17th International Conference on Sustainable Energy Technologies

21st to 23rd August 2018, Wuhan, China

Sustainable Energy
Technologies for
Eco Cities and Environment

Conference Proceedings Volume 3

Proceedings of the
17th International Conference on
Sustainable Energy Technologies – SET 2018
21st to 23rd August 2018, Wuhan China

Sustainable Energy Technologies for Eco Cities and Environment

Volume 3

Edited by

Professor Saffa Riffat, Dr Yuehong Su,
Professor Defu Liu and Professor Yingjiang Zhang

SET 2018 Admin Support
Department of Architecture and the Built Environment
Faculty of Engineering, University of Nottingham

Supported by the Conference Organising Committee:

Chair: Professor Saffa Riffat
Professor Liu Defu
Professor Zhang Yingjiang
Dustin Chen
Amy Long
Zeny Amante-Roberts
Dr Yuehong Su

Reference to a conference paper:

To cite a paper published in these conference proceedings, please substitute the highlighted sections of the reference below with the details of the article you are referring to:

Author(s) Surname, Author(s) Initial(s), 2018. 'Title of paper'. In: Riffat, Su, Liu & Zhang. ed., **Sustainable Energy Technologies for Eco Cities and Environment**: Proceedings of the 17th International Conference on Sustainable Energy Technologies, 21-23 August 2018, Wuhan, China. University of Nottingham: Buildings, Energy & Environment Research Group. Volume X, pp XX-XX. Available from: nottingham-repository.worktribe.com/ [Last access date].

ISBN-13 9780853583271

Version: 26.02.2019

Foreward

The 17th International Conference on Sustainable Energy Technologies was a significant international academic conference in the domain of world sustainable energy technologies with a theme of *Sustainable Energy Technologies for Eco Cities and Environment*. The conference aimed to provide a forum for the exchange of latest technical information, the dissemination of up-to-date research results, and the presentation of major issues that may shape future directions of human society, such as sustainable energy technology research, its application and energy security.

Held from August 21st to August 23rd, 2018, in Wuhan, China, the conference was a collaboration between the World Society of Sustainable Energy Technologies (WSSET) and the Hubei University of Technology. World-renowned experts and scholars in the area, representatives of prominent enterprises and universities attended to discuss new developments and achievements in the field, as well as promoting academic exchange, application of scientific results, university-industry collaboration and government-industry collaboration.

The papers contained in these proceedings focus on topics such as Energy Storage for the Age of Renewables; Research, Innovation and Commercialisation in Sustainable Energy Technologies; Integrating Planning & Policy, Architecture, Engineering & Economics; Energy and Environment; Engineering Thermo-physics; and Systemic Change for Cities.

Over 300 delegates from 27 countries attended SET2018; over 400 abstracts were received and 251 papers have been published in the conference proceedings. The proceedings have therefore been divided into four volumes. I hope you enjoy as much as I did the breadth of work you will find in this book.

We would like to thank all participating authors for their contributions to both the conference and to the publishing of this book. We are also indebted to our international scientific committee for their advice and seemingly endless review of papers. We would also like to thank unreservedly Celia Berry, Zeny Armante-Roberts, Amy Long, Dustin Chen for their tireless efforts in making SET2018 one of the most successful conferences we have held. Also a huge thanks to our sponsors PCM Products Ltd., Solar Ready Ltd., Positive Homes, Hubei Provincial Department of Education, Oxford University Press and MDPI.

Professor Saffa Riffat
Chair in Sustainable Energy Technologies
President of the World Society of Sustainable Energy Technologies
SET 2018 Chairman

CONTENTS

Paper Reference # **List of Papers** **Page Number**

201: Research on region segmentation algorithm oriented to solar cell surface image

Min LIU[1], Weiwei SONG[2], Juan WANG*[3], Peng WANG, Wei XIONG, Chunyan ZENG

1 Hubei Key Laboratory for High-efficiency Utilization of Solar Energy and Operation Control of Energy Storage System, Hubei University of Technology, Wuhan, 430068, P. R. China,463467853@qq.com
2 Hubei Key Laboratory for High-efficiency Utilization of Solar Energy and Operation Control of Energy Storage System, Hubei University of Technology, Wuhan, 430068, P. R. China,353977581@qq.com
3 Hubei Key Laboratory for High-efficiency Utilization of Solar Energy and Operation Control of Energy Storage System, Hubei University of Technology, Wuhan, 430068, P. R. China, happywj@hbut.edu.cn

* *Corresponding author*

With the reducing of disposable energy and the worsening of environmental pollution，solar energy，a sustainable green energy, has gained widely concerned. Similarly, solar panels as the carrier of solar power generation has attracted much attention. The quality of solar cells is an important factor affecting the efficiency of power generation, and an indispensable part of the power generation process. The segmentation algorithm for solar cell surface image segmentation has high segmentation complexity and the number of targets that needs to be manually intervened and the accuracy of semantic expression that is inaccurate. Concerning these three issues, This document of this project is to explore an image segmentation algorithm, which has the ability to learn autonomously , has high boundary fit, and the low computational complexity.The main research contents are as follows: Firstly, aiming at problem of manual intervention in superpixel segmentation, the multi-task circular convolutional neural network (Multi-mask RCNN) is proposed to train and learn the sample data with weak annotation information to achieve accurate and fast segmentation. Secondly, for low boundary fit for segmentation, it is proposed to add texture information as optimisation information to the evaluation function to guide the segmentation and ensure the integrity of edge segmentation. Finally, to solve high computing complexity, the segmented region is considered as the vertex of the graph of spectral clustering, and spectral clustering algorithm is applied to cluster the regions with similar features and semantic relatedness to achieve the accurate segmentation of the surface images of the solar panels.

Keywords: Learn autonomously, High degree of boundary fitting, Multi-mask RCNN, Spectral clustering algorithm, Semantic correlation

1. INTRODUCTION

With the gradual depletion of fossil energy, the increasing demand for clean energy at home and abroad, as well as the increase in government subsidies for clean energy, have led to a rapid increase in the demand for photovoltaic modules. As a clean energy source, solar energy has developed rapidly, and the production of silicon solar cells has also increased rapidly.In the process of solar cell production, there will inevitably be some minor defects on its surface, which will seriously affect the efficiency and service life of solar cell generation.Therefore, it is necessary to detect the defects on the surface of solar cells and remove the defective ones.

Tsai (2011) proposed to combine gradient feature with mean drift algorithm. The method firstly performs edge detection on the image. In the defect-free area of solar cells, the direction of the edge is more consistent, while the direction of the defect area is more diversified. Therefore, the gradient direction entropy is calculated in each neighbourhood window to convert the grayscale image into the entropy image. Subsequently, the entropy image is subjected to mean shift smoothing processing, and strives to suppress noise while maintaining the edge. Finally, the filtered entropy image is adaptively threshold to obtain the final test result. This method can accurately detect crack defects and corner defects, but can't accurately detect broken gate defects.

Demant (2017) proposed a surface defect detection method for solar cells based on support vector machine (SVM). In the training mode, the method acquires a set of samples marked with cracks and non-crack in advance, then, a set of local descriptors is used to extract the features, and the obtained feature vectors are used to represent the samples, and the feature vectors are sent to the SVM for training. Among them, the crack widths in the crack samples are different, which makes the sample set more representative.In the online detection, the same local descriptor is used to obtain the feature vector of the input image, and then sent to the SVM to determine whether there is a crack. Applying this method to detect low-pixel images can obtain better detection results, and the detection speed is faster. However, in practical applications, since the micro-defects can only be revealed under a high-precision camera, the pictures to be detected are generally in the order of megapixels, this is a great challenge for SVM network training.

The existing graph-based superpixel segmentation and gradient-based superpixel segmentation are used to find the optimal path or seam through the mesh to decompose the image into smaller vertical or horizontal regions. This is a method of image cutting using the best path, but one of the drawbacks of this method is the need for manual intervention, which strongly affects the speed of the output.

Based on the defects and shortcomings of the above detection methods, it is proposed to use the multi-task circular convolutional neural network to train the sample data with weak annotation information on the surface of the solar cell to realize the fast and accurate defect detection method.The method can not only detect general defects from low-pixel images and classify the defects, but also can quickly process high-pixel images and perform fine defect detection.

2. TYPES OF SURFACE DEFECTS ON SOLAR CELLS

According to the characteristics of solar cell surface defects and the design of detection algorithm, this paper divides the surface defects into three types: broken gate, shape defects and cracks. The specific form of common defects is shown in figure 1.

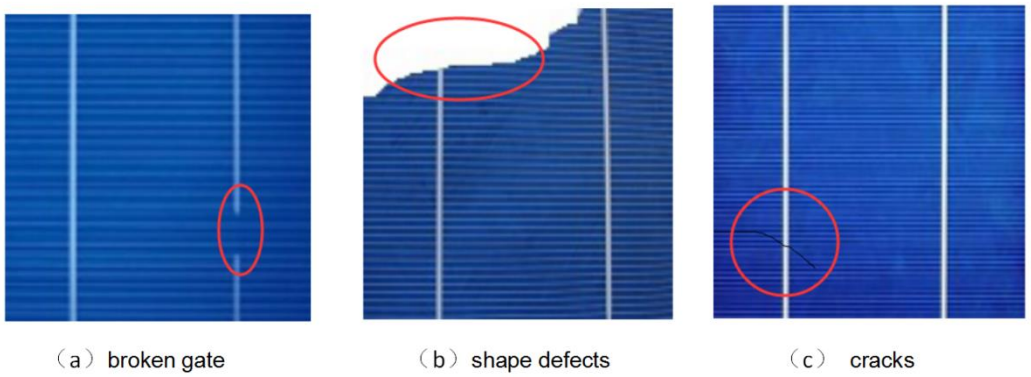

Figure 1: Common Solar Cell Surface Defects

3. SOLAR CELL SURFACE SEGMENTATION METHOD BASED ON CONVOLUTIONAL NEURAL NETWORK

The general flow of the solar cell surface segmentation method based on convolutional neural network can be summarized as follows: Imaging the surface of the solar cell, obtaining the image data of the surface of the battery, and then using various machine vision methods to detect the defect area of the image.

First, a low-pixel picture of a solar cell is obtained by a low-precision camera, and it is judged whether the picture contains a shape defect or a crack defect; then the high-pixel picture of the solar cell is obtained by a high-precision camera, and it is detected whether the picture contains broken gate defects.In this paper, the area of the solar cell chip in the digital image is defined as the target area, the grid line is defined as the target foreground, and the blue area is defined as the target background. The process of solar cell surface quality detection algorithm based on machine vision is shown in Figure 2.

The convolutional neural network overall architecture used in this paper contains a total of 28 convolutional layers, including 5 Max Pooling layers, 3 Regularization layers, 4 Upsampling layers and 1 Softmax layer. In addition to the convolutional layer before the Regularization layer, each convolutional layer is followed by the Batch Normalization layer and the PReLU activation function. After the first Regularization layer is fused with the Max Pooling layer branch, a PReLU layer is immediately followed, while the other Regularization layers are also followed by a PReLU layer.In addition, in addition to the ordinary convolutional layer, the 28 convolutional layers contain several special convolution layers, namely, deconvolution layer layer, sparse convolution layer, and full convolution layer.

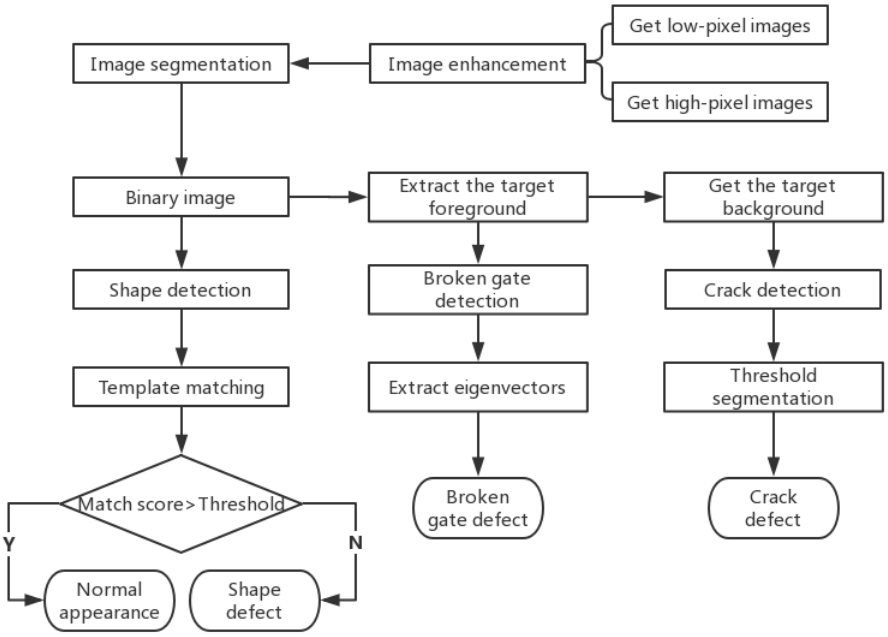

Figure 2: Solar cell defect detection process

Be universally known, the size of the receptive field is crucial in the convolutional neural network, and the large receptive field can contain more contextua information. For image semantic segmentation, the more context information is acquired, the more likely it is to successfully identify the semantic category to which the current pixel belongs. Sparse convolution expands the receptive field successfully without increasing the parameters of the convolution kernel. Sparse convolution can be defined as:

Equation 1: Sparse Convolution Formula.

$$(k *_l f)_t = \sum_{\gamma=-\infty}^{\infty} k_\gamma f_{t-l\gamma}$$

Where:

- k =the convolution kernel
- l = the sparse coefficient
- f =the sparse signal

It can be seen that the difference from the traditional convolution is that the last child is changed from f_{t-y} to f_{t-ly} , so that each convolution kernel is only in contact with the element of the multiple of l in f .

Before the training starts, the algorithm generally needs to do normalization on the input data. The specific formula is as follows:

Equation 2: Normalized formula

$$\hat{x}^{(k)} = \frac{x^{(k)} - E[x^{(k)}]}{\sqrt{Var[x^{(k)}]}}$$

Where:

- (k) =the dimensions

This is a simple normalization. In order to avoid destroying the original distribution of the learned data, reconstruct the above formula transformation:

Equation 3: Normalized formula

$$y^{(k)} = \gamma^{(k)}\hat{x}^{(k)} + \beta^{(k)}$$

Where:

- γ , β =the learning parameters

With the mini-batch batch normalized forward propagation process is as follows:

Input: a batch of input values $x:\mathrm{B} = \{x_{1...m}\}$, parameters to be learned γ , β ,

Output: $\{y_i = BN_{\gamma,\beta}(x_i)\}$.

process:

Equation 4: Calculate the batch average

$$\mu B = \frac{1}{\mathrm{m}}\sum_{i=1}^{\mathrm{m}} x_i$$

Equation 5: Calculate the batch variance

$$\sigma_B{}^2 = \frac{1}{m}\sum_{i=1}^{m}(x_i - \mu B)^2$$

Where:

- σ_B^2 =the variance

Equation 6: Normalized formula

$$\hat{x}_i = \frac{x_i - \mu B}{\sqrt{\sigma_B^2 + \varepsilon}}$$

Equation 7: Transform reconstruction formula

$$y_i = \gamma\hat{x}_i + \beta \equiv \mathrm{BN}_{\gamma,\beta}(x_i)$$

In order to enhance the nonlinear capability of the network, a nonlinear activation function must be introduced in the neural network:

Equation 8: ReLU function

$$\mathrm{ReLU} = \max(0, x)$$

Since ReLU is directly takes 0 in the negative direction, it will actually lose some information, and then there is an improved version of ReLU, mainly adding a minimum parameter α that can be learned in the negative direction, the specific formula as follows:

Equation 9: PReLU function

$$\mathrm{PReLU} = \max(\alpha x, x)$$

Where:

- α =the learning parameters

Usually α is less than 0.1, Figure 3 shows ReLU and PReLU curves.

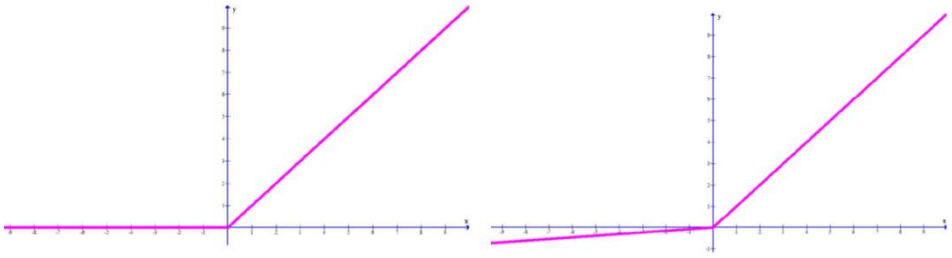

Figure 3: ReLU curve and PReLU curve

In order to solve the problem that neural network training needs to label a large amount of data, and network optimisation is difficult and the convergence speed is slow, this paper adopts the method of transfer learning to train the neural network:

1) Pre-training is performed on the collected solar cell data sets, and an initial model is obtained by initial training of the designed convolutional network.

2) In the simulation data set, the network parameters are initialized with the initial model trained in the first step, and then retrained to obtain the initial segmentation model for the solar cell surface.

3) On the manually collected and labeled solar cell dataset, using the segmentation model obtained in the second step to initialize the network weights and perform final training to obtain the high-precision model. The transfer learning method can effectively improve the accuracy of the model and improve the training speed of the model in the case of limited training samples.

4. DETECTION METHOD BASED ON CLUSTERING

The core idea of this method is to distinguish between defective areas and non-defective areas by clustering algorithms, then obtaining a binary image including only the defect area by threshold division algorithm. The following is an overview of some of the representative work in such methods. Firstly, performing smooth preconditioning the image with Gaussian filter. Secondly, edge positioning and image segmentation were performed on the image to separate a single battery block. Then, the image is segmented by the Maximum Between-Class Variance method (Otus Method), and the image is divided into a foreground part containing defects and a background part without defects. Finally, Linear detecting the segmented binary image with the Hough transform, comparing the result image with the original image that performed smooth preconditioning to get the defect.

This paper presents a new clustering algorithm for the detection of solar cell surface defects. The method uses the segmented area as the vertices of the image in the spectral clustering, and the spectral clustering algorithm is used to cluster ensemble the features similar and semantically relevant area. In the clustering stage, binary tree clustering algorithm is used to cluster the samples. Specifically, a consistency metric based on principal component analysis is proposed to evaluate each cluster. If the metric score of some cluster is the lowest, the fuzzy C-means (FCM) algorithm is adopted to split the cluster into two new clusters. Calculate the distance between each cluster center in the input data to determine whether the input data contains defects.

Let $\mathrm{B}=\{B_c, c=1,2,...,C\}$ be a sampled cluster set, and let $B_c=\{x_{c,1}, x_{c,2},..., x_{c,n_c}\}$ be a cluster C containing n_c members. In order to detect the surface defects of the solar cell, it is necessary to set the distance threshold of the cluster.Since the surface defects of each solar cell are different, and the density and spacing of the clusters are different, so we need to set the distance threshold λ for each cluster. Calculate the distance $d_{c,i}$ between the edge point and the centroid of B_c and compare $d_{c,i}$ with the distance threshold λ. If there is a cluster with $d_{c,i}$ less than λ, the test point is classified as a non-defective point. If $d_{c,i}$ is greater than the distance threshold of any cluster in B, the test point is identified as a defective point.

The method for calculating the Euclidean distance of cluster centroid o_c from point x_i to B_c is as follows :

Equation 10: Distance formula

$$d_{c,i}=\|x_i-o_c\|, \qquad x_i \in B_c$$

Where:

- o_c = the cluster centroid

The distance threshold of the cluster B_c is adaptively defined by the control limit:

Equation 11: Distance threshold formula

$$\lambda = \alpha \cdot s_c + m_c, \qquad c = 1,2,...,C$$

Where:

- λ = the distance threshold
- α =the control constant
- s_c =the standard deviation of centroid distance
- m_c =the mean of centroid distance

The distance from the test sample x' to the centroid of cluster C is:

Equation 12: Centroid distance formula

$$d_c = \left\| x' - o_c \right\|, \qquad \forall c = 1,2,...,C$$

If the distance d_c is larger than the threshold λ, the edge point x' of the tested sample is marked as 1, otherwise it is 0, that is:

Equation 13: Judgment formula

$$d_c(x') = \begin{cases} 1, & \text{if} \quad d_c(x') > \lambda \\ 0, & \text{otherwise} \end{cases}$$

If the distance is greater than the threshold of each cluster in B, identify x' as the defect point,that is:

Equation 14: Judgment formula

$$\prod_{c=1}^{C} d_c(x') = 1$$

5. IMPLEMENTATION OF IMAGE AREA SEGMENTATION

The defect detection system runs on the MATLAB platform. Before defect automatic inspection, each solar cell should be tested by experienced workers, and the artificial test results as the correct result for system verification.

In an effort to verify the correctness of the algorithm in this paper, a batch of 600 pixels with a high scrap rate of 120×120 solar cell images, which contains shape defects、broken gate and cracks defects each of 200 images . The test results of shape, broken gate and crack defects are shown in Table 1.

Table 1: appearance, broken grid and crack detection results

Type of defect	shape defect	Broken grid	Crack defect
Number of defects	200	200	200
Correctly identify the quantity	200	197	195
Correct recognition rate	100.0%	98.5%	97.5%

We conducted network training on the algorithm of this paper and the other three algorithms (mean drift algorithm, SVM and superpixel algorithm), and selected 6000 high-resolution images (2000 only contain broken gate defects, 2000 only contains shape defects, and 2000 contains only crack defects) as training samples. So as to test the recognition effect of the four algorithms, 600 different defect samples were selected as test sets and input into the designed algorithm for testing. Finally, 600 samples in the test set were input into the designed two types of algorithms for testing. The comparison results are shown in Table 2.

Table 2: The algorithm is compared with the other three algorithms

Type of defect / Experimental result	algorithm of this paper			superpixel algorithm			mean drift algorithm			SVM		
	shape defect	broken gate	crack defect	shape defect	broken gate	crack defect	shape defect	broken gate	crack defect	shape defect	broken gate	crack defect
recognition rate	100.0%	98.5%	97.5%	99.0%	93.0%	97.5%	100.0%	62.0%	99.0%	90.0%	92.5%	87.5%
calculation time/s	0.075	0.092	0.082	0.083	0.124	0.114	0.079	0.203	0.086	0.311	0.530	0.362

6. CONCLUSION

From the experiment of detecting the surface defects of solar cells, it is known that the mean shift algorithm proposed by Tsai (2011) can accurately and quickly detect crack defects and shape defects, but can't accurately detect broken gate defects.And as the experimental data is high pixel images, it brings great challenges to SVM network training.In the case of shape defect detection, broken gate detection and crack defect detection for high-pixel images, the method of this paper has high accuracy and has faster calculation speed. This paper proposes a fusion based on convolutional neural networks and clustering of the solar cell surface segmentation algorithm, it can be implemented in the manufacturing process of solar cells in common surface defect detection and reduce the related labor costs, increase the reliability of the detection and speed.The system relies on the above detection algorithm flow not only to accurately identify general defects and classify the defects, but to detect fine defects such as broken gates.

For making the system more widely used in factories, on the basis of research on the surface defect detection of solar cells, the electroluminescence image recognition of solar cells should be further studied to identify the Internal defects of the cells such as cracks and black hearts, and the internal defect detection function is added to the system to continuously improve the function of the system.

7. ACKNOWLEDGEMENTS

This work was supported in part by National Natural Science Foundation of China (61471162, 61501178, 61571182, 11605051, 41601399, 61601177); Program of International science and technology cooperation (2015DFA10940); Science and technology support program (R & D) project of Hubei Province (2015BAA115); PhD Research Startup Foundation of Hubei University of Technology (BSQD2015023,BSQD13029, BSQD13032, BSQD14028, BSQD14033); Open Foundation of Hubei Collaborative Innovation Center for High-Efficiency Utilization of Solar Energy (HBSKFZD2015005, HBSKFTD2016002);Key projects of Hubei Key Laboratory for High-efficiency Utilization of Solar Energy and Operation Control of Energy Storage System（HBSEES201701）.

8. REFERENCES

Tsai, D. M., & Luo, J. Y. (2011). Mean shift-based defect detection in multicrystalline solar wafer surfaces. IEEE Transactions on Industrial Informatics, 7(1), 125-135.

Demant, M., Welschehold, T., Oswald, M., Bartsch, S., Brox, T., & Schoenfelder, S., et al. (2017). Microcracks in silicon wafers i: inline detection and implications of crack morphology on wafer strength. IEEE Journal of Photovoltaics, 6(1), 126-135.

Chen,L.C., Papandreou,G., Kokkinos,I.,Murphy, K., & Yuille, A. L. (2015). Semantic Image Segmentation with Deep Convolutional Nets and Fully Connected CRFs. ICLR.

Shelhamer,E.,Long,J.,& Darrell, T. (2017). Fully convolutional networks for semantic segmentation. IEEE Transactions on Pattern Analysis & Machine Intelligence, 39(4), 640-651.

Zhang, L., Li, H., Shen, P., Zhu, G., Song, J., & Shah, S. A. A., et al. (2018). Improving semantic image segmentation with a probabilistic superpixel-based dense conditional random field. IEEE Access, PP(99), 1-1.

202: Research on surface image enhancement algorithms of solar cell by combining depth information

Juan WANG[1], Cong ZHOU[2], Min LIU*[3], Li ZHU[4], Cong LIU[5], Zhao ZHANG[6]

[1] *Hubei Key Laboratory for High-efficiency Utilization of Solar Energy and Operation Control of Energy Storage System, Hubei University of Technology, Wuhan, 430068, P. R. China ,happywj@hbut.edu.cn*
[2] *Hubei Key Laboratory for High-efficiency Utilization of Solar Energy and Operation Control of Energy Storage System, Hubei University of Technology, Wuhan, 430068, P. R. China,940060441@qq.com*
[3] *Hubei Key Laboratory for High-efficiency Utilization of Solar Energy and Operation Control of Energy Storage System, Hubei University of Technology, Wuhan, 430068, P. R. China,463467853@qq.com*
[4] *Hubei Key Laboratory for High-efficiency Utilization of Solar Energy and Operation Control of Energy Storage System, Hubei University of Technology, Wuhan, 430068, P. R. China, 810745390@qq.com*
[5] *Hubei Key Laboratory for High-efficiency Utilization of Solar Energy and Operation Control of Energy Storage System, Hubei University of Technology, Wuhan, 430068, P. R. China,106907393@qq.com*
[6] *Hubei Key Laboratory for High-efficiency Utilization of Solar Energy and Operation Control of Energy Storage System, Hubei University of Technology, Wuhan, 430068, P. R. China,717126483@qq.com*
* *corresponding author*

With the sustainable growth in energy demand and the escalation of energy issues, new energy resources such as solar energy, wind energy and others are rapidly developing. Solar energy, a kind of clean and environment-friendly energy,has got development for years.As a carrier of solar energy,the quality of solar cell affects the life of its module,as well as the stability and the power generation efficiency,they also affect the market competitiveness among the solar cell manufacturers.Therefore, the detection of solar cell surface has become the focus of many researches, because of its ability to measure the quality of solar cells.Current detection of solar cell surface indicates that the surface target image is weak,blurred and has low contrast. At the same time， there are problems such as the real-time performance and complexity of the algorithm are not compatible, and over-enhanced contrast exists in existing enhancement algorithms. In this issues,we intend to combine depth image information and use multi-scale Convolutional Neural Networks to locate and detect the surface target image of solar cells,there are three main contents included in this process.Firstly, the automated bias supervised learning method for automatically labeling target samples during data pre-training process is researched.Secondly, the sparse representation of image data model based on depth information is studied.Finally, the effect on the precise detection of small targets based on multi-scale convolution mechanism, combining related solutions to achieve overall optimisation of system performance is discussed. The experimental results demonstrate that the method can effectively improve the contrast of the solar cell surface, avoid the excessive contrast enhancement, and provide strong support for rapid and efficient target detection.

Keywords: multi-scale Convolutional Neural Networks, solar cell, image location, image detection

1. INTRODUCTION

Image enhancement is the basis of image processing. Applications such as object recognition and image retrieval require clear digital images as input. However, the digital image is contaminated by noise in the process of collection and storage, so image denoising is a very important issue. After years of research, the current image denoising algorithm has been able to achieve well performance while the noise intensity is weak. But, in high-noise environment, due to the low signal-to-noise ratio and insufficient information available within the image, the performance of these algorithms will rapidly decline.

The type of image noise are determined by the specific pollution process. Two common noise models are: additive and multiplicative.

There are many methods for image denoising, which have explored the characteristics of images from various aspects with effective algorithms. Denoising algorithms can be divided into three categories (Zhao, 2013):

The first type of denoising algorithm focuses on local smoothing of noise images (Paik, 1992), and strives to preserve image details as much as possible on noise removal. The most basic average filtering and median filtering in signal processing belong to this category. Among many updated algorithms, bilinear filtering, Gaussian filtering and other methods have been adopted and optimised in combination with the edge information of images. The advantage of this algorithm is that it is fast, easy to implement and understand, but the denoising effect tends to be less prominent (Han, 2004).

The second type of denoising algorithm focuses on taking advantage of features that are different in one image, such as Non-Loca (Maas, 2013), BM3D, etc. This algorithm considers the process of denoising from the perspective of the entire map, and makes full use of local smoothness, global self-similarity, etc., which has achieved good results.

The third type of denoising algorithm focuses on using the statistical properties of natural images to denoise. One of the classic ways is frequency domain filtering: frequency-domain filtering is based on the assumption that the high-frequency part of the image in the frequency domain is more likely to be noise, and the low-frequency part is more likely to be effective information, than separating noise and effective information by transforming space (Lee, 2011; Krizhevsky, 2012).

Based on the neural networks, this paper discusses the setting of the network parameters and the training techniques in combination with the characteristics of image denoising. And proposed to use linear rectification function instead of sigmoid function as neural network hidden layer activation function to further enhance the ability of neural network to solve the denoising problem.

2. NEURAL NETWORKS

Due to the randomness of the noise adding process and the lack of prior knowledge of natural images, it is difficult to find an ideal analytical method for the denoising problem. Neural networks are a good model for this highly complex multidimensional regression problem. Through the hierarchical combination of nonlinear characteristics, neural networks have a strong ability to fit various functions, and other documents have proved that each bounded continuous function can with a two-layer neural network approached with any small error, any function can be approximated with arbitrary precision using a three-layer neural network. It can be said that as long as the problem can be expressed in the form of a function, theoretically it can be considered to use the neural network as a tool for learning. Neural networks are a powerful tool for image denoising.

A neural network is essentially a nonlinear function that maps a vectorized input through several hidden layers to a vectorized output. The basic unit of a neural network is a neuron. An example of a neuron with three input parameters is shown in Figure 1. This neuron takes three input parameters x1, x2, x3 and intercept “+1” as input values, the output values is Equation 1:

Equation 1: Output values.

$$h_{w,b}(x) = f\left(W^T x\right) = f\left(\sum_{i=1}^{3} W_i x_i + b\right)$$

Where:

W = the parameter of this neuron
b= the parameter of this neuron
f= the activation function

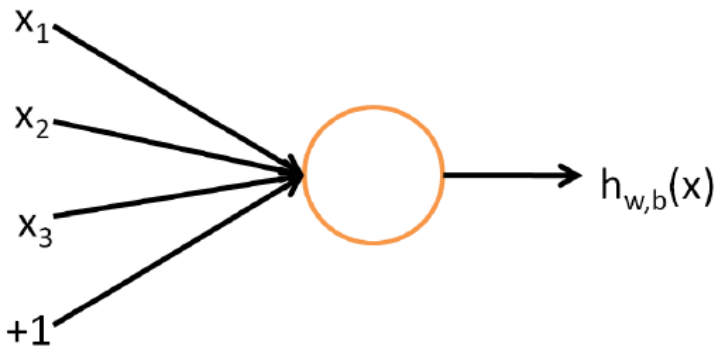

Figure 1: A neuron with three input parameters

A neural network is a combination of multiple single neurons, and the input of some neurons is called the output of other neurons to form a network. A simple example is shown in Figure 2. The circles are used here to represent the input of the neural network, and the circles marked "+1" are called Bias units. The leftmost layer of the network is called the input layer, the rightmost layer is called the output layer, and the middle layer is called the hidden layer.

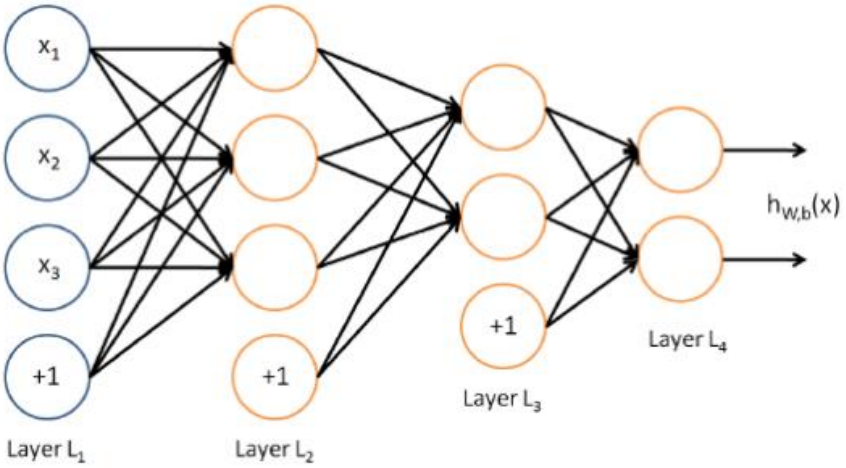

Figure 2: A simple neural network

By Equation 2, given the neural network input, we can calculate the output of the neural network layer by layer. This process is called forward propagation.

Neural network is a very complicated machine learning model. Usually we cannot obtain the analytical solution of each parameter of the neural network. For optimisation problems where an analytical solution cannot be obtained, the solution is usually performed by gradient descent. Specifically, for a single sample (x,y), the cost function is Equation 2:

Equation 2: Cost function.

$$J(W,b;x,y)=\frac{1}{2}\left\|h_{W,b}(x)-y\right\|^2$$

Where:

J = the cost function

For a data set containing m samples, the overall cost function J(W,b) can be defined as Equation 3:

Equation 3: Cost function.

$$J(W,b)=\frac{1}{m}\sum_{i=1}^{m}J\left(W,b;x^{(i)},y^{(j)}\right)+\frac{\lambda}{2}\sum_{l=1}^{nl-1}\sum_{i=1}^{sl}\sum_{j=1}^{sl+1}\left(W_{ji}^{(l)}\right)^2$$

The first item in the equation is the average error of the sample in the data set, and the second item is a weight attenuation item. Its purpose is to reduce the magnitude of the weight and prevent over-fitting. The specific mechanism

is that its additional error is proportional to the sum of the powers of the two elements in the matrix. It is known from the nature of the quadratic function that under this constraint, the parameters will tend to select values with smaller absolute values as much as possible. This approach is based on the Bayesian regularization method. When the parameters have a priori Gaussian distribution, the maximum posterior estimate is used instead of the maximum likelihood estimate.

Each iteration in the gradient descent method updates W and b according to the following Equation 4:

Equation 4: updating W and b .

$$W_{ij}^{(l)} = W_i^{(l)} j - \alpha \frac{\partial}{\partial W_i^{(l)} j} J(W,b) b_i^{(l)} = b_i^{(l)} - \alpha \frac{\partial}{\partial b_i^{(l)}} J(W,b)$$

Where:

α = the learning rate

With the update rule, the key step is to calculate partial derivatives. The classical algorithm for calculating partial derivatives of neural networks is the Back Propogation algorithm.

1. Using Equation 1 for forward propagation calculation, calculate the activation value of neurons in each layer layer by layer, expressed by a_i^{nl} , where nl represents the neuron in the first layer, i represents the neuron in this layer Serial number.

2. For each output element i of the output layer (indicated by nl), calculate the residual according to the following Equation 5:

Equation 5: calculate the residual.

$$\delta_i^{nl} = \frac{\partial}{\partial z_i^{(nl)}} \frac{1}{2} \left\| h_{W,b}(x) - y \right\|^2 = -\left(y_i - a_i^{(nl)}\right) * f'\left(z_i^{(nl)}\right)$$

For each layer of $l = nl-1, nl-2, nl-3, \ldots, 2$, the residual of the i-th node of the l-th layer is as follows Equation 6:

Equation 6: calculate the residual.

$$\delta_i^l = \left(\sum_{j=1}^{gl+1} W_{ji}^{(l)} \delta_j^{(l+1)} \right) f'\left(z_i^{(nl)}\right)$$

Calculate the required partial derivatives by the Equation 7 and Equation 8:

Equation 7: calculate the derivatives.

$$\frac{\partial}{\partial W_{ij}^{(l)}} J(W,b;x,y) = a_j^{(l)} \delta_i^{(l+i)}$$

Equation 8: calculate the derivatives.

$$\frac{\partial}{\partial b_i^{(l)}} J(W,b;x,y) = \delta_i^{(l+i)}$$

by iteratively using the steps of forward propagation and reverse conduction, we can train to get the required network model.

2.1. Denoising frame

The neural network and deep learning model is very suitable for the function of learning image patch to image patch because of its powerful expression ability. The framework of denoising using neural network is shown in Figure 3. Here we distinguish between the activation function of the hidden layer and the activation function of the output layer because the selection of the activation function of the output layer depends on the needs of the problem.

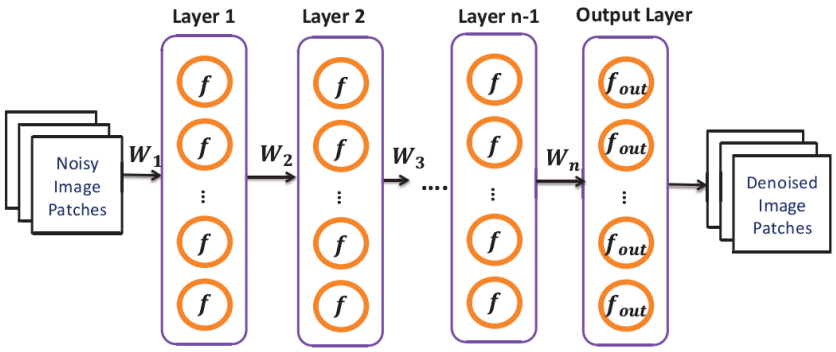

Figure 3: The framework of using neural network in denoising. f is the activation function of hidden layers and f_{out} is the activation function of the output layer.

Specifically, we first randomly select a clean picture block y from the picture data set, and then generate a corresponding noise picture block x by manually adding Gaussian white noise and the like. Then we take the vectorized noise picture block x as the input of the neural network, take the corresponding vectorized clean picture block as the output of the neural network, update the parameters of the neural network through the backward propagation, and then iterate through Gradually learn the required model.

However, the neural network itself is complex in structure and has many parameters. It also needs to consider the need for image denoising. Therefore, there are many changes and techniques.

2.2. Data preprocessing

For the denoising problem, the input noise image patch and the output denoised image patch often have different statistical characteristics, which adds a great difficulty to the problem. One possible solution is to estimate the mean variance of the output by taking the mean variance of the input and adding the standard deviation of the noise as a parameter. This kind of scheme has certain feasibility when noise is low, but when the noise becomes stronger, both the accuracy of the image denoising estimation and the denoising effect of the final model gradually become unsatisfactory: in the high noise environment, Because the range of gray values of the image pixels is defined, even the average value of the image patch changes, and the variance is more difficult to estimate.

Therefore, we choose to avoid this problem by simply mapping the pixel's gray value linearly from the interval [0, 1] to [−0.8, 0.8] and using the hyperbolic tangent function (tanh) as the activation function of the output layer. Ensure that the average of the input picture block is statistically close to zero.

2.3. Network weight initialization

The initial value of the neural network weight matrix has a significant effect on the training process and the final result. For multi-layer networks, we hope that the initial values of the network will satisfy the randomness while ensuring that the input and output of each hidden layer have the same statistical characteristics as possible. In order to achieve this, the initial value of each parameter needs to be associated with the number of nodes in the corresponding layer, and adaptive adjustment is performed according to the number of nodes in each layer. The parameters of the network initialization weight set in this work are: Layer i network parameters are uniformly distributed $\left[-4*\sqrt{\frac{6}{n_{i-1}+n_i}},4*\sqrt{\frac{6}{n_{i-1}+n_i}}\right]$, Where ni represents the number of nodes in the i-th layer.

2.4. Learning rate and inertia parameters

The setting of learning rate: A larger learning rate may make the neural network model learn faster and it may also make the neural network divergence. The work of this paper adopts an experimental approach to choose the initial learning rate: initially try 0.1, if the neural network diverges then select 0.05, then try 0.02, etc., gradually smaller initial learning rate; if the network converges but the training speed is slow, then try to learn the rate increases. In order to ensure the convergence of the neural network, the current learning rate is multiplied by 0.99 per cycle when executing the small batch processing algorithm.

Momentum: Inertia is a commonly used acceleration method in neural network training and can help the neural network to leave the flat area in the function space more quickly. The specific operation method is to additionally add a part of the last update of the weight value each time the weight matrix is updated, that is Equation 9:

Equation 9: Weight update.

$$\Delta W(t+1) = -\rho \frac{\partial E}{\partial W} + \beta \Delta W(t)$$

Where:

ρ= the current learning rate

β= the momentum, 0 ≤ β <1

2.5. Linear rectification function

Instead of using sigmoid function as the activation function of hidden layers in neural network, we propose to use the rectified linear function: $\text{rectifier}(x) = \max(0, x)$. This function is more similar to the function of the common neural activation function motivated by biological data which keeps zero when input current is below some threshold and gradually increases when input current is beyond the threshold. This change also brings several advantages which make it more suitable for our problem.

Deep neural networks using linear rectification units can be trained directly in backward propagation without pre-training. The pre-training algorithm is proposed to solve the problem of gradient dispersion in the training process of multi-layer neural network and the lack of marked training data. The problem of lack of marked training data is basically absent in the image denoising problem because an infinite amount of generation can be performed by artificially adding noise. At the same time, for the linear rectification function, there is no gradient diffusion problem that the S-shape function needs to face, because max(x, 0) is a very simple step function.

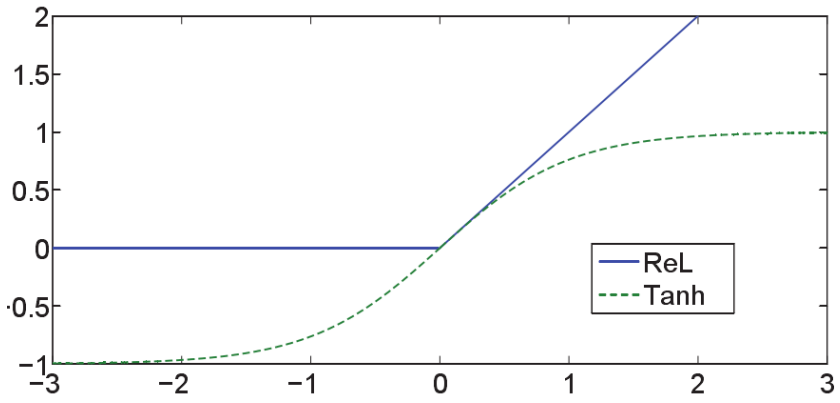

Figure 4: Rectifier linear units

In our actual training process, a multi-layer network using a linear rectification function as an activation function can be well trained even if a network parameter is randomly initialized.

2.6. Training method

In this paper, we use the small-batch training method of the gradient descent algorithm model. Each time the small-batch processing algorithm selects a fixed n sample points from the training data set, the total error of this small sample is calculated for the derivative of the weight matrix and then performed. The weights are updated and called once per cycle (Epoch). The stochastic gradient descent algorithm can be considered as a small batch processing algorithm with n = 1 and the batch processing algorithm can be seen as a small batch processing algorithm with n = N (N is the number of training data).

Compared with batch processing algorithms, small-batch processing has the advantages of faster updating of weights, online learning, fewer resources required, and randomness that can leave unoptimised local extrema points. Compared with random gradient descent, small batch processing the error curve is more stable during training and less affected by noise in the data.

3. EXPERIMENT

We used 200 solar cell images as image data sets. The resolution of these images is 120×120.Part of the image set are shown in Figure 5. Based on this data set, the experimental results obtained are shown in Figure 6.

IMG 1 *IMG 2* *IMG 3* *IMG 4*

Figure 5: Part of the picture set

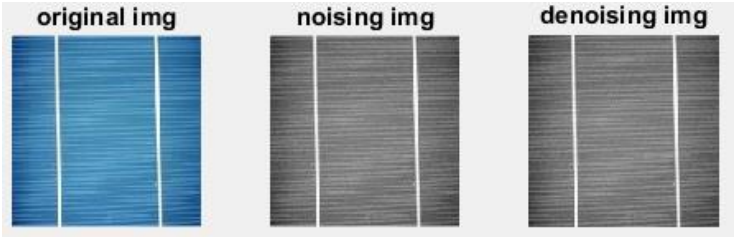

Figure 6: The result of our method

Then, we selected three scenarios of low noise (σ = 25), medium noise (σ = 50), and high noise (σ = 75) to compare our model with K-SVD algorithm and BM3D algorithm. Models of noise magnitude are trained and tested separately. The results are shown in Table 1, Table 2 and Table 3.

Table 1: Denoisng result of different methods for σ = 25 (PSNR/d B)

	σ = 25	K-SVD	BM3D	Our algorithm
IMG 1	20.55	26.33	27.50	26.91
IMG 2	21.47	28.24	29.55	29.43
IMG 3	20.72	27.03	27.83	27.59
IMG 4	21.57	29.87	31.45	33.96
IMG 5	20.22	28.82	29.58	29.17

Table 2: Denoisng result of different methods for σ = 50(PSNR/d B)

	σ = 50	K-SVD	BM3D	Our algorithm
IMG 1	15.53	21.31	23.23	23.76
IMG 2	15.74	22.69	23.69	25.42
IMG 3	15.34	22.61	23.68	24.60
IMG 4	15.25	28.32	29.87	31.02
IMG 5	14.93	24.80	26.53	26.13

Table 3: Denoisng result of different methods for σ = 75 (PSNR/d B)

	σ = 75	K-SVD	BM3D	Our algorithm
IMG 1	12.35	19.03	20.49	21.77
IMG 2	12.83	20.54	21.79	27.09
IMG 3	12.44	20.32	21.47	23.05
IMG 4	11.95	22.81	24.37	24.72
IMG 5	12.62	21.85	24.47	26.13

Finally, we put the statistical information of the peak signal-to-noise ratio of the denoised results in Table 4.

Table 4: Denoising results of different methods on test tests

Method	25/PSNR	50/PSNR	75/PSNR
K-SVD	29.10±1.64	24.61±1.57	21.33±1.47
BM3D	30.41±2.05	26.07±1.81	23.18±1.35
Our algorithm	29.95±2.01	26.79±2.03	24.83±1.80

4. CONCLUSION

In this paper, we choose neural networks with rectified linear units as hidden units in the image denoising problem. We find that by using rectified linear units can achieve better performance and faster convergence than using traditional sigmoid units. The comparison between our method and previous models indicates our model can achieve better denoising performance when additive noise is high.Next we will continue to study how to use multi-scale convolutional neural networks to achieve enhanced solar cell image contrast. So that it can be better used in solar cell surface defect detection.

5. ACKNOWLEDGEMENTS

This work was supported in part by National Natural Science Foundation of China (61471162, 61501178, 61571182, 11605051, 41601399, 61601177);

Program of International science and technology cooperation (2015DFA10940);

Science and technology support program (R&D) project of Hubei Province (2015BAA115);

PhD Research Startup Foundation of Hubei University of Technology (BSQD2015023, BSQD13029, BSQD13032, BSQD14028, BSQD14033);

Open Foundation of Hubei Collaborative Innovation Center for High-Efficiency Utilization of Solar Energy (HBSKFZD2015005, HBSKFTD2016002);

Key projects of Hubei Key Laboratory for High-efficiency Utilization of Solar Energy and Operation Control of Energy Storage System (HBSEES201701).

6. REFERENCES

Zhao, Y. (2013). Multi-level denoising and enhancement method based on wavelet transform for mine monitoring. International Journal of Mining Science and Technology, 23(1), 163-166.

Paik, J. K., & Katsaggelos, A. K. (1992). Image restoration using a modified hopfield network. Image Processing IEEE Transactions on, 1(1), 49-63.

Han, Y. (2004). Image restoration using a modified hopfield neural network of continuous state change. Signal Processing.

Maas, A. L., Hannun, A. Y., & Ng, A. Y. (2013). Rectifier Nonlinearities Improve Neural Network Acoustic Models.

Lee, H., & Hero, A. O. (2011). Efficient learning of sparse, distributed, convolutional feature representations for object recognition. International Conference on Computer Vision (Vol.24, pp.2643-2650). IEEE Computer Society.

Krizhevsky, A., Sutskever, I., & Hinton, G. E. (2012). ImageNet classification with deep convolutional neural networks. International Conference on Neural Information Processing Systems (Vol.60, pp.1097-1105). Curran Associates Inc.

Buades, A., Coll, B., & Morel, J. M. (2005). A review of image denoising algorithms, with a new one. Siam Journal on Multiscale Modeling & Simulation, 4(2), 490--530.

Burger, H. C., Schuler, C. J., & Harmeling, S. (2012). Image denoising: Can plain neural networks compete with BM3D?. IEEE Conference on Computer Vision and Pattern Recognition (Vol.157, pp.2392-2399). IEEE Computer Society.

Bengio, Y., Simard, P., & Frasconi, P. (2002). Learning long-term dependencies with gradient descent is difficult. IEEE Trans Neural Netw, 5(2), 157-166.

Estrada, F. J., Fleet, D. J., & Jepson, A. D. (2009). Stochastic Image Denoising. British Machine Vision Conference, BMVC 2009, London, UK, September 7-10, 2009. Proceedings. DBLP.

Glorot, X., Antoine, B., & Bengio, Y. (2010). Deep sparse rectifier networks. Learning/statistics & Optimisation.

Jain, V., & Seung, H. S. (2008). Natural image denoising with convolutional networks. International Conference on Neural Information Processing Systems (pp.769-776). Curran Associates Inc.

Lecun, Y., Bottou, L., Orr, G. B., & Müller, K. R. (1998). Efficient backprop. Neural Networks Tricks of the Trade, 1524(1), 9-50.

M.D. Zeiler, Ranzato, M., Monga, R., Mao, M., Yang, K., & Le, Q. V., et al. (2013). On rectified linear units for speech processing. IEEE International Conference on Acoustics, Speech and Signal Processing (Vol.32, pp.3517-3521). IEEE.

Portilla, J., Strela, V., Wainwright, M. J., & Simoncelli, E. P. (2003). Image denoising using scale mixtures of gaussians in the wavelet domain. IEEE Transactions on Image Processing, 12(11), 1338.

Pothula, A., Deepthi, C. N., & Suresh, P. (2013). A collective approach towards energy-based structure for autonomous learning. International Journal of Computer & Electronics Research, 2(3).

Rudin, L. I., Osher, S., & Fatemi, E. (1992). Nonlinear total variation based noise removal algorithms. Eleventh International Conference of the Center for Nonlinear Studies on Experimental Mathematics: Computational Issues in Nonlinear Science: Computational Issues in Nonlinear Science (Vol.60, pp.259-268). Elsevier North-Holland, Inc.

Vincent, P., Larochelle, H., Lajoie, I., Bengio, Y., & Manzagol, P. A. (2010). Stacked denoising autoencoders: learning useful representations in a deep network with a local denoising criterion. Journal of Machine Learning Research, 11(12), 3371-3408.

Xie, J., Xu, L., & Chen, E. (2012). Image denoising and inpainting with deep neural networks. International Conference on Neural Information Processing Systems (Vol.1, pp.341-349). Curran Associates Inc.

203: Cross-layer optimised high-definition video multicast in TV whitespace

Minghu WU[1], Meng LIU [2], Cong LIU*[3], Hanhui YUE[4], Sida XU[4], Zhao ZHANG[4]

[1] Hubei Key Laboratory for High-efficiency Utilization of Solar Energy and Operation Control of Energy Storage System, Hubei University of Technology, Wuhan, 430068, P. R. China, wuxx1005@163.com
[2] Hubei Key Laboratory for High-efficiency Utilization of Solar Energy and Operation Control of Energy Storage System, Hubei University of Technology, Wuhan, 430068, P. R. China, 137354181@qq.com
[3] Hubei Key Laboratory for High-efficiency Utilization of Solar Energy and Operation Control of Energy Storage System, Hubei University of Technology, Wuhan, 430068, P. R. China, 106907393@qq.com
[4] Hubei Key Laboratory for High-efficiency Utilization of Solar Energy and Operation Control of Energy Storage System, Hubei University of Technology, Wuhan, 430068, P. R. China
** Correspnding author*

Wireless video multicast is a newly arising technique for video transmission. This type of transmission technology requires a large amount of spectrum resources to transmit data. Using TV whitespace for video multicast can not only solve the problem of wireless video multicast, but also can effectively increase the spectrum utilization of TV whitespace. For the purpose of the overall received video quality, this paper presents a study of optimised real-time video multicast in TV Whitespace. Firstly, we suggest a practical and bandwidth efficient TV Whitespace video multicast framework. Under the framework, we model the TV Whitespace video multicast as a cross-layer optimisation problem, which a quasi-static spectrum access scheme based on TV whitespace is proposed to solve the problem of excessive time delay caused by frequent spectrum switching. Furthermore, considering various cross-layer design factors, adaptive modulation coding (AMC) is used in the PHY layer to improve transmission efficiency. In order to adjust the video rate equivalent to the channel conditions, scalable video coding (SVC) is exploited in our framework. Moreover, this article focuses on the issue of optimal resource scheduling, which introduce an innovative cross-layer optimised subcarrier scheduling mechanism for the TV whitespace video multicast system. The optimal scheduling problem is generalized by the scheme into a mixed integer nonlinear programming problem (MINLP), which meets the unique constraint, layer integrity constraints, limited allocation principle as well as the lower minimum rate limiting and other related real video transmission constraint. In addition, the heuristic algorithm of Binary Particle Swarm Optimisation (BPSO) is proposed by us to obtain the suboptimal solution of the optimal subcarrier scheduling problem. Finally, the effectiveness and superiority of this scheme are proved by our simulations.

Keywords: TV Whitespace, Video multicast, Cross-layer optimisation, scalable video coding

1. INTRODUCTION

Wireless network-based multicast technology is one of the research hotspots in the field of wireless networks. Multicast technology is favored by various research institutions or organizations around the world because it can greatly reduce the bandwidth consumption in data transmission and improve the efficiency of spectrum utilization. Currently, each wireless organization has released its own multicast standard, which compares the typical LTE MBMS and e-MBMS standards, the WiMAX MBS standard, and the European Telecommunications Standards Institute's (ETSI) DVB-H/DVB-T standard, and MediaFLO standards introduced by Qualcomm. In addition, the popularity of smart phone users is increasing because of the rapid development of mobile communication technologies. The portability of the mobile phone makes the mobile TV service show a wider influence than the ordinary TV. However, the frequency band allocated to mobile operators is generally high, causing excessive signal attenuation, which is not conducive to long-distance transmission. And mobile operators have to arrange multicast services on extremely limited bandwidth resources because the allocated bandwidth resources are severely limited, resulting in a very poor mobile TV user experience.

With the help of cognitive radio technology, the release of mobile TV services to cognitive wireless networks with near-infinite spectrum resources can not only greatly alleviate the extremely scarce spectrum resources of operators, but also make use of the good spectrum characteristics of cognitive frequency bands (More common TV whitespace, etc.) to greatly enhance the viewing experience of mobile TV users. However, as current research on cognitive radio technology is largely focused on how to accurately sense the working state of the primary user and how to reasonably access the licensed frequency band without affecting the primary user's work. Few people pay attention to what kind of applications a cognitive radio network is suitable for and how to customize a reasonable PHY protocol and MAC protocol for these applications. Therefore, we propose a new spectrum access scheme and a novel multicast scheduling framework to solve the video multicast problem.

2. SPECTRUM ACCESS SCHEME

The use of frequency spectrum in the initial wireless communication system is based on the static spectrum allocation strategy. The wireless communication system can only strictly follow the spectrum allocation, and authorized users occupy their own frequency bands, and select the most suitable communication from these frequency bands aisle. The dynamic spectrum access technology in cognitive radio can make use of all available channels at the right place, time and suitable working mode according to the use of the spectrum, which not only greatly increases the opportunity for the cognitive users to access the spectrum, but also improves the quality of the information transmission and the utilization of the spectrum effectively. Dynamic spectrum access is a radio technology that can dynamically select the working spectrum within a certain frequency spectrum usage authority and use the spectrum opportunities that occur in a time domain, air space, and frequency domain to communicate. Dynamic spectrum access technology is proposed in response to the three main drawbacks of existing spectrum allocation strategies: fixed distribution; poor sharing; strict restrictions on how to use spectrum.

There are many existing spectrum access schemes, including a multicast framework based on cognitive radio networks proposed by DongLin Hu et al. The framework uses a spectrum access data transmission mode for drivers. In this mode, the transmission of each data packet is divided into three parts: the perceived spectrum, transmission data packets, and user feedback acknowledge (ACK) signals.

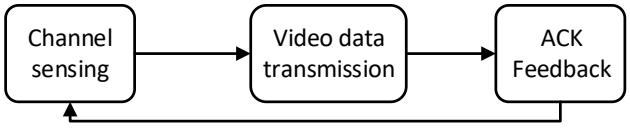

Figure 1: "opportunistic" spectrum access scheme

Because the channel reestablishment process between channel perception and data transmission will cause great delay for video transmission, the solution proposed by Hu et al. is not applicable to delay-sensitive video services. And, the spectrum access strategy used in Hu's solution can only access a single channel at a time. When there are more video programs or HD video multicast services exist, a single channel (UHF channel bandwidth value is usually 6 MHz) obviously it is not enough. To illustrate this point, the spectrum bandwidth resource requirements for different video types are listed in Table 4-1(Assume that the aspect ratio of all videos is 16:9, FPS is 30, compression is H.264/AVC standard, and the playback rate is the compressed rate). It can be seen from the table that a single UHF channel can only support at most 12 video multicasts with a resolution of 480P. The program (modulation scheme is 64-QAM), and when the modulation scheme is QPSK, a single UHF channel (6 MHz) cannot even provide bandwidth support for a 1080P video program.

Table 1: Spectrum resource requirements under different video types

Video type	Play speed	Spectrum requirements under different modulation schemes		
		QPSK	16-QAM	64-QAM
480P	356KBps	1.42MHz	0.71MHz	0.47MHz
720P	813KBps	3.24MHz	1.62MHz	1.08MHz
1080P	1829KBps	7.29MHz	3.65MHz	2.43MHz

Therefore, a quasi-static spectrum access scheme based on the TV white band is proposed by us, which solves the problem of too large time delay due to frequent spectrum switching in the Hu scheme. The CR system can access multiple consecutive available UHF channels and change its working spectrum only when one of two situations occurs. One is non-autonomous spectrum switching caused by the active user becoming active on the operating channel. The other is that when the CR base station detects a severe degradation of its current channel, it triggers spontaneous spectrum switching.

3. SYSTEM MODEL

We consider a centralized single-hop CR network collocated with several primary networks. The primary network, maybe a traditional TV broadcasting system or a wireless micro-phone system, has the priority to UHF bands. The availability of each UHF band evolves over time due to primary user transmissions. The CR network, composed by N mobile CR users (consist the CR user set N) and a CR base station, can opportunistically access these UHF bands under the premise of causing no interference to primary users. We assume the base station is equipped with S widely-tunable mnidirectional antennas, which are independent of each other and operate on different bands. Each CR user is also equipped with a single widely-tunable antenna and can communicate with the base station on any UHF bands.

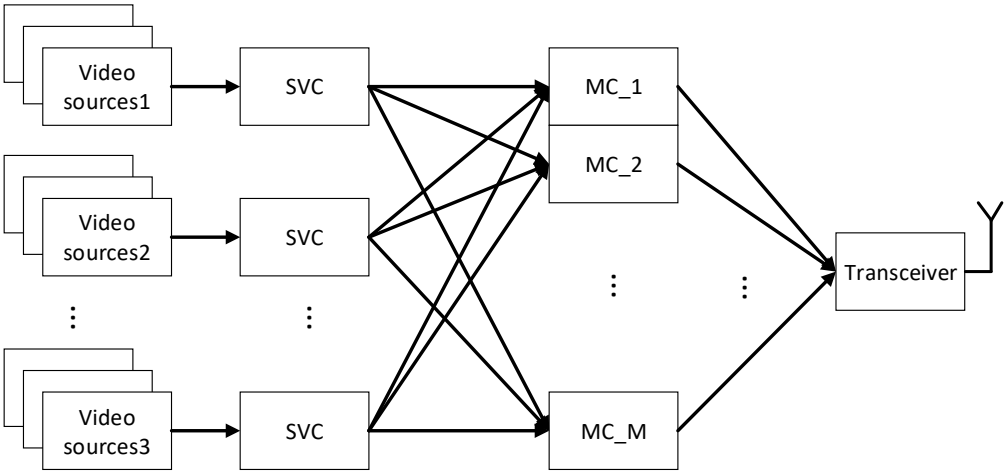

Figure 2: Scalable video multicast scheme

In order to provide the user with video quality that is consistent with the user's link quality, the base station encodes the video using SVC technology. Assume that the number of coding layers of the SVC encoder is M. After the SVC encoder, the video source is encoded into a base layer and M-1 enhancement layers. For ease of analysis, we call the video layer 1 to represent the base layer and the video layer m ($2 \le m \le M$) denotes the enhancement layer. It is also assumed that the m-th layer rate of video g is R.

The channel coding uses AMC technology and corresponds to the number of SVC encoder layers. This article considers a total of M channel coding schemes. Each coding scheme consists of a modulation scheme (Such as QPSK, QAM-16) and a forward error correction scheme (FEC) with different coding rates. In AMC, different modulation coding schemes (MCSs) have different bandwidth utilization ratio (BUR), e.g., QPSK & FEC 1/2 (code rate) has the BUR 1 (bit/s/Hz), 16-QAM & FEC 3/4 has the BUR 3. We consider N unique MCSs in this paper, and sort them according to their BUR in the increasing order, assuming the sorted list is $\{MC_1, MC_2, \ldots, MC_3\}$. Assume the entry MC_m min this list has the BUR λ_m .

In order to adjust the video rate commensurate to the channel conditions, the scalable video coding (SVC) is employed in our framework, in which each video is encoded into the base layer and the enhancement layer. The base layer can ensure basic video quality and the enhancement layer can enhances the quality of the video.

Since in SVC the base layer carries the most important data, the most reliable MC scheme should be used. Without loss of generality, we assume the base layer is always transmitted using MC_1. If a user's channel is so poor that it cannot decode the MC_1 signal, we consider it disconnected from the system. For any video g, we further divide the enhancement layer into M−1 sub-layers (for simplicity, we use the layer 1 denotes the base layer and the layer m ($m \geq 2$) denotes the sub-layer m−1). Assume the layer m in video g has rate R mg and uses MC_m.Obviously, we have $R_g = \sum_{m=1}^{M} R_g^m$ .To support the video g, at lease $BW_g = \sum_{m=1}^{M} (R_g^m / \lambda_m)$ bandwidth is needed.

4. CROSS-LAYER OPTIMISED SUBCARRIERS CHEDULING FOR VIDEO MULTICAST IN TV W HITESPACE

To further improve the overall received video quality, we introduce a cross-layer optimised subcarrier scheduling mechanism for the TV whitespace video multicast system. The subcarrier scheduling should be implemented when new spectrum sensing data arrived. In this section, we mainly answered two key problems. First, what is the optimal subcarrier scheduling? And second, how is the optimal subcarrier scheduling achieved?

4.1. Preliminaries for the optimised subcarrier scheduling

Assume that the final acquired frequency band is F and the span is WF. The system uses OFDM modulation to access the acquired frequency band. Each subcarrier has a bandwidth of Δf . The system has a total of $K = \ell BW / \Delta f$ subcarriers. Here, Where ℓ represents the OFDM frequency reuse factor. Let $k = 1, ..., K$ be the sequence number of each subcarrier, and the signal-to-noise ratio of user i on subcarrier k is $\gamma_{i,k}$. Given that a total of M different MCS schemes are assumed at the physical layer, a fixed bit error rate (BER) threshold is given. The user's signal-to-noise can be divided into M+1 different levels, defined as $\gamma_1, \gamma_2, ..., \gamma_{M+1}$. Here γ_m is calculated as:

Equation 1: The signal-to-noise of user

$$\gamma_m = \frac{2^{m-1} \ln 5 P_{ber}}{-1.5}, m = 1, ..., M+1$$

Where:

- γ_m = the signal-to-noise of user
- $\mathrm{p}_{\mathrm{ber}}$ =Bit Error Ratio

Thus, for each multicast group g, we can get the set of users on its subcarrier k that can correctly receive the video layer m, as follows:

Equation 2: A collection of users who have correctly received the video layer m

$$L_{g,m,k} = \{i \mid i \in N_g, \Upsilon_m < \gamma_{i,k} < \Upsilon_{m+1}\}$$

Where:

- $L_{g,m,k}$ = A collection of users who have correctly received the video layer m
- N_g = Each multicast group contains a collection of users

In the SVC decoding process, the high video layer needs the support of the low video layer, and the video transmission rate is decomposed into M levels, and the rate set of the video g is defined as $R_g = \{v_{g,1}, ..., v_{g,M}\}$.

Equation 3: Video g layer m transmission rate

$$v_{g,m} = \sum_{i=1}^{m} R_{g,i}, g = 1, ..., G$$

Where:

- $v_{g,m}$ = video g layer m transmission rate
- $R_{g,i}$ = the transmission rate of the video g layer m to user i

4.2. Optimal resource scheduling

In the process of resource scheduling, it is our purpose to determine the optimal mapping relationship between the subcarrier sequence {1,..., K} and the various video layer {1,..., M} of each video program {1,..., G} and to determine the optimal MCS scheme for each subcarrier. Here we use the resource scheduling criteria to maximize proportional fairness, that is, to ensure that each user obtains the video quality that matches its channel conditions as much as possible. The resource scheduling criteria are formulated as follows:

Equation 4: proportional fairness

$$U=\sum_{g=1}^{G}\sum_{i\in N_g}\log(Q_{g,i})$$

Where:

- U = proportional fairness
- $Q_{g,i}$ = user i received video quality

$Q_{g,i}$ represents user $i \in N_g$ received video quality, $Q_{g,i}$ can also be written as follows:

Equation 5: user i received video quality

$$Q_{g,i} = Q_g^B + \beta_g R_{g,i}^E$$

Where:

- Q_g^B = basic layer decoded video quality of video g
- β_g = rate-quality model basic parameters
- $R_{g,i}^E$ = accumulated enhancement layer rate for video g

5. THE SOLUTION PROCEDURE FOR SSOP

The subcarrier schedule problem (SSOP) is combinatorial in nature, the best solution can be found by exhaustive search. However, it is computationally prohibitive to find the global optimum, since there are 2^{GMK}possible subcarrier allocation schemes to be considered. In this paper, we suggest a heuristic algorithm called binary particle swarm optimisation (BPSO) for getting the suboptimal solution of the SSOP.

5.1. Overview of BPSO

The PSO, suggested by Kennedy and Eberhart, is a population-based parallel search algorithm using a group of particles (assume the particle's number NP). It is based on the behaviour of individuals of a swarm and its roots are in the zoologist's modeling of the movement of individuals within a population. It has been noticed that members of a group seem to share information among them, a fact that leads to increased efficiency of the group.

In PSO, each potential solution is represented as a particle. Two properties (position and velocity) are associated with each particle. In an D-dimensional search space, the position and velocity of i-th particle are represented as $X_i = [x_{i1}, ..., x_{iD}]$, $V_i = [v_{i1}, ..., v_{iD}]$ .Where each element has real values. Let $Pbeset_i = [p_{i1}^b, ..., p_{iD}^b]$ and $Gbeset_i = [p_{i1}^b, ..., p_{iD}^b]$ be the best position (with the best fitness value) of the i-th particle and the group's best position so far, respectively. The velocity and position of each particle is updated as follows:

Equation 6: Speed after update

$$v_{id}^{t+1} = \omega v_{id}^t + c_1 r_1 (p_{id}^b - x_{id}^t) + c_2 r_2 (g_d^b + x_{id}^t)$$

Equation 7: Position after update

$$x_{id}^{t+1} = x_{id}^{t} + v_{id}^{t+1},\ i = 1,...,NP:\ d = 1,...,D.$$

Where:

- v_{id}^{t+1} = speed after update
- ω = inertia weight
- v_{id}^{t} = before the update
- x_{ic}^{t} = prior to update
- c_1 = self-learning factor
- c_2 = group learning factor
- r_1, r_2 = random number

Applying a high inertia weight at the start of the algorithm and making it decay to a low value through the BPSO execution, which make the algorithm search globally, at the beginning of the search, and search locally at the end of the execution.

Equation 8: inertia weight update

$$\omega_t = \omega_{\max} - \frac{\omega_{\max} - \omega_{\min}}{iter_{\max}}$$

Where:

- $\omega_{\max}$ = initial weight
- $\omega_{\min}$ = final weight
- $\mathrm{iter}_{\max}$ = the maximum iteration number

The structure of the BPSO is effectively the same as that of the real-valued PSO. In BPSO, however, the position vector of a particle is a binary one. The velocity of the d-th element in the i-th particle is related to the possibility that the position of the particle takes a value of 1 or 0. It is implemented by defining an intermediate variable $S(v_{id}^{t+1})$, called a sigmoid limiting transformation, as follows:

Equation 9: intermediate variable

$$S(v_{id}^{t+1}) = \frac{1}{1 + \exp(-v_{id}^{t+1})}$$

The value of $S(v_{id}^{t+1})$ can be interpreted as a probability threshold. If a random number r, selected from a uniform distribution in [0, 1], is less than the value of $S(v_{id}^{t+1})$, the position of the d-th element in the i-th particle at iteration k+1 is set to 1 and otherwise, set to 0. In BPSO, therefore, Equation 7 for modifying the position vector is replaced as follows:

Equation 10: Position after update

$$x_{id}^{t+1} = \begin{cases} 1, & \text{if r} < S(v_{id}^{t+1}) \\ 0, & \text{otherwise} \end{cases}$$

5.2. BPSO for SSOP

Assumed $x_{i,g,m,k} = 1$ denotes in particle i, the subcarrier k is allocate to the m layer in the group g, and 0 otherwise. We now give the detailed procedures of BPSO for SSOP as follows:

1） Population initializing: In the initialization process, we first give the initial position of the particles, and the initial velocity of each particles $v_{i,g,m,k}^{0} \in [-V_{\max}, V_{\max}]$. And then We set the initial $Pbest_i$ and $Gbest$.

2） Velocity update: After setting the inertia weight by Equation 8, the i-th particle's velocity is updated by

Equation 11: Speed after update

$$v_{i,g,m,k}^{t+1} = \omega_t v_{i,g,m,k}^{t} + c_1 r_1 (p_{i,g,m,k}^{b} - x_{i,g,m,k}^{t}) + c_2 r_2 (g_{g,m,k}^{b} + x_{i,g,k,m}^{t})$$

3） Modification of Position of Particles: The position vector of the i-th particle at iteration t is modified as follows:

Equation 11: Speed after update

$$x_{i,g,m,k}^{t} = \begin{cases} 1, \text{ if } r^{t} < S(v_{i,g,m,k}^{t+1}) \\ 0, \text{ otherwise} \end{cases}$$

4） Update of $Pbest_i$ and $Gbest$: If X_i^{t+1} yields a bigger fitness value than $Pbest_i^t$, then $Pbest_i^{t+1}$ is set to X_i^{t+1} .Otherwise, $Pbest_i^t$ retained:

Equation 11: Speed after update

$$Pbest_i^{t+1} = \begin{cases} X_i^{t+1}, & \text{if } f(X_i^{t+1}) > f(Pbest_i^t) \\ Pbest_i^t, & \text{otherwise} \end{cases}$$

Also, $Gbest^{t+1}$ is set as the best evaluated position among the $Pbest_i^{t+1}$.

5） Stopping criteria: The proposed BPSO algorithm is terminated if the iteration reaches a pre-specified maximum iteration. And finally, we set the optimal solution L^* for SSOP as $Gbest^{iter_{\max}}$.

5.3. Simulations results

As shown in Figure 3, the opportunistic spectrum access method performs frequent spectrum switching operations during video transmission, which makes the accumulated switching delay much higher than the proposed scheme. In the simulation time of 900 seconds, the accumulated switching delay reaches about 165 seconds. The proposed scheme has a total switching delay of only 35 seconds. Therefore, the proposed scheme is more suitable for network deployment.

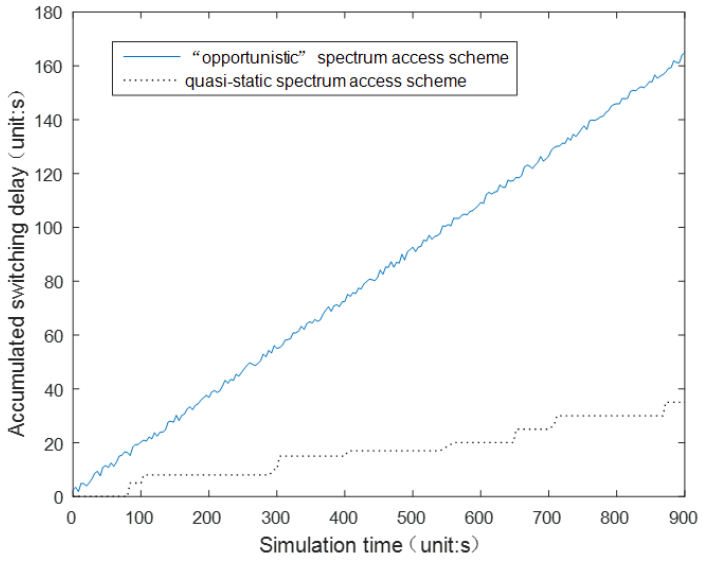

Figure 3: Accumulation switching delay comparison of different spectrum access schemes

As shown in FIGURE 4, in the case of the same number of program sources, the use of the proposed spectrum access scheme can greatly increase the quality of the received video. When using the proposed scheme, the user's decoding quality is about 4dB higher than that of the conventional scheme, which proves the superiority of the proposed scheme.

Figure 4: Different spectral access scheme video decoding quality

6. CONCLUSION

In this paper, we propose a TV whitespace scalable high-definition video multicast solution based on SVC technology. This is different from the traditional multicast-based multicast scheme based on cognitive radio networks. This article considers a spectrum utilization strategy with high spectrum utilization. Different from the traditional opportunistic spectrum access method, this paper makes full use of the long ON/OFF interval of TV whitespace UHF channels when designing spectrum access schemes, and proposes a quasi-static spectrum access method. Simulation results show that the method can greatly reduce the delay caused by spectrum switching in video multicasting and effectively improve the user experience.

7. ACKNOWLEDGEMENTS

This research was supported by National Natural Science Foundation of China (61471162, 61501178, 61571182, 11605051, 41601399, 61601177); Program of International science and technology cooperation (2015DFA10940); Science and technology support program (R & D) project of Hubei Province (2015BAA115); PhD Research Startup Foundation of Hubei University of Technology (BSQD13029, BSQD13032, BSQD14028, BSQD14033); Open Foundation of Hubei Collaborative Innovation Center for High-Efficiency Utilization of Solar Energy (HBSKFZD2015005，HBSKFTD2016002).

8. REFERENCES

Figueiredo, S., Wetterwald, M., Nguyen, T. T., Eznarriaga, L., Amram, N., & Rui, L. A. (2016). SVC multicast video mobility support in MEDIEVAL project. Future Network & Mobile Summit IEEE, 1-8.

Hua, K. L., Anistyasari, Y., Hsu, C. H., Chin, T. L., Yang, C. L., & Wang, C. Y. (2017). Multicast scheduling for stereoscopic video in wireless networks. Multimedia Tools & Applications, 76(1), 679-706.

Liu, J., Li, B., & Zhang, Y. Q. (2012). Adaptive video multicast over the internet. Multimedia IEEE, 10(1), 22-33.

Lim, W. S., & Hong, Y. G. (2017). Energy-Efficient Multicasting in IEEE 802.11 WLANs for Scalable Video Streaming. Vehicular Technology Conference IEEE, 1-5.

Tan, W. T., & Zakhor, A. (2001). Video multicast using layered fec and scalable compression. IEEE Transactions on Circuits & Systems for Video Technology, 11(3), 373-386.

Wang, L., Yang, Z., Xu, L., & Yang, Y. (2016). Ncvcs: network-coding-based video conference system for mobile devices in multicast networks. Ad Hoc Networks, 45, 13-21.

Zuo, L., Lou, J. G., Cai, H., & Li, J. (2006). Multicast of Real-Time Multi-View Video. *IEEE International Conference on Multimedia and Expo* IEEE, 1225-1228.

204: Urban short-term traffic flow prediction method based on stacked self-encoder and support vector machine

Min WU[1], Li ZHU*[2], Minghu WU[3], Yuanxin LE, Songnan LV, Xuru MA

1 Hubei Key Laboratory for High-efficiency Utilization of Solar Energy and Operation Control of Energy Storage System, Hubei University of Technology, Wuhan, 430068, P. R. China, 417534678@qq.com
2 Hubei Key Laboratory for High-efficiency Utilization of Solar Energy and Operation Control of Energy Storage System, Hubei University of Technology, Wuhan, 430068, P. R. China, julianabiding@126.com
3 Hubei Key Laboratory for High-efficiency Utilization of Solar Energy and Operation Control of Energy Storage System, Hubei University of Technology, Wuhan, 430068, P. R. China, wuxx1005@163.com

* *Corresponding author*

With the rapid development of urbanization in China, the number of motor vehicles is also increasing rapidly, and at the same time it has also caused a series of traffic problems. These include serious road traffic congestion, rising traffic accident rates, and waste of resources caused by inefficient transportation, most notably the severe congestion of road traffic. Therefore, forecasting traffic flow is the key to ease traffic congestion. To solve the above problems, this paper proposes an urban short-term traffic flow prediction model based on stacked self-encoder and support vector machine. This model utilizes the characteristics of Stacked Auto Encoder (SAE) and Support Vector Machine (SVM): SAE is used to extract features from the traffic Flow and the extracted features are input into the SVM. Then, Traffic congestion is predicted. In order to verify the validity of the model, data on buses and taxis in Wuhan are processed to extract important traffic flow parameters in traffic congestion prediction, including traffic volume, average speed, and average density. For the preprocessed data, SAE and SVM were used for model training and prediction. Then the model was modified by BP back-propagation neural network to make the model prediction error converge. The prediction results show that the SAE-SVM model has higher accuracy than the traditional prediction model, and the mean square error (MSE) and average absolute error (MAE) are low, so the SAE-SVM model is more accurate in traffic congestion prediction.

Keywords: Traffic Flow Prediction, Stacked Auto Encoder, Support Vector Machine

1. INTRODUCTION

Research on short-term traffic flow prediction in this field has been active internationally. In the past few decades, research on short-term traffic flow forecasting theory has attracted the attention of many scholars at home and abroad. Short-term traffic flow prediction has become one of the current research hotspots of intelligent transportation.

Martin, Smith, Sullivan, and Dememetsky et al. proposed models for solving various short-term traffic prediction problems, including intersection traffic forecasting, road traffic volume, and accident prediction. The earlier prediction methods mainly include autoregressive model (AR), moving average model (MA), autoregressive moving average model (ARMA), historical average model (HA) and Box-Cox method and so on. The historical average data model (conventional model) is simple and fast, but it cannot cope with emergencies. Gary A. Davis and Nancy L. Nihan (1991) applied a non-parametric regression model to predict traffic flow, and this model has higher prediction accuracy than the time series prediction model in some cases. P.C. Vythotkas (1993) proposed a traffic flow prediction model based on Kalman filter theory, and the calculation results were satisfactory. Brian L.Smith and Michael J.Demetsky (1993) used neural network methods to predict traffic flow. The prediction results had high accuracy and there was no time lag. Maschavander Voort (1996) combined neural networks with ARIMA time series models to predict traffic flow, making the ARIMA model more adaptable and portable. Corinne Ledoux (1997) established a traffic flow prediction model based on neural networks. First, a neural network was used to establish a traffic flow prediction model for each road section, and then a traffic flow prediction model for the entire road network was established. The model was then simulated using simulated data. Later, a neural network-related hybrid prediction model was established, which was slightly more accurate than an independent neural network. For different traffic conditions, the comprehensive model chooses one or several suitable forecasting methods to predict the traffic flow.

The aforementioned existing prediction models, including historical average models, time series models, non-parametric regression models, neural network models, Kalman filter models, etc., have their own advantages and disadvantages and their own adaptation conditions. Therefore, the application of a single model for the prediction of complex traffic flow is clearly beyond our control. Therefore, considering a mixed model, choose one or several model combinations in historical average method, time series method, non-parametric regression method, and neural network method.

This paper proposes a traffic flow prediction method based on deep learning. Here, a Stacked Automatic Encoder (SAE)-Support Vector Machine (SVM) hybrid model was used to learn general traffic flow characteristics, and it was trained in a layer-by-layer greedy manner. For the data currently examined, this is the first time that the SAE-SVM method has been used to represent predicted traffic flow characteristics. The spatial and temporal correlations are considered simultaneously in the model. In addition, it shows that the proposed method predicts superior performance of the flow.

2. TRAFFIC JAM RECOGNITION MODEL FRAMEWORK AND METHOD

2.1. Traffic jam recognition model framework

This paper proposes a traffic congestion identification model. The model extracts the average speed, average traffic flow density and traffic flow by processing traffic data. A road congestion recognition model based on fuzzy analytic hierarchy process is established to determine road traffic congestion levels.

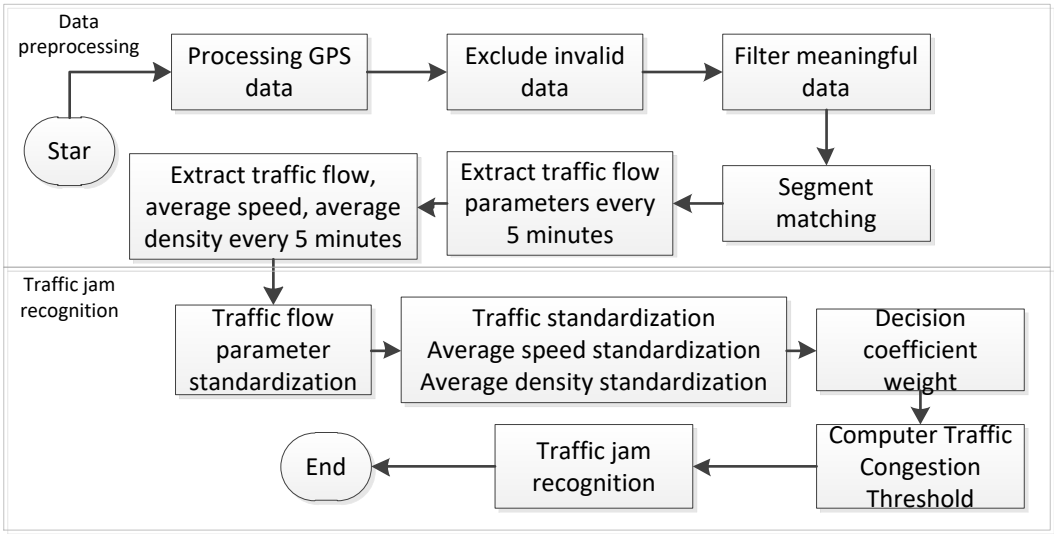

Figure 1: Example of Traffic Congestion Recognition Model

As shown in Figure 1, this traffic congestion identification model is a structural diagram. The model is divided into two parts, the data preprocessing part and traffic congestion identification part. The data preprocessing section mainly includes removing invalid data, screening meaningful data, matching road sections, and then extracting the traffic volume, average vehicle speed, and average density of each section every 5 minutes from the data of the matched road sections. Traffic congestion identification is the standardization of preprocessing traffic flow parameters. Then by determining the weights of the evaluation criteria, the traffic congestion comprehensive threshold is defined, and then the corresponding congestion situation is obtained through the threshold range.

2.2. Traffic congestion identification method

Under normal circumstances, traffic congestion occurs in the early, middle, and late periods, and abnormal changes in traffic volume, average vehicle speed, and traffic flow density occur. Therefore, the three traffic flow parameters of traffic volume, average speed and average density are used as indicators for evaluating traffic congestion. And establishing a recognition model is very favorable for the determination of road congestion. When describing road traffic conditions, based on data analysis, analyze the weight of the parameters and analyze the weights. The speed, density, and flow rate of the characteristic parameters are selected. The number of vehicles traveling within the unit of time, unit mileage, and the number of vehicles within unit mileage per unit time are used to measure road traffic conditions and determine road conditions. Among them, the road section with low speed, high density, and small flow rate is set as a congested road section.

The three characteristic parameters in the evaluation index belong to different dimension indicators. It is necessary to eliminate the dimension and normalize the processing parameters. This article uses the standard function method for processing. In the evaluation of road traffic conditions, the greater the average speed of the vehicles, the more unimpeded the roads are; the greater the traffic density, the more congestion the roads have; there is no intuitive linear relationship between traffic indicators and road congestion. Therefore, in the road congestion evaluation system, the average speed can be used as a benefit-type parameter; the flow can be used as a moderate-type parameter; and the traffic density can be used as a cost-type parameter. Therefore, the traffic congestion indicator vector can be obtained as shown in Equation 1.

Equation 1: Indicator vector

$$F^1 = \{(v_1^1, f_1^1, k_1^1), (v_2^1, f_2^1, k_2^1), \cdots, (v_n^1, f_n^1, k_n^1)\}$$

Where:

- n= the number of road segments
- v_i=the average speed of the i-th road segment
- f_i= the traffic volume of the i-th road segment
- k_i=the traffic volume of the i-th road segment

After the traffic flow parameters are standardized, the weights of the evaluation indexes need to be determined. Including the determination of two coefficients: First, the weight coefficient of the road segment based on the distance; Second, the determination of the importance of the three traffic flow parameters weight coefficient.

Traffic jams often occur on a section of a road track. For example, the location of traffic jams is relatively close to the location of the upstream intersection. The queuing behaviour caused by congestion has a large impact on the upstream intersections, and it easily leads to congestion at the upstream intersections, which also affects other road trajectories

passing through the intersections. Therefore, the degree of traffic congestion is impacted by the road from the upper intersection to weaken the radiation. The formula for establishing the distance-based weight coefficient of a road segment is shown in Equation 2.

Equation 2: Segment weight coefficient

$$W = [W_1, W_2, \cdots, W_n]; W_i = \frac{\frac{1}{s_i}}{\sum_{i=1}^{n} \frac{1}{s_i}}$$

Where

- n=the number of road segments
- s_i=the distance from the center of the i-th road segment to the upstream intersection

The parameter weight coefficients are determined using the method for calculating the maximum eigenvalue in the AHP. According to the definition of experts, it can be seen that the three parameters are important for the judgment of traffic congestion. Traffic density and speed have a more important impact on traffic congestion. The impact of traffic volume is smaller than the other two traffic flow parameters, and the final defined weight coefficient the vector is shown in Equation 3.

Equation 3: Characteristic parameter weight coefficient

$$B = [b_1, b_2, b_3] = [0.45, 0.10, 0.45]$$

Where:

- b_1= the importance weight of the average speed
- b_2= the importance weight of the traffic volume
- b_3= the importance weight of the average density

According to the obtained index vector, the weight coefficient of the road section and the weight coefficient of the characteristic parameter, the comprehensive measurement parameter is set. Its formula is shown in Equation 4.

Equation 4: Comprehensive measure parameters

$$C = WF^1 B^T$$

$$C = [W_1, W_2, \cdots, W_n] \begin{pmatrix} v_1^1 & f_1^1 & k_1^1 \\ \vdots & \vdots & \vdots \\ v_n^1 & f_1^1 & k_n^1 \end{pmatrix} \begin{pmatrix} b_1 \\ b_2 \\ b_3 \end{pmatrix}$$

$$C = b_1 \sum_{i=1}^{n} W_i v_i^1 + b_2 \sum_{i=1}^{n} W_i f_i^1 + b_3 \sum_{i=1}^{n} W_i k_i^1$$

Finally, the congestion level is determined based on the comprehensive measurement value, and the correspondence between the comprehensive measurement value and the road congestion status is shown in Table 1.

Table 1: Comprehensive Thresholds for Road Traffic Congestion

Comprehensive threshold	Very smooth	General smooth	Mild congestion	Moderate congestion	Severe congestion
city road	0.8-1	0.70-0.80	0.56-0.70	0.40-0.56	0-0.40
highway	0.76-1	0.67-0.76	0.59-0.67	0.42-0.59	0-0.42

Through the above-mentioned method, the established traffic congestion recognition model based on fuzzy function can better determine the status of traffic congestion, and has certain practical value for solving traffic congestion problems.

3. CONSTRUCTION OF FORECASTING MODEL NETWORK BASED ON SAE-SVM

3.1. Model network structure

In the learning process of the neural network, firstly, given an input, the artificial network will have an output tag, and then it will back-propagation according to the error of the current input and the tag. And network will be trained by adjusting the parameters in the network. The learning process of the automatic encoder is a process of unsupervised

learning. The input sample is not labeled, so the training process of the automatic encoder is different. As shown in Figure 2, this is an automatic encoder training process.

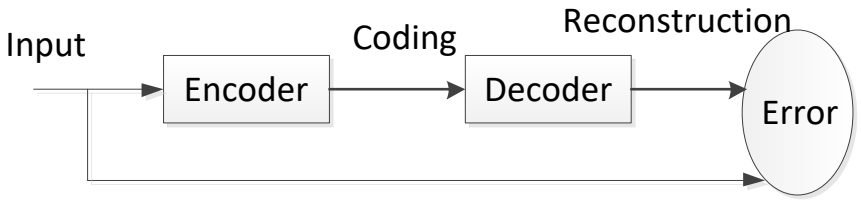

Figure 2: Training of automatic encoder

In summary, it can be concluded that the automatic encoder is an effective method for extracting data features. It usually consists of three or more layers of neural networks. One of the simplest automatic encoders consists of three layers, an input layer, a hidden layer, and an output layer. Given a set of training samples $\{x^{(1)}, x^{(2)}, x^{(3)}, \ldots\}$, where. First an autoencoder encodes $x^{(i)} \in R^d$ into a hidden layer representation y($x^{(i)}$)using equation 5, and then passes the formula 6 to y($x^{(i)}$) is decoded into a reconstructed form z ($x^{(i)}$). The formula is as follows:

Equation 5: S-function

$$f(x) = f(W_1 x + b)$$

Equation 6: S-function

$$z(x) = g(w_2 y(x) + c)$$

Where:

- W_1=a weight matrix
- b= a coded offset vector
- W_2=a decoding matrix
- c=a decoding offset vector
- f(x)、g(x)= sigmoid functions $\frac{1}{1+e^{-x}}$

The construction of the automatic encoder is relatively simple, and the mathematical representation is easy to understand, so it can be stacked better, thus forming a deep structure stacked by an automatic encoder. This formed network model is called a stacked automatic encoder (SAE). As shown in Figure 3, the stacked automatic encoder first trains the first automatic encoder. The goal is to minimize the error between the original input and the reconstructed output. After the automatic encoder is trained, the automatic encoder is used. The output is used as the input to the next automatic encoder, and so on, until the training of the remaining layers is completed. The output of the last layer can be used as an input to the predictor, initializing its parameters, and fine-tuning according to supervised standards.

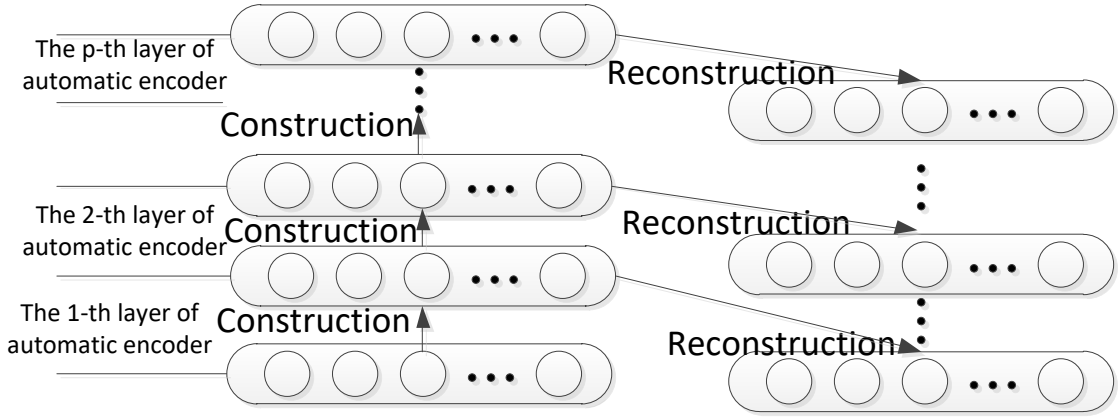

Figure 3: A simple SAE

3.2. Model training

In this paper, SAE is used to study certain traffic characteristics of traffic flow parameters. Support vector machine SVM is used at the top of SAE model. This section will focus on the establishment of the model.

For this model, you first need to define the input feature vectors that are related to the traffic volume. Due to the spatio-temporal characteristics of traffic volume, it can be found that the traffic volume between adjacent links influence each other. Therefore, the input feature vector for this model is defined in this paper as shown in Equation 7.

Equation 7: Input feature vector

$$x_i = (x_{i,t}, x_{i,t-\Delta t}, x_{i,t-m\Delta t})$$

Where:

- x=the traffic volume of the i-th section at time t.

The traffic volume at the next moment of any road section is predicted from the traffic data of the current time and the first m moments of the adjacent road sections.

The overall structure of the model is shown in Figure 4.

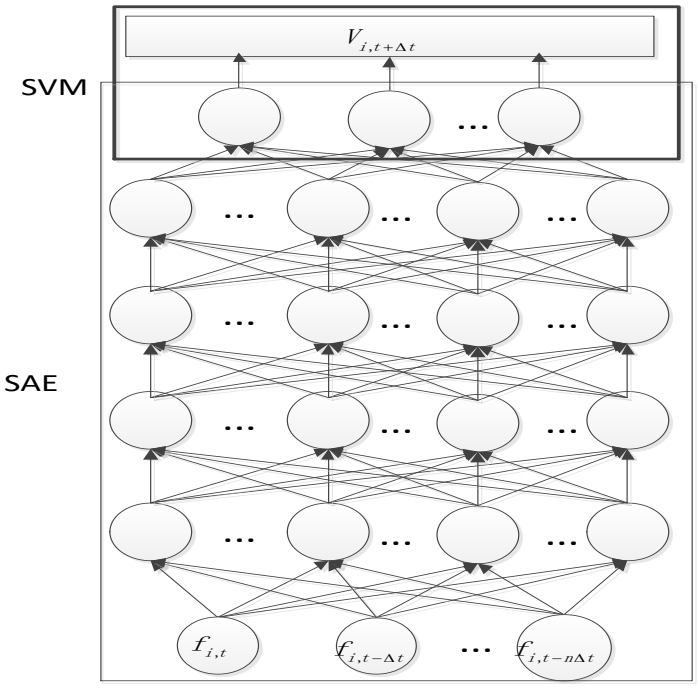

Figure 4: Traffic Forecast Model Structure

As shown in Figure 4, this paper uses a network structure of two hidden layers. When constructing the network, two automatic encoders (AEs) are used to perform the overlay. Each AE is trained layer by layer during training. The training is performed by minimizing the error between the original input and the reconstructed output, and then the output of this layer is taken as the input of the next AE. According to this method, each layer is trained sequentially, and finally a SAE learning model is obtained. The SAE output layer is removed, and the features are input into the support vector machine SVM, and the value of the traffic at the next moment is used as a label.

The input of the prediction model of traffic volume is the traffic volume of several adjacent road segments at the current moment and several historical moments. The value of the traffic volume is integer and within a certain range of values, so it can be directly used as a category label as an output. The category value to which the prediction input belongs can be regarded as a value that predicts the traffic volume of a certain section at the next moment (the average speed forecast model is the same as the traffic forecast model).

The training process of this model can be summarized in the following five steps:

(1) The training set is used as the input of the automatic encoder, the first layer is trained by minimizing the objective function, and the first layer is used as an automatic encoder.

(2) The second layer is used as an automatic encoder and the output of the first layer is used as the input of the automatic encoder.

(3) Continue the above operation and iterate to the fourth floor.

(4) The output of the last layer is used as input to the prediction layer, and its parameters are initialized at random or by supervised training.

(5) Using the BP method to supervise the parameters of all layers in a supervisory manner.

The learning function of SAE realizes the deep mining of traffic data samples and does not predict new samples. Therefore, it is necessary to use the output characteristics of the learning model as the input of the prediction layer (SVM). This paper uses the support vector machine to predict the traffic volume and then brings it into the ambiguity

function to calculate the traffic congestion threshold. Through the determination of the input feature vector and the training process of the model, this paper determines the traffic forecasting model based on SAE-SVM.

4. EXPERIMENTAL ANALYSIS

In this paper, we first present two performance measures based on SAE-SVM prediction model, average absolute error and root mean square error. In this paper, we first compare the different results of the two models based on different parameters, and separately introduce the comparison between the two prediction models and other methods of predicting traffic volume and traffic speed, and then perform a certain analysis. Finally, through the prediction of two kinds of traffic flow parameters, the traffic congestion prediction results are analyzed.

4.1. Experimental environment

The data used in this article is Wuhan taxi data for December 2014. This paper takes the data processing and parameter extraction at intervals of 5 minutes to extract the traffic volume and the average speed of the four road sections respectively. By analyzing the temporal and spatial characteristics of traffic flow parameters, the characteristics of traffic data characteristics and average speed were extracted respectively, and two SAE-SVM-based prediction models established for these two traffic flow parameters were established. Finally, based on the prediction results of these two kinds of traffic flow parameters, traffic congestion prediction is carried out. According to the phenomenon that the traffic volume and the average speed are not consistent on the working days and non-working days, this paper separates the working days from the non-working days to make predictions.

4.2. Analysis of experimental parameters

In this paper, based on the prediction model of traffic volume and average speed of traffic, the performance analysis of the prediction model mainly includes the average absolute error (MSE) and the average root error (RMSE).

Equation 8: The average absolute error

$$MAE = \frac{1}{N}\left|y_i - y_i\right|$$

Equation 9: The average root error

$$RMSE = \frac{1}{N}\sqrt{\sum_{i=1}^{N}\left(y_i - y_i\right)^2}$$

Where:

- y_i=The actual observed value
- $\hat{y}_i$=The predicted value
- n= The number of samples

In this experiment, the main research road selected in this paper is four road sections in Wuhan. Therefore, for the traffic volume of road section 1, it is necessary to analyze the traffic volume of its three adjacent road sections. The number of sub-road segments in this paper is 3, that is, the adjacent three links, so the value is 3. Then m in the above input vector formula, that is, the selected distance from the period of time, needs to be determined in this paper.

For the SAE-SVM prediction model, some input and output parameters need to be determined. In the learning feature of SAE, at present, there is no good way to determine the parameters, usually based on experience or multiple attempts. Therefore, this paper finally determines the value of the parameter based on the influence of the size of several important parameters on the prediction error. This article mainly analyzes from the following parameters: the number of hidden layers and the number of hidden layer nodes. According to simulation experiments, when the number of hidden layers is 4, the number of hidden layer nodes is 400, and the prediction accuracy is best.

4.3. Model comparison scheme

In order to verify the effectiveness of the SAE-SVM hybrid model, this paper chooses the SAE-SVM hybrid model with 4 implicit nodes and 400 nodes (nominal parameters) to compare with other predictive models, including SVR, CNN and CNNS (CNN- SVR). The three models calculated the values of MAE and RMSE for normal conditions, holidays, and abnormal weather, respectively, as shown in Table 4. From Table 4 it can be seen that the MAE and RMSE values of the SAE-SVM hybrid model are smaller than other models. None of the three models had a good prediction effect with the SAE-SVM hybrid model. The SAE-SVM hybrid model uses more unmarked data and uses layer-by-layer greedy pre-training. Compared with CNN and CNNS models, the SAE-SVM hybrid model has better extraction results, and the SVM has a good classification effect, making the hybrid model more predictive performance.

Table 4: Other Forecasting Models

	MAE			RMSE		
	SVR	CNN	CNNS	SVR	CNN	CNNS
Normal status	9.3	12.1	8.4	12.6	13.3	10.2
Holidays	10.8	13.8	8.7	13	14.6	11.1
Abnormal weather	12.3	11.3	8.1	14.2	12.1	9.8
Test set	10.2	11.5	8.2	13.5	12.9	10

5. CONCLUSION

This paper proposes a short-term traffic flow forecasting method based on stacked auto-encoder network model combined with support vector regression. A mixed model of SAE model plus SVM is designed to process traffic flow data with time-space information into a stacking automatic encoder. In the form of network input, the entire network is trained by using the objective function of SVM; the SGD stochastic gradient descent algorithm is used to ensure the full extraction of spatio-temporal characteristics of traffic flow; finally, traffic performance data of Wuhan is used to analyze the model performance. The experimental results show that the prediction model presented in this paper has higher prediction accuracy, the predicted value can keep the same with the true value, and it is less affected by external interference factors, and it is an effective traffic flow prediction method.

6. ACKNOWLEGMENTS

This research was supported by National Natural Science Foundation of China (61471162, 61501178, 61571182, 11605051, 41601399, 61601177); Program of International science and technology cooperation (2015DFA10940); Science and technology support program (R & D) project of Hubei Province (2015BAA115); PhD Research Startup Foundation of Hubei University of Technology (BSQD13029, BSQD13032, BSQD14028, BSQD14033); Open Foundation of Hubei Collaborative Innovation Center for High-Efficiency Utilization of Solar Energy (HBSKFZD2015005，HBSKFTD2016002).

7. REFERENCES

Jun Li, & Xue Mei.(2017). Deep Neural Network for Structural Prediction and Lane Detection in Traffic Scene. IEEE Transactions on Neural Networks and Learning Systems, 28(3), 690-703

Zhou Zhihua. (2016). Machine Learning, Beijing: Tsinghua University.

Yisheng Lv, Yangjie Duan, Wenwen Kang, & Zhangxi Li.(2015). Traffic Flow Prediction With Big Data: A Deep Learning Approach. IEEE TRANSACTIONS ON INTELLIGENT TRANSPORTATION SYSTEMS, (16), 805-873.

Jiang Deguan. (2016). The prediction of short-term traffic flow based on deep belief network. Journal of Hunan University, 23(1), 112-116.

Gao Xiaobo. (2017). Short-term traffic congestion prediction model based on deep learning. (Dalian University of Technology)

Lin Haitao. (2016). Research on neural network algorithm for short-term traffic flow prediction. (Nanjing University of Posts and Telecommunications)

Yin Baocai, (2015). Wang Wentong, &Wang Lichun. A review of deep learning. Journal of Beijing University of Technology, 16(2)865-873.

206: A wind-solar hybrid intelligent LED street lamp monitoring system

Xiangkui WAN [1], Jiaxin WEI[2], Fengcong LI*[3], Yuewen YAN[4]

[1] *Hubei University of Technology, No.28, Nanli Road, Hong-shan District, Wuchang, Wuhan, Hubei Province, P. R. China, wanxiangkui@163.com*
[2] *Hubei University of Technology, No.28, Nanli Road, Hong-shan District, Wuchang, Wuhan, Hubei Province, P. R. China, 395426098@qq.com*
[3] *Hubei University of Technology, No.28, Nanli Road, Hong-shan District, Wuchang, Wuhan, Hubei Province, P. R. China, 401103757@qq.com*
* *Corresponding author*

In this article,the author designs a wind-solar hybrid intelligent LED street lamp monitoring system based on wireless network, using a wireless network, realizing the work of complementary scenery intelligent LED lamps, performance monitoring and energy distribution. The system includes: wind and solar power generation equipment, LED street lamp and intelligent street lamp control equipment, battery and its management equipment, wireless network equipment, intelligent street lamp control equipment and server. The intelligent street lamp control equipment includes: an illumination sensor and a weather sensor, which are respectively used to implement illumination information and weather information around the intelligent street lamp control equipment. The battery management device includes: a battery power sensor and a charge and discharge controller for battery power detection and charge/discharge control, respectively. The wireless communication network equipment includes: a wireless local area network coordinator and a GPRS wireless communication module .The server is used to obtain traffic flow around the intelligent street lamps in real time, send control instructions to the intelligent street lamps and collect data related to the street lamp operating conditions. Through the street lamp brightness adjustment, street lamp operating conditions and the power adjustment of the wind power generation equipment, the consumption of the street lamp system to the utility power is greatly reduced, the service life of the street lamp is increased, and the worker's workload for maintaining the street lamp and the like can be greatly reduced.

This author aims to optimise the matching of wind turbines and solar cell systems, research on regional energy complementarity, intelligent street lamp control systems, and wireless communication networks. The current situation is that wind-solar hybrid street lamps are widely distributed, inconvenient for maintenance, and cannot be controlled in real time. Design scenery complementary intelligent LED street lamp monitoring system, to achieve the network of scenery and complementary LED street lamps and its energy-saving monitoring.The system has the advantages of low network input costs, low operating costs, strong real-time monitoring capabilities, convenient maintenance and management, and the ability to quickly predict, find and resolve system faults.

Keywords: Wind-solar hybrid intelligent LED street lamp, Control equipment, Wind turbines, Solar cell systems

1. INTRODUCTION

The street lamp lamping system is an important part of the urban infrastructure construction. With the advancement of urbanization in China, the scale of the city is constantly expanding, the highway mileage is constantly being refreshed, the public lamping devices of the city are closely related to people's lives, and the power consumption is very large. At present, our country's traditional street lamps are all under unified control, and they are powered by direct power grids, which are manually sent off. When there are few people driving at night, the street lamps will continue to be lit and the energy will be wasted. Many urban roads will greatly reduce their traffic flow even after the early morning, even without traffic. The street lamps need regular organization of human maintenance, a serious waste of human, material and financial resources. The wind-solar hybrid new energy system is one of the key projects supported by the National 863 Development Plan. It is a new technology and energy-saving application launched in recent years.

In view of the failure of the street lamp, it cannot be monitored and alarmed in time, the street lamp cannot adjust the brightness according to the pedestrian and the vehicle, the grid power supply is used, and the power consumption is huge. It is necessary to design a wind-solar hybrid intelligent LED street lamp monitoring system, which can realize the Intelligent control of the street lamp, self-power supply, to extend the service life of street lamps, reduce the supply of electricity to the street lamps by the power grid, monitor the working status of the street lamps in real time, and detect the faulty street lamps and handle them in time.

2. THE OVERALL COMPOSITION OF THE SYSTEM

The author aims to provide wind and lamp complementary intelligent LED street lamp monitoring system, through the sensor and intelligent street lamp controller to collect LED street lamps, batteries, wind and solar power generation equipment and other related operational parameters collected by the wireless communication network equipment to the server, the server of these parameters evaluate and identify the defective street lamp components, and then send the processed results to the relevant maintenance personnel to realize the timely monitoring and fault warning of the street lamps. The entire system includes wind-solar hybrid power generation equipment, LED street lamp and intelligent street lamp control equipment, battery and its management equipment, wireless communication network equipment, and servers as shown in figure 1.

Wind-solar power generation equipment includes two parts, a wind generator and a solar panel, for converting wind and solar energy into electrical energy. LED street lamps use battery power lamping. The battery management device includes a battery power sensor and a charge/discharge controller. The battery management device is used for battery power detection and charge/discharge control, and uploads battery power data and battery operating status information to the server. The server collects, collates, and analyzes these data, and implements the intercommunication of street lamp nodes with low battery power and sufficient battery power to realize the adjustment of the battery power of all street lamp nodes in the network. The intelligent street lamp control device obtains the lamp intensity and weather information of the environment where the street lamp is located through the lamp sensor and the meteorological sensor, and transmits it to the server through the GPRS wireless communication network. The server processes these data together with the road traffic information obtained from the web and obtains the information. A LED lamp illumination strategy plan is transmitted to the intelligent street lamp controller. The controller adjusts the illumination of the LED street lamp according to the scheme to achieve the control of the illumination of the LED street lamp. The server analyzes the data collected by the intelligent street lamp control to obtain the operating status of each street lamp, and alerts the street lamp nodes that need to be maintained to the staff. During the daytime, excess power is connected to the network for the street lamp node with sufficient battery power. At night, the battery with insufficient battery power is given support to the grid power. A strategy to turn off two street lamps and one street lamp for sections at night with little traffic. The wireless communication network equipment includes: a wireless local area network coordinator and a GPRS wireless communication module, which can receive various control commands issued by the server through a GPRS wireless communication network, but also can be converted into a wireless local area network signal, and then converted by the wireless local area network coordinator. The WLAN control command signal is forwarded to the intelligent street lamp controller via the WLAN wireless network, at the same time, the signals collected by the intelligent street lamp controller are collected and converted into a GPRS signal, then uploaded to the data packet through the GPRS wireless communication network. The server and the wireless controller based on the WLAN implement the processing of various parameters of the data collection terminal.

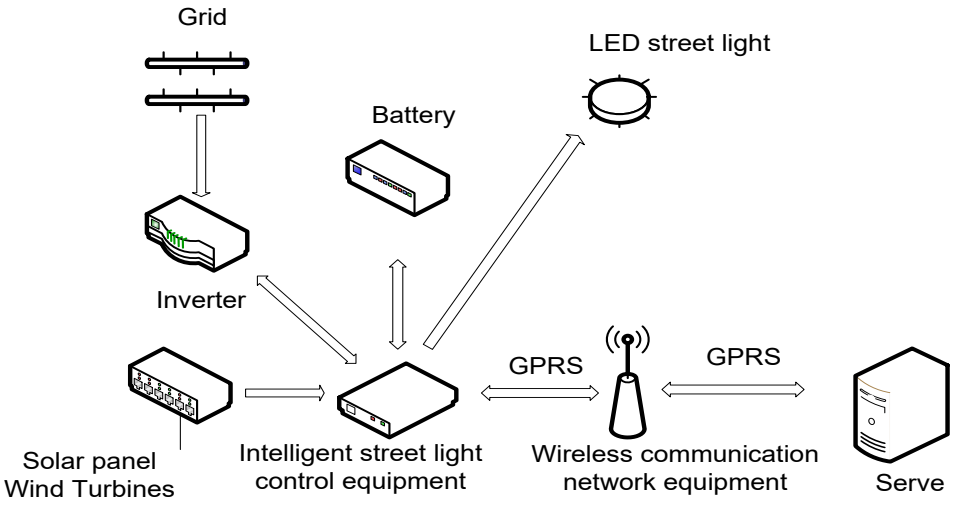

Figure 1: System structure

3. THE IMPLEMENTATION OF INTELLIGENT STREET LAMP CONTROL EQUIPMENT

During the daytime, the intelligent street lamp controller detects whether the battery power is sufficient. When the wind energy is insufficient, the battery power is difficult to saturate. If the battery power is lower than 60% at night when lamping is required, the battery power is determined to be insufficient, and the server sends the power to the server. The grid receives power requests. When the wind energy is sufficient, and the battery power is full, if the intelligent street lamp controller collects the battery power higher than 95%, it is determined that the battery power is sufficient, the intelligent street lamp controller transmits the information to the server, and the server is disconnected. Battery circuit information and excess power is transmitted to the grid through the inverter.

The intelligent street lamp controller charges the battery through a solar battery and a wind generator charging system. When the electric energy is sufficient or insufficient, when it is necessary to transmit or receive electric energy to the electric grid, the AC/DC conversion of the inverter is used to realize the conversion of the AC power and the DC power. At the same time, the intelligent street lamp controller sends the collected battery power feedback signal and the power signal sent from the grid to the system to the server through the wireless communication device.

The data at the data collection side consists of battery power, wind turbine power, solar panel power, lamp, temperature, LED street lamp voltage, current data, and weather sensors. The data control side consists of intelligent street lamp controllers and servers. The data input is composed of road traffic information, historical control records, staff instructions, and set control modes. The battery power data can determine whether the power supply mode used by the system is grid power supply or battery power supply, data provided by weather, lamp and temperature sensors, comprehensive road traffic data, determines the brightness level of the street lamp and the switch LED lamp scheme. According to the set control, the mode can control the opening and closing time of the street lamps. The control mode needs the support of data such as lamp intensity, traffic flow information, weather information, and battery power level information to complete. Through the processing analysis of the server, the purpose of intelligent control is achieved.

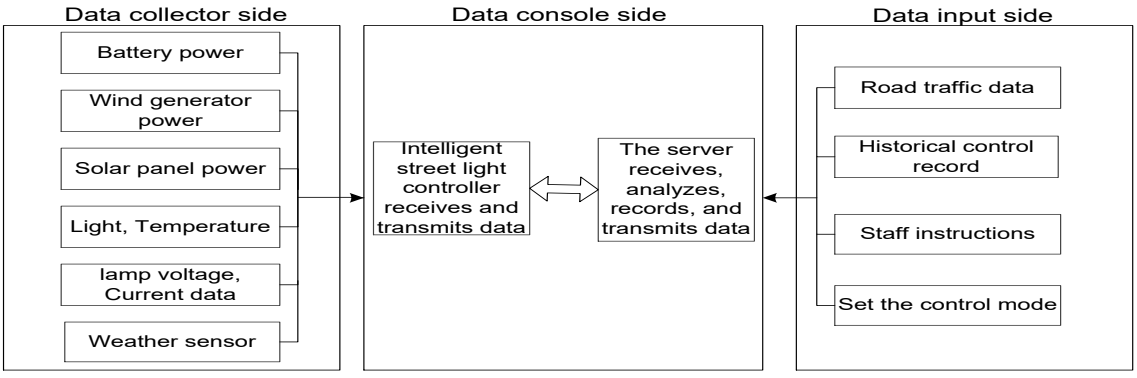

Figure 2: Intelligent street lamp control data flow structure

4. SYSTEM HARDWARE DESIGN

Figure 3 is based on the EP3C16F484C6N FPGA development board "DE0", which pin 5 "Grid-Control "and 7 pin "Battery-Control" used to control the direction of power to achieve the charge of the battery and the power generated by the power generation equipment control. Pin 13 " PWM-EN" is the LED driver chip enable terminal for controlling the brightness of the LED street lamp. Pins 15 and 17 are used for the AD data reception interface. The serial port is the interface for receiving weather sensor data. "RJ45-DE0" is the network transmission port. Lamp sensor and weather sensor are the outputs of the lamp sensor and the weather sensor. Figure 4 is a control circuit for controlling the power flow on power generation equipment, battery equipment, and LED street lamps. Figure 5(a) shown the input and output interface is the acquisition circuit, inverter is the inverter, rectifier is the rectifier, used to collect battery power data and power generation equipment power generation data and operating parameters. Power monitoer is the conversion module. Figure 5(b) is the conversion IC and the lower part is the voltage divider circuit. This circuit is to guarantee the normal operation voltage of the A/D converter module. The upper part of figure 6(a) is the external network port side, and the lower part of figure 6(b) is the LED controller. These circuits are controlled by programs stored on the FPGA development board.

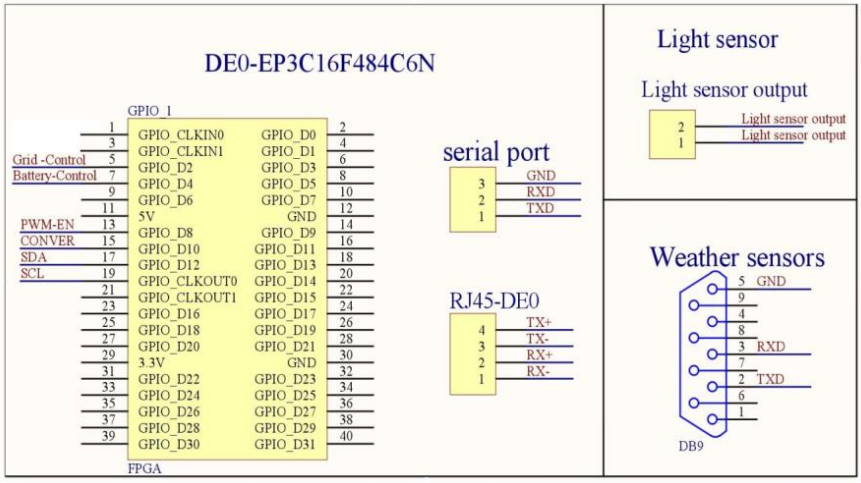

Figure 3: DE0-EP3C16F484C6N

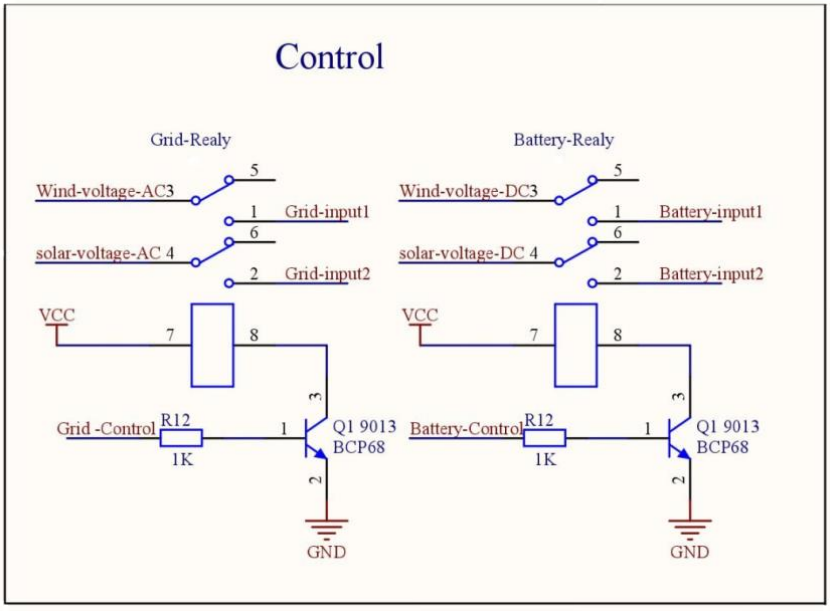

Figure 4: Control circuit

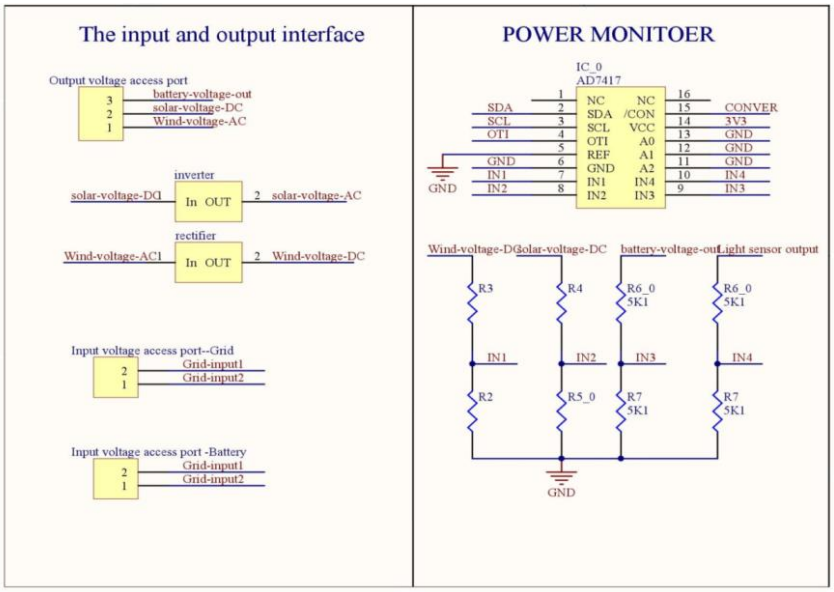

Figure 5: (a) The input and output interface (b)Power monitoer

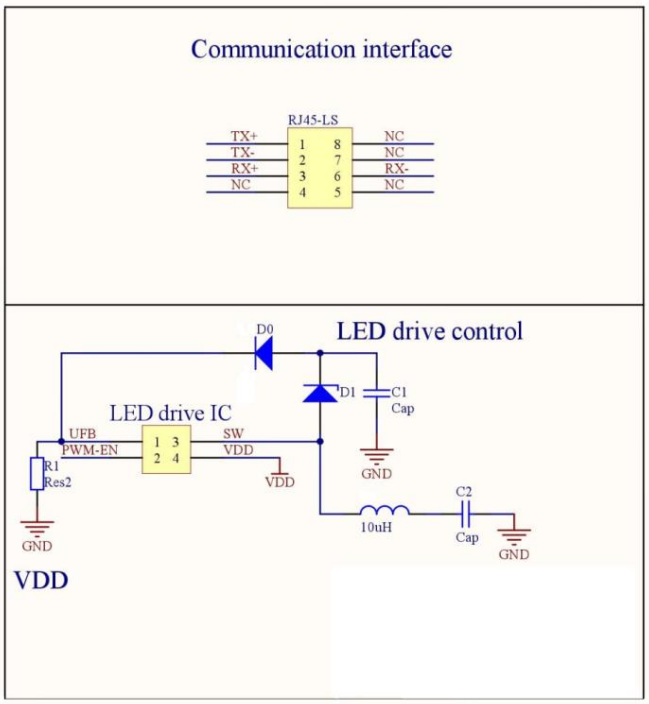

Figure 6: (a) Communication interface (b) LED drive control

5. SYSTEM MONITORING SOFTWARE DESIGN

The backstage database of the monitoring software adopts the MySQL database. The MySQL database mainly aims at a large number of controllers and transmits a large amount of data. Considering the security, stability and convenience of the software, from the design point of view, the monitoring software has the following functional modules: (1) Role assignment function for user roles. Only the management personnel can modify the relevant parameters of the intelligent street lamp controller. (2) Data display function. This function can display, analyze and count the relevant data of intelligent street lamp controller through a variety of ways. The real-time and statistical analysis data of the controller can be displayed through the curve diagram, physical simulation diagram, and relational table. Accumulated data of power consumption and power generation are dynamically displayed through dynamic curves. (3) Alarm function.Through the feedback data of the controller, it is analyzed and judged whether it belongs to the warning message of the intelligent street lamp controller. At the same time, relevant alarm information is also designed for the relevant use of the software. Alarm functions include: system alarm, communication alarm, controller the status alarms. Reflect the relevant status information and performance indicators of the intelligent street lamp

controller through the alarm information. If a fault is found, the relevant parameters of the controller can be corrected through the GPRS wireless communication network and the alarm information can be cancelled. (4) Parameter setting function.Provide display and design controller related parameter setting interface, through this interface can set the controller's relevant parameters. (5) Database function design.The monitoring software for intelligent street lamp controller real-time data analysis, statistics, a large amount of data to be stored in the database, so the database design mainly takes into account the database's index design, storage design, improve the database query efficiency .

6. CONCLUSION

In summary, the wind-solar complementary intelligent LED street lamp monitoring system can real-time understand the real-time status and historical data of each street lamp unit. The system has the advantages of reducing utility power consumption, increasing the service life of street lamps, and reducing the workload of workers in maintaining street lamps and other equipment. All operations are performed in the backstage of monitoring software. The operation is simple, intuitive, and comprehensive, which greatly improves the efficiency of maintenance and inspection of wind-solar hybrid street lamps. The use of wireless communication network equipment is an effective choice for energy conservation and environmental protection in the field of video surveillance. It is also an effective combination of the new energy industry and the Internet of things industry.

7. REFERENCES

Li Lian, & Wei Shilei. (2013). Wind-solar hybrid street lamp monitoring system based on gprs. Control Engineering, 20(4), 715-717

Xie Lei, & Zou Pengju. (2015). Wind-solar hybrid street lamp monitoring system based on zigbee and mobile 4g. Science and Technology Vision (30), 102-103.

He Weiwei, Lu Jin, & Yang Jinming. (2012). Avr-based wind and solar hybrid street lamp control system design. Journal of Illumination Engineering, 23(1), 112-116.

Si Zhize, Chen Zhijun, & An Dianqiang. (2013). Study on the control system of wind illumination led street lamps. Sichuan Electric Power Technology (3), 91-94.

Chen Lin. (2014). ZigBee-based cross-wind hybrid street lamp monitoring system design. (Doctoral dissertation, Ningxia University).

Zhang Weimin. (2013). Design and development of monitoring software based on vb wind-solar hybrid street lamp controllers. Industrial Control Computers, 26(5), 44-45.

207: Design of a household solar LED lighting system

Wei MEI[1], Zhengwang XU[2], Jiaqi YU[3], Jiarui ZHANG[4], Yuchun YI[5], Cheng CHEN[6]

[1] *Hubei University of Technology, Wuhan, China, maywayv@163.com*
[2] *Hubei University of Technology, Wuhan, China, xuzw72@163.com*
[3] *Hubei University of Technology, Wuhan, China, 757345365@qq.com*
[4] *Hubei University of Technology, Wuhan, China, 695922893@qq.com*
[5] *Hubei University of Technology, Wuhan, China, 1042048803@qq.com*
[6] *Hubei University of Technology, Wuhan, China, 1510795214@qq.com.com*

For the shortage of electricity in remote areas, many household solar LED lighting systems have been developed, but most of them have simple structure, low charge and discharge efficiency, poor stability and short battery life. Therefore, a household solar LED lighting system is designed in this paper. The system mainly uses the bidirectional BUCK/BOOST circuit as the main circuit, reducing the volume cost and reducing the switching loss of the circuit, and taking the STM32 single chip as the control core. The control strategy is as follows: (1) The battery charge and discharge management strategy based on the carrier stack thought is added to control battery charging and discharging to maximize battery life; (2) The MPPT (maximum power point tracking) algorithm based on variable step size disturbance observation method is used to improve the utilization of solar energy; (3) Based on solar panels and batteries, three charging modes are selected in different states, which are MPPT charging, constant voltage charging and floating charging to improve the efficiency of the system; (4) To protect the battery from overcharge, overvoltage and return differential, a protection strategy is designed to reduce battery damage. After testing, the system has high charge/discharge efficiency and good stability, and the service life of the battery has been effectively extended.

Keywords: Solar LED; MPPT; Battery management

1. INTRODUCTION

Nowadays, clean energy is widely advocated, and the utilization of solar energy is more common. It is not limited by geographical area and is easy to develop and utilize. In some areas with poor infrastructure, such as Africa and Southeast Asia, their electricity cannot fully cover all areas, and many areas are in a state of power shortage, which will bring adverse effects on people's life and social development. The independent solar energy system plays an important role in those areas where traditional energy is scarce or too remote to achieve grid construction.

Most of the literature about solar LED lighting system is the study of street lamps. By consulting the literature at home and abroad, their main research contents can be summarized as the main circuit design and algorithm, the main circuit design is the topology design of the DC/DC circuit and the algorithm is mainly MPPT algorithm, but the descriptions of detailed structure of the solar LED lighting system are less. There are few descriptions of the circuit design and algorithm for the market demand function. (Jin, 2014; Xiao, 2015)

In addition, the general household solar LED lighting system on the market generally only realizes the basic charge and discharge control, the basic MPPT algorithm and some personalized functions. In the product renewal problem, it only adopts the method of increasing the battery pack capacity, and does not extend the battery life through a certain control algorithm to increase the endurance time. Therefore, this paper designs a household solar LED lighting system to increase the utilization of solar energy and prolong the battery life through the hardware circuit and control strategy.

2. SYSTEM HARDWARE DESIGN

2.1. Overall structure of the system

Considering the stability and cost of the system, the overall block diagram of the system is shown in Figure 1. Among them, the red frame is the controller of the lighting system. The solar panel, the energy storage unit and the LED light three are connected through the bi-directional DC/DC main circuit in the controller. The energy storage unit is composed of the lithium battery and the 2 MOS tubes. After the voltage and current of the solar panel and the LED are collected by STM32, the control system is charged and discharged through the MOS drive and the RT9624 drive control system. After detecting the voltage through the differential circuit, the battery unit controls the state of the battery unit by SCM, so as to realize charge and discharge management.

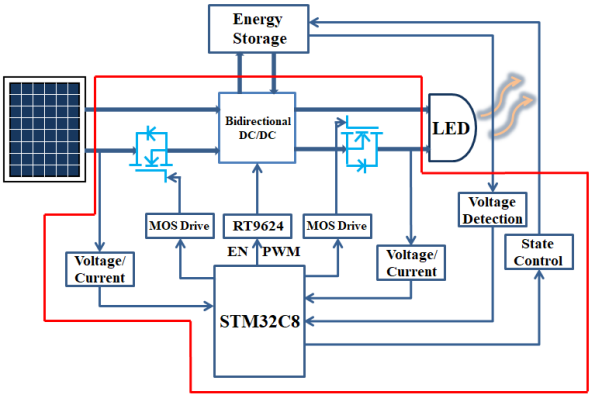

Figure 1: System framework

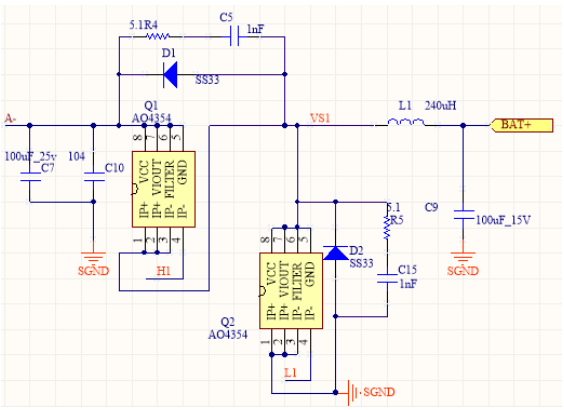

Figure 2: BUCK/BOOST bi-directional circuit

2.2. Main circuit design

The main circuit adopts BUCK/BOOST bidirectional circuit, and its circuit is shown in Figure 2.

BOOST mode: The inductance is calculated to be about 193.8μH, which generally selects 1.2 times the critical inductance and the inductance is 232μH.

BUCK mode: The inductance is calculated to be about 178.8μH, which generally selects 1.2 times the critical inductance and the inductance is 214μH.

Based on the above design requirements of BOOST circuits and BUCK circuits, this paper selects 240μH inductors.

2.3. Drive circuit design

In general, the output voltage of the battery is not matched with the required voltage of the LED lamp group. The boost and steady current of the DC-DC circuit make it fit well with the load, thus driving the LED load to run steadily and safely. In the bidirectional DC-DC circuit, there are two MOS tubes which need to be driven. Considering the cost, the RT9624 chip is used in this design. It can directly drive two MOS tubes, and the circuit is shown in Figure 3.

The driving pulse H1 and L1 produced by the RT9624 are driven by 2 MOS tubes Q1 and Q2 of the DC/DC main circuit. The PWM wave produced by STM32 is entered from the IN pin. The high-end output HO and the LO output are a pair of complementary waves, which ensures that only one of the two tubes in the bidirectional circuit is in the conduction state. The function of charge and discharge should be used.

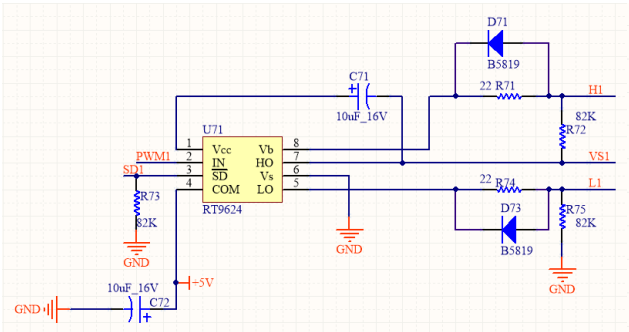

Figure 3: Drive circuit

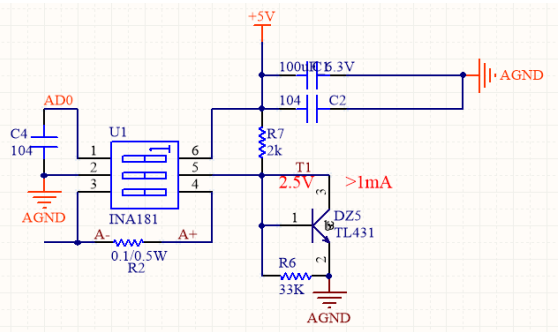

Figure 4: Current detection circuit

2.4. Current detection circuit

The current detection circuit is like Figure 4. The detection signal is sent to the main control chip by AD0. The C4 is the working capacitance of the INA181. The C1 and C2 provide the stable working voltage for INA181. R6 and R7 can detect the actual working voltage of INA181 to prevent the actual voltage from deviating from the ideal value with the error of the call flow detection, and the voltage signal passes through T1. It is given to the main control chip. When the current flows from the solar panel to the lithium battery, the voltage of the AD0 is greater than the T1 voltage; when the current flows from the lithium battery to the LED lamp, the voltage of the AD0 is less than the T1 voltage, so the INA181 can simultaneously detect the size and direction of the current in the circuit.

2.5. Battery charge and discharge management circuit

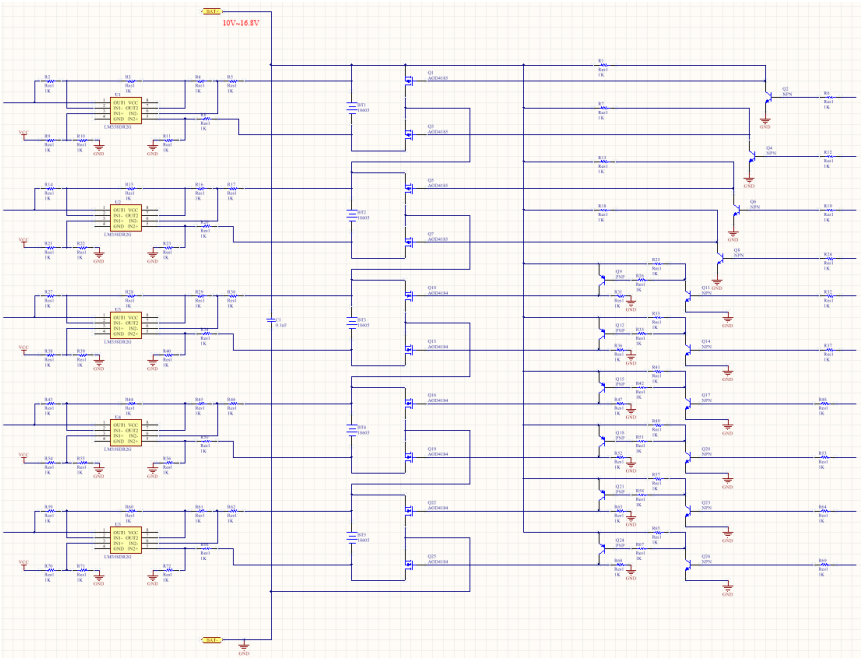

Figure 5: Battery charge and discharge management circuit

As shown in Figure 5, from left to right, respectively, differential detection circuit, energy storage unit and MOS drive circuit. The battery unit and 2 MOS tubes make up the energy storage unit. Through the differential detection circuit, the voltage of each cell is detected accurately, and the voltage of each cell is sorted by the idea of carrier layer, and the switching time of the MOS tube of each cell unit is changed by the voltage comparison.

3. SYSTEM SOFTWARE DESIGN

3.1. The idea of software overall design

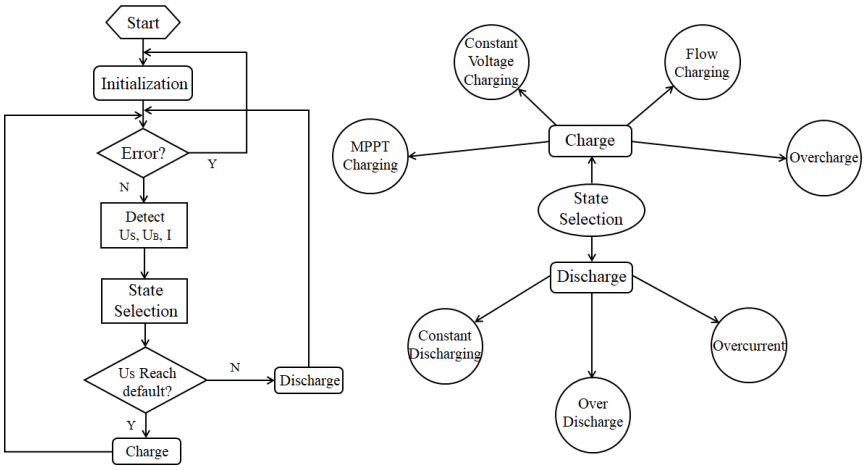

Figure 6: Software overall flow chart and state conversion diagram

As shown in Figure 6(a) main program flow chart, when the system receives the data from the host computer, the system sends the data in the memory to the host computer, and then writes the data sent by the upper computer to the memory, then the system runs with the newly received data in the memory, and the three state indicator lights in the system are used to indicate the charge, respectively. Electricity, discharge, overcharge, over discharge, and over current protection. The state switching graph, as shown in Figure 6(b), works at 1 (MPPT charging state), 2 (constant charge state), 3 (floating state), 4 (overcharge state), 5 (constant voltage discharge state), 6 (overplay state) and 7 (over current protection), according to the charge and discharge selection and judgment conditions.

3.2. MPPT algorithm based on variable step size perturbation observation method

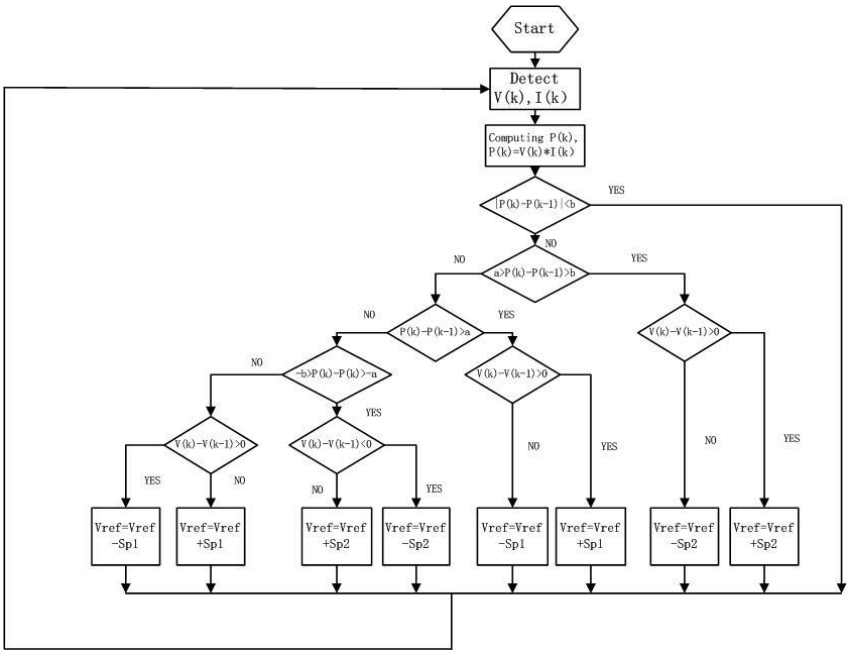

Figure 7: Variable step length MPPT algorithm flow chart

In this paper, MPPT based on variable step size perturbation method is used. The response speed and output accuracy of MPPT algorithm based on disturbance observation method are affected by the step value. The step size is larger and its response is faster but the precision is low, the step size is small and the response is slow, so the size of the step size must be determined according to the properties of the PV curve. The large step is fast approaching the maximum power point and then approaching the maximum power point with smaller step size. The algorithm flow is shown in Figure 7 (Ni, 2015).

3.3. Battery charge and discharge management strategy

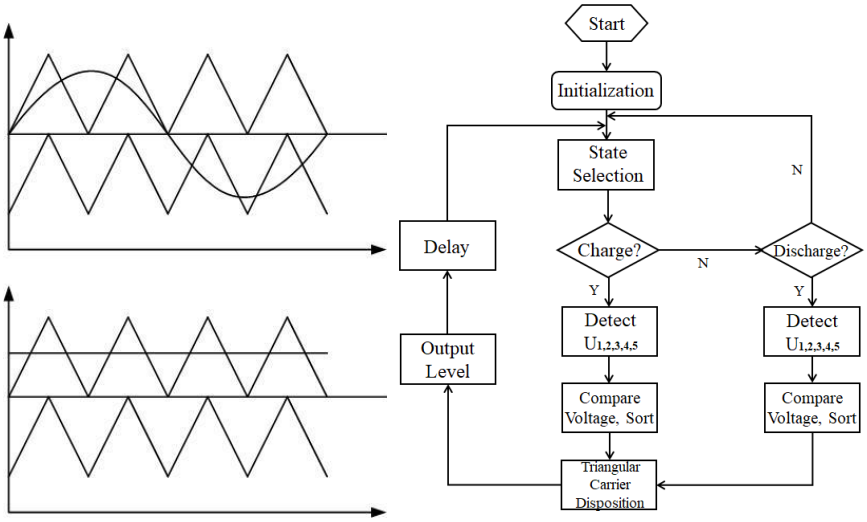

Figure 8: Flow chart of battery charge and discharge management

In the state of charge and discharge, the battery will be affected by the single cell of its worst state. In the case of discharge, the worst state battery has been discharged to the lowest limit, and the overall voltage still satisfies the discharge condition, which will greatly reduce the performance of the battery. Therefore, this paper is based on the circuit of Figure 5 as the basis of the carrier layer idea to control the MOS tube interruption in the energy storage unit. The carrier layer and the battery management strategy software flow are shown in Figure 8. (Yang, 2017; Li, 2015).

4. SYSTEM PERFORMANCE TEST AND ANALYSIS

4.1. System charge and discharge test

The system charge and discharge effect diagram, as shown in Figure 9, makes the LED terminal constant pressure at 19.3V by adjusting the PWM duty ratio. When charging, the charge is charged with a variable step length MPPT charge first, and the actual voltage of the battery is returned to the constant voltage 16.5V charge after being overcharged to lower than 16.5V when the charge is reached to 16.5V.

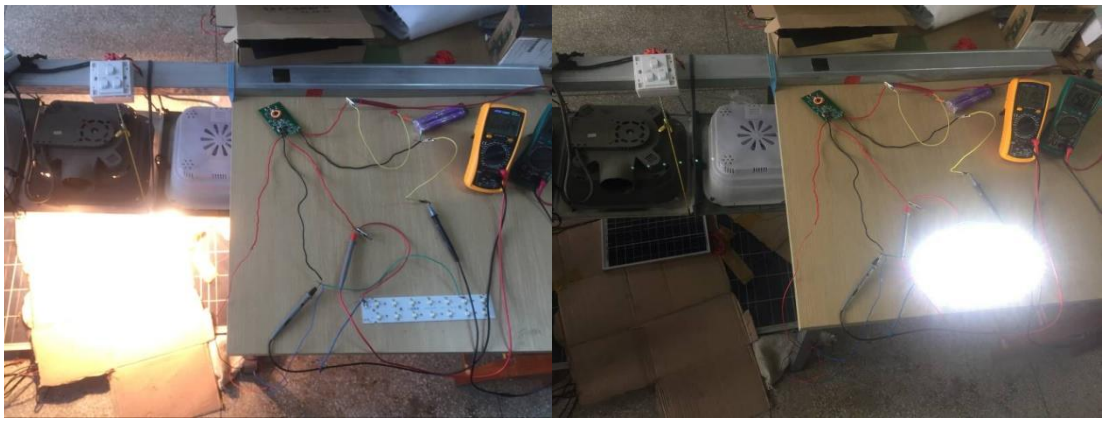

Figure 9: Charge and discharge effect

4.2. MPPT test

The simulation waveform of the variable step size disturbance observation method MPPT algorithm is shown in Figure 10. The left column is a response waveform with a smaller step length of 0.0005. The maximum power point time is longer than 0.44s, and the output power, current and voltage have good accuracy. The waveform oscillates near the maximum power point (setting a larger step 0.002). The maximum power point time of the system is shorter than 0.12s, the output power, current and voltage are low, the waveform oscillates near the maximum power point, and the corresponding waveform is not given in this paper. The one on the right is variable step response waveform, which shows that the response is fast and the output accuracy is high.

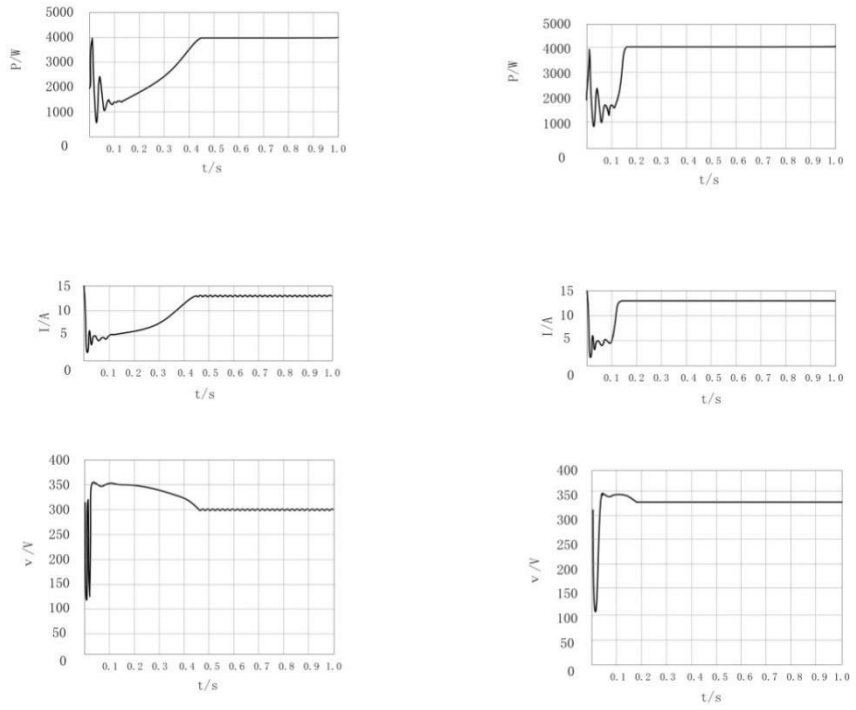

Figure 10: MPPT simulation waveform with variable step length

The actual effect diagram of the variable step length MPPT is shown in Figure 11. The blue curve (basically coincides with the green curve) is the current solar panel voltage value to magnified 100 times; the green curve is the maximum power point target voltage of the solar panel magnified 100 times, the orange curve is the charging current value magnified 1000 times, the red curve is the output power of the solar panel magnified 100 times.

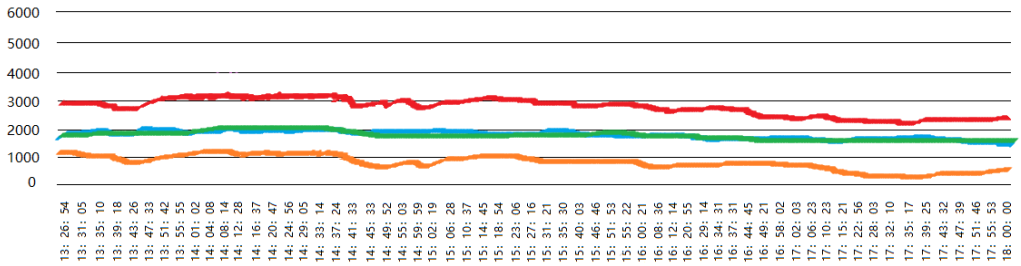

Figure 11: MPPT actual curve of variable step length

4.3. Battery management test

The discharge voltage of each single cell is shown on Table 1 and 2. Its curve is as shown in Figure 12. The actual voltage fluctuation of the battery is larger when the battery life falls, and the difference between the operating voltage and the actual voltage will become larger and larger. The lower table left four is the battery operated by the battery management strategy and the right four is the ordinary working battery. The battery discharge of the next graph is from 3.8V to 3.0V, and the left battery is longer than the right one, and the return voltage is lower than the right one. It can

be seen that the actual voltage of the left battery is closer to the working voltage, that is, the health of the left battery is better, so the battery life of the left battery is prolonged effectively by the battery management strategy.

Table 1: The discharge voltage of single cell under strategy

Time	Working Voltage	Actual voltage	Return value
15:30:00	3.82V	3.82V	0.00V
15:34:47	3.61V	3.64V	0.03V
15:38:50	3.40V	3.44V	0.04V
15:42:36	3.17V	3.23V	0.06V
15:45:06	3.00V	3.09V	0.09V

Table 2: The discharge voltage of single cell without strategy

Time	Working Voltage	Actual voltage	Return value
15:30:00	3.84V	3.84V	0.00V
15:33:12	3.62V	3.67V	0.05V
15:36:31	3.38V	3.46V	0.08V
15:39:55	3.13V	3.23V	0.10V
15:42:02	3.00V	3.14V	0.14V

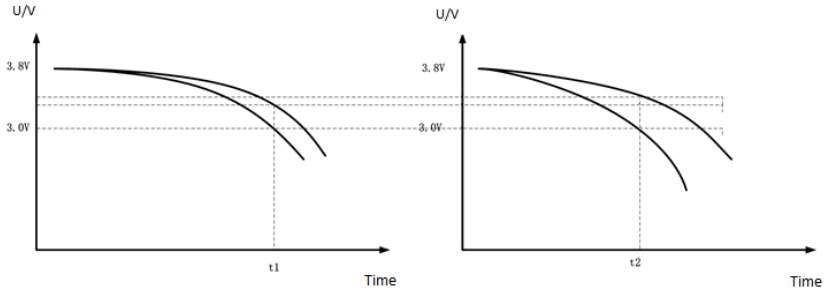

Figure 12: Battery voltage curve

5. CONCLUSION

From the performance test and analysis of the system above, it can be seen that the difference between the test results and the expected target is small. That is, the intelligent household solar LED lighting system designed in this paper is stable and reliable, and the basic charge discharge function is realized effectively under the cost condition, and the charging and discharging efficiency is effectively enhanced to prolong the system life. The application of the system has a wide range of prospects.

6. REFERENCES

Jin, B, Yu, Y, Zhu, M, 2014. Design of Solar Energy Based Intelligent LED Street Lighting Controller. *Advanced Materials Research*, 945-949, 2633-2636.

Xiao, H, Chen, L, Zhang, X, 2015. Design of intelligent controller of solar LED street lamp. *Modern Electronic Technology*, 38 (01), 153-156. (in Chinese)

Ni Y, Hao S, 2015. Motion Characteristics Analysis of P&Q Control MPPT System. *Acta Electronica Sinica*, 43 (07), 1388-1394. (in Chinese)

Yang C, Huang P, 2017. Digital Implementation and Optimisation of Multicarrier Level-Shifted PWM Algorithm. *Motor and Control Applications*, 44 (04), 47-51. (in Chinese)

Li, N, Wang, Y, Wang, Z, Zhang, H, 2015. Comparative Study of Four Kinds of Three-level Carrier-based PWM Strategies. *Electric Drive*, 45 (12), 35-40. (in Chinese)

208: Research on data storage strategy using cloud GIS in smart grid

Yuanxin LE[1], Li ZHU*[2], Minghu WU[3], Min WU, Shuai HUANG, Songnan LV

[1] *Hubei Key Laboratory for High-efficiency Utilization of Solar Energy and Operation Control of Energy Storage System, Hubei University of Technology,No.28, Nanli Road, Hong-shan District, Wuchang, Wuhan, Hubei Province, P. R. China, 495018677@qq.com*

[2] *Hubei Key Laboratory for High-efficiency Utilization of Solar Energy and Operation Control of Energy Storage System, Hubei University of Technology, No.28, Nanli Road, Hong-shan District, Wuchang, Wuhan, Hubei Province, P. R. China, julianabiding@126.com*

* *Corresponding author*

[3] *Hubei Key Laboratory for High-efficiency Utilization of Solar Energy and Operation Control of Energy Storage System, Hubei University of Technology,No.28, Nanli Road, Hong-shan District, Wuchang, Wuhan, Hubei Province, P. R. China, wuxx1005@163.com*

Cloud computing as a product of the era of big data, and its decision-making work analysis, storage and processing method can meet with the require of smart grid monitoring software running reliability and scalability. However, the requirements of the platform on performance of real-time, consistency, data privacy and security can't be satisfied by the existing cloud computing platform. As an information management platform, the GIS platform is equipped with spatial analysis capabilities, and most of the grid's power grid resources can be connection with spatial locations. Therefore, the combination of the GIS and Cloud computing can realize the input, storage, query, retrieval, processing, analysis, display and update of grid resource data and spatial data for the entire smart grid. Therefore, the input, storage, query, retrieval, processing, analysis, display and update of grid resource data and spatial data for the entire smart grid can be realized by the combination of the GIS and Cloud computing. But the current plan for the construction of power cloud GIS platform does not involve specific data storage and management methods. In view of the above issues, this paper proposes a storage strategy based on the GIS smart grid platform. Different storage methods have different advantages and disadvantages. So, the big data in the system must be classified and stored according to the performance and analysis requirements. Real-time data with very high performance requirements, such as power grid operation and equipment data, adopt real-time file system to meet the real-time performance of the data. For core business data, such as such grid marketing data, adopt traditional parallel file systems to meet the reliability of this type of data. Unstructured data, such as GIS data and Monitor video data and power enterprise management data, use a distributed file system to satisfy the large number of such data. Compared with the existing grid data, most of them use a single storage strategy, storage strategy proposed in this paper according to the characteristics of different types of data has obvious advantages on the performance of processing data.

Keywords: Data storage strategy, GIS, Cloud computing, Smart grid

1. INTRODUCTION

In recent years, the global energy problem has become more and more severe. Many countries in the world have started research work on smart grids. The basis for supporting smart grid security, self-healing, green, strong, and reliable operation is the collection, transmission, and storage of panoramic real-time data, as well as the rapid analysis of accumulated massive multi-source data. With the continuous deepening and promotion of smart grid construction, the amount of data generated by power grid operation and equipment inspection/monitoring has increased exponentially. The resulting massive data transmission and storage problems not only impose a great burden on the monitoring devices, but also limit the the leap-forward development of intelligent power systems. This requires corresponding storage and rapid processing techniques as support.

The application of cloud computing technology in the domestic power industry is still at an exploratory stage. The research content mainly focuses on the system conception, implementation ideas and prospects. In some countries, cloud computing applications are currently used for the storage and simple processing of massive data, and actual systems have been implemented and run.

Rusitschka et al (2010) analyses the real-time query requirements of different users in the power system, and designs a smart grid data cloud model for real-time data flow management, which is particularly suitable for processing mass flow data generated in the smart grid, and at the same time implements the model based on this model.

An intelligent measurement and management system for real-time data. Cloudera designed and implemented a smart grid based on the Hadoop platform on the Tennessee Valley Authority (TVA) to help the US grid manage hundreds of terabytes of PMU data, highlighting the high reliability of Hadoop and In addition, TVA developed super PDC based on the project and opened it via the open PDC project. This work will facilitate the large-scale analysis and processing of measured data and can handle other time series data of the power grid. Provide a common platform.

Japan's Kyushu Power Company uses the Hadoop cloud computing platform to perform rapid parallel analysis of massive power system user consumption data, and has developed various types of distributed batch processing application software based on this platform, which has improved the speed of data processing and effectiveness.

Birman et al (2010) have carried on the detailed analysis to the cloud computing platform applied to the smart grid, the conclusion is: The existing cloud computing platform can meet the reliability and expansibility of the smart grid monitoring software operation, but the real-time, consistency The requirements for data privacy and security are still not met and are for further study.

In China, a paper named cloud computing-based smart grid information platform focuses on the characteristics of smart grid condition monitoring and combines with Hadoop to store and manage data using virtualization technology, distributed redundant storage, and data storage mode based on column storage to ensure reliable power grid state data. And efficient management is currently only a framework. In order to solve a series of problems such as low utilization rate of resources in disaster recovery center of power system and complexity of disaster recovery business processes, a paper research on application of cloud computing in power system data disaster recovery service designed a framework and some modules of cloud computing resource management platform. Its goal is to realize the backup of ERP data of power companies, but not yet implemented.

A paper research and practice of power system cloud computing center preliminarily designed the system architecture of the power system simulation cloud computing center and the levels it belongs to: infrastructure clouds, data management clouds, and simulation computing clouds. A paper named future challenges and evolution of smart grid control centers discusses the challenges faced by the smart grid control center in the future, and proposes that the combination of the internet of things and cloud computing technology is the technical support of the new control center.

A paper named research on Hadoop-based smart grid condition monitoring data storage built a Hadoop cloud computing platform in the laboratory, designed and implemented a Hadoop-based power equipment condition monitoring storage system, and stored, keyword-queried, and parallel-processed dynamic time-series data, static data, and video data. Researches and tests of the system have verified the high reliability, good scalability, and performance advantages of data parallel access for cloud computing platforms.

A paper named smart grid big data processing technology status and challenges proposes to build a multi-level storage system for big data in the smart grid, but it is mainly aimed at historic data and cannot guarantee the processing of real-time data such as monitoring. In addition, State Grid ICT set up a big data team to tackle the big data challenge in smart grid construction. IBM collects and models big data to serve various energy industries and utilities such as smart

meter analysis, decision-based operation and maintenance, site selection based on weather data, and load forecasting and dispatching.

In summary, the storage system applied to the power grid was previously studied only for a single application. However, after the GIS system is applied to the power grid, its data has its own particularities, and its data has some characteristics different from ordinary data. In addition, there are other data services in the power system also have their own characteristics, so the research results of cloud computing in other industries can not be directly and effectively applied to the entire system using the cloud GIS smart grid. To solve this problem, this paper proposes a method of storing all kinds of data separately based on the classification based on the characteristics of the data in the GIS smart grid.

2. DATA CHARACTERISTICS

The core of power GIS system management is the power equipment. In order to describe, express and manage the equipment in the power system, it is necessary to add time, topology and other information in the traditional GIS to form the power equipment with space, attributes, topology, and operation integration model.

There are great differences in the storage structure, quantity, and operation of the four types of data in the power equipment: the device attribute data usually needs to be searched and queried according to different fields; the space data has a large amount of data and does not need to be frequently updated, and has higher spatial analysis. The requirements; topological data needs to be updated frequently, the connection relationship between equipment components is relatively complex, topology analysis often involves operations between multiple tables; equipment operation data collection frequency is high, the amount of data is large. Power GIS also manages metadata, rendering style data, power rules, etc. This type of data itself has a small amount of data, and the system needs to be acquired quickly and frequently. Complex query operations are required between tables.

In addition to the power GIS part, there are numerous marketing data in the smart grid such as electricity sales, average price of electricity sold, electricity bills receivable, electricity fee collection, and payment status. These data are similar to those of the GIS metadata and other types of data. The data volume is small, and all of them are structured data. The total amount of data is huge and complicated query operations are required between tables. In addition, because this part of the data is the enterprise core data, it must be ensured its reliability.

3. DATA STORAGE STRATEGY

According to the characteristics of various types of data described in Chapter 2, this paper divides the entire storage system into three parts. The structure of the system is shown in Figure 1.

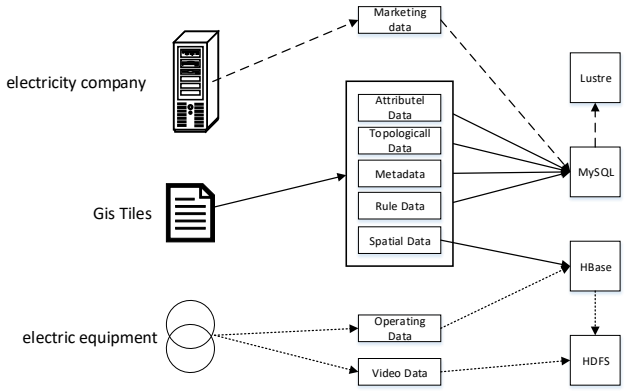

Figure 1: Storage System Framework

3.1. GIS data

The storage systems provided by cloud computing platforms are all non-relational (NotOnly SQL, No SQL) databases. Non-relational databases have slower data updates, do not support multi-table association queries, and do not provide indexes for relational databases, relations, and transaction processing functions. If you do not fully consider the characteristics of each type of data, blindly select the non-relational database for storage, it will affect the power GIS

data access performance. In fact, they are not contradictory, but they address data storage problems from two different perspectives. They complement each other.

Based on the characteristics of power GIS data and the advantages and disadvantages of the two types of databases, the grid data in the power GIS is processed through tile processing and stored in a distributed file system. Each tile is uniquely identified and a quick index is established. Stored paths are stored in a distributed database for unified management; the power device elements in the map are stored in a distributed database after being hierarchically processed, and a spatial index is established based on the spatial mapping relationship between the tiles and the elements, so that the user requests When spatial data of a region is used, an attribute query is used instead of a spatial query to avoid complicated spatial calculations.

Taking into account the limitations of non-relational databases, attribute data, topology data, metadata, and parameter data are stored in a relational database, making full use of the flexible retrieval features of relational databases to make up for deficiencies in non-relational database retrieval. This non-relational database is responsible for loading and displaying of spatial data, spatial analysis, and storage and analysis of massive operational data. Relational databases are responsible for the query of power equipment properties, topology analysis, and data management.

3.2. Electrical equipment operation data

The electrical equipment state detection system in the power system is mainly responsible for the real-time monitoring of electrical equipment for the external according to the real-time status information of these equipment to make corresponding control to achieve the purpose of maintaining the stability of the system or even through analysis to achieve system optimisation. Because the transformation of the power system state is often instantaneous, the real-time performance of the data monitored by the electrical equipment is very high. In addition, video monitoring of the status of electrical equipment has become a common method of condition monitoring, because the more HD and more details of the video can better reflect the status of the electrical equipment, so the requirements for the clarity of surveillance video are getting higher and higher. This has led to an increase in the amount of video surveillance data.

Since the NoSQL class database represented by HBase adopts a simple data model, compared with a traditional relational database, it has the characteristics of fast storage, high scalability, and random data structure, and is very suitable as a storage medium for operating data of electrical equipment. In addition, HDFS has the characteristics of large data processing and streaming file writing compared to the traditional file system and is very suitable as a storage medium for monitoring data.

3.3. Power system marketing data

Since the power company marketing data is the core data of the power company, it is mostly used for data mining of power marketing. Therefore, the data of a single time node is not a major operation object, and the data of one single time node constitutes a large file of a period of time. It is the main operating object for the user, in addition to the high reliability of the data.

Lustre is optimised for large file reads/writes, providing cluster systems with high performance I/O throughput, global data sharing environments, data storage location independence, redundancy for node failure, and clustering The reconfiguration or the quick recovery service when the server and the gateway are invalidated satisfies the needs of the high performance computing cluster system, and also satisfies the storage requirements of the power business marketing data. Therefore, the power marketing data of a single time node is first stored in a relational database according to its structure, and then it is integrated into a data file format and stored in the Lustre parallel file system.

4. TEST AND RESULT ANALYSIS

4.1. Test environment

Using four servers as hosts, the four hosts are connected by a 1 000 Mb/s switch. Each host machine virtualizes 2 computers, one of which is the Name Node management node, and the rest is used as the compute node Data Node. The virtual machine operating system is ubuntu16.04, and the configuration is 4 core CPU (Intel Core i5), clocked at 2.30 GHz, 8GB RAM, 500 GB hard disk. The experiment also prepared a server to test in a stand-alone environment, the operating system is Windows, and MySQL is installed on this host.

4.2. Data query

Experiments compare the data query performance of Stand-alone and Hadoop clusters under different data volumes. The experimental results are shown in Figure 2.

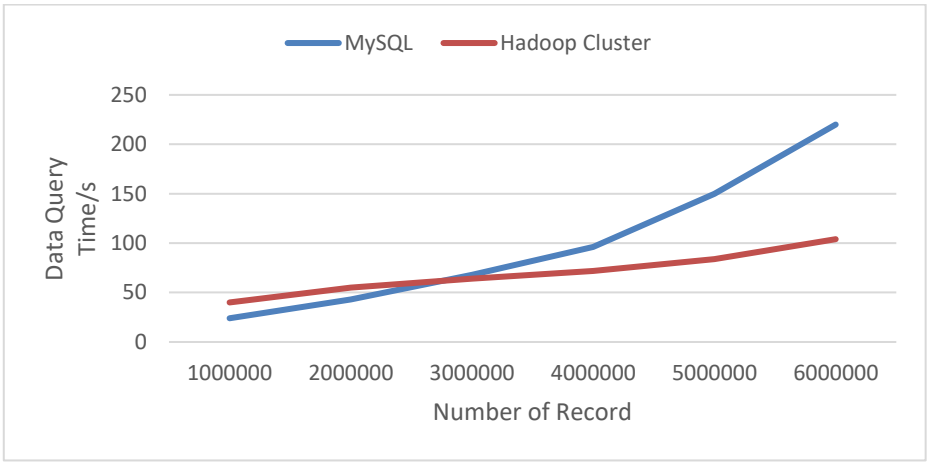

Figure 2: Data Query Time

As can be seen from the figure above, when the number of records is small, MySQL handles data query faster than Hadoop cluster, because MySQL provides a good data query mechanism. When the number of records is more than 3 million, advantages of in data processing are reflected.

5. CONCLUSION

This paper attempts to introduce a variety of storage methods into the field of power GIS data management. Based on the analysis of the characteristics of various types of data existing in smart grids that utilize cloud GIS, a data storage strategy based on classification is proposed. This storage strategy enables the stored data to have better performance in processing.

6. ACKNOWLEDGEMENTS

This research was supported by National Natural Science Foundation of China (61471162, 61501178, 61571182, 11605051, 41601399, 61601177); Program of International science and technology cooperation (2015DFA10940); Science and technology support program (R & D) project of Hubei Province (2015BAA115); PhD Research Startup Foundation of Hubei University of Technology (BSQD13029, BSQD13032, BSQD14028, BSQD14033); Open Foundation of Hubei Collaborative Innovation Center for High-Efficiency Utilization of Solar Energy (HBSKFZD2015005, HBSKFTD2016002).

7. REFERENCES

Fang X, Misra S, Xue G, et al, 2012. Smart Grid, the new and improved power grid: a survey. IEEE Communications Surveys and Tutorials (COMST), 14(4), 944-980.

Rusitschka S, Eger K, Gerdes C, 2010. Smart grid data cloud: a model for utilizing cloud computing in the smart grid domain//Smart Grid Communications (SmartGridComm), First IEEE International Conference. Gaithersburg, MD: IEEE, 483-488

Kawasoe S, Igarashi Y, Shibayama K, et al, 2012. Examples of distributed information platforms constructed by power utilities in Japan//CIGRE 2012. Paris, France: CIGRE, 108-113 .

Birman KP, Ganesh L, Renesse RV, 2010. Running smart grid control software on cloud computing architectures//Workshop on Computational Needs for the Next Generation Electric Grid, Cornell University. Ithaca, NY: DOE, 1-28.

Chen Q, Deng Q, 2009. Cloud computing and its key techniques. Journal of Computer Applications, 29(9),254-259.

Song Y, Zhou G, Zhu Y, 2013. Present status and challenges of big data processing in smart grid. Power System Technology, 37(4), 55-63 .

Zhang S, Han J, Liu Z, et al, 2009. Research on implementing spa-tial queries based on Map Reduce. Chinese High Technology Letters, 20(7), 70-74.

Wang D, Xiao K, Xiao L, 2013. Data warehouse of electric power equipment condition information based on Hive. Power System Protection and Control, 41(9), 130-135.

Xu X, Zhou J, Yang G, 2013. Data privacy protection mechanism for cloud storage based on data partition and classification. Computer Science, 40(2), 98-102.

Beraldi R, Massri K, Alnuweiri H, 2013. Erasure-coding based dissemination protocol for mobile clouds // 3PGCIC: 2013 8thInternational Conference on P2P, Parallel, Grid, Cloud and Internet Computing. Piscataway: IEEE Press, 416-421.

Jin P, Ou Y, Harder T, et al, 2012. AD-LRU: an efficient buffer replacement algorithm for flash-based databases. Data and Knowledge Engineering, 7(2), 83-102 .

209: The status and breakthrough of agricultural photovoltaic

Fangxin ZHANG[1], Ming LI[1], Xinyu ZHANG[1], Zhisen ZHANG[1], Tong WANG[1], Wen LIU[1,2*,] Jan INGENHOFF[2]

[1]Optics and Optical Engineering Department, USTC (University of Science and Technology of China), Hefei China
[2]Institute of Advanced Technology of USTC, Hefei China
**Corresponding author*

Environmental pollution and pollution haze are increasingly attracting the attention of government institutions. The Chinese government has made a commitment to the world: to vigorously develop non-fossil energies, of which solar energy is one of the most important clean energy. Because centralized photovoltaic power stations require large areas of land, most power stations are in the sparsely populated western region. But precisely because of that sparse population, solar power cannot be used locally where it is needed. Therefore, under the aspect of developing clean energy, the government has advised and encouraged the establishment of distributed photovoltaic power stations in densely populated eastern regions. However, in these densely populated areas, the per capita cultivated land is very limited. Under this background, new industries of photovoltaic agriculture have emerged. The construction of photovoltaic agricultural projects is not only happening in China, but also in Japan, Italy, Germany, and some other majorly important countries. However, problems which have seriously affected the growth of plants with traditional photovoltaic agriculture projects have become increasingly obvious. The traditional photovoltaic agriculture projects mainly adopt the following two methods: to place raised above the farm field polycrystalline silicon solar panels to achieve geometrical separation of sunlight or using amorphous silicon solar cells with inherent spectral characteristics to separate the sunlight. Neither of these two photovoltaic agriculture solutions match the spectrum requirement for photosynthesis of plants and this has gravely affected the quality and yield of crops. Thus, in China alone, the industrial scale of photovoltaic agriculture fell from a volume of 10 billion Yuan in 2015 to less than 1 billion Yuan in 2017. The solar spectrum separation technology of the team of Professor Liu Wen of University of Science and Technology of China accommodating an effective plant photosynthesis has solved the contradiction between simultaneous photovoltaic power generation and plant growth. The results show that this system scheme truly achieves the balance between plant growth and photovoltaic power generation. It can realize the efficient use of solar energy and land, save water resources, and improve the ecological environment. The introduction and promotion of this program may have far-reaching implications for agriculture, new energy and natural ecology in the future.

Keywords: agricultural photovoltaic, solar farm, spectrum separation

1. INTRODUCTION

Energy is one of the most important resources of human society. China has a very large population, but its per capita coal and oil reserves are much lower than the world's overall per capita reserves. At the same time, because of the low efficiency level of fossil energy, environmental problems arise. For example, in recent years, the pollution haze in China during autumn and winter is indisputably linked to the use of fossil fuels. This seriously affects people's health and daily life. Therefore, it is imperative to develop clean energy instead of traditional fossil energy (Lin, 2013; Zhang, 2010; Ma et al., 2005). China has abundant solar energy resources, and so far annual energy from solar based energy generation is equivalent to 2400 billion tons of standard coal (Zhan, 1988). The annual average radiation value in most parts of China is 1500kWh/m^2 (DNI). 2/3 of China's area annual sunshine duration can be above 2000 hours, which gives an enormous potential for photovoltaic development and application. Although China's photovoltaic industry started late, it has developed very rapidly thereafter. According to the data released by the National Energy Administration, the newly installed photovoltaic capacity in 2017 was 53.06 million kW, ranking first among renewable energy sources. As of the end of December 2017, the installed capacity of photovoltaic power generation in China has reached 130 million kW. However, due to the fact that most of the centralized PV power plants are located in sparsely populated areas, the situation of abandoning power has occurred from time to time. So the distributed photovoltaic has become a major highlight of China's photovoltaic market development (Li & Bao, 2018; Yuan, Xu, Zhang, Hu & Xu, 2014). In 2017, new installed capacity of distributed photovoltaic power station reached 19.4 million kilowatts, which Increased to 2.6 times last year, far exceeding the total installed capacity of distributed PV for five years. It can be predicted that this year's distributed PV will still maintain a relatively fast-growing rate. The National Energy Administration has strongly encouraged the development of distributed photovoltaic investment and construction in the 13th Five-Year Plan for Energy Development and the 13th Five-Year Plan for Renewable Energy. Distributed photovoltaic on the roof is limited to a confined number of roofs, so the village-level distributed photovoltaic will become an important development direction. Per capita arable land in China is only half of the world average. Therefore, ensuring agricultural output on the land is very important for the village-level distributed photovoltaic (Xue, 2017).

2. DEVELOPMENT STATUS AND PROBLEMS OF PHOTOVOLTAIC AGRICULTURE

Although the current photovoltaic agriculture is developing rapidly after September 2014, the State Energy Bureau has issued a notice on further implementation of the policy related to the implementation of distributed photovoltaic power generation (Liu, 2016). The accelerated development of photovoltaic agricultural industry is also closely related to the national support policy. President Xi Jinping has visited and inspected photovoltaic poverty alleviation and photovoltaic agriculture projects several times in the past two years (Ning, 2017).

But there are still a lot of challenges. The original intention of the development of photovoltaic agriculture is to develop the photovoltaic industry without affecting the plant growth, and to realize the efficient utilization of the sun light (Dinesh & Pearce, 2016). At present, the utilization of sunlight in photovoltaic agriculture can be mainly divided into two modes: geometrical splitting mode and intensity splitting mode (Jia, 2015; Hanergy, 2015; Scognamiglio, 2016).

1) Geometrical splitting mode: photovoltaic agriculture systems using a geometric light splitting are more common in photovoltaic agriculture. This construction of photovoltaic agriculture systems can currently be found in China, Japan, Italy and Germany (Rubio-Aliaga, Garcia-Cascales, Molina-Garcia & Sanchez-Lozano, 2017; Wu et al., 2018; Cossu et al., 2014). The problem is that there is either no light or uneven light on the farm land, consequently the actual lighting time is shortened resulting in critically affected crop yield and quality. This has become more and more serious, especially in areas where the land is already relatively scarce.

Figure 1: A geometrically polarized photovoltaic agricultural project

2) Intensity splitting mode: in this mode the photovoltaic cells use translucent thin film solar cells, such as copper indium selenium cells or cadmium telluride cells, which claim to be semi-transparent (Hanagy, 2015). But the common thin film solar cells have typically high absorption rates in the photosynthesis active spectrum of plants and therefore basically block the necessary plant light. Consequently, the quality of thin film solar cell technology is poor and additionally the photosynthesis of plants gets quite limited.

Figure 2: A photovoltaic agricultural project leveraging thin film solar cells

The application of spectral separation technology to photovoltaic agriculture is being studied by Sonneveld et al. of the Wageningen University in Holland. Indeed, they originally proposed the application of spectral separation to photovoltaic agriculture systems. In 2008, a greenhouse with spectral separation of photovoltaic power generation was setup (Sonneveld, Swinkels, Kempkes, Campen & Bot, 2006; Sonneueld et al., 2010). A coating on the green houses is used to reflect the 800nm-1200nm near infrared light and a photovoltaic system is used to generate power by concentrating and tracking the reflected light (Sonneveld, Swinkels & Bot, 2009). The roof of the greenhouse is made from parabolic arrays such as the reflectors in CPV systems. Thus, the coating on the groove surface can reflect the near infrared light and converge it onto the silicon modules.

Figure 3: Greenhouse photovoltaic system in Wageningen University of Holland

In 2008 -2009, Sonneveld et al. tested the system, and the annual PV power reached 20kWh/m^2. Due to the limitations of the coating reflection properties and the losses caused by the concentrator tracking system, the efficiency of the whole photovoltaic setup is only 3% (Sonneveld, Swinkels, Bot & Flamand, 2010). Because the efficiency is such low, it is difficult to apply this concept in practice. Moreover, the spectrum applied for plant growth is not accurate enough for efficient plant photosynthesis.

Another study by Loik et al. (2017) uses Wavelength-Selective Photovoltaic Systems (WSPVs) which combine luminescent solar cell technology with conventional silicon-based PV, thereby increasing efficiency and lowering the cost of electricity generation. WSPVs absorb some of the blue and green wavelengths of the solar spectrum but transmit the remaining wavelengths that can be utilized by photosynthesis for plants growing below. Numerous questions remain about the impacts of the light environment below WSPVs on plant growth for commercial crop production management or family home gardens. Results on photosynthetic and photo morphogenetic responses to growth under the dye shows that the transition of WSPVs to commercial use in greenhouse vegetable production will require better understanding of the potential impacts of WSPVs on growth across the huge diversity of crop species (Loik et al., 2017).

3. NEW PHOTOVOLTAIC FARM SOLUTIONS AND BREAKTHROUGHS

98% of sunlight energy is concentrated between 150nm ultraviolet light and 4000nm far infrared light. However, photosynthesis of plants can only use a small part of sunlight. The pigments involved in the process of absorption of photons are mainly chlorophyll A and chlorophyll B. The blue and red absorption peaks of chlorophyll A are 430 nm and 660 nm, respectively. The blue and red absorption peaks of chlorophyll B are 435 nm and 643 nm, respectively (Liu et al., 2018). It must be noted, that some other wavelengths may affect the plant growth negatively if not present. However, the required quantity of such other wavelengths is very small. The novel CPV based agriculture photovoltaic system will provide the missing wavelengths by scattered sunlight (15–20%) and satisfies the plants requirements. Therefore, it is theoretically feasible to separate the sunlight and pass through the light just needed by prosthesis. In response to these problems, Professor Liu Wen of University of Science & Technology of China proposed two solutions:

Project 1: A concentrating photovoltaic agriculture system based on the accurate spectrophotometry requirement of plant photosynthesis. In this scheme, an optical interference film is used to exactly match the transmittance spectrum with the absorption spectrum of plant photosynthesis, while the light reflection of all other wavelengths is used to generate electricity. The goal was to obtain an optical thin film with two transmission peaks at 660nm ± 20nm and 450nm ± 20nm. The reflectivity at all other wavelength was expected to be very high (~90%). Based on these requirements, a dielectric film has been designed as shown below. This film was suitable for the absorption spectra of plants and it will reduce the reflected radiation of sunlight reaching the solar cells by 17.21%. The output power of the solar cells will be cut by 19.44% through theoretical calculation (Liu et al., 2017).

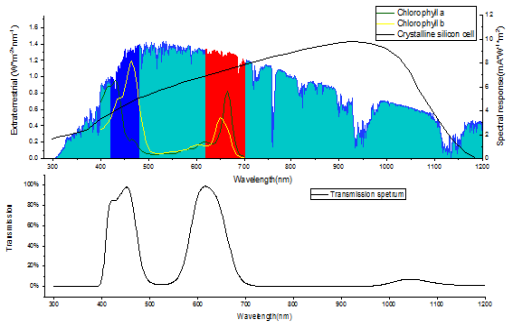

Figure 4: comparison of the transmittance spectrum between the interference film and the solar spectrum and the absorption curve of the crystalline silicon cell.

Because of the factors such as experimental conditions and cost control, it was decided to use two industrially existing polymer films with a simpler structure and stag them together. The spectrum of the two combined polymer films is shown in Figure 5a. It can be seen that film A has a better reflectivity in the 850–1150nm region, while film B has a better reflectivity in the 500–600nm region. By combining these two films, the blue curved transmission spectrum in Figure 5b is generated. The desired two peaks within the blue-light and red-light region are accomplished. The two films are manually attached to the bended glass panels.

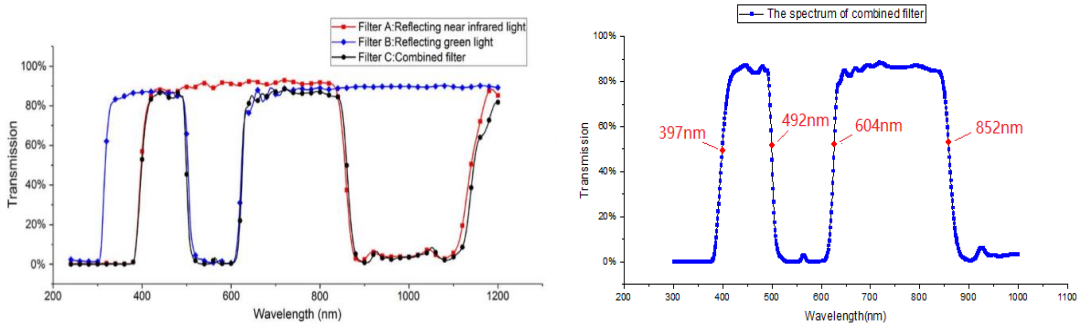

Figure 5: (a) The spectrum of the individual polymer films; (b) the spectrum of the combined polymer films

The experimental system is a concentrating system, and the plastic interference film is attached to parabolic glass panels. Red and near infrared light of 604nm-852nm and blue light of 397nm-492nm are irradiated on the lower plants by the polymer interference film, and the rest of the light is reflected by the polymer interference membrane into the focus of the parabolic glass panels carrying concentrated solar cells there.

Figure 6: PV projects have been completed in China

After measurement, the highest luminous efficiency of the system is 8.84%, and the average daily power generation efficiency is 8.37%. With a current reflected spectral range of the polymer film of 500–600nm and 850–1100nm, the agricultural photovoltaic system is ready to be used and field trials are in place. If the dichroitic polymer film is improved and multi-junction solar cells are deployed, this agriculture photovoltaic system has an enormous potential. The efficiency of the system could be as high as 14.7% using regular silicon solar cells (Antonini, Butturi, Zurru, Norton & Parretta, 2015) and as high as 30% using multi-junction GaAs/Ge solar cells (Pandey, Tyagi, Selvaraj, Rahim & Tyagi, 2016).

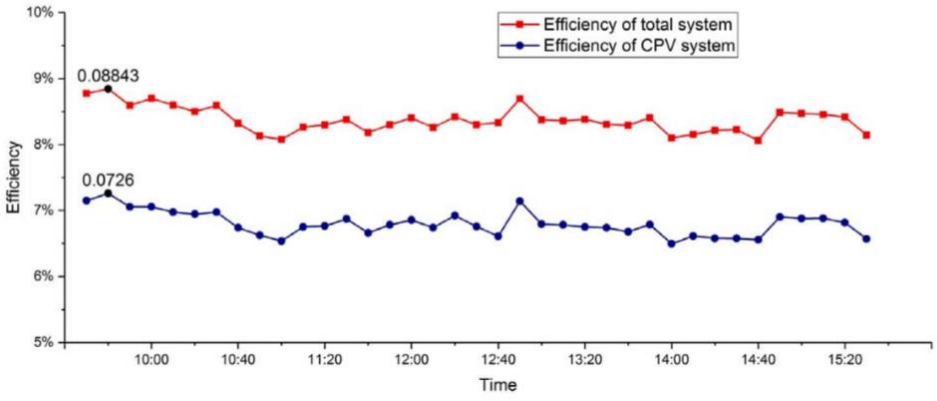

Figure 7: Test results of a PV module

At the same time, the red and blue light through the polymer interference film does not only affect positively the growth of crops, but also improves the quality and yield of crops (Ou et al., 2016). Through the cultivation and observation of three plants, such as lettuce, cabbage, cucumber and other plants, the plants under the polymer interference membrane were found to be better than the non-film control plants with respect to yield, quality and photosynthetic index. Compared with the existing photovoltaic greenhouses, the scheme has therefore a significant advantages in agriculture.

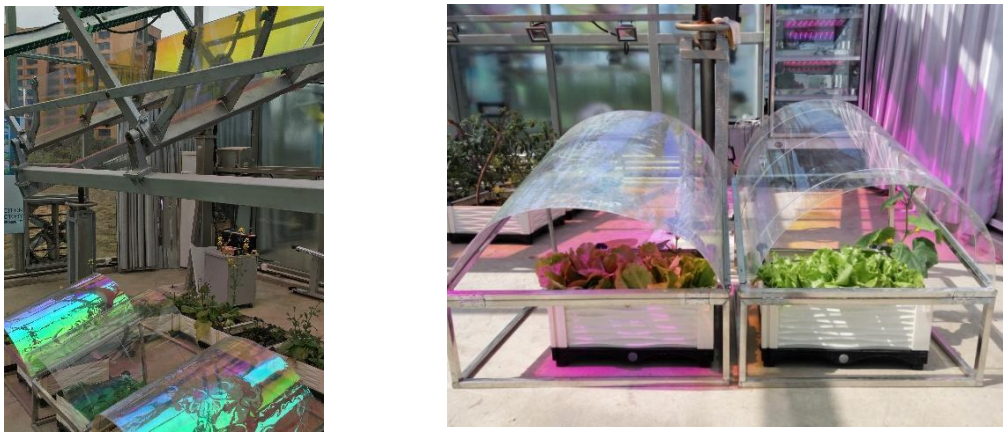

Figure 8: Light experiments with plants underneath our agriculture photovoltaic system

Table 1: Quantitative results of light experiments with plant under our agriculture photovoltaic system

	Lettuce		Cucumber		Water spinach	
	with film	without film	with film	without film	with film	without film
Height/cm	17.500	12.830	15.500	15.000	12.670	11.160
weight/g	24.719	19.382	13.416	10.626	5.135	4.615
Soluble sugar/(mg·g^{-1})	4.979	1.508	4.071	3.163	16.842	9.578
photosynthetic rate /(μmol·m^{-2}·s^{-1})	24.322	19.002	12.166	9.613	3.945	3.643

Project 2: A photovoltaic agricultural system with uniform light and adjustable intensity. The system solves the problem of non-uniform intensity of existing photovoltaic agriculture and can satisfy the growth of shade-requiring crops. By inserting a patterned glass in the middle of two conventional solar photovoltaic panels, the uniform lighting environment is realized for plants. The structure of the patterned glass as shown in Figure 9 allows the sunlight to be evenly distributed beneath both, the glass panel and the solar cell panels. This new scheme has applied for invention patent (ZL201810433650.3).

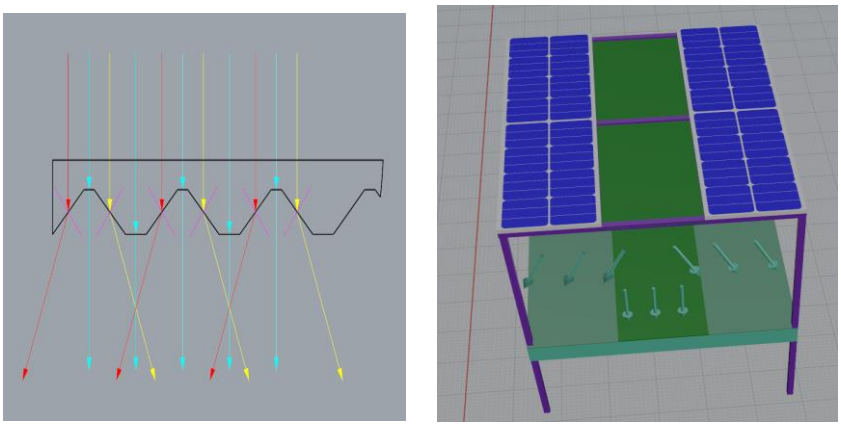

Figure 9: The structural distribution of the patterned glass and the PV pane

The length of the patterned glass should have the same dimensions as the conventional PV panels, but the width can be different. It can be adjusted accordingly to the illumination demand of the crop varieties below. The light transmittance decreases with the narrower widths but increases with large widths. The proportion of the solar panels and the glass can be 1:1, or 3:1. Different shade-plants have different requirements for the intensity of light, and the control of light intensity can make an enormous difference shade crops quality and growth conditions.

Table 2: Light intensity ratio of transmittance when size of the solar panels and the glass is 1:1

	Left shadow	Middles shadow	Right shadow
only PV panels	12%	12%	12%
PV panels with patterned glass	30%	36%	30%
Increase the transmittance	18%	24%	18%

The angle between the side wall and the vertical direction of the grooves on the lower surface of the groove glass distributor can be 45 degrees, 30 degrees or 60 degrees. At different angles, the height of solar photovoltaic panels components should be adjusted accordingly, so that the scattered light can evenly cover the lower part of the photovoltaic panels when the solar light is vertically incident at noon.

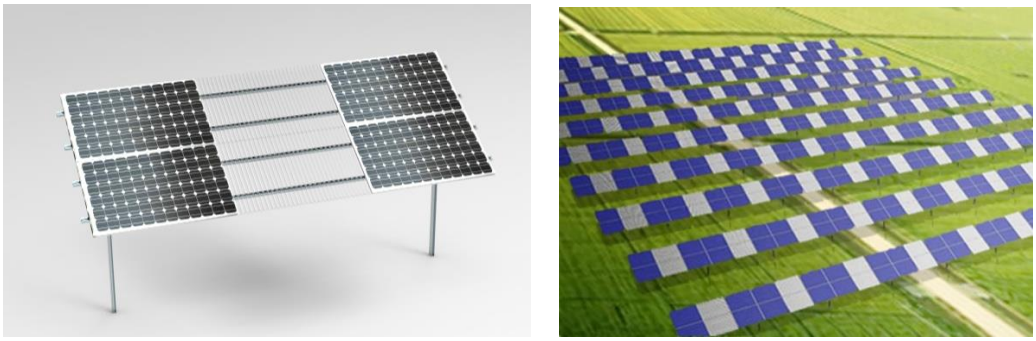

Figure 10: Schematic diagram of the principle of smoothing

Compared with the existing photovoltaic agriculture technology, the beneficial effect of this new scheme is that the light splitter is realized through the splitter of the trough glass, and the sun can be evenly distributed beneath the two sides and the middle trough glass area. Consequently, the photosynthesis of the crops is optimised. Thus, this photovoltaic agricultural system can be perfectly located on any farmland. The present invention can control the proportion of the light transmittance by adjusting the proportion of the area of the trough glass splitter, allowing to change the light intensity for the crops beneath the solar photovoltaic modules in the range of 35% and 65%. The invention also helps effectively to reduce the water evaporation of the agricultural land, avoiding lack of water during droughts. It is of great significance to improve agricultural strength in deprived areas. Test systems are currently installed in the Anhui province of China and experimental results are gathered. Furthermore, laboratory studies are under way to examine the homogenous growth of regular and shadow-corps beneath this novel system. Compared to the option 1 using concentration photovoltaic this second technique maybe a little easier to implement and be more cost effective.

4. SUMMARY AND CONCLUSION

In the future, village-level photovoltaic agricultural power stations have gradually become the main form of photovoltaic power stations, and even may be the only form of photovoltaic power stations. Agriculture photovoltaic is a promising and trend-setting technology which already has led into a beginning industrial innovative revolution (Xue, 2017; Hu & Liu, 2018). Solving existing problems, we present in this paper novel, unique and completive developments in this field. Applying concentrating photovoltaic (CPV) or regular photovoltaic (PV) and diffractive interference technology, innovative systems for agriculture photovoltaic have been demonstrated. These systems allow utilizing agricultural land and at the same time generate electricity in a cost competitive way compared to regular solar panels blocking the land from agricultural use. We have built the systems and they have an average daily power generation efficiency about 8.37%. Now the current reflected spectra area of the film for the PCV type approach is about 500nm-600nm and 850nm-1100nm. If we improve the film for spectrum separation and deploy multi-junction solar cells, this novel system and its photoelectric transformation efficiency has still an enormous potential to be increased. The efficiency of the system could be as high as 16% for regular silicon solar panel. The system may increase up to 30% with multi-junction GaAs/Ge based solar cells (Loik et al., 2017). Combined with this new agriculture photovoltaic technology, the CPV technology may get new “kinetic energy” to turn again into a rapid deployment period. The vegetables under the film grow faster and have a better quality. As for the PV type using trough patterned glass plates we can greatly and very flexibly adjust light irradiation for shade-requiring crops. Photovoltaic agricultural (APV) systems delivering uniform light and adjustable intensity belong to the intermediate solution of village-level photovoltaic agricultural power stations while concentrating photovoltaic (CPV) agriculture systems are based on the accurate spectrophotometry requirement of plant photosynthesis. Spectral separation is considered as the ultimate solution for photovoltaic agriculture industry (Li, 2018).

5. ACKNOWLEDGEMENTS

This work was supported by the Major Project of Science and Technology of Anhui Province under grant 16030701093.

6. REFERENCES

Antonini, A., Butturi, M. A., Zurru, P., Norton, M., & Parretta, A. (2015). Development of a high/low concentration photovoltaic module with dichroic spectrum splitting. *Progress in Photovoltaics, 23*(9), 1190-1201. doi:10.1002/pip.2532

Cossu, M., Murgia, L., Ledda, L., Deligios, P. A., Sirigu, A., Chessa, F., & Pazzona, A. (2014). Solar radiation distribution inside a greenhouse with south-oriented photovoltaic roofs and effects on crop productivity. *Applied Energy, 133*, 89-100. doi:10.1016/j.apenergy.2014.07.070

Dinesh, H., & Pearce, J. M. (2016). The potential of agrivoltaic systems. *Renewable & Sustainable Energy Reviews, 54*, 299-308. doi:10.1016/j.rser.2015.10.024

Hanergy (2015). Hanergy Holdings Hanergy Solar Film Technology Application in Agriculture. *Agricultural Engineering Technology (Greenhouse Horticultur*e) (10), 70-72.汉能控股 汉能太阳能薄膜技术在农业领域中的应用. (2015). *农业工程技术(温室园艺)*(10), 70-72.

Hanergy (2015). The advantages of Hanergy solar film applied to greenhouses. (2015). *Agricultural engineering technology (greenhouse gardening)* (19), 6.汉能太阳能薄膜应用于温室大棚的优势. (2015). *农业工程技术(温室园艺)*(19), 6.

Hu Runqing, & Liu Jiandong. (2018). 2017 Photovoltaic Power Generation Market Review and Outlook. *Solar Energy* (01), 14-18.胡润青, & 刘建东. (2018). 2017 年光伏发电市场回顾和展望. ***太阳能*** (01), 14-18.

Jia Qi. (2015). Prosperous NEC vigorously develops modern agriculture and takes safe and efficient green development. *Agricultural Engineering*(05), 6.嘉琦. (2015). 昌盛日电大力发展现代农业 走安全高效绿色发展之路. *农业工程* (05), 6.

Liu, L. Q., Guan, C. G., Zhang, F. X., Li, M., Lv, H., Liu, Y., . . . Liu, W. (2017). A Novel Application for Concentrator Photovoltaic in the Field of Agriculture Photovoltaics. *13th International Conference on Concentrator Photovoltaic Systems (Cpv-13), 1881*. doi:Unsp 080008-110.1063/1.5001446

Li Lijun, *Electricity and Energy*. (2018-05-14). Spectral separation technology promotes photovoltaic agricultural innovation, p. 020. 李丽旻, ***电力与能源***. (2018-05-14). 光谱分离技术助推光伏农业创新, p. 020.

Loik, M. E., Carter, S. A., Alers, G., Wade, C. E., Shugar, D., Corrado, C., . . . Kitayama, C. (2017). Wavelength-Selective Solar Photovoltaic Systems: Powering Greenhouses for Plant Growth at the Food-Energy-Water Nexus. *Earth's Future, 5*(10), 1044-1053. doi:10.1002/2016ef000531

Li Peng, & Bao Jingwen. (2018). Open a new journey for the development of the photovoltaic industry. Solar Energy (03), 23-28. 李鹏, & 包婧文. (2018). 开启光伏产业发展新征程. ***太阳能***(03), 23-28.

Liu, W., Liu, L. Q., Guan, C. G., Zhang, F. X., Li, M., Lv, H., . . . Ingenhoff, J. (2018). A novel agricultural photovoltaic system based on solar spectrum separation. *Solar Energy, 162*, 84-94. doi:10.1016/j.solener.2017.12.053

Liu, Y. P. (2016). The Development Status and Countermeasures of Photovoltaic-Ecological Agriculture in China. *Light & Engineering, 24*(3), 91-94.

Lin Zhiqin. (2013). China's long-term energy environment development strategy. China Soft Science (12), 45-57. 林智钦. (2013). 中国能源环境中长期发展战略. *中国软科学*(12), 45-57.

Ma Shenghong, Zhao Yuwen, Wang Sicheng, Kong Li, Li Anding, Zhu Ruizhao, . Bai Jianhua. (2005). The strategic position and future development direction of photovoltaic power generation in China's power energy structure. China Energy (06), 24-32. 马胜红, 赵玉文, 王斯成, 孔力, 李安定, 朱瑞兆, . . . 白建华. (2005). 光伏发电在我国电力能源结构中的战略地位和未来发展方向. *中国能源*(06), 24-32.

Ning Xiang. (2017). The status quo and development prospects of domestic distributed photovoltaic power generation industry. Energy saving (11), 14-19. 宁翔. (2017). 国内分布式光伏发电产业现状与发展前景. *节能*(11), 14-19.

Ou Langqing, He Zili, Liu Luqing, Qian Dazhao, Zhang Fangxin, Li Ming, . . Liu Wen. (2016). Effect of Red and Blue Two-channel Filter Membrane on Plant Growth. Journal of Plant Physiology(12), 1909 -1914. 欧浪情, 何子力, 刘路青, 钱大憨, 张放心, 李明, . . . 刘文. (2016). 红、蓝双通道滤光膜对植物生长的影响. *植物生理学报*(12), 1909-1914.

Pandey, A. K., Tyagi, V. V., Selvaraj, J. A. L., Rahim, N. A., & Tyagi, S. K. (2016). Recent advances in solar photovoltaic systems for emerging trends and advanced applications. *Renewable & Sustainable Energy Reviews, 53*, 859-884. doi:10.1016/j.rser.2015.09.043

Rubio-Aliaga, A., Garcia-Cascales, M. S., Molina-Garcia, A., & Sanchez-Lozano, J. M. (2017). Geographic Information System for Optimisation and Integration of Photovoltaic Solar Energy in Agricultural Areas with Energy Deficiency and Water Scarcity. *Project Management and Engineering Research, Aeipro 2016*, 181-197. doi:10.1007/978-3-319-51859-6_13

Scognamiglio, A. (2016). 'Photovoltaic landscapes': Design and assessment. A critical review for a new transdisciplinary design vision. *Renewable and Sustainable Energy Reviews, 55*, 629-661. doi:10.1016/j.rser.2015.10.072

Sonneueld, P. J., Swinkels, G. L. A. M., Campen, J., van Tuijl, B. A. J., Janssen, H. J. J., & Bot, G. P. A. (2010). Performance results of a solar greenhouse combining electrical and thermal energy production. *Biosystems Engineering, 106*(1), 48-57. doi:10.1016/j.biosystemseng.2010.02.003

Sonneveld, P. J., Swinkels, G. L. A. M., & Bot, G. P. A. (2009). Design of a Solar Greenhouse with Energy Delivery by the Conversion of Near Infrared Radiation - Part 1 Optics and PV-cells. In Y. Tuzel, G. B. Oztekin, & M. K. Meric (Eds.), *International Symposium on Strategies Towards Sustainability of Protected Cultivation in Mild Winter Climate* (Vol. 807, pp. 47-53).

Sonneveld, P. J., Swinkels, G. L. A. M., Bot, G. P. A., & Flamand, G. (2010). Feasibility study for combining cooling and high grade energy production in a solar greenhouse. *Biosystems Engineering, 105*(1), 51-58. doi:10.1016/j.biosystemseng.2009.09.012

Sonneveld, P. J., Swinkels, G. L. A. M., Kempkes, F., Campen, J. B., & Bot, G. P. A. (2006). Greenhouse with an integrated NIR filter and a solar cooling system. In B. J. Bailey, J. J. PerezParra, J. I. Montero, & B. J. Bailey (Eds.), *Proceedings of the International Symposium on Greenhouse Cooling* (pp. 123-+).

Wu Nan, Zhang Yaobang, Qi Wei, Zhang Cunbin, & Yuan Yu. (2018). Photovoltaic power generation + agriculture Unlock new models of agricultural development. Vegetables (04), 1-7. 吴楠, 张耀邦, 佘炜, 张存斌, & 袁婧. (2018). 光伏发电+农业 解锁农业发展新模式. *蔬菜*(04), 1-7.

Xue, J. L. (2017). Photovoltaic agriculture - New opportunity for photovoltaic applications in China. *Renewable & Sustainable Energy Reviews, 73*, 1-9. doi:10.1016/j.rser.2017.01.098

Yuan, J., Xu, Y., Zhang, X., Hu, Z., & Xu, M. (2014). China's 2020 clean energy target: Consistency, pathways and policy implications. *Energy Policy, 65*, 692-700. doi:10.1016/j.enpol.2013.09.061

Zhan Shuqin. (1988). Solar thermal radiation and biomass energy. *Solar energy* (04), 6-7. 战树勤. (1988). 太阳热辐射和生物量能源. *太阳能*(04), 6-7.

Zhang Yipeng. (2010). Development and Utilization of New Energy under the Background of Low-carbon *Economy. Chinese and Foreign Energy* (11), 28-32. 张一鹏. (2010). 低碳经济背景下的新能源开发和利用. *中外能源*(11), 28-32.

210: The prioritization of influencing effect on different income households' energy-saving behaviour

Wenbin DING[1], Yijie SU[2]

[1] *Hubei University of Technology, Wuhan, 10843414@qq.com*
[2] *Hubei University of Technology, Wuhan, 623702134@qq.com*

We investigate the factors influencing households' energy-saving behaviour choices. We first present a theoretical model of energy saving behaviour and energy saving willingness to determine the factors that explain households' energy consumption. Then we use ordered logistic model to discover the influencing factors of energy saving intention in different income households. Our results show the following :(1) Residents' energy-saving willingness is influenced by scenario factors and behavioural abilities. Scenario factors are more likely to influence residents' willingness to save energy than behavioural factors. (2) The acceptance of publicity and education is of great significance for promoting energy conservation, and social norms have the same effect while the former is more influential. (3) Age does not affect the energy-saving willingness. Sex of the household head can affect their willingness to save energy, in which women are more willing than men to implement relevant energy saving behaviours. (4) Energy-saving cognitive ability has a direct and significant positive impact on residents' energy-saving behaviour, but its marginal effect is much lower than the scenario factor and also lower than the energy-saving behavioural factors. According to the conclusions, we suggest some advices for better energy consumption patterns.

Keywords: Energy-saving behaviour ; Order logistic model; Energy-saving willingness

1. INTRODUCTION

Nowadays, energy resource plays a more and more significant role in promoting economic improvement and social progress. Cities are the heart of China's economic development and the main gathering areas for population, industry, and economy. As the technology develops rapidly, cities have become the main consumers of energy in the country, with energy consumption accounting for 60% of the national total. Among them, residents' energy consumption takes the main percentage of urban energy consumption. Along with the improvement of human welfare and the acceleration of urbanization, using resource brought problems of climate change and environmental pollution, making it an international issue for human being to pay attention to. Residents, as the main consumers of life energy and end consumers of energy-consuming industrial products, have great potential for energy saving and emission reduction in their lifestyle.

The study finds that residents' energy-saving willingness is influenced by scenario factors such as social norms and publicity & education and other behavioural ability factors such as cognitive ability; on the other hand, individual differences among residents have become an important factor in regulating individual behaviour, such as education, ages, sex. However, consumers with different income levels have different choices of using energy resource. In order to keep the trend with the society development, doing this research can provide policy suggestions for China's overall energy development plan, speed up the construction of "beautiful China", and deepen the concept of low-carbon life.

2. LITERATURE REVIEW

2.1. Theoretical foundations

The study of energy-saving behaviour involves a wide range of fields, including economics, management, psychology, sociology, environmental science and many other disciplines and has evolved many theories. The classical research model in the field of consumer behaviour is the Howard-Sheth Model (Howard and Sheth, 1969), which uses four variables to measure consumer purchasing behaviour: input variables, extrinsic variables, intrinsic processes, and outcome variables. Consumers form the purchase motivation after receiving the stimulus and make the final purchase decision. The Theory of Planned Behaviour (Ajzen, 1991) believes that human behaviour is the result of a well-thought-out plan. Individual behavioural attitudes, subjective norms and behavioural control cognition influence their behaviour patterns, their own psychological characteristics factors, environment and behaviour of others influence their behavioural intentions. The ABC theory shows that psychological factors and external factors control and predict individual behaviour jointly. The theory stems from Guagnano's 1995 study of household garbage collection behaviour. The study found that garbage collection behaviour (B) is the individual's attitude towards the behaviour (A). Interacts with the external environment (C) and ultimately acts on the results of the behaviour. The Value Belief Norm Theory (VBN) explains the formation and evolution mechanism of environmental behaviour through the synergy between the three variables of values, beliefs and norms (Stern et al., 1999).

As the development of research, sociology and environmental science have gradually divided into two main theoretical perspectives on the induction of environmental behaviour: one starts from the subject of behaviour and individual’s Intrinsic factors. Another starts from the external social structure, emphasizing that environmental behaviour is the external overall environment affecting individual behaviour. Therefore, the literature review of energy saving behaviour and willingness is mainly described in the two major research areas of the individual's internal factors and external situation factors.

2.2. Individual intrinsic factors

The analysis focuses on the individual characteristics related to energy saving behaviour including demographic characteristics knowledge, ability and willingness (Shi, 2016). Based on the survey data of 470 urban residents in Fuzhou, Fujian Province, they analyse the impact of low-carbon policies on urban residents' energy-saving behaviour and find that a series of low-carbon policies will not only directly affect it, but it will also be affected by some control variables such as values, mentality and age, average monthly income. Lv (2016) builds a theoretical framework of the influencing factors of urban residents' energy-saving behaviours based on the TPB, through questionnaires and structural equation models they find that energy-saving habits have a direct positive effect on energy-saving behaviour; economic factor plays a negative regulatory role in the conversion of energy-saving willingness into energy-saving behaviours. Ding (2015) uses 330 valid survey questionnaires in Wuhan and the structural equation model to make an empirical study on public awareness and acceptance of solar PV power generation. Public awareness of energy conservation has a significant positive impact on their awareness of solar photovoltaic power generation and the willingness to adopt solar-photovoltaic-power-generating equipment.

2.3. External situation factors

Identify strategies for making energy conservation activities more widely publicized and mobilized in specific environments, that is, external environmental factors that are incentivizing the implementation of energy saving

behaviours by the main body. These characteristics include reward and punishment mechanisms, social norms, and propaganda measures. Through investigating knowledge workers in office buildings, (Zhang , 2013) based on the theory of psychological ownership and TPB to establish a theoretical model, they find that attitudes are positively affecting employees to save energy, energy-saving attitudes completely influence the willingness, external publicity, perceived behaviour control and subjective norms have a positive effect on the establishment of energy saving attitudes. Based on the TPB, Mi (2016) built a theoretical model of psychological motivation for low-carbon energy consumption behaviours of urban residents. They obtained 710 valid survey questionnaires of urban residents in Xuzhou City, Jiangsu Province. Through the structural equation model, residents' low-carbon energy consumption behaviour is directly influenced by low-carbon behavioural willingness and residents' subjective norms, perceptual behaviour control, and altruistic values indirectly drive behaviours by influencing low-carbon willingness.

3. DATA SOURCE AND DESCRIPTION

We design the questions based on “Energy Conservation and Emission Reduction Handbook for the Public”. The content concerns the daily energy-saving behaviour of residents, knowledge of energy-saving, environmental responsibility, and sensitivity to energy issues etc, in order to study residents' energy-saving behaviour and energy-saving willingness. All questionnaires were distributed in web form , with all samples collected from January to September 2017. After invalid questionnaires were deleted, we finally got 498 valid samples, with the effective recovery rate at 99.6%.

3.1. Sample characteristics

It can be seen that most of interviewees are from urban area, their age tends to be young, moreover, they have generally the higher education level and more stable income. The basic situation of the investigators is relatively reasonable and distributed evenly in each category. Among the 498 interviewees, 64.66% of the total samples were male; 43.98% of households were 40-50 years old, followed by 18-30, which was 34.14%; most householders had a college education level or above, which accounted for 41.57%, only 9.24% of them had primary education or below; the family net income was the sum of income after all the expenses of the year per person, the number of each income level was relatively balanced, but in detail, 5000-10000 yuan (16.06%) and over 20,000 yuan (15.26%) of the households took relatively large percentages. However, the questionnaire was issued as a web page and it was impossible to investigate unconditional Internet users. As a result, the qualifications of the surveyed household heads were generally high, and the scope of respondents was limited.

Table 1: Summary number and percentage of the basic statistics

Category		Frequency	Percentage
Sex	Male	322	64.66%
	Female	176	35.34%
Age	Under 18	24	4.82%
	18-30	170	34.14%
	30-40	24	4.82%
	40-50	219	43.98%
	50-60	41	8.23%
	Above 60	20	4.02%
Education of the head of family	Primary school and below	46	9.24%
	junior high school	133	26.71%
	High school	112	22.49%
	University and above	207	41.57%
family net income (per person per year)	under2000	60	12.05%
	2000-3000	67	13.45%
	3000-4000	50	10.04%
	4000-5000	64	12.85%
	5000-10000	80	16.06%
	10000-15000	60	12.05%
	15000-20000	41	8.23%
	above20000	76	15.26%

3.2. Statistical analysis of relevant factors

Energy-saving behaviours.

(1) Whether the user will take the power-saving behaviour. 52.81% of the respondents said that they would turn off the lights most of the time when they leave the room. 34.94% of users often pay attention to avoid or reduce the use of air-conditioning. 36.95% of residents choose to reduce the frequency of opening and closing the refrigerator door. It can be seen that only a small part of the respondents do not pay attention to these energy-saving details. (2) Whether the user will choose bath instead of tub. 58.43% of respondents will do it every time, which may be related to family life habits. (3) Whether the user will use the daily public transport, such as taking bus, cycling. 53.21% of residents said most of the time will do. 21.89% of residents said they would do it every time. The result suggests that most residents will take "green travel" as an energy-saving act.

Table 2: Descriptive analysis of energy-saving behaviour

		Never	occasionally	About half	Mostly	every time
X1	sample number	0	26	25	263	184
	Percentage(%)	0	5.22	5.02	52.81	36.95
X2	sample number	21	86	110	174	107
	Percentage(%)	4.22	17.27	22.09	34.94	21.49
X3	sample number	15	62	83	218	120
	Percentage(%)	3.01	12.45	16.67	43.78	24.10
X4	sample number	6	46	72	265	109
	Percentage(%)	1.20	9.24	14.46	53.21	21.89
X5	sample number	6	46	72	265	109
	Percentage(%)	1.20	9.24	14.46	53.21	21.89

Scenario factors

(1) Whether the user thinks television media and other propaganda can affect energy-saving behaviour. 52.61% said they agreed, but only 8.23% of the residents totally agreed，this shows that the TV media can affect the energy-saving behaviour but the effect is not obvious. (2) Whether the user thinks their family, friends, and teachers and so on person (and others) can affect their own energy-saving behaviour. 62.85% of the residents agree with this view, from the sample sharing 3.72 can be seen, around the use of energy-saving practices can affect the user's own energy-saving behaviour.

Table 3: Descriptive analysis of scenario factors

		strongly disagree	disagree	Neither agree or disagree	Agree	Strongly agree
X8	sample number	28	139	174	128	29
	Proportion(%)	56.22	27.91	34.94	25.70	5.82
X9	sample number	70	227	113	62	26
	Proportion(%)	14.06	45.58	22.69	12.45	5.22

Behavioural factors

(1) Whether the user thinks that implementing energy-saving activities is a waste of time. The average of the survey results is 2.42, indicating that more than half of the residents disagree with this view, residents have a correct understanding of energy-saving behaviour. (2) Whether the user thinks that the pursuit of personal preference or lifestyle is far more important than the change themselves in order to save energy. 45.58% of the residents disagree, visible energy conservation has become an important concept of deep popular. (3) Does the user think that implementing energy-saving behaviour would disrupt their lifestyle and habits. 49.2% of the residents disagree, indicating that the residents to implement energy-saving behaviour have no more important impact on their own lifestyle and habits. (4) Whether the user pays more attention to the comfort and convenience of life instead of energy problem. Sample average score 2.98, 34.94% of the users choose "uncertain", and they have some hesitation in weighing their own life and energy issues. (5) Does the user think it is necessary to develop the economy before considering energy

saving and environmental protection. 41.37% of the residents disagree that residents hold the right idea in the face of serious environmental problems.

Table 4: Descriptive analysis of behavioural factors

		strongly disagree	disagree	Neither agree or disagree	Agree	Strongly agree
X10	sample number	58	245	139	41	**15**
	Proportion(%)	11.65	49.2	27.91	8.23	**3.01**
X11	sample number	201	206	46	28	**17**
	Proportion(%)	40.36	41.37	9.24	5.62	**3.41**
X12	sample number	40	262	136	48	**12**
	Proportion(%)	8.03	52.61	27.31	9.64	**2.41**
X13	sample number	8	46	141	262	**41**
	Proportion(%)	1.61	9.24	28.31	52.61	**8.23**
X14	sample number	7	47	78	313	**53**
	Proportion(%)	1.41	9.44	15.66	62.85	**10.64**

4. RESEARCH METHODOLOGY

4.1. Model setting and variable selection

Based on previous research results, we construct a theoretical model to analysis the priority order of factors that affect energy saving intention. It also analyses the impact of energy-saving scenario factors and behavioural capabilities on energy-saving willingness and the process that leads to energy-saving behaviour choices. Ordered Logistic model is an appropriate choice considering the choice of priority order.

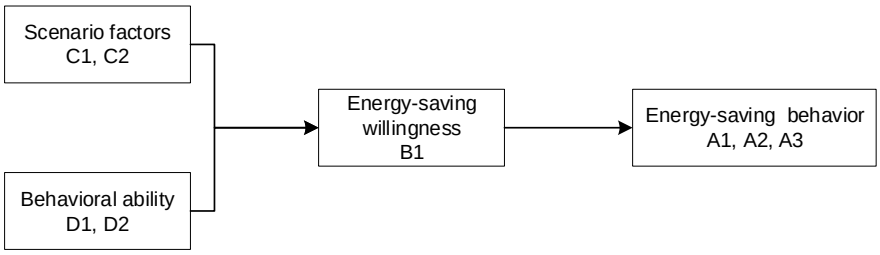

Figure 1: The theoretical model of residents' energy-saving behaviour and energy-saving willingness

This survey used the form of online questionnaires and described various specific energy-saving behaviour to make the choice easier. We used the Likert scale to perform 1-5 grade points and divided the relevant degree of recognition of energy-saving into 1-5 grades to make the respondents convenient. Each question required the respondent to choose from the frequency of 1 (never done) -5 (every time) according to their actual situation to judge their energy-saving behaviour. For the residents' energy-saving intention, a scale from 1 (totally disagree)-5 (strongly agree) was used to score items to determine the acceptance of the problem. According to the theoretical model, the specific variables selected are as follows.

Table 5: Measure indicators of formal scales

Potential variables	Observation variables	Variable name	Variable substitution	Average	Standard deviation
Energy-saving behaviour	Save electricity A1	·Close the lamp when you leave the room	X1	4.21	0.76
		·Avoid or reduce the use of air conditions	X2	3.52	1.13
		·Try to reduce the times of opening the door when got food in refrigerators	X3	3.73	1.05
	Save water A2	·Choose shower instead of basin bath	X4	4.34	0.96
	Green travel A3	·Use daily public transport such as buses, bicycles or walking.	X5	3.85	0.91
Energy-saving willingness	B1	· I am willing to sacrifice my personal interests in order to save energy and protect the environment,	X6	3.27	0.83
		·I am willing to try my best to improve or solve certain environmental problems	X7	3.84	0.92
Scenario factors	Publicity and education C1	·Tv media publics promote energy conservation, affecting individual energy conservation behaviour	X8	3.57	0.83
	Social norms C2	·Family members, friends, teachers and others' behaviours will affect individuals' energy-saving behaviours	X9	3.72	0.83
Behavioural factors	Cognitive ability D1	·Implementing energy-saving behaviours is a waste of time	X10	1.9	1.01
		·Pursuing your own lifestyle and habits is more important than changing yourself to save energy	X11	2.42	0.91
		·Energy-saving behaviour disturbs my lifestyle and habits	X12	2.46	0.87
	Ability to select D2	·First develop the economy and then consider energy consumption	X13	2.98	1
		·Compared with the energy problem, I pay more attention to the comfort and convenience of life	X14	2.49	1.05

4.2. Ordered logistic regression analysis

The results show that residents' willingness to save energy is affected by scenario factors and behavioural factors.

Under the condition of controlling other variables, for every additional unit of propaganda and education, the willingness to save energy will increase by 0.44 logit units in a good direction while the social norms will only have 0.248 logit units. In the context, contextual factors have a greater impact on energy saving intentions. The willingness to save energy has a direct impact on residents' energy-saving behaviour. The stronger residents' willingness to save energy, the greater the possibility of adopting actual energy-saving behaviour and it mainly drives residents to adopt energy-saving behaviour and green travel. social norms are positively correlated with residents' willingness to save energy. This means that residents are more subject to social regulation and the higher the frequency of publicity, the stronger their willingness to save energy. It can be seen that publicity and behavioural norms at the social level are important factors influencing energy saving intentions, and that publicity and education are more influential than social norms.

With a one-unit increase in performance capacity, the willingness to save energy will increase 0.296 logit units in a good direction, and the recognition ability will have no significant effect on the willingness to save energy.

Age does not affect the willingness to save energy, and so does gender and education.

From the perspective of ordered logitistic regression, the order of influence of energy saving behaviours for households with different income priorities is propaganda and education, energy-saving ability to select, and social norms.

Table 3: Results of logistic regression

Variables	(1) B1	(2) B1
C1	0.44***	
	(0.122)	
C2	0.248**	
	(0.121)	
D1		-0.156
		(0.153)
D2		0.296**
		(0.143)
Sex	0.27	0.296
	(0.34)	(0.337)
Age	0.234	0.289
	(0.18)	(0.179)
Education	0.309	0.309
	(0.235)	(0.234)
Family	0.174**	0.163**
	(0.08)	(0.079)
Income	-0.24	-0.266*
	(0.15)	(0.15)
Prob > chi2	0.0000	0.0169
Constant cut1	-2.59	-4.37
	(1.231)	(1.22)
Constant cut2	0.513	-1.275
	(0.752)	(0.727)
Constant cut3	2.9	1.079
	(0.737)	(0.706)
Constant cut4	5.685	3.762
	(0.776)	(0.73)

Standard errors in parentheses

*** p<0.01, ** p<0.05, * p<0.1

5. CONCLUSIONS AND SUGGESTIONS

After testing the 498 valid questionnaires, we constructed a theoretical model of residents' energy-saving behaviour and willingness. Through ordered logistic regression model, we obtained the research results: publicity and education in scenario factors and social norms had a significant positive impact on energy-saving willingness; Residents' cognitive ability has no significant effect on the willingness to save energy. Age does not affect the willingness to save energy, and so does gender and education. According to the actual situation, we propose the following suggestions：

Firstly, the government needs to increase the propaganda about green and low carbon knowledge and strengthen extensive education in energy conservation.

The research result shows that the higher level of publicity and education, the more residents are likely to save energy. The current status of the role of educational level reveals a hot issue in our country, that is, people with higher education levels are more likely to overlook energy conservation and environmental protection. The reason is that such groups pay more attention to the quality of life and are more in tune with the trend of science and technology. In addition, they are not subject to economic constraints and thus cause extravagance and waste at the level of energy consumption. Energy-saving and environmental-friendly publicity and education media can be promoted through online advertising such as advertisements, micro-films, and new media, or through schools, communities, institutions, etc., to carry out multi-perspective and multi-layered low-carbon knowledge popularization for residents to guide residents to receive psychological acceptance. Correctly implement energy-saving behaviour.

Secondly, the government should improve relevant social regulations.

According to the results of this study, social norms have a significant positive effect on residents' energy-saving willingness. Improving relevant laws and regulations will help promote residents' willingness to save energy. The government should establish a complete rewards and penalties mechanism and actively explore other incentive mechanisms, such as linking energy conservation behaviours with social models, making energy conservation and environmental protection a benchmark for the community to promote and implement, in order to promote the transformation of residents' energy-saving behaviour.

Thirdly, the government should standardize residents' energy conservation standards and provide comprehensive and daily energy-saving information.

The formulation and implementation of relevant policies should focus on the fine-quantitative research of energy efficiency products, energy efficiency grades, and energy-saving space commonly used by households. The scientific research department should work hard to develop a set of scientifically quantified energy conservation standards and information systems to help residents understand the long-term economic benefits of household energy efficiency products in the family and the potential for energy saving that is beyond estimation. It can be achieved through measures such as the production of more comprehensive green product labels.

Last but not least, the government should pay attention to education and set a good example.

The results of this paper show that the education level of residents is not significant with energy conservation behaviour. Residents have the obligation to save energy, and the government has guiding responsibilities. Whether residents are willing to implement energy-saving behaviour depends largely on the government's propaganda, guidance, and supervision. Specifically, before the implementation of energy-saving activities, the government should conduct a demonstration of the universal knowledge of energy knowledge; in the implementation process, the government should give full play to the leading role of energy-saving work; after implementation, the government should regularly implement the energy-saving methods and energy-saving effects of residents. Or irregular evaluations, audits and tests. The government is not only the maker and implementer of energy-saving regulations, but also the energy consumer.

6. REFERENCES

Ajzen,I. The theory of planned behaviour[J]. Organizational Behaviour and Human Decision Processes.1991,50(2), 179-211

Guagnano. Influences on Attitude- behaviour Relationships: A Natural Experiment with Curbside Recycling[J]. Environment and Behaviour. 1995, 27(5):699-718.

Shi H. The impact of low-carbon policies on energy conservation behaviours of urban residents [j]. journal of Beijing institute of technology (social science edition), 2016,18 (05): 42 - 51.

Lu R, Li M, Hong S. Research on the impact mechanism of urban residents' energy conservation behaviour based on the theory of planned behaviour [j]. resources and environment in arid regions, 2016,30(12):53-58.

Ding L, Shuai C, Li W, Yan Q, Guo Q. SEM - based empirical study on public awareness and willingness to adopt solar photovoltaic power generation [j]. resource science, 2015,37 (07): 1414 - 1423.

Zhang Y, Guo X, Wang Z. Research on factors influencing employee energy conservation from the perspective of psychological ownership [J]. Research on technology, economy and management,2013(03):50-54.

Mi L, Gu M, Yang J, Yu X, Liu . Psychological motivation of low carbonization of energy consumption behaviour of urban residents - taking Xuzhou city, Jiangsu province as an example [j]. resource science, 2016,38 (04): 609 - 621.

Zhang Y, Wang Z. Influencing factors of energy conservation willingness based on planning behaviour theory - taking knowledge workers as an example [j]. journal of Beijing institute of technology (social science edition), 2012,14 (06): 7 - 13.

Zhang B, Huang Z, Wen X. Marketing incentives, psychological reactions and buying intentions and behaviours of organic vegetable consumers -- empirical analysis based on the ordered Logistic regression model [J]. Agricultural technology economy,2014(02):47-56.

Chen S, Li R, Ma Y. The contradiction between intention and behaviour: a study on the classification mechanism of municipal household garbage [J]. China's population, resources and environment,2015,25(09):168-176.

Zhu D, Wang X, Tong X. Research on low-carbon production intention and behaviour of industrial enterprises [J]. Chinese population, resources and environment,2013,23(02):72-81.

Yue T, Long R, Ge S. Influence factor model of energy-saving behaviour of urban residents in jiangsu province -- based on grounded theory [J]. Journal of Beijing university of technology (social science edition),2013,15(01):34-39.

211: Synthesis of hierarchical Au/TiO_2 plasmonic nanocomposite for enhancement of photocatalytic reduction of CO_2 to CO

Jinxia XU[1,2,3],Liming WU[1,2,3],Huihu WANG[1,2,3],Fei MEI[1,2,3],Yuanming ZHOU[1,2,3], Lingyun LIU[1,2,3]

[1] Hubei Collaborative Innovation Center for High-efficiency Utilization of Solar Energy, Hubei University of Technology, Wuhan 430068, P. R. China;
[2] Hubei Key Laboratory for High-efficiency Utilization of Solar Energy and Operation Control of Energy Storage System, Hubei University of Technology, Wuhan, 430068, P. R. China;
[3] Hubei Power Grid Intelligent Control and Equipment Engineering Technology Research Center, Hubei University of Technology, Wuhan, 430068, P. R. China,xujx@hbut.edu.cn,wlm458yeah@163.com,wanghuihu@126.com, meifei777@163.com,zhouym@ hbut.edu.cn,liulingyun@ hbut.edu.cn;

The increasing worldwide consumption of fossil fuels has accelerated the global energy consumption rate and led to overproduction of the carbon dioxide, resulting in global climate change and energy crisis. Semiconductor-based photocatalytic reduction of CO_2 with H_2O to renewable hydrocarbon fuels by solar energy has attracted enormously attention in recent years. Among the semiconductor photocatalysts, Titanium dioxide (TiO_2) has been extensively used in the photocatalytic fields including water splitting, degradation of organic contaminants, and CO_2 reduction due to its cheap, non-toxic, and light stability. Herein, High specific surface area three-dimensional pine tree-like hierarchical TiO_2 nanotube array films loaded with Au nanoparticles were successfully prepared by one-step hydrothermal reaction combining with simple and feasible thermal evaporation system. These photocatalysts were characterized by scanning electron microscopy (SEM), X-ray diffraction (XRD), the elemental chemical status and compositions were analyzed with X-ray photoelectron spectroscopy (XPS). The result of the photo-reduction of CO_2 shows that the composite Au/TiO_2-branched nanotube arrays shows efficiently reduce CO_2 to CO under UV visible light irradiation, which is about 2.4 times higher than that of pure TiO_2 nanotube arrays. The Au/TiO_2 nanocomposite photocatalyst is stable with the prolonged time and reaction duration. The enhancement of photocatalytic reduction of CO_2 is attributed to the boost of plasmonic effect enhancement carrier generation and separation, higher specific surface area, faster charge transport, and superior light-harvesting efficiency for efficient charge collection. The work provides a cost-effective, flexible and clean method to develop high-performance photocatalytic reduction of CO_2 to renewable hydrocarbon fuels by solar energy.

Keywords: TiO_2 nanotube array, Au nanoparticles, plasmonic, CO_2 reduction.

1. INTRODUCTION

The increasing worldwide consumption of fossil fuels has accelerated the global energy consumption rate and led to overproduction of the carbon dioxide, resulting in global climate change and energy crisis (Habisreutinger, 2013; Ran, 2015). Therefore, the development of renewable, green and substitutive energy resources is extremely urgent. Hence, the study of CO_2 capture, storage, and transformation have been paid much more attention, the development of green and cleaning technology for CO_2 conversion is the key in the field. Since the pioneering work by Fujishima and Honda found TiO_2 electrode under UV irradiation can make the phenomenon of water decomposition hydrogen, reveals the possibility of using solar water decomposition hydrogen (Fujishima, 1972), Inoue et al. (1979) by using WO_3, TiO_2, CdS and other semiconductor materials to reduce CO_2 to CO, CH_4 and CH_3OH, HCOOH and other hydrocarbons, and analyzed the reaction mechanism of photocatalytic reduction of CO_2, opened up a new direction in the field of semiconductor-based photocatalytic reduction of CO_2 due to the process is clean, carbon-neutral and sustainable. Therefore, Semiconductor-based photocatalytic reduction of CO_2 with H_2O to renewable hydrocarbon fuels by solar energy has attracted enormously attention in recent years (Sakimoto, 2016; Liu, 2016; Li, 2012; Tu, 2014; Wang, 2016; Hirakawa, 2017). Among the photocatalysts, Titanium dioxide (TiO_2) has been extensively used in the photocatalytic fields including water splitting, degradation of organic contaminants, and CO_2 reduction due to its cheap, non-toxic, and light stability (Huo, 2012; Nie, 2014). However, the recombination of electron-hole pairs and the lack of visible light absorption limit its photocatalytic performance (Yang, 2011). Much effort has been dedicated to enhance the photocatalytic efficiency of TiO_2 in the aspect of wide responsive range to solar spectrum and efficient separation and transport of electron-hole pairs over the last couple decades (Feng, 2011; Park, 2016).

One of the most widely applied approaches to prepare highly efficient TiO_2 for photocatalytic CO_2 reduction is the surface modification of TiO_2 such as morphology, surface area, surface defects, impurity doping, metal deposition (Sheng, 2014; Yu, 2016). The three-dimensional nanostructure offers the advantage of a large surface area. Besides, the three-dimensional morphology could offer long optical paths for efficient light absorption and abundant active sites for electrochemical reactions, providing efficient transport pathway for rapid charge transport that leads to improving electron collection and electron-hole separation. Therefore, the construction of three-dimensional nanostructures is of great importance to the improvement of photocatalytic performance of TiO_2. On the other hands, the coupling semiconductors with noble nanoparticles such as Pt, Ag, Au, Cu is another promising method to enhance the reduction of CO_2 owing to the localized surface plasmon resonance (LSPR) effect of metal NPs (Tahir et al, 2017; Tahir, 2017), besides, the noble nanoparticles could act as an electron trap center to effectively prevent electron-hole recombination and increase in efficient CO_2 reduction.

Herein, High specific surface area three-dimensional pine tree-like hierarchical TiO_2 nanotube array films loaded with Au nanoparticles were successfully prepared by one-step hydrothermal reaction combining with simple and feasible thermal evaporation system. The composite Au/TiO_2-branched nanotube arrays show efficiently reduce CO_2 to CO under UV visible light irradiation. Which is attributed to the boost of plasmonic enhancement carrier generation and separation, higher specific surface area, faster charge transport, and superior light-harvesting efficiency for efficient charge collection.

2. EXPERIMENTAL

2.1. Synthesis of three-dimensional (3D) pine tree-like hierarchical TiO_2 nanotube array films

Three-dimensional tree-like TiO_2 nanotube arrays were synthesized using a hydrothermal method. The details of the synthetic procedure were described by Roh et al. (2014). Au NPs were deposited on three-dimensional pine treelike hierarchical TiO_2 nanotube array films by thermal evaporation system. Moreover, the amount of Au can be simply controlled by tuning the deposition time from 5 to 15 min, the deposition time is 5, 10, 15 min, respectively. The as-prepared samples were annealed in air at 450 °C for 10 min, subsequently. Then obtained Au NP-decorated three-dimensional pine tree-like hierarchical TiO_2 nanotube array films were named as Au(5min)/TiO_2, Au(10min)/TiO_2, Au(15min)/TiO_2.

2.2. Characterization

The morphology and microstructure of the sample was examined by SEM (S4800, Hitachi) operated at an acceleration voltage of 5 kV. The crystallinity and phase constitutions of all samples were analyzed with X-ray diffraction (XRD) (D8 Germany, Bruker Axs). The elemental chemical status and compositions were analyzed with X-ray photoelectron spectroscopy (XPS) using Mg Ka1, 2 (1253.6 eV) excitation.

The photo-reduction of CO_2 was conducted in a cylindrical steel reactor, which was vertically irradiated by a 300 W xenon lamp. The distance from sample to 300 W Xenon lamp was 18 cm. In each experiment, 4 cm^2 of nanocomposite was placed in the bottom of the cylindrical steel reactor, besides, a minimal unsealed glass bottle with 1 ml deionized water was also put in the bottom of the cylindrical steel reactor simultaneously. Then, CO_2 gas with high purity (99.999%) was pushed into the reactor until the pressure of reactor reached 0.5 Mpa. In order to

eliminate the air component, the reactor was washed 3 times by high purity CO_2 gas purging. Afterward, the light was turned on to initiate the reaction. About 0.5 ml of gas was taken out from the reactor for the analysis of CO concentration using a gas chromatograph (GC-7920 with FID detector) after 2 h.

3. RESULTS AND DISCUSSION

The microstructural and morphology detail of the prepared 3D pine tree-like hierarchical TiO_2 nanotube arrays was shown in Figure 1(a), and the insert one is the cross-sectional SEM images. The SEM images shows that the prepared 3D pine tree-like hierarchical TiO_2 nanotube arrays composing of vertically-oriented nanotube trunks with lengths of approximately 5 μm grafted with large amounts of short branches with lengths of about 300 nm were directly grown on FTO substrate by a simple one step hydrothermal method. The plan SEM image and magnified image presents that the 3D TiO_2 nanotube arrays were fully covered and arranged homogeneously on the FTO glasses with large-scale and uniform growth, and large amounts of short nanorod branches. The hierarchical architecture with lager specific surface area can enhance the absorption of dye molecules, and effectively improve charge transport by direct transport path thereby maybe improve the photocatalytic of the TiO_2.The phase purity and structure of the 3D pine tree-like hierarchical TiO_2 nanotube arrays were analyzed using XRD as shown in Figure1 (b). It can be found that diffraction peaks appeared at 25.4° and 48 °, which can be attributed to the (101) and (200) orientations of the anatase TiO_2 (JCPDS No.21-1272) (Zhang, 2000). No characteristic peak of any impurity is probed, which demonstrates that the sample fabricated by this method has high phase purity. This result shows that the 3D pine tree-like hierarchical anatase TiO_2 nanotube arrays film were successfully fabricated.

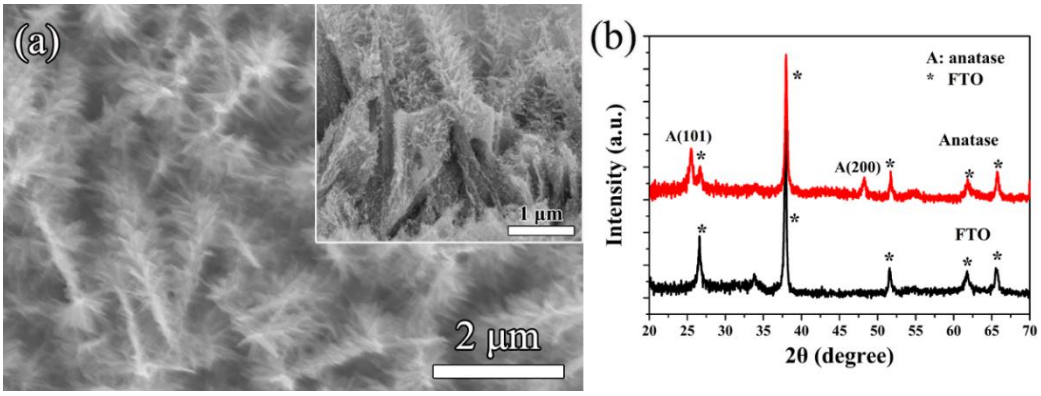

Figure 1: *(a) SEM image and cross-sectional, (b) XRD pattern of 3D pine tree-like TiO_2 nanotube arrays*.

The typical plain views SEM of Au NPs with deposited time of 5 min, 10 min and 15 min are shown in Figure 2(a), (b) and (c), and Figure 2(d), (e) and (f) is the corresponding magnified image of Figure 2(a), (b) and (c), respectively. It can be observed that Au NPs are uniformly coated on the branches of TiO_2. It is obvious that the diameter of Au NPs increases with the increase of Au deposit time. So Au NPs deposited uniformly on 3D pine tree-like hierarchical TiO_2 nanotube arrays were fabricated. The LSPR effect of Au NPs can form a strong local electronic field. Therefore, it may be form a stronger local electronic field in the hierarchical structure. So, Au NPs deposited on 3D pine tree-like hierarchical TiO_2 nanotube arrays expected with higher performance of CO_2 reduction.

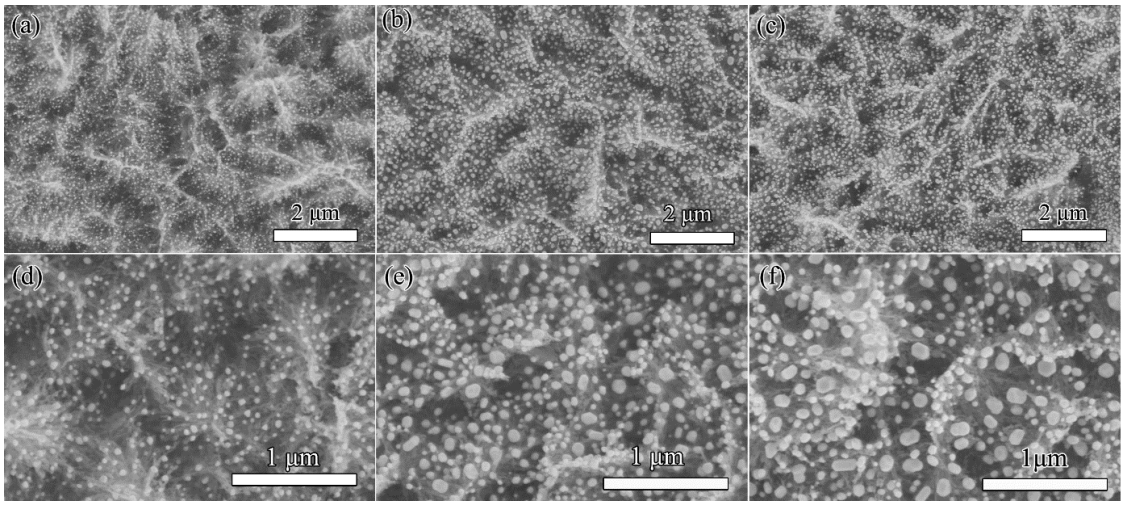

Figure 2: *The SEM image with different Au deposit time: (a) Au(5min)/TiO_2, (b) Au(10min)/TiO_2, (c) Au(15min)/TiO_2. And (d), (e), (f) is the corresponding magnified image of (a), (b) and (c), respectively.*

To further demonstrate the successful fabricated of Au NPs deposited on 3D pine tree-like hierarchical TiO_2 nanotube arrays, the elemental chemical status and compositions of Au(10min)/TiO_2 was analyzed by XPS. Figure 3(a) shows the XPS spectrum of Ti 2p. It can be observed that two peaks at binding energies of 458.5 and 464.3 eV, and that can be attributed to Ti $2p_{3/2}$ and Ti $2p_{1/2}$, respectively. The result demonstrates the state of Ti^{4+} in the anatase TiO_2 (Li, 2015). The O 1s peaks at binding energy of 529.8 eV attributed to the typical signal of Ti-O-Ti as shown in Figure3 (b) (Dumbuya, 2012). The Au 4f XPS spectrum shown in Figure3(c) consists of two peaks at 82.8 and 86.6 eV assigned to Au 4f 7/2 and Au 4f 5/2 (Li, 018), confirming that Au NPs exists in their metallic form in the Au/TiO_2 nanocomposite (Su, 2013).

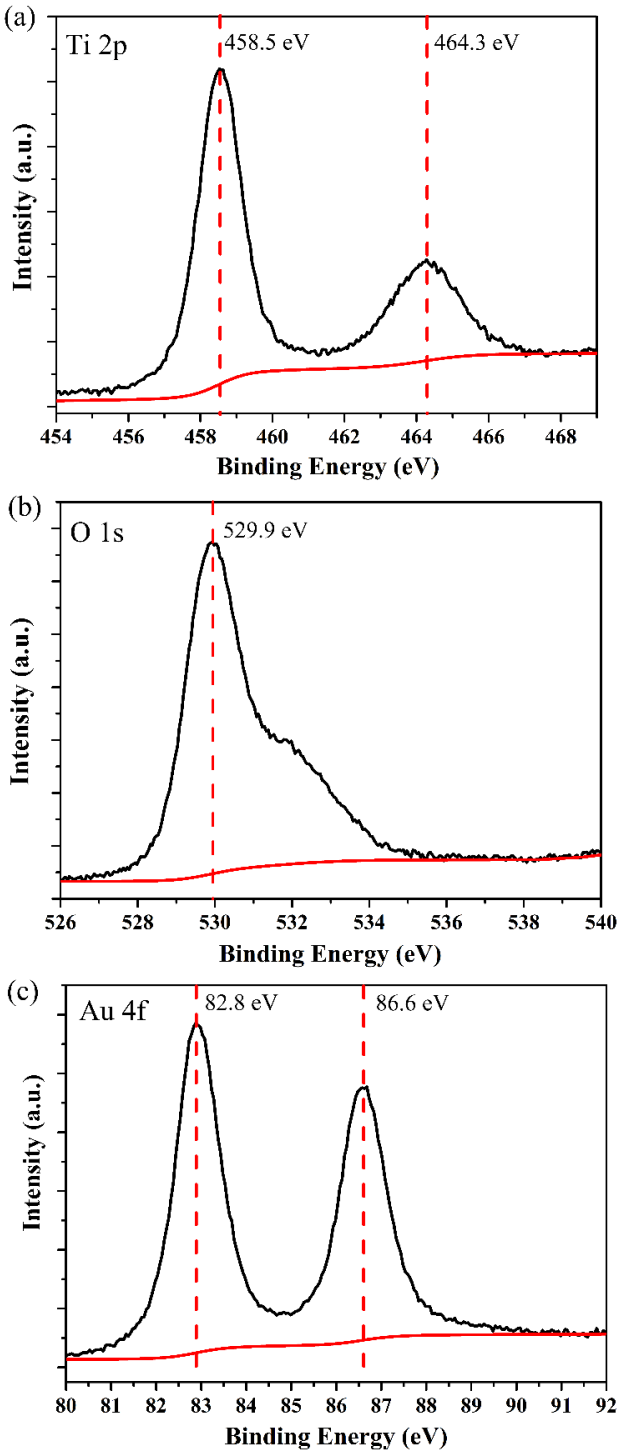

Figure 3: XPS spectra of Au (10min)/TiO_2, (a) high-resolution XPS of Ti 2p peaks, (b) high-resolution XPS of O 1s peaks, and (c) high-resolution XPS of Au 4f peaks.

Photocatalytic performance of 3D pine tree-like hierarchical TiO_2 nanotube arrays and Au(10min)/TiO_2 nanocomposites in gaseous system under UV visible light illumination are evaluated and shown in Figure 4. As it can be found in Figure 4(a), 3D pine tree-like hierarchical TiO_2 nanotube arrays and Au(10min)/TiO_2 nanocomposites have a substantial effect on the photocatalytic activity for the photoreduction CO_2. The 3D pine tree-like hierarchical TiO_2 nanotube arrays exhibit CO evolution of 5 μmol/10 g catalyst over 6 h. Meanwhile, Au (10min)/TiO_2 nanocomposites demonstrates a total CO evolution of 12 μmol/10 g catalysts over 6 h, which is about 2.4 times higher than that of pure TiO_2 nanotube arrays. To investigate the stability of Au (10min)/TiO_2 nanocomposite, cyclic performance toward the photoreduction of CO_2 to CO was carried out three months late after the first experiment. As shown in Figure4(b), the Au(10min)/TiO_2 nanocomposite maintains its high photocatalytic activity for the CO_2 photo-reduction after three months later under the same conditions, demonstrating that the Au/TiO_2 photocatalyst is stable with the prolonged time and reaction duration.

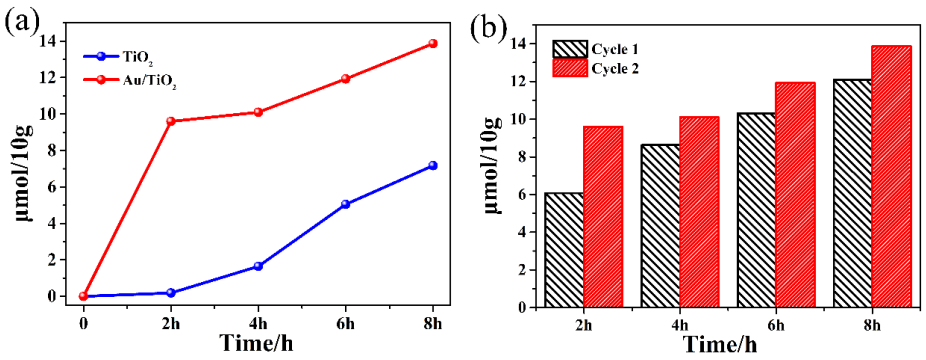

Figure 4: *(a) Dynamic CO evolution over TiO_2 and Au(10min) / TiO_2 nanocomposite, (b) the cyclic performance toward the photoreduction of CO_2 to CO over Au(10 min) / TiO_2 nanocomposite.*

During photocatalytic CO_2 reduction reaction, CO as the main products over the Au /TiO_2 catalyst as illustrated in Equations (Tahir, 2013; Tahir, 2017).

$TiO_2 \rightarrow e^- + h^+$ (1)
$H_2O + 4h^+ \rightarrow O_2 + 4H^+$ (2)
$CO_2 + e^- \rightarrow CO_2^-$ (3)
$CO_2 + 2H^+ + 2e^- \rightarrow CO + H_2O$ (4)

Based on the above experimental results, the proposed mechanism for CO_2 reduction under UV visible light irrigation over the Au/TiO_2 nanocomposite is shown in Figure 5. When the Au/TiO_2 nanocomposite is irradiated with the UV visible light source, electron-hole pairs were produced. The photoinduced electrons directly transports through the nanotube (Xie, 2010), and provides efficient transport pathway for rapid charge transport that lead improving electron collection and increasing the separation of electron-hole pair. The LSPR of Au NPs can enhance local field near the surface of NPs. Hence, there may be induced strong local electric field in the structure. The strong local electric field can increase the light capturing, and therefore boosts the generation of electron-hole pairs in Au/TiO_2 nanocomposite. Besides, due to the light scatter increase for Au/TiO_2, the optical path increases, so the absorption of light can also increase. Hence, the performance of photocatalytic reduction of CO_2 can be improved. Moreover, Au is contacted with TiO_2, Au NPs act as an electron trap effectively facilitate the separation of photo carriers, thus improve the transfer efficiency of electron and hole pairs, leading to an increased photocatalytic performance.

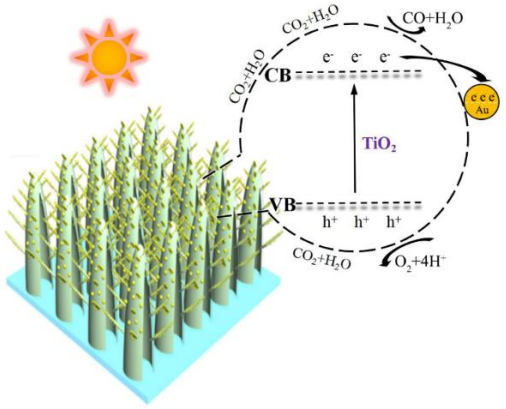

Figure 5: *The proposed photocatalytic mechanism over Au/TiO_2 nanocomposite.*

4. CONCLUSIONS

In summary, high specific surface area three-dimensional pine tree-like hierarchical TiO_2 nanotube array films loaded with Au nanoparticles were successfully prepared by one-step hydrothermal reaction combining with simple and feasible thermal evaporation system. The result of the photo-reduction of CO_2 shows that the composite Au/TiO_2-branched nanotube arrays show more efficiently reduce CO_2 to CO under UV visible light irradiation than pure TiO_2, The 3D pine tree-like hierarchical TiO_2 nanotube arrays exhibit CO evolution of 5 μmol/10 g catalyst over 6 h. Meanwhile, Au (10min)/TiO_2 nanocomposites demonstrates a total CO evolution of 12 μmol/10 g catalysts over 6 h, which is about 2.4 times higher than that of pure TiO_2 nanotube arrays. The Au/TiO_2 photocatalyst is stable with the prolonged time and reaction duration. The enhancement of photocatalytic reduction of CO_2 is attributed to the boost of plasmonic effect enhancement carrier generation and separation, higher specific surface area, faster charge transport, and superior light-harvesting efficiency for efficient charge collection.

5. ACKNOWLEDGEMENTS

The authors thank to the National Natural Science Foundation of China (No.11305056, 11304092, 51371079), the International Science & Technology Cooperation Program of China (No. 2016YFE0124300).

6. REFERENCES

Habisreutinger, S. N., Schmidt-Mende, L., Stolarczyk, J. K. (2013) Photocatalytic Reduction of CO_2 on TiO_2 and Other Semiconductors. Angewandte Chemie International Edition 52: pp.7372-7408.

Ran, J., Ma, T.Y., Gao, G., Du, X.-W., Qiao, S.-Z. (2015) Porous P-doped graphitic carbon nitride nanosheets for synergistically enhanced visible-light photocatalytic H_2 production. Energy & Environmental Science 8: pp. 3708-3717.

Fujishima, A., Honda, K. (1972) Electrochemical photolysis of water at a semiconductor electrode. Nature 238: pp. 37-38.

Inoue, T., Fujishima, A., Konishi, S., Honda, K. (1979) Photoelectrocatalytic reduction of carbon dioxide in aqueous suspensions of semiconductor powders. Nature 277: pp.637-638.

Sakimoto, K. K., Wong, A. B., Yang, P. (2016) Self-photosensitization of nonphotosynthetic bacteria for solar-to-chemical production. Science 351(6268): pp.74-77.

Liu, C., Colón, B. C., Ziesack, M., et al. (2016) Water splitting–biosynthetic system with CO_2 reduction efficiencies exceeding photosynthesis. Science 352(6290): pp.1210-1213.

Li, H., Opgenorth, P. H., Wernick, D.G., et al. (2012) Integrated electromicrobial conversion of CO_2 to higher alcohols. Science 335(6076): pp.1596-1596.

Tu, W., Zhou, Y., Zou, Z. (2014) Photocatalytic Conversion of CO_2 into Renewable Hydrocarbon Fuels: State-of-the-Art Accomplishment, Challenges, and Prospects, Advanced Materials 26: pp.4607-4626.

Wang, Z., Teramura, K., Huang, Z., Hosokawa, S., Sakata, Y., Tanaka, T. (2016). Tuning the selectivity toward CO evolution in the photocatalytic conversion of CO_2 with H2O through the modification of Ag-loaded Ga_2O_3 with a $ZnGa_2O_4$ layer. Catalysis Science & Technology 6(4): pp.1025-1032.

Hirakawa, H., Hashimoto, M., Shiraishi, Y., Hirai,T. (2017) Photocatalytic Conversion of Nitrogen to Ammonia with Water on Surface Oxygen Vacancies of Titanium Dioxide, Journal of the American of Chemical Society 139: pp.10929-10936.

Huo, P. W., Lu, Z. Y., Liu, X. L., Gao, X., Pan, J. M., Wu, D., Ying, J., Li, H. M., Yan, Y. S. (2012) Preparation molecular/ions imprinted photocatalysts of La^{3+}@POPD/TiO_2/fly-ash cenospheres: Preferential photodegradation of TCs antibiotics, Chemical Engineering Journal 198: pp.73-80.

Nie, X., Li, G.Y., Wong, P. K., Zhao, H. J., An, T. C. (2014) Synthesis and characterization of N-doped carbonaceous/TiO_2 composite photoanodes for visible-light photoelectrocatalytic inactivation of Escherichia coli K-12, Catalysis Today 230: pp.67-73.

Yang, G., Xiao, T., Sloan, J., Li, G., Yan, Z. (2011) Low-temperature synthesis of visible-light active fluorine/sulfur co-doped mesoporous TiO_2 microspheres. Chemical A European Journal 17: pp.1096-1100.

Feng, X., Sloppy, J. D., LaTempa, T. J., et al. (2011) Synthesis and deposition of ultrafine Pt nanoparticles within high aspect ratio TiO_2 nanotube arrays: application to the photocatalytic reduction of carbon dioxide. Journal of Materials Chemistry 21: pp.13429-13433.

Park, J., Jin, T., Liu, C., et al. (2016) Three-Dimenysional Graphene-TiO_2 Nanocomposite Photocatalyst Synthesized by Covalent Attachment. ACS Omega, 1(3): pp.351-356.

Sheng, X., He, D., Yang, J., et al. (2014) Oriented assembled TiO_2 hierarchical nanowire arrays with fast electron transport properties. Nano letters 14(4): pp.1848-1852.

Yu, B., Zhou, Y., Li, P., Tu, W., et al. (2016) Photocatalytic reduction of CO_2 over Ag/TiO_2 nanocomposites prepared with a simple and rapid silver mirror method. Nanoscale 8(23): pp.11870-11874.

Tahir, M., Tahir, B., Amin, N. A. S., Zakaria, Z. Y. (2017) Photo-induced reduction of CO_2 to CO with hydrogen over plasmonic Ag-NPs/TiO_2, NWs core/shell hetero-junction under UV and visible light. Journal of CO_2 Utilization, 18: pp.250-260.

Tahir, M. (2017) Synergistic effect in MMT-dispersed Au/TiO_2, monolithic nanocatalyst for plasmon-absorption and metallic interband transitions dynamic CO_2 photo-reduction to CO. Applied Catalysis B: Environmental 219: pp.329-343.

Roh, D. K., Chi, W. S., Jeon, H., Kim, S. J., Kim, J. H. (2014) High efficiency solid-state dye-sensitized solar cells assembled with hierarchical anatase pine tree-like TiO_2 nanotubes. Advanced Functional Materials 24: pp.379-386.

Zhang, W. F., He, Y. L., Zhang, M. S., Yin, Z., Chen, Q. (2000) Raman scattering study on anatase TiO_2 nanocrystals. Journal of Physics D Applied Physics 33: pp.912-916.

Li, L., Yan, J., Wang, T., Zhao, Z. J., et al. (2015) Sub-10 nm rutile titanium dioxide nanoparticles for efficient visible-light-driven photocatalytic hydrogen production, Nature Communications 6: pp.5881.

Dumbuya, K., Cabailh, G., Lazzari, R., Jupille, J., et al. (2012) Evidence for an active oxygen species on Au/TiO_2 (110) model catalysts during investigation with in situ X-ray photoelectron spectroscopy, Catalysis Today 18: pp.20-25.

Li, C., Wang, T., Zhao, Z. J., Yang, W., Li, J., et al. (2018) Promoted fixation of molecular nitrogen with surface oxygen vacancies on plasmon-enhanced TiO_2 photoelectrodes. Angewandte International Edition Chemie 57(19): pp.5278-5282.

Su, F., Wang, T., Lv, R., Zhang, J., et al. (2013) Dendritic Au/TiO_2 nanorod arrays for visible-light driven photoelectrochemical water splitting, Nanoscale 5: pp.9001-9009.

Tahir, M., Amin, N. A. S. (2013) Photocatalytic reduction of carbon dioxide with water vapors over montmorillonite modified TiO_2 nanocomposites, Applied Catalysis B: Environmental 142-143: pp.512-522.

Tahir, M., Tahir, B., Amin, N. A. S. (2017) Synergistic effect in plasmonic Au/Ag alloy NPs co-coated TiO_2 NWs toward visible-light enhanced CO_2 photoreduction to fuels, Applied Catalysis B: Environmental 204: pp.548-560.

Xie, K., Sun, L., Wang, C., Lai, Y., et al. (2010) Photoelectrocatalytic properties of Ag nanoparticles loaded TiO_2 nanotube arrays prepared by pulse current deposition. Electrochimica Acta 55: pp.7211-7218.

212: Research on matching of inter-temporal heat storage system for building foundation in Alpine area

Hanyu YANG, Jin LI, Enshen LONG*

College of Architecture and Environment, Sichuan University, Chengdu, China

The heating problem in the alpine area of western China hasn't been solved. Based on the building characteristics of small volume and low groundwater level in this area, the author proposes a heating technology scheme that uses inter-temporal heat storage of building foundation and relies on renewable energy to solve the heating problem in alpine regions. Taking a low-rise residential building in Daocheng County, Ganzi Prefecture, Sichuan Province as the research object, the Characteristic Temperature Method was used to simulate and analyze the dynamic heat load and daily heat demand of the building. Based on the daily characteristics of solar energy, an inter-temporal heat storage system for building foundation soil was constructed. The model is to study the optimisation of the inter-temporal foundation soil heat storage unit and the matching of load demand, heat storage volume and solar collector area in meeting the heating demand of the building. The results of the research indicate that the inter-temporal heat storage system for building foundation has strong feasibility and application prospects in the alpine area of western China.

Keywords: foundation heat storage; inter-temporal; heating system; load; matching

1. INTRODUCTION

There are a large number of alpine regions in China, which typical climate features are large temperature difference between day and night, low annual temperature and long duration of winter (Wu 2017; Liu 2017). For a long time, the heating problem in the alpine regions has become an important issue of concern to the government and all walks of life. However, due to factors such as the level of economic development, energy transportation conditions, and regional climate characteristics, the problem of heating in alpine regions has not been resolved (Anifantis 2017). The heat source choice in alpine areas should be based on local conditions and make full use of local resources, which can improve energy efficiency, reliability and economy. The total annual radiation in alpine areas of western Sichuan reaches 5000MJ/m^2 or more, and the annual sunshine durations exceed 1800 hours. According to the "Guidelines for the Comprehensive Treatment Technology of Rural Bulk Coal Combustion and Pollution" of the Ministry of China Environmental Protection, due to the lack of power resources and the advantages of rich solar resources, it is highly recommended to choose solar heating system in alpine areas (Lu 2017; Wang 2018).

However, how to store large amounts of solar energy in the daytime in alpine regions has hindered the development of solar heating systems. For the alpine regions, the use of solar heating in winter is prone to problems such as bursting pipes and freezing cracks. If the floor radiant heating is used, the storage tank is larger in size, higher in cost and more in heat dissipation (Siewert 2016). If the heat storage coil is combined with the building foundation, and the efficient heat storage performance of the building foundation is fully utilized, solar energy instability and intermittent defects can be overcome, which has the obvious advantage of storing solar energy across time and space (Zhao 2018). Therefore, this paper proposes a method of building foundation thermal storage heating system based on the characteristics of small volume and low groundwater level in the area，which can satisfy the indoor comfortable thermal environment, and guarantee the stability of the system, and solve the problems that traditional solar heating systems are prone to burst and freeze pipes in alpine regions.

2. BUILDING FOUNDATION THERMAL STORAGE HEATING SYSTEM

2.1. System introduction

The building foundation thermal storage heating system utilizes the huge heat storage potential of the building foundation, which can compensate for the unstable and intermittent defects of the solar heating technology, ensure the heating demand in the alpine regions, and solve the problem that ordinary solar collectors appear to burst and freeze pipes and other issues (Bonamente 2016). The system is not only simple in structure, but also has the advantages of stable performance, reliable control, and low cost. And the system can fully meet the human physiological needs because the heating is performed from the bottom to top and building's enclosure structure surface temperature is relatively high. The system consists of solar collectors, a heat retaining foundation heat storage layer and a heat storage coil. The end is equipped with a warm air blower, an expansion tank, a temperature controller and other components. Fig1 shows the schematic diagram of the building foundation thermal storage heating system.

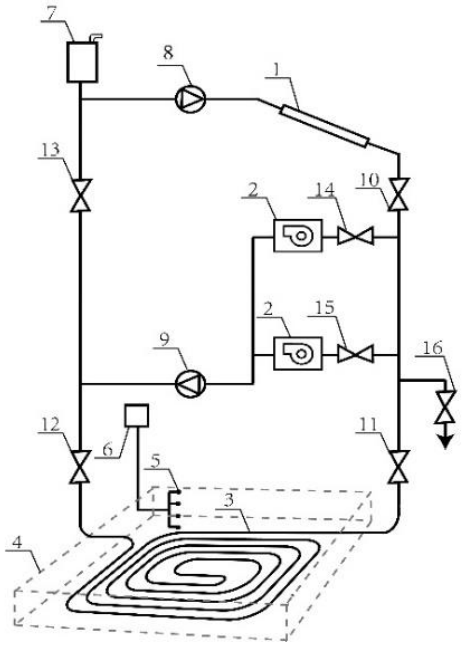

Figure 1: Schematic diagram of building foundation thermal storage heating system

1-solar collector, 2-warm air blower, 3-heat storage coil, 4-heat-retaining foundation storage layer, 5-underground temperature probe, 6-temperature controller, 7-expansion tank, 8-thermal storage circulation pump, 9-heating circulation pump, (10-16)-valves

2.2. Working principle

The system includes 3 internal circulation circuits. (1) Heating storage circuit: It is composed of solar collectors, heat storage coil, heat storage layer of foundation, thermal storage circulation pumps and valves. When the room is no heating required and the solar radiation is strong during the day. Adjust the valves and open the first circulating pumps, the solar collectors absorb solar radiation to heat the circulating water, then the heated circulating water flows into the heat storage coil that is buried in the foundation of the building, so heat can be stored in the foundation. (2) Heating release circuit: It is composed of a heat storage coil, a foundation heat storage layer, a warm air blower, heating circulation pumps and valves. When it is on cold sunny days, rainy days and nights, heat-retaining foundation storage layer releases heat storage to the rooms. In extreme weather, when the heat storage capacity of the foundation is not enough to meet the heating demands, the electric auxiliary heating of the warm air blowers in each room will start to work to meet the heating requirements. (3) Anti-freeze circuit: It is composed of solar collectors, warm air blowers, a heat retaining foundation heat storage layer, heating circulation pumps and valves; Micro-open valves can divert parts of heat into the system piping, solar collectors and the heat-retaining foundation storage layer can distribute heat to the rooms through the tube wells, which can prevent freezing in pipelines in extreme cold winter.

The length, width, and thickness of the thermal storage layer of the heat retaining foundation is determined by the local climatic conditions, the thermal performance of the enclosure structure, the areas of the solar collector, the total heating load demand of the building and the dynamic load characteristics (Li 217). The storage/release heat coil located in the heat storage layer is arranged on the foundation in the shape of spiral, and the pipes are polybutylene (PB). A certain thickness of heat insulation material is set around and at the bottom of the foundation heat storage layer. The heat insulation material is foamed concrete or foam glass, which prevents heat transfer to the surrounding and bottom, resulting in heat loss (Guo 2015); the upper part is not provided with insulation material so that the foundation dissipates heat to the upper part directly. The size of the solar collectors are determined by the heating load demand and the heat storage capacity of foundation heat storage layer, the installation azimuth, inclination angle, location latitude and longitude (Peltre 2017). The room uses warm air blowers as the main heating means, while the heat-retaining foundation heat storage layer dissipates heat to the room through the ground, pillars, walls, and floors with strong heat transfer capability, enabling passive technology to heat the room.

3. CLIMATE AND LOAD ANALYSIS

3.1. Analysis of regional solar characteristics

Daocheng County's meteorological data in Western Sichuan is selected for analysis, and the data comes from the Energyplus weather database. Hourly and daily radiation intensity of solar energy and outdoor hourly temperature have important effects on building load and energy consumption (Jradi 2017). The outdoor dry-bulb temperature hourly in this area is shown in Figure 2. The hourly and daily radiation intensity of solar energy is shown in Figures 3 and 4. The heating season in the region is calculated from Oct. 21st in the current year to Apr. 20th in the following year.

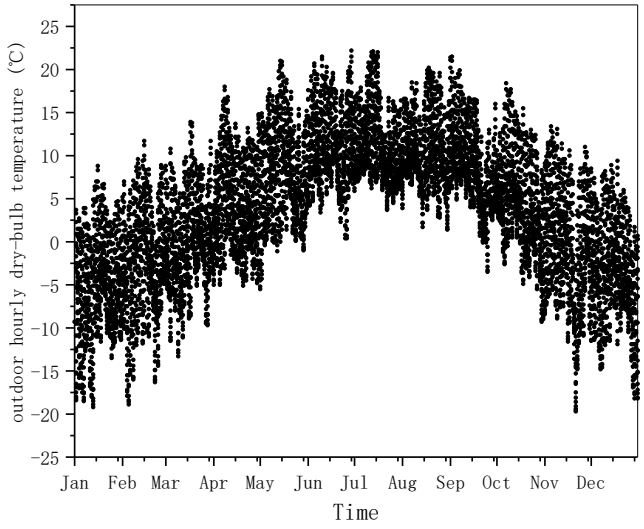

Figure 2: outdoor dry ball temperature

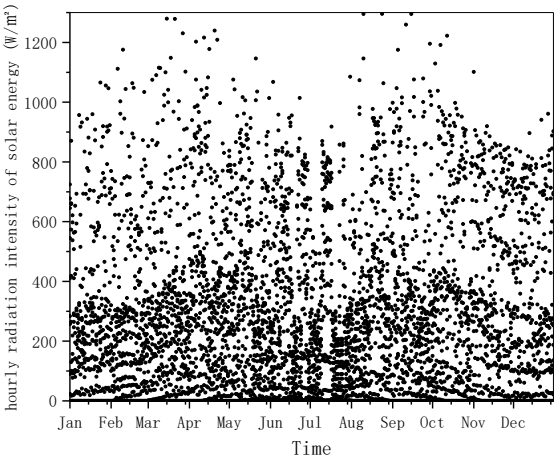

Figure 3: hourly solar radiation intensity

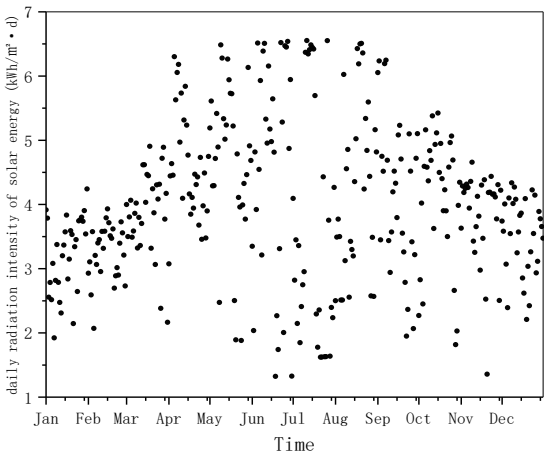

Figure 4: daily solar radiation intensity

According to statistics, there are 198 days in the area which the average daily temperature is ≤5°C, which is typical of severe cold regions with an altitude of 3750m. The annual maximum temperature is 22.2°C, the minimum temperature is -19.7°C, and the average annual temperature is 3.74°C. From figure 3 and figure 4, we can see that the region has a large amount of radiation throughout the year, of which summer can reach a maximum of 1252W/m^2, even in winter, the solar radiation can reach 1182W/m^2, and the annual solar radiation can reach 5085MJ/(m^2•a). In the heating periods, the daily average radiation amount can be captured reaches 3.28kW·h/(m^2·d), which belongs to the second-class solar energy resource-rich area.

3.2. Analysis of heating load characteristics

The building volume in Western Sichuan is relatively small. This paper takes a single building in Daocheng County as an example. The height of the building is 10.21m, and the actual heating area is 200.3m^2. The building is located in a severely cold area, therefore, the thermal insulation performance of the enclosure structure is high. The dimensions and thermal performance parameters of each orientation are shown in Table 1. Figures 5-7 are the floor plan, section view and east elevation view of the building respectively. The method of building energy consumption adopted in this paper is the characteristic temperature method (CTM) (Yang 2008; Prakash 2016), which can calculate the hourly load of the building according to the meteorological parameters and has the characteristics of strong theoretical ability, accurate hourly load calculation, and wide applicability. In addition, the CTM has been widely used in the field of building energy consumption calculation (Nguyen 2017).

Table 1: Dimensions and Thermal Performance Parameters of Enclosure Structure

Name	North Exterior Wall	North Exterior Window	South Exterior Wall	South Exterior Window	West Exterior Wall	West Exterior Window	East Exterior Wall	East Exterior Window	Roof	Ground
Area (F/m^2)	78.7	9.56	89.86	9.18	92.66	6.48	87.08	12.06	83.07	83.07
Heat transfer coefficient K (W/(m^2·℃))	0.34	2.7	0.34	2.7	0.34	2.7	0.34	2.7	0.35	0.11

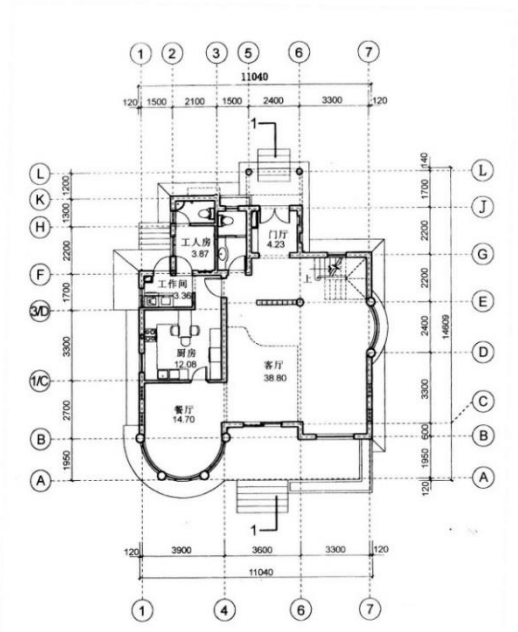

Figure 5: Ground floor plan

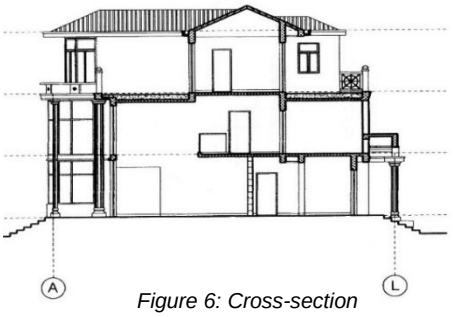

Figure 6: Cross-section

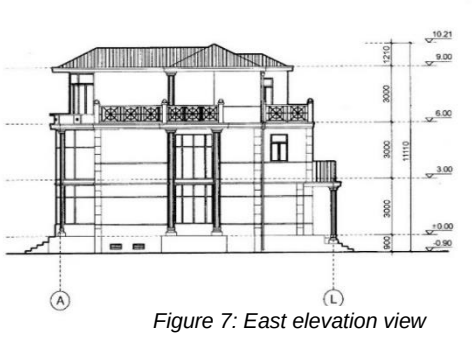

Figure 7: East elevation view

The steps of the CTM to simulate the seasonal heat load of building are as follows: Firstly, the heat transfer of the enclosure structure, solar radiation, indoor human body heat dissipation, ventilation heat and lighting device heat dissipation are separately calculated. Then, the indoor characteristic temperature can be obtained. Finally, the building's heat load can be predicted based on the characteristic temperature. This kind of dynamic load can accurately reflect the load changes of buildings at different times, and has a good effect on system selection, matching, and operation mode analysis. The indoor temperature is set at 18°C. Other setting parameters refer to "Design Code for Heating Ventilation and Air Conditioning of Civil Buildings GB50736-2012". The hourly and daily heat load distribution of the building in heating season is shown in Figure 8 and Figure 9.

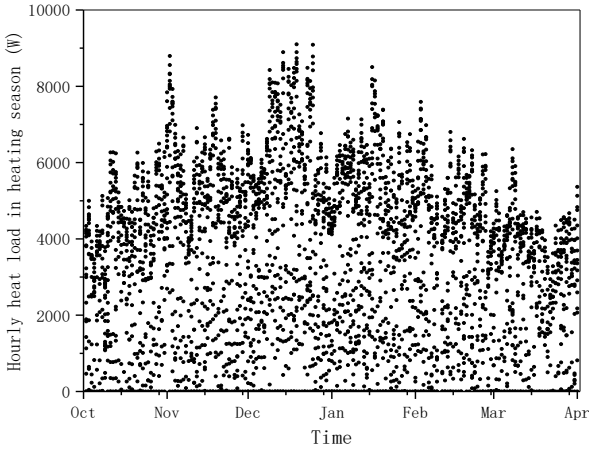

Figure 8: Hourly heat load in heating season

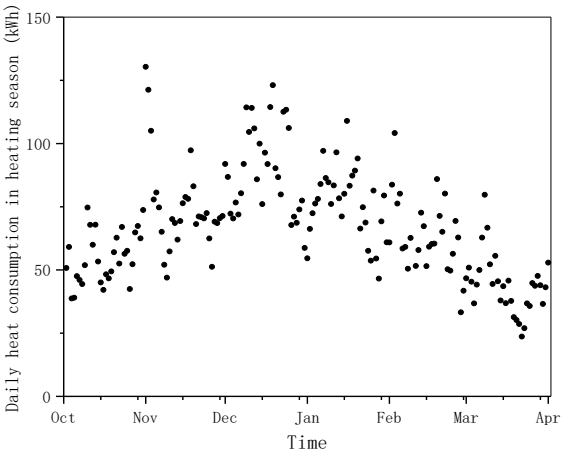

Figure 9: Daily heat consumption in heating season

4. STUDY ON SYSTEM MATCHING

The operation mode of the foundation thermal storage heating system is inter-temporal, the system makes full use of the heat storage potential of the foundation, and heats the foundation in advance through solar collectors. The heat storage should ensure that the heating season's heat consumption for the most adverse three consecutive days. The foundation where the building is located is a mixture of gravel and soil. The density is 1500kg/m^3 and the specific heat capacity is 1.4kJ/(kg·°C). In order to ensure the thermal comfort of indoor 18°C (cooler 15°C), it is more reasonable to maintain the ground temperature of the heat storage layer between 40°C and 55°C, because the floor temperature above the regenerator is relatively high, the corresponding second and third floor rooms can also transmit some heat through walls and columns to reduce the load demand; in the colder hours, the end warm air blowers have built-in electric auxiliary heat to achieve thermal environment requirements. In this mode of operation, the solar collector areas can be reduced, and the soil regenerator can also be prevented from being excessively large. Also, the capacity of the electric auxiliary thermal installation is small and the power consumption

can be greatly reduced. Perform energy simulation and optimisation matching by the CTM. The heating effect is the best when the area of the solar collector is 25m^2, the volume of the regenerator is 58.65m^3, and the electric auxiliary thermal capacity is 3kW. Among them, the solar collectors are divided into 5 groups of 5m^2 each. According to the heating demand and the amount of solar radiation to control the number of open groups, the numbers of corresponding solar collectors for each period of the heating season are shown in Table 2; The heat storage layer radiation area is the actual area of the living room plus stairs, and the thickness is 1m, which is convenient for construction. Figure 10 shows the change in the temperature of the building foundation under this matching relationship. Figure 11 shows the operating hours of daily electric auxiliary heating distribution.

Table 2: Numbers of solar collectors in each period of heating season

Period	10.21-11.20	11.21-12.1	12.2-12.20	12.21-2.20	2.21-4.1	4.2-4.20
Number of open groups	4	5	4	5	4	1
Collector area (m^2)	20	25	20	25	20	5

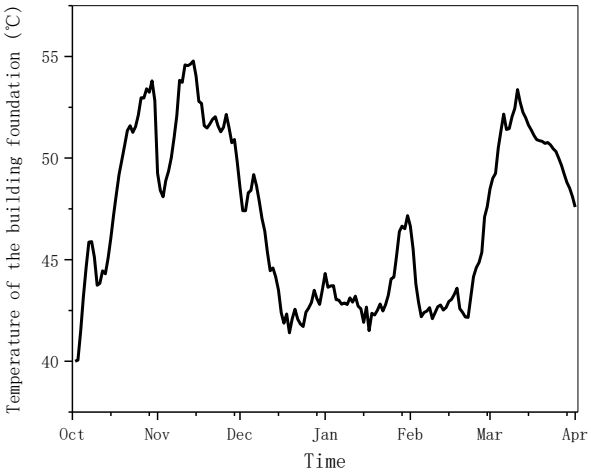

Figure 10: Temperature of the building foundation

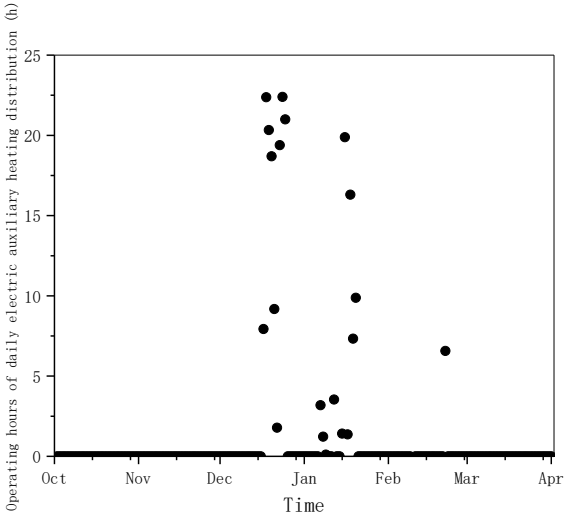

Figure 11: Operating hours of daily electric auxiliary heating distribution

It can be seen from Figure 10 that the building foundation heat storage layer has a relatively stable heating capacity throughout the heating season. The minimum temperature of the foundation is 40.0°C and the maximum is 54.8°C. Electric heating is basically not required at the beginning and end of the heating season. During the heating season, in order to use the solar energy more effectively, the numbers of solar collectors which are turned on should be determined by the actual load demand and solar radiation. Also, the temperature of the foundation will not be excessively high to reduce the indoor comfort. When it comes to the cooler period of the heating season, the heat storage capacity of the foundation will not be sufficient. The electric auxiliary in the warm air blowers are turned on for secondary heating. At the end of the heating season on April 1st, the solar radiation increases, while the heat load decreases, so the heat collection capacity of the entire groups of solar collectors has far exceeded the heating demand, just one set of solar collectors only can be turned on. As it can be seen from Figure 11, only 20 days electric auxiliary heating are required in the heating season, and the power consumption index of electric heater is 3.2 kWh/m^2, which only accounts for 4.6% of the total heating demand. The energy saving effects are significant.

5. CONCLUSION

This paper proposes an inter-temporal heat storage system for building foundation, which has strong adaptability to the features of abundant solar energy resources, small building volume, and low groundwater level in Western Sichuan, and also solves the problem of pipeline cracking in extreme weather in alpine regions. In this paper, a single building in Daocheng County of Western Sichuan is taken as an example. Under the premise of analyzing the climate and load characteristics of the region, the area of solar collectors and the volume of the regenerators are optimised and matched. The research results show that the building foundation thermal storage heating system has feasibility and obvious energy-saving effect for heating in alpine areas and has a great promoting effect on the utilization of renewable energy.

6. REFERENCES

Wu L, Liu W, Lu Z, et al. Simulation of soil temperature characteristics around ground tube in soil heat storage-exothermic process[J]. Chinese Journal of Agricultural Engineering, 2017, 33(03): 204-213.

Liu G, Luo C, Qiu Z et al. Research progress of solar-soil source heat pump combined energy supply system[J]. Refrigerating and Air Conditioning, 2017, 17(10): 8-15.

Anifantis A S, Colantoni A, Pascuzzi S. Thermal energy assessment of a small scale photovoltaic, hydrogen and geothermal stand-alone system for greenhouse heating [J]. Renewable Energy, 2017,103.

Lu Z, Qu S, Han J, et al. Research on the Applicability of Regenerative Solar Ground Source Heat Pump Coupling System in Severe Cold Area[J]. Building Science, 2017, 33(10): 97-103 (in Chinese).

Wang S, Li Y. Study on the characteristics of soil temperature field of low-temperature waste heat and heat storage ground source heat pump system[J]. Shanxi Architecture, 2018, 44(10): 179-181.

Siewert M B, Hugelius G, Heim B, Faucherre S. Landscape controls and vertical variability of soil organic carbon storage in permafrost-affected soils of the Lena River Delta [J]. Catena, 2016, 147.

Zhao Y. Research status and development prospects of solar-seasonal cross-storage heat storage heating technology [J]. Management and Technology of Small and Medium-sized Enterprises (First Quarterly), 2018(05): 135-137.

Bonamente E, Aquino A, Cotana F. A PCM Thermal Storage for Ground-source Heat Pumps: Simulating the System Performance via CFD Approach[J]. Energy Procedia,2016,101.

Li X. Simulation Study on Thermal Storage Characteristics of Solar Energy in Cross-seasonal Storage[D]. Chongqing University, 2017.

Guo L, Ma Y. Non-steady state analysis of heat transfer process of solar-soil coupled ground tube[J]. Shanxi Architecture, 2015, 41(26):143-144.

Peltre C, Gregorich E G, Bruun S, Jensen L S, Magid J. Repeated application of organic waste affects soil organic matter composition: Evidence from thermal analysis, FTIR-PAS, amino sugars and lignin biomarkers[J] Soil Biology and Biochemistry, 2017, 104.

Jradi M., Veje C., Jørgensen B.N.. Performance analysis of a soil-based thermal energy storage system using solar-driven air-source heat pump for Danish buildings sector [J]. Applied Thermal Engineering, 2017, 114.

Yang W, Shi M, Chen Z. Numerical simulation and experimental verification of solar thermal storage characteristics of U-shaped buried pipe[J]. Journal of Southeast University(Natural Science Edition), 2008(04):651-656.

Prakash O, Kumar A, Laguri V. Performance of modified greenhouse dryer with thermal energy storage[J]. Energy Reports, 2016, 2.

Nguyen A., P Pasquier., Marcotte D.. Borehole thermal energy storage systems under the influence of groundwater flow and time-varying surface temperature [J]. Geothermics, 2017, 66.

213: Study on the behaviours of a controllable loop thermosyphon used in the temperature control of a fresh food compartment

Jingyu CAO[1], Chuxiong CHEN[1], Yuehong SU[2], Jing LI[2], Michele BOTTARELLI[3], Mauro CANNISTRARO[3], Mingke HU[1], Gang PEI[1,*]

[1] University of Science and Technology of China, No.96, JinZhai Road Baohe District,Hefei,Anhui, 230026, P.R.China, peigang@ustc.edu.cn; jycao@ustc.edu.cn
[2] Department of Architecture and Built Environment, University of Nottingham, University Park, Nottingham, NG7 2RD, UK
[3] Department of Architecture, University of Ferrara, via Quartieri 8, 44121 Ferrara, Italy

The loop thermosyphon with active heat transfer control capability is a promising solution for the temperature management of the fresh food compartment of cool-storage refrigerators or other precise temperature control devices. However, the frequently start-stop operating mode of the loop thermosyphon has not received enough attention, the active temperature management behaviours of the loop thermosyphon still requires further investigation. In this study, a controllable loop thermosyphon (CLT) used in the temperature control of a fresh food compartment is developed. the start-stop of the CLT is controlled by the temperature controller with the assistance of two solenoid valves. The performances of CLT in long-term and start-stop operating modes are tested. The CLT with 35% filling ratio present highest heat transfer rate, reliable heat transfer capability, and stability for different temperatures in the fresh food compartment. Based on this filling ratio, the heat transfer rate of CLT remains higher than 40 W during the long-term operating test. The fitted equivalent heat transfer resistance increases sharply at first and then gradually decreases to 0.59 °C/W as the temperature of the fresh food compartment drops to 0 °C. When the CLT operates in the start-stop mode, the start-stop cycle decreases from 39.4 min to 27.2 min and the operating ratio increases from 12.6% to 53.7% as the temperature of the fresh food compartment rises from 2 °C to 8 °C. The results demonstrate that the precise temperature management capability of CLT is qualified as a novel temperature management device for the use in cool-storage refrigerators, as well as for other applications.

Keywords: loop thermosyphon, temperature control, fresh food compartment, start-stop

1. INTRODUCTION

The loop thermosyphon is an energy-efficient two-phase heat transfer component that can automatically operates with the assistance of temperature difference and gravity (Franco, 2012; Zhang, 2014). It is also named as the two-phase loop thermosyphon or the separate heat pipe, and has been widely applied in the traditional field of efficient heat transfer in the past few decades considering its low inner thermal resistance, high reliability, and low cost (Michaelides, 1992; Bernier, 1992; Chen, 1994). The critical heat transfer capability of the loop thermosyphons has attracted considerable attention in the fields like photo-thermal utilization of solar energy (Naghavi, 2015; Chen, 2016; Chehade, 2014), efficient heat dissipation technology (Oliveira, 2016; LI, 2016; Khodabandeh, 2004; Samba, 2013), Heating Ventilation Air Conditioning system (Yan, 2016), and nuclear technology (Nayak, 2007; Matsubara, 2016).

Besides, a growing number of researchers have been focusing on the internal two-phase flow mechanism of the loop thermosyphon in recent years. Tong et al. experimentally studied the self-regulating performance of the loop thermosyphon. Result reveals that the self-regulating ability of the loop thermosyphon is very limited and significant differences between the heat transfer loads of parallel evaporators should be avoided as much as possible (Tong, 2017). Wang et al. detailedly simulated the internal two-phase flow of a horizontal loop thermosyphon which was designed as a linear focus solar receiver. The CFD simulation results show the heat transfer mechanism of the device and also show that the U-turn structure has a notable effect on avoiding the bidirectional flow and the condenser with a certain inclination angle is beneficial for the improvement of the thermal performance (Wang, 2017; Wang, 2017). Mameli et al. put forward an advanced multi-evaporator loop thermosyphon to improve the flow motion and consequently the thermal performance. The test results show that the heat flux capability is up to five times larger with respect to the other existing wickless heat pipe technologies (Mameli, 2016). Tong et al. also paid much attention to the three typical operating states of the loop thermosyphon designed for cooling of the data center. The distribution maps and the real-time photos of the working fluid were used to describe the inner two-phase variation processes (Tong, 2017). Bodjona et al. established a transient model to simulate the complex liquid-gas variation inside of the loop thermosyphon. The flow model was solved with a specific hyperbolic solver based on Godunov method and Harten-Lax-van Leer-Contact (HLLC) Riemann solver. The closed-form of the thermodynamic state laws of the working fluid have been approximated (Bodjona, 2017).

As showed in the aforementioned applications of the loop thermosyphon, the application method of the loop thermosyphons has gradually extended with the diversification and individualization of the technology demands in various industries. Many factors that affect the inner heat transfer and two-phase flow of loop thermosyphons have been detailedly studied. However, most of the researches still place emphasis on the passive heat transfer of the loop thermosyphon, and the precise heat transfer control capability of the loop thermosyphon has not received enough attention even it has considerable potential to decrease the cost and energy consumption of the traditional heat and temperature control processes, including the temperature management of the precision instruments, electronic components, food, medicine, and vaccines (Cao, 2017).

In our previous work, a controllable loop thermosyphon (CLT) has been put forward. The internal two-phase flow of it can be artificially stopped and automatically recover at different start-stop frequencies; thus, the heat transfer rate is able to be actively adjusted in high precision (Cao, 2016; Cao, 2017; Cao, 2016). The CLT is preliminarily applied in a novel cool-storage refrigerator to precisely control the temperature of fresh food compartment. The compressor of the refrigerator can operate continuously for several hours to store cold energy in the phase change material (PCM) only in the top freezer while the CLT manages the fresh food compartment temperature; thus, it is promising in cost cutting and efficiency improvement of solar- and electric-powered refrigerators with time-of-use price policy (Cao, 2016). The authors have detailedly studied the heat transfer behaviours of the CLT; however, the practical temperature management performances of the CLT remains to be verified and researched.

In this study, a temperature control system of fresh food compartment based on the CLT has been built, the start-stop operation of the CLT is controlled by the temperature controller with the assistance of two solenoid valves. The performances of the CLT were optimised with the working fluid of R134a. The dynamic responses of the CLT and the fresh food compartment in the long-term cooling process and in the start-stop operating mode were systematically tested.

2. EXPERIMENTAL SET-UP

The experimental platform is established on the basis of the fresh food compartment of the Midea BCD-111 refrigerator, the primary components are shown in Figure 1. The evaporator section of the CLT is modified by the original evaporator of the fresh food compartment of the BCD-111 refrigerator and the condenser section is made by the inner pipe of a double-pipe helical heat exchanger. The complete CLT prototype is described in Figure 2, and the structure of the evaporator section is described in Figure 3. The R134a is selected as the working fluid based on the previous study (Cao, 2016). The main parts of the vapour line, liquid line, and condenser consist of copper, whereas the material of the heat conducting plate, the evaporator section, and its junction with the vapour and liquid lines is aluminum. Two solenoid valves are installed in the vapour and liquid lines, and their switch are simultaneously controlled by the WK-206L temperature controller. The heat transfer between the low-temperature

40% propylene glycol solution pumped from the DC-3015 thermostatic bath and the R134a is in counter-flow mode. The inner diameters of the condenser section, upper vapour, and liquid lines are 10 mm, while the inner diameter of the lower vapour and liquid lines are 4.75 mm. The inner diameter of the shell of condenser are 23 mm. Particularly, the cross section of the evaporator section of CLT is an oblateness, as shown in Figure 3. The lengths of the upper vapor line, upper liquid line, lower vapor line, lower liquid line, and condenser section are 0.57 m, 0.49 m, 0.4 m, 0.3 m and 1.34 m, respectively. The inner structure and size of the fresh food compartment is depicted in Figure 4.

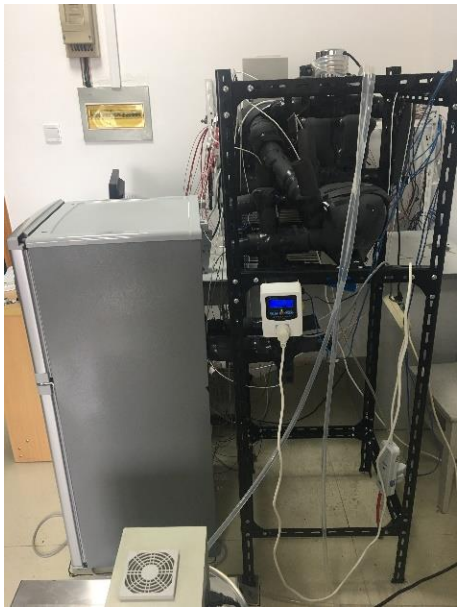

Figure 1: Test bench set-up

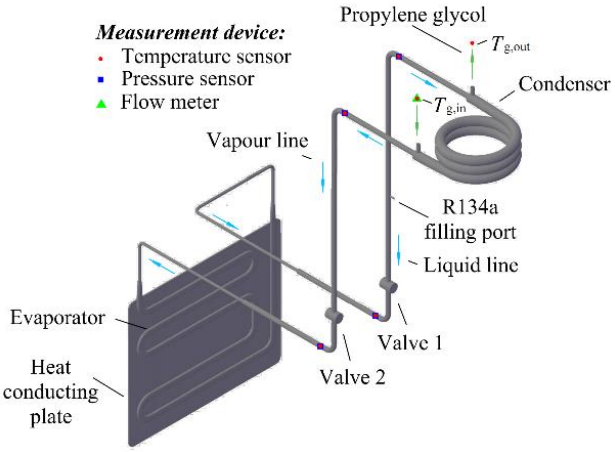

Figure 2: Concrete structure and measurement points of CLT

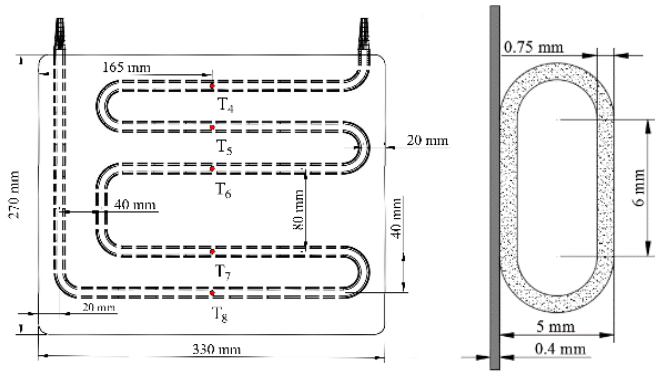

Figure 3: Structure of the evaporator and the heat conducting plate

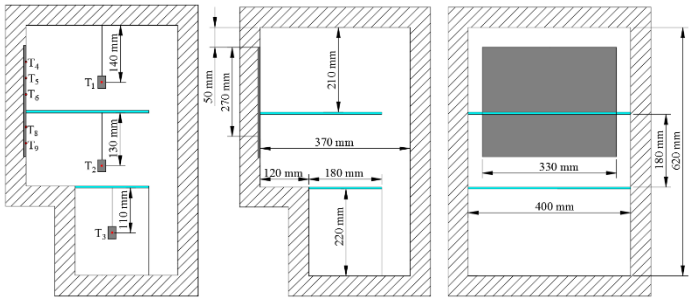

Figure 4: Structure and measurement points of the fresh food compartment

The measurement points of CLT are shown in Figure 2. To obtain the state parameters of working fluid at the inlet and outlet of the evaporator and condenser, we set 4 WZP-291 Pt100 platinum resistances and 4 JT-131 pressure sensors. The inlet and outlet temperature of the propylene glycol solution and its flow rate are also measured with WZP-291 Pt100 platinum resistances and Glass rotameter, respectively. Besides, Figure 3 and 4 show the measurement points inside of the fresh food compartment. 5 thermoelectric couples are employed to evaluate the temperature of the heat conducting plate from the inner side of the fresh food compartment. On this basis, 3 WZP-291 Pt100 platinum resistances are embedded in 3 standard copper columns to measure the air temperature in the fresh food compartment. The national test standard for household refrigerators are adequately considered when choosing the hanging position and embedded technology (PRC, 2016). An Agilent data acquisition is utilized to record the temperature and pressure measurements per 10 s. A vacuum valve, pressure gage, and electronic scale are utilized to fill and discharge R134a. Detailed information on experimental testing and monitoring devices is presented in Table 1.

Table 1: Experimental devices

Device	Specification	Range	Accuracy
Pressure sensor	JT-131	0–1000 kPa	±5 kPa
Platinum resistance	WZP-291 Pt100	-40–100 °C	±0.1 °C
Thermocouple	Type T	-200–350 °C	±0.5 °C
Flowmeter	Glass rotameter	16–160 L/h	2.5%
Electronic balance	KFS-C1	0–1 kg	±0.5 g
Temperature controller	WK-206L	0–99 °C	±0.1 °C
Thermostatic bath	DC-3015	-30–100 °C	0.1 °C
Magnetic valve	HONGSEN 1064-4	/	/
Data acquisition unit	Agilent 34970	/	/

3. EXPERIMENTAL METHODS AND CALCULATION

The flow rate of the propylene glycol solution and its inlet temperature are set to 70 L/H and -25 °C, respectively, to simulate the freezer temperature condition of the novel cool-storage refrigerator, considering the measurement accuracies of the temperature sensors and the flow meter. On this basis, the long-term heat transfer behaviours of CLT are tested under 30 g, 60 g, 90 g, 120 g, 150 g, 180 g, 210 g, 240 g, and 270 g R134a. The filling ratios of the working fluid that can be calculated based on the Equation 1 are 9%, 18%, 27%, 35%, 44%, 53%, 62%, 71%, and 80%, respectively. The comparison tests on the start-stop performances of the CLT with different R134a filling ratio under various fresh food compartment temperatures are performed. Then, the behaviours of the temperature control system that operates in stable start-stop cycles are studied when the fresh food compartment temperature varies.

To evaluate the parameters of the temperature control system with the CLT, the average temperature of the fresh food compartment T_{fre} is defined as the mean value of T1 and T2 according to the national test standard for household refrigerators while the characteristic temperature of the heat conducting plate T_{pla} is represented by average of T4, T5, T6, T7, and T8, as shown in Figure 3 and 4 (PRC, 2016).

The fill ratio of R134a in this study is defined as the ratio of volume of liquid R134a and the entire capacity of CLT:

$$R = \frac{V'}{V} = \frac{m'v'}{V} \tag{1}$$

Where: R = fill ratio of R134a (kg)
V = volume of the CLT (m^3)
V' = volume of the liquid R134a in the CLT (m^3)
m' = mass of the liquid R134a in the CLT (kg)
v' = specific volume of the liquid R134a in the CLT (kg)

The heat transfer rate of CLT is calculated at any time to monitor its transient heat transfer behaviour. The heat transfer between the CLT and the ambient is ignored considering the good thermal insulation; therefore, the heat-transfer capability of CLT can be represented by the heat-transfer capability of the condenser section:

$$Q = \rho_g \dot{V}_g Cp_g (T_{g,in} - T_{g,out}) \tag{2}$$

Where: Q = heat transfer rate of the CLT (W)
ρ = density of the propylene glycol solution (kg/m^3)
$\dot{V}_g$ = volume flow rate of the propylene glycol solution (m^3/s)
Cp_g = specific heat of the propylene glycol solution (J/kg ^oC)
$T_{g,in}$ = inlet temperature of the propylene glycol solution (^oC)
$T_{g,out}$ = outlet temperature of the propylene glycol solution (^oC)

R134a is in the undercooled and superheated state at the outlet and inlet of the condenser section, respectively. Based on the measured temperature and pressure of R134a at the evaporator inlet and outlet, the variations in the enthalpy of R134a can be obtained with the calculation software REFPROP 7.0. The mass flow rate of R134a is then calculated with the following formula:

$$\dot{M} = \frac{H_{con,in} - H_{con,out}}{Q} \tag{3}$$

Where: $\dot{M}$ = mass flow rate of the R134a (kg/s)
$H_{con,in}$ = specific enthalpy of R134a at the inlet of condenser section of CLT (kJ/kg)
$H_{con,out}$ = specific enthalpy of R134a at the outlet of condenser section of CLT (kJ/kg)

The equivalent thermal resistance of the CLT can be evaluated by:

$$R_{equ} = \frac{T_{g,in} - T_{fre}}{Q} \tag{4}$$

Where: R_{equ} = equivalent thermal resistance of the CLT ($^oC/W$)
T_{fre} = average temperature of the fresh food compartment (^oC)

4. RESULTS AND DISCUSSION

4.1. Heat transfer behaviour study on the CLT

The heat transfer rate of the CLT was tested to preliminarily evaluate the temperature management capability of the temperature control system. The door of the fresh food compartment was firstly opened until the inner temperature stabilized at the ambient temperature 16 °C, and then the door was closed and the CLT was started, the long-term operating behaviours of the system was tested for different R134a filling ratios. Figure 5 shows the average heat transfer rate of the CLT for various R134a filling ratios when the average temperature of fresh food compartment T_{fre} reaches 12 °C, 8 °C, 5 °C, and 2 °C, respectively. Given the filling ratio, the heat transfer rate decreases with T_{fre}; while given *Tfre*, it rises at first and then drops with the increasing R134a amount. The maximum heat transfer rate appears when the filling ratio increases to 35% even T_{fre} varies. When the filling ratio is lower than 27%, the insufficient R134a results in overheating at the outlet of the evaporator section and the undercooling at the outlet of the condenser section; therefore, the heat transfer rate of the CLT reduces with the decrease of the

two-phase heat transfer area of the evaporator and condenser sections. On the contrary, when the filling ratio is more than 44%, the two-phase heat transfer is disturbed by the excess liquid R134a, which also leads to the decrease of the heat transfer capability.

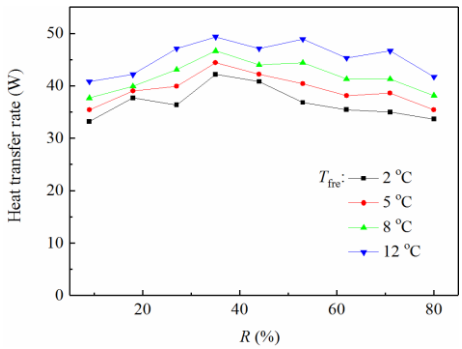

Figure 5: Heat transfer rates of CLT for different R and T_{fre}

The aforementioned test results can be analyzed combined with the states of the inlet and outlet working fluid of the CLT. Figure 6 shows the variations of the R134a temperatures at the inlet and outlet of the evaporator and condenser sections with the increasing filling ratio when T_{fre} is 8 °C and 2 °C. The overall variation tends of these temperatures remains unchanged even the heat source condition of the CLT various. The difference between the inlet temperature of evaporator $T_{eva,in}$ and the outlet temperature of evaporator $T_{eva,out}$ is higher than 30 °C when the filling ratio is 9%. When the filling ratio increases to 18%, this temperature difference is still close to 20 °C. However, this temperature difference further decreases with the increase of the filling ratio, and the values of $T_{eva,in}$ and $T_{eva,out}$ become almost the same when the filling ratio reaches 27%. Besides, the difference between the inlet temperature of condenser $T_{con,in}$ and the outlet temperature of condenser $T_{con,out}$ also shows an obvious decreasing trend. The phenomenon further certificates the overheating of evaporator and the undercooling of condenser when the filling ratio is lower than 27%. Besides, $T_{con,in}$ stabilizes at -2 °C when the filling ratio is within 27-44%, which is lower than that when the filling ratio is 9% or 18% and is obviously higher than that when the filling ratio is larger than 53%. This illustrates that the outlet R134a of the evaporator do not reach undercooling state when the filling ratio is within 27-44% whereas the outlet of the evaporator is dipped in the liquid R134a when the filling ratio is more than 53%. It should be point out that the difference between $T_{con,out}$ and $T_{eva,in}$ is obviously lower than the difference between $T_{eva,out}$ and $T_{con,in}$ because the specific heat of the gaseous R134a is much lower than that of liquid R134a when the heat gain from the ambient air and the solenoid valve is similar. The results preliminarily show that the suitable R134a filling ratio is in close proximity to 35%.

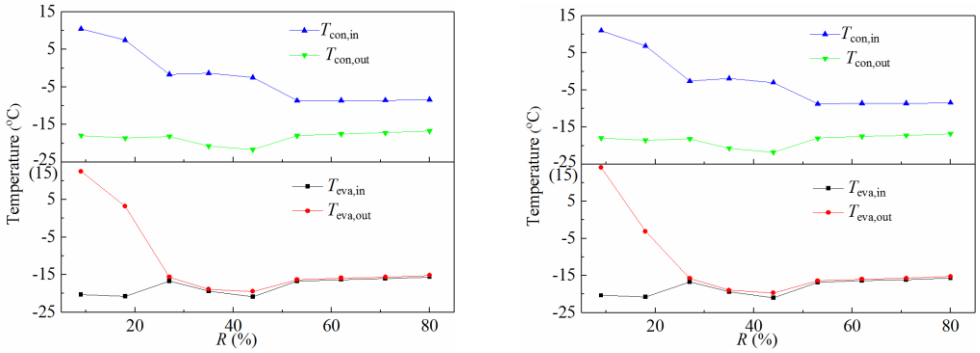

(a) T_{fre} is 8 °C *(b) T_{fre} is 2 °C*

Figure 6: The inlet and outlet temperatures of evaporator and condenser versus R for selected Tfre

Based on the preliminarily selected R134a filling ratio 35%, the long-term operating process is showed in Figure 7. The characteristic temperature of the heat conducting plate T_{pla} and the heat transfer rate Q reach relative stable states in the first 15 min, and then decrease slowly with the decreasing T_{fre}. T_{fre} decreases to 8 °C, 5 °C, 2 °C, and 0 °C in 35 min, 56 min, 90 min, and 130 min, respectively. The temperature dropping rate gradually decreases with time.

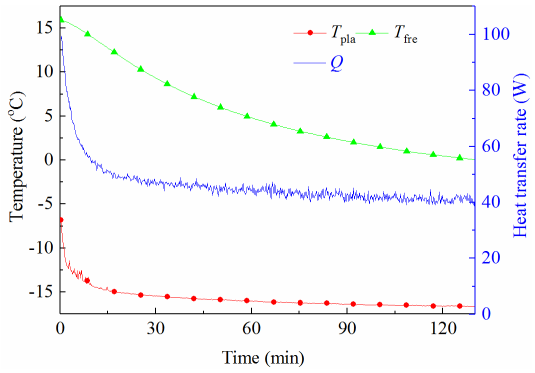

Figure 7: Variation of T_{pla}, T_{fre}, and Q in the cooling period when R is 35%

Figure 8 shows the variations of the average evaporator pressure P_{eva}, the average condenser pressure P_{con}, the fitted equivalent thermal resistance R_{fit}, and the fitted heat transfer rate Q_{fit} in the long-term test. Q_{fit} reaches approximately 40 W, P_{eva} and P_{con} fluctuate around 0.146 MPa and 0.1435 MPa, respectively, when T_{fre} is 0 °C. The decreasing trend of P_{eva} and P_{con} are similar to that of the heat transfer rate whereas R_{fit} increases sharply at first and then gradually decreases to 0.59 °C/W following the rule of Q_{fit}. The results show that the CLT with 35% filling ratio present reliable heat transfer capability and stability and that the temperature control system of fresh food compartment can be rapidly cooled by the controllable loop thermosyphon according to the national test standard for household refrigerators (PRC, 2016). This filling ratio is adopted for the following temperature control researches.

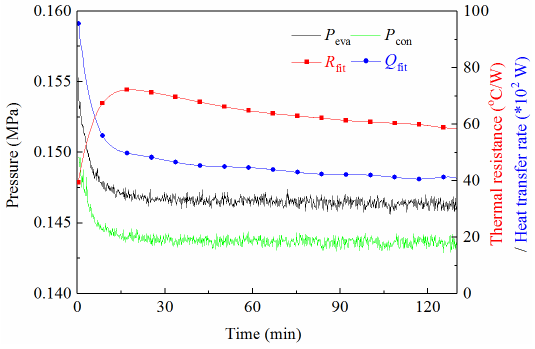

Figure 8: Variation of P_{eva}, P_{con}, R_{fit}, and Q_{fit} in the cooling period when R is 35%

4.2. Temperature adjustment capability

To test the adjustment capability of the CLT on the average temperature of the fresh food compartment, the two magnetic valves that are managed by the temperature controller were employed to switch on/off the inner flow cycle of the CLT. The average value of the upper and lower limits was varied to adjust the average value of T_{fre}, $T_{fre,ave}$, within the range of 2-8 °C. Particularly, the behaviours of the temperature control system that operates in stable start-stop cycles were studied when T_{fre} was fluctuating around 8 °C, 5 °C, and 2 °C, respectively. Figure 9 detailedly describes the stable start-stop cycles for different $T_{fre,ave}$. When $T_{fre,ave}$ is 8 °C, the start-stop cycle of CLT is about 39.4 min, the operating time within the cycle is 4.4 min, and the start-stop ratio, which is stopping time divided by operating time, is 12.6%. The upper and lower limits of T_{fre} are approximately 8.3 °C and 7.7 °C. The maximum value of T_{pla} reaches 7.3 °C and Q continuously decreases from 91.8 W to 62.9 W during the operating time. When $T_{fre,ave}$ is 5 °C, the start-stop cycle of CLT decreases to 34 min, the operating time within the cycle increases to 6.6 min, and the start-stop ratio rises to 24.1%. The maximum value of T_{pla} can only rises to 0 °C because the melting process of the ice on the heat conducting plate absorbs considerable heat and the decreasing trend of Q becomes much slower when it drops to about 55 W during the operating time. Finally, when $T_{fre,ave}$ is adjusted to 2 °C, the start-stop cycle of CLT decreases to 27.2 min, the operating time within a cycle significantly increases to 9.5 min, and the start-stop ratio obviously rises to 53.7%. The maximum value of T_{pla} cannot rise to 0 °C this time and the decreasing of Q can be clearly divided into rapid and slow descent period where the demarcation point is approximately 60 W.

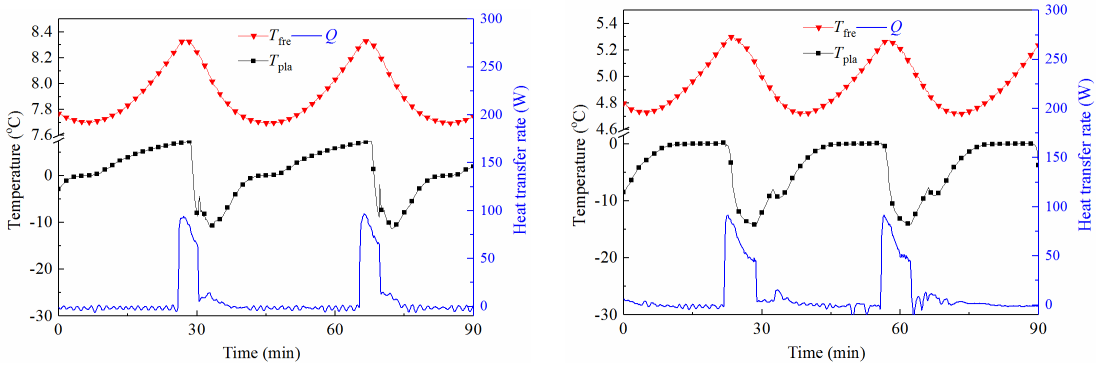

(a) $T_{fre,ave}$ = 8 °C *(b) $T_{fre,ave}$ = 5 °C*

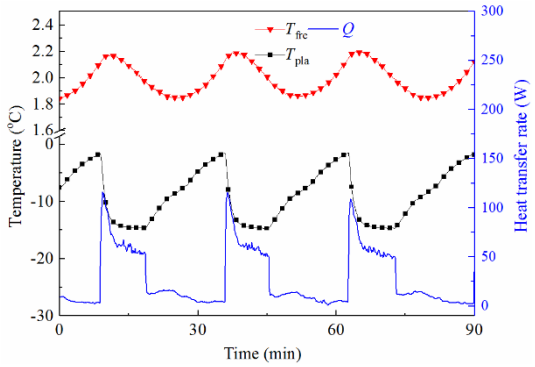

(c) $T_{fre,ave}$ = 2 °C

Figure 9: The stable on/off operating states for different $T_{fre,ave}$

More tests on the adjustment capability of the CLT were done to reveal the variation principles of the start-stop cycle and the operating ratio versus $T_{fre,ave}$. The variations are shown in Figure 10: while the $T_{fre,ave}$ gradually increases, the start-stop cycle stably decreases with the increasing operating ratio. The variation tends are relatively stable when $T_{fre,ave}$ various within 2-8 °C. The results further certificate the adjustment capability of the CLT is qualified for the temperature management of the fresh food compartment of a household compartment.

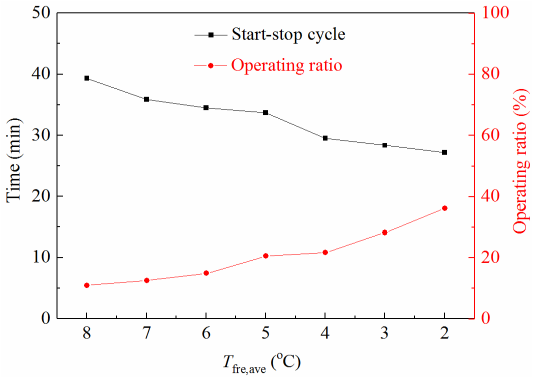

Figure 10: The start-stop cycle and operating ratio of the CLT versus $T_{fre,ave}$

5. CONCLUSIONS

In this study, a temperature management test rig is set up to analyze the precise temperature control capability of the CLT. To confirm the potential of CLT as a high-precision temperature management device in the fields of cool-storage refrigerators and other applications, we investigate its performances in long-term and start-stop operating modes. The tests on the behaviours of the CLT are completed with different R134a filling ratios and fresh food compartment temperatures. The temperature adjustment capabilities are tested. The following conclusions can be drawn:

(1) When the filling ratio increases from 9% to 80%, the heat transfer rate rises at first and then drops with the maximum value of 49.35 W. Even the temperature of fresh food compartment varies, the maximum heat transfer rate appears when the filling ratio increases to 35%. During the long-term operating test, the fitted heat transfer rate of CLT decreases to approximately 40 W when the average temperature of fresh food compartment is cooled to 0 °C. The fitted equivalent heat transfer resistance increases sharply at first and then gradually decreases to 0.59 °C/W. The results show that the CLT with 35% filling ratio present reliable heat transfer capability and stability. Thus, it is adopted for the following temperature control researches.

(2) When the average temperature of the fresh food compartment fluctuates within 7.7-8.3 °C, the start-stop cycle of CLT is about 39.4 min and the start-stop ratio is 12.6%. The heat transfer rate of CLT continuously decreases from 91.8 W to 62.9 W during the operating time. The start-stop cycle decreases and the operating ratio of CLT increases stably when the temperature of the fresh food compartment decreases. When it reaches 2 °C, the start-stop cycle of CLT decreases to 27.2 min and the start-stop ratio obviously rises to 53.7%. The results certificate the adjustment capability of the CLT is qualified for the temperature management of the fresh food compartment of a household compartment.

6. ACKNOWLEDGEMENTS

This study was sponsored by External Cooperation Program of Department of Science & Technology of Anhui Province of China (BJ2090130038), National Science Foundation of China (51476159, 51378483, 51776193), Anhui Provincial Natural Science Foundation (1608085QE96) , and the Fundamental Research Funds for the Central Universities (WK6030000066).

7. REFERENCES

Bernier M A, Baliga B R, 1992. A 1-D/2-D model and experimental results for a closed-loop thermosyphon with vertical heat transfer sections. *International journal of heat and mass transfer,* 35 (11), 2969-2982.

Bodjona S. Videcoq E, Saurel R, Chinnayy A, Benselam A, Bertin Y, 2017. Transient simulation of a two-phase loop thermosyphon with a model out of thermodynamic equilibrium. *International Journal of Heat and Mass Transfer*, 108, 2321-2332.

Chen KS, Tsai ST, Yang YW, 1994. Heat transfer performance of a double-loop separate-type heat pipe: measurement results. *Energy Conversion and Management,* 35 (12), 1131-1141.

Chen S, Yang J, 2016. Loop thermosyphon performance study for solar cells cooling. *Energy Conversion and Management,* 121, 297-304.

Chehade AA, Louahlia-Gualous H, Masson SL, Victor I, Abouzahab-Damaj N, 2014. Experimental investigation of thermosyphon loop thermal performance. *Energy Conversion and Management,* 84, 671–680.

Cao J, Pei G, Chen C, Jiao D, LI J, 2017. Preliminary Study on Variable Conductance Loop Thermosyphons. Energy Conversion and Management, 147, 66-74.

Cao J, Li J, Zhao P, Jiao D, Li P, Hu M, Pei G, 2016. Performance evaluation of controllable separate heat pipes. *Applied Thermal Engineering*, 100, 518-527.

Cao J, Pei G, Jiao D, Zhao P, Li J, Wang Y, 2017. Experimental investigation on controllable loop thermosyphon with a reservoir. *Applied Thermal Engineering*, 126, 322-329.

Cao J, Pei G, Su Y, Munir A, Li J, Wang Y. Effect of reservoir on controllable loop thermosyphon, 2016. *Bulgarian Chemical Communications*, 48 (E), 297-305.

Franco A, and Sauro F, 2012. F Loop Two Phase Thermosyphon of Small Dimensions: a review of the Experimental Results. *Microgravity Science and Technology,* 24 (3), 165-179.

Khodabandeh R, 2004. Thermal performance of a closed advanced two-phase thermosyphon loop for cooling of radio base stations at different operating conditions. *Applied Thermal Engineering*, 24 (17-18), 2643-2655.

Li T, Jiang Y, Li Z, Liu Q, Tang D, 2016. Loop thermosiphon as a feasible cooling method for the stators of gas turbine. *Applied Thermal Engineering*, 109, 449-453.

Michaelides IM, Lee WC, Wilson DR, Votsis PP, 1992. Computer simulation of the performance of a thermosyphon solar water-heater. *Applied Energy*, 41 (2), 149-163.

Matsubara K, Matsudaira Y, Kourakata I, 2016. Thermosyphon loop thermal collector for low-temperature waste heat recovery. *Applied Thermal Engineering,* 92, 261-270.

Mameli M, Mangini D, Vanoli GFT, Araneo L, Filippeschi S, Marengo M, 2016. Advanced multi-evaporator loop thermosyphon. *Energy*, 112, 562-573.

Naghavi MS, Ong KS, Mehrali M, Badruddina IA, Metselaara HSC, 2015. A state-of-the-art review on hybrid heat pipe latent heat storage systems. *Energy Conversion and Management,* 105, 1178-1204.

Nayak AK, Dubey P, Chavan DN, Vijayan PK, 2007. Study on the stability behaviour of two-phase natural circulation systems using a four-equation drift flux model. *Nuclear Engineering and Design*, 237 (4), 386-398.

Oliveira JLG, Tecchio C, Paiva KV, Mantelli MBH, Gandolfi R, Ribeiro LGS, 2016. In-flight testing of loop thermosyphons for aircraft cooling. *Applied Thermal Engineering*, 98, 144-156.

PRC. The State Standard of the People's Republic of China for household and similar refrigerating appliances, 2016. China. GB/T 8059-2016, 1-64.

Samba A, Louahlia-Gualous H, Masson S Le, Nörterhäuser D, 2013. Two-phase thermosyphon loop for cooling outdoor telecommunication equipments. *Applied Thermal Engineering,* 50 (1), 1351-1360.

Tong Z, Liu X, Jiang Y, 2017. Experimental study of the self-regulating performance of an R744 two-phase thermosyphon loop. *Applied Energy*, 186 (1), 1-12.

Tong Z, Liu X, Jiang Y, 2017. Three typical operating states of an R744 two-phase thermosyphon loop. *Applied Energy,* 206, 181–192.

Wang Y, Yang L, Wang X, Chen H, Fan H, Taylor RA, Zhu Y, 2017. CFD simulation of an intermediate temperature, two-phase loop thermosiphon for use as a linear solar receiver. *Applied Energy,* 207, 36-44.

Wang Y, Lu B, Wang X, Chen H, Fan H, Taylor RA, Zhu Y, 2017. Experimental investigation of the thermal performance of a horizontal two-phase loop thermosiphon suitable for solar parabolic trough receivers operating at 200-400 ºC. *Energy,* 132, 289-304.

Yan C, Shi W, Li X, Wang S, 2016. A seasonal cold storage system based on separate type heat pipe for sustainable building cooling. *Renewable Energy*, 85, 880-889.

Zhang H, Shao S, Xu H, Zou H, Tian C, 2014. Free cooling of data centers: A review. *Renewable and Sustainable Energy Reviews,* 35, 171-182.

215: Open system and materials of thermochemical energy storage in built environment

Yanan ZHANG[1], Yate DING[2], Auwal DODO[3], Hasila JARIMI[4], Saffa RIFFAT[5]

[1] University of Nottingham, Nottingham, UK, yanan.zhang@nottingham.ac.uk
[2] University of Nottingham, Nottingham, UK, yate.ding@nottingham.ac.uk
[3] University of Nottingham, Nottingham, UK, auwal.dodo@nottingham.ac.uk
[4] University of Nottingham, Nottingham, UK, hasila.jarimi@nottingham.ac.uk
[5] University of Nottingham, Nottingham, UK, saffa.riffat@nottingham.ac.uk

More than 40% of energy consumption occurred in building system with 36% of greenhouse gas emissions. In the UK, a major of 63% energy end-use for space heating/cooling for a comfort building condition. Thermochemical energy storage (TES) can Be a promising advanced technology in addressing massive energy use for heating and cooling in building application. The system can be an alternative to the conventional energy system because of the lower heat loss, higher energy density of the materials, more efficient and environmentally friendly.

In this paper, a novel open system of thermochemical energy storage has been shown, and different high energy density storage salts (eg $CaCl_2$, $MgSO_4$, $LiNO_3$, and $MgCl_2$) with host matrix such as vermiculite and advanced carbon were used as thermochemical heat storage (THS) materials. The aim of this paper is characterize different composite to find better performing materials with higher energy density, lower heat loss, next regeneration temperature, higher temperature lift in reaction process and higher system efficient. And some modification has been done on this The results indicate that vermiculite based composite with MgSO4 and CaCl2 as energy storage spices showed the best performance in the system and presented the optimal option. And the modified model offers a higher accuracy and efficiency than the Simplified model.

Keywords: Thermochemical energy storage (TES); energy storage materials; energy storage system; open energy storage system.

1. INTRODUCTION

Energy storage is to store generated energy at early time for later use. It comes in multiple forms, such as chemical energy, electrical potential energy, gravitation potential energy, radiation, latent heat (Paksoy, 2007) and kinetic power (Zalba, 2003). Back to the year 1780 BC, about 4000 years ago, an icehouse was first built in Mesopotamian town. That was the 1st record people using energy storage. In China, reference says that ice stored before 1100 BC. In the year 450s, an ice pot was built as a fridge. But the cost was very high, only when they were doing sacrifice or some important events, ice pot would be used. In Qing dynasty (the year 1600 to 1900), ice house was very common and people can buy some ice cream with very reasonable price. Figure 1 shows the mismatch between the solar energy and heating demand. We got lots of solar energy in summer or at daytime, but we need more heating in winter or at night. That's the reason why we need an energy storage system.

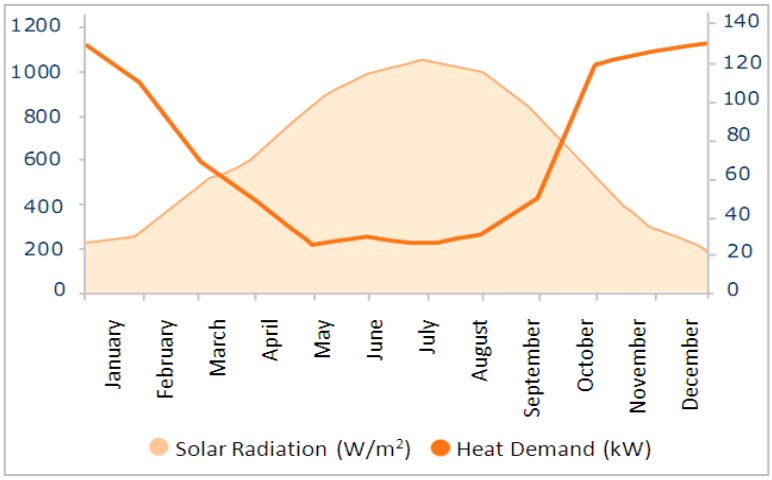

Figure 1: The mismatch between available solar energy and building heating demand.

Thermochemical energy storage (TES) is a novel technology with the advantage of high energy storage density and less heat loss. That makes it easier for long time energy storage at a relative low temperature and a large number of thermochemical energy storage materials are available. TES technologies provide more versatility to the energy plant and makes its reliance during operation hours more dependable (Prieto, 2016). Because TES technologies have the advantage of nearly no energy loss during storage and very good volumetric energy density. Normally, THS materials can store heat with very less heat loss, as long as they are proper sealed to keep the sorbent away from water (Aydin, 2015), heat will be released only when water vapor is purposely admitted (Casey, 2014; Jamiri, 2017). In thermochemical energy storage system, no matter it is a closed or open system, materials/desiccants store heat inside and separated into two parts during the storage or charging process, then the two parts can be stored separately. When heating or cooling should be provided, just simply put the two parts together, then it will release or absorb heat (Figure 2). It allows wider and more flexible usage of TES such as seasonal storage of solar energy.

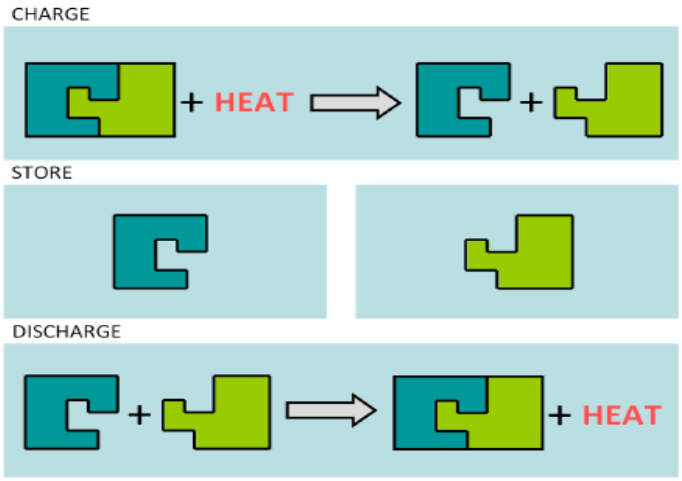

Figure 2: Thermochemical energy storage process.

Thermochemical Energy Storage (TES) system has been a hot topic in energy storage research area. At current stage, the storage stability of TES system need to be improved, which related to the TES materials parameters and properties. TES materials is one of the most important parameters that effect system performance. Thermochemical energy storage materials is an innovative and alternative energy storage source. It can store energy for later using and reduce greenhouse gas emissions as well. The materials normally has very high energy density, which can store higher energy. This report presents the details of thermochemical energy storage system and materials used in the project, include some parameters of each material, such as energy density, bulk density, water uptake, regeneration temperature and describes the fundamental phenomena in the lab work or basic test. This thermochemical energy storage system is an open loop, which is driven by low temperature heat sources, such as solar energy and waste heat recovery. An overview of thermochemical energy storage system and materials are given in the paper. TES materials using endothermic and exothermic salts to impregnate into vermiculite and silica gel to combine the new composites for the open TES system. Vermiculite is a natural, inorganic, non-toxic mineral that will swell under high temperatures (Webb, 1824). After being calcined at high temperature, the gangue tablets can rapidly expand 6-20 times in volume, and the specific gravity after swelling is 60-180kg/m^3, which has strong thermal insulation properties. Vermiculite is chemically stable and it is insoluble in water. The pH of vermiculite is 7-8, and it is non-toxic, odourless, no side effects for environment. Because of its advantages, vermiculite composites with TES salts are promising candidates for TES system.

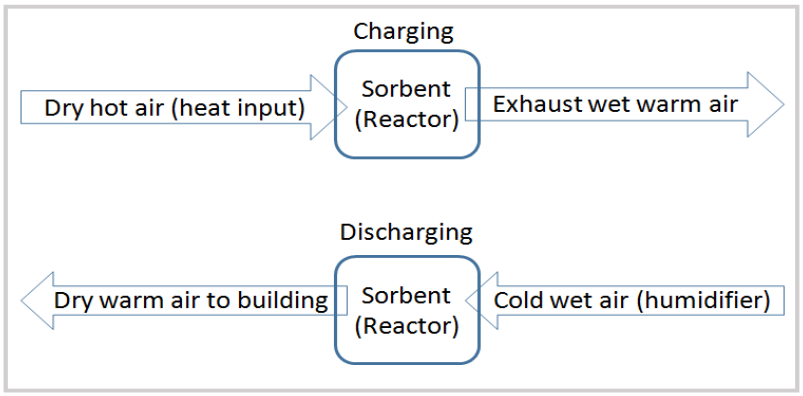

Figure 3: Operating principle of open sorption thermochemical heat storage system.

2. THERMOCHEMICAL ENERGY STORAGE MATERIALS TESTING

Thermochemical energy storage materials hold the promises of high energy density and few heat loss during energy storing and releasing. The reason is because energy is stored in a chemical reaction with combination or break of the chemical bond, and the components are stored separately. When the components get together, heat will be released (exothermic materials) or absorbed (endothermic materials). Sorbent salts such as $MgSO_4$, $CaCl_2$, LiCl, $MgCl_2$, $LiNO_3$, $NaNO_3$ and urea have a much higher energy density compared with traditional sorbents, such as silica gel and zeolite. However, there is another significant issue – these sorbents can deliquescence under some conditions and become saturated at certain relative humidity (RH) levels (Jamiri, 2017). And also, swelling and agglomeration may happen after several cycle reaction, which will affect heat and mass transfer and lead to an efficiency drop in charging and discharging process.

2.1. Inside scanning of SIM composites

Scanning Electron Microscopes (SEM) can be used to visualise the salt inside of the matrix of a SIM composite. The resolution produced is better than one nanometre. This can be used to make sure that the salt is binding uniformly inside the matrix and therefore maximising surface area and potential for mass and heat transfer.

Material characterization allows the SIM samples to be compared for the best overall material in an open loop system can be determined. The increase in porosity of samples after impregnation shows the potential of salt impregnation of host matrices in open cycle THS systems (from SEM photos).

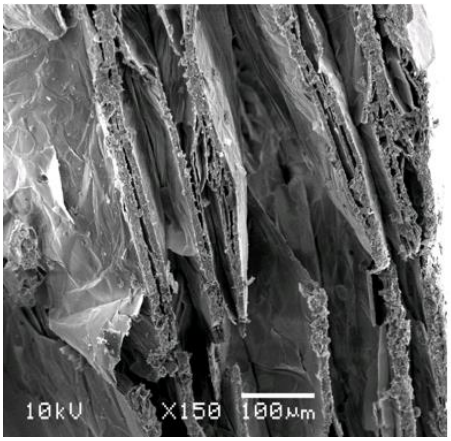

Figure 4. Vermiculite

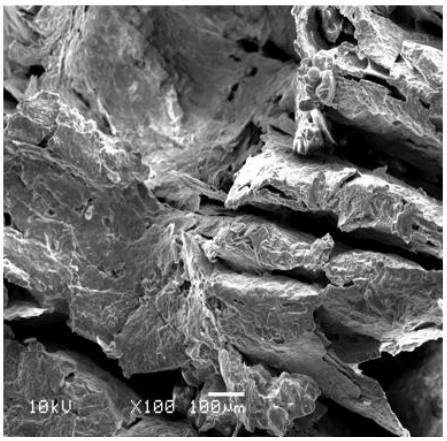

Figure 5. V-$MgSO_4$-LiCl

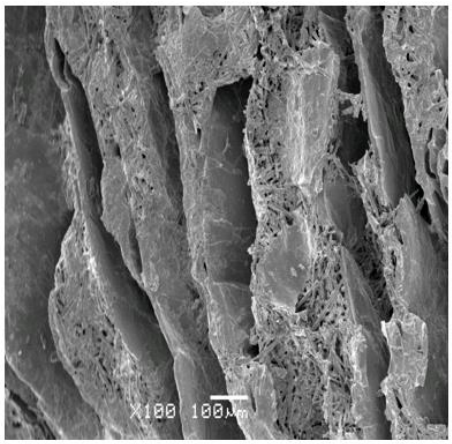

Figure 6. V-$CaCl_2$-LiCl

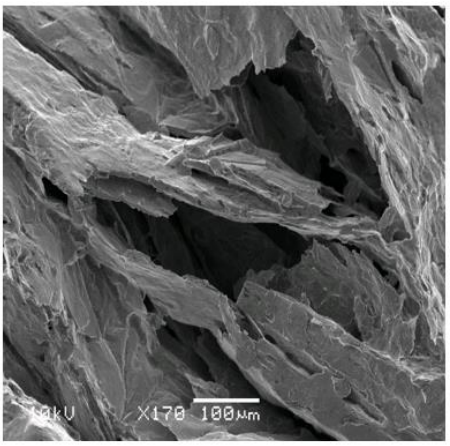

Figure 7. V-$CaCl_2$-$MgSO_4$

2.2. Energy density test for thermochemical heating and cooling materials

SDT-Q600 will be used for materials energy density test. The test materials will include thermochemical heating and cooling storage materials: vermiculite with $MgCl_2$+$LiNO_3$, vermiculite with $MgSO_4$+$CaCl_2$, vermiculite with $MgSO_4$+$MgCl_2$+$LiNO_3$, vermiculite with urea and vermiculite with $NaNO_3$.

Figure 8: SDt-Q600 for materials energy density analysis.

Sample Preparation

The Vermiculite matrix samples should be wetted two hours prior to testing so that the samples relative humidity can reach 95%, and the TES material is holding its maximum amount of water.

Testing

Before the test is performed, two empty alumina cups are placed onto the balance. One will be used to hold the sample later and the other is a reference cup. The furnace is sealed and the 'tare' function is used repeatedly until the weight reading of the sample and reference cups become within 0.1mg of one another. This process must be repeated before every sample is tested. The two cups are then heated from ambient temperature to 150°C at a constant rate of 10°C/minute in an inert argon atmosphere and cooled using ambient air whilst the weight of the cups is continuously measured along with heat flow. This gives a baseline measurement.

One cup is now filled with a sample to approximately halfway, and then the cup is placed onto the balance next to the empty reference cup. Once the balance settles slightly, the furnace is sealed, and then the balance is allowed to fully settle inside the closed furnace. The test starts, and the temperature is increased again from ambient to 150°C at a constant rate in an inert argon atmosphere then cooled using ambient air. Another graph is formed. However, we only want to know information about the sample, not the cup. Therefore, we must subtract the baseline measurement from the test measurement. This can be performed by the SDT Q600 software. To find the energy density of the sample, we take the average integral reading (J/g) in the temperature range of 30-150°C.

Results

Table 1: SDT-Q600 analysis results.

	Energy density, kJ/kg	**Regeneration temperature, °C**
V-$MgSO_4$-LiCl	990.2	74.7
V-$MgSO_4$-$CaCl_2$	1173.5	63
V-$MgSO_4$-$LiNO_3$	1000.8	81.7
V-$MgSO_4$-$LiNO_3$-$MgCl_2$	748.6	71.7
V-$NaNO_3$	872.3	82
V-Urea	727.85	54.5

According to the TA analysis results for SDT-Q600 test, for the thermochemical heating storage materials, V-$MgSO_4$-$CaCl_2$ showed the highest energy density (1173.5 kJ/kg) and lowest regeneration temperature (63 °C). Because of these characteristics, V-$MgSO_4$-$CaCl_2$ is the optimal material can be selected. For the thermochemical cooling storage materials, V-$NaNO_3$ showed the highest energy density of 872.3 kJ/kg, while V-Urea showed the lowest regeneration temperature at 54.5 °C; however, because the price of $NaNO_3$ is much higher than urea, thus, V-Urea is the better thermochemical cooling storage material.

2.3. Thermochemical heating materials sorption experiment

Sorption experiments with different materials and different salts sorption solution will be done. The adsorption liquids of the four salts solution are KNO_3, $MgSO_4$, $MgCl_2$ and LiCl. The test materials are: vermiculite with $CaCl_2$+LiCl, vermiculite with $MgSO_4$+$MgCl_2$, vermiculite with $MgSO_4$+$CaCl_2$. A sorption test is used to observe the mass of water a sample can adsorb in a set period under differing humidity. In the set up below four cases are used to create four atmospheres, each with a different relative humidity. These atmospheres are created using solutions of KNO3, MgSO4, MgCl2 and LiCl (with relative humidity level: 92%, 75%, 40% and 16%) at the bottom of each case.

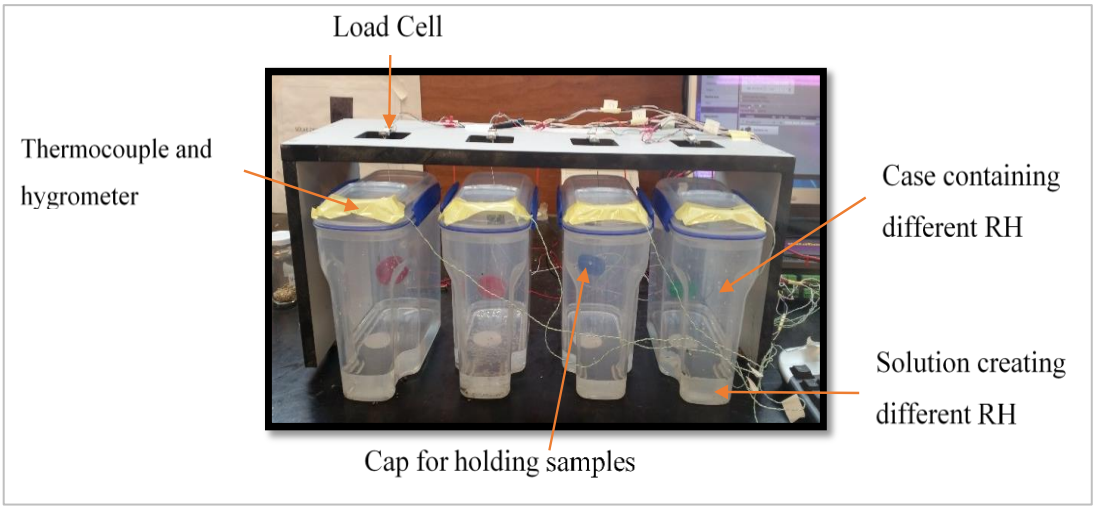

Figure 9: Sorption testing set.

Calibration

The load cell must first be calibrated before a sample can be placed into the cap. This is done in two steps:

- A reading is taken from the LoadCell with no sample in each cap. (ie. 0g in container);
- Another three readings are taken with fixed mass in each cap (2.5g, 4g and 5g);
- Everytime the mass put in the cap must be left for at least 20 minutes for the LoadCell reading to be stable.

Calibration should be done in each weight sensor (Load Cell) to record an accurate number. Before the test, different loads used in the four cups. Figures show different readings in different load cells.

Table 2: LoadCell calibration.

	Calibration 1	*Calibration 2*	*Calibration 3*	*Calibration 4*	*Formula*
Real weight, g	0g	2.5g	4g	5g	X: sensor reading; y: real reading
LoadCell1 reading, g	192	205	213	218	0.196x-37.654=y
LoadCell2 reading, g	56	68	76	81	0.196x-10.933=y
LoadCell3 reading, g	60	49	42	38	13.334-0.221x=y
LoadCell4 reading, g	35	48	55	60	0.198x-6.978=y

Samples to be tested:

- V-$CaCl_2$-LiCl (oven temp. at 200°C)
- V-$MgSO_4$-$MgCl_2$ (oven temp. at 200°C)
- V-$MgSO_4$-$CaCl_2$ (oven temp. at 200°C)
- V-$MgSO_4$-LiCl (oven temp. at 200°C)

Testing

Once the load cells have been calibrated, each cap can be filled with approximately 2g of sample. Each sample with then start to adsorb moisture from the environment around it and its mass will change. This is logged using a datalogger for at least seven days for each sample.

Results

The results show the minimum humidity for complete hydration of each salt in a time period that can be set as required.

Table 3: Sorption test results.

Water uptake, g/g	KNO_3, 92%	$MgSO_4$, 75%	$MgCl_2$, 40%	LiCl, 16%
V-$CaCl_2$-LiCl	1.75	1.55	1.15	0.5
V-$MgSO_4$-$MgCl_2$	1.65	1	0.4	0.25
V-$MgSO_4$-$CaCl_2$	2	1.6	1.3	0.4
V-$MgSO_4$-LiCl	2.5	1.8	1	0.45

As it can be seen in the above figures, KNO_3 saturated solution provides the highest humidity condition (RH=92%). $MgSO_4$ saturated solution provides second highest humidity condition (RH=75%). LiCl and $MgCl_2$ give a similar lower humidity condition ($MgSO_4$ RH=40% and LiCl RH=17%). According to the results, V-$MgSO_4$-LiCl and V-$MgSO_4$-$CaCl_2$ showed a relative high water uptake, and in the high humidity level condition, materials can normally have more water uptake. Therefore, V-$MgSO_4$-$CaCl_2$ and V-$MgSO_4$-LiCl will be better sorbents with higher water uptake in the thermochemical heat storage system.

3. AN OPEN SYSTEM FOR THERMOCHEMICAL HEAT STORAGE TESTING

Thermochemical heat storage system uses thermochemical materials act with moisture to generate heat for providing heating in built environment. This open system (Figure 10) includes power, reaction rig (to store thermochemical materials, it is the reaction place), humidifier (to supply moisture), fan (to supply decent air flow rates) and heater (for regeneration). In the real system for next step, solar PV system will replace power system, fan and heater. Thermochemical heat storage system stores solar energy in the thermochemical materials in summer/day time and release heat in winter/cool night when needed. Regeneration will take place in day time with solar energy system.

Figure 10: Open system for thermochemical energy storage materials test rig.

3.1. Chemical reaction (Hydration reaction)

A number of Thermochemical energy storage (TES) salts and matrix were chosen for an open loop THS system. These materials store energy by being dehydrated and release that energy when rehydrated. TES materials (Exothermic materials for heating and endothermic materials for cooling) are adsorbent/desiccant in the system.

$CaCl_2 + 6H_2O \rightarrow CaCl_2 \cdot 6H_2O + Heat$

$LiCl + 5H_2O \rightarrow LiCl{\cdot}5H_2O + Heat$

$MgSO_4 + 7H_2O \rightarrow MgSO_4{\cdot}7H_2O + Heat$

$(NH_2)_2CO + 2H_2O \rightarrow (NH_4)_2CO_3 - Heat$

3.2. Composite materials characterization

Because of the structure of the test rig and the big gap between the rig body and reaction mesh, moisture air cannot go through the test materials completely. Therefore, the water uptake was very low in this test. According to Figure 11, V-$CaCl_2$-LiCl had the highest water uptake 0.12g/g whilst the other two had similar 0.08g/g. However, lowest regeneration temperature is an important characteristic, and also by considering reaction temperature, V-$MgSO_4$-$CaCl_2$ shows good potential for use in open THS systems.

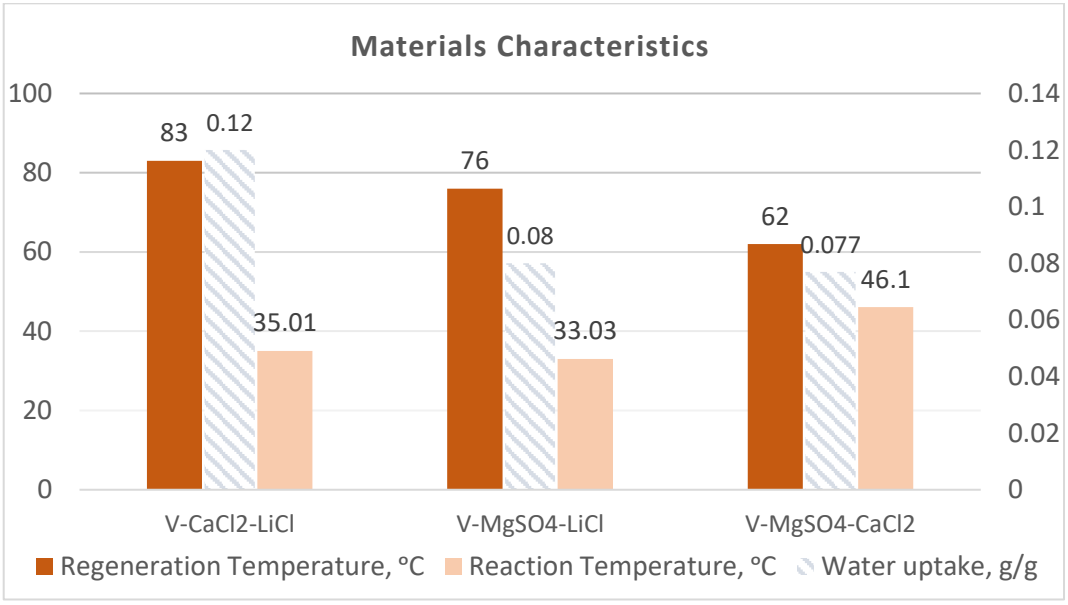

Figure 11:. Different materials characteristics.

4. CONCLUSION AND FUTURE WORK

Due to an increasing fossil fuel consumption and GHG emissions, thermochemical energy storage can be a promising advanced technology in addressing massive energy use for heating and cooling in building application, because of the lower heat loss, higher energy density of the materials, more efficient and environmentally friendly. In the project, we used different high energy density storage salts (e.g. $CaCl_2$, $MgSO_4$, LiCl, $MgCl_2$) with vermiculite as the host matrix. In this study, it characterize different composite to find better performing materials with higher energy density, lower heat loss, lower regeneration temperature, higher temperature lift in reaction process and higher system efficient.

The results of this study showed the following:

- The impregnation of the TES materials can increase porosity of the host matrix;
- The reaction temperature and the regeneration temperature showed that V-$MgSO_4$-$CaCl_2$ displays optimal characteristics for the potential of using in an open TES system for heating and V-Urea has been selected for cooling.

Future research will focus on:

- testing and analysing different salts mixture structure and performance;
- finding better way for materials reuse for long-life cycle;
- filling the gap between energy demand and supply;
- modify the current thermochemical heat storage rig for cooling teat as well;
- optimising thermochemical energy storage system for both heating and cooling with solar thermal collector driven.

5. ACKNOWLEDGEMENTS

This work is funded by the Newton Fund Institutional Links (Award ref 216229499) and Engineering and Physical Sciences Research Council (Award ref AAM118072-EOI). The authors thank the Nanoscale and Microscale Research Centre (nmRC) for providing access to instrumentation and Mrs Christine Grainger-Boultby for technical assistance.

6. REFERENCES

Paksoy, H.Ö., *Thermal energy storage for sustainable energy consumption: fundamentals, case studies and design*. Vol. 234. 2007: Springer Science & Business Media.

Zalba, B., et al., *Review on thermal energy storage with phase change: materials, heat transfer analysis and applications.* Applied thermal engineering, 2003. **23**(3): p. 251-283.

Prieto, C., et al., *Review of technology: Thermochemical energy storage for concentrated solar power plants.* Renewable and Sustainable Energy Reviews, 2016. **60**: p. 909-929.

Aydin, D., S.P. Casey, and S. Riffat, *The latest advancements on thermochemical heat storage systems.* Renewable and Sustainable Energy Reviews, 2015. **41**: p. 356-367.

Casey, S.P., et al., *Salt impregnated desiccant matrices for 'open'thermochemical energy storage—Selection, synthesis and characterisation of candidate materials.* Energy and buildings, 2014. **84**: p. 412-425.

Jarimi, H., et al., *Materials characterization of innovative composite materials for solar-driven thermochemical heat storage (THS) suitable for building application.* International Journal of Low-Carbon Technologies, 2017.

Webb, T., *Vermiculite.* American Journal of Science, 1824. **7**: p. 55.

216: Simulation analysis of shunt active power filter

Fei ZHU[1], Su WANG[2], Liang ZENG[3]

[1] School of Electrical and Electronic Engineering, Hubei University of Technology, Hubei 430068, China
[2] School of Electrical and Electronic Engineering, Hubei University of Technology, Hubei430068, China
[3] School of Electrical and Electronic Engineering, Hubei University of Technology, Hubei 430068, China

Non-linear loads appear in the power industry on a large scale, and the acquisition of high-quality electric energy has also become a universal problem. Active power filter (APF), which has the advantages of dynamic tracking and better compensation effects, has become the most efficient power electronic device in the field of harmonic pollution control. It has gradually replaced traditional passive filters and achieved rapid development. This paper first describes the basic principles of APF, the main circuit topology. The specific detection method based on the theory of instantaneous reactive power design was selected, PI control was used as the control strategy of this design, and SPWM was selected as the control method of this design. Through the analysis of the results of the Matlab/Simulink simulation, it can be concluded that the active power filter can suppress harmonics in real time.

Keywords: Three-phase three-wire system ; Active power filter ; Simulation

1. INTRODUCTION

Judging from the current technological reality, active power filter APF is still widely used alone. At the same time, after several decades of development, the APF technology method of shunt active power filter is now relatively mature (Pan, 2009; Yu, 2014; Ming, 2015; Dong, 2015; Ren Aerospace, 2012). Because the switching frequency and withstand voltage level of the power electronic devices are not high, they are basically related technologies such as multiplexing, multilevel, etc., so as to increase the frequency and withstand voltage of certain switching devices in the circuit. In this paper, the detection of harmonic currents adopts the theory of instantaneous reactive power, and the artificial neural network method is used to calculate the load too much. It is difficult to model in practical applications, and its implementation is difficult (Li, 2010). The traditional control strategy is mainly to use PI control. This article mainly controls PI on both d axis and q axis, which can reduce current tracking error.

2. THE PRINCIPLE OF SHUNT ACTIVE POWER FILTER

As shown in Figure 1, the following figure shows the principle of APF. The three-phase AC voltage on the grid side uses e_s , the output current is i_s , the load current is i_l , the compensation current generated by APF is i_c and the standard command current is i_c^* .

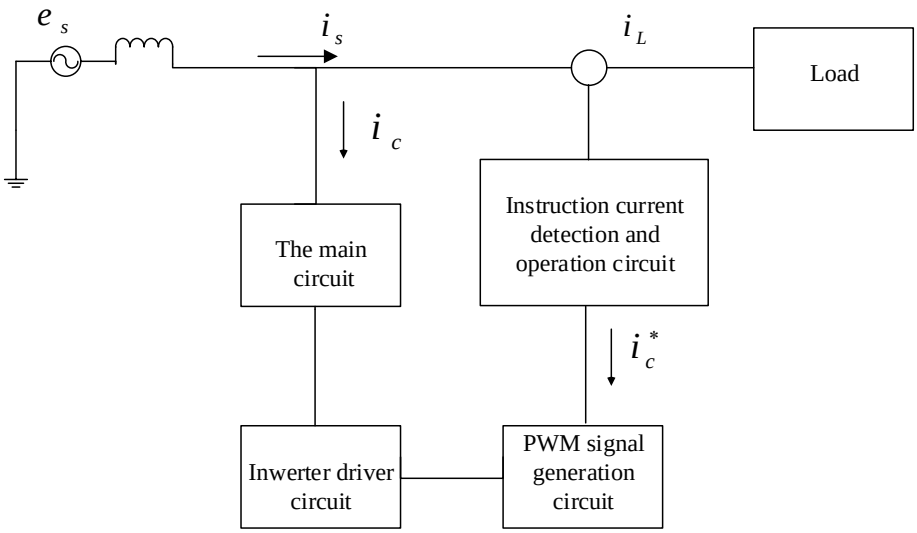

Figure 1: APF system schematic

The shunt type APF consists of a control circuit and a main circuit. Inverting and filtering are two important parts of the main circuit. The detection circuit detects the harmonics in the load to derive the command current. The command current signal is passed to the DSP and the DSP is processed, and then the DSP sends a signal to control the turning on and off of the power element IGBT to generate a series of harmonic sequences, which is the generated compensation current. These compensation currents are equal in size to the current in the grid, and are in opposite directions in phase, so that the sum of the two is zero. In this way, the harmonic currents are filtered out to meet the requirements of purifying the power grid (Chen, 2000; Peng, 2010; Cao, 2010).

3. APF MAIN CIRCUIT OVERALL TOPOLOGY

Due to the presence of harmonic currents in the power grid, the standard three-phase current is not in the form of a standard sine wave, and the harmonic currents of the power grid are cleaned by the compensation current generated by the active filter. The topology of the three-phase, three-wire, parallel APF system designed in this project is shown in the following figure:

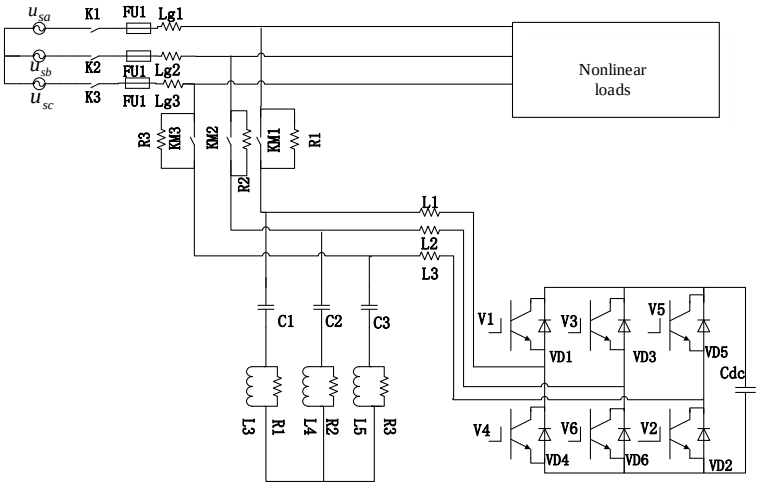

Figure 2: APF main circuit topology

As can be seen from Figure 2, the grid input, nonlinear load, inverter circuit, and filter circuit constitute the main circuit topology of the active filter design. In order to eliminate the fluctuation of the DC bus voltage generated by the AC part of the active power, the value of the capacitor C is relatively large. Inductor L and highpass passive filters are filter circuits. Grid input and non-linear loads are ancillary to this system. u_{dc} is the bus voltage on the DC side, u_{ra}, u_{rb}, u_{rc} are the output voltage of the inverter, respectively; i_{ca}, i_{cb}, i_{cc} are the compensation currents output by the filter circuit; i_{sa}, i_{sb}, i_{sc} are the output currents in the grid, respectively; i_{La}, i_{Lb}, i_{Lc} are the output currents of the load.

4. HARMONIC CURRENT DETECTION

4.1. $p-q$ theory

Akita Thai first proposed the $p-q$ theory [1], which defines instantaneous power quantities such as instantaneous active power p and instantaneous reactive power q. Later on the basis of instantaneous reactive power improvement, and later proposed the $i_p - i_q$ theory (Wu, 2009). The following mathematical modeling analysis of the theory.

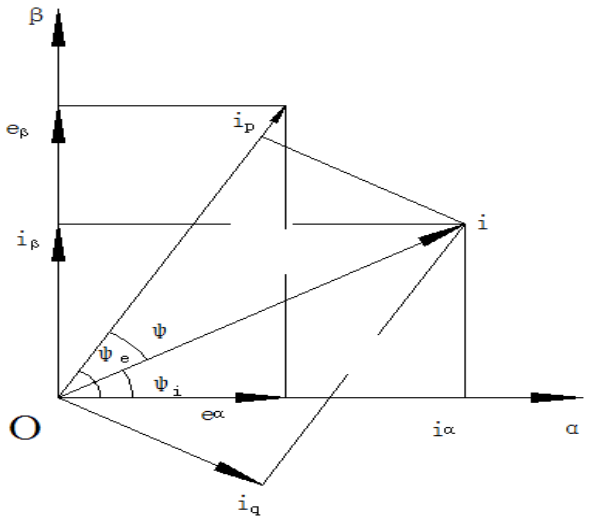

Figure 3: Voltage and current vector in $\alpha-\beta$ coordinate system

From the above vector graph we can get:

$$e = e_\alpha + e_\beta = e\angle\varphi_e \tag{1}$$

$$i = i_\alpha + i_\beta = i\angle\varphi_i \tag{2}$$

In the above equation: e and i are the moduli of vectors e and i respectively; φ_e and φ_i are the arguments of e and i, respectively.

There are vector diagrams available on the map:

$$i_p = i\cos\varphi \tag{3}$$

$$i_q = i\sin\varphi \tag{4}$$

In equations (3) and (4), $\varphi = \varphi_e - \varphi_i$, where i_p represents instantaneous active current and i_q represents instantaneous reactive current.

In a three-phase system, p represents instantaneous active power and q represents reactive power, which can be described using the following definitions:

$$p = ei_p \tag{5}$$

$$q = ei_q \tag{6}$$

Substituting Equations (3), (4), $\varphi = \varphi_e - \varphi_i$ 、 $e_\alpha = e\cos\varphi_e$, $e_\beta = e\sin\varphi_e$ into (5) and (6) yields:

$$\begin{bmatrix} p \\ q \end{bmatrix} = \begin{bmatrix} e_\alpha & e_\beta \\ e_\beta & -e_\alpha \end{bmatrix} \begin{bmatrix} i_\alpha \\ i_\beta \end{bmatrix} = C_{pq} \begin{bmatrix} i_\alpha \\ i_\beta \end{bmatrix} \tag{7}$$

Where $C_{pq} = \begin{bmatrix} e_\alpha & e_\beta \\ e_\beta & -e_\alpha \end{bmatrix}$.

4.2. $i_p - i_q$ Algorithm

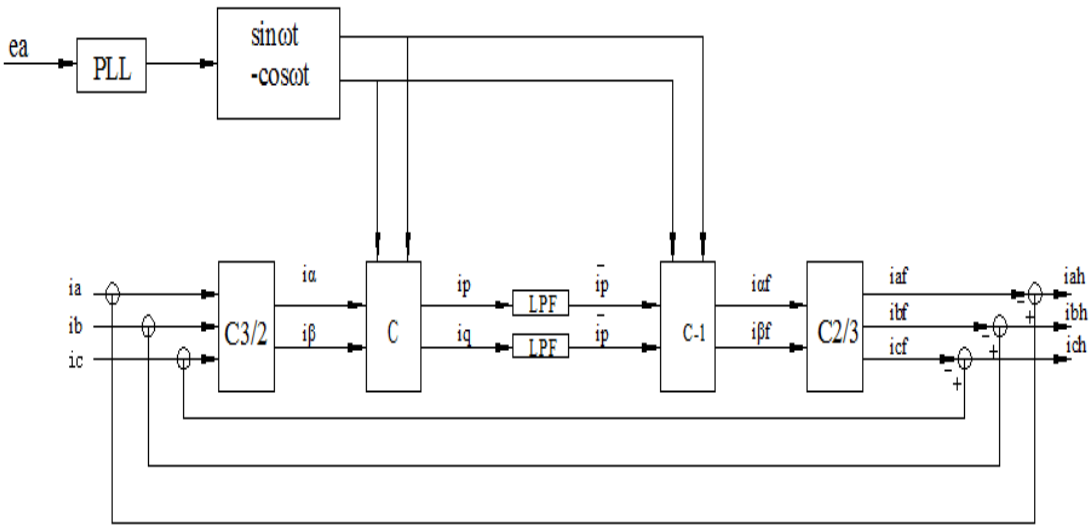

Figure 4: Schematic diagram of $i_p - i_q$ detection method

Representing the coordinate transformation from three-phase windings A, B, C to α、β、0, the same is true for $C_{2/3}$ and $C_{3/2}$, which is the coordinate transformation between α、β、0 to A, B, and C. According to the circuit diagram above, it can be seen that the three-phase currents i_a、i_b、i_c detected in the circuit are converted by $C_{3/2}$ matrix (ie, two-two transformations) to the two-phase windings α、β and the sinusoidal signal is generated by the phase-locked loop PLL. The $\sin \omega t$ and cosine signal generator -cos, the $-\cos \omega t$ ctive current component i_p and the reactive current component i_q can obtain the corresponding direct current components $\bar{i}_p$ and $\bar{i}_q$. $\bar{i}_p$ and $\bar{i}_q$ are then subjected to the $C_{2/3}$ matrix transformation (ie, two or three transformations) to obtain the corresponding fundamental wave components i_{af}、i_{bf} and i_{cf} in the α and β coordinate systems, and the fundamental wave components i_{af}、i_{bf} and i_{cf} will be detected in correspondence with them. After subtraction, we can finally get their corresponding harmonic components i_{ah}、i_{bh} and i_{ch} .

By formula (7) available:

$$\begin{bmatrix} p \\ q \end{bmatrix} = \begin{bmatrix} ei_p \\ ei_q \end{bmatrix} = \begin{bmatrix} e_\alpha & e_\beta \\ e_\beta & -e_\alpha \end{bmatrix} \begin{bmatrix} i_\alpha \\ i_\beta \end{bmatrix} \tag{8}$$

Dividing both sides of the above equation by e simultaneously yields:

$$\begin{bmatrix} i_p \\ i_q \end{bmatrix} = \frac{1}{e} \begin{bmatrix} e_\alpha & e_\beta \\ e_\beta & -e_\alpha \end{bmatrix} \begin{bmatrix} i_\alpha \\ i_\beta \end{bmatrix} \tag{9}$$

Due to $e = \sqrt{\frac{3}{2}} E_m$, finishing is available:

$$\begin{bmatrix} i_p \\ i_q \end{bmatrix} = \begin{bmatrix} \sin \omega t & -\cos \omega t \\ -\cos \omega t & -\sin \omega t \end{bmatrix} \begin{bmatrix} i_\alpha \\ i_\beta \end{bmatrix} = C \begin{bmatrix} i_\alpha \\ i_\beta \end{bmatrix} = CC_{32} \begin{bmatrix} i_a \\ i_b \\ i_c \end{bmatrix} \tag{10}$$

Where $C = \begin{bmatrix} \sin \omega t & -\cos \omega t \\ -\cos & -\sin \omega t \end{bmatrix}$.

5. SIMULATION

The simulation in this paper uses Simulink in MATLAB to build a simulation model. The simulation model of the active power filter is given below.

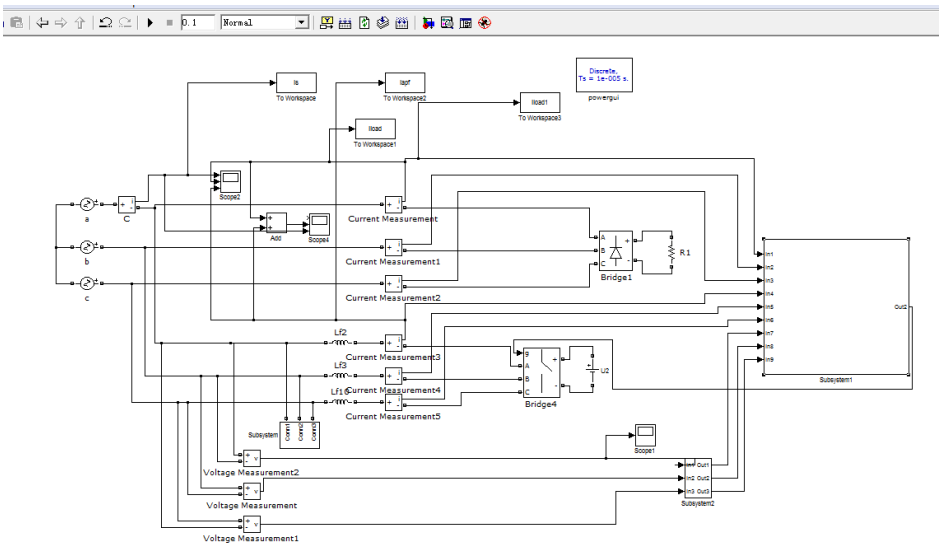

Figure 5: main circuit simulation model

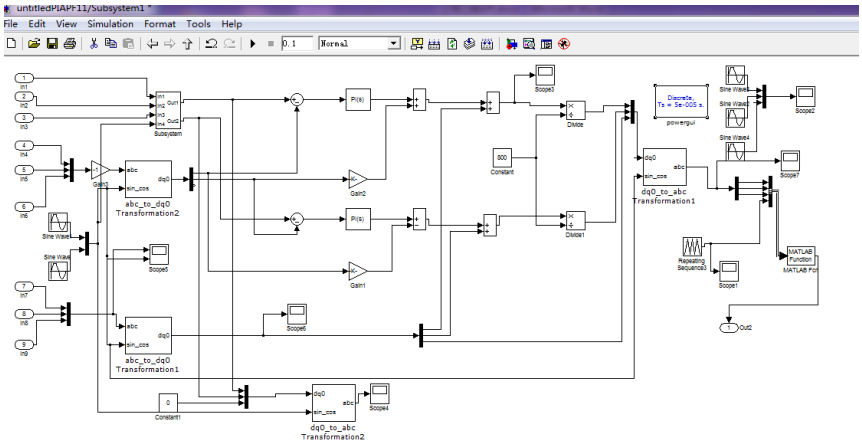

Figure 6: control circuit simulation

The parameters for voltage sources, transmission lines, filters and the load details are provided in the Table 1.

Table 1: System parameters used in Simulink

Simulation Parameters	Values	Simulation Parameters	Values
Supply Voltage(Vs)	311V	Dc Link Capacitance (C_{dc})	7960 μF
System Frequency (Fs)	50±5%Hz	Optimal values (K_p and K_i)	80 and 1.5
Passive High-pass filter(R , L , C)	4.15 Ω ;0.41mH	Filter capacitor C	36 μF
Active filter(R , L)	2.75 Ω ;1.3mH	Snubber Resistance	1000 Ω
Dc Link Voltage (V_{dc})	700V	Snubber Capacitance	1e-3F

5.1. Simulation analysis without APF

For this control, as long as the control signal of the inverter is cut off, the simulation is performed without adding the APF. The load part in this design is through a three-phase uncontrolled rectifier circuit. As shown in the figure below, the FFT analysis under load conditions, where the harmonic content THD = 30.74%.

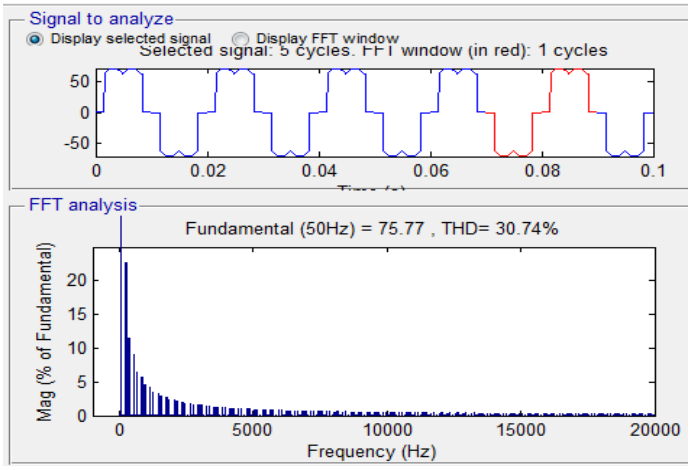

Figure 7: FFT analysis of load current before compensation

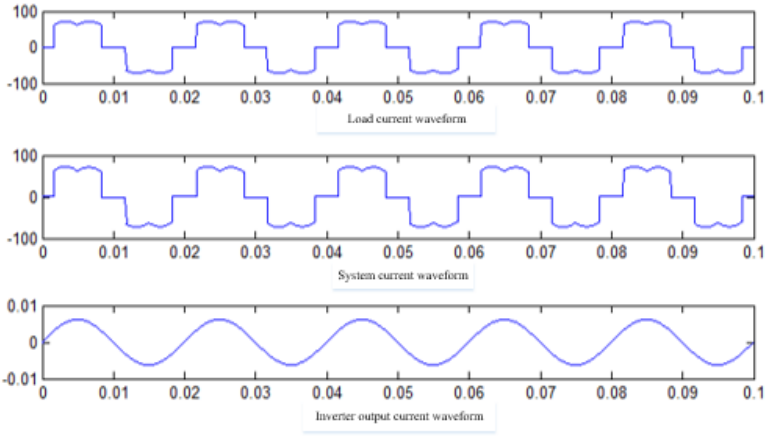

Figure 8: Current output waveform before compensation

The current is shown in Figure 8, where a, b, and c correspond to the output currents of the load, system, and inverter, respectively. As can be seen from the figure, the main harmonic current in the power grid. For the inverter output current, because the IGBT anti-parallel diode, there is a certain difference between the two sides of the voltage, when the grid of a phase voltage is higher than the sum of the power supply voltage and another phase, it will form a rectifier circuit, so will There is a relatively small current output waveform.

5.2. APF simulation waveform

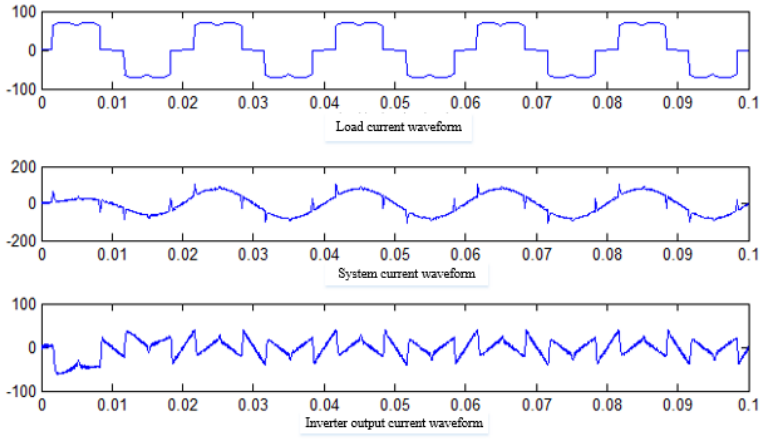

Figure 9: compensated current waveform

As shown in Figure 9, a, b, and c correspond to the output currents of the load, system, and inverter, respectively. It can be seen that the output of the inverter is harmonic current, and the output current in the grid is close to a sine wave. Perform FFT analysis below.

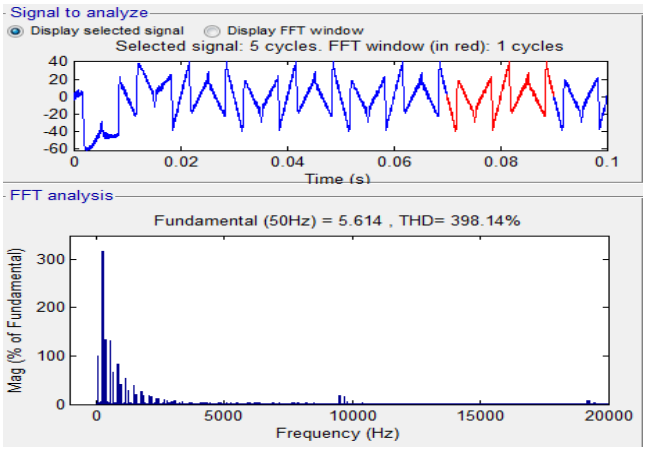

Figure 10: FFT analysis of inverter output

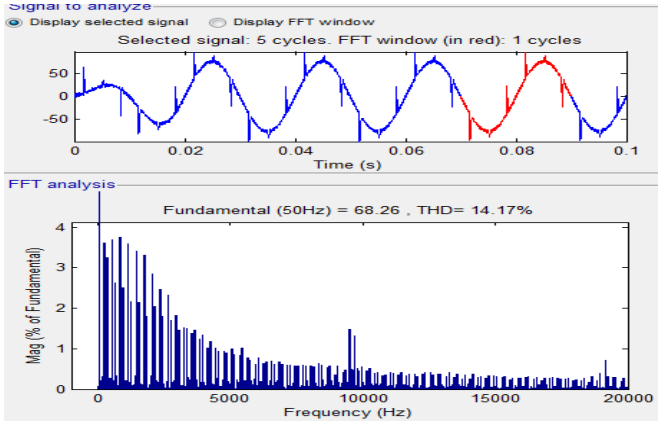

Figure 11: post-compensation FFT analysis

It can be seen from Figure 11 that the THD in the power grid drops to 14.17%. It can be seen that the harmonics have already dropped, indicating that APF can indeed perform harmonic suppression and compensation. From the above analysis and synthesis, it can be concluded that the three-phase three-wire shunt active power filter designed in this paper can play a role in suppressing harmonics.

6. CONCLUSION

This paper mainly introduces the basic principle of the APF and the main circuit topology of the APF. The specific detection method based on the theory of instantaneous reactive power design was selected, PI control was used as the control strategy of this design, and SPWM was selected as the control method of this design. Using the MATLAB/Simulink platform to build a simulation model, through the analysis of the simulation results, it can be concluded that the function of the active power filter is achieved and harmonics can be suppressed in real time.

7. REFERENCES

Akagi H, Nabae A, Kanazawa Y. Instantaneous reactive power eompensators eomprising switching deviees without energy storage components[J]. IEEE Trans. Ind. App, 1984:625-630.

Wu H. Research on hybrid active power filter based on double DSP [D]. Master thesis of Shandong University of Science and Technology, 2009.05.01:63.

Liu J, Zhang Z, Wan Y, et al. Simulation and experiment of three-phase four-wire active power filter [J]. Power Electronics Technology, 2014, 01:43-44.

Li J, Miao Z, Yu B. Research on Multi-objective Detection and Control Strategy Modeling for Active Power Filter [J]. Drive World, 2010.1:99-101.

Zhong X, Feng X, Xu Q, Chen G. Three-phase four-wire parallel APF control strategy based on ABC coordinate system[J]. Journal of Zhejiang University, 2014(5): 890-891.

Pan K. Simulation and design of parallel three-phase three-wire active power filter [D]. Dalian University of Technology, 2009:13-15.

Yu X. Research on parallel three-phase three-wire active power filter [D]. Tianjin University of Technology, 2014: 3-4.

Ming P. Research on control strategy of three-phase four-wire active power filter [D]. Tianjin University of Technology, 2015: 3-4.

Dong H. Research on 30kVA three-phase three-wire shunt active power filter [D]. Hubei University of Technology, 2015: 10-14.

Ren Aerospace. Research on active power filter based on DSP[D]. Beijing Jiaotong University, 2012:2-3.

Chen G, Lü Zhenyu, Qian Zhaoming. General Principles and Applications of Active Power Filters [J]. Proceedings of the CSEE, 2000:18-20.

Peng H, Wang H. Introduction and application of the principle of active power filter [J]. North China Electric Power Technology, 2010(1):36-37.

Cao L, Liu Y, Du H. Principle, Application and Comparison of Active Power Filter and Passive Power Filter [J].Electrical Abstracts/Technology Communication, 2010(2):50-52.

Wang L, Liu H, Wang C. Research Review of Instantaneous Reactive Power Theory [J]. High Voltage Technology, 2006, 32(2): 98-100.

Wang Z, Li M, Zhuo F. Research on instantaneous reactive power theory of three-phase circuit[J].Transactions of China Electrotechnical Society, 2013(3):98-100.

218: Industry-city integration design of eco livable city – a case study of Hou Guan Lake in Wuhan

Yan HE[1], Siwei GUO[1], Xinlai WANG[1]

[1]School of Economic and Management, Hubei University, forrof@126.com
[2]School of Economic and Management, Hubei University, 1219511689@qq.com
[3]School of Economic and Management, Hubei University, 1143140961@qq.com

The construction of ecological livable cities can't ignore the industry-city integration. Compared with other types of cities, the design emphasizes the links between industries and the livability, ecology, humanities characteristics, the function of the city and the docking with the surrounding cities. Taking Hou Guan Lake in Wuhan as an example, the paper points out the existing problems, and puts forward the design plan of the industry-city integration to provide reference for other cities to build eco livable cities.

Keywords: Industry-City Integration; Ecology; Livability; Design

1. INTRODUCTION

As people's material needs are constantly met, they began to pursue more social and psychological needs, such as more comfortable living conditions and more beautiful environments (He X.L., 2017). But the indisputable fact is that the air pollution in many cities and the decline of the living environment are not only inconsistent with people's ever-growing needs for a better life, but also restrict the development of the city's economy. Ecological livable city is an organic integration and upgrading of ecological city and livable city, which has become the goal of every local government. (Li et al, 2016). The ecology index is more embodied in the physical standards of environment, architecture, transportation and industry. The livability index reflects the harmony of nature, society and economy in the local area mainly through the satisfaction of the urban residents.

2. PROJECT BACKGROUND

2.1. Introduction of Houguan Lake ecological livable new town

Houguan Lake ecological livable new town locates in Caidian District of Wuhan, adjacent to the national eco-industrial park which is under construction - Wuhan Economic & Technological Development Zone. The area is under good protection of mountain and water resources. The coastline of the lake is natural and tortuous with green mountains and clear rivers to a unique environment. The 110 km greenway along the lake has been fully integrated, and the wetland park is the largest one to bring a pleasant garden for Wuhan. In addition to the high quality natural resources and beautiful pastoral scenery, it is also the birthplace of the "the bosom culture", and famous for historical resorts such as the tomb of Zhong Ziqi and Zhiyin Pavilion.

The ecological and industrial foundation of HouGuan Lake provides a "paradise" to undertake the industry of the main city and the transfer of the population, and a "net soil" to maintain the balance of the regional ecological environment. According to the development planning of local government, the eco livable new town of Houguan lake is mainly divided into four functional parts: Ma'anshan ecological livable plate, South Lake tourism and sightseeing plate, Gao Lake science and education culture plate and Wen Ling modern service plate. The ecological livable plate in Ma'anshan is the main residential area of the ecological livable new town of Houguan Lake, and South Lake Tourism and sightseeing plate is the core area of the ecological environment protection, where the ecological tourism and leisure tourism industry can be cultivated vigorously. Gao Lake science and education culture plate is the science and technology education base and the talent gathering center which relies on Yangtze University. Wen Ling modern service plate is an important area to undertake R&D center and financial backstage of enterprise headquarters, and vigorously develops modern services such as science and technology research and development, software industry, financial services, headquarters economy, service outsourcing, exhibition tourism.

The Sino-French ecological city is one of the major projects of the new town, which was launched jointly by the Chinese and French governments in March 2014 (Gao, 2015). In the "13th Five-Year" plan of Caidian District, it is pointed out that the city will develop medical health, cultural creativity, ecological residence, tourism and other industries, and build an ecological city which realizes the industry-city integration. This positioning also reflects the future development direction of the whole town. After 2015, the total industrial output value and fixed assets investment of Houguan Lake reached 3.195 billion and 4.33 billion Yuan respectively, increasing 10% over the previous year. The main property development and residential projects include Shimao Longwan, Zhong Heng Lake dwelling, Nanhu Peninsula, Jinqiao Princeton, Evergrand Oasis, Capitaland Huiju, Renxin Eternal Beauty and Transoceanic. The main medical and convalescent projects include the Caidian branch of Tongji Hospital, the healthy community of Union Life; and the cultural and commercial program includes Yangtze University (Wuhan campus), Chinese Wen Bo City, Hutchison Whampoa commercial city and Shimao carnival, etc.

2.2. Problems in the development of ecological livable new town

The use of land doesn't meet the needs of the ecological city. The area of new town planning is 1510.3 hectares, of which 56.5% of residential land, 1.1% for public management and service land, 14.4% for commercial service facilities, 5% for industrial land, 10.3% for transportation facilities, 0.3% for public facilities and 12.3% for green land. The M2 industrial land, which have certain interference and pollution to the environment of living and public facilities, account for 93.4% of the industrial land, and are mostly in the plastic industry, the metal products industry and the printing industry. The commercial service facilities, public management and service, public facilities and green land has less area, basically no sports facilities and cultural facilities. There are only one garbage transfer station and a drainage pumping station. The green space is mostly the park green space, but it is still not all put into operation.

Table 1: Land balance sheet of Houguan Lake

No.	code	land usage	land area(ha)	Percentage(%)
1	R	residential land	854.43	56.5
2	A	public management-services land	16.27	1.1
3	B	commercial service facilities land	217.35	14.4
4	M	industrial land	76.08	5
5	W	logistics warehousing land	1.13	0.1
6	S	transportation facilities land	155.45	10.3
7	U	public facilities land	4.01	0.3
8	G	green space	185.58	12.3
subtotal for urban construction land			1510.3	100

The heat island effect is still obvious. The new town is located in the hot-summer and cold-winter region. The air humidity around the water body is high in the scattered, massive closed waters and green space, so the summer muggy and winter cold moist phenomena is obvious. The increasing number of buildings, motor vehicles and human activities will also weaken the city's ability to mitigate the heat island effect. This will bring a great threat to the energy supply and the livable environment. Therefore, in the planning process, we must pay attention to the trend of building and road, reduce the temperature and improve the ventilation by setting air duct, green space, protecting water resources and so on.

The structure of service industry needs to be optimised. The new town is still in the preliminary stage of construction, and the total number of services is relatively small. The scale of life service industry in Houguan Lake new town is small, and business is still centralized service facilities such as Shimao carnival, etc., and is in the infrastructure construction phase. There is a general lack of street commerce in the whole area to enliven the urban atmosphere. Producer services are mainly business services, the service industry which can link manufacturing industries with manufacturing services and high knowledge services is lacking. The gaps of public services such as hospitals and education are large.

3. THE PRINCIPLES OF INDUSTRY-CITY INTEGRATION DESIGN

Livability is the most basic requirement of the ecological livable city, but it doesn't mean that the city only emphasizes the function of "city" such as "livable", thus denies the function of "industry" such as "suitable industry". On the contrary, it pays more attention to the integration of production and city. "Industry" is the premise for people to live in peace and comfort. The industry-city integration is mainly reflected in the integration of manufacturing and service industry, the integration of residence and employment, the integration of production and life, and the integration of output value and environment (He et al, 2016). Compared to industry-city integration design in the general city, the "industry" of the ecological livable city is the primary task to maintain the ecological balance, on the basis of which the social production is taken into consideration, in order to create a "livable" environment for people.

3.1. Combination of industries and urban ecological livability

In terms of the ecological environment, we must control strictly the polluting to prohibit the industry which conflicts with the ecological environment and to highlight the function of the ecological leisure area. Furthermore; we must increase the ecological input to protect and repair the natural landscape of the wetland and to build the cultural landscape, such as industry sightseeing. In terms of livability, we need to accelerate the living service industry for facilitating people, widen the field and depth of the productive service industry, and wholly promote the service industry of new town to the high-end. The most important is to ensure that the resident people have their own work by improving the employment of local residents in ecological agriculture and ecotourism projects.

3.2. Combination of the city and the humanistic characteristics

Firstly, highlight the local culture, enhance the city's soft power and hard characteristics. The former focuses on expanding the content of "the bosom culture", strengthening the local humanistic quality, integrating culture into life and building a sincere and mutual trust civilization city. The latter builds the image of architecture, landscape and so on with the background of "the bosom culture", embeds industry and products with culture, and builds the cultural brand of the city. Secondly, highlight the characteristics of natural resources. It emphasizes in creating ecological landscape and let the clear water enter into the lake, so as to protect and transform existing rivers, mountains and forests, and create a livable environment.

3.3. Combination of industries and city's functions

The ecological livable city emphasizes people-oriented principle, and the direction of industrial development must also match the requirements of urban functions. The diversified development of industries is the guarantee of benign interaction between cities and industries (Chen et al, 2013). This kind of diversification doesn't mean the more kinds

of industry, the better it is. It is embodied in the perfection of adapting to people's living and work, even adapting to the development of modernization and information development. For example, the "slow life" of the fitness, catering, express, or "Internet+" which is under the creative design, etc.

3.4. Connection of the industries and the surroundings

Strengthen the docking of new town with main city zones, industrial parks and other areas. The construction of new town and other areas of infrastructure and public service docking are accelerated in the terms of "city". The division and cooperation of new town and other regions in the industrial and value chain is emphasized in the terms of "industry". Hougan Lanke will match the surrounding manufacturing industry with the new town service industry, and transform by the technology technical research service result after combining with local advantages and characteristics.

4. THE DESIGN SCHEME OF THE INDUSTRY-CITY INTEGRATION

4.1. The position of New City

Aiming to a "Civil Garden", we will build Houguan Lake into a new city suitable for ecological recreation and livable industry in Caidian and Wuhan, attracting people in the main city and other areas to enjoy their homes here.

4.2. Integration model between the production and the city

Adopting the mode of "promoting the development of culture and tourism industry", the aim of new town’s building is to build a more suitable city with high standards and high starting points for human to habitation. Therefore, in the ecological control line, the industrial development should focus on the cultural industry, tourism industry and other services to flourish the new city.

4.3. To highlight the characteristics of livable and suitable business

In terms of livable areas, it is emphasized to protect and transform existing rivers, mountains and forests, and to create a humanistic and livable environment. In the aspect of tourism, it takes culture and agriculture leisure as the theme, combined ecotype science and technology sightseeing agriculture with confidant culture. We shall make the new town tourism brand bigger and stronger through ecotourism projects, food culture festival, and race around lake and so on. In the aspect of suitable business, we should establish a life service industry closely related to people's life, such as wholesale, retail, catering and hotels, and logistics, exhibition, creativity, real estate, which serve for the enterprises. In the aspect of suitable industry, through the development of ecological agriculture and service industry, we can improve the employment of local farmers and realize their own businesses.

4.4. Rational distribution of industrial function area

To relocate of existing industrial enterprises, agglomerate adjacent industrial parks, withdraw industrial land. The land for agriculture and forestry in the primary industry is mainly cultivated rice and wheat, while the land for the tertiary industry is divided into health industrial district, energy conservation and environmental protection industrial district, commercial culture area, ecological tourism area, living service area and business service area. The industry types and functional partitions are shown in figure 1.

We aim to building the new town into a modern service industry agglomeration area. We will focus on the construction of service industry cluster and Headquarters Economic Industrial Park in Houguan Lake’s new town, docking the manufacture cluster in Caidian, the automobile component manufacturing in Chang Fu Industrial Park, the automotive and peripheral industries in Wuhan Economic Development Zone. The former takes the health industry as the breakthrough point, promotes the comprehensive tourism, the real estate, the exhibition and other industries, and puts great effort to improve the service industry scale and the level, speeds up the emerging service industry and the high-end service. The latter supports peripheral manufacturing, the introduction of R&D institutions and small-and medium-sized incubators, the development of headquarters economy.

Figure 1: Distribution of industrial function area in Houguan Lake

4.5. Setting wind tunnel and greenway to alleviate the heat island effect

How to create open space along the road and set up the green belt and landscape that conforms to the leading direction of the city is an important starting point for mitigate the heat island effect and form an air duct. First, the road wind corridor is set up with the aid of the traffic axis. Along the longitudinal axis, the Beijing-HongKong-Macao High-Speed road and No. 101 provincial highway lead the predominant wind direction cross the Houguan Lake, using natural river ventilation corridors to take away some hot air, and then planting green belts along both sides of the lake to guide the lake wind to go deep into the city. The longitudinal axis of Yu Xian Road and Tan Huang Nan road can be configured from the urban fringe to create a permanent green belt around the city to increase the ventilation effect of the city. Along the horizontal axis of Shanghai Yu expressway, a wind corridor is set up, supplemented by a green belt along 318 provincial roads. Second, sharing green space resources, and establishing the "dot line and surface" greenbelt network in Houguan Lake's new town with combining wind tunnel, waterway, greenway, protection greenway and public park green space.

4.6. To build a characteristic home

Drawing lessons from the development concepts of characteristic town, we should build varies of distinctive homes which are suitable living, sightseeing and health and well-being. First of all, it is necessary to improve the environmental quality, and build the soft power of the city with regional characteristics and cultural brand. Yu Xian town is the largest gardening and horticultural base in Central China, and it was named the second batch of special towns in the country in August 2017. Secondly, it is necessary to establish a system of national environmental protection, from production to life and from cities to rural areas. We shall strictly deal with the prevention and treatment of waste and pollution, carry out the system of environmental information disclosure, and improve the ability of environmental management. After regulating a demonstration Garden of Ecological Residential area in Houguan Lake, we will use green buildings and advanced energy saving and emission reduction technologies.

5. CONCLUSION

Earlier studies on eco-livable cities are mainly focused on the livability and ecology of cities (Zhang et al,2012).This paper proves that the eco-livable city should also pay attention to industry-city integration, and points out the design principles and design strategies different from other types of cities with the example of Houguanhu New City in Wuhan. However, ecological livable city is a complex subject. With the increase of ecological consciousness, the social and psychological needs of the city will change and the planning scheme needs to be improved.

6. ACKNOWLEDGEMENT

This work was supported by the Education Department of Hubei province (Grant No. 16ZD022) and Institute of Wuhan Studies of Jianghan University (Grant No. 2009045).

7. REFERENCES:

He X.L.,2017.Meet the growing needs of the people for a better life. *People's Daily*,Nov.14,7.

Li H.B., Xu G.Q., 2016. Investigation, evaluation and promotion of Ecological livability in Suzhou based on the Perspective of residents' satisfaction. *Ecological economy*, 12,159-162.

Gao D.F., 2015. Chinese and French experts draw up the blueprint of ecological demonstration city. *Wuhan Evening News,* Nov.10, A02.

Liu J., Geng Q., Wang Y., 2012. The development model and planning strategy of the integrated high-tech zone of production city -- Taking the East District of Ji'nan Hi-tech Zone as an example. *Planner*, 4, 58-64.

He Y., Zeng Y.J., 2016. Transformation and upgrading of industrial park from the perspective of industry and city convergence-taking Changfu Industrial Park of Wuhan as an example. *Reform and Strategy*, 10, 29-132

Chen S.M., Zhong Y.G., 2013. A study on the interactive planning of resources-based cities with Transformation and Development-taking Pingxiang City as an example. The 15th annual meeting of the China Association of Science and Technology, 25 th annual meeting, production and City interaction and Planning Symposium proceedings.

Zhang X., Lei Z., Zhang H.W., 2012. Ecological livable city construction index and evaluation method-taking Tianjin as an example. *Urban Environment and Urban Ecology*, 2, 18-21.

220: Optical and electrical performance analysis of non-imaging low concentrating photovoltaic-thermal cogeneration system

CHANDAN[1,3], Paidisetty Sujan KUMAR[1,3], Sumon DEY[1,3], K.S. REDDY[4], Bala PESALA*[1,2]

[1] Academy of Scientific and Innovative research, Chennai-113
[2] Council of Scientific and Industrial Research- Central Electronics Engineering Research Institute, Chennai-113
[3] Council of Scientific and Industrial Research- Structural Engineering Research Centre, Chennai-113
[4] Indian Institute of Technology- Madras, Chennai-036

A concentrating solar photovoltaic thermal (CPVT) cogeneration system is a dual output (electrical and thermal energy) system which consists of a concentrator, a PV module and a heat recovery system. In the case of conventional non-tracking compound parabolic concentrator (CPC) based CPVT system, non-uniform illumination and non-uniform temperature distribution on the PVT module reduces its electrical and thermal power output. In this work, a homogeniser is optimised and integrated to the truncated 3X CPC to reduce the illumination non-uniformity at all angles (from normal incidence to the acceptance angle). Further, a scaled down CPVT system is fabricated and optical and electrical analysis has been performed under solar simulator. The experimental results show promising improvement in electrical efficiency (>50% at high incidence angles) with the incorporation of homogeniser. The study proves that for CPC-PVT systems homogenisation is necessary for realizing better electrical and thermal performance.

Keywords: *Compound Parabolic Concentrator, Homogeniser, Photovoltaic-Thermal System*, *Solar Energy*

1. INTRODUCTION

Solar PV systems are increasingly penetrating the electricity market because of the continuous decrease in the prices of silicon solar cells. The current price of a monocrystalline silicon solar cell (156 mm × 156 mm) is approximately 0.5 $/W (PV insights-Grid the World). The efficiency of the commercially available Si solar cells is still limited to 20% owing to the sub-band gap and thermalization losses (www.solarcellcentral.com/limits_page.html; Green 2011). Therefore, more than 80% of the input energy lost can be recovered as heat. Photovoltaic Thermal (PVT) and Concentrating Photovoltaic Thermal (CPVT) systems have recently gained a lot of research focus as they fundamentally aim at recovering this lost heat and provide multiple outputs from a single system (Sharaf 2015) [4]. Such systems have widespread applications in industries, domestic electricity and water heating or the outputs (electrical and heat) can be used in a secondary system viz. a cooling, desalination system etc.

In a concentrated PVT system, concentrators in the form of reflectors or refractors are used to increase the amount of radiation on a given area of solar cell (Sharaf 2015; Sharaf 2015; Yousef 2016). The main advantages of using a CPVT system is higher grade of thermal output and lower cost of the system. The concentrator reduces the cost of system by reducing the solar cell requirement but in turn increases the operating temperature of the solar cell negatively affecting its power output. The effect of temperature on the performance of the silicon solar cell is well known and has been extensively studied (Skoplaki 2009). An approximate linear decrease in efficiency at the rate of 0.4-0.6% for every degree rise in temperature is reported in the literature. The decrease in efficiency is due to the decrease in both open circuit voltage (2.2 mV/˚C) and fill factor (0.15 %/˚C) (www.pveducation.org/pvcdrom/solar-cell-operation/effect-of-temperature). Therefore, the integration of a heat recovery system to the PV cell provides double benefit of improving the electrical efficiency as well as recovering the additional heat. The electrical and thermal power output from these systems is higher but other issues such as the lifetime of PV cells, maintenance etc. need to be addressed.

The CPVT system also consists of a mounting system (fixed or tracking) (Sharaf 2015) which depends on the concentrator used. Usually low concentration system (C=2) can be fixed mounted with manual seasonal tilts. V-trough concentrators and compound parabolic concentrators are the most commonly available concentrators in this non-tracking category. The two most important and widely used terms in determining the concentrator performance are concentration and acceptance angle. Optical Concentration is defined as the ratio of power per unit area of the absorber/exit aperture to that of power per unit area at the aperture/opening. Actual concentration takes into account the curvature errors and optical losses. Acceptance angle is defined as the maximum incidence angle of the light which reaches the absorber. Compound parabolic concentrator achieves the highest acceptance angle for a given aperture (Chavez 2015) due to which they are widely used in non-tracking PV and thermal systems.

Extensive designs for PVT and CPVT systems have been explored previously to improve the performance and overall efficiency of the system. The most important problems persisting in CPC based PVT systems are non-uniform illumination and non-uniform temperature distribution on the PVT module which is the cause for faster degradation and lower performance of these systems (Sharaf 2015; Sharaf 2015; Yousef 2016). The study of non-uniform illumination on the conventional monocrystalline cell has been previously performed where the electrical output is compared between CPC (non-uniform) and V trough (uniform) and concluded that the power output and fill factor is higher for V trough (uniform) case. The difference becomes higher with increase in peak local concentration (Paul 2015). To the best of our knowledge, no study has been reported which analyses the independent effects of temperature, non-uniform illumination and non-uniform temperature distribution on the electrical parameters of a PV module. To reduce the non-uniform illumination due to CPC, secondary optical elements which act as homogenisers are used. Homogenizers are most common in high concentration multijunction cell based concentrated PV systems (Leutz 2001; Xie 2016).

As the CPC-PVT system needs to be operated without tracking or tracking with minimal seasonal adjustments, it is necessary to perform thorough optical simulation and analysis at normal (0˚) and non-zero incidence angles and study the optical and electrical characteristics. In this work, a low concentrating 2.5X LCPVT system based on compound parabolic concentrator is developed and thorough optical and electrical analysis is done to understand the effect of non-uniform illumination and non-uniform temperature distribution. Additionally, an optimised rectangular kaleidoscopic homogeniser was integrated to the 2.5X CPC herein referred as Elongated Compound Parabolic Concentrator (ECPC) and the performance is compared with the system without homogeniser. Extensive optical simulations have been performed and the final design of the concentrator is fabricated in a 3D printer (Stratasys 250mc). Optical and electrical performance of the developed lab scale model is studied under Oriel AAA solar simulator. In addition to this, a preliminary testing is performed under outdoor condition.

2. OPTICAL SIMULATION AND CONCENTRATOR OPTIMISATION

Compound Parabolic Concentrator (CPC) also known as Winston concentrator is a non-imaging concentrator and has the highest acceptance angle for given concentration and aperture (Chavez 2015). Figure 1 shows CPC with two equal parabolas described by the equation given below (Winston 1974):

$$y = \frac{x^2}{2w(1+\sin\theta)} \tag{1}$$

where, w is the absorber width and θ is half acceptance angle which is determined according to the required concentration.

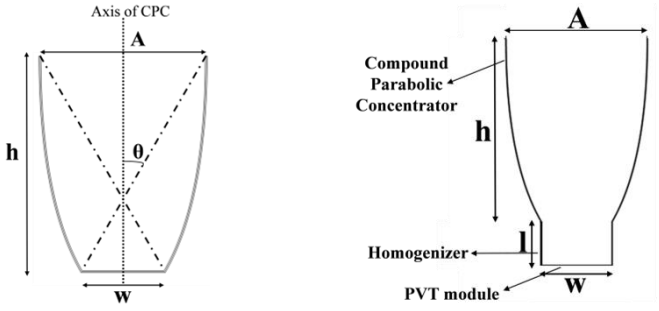

(a) (b)

Figure 1: (a) Compound parabolic concentrator (b) Compound parabolic concentrator with Homogeniser.

In the study, a symmetrical 3X CPC truncated to 2.5X with A=250 mm, w=100 mm and θ=19.47° is designed using Eq. (2) in CAD software and optical simulations have been performed using non-sequential mode of Zemax (Radiant Zemax 2014) optical simulation software.

$$y = \frac{x^2}{266.67} \tag{2}$$

A rectangular source with 10 million rays are incident on the concentrator whose reflectivity is assumed to be 0.91. The flux on the PVT module is studied by placing a rectangular detector with a pixel density of 100 × 100. For the design concentration of 2.5X, the average concentration obtained is 2.37X as some rays reach the PVT module directly and some reach after reflecting from CPC. The simulation results are shown in figure 2(b) for the both CPC and ECPC while ray tracing of ECPC at 0° angle of incidence is shown in figure 2(a). The non-uniformity of illumination is quantified by spatial non-uniformity factor (α) given by Eq. (3). Larger value of α implies greater non-uniformity.

$$\alpha = \frac{G_{\max} - G_{\min}}{G_{\max} + G_{\min}} \tag{3}$$

The 2.5X CPC is then integrated with parallel planar reflectors which act like a kaleidoscopic homogenizer herein referred to as Elongated CPC (ECPC) shown in Figure 2(a). The length of the homogeniser was varied and an optimum value considering the reflection losses and magnitude of spatial non-uniformity was found to be 35 mm. The flux pattern in Figure 2(b) shows that the non-uniformity is significantly reduced, and maximum local concentration is also reduced by 39.7% (from 4.48X to 2.70X). In the next section, the optical performance of fabricated concentrator is compared with the simulations for different angles of incidence.

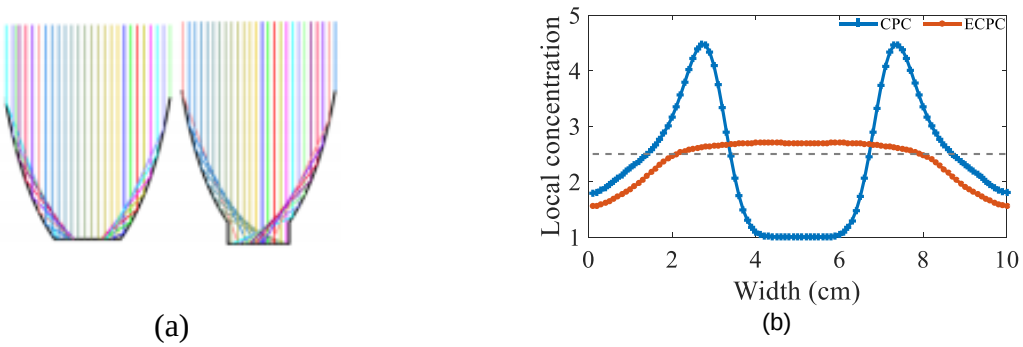

Figure 2: (a) Optical simulation ray diagram for compound parabolic concentrator and elongated compound parabolic concentrator at 0˚ angle of incidence (b) Comparison of illumination distribution at normal incidence for compound parabolic concentrator and Elongated compound parabolic concentrator.

3. FABRICATION OF THE CONCENTRATOR

A lab scale 2.5X CPVT system is then developed consisting of the concentrator, homogeniser, monocrystalline solar cell and heat recovery system. Dimensions of the concentrator are same as that of parameters used for the simulation. The concentrator is fabricated using *Stratasys Fortus 250mc* and is shown in Figure 3 below. A reflective film was then attached onto the 3D printed concentrator. A 10 cm x 10 cm heat recovery system was developed by using a 1.5 mm thick copper plate with a ¼" copper tube beneath for water circulation. Gintech make monocrystalline solar cells (2 nos.) each of dimension 5 cm × 10 cm were used. The solar cells along with the copper sheet and tube were placed on a cynthania solid insulator to avoid heat loss from sides and back. The concentrator was then integrated with the PVT module to form a 2.5X LCPVT system. The final fabricated PVT module is shown in Figure 4.

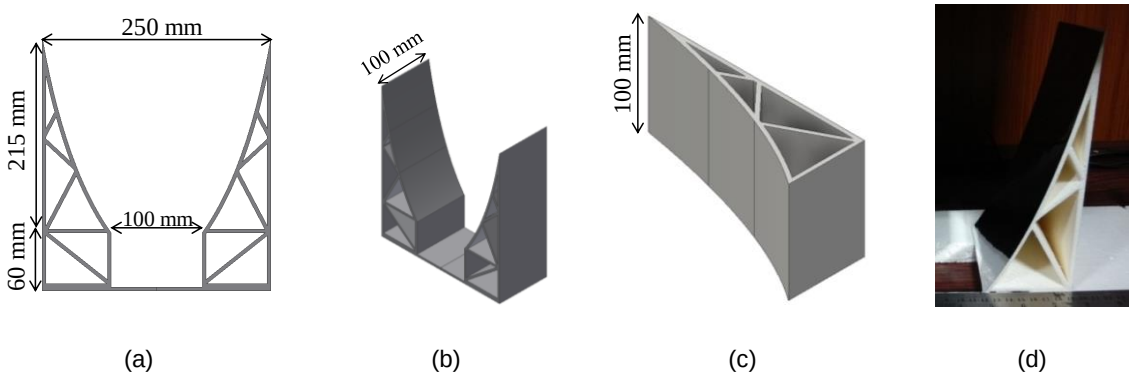

Figure 3: (a-c) CAD models of the concentrator, (d) Fabricated concentrator model.

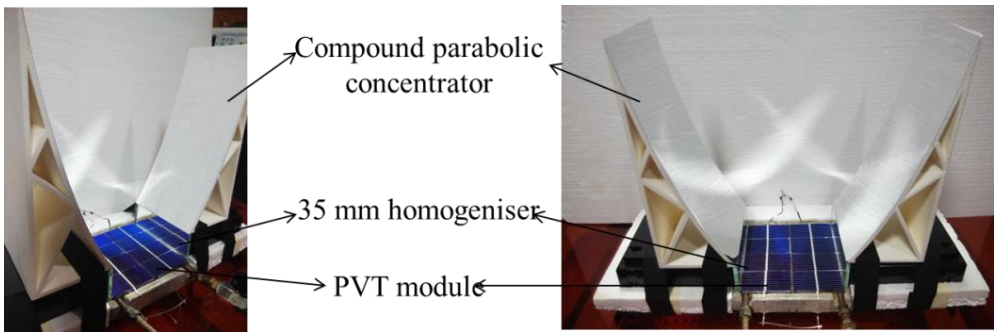

Figure 4: Developed 2.5X CPVT system

4. PERFORMANCE ESTIMATION OF THE LCPVT SYSTEM

4.1. Optical performance of the CPC and ECPC, and comparison with simulated value

Based on the optical simulation, a CPC concentrator was developed and then studied under the Oriel AAA solar simulator. A reference solar cell (4 cm^2) was used to find the intensity at different points on the absorber area of the concentrator. The reference solar cell was covered allowing only a small area of 2 mm × 2 mm for light to reach the solar cell. The sensor was placed at the positions I, III, V, VII, IX rows as shown in the Figure 5(b). The values were averaged along the column and the measured intensity profile is shown in Figure 6. The same procedure was followed for ECPC for incidence angles of 0°. Figure 6(a) show the illumination profile for 2.5X CPC while Figure 6(b) shows illumination profile for 2.5X ECPC.

The reflectivity of the reflecting film was measured by ocean optics spectrophotometers (Ocean optics USB2000+ UV-Vis-NIR (200-1100 nm) and ocean optics Flame NIR (950-1650 nm)) using a high specular reflectance standard (STAN-SSH) and the total solar reflectance was measured to be 0.91.

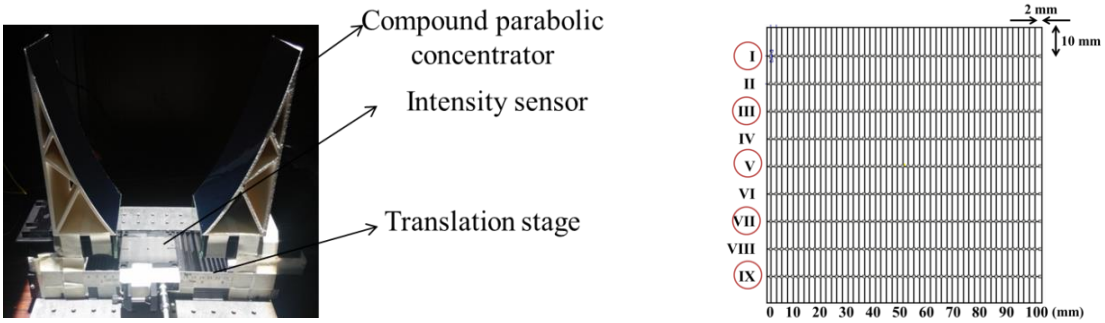

Figure 5: (a) Setup to find the intensity distribution, (b) Sensor position

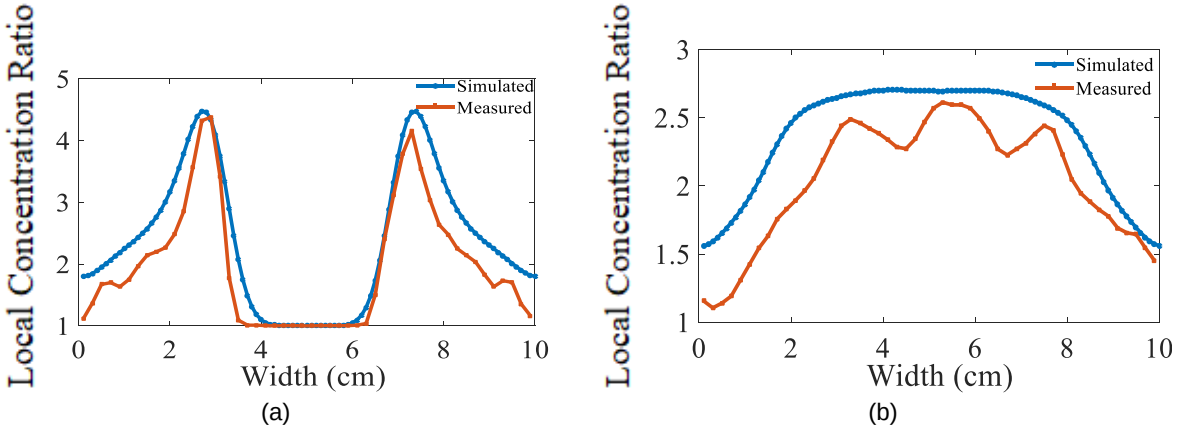

Figure 6: Comparison of simulated and actual local concentration distribution on the absorber for 0° (a) 2.5 X CPC (b) 2.5X ECPC.

Table 1: Comparison of simulated and actual average and peak local concentration for CPC

	Average concentration		Peak local concentration	
	Simulated	Actual	Simulated	Actual
0°	2.37	1.97	4.48	4.38

Table 2: Comparison of simulated and actual average and peak local concentration for ECPC

	Average concentration		Peak local concentration	
	Simulated	Actual	Simulated	Actual
0°	2.37	1.93	2.70	2.46

Figure 6 (a) shows the results for the CPC at 0° angle of incidence. Highly non-uniform illumination was measured with peak local concentration ratio reaching 4.38. This measured local concentration was in close agreement with the simulated value of 4.48 as shown in table 1. Figure 6 (b) shows results for ECPC where spatial non-homogeneity

was suppressed to a large extent with maximum concentration ratio being 2.46 when measured which was again in agreement with the simulated value that came to 2.7 as shown in table 2.

4.2. Electrical performance analysis of the LCPVT system under solar simulator

The optical analysis shows the illumination on the PVT module becomes highly uniform at all angles of incidence with the incorporation of kaleidoscopic homogeniser. It is necessary to observe this improvement in the electrical output of a PVT module. Thus, the electrical performance analysis of the 2.5 X LCPVT system were performed under solar simulator. The two solar cells in the developed PVT module were connected in series and electrical characteristics were obtained. Experiments were performed under solar simulator (*Oriel® Sol 3A Class AAA*) shown in Figure 10 at an insolation of 500 W/m^2 and the parameters were measured using *Keithley Model 2420 High Current Source Meter*. Figure 7 shows the setup under solar simulator. An industrial chiller with water as cooling medium was used to control the temperature of the PV cell and maintain it at 25˚C.

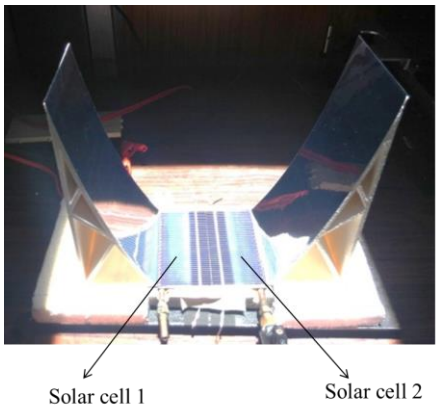

Figure 7: 2.5X Low concentrating photovoltaic thermal system under solar simulator

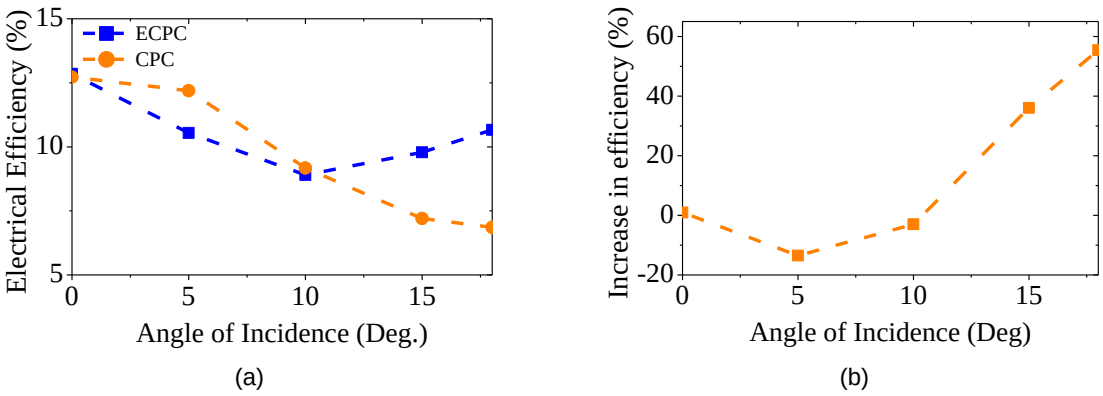

Figure 8: (a) Electrical efficiency of the cell when connected in series with cooling (b) % Increase in electrical efficiency when cells are connected in series with cooling medium

When solar cells were tested in series configuration with water as cooling medium, for the case of CPC, the electrical efficiency decreased monotonically as expected due to non-uniform illumination on the solar cells which is clearly evident in figure 8(a). The electrical efficiency was very low affected near the acceptance angle where it dropped down to 6%. In the case of ECPC, there was dip in efficiency between 5˚ and 10˚ angle of incidence. Prime reason for this dip in efficiency is because of different illumination falling on different solar cells connected in series leading to electrical mismatch between them. Further, at 5˚ and 10˚ angle of incidence, light gets reflected from the homogenizer and then spreads onto the solar cells there by losing part of it due to light reflectivity loss in the homogenizer. However, the ECPC performed significantly better at high angles of incidence, where an improvement in efficiency (>50%) is observed compared to CPC as shown in figure 8(b).

5. CONCLUSIONS

Conventional CPC design has non- uniform distribution of flux which leads to high spatial non- homogeneity and high local concentration on the cell. To overcome non-uniform distribution of flux on the solar cell, an optimised homogenizer was integrated to the CPC. With the addition of this new optical component, the maximum local concentration ratio was reduced from 4.48 to 2.7 in simulations and 4.38 to 2.46 in experiments. In solar PV modules, cells are mostly connected in series to obtain the required voltage, therefore LCPVT was tested with cells connected in series. When experiments were performed on PVT module with CPC and ECPC, it was observed that electrical output was severely affected in the case of CPC and therefore resulted in monotonic decrease in electrical efficiency at all angles of incidence. Similarly, when experiment was performed on PVT module with ECPC as concentrator, it was observed that the electrical power output of the cells connected in series increased by >50% at high incidence angle due to less spatial non-uniformity. From the optical and electrical analysis of the 2.5X LCPVT system, evaluating the performance benefits of ECPC it can be concluded that homogeniser is necessary for obtaining higher power output. In future, more outdoor testing for CPC and ECPC will be done to draw the clear conclusion between the two.

6. ACKNOWLEDGEMENT

The authors wish to thank Director, CSIR-CEERI; Director, CSIR-SERC for the resources, facilities and financial support to carry out the work fruitfully. We also take this opportunity to thank the Scientist in Charge, CSIR-CEERI for the lab facilities and fellow colleagues of CSIR and AcSIR for their kind inputs.

7. REFERENCES

PV insights-Grid the World, [Online]. Available: pvinsights.com/index.php.

http://www.solarcellcentral.com/limits_page.html

Green, M A., et al. "Solar cell efficiency tables (version 37)." Progress in photovoltaics: research and applications19.1 (2011): 84-92.

Sharaf, O Z., and Mehmet F. Orhan. "Concentrated photovoltaic thermal (CPVT) solar collector systems: Part I–Fundamentals, design considerations and current technologies." Renewable and Sustainable Energy Reviews 50 (2015): 1500-1565. [doi:10.1016/j.rser.2015.05.036].

Sharaf, O Z., and Mehmet F. Orhan. "Concentrated photovoltaic thermal (CPVT) solar collector systems: Part II–Implemented systems, performance assessment, and future directions." Renewable and Sustainable Energy Reviews 50 (2015): 1566-1633. [doi: 10.1016/j.rser.2014.07.215].

Yousef, MS., Ali K. Abdel Rahman, and S. Ookawara. "Performance investigation of low–Concentration photovoltaic systems under hot and arid conditions: Experimental and numerical results." Energy Conversion and Management 128 (2016): 82-94.

Skoplaki, E., and Palyvos JA. "On the temperature dependence of photovoltaic module electrical performance: A review of efficiency/power correlations." Solar energy 83.5 (2009): 614-624. [http://dx.doi.org/10.1016/j.solener.2008.10.008]

Available online: http://www.pveducation.org/pvcdrom/solar-cell-operation/effect-of-temperature

Chavez J. Introduction to nonimaging optics. CRC Press, 2015.

Paul, Damasen Ikwaba, et al. "The Effects of Nonuniform Illumination on the Electrical Performance of a Single Conventional Photovoltaic Cell." International Journal of Photoenergy 2015 (2015).

Leutz, R., Suzuki A, Akisawa A, and Kashiwagi T. "Flux uniformity and spectral reproduction in solar concentrators using secondary optics." In ISES solar world congress. 2001.

Xie, H, et al. "Design and performance research on eliminating multiple reflections of solar radiation within compound parabolic concentrator (CPC) in hybrid CPV/T system." Solar Energy 129 (2016): 126-146.

Winston, R. "Principles of solar concentrators of a novel design." Solar Energy 16, no. 2 (1974): 89-95. [doi: 10.1016/0038-092X(74)90004-8].

Radiant Zemax, L. L. C. "Zemax 13 Optical Design Program User's Manual." (2014).

221: Design and optimisation of non-imaging concentrator for low concentrating photovoltaic thermal co-generation system

CHANDAN[1,2], K.S. REDDY[4], Bala PESALA[1,3]

[1] *Academy of Scientific and Innovative Research, Chennai*
[2] *Council of Scientific and Industrial Research, Structural Engineering Research Centre, Chennai*
[3] *Council of Scientific and Industrial Research, Central electronic Engineering Research Institute, Chennai*
[4] *Indian Institute of Technology Madras, Chennai*

A Concentrating Photovoltaic-Thermal (CPVT) system is an integration of solar photovoltaic (PV) and solar thermal technologies along with a concentrator, which can simultaneously generate electrical and thermal output. Use of concentrators such as Compound Parabolic Concentrators (CPC), Linear Fresnel Reflector, Parabolic trough etc. helps in collecting more solar radiation which in-turn results in higher grade of thermal energy and more electrical output per unit area. CPC is a non-imaging solar concentrator where exact image of the source is not formed instead, there is a transfer of energy in the form of radiation from the source to the absorber. The non-tracking nature of this concentrator makes it unique from the other concentrators mentioned above thus reducing the cost and complexity of the system. The major drawback of the compound parabolic concentrator is the formation of nonuniform flux distribution on the absorber which can be minimized by the use of optimised homogenizer. In this work, optimised homogenizer design has been carried out for 2X, 2.5X and 3X CPC each truncated to 1.7X. The simulation results show that the optimised homogenizer significantly reduces the non-uniform illumination on the PVT absorber. In addition, simulations show that considering material requirement and acceptance angle, 2.5X CPC truncated to 1.7X is optimum design.

Keywords: Cogeneration, Compound Parabolic Concentrator, Homogeniser, Photovoltaic-Thermal, Solar Energy

1. INTRODUCTION

Solar energy is non-conventional form of energy available abundantly across the world. It has potential to solve the energy crisis of the whole world if tapped in an efficient way. In general, electricity can be produced from the solar energy in two different ways: first method uses solar photovoltaic cells for direct solar to electricity conversion while in the second case, the working fluid is heated by solar radiation to convert it into vapor, this vapor can expand in a turbine to generate electricity. Both the methods mentioned above have efficiency in the range of 15-20% (Romero, 2014; Honsberg, 2014) only. Major drawback with such existing systems is that they require huge area for installation which makes them an unattractive choice because of large capital investment and high payback periods.

In the past, a lot of research has been done on a hybrid solar PVT system combining solar photovoltaic and solar thermal technology (van Helden, 2004) which can give both hot water and electricity simultaneously. Again, such systems were not able to meet the thermal energy target as desired by industries for low temperature thermal energy requirement (Schmitt, 2016) which limits their wide range of applications. To overcome this, a concentrated photovoltaic thermal system has been explored which can capture more light and concentrate onto the solar cells thereby increasing the electrical energy output from the same cell area. However, the solar cells get more heated in this case reducing the electrical efficiency. This loss in electrical efficiency is traded off by improved grade of the thermal energy suitable for low temperature industrial process heating application.

Recently, a linear Fresnel lens (Sonneveld, 2010) for the concentration of light onto the silicon solar cell has been explored. It was observed that such system needs rigorous tracking which increases the system cost and complexity. A novel non-imaging compound parabolic solar concentrator (CPC) (Winston, 1974) has been designed on the basis of edge ray principle which completely eliminates tracking thereby reducing complexity of the system. A CPC, generally has geometrical concentration ratio in the range of 2-10X thus falling in the category of low concentration ratio (Baig, 2012). When CPCs are integrated with silicon solar cells, the concentration ratio needs to be limited to 1-2X (Sellami, 2013) because of faster degradation of solar cell (Xie, 2016) caused due to high temperature. Further, CPCs are truncated to bring down the material cost thus making them an optimal choice for CPVT application (Figure 1(a)).

Despite using CPC for LCPVT application, there is a major drawback of non-uniform illumination (Xie, 2016) on the solar cells which results in formation of hot spots (Xie, 2016). These hotspots trigger the solar cell degradation. In a recent study, it was observed that in a monocrystalline solar cell when operated under 2X CPC, the decrease in open circuit voltage, short circuit current, maximum power, fill factor, and efficiency were 1.3%, 2.3%, 4.7%, 1.15%, 4.6% (Paul, 2015) respectively. In order to overcome the non-uniform illumination (Xie, 2016) over the solar cells, a homogenizer integrated to a CPC has been explored and optimised. Such CPCs will be referred to as Elongated Compound Parabolic Concentrator (ECPC) from here on as shown in Figure 1(b). A heat exchanger is integrated below the solar cell to extract the waste heat effectively as shown in Figure 1(c).

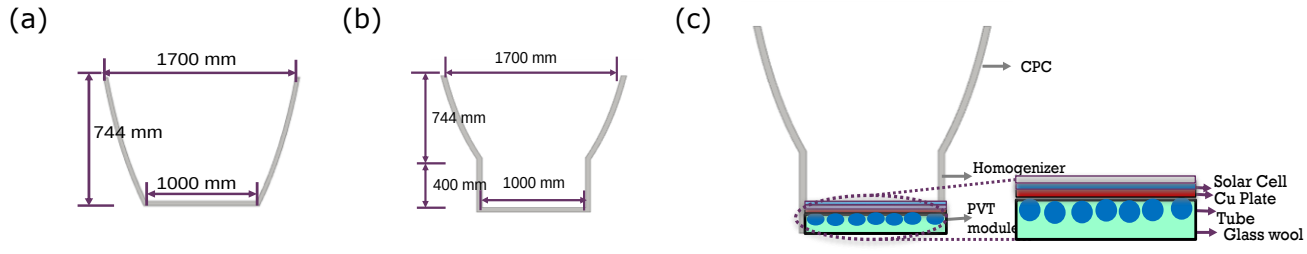

Figure 1: (a) Schematic of compound parabolic concentrator with base width of 1000 mm and Aperture width of 1700 mm (b) Schematic of compound parabolic concentrator integrated with homogenizer (ECPC) with homogenizer length of 400 mm (c) Complete LCPVT module

1.1. Design of CPC

Compound parabolic collectors are a special class of non-imaging concentrators where there is a transfer of energy/radiative flux from the source to the target (absorber/receiver) but an image of the source is not formed at the absorber (Winston, 1974). Hence, the stringent tracking requirements are reduced considerably. They are capable to attain the maximum theoretical limit of concentration for any acceptance angle unlike imaging systems. For a 2-D CPC with aperture area A_L and base area A_S, concentration ($C_{2\text{-}D}$) is given by Eq. (1)

$$C_{2-D} = \frac{n}{\sin\theta} = \frac{A_l}{A_S} \qquad (1)$$

where, C is geometrical concentration and n is the refractive index of the medium. The equation of curvature of parabola depends on the output aperture width and concentration and is given by Eq. (2)

$$y = \frac{x^2}{2(1+\sin\theta)w} \quad (2)$$

where, *w* is the absorber width and θ is half acceptance angle which is determined per the required concentration.

In this case, four different CPCs of geometrical concentration ratio 2X,2.5X and 3X each truncated to 1.7X have been explored. The design parameters of each CPC are given in table 1:

Table 1: Design parameters of the CPC

CPC Concentration ratio	Geometrical Concentration Ratio (Truncated CPC)	Absorber width (mm)	Aperture width (mm)	Height of the CPC (mm)
2X	1.7	1000	1700	1024
2.5X	1.7	1000	1700	744
3X	1.7	1000	1700	655

CPC shown in figure 1(a) is a line focusing concentrator. The non-uniformity is quantified by spatial non-uniformity factor (α) given by Eq. (3). Larger value of α implies greater non-uniformity [5].

$$\alpha = \frac{G_{max} - G_{min}}{G_{max} + G_{min}} \quad (3)$$

whereas maximum and minimum local concentration are given by Eq. (4) and Eq. (5) respectively.

$$G_{max} = \frac{I_{max}}{I_{incident}} \quad (4)$$

$$G_{min} = \frac{I_{min}}{I_{incident}} \quad (5)$$

The homogenizer is optimised based on the above-mentioned parameters i.e. spatial non-uniformity and maximum local concentration. Optimised simulations results for 2X, 2.5X and 3X ECPC each truncated to 1.7X are presented in the next section using ZEMAX (Radiant Zemax, 2014) software.

1.2. Ray tracing simulation and optimisation of the homogenizer for the ECPCs

To simulate the CPCs (2X, 2.5X and 3X each truncated to 1.7X), a rectangular source with 1 million rays were incident on the concentrator, whose reflectivity was assumed to be 0.9. The flux on the PVT module was studied by placing a rectangular detector of dimensions 1000 mm x 2000 mm. For the design concentration of 2X, 2.5X and 3X truncated to 1.7X, the average concentration obtained was 1.625,1.63 and 1.63 since some rays reached the solar PVT module directly and rest of them reached after reflecting from the CPC. Figure 2(a), 3(a) and 4(a) shows the ray tracing simulation for a normal CPC and ECPC while figure 2(b), 3(b) and 4(b) shows the magnitude and pattern of radiation flux falling on the PVT module clearly showing highly non-uniform illumination. To optimise the homogenizer, the length of the homogenizer was swept in the steps of 100 mm. At each length of the homogenizer, spatial non-uniformity and average concentration ratio are calculated. Finally, the optimised homogenizer length was chosen which had minimum spatial non-uniformity and maximum average concentration ratio as shown in Figure 2(c,d), 3(c,d) and 4(c,d).

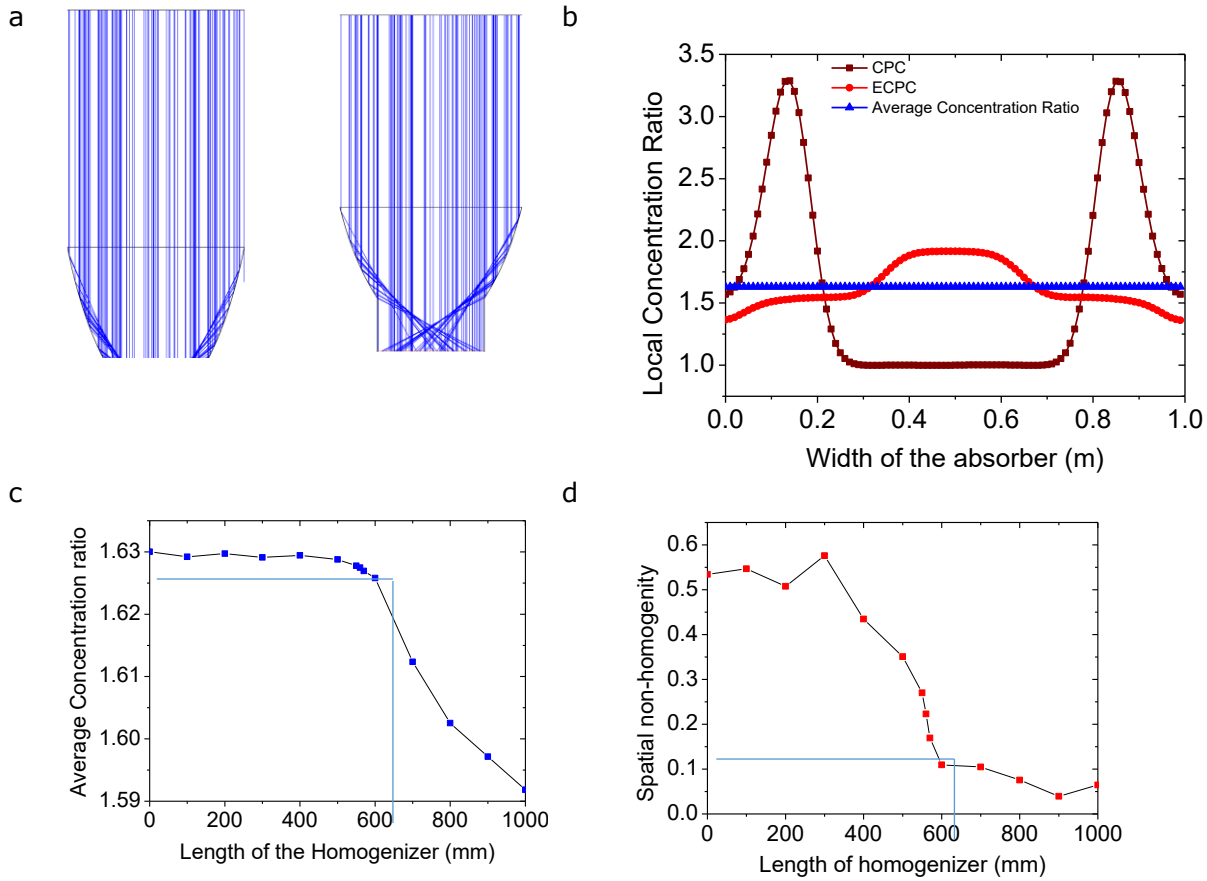

Figure 2: (a) Ray tracing simulation for 2X truncated to 1.7X (b) Flux distribution on the absorber (c) Variation of average concentration ratio with varying the length of homogenizer (d) Spatial non-homogeneity variation with length of the homogenizer.

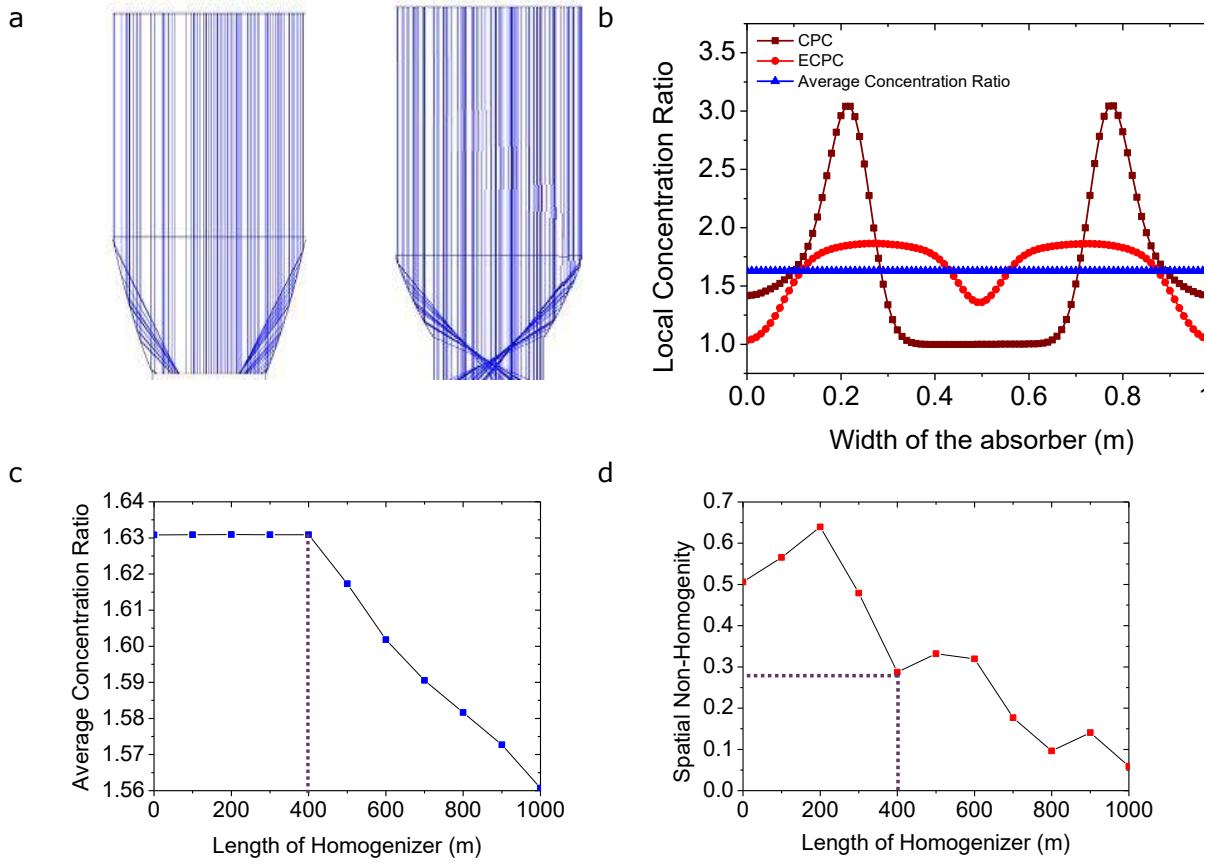

Figure 3: (a) Ray tracing simulation for 2.5X truncated to 1.7X (b) Flux distribution on the absorber (c) Variation of average concentration ratio with varying the length of homogenizer (d) Spatial non-homogeneity variation with length of the homogenizer.

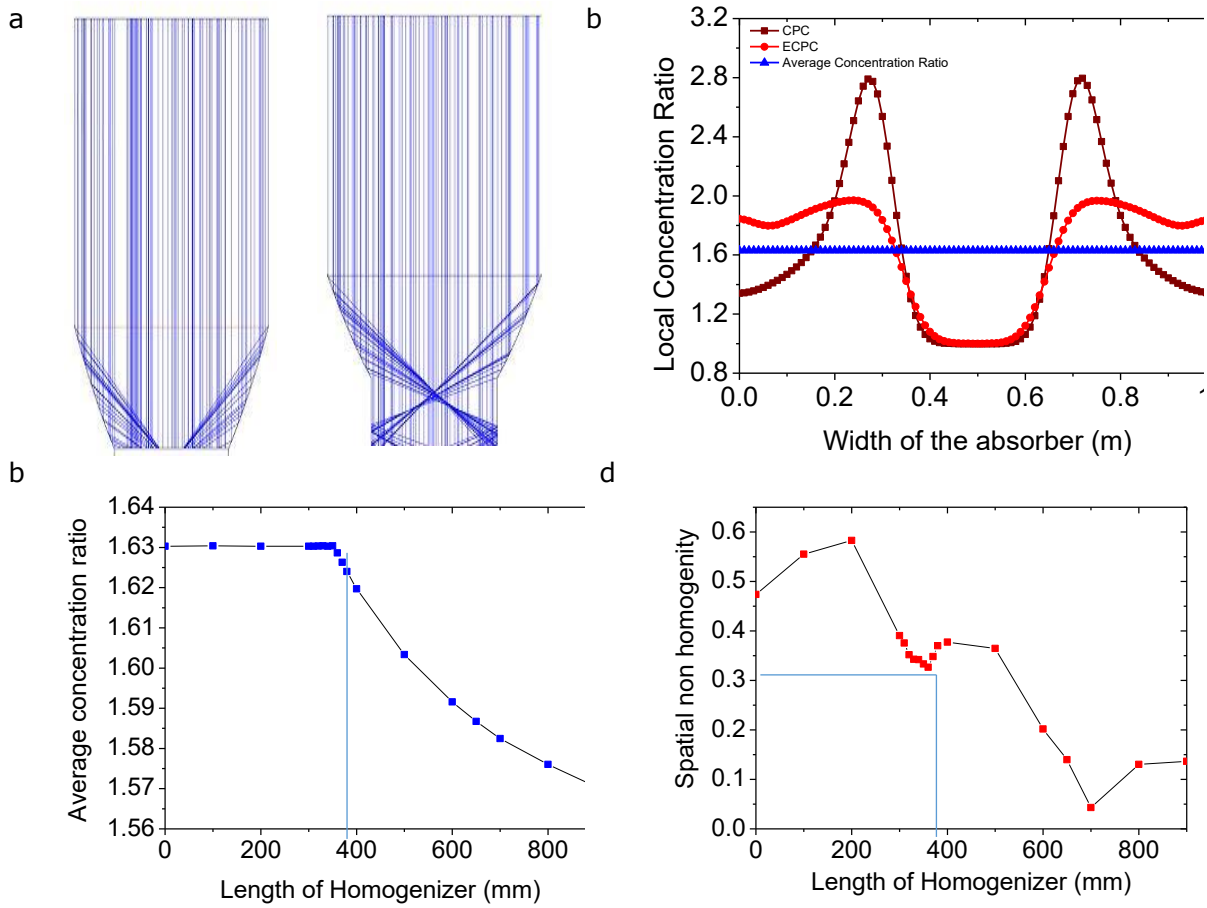

Figure 4: (a) Ray tracing simulation for 3X truncated to 1.7X (b) Flux distribution on the absorber (c) Variation of average concentration ratio with varying the length of homogenizer (d) Spatial non-homogeneity variation with length of the homogenizer.

2. RESULTS AND DISCUSSION

From the above simulation results, it can be concluded that the homogenizer plays a major role in enhancing the performance and life time of the solar cell by significantly reducing the non-uniform illumination on the PVT absorber. The spatial non-uniformity in the case of 2X, 2.5X and 3X ECPC were observed to be 0.16, 0.28 and 0.32 for homogenizer lengths of 570 mm, 400 mm, and 360 mm respectively. Although CPC of 2X truncated to 1.7X has higher acceptance angle, i.e. it can operate for a larger period during the day, the material requirement for the concentrator is 4.112 m^2 as shown in table 2 which makes it an unattractive choice. Further, 3X truncated to 1.7X has minimum material (2.97m^2) requirement but has lower acceptance angle, again limiting its deployment, therefore an ECPC of 2.5X truncated to 1.7X is a perfect trade-off between both the working hours and material requirement making it an optimal choice for the LCPVT system.

Table 2: Optimised design of the ECPC

Configuration	Curved surface area of concentrator (m^2)	Height of concentrator (m)	Length of homogenizer (m)
2X_1.7X	4.112	1.024	0.570
2.5X_1.7X	3.301	0.744	0.400
3X_1.7X	2.978	0.655	0.360

3. CONCLUSION

The comparison of optical performance of the ECPC and CPC in case of 2.5X truncated to 1.7X shows that the illumination pattern was significantly improved thus reducing the spatial non-uniformity factor by 44 % while maximum local concentration ratio is reduced from 3 to 1.86. Similar results were observed for the 2X and 3X CPC each truncated to 1.7X. In addition to this, the simulation results further demonstrate that a CPC of 2.5X

concentration ratio truncated to 1.7X is optimal for the concentrated PVT application considering both the amount of concentrator material used and the effective time of operation over the entire day.

4. ACKNOWLEDGEMENT

The authors wish to thank Director, CSIR-CEERI; Director, CSIR-SERC for the resources, facilities and financial support to carry out the work fruitfully. The first author also takes this opportunity to express his gratitude to CSIR for supporting the research work by providing SRF fellowship. Further, he is thankful to fellow colleagues of CSIR and AcSIR for their kind inputs.

5. REFERENCES

Romero M, and González-Aguilar J. "Solar thermal CSP technology." Wiley Interdisciplinary Reviews: Energy and Environment 3.1 (2014): 42-59.

Honsberg C, and Bowden S. "PVeducation.org".(access April-June 2013) http://pveducation. org/pvcdrom/properties-of-sunlight/sun-position-calculator (2014).

van Helden, WGJ, van Zolingen RJC, and Zondag HA. "PV thermal systems: PV panels supplying renewable electricity and heat." Progress in Photovoltaics: Research and Applications 12.6 (2004): 415-426.

Schmitt, B. "Classification of industrial heat consumers for integration of solar heat." Energy Procedia 91 (2016): 650-660.

Sonneveld, P, Zahn H, and Swinkels GJ. "A CPV system with static linear Fresnel lenses in a greenhouse." AIP Conference Proceedings. Vol. 1277. (2010).

Winston, R. "Principles of solar concentrators of a novel design." Solar Energy 16.2 (1974) 89-95

Baig, H, Heasman KC, and Mallick TK. "Non-uniform illumination in concentrating solar cells." Renewable and Sustainable Energy Reviews 16.8 (2012): 5890-5909.

Sellami, N, and Mallick TK. "Optical efficiency study of PV crossed compound parabolic concentrator." Applied Energy 102 (2013): 868-876.

Xie, H, et al. "Design and performance research on eliminating multiple reflections of solar radiation within compound parabolic concentrator (CPC) in hybrid CPV/T system." Solar Energy 129 (2016) 126-146.

Paul, DI, et al. "The effects of nonuniform illumination on the electrical performance of a single conventional photovoltaic cell." International Journal of Photoenergy 2015 .

Radiant Zemax, L. L. C. "Zemax 13 Optical Design Program User's Manual." (2014).

225: Review on enhancement methods for phase change materials

Mariana VELASCO-CARRASCO[1], Ziwei CHEN[2], Jorge Luis AGUILAR-SANTANA[3], Saffa RIFFAT[4]

[1] *Department of Architecture and Built Environment, Faculty of Engineering, University of Nottingham, University Park, NG7 2RD, UK, mariana.velascocarrasco@nottingham.ac.uk*
[2] *Department of Architecture and Built Environment, Faculty of Engineering, University of Nottingham, University Park, NG7 2RD, UK, ziwei.chen@exmail.nottingham.ac.uk*
[3] *Department of Architecture and Built Environment, Faculty of Engineering, University of Nottingham, University Park, NG7 2RD, UK, jorge.aguilarsantana@nottingham.ac.uk*
[4] *Department of Architecture and Built Environment, Faculty of Engineering, University of Nottingham, University Park, NG7 2RD, UK, saffa.riffat@nottingham.ac.uk*

Nowadays a mayor aspect for reducing the carbon footprint focuses on the reduction of the heating and cooling and the incorporation of energy efficient systems. It is in this regard, innovative technologies such as thermal energy storage (TES) can help boost the energy efficiency systems. Phase Change Materials or PCMs are substances that can absorb, store and release a large amount of thermal energy at relatively constant temperatures and are well suited for heat transfer and energy conversion applications where the state of the material normally varies from solid-liquid or vice-versa. The thermal performance of PCMs depends on their melting temperature, thermal conductivity, and energy storage density. The principal drawback for the PCMs application is the low thermal conductivity; to overcome this problem many researchers have focused their investigations to enhance the thermal conductivity in organic PCMs by adding nanoparticles such as carbon nanofillers, alumina and graphite. This review presents different enhancement methods to increase the thermal conductivity of the PCMs depending on the base fluids. Parrafins appear as the most common material; nevertheless further investigation is required regarding lower melting points for building application.

Keywords: cooling control, energy saving, phase change materials, thermal energy storage

1. INTRODUCTION

In recent years buildings have accounted for approximately 40% of global energy consumption and GHG emissions. This has caused a huge impact on climate change, where fossil fuels used for heating and cooling accounts for 60% of energy consumption (Huges & Cheuk-Ming, 2011), (Hughes, et al., 2011). Recent investigations predict that the impact will grow by 1.8% per year through 2050. For this reason, researchers have focused their investigations on several strategies to reduce the impact generated by heating and cooling in buildings (Akeiber, et al., 2016); one of this being the PCMs. The energy consumption for cooling is expected to increase sharply by 2050 by almost 150% globally, and by 300% to 600% in developing countries (Weinlader, et al., 2017).

Thermal energy storage (TES) is a useful technology for improving energy efficiency and energy saving (Jeon, et al., 2010). TES in buildings can be implemented by sensible heat (increasing and decreasing the temperature of the building envelopes, for example), or by latent heat (with the inclusion of phase change materials which increases thermal inertia) (Cabeza, et al., 2011).

Phase Change Materials (PCMs) are substances that can absorb, store and release a large amount of thermal energy at relatively constant temperatures (Salunke & Shembekar, 2012) and are well suited for heat transfer and energy conversion applications, where the state of the material normally varies from solid-liquid or vice-versa. The total heat addition-release to-from the PCM consists of sensible heat and latent heat. During sensible heating, the thermal energy is stored up to the initiation of melting process, whereas, the thermal energy is stored during the phase change process is known as the latent heat. One of the major advantages of the latent heat storage system is an isothermal release or gain of thermal energy. In contrast, the temperature decreases or increases during sensible cooling-heating. In a typical working temperature range, the latent heat storage capacity is about 5 to 14 times the conventional thermal energy storage materials such as masonry, rock etc. (Salunke & Shembekar, 2012). The application of the PCM has grown in recent years and it is possible to find many applications in a wide range of industries, from space applications to renewable energy in solar power, and smooth the exothermic temperature peaks in chemical reactions (Lochan & Arif, 2013).

Latent heat storage (LHS) has been qualified as the most efficient way to store thermal energy with higher storage density and smaller temperature changes when storing and releasing the heat (Farid, et al., 2004) (Zalba, et al., 2004). In LHS systems, the thermal energy is stored as latent heat in substances undergoing a phase transition (Hamdam & Elwerr, 1996).

The thermal performance of PCMs depends on the melting temperature, thermal conductivity, and energy storage density. Among those, suitable PCMs for thermal energy ideally storage required a rapid melting and solidification point (Ji, et al., 2014) (Ma, et al., 2013). There are several solutions to enhance and improve the thermal conductivity and ability to energy exchange of PCMs, such as the use of fins and heat pipes, micro and macro-encapsulation and adding nanoparticles with high thermal conductive in the PCM base fluid as nano-enhanced PCM (Ma, et al., 2013) (Khodadadi, et al., 2013).

Residential buildings have been identified as one of the few sectors that have the potential to see large energy savings through the utilization of renewable energy and green building concepts (Thanbidurai, et al., 2015). Mazzeo et al. identifies the use of high thermal performance PCMs in building envelopes as a valuable method for achieving net zero energy buildings in the near future. For buildings applications the PCMs are used to control the ambient temperatures in order to archive the thermal comfort, this can be applied in diverse components of a building, for example floors, windows, ceilings and walls (Mazzeo, et al., 2017).

2. PCM ENHANCEMENT METHODS

There are different techniques to increase the thermal conductivity and energy saving density of PCMs such as the use of extended surfaces, fins and heat pipes, micro and macro-encapsulation and adding nanoparticles with high thermal conductive in the PCM base fluid (Kasaeian, et al., 2017).

One of the most common disadvantages in organic PCMs, is the low thermal conductivity, this creates difficulties due low heat flow in thermal charging and discharging processes (Khodadadi, et al., 2013) (Wu, et al., 2013). Many researchers have proposed innovative enhancement techniques, one example is the implementation of fins and heat pipes (Salunke & Shembekar, 2012) (Sharifi, et al., 2012), insertion and dispersion of high thermal conductive materials (Khodadadi, et al., 2013), micro- encapsulation and macro-encapsulation (Salunke & Shembekar, 2012) (Delgado, et al., 2012).

According to Ji et al. and Wu et al. one commonly used technique is the dispersion of high thermal conductive nanometer-sized materials, such as nanoparticles, nanofibers, nanotubes and nanosheets, in the PCM base fluid. Resulting in the significant increase in its thermal conductivity and enhance the capability of energy exchange (Ji, et al., 2014) (Wu, et al., 2013). This emerging mixture is called nano-enhanced phase change material and is used in both passive and active applications.

2.1. Applications of nano-enhanced PCM in buildings

The nano-enhanced PCMs can be used in heating, cooling, ventilation and air-conditioning systems to reduce the incompatibility between the energy supply and the demand by the shifting and reduction of peak load and improving the energy performance of the buildings.

Some complications presented in the PCM application are the uncertainty of the speed of the moving solid–liquid interface, the interaction of nanometer-sized materials with PCM base fluids, and the highly nonlinear phase change characteristics. For this reasons, it is extremely difficult to manage with the phase change problem and reliably estimate the flow and energy transport mechanisms when the materials undergo the phase transition in the melting and solidification cycles (Ma, et al., 2013).

The first study on the use of nanometer-sized materials (i.e. nanofibers) in PCMs for improved thermal energy storage was reported by (Elgafy & Lafdi, 2005) in 2005. From this date researchers have developed a novel nano-enhanced PCM suitable for various industrial and building applications, testing and characterization of their thermal energy storage performance, and investigation of their melting and solidification characteristics (Ma, et al., 2013).

2.2. Nano-enhanced PCMs with paraffin as the base fluid

Paraffin has demonstrated a satisfactory storage performance in various applications and is one of the most commonly used organic PCMs (Memon, 2014) (Wagas & Ud, 2013) (Ho & Gao, 2009). Many studies present nanometer-sized materials in order to enhance the thermal conductivity of these organic PCMs.

Colla et al. studied the feasibility of nano-enhanced PCM containing aluminium oxide (Al_2O_3) and carbon black (CB). The thermal properties were monitored: thermal conductivity, specific heat and latent heat in both liquid and solid phases. The study presents two commercial paraffin wax with melting temperatures of 20°C and 25°C, Rubitherm RT20 and Rubitherm RT25 respectively. Thermal conductivity is measured at 14°C; the results showed that the addition of the carbon black nanoparticles leads to enhancement of 35% and 24% for the RT20/CB and RT25/CB respectively. The Al_2O_3 based nano-PCMs were found unstable (Colla, et al., 2017).

Wu et al. reported on copper nanoparticles Hitenol BC-10 was used as the surfactant. The measurement using the Fourier transform infrared (FTIR) spectrometer showed that physical interactions existed among copper nanoparticles, paraffin and HitenolBC-10. Compared to the pure paraffin, the melting time and solidification time of the mixture with a weight fraction of 1.0% copper nanoparticles were reduced by 33.3% and 31.6%, respectively (Wu, et al., 2009). Teng and Yu investigated nancomposite-enhanced phase change materials (NEPCMs) mixing paraffin with alumina, titania, silica and zincoxide particles, respectively. Using a differential scanning calorimeter the feasibility on the thermal performance was determined. Of the four particles, the paraffin combined with titania provided better heat conduction and thermal storage performance (Teng & Yu, 2012).

Ho and Gao reported on the emulsifying aluminia (Al_2O_3) nanoparticles in paraffin (n-octadecane) by means of a non-ionic surfactant, focusing on the thermo-physical properties. The results present that the thermal conductivity and dynamic viscosity of the mixture increased nonlinearly with the increase of the mass fraction of alumina nanoparticles (Ho & Gao, 2009). Paksoy and Sahan examined nano magnetite (Fe2O3) particles added to paraffin with a melting range between 56°C-58°C. The findings present that the thermal storage capacity of paraffin could increase up to 20% by addition of 10% nano magnetitite (Paksoy & Sahan, 2012).

Fan et al. investigated the effect of adding carbon nanofillers with paraffin wax in short and long carbon nanofillers and graphene nanoplates (GNPs). The experiment showed that the thermal conductivity increased with raising the loading, it is important to highlight that the enhancement depends on the size and shape of the nanofillers. In comparison to the base fluid, the thermal conductivity of the mixture dispersed with a 10% weight faction of GNPs increased up to 164% reducing the thermal interface resistance (Fan, et al., 2013).

Cui et al (Cui, et al., 2011) studied the thermal properties of carbon nanofiber (CNF) and carbon nanotube (CNT) filled with paraffin wax in order to enhance the thermal conductivity. The experimental results proved that both the CNF and CNT improve the thermal conductivity, although the CNF show to be slightly more effective. The results indicated that the dispersion of highly thermal conductive nanometer-sized materials in paraffin could substantially increase its thermal conductivity, assisting in overcoming the key barrier towards its wide application as thermal energy storage media (Ma, et al., 2013).

Zhong et al. investigated the enhancement of paraffin wax by adding graphite foam. The thermal diffusivity of the Paraffin-GF can increase 190, 270, 500 and 700 times in comparison of pure paraffin wax, moreover the study revealed that the smaller the pore size the higher thermal diffusivity and the larger pore size resulted on larger latent heat (Zhong, et al., 2010).

2.3. Nano-enhanced PCMs with other PCMs as base fluids

Apart from using paraffin as a based fluid, some researchers have focused their attention to other PCMs, for example Oya et al. who developed a new phase change composite (PCC) by implementing erythritol as PCM and graphite nickel particles as a thermal conductivity promoter. The results showed that the thermal conductivity of the mixture increased gradually with the increase of the volume fraction of the particles and their aspect ratio. The variation of the thermal conductivity could be explained well by Nielsen's equation (Oya, et al., 2013).

Zeng et al. reported on the thermal conductivity of Ag nanoparticles mixed with organic PCM (1–tetradecanol TD). The results presented that the thermal conductivity was enhanced and the thermal stability of the composite materials were closed to that of pure TD. Ag nanoparticles with multi-shape dispersed uniformly in the material, it appears that the interaction of the Ag particles and the TD is considerable small (Zeng, et al., 2007). Teng investigated the thermal conductivity of PCM with aluminia (Al_2O_3)-water nanofluid and chitosan dispersant to improve the performance of ice storage air conditioning systems. The results showed that using the appropriate concentrations of the aluminia water could improve the performance of the system (Teng, 2013).

Krishna et al. investigated a heat pipe, using nano-enhanced Phase Change Material as an energy storage medium for electronic cooling applications as presented in Table 1. The PCM was placed around the adiabatic section in the heat pipe where heat is absorbed and released depending on power inputs at the evaporator and fan speeds at the condenser. The researchers used water, tricosane and nano-enhanced tricosane, the nano enhanced PCMs were prepared by mixing different volume percentages (0.5%, 1% and 2%) of Al_2O_3 nanoparticles with Tricosane. The study revealed that the nano-enhanced PCM increases the thermal conductivity by 32%, furthermore the evaporator temperature of the heat pipe decreased 25.75%, which can lead to savings of 53% of the fan power. Overall, the nano-enchance PCM can store up to 30% of the energy supplied at the evaporator leading to a reduction in the fan power consumption (Krishna, et al., 2017).

Table 1: Thermo-physical properties of cooper, Tricosane and Al2O3 nanoparticles (Krishna, et al., 2017).

Properties	**Electrolyte cooper**	**Tricosane**	**Al_2O_3**
Thermal conductivity (W/m K)	401	0.140	30
Specific heat (kJ/kg)	0.3844	2.89	0.88
Latent heat (kJ/kg)	207	209	-
Melting point (°C)	1083.85	46	122064.85

He et al. presented a study of a nanofluid PCM containing TiO_2 nanoparticles in $BaCl_2$ aqueous solution. The experimental results showed that the thermal conductivity increased by 12.76% at -5°C, the supercooling degree was reduced by 84.92%, the latent heat and the specific heat are slightly decreased with suspending nanoparticles (He, et al., 2012).

Cai et al. examined an innovative PCM by combining lauric acid (LA), polyethylene terephthalate (PET) and silica nanoparticles (nano-SiO_2). It was reported that the nano-SiO_2 in the fibres influenced the crystallization of the LA and had an important role on the heat enthalpy of the composite fibres (Cai, et al., 2011). Kurmaresan et al. studied the behaviour of water nanofluid PCM encapsulated in a spherical container. The report concluded with savings of 6-9% in the chiller. The time of solidification of the nano-enhanced PCM was reduced between 14% to 20.2% when the fraction of carbon nanotubes was of 0.6% (Kumaresan, et al., 2013).

Guo investigated a mixture of paraffin and aluminia particles that were to be incorporate in a ceiling board. The results concluded that the PCM ceiling board saves a considerable amount of energy, although the exact percentage was not reported (Guo, 2010). Biswas et al. presented an innovative nano-PCM enhanced with graphite interconnected nanosheets. Three cooling points were selected: 21°C, 22°C, 23°C, and their results showed that during the summer, at an ambient temperature of 22°C only the PCM with a cooling point of 21°C lead to a reduction in heat gains (Biswas, et al., 2014).

The phase change heat transfer characteristics and thermal behaviour of spherically encapsulated PCM with dispersed nanoparticles is reported by Kalaiselvam et al. Table 2 compares various PCMs embedded with aluminium and aluminia nanoparticles, the study showed that the solidification time for the 60% n-tetradecane 40% n-hexadecane can reduce by 12.97% and 4.97% respectively (Kalaiselvam, et al., 2012).

Table 2: Comparison of reduction of solidification time for the PCMs in pure form and with dispersed nanoparticles (Kalaiselvam, et al. 2012).

PCM Description	Pure PCM	With aluminium nanoparticles (φ = 0.07)		With aluminia nanoparticles (φ = 0.07)	
	Time (s)	Time (s)	Time Reduction (%)	Time (s)	Time Reduction (%)
60% n-tetradecane 40% n-hexadecane	15880	13820	12.97	15090	4.97
Capric/Lauric Acid	10470	8760	16.33	9545	8.83
CaCl2.6H2O	4480	3465	22.66	3690	17.63
n-Octadecane	10795	9195	14.82	10085	6.58
n-Hexadecane	13295	11470	13.73	12640	4.93
n-Eicosane	9105	7850	13.78	8640	5.11

Colella et al. reported on a medium scale storage unit for district heating systems, designed to transfer heat from the district to building heating networks. The PCM selected was a RT100 paraffin composite and the heat transfer fluid (HTF) was water. The results show that this technology can provide higher energy storage densities (Colella, et al., 2012).

Parameshwaran et al. analysed a silver nano-based organic ester (SNOE) phase change material thermal properties. The experiment utilized spherical-shaped surface functionalized crystalline silver nanoparticles (AgNP). The experimental results revealed that dispersion of AgNP into PCM was effective; the supercooling was reduced and the latent heat capacity decreased by 7.88% in freezing and 8.9% in melting. The study concluded that the SNOE PCMs could be considered for cooling thermal energy storage (Parameshwaran, et al., 2013). In a different study Parmeshwaran et al. (Paramesshwaran, et al., 2014) investigated the thermal properties of silver-titania hybrid nanocomposite (HyNPCM), a reduction on the supercooling degree by 1.82°C was observed, while the freezing an melting times were reduced by 23.9 and 8.5% respectively.

A study focused on Bio-based PCMs with carbon nanomaterials was conducted by Yu et al. to enhance thermal conductivity. The results showed that the thermal conductivity was significantly increased, as the carbon nanomaterials loading content increased. It was concluded that the Bio PCM composites can be considered as suitable candidate for latent heat thermal energy storage (Yu, et al., 2014). Ji et al. investigated two types of multiwalled carbon nanotubes (MWNTs) which were utilized to enhance the thermal conductivity of palmitic acid (PA). The results showed an enhancement of the thermal conductivity of PA and an improved heat transfer of PA, respectively, by the functionalized MWNTs (Ji, et al., 2012).

Jiang et al investigated the thermal dynamic mechanical properties of bulk porous Al foams impregnated with organic PCMs. The study conclude that the PCMs composites could be produced by a simple and eco-friendly constant-pressure impregnation method. The shape-stabilized PCMs/Al-foam composites exhibited considerable latent thermal storage potential for good interface, the impregnation of PCMs improved the dynamic-compression yield strength, durability and resistance to oxidation of Al foams (Jiang, et al., 2012).Table 3 presents the range of PCM enhancement methods that are available, highlighting the major findings of each study.

Table 3: Synthesis table of PCM enhancement methods

PCM Type	Enhancement material	Melting Point (°C)	Findings	Drawbacks	Reference
Paraffin Rubitherm RT20 Rubitherm RT25	Aluminium oxide (Al2O3) Carbon black (CB)	20-25	Thermal conductivity was improved by using the Al2O3 and carbon black nanoparticles up to 35% for the RT20 and 24% for the RT25.	The Al2O3 based nano-PCM were found unstable.	(Colla, et al., 2017)
Paraffin	Hitenol BC-10	58-60	Thermal conductivity was enhanced from 14.2%-18.1%.		(Wu, et al., 2009)
Paraffin	Aluminia, titania, silica zincoxide	55-65	Out of all the materials tested, the titania had the best thermal conductivity.		(Teng & Yu, 2012)
Paraffin n-octadecane	Aluminia (Al2O3)	25.1-26.5	The thermophysical conductivity increase 17% by adding the aluminia.		(Ho & Gao, 2009)
Paraffin	Fe2O3	56-58	The thermal storage capacity of paraffin can increase up to 20% by addition of 10% nano magnetitite.		(Paksoy & Sahan, 2012)

Paraffin wax	Carbon nanofillers		The thermal conductivity of the mixture dispersed with a 10% weight faction of GNPs increased up to 164% owing to the reduced thermal interface resistance	Decrement of the energy storage capacity	(Fan, et al., 2013)
Paraffin wax	Carbon nanofiber (CNF)	52-54	Highly thermal conductive nanometer-sized materials in paraffin can substantially increase its thermal conductivity, in the experiment the thermal conductivity increased by 24%-40.6%.		(Cui, et al., 2011)
Paraffin	Graphite	57.85	Mesophase pitch based graphite foams with different pore size increased the thermal diffusivity of the Paraffin-GF can be enhanced 190, 270, 500, and 570 times		(Zhong, et al., 2010)
1-tetradecanol	Nano-Ag	22	The thermal conductivity was enhanced by 11%.	Apparently the interaction of the Ag particles and the TD is considerably small	(Zeng, et al., 2007)
Nano-tricosane	Al2O3		The nano-enhanced PCM increases the thermal conductivity by 32%.		(Krishna, et al., 2017)
Barium chloride	Titania particles	-8	Thermal conductivity increased by 12.76% at -5°C, the supercooling degree was reduced by 84.92%.		(He, et al., 2012)
Lauric acid Polyethylene	nano-SiO2		The nano-SiO2 in the fibres influenced the crystallization of the LA and had an important role on the heat enthalpy of the composite fibres		(Cai, et al., 2011)
DI water	Carbon	-9 /-12	Potential energy saving of 6%-9% in the cool thermal energy storage is presented by using multi wall carbon nanotubes.		(Kumaresan, et al., 2013)
Paraffin	Aluminia		It is reported that the PCM ceiling board saves a considerable amount of energy.		(Guo, 2010)
Paraffin, n-heptadecane	Graphite	19	The numerical and experimental investigation proved energy savings of 79%, while maintaining thermal comfort.		(Biswas, et al., 2014)
n-tetradecane n-hexadecane	Aluminium and aluminia	38	The solidification time for the 60% n-tetradecane40% n-hexadecane PCM embedded with the aluminium and alumina nanoparticles were expected to reduce by 12.97% and 4.97% than at its pure form respectively.		(Kalaiselvam, et al., 2012)
Paraffin RT100	Graphite	89.85-111.85	A solution based on a paraffin-graphite composite with a 15% graphite volume fraction has been found to provide higher energy storage.		(Colella, et al., 2012)
Organic ester	AgNP	6.8	The experimental results reveal that dispersion of AgNP into PCM was effective; the supercooling was reduced and the latent heat capacity decreased by 7.88% in freezing and 8.9% in melting.		(Parameshwaran, et al., 2013)
Organic ester	Silver titania		A reduction on the supercooling degree by 1.82°C is observed, the freezing and melting times were reduced by 23.9 and 8.5% respectively.		(Paramesshwaran, et al., 2014)
Bio-based	Graphite and carbon	28.13	The thermal conductivity increase for the Bio-based PCM/xGnP 5.0 wt% by 336% and the Bio-based PCM/CNT 1.0 wt% by 166%.	The superccoling increased.	(Yu, et al., 2014)
Palmic acid	Carbon	62.7-67.3	Enhancement of the thermal conductivity and heat transfer		(Ji, et al., 2012)
Stearic acids and paraffin	Aluminium	54.7-70.6	The study indicates that the Al foam composite improved the dynamic-compression yield strength, durability and resistance and proven ideal for energy saving material.		(Jiang, et al., 2012)

3. CONCLUSIONS

PCMs for building applications prove to be a compelling solution for passive cooling due its latent heat storage capacity. In the present paper, a review of enhancement methods for PCM was detailed, focusing on the nano enhancement method of the based fluid. For the organic PCMs, the paraffins stand out as the main material for the enhancement application. Paraffins have the advantage of non-corrosiveness that make them suitable for mixing with aluminia, titania and carbon which have proven to be the most common enhancement materials throughout this investigation.

It is important to highlight that most of the enhancement methods presented fail to provide suitable temperatures for building integration. Considering the human comfort, the mentioned studies melting points ranges from -9 to 111°C, with this in mind the passive incorporation in the construction sector is limited and is only at the experimental scale. Alternative applications could see the combined use of active technologies to reach the material melting point, for example, the incorporation of heat exchangers or evacuated tubes.

Incorporating nanoparticles with high thermal conductivity enhances the thermal conductivity of the PCMs, resulting in additional energy saving, nevertheless there is still a research gap in the literature for three main areas:

- New enhancement methods with lower melting points making them more adequate for building incorporation.
- Investigate enhancement methods for other materials apart from paraffins, for example hydrated salts.
- Consider new encapsulation materials as a form of PCM performance enhancement.

4. REFERENCES

Akeiber, H., Nejat, P., Majid, M. Z. A., Wahid, M. A., Jomehzadeh, F., Famileh, I. Z., Calautit, J., Hughes, B.K. R, Zaki S. A. 2016. A review on phase change material (PCM) for sustainable passive cooling in building envelopes. *Renewable and Sustainable Energy Reviews,* pp. 1470–1497.

Biswas, K., Lu, J., Soroushian, P. & S., S. 2014. Combined experimental and numerial evaluation of a prototype nano-PCM enhanced wallboard. *Applied Energy,* pp. 517-529.

Cabeza, L., Castell, A., Barreneche, C., Gracia, A., Fernandez, A. 2011. Materials used as PCM in thermal energy storage in buildings - A review. *Renewable and Sustainable Energy Reviews,* p. 1675–1695.

Cai, Y. Ke, H., Dong, J., Wei, Q., Lin, J., Zhao, Y. 2011. Effects of nano-SiO2 on morphology, thermal energy storage, thermal stability and combustion properties of electrospun lauric acid/PET ultrafine composite fibers as form-stable phase change materials. *Applied Energy,* p. 2106–2112.

Colella, F., Sciacovelli, A. & Verda, V. 2012. Numerical analysis of a medium scale latent energy storage unit for distric heating systems. *Energy ,* pp. 397-402.

Colla, L., Fedele, L., Mancin, Simone., Danza, L., Manca, O. 2017. Nano-PCMs for enhanced energy storage and passive cooling applications. *Applied Thermal Engineering,* pp. 584-589.

Cui, Y., Liu, C., Hu, S. & Yu, X. 2011. The experimental exploration of carbon nanofiber and carbon nanotube additives on thermal behaviour of phase change materials. *Solar Energy Materials and Solar Cells,* p. 1208–1212.

Delgado, M., Lazaro, A., Mazo, J. & Zalba, B. 2012. Review on phase change material emulsions and microencapsulation phase change material slurries: materials, heat transfer studies and applications. *Renewable and Sustainable Energy Reviews,* pp. 253-273.

Elgafy, A. & Lafdi, K. 2005. Effect of carbon nanofiber additives on thermal behaviour of phase change materials. *Carbon,* pp. 163–172.

Fan, L. W., Fang, X., Wang, X., Zeng, Y., Xiao, Y.Q., Yu, Z.T. 2013. Effects of various carbon nanofillers on the thermal conductivity ans energy storage properties of paraffin-based nanocomposite phase change materials. *Applied Energy,* pp. 163-172.

Farid, M., Khudhair, A., Razack, S. & Al- Hallaj, S. 2004. A review on phase change energy storage: materials and applications.. *Energy Conversersion Management,* pp. 1597-1615.

Guo, C., 2010. Application study of nanoparticle-enhanced phase change material in ceiling board. *Advanced Materials Research,* pp. 723-726.

Hamdam, M. & Elwerr, F. 1996. Thermal energy storage using a phase change material. *Solar Energy,* pp. 183-189.

He, Q., Wang, S., Tong, M. & Liu, Y. 2012. Experimental study on thermophysical properties of nanofluids as phase-change material (PCM) in low temperature cool storage. *Energy Conversion Management,* pp. 199-205.

Ho, C. & Gao, J., 2009. Preparation and thermophysical properties of nanoparticle-in-paraffin emulsion as phase change material. *International Communications in Heat Mass Transfer Journal,* pp. 467-470.

Huges, B. & Cheuk-Ming, M. 2011. A study of wind and bouyancy driven flows through commercial wind towers. *Energy and Buildings, Volume 43, Issue 10,* pp. 2964.

Hughes, B., Calautit, J. & Ghani, S. 2011. The development of commercial wind towers for natural ventilation: A review. *Applied Energy,* pp. 252-256.

Jeon, J., Seo, J., Jeon, S. & Kim, S. 2010. PCM application methods for residential building using radiant floor heating systems. *Building Environment & Materials Lab, School of Architeture Soongsil University,* pp. 156-743.

Jiang, J., Zhu, Y.; Ma, A.; Yang, D.; Lu, F.; Chen, J.; Shi, J.; Song, D. 2012. Preparation and performances of bulk porous Al foams impregnated with phase-change-materials for thermal storage. *Process in Natural Science: Materials international,* pp. 440-444.

Ji, H., Sellan, D.P., Petters, M.T., Kong, X., Ji, J., Shi, L., Ruoff, R.S. 2014. Enhance thermal conductivity of phase change materials with ultrathin-graphite foams for thermal energy storage. *Energy Environment,* pp. 1185-1192 .

Ji, P., Sun, H., Zhong, Y. & Feng, W. 2012. Improvement of the thermal conductivity of a phase change material by the fubtionalized carbon nanotubes. *Chemical Engineering Science,* pp. 140-145.

Kalaiselvam, S., Paeamesharan, R. & Haririshnan, S. 2012. Analytical and experimental investigations of nanoparticles embedded phase change materials for cooling applications in modern buildings. *Renewable Energy,* pp. 375-387.

Kasaeian, A., Bahrami, L., Pourfayaz, F., Khodabandeh, E., Yan, W.M. 2017. Experimental studies on the applications of PCMs and nano-PCMs in buildings: A critical review. *Energy and Buildings,* pp. 96-112.

Khodadadi, J., Fan, L. & Babaei, H. 2013. Thermal conductivity enhancement of nanostructure-based colloidal suspensions utilizes as phase change materials for thermal energy storage: a review. *Renewable and Sustainable Energy Reviews,* pp. 418-444.

Krishna, J., Kishore, P. & A.B., S. 2017. Heat pipe with nano enhanced-PCM for electic cooling application. *Experimental Thermal and Fluid Science,* pp. 84-92.

Kumaresan, V., Chandrasekaran, P., Nanda, M. & Maini, A. 2013. Role of PCM based nanofluids for energy efficient cool thermal storage system. *International Journal of Refrigeration,* pp. 1641-1647.

Lochan, A. & Arif, M. 2013. Phase change materials and potential applications. *International Journal of Applied Engineering Research,* pp. 147-168.

Ma, Z., Lin, W. & Sohel, M. 2013. Nano-enhanced phase change materials for improved building performance. *Renewable and Sustainable Energy Reviews,* pp. 1256-1268.

Mazzeo, D., Oliveti, G. & Arcuri, N. 2017. A method for thermal dimensioning and for energy behaviour evaluation of a building envelope PCM layer by using the characteristics days. *Energies. pp. 659*

Memon, S. 2014. Phase change materials intergarated in buildings walls: a state of the art review. *Renewable and Sustainable Energy Reviews,* pp. 870-906.

Oya, T., Nomura, T., Tsubota, M., Okinaka, N., Akiyama, T. 2013. Thermal conductivity enhancement of erythritol as PCM by using graphite and nickel particles. *Applied Thermal Engergy,* pp. 825-828.

Paksoy, H. & Sahan, N. 2012. Thermally enhance paraffin for solar applications. *Energy Procedia,* pp. 350-352.

Parameshwaran, R., Jayavel, R. & Kalaiselvam, S. 2013. Study on thermal properties of organic ester phase-change material embedded with silver nanoparticles. *Journal Thermal Analysis Calorimetry,* pp. 845–858.

Paramesshwaran, R., Deepak, K., Saravanan, R. & Kalaiselvam, S. 2014. Preparation, thermal and rheological properties of hybrid nanocomposite phase change material for thermal energy storage. *Applied Energy,* pp. 32-330.

Salunke, P. & Shembekar, P. 2012. A review on the effect of phase change material encapsulation on the thermal performance of a system. *Renewable and Sustainable Energy Reviews,* pp. 5603-5616.

Sharifi, N., Wang, S., Bergman, T. & Faghri, A. 2012. Heat pipe-assisted melting of a phase change material. *International Journal of Heat Mass Transfer,* pp. 3458-3469.

Teng, T. 2013. Thermal conductivity and phase-change properties of aqueous aluminia nanofluid. *Energy Conversion and Management,* pp. 369-375.

Teng, T. & Yu, C. 2012. Characteristics of phase-change materials containing oxide nano-additives for thermal storage. *Nanoscale Res Lett. Pp.611*

Thanbidurai, M., Panchabikesan, K., Mohan, K. & Ramaling, V., 2015. Review on phase change material based free cooling of buildings- The way toward sustainability. *Energy Storage,* pp. 74-88.

Wagas, A. & Ud, Z. 2013. Phase change material (PCM) storage for free cooling of building- a review. *Renewable Sustainable Energy Rev,* pp. 607-625.

Weinlader, H., Klinker, F. & Yasin, M. 2017. PCM cooling ceilings in the Energy Efficient Center - Regeneration behaviour of two different system designs. *Energy and Buildings,* pp. 70-77.

Wu, S., Wang, H., Xiao, S. & Zhu, D. 2013. An investigation of melting/freezing characteristics of nanoparticle-enhanced phase change materials. *Journal Thermal Analysis Calorimetry,* pp. 1127–1131.

Wu, S., Zhu, D., Li, H. & Lei, J. 2009. Thermal energy storage behaviour of Al2O3-H2O nanofluids. *Thermochimica Acta,* pp. 73-77.

Yu, S., S-G., J., Chung, O. & Kim, S. 2014. Bio-based PCM/carcon nanomaterials composites with enhcanced thermal conductivity. *Solar Energy Materials and Solar Cells,* pp. 549-554.

Zalba, B., Marin, J., Cabeza, L. & Mehling, H. 2004. Free cooling of buildings with phase change materials. *Int Refrig,* pp. 839-849.

Zeng, J., Sun, L.X., Xu, F., Tan, Z.C., Zhang, Z.H., Zhang, J. 2007. Study of a PCM based energy storage system containing Ag nanoparticles. *Journal Thermal Analysis Calorimetry,* pp. 371–375.

Zhong, Y., Guo, Q., Li, S., Shi, J., Liu, L. 2010. Heat transfer enhancement of paraffin wax using graphite foam for thermal energy storage. *Solar Energy Materials,* pp. 1011-1014.

229: Short circuit current fast blocking strategy based on solid state limiter

Yu WANG[1], Lu-jun WANG[2]

1 Hubei Key Laboratory for High-efficiency Utilization of Solar Energy and Operation Control of Energy Storage System, Hubei University of Technology, 2528582648@qq.com
2 Hubei Key Laboratory for High-efficiency Utilization of Solar Energy and Operation Control of Energy Storage System, Hubei University of Technology, silvergrass@163.com

Micro system protection is to ensure network security and stable operation, the basis of one aspect can be cut off the micro network fault through the inside and outside, on the other hand and control, communication and other units to reduce failure on the network and the impact of the stable operation of the distribution network. In the short circuit protection of communication micro-network, the traditional mechanical circuit breaker has the power of switching arc phenomenon, which limits the fault current, but brings greater security risks. The solid-state circuit breaker USES the power semiconductor to make the main switch tube, which can realize the short-circuit current fast without arc breaking, while avoiding the interference of the fault current to the grid bus voltage. A solid-state short-circuit current interrupter (LCSRSCB) based on LC series resonance circuit is proposed. In normal mode, due to the configuration of resonant structure (capacitor and reactor), the influence of the original circuit is negligible. Failure mode, by controlling the on and off the main switch tube, the topology of the LCSRSCB change for LC oscillation rectifier bridge, power grid voltage of capacitor recharge quickly, using the reverse blocking capacitor voltage short-circuit current. In order to improve the speed of the interrupter, differential protection is used to detect short-circuit status. The capacity of LC resonant structure and switching tube was selected for two operation modes, and the running loss of LCSRSCB was analyzed. Simulation and experiment are carried out to verify the effectiveness of the proposed method. Compared with the traditional blocking circuit, this circuit is simple in structure, quick in response and strong in flow. It is very suitable for ac micro grid applications.

Keywords: blocking circuit; rectifier bridge; LC resonant circuit; parameter design; resonance

1. INTRODUCTION

The protection of micro grid is one of the key problems to be solved in the development and application of micro grid. Compared with the large power grid, the micro-grid system has small capacity, more power and electronic equipment, more sensitive load and sensitive power supply, and less ability to withstand short circuit faults. As a result of the traditional ac breaker action time in more than 10 ms, such a long time will lead to exchange some of micro power grid based on power electronic technology of sensitive equipment out of work, causing failure of expanding the range of. Therefore, it is of great significance to study the short circuit current blocking strategy to improve the power supply reliability of ac micro-grid (Qi, 2015; Gharehpetian, 2015).

The fault current limiter (FCL) can limit the short-circuit capacity of the power grid and reduce the impact of short-circuit current on the power grid. FCL can be divided into two categories from the implementation principle. One is the new material FCL, such as the superconducting current limiter. Including solid-state current limiter in power electrical (SSCL) are fast action, control method, action is more flexible and low equipment cost advantages, more and more attention by many research institutions both at home and abroad (Chen, 2010; Li, 2015).

Shuai (2015) proposed a multi-function solid-state current limiter with three-phase four-bridge arm,has a voltage compensation and fault current limiting function,and the voltage stability is very high when a failture, this method is essentially a three phase flow circuit, just added the function of fault block, not the versatility. Huaxi (2017) analyzes the fault current blocking capability of common power electronic circuits, and put forward buck circuit with endogenous current blocking ability, the proposed method is limited to dc. Hagh (2009) proposed a current limiting scheme without superconducting materials, using the topology of the inductance and semiconductor devices, and the inductance current is taken as the control variable. The method is based on IGBT design and is easy to damage the ring under high voltage and high current conditions. Chen (2000) proposed a solid-state current limiter with a pure current limiting type, and the control accuracy was improved by combining the current limiting type with LC series compensation, but due to the large number of power components, complex control structure and high cost, its application prospects are limited. Fathi (2016) proposed a fault current limiter based on LC series resonance, this method can effectively block the current, but the response speed of the control strategy is slow, and LC is directly connected in case of failure, so there is resonant current.

In view of that advantage and disadvantages of the exist methods, this paper designs a fast stop strategy on the base of LC series resonant circuit, which is simple in topology, has no influence on the ac network during normal operation, and quickly shuts down the fault branch after the fault occurs, so that the power supply can be rapidly restored after the troubleshooting. Compared with traditional relay, the blocking strategy in this paper has fast response speed, flexible control method and good application prospect (Li, 2016). The structure of this paper is as follows.

The first chapter introduces the topological structure and working principle of LCSRSCB system, and analyzes the current flow path of normal working mode and fault mode.The second and third chapters put forward the control strategy of the system and the parameter design of the main components. The fourth chapter through the saber software proposed method for the simulation and set up a simple verification experiment platform, the simulation and experimental results show that compared with traditional solid-state fault current limiting block device, the system of fault current response speed, can quickly cut off the fault parts contact at the input, and easy to control, to improve the security of micro grid system has greatly significance.

2. THE PROPOSED TOPOLOGY

The typical ac micro-grid topology is shown in figure 1. Wind power generation, photovoltaic power generation and other clean energy power generation connection in the ac bus as the main energy source. The battery energy storage is connected to the ac bus to suppress the power fluctuation of the system. In figure 1, load 1 is the conventional load and load 2 is the sensitive load, which is connected to the ac bus through the circuit breaker CB1 and CB2 respectively.

Assumes a certain moment load 1 branch fault occur, during the period of CB1 not disconnect, ac busbar voltage will be obvious drop, sensitive to load 2 (for example, through frequency converter drive motor) may quit the job, if the duration of voltage sags is too long, wind power, photovoltaic power generation is likely to be tripped. Therefore, in order to ensure the power supply under sensitive load and improve the stability of the operation of micro grid, it is very important to quickly disconnect short circuit branches in micro grid.

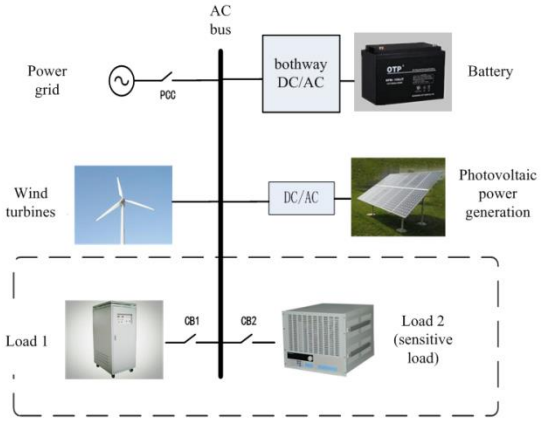

Figure 1: Strcture of typical AC microgrid

The main circuit of the proposed blocking strategy is shown in figure 2. The main circuit components are as follows: D1 and D2 are diodes, T1 ~ T6 are thyristor, C1 is resonant capacitor, and L1 is resonant inductor. The circuit has two operating modes: normal operating mode (ac mode) and fault mode (dc mode).

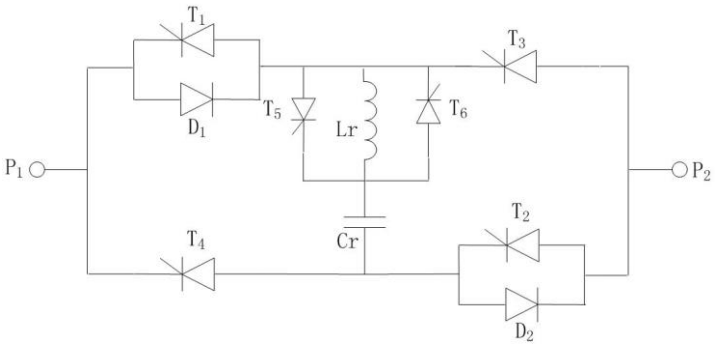

Figure 2: main circuit diagram of blocking circuit of microgrid

2.1. Normal operating mode

In normal mode, Control thyristor T1 and T2 conduction, and T3, T4, T5 and T6 are closed. At this point, the two-way current of T3, T4, T5 and T6 cannot be circulated, which can be regarded as an open circuit. The overall two-way current composed of T1/D1 and T2/D2 can be conductive, which can be regarded as a short circuit, and the equivalent circuit structure is shown in figure 3. In addition to LC resonance structure, the equivalent resistance of the line includes the sum of the resistance of the input end, cable and load end, whose value is larger than that of LC circuit. Second, the capacitance at the resonance point of ESR (equivalent resistance) is small and negligible. If the inductor and capacitor are configured to have series resonance in the circuit, the impedance of the LC resonant circuit can be ignored, almost no difference to the quality of ac power grid electricity, power grid can be stable operation.

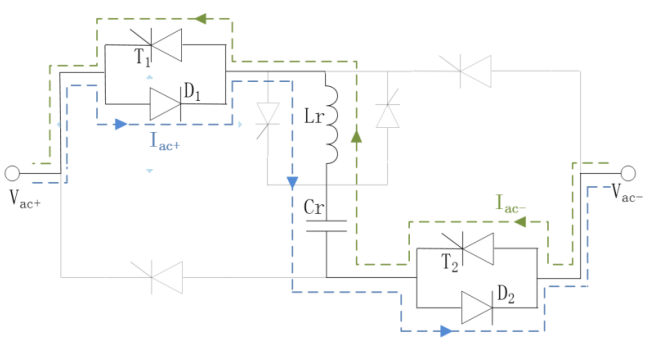

Figure 3: current path in normal mode

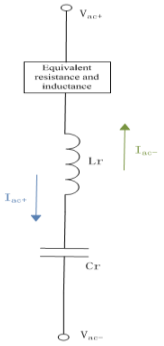

Figure 4: normal mode equivalent circuit

2.2. Fault mode

In fault mode, the control system will shut off thyristor T1 and T2 and conduct T3, T4, T5 and T6 at the time when the current exceeds the predetermined value. The new circuit topology is an ac rectification bridge added to LC oscillating circuit, the Lr is T5 and T6 bypass, rectifier voltage on the capacitor and the capacitance charging, short circuit current in the system of the energy absorbed by the capacitor, the equivalent circuit as shown in figure 4, when the capacitor voltage after reaching the maximum circuit disconnection. When the rectifier voltage makes the capacitor voltage slightly higher than the peak voltage of the micro grid, the circuit is cut off and the fault current is captured. At the initial stage of failure, the capacitor will generate oscillating harmonics to inductor reverse charge, which will affect the blocking performance. Therefore, the reverse current of the capacitor is induced in T5 branch reverse parallel T6. Among them, In figure 5,the blue arrows indicate forward current, purple arrows indicate the reverse current, the red arrow indicates the current of inductor is T5 bypass, black arrows indicate inductors are T6 bypass current. The green arrow represents the capacitor charge current I_{dc}.

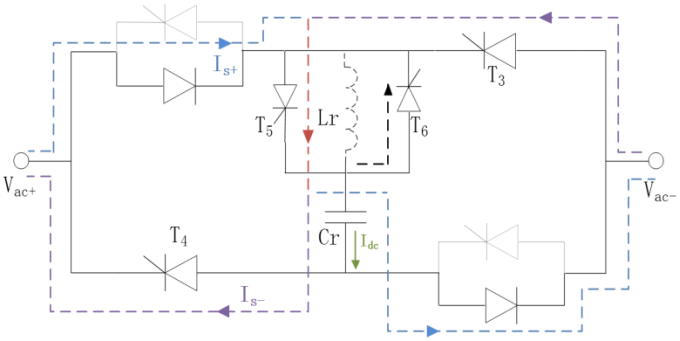

Figure 5: current path in fault mode

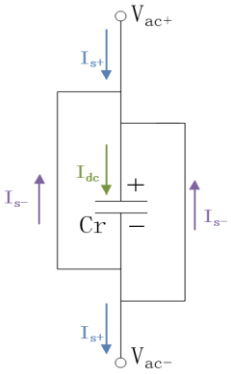

Figure 6: Equivalent circuit in fault mode

2.3. Control strategy

The block diagram of LCSRSCB control system is shown in figure 7. Adopt current differential protection strategy. Differential protection is one of the most common protection methods in relay protection, with high sensitivity and high anti-interference performance for the failure (Li, 2015). In order to improve the response time of ac micro-grid protection, differential protection is selected as the basic protection structure.

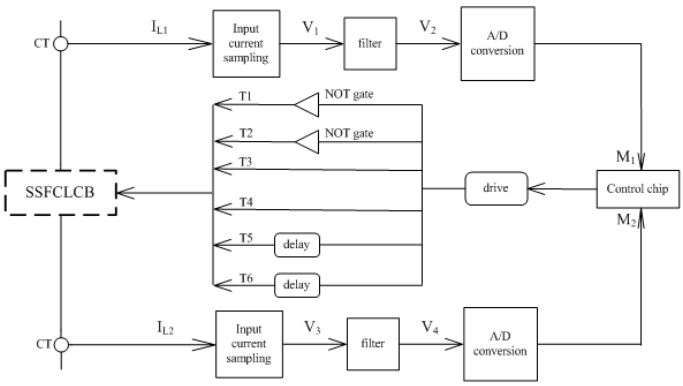

Figure 7: Control system structure

The input current and output current pass through the sampler to convert the current signal into a voltage signal，and then the noise harmonics in the voltage signal are removed through the filter and then to transmit A digital signal after A/D conversion to control chip, and finally, the power switch action is driven by the control instruction.

In normal mode, the current at both ends of LCSRSCB circuit is approximately equal, that is, $I_{L1} \approx I_{L2}$. Therefore, when I_{L1} and I_{L2} are within a reasonable range of difference values, the control chip does not issue action instructions. When the fault lines, I_{L1} and I_{L2} will appear bigger difference, when control chip detected current difference more than set threshold, immediately shut off the thyristor T1, T2, open the T3, T4, T5 delay 10 ms after open, the same time open the T6, blocking further resonance LC circuit. The 6 I/O ports of the control chip are connected with the

driving signals of 6 switch tubes respectively. The control flow of the control chip is shown in figure 8. Table 1 shows the working status of each switch tube before and after circuit failure.

Table 1: State of each switch before and after failure

	Normal mode	Failure mode	Switch between (10ms)	Second through	Failure not eliminated
T1/T2	Open	Shut down	Shut down	Open	Shut down
T3/T4	Shut down	Open	Shut down	Shut down	Shut down
T5/T6	Shut down	Open	Shut down	Shut down	Shut down

3 PARAMETER DESIGN

3.1. LC capacity selection

LC resonant circuit is an important component of main circuit and the core of block circuit. The parameter selection should consider the cost of inductors and capacitors as well as how to achieve the best blocking effect. First of all, inductor plays the role of limiting fault current in the process of failure, and capacitor plays the role of opening fault circuit in the process of failure. A capacitance with a small capacity can be charged for a shorter time and the circuit can be quickly disconnected. However, the LC circuit needs to be combined with a larger inductance, which will increase the conduction loss. If the capacity of the capacitor is too large, the charging time will be prolonged and the installation space will be a problem. Therefore, it is very important to select suitable LC circuit combination (Wu, 2015).

Table 2 summarizes the effects of different series LC combinations on the first peak current of failure and the peak of capacitor voltage. Although large capacitance will increase cost and prolong charging time, inductance will be greatly reduced, which will reduce the total loss of LC circuit and increase the accuracy of simulation experiment. The peak voltage of large capacitance in micro - grid is smaller and the capacitance is not easily broken. If the selection of small capacity (such as 10 uf), the inductance will increase sharply, the total loss of LC circuit is increased, and the small capacity of capacitance of high peak voltage (124.7 KV), in the circuit loss is bigger, the high cost of capacitance, in order to save the total cost, blocking circuit is not recommended to select this kind of capacitor. In addition, the capacitance with low equivalent resistance is selected when the actual circuit is designed, which will reduce the total impedance and loss of the circuit in ac mode. Under the working frequency of 50Hz, the combination of inductance (10mF) and capacitance (1mF) was selected in this paper.

Table 2: Circuit parameters of LC resonant circuit under different values

Capacitor value (uF)	Inductance value (mH)	First failure spike current (A)	Ac mode capacitance voltage peak (KV)	Peak capacitance voltage in dc mode (KV)
500	20	2312	2.1	22.5
450	22.2	2083	2.16	23.4
400	25	1856	2.73	24.7
350	28.5	1650	2..96	25.2
300	33.3	1432	3.3	27.5
250	40	1216	4.8	28.4
200	50	1057	5.24	30
150	100	757	12.5	39.3
100	200	523	21.4	48.9
50	1010	358	102.3	123.5

3.2. Loss analysis

The loss of LCSRSCB occurs in two parts, namely, normal running loss and fault running loss. In the normal operation of the system, the loss mainly comes from thyristor and power diode. The external impedance of LC resonant circuit can be ignored and the loss to the system is small. During the failure period, the system loss mainly occurs in thyristor conduction loss, shutdown loss, LC circuit oscillation loss, and total loss can be expressed by the formula

Equations 1: total loss of blocking circuit

$$P_{loss} = \begin{cases} P_{lc} + 2 \times P_{thy} + 2 \times P_d = i_n (R_{lc} + R_{thy} + R_d) \\ P_{lc} + 4 \times P_{thy} + 2 \times P_d = i_f (R_{lc} + 2R_{thy} + R_d) \end{cases}$$

Where:

- P_{loss}= during the fault circuit total loss(kW)
- P_{lc}= LC circuit power loss(kW)
- P_d= diode conduction loss(kW)
- P_{thy}= thyristor conduction losses(kW)
- R_{lc}= LC circuit impedance(Ω)
- R_d= diode conduction impedance(Ω)
- R_{thy}= thyristor turn-on impedance(Ω)
- i_f= short circuit current(A)
- i_n= rated current(A)

In LCSRSCB the whole operation process, the loss resulting from it should be very small, should be consider in the design of circuit components (such as inductance and capacitance) insulation, such as dielectric loss factor, avoid to produce too much additional loss.

4 PERFORMANCE EVALUATION

4.1. Simulation and analysis

Contrast experiment

In order to highlight the superiority of capacitance selection, this paper selects 100mH、100uF LC combination and 10mH、1mF LC combination of contrast experiment, observe two groups of experimental circuit of power loss and the blocking performance. In this experiment, the experimental waveform of the first set of capacitor inductance combination (10mH, 1mF) is shown in figure 8 below. The test waveform of the second set of capacitor inductance combination (100mH, 100uF) is shown in figure 9.

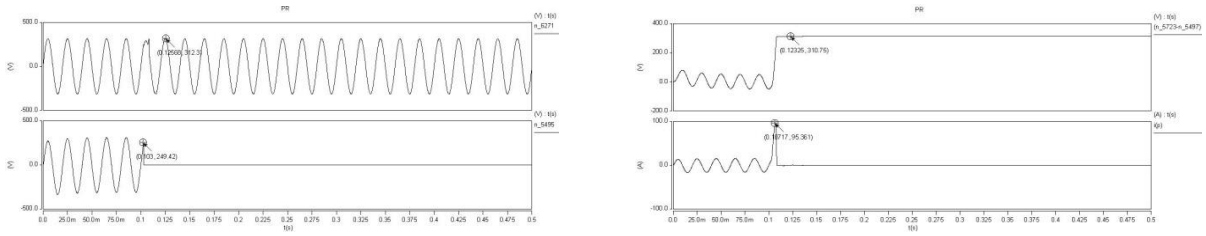

(a) input and output voltages of the circuit in case of failure *(b) line current at fault and capacitor voltage at fault*

Figure 8: The first group of LC circuit combination simulation waveform

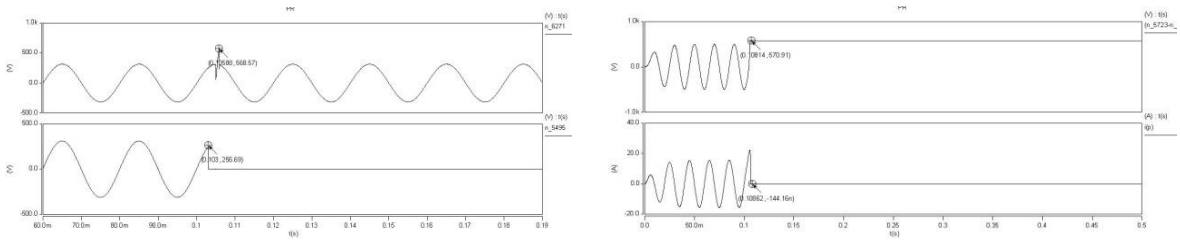

(a) input and output voltages of the circuit in case of failure *(b) line current at fault and capacitor voltage at fault*

Figure 9: The second group of LC circuit combination simulation waveform

By comparing the experiment waveforms, the first set of fault current peak of 95A, rise than 10:1, after the fault occurred 5 ms, zero line current, capacitance charging completed at the same time, the voltage of 311V or so; At the time of failure, i.e. 103ms, the output voltage will immediately drop to zero, the input voltage will be slightly fluctuated, and there will be slight fluctuation when the circuit is switched on. In the second group, the peak value of fault current is only about 22A, and the stable value of capacitor voltage is about 570V. At the same time, the

input voltage appears large overvoltage when the circuit is switched on, which has certain influence on the stable operation of the circuit. The comparison test shows that the combination of large capacitance and small inductance is more reasonable in terms of circuit stability and design cost.

Fault recovery

The failure recovery capability of LCSRSCB is shown in figure 9. As you can see from the graph (a), fault block of output voltage in steady state at the time of the peak value is 310V, and during the fault of the output voltage is zero, the output voltage at the early stage of the fault recovery has certain land, restore the steady output voltage value after 0.45s. Figure (b) represents the input is the change of ac busbar voltage and current, voltage of the input in failure time and recovery time are small fluctuations, at 0.108s moment dip voltage is 305 v, has no effect on normal operation of power system, the change of the input current and output current are the same, all recovery steady-state waveform after 0.45s.

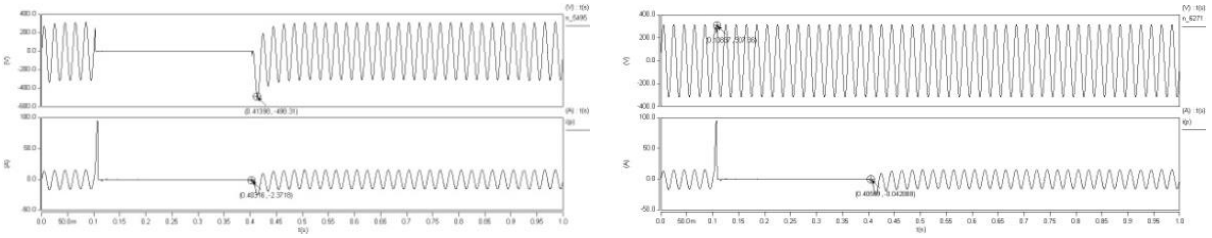

(a) output fault recovery diagram *(b) input fault recovery diagram*

Figure 10: Waveform diagram of LCSRSCB during the fault recovery phase

Through waveform figure can be found that blocking circuit in the input and output load end of the power grid and blocking circuit inside, can quickly cut off the fault current, and can in recovery after 5 ms back to steady state at the time of the waveform. The structure can quickly restore the stable operation of the system.

4.2. Experimental verification

An experimental platform using TI28335 as the core microcontroller was built. The experimental platform consists of main circuit, control circuit and drive circuit. Specific parameters are as follows: AC input for mains AC 220 V, the input inductance is 1 mH, the output resistance of 20 Ω, LC combination of inductance for 10mH, capacitance is 1000 uF.

The experimental results are shown in the figure. Figure 11 shows the output current and voltage experimental waveform. Failure in 50 ms, output voltage instantaneous zero, fault recovery in 350 ms, output voltage after failover occurred within 15 ms falling backward, in 400 ms after the return to the steady state, the output current zero after failure, failure recovery time in reverse spike, may be associated with capacitance discharge in the actual operation. Figure 12 shows the input current and voltage experimental waveform.The input current is roughly the same as the output current. The input voltage waveform in fault occurs with the momentary impulse voltage, fall slightly, at a time of fault recovery to normal, no fluctuations during circuit fault, the experiment waveforms and simulation are basically identical.

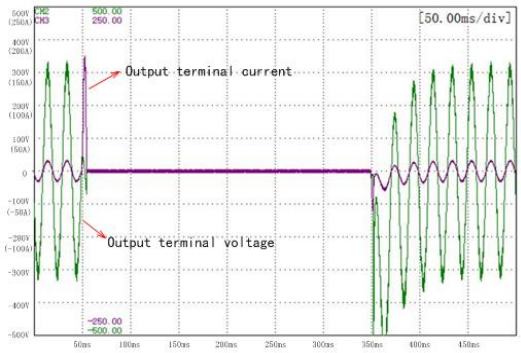

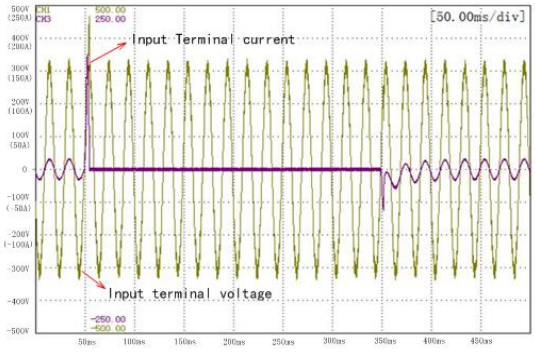

Figure 11: output terminal voltage and current waveform *Figure 12: input terminal voltage and current waveform*

The experimental results show that the fault response speed of the blocking circuit is fast, the fluctuation during the fault is small, the fault recovery speed is fast, and the fault can be attenuated to normal value within several cycles.

5. CONCLUSION

In this paper, a new LCSRSCB blocking strategy is introduced, and a simulation experiment is conducted on the circuit on this basis. Compared with the traditional blocking current limiter, it has the following characteristics:

(1) the circuit has a simple topology, and the main current passing capacity and reliability are strong based on thyristor and LC elements.

(2) differential protection is adopted as the basic protection strategy. With the solid-state current limiting circuit, the dynamic response speed is extremely fast.

(3) the method proposed in this paper can not only limit the short-circuit current, but also completely cut off the short-circuit current, which can be used as a circuit breaker.

6. REFERENCES

Qi Z, Zhou L, 2015. Summary of Microgrid Protection Research [J].*Power System Protection and Control*, 43(13): 147-154.

Gharehpetian GB, Radmanesh H, and Fathi SH, 2015. Novel High Performance DC Reactor Type Fault Current Limiter[J]. *Elect.Power Syst.Res*, vol.122,pp. 198–207.

Chen H, Lin J, Liu K, et al. 2010. Current Status of Application of Fault Current Limiter in Power System [J]. *Power System Protection and Control*,38 (7):147-151.

Li Z, 2015. Analysis of Current Research on Fault Current Limiter [J].*Electronic Test*,17 (051): 128-130.

Shuai Z, Tu C, Zou F, et al. 2015. Self Fault Diagnosis and Recovery of Multi Function Solid State Fault Current Limiter [J].*Power System Technology*, 39 (7): 1948-1955.

Huaxi Z, Pietro C, Rostan R, 2017. Fault Current Limiting Power Converters for Protection of DC Microgrids[C].//IEEE Conferences.

Hagh MT and MAbapour M, 2009. Nonsuperconducting Fault Current Limiter with Controlling the Magnitudes of Fault Currents[J].*IEEE Trans.Power Electron*., vol. 24, no. 3, pp. 613–619.

Chen J, Dong E, Zou J, 2000. Solid-State Fault Current Limiter (FCL) the Development and Application of [J]. *Relay*,28 (12): 35-37.

Fathi S H, Gharehpetian G B, Radmanesh H, et al, 2016. A Novel Solid-State Fault Current-Limiting Circuit Breaker for Medium-Voltage Network Applications[J].*IEEE Transactions on Power Delivery*. 31(1): 236-244.

Li L, 2016. Design of a New Solid State Fault Current Limiter for Direct Current Distribution Systems [J].*Power System and Clean Energy*, 32 (3): 87-91.

Li R, 2015. Study on Differential Protection Scheme for Active Distribution Network [J]. *Power System Protection and Control*, 43 (12): 104-109.

Wu H, Yuan L, Sun L, and Li X, 2015. Modeling of Current-Limiting Circuit Breakers for the Calculation of Short-Circuit Current[J].*IEEE Trans.Power Del*, vol. 30, no. 2, pp. 652–656.

231: A variable resistance variable capacitance simplified thermal model for pipe-encapsulated PCM

Tian YAN[1], Xinhua XU[1], Jiajia GAO[1], Tao XU[2], Ziye LING[3]

[1] *Huazhong University of Science & Technology, Wuhan, China, yantian@hust.edu.cn; bexhxu@mail.hust.edu.cn*
[2] *Guangzhou University, Guangzhou, China, affiliation address, 736848541@qq.com*
[3] *South China University of Technology, Guangzhou, China, zyling@scut.edu.cn*

In recent years, PCMs as the thermal energy storage media have been widely used in building envelope to improve the thermal and energy performance of buildings. Pipe-encapsulated PCM is a new type of thermal storage and insulation structure. It can be incorporated into walls, floors and ceilings simply without leakage of PCM. The recycle of PCM can be achieved by actively removing heat by the circulating fluid in the inner pipe. Numerical models are widely used for predicting the thermal characteristics of the pipe-encapsulated PCM accurately. However, all those models are computationally intensive and too complicated to be integrated with conventional building thermal and energy calculation package for simulation. Fast and feasible simplified model is essential for the simulation and application of pipe-encapsulated PCM. In this paper, a simplified thermal model composed of the PCM model and pipe model for the pipe-encapsulated PCM is developed. The PCM model is composed of four variable resistances and two variable capacitances (4R2C) and the parameters are identified using GA. An experimental setup is established, and the thermal characteristics of the pipe-encapsulated PCM with dynamic boundary condition are tested. The simplified model is validated by comparing the results of simulation and that of experiment. The mean error of internal surface temperature of PCM is 0.45℃, and the mean error of heat flow through the internal of surface inner pipe is 14.4%. It indicates that the simplified model has good accuracy for thermal performance prediction for practical applications of pipe-encapsulated PCM.

Keywords: Pipe-encapsulated PCM; Variable resistance variable capacitance PCM model; Thermal characteristics; Parameters identification; experimental validation

1. INTRODUCTION

With the rapid development of urbanization and modernization, building energy consumption is increasing day by day and the mismatch between energy supply and demand is also becoming more prominent. It is imperative to look for efficient and feasible energy-saving technologies for buildings. In recent years, thermal energy storage technology has been an efficient energy usage method to bridge the gap between energy supply and demand and increase the energy efficiency (Hamdan 1996 and Parameshwaran 2012). Phase change material(PCM) as a kind of latent heat storage media has been widely used in building envelope to improve the thermal and energy performances of buildings (Iten 2016 and Song 2018). It can be incorporated into walls, floors and ceilings in the form of microcapsules or plate and the thermal and energy performances are investigated by simulation and experiment (Delgado 2012, Kim 2017 and Kong 2017).

Pipe-encapsulated PCM is a new type of thermal storage and insulation structure, which can be easy to be incorporated into the walls of buildings. In the daytime of cooling season, the PCM encapsulated between the inner pipe and outer pipe can absorb the heat form the wall and stored that in the form of latent heat. At night, the heat of the PCM can be taken away by the working fluid in the inner pipe to realize the regeneration of the PCM. This structure can avoid leakage of the PCMs and the encapsulation process of the PCMs is also simple. It has a good application prospect in the field of building energy conservation.

Studies have been done to investigate the thermal characteristics of PCMs in buildings. Chen et al. (2008) developed non-linear numerical model for a PCM wallboard based on the effective heat capacity method. The parameters effects including the phase change temperature, specific heat and density on the thermal characteristics of the PCM were discussed. Kant, et al (2017) proposed a two-dimensional thermal model for PCM in building brick wall. The model was solved using finite element analysis method and showed good accuracy and effectiveness for predictions of thermal characteristic of PCM wall. The heat transfer characteristics of a kind of paraffin were simulated by Lamberg et al. (2004) using the effective enthalpy method and the effective heat capacity method respectively. And the feasibility of the two methods was further discussed by the experiment. Sun, et al (2016) presented a numerical mathematical model of PCM used in building envelopes based on the moving heat-source method. The model accurately predicted the position of the solid-liquid interface and the thermal performance of PCM board. The optimal melting temperatures of PCM board for different regions in China was discussed using the model. Although those numerical PCM model can predict the thermal characteristics of PCMs accurately, the computational efficiency is low, and it is too complicated to be integrated with conventional building thermal and energy calculation package for simulation. Fast and feasible simplified model is essential for the simulation and application of pipe-encapsulated PCM.

In this paper, the author developed a variable resistance variable capacitance simplified thermal model for pipe-encapsulated PCM. The parameters of PCM model are identified and the thermal characteristics including the temperature and heat flow are simulated. Further, an experiment experimental setup is established for the measurement of thermal characteristics of pipe-encapsulated PCM. The accuracy of simplified model is discussed by comparing the simulated results with experiment results.

2. DEVELOPMENT OF SIMPLIFIED MODEL

The structure of the pipe-encapsulated PCM is shown in Figure. 1*a*. It is composed of the PCM, working fluid, inner metallic pipe and outer metallic pipe. The PCM is encapsulated between the inner pipe and outer pipe to achieve the thermal storage. And the heat of PCM can be actively removed by the working fluid filled in the inner pipe. In the figure, σ_{in}, σ_{out} and σ_{pcm} *are* respectively the thickness of the inner pipe, outer pipe and PCM. d_{in} and d_{out} are respectively the internal diameters (m) of the inner pipe and outer pipe.

In order to predict the thermal characteristics of the pipe-encapsulated PCM quickly, a simplified thermal model composed of the pipe model and PCM model is developed and the assumptions of the simplified model are made as follows:

(i). The PCM is isotropic and uniform and its phase transition process occurs in the range of solidification temperature and melting temperature, [T_s,T_l].
(ii). The nodes with the same radius have the same temperature.
(iii). The specific heat and thermal conductivity of PCM is variable with the node temperature which determines its state.
(iv). The shapes and volume of PCM remain unchanged while phase changing and the influence of convection is ignorable.

Figure. 1b illustrates the elements the simplified thermal model of pipe-encapsulated PCM. Duo to the high heat conductivity coefficient and relatively small thickness of metallic pipes, it is feasible to simulate the thermal characteristics of inner pipe and outer pipe using the pipe model with two resistances and one capacitance (2R1C model). The RC parameters of pipe model are constant and the distribution of resistances for inner pipe model and

outer pipe model can be respectively determined as a half of the total resistances of inner pipe and outer pipe. For PCM, because of the latent heat of phase change, the heat mass is variable when the PCM is in various phases (solid or liquid). A variable resistance variable capacitance PCM model is developed to predicted the dynamic heat transfer characteristics. The PCM model is composed of two internal nodes (T_{p1}, T_{p2}) with four variable resistances (R_{p1}, R_{p2}, R_{p3} and R_{p4}) and two variable capacitances (C_{p1}, C_{p2}). Among this RC parameters, R_{p1}, R_{p2} and C_{p1} are variable with the temperature of node T_{p1}. R_{p3}, R_{p4} and C_{p2} are variable with the temperature of node T_{p2}. All the resistances and capacitances can be obtained by the thermophysical properties of PCM and its optimal distributions can be identified to best fit the thermal characteristic obtained by experiment, which are described in the session 3.

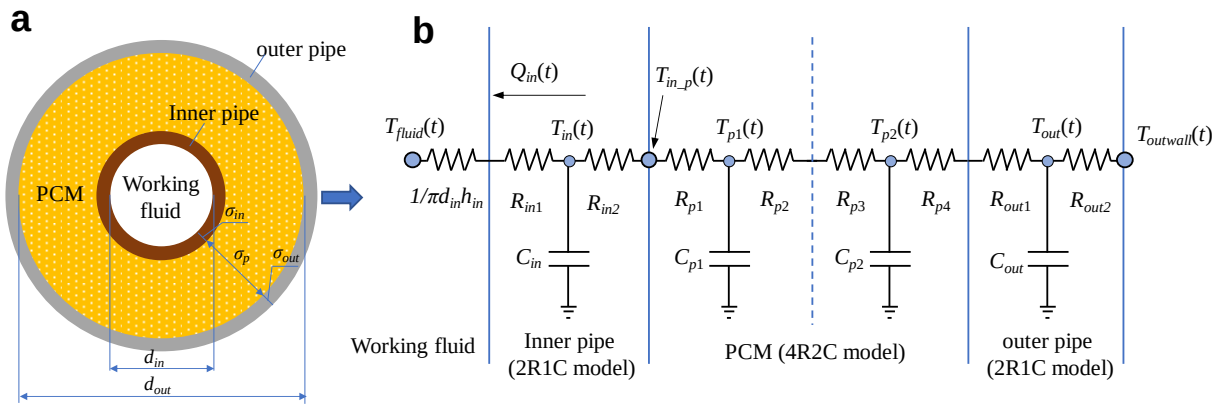

Figure 1: The structure (a) and simplified thermal model (b) of pipe-encapsulated PCM

According to the law of conservation of energy, the simplified thermal model can be expressed with the differential Equation 1 to Equation 4 as follows:

Equation 1:
$$C_{out}\frac{dT_{out}(t)}{dt}=\frac{T_{outwall}(t)-T_{out}(t)}{R_{out2}}-\frac{T_{out}(t)-T_{p2}(t)}{R_{p4}+R_{out1}}$$

Equation 2:
$$C_{p2}\frac{dT_{p2}(t)}{dt}=\frac{T_{out}(t)-T_{p2}(t)}{R_{p4}+R_{out1}}-\frac{T_{p2}(t)-T_{p1}(t)}{R_{p2}+R_{p3}}$$

Equation 3:
$$C_{p1}\frac{dT_{p1}(t)}{dt}=\frac{T_{p2}(t)-T_{p1}(t)}{R_{p2}+R_{p3}}-\frac{T_{p1}(t)-T_{in}(t)}{R_{in2}+R_{p1}}$$

Equation 4:
$$C_{in}\frac{dT_{in}(t)}{dt}=\frac{T_{p1}(t)-T_{in}(t)}{R_{in2}+R_{p1}}-\frac{T_{in}(t)-T_{fluid}(t)}{1/h_{in}\pi d_{in}+R_{in1}}$$

Where:

T= temperature (℃)

C_{out}= capacitances of outer pipe (J/m·℃)

C_{in}= capacitances of inner pipe (J/m·℃)

C_{p1}, $C_{p2=}$ capacitances of inner PCM (J/m·℃)

R_{out1}, R_{out2} = resistances of outer pipe (m·℃/W), which is a half of the total resistance of outer pipe

R_{in1}, R_{in2} = resistances of inner pipe (m·℃/W), which is a half of the total resistance of inner pipe

R_{p1}, R_{p2}, R_{p3}, $R_{p4=}$ resistances of inner PCM (m·℃/W)

h_{in} = convection coefficient (W/m^2·℃)

Further, the thermal characteristics of the pipe-encapsulated PCM can be expressed by the heat flow and the temperature of internal surface of PCM, which can be calculated by the Equation 5 and Equation 6 as follows:

Equation 5:
$$Q_{in}(t)=\frac{T_{in}(t)-T_{fluid}(t)}{1/h_{in}\pi d_{in}+R_{in1}}*l$$

Equation 6:
$$T_{in\_p}(t) = \frac{R_{in2}T_{p1}(t) + R_{p1}T_{in}(t)}{R_{in2} + R_{p1}}$$

Where:

Q_{in} = heat flow through the internal of surface inner pipe (W)

T_{in_p}= internal surface temperature of PCM (℃)

l = the length of pipe-encapsulated PCM (m)

3. PARAMETERS IDENTIFICATION

The parameters identification of simplified PCM model are actually to find out the optimal distributions of the variable resistances and variable capacitances among the nodes of the model. There are three independent parameters to be identified. And the other parameters of PCM model can be determined simply by these parameters.

GA (Genetic Algorithm) is an effective mathematical tool for the model parameters optimisation. It is feasible to identified the optimal parameters of 4R2C PCM model using GA based on the results of experiment. The parameter identification method is briefly described in Figure 2. Where β_1, β_2, β_3 are the distribution ratios of variable resistances (R_{p1}, R_{p2}, R_{p3}, R_{p4}) and variable capacitances (C_{p1}, C_{p2}). It is achieved by the GA-based estimator (optimisation objective J) which allow the temperature predicted by the simplified models to best fit the experimental results, as expressed by Equation 7. The reliable predictions of thermal characteristics can be provided by the simplified model with the variable resistances and variable capacitances determined by the optimal ratios.

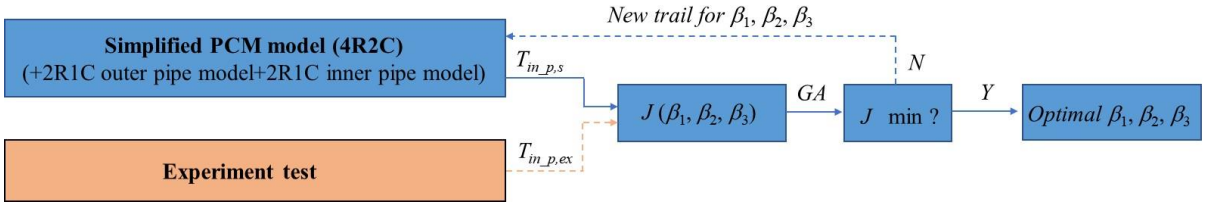

Figure 2: Parameters identification of simplified PCM model

Equation 7: Optimised objective function
$$J(\beta_1, \beta_2, \beta_3) = \sqrt{\frac{\sum_{k=1}^{n}(T_{in\_p,s} - T_{in\_p,ex})^2}{n-1}}$$

Where:

J = standard deviation of temperature (℃)

$T_{in\_p,s}$= internal surface temperature of PCM predicted by simplified model (℃)

$T_{in\_p,ex}$= internal surface temperature of PCM tested by experiment (℃)

n=the number of data points

The variable resistances (R_{p1}, R_{p2}, R_{p3}, R_{p4}) and variable capacitances (C_{p1}, C_{p2}) of 4R2C model can be determined by the independent parameters (β_1, β_2, β_3) and total resistance and capacitance of PCM, as expressed by Equation 8 to Equation 13 as follows:

Equation 8:
$$R_{p1} = \beta_1\beta_2 R_{tot\_p}(T_1)$$

Equation 9:
$$R_{p2} = \beta_1(1-\beta_2)R_{tot\_p}(T_1)$$

Equation 10:
$$C_{p1} = \beta_1 C_{tot\_p}(T_1)$$

Equation 11:
$$R_{p3} = (1-\beta_1)\ \beta_3 R_{tot\_p}(T_2)$$

Equation 12:
$$R_{p4} = (1-\beta_1)(1-\beta_3)R_{tot\_p}(T_2)$$

Equation 13:
$$C_{p2} = (1-\beta_1)C_{tot\_p}(T_2)$$

Where:

R_{tot_p}= total resistance of PCM (m·℃/W)

C_{tot_p} = total capacitance of PCM (J/m·℃)

To simplify the model, the total resistance and capacitance of PCM are variable with the temperature and can be determined simply by the Equation 14 to Equation 17 as follows:

Equation 14:
$$R_{tot\_p}(T) = \frac{1}{2\pi\lambda_p(T)} \ln \frac{d_2}{d_2 - 2\delta_p}$$

Equation 15:
$$\lambda_p(T) = \begin{cases} \lambda_s & T < T_s \\ (T - T_s)(\lambda_l - \lambda_s) / (T_l - T_s) & T_s \le T \le T_l \\ \lambda_l & T > T_l \end{cases}$$

Equation 16:
$$C_{tot\_p}(T) = \frac{1}{4}\pi(d_2^{\,2} - (d_2 - 2\delta_p)^2)\rho_p C_{p\_p}(T)$$

Equation 17:
$$C_{p\_p}(T) = \begin{cases} C_{ps} & T < T_s \\ \dfrac{C_{ps} + C_{pl}}{2} + \left(\dfrac{L}{T_l - T_s}\right) & T_s \le T \le T_l \\ C_{pl} & T > T_s \end{cases}$$

Where:

λ_p = equivalent thermal conductivity coefficient of PCM (W/m·℃)

λ_s, λ_l = thermal conductivity coefficient of PCM in solid phase and liquid phase (W/m·℃)

C_{p_p} = equivalent specific heat of PCM (J/kg·℃)

C_{ps}, C_{pl}= specific heat of PCM in solid phase and liquid phase(J/kg·℃)

L= latent heat of fusion (J/kg)

ρ_p= density of PCM (kg/m^3)

The parameters identification can be achieved by the GA driver in the optimisation tool of MATLAB. The internal surface temperature of PCM using to identify the independent parameters is tested by experiment, as described in section 4.

4. EXPERIMENT

In this section, a pipe-encapsulated PCM is prepared and an experiment facility is set up. The thermal characteristics including the surface temperature and heat flow of pipe-encapsulated PCM are tested to validate the simplified model.

4.1. Pipe-encapsulated PCM preparation

Paraffin is the common PCM with the higher latent heat and it is stable, nontoxic and low-cost. However, it will appear as liquid when temperature exceeds the melting temperature and exist the risk of leakage (Xia 2010). To perform good stability for PCM, expanded graphite (EG) is suitable supporting material for paraffin to avoid leakage because of its strong adsorption and unique network structure, and it can also improve the thermal conductivity of PCM (Zhang 2012).

In this experiment, the powdery composite PCMs containing 80wt% RT28 (a mixture paraffin) and 20wt% EG are prepared (Figure 3a). The circular PCM are easily prepared by dry pressing with the high packing density (750m^3/kg) and it can be encapsulated into the inner pipe (copper pipe) and outer pipe (steel pipe), as shown in Figure 3b and Figure 3c. The length of pipe-encapsulated PCM is 200 mm.

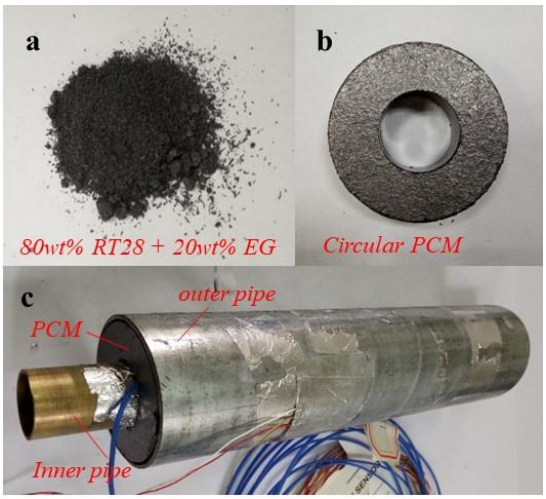

Figure 3: The powdery composite PCMs (a), circular plane (b) and pipe-encapsulated PCM

The properties and parameters of PCM, inner pipe and outer pipe are listed in Table 1. The total resistance and capacitance of inner pipe are respectively 1.54e-4 m·℃/W and 246.9 J/m·℃. And the total resistance and capacitance of outer pipe are respectively 2.06e-4 m·℃/W and 809.5 J/m·℃. The Parameters of PCM can be calculated easily by the Equation 8 to Equation 17 described in section 3.

Table 1: Properties and parameters of pipe-encapsulated PCM

Items	Phase change temperature (℃)	Latent heat of fusion (J/kg)	Density (kg/m^3)	Thermal conductivity (W/m·℃)	Specific heat (J/kg·℃)	internal / external diameter (mm)	Thickness (mm)
PCM	26.9~28.9	160 200	750	9.5	1 980	20/45	12.5
Inner pipe (copper)	-	-	8440	108.9	490	18/20	1.0
Outer pipe (steel)	-	-	7860	49.8	470	45/48	1.5

4.2. Experiment setup

The experiment setup is composed of the pipe-encapsulated PCM, Heating tap, water circulation system and data recorder, as presented in Figure 4. The electric heating tape is wound around the outer pipe surface and the PCM can be heated intermittently. The inner pipe is connected with the water circulation system which can provide the circulating water with relative low temperature (about 24℃) to cool the PCM. The outer pipe of pipe-encapsulated PCM is covered with the insulated cotton. The water circulation system is composed tank, pump, pipe system and flowmeter. In this experiment, the water pump runs with constant frequency. The water flow rate is constant and tested by the float flowmeter (±5% precision).

The temperature sensors testing surface temperature and water temperature are the T-type thermocouple with the 0.1℃ test-precision. There are four thermocouples attached on the surface of outer pipe and inner pipe, respectively. The temperature of outer surface is tested as the outer boundary condition. Two thermocouples are set in the inlet and outlet of inner pipe and the temperature of water in the inner pipe is the average value of inlet temperature and outlet temperature. The measuring points are presents in Figure 4. All data of temperature is recorded by the data recorder (Agilent Data logger 34972A) and the time step of data acquisition is 10 seconds.

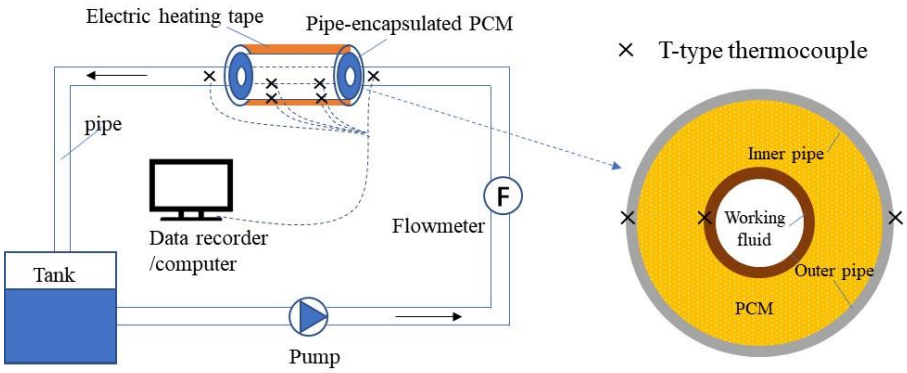

Figure 4: Experiment setup and measuring points

4.3. Experiment boundary conditions

The dynamic boundary conditions including the temperature of outer pipe surface and the average water temperature are presented in Figure 5. The temperature fluctuations of outer pipe surface are variable within the scope of 22℃ -45℃ and it is feasible to investigate the thermal characteristics of pipe-encapsulated PCM in the whole process of melting and solidification. The temperature of water in the inner pipe are near 24℃. In this study, the experiment test time is about 32000s (8.9 h). The temperature fluctuations of inner pipe are tested to identify the model parameters. And the accuracy of the simplified models can be discussed by comparing the simulated results and experiment results.

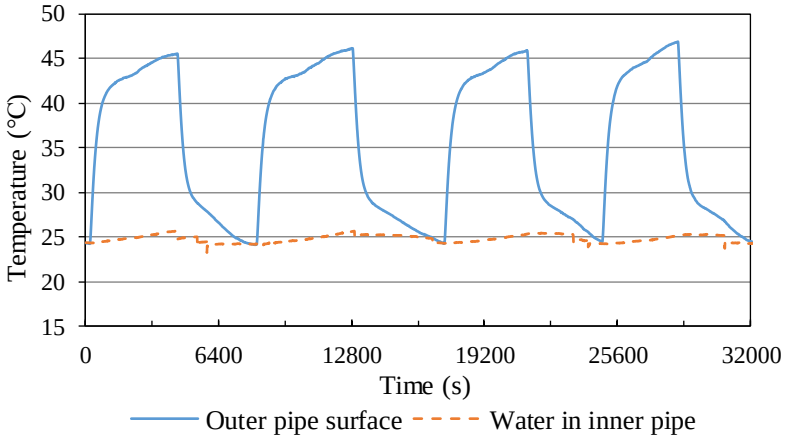

Figure 5: Experiment boundary conditions

The average flow velocity of water in the inner pipe is 0.68m/s (flow rate is 0.62 m^3/h). The Re number is about 11440 (More than 2300) which indicates that the water in the inner pipe is turbulent flow and the average convective heat transfer coefficient can be simply calculated by the Equation 18 according to the Ref. (Bergman 2011). In this experiment, the average convective heat transfer coefficient (h_{in}) is 2780 $W/m^2 \cdot ℃$.

Equation 18: Nusselt number

$$\mathrm{Nu} = hD/\lambda = 0.0265\,\mathrm{Re}^{4/5}\,\mathrm{Pr}^{0.3}$$

Where:

Nu = Nusselt number of internal turbulent flow

h= average convective heat transfer coefficient ($W/m^2 \cdot ℃$)

λ= thermal conductivity coefficient of water (0.6 $W/m \cdot ℃$)

D = internal diameter of inner pipe(m)

Pr= Prandtl number, 7.02 for 22℃ water

Re= Reynolds number

5. RESULTS

The parameters of simplified model are identified by the experiment results. The thermal characteristics of pipe-encapsulated PCM obtained by simulation and experiment are compared and the model accuracy is discussed.

5.1. Model parameters

According to the experiment results, the parameters of 4R2C simplified PCM model are identified by internal surface temperature of PCM tested by experiment with the dynamic boundary condition. The distributions of variable resistances and variable capacitances pf PCM are listed in Table 2. The RC parameters can be calculated by Equation 14 to Equation 17. And the thermal characteristics of pipe-encapsulated PCM can be quickly and efficiently predicted by the simplified model with those parameters.

Table 2: Variable resistances and Variable capacitances of simplified PCM model

Model	R_{p1}	R_{p2}	C_{p1}	R_{p3}	R_{p4}	C_{p2}
4R2C	0.098 $R_{tot\_p}(T_{p1})$	0.721 $R_{tot\_p}(T_{p1})$	0.819 $C_{tot\_p}(T_{p1})$	0.105 $R_{tot\_p}(T_{p2})$	0.076 $R_{tot\_p}(T_{p2})$	0.181 $C_{tot\_p}(T_{p2})$

5.2. Model validation

The thermal characteristics of pipe-encapsulated PCM with the dynamic boundary conditions are simulated by the simplified model. And the simplified model is validated by comparing the experiment results and simulated results. The mean error of temperature and heat flow for simplified model can be determined by Equation 19 and Equation 20 as follow:

Equation 19: Mean error of temperature

$$\Delta T_{in\_p} = \sum_{k=1}^{n} \left| T_{in\_p,s} - T_{in\_p,ex} \right| / n$$

Equation 20: Mean error of heat flow

$$\Delta Q_{in} = \sum_{k=1}^{n} \left| \frac{Q_{in,s} - Q_{in,ex}}{Q_{in.ex}} \right| / n \times 100\%$$

Where:

ΔT_{in_p}= mean error of internal surface temperature of PCM (℃)

ΔQ_{in} = mean error of heat flow through the internal of surface inner pipe (%)

$Q_{in,s=}$ heat flow predicted by simplified model(W)

$Q_{in,ex=}$ heat flow obtained by experiment(W)

The comparisons of internal surface temperature of PCM are presented in Figure 6. The internal surface temperature changes within the scope of 23.8℃ to 29.5℃ and the rate of change becomes slow when the PCM is in the phase change process. It can be observed that the temperature fluctuations predicted by simplified model match well with that tested by experiment. The mean error is 0.45℃ which indicates that the temperature predictions of simplified model with the identified parameters are accurate and acceptable.

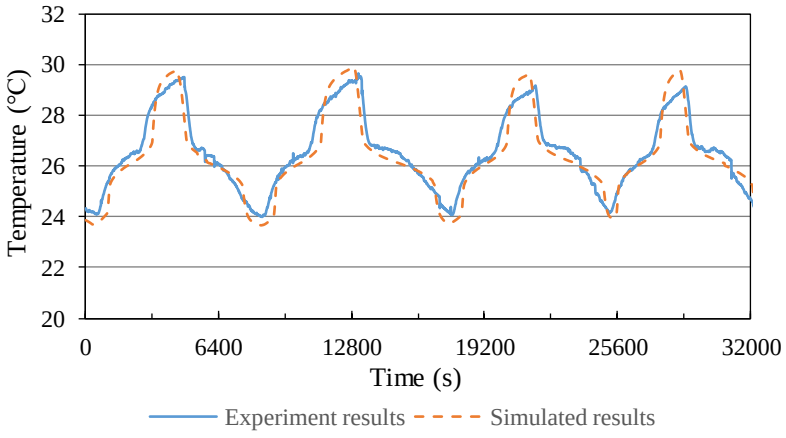

Figure 6: Internal surface temperature of PCM

The experiment results of heat flow ($Q_{in,ex}$) can be calculated by the temperature of water and inner pipe surface, as expressed by Equation 21.

Equation 21: Experiment results of heat flow

$$Q_{in,ex} = h_{in} A(T_{in,ex} - T_{water,ex})$$

Where:

A = surface area of inner pipe (m^2)

T_{in_ex}= surface temperature of inner pipe tested by experiment (℃)

T_{water_ex}= average value of inlet water temperature and outlet water temperature tested by experiment (℃)

Figure 7 shows the heat flow (Q_{in}) through the internal of surface inner pipe. The curves of heat flow predicted by simplified model nearly overlapped with the experimental results, and the mean error of heat flow is 14.4%. It indicates the simplified model has good model accuracy and it is feasible to produce the reasonable predictions of thermal characteristics of pipe-encapsulated PCM using the simplified model.

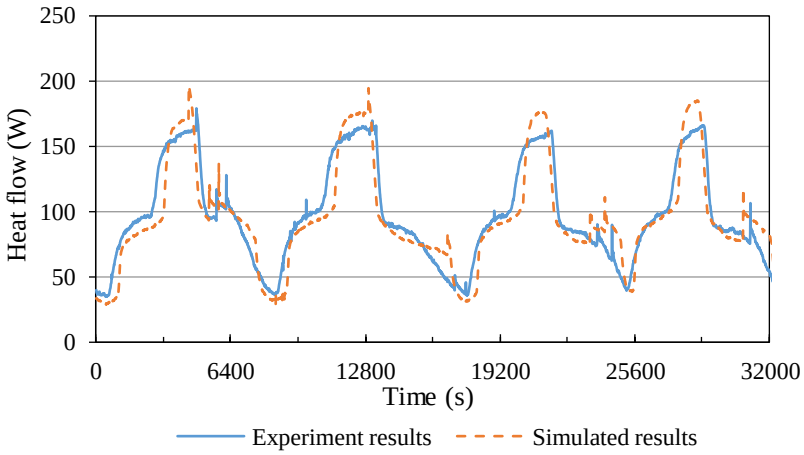

Figure 7: Heat flow (Qin) through the internal of surface inner pipe

There is a very small error between the experiment and simulation results. For model prediction, the surface temperature of outer pipe is assumed to be uniform (the mean value of four T-type thermocouple), but there is slight deviation in temperature at different surface locations of outer pipe during the experiment. In addition, the thermal conductivity coefficient and specific heat of PCM with phase change are simplified by Equation 15 and 17, which are little different from the actual parameters of prepared PCM. And there are also some measurement errors when collecting the temperature by the T-type thermocouple.

6. CONCLUSION

Pipe-encapsulated PCM is a new type of thermal storage and insulation structure. It can be incorporated into walls, floors and ceilings simply without leakage of PCM. This paper proposed a variable resistance variable capacitance simplified thermal model for pipe-encapsulated PCM. It is feasible to be integrated with conventional building thermal and energy calculation package for simulation. The PCM model is composed of four variable resistances and two variable capacitances (4R2C) and the model parameters are identified using GA. The optimal distributions of variable resistances and variable capacitances are presented and the reliable predictions of thermal characteristics of pipe-encapsulated PCM can be produced by the simplified model with those optimised parameters quickly.

The pipe-encapsulated PCM composed of the inner pipe, outer pipe and encapsulated PCM (contained 80wt% RT28 and 20wt% EG) are prepared. An experiment setup is established. The thermal characteristics of the pipe-encapsulated PCM with dynamic boundary condition are tested to validate the simplified model. The temperature and heat flow predicted by simplified model are compared with those obtained by experiment. The mean error of internal surface temperature of PCM is 0.45℃, and the mean error of heat flow through the internal of surface inner pipe is 14.4%. It indicates that the simplified model has good accuracy for thermal performance prediction for the applications of pipe-encapsulated PCM.

In this paper, the author mainly developed the proper simplified model to accurately predict the thermal characteristics of the pipe-encapsulated PCM. The energy-saving performance of the pipe-encapsulated PCM used

in the building envelope will be addressed in the further work. And the most effective usage of pipe-encapsulated PCM is also need to be studied in the future.

7. ACKNOWLEDGEMENT

This work presented in this paper is financially supported by a grant (No. 51678263) of National Science Foundation of China.

8. REFERENCES

Bergman T L., Lavine A S., Incropera F P., Dewitt D P., 2011. Fundamentals of Heat and Mass Transfer. Seventh edition. United States: John Wiley & Sons.

Chen C, Guo H, Liu Y, Yue H, Wang C, 2008. A new kind of phase change material (PCM) for energy-storing wallboard. *Energy and Buildings.*40(5), 882-890.

Delgado M, Lazaro A, Mazo J, Zalba B, 2012. Review on phase change material emulsions and microencapsulated phase change material slurries: Materials, heat transfer studies and applications. *Renewable and Sustainable Energy Reviews.* 16(1), 253-273

Hamdan.R, Elwerr.F, 1996. Thermal energy storage using a phase change material. *Solar energy*,56(2), 183-189.

Iten M, Liu S, Shukla A,2016. A review on the air-PCM-TES application for free cooling and heating in the buildings. *Renewable and Sustainable Energy Reviews.* 61,175–186.

Kant K, Shukla A, Sharma A, 2017. Heat transfer studies of building brick containing phase change materials, Solar Energy. 155, 1233-1242.

Kim H B, Mae M, Choi Y, Kiyota T, 2017.Experimental analysis of thermal performance in buildings with shape-stabilized phase change materials. *Energy and Buildings.*152, 524-533.

Kong X, Yao C, Jie P, Liu Y, QI Chengying, RONG Xian, 2017. Development and thermal performance of an expanded perlite-basedphase change material wallboard for passive cooling in building. *Energy and Buildings.*152, 547-557.

Lamberg P, Lehtiniemi R, Henell A-M. 2004. Numerical and experimental investigation of melting and freezing processes in phase change material storage. *International Journal of Thermal Sciences*. 43(3), 277-287.

Parameshwaran. R, Kalaiselvam. S, Harikrishnan.S, 2012. Sustainable thermal energy storage technologies for buildings: a review. *Renewable and Sustainable Energy Reviews.* 16(5), 2394–2433.

Song M, Niu F, Mao N, Hu Y, Deng S, 2018. Review on building energy performance improvement using phase change materials. *Energy and Buildings.*158(1),776-793.

Sun X, Zhang Q, Medina M A., Lee K O, Liao S. 2016. Parameter design for a phase change material board installed on the inner surface of building exterior envelopes for cooling in China. *Energy Conversion and Management.* 120,100-108.

Xia L., Zhang P., Wang R.Z., 2010. Preparation and thermal characterization of expanded graphite/paraffin composite phase change material, *CARBON* 48(9) 2538-2548

Zhang Z, Zhang N, Peng J, Fang X, Gao X, Fang Y. 2012. Preparation and thermal energy storage properties of paraffin/expanded graphite composite phase change material, *Applied Energy* 91(1) 426-431

232: Investigation on thermal performance of primary school dormitories mainly used at night in severe cold plateau

Fei XIONG[1], Xiaoyu SUN[1], Pengfei SI[1], Xin WANG[1], Yinping ZHANG[1]*, Xiangyang RONG[2]

1, Department of Building Science, Tsinghua University, Beijing 100084, China
2, China Southwest Architectural Design and Research Institute Co., Ltd., Chengdu 610042, China
Corresponding author. Tel.: +86-10-62772518; fax: +86-10-62773461E-mail address: zhangyp@tsinghua.edu.cn

Passive solar school dormitory is a suitable solar energy utilization mode in plateau because of maintenance-free, easy to operate, economical and energy-saving. For such buildings, the indoor thermal comfort range or rather acceptable temperature range is different from that in plain areas. Few studies on the thermal performance of such buildings have been found in the literature. For primary school dormitories, the indoor temperature during night contributes most for thermal comfort of the pupils living in them. Their ages are between 7 to 12 years old. This study was conducted in four primary schools in the Western Sichuan Plateau in China. The building basic information was collected. The indoor and outdoor meteorological parameters were measured. The pupils' thermal sensation was investigated by questionnaires. It's found that: (1) The wall of the Western Sichuan Plateau are mainly made of 200-370mm concrete blocks with an overall heat transfer coefficient of 2.5 to 3.4 W/m^{2}K, and the overall heat transfer coefficient of single glass window is 5.5 W/m^{2}K; (2) The thermal insulation performance of the building envelope is extremely poor; (3)During the test, the indoor air temperature during night varied from 1.1 to 7.6℃ while the outdoor air temperature varied from -7.4 to 4.8℃. In the coldest period of the winter, about two-thirds of the rooms have experienced indoor freezing, and about half of the students have experienced frostbite in winter. The relationship between thermal sensation and indoor air temperature was found and the thermal expected temperature was estimated to be 12°C. Pupils are accustomed to wearing thick clothes whose average thermal resistance is about 1.58 clo. The research results are helpful for the design of passive school dormitories in severe cold plateau.

Keywords: Passive house; Thermal performance; School dormitories; Severe cold plateau

1. INTRODUCTION

China's plateau region is rich in solar energy resource and has the potential for large-scale development and utilization of solar energy resource (Yi, 2013; Weidong, 2005). Passive solar energy utilization technology is considered to be the most suitable solar energy utilization mode for buildings in the severe cold plateau because of maintenance-free, convenient operation, economical and energy-saving (Ralegaonkar, 2010; Schnieders, 2015).

Indoor thermal environment can significantly influence human health and comfort. Li et al. took the indoor design temperature of the solar house in winter to 12 or 14°C (Yuanzhe, 1993). Zhang suggested that the minimal indoor air temperature in the passive solar room should not be lower than 8°C, and the daily average temperature should not be lower than 11°C (Yang, 1999). Xiao suggested that for remote Tibetan dwellings, the indoor design temperature was 10.0°C and the minimum temperature of the whole day was not less than 6.0°C (Wei, 2010). There are some studies on the thermal environment of school buildings in the plains (Bin, 2017; Kwok, 2003; Xia, 2003). However, for passive solar school dormitories in severe cold plateau，the indoor thermal comfort range or rather acceptable temperature range is different from that in plain areas. Few studies have been found in the literature. The indoor temperature during night contributes most for thermal comfort of the pupils living in them. In order to understand more about the thermal environment of the primary school dormitories in the cold plateau area, we conducted field tests and questionnaire surveys in 4 primary schools in the Western Sichuan Plateau in China. At the same time we calculated the envelope insulation after consulting the relevant staff.

2. RESEARCH METHODS

2.1. Time and location

The period of the study was 24–30, March 2018 (the range of the daily average outdoor air temperature was -0.1℃–4.1℃). The studies were conducted in 4 primary school dormitories (Figure 1) in Aba County, Aba Tibetan and Qiang Autonomous Prefecture, Sichuan Province, a severe cold area in the climate division. An Qiang Central Primary School dormitory was an old building in a remote area with poor construction level. Qiu Ji Ma Central Primary School dormitory was newly built in a remote area and the construction level had been certainly improved. No. 3 Primary School in Aba County dormitory was an old building in the county seat which represented a high level of primary school dormitories more than ten years ago. Xia Re Er primary school dormitory represented the highest level of current local primary school dormitories. During the field study, the indoor temperature changed without any space heating facilities. The pupils lived in dormitories from 8:00pm to 6:30am. Questionnaire survey was conducted before bedtime and after getting up in dormitories.

Figure 1A: An Qiang Central Primary School

Figure 1B: Qiu Ji Ma Central Primary School

Figure 1C: No. 3 Primary School in Aba County

Figure 1D: Xia Re Er primary school

2.2. Respondents

The total number of respondents was 211 (with 113 boys and 98 girls). All respondents were primary students, and most of them were 10-12 years old (Table 1). All respondents were Tibetan children who had lived on the cold plateau for generations to come. They went home once every two weeks.

Table 1: Respondents' sex and age distribution

Sex	Age	Amount
Male	≤10	8
Female	≤10	5
Male	10-11	43
Female	10-11	36
Male	≥12	62
Female	≥12	57

2.3. Equipment and questionnaire

This study was comprised of measurements of indoor environmental parameters and investigations of respondents' subjective sensations. These two parts were carried out simultaneously. Indoor environmental parameters including air temperature (Ta), and solar radiation intensity (I), carbon dioxide concentration. The accuracy of the equipment was shown in Table 2. For the measurements, the sensors were placed beside the respondent, 1.0 m above the floor. Questionnaire includes the objective indoor thermal environment (frozen, frostbite), respondents' information (sex, age), life habits (activities, clothing), subjective assessments of the environment (thermal sensation, thermal expectations, satisfaction level). The most important question was in regards to their thermal sensation vote. Based on the ASHRAE index (2004), the evaluation had 7 levels, from -3 to +3 (Table 3)

Table 2: The accuracy of the equipment

Test parameters	Equipment	Accuracy	Sampling frequency
Air temperature	Tianjian Huayi automatic recording thermometer WZY-1	±0.4℃	Every 5 minutes
Solar radiation intensity	Automatic recording solar energy meter TES-132	±10W/m^2	Every 5 minutes
Carbon dioxide concentration	Qing Da Jian Huan CO2 Automatic recorder	±75ppm	Every 1 minute

Table 3: TSV index

Level	Thermal sensation	Level	Thermal sensation
-3	Cold	-2	Cool
-1	Slightly cool	0	Neutral
+1	Slightly warm	+2	Warm
+3	Hot		

3. RESULTS AND DISCUSSION

3.1. Building envelope

There were both existing buildings and new buildings in the researched dormitories. They were somewhat unreasonable in the design and construction process. For example, An Qiang Central Primary School dormitory was an old dormitory with a single-layered glass window on the south side. It could make the sun shine in during the daytime. But it had wooden doors with big seams. Qiu Ji Ma Central Primary School dormitory was newly built in 2015 with a construction cost of 3,000 yuan per square meter. It had thick metal doors and double-layered glass windows with good air tightness. But there was a 1.5-meter-wide corridor on the south side, and the sun could not shine into the room. The third elementary school dormitory had rooms on both sides of the north and south, with a 1.5m wide corridor in the middle. The sun could shine into the south room but not into the north room which made the indoor thermal environment in the north side rooms much worse than that in the south side rooms.

In general, among the primary school dormitories, building orientation design was partly irrational which made insufficient heat gain. The wall of the Western Sichuan Plateau was mainly made of 200-370mm concrete blocks with an overall heat transfer coefficient of 2.5 to 3.4 W/m^{2}K, and the overall heat transfer coefficient of single glass window was 5.5 W/m^{2}K. It was seen that the thermal insulation performance of the building envelope was extremely poor. Poor construction levels and severe infiltration had further deteriorated the indoor thermal environment.

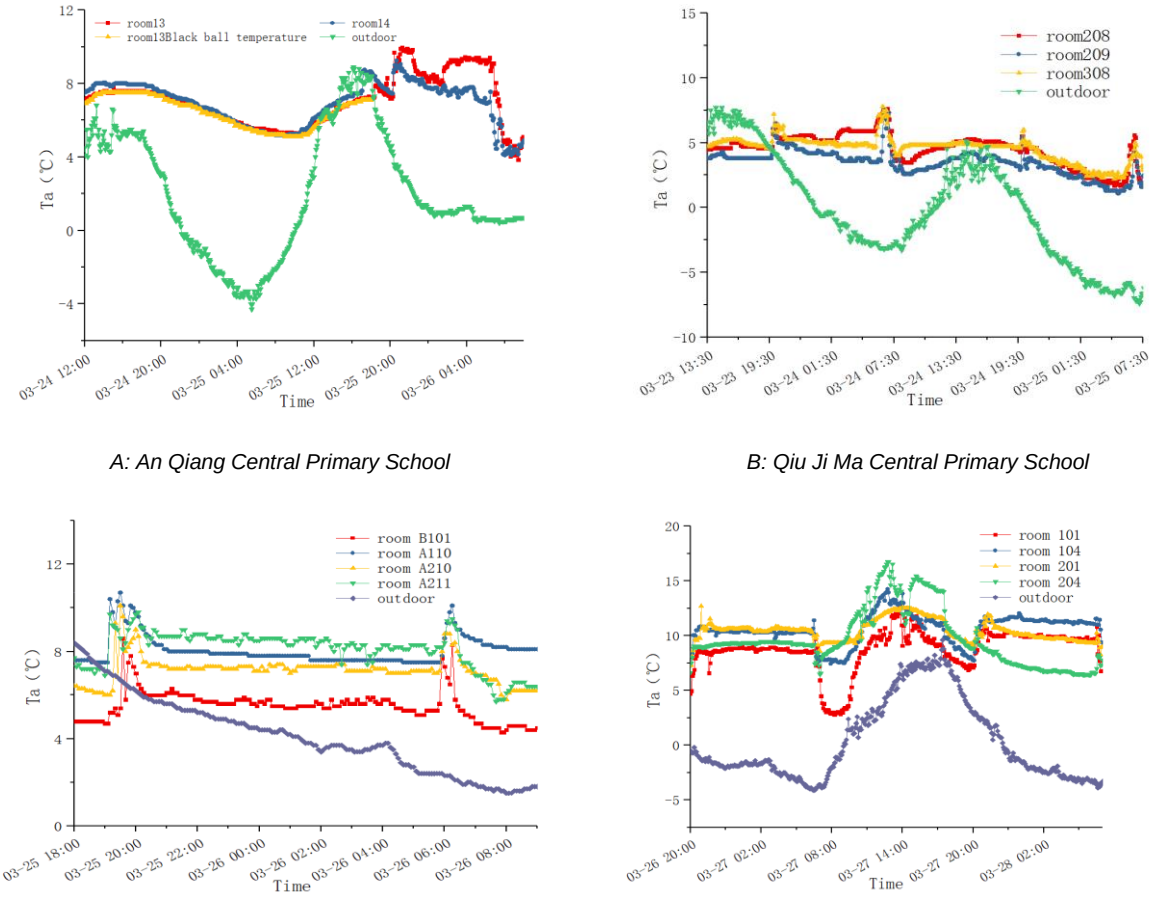

A: An Qiang Central Primary School

B: Qiu Ji Ma Central Primary School

C: No. 3 Primary School in Aba County

D: Xia Re Er Primary School

Figure 2: Indoor air temperature of different rooms

The indoor air temperature changed without any space heating facilities. During the field study, the pupils lived in dormitory from 8:00pm to 6:30am. Indoor air temperature of different rooms in 4 school dormitories was shown in Figure 2. For An Qiang Central Primary School dormitory, it had poor air tightness and sufficient heat gain. The indoor air temperature during night varied from 3.1 to 10.0℃ while the outdoor air temperature varied from -4.3 to 8.9℃. For Qiu Ji Ma Central Primary School dormitory, it had good air tightness and insufficient heat gain. The indoor air temperature during night varied from 1.1 to 7.6℃ while the outdoor air temperature varied from -7.4 to 7.7℃. For No. 3 Primary School in Aba County dormitory, the indoor air temperature of the north room (B101, A210) was lower than that of the south room (A110, A211). For Xia Re Er Primary School dormitory, the indoor average air temperature was about 10℃, slightly higher than the other three. At the coldest time of the year, the indoor thermal environment would be even worse.

Due to conditions, we did not test the indoor air temperature during the coldest time of the year. We got the general situation through questionnaires. 46.92% of the students had suffered frostbite (Figure 3), hand frostbite seriously affected their lives and learning. 64.93% of the dormitories had experienced frozen in the room (Figure 4). When the dormitories became frozen, it also caused inconvenience for the students to clean the dormitories. This also made the dormitories' air quality unsatisfactory, which seriously affected the life and health of the students. It reflected the poor living conditions of the students.

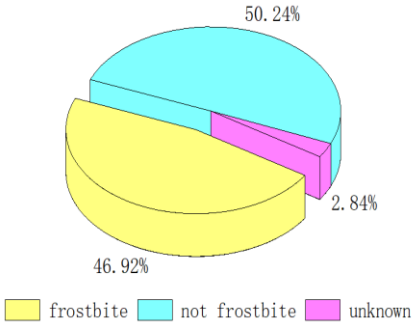

Figure 3: Respondents frostbite

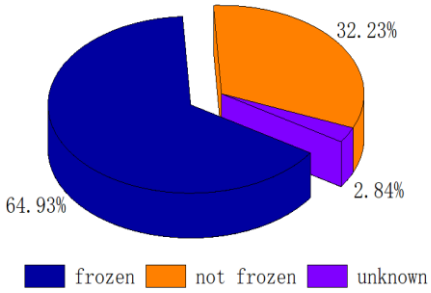

Figure 4: Whether frozen indoor

3.2. Thermal sensation

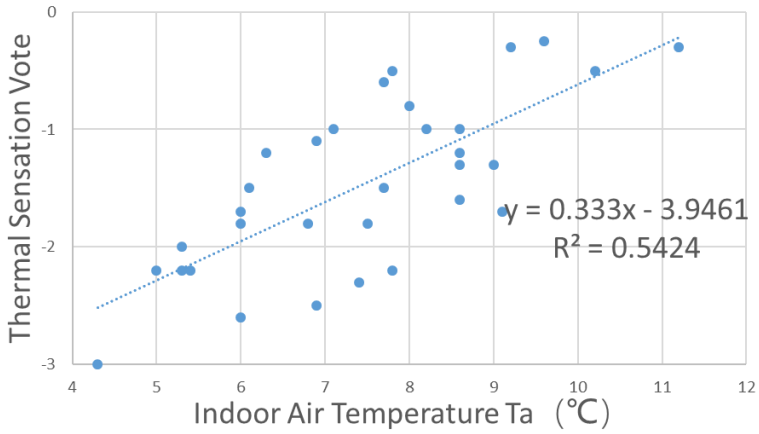

Figure 5: The relationship between indoor temperature and thermal sensation

During the field study, the indoor air temperature was continuous measured. The respondents' thermal sensation was determined by questionnaire. Each respondent filled out the questionnaire twice (before bedtime and after getting up in the dormitory)

A relationship between indoor temperature and thermal sensation was found. The thermal sensation vote value corresponding to each point on this chart was the average value of the thermal sensation of several people in the same room.

Equation 1: The relationship between indoor temperature and thermal sensation

$$TSV = 0.333t_a - 3.946 \quad (1)$$

where, TSV - thermal sensation vote, t_a – indoor air temperature, ℃.

According to formula (1), when TSV is equal to 0, T_a is 11.9℃ .According to the results of this study, the thermal expected temperature in the winter is 11.9 ◦C.

3.3. Thermal expectations and satisfaction

From the results of the previous section, the thermal expected temperature for these children in the winter is 11.9◦C. It is lower than the results of many related studies. In order to analyze the reasons, we also investigated the satisfaction and heat expectations of the respondents.

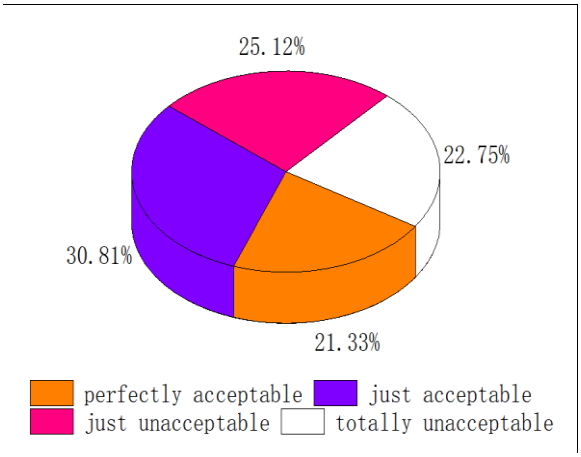

Figure 6: Respondents' acceptance level

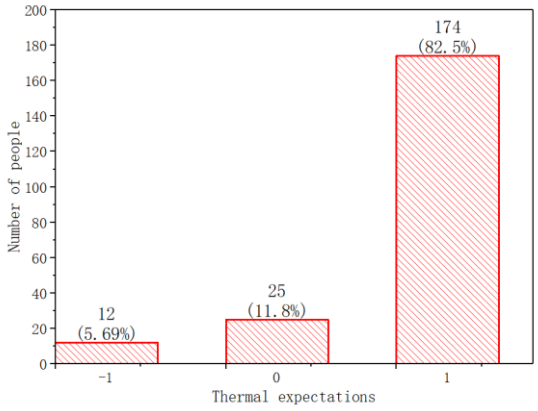

Figure 7: Respondents' thermal expectation

Figure 6 showed the respondents' acceptance level to the indoor environment during the survey. From Figure 6, more than 50% of the respondents felt acceptable for the existing thermal environment. Less than a quarter of them felt totally unacceptable. But if conditions permit, more than 80% of the respondents expected the indoor environment to be warmer, which was shown in Figure 7 (-1: to be cooler, 0: maintain, +1: to be warmer). In the environment that deviates from thermo-neutrality (or non-heated environment), people will show stronger adaptability to the environment. Influenced by natural selection, the Tibetan people can already adapt to the severe cold environment they live in.

3.4. Clothes thermal resistance

In the questionnaire, a variety of options were provided for the type of clothing, and respondents selected the options that suit their actual wearing. The clothing classification and value of clothing thermal resistance was mainly based on the relevant provisions in the ASHRAE Handbook (2001). The clothing classification methods used in this study and the clothing thermal resistance values were shown in Table 4.

Table 4: Clothing classification and thermal resistance value of single garment thermal resistance

	classification	thermal resistance	classification	thermal resistance	classification	thermal resistance
coat	Down jacket /Cotton clothing	0.55	Windbreaker	0.4	Casual sports jacket	0.3
tops	Suit tops /jacket	0.25	Sweater	0.25	Wool vest	0.15
	Pajamas	0.2	Long-sleeved shirt	0.2	Short-sleeved shirt	0.15
bottoms	Suit pants/jeans	0.2	Cotton trousers	0.3	Wool pants/trousers	0.25
	pyjama trousers	0.2	shorts	0.1		
Shoes and socks	sock	0.02	stocking	0.05	leather shoes/sports shoes	0.1
	Cotton slippers	0.05	sandals	0.02		

Equation 2: The thermal resistance of a set of garments can be obtained through the thermal resistance of a single garment (Zhu, 2010)

$$I_{cl} = 0.835\sum_{i} I_{clu,i} + 0.161 \quad (2)$$

where: I_{cl} - thermal resistance value of a set of garments, clo (1clo = 0.155m^2 · K/W); $I_{clu,i}$ - the thermal resistance of the individual piece of the i-th garment, clo.

According to calculations, children's clothes thermal resistance was 1.58clo. They wore thick clothes indoors or outdoors which helped them resist the cold. In addition, they also increased the amount of activity to generate heat. In short, they were already accustomed to taking various measures to withstand the cold.

4. CONCLUSIONS

We conducted field test and questionnaire survey in 4 primary schools in the Western Sichuan Plateau in China. In terms of objective factors, building envelope heat transfer coefficient and respondents' clothes thermal resistance were calculated. The indoor air temperature in different rooms was tested. In terms of subjective factors, respondents' thermal sensation, acceptance level, and thermal expectation were investigated and analyzed. According to the results of this study, we can conclude that:

1) The existing school buildings in severe cold plateau have poor insulation properties. There are no insulation materials in the external walls and most of them are 200-370mm concrete blocks with an overall heat transfer coefficient of 2.5 to 3.4 W/m^2K. The overall heat transfer coefficient of single glass window is 5.5 W/m^2K. It is seen that the thermal insulation performance of the building envelope is extremely poor. There is no active heating measures.

2) In the coldest period of the winter, the indoor air temperature is below zero and the indoor environment is harsh. 46.92% of the students have suffered frostbite. It seriously affects the life and health of the students.

3) In the environment that deviates from thermo-neutral (or no heating), pupils wear thick clothes and have a large amount of activity. They are more capable of adapting to severe cold conditions. The thermal expected temperature is about 12°C, and it verifies the value of relevant literature to some extent.

5. ACKNOWLEDGEMENTS

This study is supported by National Key Research and Development Program of China (2017YFC0702600) and the National Natural Science Foundation of China (51708532).

6. REFERENCES

Yi J, Ya F, Xiangyang R, Yungang P, Xiangzhao F, 2013. Discussion on urban heating mode for Lhasa [J]. HV&AC, 436):1-7, in Chinese.

Weidong G, 2005. Tibet Development Forum.

Ralegaonkar R V, Gupta R, 2010. Application of passive solar architecture for intelligent building construction: A review [J]. Energy Education Science and Technology Part A-Energy Science and Research. 26(1):75-85

Schnieders J, Feist W, Rongen L, 2015. Passive Houses for different climate zones [J]. Energy and Buildings.105:71-87

Yuanzhe L, Hongfa D, Xiande F, 1993. Passive solar house design manual [M]. Energy Press.

Yang Z, 1999 .Analysis and suggest of thermal environment in the passive solar house [J]. J. Xi'an Inst. of Metall. & Cons. Eng. In Chinese

Wei X, 2010. Study of the Direct-gain Solar Heating in Remote Southwest Tibet [D]. Tsinghua University.

Bin S, 2017. Field study to compare and evaluate winter indoor thermal and health conditions of school buildings with different envelopes [J]. Architectural Science Review, 60(1):40-48

Kwok AG, Chun C, 2003. Thermal comfort in Japanese schools [J]. Solar Energy, 74(3):245-252.

Xia B, 2003. Research on the Indoor Thermal Environment of Student Dormitory in Universities [D], Xi'an University of Architecture & Technology, 2003. In Chinese.

ASHRAE, ANSI/ASHRAE Standard 55-04, 2004. Thermal Environmental Conditions for Human Occupancy, American Society of Heating, Refrigerating and Air-Conditioning Engineers, Inc., Atlanta.

ASHRAE, 2001.The American Society of Heating, Refrigerating and Air-conditioning Engineers. 2001 ASHRAE Handbook, Fundamentals (SI). Atlanta.

Zhu Y, Zhang Y, Li X, Qin Y, Zhan Q, 2010. Built Environment [M]. Beijing: China Architecture & Building Press.

233: A model-based control strategy for space humidity of an independent dehumidification system

Jiajia GAO[1], Yuan ZHANG[2], Xinhua XU[3], Tian YAN[4], Hang WAN[5]

[1]Huazhong University of Science & Technology, Wuhan, China, jiajiagao@hust.edu.cn;
[2]Huazhong University of Science & Technology, Wuhan, China, xiamu@hust.edu.cn;
[3]Huazhong University of Science & Technology, Wuhan, China, bexhxu@mail.hust.edu.cn;
[4]Huazhong University of Science & Technology, Wuhan, China, yantian@hust.edu.cn;
[5]Huazhong University of Science & Technology, Wuhan, China, wanhang111@hotmail

Air-conditioning system is widely used for cooling/heating buildings to provide a comfortable thermal and humid environment. It is well known that both thermal process and humid process are uncertain, nonlinear and dynamic. In many systems, the temperature and humidity are controlled independently. It is more difficult to achieve a robust and accurate humidity control than the temperature control in real systems. This paper proposes a model-based control strategy for space humidity of an independent dehumidification system, which works by regulating water flow rate of cooling coil. The aim is to improve the robustness and accuracy of the space humidity control. In this control strategy, a supply air moisture content prediction model is developed to predict the system demand supply air moisture content based on the real-time humidity load and the space moisture content. The predictive value is used as the set-point and controlled by adjusting the cold water valve opening. It can guarantee that the dehumidification capacity of the dehumidification system is always satisfied the humidity load demand. Then the robust control of the space humidity is realized. Further, TRNSYS software was used to build a simulation platform of the independent dehumidification system to test the control performance of the proposed control strategy. The test results show that compared with the conventional method that tracks the space humidity by PI control algorithm directly, the proposed control strategy can improve the robustness and accuracy of the space air humidity control significantly.

Keywords: Dehumidification system, Model-based, Humidity control, Robust control

1. INTRODUCTION

According to statistics, people in modern society spend as much as 80% of their time in buildings (Charles J 1989). Therefore, indoor environment is very important for people's working and healthy. Humidity is a main indicator of the indoor comfort. It not only affects the comfort of the human body, but also results in many other serious consequences such as walls and furniture mildew and decay.

Air-conditioning system is widely used to provide a comfortable thermal and humid environment for buildings (Vakiloroaya 2014). However, the space thermal and humid environment is not really well controlled in many buildings especially the space humidity (Yan 2014), because both thermal process and humid process are uncertain, nonlinear and dynamic (Huang 2010). Usually, the space temperature and humidity are controlled by one air-conditioning system. The heat and moisture coupling method is generally adopted to produce low-temperature and dry supply air to remove residual heat and moisture synchronously. In this method, the heat and moisture ratio in the air-conditioning process can only be changed within a small range. However, the large heat and moisture ratio in many real buildings may be needed. It means sometimes the residual heat and moisture may not be removed at the same time. In this case, the common process mode is to satisfy the temperature control preferentially and sacrifice the humidity control.

A good method to avoid the above problem is to control the temperature and humidity by two independent air-conditioning systems (Zhang 2012). The space temperature is regulated by one air-conditioning system, and the space humidity is controlled by an independent dehumidification system. The commonly used independent dehumidification methods includes solution dehumidification, rotary dehumidification and surface cooling dehumidification. In the independent surface cooling dehumidification system, the space humidity is usually controlled by using conventional proportional-integral (PI) control algorithm, which tracks the space humidity by regulating the opening of cold water valve directly. As we know, the hysteresis is significant in the whole control process since the humid inertia of the space air is large. The control performance of the PI control may vary significantly with the operating conditions because of the lack of appropriate tuning and the control process may become sluggish or oscillatory at certain times (Salsbury 2005 and Huang 2010). In the real systems, the control performance of the space humidity is always unsatisfactory. Therefore, it is necessary to develop an advance control strategy for the independent surface cooling dehumidification system to improve the control performance of space humid environment. However, very few published research works have addressed the control methods to improve the robustness and accuracy of the space humidity control for the independent dehumidification system.

This paper proposes a model-based control method for the space humidity control of an independent surface cooling dehumidification system to improve its robustness and accuracy. It is well known the response of the supply air humidity is quick to the water flow rate change inside the cooling coil. In this proposed control method, a supply air moisture content prediction model is developed and used to predict the system demand supply air moisture content according to the real-time humidity load condition and space humidity. The aim is to transfer the variation of the space humidity and the humidity load to the supply air moisture content. The cooling water flow rate just needs to be regulated to track the predicted supply air moisture content. By this control method, the response of the control process is more timely, which may achieve a more robust and accurate space humidity control.

2. DESCRIPTION OF THE INDEPENDENT DEHUMIDIFICATION SYSTEM AND THE CONTROL METHOD

A typical independent dehumidification system is illustrated in Figure 1, where the supply air flow rate is constant. The supply air consists of the fresh air from outdoor and the returned air from the conditioned space. It is dehumidified by the coil, and then delivered to the air-conditioning area to regulate the space humid environment. The space air humidity can be controlled by a water valve according to the space humidity measurement and its set-point.

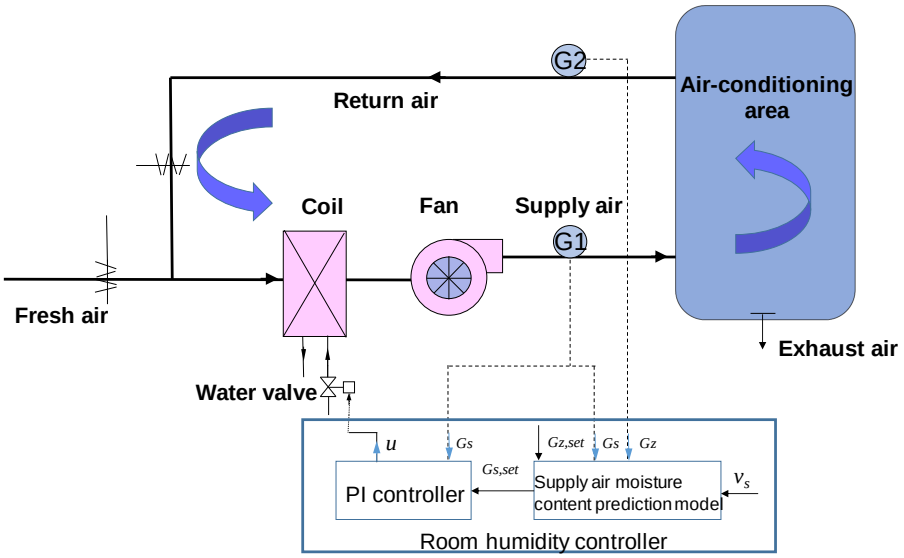

Figure 1: Schematic diagram of a typical independent dehumidification system and its control

Normally, the PI controller is used to track the space humidity directly by regulating the opening of the water valve. It is well known that the air-conditioning includes two important processes. One is the air-handling process in the air handling unit when the air passes through the cooling coil, the other is the air-conditioning process in the room when the supply air is delivered to the indoor space and mixed with the indoor air. It absorbs the heat and moisture of the indoor air, and finally is drawn back. The air-handling process in the air handling unit is a quick response process. However, the air-conditioning process in the room is a slow response process because of significant humid inertia of the building mass and the large volume of the indoor air. That means the conventional PI controller in this system regulates the water valve in the quick response air-handling process for controlling the space humidity in the slow response air-conditioning process of the indoor air. Therefore, the control performance of the space humidity in real systems by using the conventional PI control is usually not well.

As mentioned above, the air-handling process in the air handling unit is a quick response process. The supply air humidity responses to the change of the water flow rate quickly in the independent dehumidification system. That means the supply air humidity set-point can be quickly and reliably tracked by regulating the water flow rate. By considering the coupling of the quick response in the air-handling process and the slow response in the air-conditioning process of the indoor air, a model-based control method is proposed according to the dynamic characteristics of the space humidity change as shown in Figure 1. It aims to enhance the robustness and accuracy of the space humidity control of the independent dehumidification system. The proposed control method consists of a supply air moisture content prediction model and a PI controller. The basic idea of this control method is to transfer the variation of the space humidity and the humidity load to the supply air humidity, and then track the supply air humidity by using a PI controller.

The control loop of this control method is shown in Figure 2. The space humidity will change when the humidity load disturbance imposes on the air-conditioning space. The humidity sensors measure the real-time space moisture content G_z (usually measured in the return air duct) and supply air moisture content G_s simultaneously. The measurement is used as input for the supply air moisture content prediction model. This model may calculate the demand supply air moisture content at the next time step based on the space moisture content set-point $G_{z,set}$. This demand supply air moisture content is the input of the PI controller as a set-point $G_{s,set}$, then the water valve opening u can be calculated according to the feedback supply air moisture content G_s. This opening signal is used to regulate the water valve to change the water flow rate Mw. Then the demand supply air humidity is tracked, and the space humidity control is realized finally.

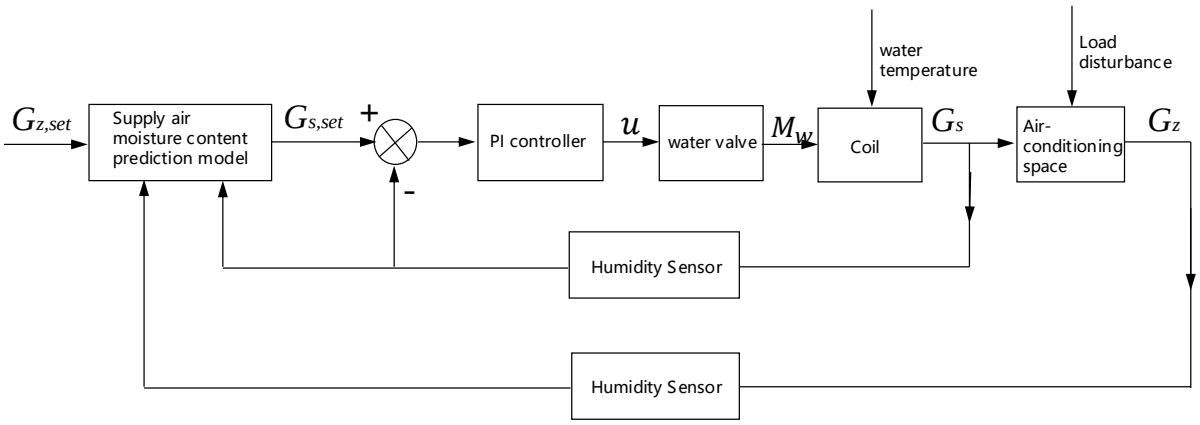

Figure 2: Cascade control loop of space humidity

3. CONTROL ALGORITHMS

3.1. Supply air moisture content prediction model

As mixing ventilation is used in the air-conditioning area, the supply air and the room air is assumed to be well mixed (Underwood 1999 and Yuan 2006). In this case, the dynamic process of the space moisture content change in the air-conditioning space can be described by Equation 1.

$$\text{Equation 1:} \qquad \rho_a V_z \frac{dG_z}{dt} = \rho_a v_s (G_s - G_z) + q_z$$

Where:

ρ_a = air density (g/m^3)

V_z = space volume (m^3)

v_s = supply air flow rate (m^3/s)

q_z = humidity load of the zone (g/s)

The supply air moisture content prediction model is developed based on the dynamic model of Equation 1. Firstly, Equation 1 is discretized with a sampling interval h as Equation 2 and α_1 and α_2 are given by Equation 3.

$$\text{Equation 2:} \qquad G_{z,k+1} = G_{z,k} + \alpha_1 v_{s,k} (G_{s,k} - G_{z,k}) + \alpha_2 q_{z,k}$$

$$\text{Equation 3:} \qquad \alpha_1 = h / V_z, \alpha_2 = h / \rho_a V_z$$

Where:

k = current time instant

α_1, α_2 = model parameters

In the independent dehumidification system, the supply air flow rate v_s is constant and then the system demand supply air moisture content $G_{r,k}$ can be calculated by Equation 4, which is inferred according to the references (Huang 2011 and Gao 2015), $e_{z,k}$ and γ are given by Equation 5 and Equation 6.

$$\text{Equation 4:} \qquad G_{r,k} = e_{z,k} + G_{z,set} - \frac{(1-\gamma) e_{z,k} + \alpha_2 \zeta_{z,k}}{v_{s,k} \alpha_1}$$

$$\text{Equation 5:} \qquad e_{z,k} = G_{z,k} - G_{z,set}$$

$$\text{Equation 6:} \qquad 0 < \gamma < 1$$

Where:

$\zeta_{z,k}$ = a parameter on the humidity load (g/s)

$e_{z,k}$ = supply air moisture content tracking error at time k(g/kg)

γ = user-defined parameter

Take $G_{r,k}$ as the supply air moisture content set-point $G_{s,set,k}$, then the water valve opening is adjusted by the PI controller to track this set-point based on the feedback real-time supply air moisture content $G_{s,k}$. With the prediction model of Equation 4, the closed-loop dynamic process of the space moisture content control will become Equation 7 when the PI controller tracks the supply air moisture content well, i.e., $G_{s,k} \approx G_{r,k}$. It can be seen that the tracking error $e_{z,k}$ will approach to zero at the steady state if the selection of γ satisfies Equation 6 and $\zeta_{z,k}$ is close to the actual humidity load $q_{z,k}$. Hence the space humidity control is achieved.

Equation 7: $$e_{z,k+1} = \gamma e_{z,k} + \alpha_2 (q_{z,k} - \zeta_{z,k})$$

In the prediction model of Equation 4, the calculation of the humidity load parameter $\zeta_{z,k}$ is a major task. Humidity load always changes with the outdoor weather condition as well as the indoor humidity load condition, such as the number of occupants. The humidity load is a time-dependent variable, and it is very difficult to predict the current humidity load $q_{z,k}$ accurately. One simple way to estimate the humidity load at steady state is based on the circulating air mass balance, as shown in Equation 8, which is derived from Equation 1 when dT/dt approaches to zero.

Equation 8: $$q_{z,k} = \rho_a v_{s,k} (G_{z,k} - G_{s,k})$$

Considering the dynamic process of the measuring devices, a forgetting factor λ is used to smooth the estimated humidity load by Equation 8 (Wang 2000), as shown in Equation 9. The range of λ is given by Equation 10. Based on the calculated real-time humidity load, the humidity load parameter $\zeta_{z,k}$ can be updated online, as is shown in Equation 11.

Equation 9: $$\hat{q}_{z,k} = \lambda \hat{q}_{z,k-1} + (1-\lambda) q_{z,k}$$

Equation 10: $$0 < \lambda < 1$$

Equation 11: $$\zeta_{z,k} = \hat{q}_{z,k}$$

3.2. PI control algorithm

The PI control is used to track the supply air moisture content set-point in the proposed control method. The control law is shown by Equation 12.

Equation 12: $$u_k = u_{k-1} + K_p (1 + \frac{h}{2T_i}) e_{z,k} + K_p (\frac{h}{2T_i} - 1) e_{z,k-1}$$

Where:

u_k = water valve opening

K_p = control gain

T_i = integral time (s)

When the PI controller is tuned, the controlled process is assumed to be modeled as a first-order and time-delay process (Seborg 1989 and Xu 2004), which can be given in the following form.

Equation 13: $$G(s) = \frac{K}{T_s + 1} e^{-\tau s}$$

Where:

K = steady-state gain

T = time constant

τ = pure delay time of the process response

A technique of graphical fitting of the first-order model using the step test is utilized to determine the unknown process parameters. Then, the PI control parameters K_p and T_i can be calculated based on the process parameters as follows (Seborg 1989).

Equation 14: $$K_p = \frac{0.9T}{K\tau}$$

Equation 15: $$T_i = 3\tau$$

It should be noted that the PI control will be also used as a comparison control to compare with the proposed control method.

3.3. Implementation process

The specific implementation process of the proposed control algorithm is summarized as below:

Initialization

(i). Determine the supply air flow rate v_s, which can be measured in the real system;
(ii). Define the room moisture content set-point $G_{z,set}$, specify the user-defined parameter γ inside the range specified by the Equation 6 and the forgetting factor λ inside the range specified by the Equation 10;
(iii). Initialized the humidify load $\hat{q}_{z,k-1}$;
(iv). Set the PI control parameters K_p and T_i by using the step test.

At each sampling time

(v). Calculate the humidity load parameter $\zeta_{z,k}$ by Equation 9;
(vi). Calculate the tracking error e_{zk} by $e_{z,k}=G_{z,k}-G_{z,set}$, and the required supply air moisture content $G_{r,k}$ by Equation 4;
(vii). Input $G_{r,k}$ to the PI controller as the supply air moisture content set-point $G_{z,set,k}$; and track this set-point by the PI controller according to the measured real-time supply air moisture content $G_{s,k}$;
(viii). Update $\hat{q}_{z,k-1}$ and wait for the next sampling time.

4. CONTROL PERFORMANCE TESTS

4.1. Boundary conditions

A platform for dynamically emulating the operation of an independent humidification system was developed to evaluate the control performance of the proposed model-based control method. This simulation platform was built by using a Transient Simulation Program TRNSYS (TRNSYS 2004). The components of concern are the building model, the cooling coil model, the fan model, the water valve model and the auxiliary models such as sensor and actuator models, etc. The building room is an open plan office, which has the area of 196 m^2 and the floor height of 3m. An independent dehumidification system serves this building room by maintaining the space relative humidity to a user-predefined set-point. This independent dehumidification system as shown in Figure 1. The design supply air flow rate is 7000 m^3/h. The design supply chilled water flow rate and temperature are 2.03kg/s and 7℃ respectively.

A summer day was taken as a typical case to evaluate the control performance of the proposed control method. The room temperature is constant at 25℃, which is controlled well by another independent air-conditioning system. The outside air flow rate was designed based on the occupancy and occupied area according to the standard (ASHRAE 2013). The designed outside air flow rate for each occupancy was 30m^3/h, and the occupancy number was 30. The profiles of the outdoor air temperature and relative humidity of the test day is illustrated in Figure 3. And Figure 4 illustrates the internal mass gain of the test day. Note that a significant variation occurs from 12:00 to 14:00 because most of the occupants go out for lunch during this interval. The independent dehumidification system works from 8:00 to 18:00, and the sampling interval of the proposed control algorithm is 15s.

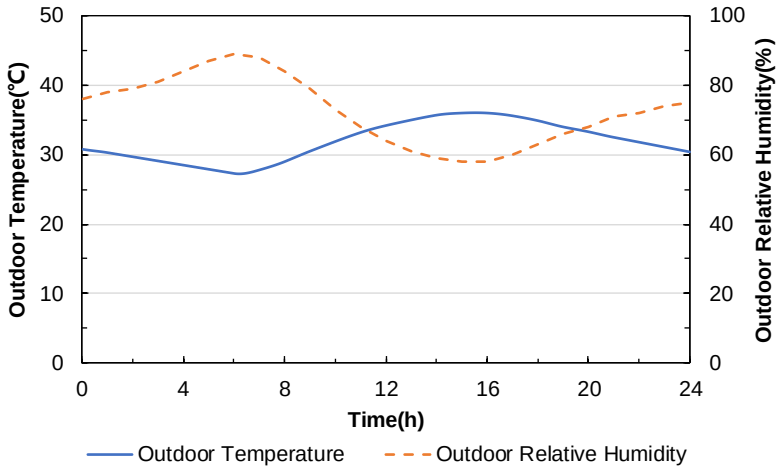

Figure 3: Profiles of outdoor air temperature and relative humidity

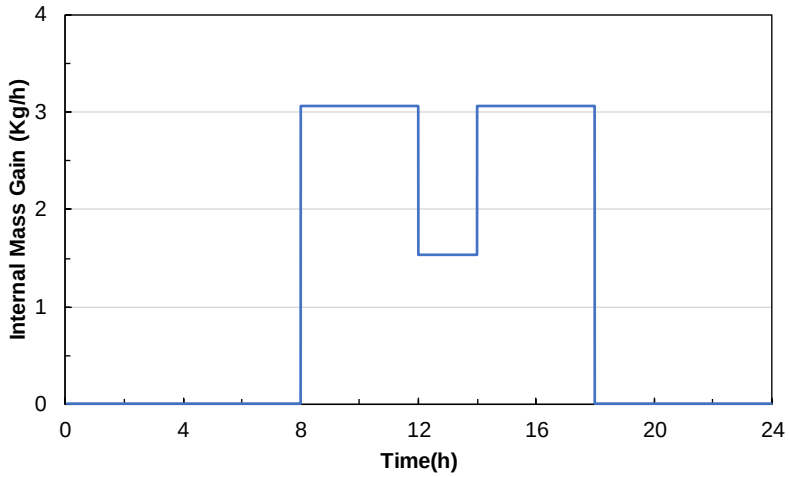

Figure 4: Profiles of the internal mass gain

For the proposed model-based control algorithm, the parameters needed to be specified were the user-defined parameter γ and the forgetting factor λ of the supply air moisture content prediction model and the control parameters K_p and T_i of the PI controller. The selections of γ and λ are limited in their feasible range described by Equation 6 and Equation 10. Normally a larger γ leads to a slow response of the controller; while a smaller one leads to a fast response of the controller. The selection of λ only affects the steady state performance as a filter, and a larger λ makes the variable $\zeta_{z,k}$ smoother and becomes less sensitive to the frequent variations of the humidity load.

In this test, the parameter γ was set as $\gamma = 0.6$, and λ was set as $\lambda = 0.8$. The control parameters K_p and T_i of the supply air humidity PI controller were determined based on the step response tests of the system, $K_p = 5$, $T_i = 120$s. It should be noted that these PI control parameters are different with that of the conventional space humidity PI control in the comparison case.

4.1. Evaluation of control performance

In this test, the space temperature is 25℃ and the relative humidity set-point is 60%. In this case, the space moisture content as the control objective in the proposed method is calculated, i.e., 11.9g/kg. Figure 5 gives the control performance of the space relative humidity when the proposed control method and the conventional PI control method were respectively used.

It can be seen that the proposed control method can maintain the space relative humidity at the set-point well, and when the humidity load changes drastically during the lunch time, it can still reject the disturbance of the internal mass gain well and achieve the stable control of the space relative humidity quickly. During the air-conditioning system operation stage in the test day, the space relative humidity average absolute control error is 0.29%. When the conventional PI control is used to track the space relative humidity directly, the control parameters $K_p = 1.5$ and $T_i = 150$s, which are well tuned in the test day. It can be seen that the control performance is not good. When the humidity load changes drastically during the lunch time, the conventional PI controller cannot response quickly, it makes the space relative humidity fluctuate greatly. During the air-conditioning system operation stage in the test day, the average absolute control error of the space relative humidity is 0.40%.

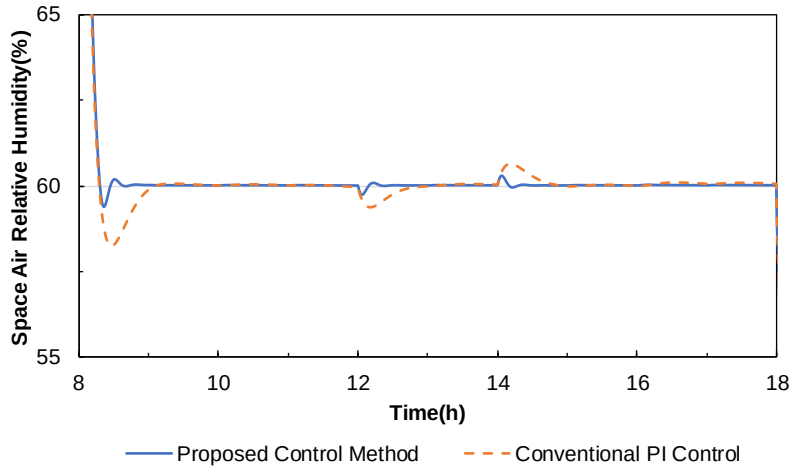

pace *relative* humidify

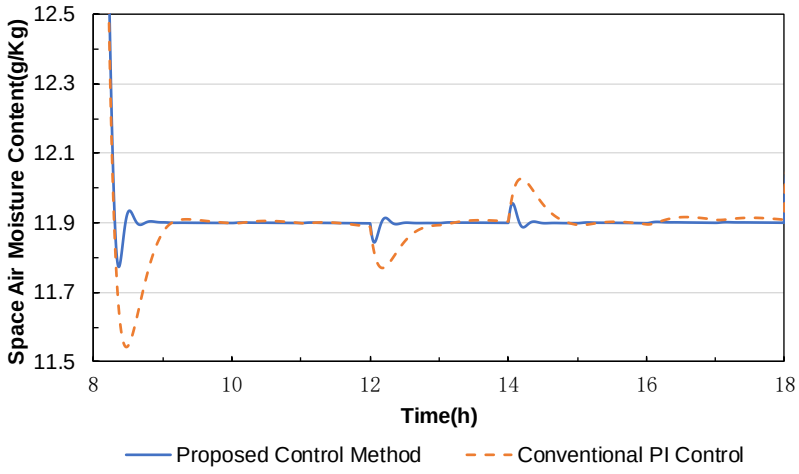

Space moisture content

Figure 5: Control performance of space relative humidity by using the proposed control method and the conventional PI control

The control signals of cold water valve in both the proposed control method and the conventional PI control were also compared in Figure 6. It can be seen that the cold water valve responded quickly to the significant changes of humidity load when the proposed control method is used. This is because that the variations of the space relative humidity and the humidity load were directly transferred to the change of the supply air moisture content in the proposed control method and the water valve responded quickly to the supply air moisture content change. When the conventional PI control was used, the response of the water valve was slow. This is because that the conventional PI control cannot respond the humidity load variation directly, and it responded after the humidity load variation transferred to the space relative humidity. It is a large thermal inertia process.

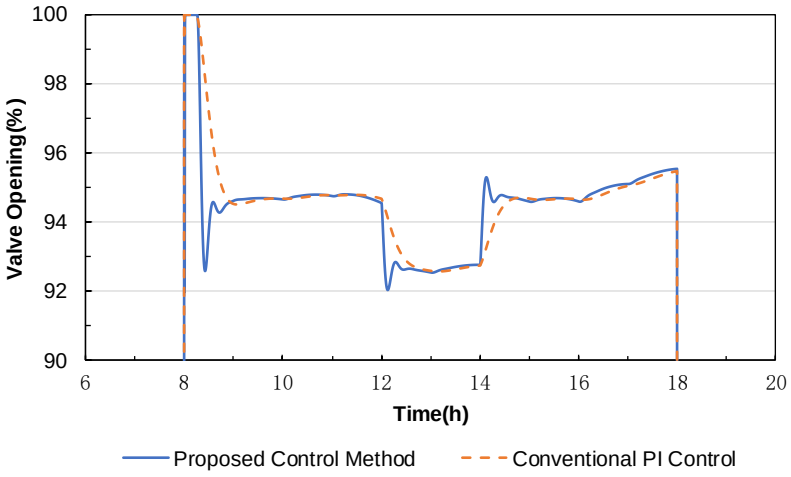

Figure 6: Water valve control signals by using the proposed control method and the conventional PI control

Figure 7 gives the variation of the supply air moisture content when the proposed control method was used. It can be seen that the supply air moisture content prediction model responded quickly to get the corresponding supply air moisture content set-point when the humidity load conditions changed significantly. The PI controller in the proposed control method can track the supply air moisture content set-point well although some lag appeared in the rapidly changing places of the humidity load conditions. It was the critical point to achieve the robust and accurate control of the space relative humidity.

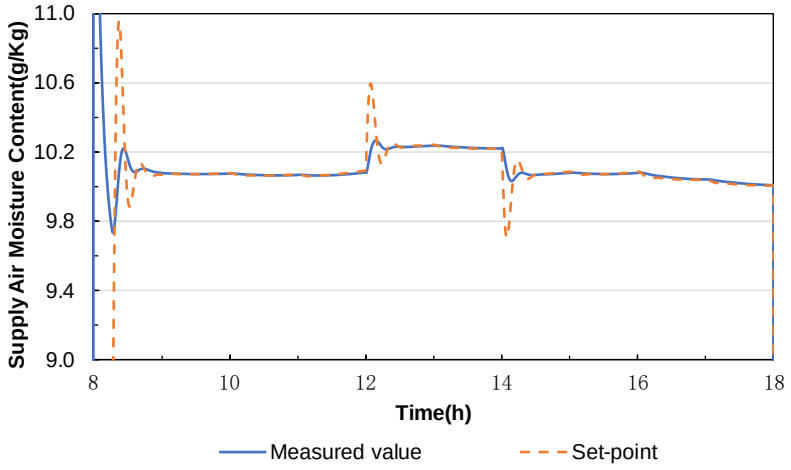

Figure 7: Variation of supply air moisture content by using the proposed control method

5. CONCLUSION

This paper proposes a model-based control method for the space humidity control of an independent dehumidification system, aiming to improve the robustness and accuracy of the space air humidity control. This control method consists of a supply air moisture content prediction model and a PI controller. The supply air moisture content prediction model is used to predict the system demand supply air moisture content based on the real-time humidity load and space humidity. The PI controller is used to track the predicted supply air moisture content by adjusting the opening of the water valve. TRNSYS software was used to build a dynamical simulation platform of an independent dehumidification system to test the control performance of the proposed control method. The test results show that the proposed control method has better dynamic regulation characteristic and load tracking ability comparing with the conventional PI control. The space relative humidity was controlled more robustly and accurately in a summer typical day. The proposed control method in this paper has a few control parameters and they are easy to be set, so it has great potential to be used in the actual independent dehumidification system.

6. ACKNOWLEDGEMENT

This work presented in this paper is financially supported by a grant (No. 51678263) of National Science Foundation of China.

7. REFERENCES

ASHRAE. ASHRAE Standard 62.1–2013. Ventilation for Acceptable Indoor Quality, Atlanta, 2013.

Charles J, Helen C, Datta V, 1989. Indoor Ozone Exposures. Air & Waste Management Association, 39(12): 1562-1568.

Gao J, Huang G, Xu X, 2015. Space temperature control of a GSHP-integrated air-conditioning system. Energy and Buildings, 108: 127-136.

Huang G, 2011. Model predictive control of VAV zone thermal systems concerning bi-linearity and gain nonlinearity. Control Engineering Practice, 19(7): 700-710.

Huang G, Wang S, Xu X, 2010. Robust model predictive control of VAV air-handling units concerning uncertainties and constraints. HVAC&R Research, 16(1): 15-33.

Salsbury TI, 2005. A survey of control technologies in the building automation industry. IFAC Proceedings Volumes, 38(1): 90-100.

Seborg DE, Edgar TF, Mellichamp DA, 1989. Process dynamic and control. New York: John Wiley & Sons.

Underwood CP, 1999. HVAC control systems: modelling, analysis and design. London & New York: E&RN Spon.

Vakiloroaya V, Samali B, Fakhar A, Pishghadam K, 2014. A review of different strategies for HVAC energy saving. Energy conversion and management, 77: 738-754.

Wang S, Jin X, 2000. Model-based optimal control of VAV air-conditioning system using genetic algorithm. Building and Environment, 35: 471-487.

Xu X, Wang S, Shi W, 2004. A robust sequencing control strategy for air-handling units. Building Services Engineering Research and Technology, 25(2): 141-158.

Yan B, Long E, Meng X, Zhang Y, Hou D, Du X, 2014. Influence of user behaviour on unsatisfactory indoor thermal environment. Energy Conversion and Management, 86: 1-7.

Yuan S, Perez R, 2006. Multiple-zone ventilation and temperature control of a single-duct VAV system using model predictive strategy. Energy and Buildings, 38:1248-1261.

Hang X, Xiao F, Li S, 2012. Performance study of a constant temperature and humidity air-conditioning system with temperature and humidity independent control device. Energy and Buildings, 49:640-646.Z

234: QUB/e: validation of a transient method for determining whole building thermal performance and building element U-values in situ under actual operating conditions

Vasileios SOUGKAKIS[1,3], Christopher WOOD[1], Johann MEULEMANS[2], Mark GILLOTT[1], Tom COX[3]

[1] The University of Nottingham, University Park, Nottingham, NG7 2RD, UK, Vasileios.Sougkakis@nottingham.ac.uk
[2] Saint-Gobain Recherche, 39 quai Lucien Lefranc B.P.135, F-93303 Aubervilliers, France, Johann.Meulemans@saint-gobain.com
[3] Saint-Gobain Delegation UK and Ireland, East Leake, Leicestershire, LE12 6HX, UK, Tom.Cox@saint-gobain.com

Growing evidence in recent years has suggested that a difference exists between the design and the as-built thermal performance of UK dwellings. This difference commonly known as the 'performance gap' may have serious implications on the UK government's emissions reduction targets. Determining the theoretical design thermal performance of whole dwellings (Heat Loss Coefficient, HLC) and building elements (U-value) can be straightforward; however in situ measurements of actual thermal performance can be much more difficult to achieve. Several methods have been developed to measure these properties in situ with the most common usually involve quasi-steady state conditions that necessitate long testing periods. The duration of such tests is deemed impractical from a building access perspective and wider uptake has therefore not been achieved.

The QUB/e method, developed by Saint-Gobain, is a dynamic method used to experimentally measure in-situ the thermal performance of a building in order to determine the whole dwelling HLC and U-values. The method is an advancement on the usual quasi-steady methods as it has the benefit of being able to be performed typically in a single night without occupancy. Validity of results has been demonstrated in a climate chamber under controlled conditions in a previous work. In this work, validation of the QUB/e method is performed under actual operating conditions by conducting a series of measurements on a daily basis in a modern well-insulated property located at the University Park Campus, University of Nottingham. Results were compared to those obtained with quasi steady-state measurements; the HLC was compared to that obtained with a coheating test and the U-values with those obtained by means of the procedure as per BS ISO 9869-1:2014 average method. Good agreement was found for both the HLC (7.5% relative difference between the two methods on average) and the U-values (in most cases the relative difference of the quasi-static and dynamic methods was approximately 2% while in one instance it was 12.5% on average), thereby increasing confidence in the ability of the QUB/e method to provide reliable results and highlights its potential to test the actual performance of buildings.

Keywords: QUB/e method, Coheating test, ISO 9869, Heat Loss Coefficient, U-value

1. INTRODUCTION

Building regulations in the UK have been setting progressively stricter requirements over the last years on the energy efficiency of new-built dwellings in order to reduce greenhouse gas emissions from the domestic sector that currently accounts for 27% of the country's final energy consumption (DBEIS, 2016). However, it has been found that the design thermal performance is often inconsistent with the actual as-built thermal performance of a dwelling. This difference is commonly referred to as the 'performance gap' and is considered a significant risk that may compromise the efforts on reducing greenhouse gas emissions. Calculating the thermal performance of a dwelling is part of the regulatory process using the UK Government's Standard Assessment Procedure (SAP) and is based on information of the building geometry, location, surroundings and material properties (DECC, 2014). In contrast, assessing the as-built performance is not as simple and straightforward.

Several methods have been developed to determine the actual as-built thermal performance of the building fabric in situ. With regards to whole building thermal performance, the coheating test is perhaps the most widely used. The coheating test is a quasi-steady state method that determines the Heat Loss Coefficient (HLC) of a building by maintaining a fixed internal elevated temperature using heaters and fans and monitoring the power required to do so as well as the external temperature and weather conditions. Despite the wide acceptance of the method by industry and research institutions, it is not considered practical as it involves long testing periods (typically 2 – 4 weeks) and is restricted during the heating season when external temperature and the levels of solar radiation are typically low. In terms of elemental performance, the BS ISO 9869-1:2014 Standard describes the recommended procedure for determining the U-value of building elements in-situ with the 'average method' being the most commonly used analysis technique. This method considers measuring the heat flow at the surface of a building element and temperatures at each side of that element and averaging them over long periods of time so that heat storage effects are minimised (i.e. quasi-steady state conditions are assumed); again long testing periods are usually required in order to meet the criteria set by the average method.

Alternatively, other methods that require shorter testing periods have been developed (e.g., see Janssens 2016 and references therein). In this paper the performance of the QUB/e method to measure both whole house HLC and building element U-value in much shorter period is evaluated. The method builds on the QUB method, a dynamic method developed by Saint-Gobain to determine the as-built HLC of dwellings typically within one night; based on the same analysis principle the QUB/e method takes into account the heat flow on building elements to determine the U-values. The ability of the QUB/e method to provide reliable results, has been demonstrated numerically (Alzetto et al., 2014) and experimentally in a climate chamber under steady conditions as well as (Meulemans et al., 2016, Alzetto et al, 2018a). Several studies have also reported on the performance of method under actual climatic conditions in different regions of Europe (Alzetto et al, 2018b, Meulemans, 2018). With regards to investigating the performance of the QUB/e method in the UK climate a long-term study was conducted in a property in Nottingham; repeatability and consistency of the results as well the effect of weather conditions were examined (Sougkakis et al, 2017).

However, that work was conducted in a poorly insulated property. In this work, results from a series of QUB/e tests performed on a daily basis in a well-insulated property in the UK climate are presented. In addition, a coheating test was also performed to determine the HLC and data from the heat flow meters during this test were also analysed considering the BS ISO 9869-1average method. The aim was to assess the ability of the QUB/e method to deliver consistent results and assess its performance against well-established quasi-static methods.

2. IN-SITU EXPERIMENTAL METHODS

In the following sections a brief description of both the quasi-steady state and the QUB/e methods is presented.

2.1. Quasi-steady state methods

Coheating method

The method statement for the coheating test is described by Johnston et al. (2013). In summary, the test procedure involves heating the building with electrical heaters to a fixed elevated temperature, significantly higher than the mean external temperature (usually 25^{o}C) so that an adequate temperature difference between internal and external environment is achieved (ΔT). Fans are also used to mix the air and achieve homogeneous temperatures throughout the building. Internal zone temperatures, the external temperature and the power consumption of the fans and heaters are monitored. The HLC is then determined by plotting the daily average electrical consumption against the daily average difference between the average internal and external temperatures (Johnston et al., 2013). This is usually referred to as 'uncorrected HLC'. In order to account for the effect of solar gains, which are a major contributor to the heat gains of a house when performing a coheating test the following simplified steady-state energy balance is considered:

Equation 1: Energy balance in a coheating test

$$Q_{elec} + Q_{solar} = Q_{loss}$$

Where

- Q_{loss} = the rate of heat loss of the dwelling (W). This is the product of the Heat Loss Coefficient, HLC (W/K) and the temperature difference between the average internal and average external temperature, ΔT (K)
- Q_{elec} = the power consumption of the electrical heaters (W)
- Q_{solar} = the solar gains (W). This is the product of the solar aperture, R (m^2), and the solar irradiance, S (W/m^2),

Therefore Equation 1 can also be expressed:

Equation 2: Expanded energy balance in a coheating test

$$Q_{elec} + R \cdot S = HLC \cdot \Delta T$$

Solar gains can be accounted for by measuring the solar irradiance, S, using a pyranometer and calculating the solar aperture, R. There are two main methods for calculating the solar aperture and therefore the solar corrected HLC. The first is through multiple regression analysis where Q_{elec} is the dependent variable and the daily average temperature difference, ΔT, and solar irradiance, S are the independent variables. The second is the 'Siviour method' where Equation 2 is rearranged as follows:

Equation 3: Energy balance for the 'Siviour method'

$$\frac{Q_{elec}}{\Delta T} = HLC - \frac{S}{\Delta T} \cdot R$$

The HLC is then determined by plotting a graph of the daily average values of the $Q_{elec}/\Delta T$ at the y-axis and the $S/\Delta T$ at the x-axis and fitting a regression line. The HLC is the intercept of the line at the y-axis and the solar aperture, R, is the slope of the line (Johnston et al., 2013).

There is no specific requirement on the duration of the test, however Johnston et al. (2013) suggested that a minimum of 1 week is expected after a building has been thermally saturated (i.e. reached quasi-steady state) ranging to 3 weeks depending on the construction type and the weather conditions, while Stamp (2015) reported on duration of published tests varying from 6 to 32 days.

BS ISO 9869-1:2014 – Average method

BS ISO 9869-1:2014 describes the procedure for determining the U-values of building elements in-situ with the use of heat flow meters. The average method is based on the assumption that after a significant amount of time, the average values of the temperature and density of heat flow rate are approaching steady state conditions (BSI, 2014). The analysis is based on dividing the mean heat flux through a building element by the mean temperature difference between the internal and external side of that element over a long period of time (Equation 4). The duration of the test is determined by specific criteria that have been set to assume quasi-static conditions are met; the test is completed once the resistance value obtained over different sub-periods of the whole test period does not deviate more than ±5% (BSI, 2014).

Equation 4: Thermal transmittance (ISO 9869-1:2014 average method)

$$U = \frac{\sum_{j=1}^{n} q_j}{\sum_{j=1}^{n} (T_{ij} - T_{ej})}$$

Where:

- U = thermal transmittance of the building element (W/m^2)
- q_j =density of heat flow rate at time step j (W/m^2K)
- T_{ij}, T_{ej} = internal and external environmental temperature at time step j (K)

In practice, when both internal and external temperatures fluctuate on a daily basis, it may be difficult for these criteria to be met which may result in significantly long testing periods. However, when this method is applied when a coheating test is performed (i.e. internal temperature remains stable) the required testing period to meet the criteria is reduced (Stafford et al, 2014). In any case the minimum (normative) test duration is 3 days for the most favourable conditions and lightweight elements.

2.2. The QUB/e test

The QUB/e method is a dynamic method developed by Saint-Gobain to determine the HLC of a building and the U-values of building elements in a single night without occupancy. The QUB/e test commences after sunset and finishes before sunrise of the following day (Figure 1Figure 1 (left)). The principle of the method to determine the HLC is based on a single resistance and capacity model where the building is represented by a global thermal resistance R (the reciprocal of HLC of the building) and a global capacitance, C (the internal heat capacity) (Mangematin et al., 2012; Pandraud and Fitton, 2013; Pandraud et al., 2013). Internal and external temperature nodes (T_{int} and T_{ext} respectively) are considered homogeneous and heat exchange between the two nodes occurs through the thermal resistance, R. Therefore, the energy input, P, is heat lost through the envelope and stored/released by the thermal mass of the fabric. This is described as follows:

Equation 5: Energy balance for an RC model

$$P = \frac{T_{int} - T_{ext}}{R} + C\frac{dT_{int}}{dt}$$

In the above equation there are two unknowns R (i.e. the reciprocal of the HLC) and C. The HLC of a building can then be determined by using two different constant powers in two different phases (respectively noted 1 and 2) and solving Equation 5 (Pandraud et al., 2014). To achieve this, the test comprises two phases of equal duration; the heating phase (phase 1) when a constant power, P_1, is injected to the dwelling and the cooling phase (phase 2) when the building is typically allowed to cool down (i.e. $P_2 \approx 0$). The temperature and power profile during the two phases of a QUB test is presented in Figure 1 (right) below.

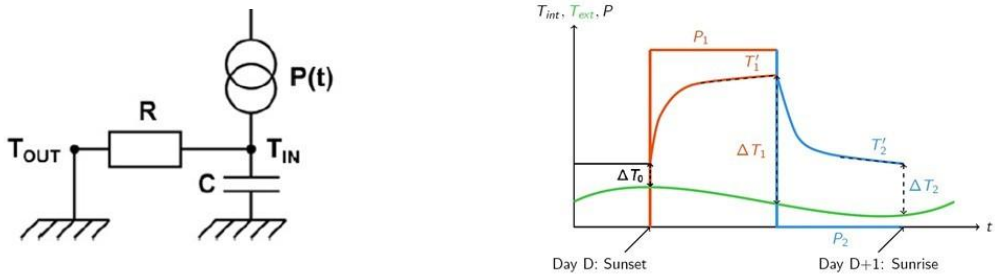

Figure 1: RC model used in the QUB method (left) and evolution of temperature and power during a QUB measurement (right)

The HLC is provided by the following formula (Meulemans et al., 2016):

Equation 6: Heat Loss Coefficient (QUB/e method)

$$HLC = \frac{T'_2 P_1 - T'_1 P_2}{T'_2 \Delta T_1 - T'_1 \Delta T_2}$$

Where:

P_i = Power input during phase i (W)

T'_i = Slope of the temperature profile at the end of phase i (defined as the $t_i - \min(t_i/2, \tau)$, where t_i is the duration of the ith phase and τ = 2 hours)

ΔT_i = Internal to external temperature difference at the end of phase i (K)

The same analysis method is applied to determine the U-value of building elements by substituting in Equation 7 the density of heat flow rate at the surface of the element (instead of the power) and the temperature in the vicinity of the surface (instead of the ambient temperature) (Meulemans et al., 2016):

Equation 7: Thermal transmittance (QUB/e method)

$$U = \frac{T'_2 q_1 - T'_1 q_2}{T'_2 \Delta T_1 - T'_1 \Delta T_2}$$

Where:

q_i = density of heat flow rate in phase i (W/m^2K)

T'_i = the slope of the temperature profile in the vicinity of the element surface in phase i

ΔT_i = temperature difference between this internal temperature and the external temperature (K).

The Taylor series method for uncertainty propagation (Coleman & Steele, 2009) is used to compute the relative uncertainty associated to the HLC and the U-values.

The accuracy of the method is dependent on a dimensionless parameter inherent to the QUB method, the α-parameter (Pandraud et al., 2014). This is determined by:

Equation 8: α-parameter

$$\alpha = 1 - \frac{HLC_{ref}\Delta T_0}{P_1}$$

Where,

- HLC_{ref} = the reference Heat Loss Coefficient (theoretical or determined experimentally) (W/K),
- ΔT_0 = the initial temperature difference between the interior and the external environment (K) as shown in Figure 1 (right)
- P_1 = the power input during the heating phase (W).

It has been demonstrated that the α-parameter has minimum effect on the resulting HLC for values $0.4 < \alpha < 0.7$, while for $\alpha > 0.7$ there is usually an overestimation of the HLC mostly at very short tests (Pandraud et al., 2014; Meulemans et al., 2016, Sougkakis, 2017). Hence, meeting this criterion is considered a measure of confidence level for test accuracy.

3. MATERIALS AND METHOD

The tests were carried in a detached house located at 6, Green Close, at the Creative Energy Homes site at the University of Nottingham Park Campus. The house was completed in 2008 and achieved level 4 of the UK's Code for Sustainable Homes. The design of the house considered a fabric first approach; the walls and roof had a design U-value of $0.15W/m^2K$. Ground floor walls were built with Insulating Concrete Formwork (ICF) construction and the first floor walls and roof were constructed with timber Structural Insulated Panels (SIPs). The south façade is a sunspace with internal and external fully glazed surfaces. The north wall has small windows while the east and west walls do not have any windows (BASF, no date). The ground and first floor plans of the house are presented in Figure 2 below.

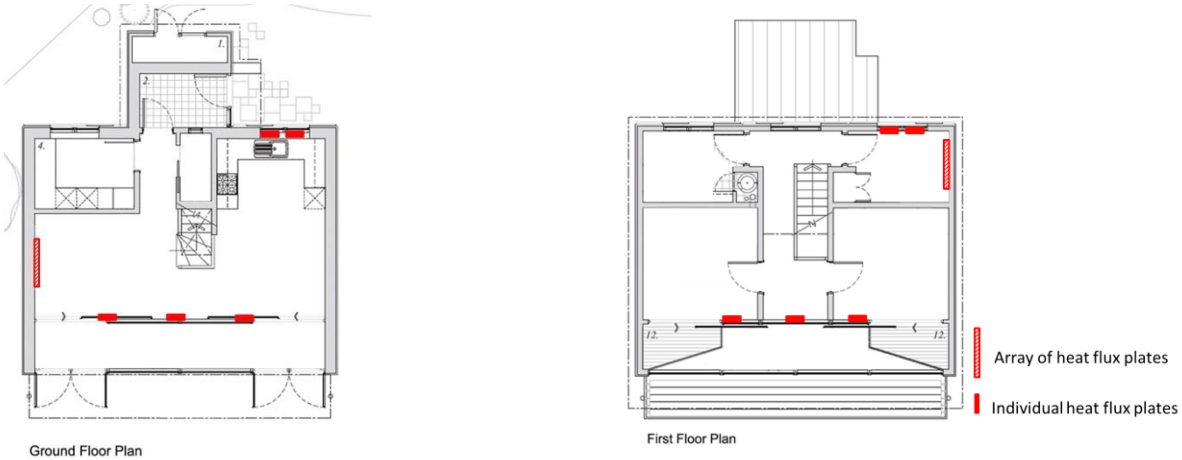

Figure 2: Ground floor (left) and first floor plan (right) of the test house and location of heat flux sensors

In order to perform the quasi-static and dynamic tests the following parameters were required to be monitored: internal ambient temperatures in the different zones, external air temperature, heat flux at the surface of the building elements of interest, temperature at the vicinity of these elements and power input. During the coheating test, temperatures at the different locations were measured with the use of Platinum RTD sensors (PT100) and the heat flux was measured with the use of HUKSEFLUX HFP01 sensors. Heat flux sensors were installed at the ground and first floor walls (an array of heat flux sensors was installed in each wall area to obtain an average U-value), the external windows and the internal sunspace windows as shown in Figure 2. The energy consumed by the heaters was monitored by pulse meters. Data were stored in two Datataker DT85 loggers with two CEM-20 expansion modules. Two Skye SKS-1110 pyranometers were installed externally in the south façade in order to obtain an average measurement of the south facing vertical solar irradiance. This was then used to account for the solar gains in the resulting HLC.

The QUB/e measurement was performed with the use of the prototype kit developed by Saint-Gobain. This comprises wireless Fibaro sensors to measure air temperatures and Fibaro wall plugs for measuring power input in order to determine the HLC of the building. The U-values during the QUB/e measurements were derived using data from the same heat flux plates and temperature sensors that were used at the coheating test in order to compare the U-values determined with the two methods at exactly the same locations. The schedule for each set of measurements is presented in Table 1 below.

Table 1: Testing schedule of quasi-static and dynamic measurements

	From	To
Quasi-static measurements (coheating, ISO 9869-1:2014)	04.11.17	26.11.17
Dynamic measurements (QUB/e)	27.11.17	19.12.17

The coheating test was conducted in November 2017 over a period of 22 days. As the south façade had such a large area of glazing, special consideration had to be given to minimise the effect of solar gains through the sunspace. It was considered that the dwelling could be subject to great swings in solar gains, and at times of high solar radiation, this heat gain could dominate the heat input to the dwelling, which may lead to difficulties maintaining the internal fixed temperature. It was therefore decided in order to mitigate this effect that the blinds in the external glazing of the sunspace would be kept closed while windows that did not have blinds would be covered with aluminium foil to reflect incoming radiation. In addition, the top windows were left open (Figure 3). Therefore, the heated area of the house did not include the sunspace. This arrangement was kept the same throughout the whole course of the quasi-static and dynamic measurements.

Figure 3: External view of the south façade of the dwelling with the location of the pyranometers. Most glazed areas were covered to minimise the effect of solar radiation

4. RESULTS AND DISCUSSION

To determine the HLC of the house, recorded data of ambient temperatures (internal and external), power consumption of heaters and south vertical solar radiation were averaged on a daily basis. This resulted in obtaining 22 data points for the analysis during the coheating test. In order to smooth the effects of thermal mass, data were aggregated from 06:00 am until 05:59 am the following morning in order to allow for solar gains to be readmitted back to space (Everett, 1985, Johnston et al, 2013). The result of the coheating test using Multiple Linear Regression analysis is presented in Figure 4 below. The south vertical irradiance measured was used as the independent variable. For better visualisation in a 2-D diagram, the solar aperture calculated by the MLR analysis was multiplied by the daily average solar irradiance measured to determine the average daily solar gains. These gains were then added to the average daily power consumed by the heaters. In other words, the y-axis of Figure 4 represents the sum of electrical power and the solar gains (Q_{elec} and Q_{solar} in Equation 1). MLR analysis in general

has been reported as statistically better in correcting the HLC for solar gains than Siviour Analysis as it treats both solar irradiance, S, and the temperature difference ΔT as independent variables (Baker, 2015). Bauwens and Roels (2014) also recommended the use of MLR analysis as the Siviour analysis may lead to unreliable results when ΔT is close to 0 K. However, the test protocol considers a minimum ΔT of 10 K and it has been shown in literature that both methods result in very similar values HLC (Stamp, 2015).

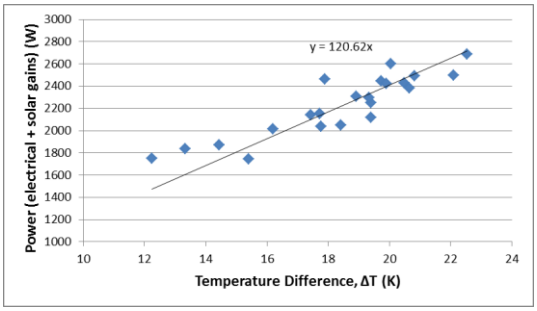

Figure 4: Multiple Linear Regression Analysis of coheating results

The HLC was found to be 120.6 ± 3.5 W/K when using the MLR analysis. This value will be referred to as HLC_{static}. For reasons of comparison, it should be mentioned that the Siviour analysis resulted to a HLC of 122.5 ± 3.8W/K which is consistent with the literature findings suggesting that the two methods lead to very similar results. As the sunspace was unheated, the internal glazing of the sunspace that was the boundary of the heated space was not in direct contact to the external conditions (despite the fact that the windows were left open the area in the sunspace was consistently in a somewhat higher than the external temperature). For this reason the HLC_{static} was adjusted by subtracting the heat loss from that area (in W/K) as described in Equation 9 9. The adjusted HLC, $HLC_{static,adj}$ was 105.2 W/K ± 3.5 W/K. This is the reference quasi-static HLC against which the QUB/e results will be compared.

Equation 9: Adjusted HLC

$$HLC_{adj} = HLC - U_{sunspace,eff} \cdot A_{sunspace}$$

Where,

- HLC_{adj} = the adjusted HLC that considers heat losses only from those elements in contact to the external temperature (W/K)
- $U_{sunspace,\ eff}$ = the effective U-value of the internal glazing that is in contact to the sunspace (W/m^{2}K)
- $A_{sunspace}$ = the area of the internal glazing that is in contact to the sunspace (m^2)

With regards to the dynamic tests, in total 20 QUB/e tests were performed between November and December 2017. In all these tests the power input and the internal temperature were controlled such as to keep the α – parameter within the recommended limits (0.4 < α < 0.7) and therefore all results were considered reliable. The HLC was calculated on a daily basis (HLC_{QUB}). The average HLC_{QUB} from all QUB/e tests was found 114.0 ± 2.9 W/K. The adjusted HLC ($HLC_{QUB,adj}$) was then determined by subtracting the heat losses to the sunspace according to Equation 9 9. The average $HLC_{QUB,adj}$ was 97.2 ± 2.8 W/K This was in good agreement with the coheating results; the relative difference between $HLC_{QUB,adj}$ and $HLC_{static,adj}$ was 7.6%. Results plotted against the dimensionless parameter α are shown in Figure 5 below.

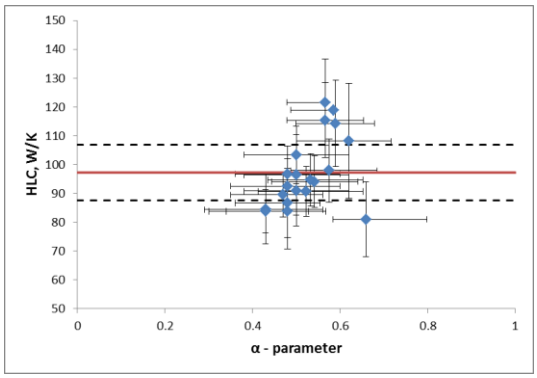

Figure 5: Summary of QUB/e results plotted against the a-parameter

It should be noted that each data point in Figure 5 shows the HLC calculated for that night (in contrast to Figure 4 where one HLC is calculated from all data). The average HLC of the QUB/e tests is shown with the red solid horizontal line in Figure 5; the black dashed lines represent the ±10% deviation from the mean. It can be seen that most of results fell within the ±10% band (or very close to it) with a few occasions where this was slightly higher (in one instance reaching +20%). This was consistent with the findings reported in a previous study regarding the repeatability of the method in a poorly insulated property of masonry construction under two different levels of airtightness (Sougkakis, 2017). It also suggests that repeatability of the QUB/e method was similar regardless of the levels of insulation of the building investigated. However, further work will be required in order determine whether the larger deviations were the result of specific weather conditions. With regards to the α-parameter calculation, the HLC_{static} determined with the coheating test was used as the HLC_{ref} in Equation 8.

To determine the elemental performance, heat flux sensors were installed at the external walls, the external window panes and the internal glazing of the sunspace in each floor. The U-value was then calculated considering the procedure set by BS ISO 9869-1:2014 and the QUB/e analysis (Equation 4 and Equation 7 respectively). In order to comply with the ISO 9869 requirements, U-values from heat flux sensors that were installed on areas away from thermal bridges are reported here, i.e. at clear wall areas and centre of pane (in the case of glazing U-values). In total, 17 heat flux sensors were installed in locations away from thermal bridges; 7 on the walls, 4 on the external windows and 6 on the internal glazed areas. The U-values calculated with the two methods are presented in Figure 6 and Figure 7 below. In the graphs the x-axis shows the ISO-9869 U-values and the y-axis the QUB/e U-values. This allows visualising where the QUB/e values stand compared to the quasi-static ones. The red dashed lines show the ±28% uncertainty limits of the U-value calculation suggested by the ISO Standard. For ease of comparison the x=y line was also plotted (diagonal). Similarly to reporting HLC values, the static method (ISO 9869) resulted in one U-value for each sensor; the whole testing period was chosen for the analysis in order to increase confidence on the results (as averaging of the heat flows and temperatures would be over a large period of time) and also to obtain the U-values from all sensors over the same averaging period. In most cases the ISO 9869 criteria were met within 4 days, while in one case after 7 days of testing. On the other hand the QUB/e method was able to determine the U-values on a daily basis (i.e. 20 results per sensor were obtained during the dynamic testing period).

Results from the sensors installed at the ground floor and first floor walls are shown in Figure 6 (left and right respectively). It can be seen that in the first floor wall (Structural Insulated Panel construction) there was very good agreement between the dynamic and quasi-static results since the QUB/e U-values were very close to the quasi-static ones both in terms of mean value from all tests as well as the individual values and well within the uncertainty limits. With regards to the ground floor wall (Insulating Concrete Formwork construction) it can be seen that there was also good agreement between the two methods, however there was larger dispersion of the dynamic U-values. As a result, the average dynamic U-value was very close to the quasi-static one but the individual values had a larger deviation from the mean. Nevertheless, in almost all cases the QUB/e U-values were within the ±28% uncertainty band. It is believed that the larger dispersion observed on the ICF wall is due to the increased levels of thermal mass of this construction type compared to SIP panels; however, further work is required to verify this.

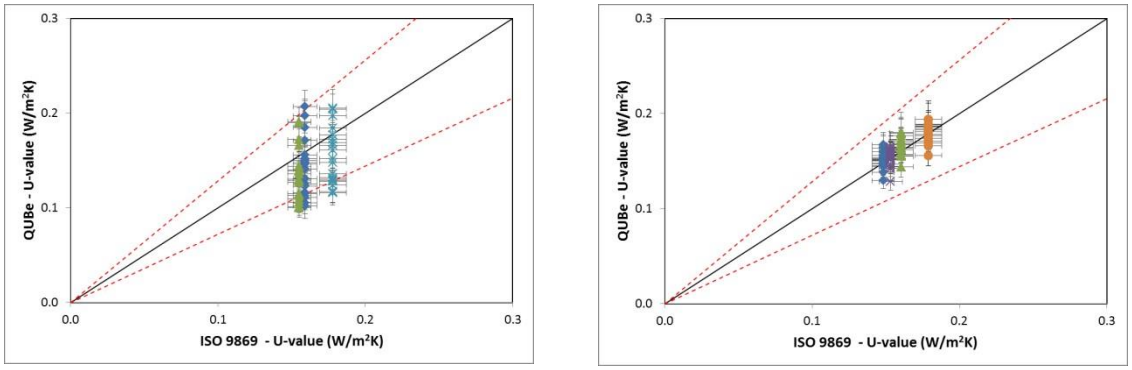

Figure 6: U-values of the ground floor wall (left) and the first floor wall (right) determined with the ISO-9869 and QUB/e method

The U-values determined at different locations of the external windows and the internal curtain wall of the sunspace is presented in Figure 7; these are all centre of pane U-values. It should be noted that the U-values obtained for the internal sunspace glazing presented here were in fact the actual U-values (not the effective U-values used in Equation 9 9); these were calculated considering the temperature difference between the heated space and the unheated sunspace in the vicinity of the glazing. It can be seen that in all cases there is good agreement between the two methods as the dynamic U-values were quite close to the quasi-static ones at all times and well within the uncertainty limits. This was particularly the case for the internal glazing of the sunspace where the external temperature considered (i.e. the temperature in the sunspace) was more stable than the actual external temperature. The internal curtain wall of the sunspace consisted by double glazed panels and two opaque uPVC panels to ensure privacy in the bedrooms. In total six sensors were installed on the curtain wall, four on the glazed panels and two on the uPVC panels (that are marked separately in Figure 7 (right)).

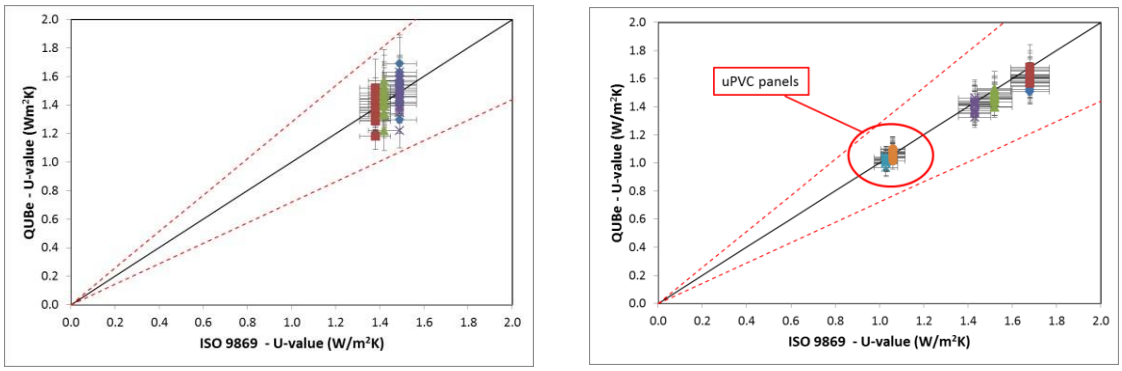

Figure7: U-values of external windows (left) and internal sunspace glazing and panels (right) determined with the ISO-9869 and QUB/e method

The average U-values for each building element determined with the two methods are shown inTable 2. It can be seen that both methods result in very similar U-values. The maximum relative difference was observed in the ground floor wall (ICF) where the QUB/e method underestimated the U-value by approximately 12.5%. Practically the same U-values were observed for the first floor wall (SIP), the internal sunspace curtain wall and the external windows (centre of pane). A maximum relative difference of about ±2% was observed. It should also be noted that there does not appear systematic overestimation or underestimation of U-values when using the QUB/e method.

Table2: Average U-values determined with the ISO 9869 and the QUB/e method

	ISO 9869 U-value (W/m²K)	**QUB/e U-value (W/m²K)**	**Relative difference**
Ground Floor wall	0.16 ± 0.03	0.14 ± 0.01	-12.5%
First Floor Wall	0.16 ± 0.02	0.16 ± 0.00	1.4%
External windows	1.44 ± 0.20	1.44 ± 0.02	-0.3%
Internal sunspace glazing	1.58 ± 0.22	1.545 ± 0.01	-2.0%
Internal sunspace vinyl panels	1.04 ± 0.21	1.04 ± 0.00	-0.74%

5. CONCLUSIONS

The findings from an in situ monitoring study conducted to assess the performance of the QUB/e method under actual operating conditions against more widely used quasi-static methods was presented in this paper. The QUB/e method is able to estimate the HLC of a building and the U-values of building elements within just one night, significantly less than the 2-4 week period required for a coheating test or other quasi steady-state methods (Janssens, 2016). The performance of the QUB/e method was assessed in a well-insulated detached dwelling located in the University Park campus, University of Nottingham from November until December 2017. The objectives of the study were to:

- Assess the HLC of the house derived with the QUB/e method and compare against that obtained with a coheating test;
- Evaluate the ability of the method to provide reliable and consistent results on a daily basis in a dwelling with high levels of insulation for the UK weather conditions;
- Assess the U-values of external building elements obtained with the QUB/e method against those obtained using the average method of BS ISO 9869-1:2014.

Results suggest that the method was able to provide reliable results in terms of both the whole building HLC and the building element U-values. On average the relative difference between the corrected HLC calculated with the coheating and the QUB/e test was 7.6%. In addition, the QUB/e method was found to have reasonable repeatability since most results were within ±10% from the mean with some cases within ±15%. This was consistent with previous findings reported by Sougkakis et al. (2017) from the in situ study conducted in a poorly insulated property, suggesting that the method had similar levels of performance regardless of the levels of insulation. In addition, the U-values determined were very close to those obtained with the average method of the BS ISO 9869-1:2014 Standard; a maximum of 12.5% relative difference was observed on average in one wall, while in the rest of building elements (SIP wall and glazed surfaces) the U-values were practically the same on average (with maximum difference of approximately 2% between the two methods). Some degree of variation was observed on a daily basis but the values were well within the uncertainty limits the suggested by the ISO Standard. These results were

consistent with previous findings reported by Meulemans (2018) from in situ measurements (QUB/e and ISO 9869-1) undertaken in a multi-storey residential building in Sweden.

Therefore, the QUB/e method is considered to have performed well in comparison to the quasi- static methods for determining both the whole building HLC and element performance.

The QUB/e method is less intrusive and requires much shorter period than the conventional long-term quasi-static methods. Consequently, the QUB/e method allows for obtaining a series of results on a building's performance parameters on a daily basis during a specified testing period (rather than obtaining one result over the whole testing period that is the case with the coheating and ISO-9869 method). Furthermore it is able to derive both the building's HLC and U-values in-situ, while a separate method is required to determine each of these parameters using the conventional quasi-static methods. For these reasons, the method has great potential as a research tool as well as a building diagnostics tool to be used by industry. The findings of this work, the first field study in a well-insulated property in the UK, support previous evidence and increase confidence on the ability of the QUB/e method to provide reliable results in the field. Additional work is required to evaluate the effect of the weather conditions on the resulting HLC and U-values, particularly the effect of the wind and temperature that has been shown previously in an uninsulated property that is a factor which may affect the results. Furthermore, similar studies in buildings that are more representative of the current building stock in the UK will be useful for the wider verification of the results and the broader acceptance of the method by researchers and building performance practitioners.

6. ACKNOWLEDGEMENTS

The authors gratefully acknowledge funding received from Saint-Gobain and Innovate UK under the KTP009930 project.

7. REFERENCES

Alzetto, F, Gossard, D, Pandraud, G, 2014. Mesure rapide du coefficient de perte thermique des bâtiments. Proceedings of Ecobat Sciences et Techniques. Paris, France

Alzetto, F, Farmer, D, Fitton, R, Hughes, T, Swan, W, 2018a. Comparison of whole house heat loss test methods under controlled conditions in six distinct retrofit scenarios. Energy and Buildings, 168, pp 35 – 41

Alzetto, F, Pandraud, G, Fitton, R, Heusler, I, Sinnesbichler, H, 2018b. QUB: a fast dynamic method for in-situ measurement of the whole building heat loss. Energy and Buildings, (Accepted manuscript)

Baker, P, 2015. A retrofit of a Victorian terrace house in New Bolsover: A whole house thermal performance assessment. Tech. rep. Historic England & Glasgow Caledonian University.

BASF, no date. Building a Sustainable Future: The BASF House - UK Project [online], BASF plc. Available at: www.nottingham.ac.uk/creative-energy-homes/documents/basfhousebrochure.pdf [Accessed: 14th June 2018]

Bauwens, G, Roels, S, 2014.Co-heating test: A state-of-the-art. *Energy and Buildings*,82,pp 163– 172

BSI, 2014. BS ISO 9869-1:2014 - Thermal insulation – Building elements – In situ measurement of thermal resistance and thermal transmittance - Part 1: Heat flow meter method.

Coleman, H W. and Steele, G W., 2009. *Experimentation, Validation, and Uncertainty Analysis for Engineers*. John Wiley & Sons, Inc., Hoboken, New Jersey.

DBEIS, 2016. Digest of United Kingdom Energy Statistics (DUKES) - Energy: Chapter 1. Department for Business, Energy and Industrial Strategy

DECC, 2014. The Government's Standard Assessment Procedure for Energy Rating of Dwellings 2012 edition. Garston: BRE

Everett, R, 1985. Rapid Thermal Calibration of Houses; Open University Energy Research Group: Milton Keynes, UK, 1985.

Jannsens, A, 2016. Overview of Methods to Analyse Dynamic Data. International Energy Agency, EBC Annex 58, Reliable building energy performance characterisation based on full scale dynamic measurements. Leuven: KULeuven

Johnston, D, Miles-Shenton, D, Farmer, D and Wingfield, J, 2013. Whole House Heat Loss Test Method (Coheating). Leeds (UK): Leeds Metropolitan University

Mangematin, E, Pandraud, G and Roux, D, 2012. Quick measurements of energy efficiency of buildings. Comptes Rendus Physique, 13 (4), pp. 383–390.

Meulemans, J, Alzetto, F, Farmer, D and Gorse, C, 2016. QUB/e – A novel transient experimental method for in situ measurements of the thermal performance of building fabrics. In: Gorse, C. and Dastbaz, M. (eds), International SEEDS conference 2016: Sustainable Ecological Engineering Design for Society, 14-15 September, 2016, Leeds (UK). Leeds (UK): Leeds Beckett University

Meulemans, J, 2018. An assessment of the QUB/e method for fast in situ measurements of the thermal performance of building fabrics in cold climates. In: The 9th International Cold Climate Conference - Cold Climate HVAC 2018 – Sustainable Buildings in Cold Climates, 12-15 March 2018, Kiruna (Sweden).

Pandraud, G and FITTON, R, 2013. QUB: Validation of a Rapid Energy Diagnosis Method for Buildings. In: IEA–EBC Annex 58, 4th Expert meeting, 8–10 April 2013, Holzkirchen (Germany)

Pandraud, G, Mangematin, E, Roux, D. and Quentin, E,2013. QUB: a new rapid building energy diagnosis method. In: Kabele, K., Urban, M., Suchý, K. and Lain, M. (eds), Proceedings of CLIMA 2013, the 11th REHVA World Congress and the 8th International Conference on IAQVEC, 13–19 June 2013, Prague (Czech Republic). Prague (Czech Republic): Society of Environmental Engineering (STP).

Pandraud, G, Gossard, D and Alzetto, F, 2014. Experimental optimisation of the QUB method. In: IEA–EBC Annex 58, 6th Expert meeting, 14–16 April 2014, Ghent (Belgium)

Sougkakis, V, Meulemans, J, Alzetto, F, Wood, C, GILLOTT, M and COX, T, 2017. An assessment of the QUB method for predicting the whole building thermal performance under actual operating conditions. In: Gorse, C. (Ed.) International Sustainable Ecological Engineering Design for Society (SEEDS) Conference 2017–Conference Proceedings, 13–14 September 2017, Leeds (UK). Leeds Beckett University.

Stafford A, Johnston, D, Miles-Shenton D, Farmer D, Brooke-Peat M and Gorse C. Adding value and meaning to coheating tests. Structural Survey, 32(4):331–42, 2014.

Stamp S, 2015. Assessing Uncertainty in co-heating tests: Calibrating a whole building steady state heat loss measurement method. PhD thesis, University College London.

235: Economic and environmental analysis of innovative greenhouse

Dewanto HARJUNOWIBOWO [1,2], Yate DING [1], Siddig A. OMER[1], Saffa B. RIFFAT[1]

[1] *Department of Architecture and Built Environment, Faculty of Engineering, University of Nottingham, University Park, NG7 2RD Nottingham, UK, dewanto.h@nottingham.ac.uk, saffa.riffat@nottingham.ac.uk*
[2] *Department of Physics Education, Sebelas Maret University, Jl Ir Sutami 36A, Surakarta, 57126, Indonesia*

In planning an industry, a financial appraisal is inevitable. As well as an agricultural business, an assessment of the building and the technologies applied to support the viability of the crop should be carried out correctly. Because of the superiority of the Discounted Cash Flow method in considering inflation and future cost changes, the payback period achieved will be closer to reality.

Based on careful calculations of the proposed greenhouse with a sophisticated system and the ability to generate independent electrical energy from the sun, it was found that the discounted and non-discounted payback period can be obtained in the 14th year and 11th year respectively, with an Internal Rate of Return (IRR) greater than the loan discount rate. Moreover, the greenhouse gas emission could be cut up to 68% compared to the conventional greenhouse. Thus, for the building and its system of 25 years lifespan, this is attractive and feasible to be financed.

Keywords: Discounted cash flow, greenhouse gas, IRR, NPV, Payback period

1. INTRODUCTION

An undertaking's monetary investigation is envisioned to determine the profit of an investment; appraising many alternatives to find the optimum use of resources while weighing its profit-cost ratio. Determining the behaviour of two types of costs, fixed and variable, in a greenhouse business is an ordinary way to find the relation between investment and profitability. Fixed costs are associated to the spent whether or not there is production, such as the investment building, equipment, property taxes, and legal bills. Whereas, variable costs in an economic analysis of a greenhouse are related to the production cycle, for instance, seeds, fertilizers and perlite bags.

Compared to the Return of Investment (ROI) method, DCF method is superior since the time value of money is incorporated. Moreover, DCF can estimate the future cash flow of the investment (Sinclair, 2010). The DCF development analysis requires the need to describe the scheme within which investment prices, operating cash flow in. Besides, the in-activity costs are calculated over the time period under scrutiny and processed in conjunction with various related. It means cash flow identification is needed. Therefore, some performance and economic analysis of cultivation greenhouses have been done.

A discounted life cycle cash flow analysis has been used on two solar kilns design for over 20 years' service life (Hasan et al., 2016). This financial analysis could determine the most profitable and environmentally beneficial of two different solar kilns. While another reference used the DCF analysis for an indoor sports arena building for 27 years (Copiello, 2016). Additionally, DCF analysis for the yield of crop inside the modified net house, PE covered greenhouse, and conventional net house has been done for 20 years lifetime (Sethi et al., 2009). It was found that modified net house produces the highest yield and the fastest payback period (5.2 years) compared to the conventional net house (6.5 years) and PE covered greenhouse (10.5 years). Furthermore, a financial analysis of a greenhouse and its modification has also been conducted in India (Banik & Ganguly, 2017). A novel scheme system of a desiccant assisted distributed fan-pad ventilated greenhouse to decrease the humidity was proposed for tropical and subtropical country. The net present value (NPV) and payback period calculation for 15 years resulted in $9090 and about 6 years, respectively.

The aforementioned greenhouse financial investigation merely assesses energy dependent building and its production. However, it is hard to find an investigation of financial on a greenhouse project which is purposed to be more independent in energy by using solar PV panel and seasonal underground heat storage. Therefore, the main focus of this analysis is to find the direct reimbursement of the investment in renewable technologies, thermal storage, and electrical saving benefit. Hence, the technologies considered for cost were not only photovoltaic panels and double glazing modules but also the Heat pump and the heat exchanger too.

The financial analysis uses DCF and non-DCF to find NPV, IRR, and the Payback period of the new system compared to the conventional greenhouse. Linked to this analysis, an environmental study was also performed to observe the reduction of carbon dioxide emissions with the utilization of renewable technologies. As described in energy efficiency section of the introductory chapter, the main strategy for climate change is directly related to the efficiency of energy. When improving the performance of some process, not only economical savings are being obtained but also fewer resources are being consumed, therefore, the emission of pollutants is minimal.

Regarding the environmental analysis, life-cycle assessment (LCA) is one of the effective methods to analyse the greenhouse gas (GHG) emissions of a particular heating system throughout its life cycle (Zheng et al., 2016). LCA is a standard assessment methodology for potential environmental and the impacts of the products and resources used against human health (Bartzas et al., 2015). LCA could assist decision-making, marketing by identifying the product improvements to the environmental performance in different life cycle stages (Curran, 2013; Islam et al., 2016; Brandão, 2017).

2. METHODOLOGY

The selected method of study was to determine the profitability of implementing passive and active technologies for production in agriculture industry (more specifically production using greenhouses) to determine the efficiency of the energy produced, against the cost of conventional energy resources.

2.1. Population/sample of the study

From the population of a full economic analysis; this study was performed only analysing the main mechanisms involved in the renewable energy production. Some variable costs and some fixed cost such as insurance for all building materials and its equipment were also been neglected. Also, costs of installation and transportation were avoided to facilitate the comparison between technologies. But consider the costs of maintenance annually for all system i.e. fan coil, Heat pump, while others vary such as inverter every 16 years, and cladding per 10 years as described in Table 4.

2.2. Location

For location purposes, all prices were presented in sterling British pound (GBP) currency. According to prices of electricity, the E.ON Company of electricity was considered for the city of Loughborough.

2.3. Limiting condition

The analysis was performed comparing two types of greenhouses with different configuration systems. Firstly, the conventional greenhouse using single glazing (SG), HPS lamps, and electric heaters, while the proposed greenhouse using double glazing (DG), Ground Source Heat Pump, solar photovoltaic panels, seasonal underground thermal storage, LED, and the supporting elements and equipment. The lifespan used in this study is 25 years.

In order to be fair, the electrical loads of both buildings are obtained by Energyplus simulation for a year using Nottingham weather data which is close to Loughborough. The design of the building can be found in (Harjunowibowo et al., 2017). The indoor temperature setting is 20 ^{o}C. Whereas, the PV's electrical generation is taken from the real annual data field.

2.4. Electricity pricing and GHG emissions per kWh

The price of electricity presents a wide variation between countries, and even between localities in the same country. In the case of UK, the price of electricity varies according to the location and provider. The cost of electricity is given by kWh and is determined by the cost of production. The tariff chosen for this analysis was E.ON Energy plan with a variable price given the inconstancy of the energy required according to the production obtained by PV installation. The unit normal rate is 14.140p per kWh for the city of Loughborough (EON, 2018). Given that all previous analysis was performed under climatological conditions of Loughborough.

Three stages of the study were followed in order to find all costs of electricity to compare. SG load refers to the electricity load required when the greenhouse cladding material is clear single glazing 6mm without thermal insulation and renewable electricity generation. DG load is the analysis case where the building has a double glazing insulation, in this case, it is triple wall Polycarbonate equipped with solar PV panels. The PV panels are installed around surrounding walls and rooftop.

The amount of GHG emitted to the atmosphere from electricity generated also present variations not only of its location but also according to the resources used, whether it is from coal, oil or natural gas, the amount emitted varies. In the case of the UK, most of the electricity is generated from fossil fuel burning a 30% of natural gas, 23% of coal and less than 1% from oil (DBEIS, 2017a). In this calculation, a total amount of greenhouse gas factor of 0.38443 was used (DBEIS, 2017b). Electricity prices will rise by 13.8% in 2018 (UKPower, 2018). The UK discount rate is assumed 6.9% for 8 years payback of loan (uSwitch, 2018).

2.5. Evaluation of Economics Assessment

The Net Present Value (NPV) expresses the sum of all the ingoing and outgoing cash flows, once they have been discounted at a given discount rate. The NPV formula is governed by Equation 1 (Osborne, 2010):

$$NPV = CF_o + \sum_{i=1}^{n} \frac{CF_i}{(1+r)^n} \quad (1)$$

where CF is the sum of the net cash flow or cash balances, which in turn overall form the cash flow in order to be discounted at the rate r, while i reflects each time unit of analysis throughout the time span n.

Moreover, the Internal Rate of Return (IRR) represents a relative measure of the profitability has the property to make null the NPV (Copiello, 2016). In other words, the IRR is the highest possible discount rate when NPV=0 at the end of the lifecycle. IRR is also crucial for the estimate of the upper level of interest rate for the loan. Appropriately, the higher the IRR value, the more possibilities exist to determine the requisite amount of investment expense on the market. Besides, the higher the value of IRR and the difference (IRR – r), the higher value of NPV and the more stable is the project (lesser risks) (Kharitonov & Kosterin, 2017). The IRR formula is governed by Equation (2 (Osborne, 2010):

$$IRR = CF_o + \sum_{i=1}^{n} \frac{CF_i}{(1+r)^n} = 0 \quad (2)$$

If NPV > 0 and IRR > r meaning the investment generates profit and is feasible to do. Additional burdens may be charged to the project until the NPV close to zero. Therefore, the project does not generate profit if NPV = 0 and IRR = r, so-called discounted cash flow payback period. Furthermore, if NPV < 0 and IRR < r then the project is not recommended to be funded since it losses.

2.6. Cost analysis of equipment

The renewable energy production equipment of the greenhouses is shown in Table . The prices were obtained from the manufacturer companies and distributors in 2015, therefore prices are subject to variation.

Table 1: Greenhouse cost analysis

Unitary prices	Sterling Pounds £	Unit	Area	Quantity	Total £
Ground-source Heat Pump 5 kW	6,631	Piece		1	6,631
Flexi type fan coil unit	1,762	Piece		1	1,762
200 litres heat pump water tank storage	1,080	Piece		1	1,080
Pump 240V	240	Piece		2	480
278W LED grow lights - Aluminum	299.95	Piece		20	5,999
HPS Poultry/Greenhouse Light - 150 Watt	86.91	Piece		20	1,738
a-Si Photovoltaic Module	165	m^2	49	34	5,610
Inverter 2.5-1 165-440V 50/60Hz 2.5KW	1,530	Piece		4	6,120
Solar Panel 265 W	150	Piece		26	3,900
5Kw portable industrial electric fan heater	119	Piece		2	238
Structure					
Seasonal Heating: Insulation foam, 24 pcs double pipe heat exchanger, piping					1,000
Stainless Steel Structure					21,642
Cladding					
Polycarbonate sheet-Clear-16 mm	32.26	m^2		86	2,774
Single Glazing - Clear - 6mm	70.20	Panel		48	3,370
Total cost (excluding labour)	5X polycarbonate Total				56,998
	Single Glazing walls Total				26,988
building maintenance (5%) - discount of 25%	5X polycarbonate Total				17,099.51
	Single Glazing walls Total				8,096.35
VAT (20% of profit)	5X polycarbonate Total				3,419.90
	Single Glazing walls Total				1,619.27
Total capital cost + Labour (assume 10% total cost)	5X polycarbonate Total				51,868.51
	Single Glazing walls Total				24,558.93

3. RESULTS AND DISCUSSIONS

This economic study was performed for both configurations and presented in two results. Firstly, time of investment payback comparing the cost of technology against the savings occurred from electricity output. Secondly, the total amount of profit obtained from the implementations made after paying the equipment; considering a lifetime of 25 years.

3.1. Specifications

In Table 2, it shows the prices related to the first two cases of load requirement, the amount of electrical load required to achieve comfort temperatures for both cases and the cost of electricity that should be paid. The SG load case represents a case where an owner of a greenhouse without any thermal improvements has to pay. The second, DG is the amount of electricity that is required to fulfil from the renewable PV modules in order to evaluate the electricity production.

Table 2: Cost analysis of kWh for cases SG and DG load

Month	SG load			DG load		
	Electrical load kWh	Cost GBP	GHG Kg/kWh	Electrical load kWh	Cost GBP	GHG Kg/kWh
Jan	3,006.76	£425.16	1,155.89	839.73	£118.74	322.82
Feb	2,508.36	£354.68	964.29	699.43	£98.90	268.88
Mar	2,035.08	£287.76	782.34	601.16	£85.00	231.11
Apr	1,507.79	£213.20	579.64	459.86	£65.02	176.79
May	835.18	£118.09	321.07	337.13	£47.67	129.60
Jun	595.45	£84.20	228.91	258.61	£36.57	99.42
Jul	282.32	£39.92	108.53	225.87	£31.94	86.83
Aug	407.63	£57.64	156.70	257.11	£36.36	98.84
Sep	854.13	£120.77	328.35	347.53	£49.14	133.60
Oct	1,582.89	£223.82	608.51	506.87	£71.67	194.85
Nov	2,343.56	£331.38	900.93	690.01	£97.57	265.26
Dec	2,927.85	£414.00	1,125.55	831.62	£117.59	319.70
Total	18,886.98	£2,670.62	7,260.72	6,054.92	£856.17	2,327.69

In Table 3, it shows the breakdown of elements analyses observing that the benefit of applying PV has a total saving of £2,487.32 in the first year. When considering a lifetime of 25 years, the implementation of this renewable technology can produce an annual gain of £672.87 from electricity generated by the greenhouse cladding elements. For the total capital cost of £51,868.51 for the proposed system, the discounted payback period could be achieved in 14.3 years. While for non-discounted payback period takes 11 years only as can be seen in Table 4.

Table 3: Money saving analysis

	Unit	Amount
The energy required for initial loads	KWh	18,886.98
Annual cost from conventional GH	GBP	2,670.62
· Annual electricity purpose greenhouse		
The annual energy required for loads	KWh	6,054.92
Annual energy supplied by PV	KWh	4,758.60
Total annual energy is taken from the grid	KWh	1,296.32
· Cost of electricity		
Cost of electricity per KWh	GBP	0.14
Total paid for electricity from the grid without renewable energies	GBP	856.17
Total paid for electricity from the grid with renewable energies	GBP	183.30
Annual total saved	GBP	672.87
Annual saved compare to conventional GH	GBP	2,487.32

The bar chart in Figure 1 reveals the monthly electrical bill produced by the conventional and renewable system for heating and cooling. Since the high U-value of single glazing, it has a big impact on the energy consumption of the conventional system. Compared to the renewable system which is equipped with low U-value double glazing and high-efficiency ground source heat-pump, there is a big difference. The electricity intake from the PV panels adds a remarkable saving as shown in Figure 2 and Figure 3.

Figure 4 shows that the payback period for both methods have rocketed exponentially. For the 25 lifespan, the proposed system could gain profit higher than the investment cost. Since the payback period is calculated with not taken into account of crops yield, then a shorter payback period could be achieved.

Table 4: Payback period calculation based on UK loan discount rate

Year	Cash flow in	Cash flow out	Net Cash flow (FV)	Present Value	Discounted Payback Balance	Non-Discounted Payback Balance
0	-£51,868.51	£0.00	-£51,868.51	-£51,868.51	-£51,868.51	-£51,868.51
1	£2,487.32	£209.00	£2,278.32	£2,131.26	-£49,737.25	-£49,590.19
2	£2,830.57	£209.00	£2,621.57	£2,294.07	-£47,443.18	-£46,968.62
3	£3,221.19	£209.00	£3,012.19	£2,465.75	-£44,977.43	-£43,956.43
4	£3,665.71	£209.00	£3,456.71	£2,646.99	-£42,330.44	-£40,499.72
5	£4,171.58	£209.00	£3,962.58	£2,838.50	-£39,491.94	-£36,537.14
6	£4,747.26	£209.00	£4,538.26	£3,041.05	-£36,450.89	-£31,998.88
7	£5,402.38	£209.00	£5,193.38	£3,255.41	-£33,195.48	-£26,805.50
8	£6,147.91	£209.00	£5,938.91	£3,482.45	-£29,713.03	-£20,866.60

9	£6,996.32	£209.00	£6,787.32	£3,723.05	-£25,989.98	-£14,079.28
10	£7,961.81	£2,983.36	£4,978.45	£3,978.16	-£23,435.41	-£9,100.83
11	£9,060.54	£209.00	£8,851.54	£4,248.78	-£19,186.63	-£249.29
12	£10,310.90	£209.00	£10,101.90	£4,535.97	-£14,650.66	£9,852.61
13	£11,733.80	£209.00	£11,524.80	£4,840.87	-£9,809.79	£21,377.41
14	£13,353.06	£209.00	£13,144.06	£5,164.66	-£4,645.13	£34,521.47
15	£15,195.79	£581.00	£14,614.79	£5,371.89	£726.75	£49,136.26
16	£17,292.80	£710.00	£16,582.80	£5,701.84	£6,428.59	£65,719.06
17	£19,679.21	£209.00	£19,470.21	£6,262.53	£12,691.12	£85,189.27
18	£22,394.94	£209.00	£22,185.94	£6,675.43	£19,366.55	£107,375.21
19	£25,485.44	£209.00	£25,276.44	£7,114.42	£26,480.97	£132,651.66
20	£29,002.44	£3,463.36	£25,539.08	£7,454.84	£33,205.33	£158,190.73
21	£33,004.77	£209.00	£32,795.77	£8,077.67	£41,283.00	£190,986.50
22	£37,559.43	£209.00	£37,350.43	£8,605.70	£49,888.70	£228,336.93
23	£42,742.63	£209.00	£42,533.63	£9,167.38	£59,056.08	£270,870.56
24	£48,641.11	£209.00	£48,432.11	£9,764.92	£68,820.99	£319,302.68
25	£55,353.59	£209.00	£55,144.59	£10,400.64	£79,221.64	£374,447.27
NPV				£79,221.64		
IRR				13.83%		
Discounted Payback period					14.32 Years	
Non-Discounted Payback period						11.02 Years

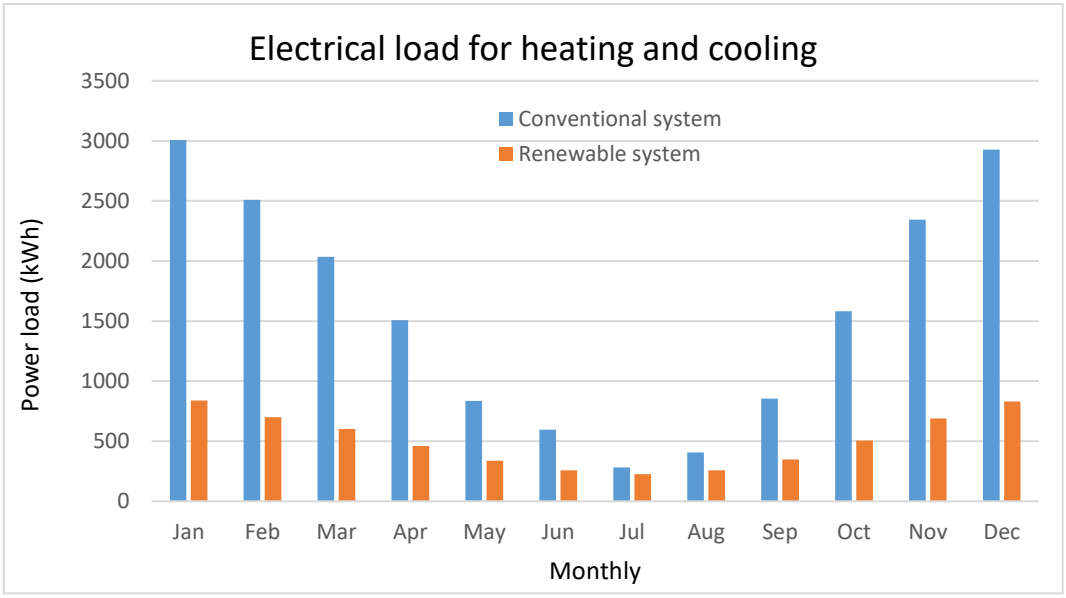

Figure 1: Average electrical loads needed by the buildings per year

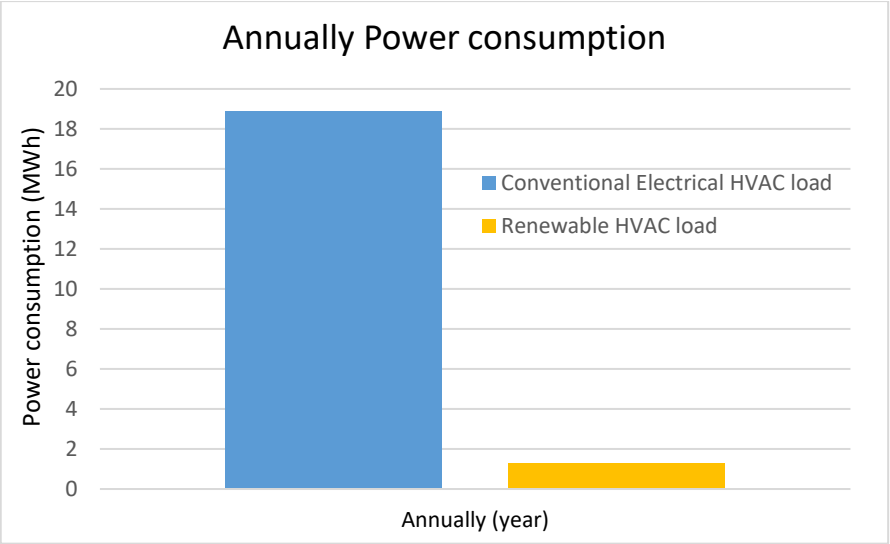

Figure 2: The annual average power consumption of the buildings

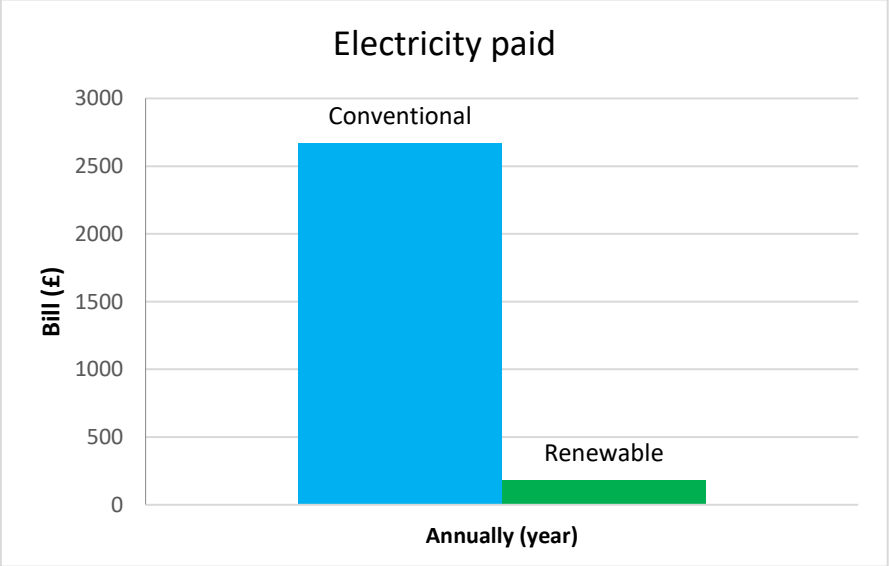

Figure 3: Electric bills paid by both buildings per year

3.2. Environment analysis

The UK Government issued policies at earth protecting by diminishing GHG by means of 80% up to 2050 (DECC, 2015). Therefore, the LCA is conducted to assess the impact of the renewable greenhouse system to its environmental and human health. The LCA calculation is based on the desired temperature by utilizing electrical power and natural gas resource. Focusing on the third quarter in the UK, Figure 5 reveals that the total electricity generated in 2017 was 74.4 TWh lower than in 2016 by 2.2 %, while gas reached a record low of 39.10 % of total generation (down 4pp) in Q3 2017. The reduction is a consequence of nuclear and non-thermal renewable energy supply increasing. Renewables generation moved up 8.9 %, primarily thanks to solar and wind capacity increasing.

Furthermore, the total energy production was 28.6 million tonnes of oil equivalent in 2017, 2.8 % lower than in 2016 as shown in Figure 6. Because of low production levels in August and September 2017, the gas production dropped by 10.7 % compared to in 2016. Moreover, primary electricity output of 2017 was lower than in 2016 by 0.3 %, meanwhile, the output from renewable was 11.9 % higher than the same period in 2016.

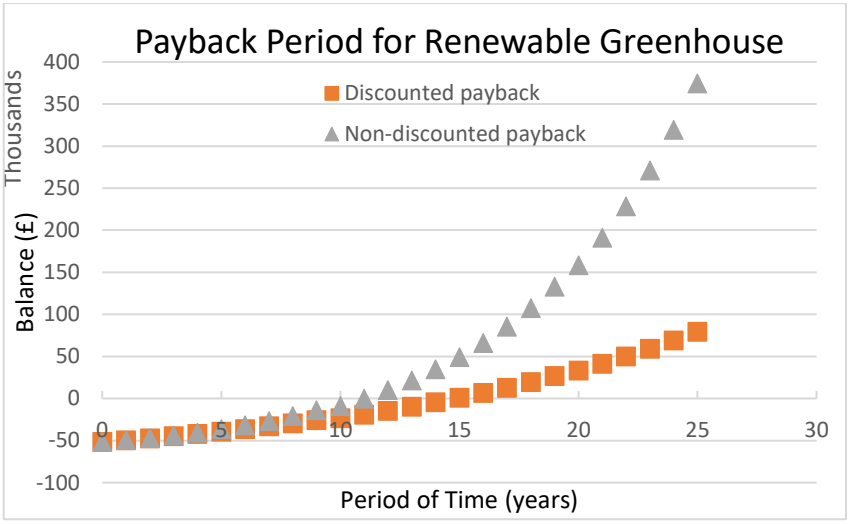

Figure 4: The payback period for the proposed greenhouse in 25 years lifespan

For electricity consumed (includes grid losses), the electricity generation emission factors respectively from CO_2, CH_4, N_2O, are 0.39108, 0.00070, and 0.00234 (DBEIS, 2017b). In this calculation, a total amount of greenhouse gas factor of 0.38443 was used. While for natural gas, the heat generation emission factor from CO_2e, CO_2, CH_4, and N_2O are 0.20463, 0.20423, 0.00029, and 0.00011, respectively. Therefore, the total amount of the emission factor for the calculation is 0.40925 (DBEIS, 2017c). Based on the calculation, a reduction of 68% GHG can be achieved for the greenhouse's second configuration as shown in Table 2.

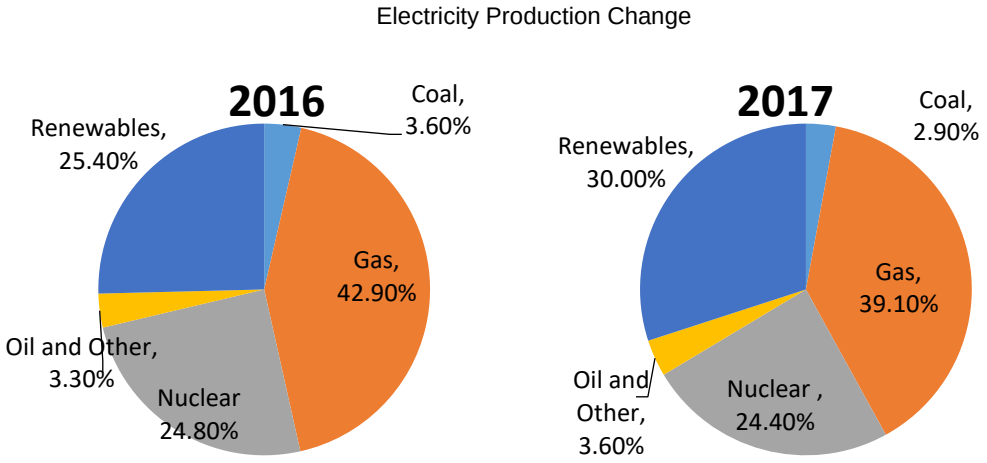

Figure 5: The electricity source composition in quarter 3 (DBEIS, 2017a)

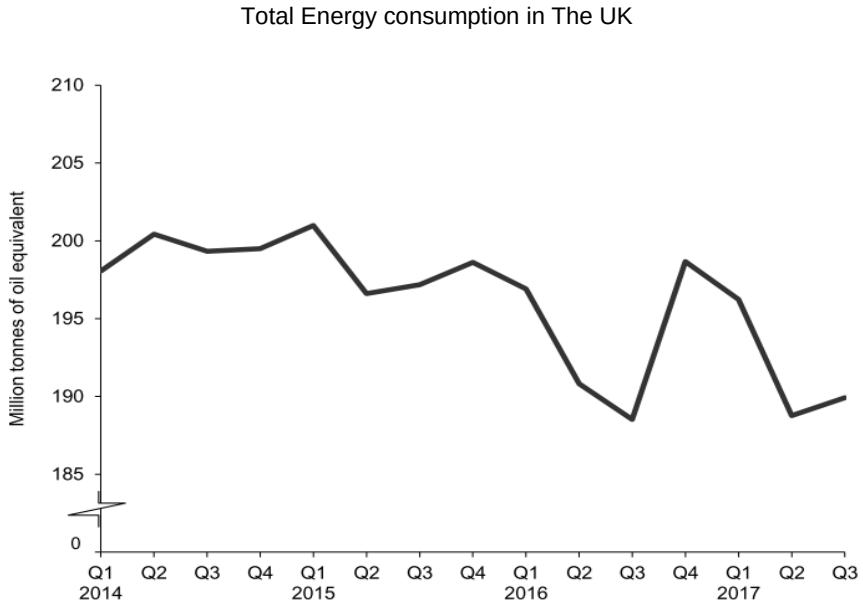

Figure 6: The UK energy consumption (DBEIS, 2017a)

4. CONCLUSIONS AND RECOMMENDATIONS

The observed results are in substantial agreement with the expected from the difference in costs of both technologies, given that the greenhouse proposed systems have a considerably reduced price. In an industry which main cause of money outflow is constituted by variable costs, the implementation of renewable technologies with a short payback time economically is attractive. Furthermore, it can be observed that the feasibility to generate electricity for an “active energy used greenhouse” has not only an economic profit but also allowing to optimise land by locating the electricity generation technologies in the cladding elements of the greenhouse.

It was found that the discounted and non-discounted payback period can be obtained in the 14th year and 11th year respectively, with an IRR greater than the loan discount rate. Moreover, the greenhouse gas emission could be cut up to 68% compared to the conventional greenhouse. Therefore, the proposed greenhouse has potential to be a zero-energy greenhouse in terms of energy, environmental-friendliness, and reduce the greenhouse gas emission in harmony with government policy.

5. ACKNOWLEDGEMENT

The authors would like to greatly acknowledge to Innovate UK, DIKTI Scholarship and Doctoral Grant UNS No.623/UN27.21/PP/2017, for their funding support.

6. REFERENCES

Banik, P. & Ganguly, A. , 2017. Performance and economic analysis of a floricultural greenhouse with distributed fan-pad evaporative cooling coupled with solar desiccation. *Solar Energy*. 147:439–447. DOI: 10.1016/j.solener.2017.03.057.

Bartzas, G., Zaharaki, D. & Komnitsas, K. , 2015. Life cycle assessment of open field and greenhouse cultivation of lettuce and barley. *Information Processing in Agriculture*. 2(3–4):191–207. DOI: 10.1016/j.inpa.2015.10.001.

Brandão, M. , 2017. Hybrid life cycle assessment (LCA) does not necessarily yield more accurate results than process-based LCA Article in Journal of Cleaner Production · March 2017. *Journal of Cleaner Production*. 150(March):e167–e168. DOI: 10.1016/j.jclepro.2017.03.006.

Copiello, S. , 2016. A Discounted Cash Flow variant to detect the optimal amount of additional burdens in Public-Private Partnership transactions. *MethodsX*. 3:195–204. DOI: 10.1016/j.mex.2016.03.003.

Curran, M.A. , 2013. Life Cycle Assessment: A review of the methodology and its application to sustainability. *Current Opinion in Chemical Engineering*. 2(3):273–277. DOI: 10.1016/j.coche.2013.02.002.

DBEIS., 2017a. *UK Energy Statistics, Q3 2017*. London. Available: https://www.gov.uk/government/uploads/system/uploads/attachment_data/file/669764/Press_Notice_December_2017.pdf.

DBEIS. , 2017b. *2017 government GHG conversion factors for company reporting: methodology paper for emission factors*.

DBEIS., 2017c. *Greenhouse gas reporting - Conversion factors 2017*. Available: https://www.gov.uk/government/collections/government?conversion?factors?for?company?reporting.

DECC., 2015. *Government response to the Committee on Climate Change. Progress on meeting carbon budgets and preparing for climate change - Summary Document*. London.

EON, U. , 2018. *Our gas and electricity tariffs*. Available: https://www.eonenergy.com/for-your-home/products-and-services [2018, March 29].

Harjunowibowo, D., Yate, D., Omer, S.A. & Riffat, S.B. , 2017. Reducing Greenhouse Energy Consumption using Novelty Rooftop: A Simulation. In *16th International Conference on Sustainable Energy Technologies – SET 2017*. bologna. 1–10.

Hasan, M., Zhang, M., Wu, W. & Langrish, T.A.G. , 2016. Discounted cash flow analysis of greenhouse-type solar kilns. *Renewable Energy*. 95:404–412. DOI: 10.1016/j.renene.2016.04.050.

Islam, S., Ponnambalam, S.G. & Lam, H.L. , 2016. Review on life cycle inventory: methods, examples and applications. *Journal of Cleaner Production*. 136:266–278. DOI: 10.1016/j.jclepro.2016.05.144.

Kharitonov, V.V. & Kosterin, N.N. , 2017. Criteria of return on investment in nuclear energy. *Nuclear Energy and Technology*. 3(3):176–182. DOI: 10.1016/j.nucet.2017.08.006.

Osborne, M.J. , 2010. A resolution to the NPV-IRR debate? *Quarterly Review of Economics and Finance*. 50(2):234–239. DOI: 10.1016/j.qref.2010.01.002.

Sethi, V.P., Dubey, R.K. & Dhath, A.S. , 2009. Design and evaluation of modified screen net house for off-season vegetable raising in composite climate. *Energy Conversion and Management*. 50(12):3112–3128. DOI: 10.1016/j.enconman.2009.08.001.

Sinclair, D.R. , 2010. Capital budgeting decisions using the discounted cash flow method. *Canadian Journal of Anesthesia/Journal canadien d'anesthésie*. 57(7):704–705. DOI: 10.1007/s12630-010-9304-6.

UKPOWER. , 2018. *What will the latest energy price hikes mean for you?* Available: https://www.ukpower.co.uk/gas_electricity_news/energy-price-hikes [2018, March 29].

USWITCH. , 2018. *Compare loans*. Available: https://www.uswitch.com/loans/ [2018, April 16].

Zheng, M., Fang, R. & Yu, Z. , 2016. Life Cycle Assessment of Residential Heating Systems: A Comparison of Distributed and Centralized Systems. *Energy Procedia*. 104:287–292. DOI: 10.1016/j.egypro.2016.12.049.

237: Optimisation of hierarchical protection and control system for Smart Substation

Shiyi XIAO[1,3],Tiezhou WU[1,2], Fanfan YANG[3], Linxin GUO[1,2], Yan LI[1], Yueyang WANG[4]

1 School of Electrical and Electronic Engineering, Hubei University of Technology, Wuhan 430068, 348371285@qq.com.
2 Hubei Collaborative Innovation Center for High-efficiency Utilization of Solar Energy, Hubei University of Technology, Wuhan 430068,348371285@qq.com.
3 Anqing power supply company,Anqing,246003,348371285@qq.com.
4 Sifang Protection (Wuhan) Software Ltd., Wuhan,246003,348371285@qq.com.

1. INTRODUCTION

In recent years, the domestic smart substation construction rapidly, as well as technology development. From the first generation of smart substation to a new generation of smart substation, new technology and new equipment in the secondary system continuously introduced, in which hierarchical protection control system is a novel. Integrated application of smart substation hierarchical protection control system refers to the power cut data information, through the distribution and coordination of function configuration, realize the coordination of time dimension, spatial dimension and functional dimensions, implements the transfer of protection control information from the single point to multipoint, from components oriented to the system oriented, from object-oriented to function-oriented, enhance protection reliability, sensitivity and selectivity, ascension performance of grid relay protection and control system (Song 2014).Hierarchical protection is a multidimensional hierarchical relay protection system based on local protection layer and coordinated between station area and wide area protection. Among them, the local protection layer technology is oriented to the protection of a single protected object. It makes independent decisions with the information of the protected object and realizes reliable and rapid removal of the fault. Station area protection control for substation using multiple objects within the station of voltage, current, switch and status information of regional protection device, realize the protection of redundancy and optimisation, and improve the safety of the substation level automatic control function. Wide area protection is oriented to regional power grid (multiple substations). It makes use of the comprehensive information of multiple stations, makes unified judgment and decision, and realizes related protection and stability control. These three layers of protection connect with each other in space and time, which can realize the cooperative control of protection and the coverage of the whole range protection function of power grid (Gao 2012).

2. ARCHITECTURE OF HIERARCHICAL PROTECTION CONTROL SYSTEM

2.1. Design of system architecture

Hierarchical control system configures multiple protection on ground level protection, station area protection and

Smart substation is an important part of smart grid. The safe and stable operation of the grid cannot be separated from the protection equipment. Therefore, it is necessary to optimise the protection control system of substation. Hierarchical protection of power grid includes three levels: prefecture level protection, station area protection and wide area protection. The technology of hierarchical protection is the inevitable product of smart grid development process which is characterized by informatization, automation and interaction. Compared with traditional relay protection, the system has great changes in principle and implementation mode, and its performance also has great progress. In this paper, a new generation of Smart substation hierarchical protection control system architecture is discussed. And the configuration scheme and coordination scheme are proposed to achieve the coordination and unity of relay protection and safe control, in order to adapt to the trend of power grid interconnection and complex, changeable operation requirements. Combining with a practical case of 110kV substation, this paper analyses the protection configuration scheme at prefecture level and station level, and puts forward the optimisation and integration scheme of interval layer equipment and process layer equipment.

Keywords: Smart substation; Hierarchical protection; Prefecture level protection; Station area protection

wide-area protection in time dimension, space dimension, function dimension.

2.2. In the time dimension

There is no delay action (20~30ms) for all kinds of primary protection in local protection, and the reserve protection realizes mutual cooperation through piecewise delay. In order to meet the selectivity and reliability, the rapidity of protection (0.8~1.2s) is sacrificed. Station area and wide area protection control uses comprehensive information to accelerate local reserve protection (0.3~0.5s). Coordination and cooperation of protection and stability control at all levels (Cai 2014). Coordination of protection and stability control at all levels to improve relay protection performance and stability control level, as shown in Figure1.

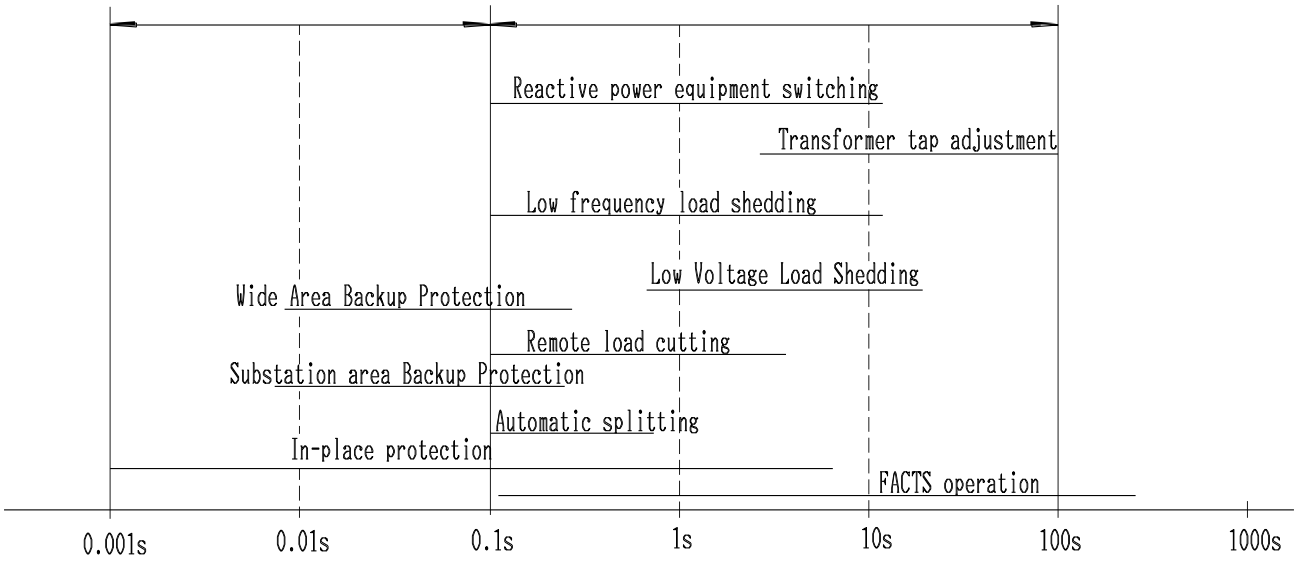

Figure1: Time distribution of relative functions of hierarchical protection & control system

2.3. In the spatial dimension

Local protection realizes "close-in defense" against a single object; Station protection and control integrated use of information within the station to achieve integrated defense within the station; Wide area protection and control integrated use of inter-station information to achieve comprehensive defense of the entire network. The combination of hierarchical protection and control points realizes the comprehensive protection of regional power grid.

2.4. In the functional dimension

Local protection aims to isolate fault elements quickly and reliably, and makes independent decisions with the information of individual components, so as to achieve rapid and reliable component protection. Station area protection control to optimise control configuration, improve protection control system performance, for the purpose of using total station information centralized decision-making, realizes the flexible and adaptive bus protection, failure protection, components and implement reserve protection for the shoot, low cycle/low voltage load shedding control function (Zheng 2014). Wide-area protection control in order to improve the system stability control automatic and intelligent level, for the purpose of using a substation panoramic data information within the region to implement wide area reserve protection, protection fixed value adjustment, optimising control strategy, implementation of protection and control in the area of coordination.

3. HIERARCHICAL PROTECTION CONTROL CONFIGURATION SCHEME

3.1. Configuration scheme on the ground level

Based on the existing protection configuration scheme, the ground level protection should be as close as possible to the primary equipment layout and installed in the local outdoor cabinet, the integrated control cabinet or the prefabricated equipment compartment.

(1) 220kV and above voltage grade lines are equipped with independent protection functions according to the principle of dual-use, and 110(66) kV voltage grade is equipped with protection functions according to a single set. The line protection device should be arranged in the local outdoor cabinet or sink control cabinet to protect the direct mining jump. When conventional transformer is used, the protection can be sampled directly by cable. When the protection function is integrated with the integrated design of combination unit and intelligent terminal, the local

protection can only be configured with the main protection function, and the reserve protection function is realized by the station domain protection.

(2) 220kV and above voltage grade lines are equipped with independent bus protection function according to the principle of dual-use, and 110(66) kV voltage grade is equipped with bus protection function according to a single set. The protection device is arranged in the prefabricated equipment cabin, which can be adopted by network trip on the premise of ensuring reliability and quick operation.

(3) 220kV and above voltage grade lines are equipped with independent main reserve protection function of transformer according to the principle of dual-use. 110(66) kV voltage grade is configured with single set of protection function, and main protection is separated with reserve protection. The equipment should be arranged in the prefabricated equipment compartment when the main and rear integration configuration is made. Reserve protection will appropriate change arrangement in outdoor cabinet on the spot while main protection equipment cabin layout in precast type when protection is separated.

3.2. Configuration scheme on substation-area level

220kV and above voltage grade adopted the protection configuration, the doubling of substation area differential protection configuration principle reserve protection, cooperate with in situ protection to accelerate the reserve protection action. Overloading, low frequency and low voltage load reduction are realized by using station domain information optimisation (Li 2011). 110kV and below voltage levels are equipped with a single set of protection configuration, and the station domain protection is equipped with main protection of each element to realize asymmetric redundancy of protection. Also equipped with differential principle of station area reserve protection and overloading, low frequency, low voltage load reduction control functions. The function configuration of the substation-area protection and control is shown in table 1.

Table 1: Function configuration of substation-area protection & control

Number	classification	functional module	Functional description
1	Redundancy protection	Line protection, main transformer protection, busbar protection, sectional protection.	Redundancy as a single set of configuration protection
2	Optimised reserve	Fast fault location	Fast fault location based on multi-point information, with local protection to accelerate fault removal.
		110kV failure protection	Failure protection function of circuit breaker
		35 (10) kV bus protection	Simple busbar protection based on GOOSE information
3	Automatic safety control	Low cycle low pressure load reduction	Integrated low cycle low voltage load shedding function to optimise load shedding strategy
		Station domain preparation	Voltage grade in the station
		Overloading of main transformer	Overload connection of main transformer and average load distribution
4	Wide area protection control	Wide area protection control sub station	Station information collection, processing, sending, wide area information check and execution.

The station area protection control device is arranged in the precast equipment cabin or the two equipment room, and the single set is configured.

3.3. Configuration scheme on wide area

Wide area protection control is oriented to the regional power grid. Its functions include 2 aspects: relay protection and automatic safety control. The wide area protection is equipped with the reserve protection of the differential principle and completes the reserve protection of the connection lines between substations; the wide area control has the functions of power network topology analysis, power flow analysis, reserve protection fixed value adjustment, stable prediction, emergency control and so on (Wang 2013). The typical functional configuration of wide area protection control is shown in Table 2.

Table 2: Function configuration of wide area protection & control

Number	classification	functional module	Functional description

1	protection	Accurate fault location	Fast fault location based on multi-point information and acceleration with the protection of junction area to remove the obstacle.
		Wide area reserve protection	Using differential principle to locate faults and optimise local reserve protection
		Adaptive fixed value	Adaptive calculation based on system operation mode and topology change.
2	Low cycle low pressure load reduction	Low cycle low pressure load reduction	Optimisation of load cutting strategy
		Coordination of protection and security	Prevention of blackout, cutting load and cutting load
		Stability assessment and political and police officers	Observation of the state of the power grid, automatic evaluation and early warning

4. MAIN FEATURES OF THE HIERARCHICAL PROTECTION AND CONTROL SYSTEM

1) Functional stratification to improve the overall performance. In order to improve the selectivity, speed and reliability of the reserve protection, the coordination of protection action is improved by the coordination of the local protection, the substation area reserve protection and the wide area reserve protection. Substation area protection and wide area protection increase the redundancy of protection configuration, especially for 110kV and below voltage level substations.

2) Local protection for individual components and equipment protection. When the conditions are allowed, the equipment can be protected near a equipment arrangement, the secondary wiring is simplified, the speed of the operation is fast, the secondary equipment is strong, and the maintenance is easy. It is beneficial to the modular design and installation (Song 2013). On the other hand, for low voltage level components (such as 35kV system), the protection can be integrated, one device can protect multiple intervals, simplify the network structure in the station, and reduce operation and maintenance.

3) The substation area protection control is oriented to function, so as to enhance the protection and control performance of substation. Using the advantage of information sharing (such as avoiding the impact of TV and TA on protection by the sharing of adjacent TV and TA data), it can improve the reliability and speed of protection, and also develop the protection strategy of multiple criteria decision. For different voltage level substations, the station domain functions are integrated with control functions such as self-switching, small current grounding line selection, low cycle / low voltage load reduction and so on, reducing two equipment layout and optimising control strategy.

4) Wide area protection controls global optimisation and to achieve coordination between protection and stable control. Reserve protection based on wide area information can realize line reserve protection within the scope of regional power network and improve the speed and selectivity of reserve protection. For the wide area reserve protection of 110kV system, it has second reserve protection functions, which adds redundancy of protection. The operation state of the power grid is analysed and evaluated using the panoramic data information of each substation, and the effect of the fault removal on the safety and stability of the system is analysed, and the corresponding control measures are taken to achieve the coordination and optimisation of the relay protection and automatic control function. In case of cascading failures, coordinate protection devices (Li 2013).

5. APPLICATION EXAMPLES

The electrical main wiring diagram of one 110kV substation is show in Figure 2. The high voltage side is inner bridge connection, and the low voltage side is single bus section connection. The substation area protection needs the reserve protection of the station area. Now let’s further analysis the configuration scheme of the substation.

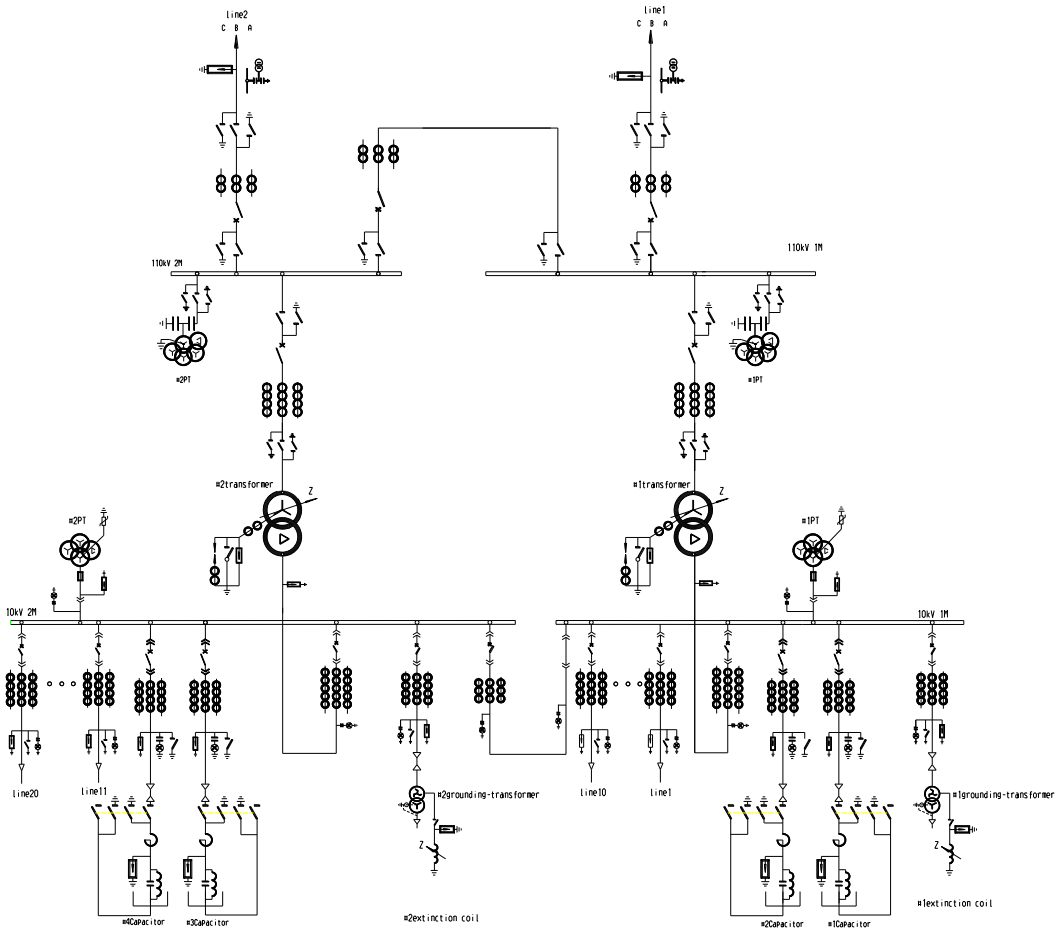

Figure 2: The electrical main wiring diagram of a 110kV substation

5.1. Local protection configuration

There are two transformers in this station, the protection of transformer is protected by micro type protection device. Each transformer is set up with one main transformer protection cabinet and one main transformer body intelligent control cabinet. The transformer protection cabinet is arranged in the secondary equipment room. The main transformer's intelligent control cabinet is placed near the main body of the main transformer.

The main transformer body intelligent control cabinet is equipped with one integrated device and two integrated units of the intelligent terminal for non-electric power protection. Differential protection is the main protection. The reserve protection on the high voltage side has the overcurrent protection in the direction of compound voltage lock, the overcurrent protection of compound voltage lock and the overload protection (Chen 2014). In addition, two stages zero-sequence over-current protection and gap zero-sequence over-current and over-pressure protection are installed on the high-voltage side. The low-voltage side is equipped with a two-stage compound voltage lock over current protection. The intelligent control cabinet of the main transformer body is arranged beside the main transformer to realize the measurement, control and non-electric power protection of the main transformer body, load regulating switch, neutral point isolating switch, etc.

The 10kV utility line, capacitor and grounding transformer are installed in the corresponding switchgear by microprocessor-based protection and measurement and control integrated device. Protection of 10kV lines are equipped with three stages of interphase current protection, overcurrent protection, reclosing, low cycle load reduction and other functions; 10kV capacitor protection is equipped with three stages of interphase current protection, open triangle voltage protection, overvoltage and voltage loss protection functions; 10kV grounding transformer station variable protection configuration micro current quick break protection, overcurrent protection (Li 2013).

The transformer protection sampling and tripping adopt the "direct sampling direct jump" mode. The main transformer differential and reserve integrated protection devices with dual configuration are respectively connected to A and B merging units. The switch quantity of the fault recording device, the GOOSE message of the fault signal and the SV message of the sampled value are all transmitted by the process layer network, and the 110kV self-

input device adopts the " direct sampling direct jump " mode, and the other GOOSE message information is transmitted by network mode (Yin 2012).

5.2. Station area protection configuration

110kV and below substation area protection, integrated centralized reserve protection function, to achieve redundant configuration. The station area protection configuration of 110kV substation is as follows:

1) The two lines of 110kV protection (include distance protection, over current protection and reclosing function and so on).

2) Overcurrent protection of 110kV bus.

3) Protection of The 10kV lines (include overcurrent protection, reclosing function and so on).

5.3. Wide area protection configuration

Wide area protection control of 110kV and the below voltage level include the function focuses on the relay protection of the local grid, the main station can be set in the 110kV substation or the 220kV and above voltage grade substations. When the main station is set up in the 220kV substation, the mainframe and the substation of the field protection layer are only oriented to the voltage level of 110kV and the following station and the related power grid outside the station, and the main station of the protection host and the stability control system is configured independently (Liu 2010).

In order to ensure the reliability of the operation, two sets of wide area layer protection and control hosts should be configured, two sets of machines run at the same time and alternate with each other. One is able to perform the protection and control functions while a set of failures, overhaul or off-line configuration occurred, the other one is still able to perform the protection and control functions on line.

6. CONCLUSION

In view of the new function and performance requirements of relay protection for the development of smart grid, a protection scheme for regional power grid is proposed in this paper, the hierarchical protection control system. The hierarchical protection system is an innovation to the protection device, which can not only quickly remove the fault, but also solve the change of the reserve protection easily by the operation mode (Xu 2009). Due to the problems of coordination and long action time, the wide area protection can also serve as main protection which enrich the protection system. With the new generation of smart substation related technology exploration and application, the smart substation hierarchical protection system will be further promoted and applied. A complete and sound hierarchical protection system will play a prominent role in building the line of security and stability of the power grid.

7. REFERENCES

Song, X, Liu, K, (2014).New Generation Research and Design of the New Generation Smart Substation[M].Beijing,China Electric Power Press,

Gao D, Zhi Q, Zhu L, (2012) .Research on protection configuration scheme of Smart Substation[J],power system protection and control,40(1),68-71.

Cai Y, Zhang D, Meng B, (2014).Technology and Engineering Application of the New Generation of Smart Substation[M],Beijing,China Electric Power Press.

Zheng Y, (2014).Secondary Device and Technology of Smart Substation[M],Beijing,China Electric Power Press.

Li Z, Yin X, Zhang C, (2011). System Construction and Fault Identification of Wide Area Protection in Subarea.Construction and fault identification [J]. Journal of Chinese lectrical Engineering Science, 31 (28): 95- 10.

Wang Y, (2013). Research of the Hierarchical Protection System Based on Smart Substation[J]. NORTH CHINA ELECTRIC POWER.09,27-30.

Song X, Li Y, Li J et al (2013).Hierarchical Protection & Control System for New Generation Smart Substation [j].Electric Power Construction.34(7),24-29.

Li Y, (2013). Study on the scheme & Reliability of Hierarchical Protection and Control System for New Generation Smart substation [D]. Beijing: Beijing Jiaotong University.

Chen G, Zhang, Z, Yin X, (2014). Design on hierarchical system for relay protection Net Topology Structure [J]. Power System Protection and Control, 40 (4),63-70.

Li Z, (2013) Study on Construction Mode and Key Technologies of Smart Grid Hierarchical Protection[D].Wuhan,Huazhong University of Science and Technology.

Yin X, LI Z, LIU Y, LIU B, (2012). Discussion on wide area relay protection and fault elements identification[J].Power system protection and control, 40 (5): 1 - 9.

Liu Z, (2010). Smart grid technology[M].Beijing:,China Electric Power Press.

XuT, Yin X, You D, et al, (2009). Analysis of System Function and Feasible Structure for wide area protection [J].Power system Unified protection and control, 38 (1): 93-97.

240: Using cluster analysis to evaluate the green M&A performance of manufacturing enterprises in China

Yingchun SONG[1], Wanjie HUANG[2]

[1] *School of Economics and Management, Hubei University of Technology, 7862659@qq.com*
[2] *School of Economics and Management, Hubei University of Technology, 421243406@qq.com*

Enterprise green development is a new development path. To effectively track M&A performance of manufacturing enterprises, this paper is based on M&A of the iron and steel enterprises, building a three-layer index system including M&A economic performance, environmental performance and social performance index, and using cluster analysis to evaluate the change of the M&A performance. The research results show that in the context of green development, there are two extremes in the post-merger performance of enterprises. Some enterprises have obtained higher economic performance and social performance through M&As. The other enterprises have obtained higher environmental performance through M&As. However, there are no enterprises obtained with higher economic performance, environmental performance and social performance at the same time. Therefore, it is a long way to balance the development of the economic prosperity, environmental protection and social welfare in future. The innovation of this paper is based on the Theory of Triple Bottom Line building a three-layer M&A performance index system, then using the hierarchical cluster analysis method to analyse M&A performances of manufacturing enterprises, and the result is more targeted.

Keywords: Green development, Iron and steel enterprises, Cluster analysis, M&A performance

1. INTRODUCTION

The Report of the 19th CPC National Congress proposed that we must establish and implement the concept of ecological civilization development that Green Mountain is the gold mountain and silver mountain, and promote green development, strive to resolve outstanding environmental problems, and insist on the harmonious coexistence between the human and nature. With the proposal for the *13th Five-Year Plan Outline*, *"*changing the mode of economic development as the main development line and achieve green development" is now a model of all walks of life , which is of great significance to establish a corporate image and improve enterprise efficiency. Promoting green recycling and sustainable development, eliminating high-consumption and high-pollution products and technology as soon as possible, and completely changing the approach of the corporate development is an important guarantee for sustainable economic development of the company.

The Iron and steel enterprises plays a unique role in China's industrialization and is the pillar industry of the national economy. With the rapid development of iron and steel industry, China's steel industry has experienced serious overcapacity and environmental pollution. Merger and acquisition is an effective means to solve the overcapacity and environmental pollution in China's iron and steel industry. Through merger and acquisition to absorb other enterprise advanced green technologies, green technology, integrated iron and steel industry to develop green products, to achieve energy conservation and emissions reduction and resource optimisation, promote the green development of iron and steel enterprises.

2. LITERATURE REVIEW

2.1. A Summary of Research on the Green M&A

The Green M&A are extended by broad technology M&A. The first study on the theory of the Technology M&A was made in 1975.Williamson preliminary expounded the development motives of the Technology M&A, followed by Agrawal (1992), Grant (1996), Lehto & Lehtoranta (2004) and Granstrand (2005) attributed the underlying drivers of the Technology M&A by companies to obtaining the required technical resources. Domestic research on the Technology M&A started slightly. Liu (2004) conducted a systematic research on the Technology M&A. He believes that the Technology M&A refers to M&A of small to medium-sized enterprise by large. It is the beginning of research on domestic the Technology M&A. Since then, the overall research framework for the Technology M&A has gradually begun. The connotation of the green M&A and the Technology M&A is consistent with technology acquisition and promotion, but the connotation of the Green M&A is not limited to this. Chao and Zhou (2012) regard the Green M&As as the M&A which based on acquiring or expanding their green competitive advantages. Although domestic and foreign scholars have made some explorations of the Green M&A, there is a lack of research on the Green M&A performance evaluation, which provides a direction for the study of this article.

2.2. A Summary of Researches on Green M&A Performance Evaluation

Domestic and abroad scholars have a long history of research on the performance evaluation of enterprises. The research direction covers all aspects, which methods and indicators cover a wide range, from the earlier single cost accounting to the more comprehensive Wall method and DuPont Analysis, Performance Appraisal Methods, and Economic Value Added. With the complication of economic activities, the enterprise performance evaluation developed from a simple financial performance evaluation to a combination of financial performance and non-financial performance indicators, then brought out comprehensive performance evaluation methods such as Career smart Balanced Score Card, Triple Bottom Line and Performance Prism. Elkington (1998) pointed out that three basic bottom lines of the survival and development of the companies are the profits, environmental protection and social responsibility, which are equally important to the company. If these three bottom lines are not adhered to, the company will not be able to achieve the goal of sustainable development. This is the triple bottom line theory. Chinese scholars have conducted many explorations based on the triple bottom line theory. Based on the theory of contingency, Wen (2010) constructed a hierarchical variable comprehensive evaluation model for corporate triple performance. Zhao (2010) applied the Analytic Hierarchy Process to construct a “triple performance” systematic framework for the Farmer professional cooperatives. Based on the triple bottom line theory and vector evaluation theory, He (2014) constructed an ecotourism performance evaluation system including economic performance, ecological performance and social performance and established a triple performance static and dynamic evaluation model of ecotourism. The study of corporate performance evaluation by domestic and abroad scholars provides a theoretical basis and ideas for the construction of the Green M&A triple performance evaluation system. Based on the triple bottom line theory, this paper will build a triple performance evaluation system from economic, environmental and social perspectives to measure corporate greenness M&A performance.

About Green M&A and M&A performance evaluation, scholars have carried on the related research, combined with some new perspectives, interdisciplinary between also produced many new performance evaluation method, have greatly enriched the existing research results. However, there are still some shortcomings, especially the lack of in-depth studies on the classification of M&A performance and evaluation under the green background. Therefore,

based on the research of scholars, this paper intends to evaluate the M&A performance of manufacturing enterprises in the text of green development by using cluster analysis.

3. MERGER AND ACQUISITION EVENTS AND DATA PROCESSING OF IRON AND STEEL ENTERPRISES IN THE CONTEXT OF GREEN DEVELOPMENT

3.1. Merger and acquisition of iron & steel enterprises

From 2010 to 2013, the China government issued a series of documentation through relevant departments to promote the green development of enterprises through mergers and acquisitions. In 2010, the State Council issued the *Opinions on Promoting Enterprises Mergers and Restructuring*, effectively accelerating the transformation of the economic development pattern and structural adjustment and improving the quality and efficiency of development. In 2013 Ministry of Industry and Information Technology and China Federation of Industrial Economics released about *Guideline on Accelerate the Key Industries Enterprise Mergers and Restructuring* , put forward the objective, the iron and steel industry mergers and acquisitions in 2015, the top ten iron and steel enterprises group industrial concentration has reached around 60%, developing 3 to 5 enterprise groups which have a strong core competitiveness and international influence, developing 6 to 7 enterprise groups which have strong regional market competitive power. In the same year, the State Council also issued the *Guidance on Resolving the Serious National Policy Contradictions on Production Capacity,* to actively and effectively guide the work of resolving overcapacity in iron and steel and other industries. In this green development background, iron and steel enterprises have implemented a series of mergers and acquisitions.

3.2. M&A performance evaluation index system and sample data processing

Ellington (1998) proposed the Triple Bottom Line for the first time, which basically means that enterprises should pay attention to the balanced development of economic prosperity, environmental protection and social welfare in the process of development. It indicates that a sustainable enterprise needs to have significant performance in economic performance, environmental performance and social performance, namely *Triple Performance.* Based on the *Triple Bottom Line Theory* of Ellington (1998), this paper constructs a M&A performance evaluation index system of iron and steel enterprises (see table2 for details).

Economic Performance Index

The fundamental purpose of the survival and development for a company is to pursue the maximization of economic benefits. The steel companies achieve the goal of optimising resource allocation through the Green M&A, thereby enhancing corporate value. The performance of the Green M&As is closely related to the business performance after M&A. Therefore, the economic performance should be determined first when constructing the triple performance evaluation system for the Green M&A of the steel companies, which is reflected through financial indicators. This article follows the principles of scientific and practicality, and refers to" the Interim Measures for the Administration of Comprehensive Performance Evaluation of Central Enterprises" issued in May 2006 and "the Detailed Implementation Regulations for Comprehensive Performance Evaluation of Central Enterprises" issued in September 2006 by the State-owned Assets Supervision and Administration Commission of the State Council ,combined with the "CASS-CSR1.0",the "CASS-CSR2.0",and the "General Framework for the Compilation of Corporate Social Responsibility Reports in China" standard on financial indicators, including profitability, solvency, operational capacity, and development capacity this 4 aspects to design economic performance indicators(The specific content C1-C4 of the indicator is shown in Table1).

Environmental Performance Index

Environmental performance mainly describes the responsibility contribution of companies to energy conservation, emission reduction, and environmental protection. There is no uniform evaluation standard for environmental performance at present and Chinese scholars are still exploring this. In 2015, the Ministry of Industry and Information Technology issued the “Standards for the Production and Operation of the Steel Industry” and other documents that regulate the green development of the steel enterprises, particularly the energy, fresh water consumption, and the emission of COD, dust, SO_2, and nitrogen oxides of the iron and steel enterprises. And them also made specific requirements for the company's environmental protection reform and other indicators. The steel enterprises through the Green M&A to absorb the target company's advanced green technology, invest in R & D costs after M&A for product development, and turn the green technology into green products. On the other hand, energy consumption such as water and electricity are reduced, and the impact of industrial waste gas waste water and waste slag on society is reduced through various environmental system settings in the daily operation and management process, then the purpose of the green development for the steel companies after the Green M&A is achieved. Therefore, this paper combines the above documents and the standards and regulations of the "ISO26000", "CASS-CSR1.0", "CASS-CSR2.0" and "General Framework" to design environmental performance indicators from green management and green production aspects (The specific content C5-C6 of the indicator is shown in Table 1).

Social Performance Index

In addition to the goal of maximizing corporate value, the steel companies also shoulder social responsibilities such as taxation, donations, and employment. On the one hand, companies absorb advanced green technologies, increase investment in safety production, improve product quality, and achieve product liability through the Green M&A. On the other hand, the transformation and upgrading of the steel companies through the Green M&A will provide more new employment channels and jobs for the society. What's more, the steel companies provide employees with a safe working environment, improve their wages and salaries, and safeguard employee benefits through the green transformation. Based on the above analysis, the author designed social performance index from the perspectives of product responsibility, employee responsibility and social impact, which eliminated index that have been selected as economic performance and environmental performance. And she reviewed some of the customer responsibility index in the market performance from the "General Framework" such ad customer satisfaction, credit rating, number of technicians and number of national patents that were incorporated into the social performance index. This performance system including total number of employees, total salary, equal employment, employee training, investment in production safety, total tax payment, and social donation these 11 indexes (The specific content C7-C9 of the indicator is shown in Table 1).

The economic performance data of iron and steel enterprises from the annual report and the China Stock Market & Accounting Research(CSMAR) database, environmental performance and social performance data mainly comes from corporate social responsibility report. After manual to collect the original data dimensionless processing. Then, the standardized data are calculated by using the normalization formula, and the performance index data of iron and steel enterprises are obtained.

Table 1: M&A performance evaluation index system of iron and steel enterprises

First Level Index	Second Level Index	Third Level Index
A M&A Performance	B1 Economic Performance	C1 Profitability
		C2 Solvency
		C3 Operational capacity
	B2 Environmental Performance	C4 Development capacity
		C5 Green operation
		C6 Green production
	B3 Social Performance	C7 Product liability
		C8 Employee responsibility
		C9 Social influence

According to this framework, the M&A performance was calculated by using the catastrophe progression method. The specific method can be seen in Song & Huang (2018). This part is not the focus of this paper.

4. CLUSTER ANALYSIS AND EVALUATION OF M&A PERFORMANCE OF IRON AND STEEL ENTERPRISES

4.1. Cluster analysis

Clustering analysis is to point to in the absence of prior knowledge, according to the nature of the sample correlation or similarity to the automatic classification of multiple classification results, each category of individuals with similar characteristics, different categories of individual differences in the larger a analysis method. According to different clustering methods, clustering can be divided into system clustering, K mean clustering and fuzzy clustering. The system clustering method is chosen in this paper. System clustering, also known as hierarchical clustering, first of all, think will each singular sample, with a kind of method to calculate the distance between each sample, the distance between the nearest two samples into a class; Then calculate the distance between the new class and other classes and combine the two closest samples into one class. And so on and so on, gradually reduce the categories until all the samples are merged into one. In this paper, system clustering analysis is based on the Euclidean distance function and the least square deviation.

Equation 1: Euclidean distance

$$D_{jk} = \sqrt{\sum_{l=1}^{n} (X_{ij} - X_{ik})^2}, 0 < D_{JK} < \infty$$

Where:

D_{jk} = Euclidean distance

n=the number of M&A performance of iron and steel enterprises

X_{ij} = the ith M&A performance of j iron and steel enterprises

D_{ik} = the ith M&A performance of k iron and steel enterprises

4.2. The result of cluster analysis

Based on iron and steel enterprises M&A performance in 2014 and 2016 as a variable, the index system of green development under the background of the iron and steel enterprises M&A performance is composed by economic performance, social performance and environmental performance of three secondary index. Five iron and steel enterprises of MAGANG, ANGANG, TAIGANG, BAOGANG AND SANGANG were taken as the research samples. In 2015, the macro-economic environment of the steel industry was severe, and the steel demand intensity continued to decline，M&A events before and after in 2015 were selected for comparative analysis. In this paper, SPSS19.0 was used for system clustering analysis and the following results were obtained: (see Figure 1 and Figure 2 for details).

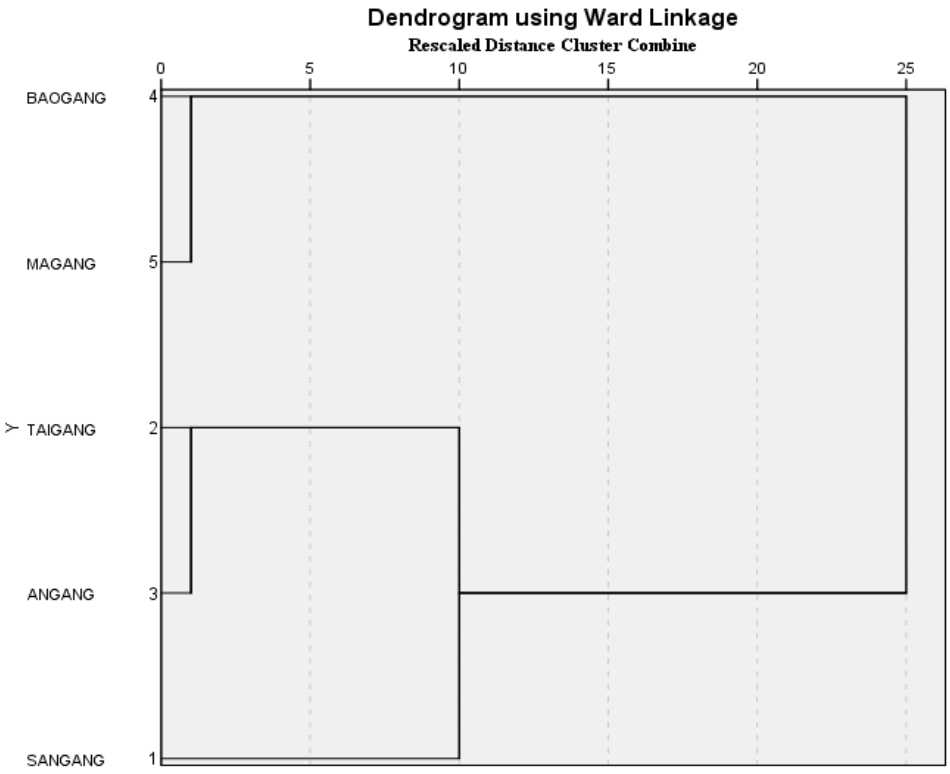

Figure 1: 2014 M&A performance of iron and steel enterprises cluster trees

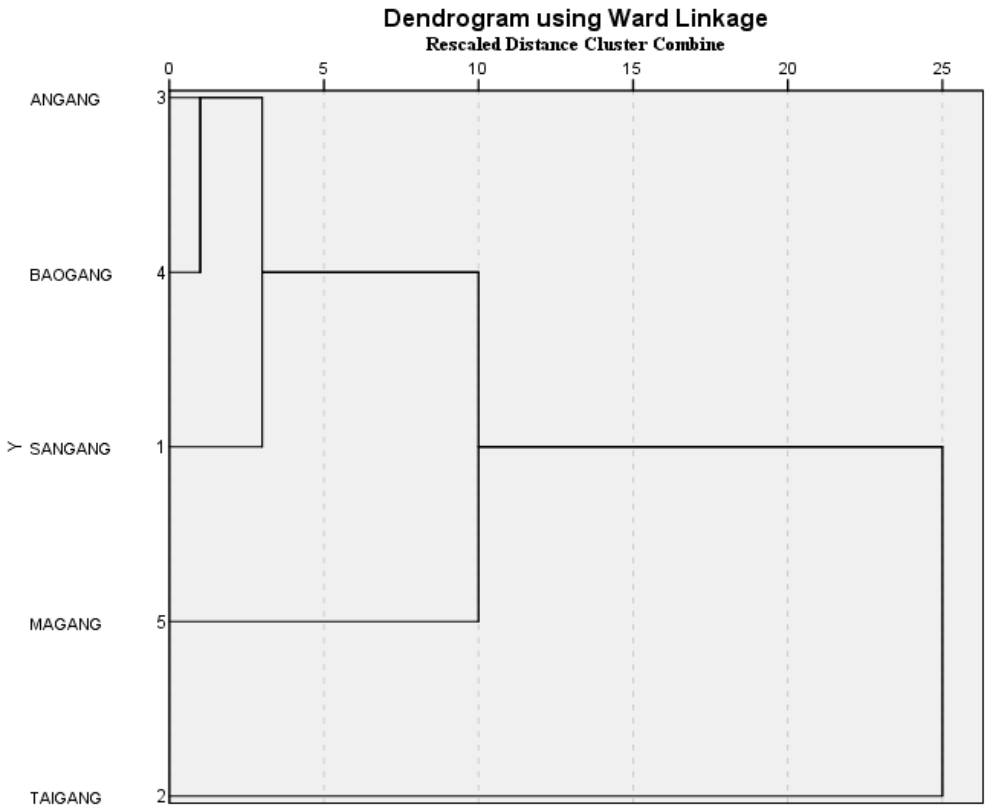

Figure 2: 2016 M&A performance of iron and steel enterprises cluster trees

As can be seen from table 2，the results of cluster analysis are two types. The first type of enterprises is MAGANG, ANGANG, TAIGANG, BAOGANG. The second type is SANGANG. According to the result of cluster analysis, this paper will further evaluate the M&A performance of iron and steel enterprises in the context of green development from three secondary indicators of economic performance, environmental performance and social performance.

Table 2: Cluster Analysis Results of M&A Performance of Iron and Steel Enterprises in 2014 and 2016

Category	The sample enterprises	
	2014	2016
Class 1	SANGANG, TAIGANG, ANGANG	SANGANG, ANGANG, BAOGANG, MAGANG
Class 2	BAOGANG, MAGANG	TAIGANG

5. ANALYSIS OF M&A PERFORMANCE OF IRON AND STEEL ENTERPRISES

5.1. Economic performance analysis

Economic performance refers to the maximization of economic benefits in the survival and development of enterprises. Through mergers and acquisitions, iron and steel enterprises s achieve the goal of optimising resource allocation and improving enterprise value. Therefore, the economic performance mainly reflects the operating results and financial status of enterprises after M&A. The comparison of M&A economic performance of iron and steel enterprises in 2014 and 2016 is shown in table 3.

Table 3: Comparison of M&A economic performance of iron and steel enterprises in 2014 and 2016

Category		2014		2016
Class1	SANGANG	0.9255	SANGANG	0.8831
	TAIGANG	0.9127	ANGANG	0.9635
	ANGANG	0.9513	BAOGANG	0.9451
			MAGANG	0.9356
	Mean	0.9298	Mean	0.9318
Class2	BAOGANG	0.9123	TAIGANG	0.9032
	MAGANG	0.9302		
	Mean	0.8834	Mean	0.9032

In 2014, the average M&A economic performance of the first-class iron and steel enterprises was 0.9298, higher than that of the second-class iron and steel enterprises (0.8834). However, the M&A economic performance of the first-class iron and steel enterprises was obviously better than that of the second-class iron and steel enterprises in 2016. The economic performance of the first-class iron and steel enterprises was 0.9018 in 2016, which not only was better than that of the year in 2015, but also was better than that of the second-class iron and steel enterprises. Many iron and steel enterprises have achieved higher economic performance through merger and acquisitions.

5.2. Environmental performance analysis

Environmental performance is mainly referring to the enterprise responsibility in the aspect of energy conservation and emissions reduction, environmental protection. Through mergers and acquisitions, iron and steel enterprises, on the one hand, absorb the advanced green technology from target enterprise. After M&A, invest in R&D in terms of product development, and transfer the green technology into green products. On the other hand, through a variety of environmental system settings, iron and steel enterprises reduce the energy consumption of water, electricity, etc., reduce industrial waste gas, waste water and waste residue emissions influence and harm to society during the process of the daily management. And iron and steel enterprises realize the green development after M&A. The comparison of M&A environmental performance of iron and steel enterprises in 2014 and 2016 is shown in table 4.

Table 4: Comparison of M&A environmental performance of iron and steel enterprises in 2014 and 2016

Category		2014		2016
Class1	SANGANG	0.4310	SANGANG	0.8256
	TAIGANG	0.5646	ANGANG	0.8536
	ANGANG	0.5693	BAOGANG	0.9632
			MAGANG	0.9747
	Mean	0.5216	Mean	0.9043
Class2	BAOGANG	0.6998	TAIGANG	0.9713
	MAGANG	0.7053		
	Mean	0.8834	Mean	0.9713

In 2014, the average M&A environmental performance of the first-class iron and steel enterprises was 0.5216, which was significantly lower than that of the second-class iron and steel enterprises in the same year, which was 0. 8834. Later, M&A environmental performance was improved obviously in 2016, which was 0.9043 in 2016, was much better than that of the first-class iron and steel enterprises were in 2014. Due to BAOGANG and MAGANG were classified to the first-class, the M&A environmental performance of first-class iron and steel enterprises was much better than before. Although, the first-class iron and steel enterprises made a big progress in 2016, the second-class iron and steel enterprises also made a bigger progress than that of the first-class iron and steel enterprises (0.9713). From the perspective of the average M&A environmental performance of iron and steel enterprises in five years, the second-class iron and steel enterprises have a slight advantage.

5.3. Social performance analysis

In addition to the goal of maximizing enterprise value, iron and steel enterprises also shoulder social responsibilities such as tax payment, donation and employment. On the one hand, iron and steel enterprises absorb advanced green technologies through mergers and acquisitions, increase investment in safe production, improve product

quality and realize product responsibility. On the other hand, through mergers and acquisitions to achieve the transformation and upgrading of iron and steel enterprises, to provide more new employment channels and jobs for the society; In addition, through green transformation, iron and steel enterprises provide safe working environment for employees, improve their salary and treatment, and maintain their welfare. The comparison of M&A social performance of iron and steel enterprises in 2014 and 2016 is shown in table 5.

Table 5: Comparison of M&A social performance of iron and steel enterprises in 2014 and 2016

Category		2014		2016
Class1	SANGANG	0.9017	SANGANG	0.8761
	TAIGANG	0.8120	ANGANG	0.9077
	ANGANG	0.9591	BAOGANG	0.8130
			MAGANG	0.8719
	Mean	0.8909	Mean	0.8672
Class2	BAOGANG	0.8858	TAIGANG	0.7114
	MAGANG	0.8993		
	Mean	0.8926	Mean	0.7114

In 2014, the average M&A social performance of the first-class iron and steel enterprises was 0.8909, lower than that of the second-class iron and steel enterprises of the same year. But In 2016, the average M&A social performance of the first-class iron and steel enterprises was 0.8672, lower than that of first-class iron and steel enterprises in 2014. But higher than that of the second-class iron and steel enterprises of the same year (0.7114). According to the average M&A social performance of the iron and steel enterprises in 2016, the first-class iron and steel enterprises have a slight advantage.

6. CONCLUSION

In the context of green development, this paper based on M&A of the iron and steel enterprises, building a three-layer M&A performance index system including economic performance, environmental performance and social performance index. Using clustering analysis, the evaluation of the changes of the three difference M&A performances. The results show that in the context of green development, MAGANG, ANGANG, BAOGANG and MAGANG have achieved higher economic performance and social performance through M&As, while TAIGANG has achieved higher environmental performance and social performance through M&As. In future manufacturing enterprises should balance the economic prosperity, environmental protection and social welfare during the process of mergers and acquisitions.

7. ACKNOWLEDGEMENTS

This study was supported by 2017 Annual Research Plan Project of Hubei Department of Education (Project No. D20171401); Doctor's research of Hubei University of Technology Start Fund Project (Project No. BSQD13075)

8. REFERENCES

Elkington, J., 1998. Partnerships from cannibals with forks: The triple bottom line of 21st - century business. *Environmental Quality Management*, *8*(1), pp.37-51.

Williamson, O.E. and Markets, H., 1975. Analysis and antitrust Implications: A study in the Economics of Internal organization.

Agrawal, A., Jaffe, J.F. and Mandelker, G.N., 1992. The post - merger performance of acquiring firms: a re - examination of an anomaly. *The Journal of finance*, *47*(4), pp.1605-1621.

Granstrand, O., 1998. Towards a theory of the technology-based firm1. *Research policy*, *27*(5), pp.465-489.

Lehto, E.L.O. and Lehtoranta, M.O., 2004. Becoming an acquirer and becoming acquired. *Technological Forecasting and Social Change*, *71*(6), pp.635-650.

Liu K, 2004. Enterprise Technology M&A Strategy and Management. Beijing: China Financial Publishing House, pp.31-33.

Xu Z, Zhou C.,2013.The Begining of the Green M&A. *Finance Communication*,(04),pp.36-38.

Wen S., 2010. A Comprehensive Evaluation Model of Hierarchical Variable Weight for Enterprise Triple Performance - Based on the Perspective of Sustainable Development Strategy. *Accounting Research*,12, pp.82-87.

Zhao R, Yang L, 2010.Research on Triple Performance Evaluation of Resource-based Enterprises under the Background of Circular Economy. *Guangdong Agricultural Sciences*,37(04), pp.380-382+392.

Zhao J, 2010.Study on the "Triple Performance" Evaluation Model of Farmers' Professional Cooperatives *Agricultural Technology Economy*, (02), pp.119-127.

He H, 2014.Construction of Triple Performance Evaluation Index System in Qinba Mountainous Ecotourism Area in Southern Shaanxi Province. *Shanxi University of Technology (Social Science Edition)*, (04), pp.34-39.

Song Y, Huang W.,2018. Analysis on the green M&A performance of manufacturing enterprises based on the catastrophe progression method. *Finance and Accounting Monthly*, (12). pp.41-47.

241: An analysis of the intervention effect of government green procurement on green transformation

In the example of government procurement of new energy vehicles

Liangmei LIAO [1], Shan SU [2]

[1] School of Economics and Management, Hubei University of Technology, 529722228@qq.com
[2] School of Economics and Management, Hubei University of Technology, 954093363@qq.com

Based on externality theory and public goods theory, this paper studied the government's green procurement intervention of supplier behaviour under the completely competitive market structure and imperfectly competitive market structure, and then theoretically demonstrated the effect of environmental pollution intervention on China's new energy vehicles. The government procurement as an example analysed the green intervention effect of government green procurement. According to the theoretical and practical argumentation conclusions, the following measures were proposed: further expand the scale of government green procurement; give green product purchase prices to be tilted; improve green standards or evaluation systems and establish and improve government green procurement regulations.

Keywords: Government green procurement; Green transformation; New energy vehicles

1. INTRODUCTION

Energy shortages and environmental pollution have become a worldwide problem. Since the Reform and opening-up, the rapid development of China's economy has highlighted and aggravated the severity of these two issues. In order to control pollution, the Chinese government has used economic, legal and administrative means to carry out pollution control actions and achieved certain results. The Assessment Report on China's Environmental Air Quality Management (2017) pointed out that with the improvement of the environmental protection system and the strengthening of environmental protection supervision, the pollution of various particulate matter in China has generally improved in 2016, and most of the provinces and cities have realized the improvement of "atmospheric ten" in advance. In 2016, the average reduction in PM2.5 key control areas in Beijing, Tianjin, Hebei, Shandong, Shanxi, Shanghai, Jiangsu, Zhejiang, the Pearl River Delta and Chongqing 10 provinces (municipalities directly under the Central Government) was 7.8%, including Beijing-Tianjin-Hebei and the surrounding areas PM2.5 pollution during heating period is still more serious. Environmental monitoring indicates that the pollution of motor vehicle exhaust has become an important source of air pollution in China and is an important cause of fine particulate matter and photochemical smog pollution.

In order to solve the problem of energy shortages leading to energy security, our government has actively developed new energy sources such as wind power, nuclear power, and solar energy. New energy vehicles have the advantages of reducing pollution, saving energy and high efficiency, and can be a good combination of energy and pollution problems. How to develop new energy vehicles, increase market acceptance, and achieve green transformation require in-depth research. This article intends to demonstrate the intervention effect of government green procurement on the green transformation from the perspective of manufacturers and market structure. The new energy vehicle is used as an example to test the effect.

2. THEORETICAL BASIS AND RESEARCH HYPOTHESIS

The main body of environmental pollution is the enterprise and individuals; the recipient of environmental pollution is public resources such as air, water and soil. To study its root causes, the former applies the externality theory, and the latter applies the theory of public goods to explain it. Therefore, this paper takes the externality theory and public goods theory as the theoretical basis of the study.

2.1. Theoretical basis

Externality theory

The theory of externality first originated from Alfred Marshall (1842-1924), the concept of "external economy" proposed by Marshall, and the most representative scholar afterwards was Arthur Cecil Pigou (1877-1959) and Ronald H. Coase (1910-2013). The concept of "external economy" proposed by Marshall in "The Principles of Economics" published in 1890. To sum up, we define from the subject of externality: "Externality refers to the situation where production or consumption imposes uncompensated costs on other groups or gives benefits without compensation"—Samuelson and Nord House. Defined by external acceptors: "Externality is used to represent some of the inefficiencies that arise when certain benefits or costs of an action are not considered by the decision maker; that is, some benefits are given or some of the costs are imposed on those who did not participate in this decision"—Randall. The increasing pollution of the environment is because humans have always regarded environmental resources as free resources. The destruction of environmental resources caused by competitive use has not been reflected in its costs, resulting in external diseconomy (negative externalities); environmentalists give other beneficiaries the benefits brought are also not remunerated at their prices, creating external economics (positive externalities).

How to correct externalities, Pigou argues that internalization of externalities can be achieved by subsidizing those who cause taxation and positive externalities caused by negative externalities. This policy proposal was later called the "Pigou tax". According to Pigou's claim, those who pollute the environment should be taxed, and those who protect the environment should be subsidized to eliminate pollution and protect the environment.

Although the externality originated from the failure of the market mechanism, Coase still insisted that "the market is good" and the externality problem should be solved by the market. To this end, it put forward the famous Coase theorem: If transaction costs are zero, no matter how the rights are defined, the optimal allocation of resources can be achieved through market transactions and voluntary negotiation; if the transaction costs are not zero, institutional arrangements and choices are important. This means that the solution to the externality problem may be to replace the Pigou taxation with a voluntary negotiation in the form of market transactions.

With the growing environmental problems in the 1970s, market economies have begun to actively explore concrete ways of realizing the internalization of externalities. As a result, the Coase theory has been put into practical use. The emissions trading system in the field of environmental protection is a concrete application of the Coase theory. The successful practice of Coase's theory further shows that "market failure" is not a necessary and sufficient

condition for government intervention, and government intervention is not necessarily the only way to solve the "market failure".

Public Goods Theory

The study of the theory of public goods in the modern economy began with Paul A. Samuelson (1915-2009). He believed that public goods mean that the consumption of a certain product by each person does not cause others to reduced consumption. On this basis, the further research and improvement of the manager Richard Abel Musgrave (1910-2007) and others gradually formed the two major characteristics of public goods, namely the non-competitiveness of consumption and non-exclusive. The non-competition of consumption means that adding additional consumers will not affect the consumption level of other consumers, or that the marginal cost of increasing consumers is zero; the non-exclusiveness of consumption means that the consumption of an item is not possible to exclude others.

In addition to the contributions made by Musgrave in the development of public goods, he first quoted the economic concept of "Merit Goods" in the article "Multiple Theory of Budget Decisions", and later used the concept of "Demerit Goods", which has caused great controversy in the field of economics. Musgrave defined beneficial products as "products that increase production through policies that interfere with personal preferences", which means that beneficial products are mainly provided by the state. Harmful goods are those that are taxed or banned by the government to reduce consumption, such as tobacco, alcohol, and drugs. In 1959, Musgrave once again pointed out in the "Fundamental Principles" that beneficial products refer to items that are beneficial to consumers but are under-consumed due to consumers' ignorance. Given the ambiguity of the term "preference", some scholars later argued that beneficial products are items that the government should provide by formulating policies that interfere with individuals' willingness to pay.

Government green procurement is an important means of implementing green transformation

Judging from the characteristics of public finances, meeting the public needs of society is its main goal and the focus of its work. Energy saving and environmental protection have become an urgent need for the overall interests of the entire society. Supporting environmental protection, purchasing energy-saving products is an important function of public finances. Therefore, "green procurement" should be an important part of public finances.

The air, water and other items have the characteristics of public goods. The market mechanism will cause pollution and destruction. The public goods theory believes that the public property rights arrangements for public goods are more effective. As a result, government intervention is necessary. The government's green procurement refers to a series of policy measures, such as preferential procurement and prohibition of procurement, from the perspective of social resources and environmental public interests in government procurement. Through large purchasing power, priority is given to the purchase of environmentally friendly products that have less negative impact on the environment. To promote the improvement of corporate environmental behaviour, thus promoting and demonstrating the role of social green consumption. Ultimately promote the improvement of the environment and achieve the goal of resource conservation. Government green procurement should be an important means to provide beneficial products, overcome negative externalities, and realize green transformation.

2.2. Research hypothesis

- product is homogeneous product, with same market demand curve and market price

-The product's Manufacturers, A and B, are main market suppliers. Manufacturer A lays stress on environmental protection, it produces green product without polluting environment. On the contrary, manufacturer B caused environmental pollution while producing products but was not punished. Manufacturer B produces pollution type ordinary products, so manufacturer B's cost is lower than manufacturer A's.

-The cost function of manufacturer A and manufacturer B is incremental. We can know from 2 that manufacturer A's marginal cost line is higher than manufacturer B's.4. The government purchases the product for a fixed amount. Before the government implements green procurement, it selects the product of the B manufacturer. After the government implements green procurement, it selects the product of the manufacturer A. The government's implementation of green procurement does not change the market structure.

-The government purchase a certain quantity of a product, before carrying out green procurement, the government chose manufacturer B's products, and after carrying out green procurement, the government chose manufacturer A's products. Carrying out green procurement doesn't change market structure.

3. THE INTERVENTION EFFECT OF GOVERNMENT GREEN PROCUREMENT

According to two types of market structure---fully competitive market and non-competitive market, the influence of carrying out green procurement on manufacturers will be analysed to achieve government intervention in ecological environment.

3.1. Fully competitive market

According to hypothesis condition, product's market structure is fully competitive, which means manufacturer A and manufacturer B are both facing the same market demand line AR and marginal income line MR, and the lines are both horizontal lines. As shown in figure 1, manufacturer A 's marginal cost line is MC_A and manufacturer B's marginal cost line is MC_B , and MC_A is higher than MC_B . Out of the principle of maximizing profit, marginal income is marginal cost, and manufacturer A's optimal production scale is Q_{A1} ,manufacturer B's optimal production scale is Q_{B1} , manufacturer A's profit is $\Delta A_1 P_E C_A$, and manufacturer B's profit is $\Delta B_1 P_E C_B$, because MC_A is bigger than MC_B , $\Delta B_1 P_E C_B$ is higher than $\Delta A_1 P_E C_A$. Therefore, market failure and market distortion come, which means market principle of profit maximization encouraged manufacturer B's production which is harmful for the environment, while restricted environmental-friendly manufacturer A's production.

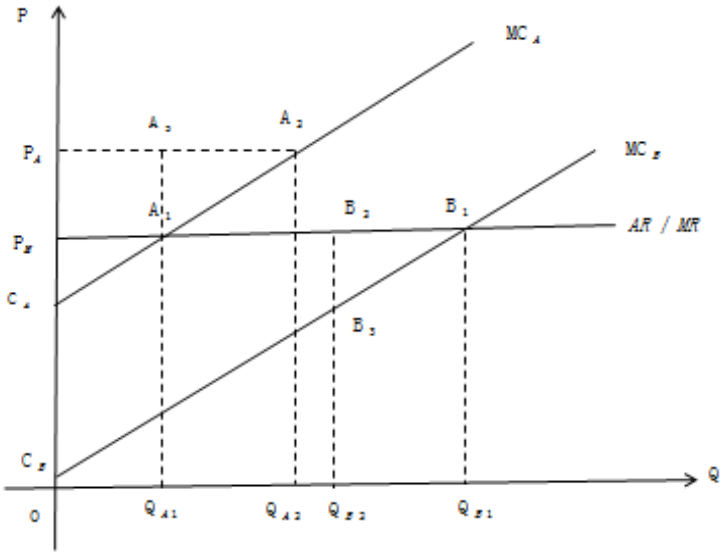

Figure 1: Fully Competitive Market

If the government's procurement quantity of the product is Q_F , before carrying out green procurement, the government chose manufacturer B to purchase products and the quantity of the product is Q_F = B_2B_1 . As shown in figure 1, manufacturer B's profit from government procurement is $\Delta B_1 B_2 B_3$. After carrying out green procurement, purchased product should be environmental protective, so government procurement shifts from manufacturer B to manufacturer A, procurement quantity remains the same Q_F .If manufacturer A accepts government procurement, and adds its production scale Q_{A1} to Q_{A2}, Q_{A1} and Q_F added together are Q_{A2}, then profit maximization principle decides that the lowest price could be accepted by manufacturer A is P_A, the cross point A_2 between Q_{A2} and MC_A. If the government accepts the price, the deal is completed, or manufacturer A will not accept government procurement. I f the deal is completed, the government accepts manufacturer A's quantity of sale Q_F (A_3A_2), then manufacturer A's profit will be $\Delta A_1 A_2 A_3$. At the same time, the government stops purchasing

products from manufacturer B, manufacturer B's production and sales will go down Q_F (B_1B_2), therefore, the profit will go down $\Delta B_1B_2B_3$.

3.2. Non-competitive market

In terms of hypothesis condition, market structure of product is non-competitive market, and manufacturer A and manufacturer B have the same market demand line AR and marginal income line MR, which are both straight lines leaning from upper left to lower right. As shown in figure 2, manufacturer A's marginal cost line is MC_A , and manufacturer B's marginal cost line is MC_B , and MC_A is higher than MC_B . Out of the principle of maximizing profit, marginal income is marginal cost, and manufacturer A's optimal production scale is Q_{A1} ,because A_1 is the cross point between Q_{A1} and AR, market price is P_{A1} .Manufacturer B's optimal production scale is Q_{B1} , because B_1 is the cross point of Q_{B1} and AR, market price is P_{B1} . Manufacturer A's profit is $C_AE_{A1}A_1P_{A1}$,Manufacturer B's profit is Manufacturer A's profit is, because MC_A is higher than MC_B , which causes $C_BE_{B1}B_1P_{B1}$ higher than $C_AE_{A1}A_1P_{A1}$.

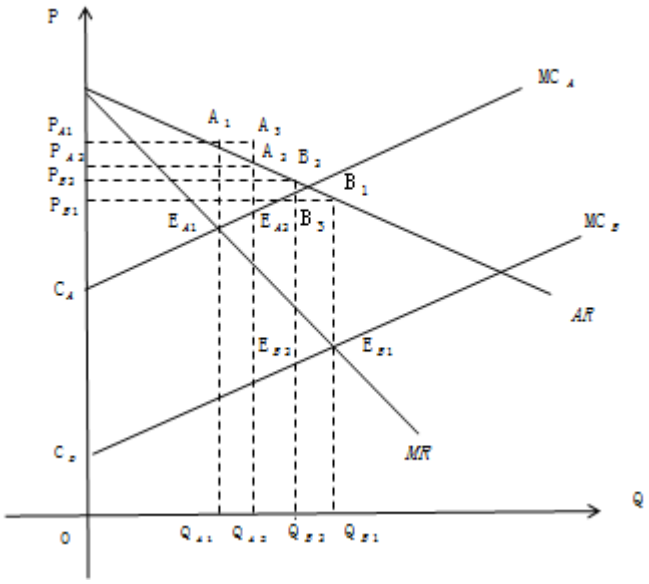

Figure 2: Non-competitive Market

Similarly, if the quantity of government procurement is Q_F , before carrying out green procurement, the government chose manufacturer B to purchase products and the quantity of the product is Q_F = $Q_{B2}Q_{B1}$. As shown in figure 1, manufacturer B's profit from government procurement is $E_{B2}E_{B1}B_1B_3$. After carrying out green procurement, government procurement shifts from manufacturer B to manufacturer A, procurement quantity remains the same Q_F . The government purchases products from manufacturer A at the original price P_A , and manufacturer A'S production scale will goes up to Q_{A2} , and Q_{A1} added Q_F together is Q_{A2} . If the government accepts manufacturer A's quantity of sale Q_F (A_3A_2), manufacturer A's profit will go up $E_{A1}E_{A2}A_3A_1$. Manufacturer A can choose new market price like P_{A2} as government procurement adds the demand for the products, while manufacturer A's market share will increase, and its price competitiveness will increase as well. At the same time, the government will no longer purchase products from manufacturer B, so manufacturer B's production and sales will decrease Q_F

($Q_{B1}Q_{B2}$). In order to keep price competitive advantage, manufacturer B will take the measure of keeping the same market price to decrease the profit of $E_{B2}E_{B1}B_1B_3$. If manufacturer B reprices in terms of demand curve and increase price (like P_{B1} goes up to P_{B2}) because of demand decreased, which will weaken product's market price competitiveness and decrease market share.

3.3. Conclusion

-If the government didn't implement green procurement, and the manufacturers that would cause pollution wouldn't be punished, the principle of maximizing profit will encourage the development of manufacturer B that would do harm to environment and restrict the development of environment-friendly manufacturer A, therefore, market failure, market distortion and "public tragedy" that cause environmental pollution will continue to exist.

-The implement of green procurement will make green products have substitution effect on not-green product. The magnitude of the substitution effect depends on the quantity of government procurement. The substitution effect is promotional to the quantity of government procurement.

-The implement of green procurement will make non-green products have transformation effect on green product. In order to sustain and improve market competitiveness, manufacturer B has to choose to transform from polluting product to non-polluting product, especially when local government's procurement is great or is becoming greater.

-Under the circumstance of green procurement constantly increase, ecological environment will be improved as green product is increasing and non-green product is decreasing. Accordingly, the government's intervention towards environmental pollution caused by market failure and market distortion will be more effective.

4. OBVIOUS GREEN PROCUREMENT INTERVENTION EFFECT THAT OUR COUNTRY HAS ON NEW ENERGY VEHICLE

It's reported by Ministry of Public Security that China's tenure of vehicle is 310 million, among them the tenure of new energy vehicle is 1.53 million which is 0.7% of the total number (16:54:14 January 15th, 2017 from China News). Annual report on Environmental Management of China's Motor vehicles in 2017 shows that China was the largest country in motor vehicle production and sale for the past 8 years. Automobile exhaust gas pollution is a great cause of air pollution, an important reason of fine particulate matter and photochemical smog pollution. Pollution prevention and control has aroused the attention of the government. To decrease air pollution in cities and carbon emission and create a leading industry in the world that can improve employment and export and decrease oil dependency on Mid-east to ensure energy security, new energy vehicle industry is included in the list of strategic emerging industry planning by our government and in the ten key development fields of made in China 2025. The new energy vehicle industry that has high efficiency and low noise and can save fuel energy, reduce exhaust gas emissions. The government should take measures such as financial subsidies, tax preferences, government procurement to support the development of new energy vehicle.

In August 2008, the State Department informed and required to include clean energy vehicle and new energy vehicle in the list of government procurement. Some new energy vehicles like BYD's f3dm dual Model Electric vehicle, Chang'an hybrid car Jaxun and FAW Toyota Hybrid Car Price were in the Central Government Organ Automobile Agreement Supplier Automobile Manufacturer 2009-2010, which symbolizes new energy vehicle is included in government procurement. In February 2011, the government has made clear the target of the priority purchase of the new energy vehicle of its own brand, and the detailed regulations for the management of vehicle models have been issued. In 2014, National administration bureau, the Ministry of finance and other four ministries has pointed out that government agencies and public services can't have less 30% of new energy vehicles for each year's equipment. And the some recent years' requirements are as followed: not less 10% in 2014, not less 20% in 2015, and not less 30% in 2016, and the percentage in following years must goes up. Energy Saving and New Energy Automobile Industry Development Plan 2012-2020 puts forward that domestic pure electric vehicles and plug-in hybrid electric vehicles will produce and sell 500000 vehicles in 2015 and 5 million in 2020.

By the end of 2015, the accumulative number of electric vehicles popularized and applied in Beijing has reached 35900, and only in 2015, 23500 new electric vehicles were added, and the promotion and application of electric vehicles increased significantly, and the overall scale ranked first in the country. Public transport, sanitation, rental and other areas of public services reached 16200, accounting for 45.13%.

In 2016, Taiyuan replaced 8292 taxis in the city with electric vehicles and became the first city to make all the taxis become power-driven. Turning oil-driven to power-driven is helpful for improving air quality. According to the analytical results of air pollution sources in Taiyuan, in Taiyuan's pm2.5 pollution, the proportion of motor vehicle exhaust gas reached 16. Taiyuan's Taxi electrolysis is expected to reduce emissions by 7.0 tons of pm2.5 per year.

With the support of the central and local governments in the form of government procurement and subsidies, new energy vehicles in China are developing rapidly, ranked top in the world, as shown in figure 3 and figure 4. In terms of statistics, the productions and sales of new energy vehicle has respectively achieved 794 thousand and 777 thousand, increasing of 53.8% and 53.3%, accounting for 63.3 times and 60.7 times of 2012. The productions and sales of new energy vehicle has been ranked first in global production and sales for 3 years, accounted for more than half of the world's new energy car market. The effect of government intervention on green transformation was remarkable (Liaowang: Alert to the risk of excess capacity of new energy vehicles 2018-04-03 07:28:50 Source: Liaowang News Week).

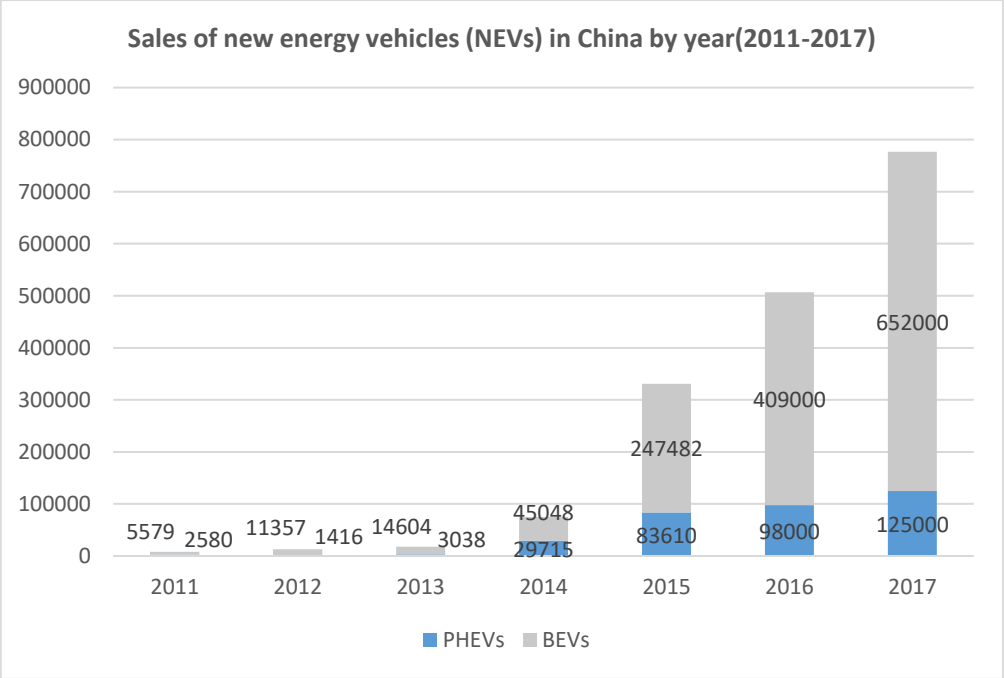

Figure 3: Sales of new energy vehicles

Note: NEVs includes passenger cars and commercial vehicle, such as buses, sanitation trucks, and other heavy-duty vehicles.

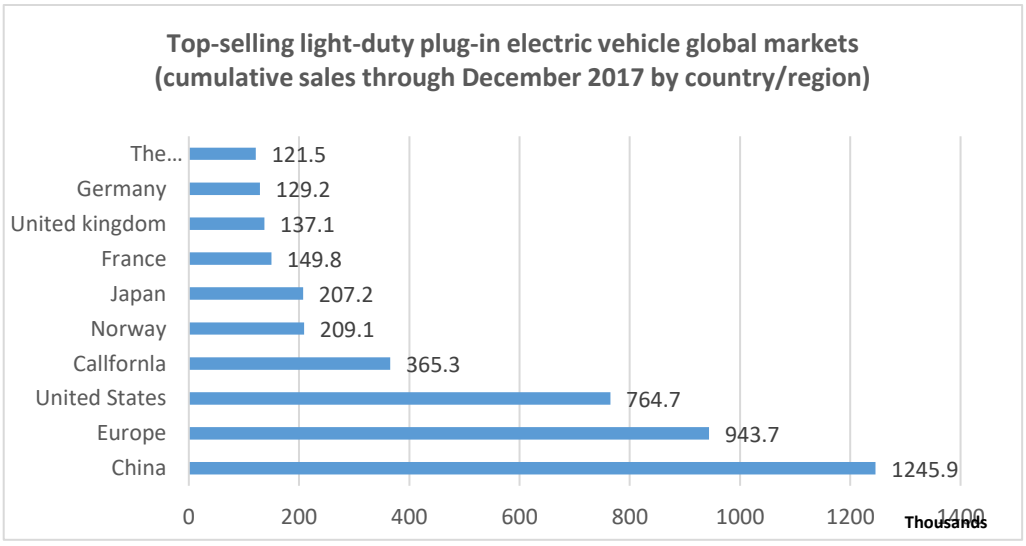

Figure 4: global markets

5. DRAWING LESSONS FROM OTHER COUNTRIES' EXPERIENCES AND IMPROVING GOVERNMENT GREEN PROCUREMENT PROPOSALS

5.1. Further expanding the scale of government green procurement

The concept and practice of government green procurement originally originated in developed countries such as Germany, Norway, Sweden and the United States, and achieved good results in practice. EU green procurement accounted for an average share of government procurement of 19%, and 50% of Sweden, 40% of Denmark and 30% of Germany, China's government's green procurement started late and grew rapidly. In 2013, in the procurement of energy-saving and environmentally friendly products, the nation's compulsory and preferential procurement of energy-saving and environmental protection products reached 183.91 billion yuan and 143.49 billion yuan, respectively. 86% and 82% of similar products. The two together account for 20% of the national government procurement amount. The gap between China and the developed countries has gradually narrowed. It is suggested that China increase the proportion of government procurement and GDP, and further expand the scale of government green procurement. The green procurement of new energy vehicles draws on the practice of the United States (the US announced in 2015 that all official vehicles of its government departments have been purchased as new energy vehicles), and gradually achieved the public goods attributes of all official vehicles and public taxis in government departments. All cars are purchased as new energy vehicles.

5.2. Inclining the purchase price of green products

To join the GPA (Government Procurement Agreement), China's government green procurement green to achieve the above-mentioned good ecological effect is also to pay the price, the government green procurement is not only a government action, but also a market economy behaviour, the government green procurement objectively inevitable Follow the laws of market economy. The cost of government green procurement payment includes not only the cost of procurement, but also the cost of use, recovery, and final disposal costs. Compared with ordinary products, green products have higher costs because of the green technology and production, so their market prices are higher than those of ordinary products, and the cost of use, recycling, and final disposal costs are taken into account. Government procurement costs will no doubt It will increase more than purchasing ordinary products. Of course, not all green procurement will increase government procurement costs. Although the initial cost of some green products is higher at the time of procurement, the cost of use and the final disposal cost are lower. From the viewpoint of the entire product life cycle, the comprehensive cost may be lower than that of ordinary products, such as energy-saving products, and its purchase cost is high, but its use cost is lower.

The higher costs of government procurement of green products are in conflict with the limited procurement budget. To avoid and reduce conflicts, the government needs to fully consider green products in its development process to improve environmental protection and safety in the preparation of procurement budgets and the formulation of procurement regulations and policies. In terms of costs, etc., the necessary price inclinations are given in the bidding management methods and procedures.

5.3. Perfecting green standards or evaluation system

Only the true sense of whether green products can effectively substitute for non-green products, if the government purchases only nominal green products, in essence "pseudo-green products", the market has implemented the implementation of green products for non-green products. The substitution of products, this kind of substitution is merely a kind of "pseudo substitution", in fact because it can't improve the environmental pollution, the intervention that the government pays high purchase cost is invalid. Therefore, a clear green standard or evaluation system is an important guarantee for the effective intervention of environmental pollution through government green procurement. It is recommended that China strengthen the certification of green product environmental labelling, complete the integration with the green standards of GPA member states as soon as possible, and maintain and harmonize with other GPA member countries in terms of the design of environmental certification systems, the formulation of green standards, and the certification of environmental label products. In terms of new energy vehicles, while strengthening the standardization management of domestic new energy vehicles, it is necessary to closely follow the development of the global new energy automotive industry, strengthen international exchanges and coordination, and promote the internationalization of Chinese standards.

5.4. Establish and improve government green purchasing regulations

As a means of interfering with "market failures", government green procurement also has the problem of "government failure". To prevent government rent-seeking, fraud, corruption, etc. during the green procurement process, strengthening legal norms is to ensure the fairness of government green procurement. And the important guarantee of efficiency. The United States issued a presidential decree in 1991, which stipulated that the government purchases green product lists; Canada's environmental responsibility procurement law requires the government to use environmental labelling products; Japan started the implementation of the green procurement law in 2001, and it can be said that the legislation is a success for developed countries to implement government

greening. The important guarantee of purchase. At present, China's government green procurement is still in its infancy. Therefore, the formulation and improvement of relevant legal systems is the primary issue in the use of environmental measures in China's government procurement. In the long run, China should formulate a special “Government Green Procurement Law”, which clearly stipulates the formulation and publication of the government's green procurement principals, responsibilities, green procurement standards, and green procurement lists. At present, China's “Government Procurement Law” has been enacted for six years and has related principle provisions. Therefore, under the framework of this law, it is possible to formulate and promulgate government green purchasing regulations or methods that suit China's national conditions. Internal promotion provides strong legal protection.

6. REFERENCES

Su W L. On Government Green Procurement and Promotion of Ecological Civilization Construction[J]. Theoretic Observation, 2014(03).32-33

Zhao F. The fulcrum of inciting China's new energy vehicle consumer market lies in the implementation of long-term government procurement policies[J]. Modern Industrial Economy, 2013(07):28-32

Guo Y. Green Public Procurement under the Opening Condition [J]. Green Economy, 2012(02):142-145

Xu G. Analysis of Effects and Solutions of Government Green Procurement under the Perspective of Low-Carbon Economy [J]. Ecological Economy. 2011(3):121-125

Ma X, Yang P. Government Green Purchasing under GPA Framework [J]. China State Finance, 2011(06):65-66

New energy vehicles in China, https://en.wikipedia.org/wiki/New_energy_vehicles_in_China

Wood D G. Federal procurement - Government agencies’ purchases of recycled-content products [N]. Natural Resource and Environment Issues, 2002-07 -11.

Scot C. Finding the best green value: strategies balance cost, human health and environment concerns [J]. Government procurements, 2005(1): 17.

242: Numerical study of natural convection from a vertical array of elliptic cylinders

Zhaohui HE[1,2], Jinrong ZHU[1,2], Chunfu CHENG[2], Jinye ZHANG[2], Ni HU[2]

[1] Hubei Collaborative Innovation Center for High-efficiency Utilization of Solar Energy，Hubei University of Technology，Wuhan，Hubei，China, 430068
[2] School of Science，Hubei University of Technology，Wuhan，Hubei，China, 430068

This study investigates natural convection heat transfer from a vertical array of five elliptic cylinders numerically. The axis ratio of each cylinder changes in the range from 0.25 to 0.75.ANSYS18.0 is used to study a two-dimensional natural convection for Rayleigh numbers varying in range of 10^3 to 10^5.The effect of the axis ratio and center-to-center separation distance from 2 to 5 cylinder major axis are examined. The average Nusselt number of each individual cylinder and the array are investigated to describe the strength of heat transfer. As the separation distance increases, the average Nusselt number of the bottom cylinder in the array basically unchanged, and the average Nusselt number of downstream cylinder increases. The average Nusselt number of the array increases with increasing the Rayleigh number and cylinder spacing.

Keywords: Natural convection; Elliptic cylinder; Vertical array; flow diverters; Numerical simulation

1. INTRODUCTION

Natural convection heat transfer from pipes and tubular arrays are relevant to many industrial applications, such as heat exchangers, air conditioning industries, and cooling of electronic devices. Many investigations have dealt with the heat transfer from single cylinder (Churchill 1975; Saitoh 1993; Chouikh 2000; Misumi 2003) or an array of cylinders (Demir 2010; Grafsronningen 2013; Kitamura 2016; Mustafa 2017). The natural convection heat transfer from a cylinder in an array is quite different from a single cylinder due to the interaction of the flow fields around neighbouring cylinders.

Eckert and Sorhngen 1948) firstly studied the natural heat transfer from horizontal cylinders in a vertical array. They used three cylinders of 22.3 mm diameter in vertical and found that the heat transfer from the lowest cylinder in the array remained the same as a single cylinder. The same type of results were obtained by Yang Shiming (1997), who studied heat transfer from a vertical array of three heated cylinders in high Rayleigh numbers. It was found that the heat transfer of the bottom cylinder is the same as a single cylinder, the middle cylinder improved with respect to the single cylinder and the upper cylinder is between the two.

Corcione et al (2005) numerically investigated steady laminar free convection flow from a vertical array of 2-6 circular cylinders. The center to center separation distances from 2 up to more than 50 cylinder-diameters were studied over the range of Rayleigh numbers from 5×10^2 to 5×10^5.It was found that the heat transfer rate at any downstream cylinder may either enhance or degrade with respect to that for a single cylinder, depending on the location of the cylinder in the array and the tube-spacing.

Hyun Sik Yoon et al. (2012) numerical studied the natural convection in a cooled square enclose with two inner heated circular cylinders with the same diameter for different Rayleigh numbers varying in the range of 10^3 to 10^5.They considered the effect of the radius of inner cylinders and found that the average Nusselt number of the inner cylinders decreases with increasing the radius. Unsteady natural convection heat transfer from two horizontal cylinders has also been reported by Quentin Pelletier et al. (2016). They investigated the natural convection from a pair of isothermally heated horizontal cylinders in water for Rayleigh number from 1.7×10^6 to 5.3×10^6 and spacing between 2 and 4 diameters. They found that a maximum enhancement of Nusselt number is Ra=5.3×10^6 and S=3.5D.

Generally, change the circular cylinder into elliptical is an acceptable way to enhance the natural convection heat transfer of the cylinder array. Memory et al (1997) reported that the elliptical cylinder has a nearly 11% improvement in the mean heat transfer coefficient of an elliptic cylinder compared to a circular cylinder. R.Y.Sakr et al (2008) experimental and numerical studied natural convection heat transfer from a horizontal elliptic cylinder. They considered the effect of tube orientation angle and axis ratio of elliptic cylinder on heat transfer, and found that the average Nusselt number decreases with the increase of the elliptic cylinder orientation angle from the position where its major axis is horizontal to the vertical. Corcione et al (2009) reported a muti-Prandl correlating equations for free convection heat transfer from a horizontal elliptic cylinder. Liao et al. (2012) investigated the influences of a confined elliptic cylinder at different aspect ratios and inclinations on the laminar natural and mixed convection flows.

T.Yousefi and M.Ashjaee (2007) experimentally investigated natural convection heat transfer from vertical array of five horizontal isothermal elliptic cylinders. The axis ratio was kept constant to 0.67. The investigation was performed in air for center-to-center separation distance from 2 to 5 cylinder major axis and for Rayleigh numbers from 10^3 to 2.5×10^3. They found that the average Nusselt number of the array increases with increasing the Rayleigh number and cylinder spacing.

Therefore, the present paper aims to study on the effect of the axis ratio of elliptic cylinders in a vertical array on the natural convection heat transfer. The influence of cylinder spacing and Rayleigh numbers are also examined.

2. MATHEMATICAL MODEL

Figure 1 shows the geometry in which natural convective heat transfer is studied in this work. It consists of a vertical array of five horizontal isothermal elliptic cylinders. The cylinder major axis is a, minor axis is b. The axis ratio (AR=b/a) of the cylinder changes in the range from 0.25 to 0.75. The numerical study is carried out by using Finite-Volume-Method (FVM). The investigation is performed in air for center-to-center separation distance (S) from two to five cylinder major axis and for Rayleigh numbers based on the cylinder major axis in the range between 10^3 and 10^5.

The dimensionless governing equations for two-dimension, steady, laminar, and incompressible flow with Boussinesq approximation can be written as:

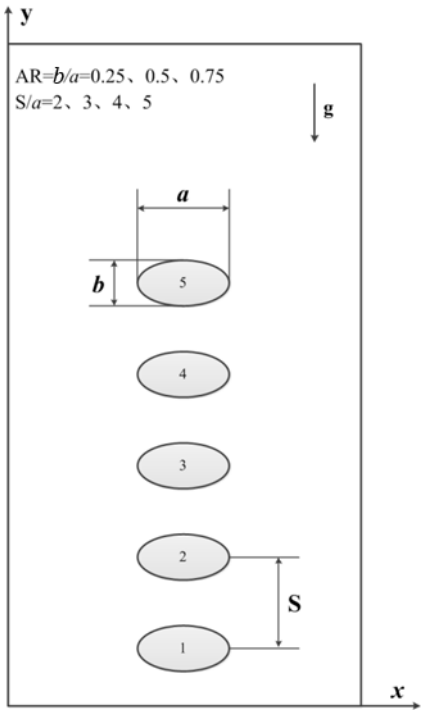

Figure 1: Geometry describing the physical problem

$$\frac{\partial u}{\partial x}+\frac{\partial v}{\partial y}=0 \tag{1}$$

$$u\frac{\partial u}{\partial x}+v\frac{\partial u}{\partial y}=-\frac{\partial P_d}{\partial x}+\left(\frac{\partial^2 u}{\partial x^2}+\frac{\partial^2 u}{\partial y^2}\right) \tag{2}$$

$$u\frac{\partial v}{\partial x}+v\frac{\partial v}{\partial y}=-\frac{\partial P_d}{\partial y}+\left(\frac{\partial^2 v}{\partial x^2}+\frac{\partial^2 v}{\partial y^2}\right)+GrT \tag{3}$$

$$u\frac{\partial T}{\partial x}+v\frac{\partial T}{\partial y}=\frac{1}{Pr}\left(\frac{\partial^2 T}{\partial x^2}+\frac{\partial^2 T}{\partial y^2}\right) \tag{4}$$

The following dimensionless variables are used: $P_d = P/\rho u_0^2$, $T=(T-T_0)/\Delta T$, $Pr=\nu/\alpha$, $Ra=g\beta\Delta TL^3/\nu\alpha$

The local Nusselt number of each individual cylinder in the array is determined as follows:

$$\mathrm{Nu}=\frac{h}{k_\mathrm{f}}=-\frac{k_\mathrm{w}a}{k_\mathrm{f}\left(T_w-T_\infty\right)}\cdot\left.\frac{\mathrm{d}T}{\mathrm{d}r}\right|_{r=0} \tag{5}$$

Where k_f is the air thermal conductivity at film temperature, which is defined as:

$$T_\mathrm{f}=\frac{T_w+T_\infty}{2} \tag{6}$$

The average Nusselt number of the array is obtained as the arithmetic mean value of the average Nusselt numbers of the individual cylinders in the array:

$$\overline{Nu_a}=\frac{1}{5}\sum_{i=1}^{5}\overline{Nu_i} \tag{7}$$

3. GRID INDEPENDENCE TEST, AND VALIDATION

3.1. Grid generation

Figure 2 shows a typical mesh of the numerical model for AR=0.5, S/a=2. The calculation domain is divided into two parts. In the inner part, the mesh around the elliptic cylinders is discretized using triangular cells. The left and right part of the calculation domain is discretized with rectangle cells.

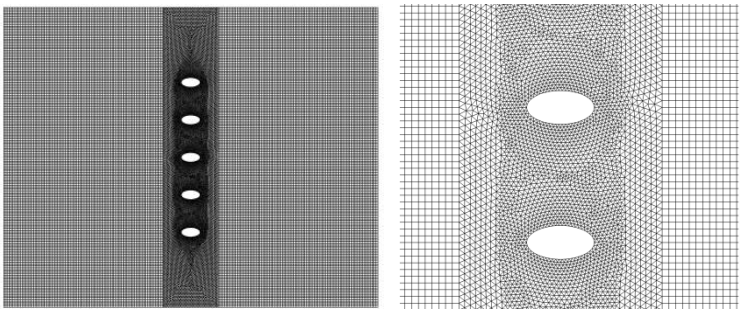

(a) (b)

Figure 2: Overview of the two-dimensional mesh (a), and close-up view of the cylinders from structured mesh around the elliptic cylinders (b) for AR=0.5 S/a=2.

Table 1 shows the effect of grid size on the average Nusselt number for the array of five elliptic cylinder (S/a=2, Ra=10^3).Increasing the number of cells more than 257348 did not increase the accuracy of average Nusselt number. It was found that the number of computational cells was fixed to 257348 after doing the grid independence test.

Table 1: Comparison of the simulated Nusselt number for different uniform grid with experimental result of Ref[18] for grid-independence test

Grid	43981	87962	175924	257348	351848	Ref[18]
$\overline{Nu}$	3.10	2.642	2.381	2.281	2.280	2.288

3.2. Validation

Figure 3 and Figure 4 show the comparison of the experimental data with T.Yousefi et al.[18]. In this comparison, the axis ratio (b/a) is kept constant to 1.49. The center-to-center separation distance is from two to five cylinder major axis for Rayleigh number in the range between10^3 and 2.5×10^3.

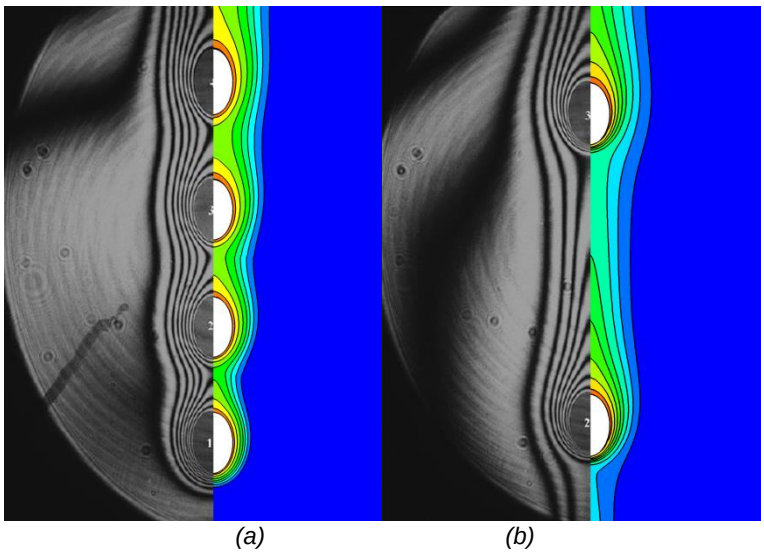

(a) *(b)*

Figure 3: Comparison of the temperature field with T.Yousefi et al. for the array first through fourth cylinder for S/a=2 and Ra=2×10^3(a) and second and third cylinder for S/a=5 and Ra=2×10^3(b).

Figure 3 shows the comparison of the temperature field with T.Yousefi et al. for the array first through fourth cylinder for S/a=2 and Ra=2×10^3(a) and second and third cylinder for S/a=5 and Ra=2×10^3(b). Figure 4 is the comparison of average Nusselt number of any individual cylinder in the array (a) and average Nusselt number of all the cylinders in the vertical array (b).It means in both individual cylinder and all the cylinders, the present numerical results agree well with the previous results.

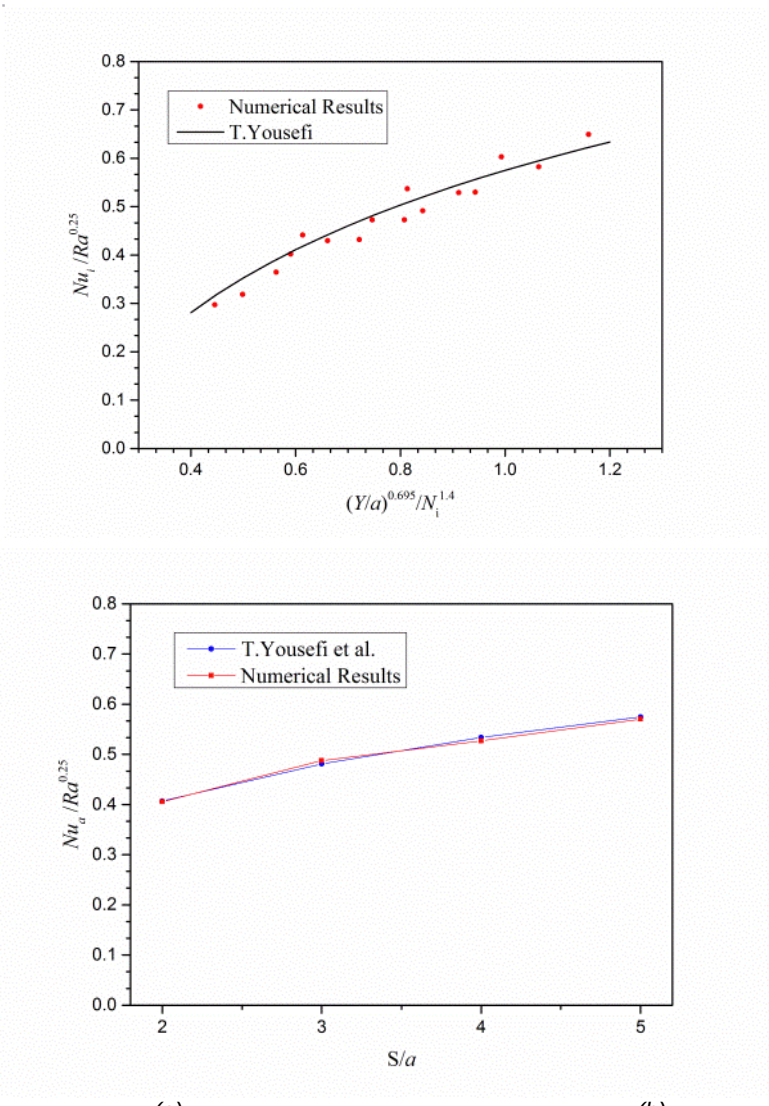

(a) (b)

Figure 4: Comparison of average Nusselt number with T.Yousefi et al. for the individual cylinder in the array (a) and all the cylinders in the vertical array (b).

4. NUMERICAL RESULTS

Natural convection heat transfer from the vertical array of five horizontal isothermal elliptic cylinders has been studied. The axis ratio of the cylinder is from 0.25 to 0.75.The range of Rayleigh is from 10^3 to 10^5.

4.1. Temperature contour

Figure 5 shows the contours of static temperature over the array of elliptic cylinders with varying AR and separation spacing for Rayleigh number from 10^3 to 10^5.It is clear that the temperature contours are symmetric about the minor axis of any case. Also, it is observed that as the Rayleigh number increases the temperature gradient around the cylinders increases, indicating that the heat transfer increases. Another phenomenon can be seen from the figure is that the isotherms has double peak in some case. It is due to the effect of the raising plume of the bottom cylinder.

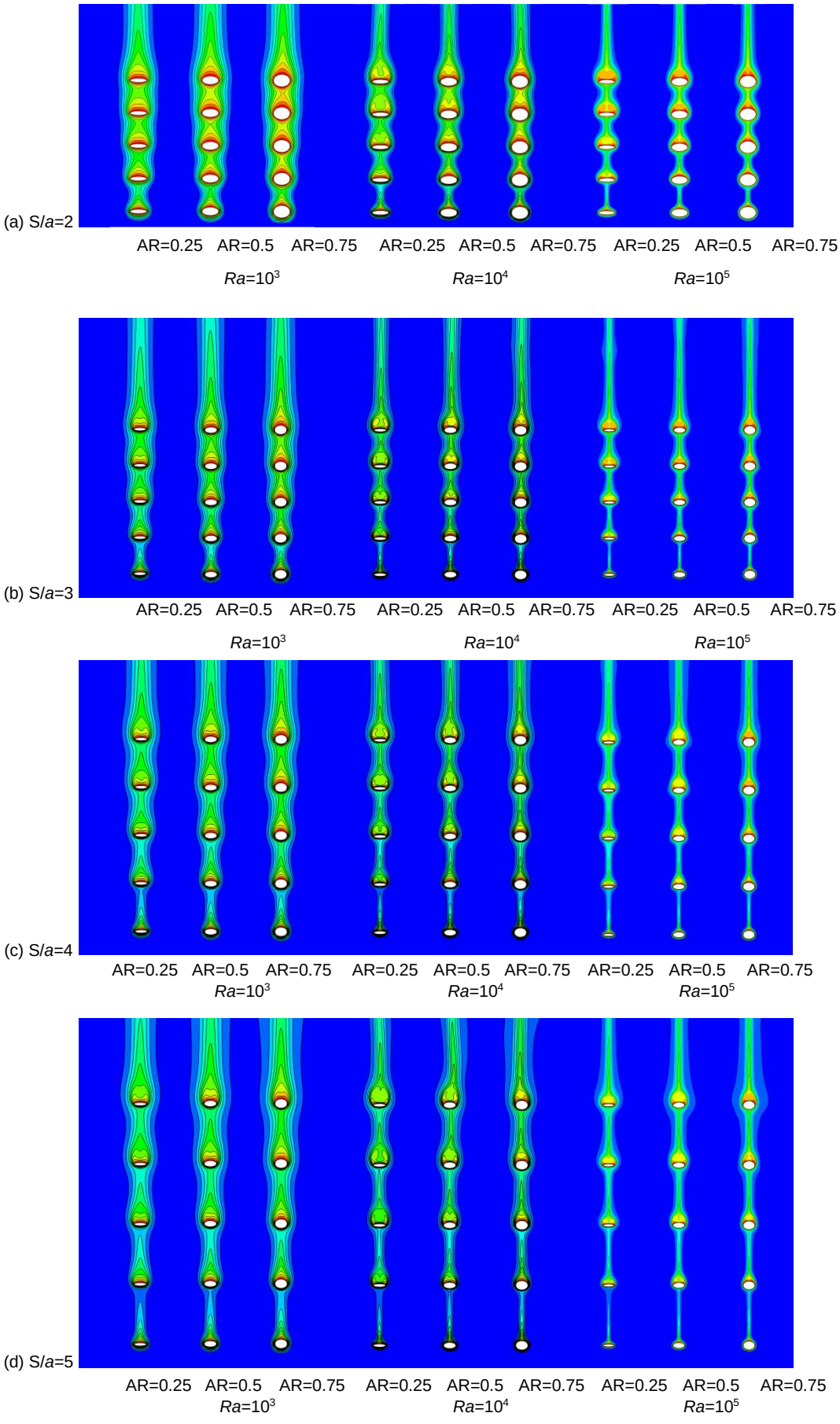

Figure 5: Temperature contours with various spacing betweent 2 to 5 cylinder major axis for $Ra=10^3$ to 10^5 AR=0.25 to 0.75 (a:S/a=2; b:S/a=3; c:S/a=4; d:S/a=5)

4.2. Heat transfer from each individual cylinder in the array

Figure 6 is variations of the average Nusselt number for individual elliptic cylinder in the array for Rayleigh numbers from 10^3 to 10^5. Three colour and four symbol of the line are used in each figure in order to distinguish the AR and S/a. It can be observed that the Nusselt number of the bottom cylinder (C1) in the same AR do not change with the change of S/a, and the Nusselt number from C2 to C5 is shown a decrease tendency in any case. It can be seen that the Nusselt number of each cylinder in the array decreases monotonically with the rise of AR.

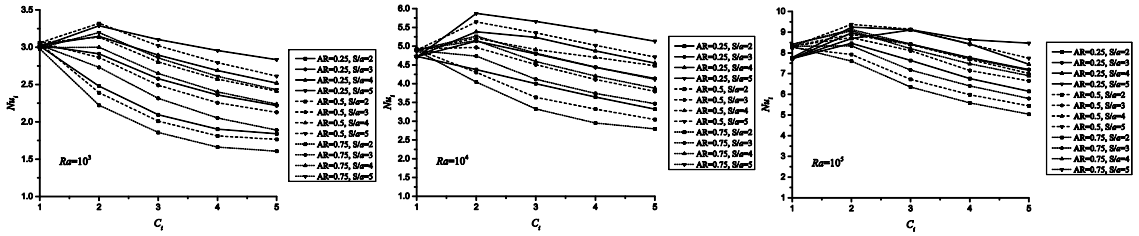

(a) Ra=10^3 (b) Ra=10^4 (c) Ra=10^5

Figure 6: Variations of the average Nusselt number for individual elliptic cylinder in the array for Rayleigh numbers from 10^3 to 10^5

4.3. Heat transfer from the array

Figure 7 is variations of the average Nusselt number of the array versus dimensionless cylinder spacing S/a for Rayleigh number from 10^3 to 10^5. As seen from the figure, the average Nusselt number of the array ($\overline{Nu_a}$) is increased by increasing Rayleigh number and decreased by increasing AR. The average Nusselt number of the array is increased by increasing S/a. It is the same tendency of the individual cylinder.

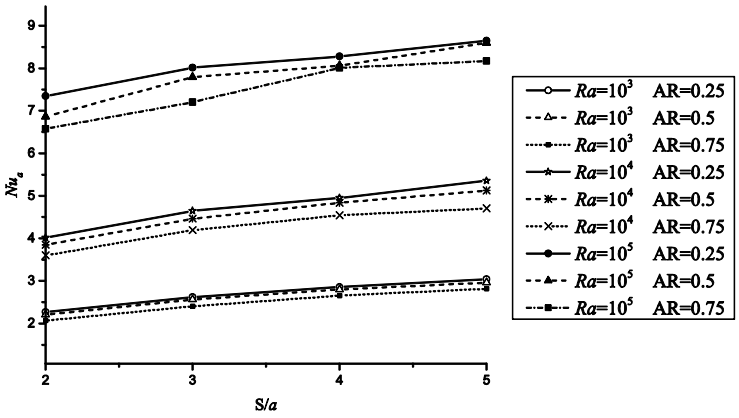

Figure 7: Variations of the average Nusselt number of the array versus S/a for different AR for Rayleigh number between 10^3 to 10^5

The numerical results for average Nusselt number of all the cylinders in the vertical array may be correlated to the Ra, S/a and AR, by the following equation:

$$\overline{Nu_a} = Ra^{0.25}\left[0.183\ln(S/a)+0.28\right]\times(1-0.25\,\mathrm{AR}) \tag{8}$$

$$2 \le S/a \le 5$$

$$0.25 \le \mathrm{AR} \le 0.75$$

$$10^3 \le Ra \le 10^5$$

The numerical results with its correlation Eq.(8), are presented in Figure 8

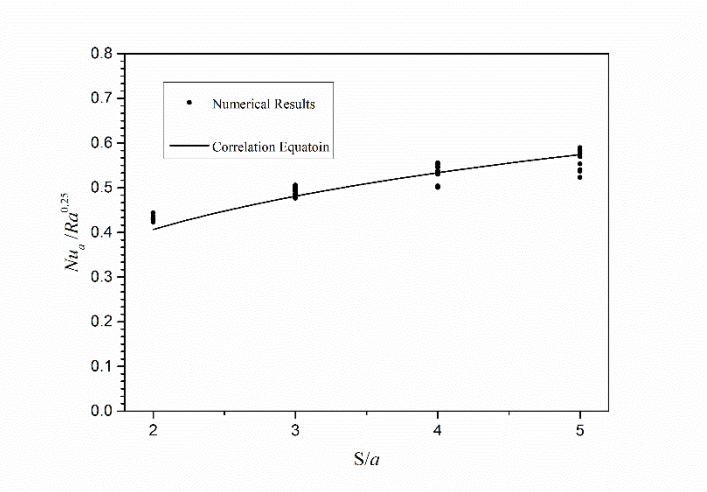

Figure 8: Comparison of the Numerical results with the Eq.(8)

5. CONCLUSIONS

The average Nusselt number of individual cylinder and all cylinders of the array increase with increasing Ra from 10^3 to 10^5.

The Nusselt number from the bottom cylinder in the array at any Rayleigh number and for each cylinder space is basically unchanged, and the Nusselt number of the second to fifth cylinder is increase with increasing cylinder spacing.

The average Nusselt number of the array decreases with increasing AR from 0.25 to 0.75.

6. REFERENCES

Churchill SW, Chu HHS, 1975. Correlation equations for laminar and turbulent free convection from a horizontal cylinder. *International Journal of Heat and Mass Transfer*, 78(9), 1049-1053.

Saitoh T, Sajiki T, Maruhara K, 1993. Bench mark solutions to natural convection heat transfer problem around a horizontal circular cylinder. *International Journal of Heat and Mass Transfer*, 36(5), 1251-1259.

Chouikh R, Guizani A, El Cassi A, Maalej M, Belghith A, 2000. Experimental study of the natural convection flow around an array of heated horizontal cylinders. *Renewable Energy*, 21(1), 65-78.

Misumi T, Suzuki K, Kitamura K, 2003. Fluid flow and heat transfer of natural convection around large horizontal cylinders: experiments with air. *Heat Transfer-Asian Research*, 32(4), 293-305.

Demir H, 2010. Experimental and numerical studies of natural convection from horizontal concrete cylinder heated with a cylindrical heat source. *International Communications in Heat and Mass Transfer*, 37(4), 422-429.

Grafsronningen S, Jensen A, 2013. Natural convection heat transfer from three vertically arranged horizontal cylinders with dissimilar separation distance at moderately high Rayleigh numbers. *International Journal of Heat and Mass Transfer*, 57(2), 519-527.

Kitamura K, Mitsuishi A, Suzuki T, Kimura F, 2016. Fluid flow and heat transfer of natural convection induced around a vertical row of heated horizontal cylinders. *International Journal of Heat and Mass Transfer*, 92, 414-429.

Mustafa AW, Zahi JA, 2017. Constructal design of elliptic tubes cooled by natural convection. *International Journal of Energy and Environment*, 8(3), 279-290.

Eckert ERG, Soehngen EE, 1948. Studies on heat transfer in laminar free convection with the Mach-Zehnder in interferometer. AF Technical Reports, 5747, USAF Air Material Command, Wrigh-Paterson Air Force Base, Ohio.

Yang S, Jiang C, Xu J, Fan Y, 1997. High rayleigh number natural convection heat transfer from vertical array of horizontal cylinders. *Journal of Engineering Thermo Physics*, 18(5), 588-591.

Corcione M, 2005. Correlating equations for free convection heat transfer from horizontal isothermal cylinders set in a vertical array. *International Journal of Heat and Mass Transfer*, 48(17), 3660-3673.

Yoon HS, Jung JH, Park YG, 2012. Natural convection in a square enclosure with two horizontal cylinders. *Numerical Heat Transfer*, *Part A,* 62, 701-721.

Pelletier Q, Murray DB, Persoons T, 2016. Unsteady natural convection heat transfer from a pair of vertically aligned horizontal cylinders. *International Journal of Heat and Mass Transfer*, 95, 693-708.

Memory SB, Adams VH, Marto PJ, 1997. Free and forced convection laminar film condensation on horizontal elliptical tubes [J]. *International Journal of Heat and Mass Transfer*, 40(14), 3395-3406.

Sakr RY, Berbish NS, Abd-Alziz AA, Hanafi AS, 2008. Experimental and numerical investigation of natural convection heat transfer in horizontal elliptic annuli. *International Journal of Chemical Reactor Engineering*, 4(2), 138-155.

Corcione M, Habib E, 2009. Multi-Prandtl correlating equations for free convection heat transfer from a horizontal tube of elliptic cross-section. *International Journal of Heat and Mass Transfer*, 52(5-6), 1353-1364.

Liao CC, Lin CA, 2012. Influences of confined elliptic cylinder at different aspect ratios and inclinations on the laminar natural and mixed convection flows. *International Journal of Heat and Mass Transfer,* 55(23-24), 6638-6650.

Yousefi T, Ashjaee M, 2007. Experimental study of natural convection heat transfer from vertical array of isothermal horizontal elliptic cylinders. *Experimental Thermal and Fluid Science*, 32, 240-248.

243: Self-cleaning characteristics of mesoporous nano-crystalline TiO_2-SiO_2 thin films

Chen CHEN[1], Xinguo MA[1,2], Shijie DONG[2], Xiaobo CHEN[3], Chuyun HUANG[1,2]

[1] School of Science, Hubei University of Technology, Wuhan 430068, China
[2] Hubei Collaborative Innovation Center for High-efficiency Utilization of Solar Energy, Hubei University of Technology, Wuhan 430068, China, maxg2013@sohu.com
[3] Department of Chemistry, University of Missouri-Kansas City, Kansas City, MO64110, USA

Since titanium dioxide was found to exhibit super-hydrophilicity under ultraviolet light, researches on titanium dioxide self-cleaning films have also been continuing. It has been proved that mesoporous structure of the film can improve its optical transmittance, reduce the light reflection, and improve the utilization of light, thus enhancing its photocatalytic activity. The doping of SiO_2 in TiO_2 can increase the number of hydroxyl groups on the surface of the film, inhibit the transformation of TiO_2 crystals and increase the specific surface area, thus improving its photocatalytic activity and reduce the contact angle of water droplets, and eventually enhancing the self-cleaning effect of the film. In this paper, the effects of different volume fractions of SiO_2 on the surface morphology, mechanical stability, wettability and photocatalytic activity of TiO_2 films are explored in great detail. It has been found that the film shows a smooth, crack-free surface morphology at a volume fraction of 20% SiO_2. After exposure to ultraviolet light, a contact angle of 0.75° can be obtained in a short time, and the film exhibits super-hydrophilicity. Moreover, a low contact angle is maintained for a long time after the lighting is stopped. Methyl orange is adopted to evaluate its photocatalytic performance. Under ultraviolet light, it can be almost completely degraded in a short time, showing great photocatalytic activity. All the mesoporous films prepared exhibit good optical permeability. At the same time, it has been found that the films prepared are of good adhesion and maintain acid and alkaline resistance under natural conditions.

Keywords: TiO_2-SiO_2 thin film; mesoporous; self-cleaning; photocatalysis

1. INTRODUCTION

Since Fujishima et al (2010) discovered that TiO_2 film shows superhydrophilicity after being irradiated by ultraviolet light in 1997. Because of its potential application value in self-cleaning and other fields, this property has attracted wide interest from domestic and foreign researchers (Kyou-Hwa 2011; Aita 2007; Paz 1995). When the surface of each type of glass or lens is coated with nano-TiO_2, rain or mist attached to the surface of the glass will not form water droplets and rapidly spread into a uniform water film, thereby not affecting people's sightlines (Ohtani 2014). The surface coated with nano-TiO_2 film has super-hydrophilicity, so that oil stains are not easily adhered, and even if the adhesion is combined with the outer water film, it is easily detached from the surface under external wind and water leaching conditions and achieves the self-cleaning function (Duan 2009).

However, a single TiO_2 film can only produce superhydrophilicity under UV light, and the adhesion between the film and the supporting substrate is not strong, which limits its use in technology (Zhang 2008). Therefore, most of the current researches have centered on the modification of TiO_2 ultra-hydrophilic thin films (Yu 2006; Yu 2002). Surfactants have a biparental function and can further improve the surface microstructure of the film by affecting the dispersion state and surface properties of the nanoparticles. Li et al. (2008) used surfactant-modified nano-TiO_2 to synthesize nano-TiO_2 thin films that were not irradiated with ultraviolet light but had ultra-hydrophilicity. Liu et al. (2002) used sol-gel method and dip pulling method to prepare TiO_2/Fe_2O_3 composite film on ordinary glass slides. It was found that the hydrophilic energy of the film varies with the Fe_2O_3 mass fraction, when the Fe_2O_3 mass fraction is 0.05%~0.1%，an ultra-hydrophilic film with a contact angle of 0° was obtained. Because of its unique structure, mesoporous materials show a good application prospect in the fields of catalysis, adsorption and separation, host-guest chemistry, and so on, which has ignited the upsurge of research on mesoporous materials (Kresge 1992). Compared with ordinary titanium dioxide, mesoporous titanium dioxide has an ordered pore structure and a higher specific surface area which makes it more advantageous in the field of photocatalytic self-cleaning. Studies have shown that the addition of SiO_2 contributes to the adsorption of hydroxy groups on the surface of the TiO_2 film, thereby improving its hydrophilicity (Yu 2001; Machida 1999; Zhai 1998). Yin (2003) found that the addition of SiO_2 not only affects the grain growth during the calcination process, but also enhances the permeability of the film, and at the same time increases the acidity of the film to increase the surface hydroxyl concentration, thereby increasing the surface hydrophilicity.

In this research, mesoporous TiO_2 materials were prepared by sol-gel method. Mesoporous materials were coated on glass substrates with self-made simple liquid flow method to produce self-cleaning mesoporous TiO_2-SiO_2 films of high adhesion, transparency, and high degree of wettability. Under short-time UV irradiation, the contact angle of the coating rapidly reduced to less than 0.75°, showing its super-hydrophilicity. At the same time, the effect of different volume fraction of SiO_2 sol in TiO_2 on surface morphology, stability, wettability and photocatalytic activity was studied in detail.

2. EXPERIMENTAL SECTION

2.1. Materials

Tetra-n-butyl titanate (TBOT, AR), tetraethylorthosilicate, anhydrous ethanol, and acetic acid were purchased from Sinopharm Group Chemical Reagent Co., Ltd. Concentrated hydrochloric acid was purchased from Xinyang Chemical Reagent Factory. P123 (Mn 5800) and polyethylene glycol PEG (Mn 2000) were purchased from Macleans. Deionized water was made in the laboratory. All chemicals were analytically pure and used without further purification.

2.2. Preparation of thin films

Sol-Gel method was used to prepare mesoporous TiO_2 and SiO_2 sol, and then different proportions of SiO_2 were added to TiO_2 and stirred. Mix 0.5 g of P123 and 1.5 g of PEG into 100 mL of anhydrous ethanol, stir it violently with magnetic force for 10 min, and then ultrasonically heated it at 60 °C and dispersed it for 30 min. Add 20 mL of butyl titanate dropwise to the stirred anhydrous ethanol under magnetic stirring. Add 10mL of anhydrous ethanol, 5mL of acetic acid and 5mL of concentrated hydrochloric acid and 15mL of deionized water into the mixture prepared before, mix and stir it for 30min, ultrasonically heat it at 40 °C and shake it for 15min. in the end the mesoporous TiO_2 sol is obtained. Similarly, mesoporous SiO_2 sol can be produced. Dip clean silicate glass pieces in concentrated H_2SO_4 and NaOH for 24 hours and then put them into anhydrous ethanol for later use. Take out the processed clean glasses and seal one side was with a corrosion-resistant tape, and at last vertically fix the glass pieces in a special separatory funnel. Mix the mesoporous TiO_2 sol and the mesoporous SiO_2 sol mixed with different proportions, stir it magnetically for 30 minutes, ultrasonically shake it for 30 minutes, and dry it in a drying oven at 80℃ for 30 minutes. Then, the desired mixed sol can be obtained. Pour the mixed sol into a separatory funnel and immerse the glass pieces into the liquid. Turn on the flow switch to make the sol left on the glass pieces slowly, that is, to coat a transparent film on the surface of the glass pieces Take out the glass and dry them in a drying oven at 80°C for 30 min. After drying, strip the corrosion-resistant tape from the glass and heat them in a boiling furnace to

450 °C at 100 °C/h. Preserve the heat for 1 hour and then slowly cool them to room temperature. In this way, the mesoporous TiO_2-SiO_2 film was obtained.

2.3. Characterization

Ultraviolet spectrophotometer was used to study the transmittance of the film. SEM was employed to characterize the structural morphology of the film. The hydrophilicity of the film was represented by the contact angle, and the adhesion of the film was investigated through a standard grid method.

2.4. Photocatalytic activity and self-cleaning measurements

Under certain conditions, the property of keeping the surface clean and not easily contaminated is Self-cleaning. The self-cleaning and photocatalytic properties of the prepared samples were evaluated through oleic acid (purity greater than 60.0% (mass fraction)) and methyl orange. The self-cleaning properties of the photocatalytic material were evaluated by testing the minimum contact angle of the sample. Firstly, attach organic material (pretreatment) to the surface of the sample. Then irradiate it with a certain amount of ultraviolet light, measure the changes in the contact angle during the process and finally characterize the self-cleaning property of the sample (Sangchay 2014).

3. RESULT AND DISCUSSION

3.1. Morphology

The SEM image of powders and thin films are shown in Figure 1.The pure TiO_2 powder particles and the powder of de TiO_2-SiO_2 system SEM are shown in Figure 1 (a) and (b). From (a) and (b), it can be clearly seen that the pure TiO_2 particles have agglomeration phenomenon, which reduces the specific surface area of the catalyst, and leads to a decrease in its photocatalytic efficiency. The SEM images of the mesoporous TiO_2-SiO_2 films and the pure TiO_2 film are shown in Figure 1. (c) and (d). Compared (c) with (d), it is obvious that the image (c) shows a porous structure. On the one hand, the porous structure can reduce the reflection of light and enhance the light utilization efficiency of the film. On the other hand, it also can enhance the adsorption of dyes, thereby enhancing the photocatalytic effect. At the same time, the porous structure can greatly increase the surface roughness of the film to increase the specific surface area and increase the adsorption of hydroxyl to enhance the hydrophilicity of the film. Meanwhile, the addition of SiO_2 can increases the hydroxyl content of the film surface and increases the hydrophilicity of the film.

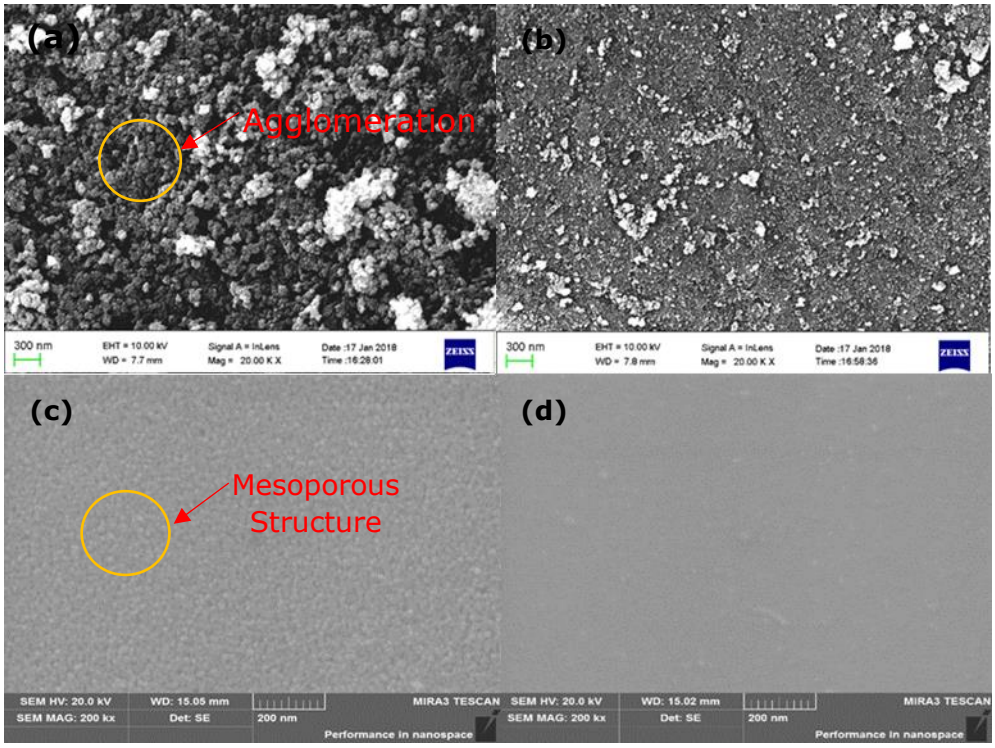

Figure 1: The SEM of powder(300nm) and films(200nm) (a) the pure TiO_2 powder; (b) the TiO_2-SiO_2 powder; (c) the TiO_2-SiO_2 mesoporous thin film; (d) the pure TiO_2 thin film .

3.2. Optical properties

The images of the optical transmission of TiO_2-SiO_2 (T-S) films and TiO_2 films at different volume fractions and photos of TiO_2-SiO_2 and TiO_2 films under a metallographic microscope are shown in Figure 2. From Figure 2. (a), it can be seen that all the films exhibit very high transmission, mainly due to the presence of mesoporous in the film, which reduces the reflection of the film. At the same time, the transmittance of TiO_2-SiO_2 film is higher than that of TiO_2 film, mainly because the SiO_2 can enhance the light transmittance of the film. The images of TiO_2 films and TiO_2-SiO_2 films under a metallographic microscope are shown in Figure 2. (b)(c)(d)(e)(f). From image (b), we can find that the TiO_2 film has many cracks, and the film formation quality is poor, and a colourful texture appears. The films in the image (b) and (c) shows less cracks and the image (e) and (f) shows smooth and uniform. It is mainly because SiO_2 can improve the adhesion between the film layer and the glass substrate and reduce the visual colour difference (Bai 2017) and light reflection, and finally improve the utilization of light.

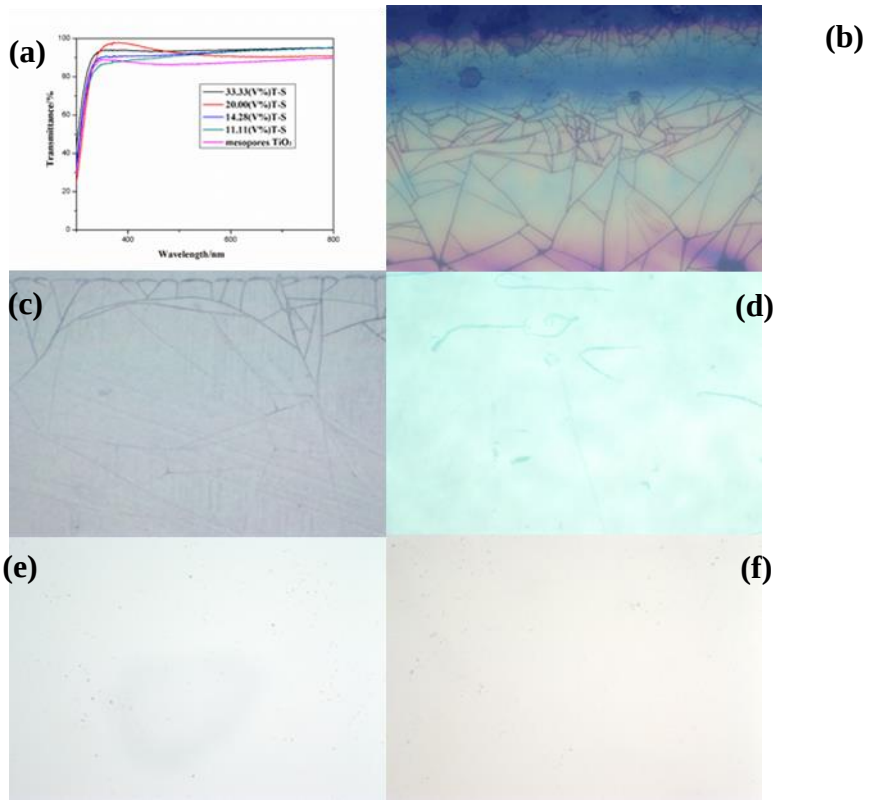

Figure 2: (a) The optical transmittance of films with different compositions ; (b)~ (f) the photos of TiO_2 films and different V % of TiO_2-SiO_2 (T-S) films under a metallographic microscope

3.3 Superhydrophilicity

The hydrophilicity of the film was evaluated mainly by the water contact angle (θ). When the contact angle was lower than 90° and higher than 5°, it shows hydrophilicity. While then θ was lower than 5°, it showed superhydrophilicity. The contact angles of water droplets for films with different composition ratios are shown in Figure 3. As it can be seen from the figure 3 (a) and (b), both the pure TiO_2 and the mesoporous TiO_2 have a slightly larger contact angle after light irradiation. The mesoporous TiO2 has a smaller contact angle than the pure TiO2 mainly because the water droplet is adsorbed on the surface of the film in the frontal concave hole and forms a solid-liquid composite surface with the film surface, and the remaining water droplets are spread on the solid-liquid composite surface. Therefore, water spreads faster on a porous surface than on a flat surface and the contact angle is smaller. With the addition of SiO_2, the contact angle of the film rises at the beginning and then decreases. The main reason is that when SiO_2 is introduced, SiO_2 can inhibit the grain transformation and grain growth of the TiO_2, which increases the specific surface area of the film and increase the surface hydroxyl group of the composite film (Yang 2013), and enhance the adsorption capacity of water raises, finally leading to the superhydrophilicity of the composite film. When the Si (V%) content reaches 20%, the water contact angle is the best at 0.75°. When the amount of SiO_2 is too large, the surface of the composite film will be occupied by more SiO_2, and the photocatalytic activity will be reduced, and the hydrophilic nano-domains will not be easily generated by light excitation, so its hydrophilicity is also reduced.

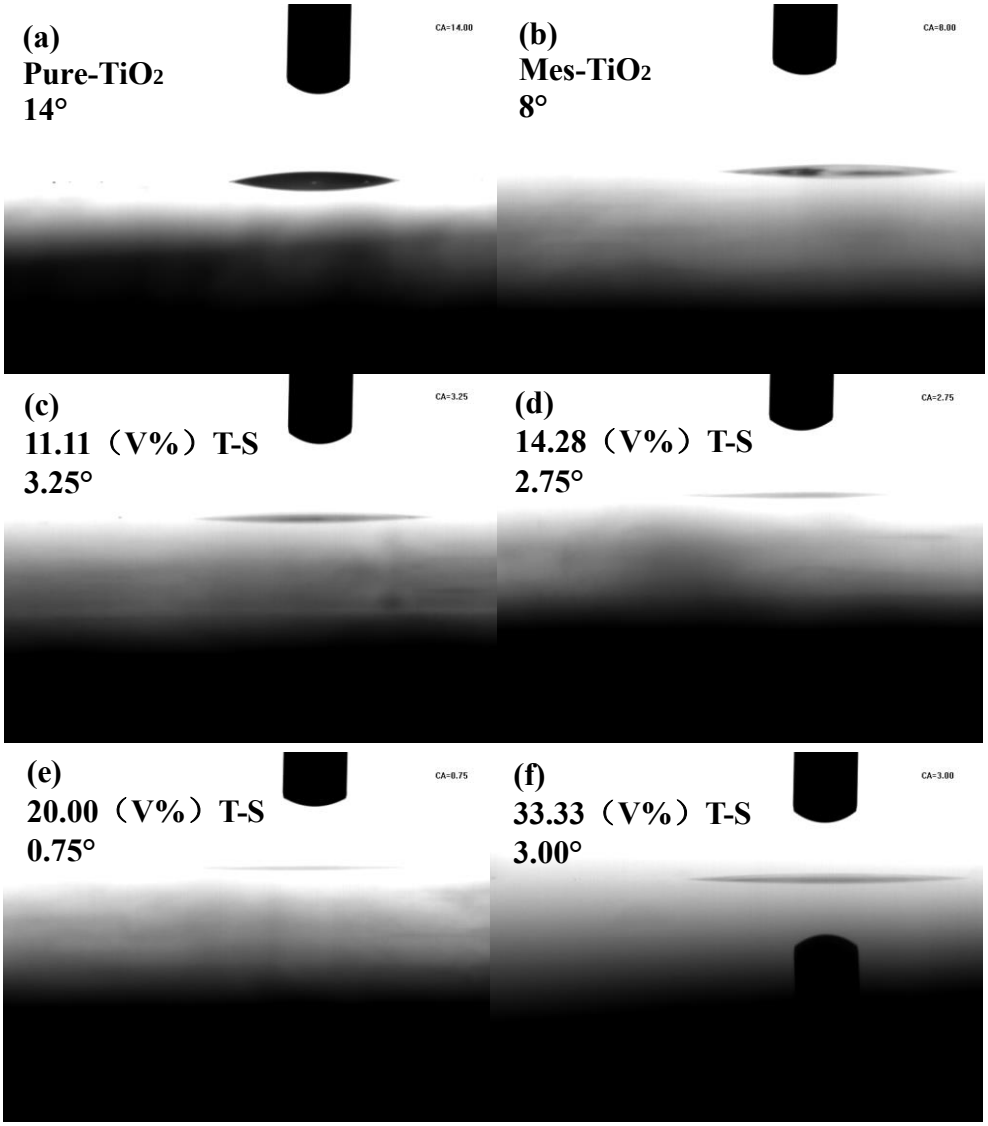

Figure 3: Contact angle of different films after light irradiation for 30 minutes. (a) (b) the Pure-TiO2 and Mesoporous TiO2;(c)~(f)the different V % of TiO2-SiO2 films.

3.4. Photocatalytic properties

Degradation of methyl orange was used to evaluate the catalytic performance of the catalyst. After the prepared sol is dried into a gel, the colloid is crystallized into a catalyst powder in a horse boiling furnace under the same conditions as the thin film is crystallized in high-temperature, and then powder is washed and dried. Take 15mg of methyl orange, and dissolve it in 1L of deionized water, then stir to make it dissolve evenly. Put 20 mg of catalyst powders of different compositions into 50mL of methyl orange solution and decompose it catalytically under ultraviolet light. The efficiency of photodegradation of methyl orange by different compositions of catalysts and the absorbance of different compositions of catalysts are shown in Figure 4. From Figure 4. (a) we can get that TiO_2 has the highest absorbance, with the incorporation of SiO_2, the absorbance gradually decreases. This is mainly in the ultraviolet region, only TiO_2 can absorb ultraviolet light under illumination. When the amount of SiO_2 is gradually increased, SiO_2 will coat TiO_2 and reduce its absorbance, affect its light energy utilization, and thus reduce its photocatalytic effect. From Figure 4. (b) we can find that the photocatalytic effect of pure TiO_2 is poor, and the effect of mesoporous TiO_2-SiO_2 system is obviously better than that of pure TiO_2.This is because the introduction of SiO_2 mainly improves the surface acidity of TiO_2, and the surface acidity can contribute to the formation of strong hydroxyl groups on the surface of the film. These hydroxyl groups can capture light generated holes, inhibit the recombination of electrons and holes, and the strong oxidized hydroxyl generated can increase the photocatalytic efficiency. At the same time, the increase of surface acidity can also form a better adsorption site, improve the adsorption effect on methyl orange and be more easily degraded. SiO_2 also inhibits the transformation of TiO_2 from anatase to rutile phase, and anatase TiO_2 has a better photocatalytic effect (Paušová 2014). The photocatalytic effect of TiO_2-SiO_2 film with mesoporous structure is better than that of ordinary TiO_2-SiO_2 film, which can be mainly attributed to its mesoporous structure. The mesoporous structure of the film reduces the reflection of light and enhances the

absorption of light. The utilization of light improves the photocatalytic effect. This kind of structure also enhances the adsorption of methyl orange, which facilitates photodegradation. In the figure, as the amount of SiO_2 gradually increases, the photocatalytic effect increases at first and then decreases. The main reason is that the introduction of Si can increase the photocatalytic efficiency. However, when the amount of Si further increases, the TiO_2 particles are easily coated with SiO_2. As SiO_2 itself is of no photocatalytic activity, it will reduce its catalytic effect. Therefore, a better photocatalytic effect can be obtained by introducing SiO_2 reasonably.

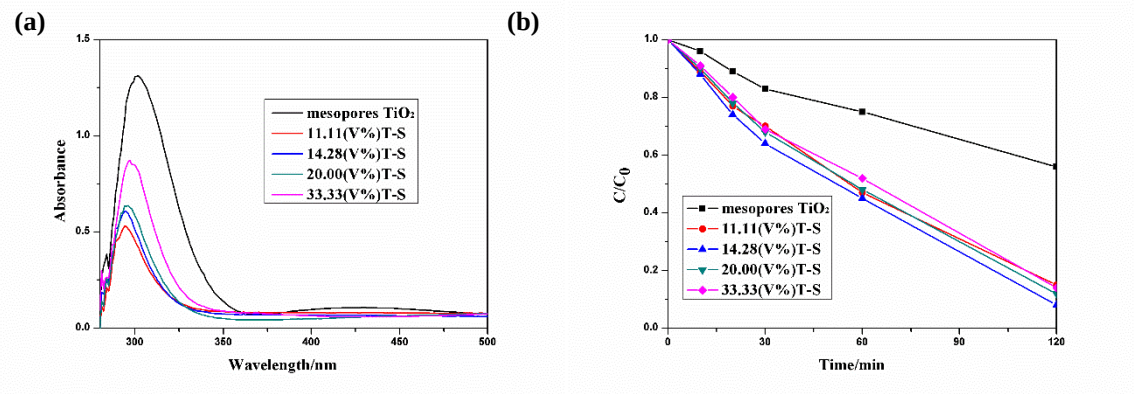

Figure 4: (a) the absorbance of different flims; (b) Photodegradation of Methyl Orange in Different Composition Photocatalysts

3.5. Film stability

The standard cross-cut method was used to measure the adhesion of the film and further to verify the mechanical properties of the film (Fateh 2013). Meanwhile the hydrophilicity of the film was measured after a week's light irradiation to check the stability of the film. The prepared film was soaked in concentrated sulfuric acid and hydrogen hydroxide respectively for 3 days and was preserved in the dark for a week. The adhesion test before and after the acid-base treatment are shown in Figure 5. From Figure 5.(a) and (b),it can be found that the TiO_2 film appears cracks after the treatment.Figure 5.(c) and (d) show that there is no change in the TiO_2-SIO_2 film before and after the treatment, indicating that the adhesion of the TiO_2-SiO_2 film with the substrate and the stability is better than the TiO_2 film. The water contact angles before light irradiation, after 30minutes light irradiation, and after one week of dark treatment are shown in Table1. It can be found that the film still maintains good hydrophilicity after one week, and even when the amount of SiO_2 is 20%, it still maintains 2° and exhibits super-hydrophilic. This mainly due to that when TiO_2 is composited with SiO_2, the physical adsorption of water on the surface of the TiO_2-SiO_2 film diffuses to SiO_2 under light irradiation and is adsorbed by SiO_2, which as result becomes a stable physical adsorption water layer. When light irradiation is stopped, the adsorbed water on the surface of SiO_2 can stabilize the Ti^{3+} and -OH structures on the surface of the TiO_2, and the TiO_2 surface can maintain hydrophilic properties for a long time in the dark. Therefore, the prepared films have good stability.

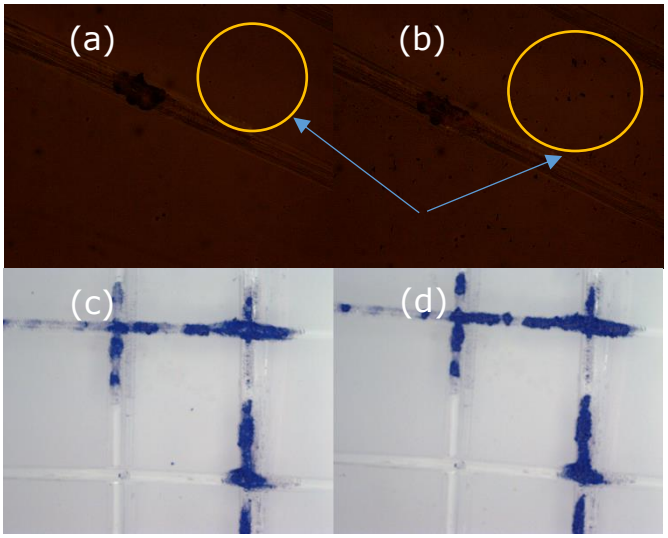

Figure 5: Adhesion of thin films after soaking in H_2SO_4 and NaOH.(a) the TiO_2 film before treatment;(b) the TiO_2 film after treatment;(c) the TiO_2-SiO_2 film before treatment; (d) the TiO_2-SiO_2 film before treatment.

Table 1: Contact angle (θ) before and after 30min light exposure and one week after dark

Film	Pure-TiO_2	Mes—TiO_2	11.11（V% ）T-S	14.28（V% ）T-S	20.00 （V%）T-S	33.33 （V%）T-S
Before lighting (θ)	22°	15.25°	7.25°	6.5°	5.5°	8°
After lighting 30min (θ)	14.00°	8°	3.5°	2.75°	0.75°	3°
A week after dark (θ)	18.25°	10.5°	5.25°	4.5°	2°	5.5°

4. CONCLUSION

A self-made liquid flow device was used to obtain mesoporous TiO_2-SiO_2 thin films by using Sol-Gel method and P123 and PEG as mixed template agents and incorporating different ratios of SiO_2 to TiO_2. Through the measurement on characterization of the film, optical properties, wetting properties, catalytic activity and stability, the following conclusions can be drawn: The mesoporous structure of the film can reduce light reflection, improve the utilization of light, and enhance the photocatalytic activity. At the same time, mesoporous mesopores can enhance the adsorption of water to the film and improve its superhydrophilicity. The incorporation of SiO_2 can increase the number of hydroxyl groups on the surface of the film, thereby improving the hydrophilicity of the film, and increasing the specific surface area of the photocatalytic film and finally enhancing the photocatalytic activity. In the meantime, the incorporation of SiO_2 can improve the adhesion between the film and the substrate, enhance the stability of the film, and stabilize the hydroxyl and Ti^{3+} on the surface of the film in the absence of light, thereby maintaining long-lasting hydrophilicity and even super-hydrophilicity;It was found that when the SiO_2 incorporation ratio is 20%, the prepared mesoporous TiO_2-SiO_2 film has the lowest contact angle, higher photocatalytic activity and optical transmittance, and has good stability and sustained hydrophilicity and showed self-cleaning properties.

ACKNOWLEDGEMENTS

This work was supported by the National Natural Science Foundation of China (51472081), Cooperative Foundation of China-UK Research and Innovation Bridges (2016YFE0124300), the Foundation for High-Level Talents (GCRC13014) and Leading Plan of Green Industry (YXQN2016005), the Development Funds of Hubei Collaborative Innovation Center (HBSKFMS2015004, HBSDB201704，HBSDY201713). X. C. appreciates the support from the U.S. National Science Foundation (DMR-1609061), and the College of Arts and Sciences, University of Missouri Kansas City.

REFERENCES

Wang, R., Hashimoto, K., Fujishima, A., Chikuni, M., Kojima, E., & Kitamura, A., et al. (2010). Photogeneration of highly amphiphilic tio2 surfaces. *Advanced Materials, 10*(2), 135-138.

Kyou-Hwa, P., Jai-Young, K., Seong-Kyun, K., & Seong-Joo, H. (2011). Wettability and cellular response of uv light irradiated anodized titanium surface. *Journal of Advanced Prosthodontics, 3*(2), 63-68.

Aita, H., Ohata, N., & Ogawa, T. (2007). Accelerated Osseointegration around Light-induced Super-amphiphilic Titanium Surface. (Vol.51).

Paz, Y., Luo, Z., & Heller, L. R. A. (1995). Photooxidative self-cleaning transparent titanium dioxide films on glass. *Journal of Materials Research, 10*(11), 2842-2848.

Ohtani, B. (2014). Photocatalyst. 1529-1532.

Duan, Q. (2009). Research progress of the self-cleaning glass. *New Chemical Materials*.

Zhang, H., Hai-Yong, Y. U., Wang, Q., & Deng, Y. M. (2008). Research of the influence of concrete designed value to corrosion of the steel bar under chloride environment. *Development & Application of Materials*.

Yu, J., Zhou, M., Yu, H., Zhang, Q., & Yu, Y. (2006). Enhanced photoinduced super-hydrophilicity of the sol–gel-derived tio2, thin films by fe-doping. *Materials Chemistry & Physics, 95*(2), 193-196.

Yu, J. C., Yu, J., Ho, W., & Zhao, J. (2002). Light-induced super-hydrophilicity and photocatalytic activity of mesoporous tio2, thin films. *Journal of Photochemistry & Photobiology A Chemistry, 148*(1), 331-339.

Jing, L., Li, S., Song, S., Xue, L., & Fu, H. (2008). Investigation on the electron transfer between anatase and rutile in nano-sized tio 2, by means of surface photovoltage technique and its effects on the photocatalytic activity. *Solar Energy Materials & Solar Cells, 92*(9), 1030-1036.

Liu, Q. J., Wu, X. H., Liu, Q., & Wang, B. L. (2002). Study on super-hydrophilicity property of tio2 thin films. *Journal of Functional Materials & Devices, 8*(3), 238-242.

Kresge, C. T., Leonowicz, M. E., Roth, W. J., Vartuli, J. C., & Beck, J. S. (1992). Ordered mesoporous molecular sieves synthesized by a liquid-crystal template mechanism. *Nature, 359*(6397), 710-712.

Yu, J. G., Zhao, X. J., Chen, W. M., Lin, L., & Zhang, A. L. (2001). Photocatalytic activity and hydrophilic property of tio2/sio2 composite nanometer thin films. *Acta Physico-chimica Sinica, 17*(3), 261-264.

Machida, M., Norimoto, K., Watanabe, T., Hashimoto, K., & Fujishima, A. (1999). The effect of sio2 addition in super-hydrophilic property of tio2 photocatalyst. *Journal of Materials Science, 34*(11), 2569-2574.

Zhai, J. W., Zhang, L. Y., & Lao, X. (1998). Diffusion of phase boundary and crystallization behaviours for tio2/sio2 composite films. *Journal of Inorganic Materials, 13*(1), 78-82.

Yin, Y. S., Guan, K. S., & ZHAO Hong nan. (2003). Effect of sio2 addition on surface structural and super-hydrophilic property of tio2 films. *Chinese Journal of Nonferrous Metals*.

Sangchay, W. (2014). Effect of calcinations temperature on microstructures, photocatalytic activity and self-cleaning property of TiO2 and SnO2/TiO2 thin films prepared by sol-gel dip coating process. International Conference on Experimental Mechanics 2013 and Twelfth Asian Conference on Experimental Mechanics (Vol.9234, pp.320-2). International Society for Optics and Photonics.

Bai, Z., Hu, Y., Yan, S., Shan, W., & Wei, C. (2017). Preparation of mesoporous sio2/bi2o3/tio2 superhydrophilic thin films and their surface self-cleaning properties. Rsc Advances, 7(4), 1966-1974.

Yang, C. X., Huang, H., Huang, T., & Yue, S. (2013). Preparation and superhydrophilic mechanism of porous tio2/sio2 composite thin film. Applied Chemical Industry.

Paušová, Š., Krýsa, J., Jirkovský, J., Prevot, V., & Mailhot, G. (2014). Preparation of tio2-sio2 composite photocatalysts for environmental applications. Journal of Chemical Technology & Biotechnology, 89(8), 1129-1135.

Fateh, R., Dillert, R., & Bahnemann, D. (2013). Preparation and characterization of transparent hydrophilic photocatalytic tio2/sio2 thin films on polycarbonate. Langmuir, 29(11), 3730-9.

244: Development of electronic gear box technology for HNC-8 CNC system

Guolong DING[1], Yali ZHANG[2], Daxing ZHAO[3], Zikai ZHANG[4]

[1] School of Mechanical Engineering, Hubei University of Technology, Wuhan, dingguolong@tom.com
[2] School of Mechanical Engineering, Hubei University of Technology, Wuhan, zhangyali19921005@126.com
[3] School of Mechanical Engineering, Hubei University of Technology, Wuhan, zdx008@126.com
[4] Chongqing Machine Tool (Group) Co., Ltd, Chongqing, zhangzikai@chmti.com

There is a big gap between the domestic CNC system and the imported system in gear hobbing process. The key problem lies in the poor function of the electronic gearbox in the domestic system and the low control precision of the following movement of each feed shaft and the hob spindle. Aiming at CNC gear hobbing machine with six-axis and four-link, the hobbing process is analyzed and the movement relationship model of hob spindle and each feed shaft are established. The characteristics of the open PLC interface of HNC-8 CNC system are studied. Based on the interface with an interpolation period of 1 millisecond, PID control algorithm is adopted to carry out the master-slave following motion control technology and develop the functional module of electronic gearbox for hobbing machine. The hardware and software experimental platform of motion control is built based on HNC-818B/M system to verify the function of electronic gearbox. The test results show that the motion control algorithm of the proposed electronic gearbox is reasonable and feasible, which provides a method for the development of the electronic gearbox of the domestic CNC system.

.

Keywords: gear hobbing process; master-slave motion control; HNC-8 CNC system; electronic gearbox

1. INTRODUCTION

Hobbing processing has good adaptability and high productivity. It is widely used in gear processing. However, the machining accuracy of gear is easily affected by the accuracy of parts, the structure of the tool and machine along with the accuracy of the whole process system. The traditional inline drive cannot meet the requirement of high precision machining by changing the gear in the gearbox. The electronic gear drive is driven by the servo device directly or through a short transmission chain. The internal transmission relationship is guaranteed by the software and the electronic circuit, so that the strict requirements for the transmission can be achieved.

In 1960s, Loxham proposed the concept of "Electronic Gearbox", then the British Cranfield Unit of Precision Engineering (CUPE) pioneered the electronic gearbox implemented by electronic hardware in the world. Dinsdale et al. first realized the phase-locked loop electronic gear and put forward the Cranfield "electronic gearbox" theory, then verified the application prospect of the electronic gearbox technology in the gear grinder (Dinsdale, 1982). Takeuchi et al. proposed the electronic gearbox realized by software. It has a wide transmission range, but the stability and static error of the system still cannot be effectively solved (Takeuchi, 1993). With the application of foreign electronic gearbox technology, many domestic scholars have gradually started the research on the realization method of electronic gearbox. Quan et al. proposed a software electronic gearbox, which is implemented by a microcomputer (Quan, 1999). Frequency doubling and closed loop control are adopted and a divider is introduced to eliminate the influence of feedback frequency multiplier on stability. Zhuang et al. studied the realization and control strategy of the electronic gearbox and pointed out that the electronic gearbox with phase-locked loop has unique advantages in the steady state and precision, but there are obvious defects in the dynamic performance and anti-interference performance (Zhuang, 2001). Xiong et al. researched the basic structure and information processing of the software gearbox, then discussed the internal transmission structure of the CNC gear shaper based on the principle of electronic gearbox (Xiong, 2008). HU et al. designed the transmission scheme of the electronic gearbox based on the linkage movement model of the hobbing processing scheme of the non-circular spur gear and the helical gear (Hu, 2009). Tian et al. set up a new theory model of gear hobbing electronic gearbox on the basis of gear processing technology (Tian, 2015) and studied the realization and structure of EGB in the embedded CNC system based on ARM+DSP+FPGA (Tian, 2016). By studying the control error analysis, estimation and compensation in the process of gear hobbing, a kind of new architecture which is connected by EGB and cross coupling controller, is proposed to improve the control precision of the electronic gearbox (Tian, 2016). Han et al. analyzed the cause of the generation error of the electronic gearbox and put forward the synchronous coupling control method to improve the control accuracy of the electronic gearbox (Han, 2017).

Currently, the research on the technology of electronic gearbox (EGB) have been generally based on imported CNC systems such as SIMENS form Germany and FANUC form Japan. The EGB technology was seldom used in domestic CNC system. The key problem was the low precision of electronic gearbox in the domestic system. In view of the CNC gear hobbing machine with six-axis and four-link, an electronic gearbox motion control algorithm was proposed based on the domestic HNC-8 CNC system. The feasibility and correctness of the proposed electronic gearbox were verified by the function experiment on the secondary development platform. It provided a method for the realization of the electronic gearbox technology on domestic CNC system.

2. ANALYSIS OF GEAR HOBBING PROCESS

The gear hobbing machine with six-axis and four-link has five feed shafts and a servo spindle as shown in Figure 1.

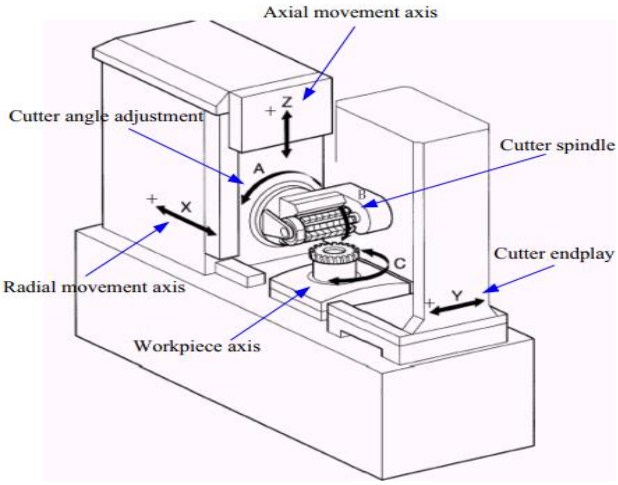

Figure 1: Overall structure of gear hobbing machine with six-axis

The motion of gear hobbing machine is mainly composed of four kinds of motion: cutting motion; feeding motion of each shaft; tooth dividing movement; and differential transmission. When machining different types of gears, the additional motion is different and the meshing relationship between the axes and C-axis is different. In the hobbing process, the coupling equation between C-axis and other guide shafts is:

Equation 1: Coupling equation between C-axis and other shafts

$$n_C = k_B \frac{Z_B}{Z_C} n_B \pm k_Y \frac{360 \cos \gamma}{\pi m_n Z_C} v_Y \pm k_Z \frac{360 \sin \beta}{\pi m_n Z_C} v_Z$$

Where:

k_B = coefficient related to the thread direction of the gear

k_Y = coefficient related to the thread direction of the gear

k_Z = coefficient related to the thread direction of the gear

n_C = rotation speed of workpiece (r/min)

n_B = rotation speed of tool (r/min)

v_Y = moving speed of Y-axis (mm/min)

v_Z = moving speed of Y-axis (mm/min)

Z_B = number of hobbing cutter

Z_C = number of teeth of gear workpiece

β = helix angle of the workpiece

γ = helix angle of the hobbing cutter

There are four kinds of hobbing technology for the gear hobbing machine with six-axis and four-link:

(1) When processing the spur gear axially, B-axis is operated in the speed mode. The coupling relationship between the C-axis and B-axis is performed as follows:

Equation 2: Coupling equation between C-axis and B-axis

$$n_C = \frac{Z_B}{Z_C} n_B$$

(2) When processing the helical gear axially, B-axis is operated in the speed mode. The coupling relationship among the C-axis, B-axis and Z-axis is performed as follows:

Equation 3: Coupling equation among C-axis, B-axis and Z-axis

$$n_C = \frac{Z_B}{Z_C} n_B \pm \frac{360 \sin \beta}{\pi m_n Z_C} v_Z$$

(3) When processing the spur gear in tangential direction, B-axis runs in the speed mode and the tangential feed shaft(Y-axis) produces an additional motion. The coupling relationship among the C-axis, B-axis and Y-axis is performed as follows:

Equation 4: Coupling equation among C-axis, B-axis and Y-axis

$$n_C = \frac{Z_B}{Z_C} n_B \pm \frac{360 \cos \gamma}{\pi m_n Z_C} v_Y$$

(4) When processing the helical gear in tangential direction, B-axis runs in the speed mode. Both the tangential feed shaft(Y-axis) and the axial feed shaft(X-axis) produce additional motion. The coupling relationship among the C-axis, B-axis and Z-axis and Y-axis is performed as follows:

Equation 5: Coupling equation among C-axis, B-axis and Z-axis and Y-axis

$$n_C = \frac{Z_B}{Z_C} n_B \pm \frac{360 \cos \gamma}{\pi m_n Z_C} v_Y \pm \frac{360 \sin \beta}{\pi m_n Z_C} v_Z$$

High precision gear hobbing mostly adopts intermittent low speed cutting and the cutting force is small with a large impact during the processing. The hobbing cutter shaft runs in the mode of main shaft, and it not only cuts the workpiece, but also participates in the internal transmission with the other shafts. The traditional mechanical gear structure is difficult to ensure the machining precision. The numerical control hobbing machine produced by the domestic major gear machine manufacturers adopts imported CNC system and integrates the function of electronic gearbox to replace the traditional mechanical inline drive chain, so that the gear hobbing machine can process

various types of gear without changing the mechanical structure, furthermore, the machining precision and efficiency are improved meantime.

3. STRUCTURE AND PRINCIPLE OF ELECTRONIC GEARBOX

Electronic gearbox, that is, electronic gear control module, is a system with accurate transmission ratio of gearbox, which is composed of three parts of motion detection, motion information processing and executive mechanism, as shown in Figure 2. The main motion signal is detected and then processed through the motion information processing module after detection and finally becomes the control signal of slave movement to realize the specific transmission of motion mechanism.

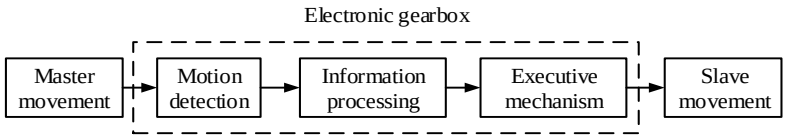

Figure 2: Schematic diagram of electronic gearbox

The electronic gearbox utilizes the computer and numerical control technology to replace the mechanical inline drive chain and realizes the flexible fixed ratio transmission of multi-shaft. Compared with the mechanical inline transmission chain, the electronic gear control module can not only improve the precision of the fixed transmission, but also have high flexibility. According to the actual process demand, it can be flexible to change the synchronous relationship between multi-shaft, so as to realize the complex and changeable processing requirements.

From the point of the structural form, the electronic gearbox can be divided into the type of parallel and master-slave. The parallel electronic gearbox is based on the fixed value control, while the master-slave electronic gearbox is based on the tracking servo. The structural model of the two electronic gearboxes is shown in Figure 3.

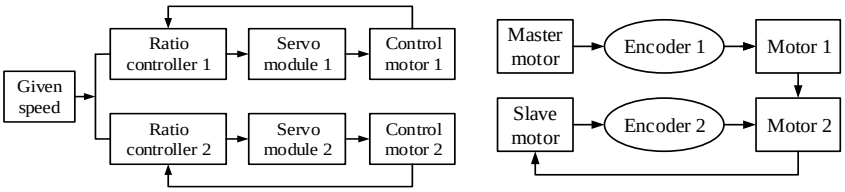

a. parallel type *b. master-slave type*

Figure.3: Structural model of electronic gearbox

The parallel electronic gearbox calculates the position of all shafts of the hobbing machine before processing and sets the position value as the command of each shaft at the corresponding time, then makes the compensation by comparing the theoretical calculation value and the real time position, thus realizing the following transmission between the shaft.

The master-slave electronic gearbox, that is, the tracking and following control of master motion from slave motion, detects the master motion through the encoder and transforms the motion signal into the given signal to the slave motion. The deviation value obtained by comparing the given signal with the feedback signal of the slave motion is adjusted by the controller to realize the planned motion law of the electronic gearbox.

The master-slave electronic gearbox can timely and accurately control the output of the slave shaft according to the change of the master shaft, so as to ensure that the transmission relationship between the master-slave motion remains unchanged. In view of the CNC hobbing machine with six-axis and four-link, taking into account the requirements of gear hobbing in transmission precision, economy and control ability, the master-slave electronic gearbox is selected as the synchronous control system of hobbing.

4. FOLLOWING CONTROL TECHNOLOGY OF ELECTRONIC GEARBOX ON HNC-8

4.1. Secondary development system of HNC-8 CNC system

The secondary development software platform of HNC-8 can be divided into three leaves of HMI, API and NCU. HMI is the human-machine interaction interface, through which users can complete the operation of CNC machine

tools. API is the interface layer, providing HMI access to functions of NC and others. NCU is the core layer, which can realize various control functions of NC. The information interaction between the three levels is accomplished through the built- in interface of the system.

In this paper, the development of the motion control module of the electronic gearbox is carried out at the NCU level of the HNC-8 CNC system, and its development flow is shown in Figure 4.

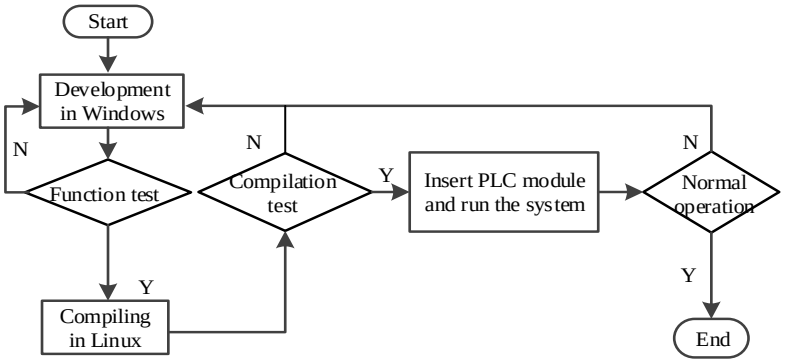

Figure 4: Secondary development flow of HNC-8 CNC system

4.2. Electronic gearbox based on PLC of HNC-8 CNC system

The PLC module of HNC-8 system interacts with the external device through the interface of I/O. After determining the control object and calculating the number of the corresponding input/output signals, the corresponding interface can be allocated for the device. The PLC execution module has 3 executive control interfaces: initialization program interface, first level program of PLC1 and second level program of PLC2. The initialization program is executed only once at the beginning of the system, meaning that the sequential program starts being executed. The first level program is executed every scanning cycle (1 millisecond), which is the main component of the sequential program. The second level program is executed every *n* millisecond, and *n* is the number of divisions of the second level program. When the sequential program being executed, the second level program will be automatically segmented. The loop execution of the PLC sequential program is shown in Figure 5.

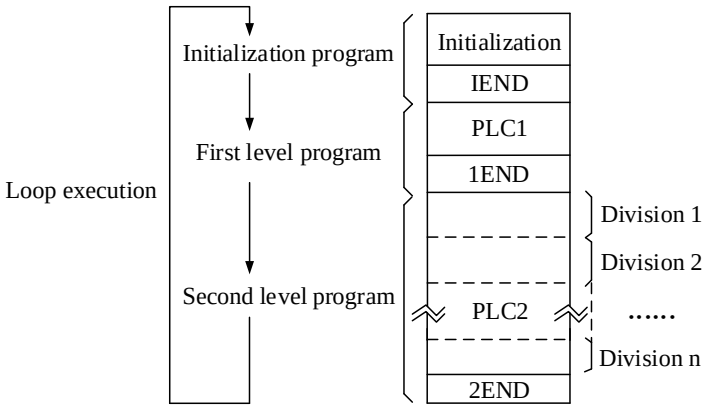

Figure 5: Sequential control of PLC module of HNC-8 system

In the PLC1 module, the function of the electronic gearbox is realized by using several interfaces. The main function of the above interface is to get the actual position of the machine, set the register specified in the parameter and set the real-time instruction position, etc. The EGB technology is realized through the information transmission among the programming of G code, the bus of HIO-1000 and the cyclic scanning of PLC (shown in Figure 6).

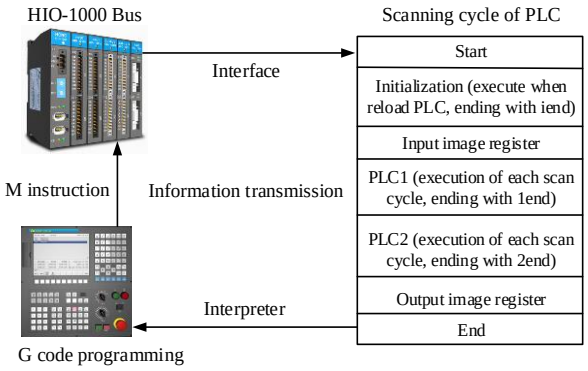

Figure 6: Information transmission of PLC module of HNC-8 system

The information interaction between the PLC module and the G code program is completed by the M instruction. This study developed a pair of M instruction to complete the opening and closing of the electronic gearbox, that is, the instruction of M80 and M81. The R register is allocated for the instruction pair to record the state response to the M instruction in PLC, and the corresponding relationship between the instruction and the register is shown in Table 1.

Table1: Corresponding relationship between M instruction and R register

M instruction	Function	R register
M80	Opening of EGB	R170.0
M81	Close of EGB	R170.1

When the G code interpreter is interpreted to the M instruction, it will automatically call the sequence control command line in PLC related the instruction to achieve the corresponding control. The interaction process between G code interpreter and PLC for M80-M81 instruction pairs is shown in Figure 7.

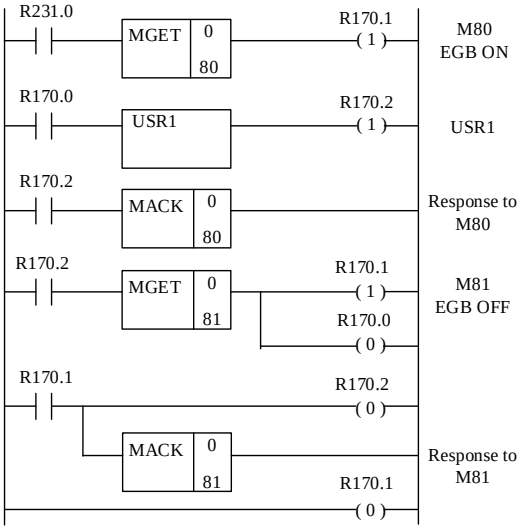

Figure.7: Interaction process between G code interpreter and PLC

5. SIMULATION AND EXPERIMENT OF ELECTRONIC GEARBOX

5.1. Simulation of the electronic gearbox in Linux

The electronic gear control module was simulated and tested in Linux. The theoretical relation of the test case in the simulation can be expressed as follows:

Equation 6: Coupling equation in the simulation and test

$$y = y_0 + \Delta y = y_0 + a * \Delta x_1 + b * \Delta x_2 + c * \Delta x_3$$

Where:

y_0 = initial position of the slave shaft

Δy = position increment of the slave shaft

Δx_1= position increment of the first master shaft

a = following coefficient between the first master and slave shafts

Δx_2 = position increment of the second master shaft

b = following coefficient between the second master and slave shafts

Δx_3 = position increment of the third master shaft

c = following coefficient between the third master and slave shafts

The following movement simulation of the linear shaft and the rotating shaft of the developed electronic gearbox was carried out in Linux. The simulation results are shown in Figure 8 and Figure 9.

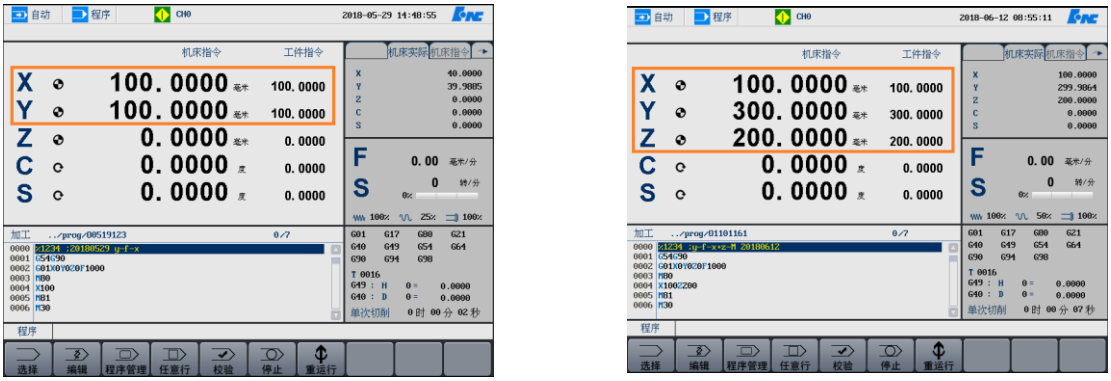

Figure 8: Following movement simulation of the linear shaft in Linux

The linear shaft following motion simulation took Y-axis as the slave shaft, X-axis and Z-axis as the master shafts. The initial positions of three shafts were 0 mm and the position increment of X-axis and Z-axis were set to be 100 mm and 200 mm respectively, and the following coefficient between the master-slave motion was 1.

When Y-axis is following with X-axis, the position increment of Y-axis can be calculated to be Δy =100 mm according to Equation 6. At this time, the instruction position of Y-axis should be 100 mm. When Y-axis is following with X-axis and Z-axis, the position increment of Y-axis can be calculated to be Δy =100+200=300 mm according to Equation 6. At this time, the instruction position of Y-axis should be 300 mm.

As shown in Figure 8, the position of the Y-axis was consistent with the theoretical calculation, which verified that the developed electronic gearbox could realize the following between a single linear shaft and multi shafts.

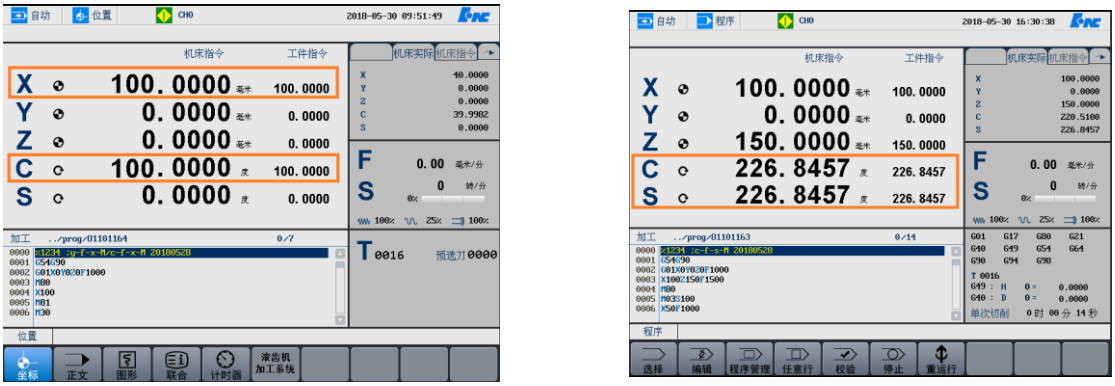

Figure 9: Following movement simulation of the rotating shaft in Linux

The rotating shaft following motion simulation took C-axis as the slave shaft, X-axis and S-axis as the master shaft. The initial positions of three shafts were 0 mm/0° and the position increment of X-axis was set to be 100 mm, the rotational speed of S-axis was 100 r/min. The following coefficient between the master-slave motion was 1.

When C-axis is following with X-axis, the position increment of C-axis can be calculated to be Δy =100 mm according to Equation 6. At this time, the instruction position of Y-axis should be 100 mm. S-axis is the spindle of the hobbing machine and runs in the speed mode in the hob process, the actual position of which is related to the speed. When C-axis is following with S-axis, the instruction position is followed with the real-time position of S-axis.

As shown in Figure 9, the position of C-axis was consistent with the theoretical calculation, which verified that the developed electronic gearbox could realize the following between rotating shaft. The feasibility of the developed electronic gearbox based on the open interface of PLC module of HNC-8 system is verified through the simulation of the linear shaft and the rotating shaft in Linux.

5.2. Experiment of electronic gear box in platform

Based on the secondary development platform of HNC-8, the software and hardware platform of the electronic gearbox module was built and the acquisition and analysis of the off-line data from the platform was carried out through the servo adjustment tool of SSTT. The experimental platform is shown in Figure 10.

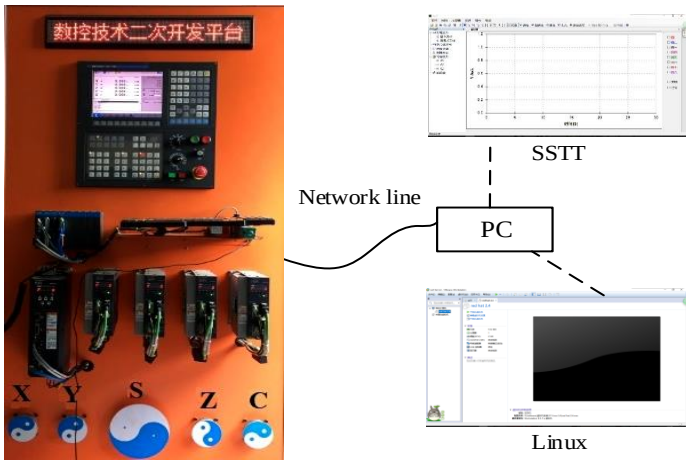

Figure 10: Experimental platform of the electronic gearbox

Data acquisition and analysis of position and error in the following motion of linear shaft

The linear shaft following motion test was carried out on the experimental platform. The test took Y-axis as the slave shaft, X-axis and Z-axis as the master shafts. The initial positions of three shafts were 0 mm and the position instruction of X-axis and Z-axis were set to be 100 mm and 200 mm respectively, so that the position increment of Y-axis is calculated to be 300 mm and the theoretical position is 300 mm. The position trajectories obtained through the servo adjustment tool of SSTT are shown in Figure 11.

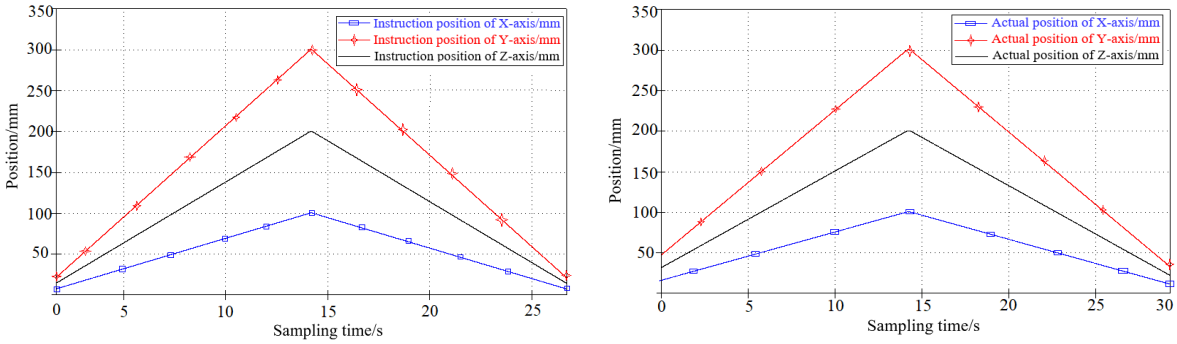

a. Instruction position of X-axis, Y-axis and Z-axis

b. Actual position of X-axis, Y-axis and Z-axis

Figure 11: Position trajectories of the linear shaft following motion

Using MATLAB to analyze the location data obtained from the linear shaft following experiment, the distribution chart of the following error can be expressed as shown in Figure 12.

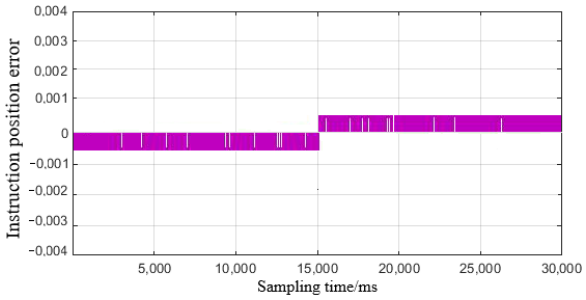

a. Instruction position err of Y-axis

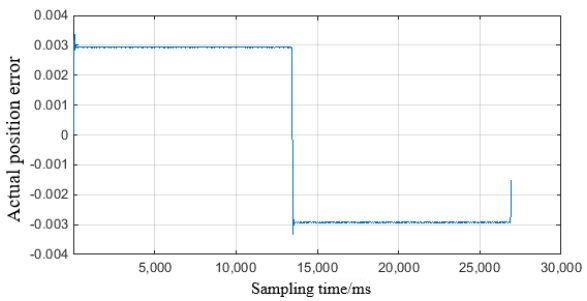

b. Actual position error of Y-axis

Figure 12: Following error of the linear shaft following motion

As shown in Figure 11 and Figure 12, it can be observed that the instruction position of Y-axis is basically the same as the sum of X-axis and Z-axis and the actual position trajectory is consistent with the sum of X-axis and Z-axis. The instruction following error can be accurate to 1 u, and the actual following error is less than 0.003 mm, thus explaining that the electronic gear control module developed in this study can realize the following motion between the linear shaft.

Data acquisition and analysis of position and error in the following motion of rotating shaft

The rotating shaft following motion test was carried out on the experimental platform. The test took C-axis as the slave shaft, S-axis as the master shafts. The rotational speed of S-axis was set to be 100 r/min and its position signal ranges from 0° to 360°. The position trajectories obtained through the servo adjustment tool of SSTT are shown in Figure 13.

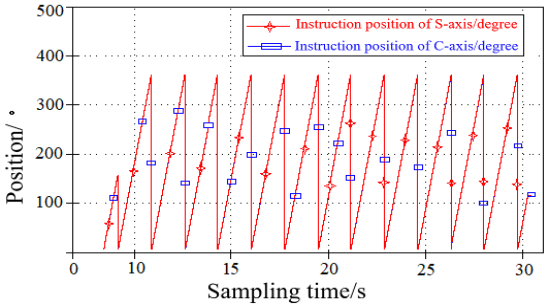

a. Instruction position of C-axis

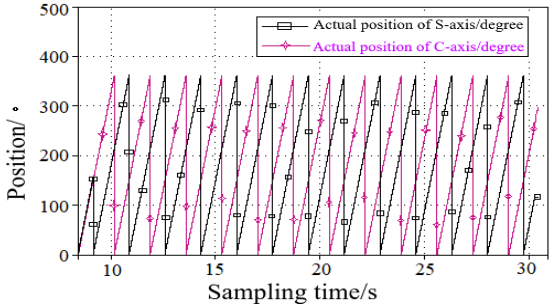

b. Actual position of C-axis

Figure 13: Position trajectories of the rotating shaft following motion

As shown in Figure 13, it can be seen that the position of C-axis is basically the same as that of the S axis and there is a lag in the actual position trajectory. Because S-axis is a servo spindle during the hobbing process. When the tracking servo principle is used to control the slave motion, since the input signal of the master motion is a random variable, there must be a tracking lag. The PID adjustment algorithm is used to compensate the lag, so as to improve the control ability of motion following changes. The position trajectories obtained through SSTT after PID adjustment is shown in Figure 14.

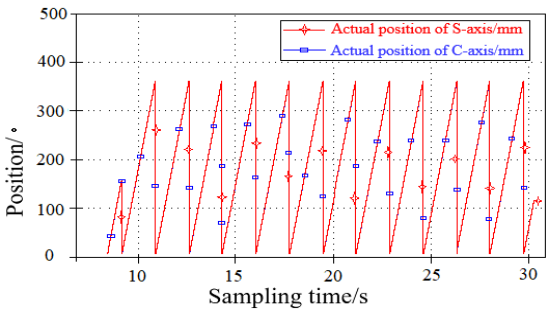

Figure 14: Actual position of S-axis and C-axis after PID adjustment

Using MATLAB to analyze the location data obtained from the rotating shaft following experiment, the distribution chart of the following error can be expressed as shown in Figure 15.

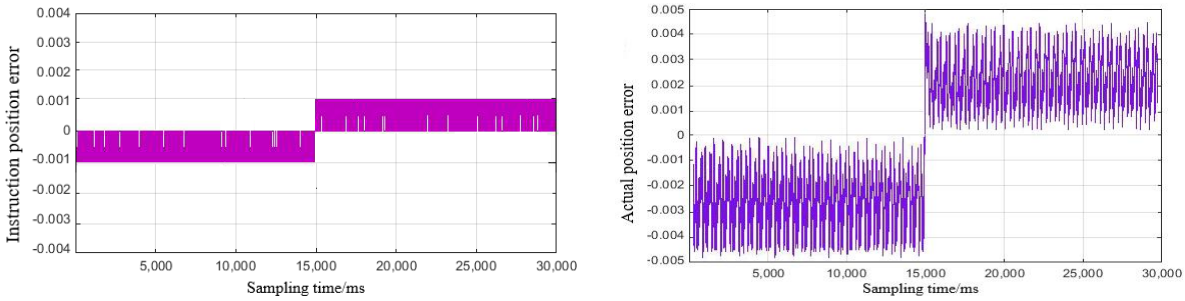

a. Instruction position error of C-axis

b. Actual position error of C-axis

Figure 15: Following error of the rotating shaft following motion

After the adjustment of PID algorithm, C-axis basically follows S-axis, and the actual following error is less than 0.005 °, which shows that the electronic gear control module developed in this study can realize the following motion between the rotating shaft.

6. CONCLUSION

Based on the CNC hobbing machine with six-axis and four-link, the gear hobbing processing is analyzed and the motion model between the hob shaft and the feed shaft in the machining process of different types of gear are established. Aiming at the HNC-8 CNC system, the characteristics of PLC interface are studied and the function of electronic gearbox based on the interface with an interpolation period of 1 millisecond is developed. The relevant algorithm of the developed electronic gearbox control module is simulated in Linux system and tested on an experimental platform. The simulation and experimental results show that the electronic gear box of PLC module of HNC-8 system can basically realize the linear following between the linear shaft and the rotating shaft. The following ability of the electronic gearbox module can be improved by using the feed forward algorithm of PID.

The electronic gearbox proposed in this study can be integrated into the multi-shaft follower control of machine equipment to improve the tracking precision of each shaft and the synchronization between the multi-shaft.

7. REFERENCES

Dinsdale, J., Jones, P. F., Thorneycroft, M., & Loxham, J. (1982). The Electronic Gearbox - Computer Software Replaces Mechanical Couplings. CIRP Annals - Manufacturing Technology, 31(1), 247-249.

Takeuchi, T., & Katagiri, T. (1993). Motor Control Apparatus for Controlling the Position of a Motor-driven Object. US, US5235262.

Quan J Z, Tan W M, & Yin H Y. (1999). Research on Realizing Method of Electronic Gearbox with Computer Software. MECHATRONICS (3), 20-22.

Zhuang L, Zuo D W, Wang M, & You Y P. (2001). Research and Application of Electronic Gear-Box. Machine Design and Manufacturing Engineering, 30(2), 48-50.

Xiong X W, Zhang Z Y, & Liao C J. (2008). On the Inner-link Transmission Structure of a CNC Gear Shaper. Mechanical Science and Technology for Aerospace Engineering, 27(6), 793-798.

Hu C B, Tian F Y, & Jian Y C. (2009). Application of the Electrical Gearbox in the Hobbing Non-circular Gear. Machinery Design & Manufacture (12), 79-81.

Tian X Q, Han J, & Xia L. (2014). Research and Implementation of High Speed and High Precision Electronic Gearbox Technology. China Mechanical Engineering, 25(1), 11-16.

Tian, X. Q., Han, J., & Xia, L. (2016). A New Electronic Gearbox for Gear Hobbing Machines. Proceedings of the Institution of Mechanical Engineers Part B Journal of Engineering Manufacture, 230(5).

Tian, X. Q., Han, J., & Xia, L. (2015). Precision Control and Compensation of Helical Gear Hobbing via Electronic Gearbox Cross-coupling Controller. International Journal of Precision Engineering & Manufacturing, 16(4), 797-805.

Han, J., Wu, L., Yuan, B., Tian, X., & Xia, L. (2017). A Novel Gear Machining CNC Design and Experimental Research. International Journal of Advanced Manufacturing Technology, 88(5-8), 1711-1722.

246: The prototype construction and thermal efficiency evaluation of dish-type concentrator photovoltaic system

Xiaowei CHEN[1,2], Hui LV[1,2*], Yue HU[1,2], Huiliang ZHOU[1,2], Jun LIAO[1,2], Jin LI[1,2], Yuehong SU[3], Saffa RIFFAT[3]

[1] Hubei Collaborative Innovation Center for High-efficiency Utilization of Solar Energy, Hubei University of Technology, Wuhan 430068, PR China
2 School of Science, Hubei University of Technology, Wuhan 430068, PR China
3 Department of Architecture and Built Environment, University of Nottingham, Nottingham NG7 2RD, UK
**Corresponding author: lvhui@hbut.edu.cn*

The dish concentrating solar technology has attracted more attention due to its high light-comprehensive axis tracking is taken as the object, whose tracking control and energy conversion characteristics are studied in-depth. Specifically, the dish-type concentrator photovoltaic system is described in detail from the following three parts: concentrating power generation system, tracking control system, and cooling system. As the main control model, an independently designed closed-loop tracking control system is used based on PLC, which operating every 60 seconds with the tracking accuracy under 1%. In order to demonstrate the tracking accuracy of the system, some experiments are carried out on this platform, including measuring the outer wall temperature of the secondary reflection unit by thermocouples and recording the temperature distribution of the focus spot by infrared camera. Finally, thermal dynamic analysis is carried out to evaluate the overall performance and energyflow characteristics of the photovoltaic system.

Keywords: dish concentrating, dual axis tracking, thermal efficiency evaluation

1. INTRODUCTION

With the increasing development of the world economy, the fossil energy resource is depleting rapidly, which making the environmental pollution more and more serious. As a renewable energy resource, solar energy has become one of the alternative energy resources urgently needed for human development due to its unlimited storage, universality and economy (Stein 2011; Gerstmaier 2011; Mcdonald 2009; Kinsey 2011; Menard 2012). Direct utilization is ineffective because of the low energy density of solar energy, which increasing the device scale and initial investment and affecting its commercial applications. In order to solve the above issue, the concentrating technology is getting more and more attention. Generally, the solar concentrating power generation technology can mainly be divided into four different categories: tower type, trough type, Fresnel type and dish type, which is one of the most feasible approaches due to its high tracking accuracy, concentration efficiency, and thermal power generation efficiency. Research shows that the solar thermal power conversion efficiency of the dish solar thermal power system is up to 85%, and the photoelectric conversion efficiency is as high as 31.25% (King 2004; Wang 2013; Jaramillo 2008; Jones 1995; Yong 2008).

At present, many scholars have conducted a lot of research on dish-type concentrator photovoltaic system in order to further increase the energy efficiency. Jaramillo et al (2008) analyzed experimentally and theoretically the thermal energy and temperature distributions obtained in the focal plane. Jones et al (1995) took the geometry of the reflecting and receiving surfaces and the uncertainty of the reflecting surface into account. The energy distribution on the cylindrical central axis receiver was compared and analyzed, and the proposal for such a concentrating system was given. Shuai et al (2008) applied a Monte-Carlo analysis to the dish-type concentrating system. The effect of the introduction of solar shape and reflection surface error on the performance of concentrating radiation was studied. Du Shenghua et al (2006) also used the Monte-Carlo method to analyze the affection of non-parallelism of solar light, tracking accuracy, and reflection aperture ratio on the energy distribution of focal plane. Liu Ying et al (2007) also proposed a new method for calculating the distribution of energy flow in the focal plane using the finite element method (Muller 2011; Rodrigo 2015).

Researches mentioned above indicate the affection of the focus spot on the power generation efficiency and provide valuable ideas for uniform the focus spot in some extent. There are many factors affect the focus of light spot, such as the dish structure, the cell cooling system, and the tracking accuracy of the dish system. In order to analysis the energy distribution characteristics of the focus spot, a solar-dish system experimental platform is set up in this paper, which including concentrating power generation system, tracking control system, and cooling system. After the overall design of the flatness and structure of the dish surface, the infrared camera is used to observe the focus spot in real time, which dish losed that there is a large space to improve the spot uniformity. Besides, four thermal resistances installed on the outer wall of the secondary reflection unit and the data of Infrared camera are used to judge the system tracking accuracy. Moreover, a water cooling circulation system was designed to guarantee the cell operation.

2. CONSTRUCTION OF DISH-TYPE CONCENTRATOR PHOTOVOLTAIC SYSTEM

As shown in Figure 1, the dish-type concentrator photovoltaic system is divided into three parts: dish concentrator system, tracking system and cooling system. A dual axis tracking control system consisting of a deceleration motor, a rod motor and a photoelectric sensor, so that the sun can keep the sun vertically on the concentrator. The concentrator is mounted on a two axis tracking device to keep the sunlight perpendicular to the entrance plane of the condenser.

The incident sunlight is uniformly distributed on the concentrating solar cell surface through the secondary reflection unit. The cooling water is pumped from water tank to cool down the secondary reflection unit and the solar cell. Then, the surplus heat taken away by cooling water is recovered subseqently to increase the overall energy utilization efficiency. The heat of the cooling system is measured by the test system, and the temperature of the outer wall of the secondary reflection unit is collected to realize the overall analysis of the dish-type concentrator photovoltaic system.

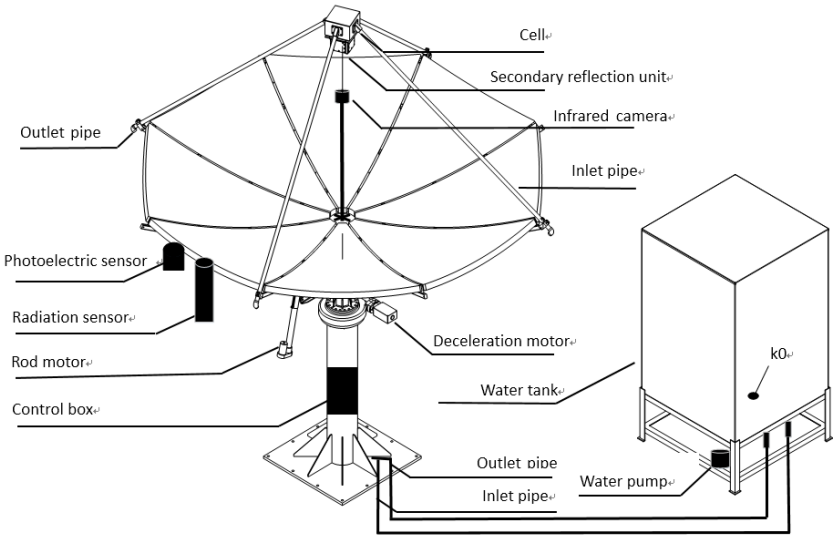

Figure 1 Dish-type concentrator photovoltaic system schematic

2.1. Tracking control system

The system tracking accuracy is the premise for efficient operation of the dish-type concentrator photovoltaic system. The tracking control system is mainly composed of photoelectric sensor, rod motor and deceleration motor, as shown in Figure 1. Specifically, there are four photosensitive resistors in the sunlight sensor, whose resistance values can be changed with the sun's position.

When the four resistances is different, the disk tracking system will operate. On one hand, the deceleration motor drives the corresponding mechanical structure to make the concentrator rotating from east to west to track the azimuth of the sun. On the other hand, the rod motor drives the concentrator to rotate around the push rod to track the sun's height angle. Until the resistance error of the four photosensitive resistors is less than 0.1, the tracking control will stop operation and the sunlight is believed incident perpendicularly. Moreover the rod motor and the decelerating motor adopt brushless motor and gearbox to improve the motion accuracy.

The system adopts Siemens PLC-1200 as the main controller which installed in the control box. The control system is divided into two kinds of tracking modes in Figure 2: time tracking and sunlight tracking. When the weather is clear, the radiation intensity is higher than the threshold set by the photoelectric sensor. The control system automatically enters the sun tracking mode. At the same time, if the radiation intensity is lower than the threshold of the sensor sensor, the system automatically enters the time tracking mode and calculates the sun azimuth and height angle at this time, and drives the motor. The motor feedback data is collected to detect the angle of motor operation.

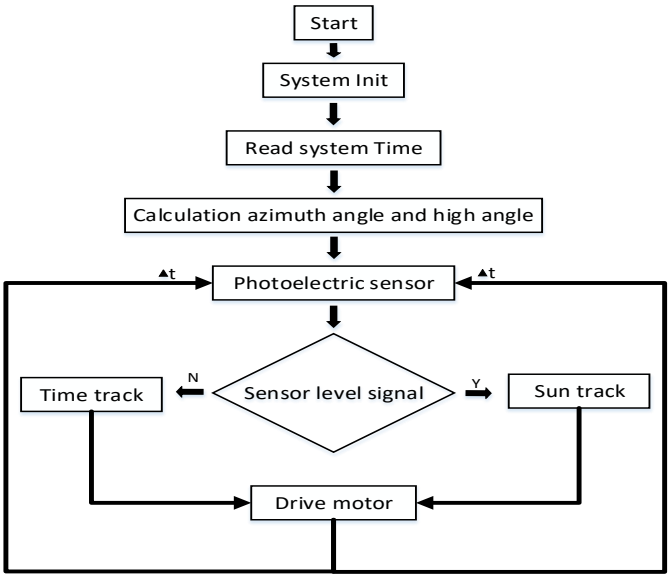

Figure 2: Tracking control flow chart

2.2. Cooling system

Under the action of double axis tracking, the sunlight is reflected by the concentrator, and all the energy is concentrated in the secondary reflection unit. Most of the energy is converted to the cell, the small part is reflected on the surface of the cell, and the dish system has a high concentration, so there is still a lot of energy converted from light energy to heat. Under the cooling structure (such as the water cooling structure of the cell in Figure 3 and the water cooling structure of the outer wall of the two reflection unit), this part of the energy is taken away by the cooling water so the cell can run efficiently .

The water cooling structure on the outer wall of the two reflection unit is prevented from damaging the reflective film on the outer surface, as shown in Figure 3 (left). At the same time, because the solar cell can only absorb the solar light of a specific band, the radiation that is not used will be converted into thermal energy, and the high temperature affects the efficiency of the cell. Therefore, in order to maintain the efficient operation of the cell in the dish-type concentrator photovoltaic system, the bottom of the cell board is equipped with cooling devices. At the beginning of the experiment, the price of the cell is too expensive, a copper plate is used instead of a panel to measure, and after the stability of the whole cooling system is verified, using solar cells instead of copper plates for measurement. The bottom cooling system is shown in Figure 3 (right). At the same time, the design structure of the U shape increases the contact area between the water and the inner wall, making the cooling system more effective.

The cooling water of the entire system is provided by water tank. The cooling water passes through the water pump and enters the inlet pipe. A part of the cooling water passes through the outer wall of the secondary light unit. A part of the cooling water flows through the copper plate heat dissipation structure and then passes through the outlet pipe. Cooling water takes away heat from the system and is stored for later use, as shown in Figure 1.

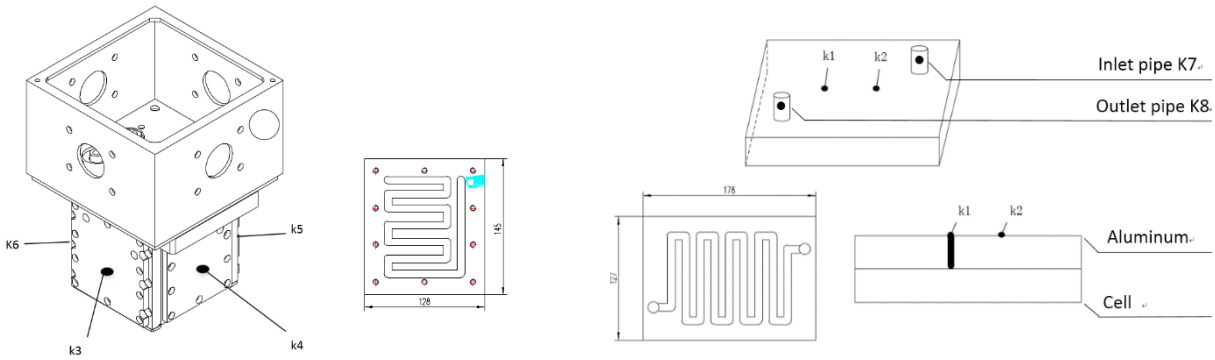

Figure 3: The two reflection unit (left 1), cooling structure (left 2). Cooling structure of cell (right), K1~K6 are thermal resistors.

2.3. Dish-type concentrating system

Under the premise of system tracking control and water cooling system, solar cells convert solar energy into electrical energy. However, due to the small density of the solar radiation energy, the vertical incident solar light is converged to the entrance of the two reflection unit through the concentrator's reflection and focusing, thus increasing the energy density at the entrance of the two reflection unit. At the same time, the gathering light of the entrance is reflected by the surface of the two reflection unit, which makes the gathering light evenly distributed on the surface of the cell, so that the solar cell can absorb the solar energy into electric energy as much as possible.

The solar disk concentrator used in the dish-type concentrator photovoltaic system has a regular octagonal cross section and a diameter of 384cm. In order to increase its mechanical strength and reduce the production difficulty, each paraboloid consists of three sub-mirrors. Under the joint action of the eight sub-mirrors, a dish-shaped converging unit with a converging ratio of 570:1 is formed. The specific parameters of each sub-mirror are shown in Figure 4.

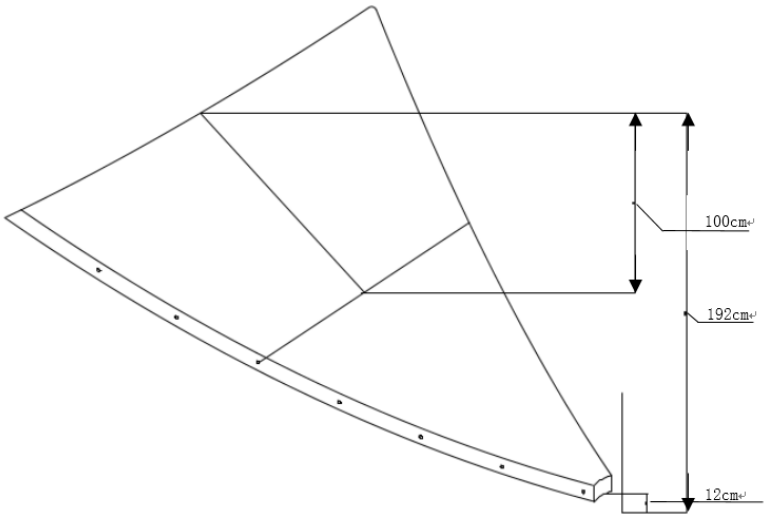

Figure 4: Concentrator sub-mirror

3. EXPERIMENTAL METHOD AND SYSTEM VERIFICATION

3.1. Experimental method

In order to analyze the thermal efficiency of the dish-type concentrator photovoltaic system. At the beginning of the experiment, the pump is first opened to ensure the heat dissipation of the system. At the same time, the software on the computer records the irradiated data of each temperature measuring point in real time and displays them. The control system automatically enters the automatic control state and tracks the sun operation, and judges the data of the four temperature measurement points of k3-k6. The infrared camera collects the data when the interpolation difference value of the side temperature measurement point is within the range of 0.1.

In order to verify the feasibility and actual performance of the disk tracking control system, four thermal resistors are placed on the outer wall of the secondary reflection unit. As shown on the left of Figure 3, four temperature points are located in the positive center of the outer wall of the two secondary unit. When the inner wall of the focusing spot is reflected to the bottom of the concentrator, if the distribution of the spot is uneven, the temperature of the relative thermistor will not meet the requirement, and At this point the tracking control system needs to be recalibrated.

In order to obtain the distributed image of the solar input, the infrared camera is used to record the information of the spot in real time. Meanwhile, the image can also be used as an auxiliary means to calibrate the control system accurately, so as to obtain better tracking precision. The actual effect diagram of the dish solar concentrator is shown in Figure 5. The DNI radiation sensor is installed at the edge of the dish surface to measure the sunlight intensity in real time. At the same time, the inlet and outlet of the test bed also measure the inlet and outlet water temperature by the thermal resistance, and the thermal efficiency of the experimental table can be reflected by the temperature of the inlet and outlet.

Figure 5: Dish-type concentrator photovoltaic system

3.2. Theoretical analysis

According to the above experimental measurements, the total energy of the dish-type concentrator photovoltaic system at the entrance of the secondary reflection unit is calculated as follows

$$Q_{in} = G_D \cdot \gamma \cdot \rho_m \cdot F_{shape} \cdot F_{dirt} \quad (1)$$

ρ_m is the specular reflection, F_{shape} is the mirror shape factor, and F_{dirt} is the dust influence factor, γ are the theoretical converging ratios, which are calculated here according to 570, G_D is the direction data.

The energy at the entrance is reflected on the surface of the two reflector units, evenly distributed on the surface of the cell. It shows that the energy at the bottom of the two reflection unit is actually

$$Q^{'} = \rho_m \cdot Q_{in} \quad (2)$$

According to Eq(1) can calculate the cooling water away energy

$$Q_w = m \cdot c \cdot (t_{out} - t_{in}) \quad (3)$$

Among them, the total energy Q_w taken away by the cooling water, m is the quality of the cooling water, in units of kg, the specific heat capacity of the cooling water 4200 $kJ/(kg*°C)$, t_{out} and t_{in} the temperature difference between the inlet and outlet.

At the same time, the overall energy balance equation of the system can be obtained

$$Q^{'} = Q_w + \Delta Q \quad (4)$$

Among them, ΔQ the heat dissipation of the system. The total energy generated by the system is the energy taken away by the cooling water. At the same time, the test platform is designed with a dish concentration system with a condenser ratio of 570. Therefore, the thermal efficiency of the system is

$$n = \frac{Q_w}{Q^{'}} * 100\% \quad (5)$$

3.3. Experimental verification

Tracking control system verification

During the operation of the disk control system, PLC controller takes 2Hz frequency to collect the temperature data of the four thermistors of the secondary reflection units and save the DNI data at the same time. The experiment preserves the data from 9 to 14 points. The amount of data is too large, only part of the data is intercepted that the system has just started to run.

At the beginning of operation, the radiation intensity is 0, and the temperature of the four observation points of the secondary reflector unit is equal. When the system automatically enters the tracking mode, the thermal resistance temperature of the south face presents a wave peak at 9:33 in 45 seconds, representing the focus spot from the south to the secondary reflection unit. As the control system automatically tracks the sun, when the sunlight is incident on the concentrator vertically, the temperature of the outer wall of the secondary reflector unit enters an equilibrium state, at which time the representative control system completes an automatic tracking.

At the same time, when the focus spot just enters the secondary reflector unit, the intensity of radiation increases first, and the control system is tracking the state slowly, as shown in the phase 1 of Figure 6. When the focus spot is entered from the edge to the center, the control system will calibrate the tracking precision many times, and the radiation intensity also presents a slow growth state, as shown in phase two in Figure 6. in phase three in Figure 6, the radiation intensity presents a regular change, and the difference of the two trough is 71 seconds, exactly corresponding to the control system calibration once every 70 seconds.

The transformation of the radiation intensity value reflects the change of the state when the system completes a tracking. At the same time, the thermistor value of the outer wall of the secondary reflector unit reflects the tracking accuracy of the system.

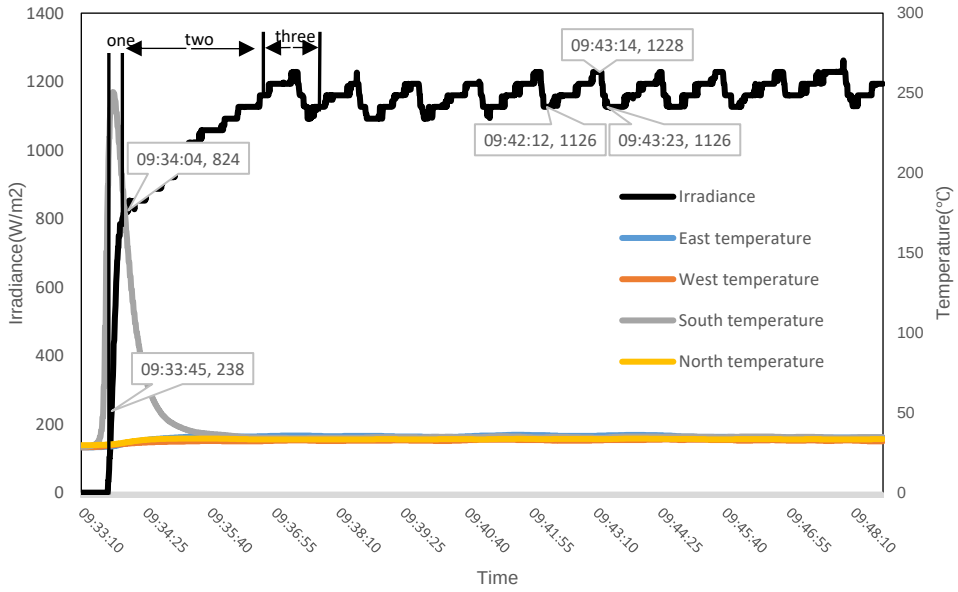

Figure 6: The temperature of the outer wall of the secondary reflection unit and Irradiation intensity data

Cooling system verification

This experiment mainly verified the function of the dish-type concentrator photovoltaic system, so the initial use of copper (cooling structure same as concentrating solar cells) to replace the cell for testing. K1-2 thermistor installation position shown in Figure 3, through Figure 7 It can be seen that the temperature at the back of the cell fluctuates back between 39-41°C. At the same time, the temperature of the thermistor K1 is higher than K2. This is because the thermistor K1 cling to back of the cell. Within this temperature range, the concentrating solar cell can work normally, which means that the cooling system of the dish-type concentrator photovoltaic system has played a vital role. It provides the cooling protection for the later installation of concentrating solar cells for testing.

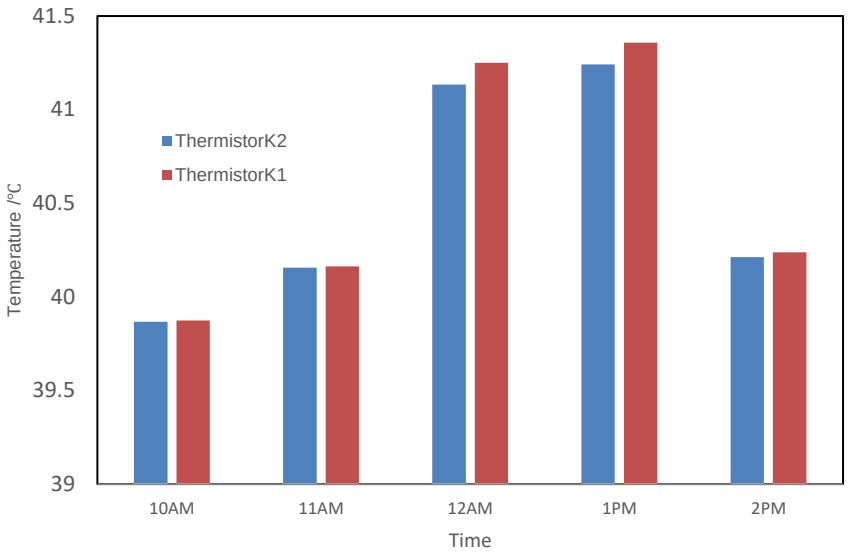

Figure 7: The back temperature of the copper

Dish concentrating system verification

In the experiment, the infrared camera collects the spot image from 10Am to 2Pm. 500 images are collected at each point. The same temperature upper and lower limit is set in the Xenics (infrared camera supporting software), and 5 image of spot are shown in Figure 8.

The right image in this Figure shows the same temperature upper and lower limit for the 5 images in the software. As time goes on, the temperature in the concentrator is getting higher, and the image colour is getting brighter. It is obvious that the colour in the concentrator is brighter than the edge in any picture. From this point of view, the design of the dish-type concentrator photovoltaic system is reasonable and can converge the vertical incident sunlight into the concentrator.

But in each image, it can be seen that the colour of at the bottom of the secondary reflector unit is different, and that there is a high temperature anomaly (dark blue) in the lower left corner of the image. The reason is that the reflective film on the outer wall of the cylinder is partially melted under the high temperature condition. This is also a point to be improved in the later experiment.

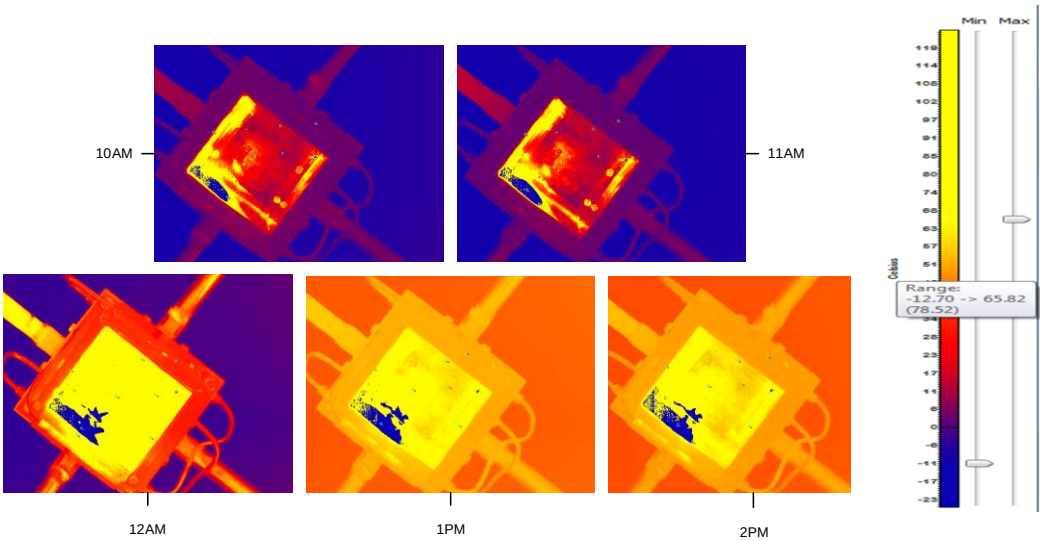

Figure 8: Focal spot image

4. THERMAL EFFICIENCY EVALUATION

In order to measure the thermal efficiency of the dish-type concentrator photovoltaic system, in the process of real-time observation of the spot image experiment, the temperature of the cooling water at the inlet and outlet is

measured and recorded at the same time, and all the energy taken away by the cooling water can be calculated by Eq(3). As shown in Table 1.

Table 1: Heat taken away by the cooling water

Time	*10AM*	*11AM*	*12AM*	*1PM*	*2PM*
Inlet temperature（°C）	*31.50*	*31.78*	*32.61*	*32.14*	*32.11*
Outlet temperature（°C）	*36.84*	*37.67*	*38.42*	*38.40*	*38.75*
Cooling water rated flow	*12.7*	*12.7*	*12.7*	*12.7*	*12.7*
Heat taken away by cooling water（MW/m2）	*0.31*	*0.34*	*0.34*	*0.37*	*0.33*
Thermal efficiency（%）	*34.5*	*40.4*	*45.4*	*49.4*	*55.6*

As can be seen from the table, the outlet temperature is less than 40 degrees, the water temperature is not sufficient for direct use, and energy storage devices such as heat pump devices should be added later. Increase water temperature and reuse.

From the table we can see that the cooling water takes less than half of the total energy. The proportion is low. One of the important reasons is that the copper plate is used instead of the cell, the absorption rate of sunlight on the surface of the copper plate is greatly different from the absorption of sunlight by the cell. It can be seen that the entrance of the secondary reflector light unit is very bright from Figure 5, indicating that a large part of the sunlight is reflected by the cell surface into the air.

5. CONCLUSION

The dish-type tracking control system and the cooling system are verified in this paper, which is based on the independent design of the dish-type concentrator photovoltaic system. The image of the spot is recorded in real time by the infrared camera and the temperature of the outer wall of the secondary reflector unit. At the same time, through the temperature data of the cell backplane, the effect of the cooling system of the experimental platform is analyzed, which can well meet the normal working temperature of the concentrating solar cell. Finally, through experiments, the temperature of inlet and outlet pipes is recorded and analyzed, and the heat utilization efficiency of dish type test stand is calculated. The above experiments verify the performance of the dish-type concentrator photovoltaic system.

6. ACKNOWLEDGEMENT

The authors gratefully acknowledge Hubei Collaborative Innovation Center for High-efficiency Utilization of Solar Energy, Hubei University of Technology, for its Open Foundation under Grant No. HBSKFTD2016001. This work was also supported partly by the National Undergraduate Training Programs for Innovation and Enterpreneurship under Grant No. 201710500008, in part by the International Science & Technology Cooperation Project of Wuhan Science and Technology Bureau under Grant No. 2017030209020254, and in part by the International Science & Technology Cooperation Program of China under Grant No. 2016YFE0124300.

7. REFERENCES

Stein, J S, Cameron, C P. PV performance modeling workshop summary report.[J]. Office of Scientific & Technical Information Technical Reports, 2011.

Gerstmaier T, Gomez M, Gombert A, et al. Validation of the PVSyst Performance Model for the Concentrix CPV Technology[J]. 2011, 1407(1):366-369.

Mcdonald M, Dittmer J. Accurate energy predictions for tracking hcpv installations[J]. 2009.

Kinsey G S, Stone K, Brown J, et al. Energy prediction of Amonix CPV solar power plants[J]. Progress in Photovoltaics Research & Applications, 2011, 19(7):794-796.

Menard E, Wagner W, Furman B, et al. Multi-physics circuit network performance model for CPV modules/systems[J]. 2012:002268-002272.

King D L, Kratochvil J A, Boyson W E. Photovoltaic Array Performance Model[J]. 2004.

Wang Y; Research on comprehensive utilization system of solar panel concentrator and power generation [D]. University of Science & Technology China.2013

Jaramillo O A, Pérez-Rábago C A, Arancibia-Bulnes C A, et al.. A flat-plate calorimeter for concentrated solar flux evaluation[J]. Renewable Energy, 2008,33(10):2322-2328

Jones P D, Wang L, Concentration distributions in cylindrical receiver/paraboloidal dish concentrator systems[J]. Solar Energy, 1995, 54(2):115-123

Yong S, Lin X X, Tan H P. Radiation performance of dish solar concentrator/cavity receiver systems[J]. Solar Energy, 2008,82(1)：13~21

Du S, Xia X, Tang Y. Numerical study on the influence of sun's non parallelism on solar energy aggregation [J]. solar energy, 2006, 27 (4): 388-393.

Liu Y, Dai J, Lang Z, et al. Finite element analysis of the energy distribution of the focal plane of a rotating parabolic concentrator [J]. Acta optica Sinica, 2007, 27 (10): 1775-1778.

Gombert A, Heile I, Gomez M, et al. Field Experience Of Concentrix Solar's CPV Systems In Different Climatic Conditions[C]// American Institute of Physics, 2011:327-330.

Muller M, Marion B, Rodriguez J, et al. Minimizing Variation In Outdoor CPV Power Ratings[C]// American Institute of Physics, 2011:336-340.

Rodrigo P, Micheli L, Almonacid F. The High-Concentrator Photovoltaic Module[M]// High Concentrator Photovoltaics. Springer International Publishing, 2015:115-151.

247: Simulation research on temperature field and magnetic field coupling based on magnetic drive inspection robot

Xianjin XU[1], Chenghui LIU[1], Haoda CHEN[1], Yunlong, WANG[1], Yu YAN[2,3]

[1] College of Mechanical Engineering, Hubei University of Technology, Wuhan, Hubei province, China, 15926411039@163.com
[2]State Grid of Hunan Electric Power Company, Changsha, Hunan province, China, 942498195@qq.com
[3]State Grid Corporation Laboratory of Live-working Inspection and Intelligent Operation Technology, Changsha, Hunan province, China, 309993182@qq.com

In order to solve the slippery problem for a two-arm-wheel combined inspection robot, a magnetic maglev system based on the magnetic field of high voltage direct current (HVDC) is proposed. The magnetic system contains two parts: magnetic levitation and magnetic drive. The levitation part overcomes the gravity of the robot by the ampere force which is generated by current-carrying coils in the magnetic field of HVDC. The drive part takes the ampere force generated by current-carrying coils in the magnetic field of HVDC as the driving force. This method replaces the traditional means that the inspection robot is driven by a motor and a wheel rail. The levitation force and the driving force were calculated in theory. The relationship between the size of the physical model and the number of turns of the coil was under consideration. The COMSOL software was used to simulate the two models respectively. During the magnetic field calculation, the mean magnetization curve and the loss curve of the material are updated according to the current temperature field simulation results, and then the temperature rise is calculated based on the current magnetic field loss calculation. So repeated iterative until the end of the coupling. The simulation results show that: in the process of magneto-thermal coupling, the temperature has a significant influence on the magnetic permeability of the magnetic core, thus affecting the magnetic driving force. In view of this, the thermal-magnetic coupling simulation is performed again for the open box optimisation design of the outer box body.The results show that the magnetic levitation method and the magnetic drive method is feasible in theory, and the model is correct and effective, which is of great practical significance to the physical realization of the inspection robot.

Keywords: Ampere force, HVDC, Inspection robot, Magnetic system, Modelling, Simulation

1. INTRODUCTION

Since the late 1980s, the use of mobile robots on the overhead high-voltage circuit inspection has become a hot topic in the field of robot at home and abroad (Zhu 2009; Zhang 2007; Zhou 2004). Canada's Quebec Hydro and KEPCO and JPS are typical representatives of high-voltage circuit inspection robots abroad. The former developed a "LineScout" inspection robot (Pouliot 2008; Montambault 2008) .The latter for the multi-split wire developed a patrol robot "Expliner" (Debenest 2008). A more prominent technical problem is the problem of traveling wheel slip. Most of the high-voltage inspection robots studied at home and abroad use the structure of wheel-arms, and the static friction force traction robot moves between the driving wheel and the surface of the line. When the surface of the line is complicated (such as icing), the static friction is not enough to overcome the gravity thus slipping. The slip will seriously affect the robot inspection efficiency, increase the energy burden of the robot, damage to the transmission line. When the slippery is serious, the robot becomes difficult to control. Slip is the inherent problem of wheel drive.

The technology of magnetic levitation train (Cheng 2003; Chen 2014; Tang 2003) and linear motor (Mao 2007; Chen 2015) provides a new way to solve the problems such as slipping of inspection robot. The magnetic levitation method and magnetic drive method described in this paper are different from those of maglev train technology The magnetic principle that the same sex repel each other and the opposite sex attract each other lays the foundation of the levitation of the train, but by the use of HVDC transmission lines around the magnetic field and reasonable arrangement of coils, the magnetic levitation part overcomes the robot's own gravity by the Ampere force generated by current-carrying coil in the magnetic field. The magnetic drive part regards the Ampere force generated by current-carrying coils in the magnetic field as the driving force of the traction robot to replace the wheel drive mode, thus completely solves the problem of inspection robot slipping.

2. DESIGN OF THE OVERALL STRUCTURE OF INSPECTION ROBOT

The domestic and foreign research of high-pressure inspection robots have been mostly wheel-arm structure so far. The kind of inspection robots is not compact, large-size, overweight, lowly efficient, and poor resistance to wind load and other defects. In order to realize magnetic levitation and magnetic drive, the magnetic levitation inspection robot is designed as intermediate cylindrical shape, both ends curved shape (to reduce the air resistance during operation). The overall structure of inspection line robot is designed as shown in Figure 1. The robot magnetic levitation system includes magnetic suspension system and magnetic drive system. The magnetic levitation system and the magnetic drive system are adhesive together, while the use of magnetic drive system cascade can increase the driving force.

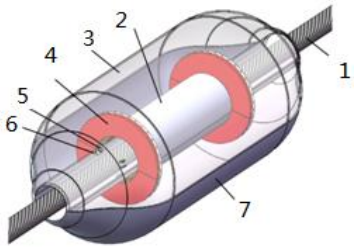

1-High-voltage lines; 2- Magnetic suspension system; 3-Upper body

4- magnetic drive system; 5- Small roller holder; 6- Small roller; 7-Lower body

Figure 1: The Overall Structure of Magnetic Inspection Robot

3. REALIZATION PRINCIPLE OF THE MAGNETIC LEVITATION SYSTEM

3.1. Magnetic levitation principle analysis and model design

According to the properties of the toroidal magnetic field determined by the DC, the current-carrying coil is arranged rationally around the high-voltage conductor. So that the current-carrying coil is subjected to the work force in the magnetic field around the high-voltage line. The Ampere force is too small to overcome the gravity of the robot itself to suspend the robot on the high-voltage line. L2, the long side of the current-carrying coil, is placed in the soft magnetic material for the properties of soft magnetic materials, high permeability. In contrast, L1 placed in the weak magnetic material (Air, etc.). By this, the Ampere force applying to the coil is upward, so as to meet the robot's own gravity requirements. So, the robot can be levitated. The magnetic levitation of the physical model is shown in Figure 2.

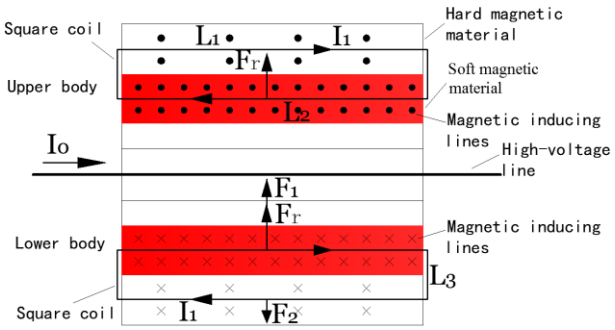

Figure 2: Magnetic levitation physical model

In order to improve the stability of the robot inspection movement, the magnetic levitation system model of the inspection robot is designed to be rounded to facilitate nesting inside the overall structure of the robot which is shown in Figure 3. To prevent the leakage of magnetic, L2, the long side of the coil is seamlessly embedded in the soft magnetic material by the 3D printing or sintering process. At the same time, in order to reduce the difficulty in the manufacturing process of the magnetic suspension system, the long side end of the coil L2 can be connected by welding, Side in the weak magnetic material. Magnetic suspension system is designed into the upper and lower body parts to meet the demands of opening and closing. The current-carrying coil are wrapped around the levitation system.

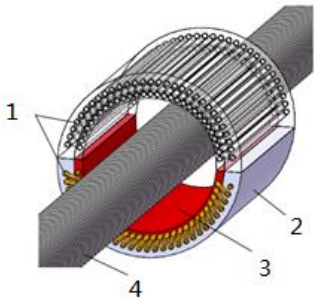

1-Current-carrying coils; 2-Hard magnetic material; 3-Soft magnetic material; 4-High-voltage lines

Figure 3: Entity model of magnetic levitation system

Because the current carrying coil and the ring magnetic induction line are perpendicular to each other, that is $\theta = 90^{\circ}$ according to Ampere's law the Ampere force of the effective edge can be obtained. $F = BIL\sin 90^{\circ} = BIL$

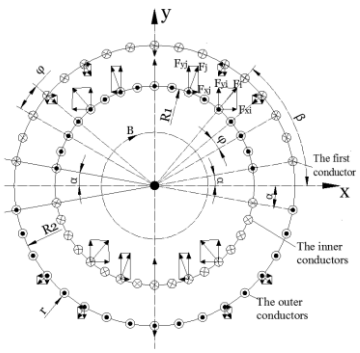

Figure 4: Force Analysis of the Model Cross Section Coils

According to the analysis model of cross section of magnetic suspension system of Figure 3, because the outer wire in weak magnetic material (such as in the air), the strength of the magnetic field where the outer conductor by

the Biot-Savart's law is: $B_2 = \frac{\mu_0 I_0}{2\pi R_2}$ Where: ***I₀*** is for the high-voltage wire current;***R₂*** is for the outer ring wire and the distance between the high-voltage line, that is, the radius of the circle where the outer wire.

The Ampere force of the inner wire can be expressed as

$$F_1 = \frac{\mu_0 \mu_r I_0 I_1 L_2}{2\pi R_1} \tag{1}$$

Where: ***L₂*** is the length of the long side of the wire in the soft magnetic material.Assuming that the angle between the first wire and the X axis is α , the angle between the root wire and the X axis is β ,so there is

$$\beta = \alpha + \phi(i-1) \quad (\text{among } i = 1,2,3...n) \tag{2}$$

By the formula (2), the components of the Ampere force in the Y axis direction can be obtained for a single coil

$$F_y = (F_1 - F_2)\sin\left[\alpha + \phi(i-1)\right] \tag{3}$$

The winding of the upper and lower body of the magnetic levitation system is symmetrically arranged, so the levitation force of the whole system is

$$\begin{aligned} F_{f\,2n} = {} & 2(F_{1y1} + F_{1y2} + \cdots + F_{1ym} + \cdots + F_{1yn}) \\ & -2(F_{2y1} + F_{2y2} + \cdots + F_{2ym} + \cdots + F_{2yn}) \end{aligned} \tag{4}$$

Where: ***F₁ym*** is the component force of the ampere force in the Y-axis direction of the ***m***-th inner ring conductor placed in the soft magnetic material; ***F₂ym*** is the component force of the ampere force in the Y-axis direction for the ***m***-th outer ring conductor placed in the hard-magnetic material.

Substituting formula (3) into formula (4), we get the resultant force of the ***2n*** current-carrying coils in the y-axis direction

$$\begin{aligned} F_{f\,2n} = {} & 2\left(F_1 - F_2\right)\{\sin\left[\alpha + \phi\times(1-1)\right] + \\ & \sin\left[\alpha + \phi\times(2-1)\right] \\ & +...+\sin\left[\alpha + \phi(m-1)\right]+...+ \\ & \sin\left[\alpha + \phi(n-1)\right]\} \\ = {} & 2(\frac{\mu_0 \mu_r I_0 I_1 L_2}{2\pi R_1} - \frac{\mu_0 I_0 I_1 L_1}{2\pi R_2})\times \\ & \sum_{i=1}^{n}\sin[\alpha + \phi\times(i-1)] \end{aligned} \tag{5}$$

3.2. Magnetic drive principle analysis and model design

The current-carrying coil is arranged in the magnetic field around the HVDC lines, and the Ampere force is used as the driving force of the direct traction robot. The magnetic drive physical model is shown in Figure 5.***L₅*** ,a long side of the rectangular current carrying coil is placed in the soft magnetic material, and a corresponding long edge is placed in the hard magnetic material. As is shown in Figure 5, magnetic drive system is also divided into upper and lower body parts. Current-carrying coils are wrapped in the upper body and the lower body. Its processing technology is similar to the magnetic levitation system.

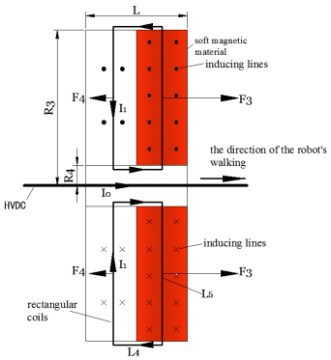

Figure 5: Physical Model of Magnetic Drive

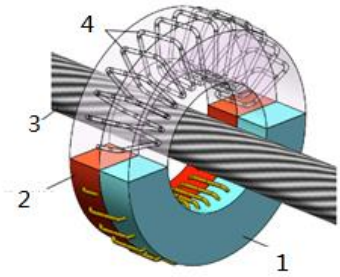

Figure 6: Entity Model of Magnetic Drive

The length of the magnetic field on each side of the coil of varies, so the Ampere force of the long side of the rectangular coil placed in the weak magnetic material: $F_4 = \int_{R_4}^{R_3} \frac{\mu_0 I_0}{2\pi r} I_1 dr$

Where: ***R₃*** and ***R₄*** is respectively for the vertical distance between the HVDC transmission line and the upper and lower sides of the coil the coil; ***I₀*** is for the high-voltage line current; ***I₁*** is for the current-carrying coil current.

The other long side of the current carrying coil is placed in the soft magnetic material, and its strengthened magnetic induction ***B₃*** is $B_3 = \frac{\mu_0 \mu_r I_0}{2\pi r}$ .The Ampere force of the long side ***F₃*** is: $F_3 = \int_{R_4}^{R_3} \frac{\mu_0 \mu_r I_0}{2\pi r} I_1 dr$

As the magnetic drive system is composed of two symmetrical body, the winding coil is arranged symmetrically up and down with the high voltage line as the center line. The Ampere force of the short side of the rectangular coil of the upper body is canceled by the amber force of the short side of the rectangular coil of the lower body. That is,***F₀*** ,the resultant force of a single coil is: $F_0 = F_3 - F_4$. Without considering the coupling of the magnetic field and other cases, the total driving force of the magnetic drive system is: $F_{d2n} = 2nF_0$. Where: ***n*** is the upper body (or lower body) winding coil turns.

The robot travels on the high-voltage line by the guide wheel, and the friction is rubbing friction, which is negligible. Considering the sag of the overhead high voltage line, the robot needs more traction in the uphill section with sagging. Suppose the line slope is shown in Figure 7. To make the robot walk on the high voltage line, the following conditions must be satisfied:

$$F_{resul\tan t} \geq G\sin\lambda\,. \tag{6}$$

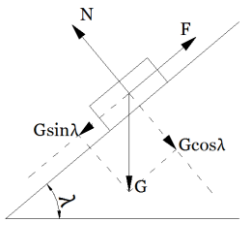

Figure 7: Force Analysis of the Body in Slope Sections

4. SIMULATION ANALYSIS AND THEORETICAL FORCE CALCULATION

4.1. Establishment of simulation physical model

In view of the magnetic levitation system, as the closer to the high voltage line surface, the stronger the magnetic field strength of the coil, we take $R_1 = 0.0425m$, $R_2 = 0.05m$; In order to make the levitation system more light, the extraction method is adopted $L = 0.3m$; In order to facilitate the opening and closing movements of the upper

and lower bodies, the $\alpha=0^{\circ}$ is adopted. Combined with the characteristics of the solid model, according to the above parameters to establish magnetic levitation two-dimensional simulation model shown in Figure 8.

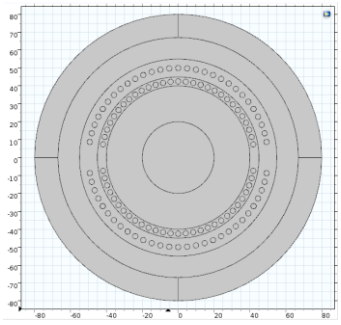

Figure 8: Simulation Model Of Maglev Two-Dimensional

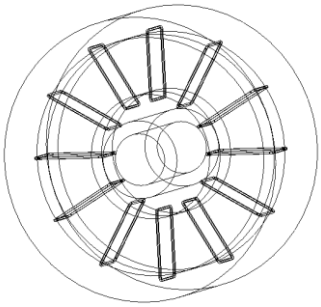

Figure 9: Simulation Physics Model

4.2. Simulation analysis

Firstly, the material properties of the magnetic suspension system model are set, the physical field is selected as the magnetic field, the setting surface thickness is 0.3m, the external current density of the high voltage line is $1000/(0.02\times0.02\times\pi)A/m^2$, the outer current density of the coil is $10/(0.0015\times0.0015\times\pi)A/m^2$, and all the coil calculation is added. The mesh partition is divided into three parts by using the free-cut triangular mesh. The solution of the steady-state solver is used to solve the model. Under the same model conditions, the coil current size unchanged, only to change the size of high voltage current, respectively, by simulation to high voltage current size of 500A, 1000A, 1500A simulation shown in Figure 10.

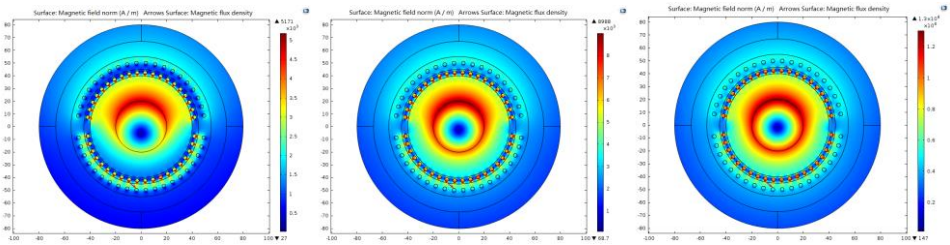

(a) $I_0=500A$ (b) $I_0=1000A$ (c) $I_0=1500A$

Figure 10: Simulation of Different High-voltage Current Conditions

According to the above two-dimensional simulation diagram can be seen: in the coil turns, coil current and other conditions are the same circumstances, with the high voltage current increases, the surrounding magnetic field strength continues to increase.Based on the two-dimensional simulation model (on Figure 10) to take a x = 0 two-dimensional line, simulation figure curve arc length and the magnetic flux density model shown in Figure 11.

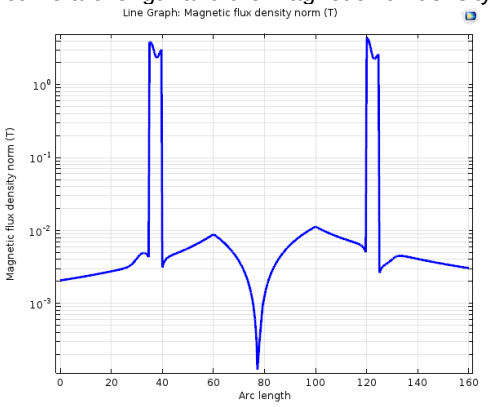

Figure 11: Curve Relation Curve of Arc Length Magnetic Flux Density

In the case of high-voltage current of 500A, 1000A and 1500A, the magnetic levitation system is obtained in x, y and z direction. The magnitude of the amber force on the table is shown in Table 1, where the amber force in the y direction is the levitation force of the robot (the negative data in Table 1 indicates that the ampere force is opposite to the original direction).

Table 1: Simulation results of Ampere force in the three axis direction

F/N	$I_0 = 500\,A$	$I_0 = 1000\,A$	$I_0 = 1500\,A$
z	8.8×10^{-3}	1.31×10^{-4}	1.79×10^{-4}
χ	3.4×10^{-2}	-1.048	1.766
y	207.78	415.59	623.40

For the study the change of the magnetic levitation force with the number of turns of the coil, the rule of the model coil is first analyzed (see Figure 12). The coil at each point on the circumference of the ampere force is not equal, specify the number 1 to 4 coil for the fixed point (the position is not fixed), and then each model gradually increase the 4 turns coil (up and down the body of the 2 turns), the upper and lower body coil and other center of the circle evenly distributed. Different turns of the coil model in the high voltage current of 1000A are simulated. Figure 16 (a) and (b) are the two-dimensional model of the magnetic levitation system with the number of turns of 20 and 58, respectively.

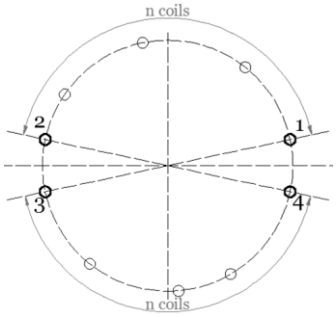

Figure 12: Coil Addition Distribution

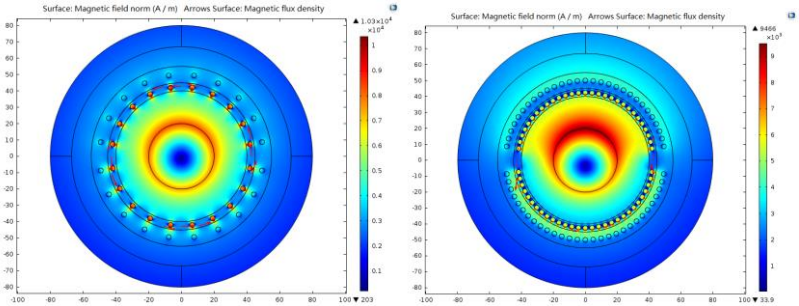

(a) 20 turns (b) 58 turns

Figure 13: Two-dimensional Model Simulation

It can be seen from the simulation diagram that: the distribution of the current density in the cross section of the high voltage line is that the edge is larger than the center; the skin effect is obvious. The magnetic field around the coil embedded in the soft magnetic material in Figure 13 (a) is stronger than that in the hard magnetic material. The magnetic field strength of the cross section of the coil shows a strong radial magnetic field, while the two sides are weak. When the turns of coils increase, the magnetic flux density immediately above the high voltage line gradually increases, and the bottom of the magnetic flux density gradually weakened. The direction of the magnetic induction line generated by the high voltage line and the direction of the magnetic induction line generated by the current carrying coil are determined by the right-hand rule. When the direction of the former coincides with the latter direction, the magnetic field strength is strengthened; when the direction of the former is opposite to the latter direction, Weakened. When the number of turns is 58, the simulation results are:

$$
\begin{aligned}
F_{58y} &= 588.45N \\
F_{58x} &= -1.66N \\
F_{58z} &= 2.11\times10^{-5}N
\end{aligned}
\tag{7}
$$

In the case of the number of coils of the magnetic suspension system calculated by software, 20, 24, 28, ..., 56, 60, the size of the amperage force in the x, y and z directions of the suspension system is F_x, F_y and F_z, where the y direction of the Ampere force F_y is for the robot's levitation force. According to the different number of turns of the coil ampere force is in the axial direction of the magnetic levitation system size, rendering the ampere force size changes with the number of turns of the coil by using the OriginPro software. The theoretical values and simulation values of the comparison are shown in Figure 14 (the figure axis is negative that the ampere force is opposite to the direction of the original set). It can be seen from Figure 14 that the simulation value of F_y is always larger than the theoretical value. With the increase of the number of turns, the closer the theoretical value of F_y is to the simulation value. The simulation value of F_y increases with the number of turns. Since F_z is one millionth of F_y, it is not shown.

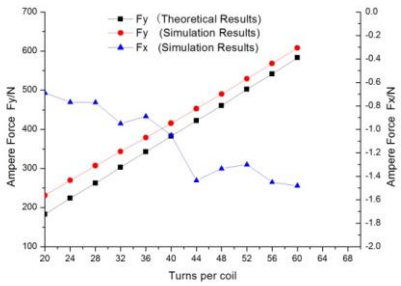

Figure 14: Comparison of Theoretical and Simulated Values

The magnetic material properties is set. The physical field is selected for magnetic field. Coil type is numeric and the number of turns of each coil is a coil. The coil current is 10A. Under the high voltage current of 500A , 1000A, 1500A three conditions high-voltage line current density is set. According to the boundary conditions of magnetically insulated magnetic insulation interface, set the current direction of the coil; mesh free mesh refinement of tetrahedral mesh division method by setting the extreme; automatic calculation of current and steady-state solution of the model is solved by simulation calculation, are shown in Figure 15 under three different high-voltage current coils for simulation of section 12 turn.

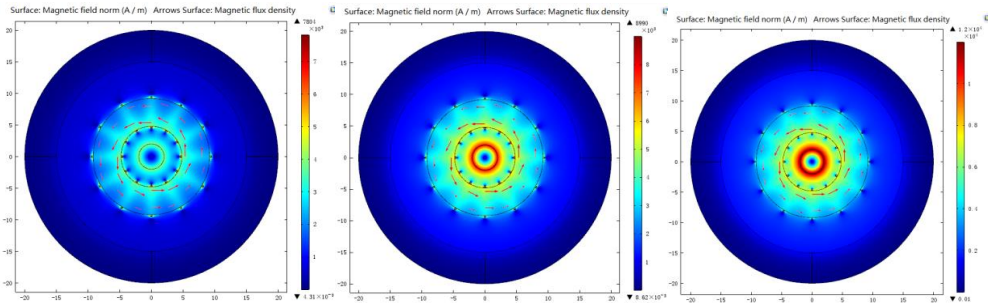

(a) I_0=500A (b) I_0=1000A (c) I_0=1500A

Figure 15: Same Model In Different Conditions of High-voltage Current Simulation Sectional Charts

According to the above simulation section, it can be seen that with the increase of the high voltage current, the magnetic field intensity increases continuously under the condition that the number of turns on the coil and the coil current are the same.

Table 2: Simulation Results of Ampere Force Magnitude in

Three Axis Direction of the Same Turn Coil Under Different High-Voltage Current

F/N	$I_0 = 500A$	$I_0 = 1000A$	$I_0 = 1500A$
z	-6.2929	-11.942	-17.604
x	8.8×10^{-3}	-3.2×10^{-3}	-7.5×10^{-3}
y	3.4×10^{-2}	8.7×10^{-2}	0.1643

The magnetic drive magnitude is calculated by changing the number of turns of the coil. Figure 16 shows the number of coils, and 8 and 16 are used to simulate the magnetic drive system model.

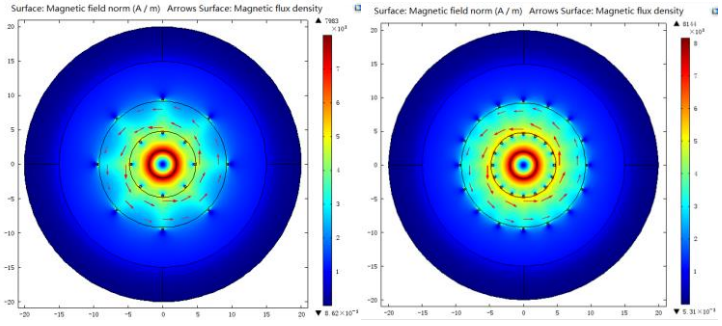

(a) 8 coil simulation cross sections *(b) 16 coil simulation cross sections*

Figure 16: Sectional Charts of Model Simulation at the Same High-voltage Current

It can be seen from the simulation chart that the eight points on the outer diameter of the magnetic drive system in Figure 16 (a) are the cross section of the coil, and the magnetic field strength on both sides of the coil cross section is stronger; Figure 16 (b) is similarly analysed. The magnetic field vector generated by the high-voltage line and the current carrying coil judged by the right-hand rule are consistent.

4.3. Theoretical force calculation

Without considering the magnetic field coupling and other factors, according to the required size of the magnetic levitation force, in the range of the number of turns to meet the coil under the conditions of the upper and lower body winding coil number to be taken $n = 29$; by formula (10) the theoretical levitation force of the model is:

$$F'_{f2n} = 2\left(\frac{\mu_0 \mu_r I_0 I_1 L}{2\pi R_1} - \frac{\mu_0 I_0 I_1 L}{2\pi R_2}\right) \times \sum_{i=1}^{n} \sin\left[\alpha + \phi \times (i-1)\right] \approx 562N \tag{14}$$

5. CONCLUSION

Through the simulation analysis of the magnetic suspension system model and the magnetic drive system model, the following conclusions can be drawn: In comparison of formula (7) and (8), it can be seen that the theoretical value of magnetic levitation force is very close to the simulation value, which proves the validity of the magnetic levitation model proposed in this paper; Because the magnetic suspension system produces magnetic coupling, the magnetic induction line is biased and the component force is produced in the direction of x and y, the theoretical calculation value of the magnetic levitation force F'_{f2n} is not equal to the simulation value F_{58y} ; In magnetic drive system when the coil number increases exponentially, the ampere force is greater than the value of times, is not a

linear relationship; when the current is changing the direction of current carrying coil, the driving force can be produced in the opposite direction and slow-motion control of robot.

6. REFERENCES

Zhu Xl, Zhou JP, Wang HG, et al. Experiments and Mechanism of Obstacle Negotiation of an Inspection Robot for Transmission Lines[J]Chinese Journal of Mechanical Engineering,2009,45(02):119-125.

Zhang Y, Liang Z, Fu S, et al. Structure-Constrained Obstacle Recognition for Transmission Line Inspection Robot[J].Robot, 2007,29(1):1-6.

Zhou FY, Wu A, Li Y, et al. Development of mobile robot for inspection of high voltage overhead power transmission lines[J].Automation of Electric Power Systems, 2004,28(23):89-91.

Pouliot N, Montambault S, Geometric design of the LineScout, a teleported robot for power line inspection and maintenance [C]//Proceedings-ICRA 2008 , Pasadena Conference center , Pasadena, CA, USA, 2008: 3970-3977.

Montambault S, Pouliot N, Design and validation of a mobile robot for power line inspection and maintenance [C]//6th International Conference on Field and Service Robotics-FSR2007,Chamonix,France;Springer,2008:495-504.

Debenest P. Expliner-robot for inspection of transmission lines[C]//Proceedings-ICRA 2008, Pasadena Conference Center, Pasadena, CA, USA, 2008:3978-3984.

Wu GP, Cao H, Pi Y, et al. An autonomous inspection robot for high voltage bundled transmission line and its application[J]. Engineering Journal of Wuhan University, 2012,45(01):96-102.

Wu GP, Xiao XH, Xiao H, et al. Development of a Mobile Inspection Robot for High Voltage Power Transmission Line[J]. Automation of Electric Power Systems, 2006, 30(13): 90-107

Wu GP, Dai JC, Guo YL, et al. Infrared Ray Detection and Fault Diagnosis of Mechanical Fault on High Voltage Lines[J].Chinese Journal of Scientific Instrument, 1999, 20(06): 571 -574.

Cheng JF. Development and Application of Magnetic Levitation Trains[J].Rolling Stock, 2003, 41(11): 13-17.

Chen Q, Li XL, Liu S. Nonlinear PID Controller for the Magnetic Levitation System[J].Electric Drive for Locomotives, 2014 (01): 52-54

Tang S. The research and development overview of Maglev linear motor-driven[J].Micro-motor,2003,36(04):51-55.

Mao JH, Luo JH, Jiang Q, et al. Design of Magnet Arrays for a Permanent Magnetic Linear Motor[J]. Journal of Xi'an Jiao tong University, 2007 , 41(03): 353-357.

Chen TF, Deng JM, Tang JX, et al. Break maglev linear motor maximum acceleration tracking control[J].Control Engineering,2015, 22(01):8-13.

Hao Y, Wang ZY, Yang M, et al. Research Optimisation of Space between Polar Conductor for $\pm$ 800kV UHVDC Transmission Line[J].Power System and Clean Energy, 2012, 28(01): 49-53.

249: Plasmonic enhancement of the properties of Dye-sensitized solar cells by Au nanocubes in composite photoanode

Hu XIE[1,3], Mengdai LUOSHAN[1,2*] , Chuyun HUANG[1,3*], Xinguo MA[1,3]

[1] School of Science, Hubei University of Technology, Wuhan 430068, China, 2289728371@qq.com
[2] Hubei Collaborative Innovation Center for High-efficiency Utilization of Solar Energy, Hubei University of Technology, Wuhan 430068, China, 455658743@qq.com
[3]Hubei Collaborative Innovation Center for High-efficiency Utilization of Solar Energy, Hubei University of Technology, Wuhan 430068, China, 6981605@qq.com
*Corresponding authors

A series of TiO_2 nanocomposite photoanodes with different amounts of Au nanocubes are prepared by a ball milling method and applied to assemble a series of dye-sensitized solar cells (DSSCs). The gold nanocubes demonstrate unique optical properties of the high photoluminescence quantum yield. The influences of the Au nanocubes on the performance of the photoanode and dye-sensitized solar cells were investigated. Studies demonstrated that by introducing the Au nanocubes, the intensity of the light-absorption spectra of the photoanodes and the photon capture ability of the dye molecules are significantly increased. The optimal performance with a Jsc of 15.32 $mA \cdot cm^{-2}$ and PCE of 6.708% are obtained in the DSSCs with the hybrid composite photoanodes, higher than those of the conventional DSSCs (based on pure TiO_2 photoanodes), respectively. The significant improvements in the properties of the optimal DSSCs are mainly attributed to the increase of the light-absorption of the dye due to the localized surface plasmon resonance.

Keywords: Au nanocubes; Surface plasmon resonance; Dye-sensitized solar cells; Photoelectric conversion efficiency

1. INTRODUCTION

Dye-sensitized solar cells (DSSCs) have attracted extensive attention as a promising alternative to traditional silicon-based photovoltaic devices due to its relatively simple fabrication methodology and high photoelectric conversion efficiency (Kong 2007; Hagfeldt 2010; Zhang 2013). Typically, a conventional DSSC device is comprised of TiO_2 nanocrystalline photoanode film which adsorbed by a monolayer dye molecules, a Pt-coated conductive glass as counter electrode and an electrolyte solution with a redox couple iodide/triiodide between the electrodes (O'Rega 1991; Schmidt-Mende 2005; Jena 2012). In order to obtain high photoelectric conversion efficiency (PCE) in DSSCs, kinds of efforts have been directed at controlling the TiO_2 photoanodes with various morphologies and textures (such as nanorods, nanosheets, mesoporous spheres), dopants and dyes capable of effectively absorbing visible and near-infrared light (Bach 1998; Pichot 2000; Ragoussi 2015). Among all the components of a DSSC, the monolayer of dye molecules plays a significant role in light-absorbing and photo-stimulated carriers generating (Liu 2009; Chandiran 2013; Leijtens 2013). Thus, the amounts of dye molecules that adsorbed by photoanodes and the light-harvesting efficiency (LHE) of the dye molecules would determine the efficiency of DSSCs to a great extent. Therefore, enhancing the LHE of the dye should be an effective way to optimise the whole performance of the DSSCs.

Recently, localized surface plasmon resonance(LSPR) of metal nanostructures has been regarded as a promising way to improve the LHE of photovoltaic devices (Au 2008; Chen 2009; Huang 2012). These noble metal nanocrystals have large surface area-to-volume ratios and spatial confinement of the free electrons. These significant properties improve their chemical reactivity and surface bonding performance, as well as nonlocal dielectric responses, plasmon-enhanced spectroscopies. When the noble metal nanoparticles are exposed to light, the free oscillating electrons in the conduction band of the metal particles interact with the electromagnetic field of the incident light wave under the same frequency, and then coupled with each other to form a collective oscillation.Under resonant excitation, the energy of the corresponding incident light wave photons is almost entirely in the form of surface plasmons locally in the metal surface, so that the local electromagnetic field of the metal surface is enhanced to some extent. Most of the noble metal nanostructures are prepared by seed-mediated growth method, which was developed from the preparation of differently shaped monometallic nanocrystals. This method is considered to be the most efficient and low cost method for tuning the shape and size of metal nanostructures compare to electrochemical reduction and different physical methods. Various metallic nanostructures have been synthesized and introduced into DSSCs to investigate their effects on the performance of devices (Huang 2006; Skrabalak 2008; Wang 2011). The studies showed that the coupling of plasmonic near-fields produced by metallic nanostructures with the sensitizers could optimise the light-adsorption of dye molecules and also could provide more reaction hot-spots for the photocatalysis processes (Lu 2010; Gong 2012). For instance, DSSC based on the Ag nanowires had a higher efficiency compared to DSSCs fabricated with no metal nanostructures, which represents potential access for improving the PCE of DSSCs (Ran 2017). DSSC doping 0.15 wt% Ag nanoparticles had an enhanced PCE of 5.33% (Guo 2013). The DSSCs made with TiO_2-Au nanocomposite are found to yield a much superior performance than the cells made with only TiO_2 nanoparticles (Muduli 2012). Furthermore, the results indicated that gold nanoparticles are generally more chemically stable than Ag nanoparticles when they are dispersed in aqueous solutions (Jiang 2012; Song 2012).

In this study, we propose a versatile bottom-up approach to assemble uniform monodisperse Au nanocubes and applied for the first time to improve the performance of DSSCs to the best of our knowledge. A series of different amounts of Au nanocubes were incorporated into conventional TiO_2 nanocrystalline films to form the composite photoanodes for the DSSCs. The influence of the Au nanocubes on the performance of the DSSCs and the mechanisms of their effects were investigated.

2. EXPERIMENTAL

2.1. Materials

Commercial TiO_2 powder (P25) was purchased from Evonik Degussa (New Jersey). Ethanol (EtOH, 95%), Triton-X100, acetylacetone, Gold chloride trihydrate($HAucl_4 \cdot 3H_2O$≥99.0%), silver nitrate($AgNO_3$, ＞99.8%), sodium borohydride($NaBH_4$,96%), L-ascorbic acid(AA, ＞99.7%) were purchased from Sinopharm Chemical Reagent Co.Ltd(Shanghai，China), Cetyltrimethylammonium bromide(CTAB, ≥99.0%) were purchased from Sigma-Aldrich Co. Ru dye and *cis*-di(thiocyanato)-bis(2,2'-bipyridyl-4,4'-dicarboxylate) ruthenium(N719) were purchased from Solaronix(Switzer-land). Iodine (I_2, 99.8%) was acquired from Beijing Yili chemicals (China). Lithium iodide (LiI, 99%) and 4-*tert*-butylpyridine (TBP) were purchased from Acros. Fluorine-doped SnO_2 conductive glasses (FTO, sheet resistance 10-15Ωsq^{-1}, Asahi Glass, Japan) were used as the substrate for the deposition of mesoporous nanocrystalline TiO_2 film. Deionized water with a resistivity of 18 MΩ cm used in experiment was prepared using an ultrapure water system.

2.2. Synthesis of Au nanocubes

The Au nanocubes were prepared by using a seed-growth method which contains a two-step process as reported previously (Liu 2013). Au seeds were synthesized by adding 0.6 mL of an ice-cooled $NaBH_4$ aqueous solution (10 mM) into a 7.8 mL aqueous solution which contains $HAuCl_4$ (0.25 mM) and CTAB (100 mM), generating a brownish solution. The seed solution was kept undisturbed for 1 h at 37 °C to ensure complete decomposition of $NaBH_4$ remaining in the solution. The growth solution containing 0.8 mL $HAuCl_4$ (10 mM), 6.4 mL CTAB (100 mM) and 31.2 mL H_2O was mixed uniformly, then a 3.8 mL AA aqueous solution (100 mM) was added and the growth solution turned colourless. Next, a 0.02 mL seed solution that was diluted 10 times by water was added into the growth solution. The resultant mixture solution was mixed by gentle inversion for 10 s and then left undisturbed overnight.

2.3. Fabrication of photoanodes and DSSCs

TiO_2 pastes were produced by ball milling the TiO_2 powder. The TiO_2 pastes containing different amounts of Au nanocubes were synthesized by incorporating different amounts of Au nanocubes into the TiO_2 pastes according to a series of mass ratios (Au:TiO_2=0, 0.2%, 0.4%, 0.6%, 0.8%, 1.0%). Doctor blade method was used to prepare photoanodes using the mixture paste, followed by sintering at 500 °C for 15min. Then, these photoanodes were sensitized by immersing them into a solution of *cis*-di(thiocyanato)-bis(2,2'-bipyridyl-4,4'-dicarboxylate) ruthenium(N719) with a concentration of 500 μM in a mixture of EtOH and *tert*-butyl alcohol (volume ratio:1/1) at 60 °C overnight. Then these sensitized photoanodes were washed with DI water and EtOH in order to remove excess dye molecules on the surface of these nanocrystalline TiO_2 films and then dried in an oven at 60 °C. The Pt counter electrodes were obtained by depositing a thin film of Pt via magnetron sputtering. These photoanodes and platinized counter electrodes were then assembled to form a DSSC by sandwiching a redox (I^-/I_3^-) electrolyte solution.

2.4. Characterization

The morphology of the Au nanocubes was characterized by transmission electron microscopy (TEM, JEM-2010FEF(UHR)) characterization. The chemical species of the Au nanocubes were analyzed by Energy-dispersive X-ray spectroscopy (EDX, GENESIS70000). The UV-vis absorption spectra of these samples were obtained on a UV-vis-NIR spectrophotometer (Cary 5000, Varian). The photo-current-voltage (*J*-V) characteristics of the DSSCs were measured under an irradiance of 100 $mW \cdot cm^{-2}$(AM 1.5 simulated illumination (Newport, 91192, Global)) at an effective irradiated area of 0.25 cm^2. Electrochemical impedance spectra (EIS) were obtained by a computer controlled electrochemical workstation CHI660C (Shanghai, China) with a frequency range from 100 kHz to 0.1 Hz in the condition of open circuit under 100 $mW \cdot cm^{-2}$ irradiation. The amount of dye loaded on each photoanode was checked by desorbing the dye from the photoanode into 0.1 M NaOH aqueous solution and measuring the UV-Vis absorbance spectra of the dye solution.

3. RESULT AND DISCUSSION

3.1. Characterization of the Au nanocubes

The morphologies of as-prepared Au nanocubes with uniform diameter were obtained by TEM. As shown in Figure 1a and b, the original Au nanocube monomers had a cube-like shape with an average edge length of 40 nm. It is easy to find that the surface of these nanocubes are very smooth. Furthermore, as shown in Figure 1c, the EDS pattern confirms that these nanoparticles are composed of Au element. Figure 1d shows a UV-vis absorption spectra of the Au nanocubes dispersed in DI water, it can be noted that the LSPR peak of the Au nanocubes was centered at 530 nm. Due to the structural anisotropy of the Au nanocubes, the status of electron oscillation is equal in each directions, which thereby result in only one unique surface plasmon resonance mode.

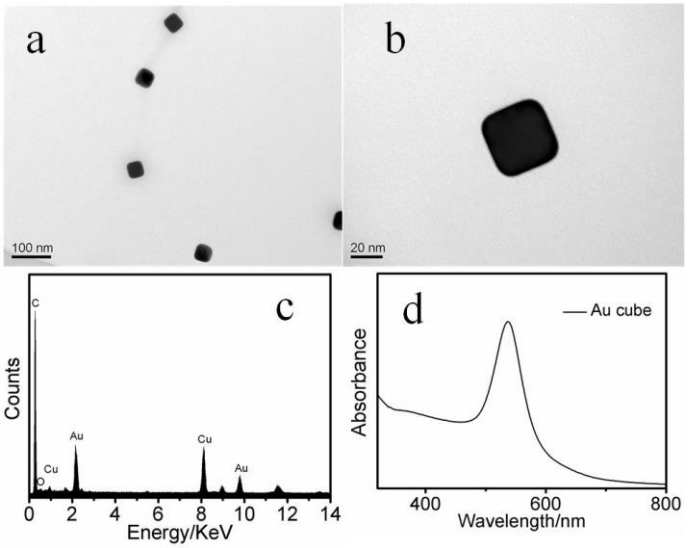

Figure 1: (a) TEM images of the as-synthesized Au nanocubes (b) A magnified TEM image of an individual Au nanocube (c) EDS pattern of the Au nanocubes (d) UV-vis absorption spectrum of Au nanocubes obtained in DI water.

3.2. Influences of the Au nanocubes on the performance of the photoanode

In order to assess the effect of the LSPR of Au nanocubes on the light absorption of dye adsorbed in the films, mesoporous TiO_2 films with different amounts of Au nanocubes incorporated were prepared by doctor-blading and measured, as shown in Figure 2a. The light absorption of the composite films increased obviously with the increase of the Au nanocubes in the films especially in the visible region when compare to the pure TiO_2 nanocrystalline film. And this enhancement in light-adsorption mainly attributed to the LSPR effect of these noble metal nanoparticles. In Au nanocubes incorporated films, light can effectively couple with plasmon due to the LSPR effect and optimise the optical density around Au nanocubes, then the dye molecules located around these Au nanocubes can absorb more photons as a result. In order to confirm our inference, the amount of dye absorbed in each film was measured by UV-vis absorption measurements, shown in Figure 2b. The UV-vis absorption spectra of the dye desorbed from the TiO_2 films measured in NaOH solution. It is noted that in the whole visible region, the intensity of the absorption peak of the dye desorbed from the dye-sensitized TiO_2 films with Au nanocubes are higher than that of the pure TiO_2 films. And as the amounts of the Au nanocubes increase, the intensity of the absorption peak becomes stronger, resulting in the higher LHE of photoanodes and better performance of DSSCs.

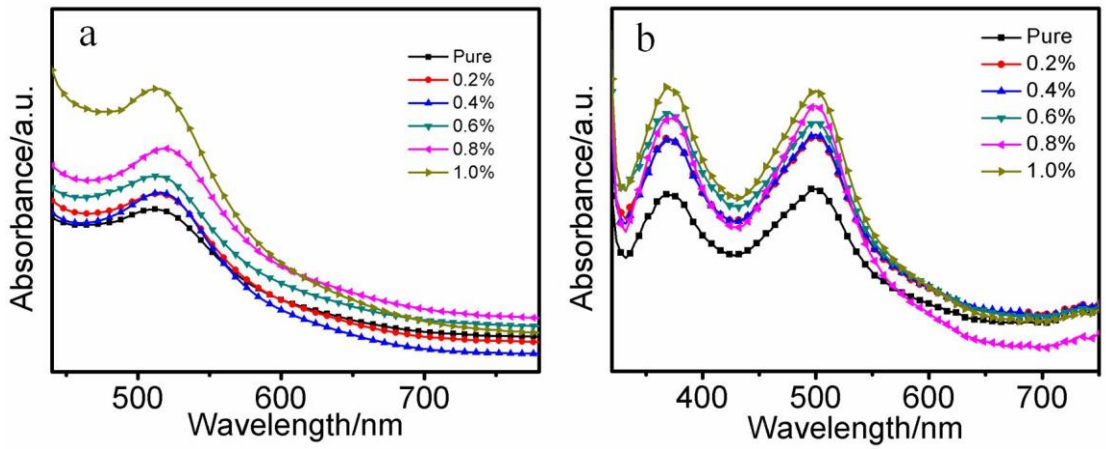

Figure 2: (a) UV-vis absorption spectra of the TiO_2 films containing different amounts of Au nanocubes after sensitization. (b) Absorption spectra of the dye desorbed from TiO_2 films with different amounts of Au nanocubes.

To investigate the effect of LSPR on the whole performance of DSSCs, a series of DSSCs incorporated different amounts of Au nanocubes were prepared. The photocurrent density-voltage (*J*-V) characteristics of these DSSCs are presented in Figure 3a, and the performance parameters are shown in Table1.

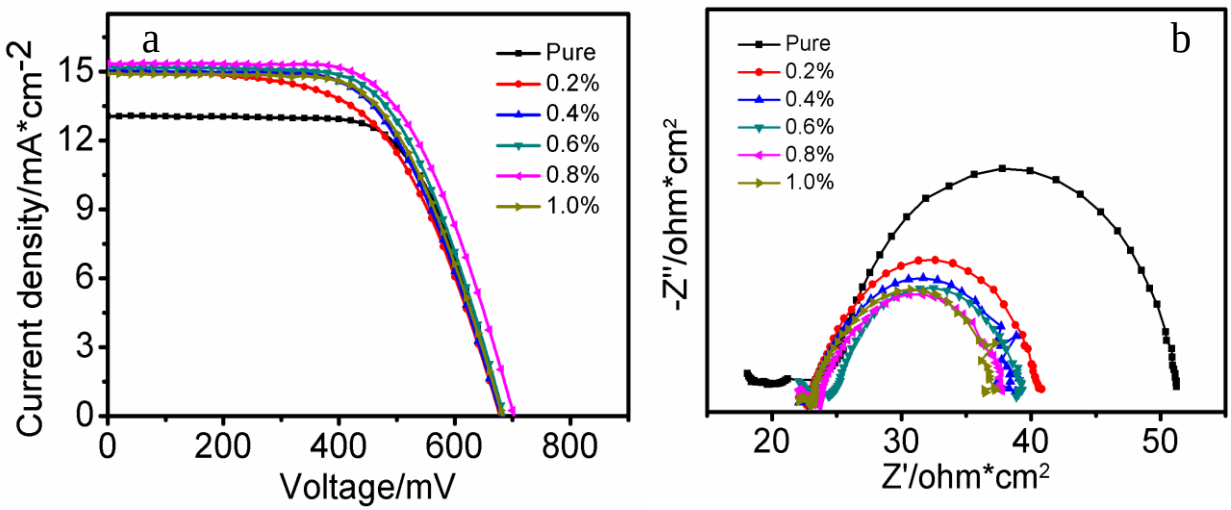

Figure 3: J-V curves (a) and Nyquist plots (b) of DSSC devices based on different amounts of Au nanocubes incorporated photoanodes.

Table 1: performance parameters of the DSSCs varing with different contents of Au nanocubes

contents of Au nanocubes	J_{SC}(mA·cm^{-2})	V_{OC}(mV)	FF(%)	Ƞ(%)
0	13.048	678	0.67	5.894
0.2%	14.97	677	0.58	5.86
0.4%	15.03	679	0.61	6.197
0.6%	15.19	685	0.62	6.497
0.8%	15.32	703	0.62	6.708
1.0%	14.91	681	0.62	6.28

As can be seen from the *J-V* curves, the short-circuit current density (J_{sc}) exhibits obviously change with different amounts of Au nanocubes. When the amounts of Au nanocubes increase, the J_{sc} increase significantly. For the DSSC containing 0.8wt% of the Au nanocubes, the optimised performance with a J_{sc} of 15.32 mA·m^{-2}, V_{oc} of 703 mV and η of 6.708% is achieved, exhibiting a ~14.47%, ~3%, ~12% enhancement respectively in comparison with those of the DSSCs with pure TiO_2 photoanode. Due to oscillating conduction electrons of Au nanocubes could resonate with the electric field of incident light at around 530 nm, resulting in LSPR localized in the vicinity of Au nanocubes. The LSPR effect could stimulate dye molecules more effectively and then optimise the light-absorption and photocurrent generation. However, with further increasing the amounts of Au nanocubes, the J_{sc} decrease accordingly. This could be attributed to an excess amount of Au nanocubes in the TiO_2 films that may reduce the effective surface area of the TiO_2 films and increase of charge carrier recombination reverse.

Electrochemical impedance spectroscopy (EIS) analysis has been regarded as a powerful tool for investigating the kinetics of electrochemical processes occurring in DSSCs (Luoshan 2015). In order to further study the performance of the photoanodes incorporated, EIS measurements were carried out on an electrochemical work station under AM 1.5 sunlight irradiation (Luoshan 2016). Nyquist plots of DSSC devices based on different amounts of Au nanocubes incorporated photoanodes are shown in Figure 3b. As the performance of the Au nanocubes induced photoanodes is the key in this study, we focus on the second circle (R_2) of the curves. It can be calculated that the charge transfer resistance of the TiO_2/dye/electrolyte interface retained its value after incorporated Au nanocubes into the TiO_2 membrane. The smaller R_2, the less recombination reaction of electrons with triiodide ions and the excited dye at the TiO_2/dye/electrolyte interface, and thus a higher J_{sc}.

4. CONCLUSIONS

In summary, a series of composite TiO_2 films incorporated with different amounts of Au nanocubes were prepared and applied to make DSSCs. Influences of the unique structure of the Au nanocubes on the properties of the photoanode and DSSCs were investigated. Studies indicated that, the ability of light-absorption of the TiO_2 photoanodes amd the photon capture ability of the dye molecules were significantly increased, and J_{sc} were optimised as a result. The optimal properties were obtained in a DSSC with J_{sc} of 15.32 mA·cm^{-2} and η of 6.708% at Au nanocubes content of 0.8 wt%. The enhancement of J_{sc} and η mainly attributed to the increase of light-coupling and absorption of dye due to the LSPR effection of Au nanocubes.

5. ACKNOWLEDGEMENTS

We gratefully acknowledge the Development Funds of Hubei Collaborative Innovation Center (HBSKFZD2017004, HBSKFMS2015004) and University Students Science and Technology Innovation Fund of Hubei Collaborative Innovation Center for High-efficiency Utilization of Solar Energy (HBSDY201616).This work was also supported by the National Natural Science Foundation of China (51472081),Cooperative Foundation of China-UK Research and Innovation Bridges (2016YFE0124300), the Foundation for High-Level Talents (GCRC13014) and Leading Plan of Green Industry (YXQN2016005).

6. REFERENCES

Kong FT, Dai SY, Wang KJ, 2007. Review of recent progress in dye-sensitized solar cells, *Advances in OptoElectronics*, 2007(March), 1–13.

Hagfeldt A, Boschloo G, Sun L, et al. 2010. Dye-sensitized solar cells, *Chemical Reviews*, 110(11), 6595–6663.

Zhang S, Yang X, Numata Y, et al. 2013. Highly efficient dye-sensitized solar cells: progress and future challenges, *Energy & Environmental Science*, 6(5), 1443.

O'Regan B, Grätzel M 1991. A low-cost, high-efficiency solar cell based on dye-sensitized colloidal TiO_2 films, *Nature*, 353(6346), 737–740.

Schmidt-Mende L, Bach U, Humphry-Baker R, et al. 2005. Organic dye for highly efficient solid-state dye-sensitized solar cells, *Advanced Materials*, 17(7), 813–815.

Jena A, Mohanty SP, Kumar P, et al. 2012. Dye sensitized solar cells: A Review, *Transactions of the Indian Ceramic Society*, 71(1), 1–16.

Bach U, Lupo D, Comte P, et al. 1998. Solid-state dye-sensitized mesoporous TiO_2 solar cells with high photon-to-electron conversion efficiencies, *Nature*, 395(6702), 583–585.

Pichot F, Pitts J R, Gregg B A 2000. Low-temperature sintering of TiO_2 colloids: application to flexible dye-sensitized solar cells, *Langmuir*, 16(13), 5626–5630.

Ragoussi ME, Torres T 2015. New generation solar cells: concepts, trends and perspectives, *Chemical Communications*, 51(19), 3957–3972.

Liu B, Aydil E S 2009. Growth of oriented single-crystalline rutile TiO_2 nanorods on transparent conducting substrates for dye-sensitized solar cells, *Journal of the American Chemical Society*, 131(11), 3985–3990.

Chandiran AK, Comte P, Humphry-Baker R, et al. 2013. Evaluating the critical thickness of TiO_2 layer on insulating mesoporous templates for efficient current collection in dye-sensitized solar cells, *Advanced Functional Materials*, 23(21), 2775–2781.

Leijtens T, Lim J, Teuscher J, et al. 2013. Charge density dependent mobility of organic hole-transporters and mesoporous TiO_2 determined by transient mobility spectroscopy: Implications to dye-sensitized and organic solar cells, *Advanced Materials*, 25(23), 3227–3233.

Au L, Lu X, Xia Y 2008. A comparative study of galvanic replacement reactions involving Ag nanocubes and $AuCl^{2-}$or $AuCl^{4-}$, *Advanced Materials*, 20(13), 2517–2522.

Chen H, Sun Z, Ni W, et al. 2009. Plasmon coupling in clusters composed of two-dimensionally ordered gold nanocubes, *Small*, 5(18), 2111–2119.

Huang M H, Lin PH 2012. Shape-controlled synthesis of polyhedral nanocrystals and their facet-dependent properties, *Advanced Functional Materials*, 22(1), 14–24.

Huang CJ, Chiu PH, Wang YH, et al. 2006. Synthesis of the gold nanocubes by electrochemical technique, *Journal of The Electrochemical Society*, 153(8), D129.

Skrabalak S E, Chen J, Sun Y, et al. 2008. Gold nanocages: synthesis, properties, and applications, *Accounts of Chemical Research*, 41(12), 1587–1595.

Wang J, Gong J, Xiong Y, et al. 2011. Shape-dependent electrocatalytic activity of monodispersed gold nanocrystals toward glucose oxidation, *Chemical Communications*, 47(24), 6894.

Lu CL, Prasad KS, Wu HL, et al. 2010. Au nanocube-directed fabrication of Au−Pd core−shell nanocrystals with tetrahexahedral, concave octahedral, and octahedral structures and their electrocatalytic activity, *Journal of the American Chemical Society*, 132(41), 14546–14553.

Gong J, Zhou F, Li Z, et al. 2012. Synthesis of Au@Ag core–shell nanocubes containing varying shaped cores and their localized surface plasmon resonances, *Langmuir*, 28(24), 8959–8964.

Ran H, Fan J, Zhang X, Mao J, Shao G. 2017. Enhanced performances of dye-sensitized solar cells based on Au-TiO_2 and Ag-TiO_2 plasmonic hybrid nanocomposites, *Applied Surface Science*, 430, 415-423.

Guo K, Li M, Fang X, et al. 2013. Preparation and enhanced properties of dye-sensitized solar cells by surface plasmon resonance of Ag nanoparticles in nanocomposite photoanode, *Journal of Power Sources*, 230(10), 155-160

Muduli S, Game O, Dhas V, et al. 2012. TiO_2-Au plasmonic nanocomposite for enhanced dye-sensitized solar cell (DSSC) performance. *Solar Energy*, 86(5), 1428-1434.

Jiang R, Chen H, Shao L, et al. 2012. Unraveling the evolution and nature of the plasmons in (Au Core)-(Ag Shell) Nanorods, *Advanced Materials*, 24(35), OP200-OP207.

Song HM, Anjum D H, Khashab N M 2012. Shape-controlled synthesis of Au@Pd core-shell nanoparticles and their corresponding electrochemical properties, *RSC Advances*, 2(9), 3621.

Liu XL, Liang S, Nan F, et al. 2013. Solution-dispersible Au nanocube dimers with greatly enhanced two-photon luminescence and SERS, *Nanoscale*, 5(12), 5368.

Luoshan M, Li M, Liu X, et al. 2015. Performance optimisation in dye-sensitized solar cells with β-$NaYF_4$: Er^{3+}/Yb^{3+} and graphene multi-functional layer hybrid composite photoanodes, *Journal of Power Sources*. Elsevier, 287, 231–236.

Luoshan M, Bai L, Bu C, et al. 2016. Surface plasmon resonance enhanced multi-shell-modified upconversion $NaYF_4$:Yb^{3+},Er^{3+}@SiO_2@Au@TiO_2 crystallites for dye-sensitized solar cells, *Journal of Power Sources*. Elsevier B.V, 307, 468–473.

250: Human-machine interaction intention recognition technology based on D-S evidence theory

Xueyuan ZHANG[1], Liping YU[2], Ge LIU[3], Di ZHAO[4]

[1] School of Mechanical Engineering, HBUT, Wuhan, 328040576@qq.com
[2] School of Mechanical Engineering, HBUT, Wuhan, 523182137@qq.com
[3] School of Mechanical Engineering, HBUT, Wuhan, 646605009@qq.com
[4] School of Mechanical Engineering, HBUT, Wuhan, zhd_hbut@126.com

Human intention recognition plays an important role in human-machine collaboration. In this paper, the intention recognition method for target capture is studied, a vision based method is used in the human-computer interaction, and the trajectory of the body's upper extremity is taken as the main criterion. The user interaction intention model is established by using the multi-dimension judging factor. Then the target fast judging algorithm is optimised by adopted the D-S theory to realize the intention factor fusion. Experiment results show that the intention-identification method proposed in this paper can quickly and accurately identify the operator's grasping intentions and serve human-computer collaboration. The comparison experiments show that the multi-dimensional factor intention identification method is more accurate and more effective than the single factor method.

Keywords: Intention recognition; D-S theory; machine vision; human-robot collaboration

1. INTRODUCTION

At present, in the Human-Robot Collaboration (HRC) operation, most of the control of the robot is directly controlled by a person. This method is timely and easy to implement, but the efficiency, fluency and adaptability of human-computer interaction are easily affected. Psychological research shows that when two interactive objects are collaborating, one of the objects will always tend to predict the potential actions of interactive objects and take corresponding countermeasures according to the predicted actions to achieve safe and correct collaboration. The first task for robots to complete the natural HRC process is to predict human intentions.

In the existing research, many scholars have made many breakthroughs based on the natural human-computer cooperation of intention recognition. For example, Song and Kyriazis et al. (2013) obtain the state of action images by observing the sequence of action images transmitted or captured by users' hands and encoding them, so that the robot can learn the interaction intention of users' hands. Jang and Mallipeddi et al. proposed a method based on eye movement patterns and changes in pupil size to identify potential intentions of users, allowing the robot to predict user intentions (Jang, 2014). Wang and Deisenroth et al. proposed to model the probabilistic model with intention-driven intention-driven dynamic model (IDDM) and use Bayes' theorem to infer the intent of the observed motion (Wang, 2013). Elfring and Molengraft et al. used the growth hidden Markov model (GHMMS) to summarize the user's typical motion pattern, compared with the traditional constant velocity model, the hidden Markov model can significantly improve the estimation of the user's intention position (Elfring, 2014). Gehrig and Krauthausen et al. proposed multi-level (intention, action, movement) information fusion modeling for intention prediction of user movement (Gehrig, 2011).

The above research shows that the robot can achieve prediction or recognition of user interaction intention by extracting user motion features or mixing user motion interaction information. In this article, the author has constructed a user interaction intent model and used the intent recognition algorithm based on Dempster-Shafer (D-S) evidence theory to determine the robot's intention to capture the human, thus predicting the user's actual intention expression, as shown in Figure 1.

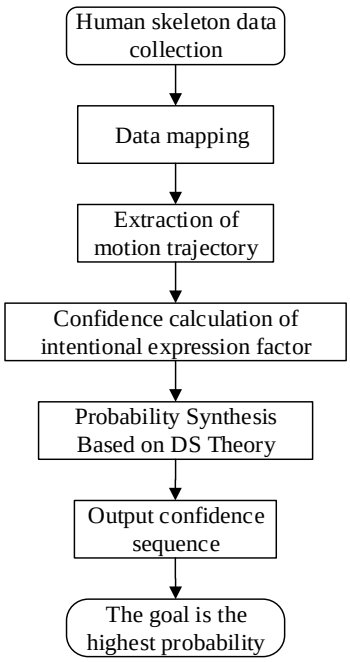

Figure 1: Flow chart of intention judgment based on D-S evidence theory

2. USER INTERACTION INTENTION MODEL

The prediction of the user's intention by the robot is not through command input or human-computer question and answer, but by giving feedback by sensing and analyzing the information generated by the interactive environment and user actions. The premise of the robot's perception and recognition of the user's intention is to model the user's interaction intention and to understand the purpose of the user interaction through the intention model, so as to effectively improve the human-computer interaction efficiency. This article has designed an intent model that is suitable for humans to grasp the operation of an object. Its model is expressed as follows:

Equation 1: Intent model.

$$I = \left\{ R_o, H_u, G, B_e, O_p, H_g, R_h \right\}$$

Table 1: User interaction intention model parameter table

Parameter	Meaning	Content
Ro	Robot System Properties	Robot motion parameters and cooperative operation service modules that can be provided
Hu	User system properties	Interactive limb type, user position relative to robot space, operator's upper body movement information
G	Target attribute	Target space coordinates
Be	Interaction behaviour attributes	Including user interaction gestures, voice commands, line of sight, facial expressions, sports trends
Op	Interaction properties	Including the implementation of single-step operation type parameters and continuous action set
Hg	User and target related attributes	User orientation, target included in user motion range
Rh	User system and robot system related properties	User system and robot system coordinate system transformation matrix

In this study, the end point of the human body's upper limb movement in the field of view of the robot camera is taken as the predicted movement target point. The object that predicts the position of the target point is defined as the user's possible grasping operation intent, and is also the cooperative crawling intention of the robot in the human-robot cooperative operation.

Equation 2: Target attribute.

$$G = \{g_1, g_2, \cdots, g_i\}$$

Where, $g_i \in R^3, i = 1, 2, 3, \cdots, \mathrm{N}$.

$g_i(gx_i, gy_i, gz_i)$ indicates the user's intention to crawl, (gx_i, gy_i, gz_i) represents the spatial coordinates of the target in the robot motion coordinate system. G is all potential intentional target sets. In order to facilitate the experimental feasibility, limiting the crawling intention g can only be one of the limited goal set G . Parameters not mentioned in this article are set to default values, which are set to 1.

3. INTENTION RECOGNITION BASED ON D-S EVIDENCE THEORY

3.1. Data mapping

In the human-computer interaction, the user and the robot are in the same three-dimensional workspace, and the robot captures the real-time movement trajectory of the user's crawling operation through the depth camera. In order to facilitate the real-time robot grab operation, it is necessary to map the depth camera space coordinates and the robot motion space coordinates (Schaal 1999). $F^{\mathrm{c}} = (x^{\mathrm{c}}, y^{\mathrm{c}}, z^{\mathrm{c}})$ is the depth camera space coordinate and $F^{\mathrm{r}} = (x^{\mathrm{r}}, y^{\mathrm{r}}, z^{\mathrm{r}})$ is the robot motion space coordinate.

Equation 3: Data mapping.

$$F^{\mathrm{r}} = R_{\mathrm{c}}^{\mathrm{r}} F^{\mathrm{c}} + T_{\mathrm{c}}^{\mathrm{r}}$$

$F^{\mathrm{c}}, F^{\mathrm{r}}$ are the real-time motion data of the depth camera space and the robot motion space in real time. $R_{\mathrm{c}}^{\mathrm{r}}, T_{\mathrm{c}}^{\mathrm{r}}$ are the rotation matrix and the translation matrix from the camera coordinate system to the robot motion coordinate system (Schaal 2013).

The depth camera captures depth image information F^{c}, and the colour camera captures interactive colour image information $F^{I}=(u,v)$. In order to perform interactive information fusion, it is necessary to separately map the coordinates of the user's skeleton space captured by the depth camera and the coordinates of the target object space and the coordinates of the image captured by the colour camera. Because the resolution of the depth image and the colour image and the origin of the coordinate system are not uniform, the coordinate conversion can be performed in the following way:

Equation 4: Coordinate transformation.

$$\begin{bmatrix} u \\ v \\ \alpha \end{bmatrix} = \begin{bmatrix} \frac{1}{\mathrm{d}x^{c}} & 0 & x_0^{c} \\ 0 & \frac{1}{\mathrm{d}y^{c}} & y_0^{c} \\ 0 & 0 & 1 \end{bmatrix} \begin{bmatrix} x^{c} \\ y^{c} \\ \alpha \end{bmatrix}$$

In the formula, u,v represents colour image pixel point coordinates, the unit is px (pixels); x_0^{c}, y_0^{c} represents the depth image pixel coordinates in units of mm; α is the depth image and colour image resolution conversion factor; the unit of $1/\mathrm{d}(...)$ is px/mm.

3.2. Intention expression factor

Intent expression factor refers to the characteristics that can capture the user's grasping intention during the arm grabbing motion, such as the hand movement speed, the movement acceleration, the azimuth of the hand movement direction and the target, and the Euclidean distance between the arm and the target. , the user's hand grab gestures. The intention expression factor in this paper is the Euclidean distance S_i between the user's hand movement trajectory and the potential target, the azimuth θ_i between the speed direction of the user's hand movement trajectory and the potential target, and the relative velocity vector v_i^{*} between the user's hand movement trajectory and the potential target, ,as shown in Figure 2.

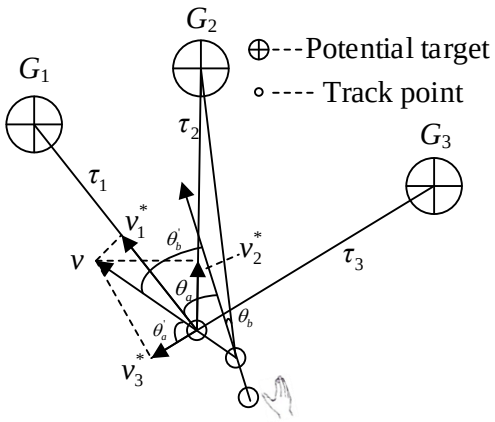

Figure 2: Relationship between hand trajectory and potential targets

The Euclidean distance between the user's hand movement trajectory and the potential target is denoted by S_i:

Equation 5: The Euclidean distance.

$$S_i = \sqrt{(gx_i - tx)^2 + (gy_i - ty)^2 + (gz_i - tz)^2}$$

In the interaction process, the smaller the Euclidean distance S_i between the end point *t* of the motion trajectory and the potential target, the greater the probability PS_i that the potential target is captured, i.e., $PS_i \propto 1/S_i$ .In the interactive process, it is stipulated that every crawl must select a certain target, i.e., $\sum_{i=1}^{N} PS_i = 1$. Because the distribution of each dimension component of the data in the standard Euclidean distance is not the same, it is necessary to "normalize" each component, that is to say, the mean and variance are equal, and the variance is the second-order distance. Therefore, let the target capture probability mapping function based on S be:

Equation 6: The target capture probability mapping function based on S.

$$PS_i = \frac{S_i^{-2}}{\sum_{i=1}^{N} S_i^{-2}}$$

The azimuth between the speed direction of the user's hand movement trajectory and the potential target is denoted by θ_i , and the vector of the hand movement trajectory point and the potential target is defined as τ ,

Equation 7: Vector of hand trajectory points and potential targets.

$$\tau_i = \left[gx_i - tx, gy_i - ty, gz_i - tz \right]^T$$

The velocity vector ν of the user's hand movement trajectory can be given by two consecutive movements of the trajectory points, and $t^{'}(tx^{'}, ty^{'}, tz^{'})$ denotes the coordinate of the previous hand's movement trajectory point.

Equation 8: The velocity vector of the hand movement trajectory

$$\nu = \left[tx - tx^{'}, ty - ty^{'}, tz - tz^{'} \right]$$

According to the vector angle calculations are： $\cos\theta_i = \frac{\nu \cdot \tau_i}{|\nu||\tau_i|}$

Equation 9: The azimuth.

$$\theta_i = \arccos \frac{(gx_i - tx)(tx - tx^{'}) + (gy_i - ty)(ty - ty^{'}) + (gz_i - tz)(tz - tz^{'})}{\sqrt{(gx_i - tx)^2 + (gy_i - ty)^2 + (gz_i - tz)^2} * \sqrt{(tx - tx^{'})^2 + (ty - ty^{'})^2 + (tz - tz^{'})^2}}$$

In the interaction process, the smaller the velocity vector of the user's hand movement trajectory and the azimuth angle θ_i of the target, the more likely the movement tendency of the hand is close to the target, and the probability $P\theta_i$ that the potential target is captured is greater, $P\theta_i \propto 1/\theta_i$,as shown in Figure 2.

According to the relationship between hand movement speed and the potential target azimuth and target capture probability, this paper makes $\sum_{i=1}^{N} \theta_i = \theta_s$. There must be a goal to be crawled during the final interaction, i.e., $\sum_{i=1}^{N} P\theta_i = 1$ .Therefore, let the target capture probability mapping function based on *θ* be:

Equation 10: The target capture probability mapping function based on θ.

$$P\theta_i = \frac{\theta_i^{-1}}{\sum_{i=1}^{N} \theta_i^{-1}}$$

The relative motion velocity vector between the velocity vector of the user's hand and the potential target during the interaction can be represented by v_i^* , $v^* = v * \cos\theta$, as shown in Figure 2.

Equation 11: Relative motion velocity vector.

$$v_i^* = v \cdot \frac{\tau_i}{|\tau_i|}$$

And because the size of the vector module connecting the trajectory of the hand with the potential target is the Euclidean distance S_i between the trajectory of the arm and the target, after the conversion, the calculation process of v_i^* can be expressed as:

Equation 12: Relative motion velocity vector.

$$v_i^* = \frac{1}{S_i} \cdot \begin{bmatrix} (gx_i - tx)(tx - tx') + (gy_i - ty)(ty - ty') + \cdots \\ (gz_i - tz)(tz - tz') \end{bmatrix}$$

The direction of the relative velocity vector v* represents the tendency of the potential target to be captured. The larger the potential velocity vector model, the more potential targets may be captured, i.e., $Pv_i \propto v_i^*$。Considering that there must be a goal to be captured during the final interaction, i.e., $\sum_{i=1}^{N} Pv_i = 1$。Due to the closeness of the velocity parameter curve and the natural exponential function in the human upper limb movement, an exponential function was chosen [15]. Let the target capture probability mapping function based on v^* be:

Equation 13: The target capture probability mapping function based on v^*.

$$Pv_i = \frac{e^{v_i^*}}{\sum_{i=1}^{N} e^{v_i^*}}$$

3.3. Based on D-S evidence theory intention identification

The set G is called a recognition frame or hypothesis space.

In the process of the user's arm movement, the probability that the target is captured is represented by *P*, and P_i represents the probability that the Ith target is captured after making a decision based on the D-S evidence theory at this moment. Each target needs to consider these three intention expression factors S, θ, v. PS_i、$P\theta_i$、Pv_i denote the confidence of the target I under the evaluation of the intent expression factor S、θ、v, respectively.

Using the combination of D-S evidence theory and the Dempster rule of evidence synthesis, the combined mass function for each target is calculated (Ravichandar 2016):

Equation 14: The combined mass function for target.

$$(PS_i \oplus P\theta_i \oplus Pv_i)(g_i) = ((PS_i \oplus P\theta_i) \oplus Pv_i)(g_i)$$

Evidence synthesis is completed and the final multi-evidence fusion is achieved for each target's mass function set $P = \{P_1, P_2, \cdots, P_i\}$.

Equation 15: Probability of getting captured.

$$\begin{aligned} P_i &= m(g_i) = (PS_i \oplus P\theta_i \oplus Pv_i)(g_i) \\ &= K^{-1} \cdot \sum_{g_1 \cap g_2 \cap \cdots \cap g_n = g_i} \prod_{1 \le i \le n} PS_i(g_i) * P\theta_i(g_i) * Pv_i(g_i) \end{aligned}$$

Where K is the normalization constant

3.4. Algorithm optimisation

To further optimise the algorithm, this article adds probability selection links. When the probability of a certain target being fetched is greater than or equal to 0.5 and continues to increase when a certain moment is merged with a

multi-intent expression factor, the system can directly determine the target as a target for capture, and output the probability as 1 to exclude other targets, as shown below.

Equation 16: Judged grab target.]

$$\max(P) = \begin{cases} m(g_i) & \max(m(g_i)) < 0.5 \\ 1 & m(g_i) \geq 0.5 \end{cases}$$

If the system cannot recognize the current intention, the previous frame intention is taken as the intention of this cycle.

Equation 17: The final target captured.]

$$G_t = \begin{cases} g_i & m(g_i) = \max(P) \\ G_t^{'} & G_t^{'} \textit{ is the previous frame prediction} \end{cases}$$

The final prediction of the interaction intention is $G_t = g_i$.

4. SIMULATION

In this paper, an experiment for the robot to judge the intention of people to grab the object is designed to verify the intention recognition algorithm based on D-S theory. The system configuration is as follows: Microsoft Kinect 2.0 somatosensory controller collects human bone data; Visual Studio 2013+ Kinect for Windows SDK V2.0+OpenCV reads human bone data, draws human skeleton feature points, and records and records bone feature data in real time. The data sampling period is 1/30 s. Among them, the controller actively visually captures the space coordinate and quantity of the user's capture intention, and uses OpenCV to convert to the real-time interactive interface.

Four experimental objects g1、g2、g3，g4 (from left to right) are randomly placed on the experimental table to perform grab verification, randomly grab one of the targets, monitor experimental data, and complete the experimental process. The experimental process is shown in Figure 3.

The graph (a), (b), (c), (d) four graphs are in turn the prediction of the user interaction intention during the arm movement, and the green circle indicates that the target is the user's grasping intention. According to figure 3, the user's grasping intention is G3. The red curve is the actual movement trajectory of the user arm, and the Yellow dashed line represents the vector of the end point of the user arm movement trajectory pointing to the potential target.

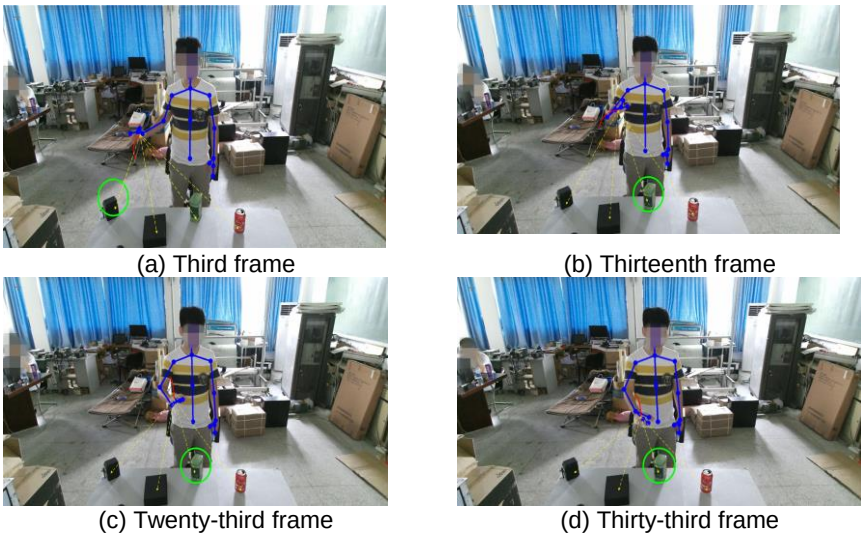

(a) Third frame (b) Thirteenth frame

(c) Twenty-third frame (d) Thirty-third frame

Figure 3: intention recognition experiments for grasping targets at different times

In the process of grabbing the experiment, the user's intention is actually expressed by multiple intentional expression factors. Figure 4 shows each target crawl probability sequence in the intention recognition algorithm based on different intent expressive factors and D-S evidence fusion in grabbing g_3.

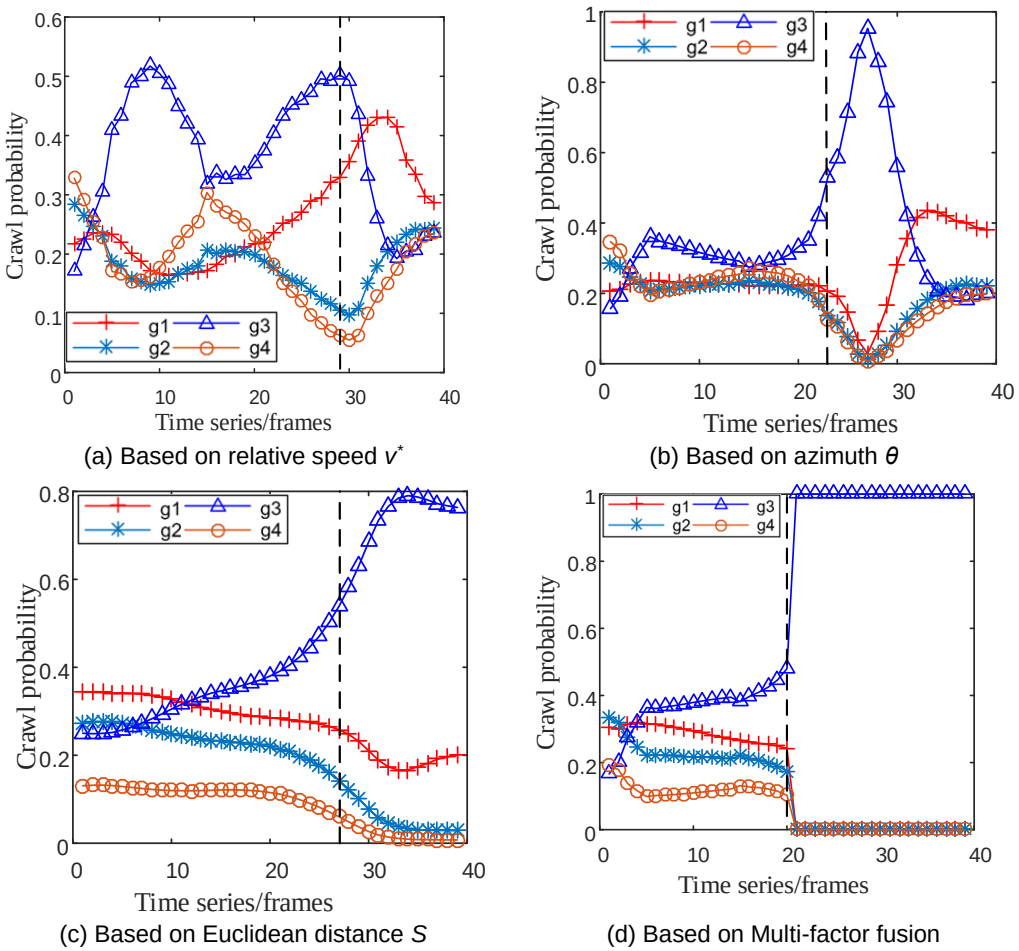

Figure 4： Grab probability of each target under the judgment of different intention factors

The dashed line indicates the number of frames that can determine the capture intention under different intention expression factors. The following conclusions can be drawn:

In the process of arm motion, the target judgment based on relative velocity v^* needs nearly 30 frames, and the probability of early real target and interference target fluctuates greatly; the target judgment based on azimuth angle θ is nearly 25 frames, and the probability of the earlier real target and the interference target is relatively close, and the distinction is not strong. Both of the latter's actual target probabilities are decreasing rapidly, so the recognition effect is very poor, and it is even easy to cause misjudgement.

Although the target based on the Euclidean distance S can accurately identify the real target, the convergence speed is slow. The target judgment based on the multi-intent expression factor can quickly and accurately recognize the real target at about 20 frames.

Compared with the single intention expression factor target grasping probability experiment, the multi intention expression factor fusion intention recognition algorithm can quickly converge, and the prediction time can be reduced by more than 25% on the basis of accuracy, and the validity and correctness of the algorithm is verified.

5. SUMMARY

In this article, the author has attempted to establish the intention model when man grabs the object, obtained the motion of the human through the depth camera, expressed the intention in a natural interactive way, and used the D-S argument to fuse the intention recognition algorithm of the intentional expression factor. Experiments show that the algorithm converges to the real intention more quickly than the single-intent expression factor, so it has higher accuracy and credibility in intention recognition and has practical application value in human-computer interaction.

6. REFERENCES

Liu T, Wang J, Meng Q H. Human robot cooperation based on human intention inference[C]// International Conference on Robotics and Biomimetics, 2015:73-6.

Baldwin D A, Baird J A. Discerning intentions in dynamic human action [J]. Trends in Cognitive Sciences, 2001, 5(4):171-178.

Feng Y, Jia Q, Wei W. Evaluation Method of Human-Computer Interaction Participation Based on Dynamic Bayesian Network[J]. Robotics, 2018, 40(2): 169-177.

Zhao D, Yang B, Liu G, et al. Prediction of User Operation Intent Based on Human-robot Collaboration[J]. Science Technology and Engineering, 2017, 17(16):242-247.

Tsai C S, Hu J S, Tomizuka M. Ensuring safety in human-robot coexistence environment[C]//IEEE/RSJ International Conference on Intelligent Robots and Systems,2014:4191-4196.

Nikolaidis S, Ramakrishnan R, Gu K, et al. Efficient Model Learning from Joint-Action Demonstrations for Human-Robot Collaborative Tasks[C]// Tenth ACM/IEEE International Conference on Human-Robot Interaction,2015:189-196.

Wang C, Zhao Y, Lin C Y, et al. Fast planning of well-conditioned trajectories for model learning[C]// IEEE/RSJ International Conference on Intelligent Robots and Systems, 2014:1460-1465.

Song D, Kyriazis N, Oikonomidis I, et al. Predicting human intention in visual observations of hand/object interactions[C]//IEEE International Conference on Robotics and Automation, 2013:1608-1615.

Jang Y M, Mallipeddi R, Lee S, et al. Human intention recognition based on eyeball movement pattern and pupil size variation[J]. Neurocomputing, 2014, 128(128):421-432.

Wang Z, Deisenroth M P, Amor H B, et al. Probabilistic movement modeling for intention inference in human-robot interaction[J]. International Journal of Robotics Research, 2013, 32 (7):841-858.

Elfring J, Molengraft R v d, Steinbuch M. Learning intentions for improved human motion prediction [J]. Robotics & Autonomous Systems, 2014, 62 (4):591-602.

Gehrig D, Krauthausen P, Rybok L, et al. Combined intention, activity, and motion recognition for a humanoid household robot[C]//IEEE/RSJ International Conference on Intelligent Robots and Systems, 2011:4819-4825.

Schaal S. Is imitation learning the route to humanoid robots [J]. Trends in Cognitive Sciences, 1999, 3(6):233.

Ravichandar H C, Dani A P. Human Intention Inference Using Expectation-Maximization Algorithm With Online Model Learning [J]. IEEE Transactions on Automation Science & Engineering, 2016, PP(99):1-14.

Zhang X. Evidence theory and decision making, artificial intelligence [M].Beijing: China Renmin University Press,1993.26-36.

Yang N. Human body movement coordination law and its parametric description [D]. Tsinghua University, 2001.

251: Enhancing visible-light photocatalytic activity of $BiPO_4$ via hybridization of graphene based on a first-principles study

Chang SHU[1], Jisong HU[1], Yang WEI[1], Xinguo MA[1,2]

[1] School of Science, Hubei University of Technology, Wuhan 430068, China
[2] Hubei Collaborative Innovation Center for High-efficiency Utilization of Solar Energy, Hubei University of Technology, Wuhan 430068, China, maxg2013@sohu.com

Interfacial bonding and electronic properties are very important for understanding the photocatalytic activity of heterojunction. However, theoretical research is still lacking in $BiPO_4$(100)/graphene heterojunction. In this study, the photoelectrochemical properties of the $BiPO_4$(100) surface were modified through the introduction of graphene, and the corresponding effect of interface cohesive interaction on the charge redistribution and the band edge of $BiPO_4$(100)/graphene heterojunction was investigated by first-principle calculations incorporating semiempirical dispersion-correction schemes. The results indicated that $BiPO_4$(100) and graphene were in parallel contact and formed a stable van der Waals heterojunction with low lattice mismatch. In addition, it was identified by analyzing the energy band structures and the three-dimensional charge density difference that to couple with graphene, the $BiPO_4$(100) layer in interface took an obvious electron accumulation. It was identified that the hybridization between the two components induces a decrease of band gap and then an increase of optical absorption of $BiPO_4$(100) in visible-light region. Combining the decrease of the band gap of $BiPO_4$ in heterojunction, the potential of the conduction band minimum of $BiPO_4$(100) in heterojunction increased to -1.84 eV, which enhanced its reduction capacity. These results demonstrated that the heterojunction of $BiPO_4$(100)/graphene exhibited higher quantum efficiency under visible-light irradiation. A deep understanding of the microcosmic mechanisms of interface interaction and charge transfer in this system can be helpful for fabricating $BiPO_4$-based heterojunction photocatalysts. Moreover, our work may provide insights for understanding of the mechanism of $BiPO_4$(100)/graphene heterojunctions on photocatalytic activity, which also help in designing other new heterojunction combinations.

Keywords: $BiPO_4$(100)/graphene, heterojunction, first-principles, interface, photocatalytic

1. INTRODUCTION

$BiPO_4$ is one of the new promising photocatalytic materials for O_2 evolution from water-splitting, and organics degradation under visible-light irradiation (Pan 2015; Pan 2010). It is well known that $BiPO_4$ with three polymorphs: monoclinic $BiPO_4$ (SG: P21/n, nMBIP), monoclinic $BiPO_4$ (SG: P21/m, mMBIP) and hexagonal $BiPO_4$ (SG: P3121, HBIP) (Pan 2010; Wang 2017). Among them, nMBIP with a band gap of 3.8 eV and a valence band (VB) edge at approximately 3.4 V vs. NHE is the most common phase under ambient conditions and exhibits the highest photocatalytic activity in three crystal phases under UV irradiation (Pan 2015; Wang 2017). Various successful modifications have been made to improve the photocatalytic activity of $BiPO_4$, such as controlling morphologies (Pan 2010; Wang 2017), doping (Liu 2014; Di 2016), and coupling with metal oxide semiconductors or carbon materials (Wu 2013; Lin 2015; Lv 2018; Zhu 2017). Among those strategies, construction of $BiPO_4$-based heterojunctions by surface hybridization with π-conjugated materials has been shown in enhancing its photocatalytic performance. Examples include graphene/$BiPO_4$ (Lu 2012; Wang 2014), graphene oxide/$BiPO_4$ (Lv 2015; Zhang 2014; Pan 2014), polyaniline/$BiPO_4$ (Yu 2018), CuTCPP/$BiPO_4$ (Zhang 2017), and so on.

It is well known that graphene is an electronic collector and transporter, which can be used to improve the performance of various energy conversion and storage devices or as a carrier of a catalyst. Graphene has high carrier fluidity, which makes it a dopant regulating the electronic structure of $BiPO_4$ to adjust the energy level of $BiPO_4$ and improve its carrier fluidity. Heterojunction photocatalysis on $BiPO_4$ is frequently reported, for example, the successful synthesis of g-C_3N_4/$BiPO_4$ heterojunction have been proved to have great potential in promoting the performance of photocatalyst (Xia 2017). However, there are no theoretical reports on $BiPO_4$(100)/graphene heterojunction photocatalysts. In our previous calculations, the lattice of these two materials can match well. Therefore, the contact of $BiPO_4$(100) slab and graphene sheet will form a stable heterojunction. This structure is expected to promote electron hole pair separation, increase the visible absorption rate and form a suitable redox potential.

This paper mainly deals with the mechanism of photocatalytic activity of $BiPO_4$(100)/graphene heterojunction. The structural stability, electronic properties of $BiPO_4$(100)/graphene heterojunction, and their applications in photocatalysis were studied. The electronic properties of $BiPO_4$(100)/graphene heterojunction mainly include band gap, charge transfer and interfacial action, especially the change of the conduction band (CB) and valence band (VB) potential before and after the contact of $BiPO_4$(100) and graphene by using density functional theory (DFT). The interaction between them adjusted the CB and VB edge position of $BiPO_4$(100). At the same time, the space charge region formed by $BiPO_4$(100) and graphene promotes the effective separation of electron hole pairs. The $BiPO_4$(100)/graphene heterojunction exhibits high photocatalytic activity under visible light irradiation.

2. CALCULATION METHODS

All calculations were accomplished using the ultrasoft pseudopotentials (USP) with the exchange and correlation in the Perdew-Burke-Ernzerhof (PBE) (Perdew 1996) formalisms of DFT as implemented in the CASTEP code (Ceperley 1980). In USP calculations, to describe correctly van der Waals (vdW) interactions, a hybrid semiempirical solution from Tkatchenko and Scheffler (TS) scheme was given to introduce damped atom pairwise dispersion corrections of the form C6R-6 in the DFT formalism (Tkatchenko 2009). The dispersion-corrected total energy E_{total} is represented as:

$$E_{\text{total}} = E_{\text{KS-DFT}} + E_{\text{vdW}} \tag{1}$$

where $E_{\text{KS-DFT}}$ is the conventional Kohn–Sham DFT energy and E_{vdW} is the dispersion correction. The semiempirical approach provides the best compromise between the cost of first-principles evaluation of the dispersion terms and the need to improve non-bonding interactions in the standard DFT description. The valence atomic configurations were C: $2s^2 2p^2$, O: $2s^2 2p^4$, P: $3s^2 3p^3$, Bi: $6s^2 6p^3$, respectively. A cutoff energy of 400 eV and a Monkhorst–Pack k-mesh of 6 × 3 × 3 are used. All calculations with the denser meshes ensure that the results are fully converged. Geometry optimisations were done before the calculation of properties, and the self-consistent convergence accuracy was set at 1×10^{-5} eV per atom. The convergence criterion for the maximal force on atoms is 0.05 eV/Å^{-1}. The maximum displacement is 2×10^{-3} Å, and the stress is less than 0.02 GPa.

3. CALCULATION MODELS

A geometric model of $BiPO_4$(100)/graphene heterojunction was established by using supercell method. The model contained $BiPO_4$(100) and graphene in parallel. In this paper, several crystal faces of $BiPO_4$ were studied in advance. The results are shown in Table 1. As can be seen from the Table 1, the surface energy and total energy of $BiPO_4$(100) surface are the lowest, and the mismatch of the angle between α, β and γ is less than 2%. Therefore, $BiPO_4$(100) surface was selected as the research object. The 1 x 2 $BiPO_4$(100) (a=7.03 b=12.82) is used to construct the heterojunction with the 3 x 3√3 graphene (a=7.38 Å, b=12.82 Å) layer. The result of geometric optimisation structure is shown in Figure 1. In order to obtain the most stable heterojunction, we move the graphene sheet along the X and Y direction (about half a graphene ring). We found that the energy difference is only 0.01eV

before and after movement. This indicated that the stacking mode has little effect. And then, the lattice mismatch rate was 5%, 0.2% in X and Y directions, respectively, which indicated that the model was reasonable (⩽5%). After the geometric optimisation, the minimum interlayer spacing between $BiPO_4$(100) and graphene lamellae was calculated to be 3.3 Å, which is consistent with the results of other graphene-based semiconductor composites. A vacuum layer of 15 Å is used to isolate the slab as the boundary condition, which according to other previous work, is good enough to make interactions between neighbouring slabs negligible.

Table 1: Surface energy and total energy of four main crystal faces of $BiPO_4$

Surface	Lattice parameters			Surface energy /eV	Total energy /eV
	α	β	γ		
$BiPO_4$(001)	90°	92°	90°	1.094	-8322.3
$BiPO_4$(100)	89°	90°	92°	0.286	-8327.7
$BiPO_4$(010)	87°	98°	102°	0.437	-8326.9
$BiPO_4$(011)	88°	91°	79°	1.214	-8326.7
Graphene	90°	90°	89.7°	—	—

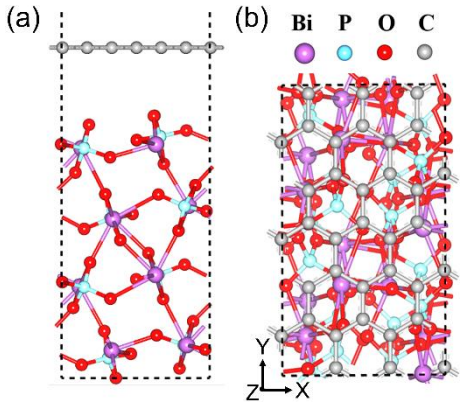

Figure 1: (a) The side and (b) top views of the $BiPO_4$(100)/graphene heterojunction.

4. DISCUSSION

To investigate the thermodynamic stability of the $BiPO_4$(100)/graphene heterojunction, the interface cohesive energy was taken as follow equation:

$$E_{coh} = [E(\text{hetero}) - E(\text{graphene}) - E(BiPO_4(100))]/A \quad (2)$$

where E(hetero) , E(graphene) and $E(BiPO_4(100))$ represent the total energies of the relaxed $BiPO_4$(100)/graphene heterojunction, isolated graphene and isolated $BiPO_4$(100) sheet, respectively. Additionally, A represents the surface area of slab model. Obviously, the chemical bonds of $BiPO_4$(100) or graphene in the plane are very strong, and the interlayer force is relatively weak. It is because of this weak interlayer force that it is prone to chemical abscission in the process of photocatalytic reaction, resulting in a larger surface area. According to formula (2), the cohesive energy of $BiPO_4$(100)/graphene heterojunction was calculated. It is easy to know that negative value represents a stable interaction between the two layers. It was calculated that the formation energy of $BiPO_4$(100)/graphene heterojunction was -3.75 eV, and the cohesive energy of the interface is 2.04 eV/nm^2, which was in accordance with the standard vdW cohesive energy interval 1.3-2.1 eV/nm^2 in the previous theoretical calculation (Björkman 2012). Therefore, the interlayer of $BiPO_4$(100) and graphene exhibited a typical physical adsorption, that was, $BiPO_4$(100)/graphene heterojunction was typical vdW heterojunction, which is similar to the results of Hu et al (2018).

In order to investigate the photocatalytic activity of $BiPO_4$(100)/graphene heterojunction, the band structures of $BiPO_4$(100), graphene and $BiPO_4$(100)/graphene heterojunction were calculated, respectively, as shown in Figure 2. $BiPO_4$(100) showed an indirect band gap of 3.40 eV, which was slightly lower than the theoretical value of $BiPO_4$ in the bulk phase of 3.80 eV (Lu 2012). The CB bottom and VB top of $BiPO_4$(100)/graphene heterojunction formed a small direct band gap of 0.11 eV. The heterojunction was known as a p type system by Figure 2(c), and the hybrids of $BiPO_4$(100) and graphene could open the band gap of graphene.

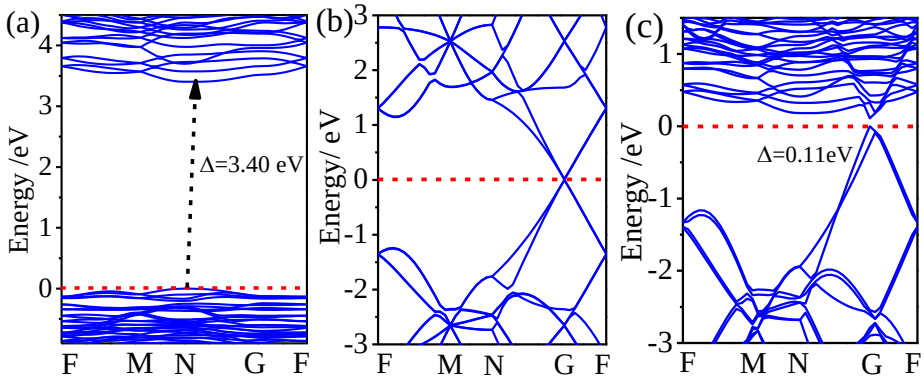

Figure 2: Calculated band structures of (a) $BiPO_4$(100) slab, (b) graphene, and (c) $BiPO_4$(100)/graphene heterojunction within GGA-PBE formalism. Fermi level is set to zero denoted as a red dashed line.

In order to better understand the micromechanics of the interlayer interaction in $BiPO_4$(100)/graphene heterojunction, the total density of states (TDOS) and partial density of states (PDOS) of the heterojunction were analyzed, as shown in Figure 3. For $BiPO_4$, the VB was composed of O 2p orbitals, whereas the CB was composed of Bi 6p orbitals. For the $BiPO_4$(100)/graphene heterojunction, the new VB maximum (CBM) and CB minimum (VBM) are mainly contributed by the p_z orbital of the C atoms. Thus, the hybridization between the $BiPO_4$(100) surface and graphene resulted in a serious decrease of the band gap of $BiPO_4$ in the interface. And the charge transfer was supposed to take place from O 2p hybrid orbitals to Bi 6p orbitals upon photoexcitation. As consequence, the introduced states neighbouring the Fermi level greatly enhanced the carrier mobility, which was beneficial to the effective separation of the photoinduced electron-hole pairs.

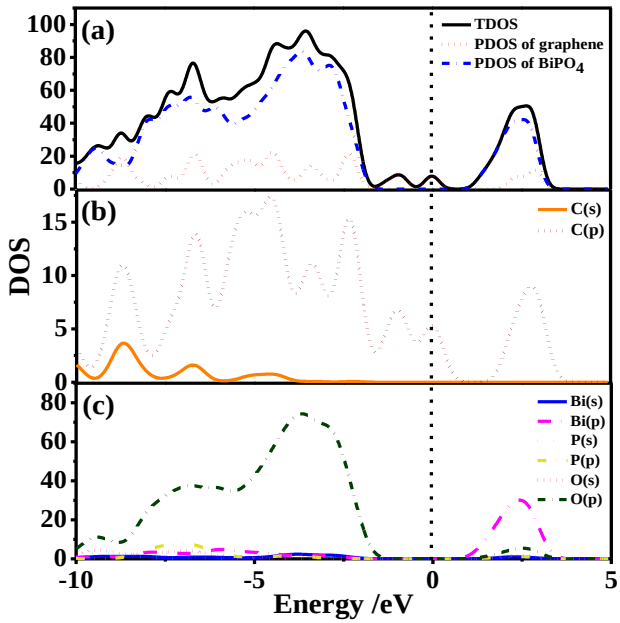

Figure 3: (a) Calculated TDOS of $BiPO_4$(100)/graphene heterojunction and PDOS of graphene and $BiPO_4$(100). (b) The calculated PDOS of C atoms in graphene. (c) The calculated PDOS of Bi, P and O atoms in $BiPO_4$(100). The vertical line is Fermi level.

The formation of heterojunction changed the electrical properties of $BiPO_4$(100) and graphene, which was mainly caused by interlayer binding, leading to the redistribution of charges in the interface. Figure 4 showed the charge density difference of the $BiPO_4$(100)/graphene heterojunction, in which the yellow and blue region indicated an electron decrease (positive charge aggregation) and an electron increase (negative charge aggregation). It can be seen that the formation of the heterojunction interface caused the partial charge from graphene transfer to the O atoms of $BiPO_4$(100), so that more negative charge was gathered at the O atom in BiPO4(100), and holes was gathered on the C atoms above the O atoms, and the internal electric field was formed in some vertical interfaces.

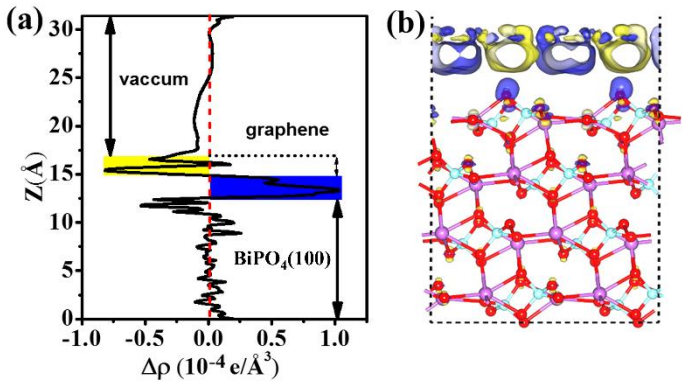

Figure 4: Planar-averaged electron density difference Δρ(z) for $BiPO_4$(100)/graphene heterojunction. Above and below the zero areas indicate electron depletion and accumulation, respectively.

The energy level matching between the two components is essential for understanding charge transfer and separation in the heterojunction interface. Therefore, in order to clarify these changes, we estimated the band edge energies of the CB and VB of $BiPO_4$ and graphene from the absolute electronegativity and band gap of the atom as follows:

$$E_{VB} = \chi + 0.5E_g + E_e \quad (3)$$

$$E_{CB} = E_{VB} - E_g \quad (4)$$

where χ is the absolute electronegativity of the semiconductor. E_e is the energy of free electron on the hydrogen scale (4.5 eV). E_{CB}, E_{VB} and E_g are the band edge energies of the CB and VB and the band gap of semiconductor, respectively. The CB and VB position of $BiPO_4$(100) is 0.09 and 3.89 eV respectively, as shown in Figure 5 (d). When the two contacts formed a heterojunction, the position of CB and VB changed with the level of Fermi level. The calculated work function of the four layers $BiPO_4$(100)/graphene heterojunction was 4.82 eV which between the work functions of $BiPO_4$(100) and graphene, which was caused by the charge transfer of the interface.

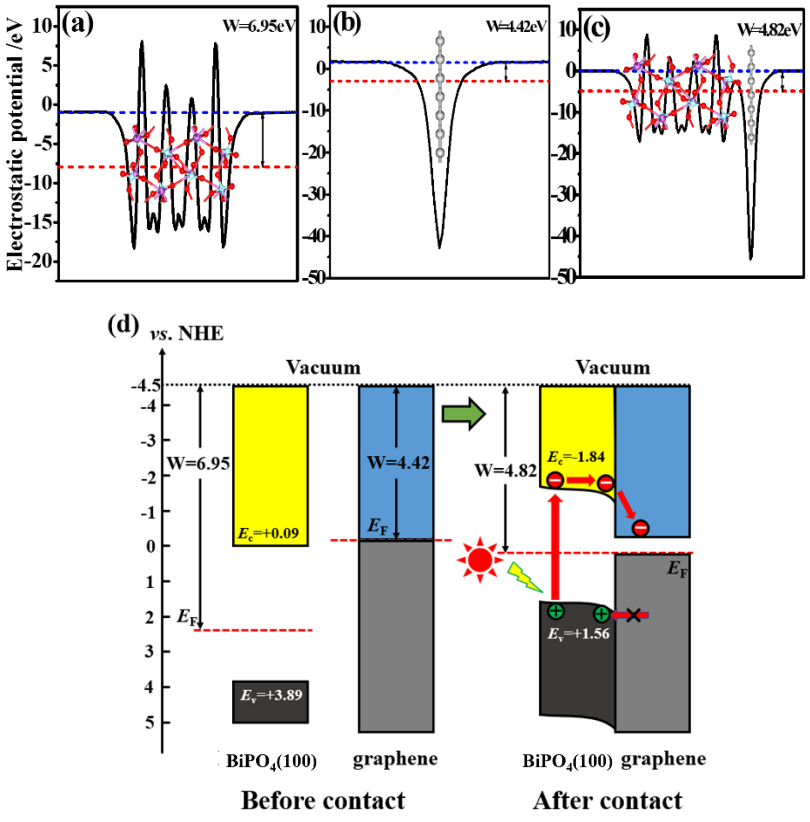

Figure 5: Calculated work function of (a) $BiPO_4$(100), (b) graphene and (c) $BiPO_4$(100)/graphene heterojunction. The blue and red dashed lines denote the vacuum energy level and Fermi level, respectively. (d) Diagram of the band edge positions before and after contact of $BiPO_4$(100) and graphene.

The work function of the material is an important parameter, which determines the direction of electrons flowing at the heterojunction interface. Therefore, it is usually used as an intrinsic reference with alignment. Here, the work function was calculated and the corresponding energy level lineup diagrams for $BiPO_4$ and graphene before and after equilibrium are plotted in Figure 5. The work function is defined as follows:

$$\Phi = E_{vac} + E_F \quad (5)$$

where E_{vac} is the energy of a stationary electron in the vacuum near the surface. E_F is the Fermi level. The calculated electrostatic potentials for graphene, the $BiPO_4$(100) sheet, and the $BiPO_4$(100)/graphene interface are demonstrated in Figure 5a–c. The calculated work function of $BiPO_4$(100) (6.95 eV) was larger than that of graphene (4.42 eV). The electrons in graphene with a low work function flow into $BiPO_4$(100) with a high work function, after the formation of $BiPO_4$(100)/graphene heterojunction. It can be inferred that the $BiPO_4$(100) layer accumulated negative charges. In the meantime, the graphene layer gathered positive charges. Under visible light irradiation, electrons transferred from graphene to $BiPO_4$.

According to the thermodynamic equilibrium condition, the Fermi level of the two components will be balanced under the action of electric field force and diffusion force. The Fermi level of the $BiPO_4$ shifted upward 2.13 eV, and the Fermi level of the graphene shifted downward 0.40 eV. The band gap of $BiPO_4$(100) was reduced by 0.40 eV because of the hybridization in the heterojunction, causing the CB to move down about 0.20 eV. The CB of $BiPO_4$(100) moves upward about 1.93 eV, so the CBM was -1.84 eV. It can be further deduced that the VBM was about 1.56 eV. It can be seen that the introduction of graphene makes the CBM edge position of $BiPO_4$(100) change from positive to negative, resulting in strong reduction ability of photogenerated electrons. When $BiPO_4$(100) contacted with graphene, its CB potential changed from 0.09 eV to -1.84 eV, which was more negative than H^+/H_2 (0 eV) and $O_2/O_2^{\cdot -}$ (-0.28 eV), thereby reducing H^+ to H_2. While partial photoelectron and oxygen molecular reactions can produce superoxide radical anions ($O_2^{\cdot -}$) with strong oxidation ability to degrade some organic pollutants.

5. CONCLUSION

The interfacial bonding and electrical properties of $BiPO_4$(100)/graphene heterojunction were investigated by DFT in detail. The calculated interfacial cohesive energy shows that $BiPO_4$(100) and graphene were in contact and formed a stable vdW heterojunction. Through the calculation of the band structure, it was found that the $BiPO_4$(100)/graphene heterojunction with a smaller band gap. The 3D density of difference diagram further indicated that the built-in electric field of graphene toward $BiPO_4$(100) was formed at the interface. By analyzing the CB and VB positions based on work function between the two components, it can be found after equilibration of the $BiPO_4$(100)/graphene interface that the electrons receiving photon energy in the $BiPO_4$(100) layer continuously flow into the C p orbital of graphene under visible-light irradiation, in which the electrons cannot migrate back to $BiPO_4$(100) and thus were trapped in graphene, facilitating the separation of photogenerated carriers. The CB edge position of $BiPO_4$(100) changed to −1.84 V, which was more negative than that of H^+/H_2 (0 V), thereby reducing H^+ to H_2. In addition, the CB edge position was also more negative than that of $O_2/O_2^{\cdot -}$ (−0.28 V), which can produce superoxide radical anions ($O_2^{\cdot -}$) to decompose organic pollutants. In short, the incorporation of graphene into $BiPO_4$(100) facilitates the separation of photogenerated e^-/h^+ pairs and the enhancement of visible-light absorption. The present investigation is useful in the wider development of new $BiPO_4$-based heterojunction photocatalysts.

6. ACKNOWLEDGEMENTS

This work was supported by the National Natural Science Foundation of China (51472081), Cooperative Foundation of China-UK Research and Innovation Bridges (2016YFE0124300), the Foundation for High-Level Talents (GCRC13014) and Leading Plan of Green Industry (YXQN2016005), the Development Funds of Hubei Collaborative Innovation Center (HBSKFMS2015004, HBSDB201704, HBSDB201514). X. C. appreciates the support from the U.S. National Science Foundation (DMR-1609061), and the College of Arts and Sciences, University of Missouri Kansas City.

7. REFERENCES

Pan C, Zhu Y, 2015. A review of $BiPO_4$, a highly efficient oxyacid-type photocatalyst, used for environmental applications. *Catalysis Science & Technology*, 5(6), 3071-3083.

Pan C, Zhu Y, 2010. New type of $BiPO_4$ oxy-acid salt photocatalyst with high photocatalytic activity on degradation of dye. *Environmental Science & Technology*, 44(14), 5570-5574.

Wang J, Li J, Li H, Duan S, Meng S, Fu X, Chen S, 2017. Crystal phase-controlled synthesis of $BiPO_4$ and the effect of phase structure on the photocatalytic degradation of gaseous benzene. *Chemical Engineering Journal*, 2017, 330, 433-441.

Liu Y, Lv Y, Zhu Y, Liu D, Zong R, Zhu Y, 2014. Fluorine mediated photocatalytic activity of $BiPO_4$. *Applied Catalysis B Environmental*, 147(14), 851-857.

Di J, Chen J, Ji M, Zhang Q, Xu L, Xia J, Li H, 2016. Reactable Ionic Liquid Induced Homogeneous Carbon Superdoping of $BiPO_4$ for Superior Photocatalytic Removal of 4-Chlorophenol. *Chemical Engineering Journal*, 313, 1477–1485.

Wu S, Zheng H, Lian Y, Wu Y, 2013. Preparation, characterization and enhanced visible-light photocatalytic activities of $BiPO_4$/$BiVO_4$ composites. *Materials Research Bulletin*, 48(8), 2901-2907.

Lin X, Liu D, Guo X, Sun N, Zhao S, Chang L, Zhai H, Wang Q, 2015. Fabrication and efficient visible light-induced photocatalytic activity of Bi_2MoO_6/$BiPO_4$ composite. *Journal of Physics & Chemistry of Solids*, 76, 170-177.

Lv H, Wu X, Liu Y, Zhang P, Cao Y, Ren H, 2018. Photoreactivity and mechanism of $BiPO_4$/WO_3 heterojunction photocatalysts under simulant sunlight irradiation. *Ceramics International*, 44(6), 6786–6790.

Zhu Y, Wang Y, Ling Q, Zhu Y, 2017. Enhancement of full-spectrum photocatalytic activity over $BiPO_4$/Bi_2WO_6 composites. *Applied Catalysis B Environmental*, 100, 222-229.

Lu B, Ma X, Pan C, Zhu Y, 2012. Photocatalytic and photoelectrochemical properties of in situ carbon hybridized $BiPO_4$ films. *Applied Catalysis A General*, 435-436(17), 93-98.

Wang C, Zhang G, Zhang C, Wu M, Yan M, Fan W, Shi W, 2014. A facile one-step solvothermal synthesis of bismuth phosphate–graphene nanocomposites with enhanced photocatalytic activity. *J Colloid Interface Sci*, 435(435), 156-163.

Lv H, Shen X, Ji Z, Qiu D, Zhu G, Bi Y, 2015. Synthesis of graphene oxide-$BiPO_4$ composites with enhanced photocatalytic properties. *Rsc Advances*, 5(72), 58777-58783.

Zhang Y, Shen B, Huang H, He Y, Fei B, Lv F, 2014. $BiPO_4$/reduced graphene oxide composites photocatalyst with high photocatalytic activity. *Applied Surface Science*, 319(1), 272-277.

Pan B, Wang Y, Su W, Wang X, 2014. Nanocomposite of $BiPO_4$ and reduced graphene oxide as an efficient photocatalyst for hydrogen evolution. *International Journal of Hydrogen Energy*, 39(25), 13527-13533.

Yu W, Cheng Y, Zou T, Liu Y, Wu K, Peng N, 2018. Preparation of $BiPO_4$-Polyaniline Hybrid and its Enhanced Photocatalytic Performance. *Nano Brief Reports & Reviews*, 13(1), 1850009–1850018.

Zhang Z, Liu H, Xu J, Zeng H, 2017. CuTCPP/$BiPO_4$ composite with enhanced visible light absorption and charge separation. *Journal of Photochemistry & Photobiology A Chemistry*, 336, 25-31.

Xia J, Zhao J, Chen J, Di J, Ji M, Xu L, Chen Z, Li H, 2017. Facile fabrication of g-C_3N_4/$BiPO_4$ hybrid materials via a reactable ionic liquid for the photocatalytic degradation of antibiotic ciprofloxacin. *Journal of Photochemistry & Photobiology A Chemistry*, 339, 59-66.

Perdew J P, Burke K, Ernzerhof M, 1996. Generalized Gradient Approximation Made Simple. *Physical Review Letters*, 77(18), 3865-3868.

Ceperley D. M, Alder B. J, 1980. Ground State of the Electron Gas by a Stochastic Method. *Physical Review Letters*, 45(7), 566--569.

Tkatchenko A, Scheffler M, 2009. Accurate molecular van der Waals interactions from ground-state electron density and free-atom reference data. *Physical Review Letters*, 102(7), 073005-073008.

Björkman T, Gulans, A, Krasheninnikov A. V, Nieminen R.M, 2012. Van der Waals Bonding in Layered Compounds from Advanced Density-Functional First-Principles Calculations. *Physical Review Letters*, 108(23), 235502.

Hu J, Ji G, Ma X, He H, Huang C, 2018. Probing interfacial electronic properties of graphene/$CH_3NH_3PbI_3$ heterojunctions: A theoretical study. *Applied Surface Science*, 440(15), 35-41.

Ma X, Wei Y, Wei Z, He H, Huang C, Zhu Y, 2017. Probing π-π stacking modulation of g-C_3N_4/graphene heterojunctions and corresponding role of graphene on photocatalytic activity. *Journal of Colloid & Interface Science*, 508, 274-281.

253: Recent progress of the application of plasma technology in sustainable energy

Jixiong XIAO[1], Jun CHEN[2], Anfei XU[3], Huafeng CAI[4], Yunhao JIANG[5]

[1]Hubei Key Laboratory for High-efficiency Utilization of Solar Energy and Operation Control of Energy Storage System, Hubei University of technology, Wuhan, 430068, P. R. China, xiaojixiong0738@163.com
[2]Hubei Key Laboratory for High-efficiency Utilization of Solar Energy and Operation Control of Energy Storage System, Hubei University of technology, Wuhan, 430068, P. R. China, chenjunhbut@126.com
[3]Hubei Key Laboratory for High-efficiency Utilization of Solar Energy and Operation Control of Energy Storage System, Hubei University of technology, Wuhan, 430068, P. R. China, 20602728@qq.com
[4]Hubei Key Laboratory for High-efficiency Utilization of Solar Energy and Operation Control of Energy Storage System, Hubei University of technology, Wuhan, 430068, P. R. China, 37715457@qq.com
[5]Hubei Key Laboratory for High-efficiency Utilization of Solar Energy and Operation Control of Energy Storage System, Hubei University of technology, Wuhan, 430068, P. R. China, 407307716@qq.com

With the rapid development of modern human society and economy, how to achieve sustainable energy development is one of the key issues that human beings are facing. Fortunately, in the last two decades, the flourishing development of plasma technology and its applications in the field of energy technologies have provided more and more choices for the sustainable energy development. At present, the application of plasma technology in the field of energy mainly includes the following seven aspects: (1) Controlled nuclear fusion, which including magnetic confinement fusion and inertial confinement fusion; (2) solar cells and new photovoltaic materials; (3) Plasma-catalytic conversion of CO_2 into value-added chemicals and fuels; (4) new types of energy storage materials and super capacitors; (5) Magnetic fluid power generation; (6) Plasma gasification for power & heat generation and assisted combustion. This paper is intended to provide a comprehensive overview of the recent progress of such application of plasma technology in the field of sustainable energy technologies. The recent researches and technological advances in those topics are presented and the development trends are analyzed. Then, the future challenges of the application of plasma technology in the field of sustainable energy are also discussed.

Keywords: sustainable energy development, plasma technology, energy technology

1. INTRODUCTION

In September of 2015, the UN proposed 17goals of the world conservation strategy for sustainable development, which has adopted by 70 countries (Chernyak et al., 2017: page 126). Among these 17 goals, 9 can be achieved with the help of plasma technology: "zero hunger", "good health and well-being", "clean water and sanitation", "affordable and clean energy", "decent work and economic growth", "sustainable cities and communities", "responsible consumption and production", "life below water", "life on land". Among these goals, how to reduce the use of fossil fuels and pollution emission and how to replace the fossil fuels with renewable sources of energy are two of the most important for sustainable development.

The energy production and utilization of the human society has experienced the evolution from firewood era to coal era, then to the oil and gas era. The huge leap in each energy age has greatly spurred the great-leap-forward development of human economy and society. Therefore, the sustainable development of energy has a very important significance for the sustained and rapid development of human economy and society (Tester et al., 2012: page 2-44). In the past few decades, Humanity has made many important advances in the energy domain of sustainable energy technologies, such as controlled nuclear fusion technology (Miyamoto et al., 2016: page 5-9), solar energy utilization technology(Kabir et al., 2018: page 894-900), catalytic carbon dioxide conversion to fuel (Kim et al., 2016: page 45-72), new types of energy storage materials (Tyczkowski et al., 2011: page 341-344) and supercapacitor technologies (Vangari et al., 2013: page 72-78), etc. After scrutinizing all of all these technological advances, we will find that, plasma technology plays a very important role in almost all these areas, and it can be regarded as one of the important engines for the development of sustainable energy technologies.

Plasma is viewed as the fourth state of a matter apart from solid, liquid, and gas, and is a partially or completely ionized gas, which is consisting of a large number of free electrons, positive ions, neutral atoms and molecules (Harry et al., page 1-4). Generally, it is approximately electrically neutral on a macroscopic scale and contains almost equal positive and negative charges everywhere.

The macroscopic temperature of the plasma depends on the temperature of the heavy particles. According to the plasma temperature, plasma can classified as high temperature plasma and low temperature plasma (Richard et al., 2014:1-3). For high temperature plasmas, the electron temperature (T_e) and ion temperature (T_i) are identical and the temperature generally range from 10^2~10^6 eV with full ionization. It only found in some of the most extreme environments in the universe, such as the fixed star. However, in order to achieve controlled nuclear fusion, it has become obtainable in the laboratory by using magnetic confinement technology and high energy laser technology in the last few decades (Miyamoto et al., 2016: page 5-9). Nuclear fusion reactions fuse two lighter atomic nuclei to form a heavier nucleus and releasing energy. The fusion reaction that is most easily achieved in nature is D-T fusion reaction, and it has lasted 5 billion years in the sun. Controlled nuclear fusion has many advantages. First, there are abundant sources of raw materials. It is estimated that there are 45 trillion tons of deuterium in seawater on Earth, so it can be said that deuterium is an inexhaustible resource of energy material. Although there is no tritium in nature, it can be produced in large quantities by bombarding lithium fluoride, lithium carbonate, or a lithium-magnesium alloy by neutrons generated from a reactor, and seawater also contains a large amount of lithium. Therefore, once the practicalization of controlled nuclear fusion is realized, the energy problem of human sustainable development will also be solved. Second, fusion energy can be clean and free from pollution. Nuclear fusion differs from nuclear fission in that the substances produced after the reaction are inert gases, so it will not produce high-level nuclear wastes like their fission counterparts. On the other hand, there is no combustion during the process of the nuclear fusion reactor, so it will not emit CO_2 and other gases that may cause the green-house effects and pollute the atmosphere. Third, it is very safe and reliable. The amounts of fuel used for fusion are small compared to fission reactors. In addition, as long as any one of the fusion reaction conditions is removed, the reaction will be completely stopped, and there will be no nuclear fuel decay heat produced, which is the main reason for many fission power reactor accidents.

Therefore, fusion energy seems to be an ideal or a very attractive solution to solve the energy problem of the human's sustainable development in the future. However the problem is that extracting net energy from fusion is very difficult to achieve in a controlled manner. This difficulty arises from the need to confine the reactants for a sufficient time with a very high temperature (~10keV) for them to burn, which should be satisfied the so-called Lawson criterion (Jeffrey F,2007: page 82-83). The main purpose of high-temperature plasma technology is how to heat the plasma to extremely high temperatures and maintain a confinement time long enough to overcome the Lawson criterion, achieve fusion ignition conditions.

Over the past 50 years, two predominant approaches have emerged: magnetic confinement and inertial confinement by laser. At present, although most scholars believe that it will still take decades to realize the commercialization of fusion energy, human beings have made many important breakthroughs in these two different technological fields. For example, in the field of magnetic confinement fusion, a stable 101.2s steady-state long-pulse high confinement plasma operation (with ne=$3.0\times10^{19}/m^3$, Te=4.0KeV) was achieved firstly in the world by using pure RF wave heating in EAST (Liu et al., 2017: page 95). In the laser inertial confinement fusion (ICF) field, Hurricane reported the achievement of fusion fuel gains exceeding unity on the US Nation Ignition Facility Using a 'high-foot' implosion method(Hurricane et al., 2014: page 1). These important technological advances mean that Human beings are getting closer and closer to breaking the plasma energy breakeven point (or plasma power

amplification factor) Q=1(it describes the moment when plasmas in a fusion device release at least as much energy as is required to heat them).

Different from the generation of high temperature plasma, the production of low temperature plasma is much easier. The main methods are glow discharge, corona discharge, dielectric barrier discharge, radio-frequency discharge, sliding arc discharge, jet discharge, atmospheric glow discharge (Lu et al., 2014: page 1-36). For low temperature plasma, according to the thermal equilibrium state of electrons and ions (neutral particles), it can also be classified as non-thermal equilibrium plasma and thermal equilibrium plasma. When the electron temperature is much larger than the ion temperature (T_e>> T_i), it is called as non-thermal equilibrium plasma or cold plasma, and its electron temperature T_e is generally greater than 10^4K, but the ion temperature T_i only about 300~500K. In cold plasma, on the one hand, the electrons have high enough energy to make gas / atomic excitation, dissociation or ionization, on the other hand the system is kept at a low temperature and near or slightly higher than ambient temperature. An important feature of non-equilibrium cold plasma is its ability to generate a unique 'one pot' cocktail of biologically active agents (Misra et al., 2017: page 75), which makes it have many advantages in the applications of material surface modification, vapor deposition and catalysis. Therefore, it is widely used in the field of solar cells and the preparation of the next generation of photovoltaic materials, Plasma-catalytic conversion of CO_2 into value-added chemicals and fuels, nanostructure fabrications of new energy materials to enhanced energy storage performance, Preparation of new energy materials and supercapacitors, and other new energy field. For thermal plasma, it has higher temperature and $T_e \approx T_i \approx 10000$K. In general, the thermal plasma in strict sense is difficult to achieve in practical applications or in the laboratory. But It is easier to form a plasma in which the various particle compositions are close to equilibrium and the temperature is approximately equal, i.e. a local thermal equilibrium plasma. The temperature of the local thermal equilibrium plasma is generally about 1×10^3~2×10^4K, and it can be produced at high atmospheric pressure. As the thermal plasma with the characteristics of high temperature, high enthalpy and high reactivity, it is very suitable for the synthesis of new energy nanomaterials, energy generation from waste treatment by plasma gasification, magnetohydrodynamic (MHD) power generation, auxiliary combustion technology for traditional chemical fuels, clean coal technologies and so on.

As mentioned above, plasma technology, especially the low temperature plasma technology has been applied in almost all the fields of sustainable energy technologies. The purpose of this review is to provide the recent progress of the application of plasma technology in the field of sustainable energy. The rest of this paper is organized as follows. In Section II, the applications of the high temperature plasma technology in controlled nuclear fusion is presented. The basic principle, typical scientific facilities and latest research progress and current major technical challenges are also given and discussed. In Section III, the applications of nonequilibrium plasma in photovoltaic cell, plasma-catalytic conversion of CO_2 into syngas and fuel, preparation of new energy mater and supercapacitor are described. In Section IV, the applications of thermal plasma in the fields of synthesizing new energy materials, waste disposal & power generation by plasma gasification, MHD power generation, and auxiliary combustion and clean utilization of conventional chemical fuels are discussed. In Section V, concluding remarks are made.

2. HIGH TEMPERATURE PLASMA TECHNOLOGY AND CONTROLLED NUCLEAR FUSION

Although the first release of man-made thermonuclear energy via H-bomb took plasma in 1952, but the problem of how to control this sudden release in a controlled way, for the purpose of generating electric power, is still with us today (Miyamoto et al., 2016: page 5-6). In order to achieve fusion thermonuclear fusion, the average kinetic energy or the temperature should be very enough. After reaching sufficient temperature, given by the Lawson criterion, the energy of accidental collisions within the plasma is high enough to overcome the coulomb barrier and the particles may fuse together. The key problem in achieving thermonuclear fusion is how to confine the hot plasma. However, due to the high temperature, the plasma cannot be in direct contact with the reactor, so it has to be located in a vacuum. Besides, high temperatures imply high pressures and the plasma tends to expand immediately and some force is necessary to act against it. One force capable of confining the fuel well enough to satisfy the Lawson criterion is gravity. The mass needed, however, is so great that gravitational confinement is only found in stars. That is why nuclear fusion can only be achieved about 15 million degrees Celsius in the core of the solar because its central pressure as high as 200 billion atmospheres. By comparison, if human beings want to achieve thermonuclear fusion, they need to heat the fuel up to 200 million degrees with a required value of electron density n_e multiplied by energy confinement time τ_E. As the temperature of the plasma has to be so high that there is no possibility of containing the hot plasma in any conventional vessel. Even the most refractory materials, such as graphite, ceramics, or tungsten, would evaporate. There are two options. One is to use a magnetic field to form a barrier between the hot fuel and the wall. The electrical charges on ions and electrons can prevent them from moving directly across a magnetic line of force so that the charged particles will be captured by the magnetic line of force and make spiral motions along the direction of the field. In this way a magnetic field can be used to guide the charged particles and prevent them from hitting the surrounding solid walls. This is the basic principle of magnetic confinement fusion (MCF). The second option is to compress the fusion fuel and heat it so quickly with high power laser irradiation that fusion takes place before the fuel can expand and touch the walls. This is called inertial confinement fusion (ICF).

2.1. Magnetic confinement fusion

Magnetic confinement if one of two major branches of fusion energy research. According to Lawson criterion, achieving fusion reaction require high temperature with sufficient density and energy confinement. At these temperatures, no material container could withstand the extreme heat of the plasma. Magnetic confinement fusion attempts to create these conditions by using the electrical conductivity of the plasma to contain it with magnetic. The basic concept can be thought of in a fluid picture as a balance between magnetic pressure and plasma pressure, or in terms of individual particles spiralling along magnetic field lines.

The earliest proposed magnetic field configuration is magnetic mirror. However, as the magnetic mirror is a open confinement, plasma would quickly escape sideways through the confinement fields, which called as end loss. This would occur in any machine with convex magnetic fields, which existed in the centre of the mirror area. Although several mirror machines were developed by Russia (GOL-3, GDT, AMBAL-M), Japan (GAMMA-10), Korea (HANBIT) and so on, keV level plasma temperature and an energy confinement time of ~0.05s are the highest parameters achieved by tandem mirror machines. Due to its simple and compact structure, flexible operation, low cost and low tritium consumption, it is very suitable as a neutron source for testing fusion materials. Therefore, research on such machines is currently mainly focus on how to improve its performance to meet the needs of fusion materials testing.

Despite repeated failures, the exploration of magnetic confinement has never stopped. Subsequently, a series of new magnetic configuration for magnetic confinement were proposed, such as tokamak, reversed--field pinch, stellarator, spheromak, field-reversed configuration, levitated dipole. In these magnetic confinement configurations, tokamak and stellarator are considered as the most promising options and both of them are closed confinement systems.

Since the tokamak was invented in the old Soviet Union by Andrei Sakharov and Igor Tamm, tens of experimental tokamak machine has been built, such as TFTR(USA), Alcator C-Mod (USA), DIII-D(USA), STOR-M (Canada), HL-2A (China), EAST (China), JT-60 (Japan), KSTAR (South Korea), JET (Europe), Compass (Europe), ASDEX Upgrade (Germany), T-15(Russia), TCV(Switzerland), MAST(UK) (Huang et al., 2018: page 4). Among them, the representatives of the large tokamaks in the world are DIII-D, JET, JT-60, EAST, KSTAR. Several scientific milestones have been achieved on tokamak machines. In 1978, the PLT demonstrated the ion temperature was raised to 7.6KeV by a neutral beam injection (Zhu,1990: page 117). In 1982, the high confinement mode (H mode) was first discovered on the ASDEX Upgrade (Li, 2016: page 89). In 1986, TFTR used a 16MW high-power neutral beam injection to obtain a 200-million-degree plasma and generated a 10 kW fusion power with Q ~0.27 (Li, 2016: page 89). In December 1997, JT-60 achieved a equivalent energy gain factor 1.25 with DT reaction by DD fusion experiments, which basically proved the scientific feasibility of magnetic confinement fusion (Li, 2016: page 89). In 1991, the JET demonstrated the first large-scale test of the D/T reaction could produce a maximum of about of 1.7 MW in a short pulse of about 2 s (corresponding to Q~0.15) and produced a maximum fusion power larger than 16MW. Six years later, in 1997, the JET tokamak machine produced a maximum fusion energy of 75 MJ (Q~0.65) and the equivalent steady-state Q becomes 0.94 after correcting for transient effects (Romanelli, 2015: page 8).

Until now, these are the highest fusion powers and Q values produced by a fusion reactor and the value of Q is very close to break the plasma energy breakeven point. Recently, China's EAST made an important advance by achieving a stable 101.2s steady-state high confine plasma, setting a new world record in long-pulse H-mode operation in 2017(Liu et al., 2017: page 95). All these achievements show that mankind is getting closer and closer to realizing the dream of controlled fusion. The representative of the next stage of magnetic confinement will be ITER (International Thermonuclear Experimental Reactor), which is the largest joint project in the world and is being jointly build by the US, EU, China, India, Japan, South Korea, and Russia (Hemsworth et al., 2009: page 1-2 and Lehnen et al., 2014: page 1-2). At present, the ITER project has begun to enter the assembly phase and the first plasma is expected to be produced in 2025. This machine has been designed specifically to (Lehnen et al., 2014: page 1-3): (1) produce a ten-fold return on energy (Q=10), or 500 MW of fusion power from 50 MW of input heating power. ITER will not capture the energy it produces as electricity, but—as first of all fusion experiments in history to produce net energy gain—it will prepare the way for the machine that can; (2) Demonstrate the integrated operation of technologies for a fusion power plant. ITER will bridge the gap between today's smaller-scale experimental fusion devices and the demonstration fusion power plants of the future. (3) Achieve a deuterium-tritium plasma in which the reaction is sustained through internal heating. Scientists are confident that the plasmas in ITER will not only produce much more fusion energy, but will remain stable for longer periods of time; (4) Test tritium breeding. The world supply of tritium (used with deuterium to fuel the fusion reaction) is not sufficient to cover the needs of future power plants. ITER will provide a unique opportunity to test mockup in-vessel tritium breeding blankets in a real fusion environment. (5) One of the primary goals of ITER operation is to demonstrate the control of the plasma and the fusion reactions with negligible consequences to the environment. After completing these goals, scientists will proceed to the design and construction of the demonstration reactor. In additional, taking into account the serious delay in the progress of the ITER project, China is now actively promoting the Chinese version of the ITER plan - CFETR (China Fusion Engineering Test Reactor) (Wan et al., 2017: page 1-3).

In addition to tokamak, the stellarator is also a magnetic confinement fusion device of great concern. In 1958, Spitzer proposed the concept of stellarators. Unlike tokamaks, the stellarator's toroidal and poloidal magnetic fields are all provided by external coils. Therefore, in the absence of plasma current, the stellarator remains effectively

confine the charged particles. The stellarator avoids the problem of the disruption caused by the plasma current and therefore it can more easily achieve steady-state operation. Currently, the representative device of the stellarator is Germany's Wendelstein 7-X (W7 -X) (Wurden et al., 2017: page 1-2). The total cost of the facility was 370 million Euros. The first discharge produced a helium plasma on December 10, 2015, and the first discharge on February 3, 2016 produced a high temperature of 80 million kWh, continuing 1 /4 s of hydrogen plasma. The future development of W7-X deserves attention.

2.2. Inertial confinement fusion

Since Nuckools first proposed the idea of compressing a tiny target with high-power lasers to bring thermonuclear fuel to ignition conditions, Inertial confinement fusion (ICF) by laser has become a basic approaches to achieve the desired controlled thermonuclear fusion (Zohuri, 2016: page 93). Compared with magnetic confinement attempting to prevent particles in plasma of moderate particle density (10^{14}–10^{15} cm^{-3}) from leaving the reaction volume by thermal velocity for long period (e.g., ≥1 s), inertial confinement follows the opposite path to produce extremely dense plasma with a very short confinement time by using high-energy laser or beam of particles. To achieve conditions under which inertial confinement is sufficient for efficient thermonuclear burn, a capsule (generally a spherical shell) containing thermonuclear fuel is compressed in an implosion process to conditions of high density and temperature.

ICF can be implemented with different driving sources. Currently, it mainly includes laser driving and magnetic field driving (Z pinch) and heavy ion drivers, but laser driven inertial confinement fusion is the mainstream solution. There are two driving methods for laser-driven ICF: direct drive (Craxton et al., 2015: page 1-2) and indirect drive (John, 1995: page 1-2). In direct drive, the laser beams aimed directly at the target containing D-T thermonuclear fuel (ICF capsule) to achieve fusion ignition and trigger a large number of fusion reactions and the laser energy is transferred to electrons by means of inverse bremsstrahlung or a variety of plasma collective processes. In indirect drive, the driver energy (from laser beams or ion beams) is first absorbed by a high-Z metal enclosure (hohlraum). The material heated by the laser beams to emit strong x rays, which drive the capsule implosion. Direct drive requires enough laser beams to irradiate the surface of the target to achieve uniform irradiation. The indirect drive uses a hohlraum to convert the laser into a soft X-ray firstly. The hohlraum is a metal cavity with the cavity wall is made of high Z materials (usually is Au or U, etc.). At present, it is mostly cylindrical (spherical or elliptical can also be used). At both ends of the cavity there is a perforation (for other shapes, the position may be different). The target is placed in the center of the hohlraum, and the laser beams enter it through the perforation and irradiate to the inner wall. The absorption of the laser energy by the inner wall material causes the temperature of it to rise sharply to be melted into a plasma to emit strong X--rays, then the X--rays act on the target pill by transportation.

In a sense, indirect drive can be regarded as a direct drive with a very wide band of very short wavelength. The energy efficiency of the direct drive is high, but the uniformity of the beam intensity distribution is very demanding, and the hydrodynamic instability caused by the surface disturbance of the target pellet is more serious. The advantage of indirect drive is that the X-ray transport is very fast, so it can be easily irradiate the target uniformly, and the X-ray penetration is deep, the ablation rate is fast so that the pressure to drive the implosion is high, and at the same time it has a better inhibitory effect on hydrodynamic instability. Of course, as the laser energy of the indirect drive needs to be converted into X-ray energy in the hohlraum first, the energy loss during the conversion process, the absorption ability of the cavity wall to the laser energy, and the energy loss in the laser inject into the perforation will result in low energy efficiency.

Up to now, the world's major laser confinement facilities are NIF(USA), OMEGA(USA),SG-II(China), SG-III(China), SG-IV(China, under construction), GEKKO XII (Japan), HIPER (EU), LMJ(France) and so on (Betti et al., 2016:page 1-3 and Pfalzner, 2006: page 39). Research in this area is mainly concentrated in the United States, China and the European Union and the United States is undoubtedly the absolute leader.

The research on the use of high-power lasers to drive fusion reactions is part of the US nuclear safety program and mainly concentrated in the American Lawrence Livermore National Laboratory (LLNL) and University of Rochester. The development of the current NIF (belonging to LLNL) (Betti et al., 2016:page 1-3) and the OMEGA (belonging to University of Rochester) (Regan et al., 2016: page 1-2, Bose et al., 2016: page 1 and Bose et al., 2018: page 1-2) facilities run through the whole ICF research process in the United States. The ICF study in LLNL laboratory can date back to the 70s of the last century. In 1974, the LLNL laboratory set up a Janus laser facility with twin channel. In 1975, the CYCLOPS system with the output energy~100 Joule was set up, then the first laser driven implosion experiment was completed on it, and about 10^4 of the neutron yield was obtained. This result increased the confidence of the indirect drive and further promoted change of the driving method from direct drive with a uniform irradiation to indirect drive with a irradiation from two end faces. In 1979, the NOVA plant was built and it reached full capacity in 1985. Between 1986 and 1990, significant advances were made in the physics of indirect-driven targets using NOVA. Experimental and quantitative simulations demonstrated the symmetry control of implosions and completed the first quantitative R-T instability experiment (Remington et al., 1997: page 1997-1999 and Dimonte et al., 1993: page 1806-1808). In early 1993, the United States Department of Energy (DOE) signed and approved the concept design and construction plan for the National Ignition Facility (NIF). NIF is the first laser system designed to demonstrate ignition and thermonuclear burn of deuterium-tritium-filled capsules and has been operational and conducting experiments since late in 2009. It has the ability of delivering 1.8 MJ at 500 TW of 0.35-lm light to a target (Edwards et al., 2013: page 1-2 and Lindl et al., 2014: page 2-4). So far, laser-fusion implosions

at NIF have achieved more than half of the value of Pτ required for thermonuclear ignition (Hurricane, et al., 2014: page 1). Although ignition remains an elusive goal, NIF implosions have demonstrated, for the first time, a fusion yield exceeding the total energy (thermal and kinetic) of the D-T fuel.

The OMEGA facility at the University of Rochester (NRL) was completed in 1979. The purpose of the system construction was to explore important physical issues in the ICF direct drive approach, including uniform irradiation, fluid dynamic instability, laser-plasma interactions, etc. The OMEGA has 60 beam lasers and can deliver up to 500 J per beam (a total of 30 kJ) at a wavelength of 351 nm, in a variety of pulse shapes with a 4 ns maximum duration and a total peak power of 30 TW. According to recent experimental and simulation results on OMEGA, it was estimated that the best performing implosion on OMEGA extrapolated to NIF scales, i.e., with the same illumination configuration and laser target coupling, would produce 125 kJ of fusion energy, five times the fusion yield of indirect drive (Bose et al., 2016: page 1).

Overall, a series of important technological advances made by humans in the field of high temperature plasma in the last forty years have made controlled nuclear fusion technology no longer a distant dream. Especially in the field of magnetic confinement, with the completion and operation of ITER, the design and construction of demonstration reactors in the next two decades will be a high probability event.

3. THE APPLICATION OF NONEQUILIBRIUM PLASMA TECHNOLOGY IN SUSTAINABLE ENERGY

3.1. Plasma technology in Photovoltaic cells

In contrast to fossil fuels, photovoltaic (PV) solar energy is considered as a possible solution of the climate change or global warming problems since PV solar cells can provide electricity without producing carbon dioxide and other greenhouse gas emissions (Fraas et al., 2010: page 12-13). According to the different materials used, solar cells can be divided into crystalline silicon cells, silicon-based thin film cells, multi-component thin film cells, organic solar cells, etc. (Kabir et al., 2018: page 896 and Goetzberger et al., 2003: page 1-46). Among them, silicon solar cells are currently the most developed mature and dominate the photovoltaic (PV) industry. As low-temperature plasma technology has many advantages in chemical vapor deposition (CVD), surface treatment of materials, nanomaterial synthesis, organic material polymerization, etching, etc., it can be applied to almost every field of solar cells. Plasma enhanced vapor deposition (PECVD) has the following advantages over the atmospheric pressure (APCVD) and low pressure (LPCVD) methods (Fraas et al., 2010: page 168-171 and Duerinckx et al., 2002: page 233): (1) high deposition rate; (2) low deposition temperature, which does not cause phase charge or deformation of the substrate; (3) easy to obtain relatively uniform components so that the film with high quality; (4) the composition of the film can be changed continuously by adjusting the ratio of the gas flows.

Because of this, it has many important applications in the field of silicon solar cells, mainly including (Bosio et al., 2010: page 31-41 and Duerinckx et al., 2002: page 233): (1) the preparation of antireflection and passivation film for silicon solar cells. Compared with other methods, the PECVD has the characteristics of low reaction temperature, fast deposition rate, high adjustable range of refractive index and high content of hydrogen in the deposited film, is the most common method. In order to increase the efficiency of the silicon cell, it is usually necessary to reduce the reflection on the surface of the solar cell and it also needs to be passivated to reduce the combined action of the minority carrier caused by surface defects, there by the efficiency of the solar cell can be improved greatly. At present, the main antireflection materials are TiO2, SnO2, SiO2, SiNx, Al2O3 and so on. Based on the antireflection and passivation film prepared by PECVD, the photoelectric conversion efficiency of the passivation film can be increased by more than 50%, and the overall conversion efficiency can reach about 20%. (2) plasma etching processes for removal of phosphorus silicate glass (PSG) or parasitic emitters, for wafer cleaning as well as masked and mask-free surface texturization. In the standard solar cell production sequence, the PGS formed during the phosphorus diffusion at the Si surface is removed by diluted hydrofluoric acid (HF). This process can also be achieved by a plasma etching process with a selectivity of >10 (etch rate of PSG/etch rate of Si). The removal of residuals from a crystalline Si wafer surface is an important process needed typically before the deposition of thin layers. This surface cleaning process can be done by means of Si removal by etching with fluorine containing gases like SF6.

In contrast to conventional wet cleaning methods have problems with excessive etching and degradation, plasma etching process with higher particle removal efficiency and no charge-buildup damage. As we known, texturisation of the silicon wafer surface can increase the collection of photons. A great advantage of a plasma texturisation process (masked or mask-free) is its independence of the crystal orientation of the substrate. Hence, also low-cost mc Siwafers can be effectively textured. (3) Preparation of amorphous silicon thin films. Amorphous silicon thin-film solar cells have the advantages of low production cost, light weight, suitable for mass production, good high temperature performance, low light response, and high charging efficiency, so that it has a broad prospect. Compared with other methods such as reactive sputtering and electron beam evaporation, PECVD employs a series of deposition chambers that form a continuous process in production to enable mass production. At the same time, amorphous silicon solar cells are very thin so that they can be stacked or can use a suitable masking process on one plane, making multiple cells in series at a time to obtain a higher voltage. (4) Preparation of amorphous

/crystalline silicon heterojunction with intrinsic thin layer (HIT) solar cells. The high efficiency of the HIT battery is impressive, and the HIT battery produced by Japan Sanyo in 2015 created a world record of 25.6% efficiency in laboratory. Although the current heterojunction solar cells have problems in mass production, it combines low-temperature manufacturing of thin-film photovoltaic cells, and has many advantages such as high efficiency, high stability, and low cost, is an important research focus in the field of solar cells. The key technology of HIT solar photovoltaic cells is the deposition of a-Si:H films. PECVD is currently widely used to deposit intrinsic and doped a-Si:H films. Meanwhile, hot filament chemical vapor deposition (HWCVD) is also considered to be very promising.

As mentioned above, low-temperature and low-pressure plasma technology has achieved great success in the field of solar cells, and it can be said that it is everywhere. There is no doubt that leaving the low-temperature and low-pressure plasma technology will bring great difficulties to the commercialization of solar cells, and the prospect of the photovoltaic market will not be as bright as it is now.

Compared with low-pressure plasma discharge technology, atmospheric pressure discharge plasma does not require complicated and expensive vacuum equipment, and has the advantages of low cost, low energy consumption, and high efficiency. With the impressive technical progress achieved in atmospheric pressure discharge plasma technology over the past decade, currently it has very important applications in film deposition, surface modification, material preparation, biomedicine, environmental purification, and food safety control. Mariotti gives an overview of the application of low-temperature atmospheric pressure plasma (APPs) processing in "Green" third generation photovoltaics and demonstrates low-temperature APP technologies can produce the full range of materials required for 3-Gen PV device fabrication (Mariotti et al., 2016: page 70-85). In addition, atmospheric pressure discharge plasma technology can also be used for solar panel cleaning. Traditional solar panel cleaning methods need to consume large amounts of water and are not environmentally friendly. The simulation and experimental results carried by Cui (Cui et al., 2017: page 328-334) show that atmospheric pressure dielectric barrier discharge (DBD) plasma can effectively remove the contaminants adhering on the surface of the solar cell panels for a long time, and has the advantages of simplicity, effectiveness and no pollution.

Another important application of plasma technology is to improve the photoelectric conversion efficiency of organic solar cells (OSCs) (Choy et al., 2013: page 1-2). Since the OSCs are invented in 1990s，as using organic semiconductors as the active material for photoelectric conversion, they have the advantages of low cost, low thickness, light quality, simple manufacturing technology and suitable for making large area flexible devices and have become one of the most dynamic and promising research frontiers in the field of new materials and new energy. Due to the low energy conversion efficiency of current organic solar cells, large-scale applications cannot be realized. However, this problem can be solved by the introduction of surface plasmons of metal nanoparticles and nanostructures to increase the photoelectric conversion efficiency of the OSCs. Atwater gave a detailed overview of the recent progress of plasmonics technology for improving the energy conversion efficiency in the field of organic solar cells (Atwater et al., 2010: page 205-211).

3.2. Plasma-catalytic conversion of CO_2 into value-added fuels and chemicals

As a major greenhouse gas, CO_2 contributes more than 50% of the man-made greenhouse effect among all the greenhouse gases. It is estimated that emit 10 billion tons of CO_2 into the atmosphere each year through various fossil fuels, but less than 100 million tons are used by humans (Liu et al., 1999: page 119). This not only exacerbates the waste of CO_2 resources, but also exacerbates the greenhouse effect. Therefore, the effective utilization of CO_2 recycling has become a hot issue of great concern to all countries in the word. At present many methods have been used to convert CO_2 in to value-added fuels and chemicals, for examples, CO_2 reforming of CH_4 for hydrogen production (Tao et al., 2011: page 113-122), CO_2 hydrogenation for synthesis of amonia (Peng et al., 2018: page 597-599), methane (Nozaki et al., 2013: page 29-30) and direct splitting of CO_2 into CO (Mei et al., 2015: page 1-2) and so on. However, CO_2 molecule has a very low energy content and with high stability, a large amount of additional energy (that would induce more CO_2 emissions) is required for the activation of CO_2 in the conventional CO_2 conversion process so that the efficiency-cost ratio is very low. Recently, the unusual plasma chemistry, especially the no-thermal plasma has been considered as an attractive alternative to the conventional thermal or catalytic route for value-added fuels and chemicals (Sakakura et al., 2007: page 2365-2367). Until now, many different types of plasma have been used for CO_2 conversion, including dielectric barrier discharges (DBDs) (Paulussen et al., 2010: page 1-2), corona discharges, glow discharges, microwave discharges, radio frequency discharge and gliding arc discharges.

The applications of low-temperature plasma technologies in CO_2 utilization can be divided into two categories (Liu et al., 1999: page 124-126): (1) indirection conversion of carbon dioxide and (2) direct conversion of carbon dioxide. For indirection conversion technology routes, the typical application is CO_2-CH_4 reforming to produce syngas and then converted to more valuable hydrocarbons using non-thermal plasmas in the absence of a catalyst. This process involves reactions of producing carbon monoxide or syngas. Compared with non-thermal plasma method, it was found that the energy cost and energy efficiency in warm plasmas (e.g. gliding arc and spark) are much better than those in cold plasmas (e.g. DBD and corona) at a comparable range of reactant conversion. Another indirect CO_2 utilization is the case of the syngas formation from CO_2 and H_2S mixture using microwave discharge. The products contain the elements sulfur and syngas with a 1/1 ratio of H2/CO. Potapkin et al. demonstrated this reaction to be a two-stage process (Liu et al., 1999: page 125): H_2S is first dissociated plasma-chemically and hydrogen is

produced. Then, the hydrogen reacts with CO_2 to generate water and CO. The overall effect of carbon dioxide was to increase the conversion of H_2S but reduce the hydrogen yield. For direct conversion of carbon dioxide, the main applications include: (1) methanol formation by CO_2 hydrogenation in the presence/absence of a catalyst; (2) synthesis of aldehydes from carbon dioxide and methane, (3) more valuable hydrocarbons from water and carbon dioxide, for examples, methanol, oxalic acid, H_2O_2, CH_4,acetone, C_3 and C_4 alcohols; (4) direct higher hydrocarbon (C_2 hydrocarbons) formation from CO_2 and CH_4.

3.3. New types of energy storage materials and supercapacitors

Electrochemical new energy technology is a reasonable solution that is currently considered to deal with the energy crisis. Electrode material, including electrocatalyst, is an important part of the electrochemical energy storage and conversion device and is also one of the key factors that affect the efficiency of energy storage and conversion. Therefore, the development of high performance electrode materials / electrocatalysts plays an important role in accelerating the application of electrochemically renewable new energy technologies. Nowadays, low temperature plasma, such as glow discharge plasma, corona plasma, DBD plasma, microwave plasma and RF plasma, due to their high electron temperature, low gas temperature and high energy characteristics, has a wide range of applications in the preparation and modification of renewable energy electrode materials because of their high electron temperature, low gas temperature and high energy characteristics (Dou et al., 2018: page 1-2). The plasma process can be simply described as follows (Dou et al., 2018: page 4-20 and Kobayashi, 2015: 1-2): the energetic radicals first attack the surface of materials and then a series of physical and chemical reactions occur during the energy exchange (from energetic radicals to substrate materials), then the redundant reactants are removed from the material surface and thus change the physical and chemical properties. In contrast to traditional methods, plasma process has a higher efficiency and may bring soft reaction conditions with reducing the reaction temperature. The main applications of plasma process in this field include (Dou et al., 2018: page 21 and Ouyang et al., 2016: page 17801-17802): (1) Nonthermal plasma technology assist the modification and/or the preparation of three composting the polymer electrolyte membrane fuel cells (PEMFCs) to improve their performance, including the oxygen reduction reaction (ORR) electrocatalysts in cathodes and the fuel oxidation reaction (FOR) electrocatalysts in anode as well as the membranes as a core part in PEMFCs; (2) Preparation proton exchange membrane for PEMFCs by using plasma polymerization technology; (3) Improving the performance of Li-Ion Batteries by the modification or synthesis of electrode material (including anode and cathode) with the assistance of plasma;(4) Supercapacitors. For example, using oxygen plasma process or doping of heteroatoms into the carbon-based materials of electrochemical double layer capacitors (EDLCs) and Preparation of metal oxide/carbon materials hybrids as supercapacitor nelectrode material by PECVD process to improve the performance of supercapacitors.

4. THE APPLICATION OF WARM PLASMA TECHNOLOGY IN SUSTAINABLE ENERGY

4.1. Magnetic fluid power generation

Nowadays, the generation of electric power through the conventional systems (thermal and hydro electric) is no longer sufficient to meet the increasing industrial and commercial usage. Therefore, an alternative energy conversion system is currently being sought. Magnetic fluid power generation (MHD) technology (Murakami et al., 1999: page 605 and Mikheev, 2006: page 242), as a new type of direct thermal power generation, has been successfully experimented since the late 1950s, and its remarkable advantages of high efficiency and low pollution have attracted the attention of many countries, such as Russia and the United States. Japan and China have included magnetic fluid power generation in their national plans and have provided long-term sustained support.

At present, the main working medium for MHD power generation is the combustion gas, inert gas, or alkali metal vapor generated by the combustion of fossil fuels (coal, oil, and natural gas). When combustion gases are used, a small amount of additives (commonly used potassium carbonate), also known as "seeds", should be added to obtain enough ionization degree, which allows the gas temperature below 3000K to obtain sufficient conductivity. For monoatomic gases, the use of hydrazine as an additive allows the operating temperature to be reduced to 1500 K. Liquid metal fluids are liquid phase working medium formed by the injection of liquid metal into steam or fluid streams.

Although the feasibility of MHD power generation has long been proven, there are still many problems to be solved in its commercialization (Murakami et al., 2011: page 185201, Murakami et al., 2011: page 185202, Tanaka et al., 2014: page 4020): (1) Efficiency and longevity. At present, the efficiency of the magnetic fluid-steam combined power generation is achieved in a short period of time. How to obtain high efficiency under long-lived conditions is still a problem to be solved; (2) The recycling efficiency of "seeds" is too low. At present, the recovery efficiency of seeds is only 20%, which leads to excessive consumption; (3) developing new electrodes that can work for a long time under high temperature parameters; (4) The huge superconducting magnets required; (5) When using the most abundant coal as the combustion working medium, the problem of coal slag discharge, the effect and separation between the slag and the seed still need to be solved and not yet reached the requirement of practical application.

4.2. Plasma gasification for power & heat generation and assisted combustion

In general, the plasma temperature of the hot plasma is in the range of 1 to 10 K, which is basically close to the thermodynamic equilibrium. Since the temperature of the thermal plasma is very high, the material can be melted, decomposed, and phase-transformed effectively. Therefore, the thermal plasma has important applications in the fields of waste disposal power generation, assisted coal gasification combustion (Fabry, 2013: page 421-422 and Suo et al., 2017: page 3). The most basic component of thermal plasma pyrolysis / gasification / combustion supporting system is plasma generator, also known as plasma torch. There are three types of plasma generators that are used in such fields and have industrial application value (Tang et al., 2013: page 840-842): (1) arc plasma torches with DC/AC discharge; (2) High frequency induction plasma torch with high-frequency induction discharges; (3) microwave plasma torch with microwave discharge at atmospheric pressure.

When waste is treated with warm plasma, the waste is placed in it and the high thermal density and high reactive activity of the plasma will lead to many high temperature chemical reactions, such as (1) plasma dissociation. The garbage will be cracked into small molecules under anaerobic or oxygen-limited conditions with the action of the thermal plasma; (2) plasma gasification. Organic matter in garbage can be converted into calorific value gas under anoxic conditions, such as syngas containing CO, H2 and CH4. (3) plasma melting. The inorganic components in waste are melted and solidified under high temperature condition and transformed into vitrified substances. Heavy metals and harmful substances are fixed in the vitreous body. Compared with the conventional heat treatment method of waste, the advantages of plasma gasification technology are: (1) flexible and efficient. Due to the high temperature of the plasma gasification treatment, almost all organic matter can be converted into synthesis gas, while inorganic substances are converted into glass slag, so that all kinds of waste can be treated at the same time. Meanwhile, the power generation efficiency of the plasma gasification technology with high power generation efficiency and can reach as high as 39%, but the conventional incineration method can hardly exceed 22%. (2) environmental protection. Plasma gasification technology is carried out under anoxic conditions, with less emissions of greenhouse gases and other harmful gases, which is only about half that of the conventional methods. The temperature of the plasma gasification is generally about 1500 degrees. At that temperature, the organic matter is completely decomposed, no dioxins are produced, and the harmless vitreous slags can be used as a building material. (3) Economicality. Although the plasma gasification process is more complex, it is economically feasible; receiving garbage can charge a certain amount of garbage disposal fee, the electric energy produced can be sold to the power grid; it can also recover metal and valuable plastics from the recycled waste, and the gasified slag can be used to produce construction materials, such as rock wool and building bricks. Because of less residue (~1/5 of the traditional method), it can also save the cost of transporting rubbish.

The stability and power consumption of thermal plasma treatment are two major problems that impede the development of plasma gasification technology. The economy of plasma gasification technology is the most important factor in waste treatment. With the continuous development of plasma gasification technology, the power consumption of plasma torch has dropped from 35% in the past to 20% now, the life and stability of plasma torch have been greatly increased, the economy of plasma pneumatic technology has been greatly improved, and plasma gasification technology has gone from basic research to industrial application.

Another important application of thermal plasma is assisted coal gasification and combustion. There are currently three main types of processes (Messerle et al., 2016: page 172-173,): (1) Oxygen plasma gasification (Matveev, et al., 2008: page 2948). The reaction of coal in oxygen plasma similar to conventional coal gasification is called oxygen plasma gasification, but this method generates large amounts of carbon dioxide during the process and the value of industrial production is low; (2) H_2O-Ar plasma gasification (Bao et al., 2006: page 223). Coal gasification in H_2O-Ar plasma is significantly different from coal pyrolysis in H2-Ar plasma. Many researchers pointed out that assuming that the heat supply in the entire gasification process can be guaranteed, the temperature in the entire reaction zone should be greater than 1400 K and meet the hydrodynamic conditions, the pulverized coal will be completely gasified with the increasing of the diffusion rate of water vapor and the residence time of the pulverized coal in the reactor. The absence of solid phase products is the main difference between plasma gasification and plasma pyrolysis of bituminous coal to produce acetylene.(3) steam plasma gasification (Shin et al., 2013: page S520). Steam is used as the main gasification agent and working gas of the plasma generator. If a non-steam plasma generator such as air or other non-oxidizing gas is used as the working gas, steam must be added at the anode inlet. This is currently the most widely used process.

Thermal plasma coal gasification has the following advantages (Fabry et al., 2013: page 421-422): (1) High energy density in the reaction zone and high production intensity of the equipment; (2) High gasification efficiency (more than 90%), high selectivity, and high product calorific value; (3) Since sulfur and nitrogen in coal will be converted to low oxidation substances under the high-energy and reducing environment, which can reduce the emission of the harmful gas, such as high-oxidation nitrogen oxides and sulfur oxides and make it environmentally friendly; (4) It is easy to automate and optimise the entire process. (5) as the temperature of the reaction mixture is as high as 3000K, there is no special requirement for raw coal, and the inferior coal can be used for gasification, which greatly reduces the production cost.

5. CONCLUSION

With the rapid development of plasma technology in the past ten years, plasma technology is becoming more and more widely used in the field of sustainable energy. As mentioned in this review, currently, plasma technology has many important applications in controlled nuclear fusion, solar cells, preparation of new energy materials, MHD power generation, plasma gasfication of waste to power generation, assisted coal gasification and combustion. It can be said that plasma technology is an important booster engine for energy sustainable development. Although the application of plasma technology in some of these applications is not mature, it still remains to be further studied, but plasma technology has shown great potential in the application of energy sustainable development.

6. ACKNOWLEDGEMENTS

This work is supported by National Nature Science Foundation of China (Nos. 61771187 and 11075123).

7. REFERENCES

Atwater H A, Polman A, 2010. Plasmonics for improved photovoltaic devices. Nature Materials, 9: 205- 213

Betti R, Hurricane O. A, 2016. Inertial-confinement fusion with lasers. Nature Physics, 12: 435-448

Bose A, Betti R, Mangino D, et al., 2018. Analysis of trends in experimental observables and reconstruction of the implosion dynamics for direct-drive cryogenic targets on OMEGA. Physics of Plasma, 25: 062701

Bose A, Woo K. M, Betti R, et al., 2016. Core conditions for alpha heating attained in direct-drive inertial confinement fusion. Physical Review E, 94: 011201

Bosio Alessio, Romeo Alessandro, 2010. Thin film solar cells: Current status and future trends. New York: Nova Science Publishers

Bao W. R, Chang L. P, Lu Y. K, 2006. Study on main factors influencing acetylene formation during coal pyrolysis in arc plasma. Process safety and environmental protection, 84: 222-226

Chernyak V. Y, Nedybaliuk O. A, Tsymbaliuk O. M, et al., 2017. Plasma chemistry for concept of sustainable development. Problems of Atomic Science and Technology, 1: 126-131

Chu P. K, Lu Xinpei, 2014. Low temperature plasma technology: Methods and Applications. London, New York: CRC Press

Craxton R. S, Anderson K. S, Boehly T. R, et al., 2015. Direct-drive inertial confinement fusion: A review. Physics of Plasmas, 22: 110501

Duerinckx F, Szlufcik J, 2002. Defect passivation of industrial multicrystalline solar cells based on PECVD silicon nitride. Solar Energy Materials & Solar Cells, 72: 231-246

Cui Weisheng, Liu Wenzheng, Wang Tahan, et al., 2017. The Application of atmospheric pressure dielectric barrier discharge plasma on the cleaning of photovoltaic panels. IEEE Transactions On Plasma Science, 45: 328-334

Choy W. C. H, 2013. Organic solar cells: Materials and Device Physics. New York: Springer-Verlag London

Dimonte Guy, Remington B, 1993. Richtmyer meshkov experiments on the Noava laser at high compression. Physical Review Letters, 70: 1806-1809

Dou Shuo, Tao Li, Wang Ruilun, et al., 2018. Plasma- assisted synthesis and surface modification of electrode materials for renewable energy. Advanced Materials, 30:1705850

Edwards M. J, Patel P. K, Lindl J. D, et al., 2013. Progress towards ignition on the nation ignition facility. Physics of Plasmas, 20: 070501

Fabry F, Rehmet C, Rohani V, et al., 2013. Waste Gasification by Thermal Plasma: A Review. Waste Biomass Valor, 4: 421-439

Fraas L, Partain L, 2010. Solar Cells and their applications. Second Edition. Hoboken, New Jensey: John Wiley & Sons

Goetzberger A, Hebling C, Schock H. W, 2003. Photovoltaic materials, history, status and outlook. Materials Science and Engineering: R: Reports, 40: 1-46

Hemsworth R, Decamps H, Graceffa J, et al., 2009. Status of the ITER heating neutral beam system. Nuclear Fusion, 49: 045006

Huang C, Li L, 2018. Magnetic confinement fusion: a brief review. Frontiers in Energy, 5: 1-9

Hurricane O. A, Callahan D. A, Casey D. T, et al., 2014. Fuel gain exceeding unity in an inertially confined fusion implosion. Nature, 506: 343-348

Jeffrey F, 2007. Plasma physics and fusion energy. New York: Cambridge university press

Lindl J, 1995. Development of the indirect drive approach to inertial confinement fusion and the garget physics basis for ignition and gain. Physics of Plasmas, 2: 3933

Kabir Ehsanul, Kumar Pawan, Kumar Sandeep, 2018. Solar energy: Potential and future prospects. Renewable & Sustainable Energy Reviews, 82: 894-900

Kim Hyun Ha, Teramoto Yoshiyuki, Ogata Atsushi, et al., 2016. Plasma catalysis for environmental treatment and energy applications. Plasma Chemisty & Plasma Processing, 36:45-72

Kobayashi Akira, 2015. Application of advanced plasma technology to energy materials and environmental problems. AIP Conference Proceedings, 1657: 030004

Lehnen M, Aleynikova K, Aleynikov P. B, et al., 2014. Disruptions in ITER and strategies for their control and mitigation. Journal of Nuclear Materials, 463: 39-48

Li Jiangang, 2016. The status and progress of tokamak research (in Chinese). Physics, 45:88-97

Lindl J, Landen O, Edwards J, et al., 2014. Review of the nation ignition campaign 2009-2012. Physics of Plasmas, 21: 020501

Liu C, Xu G, Wang T, 1999. Non-thermal plasma approaches in CO_2 utilization. Fuel Processing Technology, 58: 119-134

Liu C, Zhang L, Cao L, et al., 2017, Current status and upgrade activities on the guard limiter of 4.6GHz lower hybrid antennas for EAST tokamak. Fusion Engineering and design, 125:93-97

Mariotti D, Belmonte T, Benedikt J, et al., 2016. Low-temperature atmospheric pressure plasma processes for "Green" third generation photovoltaics. Plasma Processes and Polymers. 13: 70-90

Matveev I. B, Messerle V. E, Ustimenko A. B, 2008. Plasma gasification of coal in different oxidants. IEEE Transactions on plasma science, 36: 2947-2954

Harry John. Ernest, 2010. Introduction to plasma technology: Science, Engineering and Applications. Weinheim: WILEY-VCH Verlag & Co. KGaA

Mikheev A. V, Kayukawa N, Okinaka N, et al., 2006. High-temperature coal-syngas plasma characteristics for advanced MHD power generation. IEEE Transactions On Plasma Science, 21: 242- 249

Misra N. N, Cheorun Jo, 2017. Applications of cold plasma technology for microbiological safety in meat industry. Trends in Food Science & Technology, 64: 74-86

Miyamoto Kenro, 2016. Plasma Physics for Controlled Fusion. Second Edition. Berlin, Heidelberg: Springer Berlin Heidelberg

Mei Danhua, Zhu Xinbo, He Yaling, 2015. Plasma-assisted conversion of CO_2 in a dielectric barrier discharge reactor: understanding the effect of packing materials. Plasma Source Science and Technology, 24: 015011

Murakami T, Okuno Y, 2011. Magnetohydrodynamic electrical power generation using convexly divergent channel I Experimental demonstration. Journal of Physics D: Applied Physics, 44: 185201

Murakami T, Okuno Y, 2011. Magnetohydrodynamic electrical power generation using convexly divergent channel: II. Experimental demonstration. Journal of Physics D: Applied Physics, 44: 185202

Murakami T, Okuno Y, Kabashima S, 1999. Plasma Stabilization and Improvement in the Performance of a Nonequilibrium Disk MHD Generator by a Radio-Frequency Electromagnetic Field. IEEE Transactions On Plasma Science, 27: 604-612

Nozaki Tomohiro, Okazaki Ken, 2013. Non-thermal plasma catalysis of methane: Principles, energy efficiency and applications. Catalysis Today, 211: 29-38

Ouyang Bo, Zhang Yongqi, Wang Ying, et al., 2016. Plasma surface functionalization induces nanostructuring and nitrogen-doping in carbon cloth with enhanced energy storage performance. Journal of Materials Chemistry A, 45: 17801-17808

Pfalzner S, 2006. An introduction to inertial confinement fusion. Boca Raton: CRC press

Paulussen Sabine, Verheyde Bert, Tu Xin, et al., 2010. Conversion of carbon dioxide to value-added chemicals in atmospheric pressure dielectric barrier discharges. Plasma Sources Science and Technology, 19: 034015

Peng Peng, Chen Paul, Schiappacasse Charles, et al., 2018. A review on the non-thermal plasma-assisted ammonia synthesis technologies. Journal of Cleaner production, 177: 597-609

Regan S. P, Goncharov V. N, Igumenshchev I. V, et al., 2016. Demonstration of Fuel Hot-Spot Pressure in Excess of 50 Gbar for Direct-Drive layered Deuterium-Tritium Implosions on OMEGA. Physical Review Letters, 117: 025001

Richard Fitzpatrick, 2014. Plasma Physics: an introduction. London, New York: CRC Press

Romanelli F, 2015. Overview of the JET results. Nuclear Fusion, 55: 104001

Remington B. A, Kane J, Drake R. P, et al., 1997. Supernova hydrodynamics experiments on the Nova laser. Physics of plasmas, 4: 1994-2003

Sakakura Toshiyasu, Choi Jun-Chul, Yasuda Hiroyuki, 2007. Transformation of Carbon Dioxide. Chemical Reviews, 107: 2365-2387

Suo Yang, Nagaraja S, Sun Wenting, et al., 2017. Multiscale modeling and general theory of non-equilibrium plasma-assisted ignition and combustion. Journal of Physics D: Applied Physics, 50: 433001

Shin D. H, Hong Y. C, Lee S. J, et al., 2013. A pure steam microwave plasma torch: Gasification of powdered coal in the plasma. Surface & Coatings Technology, 228: S520-S523

Tanaka M, Murakami T, Okuno Y, 2014. Plasma Characteristics and Performance of Magnetohydrodynamic Generator With High-Temperature Inert Gas Plasma. IEEE Transactions On Plasma Science, 42: 4020-4025

Tang L, Huang H, Hao H, et al., 2013. Development of plasma pyrolysis-gasification systems for energy efficient and environmentally sound waste disposal. Journal of Electrostatics, 71: 839-847

Tao Xumei, Bai Meigui, Li Xiang, et al., 2011. CH_4 - CO_2 reforming by plasma - challenges and opportunities, Progress in Energy and Combustion Science, 37: 113-124

Tester JW, Drake EM, Driscoll MJ et al., 2012. Sustainable Energy: Choosing Among Options. Second Edition. Cambridge, Mass: MIT Press

Tyczkowski Jacek, 2011. New Materials for innovative energy systems produced by cold plasma technique. Functional Materials Letters, 4: 341-344

Vangari M, Pryor T, Li Jiang, 2013. Supercapacitors: review of materials and fabrication methods. Journal of energy engineering, 139: 72-79

Wan Yuanxi, Li Jiangang, Liu Yong, et al., 2017. Overview of the present progress and activities on the CFETR. Nulcear Fusion, 57: 102009

Wurden G. A, Biedermann C, Effenberg F, et al., 2017. Limiter observations during W7-X first plasma. Nuclear Fusion, 57: 056036

Zhu S, 1990. History of research on the study of nuclear fusion (in Chinese). Physics, 19:113-117

254: Alternate processes for energy efficiency in non-centrifugal cane sugar industry-an analytical study

Srinivas MORAPAKALA[1], Prudhviraj SUNKARA[2], KS REDDY[3], Ayush VARSHNEY[4], Navaneeth KUNCHAM[5]

[1,2,4,5]Department of Mechanical Engineering, Birla Institute of Technology and Science Pilani, Hyderabad Campus, Telangana, India, [1]morasrini@hyderabad.bits-pilani.ac.in; [2]p20170445@hyderabad.bits-pilani.ac.in; [4]ayush.varshney9@gmail.com; [5]f20150022@hyderabad.bits-pilani.ac.in
[3]Heat Transfer and Thermal Power Laboratory, Department of mechanical engineering, IIT Madras, Chennai, ksreddy@iitm.ac.in

Non-centrifugal cane sugar, known as Jaggery, is a condensed form of sugarcane juice and is conventionally produced by evaporation of water in juice using bagasse as fuel. Owing to the low furnace efficiency of around 20%, the traditional method of water removal through evaporation process requires an energy demand of 62.902 MJ/kg of jaggery. In the pursuit of improving energy efficiency in this small scale unorganized rural industry sector in India, an analytical approach for water removal through a combination of freezing and evaporation processes is presented in this paper. Thermal analyses and associated analytical computations are conducted to assess the energy demands for water removal from sugarcane juice using evaporation, freezing and various combinations of both evaporation and freezing processes. The comparative study taken up showed that water removal from juice using freezing process requires an energy demand of just 21.032 MJ/kg of jaggery for a refrigeration unit of 0.5 coefficient of performance (COP).The obtained analytical data also indicates an energy demand ranging from 121.206 MJ/kg of jaggery to 3.749 MJ/kg of jaggery for water removal percentages varying from 10% to 90% by freezing and the remaining by evaporation process, with corresponding ranges of furnace efficiency and COPs being 10% to 90 % and 0.5 to 4.5, respectively. The combined process seems to be a viable option among the three, owing to the practical constraints faced in the pure freezing process and higher energy demands involved in the conventional process.

Keywords: jaggery, evaporation, freezing, energy demand

1. INTRODUCTION

Jaggery, the non-centrifugal cane sugar, is a traditional sweetener consumed in Asia, Africa, Latin America and the Caribbean (Sardeshpande et al , 2010: 4740-4747). It contain 65-85 % sucrose, 10-15% reducing sugar, 3-10% moisture and remaining are insoluble matter such as fat, proteins, minerals, iron and phosphorus (Jagannadha Rao et al, 2007: 95-102). It is a condensed form of sugarcane juice which is conventionally produced by evaporation of water in the juice. Bagasse, (the remaining material after the juices is extracted from the sugar cane) is used as a primary fuel in jaggery making furnaces to affect this evaporation process. Before using this bagasse as a fuel, it is dried since it contains around 50-60% moisture as reported (Jagannadha Rao et al, 2007: 95-102). These furnaces being very rudimentary in nature with not much of controls to maintain correct air-fuel ratios, have very poor heat utilization efficiency of approximately about 15% (Sharon et al, 2013: 22-25). With an intention to improve these furnace efficiencies modified versions of these furnaces have been investigated. An improved furnace design using 2-pan and parallel fins has reported the heat utilization efficiency of 30% (Anwar, 2010: 360-364) . A further study using 4-pan showed a heat utilization efficiency of furnace about 50-60% (Shiralkar et al, 2014: 36-48). These and other literature & field surveys reveal that such kind of investigations primarily focused on improving the furnace designs to improve the energy efficiency in the Jaggery making process. As a slight deviation from these, a freeze pre-concentration of sugarcane juice was studied by Rane and Uphade (Rane and Uphade, 2015: 370-381). It has been reported that freeze concentration from 20°Brix to 40°Brix using a reversible heat pump saves bagasse during initial 63% water removal. In this paper, an attempt has been made to assess the energy requirements of jaggery production by removing water using three techniques namely (a) conventional evaporation process, (b) through pure freezing and (c) combination of evaporation and freezing process for different ratios of water removal, with view to find the energy efficient way (among the above three) to remove the water from cane juice to produce jaggery.

2. THERMAL MODELLING FOR ENERGY DEMAND ASSESSMENT

Figure 1 depicts typical distribution of water, jaggery and bagasse of given sample of a freshly harvested sugar cane. Nearly 65% (by weight) of the sugar cane, is juice while the remaining mass is bagasse. The freshly extracted juice contains mostly water and 12% of jaggery which is the final quantity of jaggery produced (Sardeshpande et al , 2010: 4740-4747). The bagasse usually contains 45% of moisture which is dried (by open solar drying or by other drying processes) to obtain dry bagasse of 8-10% moisture content making it a very useful fuel for burning. The preliminary mass balance equations are as represented by equation (1) to equation (5). Table 1 indicates the nomenclature of various parameters used in the thermal modelling and associated analyses & computations.

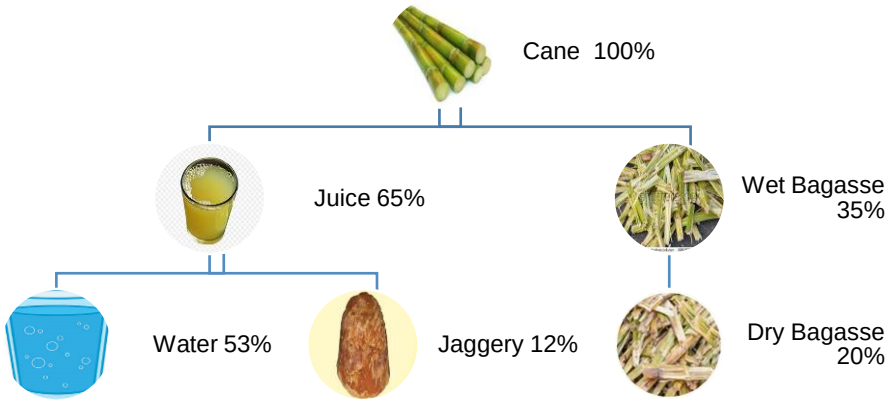

Figure 1: Mass balance

Equation 1: Mass of the cane.

$$M_{cane} = \frac{M_{jag}}{0.12}$$

Equation 2: Mass of juice extracted from the cane

$$M_{juice} = M_{cane} * 0.65$$

Equation 3: Mass of water present in juice

$$M_w = M_{juice} - M_{jag}$$

Equation 4: Mass of water in bagasse.

$$M_{wb} = M_{cane} - M_{juice}$$

Equation 5: Mass of dry bagasse.

$$M_{db} = \frac{20}{35} * M_{wb}$$

T*able 1: Nomenclature of various parameters used in the modelling, analysis and computations*

Parameter	Description of parameter	Parameter	Description of Parameter
Brix1	Brix value for fresh juice	L.H.V	Latent heat of vaporization for water (J/kg)
Brix2	Brix value after removal of certain percentage of water	M_{cane}	Mass of crushed cane (kg)
Brix3	Brix value of hot syrup	M_{db}	Mass of dry bagasse (kg)
$C_{p, hs}$	Specific heat of hot syrup/concentrated juice (J/kg-K)	M_{jag}	Mass of jaggery produced (kg)
$C_{p, j2}$	Specific heat of remaining juice after freezing (J/kg-K)	M_{juice}	Mass of juice extracted from cane (kg)
$C_{p, j1}$	Specific heat of fresh juice (J/kg-K)	M_w	Mass of water in bagasse (kg)
E_{jf}	Energy demand for jaggery formation process (MJ)	M_{wb}	Mass of water in bagasse (kg)
E_{comb}	Total energy demand in combined process (MJ)	T_{amb}	Ambient temperature (°C)
E_{cool}	Cooling energy demand in combined process (MJ)	T_{boil}	Boiling temperature for cane juice (°C)
E_{heat}	Heating energy demand in combined process (MJ)	T_{freeze}	Freezing temperature of water in juice (°C)
$E_{p, freeze}$	Energy demand for pure freezing process (MJ)	T_{strike}	striking temperature for jaggery formation (°C)
$E_{p, vap}$	Energy demand for conventional evaporation process (MJ/kg)	x	Percentage of water removed through freezing in combined process
E_{fp}	Energy demand for freezing process (MJ)	η	efficiency of furnace (%)
L.H.F	Latent heat of fusion for water (J/kg-K)	COP	Coefficient of Performance

2.1. Water removal through evaporation process (conventional process)

The conventional process used for jaggery production involves evaporation of entire water content of the juice by burning bagasse. Figure 2 depicts this conventional process. The sugarcane is crushed in a vertical or horizontal 3-roller machine where the latter type has a slightly higher efficiency and hence is the preferred one. These machines are run by electrical motors in the modern plants (Sharon et al, 2013: 22-25).

The extracted juice containing around 80% water is to be evaporated by supplying the necessary heat. Various stages of this entire heating process are as shown in Figure 2. Sensible heating of juice starts at the ambient temperature and continues till boiling point is reached. During this process, certain additives like bhendi, calcium carbonate and phosphoric acid is added in measured quantities to maintain the pH of the solution. Once it has attained boiling temperature, the water present in the juice is evaporated by supplying the required latent heat. After this stage, any floating residue present in the juice is removed to give a concentrated hot syrup. The hot syrup containing high sucrose content (65-85%) is to be raised to a striking temperature (usually 118°C), where it converts itself into a semi-solid paste which doesn't stick to the container and can be easily cooled and moulded to form jaggery (Sardeshpande et al , 2010: 4740-4747). The energy balance and associated equations for the entire process could be represented by equation (6) to equation (8).

Equation 6: Energy demand for conventional evaporation process.

$$E_{p,evap} = \left(M_w + M_{jag}\right) * C_{p,j1} * (T_{boil} - T_{amb}) + M_w * L.H.V + M_{jag} * C_{p,hs} * (T_{strike} - T_{boil})$$

Equation 7: Specific heat capacity of fresh juice.

$$C_{p,j1} = 4187 * (1 - 0.006 * Brix1)$$

Equation 8: Specific heat capacity of hot syrup/concentrated juice.

$$C_{p,hs} = 4187 * (1 - 0.006 * Brix3)$$

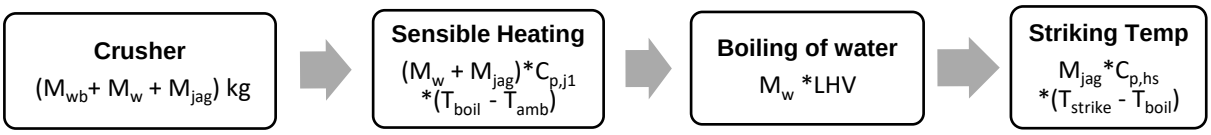

Figure 2: Process Flowchart of Conventional Process

2.2. Water removal through freezing process

Compared to the conventional process, in this new process, the water removal from the juice is affected by subjecting the juice to refrigeration process. The temperature of the fresh juice is reduced from the ambient temperature to a temperature of about -1.5° C, which is the freezing point of the mixture (Rane and Uphade, 2015: 370-381). The ice formed in the juice is removed to obtain high concentrated syrup. Temperature of this syrup is then raised to striking temperature to form jaggery. The process is represented in Figure 3. The associated energy balance and allied equations could be represented by equation (9) to equation (10).

Equation 9: Energy demand for pure freezing.

$$E_{p,freeze} = \left(M_w + M_{jag}\right) * C_{p,j1} * \left(T_{amb} - T_{freeze}\right) + M_w * L.H.F$$

Equation 10: Energy demand for jaggery formation

$$E_{jf} = M_{jag} * C_{p,hs} * (T_{strike} - T_{freeze})$$

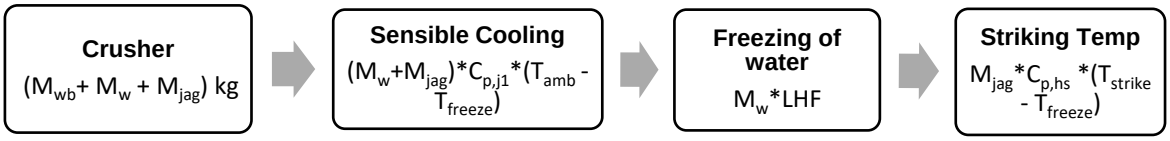

Figure 3: Process Flowchart of Freezing Process

2.3. Water removal through combined process

In this combined process both freezing and evaporation techniques are utilized for removal of water from the juice. Initially, the freezing process is performed to remove certain percentage of water (x) from the juice. The remaining water is heated and evaporated to form jaggery. The specific heat value of the juice after freezing, changes due to a change in Brix value. The new Brix can be calculated using simple linear approximation considering the concentration of sucrose (Brix) varying from the initial Brix value to 100% concentrated solution (equation 11) (Hugot. E, 1986: 1166) . The process flow diagram is as shown in Figure 4. The associated energy balance and allied equations are as represented by equation (12) to equation (15). As obviously it is, these equations suggest that the total energy requirements for jaggery productions would be different for different percentages of water removed through freezing.

Equation 11: Brix value after removal of some percentage of water

.

$$Brix2 = \frac{Brix1}{1 - \left(1 - \frac{Brix1}{100} * x\right)}$$

Equation 12: Cooling energy demand in combined process.

$$E_{cool} = \left(M_w + M_{jag}\right) * C_{p,j1} * \left(T_{amb} - T_{freeze}\right) + x * M_w * L.H.F$$

Equation 13: Heating energy demand in combined.

$$E_{heat} = \left((1-x) * M_w + M_{jag}\right) * C_{p,j2} * \left(T_{boil} - T_{freeze}\right) + (1-x) * M_w * L.H.V + M_{jag} * C_{p,hs} * (T_{strike} - T_{boil})$$

Equation 14: Total energy demand in combined process.

$$E_{comb} = E_{cool} + E_{heat}$$

Equation 15: Specific heat of remaining juice after freezing.

$$C_{p,j2} = 4187 * (1 - 0.006 * Brix2)$$

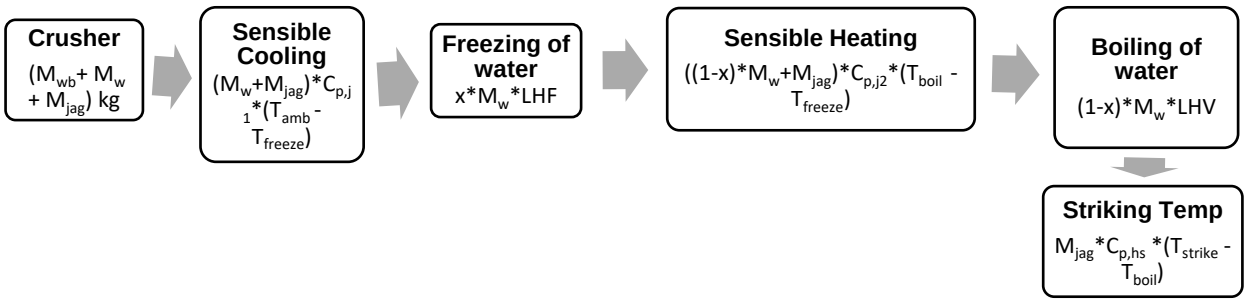

Figure 4: Process Flowchart of Combined Process

Comparison of the total energy requirements for several percentages of freezing and heating loads with several furnace efficiencies and COP of freezing units could be done using equation (16) to equation (18). The first and second term of equation (18) represents heating and cooling energy input respectively.

Equation 16: Energy demand for conventional evaporation process

$$Ep, vap = \frac{\boldsymbol{E_{p,evap}}}{\boldsymbol{\eta}}$$

Equation 17: Energy demand for freezing process

$$E_{fp} = \frac{\boldsymbol{E_{p,freeze}}}{\boldsymbol{COP}} + E_{jf}$$

Equation 18: Total energy demand in combined process

$$E_{comb} = \frac{\boldsymbol{E_{heat}}}{\boldsymbol{\eta}} + \frac{\boldsymbol{E_{cool}}}{\boldsymbol{COP}}$$

3. ENERGY DEMAND ASSESMENT

The energy demand per kg of jaggery could be calculated, for all the above three cases using above presented thermal model. A preliminary mass balance results in the mass of cane, juice, bagasse as given in Table 2. The assumed data to proceed with the computations are as given in Table 3. Initial value of Brix of freshly extracted sugarcane juice is assumed to be 20. The value of Brix of the liquid jaggery when the maximum possible amount of water removal took place generally varies from 65% to 85% (Shrivastav et al., 2016: 198-202). In the present analysis an average value of 75% had been taken for Brix 3. The amount of water removed from the refrigeration process in the combined process is varied giving us the corresponding new Brix values and specific heat values for the remaining juice which undergoes evaporation process to remove the left-out water. The computed values of these new Brix 2 and associated specific heat values are as given in Table 4.

Table 2: Mass of cane, juice, and bagasse

Constitute	Mass (kg)
M_{cane}	8.333
M_{juice}	5.417
M_{w}	4.417
M_{wb}	2.916
M_{db}	1.666

Table 3: Assumed values for different parameters

Parameter	Value
T_{amb}	25° C
T_{boil}	100° C
T_{strike}	118° C
T_{freeze}	-1.5° C
$L.H.V$	2500 KJ/kg-K
$L.H.F$	2230 KJ/kg-K
$Brix1$	20
$C_{p,j1}$	3684.56 J/kg-K
$Brix3$	75
$C_{p,hs}$	2302.85 J/kg-K

Table 4: Brix2 and specific heat values for different percentages of water removed through freezing

y (% Water Removed)	Brix 2	$C_{p,j2}$ $(\frac{J}{kg-K})$
10	21.739	3640.87
20	23.809	3588.857
30	26.315	3525.895
40	29.411	3448.118
50	33.333	3349.6
60	38.461	3220.769
70	45.454	3045.091
80	55.555	2791.333
90	71.428	2392.571

The data presented in Tables 2, 3 and 4 were used to find the energy requirements for all three processes. The energy demand for the conventional process (which mainly depends on furnace efficiency) can be reduced significantly by improving the furnace design. The energy demand for varied values furnace efficiencies and COPs were obtained by using the above thermal model and the results are as shown in Table 5 and Table 6. The energy demand for freezing process (which mainly depends on the COP of the refrigeration unit) gives the lowest energy input requirement amongst the three processes.

Table 5: Energy demand for jaggery production using evaporation for different furnace efficiencies

Furnace Efficiency, η (%)	Energy Demand (MJ/kg of Jaggery)
10	125.804
20	62.902
30	41.934
40	31.451
50	25.160
60	20.967
70	17.972
80	15.725
90	13.978

Table 6: Energy demand for jaggery production using freezing process for different COPs:

COP	Energy Demand (MJ/kg of Jaggery)
0.5	21.032
1	10.653
1.5	7.194
2	5.464
2.5	4.426
3	3.734
3.5	3.240
4	2.869
4.5	2.581

Figure 5 and Figure 6 are the representative figures that present the individual heating and cooling energy demands for varied COPs, furnace efficiencies and percentages of water removed through freezing. From these and similar other graphs, following observations could be made. (a) As the furnace efficiencies are increasing, the heating energy demand is coming down. For instance, as the furnace efficiency is increasing from 20% to 30%, for percentage of water removed through freezing = 10%, the heating energy demand is decreasing from 58.88 MJ/kg of Jaggery to 39.25 MJ/kg of Jaggery. (b) For a given furnace efficiency, for all percentages of water removed through freezing, as the COP is increasing, the cooling energy demand is decreasing. For instance, for a furnace efficiency of 20% and for percentages of water removed through freezing = 50%, as COP is increasing from 0.5 to 4.5, the cooling energy demand is decreasing from 10.84 MJ/kg of Jaggery to 1.2 MJ/kg of Jaggery. (c) As the COP is increasing above 3 for any percentage of water removed through freezing, the cooling energy demand is not decreasing considerably when compared to increase in COP from 0.5 to 3. For instance, for a furnace efficiency of 30% and for a percentage of water removed through freezing = 80%, as COP is increasing from 3 to 4.5, the cooling energy demand is decreasing from 2.39 MJ/kg of Jaggery to 1.86 MJ/kg of Jaggery. But when COP is increasing from 0.5 to 2, the cooling energy demand is decreasing from 16.75 MJ/kg of Jaggery to 13.57 MJ/kg of Jaggery.

The total energy demand for varied values of (x) for different COPs of freezing systems and different furnace efficiencies was calculated using the above presented model. While a big database giving energy demands for various scenarios was obtained, outcomes of these computations for furnace efficiencies of 20% and 30% are presented in Figure 7 and Figure 8. From these figures and the data base, it could be observed that (a) for a given furnace efficiency (e.g. 20% and 30%), as the percentage of water removed through freezing is increasing, the total

energy demand is decreasing. For instance, for a COP of 0.5 and furnace efficiency of 20%, the energy demand is decreasing from 62.9 MJ/kg of Jaggery to 22.3 MJ/kg of Jaggery. (b) For a given furnace efficiency, as the COP of the refrigeration system is increasing, the total energy demand is decreasing. For instance, for a furnace efficiency of 30% and percentage of water removed through freezing is 50%, the energy demand is decreasing from 32.87 MJ/kg of Jaggery to 23.38 MJ/kg of Jaggery. (c) For a given COP, with increase in furnace efficiencies, the total energy demand is decreasing. For instance, as the furnace efficiency is increasing from 20% to 30% for a COP of 2, for percentage of water removed through freezing is 80%, the total energy demand is decreasing from 24.1 MJ/kg of Jaggery to 17.27 MJ/kg of Jaggery. (d) Overall, the obtained analytical data also indicates an energy requirement ranging from 121.206 MJ/kg of jaggery to 3.749 MJ/kg of jaggery for the water removal (percentages from 10% to 90%) by freezing/evaporation (freezing and evaporation) percentages ranging from 0.1 to 0.9. For this range of energy demand, the corresponding ranges of furnace efficiencies are from 10% to 90% and COP ranges are 0.5 to 4.5.

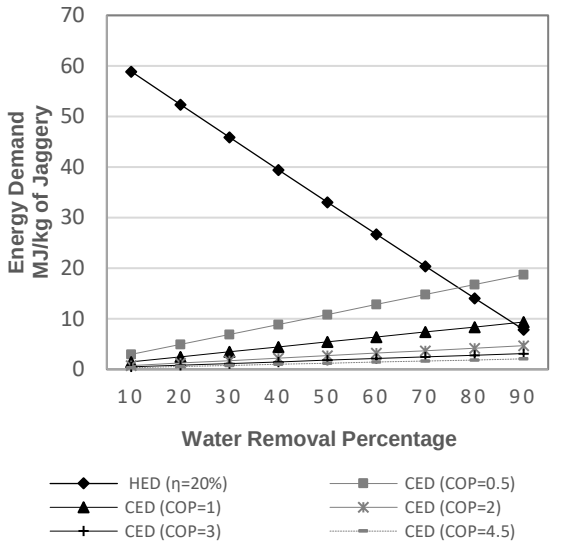

(HED = Heating energy demand, CED = Cooling energy demand)

Figure 5: Energy Demand for Furnace Efficiency 20% and various COPs

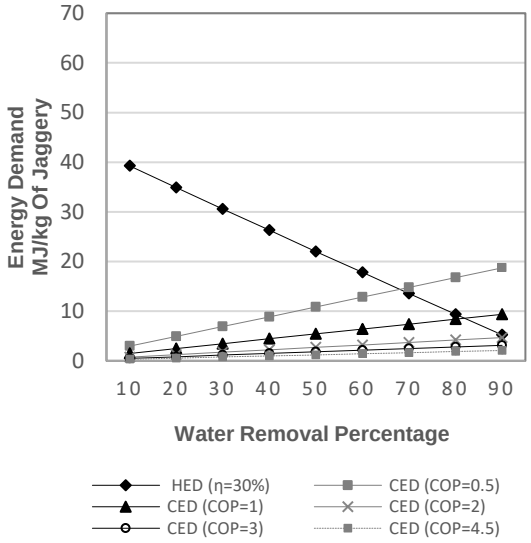

(HED = Heating energy demand, CED = Cooling energy)

Figure 6: Energy Demand for Furnace Efficiency 30% and various COPs

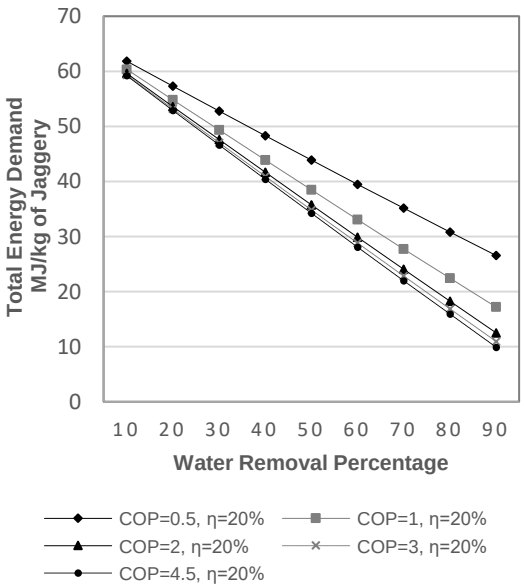

Figure 7: Total Energy Demand for Furnace Efficiency 20% and various COPs

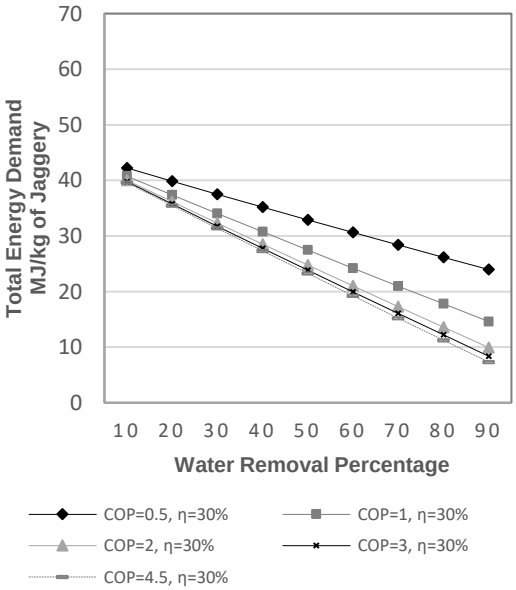

Figure 8: Total Energy Demand for Furnace Efficiency 30% and various COPs

From the energy demand computations for the three processes, it is clear that water removal by pure freezing seems to be the best option by far requiring only 21.032 MJ/kg jaggery of energy even for a refrigeration system of COP 0.5. While this is true analytically, it is seen that 100% of the water content in juice cannot be removed just by freezing because the sucrose-water phase equilibrium diagram shows that the freezing process is limited by the eutectic point (Rane and Uphade, 2015: 370-381).This eutectic point gives the minimum temperature to which the

solution can be cooled limiting the maximum water removal to 63%. Any further cooling will result in freezing of the sucrose or sugar content in the juice. Hence water removal by a combination of freezing and evaporation processes is to be contemplated in such a way that water removal through freezing is to be limited to 63%. Undertaken computations indicate that the total energy demand for this combination of 63% water removal by freezing and 37% water removal by evaporation ranges from 39.49 MJ/kg jaggery (for a furnace efficiency of 20% and COP of 0.5) to 37.49 MJ/kg jaggery (for a furnace efficiency of 30% and COP of 0.5). This suggest that, for minimizing the energy demand in jaggery making, efforts may be made to improve the process lines, furnace designs and refrigeration units to have higher efficiencies and higher COPs.

4. CONCLUSION

Compared to refined sugar, non-centrifugal sugar (Jaggery) is an alternate sweetener that contains nutritious molasses which is retained during the preparation process. Jaggery is conventionally produced by evaporating the water in sugarcane using bagasse as fuel. These conventional techniques, employed in the large unorganised industrial sector in India, are highly energy inefficient thereby resulting in higher energy demand, fuel shortages and associated demerits. Analytical assessments were attempted to find alternate jaggery production method that reduces the energy demand in jaggery making. Thermal modelling of three processes for water removal through (a) evaporation (b) freezing and (c) combination of evaporation and freezing was presented in this paper. These models were used to assess the energy demands in these three processes. A large data base was created for the computed energy demands for various percentages of water removed, furnace efficiencies and refrigeration COP's. It had been observed that energy demand was reduced with increase in furnace efficiencies and COPs. It had also been observed that energy demand was less when large amount of water was removed by freezing process. However, since the sucrose solidifies and combines with ice if more than 63% of water was removed by freezing, it was identified that, for minimizing energy demand, 63% of water can be removed by freezing and remaining by evaporation. The combined process seems to be a viable option to move forward as the energy demands are quite low compared to the conventional process. This can further help in saving fuel required for evaporation process. Since, it is seen that refrigeration units involving higher COPs have not shown remarkable reduction in cooling load requirements, thus a refrigeration system utilizing low-grade energy (such as solar energy, industrial waste heat) can be considered for these refrigeration purposes.

5. ACKNOWLEDGEMENTS

The work presented here in this paper is a part of the project "Sustainable technological solutions for energy efficiency in jaggery industry (STEEJ)" funded by Royal academy of Engineering (RAE) vide project reference # IAPP1R2\100083. The authors gratefully acknowledge the RAE for funding this project.

6. REFERENCES

Anwar, S. I. (2010) 'Fuel and energy saving in open pan furnace used in jaggery making through modified juice boiling/concentrating pans', *Energy Conversion and Management*. Elsevier Ltd, 51(2), pp. 360–364. doi: 10.1016/j.enconman.2009.09.033.

Hugot, E. (1986) 'Handbook of Cane Sugar Engineeirng', p. 1166.

Jagannadha Rao, P., Das, M. and Das, S. (2007) 'Jaggery – A Traditional Indian Sweetener', *Indian Journal of Traditional Knowledge*, 6(1), pp. 95–102.

Rane, M. V. and Uphade, D. B. (2015) 'Energy Efficient Jaggery Making Using Freeze Pre-concentration of Sugarcane Juice', *Energy Procedia*. The Author(s), 90(December 2015), pp. 370–381. doi: 10.1016/j.egypro.2016.11.204.

Sardeshpande, V. R., Shendage, D. J. and Pillai, I. R. (2010) 'Thermal performance evaluation of a four pan jaggery processing furnace for improvement in energy utilization', *Energy*. Elsevier Ltd, 35(12), pp. 4740–4747. doi: 10.1016/j.energy.2010.09.018.

Sharon, M. E. M., Abirami, C. K. and Alagusundaram, K. (2013) 'Energy Losses in Traditional Jaggery Processing', *Indian Food Industry Magazine*, 32(3), pp. 22–25.

Shiralkar, K. Y., Sravan , K. K., Narendra, G. S., Sanjay, M.M. (2014) 'Energy improvements in jaggery making process', *Energy for Sustainable Development*. Elsevier Ltd, 18(1), pp. 36–48. doi: 10.1016/j.esd.2013.11.001.

Shrivastav, P., Abhay, K.V., Ramanpreet, W., Rehana, P., Arun, K. S., . (2016) 'Pharmaceutical Jaggery : a Revolution in the Field of Natural Sweeteners', *European Journal of Pharmaceutical and Medical Research*, 3(3), pp. 198–202. Available at: http://www.ejpmr.com/admin/assets/article_issue/1456712434.pdf.

256: Design of three-phase electric energy detection system

Jiarui ZHANG[1], Zhengwang XU[2], Yuchun YI[3], Cheng CHEN[4], Wei MEI[5], Jiaqi YU[6]

[1]Hubei University of Technology, Wuhan, China,jrzhang1994@sina.com
[2]Hubei University of Technology, Wuhan, China, xuzw72@163.com
[3]Hubei University of Technology, Wuhan, China, 15871350521@163.com
[4]Hubei University of Technology, Wuhan, China, 1510795214@qq.com
[5]Hubei University of Technology, Wuhan, China, 790534374@qq.com
[6]Hubei University of Technology, Wuhan, China, 757345365@qq.com

With the rapidly development of economy and technology, the needs of electricity become increasing in production and living. The production of electricity is limited, while there are some energy wasted or electricity unreasonable used in life. Thus to realize the concept of sustainable development, must be guaranteed energy used efficient, reasonable and low loss to bring more benefits to human beings. A power energy detection system is designed. ATT7022CU chip acquires three-phase electric energy parameters through transformers, with STC90C58AD as the main control chip of data receiving module can receive transmited data from data acquisition module. The detection system can transmit all data information to the upper computer by wireless module, and the upper computer can handle the corresponding position through the algorithm. Through the experiment of current and voltage acquisition, the real time and precision of the detection system for power parameter acquisition can be explained according to the data collection results. The system can reduce the loss of power, improve the efficiency of energy, and have large market space of application.

Keywords: electrical energy detection; ATT7022CU; transformer

1. INTRODUCTION

Energy conservation and environmental protection is the key to sustainable development strategy in the 21st century. At present, in China, most of the household electricity supply fails because of overloading or external factors, such as lightning, strong wind and animal damage. And reasons of power loss because of electricity power did not make full use of, such as in a certain period of time without using a certain electrical appliances with the electric equipment is still running, or personnel during the rest time to leave but forget to turn off electrical appliances, thus caused energy waste of electric power.

Aiming at these problems, a power energy detection system is designed for daily using electricity. In recent years, most of the relevant studies were based on STM32 (Zhang, 2010: 90-93), which used digital-to-analog conversion and related algorithms to collect data (Li, 2016: 263-266). Although this method is low cost, it has a small measurable range and complex software design. There are also some detection methods similar to the one in this paper. The ATT7022 series chips are detected and read real-time data by means of mutual inductor and electric energy (Hu, 2016: 59-61). However, the function is single, limited to data detection, and it does not analyze the test data and deal with the running state of the power system (Ni, 2015: 48-51). Power detection system designed in this paper, it can not only real-time monitoring and display circuits of electricity parameters, but also transmit the collected data to the upper computer for processing. PC and make the corresponding feedback, the running state of the paragraphs in the control circuit to reduce the loss of electrical power, guarantee the stability of the circuit system run efficiently. After further improvement, the control system can also be applied to high voltage power transmission sites.

2. SYSTEM COMPOSITION

The structure of the system is shown in figure 1. The ATT7022CU chip collects voltage and current in the three-phase circuit respectively through the voltage transformer and current transformer. ATT7022CU transmits the collected data to the data receiving chip STC90C58AD through SPI protocol, and the data received by STC90C58AD chip can be displayed or transmitted to the upper computer in real time.

The ATT7022CU, a professional power measurement chip, is responsible for collecting the system to provide the accurate date. In normal operation without power off, power supply is provided by the power module. In the case of power off, the external lithium battery is automatically switched to provide power for the clock chip to ensure its continuous operation (Hu, 2016: 59-61). Using STC90C58AD as the detection system of MCU, realize to read and write operations and scheduling system peripheral modules, complete the internal operation, storage and communications, and other functions. Gathering the appropriate data can be real-time display by LCD (Liquid Crystal Display). The external storage module uses EEPROM memory as the acquisition data storage chip to provide the stored historical data for the system. Industrial RS485 interface is adopted to transmit the received data to the upper computer through the wireless transmitting module NRF905 (Liu, 2014). PC using algorithm analysis, in combination with the practical situation of collection sites is analyzed, and the corresponding area make the instruction. To control the load usage in this area, so as to reduce the power consumption and improve the efficiency.

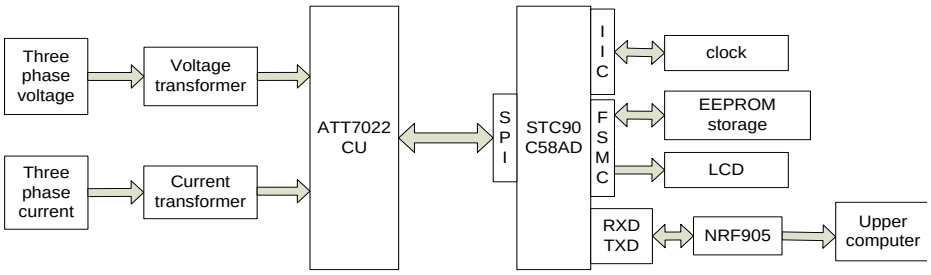

Figure 1: System architecture

3. HARDWARE CIRCUIT

3.1. Power parameter acquisition module

The main control chip is ATT7022CU electricity parameter acquisition module. ATT7022CU chip integrates all second-order sigma-delta ADC, reference voltage circuit, and all power, energy, effective value, power factor and frequency measurement of digital signal processing circuit. It can measure each phase and the conjunction of active power, reactive power, apparent power, active energy and has no function. Every phase current, voltage RMS, power factor, phase Angle, frequency and other parameters can also be measured. Fully meet the requirements of the three-phase compound rate multifunctional meter.

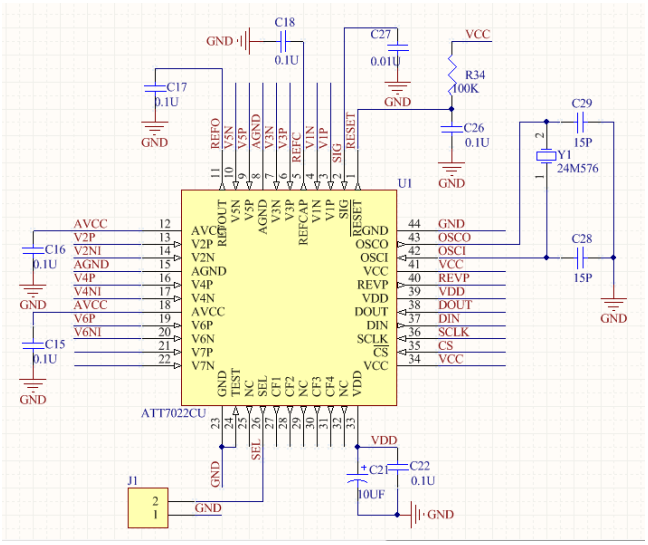

Figure 2: Power acquisition module main control circuit

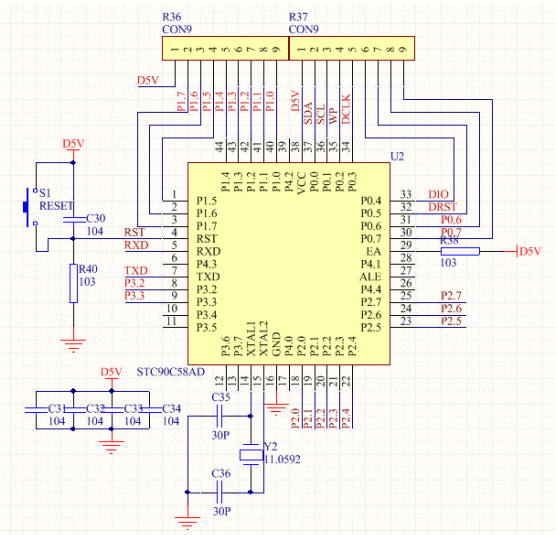

Figure 3: Main circuit of data receiving module

As shown in figure 2, V1P/V1N, V3P/V3N and V5P/V5N are positive and negative analog input pins of input A, B and C phase current channels respectively. V2P/V2N, V4P/V4N and V6P/V6N are positive and negative analog input pins of input A, B and C phase voltage channels respectively. Voltage parameters in the operating line are collected by the external voltage transformer (Han, 2006: 251-255). The ATT7022CU is an in-chip integrated 19-bit ADC and SPI serial communication interface. It works in slave mode and has 7 analog input channels, which are divided into current and voltage channels. The normal work of the current channel for the highest signal level for the +/-0.7 V (p), current channel has a programmable gain amplifier, magnification of 1, 2, 8, 16, and within two pins are ESD protection circuit. The dc offset voltage of input pins V2P and V2N is provided by the reference voltage of 1.2V in the chip REFCAP.

3.2. Power parameter receiving module

Figure 2, resistance and capacitance of the anti aliasing filter, remove the acquisition of some uncertain signal interference caused by the useful signal, and to restrain or eliminate aliasing phenomenon influence on data acquisition. The anti-aliasing filter can not only attenuate and filter useless signals, but also provide a buffer for transient energy generated by ATT7022CU conversion. The ATT7022CU transmits the metering parameters between SPI port and main control board provided by it.

Characteristics by above knowable, using the high performance and low power consumption STC90C58AD as system core processor and multi-functional three-phase meter can chip ATT7022CU as power data acquisition unit.This system can simplify the complexity of the hardware system design of the traditional power monitor, improve the running speed of the system and reduce the power consumption of the system.

Figure 3 shows the main control chip STC90C58AD and some peripheral auxiliary circuits. Through SPI bus protocol, power parameter data collected by data acquisition module are received (Liu, 2013). Data received can be displayed on the LCD screen. In order to realize real-time monitoring of each branch by the upper computer, the main control chip can transmit data to the upper computer in real time through wireless transmission module. The upper computer processes the data according to the received data, analyzes the running state of each branch and controls it accordingly.

4. CONTROL METHOD

Firstly, the system is initialized, and then the voltage parameter on the load and the current parameter on the branch are respectively collected by the voltage transformer and current transformer on the power parameter acquisition module. Then, the power parameter acquisition module transfers the collected data to the data receiving module. Data receiving module according to the received data to PC through wireless transmission module (Yu, 2015: 69-72). PC can judge the running state of the circuit. Main gathering above the load voltage and branch current. The control program is shown in figure 4. The specific control methods are as follows:

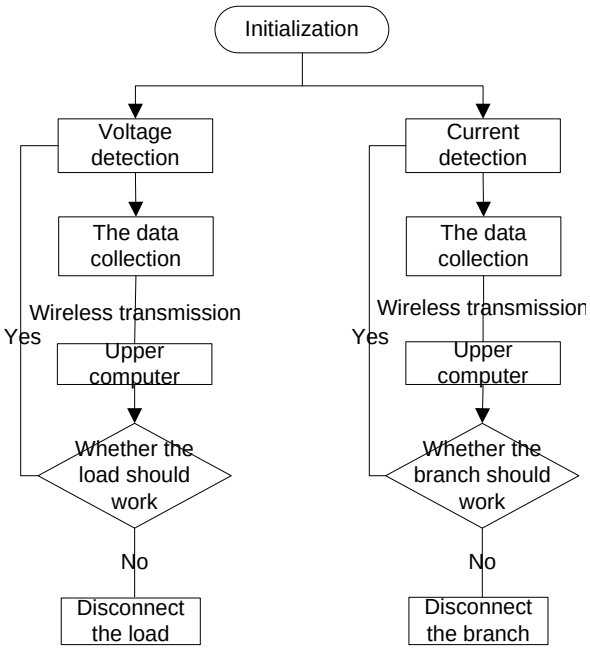

Figure 4: Flow chart of control program

When determining whether the load should work, it is the upper computer that compares the detected line voltage parameters with the actual rated voltage of the load. If the voltage deviation value is within the allowable error range, further judgment is made on whether the load needs to be operated. If the position should be in a dormant state at this time without being in a working state, or if the person in the position has left and forgotten to turn off the power equipment, it is deemed that the load or branch need not be run. If both conditions are met, continue running, otherwise the upper computer issues an instruction to disconnect the load. Similarly, when judging whether the circuit branch should work, the upper computer compares the current parameters of the detected circuit with the rated current of the circuit. If the current deviation value is within the allowable error range, continue to determine whether the branch needs to be run. If both conditions are satisfied, the branch will continue to operate, otherwise the upper computer will issue instructions to control the branch off.

This control method can intelligently control the position that is in the running state without operation, and can realize remote control without the on-site operation of personnel. It not only realizes the intelligence of power system operation, but also can save a lot of power to reduce the loss and improve the efficiency of power utilization.

5. EXPERIMENTAL TEST

According to the foregoing, the experimental platform is built by the electric energy acquisition module and the electric energy parameter reception module, the single-phase current and voltage acquisition test experiment is carried out. Other parameters such as active power, reactive power and power frequency can be monitored in real time.

5.1. Current test

As shown in figure 5, in order to limit current size are meet current range within the scope of transformer in single-phase power supply series access three 51Ω resistance as load. At the same time series in the circuit into the multimeter, used to detect line size and module in the current size of current data collected were compared. A wire in the loop is passed through any center of the three current transformers. At this point, the experiment takes phase B as an example. The experimental test results are shown in figure 5. The current size of the ammeter in the circuit is 1.49A, and it can be seen from the LCD screen that the current detected by the current transformer in the power acquisition module is 1.49A. Comparing the two test results, the error is 1% within the allowable range. In order to avoid the randomness of an experiment, several groups of data were measured as shown in table 1.

Table 1: Current accuracy test

Number	Liquid crystal display（A）	Ammeter display(A)	Error rate
1	0.20	0.18	2%
2	0.49	0.48	1%
3	1.50	1.49	1%
4	2.32	2.30	2%
5	4.43	4.42	1%

According to the data analysis in table 1, the measurement accuracy of this detection system is about 1% within the detection range of the mutual inductor in this system.Therefore, the feasibility of using the system to detect the electric energy parameters in the circuit is illustrated.

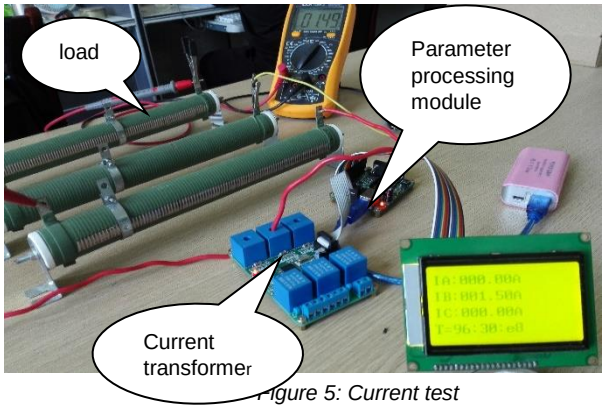

Figure 5: Current test

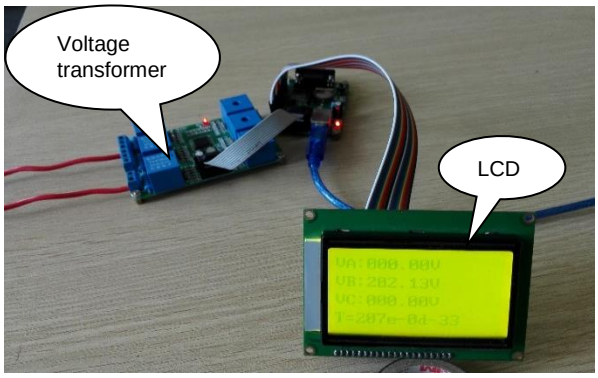

Figure 6: Voltage test

5.2. Voltage test

In order to ensure the accuracy of the various parameters, a similar approach is used to detect the voltage parameter. As shown in figure 6, access to the single-phase power supply, only tests voltage, so don't connected to the load directly to the zero line of single-phase power supply respectively connected to the voltage transformer corresponding port, at this time or in the same phase B, for example.Figure 6 LCD shows the real-time voltage value of the access voltage at this time, indicating that the single-phase voltage at this time is 202.13V. If the load is connected and the voltage parameters at both ends of the load are collected. The upper computer can judge according to the control procedure.

6. CONCLUSION

In order to realize high efficiency utilization of electric energy, a kind of electric energy detection system is designed in this paper. Everywhere in the system can real-time monitor the power lines are in operation.If the collected data is sent to the upper computer for processing, the upper computer can solve the energy waste problem caused by improper use of electric energy in daily life. It can greatly improve the efficiency of electricity utilization, no manual operation, intelligent and convenient, and has a good application prospect.

7. REFERENCES

Zhang X, Qi X, Li S, 2010. Design of power data acquisition system based on STM32. Electronic measurement technology,33 (11) : 90-93.

Li Z, Liu H, Pei C, Wu Z, 2016. STM32 grid short-circuit fault indicator design. Journal of wuhan university of technology (information and management engineering edition), 38(02): 263-266.

Hu Y, 2016. Design of dual-external remote control system based on ATT7022. Information technology and information technology, (07): 59-61.

Ni J, Tan E, Yao P, 2015. Design of ATT7022E and STM32 multi-functional power monitor. Foreign electronic measurement technology, (05): 48-51.

Liu L, 2014. Research on intelligent meter reading system based on Internet of Things technology. Jilin: Northeast Electric Power University.

Han R, Meng F, 2006. Study on a new electronic Watt - hour meter. Journal of Taiyuan University of Science and Technology, 27 (4) : 251-255.

Liu S, 2013. Research and design of multi-function electric quantity measurement instruments based on DSP. Nanchang: Nanchang Hangkong University.

Yu Z, Zhao R, Xia J,2015. Design of network intelligent power monitor based on S3C2410 and ATT7022B. Shandong electric power technology, 43 (03): 69-72.

257: Researching on multiple "Phase Hopping" AC-AC frequency conversion circuit

Yuchun YI[1], Zhengwang XU[2], Jiarui ZHANG[3], Cheng CHEN[4], Jiaqi YU[5], Wei MEI[6]

1Hubei University of Technology, Wuhan, China, 15871350521@163.com
2Hubei University of Technology, Wuhan, China, xuzw72@163.com
3Hubei University of Technology, Wuhan, China, 695922893@qq.com
4Hubei University of Technology, Wuhan, China, 1510795214@qq.com
5Hubei University of Technology, Wuhan, China, 757345365@qq.com
6Hubei University of Technology, Wuhan, China, 790534374@qq.com

Power energy occupies a very central position in all clean energy, and our country also puts a considerable amount of resources in the research and development of electric power. In actual industrial production, the most obvious measure to response the slogan of saving resources actively is the use of cycloconverter. The main characteristics of the motor working condition can be fully used according to this technology. It can not only reduce energy consumption, but also can make performance of the motor in the state of starting improved on a certain basis and accuracy of the motor and load device has great improvement when working state. "Phase hopping" cycloconverter is developed based on traditional cycloconverter. It can increase the output frequency to close to the line frequency, and has the advantages of no circulation current and no dead zone. By combining multiple-stage cycloconverters technology, "phase hopping" cycloconverter can regulate the output voltage and output frequency at the same time. Relative to current frequency converters, it has advantages of large capacity, high voltage level and low cost. The fundamental idea of "phase hopping" is introduced based on the reverse parallel bridge circuit. Taking a sixfold circuit as an example, all of possible voltage results are analyzed according to the voltage vector superposition method, the scope of the voltage variation is summarized from the results. Four groups are chosen as instance and performed simulation with MATLAB in the condition of constant voltage to frequency ratio. Then an experimental platform is set up and the experimental analysis has been carried on. The experimental results are in good agreement with theoretical and simulation studies.

Keywords: Cycloconverters, Multiple-stage, Vector superposition, MATLAB

1. INTRODUCTION

The "phase hopping" alternating frequency conversion connect the output end to the input of different phase using on and off of thyristor, then the frequency conversion is realized. Therefore, it is called "phase hopping" frequency conversion.Direct use of "jump phase" frequency conversion can obtain the output frequency of far ultra traditional alternating frequency conversion frequency, the output frequency can be close to the power frequency, and in the frequency conversion process, there are no circulation and no dead zone. However, output frequency of single phase "phase hopping" in variable frequency conversion circuit can change, output voltage is difficult to change. Combined with the traditional multiple technology, we can make use of the characteristics of independent various heavy output. Vector superposition is carried out for each output voltage (Agarwal, 2012). Different output voltages are obtained by using different angles between different vectors. This technology has a good application prospect in high voltage, high capacity and high output frequency (Komeda, 2017).

2. THE PRINCIPLE OF SINGLE-PHASE MULTIPLE "PHASE HOPPING" FREQUENCY CONVERSION

Multiple "phase hopping" frequency conversion is improved based on single AC-AC frequency conversion. In order to solve the problem of voltage change, the traditional multiple technology was combined with "phase hopping" frequency conversion technology, we can get the actual application of multiple phase "phase hopping" frequency conversion circuit, as shown in figure 4 is sixfold "phase hopping" AC-AC frequency conversion circuit.

In Figure 1, D1D2D3D4D5D6 are basic hand over frequency conversion circuit made up by two same bridge rectifier circuit composed of the parallel, through phase-shifting transformer it input six independent set of three-phase power supply, of which the phase of A1A2A3A4A5A6 differ 10° respectively as same as B1B2B3B4B5B6 and C1C2C3C4C5C6. Because the six groups of three phase power are independent of each other, D1D2D3D4D5D6 will work independently, each weighing circuit output respective an input line voltage, six line voltage combined into six heavy total output voltage of the circuit. For each line voltage is sine wave, the additive of them is vector addition, when the angle between them are different size of voltage vectors are different.For the convenience of analysis, each of the six voltages that can be output can be represented by BC, BA, CA, CB, AB and AC. There are 1~6 differences between six weights, such as BC1, BC2, BC3, BC4, BC5, and BC6. All 36 voltages are represented by vectors, with BC1 as the axis horizontal axis in Figure 2 (DU, 2000:1592-1594).

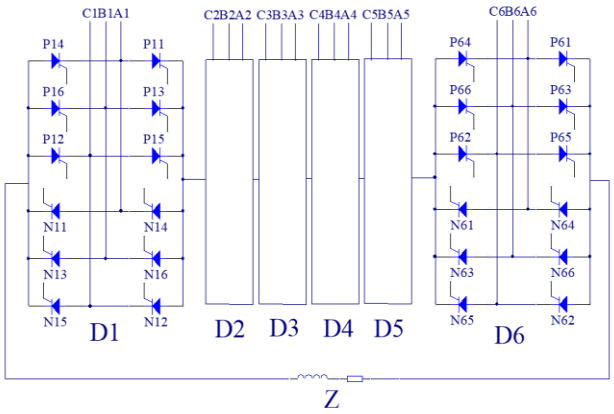

Figure 1: Sixfold "jump phase" alternating current frequency conversion circuit

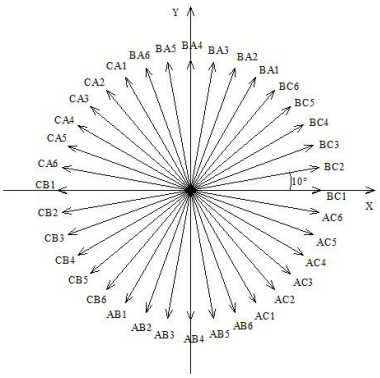

Figure 2: The voltage vector diagram of the hexagonal circuit

Let's suppose that each of these vectors is 1, and we can represent each voltage in coordinates, and they are BC1(cos0°，sin0°)，BA1(cos60°，sin60°)，CA1(cos120°，sin120°)，CB1(cos180°，sin180°)，AB1(cos240°, sin240°)，AC1(cos320°，sin320°)，BC2(cos10°，sin10°) and so on。 The value of the output voltage $|U_{out}|$ is

$$\left|U_{out}\right| = U_0\sqrt{(\cos\theta)^2 + (\sin\theta)^2} \tag{1}$$

Where U_0 is the input line voltage amplitude, according to the above assumption, the value is 1, cosθ and sinθ is the component of the total output voltage of the circuit on the horizontal axis and the vertical axis, and the relationship between them and the input quantity is

$$\cos\theta = \cos\theta_1 + \cos\theta_2 + \cos\theta_3 + \cos\theta_4 + \cos\theta_5 + \cos\theta_6 \tag{2}$$

$$\sin\theta = \sin\theta_1 + \sin\theta_2 + \sin\theta_3 + \sin\theta_4 + \sin\theta_5 + \sin\theta_6 \tag{3}$$

Because each has six different line voltage circuit, from six in the double circuit line voltage into the formula (1), a total of 6×6×6×6×6=46656 different situation, through computer programming calculation, this 46656 different situations six heavy voltage superposition of different voltage amplitude there are 690 species, distributed in the range of 0.026 ~ 5.736, the output voltage range of 0.026 times to 5.736 times the size of the input voltage. It can be considered that the voltage can be changed continuously (Babaei, 2011).

3. SIMULATION

This article uses the simulation effect of frequency and constant voltage frequency ratio. Four sets of data were selected from the above 690 output.

3.1. Simulation model

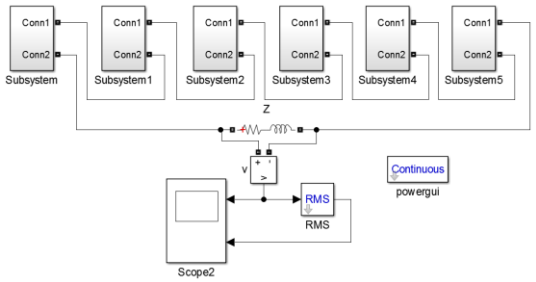

Figure 3: The simulation model of the six-fold "phase hopping" frequency conversion

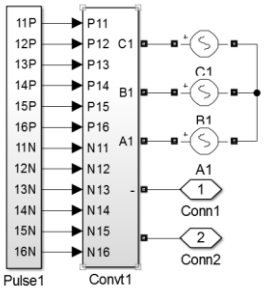

Figure 4: Internal structure of subsystem

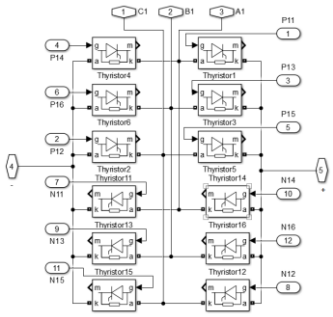

Figure 5: Internal structure of Convt

As shown in Figure 3 is six serious "jump" simulation model of variable frequency. Figure 4 is one circuit simulation model, including trigger pulse generation model. Figure 5 simulation model for the inside of a single circuit. By combining the complex circuit elements together, the simulation model is clear and easy to understand, and Z is the resistance load.

According to the principle of the output constant voltage frequency ratio simulation parameters are set. At the time when the output frequency of 50 Hz, the proportion of the output voltage of 2500 V, U/f = 50, set the maximum line voltage is 2500V output, while the output phase voltage as the input line voltage of 5.7368 times, so the input phase voltage of the three-phase power supply is roughly 2500 / (5.7368×√3) = 358 V. Simplicity, set up six heavy circuit of input phase voltage is 358 v, the sense of resistance load resistance for 5 Ω, inductance is 30 mh.

3.2. The analysis of simulation waveform

According to the calculation of U/f=50, the output phase voltage of 42.86Hz output is 2143V. The following case is selected from 690 cases for each weight output. The resulting simulation waveform is shown in Figure 6.

$$AC1(\sin 300°, \cos 300°) + BC2(\sin 10°, \cos 10°) + BC3(\sin 20°, \cos 20°) +$$
$$BC4(\sin 30°, \cos 30°) + BC5(\sin 40°, \cos 40°) + BC6(\sin 50°, \cos 50°)$$

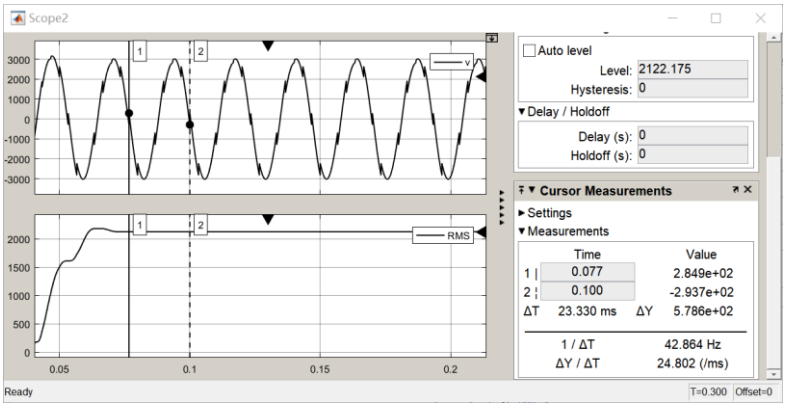

Figure 6: Simulation waveform of 42.86HZ

As can be seen from the Figure 6, the output frequency is 42.86HZ, and the output voltage fluctuates between 2122V. According to output waveform in figure 10, the voltage and frequency are accord with the theoretical analysis. The waveform distortion caused by the jump is small, illustrate its harmonic content is low, the four cases can be got through the simulation analysis of total harmonic distortion rate of 5.97% respectively, in the fan and pump drive system can be used directly or with small capacity harmonic treatment device is used.

4. EXPERIMENTAL VERIFICATION

4.1. The experiment platform

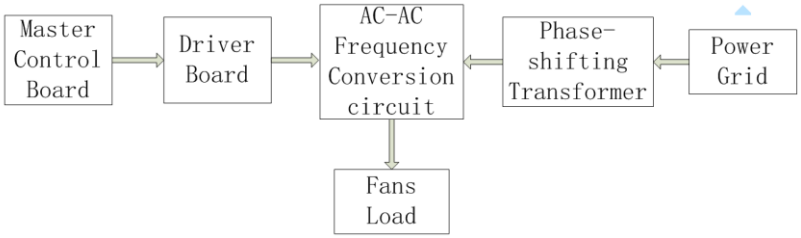

Figure 7: experiment platform

In order to verify the theory of "phase-hopping" frequency conversion, an experimental platform was set up, several experiments were carried out at a low voltage level, and valuable experimental data were obtained.As shown in figure 7, it is a block diagram of the experimental platform, mainly including: master control board, driver board, AC-AC frequency inverter, phase-shifting transformer and fan load.The main control panel USES Cyclone Ⅲ series CPLD, which is EP3C16Q240C8. Its main function is to output the pulse signal required for the crystal gate pipe.The drive plate provides the power amplification function of the trigger pulse. The drive plate also has auxiliary parts such as synchronous detection circuit, current detection circuit and resistance capacitance absorption circuit.The load of the frequency converter circuit is a 2.2kW /220V fan, and the output frequency of the converter can be directly observed by changing the fan speed.

4.2. The analysis of experimental results

On the above six-fold experimental platform, the experimental output waveforms of 42.86Hz frequencies were obtained by setting trigger control signals, as shown in Diagram of Figure 8. The blue wave as the reference input line voltage waveform, the yellow waveform is output current waveform, according to the output frequency 1/ΔT can read in frequency converter. It can be seen that the above theoretical analysis and simulation are in accordance with the above chapters, which verify the correctness of the above chapters' theoretical analysis and simulation analysis.

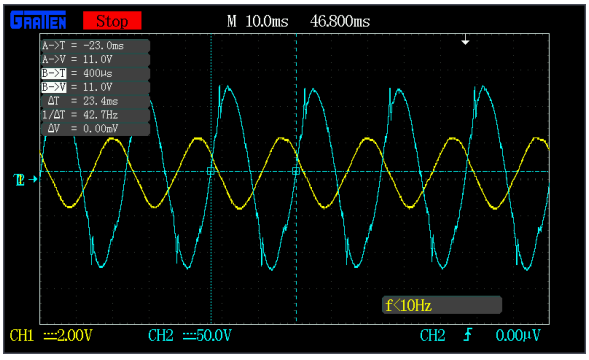

Figure 8: Experimental waveform of triplex "phase-hopping" frequency conversion

5. CONCLUSION

"Phase hopping" frequency conversion method on the basis of the traditional hand over frequency increase the trigger time interval, and triggered thyristor of positive and negative groups at the same time and maintain output is always connected to the same input method. So that the inverter circuit output is close to the high frequency of power frequency, and it overcome the traditional hand over frequency conversion circulation and dead zone.By combining multiple technologies, "Phase hopping" frequency conversion method can gain the ability of voltage regulation, at the same time the system capacity and voltage level are expanded, and the output harmonic content is reduced,"Phase hopping" frequency conversion method can be widely used in the frequency control and speed regulation of fan and pump drive system .

6. REFERENCES

Agarwal A, Agarwal V, 2012. FPGA based variable frequency AC to AC power conversion. Electric Power Systems Research, 90:67-78.

Komeda S, Fujita H, 2017. A High-Frequency Cycloconverter Based on a Phase-Shift Control Method. Electrical Engineering in Japan, 201(3):43-52.

Du Q, Wang X, Chen L, 2000. A fuzzy control algorithm to shape the output waveform ofphase-controlled frequency converters.Intelligent Control and Automation, 2000. Proceedings of the, World Congress on.1592-1594 vol.3.

Babaei E, 2012. A new PWM based control method for forced commutated cycloconverters. Energy Conversion & Management, 53(1):305-313.

260: Analysis of the transmittance of the different coated glass

Jiachen CUI[1,2],Qinghua LV[1,2],Weidong BAO[1,2],Hui LV[1,2], Saffa RIFFAT[1],Yuehong SU[1]

[1]Hubei Collaborative Innovation Center for High-efficient Utilization of Solar Energy，Hubei University of Technology
[2]School of Science, Hubei University of Technology, Hubei, Wuhan, 430068

With the development of coating technology, the application of optical film is increasingly widespread, involving defense, communications, energy and other fields. Among all optical films, antireflective films play an important role and are the most commonly used optical films. Therefore, how to use an optical film having different characteristics to obtain a desired glass transmittance is the subject of current research. In this paper, the coated glass with different functional glass layers has been modulated ZEMAX® software, and the transmittance of the coated glass were analyzed in different wavelengths.

Keywords: Optical films; Transmittance ; Zemax; Different wavelength

1. INTRODUCTION

As an optical material, glass has excellent optical transmission properties in the ultraviolet, visible, infrared, and other wavelengths. Therefore, glass has important application value, In general, the transmittance of the coated glass is low. In order to make the glass have a better transmittance, there are mainly three methods used, namely, reducing absorption, increasing trap structure and reducing reflection. The most common method is coating. The glass coating is made of nano-materials on the surface of the glass to form a high-efficiency AR coating to reduce reflections and increase the transmittance (Li 2017). As a deep processing method of glass, the glass coating technology is to reduce the reflection of light by coating an antireflection film on the glass surface and using the phase interference in the two media of the antireflection film and the glass to cancel out the emitted light.

2. OPTICAL FILM

The optical film refers to a dielectric film, a metal film, or a dielectric metal film that is plated on one or more layers on an optical element or on an individual basis to change the light wave transmission characteristics. Most optical films are used to change the transmission characteristics of light waves through interference, and the interference effect changes with the wavelength. After the light passes through the optical film, the transmission, reflection, polarization, and phase of light at different wavelengths may change differently.

3. MEMBRANE ANALYSIS

3.1. Ultraviolet absorption layer

The surface of glass is often affected by climatic and environmental factors.It attached easily to dust and other pollutants which reduces the transmittance of the glass and the efficiency of film generation seriously. Using the self-made anatase nano TiO_2 thin film with high catalytic activity and good chemical stability, combining TiO_2 film with glass can absorb UV light very strongly, enabling glass to be exposed to sunlight and atmosphere for a long period of time and the performance will not be aged seriously.

In practice, the binding of SiO_2 to glass is relatively easy, while the combination of TiO_2 and glass is more difficult. in order to ensure the perfect combination of film and glass, SiO_2 is coated on the outside of TiO_2. This structure makes TiO_2 not directly bond with glass, so that the film can be permanently and firmly “long” on the surface of the component glass, and can maintain 25 years of service life. Therefore, in editing the film material, it is necessary to first plate a single 200nm SiO_2 and then a single layer 75nm TiO_2 (Nagel 2001), which are required to be plated on the outer surface of the glass. The results of simulation in the 0.38um-0.85um band are shown in Figure 1. Because the specific properties of TiO_2 material itself have strong absorption in the ultraviolet region, the transmittance is lower than 5%. The method of defining the material in addition of *ZEMAX*®, the method of defining the material in *ZEMAX*®, since there is no data in the ultraviolet absorption strongly, the film will be defined in the *ZEMAX*® according to the refractive index of 0.38 um, so no analysis is performed here.

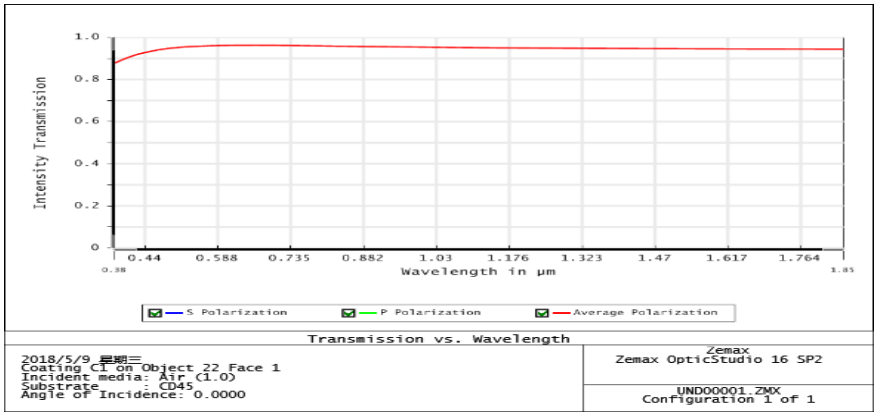

Figure 1: Transmission of Ultraviolet absorption layer in the visible band

From the above picture, we can see that the wavelength is 0.38um, T=0.8803, and up to 0.6404um, the maximum transmission rate reaches 95.28%, then it begins to fall, the final stability of 95%, the average transmittance of the Ultraviolet absorption layer is 94.5% in the visible band.and the uncoated film has an average visible light transmittance of 93%, and the transmittance of the coating is increased by 1%-2%. The film can improve the light transmittance while maintaining the optical properties of the glass, in line with the properties of the TiO2 material (Yang 2010).

3.2. Infrared absorption layer

Since the amorphous silicon optical film material has a low infrared absorption coefficient, a high refractive index (3.0-4.0) (Zhang 2017; Wagner 2017), a high conversion rate of microcrystalline silicon, a high absorption coefficient, and infrared light power generation. Therefore, in this paper, μC-Si is used as a material for absorbing films in ZEMAX®, and μ-Si material is used for analyzing the transmittance in the infrared band. In Figure 1, the backside of the glass is coated with a 600 nm μc-Si film (Minot 1976). The simulation results are shown in Figure 2.

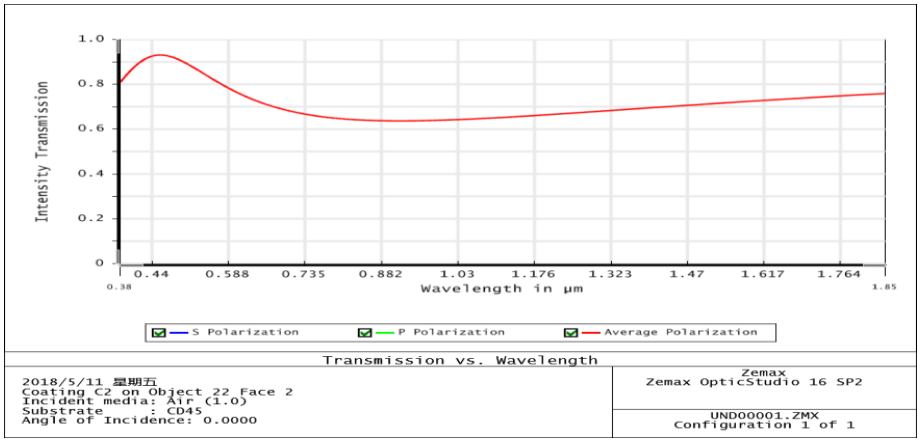

Figure 2: Transmission of the μ-Si film in the infrared band

From the above analysis, we can see that at 0.38um, T = 0.8112, at 0.45um, the transmittance reaches a peak T=0.93 and then it begins to fall. At 0.95um is minimized and T=0.6414. Then it starts to rise. At 1.42um, T=0.7, the transmission rate will continue to rise. It can be seen from Figure 3 that the transmittance between 0.76um and 1.03um is very low, the μc-Si film has a very strong absorption effect in this area, and after 1.03um, the transmittance is low and the transmittance is increasing, the effect is not ideal.in order to make full use of infrared light, a layer of low-E film is coated on the outer surface of 3-glass so that the infrared light is reflected to Infrared absorption layer on the rear surface of the 2- glass. The metal film layer adopts Ag film on the basis of considering the process and cost. In the application of silver film, the transition layer and protective layer usually need to be plated, such as the silver film as the outer reflector, using Al_2O_3 as the transition layer, and SiO as the protective layer (Li 2010). However, the thickness of the silver film is not too thick, considering that the metal film layer also has a large reflection of visible light. Therefore, Al_2O_3 100nm, Ag 3.2nm, SiO 100nm, MgF_2 250nm are plated on the outer surface of the 3-glass. MgF_2 is used to increase the transmittance of visible light (2.4 will be described in detail), and the simulation results are shown in Figure 3.

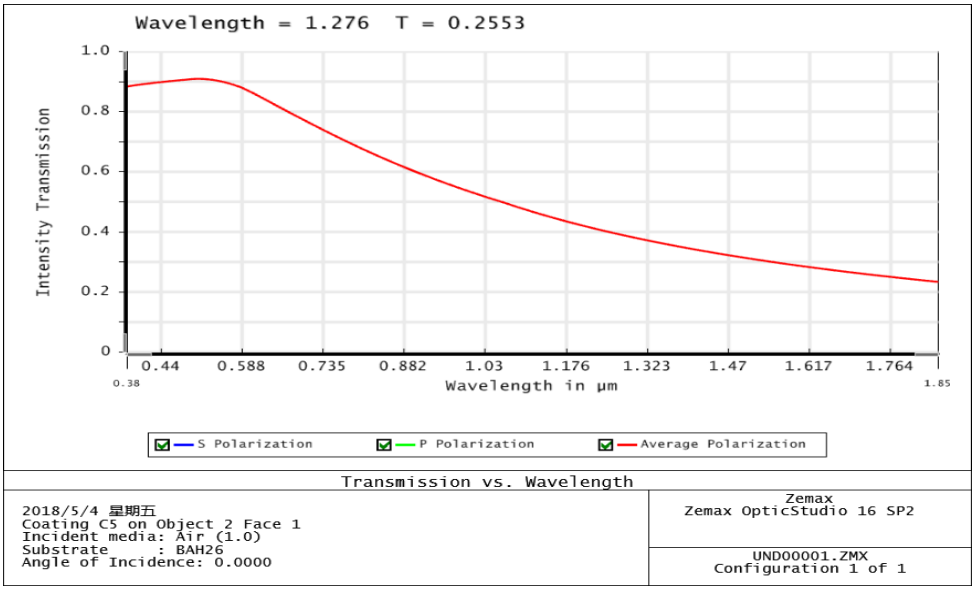

Figure 3: Reflectance of the low-E film in the infrared band

From Figure 3, we can get T=0.88 at 0.38um and then at 0.50um.The transmittance reaches a peak of T=0.91 and then it begins to fall, at 0.76um, T=0.62, at 1.85um, T=0.21, the transmittance in the infrared band has been reduced and the corresponding reflectivity is getting higher and higher.The average transmittance of visible light is about 80% which is in accordance with the low-E glass transmittance of (Wang 2013).

3.3. AR coating

The high transmittance of glass is mainly achieved by the anti-reflection principle of the coating. According to the coating application process, there are two sets of mechanisms that contribute to the anti-reflection process (Zhu 2010). Here we mainly introduce the first type.

The first is interfered with the optical subtraction mechanism.that is when the light is irradiated on the surface of the two medium with different refractive index,a part of the light travels through the interface and the other part of the light will reflect on the surface. If the light is incident perpendicularly, the ratio of the intensity of the reflected light to the incident light (i.e. reflectivity) depends on the ratio of the refractive index of the two adjacent media.

$$R=\left(\frac{1-n_1/n_0}{1+n_1/n_0}\right)^2 \cdot \qquad 1$$

Assuming that light is incident from the air to the glass, the surface reflectivity of R will depend only on the refractive index of the glass because n_0 (the refractive index of the air) is 1. The refractive index of the ordinary optical glass is about 1.52. Beacause the absorption of light in the optical glass is very weak, it is negligible. Therefore, the ratio of light intensity to the incident intensity of a plate glass (the transmittance T) can be easily calculated by the following formula. · ·

$$T=\frac{4n_1}{(1+n_1)^2} \qquad 2$$

However, after a layer of film medium is added to the surface of the glass, the light passes through the transmission model of the single layer film medium And the incident light is reflected at the two interfaces respectively.and the two beams of interference are formed. When the difference between the two beams of reflected light is two times the thickness of the film.the product of the film thickness and the refractive index is 1/4 of the reference wavelength. the optical path difference between two beams is just half the wavelength, thus interference cancellation occurs.T

In the application, due to factors such as cost, the materials used for the antireflection coating under normal circumstances are magnesium fluoride with a refractive index of 1.38 or silica with a refractive index of 1.45. With the use of magnesium fluoride in this article, a layer of MgF_2 film is plated on the outer surface of the glass. Because of this material in the zemax, it is not described in detail. The simulation results are shown in Figure 4, Figure 5. It is indicated that the purity of the glass in the zemax, the glass library is higher than the actual, so the transmission rate is higher than the actual 2%-4%, but it will not affect the analysis of the film layer. ".

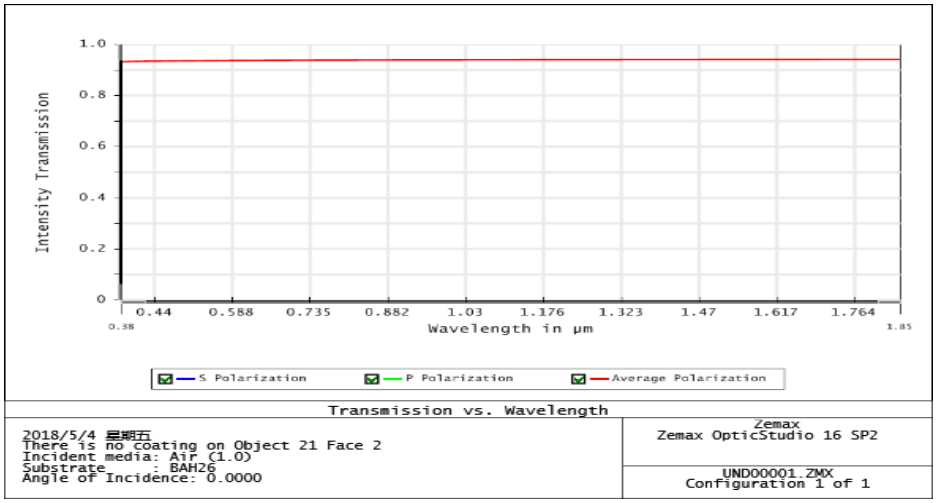

Figure 4: Uncoated film in visible light transmission

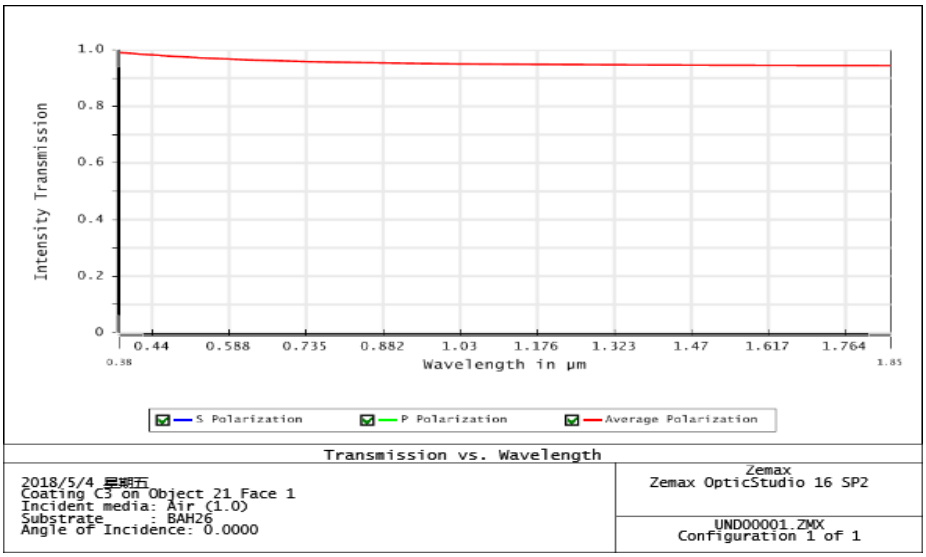

Figure 5: Transmission of AR-coated film in visible light

We mainly consider the transmittance of visible light. In the Figure 4, the average transmittance of the visible light is about 93.5% in the undercoat glass surface. The average transmittance of the glass surface with the film is about 96.5% in the Figure 5. The transmittance of visible light after glass-coated antireflection coating has increased by about 3%.

4. CONCLUSION

This paper mainly uses *ZEMAX*®software to simulate and analyze the optical properties of each layer of glass.

(1) The TiO_2 material used in the Ultraviolet absorption layer absorbs strongly in the ultraviolet wavelength region. At the same time, the transmittance after coating is increased by 1.5%, making the average visible light transmittance about 94.5%. From the simulation results, the average visible light transmittance is over 92.5%, which satisfies the requirement of not less than 92.5% of the photovoltaic transmission (Minot 1976).

(2) the infrared absorption layer is made of micro crystalline silicon material and has high transmittance in the visible light band. It has strong absorption in the infrared wavelength range between 0.76um and 1.03um.

(3) the silver film is used for the low-e film layer. While ensuring the average transmittance of the visible light transmittance of 80%, the infrared light reflection effect is also obviously.

(4) the anti-reflection film is made of mgf_2 material, and the average transmittance of the glass after coating is increased by about 3%. Therefore, the visible light transmittance of the glass can be improved by appropriately setting the antireflection film on the glass surface.

5. ACKNOWLEDGEMENT

This work was supported by International Science & Technology Cooperation Program of China (No. 2016YFE0124300)

6. REFERENCES

Li, J, 2017.Crystal silicon solar cell development status and trend analysis[J]. Science and Technology Innovation and Application,(01):18.

Nagel H, Metz A, Hezel R. PorousSiO2 films prepared by remote plasma-enhanced chemical vapor deposition –a novel antireflection coating technology for photovoltaic modules[J]. Solar Energy Materials & Cells, 2001 (65): 71-77.

Yang J, 2010.Preparation of wave temperature of TiO2 coating and its micro-mechanical properties[C]; Yanshan University.

Zhang, X, 2017.Application Research of Antireflective Self-cleaning Photovoltaic Module Nanofilm Layer[C]; Beijing Jiaotong University. ·

Wagner S. Amorphous silicon: Vehicle and test bed for large-area electronics.physica status solidi. 2010,2017(3):501-509

Li Z; Zhang XW; Han G, 2010.Electrical and optical properties ofboron-doped nanocrystalline silicon films deposited by PECVD[J].physica status solidi.,207(1):144-148 [6] Hao,Xiaoyong; Li,Ru,2006i.Structure and optical properties of microcrystalline silicon thin films[J]. Acta Physica Sinica, (01):55

Wang Z, 2013.Thin film optics and vacuum coating technology[M]. Harbin Institute of Technology Press.

Zhu G; Zhu W, 2010. Low-E vacuum forging film process and equipment[J]. Guangdong Vacuum Society 2010 Annual Conference and Guangdong Province vacuum and low carbon technology exchange conference proceedings · · · ·

Minot M J. Sing-layer, gardaient refractive index antireflection films effective from 0.35 to 2.5 μ[J].J.Opt. Soc. Am, 1976, 66(6):515-519.

261: A quantitative evaluation on ecological city construction level of urban agglomeration in the middle reaches of Yangtze River

Yanhua ZHANG[1,2,3], Tongyu LI [1], Zixi YU [1]

[1] the College of Economic and Management, Hubei University of Technology, Nanli Road No.28, Hongshan District, Wuhan City, Hubei Province, China, 2039076986@qq.com
[2] the Research Center of Circular Economy Development in Hubei, Nanli Road No.28, Hongshan District, Wuhan City, Hubei Province, China
[3] the Collaborative Innovation Center of Regional Industrial Ecology Development, Hubei University of Technology, Nanli Road No.28, Hongshan District,Wuhan City, Hubei Province, China

Eco-city has become an inevitable product of sustainable development of the world's cities. Based on the eco-city concept and the index system proposed at home and abroad, we inherit the basic ideas and principles of the relevant theoretical concepts of ecological cities at home and abroad. Starting from the ecological and ecological city development model, we believe that ecological cities are based on the concept of ecological civilization to establish a coordinated and sustainable human habitat for economic, social and natural development. We explores further, and establishes an index system based on three subsystems: living and working in peace, resources and environment, and development potential. Through factor analysis methods, it is applicable to city-level cities in the middle reaches of the Yangtze River. The 28 eco-city developments were ranked for evaluation. According to the scores and development status of the factor analysis model of each ecological city, the development level of the ecological city in the middle reaches of the Yangtze River is divided into three stages: developed ecological city, developing ecological city, and backward ecological city. The ecological cities in the prefecture-level cities in the middle reaches of the Yangtze River include 10 developed ecological cities such as Wuhan, Nanchang, Changsha, Yingtan, Jingdezhen, Xinyu, Ezhou, Xiangtan, Huangshi, Pingxiang; 6 developing ecological city such as Yichun, Zhuzhou, Jingmen, Jiujiang, Loudi, Changde; 12 backward ecological cities such as Fuyang, Fuzhou, Jingzhou, Huanggang, Yiyang, Yueyang, Xiaogan, Ji'an, Shangrao, Hengyang, Changde, Xianning. The proportion of developed and developing ecological cities in the middle reaches of the Yangtze River has reached 57.14%. Among them, the level of ecological cities in Jiangxi Province is higher than those in Hubei and Hunan.

Keywords: Urban agglomeration in the middle reaches of the Yangtze River, factor analysis, index system, phase division of ecological cities,ecological city

1. RESEARCH BACKGROUND

In the environment where the deterioration of the ecological environment, depletion of resources, global warming and other issues are endangering the sustainable development of countries around the world, the pursuit of green development has become the consensus of all countries. Eco-city has become an urban development model that pursues the greatest degree of reduction of resource consumption, protection of the ecological environment, and construction of a socially livable city, and is consistent with the concept of sustainable development. Wuhan City Circle, Changsha-Zhuzhou-Xiangtan City Cluster, and Central Poyang Lake City Cluster with Wuhan, Changsha, and Nanchang as hubs are developing very rapidly. They have formed a number of small and medium-sized cities and small towns with distinctive features, and have a relatively large ecological capacity (Liu 2015).

2. LITERATURE REVIEW

2.1. Literature review on the related theories of eco city

In recent years, domestic and foreign scholars have conducted in-depth research on ecological cities from different perspectives. We inherit the basic ideas and principles of the relevant theoretical concepts of ecological cities at home and abroad. We believe that ecological cities are based on the concept of ecological civilization to establish a coordinated and sustainable human habitat for economic, social and natural development. The urban development model of vigorous economic development, efficient use of resources, a healthy cycle of ecology, a clean and beautiful environment, social living, and a comfortable and healthy life is a mutually beneficial symbiotic structure formed by the integration of nature, cities, and people as an organic whole.

Table 1: Eco-city concept

Theory	The origin of the concept	Eco-city concept
Urban ecological development	UNESCO	Ecological city "is the result of urban ecological development; it is a human living form of social harmony, economic efficiency and ecological virtuous cycle. It is a mutually beneficial symbiotic structure formed by the integration of nature, cities and people into an organic whole" (Zhang 2015)
	Song Yongchang	Eco-city should be a city with beautiful environment, healthy and comfortable life, best use of human resources, best use of resources, harmonious development of humans and nature, and an ecologically sound cycle (Song 1999)
Ecological city construction	Kline	A typical ecological city should include four features that are integrated with natural ecology, economic security, and high quality of life, and that those in power can be responsible (Kumar 2014)
Ecological city development model	Gu Xiaoyan	“Eco-city is a mode of urban development that seeks to minimize resources and energy consumption, protect the environment, and build a livable environment. It is also a new direction for the transformation and development of China’s industrialization and urbanization under the background of ecological civilization (Gu 2015)
Ecological principles	Mi Kai and Peng Yu	“Eco-city is a type of society-economically-natural coordinated development based on ecological principles. It is mainly used in urban planning, design and management.” (Mi 2014)

2.2. Literature review of eco city index construction

Foreign scholars have more in-depth research on the eco-city index system. Simon Joss (2010) pointed out through research that when choosing an eco-city construction indicator, it should be considered from three aspects: the scale of indicators, the areas covered by the indicators, and the indicators Available policy support (Joss 2010). Andy Scerri and Paul James (2010) pointed out that when formulating eco-city indicators, the influencing factors considered should include the social sciences, fully study the value of qualitative indicators, and formulate indicators that allow residents to be willing to accept (Scerri 2010). For the research and establishment of the eco-city index system by domestic scholars and institutions, we summarizes the following 11 eco-city index systems.

Table 2: the 11 indicator system of experts

The source of the index	Index setting dimension	The ecological index
Ye Zuda (2014)	Urban functions, green transportation, energy and resources, ecological environment, green building and social harmony.	The comprehensive volume rate of construction land, the proportion of clean energy public transportation, the proportion of renewable energy, the classification and collection rate of domestic waste, the local plant index, the employment housing balance index, etc.
Mi Kai, Peng Yu (2014)	Ecological environment, economic development and social progress	Poor air quality and medium days, recycled waste (or utilization), the proportion of environmentally friendly products in total consumption, public transport coverage, the number of juvenile delinquency cases, etc

Zhou Junqing (2014)	Environmental friendliness, resource conservation, scientific development and social harmony.	Per capita public green area, garbage utilization rate, employment housing balance index, affordable housing ratio, etc.
Qiu Baoxing (2012)	Social, economic, environmental, resource classes	The proportion of affordable housing, regional economic coordination, natural wetland net loss, hazardous waste and domestic waste (harmless) treatment rate, etc
Li Xun, Liu Yan (2011)	Resource saving, environmental friendliness, economic continuity, social harmony, and innovation leading	The utilization rate of regenerated water resources, the utilization rate of domestic waste resources, the energy consumption of unit GDP, the collection of the per capita public library, the level of the classification and recovery of municipal solid waste, etc.

2.3. Literature review of ecological city stage division

There are few experts and scholars studying the division of ecological city stage now. Most experts and scholars only evaluate the development level of the ecological city and rank the development of different ecological cities in a certain region. Guan Hailing and Sun Yujun (2012) make a comprehensive evaluation on the development of low carbon ecological cities in the province of China, and to the low carbon eco city in the whole country (Guan 2014). The regional division is divided into eastern, central and western regions. It is considered that the low carbon eco cities in the eastern provinces have a higher level of development, and the development level of the provinces in the middle and western regions is low. Ding Ding (2015) divided 36 low carbon pilot cities in China into four categories, namely, the leading type, the latter type and the exploratory type four. The development level of the urban agglomeration of the middle reaches of the Yangtze River is divided into three stages: the developed ecological city, the developing ecological city and the backward ecological city.

3. THE INDEX SYSTEM OF ECOLOGICAL CITY

3.1. Construction principle of eco city index system

Ecological city construction, that is, building a compound ecological city of sustainable development ("eco city green paper 2015"), in the process of urban sustainable development and complex ecological development, the index quantized can reflect the operating state of the evaluation subsystem and the index elements of various aspects of the urban agglomeration in the middle reaches of the Yangtze River. Therefore, the evaluation of the analysis students The index system should be set up when the development level of a city is developed. When constructing the index system of eco city, we should follow the principles of scientificity, systematization, coordination and maneuverability.

3.2. Index selection and naming of Ecological City

We establishes an index system to evaluate ecological cities from the three subsystems of living and working in peace and contentment, resources and environment, and development potential. With reference to the establishment of the index system of internal and external experts, 13 indicators have reference to the establishment of the index system of internal and external experts, 13 indicators have been selected.

Table 3: Eco city development index system

Total target layer	Sub target layer	Standard layer	Index layer	Calculation formula
Ecological city construction level of urban agglomeration in the middle reaches of the Yangtze River	living and working in peace and contentment	The degree of infrastructure construction	LPG supply per 10000 people	LPG gas supply / year-end total population (10000 persons)
			Number of ordinary college students per 10000 people	Number of students in Colleges and universities / end of the year (10000 persons)
			Every ten thousand people have a bus (car)	
			Per capita GDP	Total GDP / total population at the end of year
		Comfort level of residence	Green coverage rate of built-up area (%)	Green area of built-up area / built-up area * 100%
	resource and environment	Environmental friendliness	Per capita industrial smoke and dust removal	Industrial dust removal / total population at the end of the year
			Emission of sulphur dioxide per capita	
		Sustainability of resources	Natural population growth rate (per thousand)	(number of births per year - number of deaths per year) / annual average number x 1000 per thousand
			Comprehensive utilization of industrial solid waste (%)	The total amount of industrial solid waste / industrial solid waste utilized is 100%.

	the development potential	Economic development potential	GDP growth rate	The comparable price of GDP/ this year is comparable to that of GDP * 100%-100%.
			The number of theaters per million people.	Number of theaters / year-end total population (millions of people)
		Personal development potential	Per capita educational expenditure	Education expenditure / total population at the end of the year
			Mobile phone number of users at the end of the year	

Living and working in peace and contentment subsystem: Per 10000 people of LPG supply (tons), the number of ordinary higher school students per 10000 people (people), every 10000 people with bus (car) and per capita GDP (yuan) mainly reflect the people's life, travel and learning in the city, so it is named as the establishment of infrastructure. The green coverage rate (%) reflects the living environment and living environment of the people, so it is named comfort degree.

Resource and environment subsystem: The target per capita industrial soot removal (kilogram) and the per capita emission of industrial sulfur dioxide (kg) mainly reflect the environmental pollution and environmental protection of the city, so it is named environmental friendly. The natural growth rate of the target population (per thousand) and the comprehensive utilization rate of industrial solid waste (%) mainly reflect the status of urban population resources and resources utilization, so it is named as resource sustainability.

The development potential subsystem: The index GDP growth rate and the number of theaters per million people are mainly reflected in the booming economic development of the city, so it is named the potential of economic development. The per capita educational expenditure (yuan) and the number of users at the end of the year of the mobile phone (tens of thousands of households) mainly reflect the favorable conditions for the individual development of the urban residents, so they are named as individual development potential.

4. BASED ON FACTOR ANALYSIS, THE EVALUATION OF ECOLOGICAL CITY IN THE MIDDLE REACHES OF THE YANGTZE RIVER

4.1. Sample selection and data sources

We obtained data from the statistical yearbooks of cities from 2005 to 2016, the statistical yearbook of China, and the regional statistical yearbook of China. We used SPSS software to analyze the data from 2005 to 2016 for the eco city of the middle reaches of the Yangtze River (He 2015). After the standardized processing of sample data, the KMO value is 0.623, more than 0.5, the significant level of the statistical value of Bartlett sphere is 681.270, which indicates that the number of samples is sufficient and the correlation coefficient matrix is non unit matrix, so the factor analysis can be carried out (Fang 1989). Taking the common factor extracted by factor analysis as shown in Table 4, 6 common factors were extracted, and the cumulative variance contribution rate was 72.086%.

Table 4: Total variance decomposition table

No.	The sum of the squared loads of the rotated factors		
	Characteristic root	Variance contribution rate	Cumulative variance contribution rate
1	3.028	23.291	23.291
2	1.817	13.979	37.269
3	1.328	10.215	47.485
4	1.137	8.747	56.232
5	1.04	7.996	64.228
6	1.022	7.858	72.086

4.2. The rationality test of the index system

The factor analysis method is used to rank the comprehensive evaluation of the ecological city development level. The data after the finishing are entered into the SPSS16.0 software, the correlation coefficient matrix of each variable is calculated and its eigenvalues are calculated.

Table 5: The load coefficient of common factor after rotation

Public factor	factor	Orthogonal rotation	Oblique rotation
The degree of infrastructure construction	LPG supply per 10000 people (tons)	0.861	0.851
	Number of ordinary college students per 10000 people	0.834	0.789
	Every ten thousand people have a bus	0.804	0.786
	Per capita GDP	0.698	0.765
Comfort level of residence	Green coverage rate of built-up area (%)	0.933	0.859
Environmental friendliness	Per capita industrial smoke and dust removal	0.873	0.863
	Emission of industrial sulphur dioxide per capita	0.873	0.825
Sustainability of resources	Natural population growth rate (per thousand)	-0.737	-0.709
	Comprehensive utilization of industrial solid waste (%)	0.728	0.641
Economic development potential	GDP growth rate	0.758	0.652
	Theater per million people. Number of theaters	0.519	0.605
Personal development potential	Per capita education expenditure	0.798	0.772
	Mobile phone number of users at the end of the year (tens of thousands of households)	-0.54	-0.605

First the amount of LPG supply per 10000 people, the number of ordinary higher school students per 10000 people, the bus and the per capita GDP per 10000 people are large, and the symbol is consistent, which indicates that the positive correlation between the three people is strong and can be classified as the infrastructure construction degree; second public factors in the industrial smoke and dust removal per capita are removed. Both the amount and the per capita industrial sulfur dioxide emission factor load are both large and consistent, indicating that the positive correlation between the three is strong and can be classified as environmental friendliness; the natural growth rate (per 1000) and the comprehensive utilization ratio (%) factor of industrial solid waste in third public factors are larger, and the opposite sign shows the reverse between the two. The relationship can be summed up as resource sustainability; the GDP growth rate in fourth public factors and the theater of every million people. The number of theaters is larger and the symbol is consistent, indicating that the positive correlation between the three parties is strong and can be classified as the economic development potential; fifth of the fifth public factors and the number of users of the mobile phone at the end of the year are compared. Large, and the opposite sign, indicating the reverse relationship between the two, can be classified as the individual development potential; the sixth public factor of the built-up area afforestation rate (%) factor load is larger, can reflect the living comfort level. The division of the six types of public factors is consistent with the previous benchmark analysis, thus fully demonstrating the rationality of the index system for constructing the eco city in this paper (table 5).

4.3. Result of factor analysis

We used SPSS software to mark the development of 28 eco cities in the cities of the middle reaches of the Yangtze River from 2005 to 2016. From 2005 to 2016, we can see that Wuhan, Changsha, Xinyu, Nanchang, Ezhou, Jingdezhen, Huangshi and Pingxiang are in the top ranking, and the top 10 are in the first place every year. Since the new ecological city will be added almost every year, the ranking of some ecological cities will change greatly. It seems to be backward in ranking. In fact, it has always been at the end of the city, such as Fuzhou and Jingzhou (figure 1).

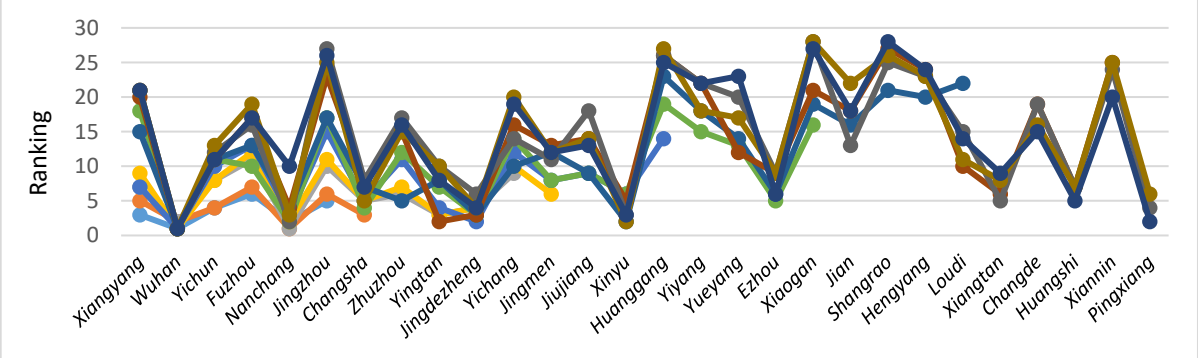

Figure 1: Comparison ranking of eco-cities from 2005 to 2016

5. DEVELOPMENT STAGES OF ECO CITY IN THE MIDDLE REACHES OF YANGTZE RIVER

Based on the above analysis, we divide the 28 eco cities into three types: the developed ecological cities, the developing ecological cities and the backward eco cities.

The developed eco cities basically meet score>0, and the urban construction of ecological city has strong momentum, which includes 10 ecological cities, including Wuhan, Nanchang, Changsha, Yingtan, Jingdezhen, Xinyu, Ezhou, Xiangtan, Huangshi and Pingxiang.

The developing ecological city is changed from score<0 to score>0, and the scores are obviously rising. The cities with good ecological city construction include 6 ecological cities in Yichun, Zhuzhou, Jingmen, Jiujiang, Loudi and Changde.

The backward ecological cities basically meet score<0, and the cities with poor ecological urban construction have no obvious improvement trend, including 12 ecological cities, including Xiangyang, Fuzhou, Jingzhou, Huanggang, Yiyang, Yueyang, Xiaogan, Ji'an, Shangrao, Hengyang, Changde and Xianning.

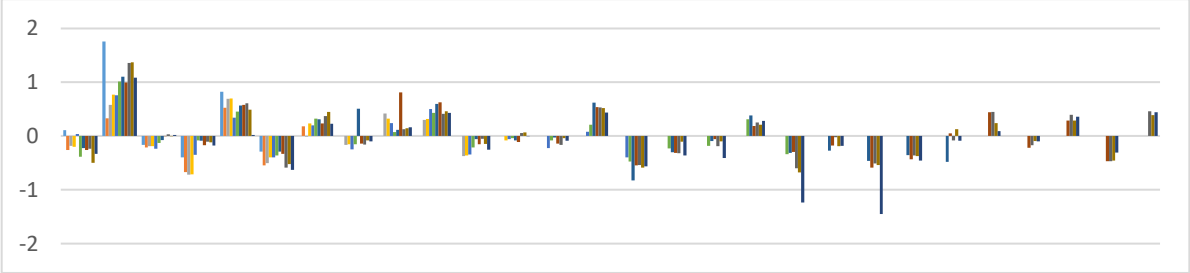

Figure 2: scores of eco-city in 2005-2016

After dividing the ecological cities into three types of developed eco cities, developing eco cities and backward eco cities, we have found that among the three provinces of Jiangxi, Hubei and Hunan in the middle reaches of the Yangtze River, the types of ecological cities can be seen in Table 6. Among them, the proportion of the developed and developing ecological cities in the urban agglomeration of the middle reaches of the Yangtze River is 57.14%, and the development level of the urban agglomeration in the middle reaches of the Yangtze River shows a good situation.

Table 6: Distribution table of ecological cities in three provinces

province	developed ecological cities	Developing ecological cities	backward ecological cities	Proportion of developed and developing ecological cities
Jiangxi	Nanchang,Yingtan, Jingdezhen, Xinyu, and Pingxiang	Yichun, Jiujiang, and Loudi	Ji'an, Shangrao and Fuzhou	72.73%
Hubei	Wuhan,Ezhou, and Huangshi	Jingmen	Xiangyang,Jingzhou,Huanggang,Xiaogan,and Xianning.	40%
Hunan	Changsha、Xiangtan	Zhuzhou、Changde	Yiyang, Yueyang,Hengyang, and Changde	50%
total	10	6	12	57.14%

6. ANALYSIS AND SUGGESTIONS ON THE DEVELOPMENT OF THREE TYPES OF ECOLOGICAL CITIES

6.1. Analysis and suggestions on the development of developed eco-city

Living and working in peace and contentment eco cities: first, the developed ecological cities of infrastructure construction, such as Wuhan, Nanchang and Changsha, all three cities are provincial capital cities, with a long history and perfect facilities. The two is the developed comfortable eco city, such as Xinyu, Ezhou, Xiangtan, Huangshi and Pingxiang. The green coverage rate of the built-up area is relatively high.resource and environment type developed eco cities: such as Yingtan, resources sustainability and environmental friendliness in this area are more prominent.developing potential developed eco cities: for example, Jingdezhen, the region's economic

development potential and personal development potential are more prominent, especially its personal development potential, which is due to the better development of education and communication in the region.

6.2. Analysis and suggestions on the development of the developing ecological city

The overall development of ecological cities, such as Yichun, Jingmen and Changde, has been continuously optimised in three aspects, such as living and music, resource environment and development potential for the last ten years, and the level of ecological urban development has been steadily rising. Ecological cities in the development of single item, such as Zhuzhou, Jiujiang and Loudi, three regions have developed better in one or two areas, but they have not been able to develop in an all-round way, and the development level of the ecological cities is not stable.

6.3. Analysis and suggestions on the development of the developing ecological city

Through the analysis of the sub-system score of the backward ecological cities, we found that most of the backward ecological cities have low development level in two aspects, such as living, music and development potential, and the development level of the resource environment subsystem is relatively good. Backward eco city has slow economic development and backward construction of various facilities, but its natural resources are abundant and its environment is beautiful.

7. REFERENCES

Liu J, Sun W, Hu W, 2015. Eco city green paper [M]. Beijing: Social Science Literature Press.1-30.

Zhang Q, Deng X, Zhou Q, 2015. The concept, mode and resource utilization efficiency of urban ecological management [J]. China population, resources and environment,25 (06), 142-151.

Song Y, Qi R, 1999. Index system and evaluation method of eco city [J]. Urban environment and urban ecology, 10(05),16-19.

Kumar A, Shaw S R, 2014. 'Eco-city' to 'disaster-resilient Eco-community': A Concerted Approach.

Gu X, 2015. "Curitiba experience" and its inspiration for the construction of Wuhan Sino French eco city [J]. Yangtze River forum, 15 (04), 43-47.

Mi Kai, Peng Yu,2014. Index system of foreign eco city and its application status analysis [J]. China population, resources and environment,24 (S3), 129-134.

Joss S, 2010. Eco-cities-a Global Survey 2009[J].WIT Transactions on Ecology and the Environment,129, 239-25.

Scerri A, James P. Accounting for Sustainability: Combining Qualitative and Quantitative Research in.

Ye Z, 2014. Analysis framework of control detailed planning management system in low carbon ecological urban area -- Taking Taihu eco city project in Wuxi as an example, [J]. Urban development research,21 (07), 91-99.

Zhou J, Xu L Q, He B, 2014. Research on the development of new towns in eco sensitive areas based on elastic thinking -- Taking Huashan ecological new town in Wuhan as an example of [J]. Urban planning, 20 (06), 77-84.

Qiu B, 2012. Situation and task of low carbon eco city construction in China [J]. Urban planning, 12,36 (12), 9-18.

Li X, Liu Y, 2011. Current situation, problems and Countermeasures of the development of low carbon eco city in China [J]. Journal of urban planning, 34 (04), 23-29.

Guan H, Sun Y, 2014. Comprehensive evaluation of the development level of low carbon eco city in China province based on factor analysis [J]. Technology economy, 31 (07), 91-98.

Ding D, 2015. Evaluation of low carbon pilot cities based on index system [J]. China population, resources and environment,10,34-38.

He X, 2015. Multivariate statistical analysis [J]. Beijing: Renmin University of China press, 31,113 -169.

Fang K, 1989. Practical multivariate statistical analysis [M]. Shanghai East China Normal University press,18-20.

264: The study of the growth model of enterprises in Hubei province: “pollution” or “environmental protection”

Based on the research of China’s industrial enterprises database

Yanhua ZHANG[1,2,3], Guilan HUANG[1], Qingwei HU[1]

[1] the College of Economic and Management, Hubei University of Technology, Nanli Road No.28, Hongshan District, Wuhan City, Hubei Province, China, 2039076986@qq.com
[2] the Research Center of Circular Economy Development in Hubei, Nanli Road No.28, Hongshan District, Wuhan City, Hubei Province, China
[3] the Collaborative Innovation Center of Regional Industrial Ecology Development, Hubei University of Technology, Nanli Road No.28, Hongshan District,Wuhan City, Hubei Province, China

With the rapid economic development, environmental pollution has become more and more serious, and the traditional “pollution-for-growth” economic growth model with high mining, low utilization, and high emissions has been increasingly unable to meet the requirements of modern sustainable development concepts. A big consumer of energy, its development model has always been the focus of attention. This paper analyzes the sales growth model of industrial enterprises in Hubei Province using the microscopic data of industrial enterprises in 2004 and the sales growth rate of industrial enterprises in 2005-2009, and analyzes the impact of the level of corporate environmental pollution on its sales growth rate. In this paper, the environmental pollution situation and economic growth pattern of enterprises are measured by whether enterprises are charged with pollutant discharge fee or not The Study found that the sustainable development model in growth than to pollution for more economic growth, is not business of collecting fees for discharging pollutants on the show higher sales growth, indicates that the development of environmental protection enterprises to get faster The“pollution-for-growth”model does not necessarily bring economic growth to enterprises, which indicates that pollution is not a long-term solution for enterprises to develop. The conclusions obtained in this paper provide a reference for promoting energy conservation transformation of industrial enterprises.

Keywords: Sustainable Development; Pollution Growth; Environmental pollution;

1. INTRODUCTION

With the rapid development of our country's society, the rapid growth of the industrial industry has promoted the growth of the national economy and has become China's help to catch up with the developed countries. However, the development of the industrial industry has brought serious harm to the natural environment and the human living environment. In particular, environmental pollution has become a key factor that seriously hinders China's continued development. The unreasonable use of energy and waste cannot be ignored, and some economic development methods lead to There are too many capital inputs, and many companies only use a large amount of resources and energy to increase their production capacity. Rapidly disappearing resources, serious environmental pollution, and degraded ecosystems, the "barbaric" development method at the expense of the environment is no longer suited to the needs of the current society. Therefore, it is particularly important to promote China's economic development model from unsustainable to sustainable, from extensive to intensive, and from a "high-carbon economy" to a "low-carbon economy." In order to accelerate the transformation of our country's economy, we need to study the current economic development model. This paper takes Hubei Province as an example to study the economic growth pattern of industrial enterprises, and analyzes how the level of environmental pollution affects the sales growth of enterprises, so as to obtain the microscopic mechanism of economic growth of industrial enterprises.

In the past, China's economic growth mode has been widely discussed. It is generally believed that there are two growth modes. Some researchers believe that environmental pollution is still an important factor in China's economic growth. There are phenomena of "pollution for growth". Other researchers believe that China's economy is generally consistent with the "sustainable development model." It is difficult for these studies based on macro-data analysis to explain in detail the operating behaviour of micro-industrial enterprises. Therefore, the underlying reasons for China's economic growth have not been exposed. Zhao Wenjuan (2012) used panel data from the micro-level of large and medium-sized industrial enterprises in China in 1996-2009 to study the impact of foreign technology introduction and domestic technology introduction on China's economic growth through fixed-effect variable coefficient models. Zhang Yanlei et al. (2015) analyzed the sales growth model of industrial enterprises in China based on the microscopic data of industrial enterprises, and the influence of environmental pollution levels on the growth of corporate sales. Zhao Changwen and Xu Zhaoyuan (2013) assessed the transformation and upgrading of Chinese companies since the financial crisis through field surveys and questionnaire surveys. The above studies have analyzed the environmental pollution of industrial enterprises and the economic development model of industrial enterprises from a micro perspective, but there are still some deficiencies:

- The research perspective is single. The corporate economic-environmental system is not only a huge and very complex system, it can not simply include one or two factors, such research can not explore in detail the relationship between environmental pollution and corporate economic development model.
- The study only analyzes the two economic development models, but does not delve into the specific methods and measures that change from "pollution for growth" to "sustainable discovery".
- The data lacks representativeness. There is no analysis based on the data of Chinese industrial enterprises above designated size or only the major indicators, but as the remaining control variables, there is no reference to the selection basis.

This paper takes Hubei Province as an example, and analyzes the sales growth model of industrial enterprises from the microscopic point to get the evolution of the macroeconomic model. If industrial companies reduce their exposure to environmental pollution and establish an environmental image in exchange for rapid sales growth, they have already achieved a "sustainable development" model. On the contrary, if companies increase their sales by shirking environmental responsibility, it means that they adopt the "pollution-for-growth" development model. This paper analyzes the environmental pollution status of industrial enterprises through whether they are charged with pollutant discharge fee and the amount of pollutant discharge fee. First of all, it analyzes whether environmental protection enterprises that are not charged with pollutant discharge fees can achieve high sales growth rate. Second, it analyzes the enterprises that are charged with pollutant discharge fees in the sub-samples. Compared to previous studies, this paper has the following contributions:

- This article explores the macroeconomic development model from a micro perspective, analyzes two growth models of "sustainable development" and "pollution for growth", supplementing the previous research insufficiency;
- The best way for the development of industrial enterprises is to choose the basis for the "sustainable development" model;
- The data selection is well-founded and the data used is derived from the "China Industrial Enterprise Database" published by the China Bureau of Statistics. It is the most authoritative micro-enterprise data available now. Relatively more time-sensitive than previous studies to ensure the correctness of the conclusions.

2. ANALYSIS OF MICRO-MECHANISMS, SOURCES OF DATA, AND STATUS OF CHARGES FOR DISPOSING POLLUTANTS IMPOSED ON INDUSTRIAL ENTERPRISES

2.1. Analysis of the micro-mechanism of the "sustainable development" and "pollution-for-growth" development model

There are two types of corporate economic growth models, namely “for pollution” and “sustainable development”. Byrne (1997) believes that economic growth is mostly at the expense of the environment, resulting in “for pollution”. Tang Weibing (2014) and other scholars believe that investment in technology in environmental protection will not only promote the improvement of the ecological environment, but also stimulate domestic demand and increase employment opportunities. This is a necessary condition for sustainable development. China's environmental pollution occurs mainly in the production process of industrial enterprises. Therefore, the use of micro-data of industrial enterprises is more suitable for analyzing China's macroeconomic "growth for pollution" and "sustainable development" growth model.

Industrial economy is the main body of China's macro economy. In the long run, the growth in the sales of industrial enterprises at the micro level is an important force for stimulating macroeconomic growth. Industrial enterprises can obtain good environmental performance by gaining consumer recognition of enterprises and increasing production efficiency, upgrading production equipment, reducing environmental pollution, and using waste, and increasing the sales growth rate of enterprises. This can correspond to the "sustainable development" macroeconomic development model. If the delay in production equipment is upgraded or a low-cost and highly polluting production equipment is used to obtain the advantages of production cost, a higher sales growth rate can be obtained. This kind of development model that seeks economic growth by destroying the environment is consistent with the macro development model of “pollution-for-growth”.

2.2. Sources of data

The data used in this paper was obtained from the "China Industrial Enterprise Database" published by the China Bureau of Statistics. The data of micro-industrial enterprises in Hubei Province was used as an example to analyze the impact of environmental pollution on its sales growth rate, and the use of industrial enterprises was charged with charges for disposing pollutants. Situation to measure its level of environmental pollution. Of the industrial enterprise data released in 1995-2013, only 2004 included figures on pollution discharge fees. In addition, the Chinese environmental protection agencies still enforced the "Standard Management Measures For Collection Of Pollution Discharge Fees " issued in 2003. Therefore, this article uses Hubei Province's industry in 2004. Corporate census data.

According to the survey data of industrial enterprises above designated size in Hubei Province from 2005 to 2009, the sales growth rate of industrial enterprises was calculated to analyze the impact on the development of enterprises after the 2004 collection of pollution discharge fees. Although the "China Industrial Enterprise Database" enterprise data is up to 2013, it is only open to the outside world in 2009. Since then, the data has not been disclosed to the public. The data in this paper is available for the latest data. The data for 2005-2009 has been widely used by scholars at home and abroad, so it is still meaningful to study these data. Such as Bao Qun (2011), Chen et al. (2011), Kotabe et al. (2010) and so on. This paper merges the census data of Hubei Province in 2004 by the National Bureau of Statistics and the survey data of industrial enterprises above designated size in Hubei Province from 2005 to 2009. Delete missing variables, abnormal variables and the final 1,333 sample industrial enterprises were obtained, of which 578 were to collect pollution discharge fees.

2.3. The status of pollution discharge fees imposed on industrial enterprises

China currently adopts a method of collecting pollution fees from polluting enterprises to deal with environmental pollution. In 2003, the State Council promulgated "Standard Management Measures for Collection of Pollution Discharge Fees", and it will come into effect on July 1 of the same year. Enterprises that directly discharge pollutants into the environment must pay pollution discharge fees in accordance with the provisions of the Measures. In addition, it also includes specific pollution discharge fees collection standards and calculation methods. Therefore, the environmental pollution of industrial enterprises is to some extent reflected by whether the company has been charged with pollution discharge fees and the amount of pollution discharge fees collected. If an enterprise is levied pollution discharge fees, it means that the company has caused pollution to the environment during the production process. The higher the company's pollution discharge fees are, the more pollutants the company emits, and the more serious the pollution and damage to the environment will be.

Table 1 shows the status of pollution discharge fees collected by sample industrial companies. Among all 1,333 sample industrial enterprises, 578 companies were levied with pollution discharge fees, accounting for 43.36% of the total sample. 1333 industrial enterprises were charged an average of 13.851 million yuan in pollution discharge fees. There is a big difference in the amount of pollution discharge fees collected between different companies. The standard deviation is 1.5402 million yuan, and the minimum is 1,000 yuan and the highest is 35.727 million

yuan. The proportion of pollution discharge fees to operating income averaged 0.14%, the standard deviation was 0.0039, and the highest value was 0.0709. The absolute amount of pollution discharge fees imposed on industrial enterprises accounts for a small proportion of their operating income. The absolute amount of pollution discharge fees levied by industrial companies is small as a percentage of their revenues, which gives highly polluting industrial companies an incentive to trade in growth by paying pollution charges and polluting the environment

Table 1: The situation of pollution discharge fees imposed on sample industrial enterprises

A： The number and relative proportion of industrial enterprises affected by pollution discharge fees

	Enterprises with pollution discharge fees	Enterprises that have not been levied pollution discharge fees	Master Samples
Number of sample industrial enterprises (units)	578	755	1333
The proportion of the total sample (decimal)	0.4336	0.5664	

B： The absolute amount of pollution discharge fees and its relative proportion of operating revenue

	mean value	median	Standard deviation	Minimum value	Maximum value
The absolute amount of pollution discharge fees(ten thousand yuan)	13.851	1.2000	154.0190	0.1000	3572.7
pollution discharge fees as a percentage of operating revenue	0.0014	0.0005	0.0039	0.0000	0.0709

2.4. The collection of pollution discharge fees in various industrial sectors and the definition of “highly polluting industries”

In this paper, the environmental pollution level of the industrial industry is compared according to the relative proportion of the industrial enterprises that are charged with the pollutant discharge fee and the amount of the pollutant discharge fee, and divide the sample industry into two types of industries: “high pollution” and “low pollution”. The industrial sector is based on the two-digit industry code in the "National Economic Sector Classification." The industrial sector division is based on the two-digit industry code in the “national economic industry classification”. This article compares the environmental pollution levels of various industries by the three indicators of “The proportion of enterprises in the industry charged with pollution discharge fees”, “The average amount of pollution discharge fees levied on an enterprise”, and “The average proportion of pollutant discharge fee in business income of enterprises”. To comprehensive analysis of the industry environment pollution level, the principal component analysis was used to construct a comprehensive index, the principal components can explain the variance of 0.6152 changes, representative is stronger, which can be used to analyze the industry's overall environmental pollution levels. “The proportion of enterprises in the industry charged with pollution discharge fees”, “The average amount of pollution discharge fees levied on an enterprise”, and “The average proportion of pollutant discharge fee in business income of enterprises” and the factor loads of all three indexes were positive, respectively, 0.845, 0.582, 0.891. Therefore, all three indicators are positively related to the principal component indicators. The larger the value, the stronger the correlation. According to the factor load, the main components of the environmental pollution levels of various industrial sectors are calculated. The results are shown in Table 2. Since the load of the three index factors of the principal component load is positive, the larger the value of the principal component, the higher the corresponding value of the industrial production process. The more serious the pollution.

According to the data analysis, the overall pollution level of the non-ferrous metal mining industry is the highest. Among the sample industrial enterprises, there is only one enterprise in the industry. This company has also been levied pollution discharge fees, and the levied pollution discharge fees accounted for the company's operating income ratio 0.0014. The value of the main components of waste and waste materials recycling and processing industry is the lowest. In this sample, there are only three waste recycling companies and waste materials recycling and processing industries, and these three companies have not been levied pollution discharge fees. In addition, the overall pollution levels of textile, clothing, shoes and hats are the lowest , In the industry, 0.1905 enterprises were charged with pollution discharge fees ,. The average industry pollutant discharge fee is only 0.4571 million yuan, However, the average proportion of pollutant discharge fee in enterprise operating income is less than 0.01%.

This paper divides the industry into "high pollution industry" and "low pollution industry" based on the principal component index. But consider the different levels of environmental pollution in different industries, this paper will refer to the list of listed companies' classified management of environmental protection verification industry released in 2008. List of the management of thermal power, steel, cement, electrolytic aluminium, coal, metallurgical, chemical, petrochemical, building materials, paper making, brewing, pharmaceutical, fermentation, textile, leather and mining and other 16 classes make further subdivision of heavy pollution industry. Although on July 13, 2016, the ministry of environmental protection issued the decision of the ministry of environmental protection to abolish some regulations and normative documents of environmental protection departments, the list of listed companies on the management of environmental protection inspection industry classification was annulled. However, considering the number of years of data selected in this paper, we can still refer to it to classify the high and low pollution industries. Table 2 shows the pollutant discharge fee levied by high and low polluting industries and the main component index of the environmental pollution level of the industry. Where, the value of the principal

component of "high pollution industry" is greater than or equal to 0.0836, The average value is 0.7887, Including non-ferrous metal mining, paper and paper products, chemical raw materials and chemical products, Because the industry is enterprise of collecting fees for discharging pollutants on the amount of the expropriation and the industry enterprise is the average amount is larger, collecting fees for discharging pollutants on the combined with the policy of the division, so the chemical fiber industry and black metal smelting and rolling processing industry still belong to "polluting industry" .The average principal component value of "low pollution industry" is -0.5811, Including leather, fur, feather (wool) and its products, food manufacturing, etc. Among them, only a small number of furniture enterprises have been charged with pollution discharge fees in the whole sample, and only one enterprise has been charged with a large amount of pollution discharge fees. Therefore, the average amount of pollutant discharge fee levied by enterprises is increased, leading to a large index of the main component, According to the division of policy, accordingly, furniture industry is divided in "low pollution industry". In all 1,333 sample industrial enterprises, there are 467 "high pollution industries" and 866 "low pollution industries".

Table 2: main component indicators of environmental pollution levels of various industrial industries and the situation of pollutant discharge fees levied

Industrial industry	Principal component index	Percentage of pollution discharge fees levied in the industry (Decimal)	The average amount of pollution discharge fees levied on enterprises (ten thousand yuan)	pollution discharge fees account for the average proportion of business revenue (Decimal)
High pollution industry				
non-ferrous metals mining and dressing	2.2758	1.0000	1.0000	0.0014
paper making and paper products industry	2.0141	0.5652	6.3848	0.0014
Manufacture of chemical materials and chemicals	1.7820	0.6186	5.1729	0.0012
Nonmetallic mineral products	1.5140	0.6134	3.5924	0.0012
Wood processing and wood, bamboo, rattan, brown, grass products	0.9017	0.6667	1.9000	0.0008
Coal mining and washing	0.8776	0.4444	2.6111	0.0011
Pharmaceutical industry	0.7025	0.5091	3.6164	0.0007
Non - ferrous metal smelting and rolling industry	0.6060	0.3333	9.3667	0.0002
Non-metal mining and selection	0.5421	0.4000	2.4880	0.0009
Ferrous Metals Mining and Dressing	0.2604	0.4000	1.9500	0.0008
Beverage Manufacturing	0.1461	0.5313	2.3750	0.0003
Petroleum processing, coking and nuclear fuel processing industries	0.0836	0.3333	0.8333	0.0009
Chemical fiber manufacturing	-0.3657	0.2500	3.7500	0.0003
Black metal smelting and rolling industry	-0.2985	0.3333	3.2250	0.0002
Low pollution industry				
Furniture manufacturing	1.2864	0.6000	1.2600	0.0013
Food manufacturing industry	0.0007	0.3684	2.7053	0.0005
Transportation equipment manufacturing industry	-0.1054	0.4844	1.9688	0.0003
Art Products and Other Manufacturing	-0.1708	0.6667	0.0667	0.0001
Farm and sideline food processing industry	-0.1950	0.4806	1.0620	0.0003
Specialized equipment manufacturing	-0.2477	0.3462	1.7019	0.0005
Leather, fur, feather (wool) and its products	-0.3510	0.2857	1.3571	0.0005
General equipment manufacturing	-0.4669	0.4412	0.5520	0.0002
Manufacture of Metal Products	-0.5356	0.3571	0.5810	0.0003
Reproduction of printing and recording media	-0.5507	0.3125	1.6406	0.0003
plastic product industry	-0.6815	0.3333	0.5452	0.0003
Manufacture of Rubber	-0.7183	0.3750	0.2750	0.0002
Textile industry	-0.7651	0.3145	0.8339	0.0002
Culture, education and sports goods manufacturing	-1.0028	0.1667	0.2833	0.0004
Electrical machinery and equipment manufacturing	-1.0871	0.2500	0.2893	0.0001

Instrumentation and culture, office machinery manufacturing	-1.1635	0.1579	0.4000	0.0002
Manufacturing of communications equipment, computers and other electronic equipment	-1.1954	0.2143	0.2107	0.0001
Textile clothing, shoes, hats manufacturing	-1.2317	0.1905	0.4571	0.0001
Waste resources and waste materials recycling and processing industry	-1.8602	0.0000	0.0000	0.0000

3. RESEARCH DESIGN AND DESCRIPTIVE STATISTICS

3.1. Research design

In order to study the mode of sales growth of industrial enterprises in Hubei Province, we transform it into the relationship between the level of environmental pollution and the sales growth rate of industrial enterprises. We use the micro data of industrial enterprises in Hubei Province, and use econometrics to process and regress data. The model explanatory variable is the environmental pollution situation of industrial enterprises in Hubei Province in 2004, that is, "whether to be levied for pollutant discharge fee" and "the amount of operating income by levied discharge fee", which is explained as the annual average annual sales growth rate of industrial enterprises in Hubei province for 2005-2009 years. In view of the fact that the industrial enterprise database has only published details of the pollution discharge feess in 2004, the pollution discharge feess after 2004 are included in the enterprise management fees. In view of the cause of the enterprise's pollution to the environment is the backwardness of technology and the old equipment in the production source and production process, and for the industrial enterprises, especially the industrial enterprises above the scale, the innovation of the production process and the equipment renewal are difficult to complete in the short term. Therefore, we can make a false determination of the level of enterprise pollution to the enterprises in the short term. Sales growth will still have an impact and data availability.

In this paper, the sample industrial enterprises are divided into two categories according to "Whether or not the discharge fee of an enterprise is levied ", and the two indicators of "whether to be levied for pollutant discharge fee" and "the proportion of pollution discharge fees to operating income" are constructed respectively. For all samples, the index of "whether to be charged for pollution discharge feess" is a virtual variable of 0 or 1. Taken as 1, it means that enterprises are charged with pollution discharge feess, no technological innovation, and pollution to the environment, It is taken as 0, which means that the waste discharge fee is not charged, that is, the process, technology and equipment are reformed, and the clean production does not pollute the environment, and the "sustainable development" model is adopted. According to the index "the proportion of pollutant discharge in the business income" as a continuous variable, the more the value of the discharge fee accounts for the value of the operating income, the more serious the pollution of the enterprise is. This paper first chooses linear regression model to analyze, but the result is not significant. Therefore, a logarithmic linear regression model is constructed.

The model is as follows :

$$\ln\text{SalesGrowth} = \alpha + \beta_1 Pollution\_dummy + \beta_2 Controls + \varepsilon \qquad (1)$$

$$\ln\text{SalesGrowth} = \alpha + \beta_1 PollutionFrees/Sales + \beta_2 Controls + \varepsilon \qquad (2)$$

The SalesGrowth are annual average sales growth rate for sample industrial enterprises in 2005-2009 years. The Pollution_dummy are "Virtual variable" whether the enterprise is charged for pollutant discharge". The PollutionFrees/Sales are "the proportion of pollution discharge feess in operating income". The controls are other control variables. The ε is a residual item.

In addition to the main explanatory variables, this paper selects the size of the enterprise, whether it is the state-owned enterprise, the age of the enterprise, the rate of profit, the ratio of assets and liabilities, the proportion of fixed assets, the proportion of the intangible assets, and the advertising of the enterprises as the other control variables. In addition, the industry dummy variables based on the two digit industry code division are added to exclude the gap caused by the regional industry. The size of the enterprise is replaced by the logarithm of the total assets of the enterprise. The age of the enterprise is standardized by the business year of the enterprise. The asset liability ratio is the proportion of the total assets of the enterprise. The proportion of the fixed assets and the intangible assets is the ratio of the fixed assets and the intangible assets to the total asset ratio, and the sales profit rate is the total profit. The proportion of the income of the industry. In this paper, the ratio of sales growth rate, the proportion of discharge fee to operating income, the ratio of assets and liabilities, the proportion of fixed assets and the proportion of intangible assets are Winsorize with at the end of the bilateral 1%, and the abnormal variables are excluded. In order to reduce the correlation between variables, we choose industrial sales as denominator to calculate the index "the proportion of the collected pollution discharge feess to the operating income"

It is assumed that the level of environmental pollution will have an impact on its sales growth rate. In order to test the universality of the hypothesis, the two models of high polluting industries were analyzed by principal component analysis respectively. If the hypothesis is established, the environmental pollution level coefficient of the "high polluting industries" sample will also meet the hypothesis requirements.

3.2. Descriptive statistics

Table 3 shows descriptive statistics of dependent variables and major independent variables, including mean, median, standard deviation, and maximum and minimum. The explanatory variable "the proportion of pollution discharge fees to business income" is described by 578 sample enterprises, and the other variables are calculated by 1333 sample industrial enterprises. It can be seen from the table that the average annual sales rate of the sample industrial enterprises in 2005-2009 years is 0.0687 and the maximum is 0.417. The average value of "pollution discharge fees" is 0.4336, and 43.36% of the sample industrial enterprises have been charged with pollution discharge fees. In the 578 sample industrial enterprises that were charged with pollution discharge fees, the pollution discharge fees accounted for an average of 0.14% of the operating income, the highest was only 7.09%. It can be seen that the expropriation of enterprise discharge fee is not high for business income. The enterprise has a full motive to gain high profit by reducing the cost of pollution to fill the loss caused by the cost of pollutant discharge, and to gain the growth of the enterprise sales at the expense of the environment. The average enterprise size is 9.8608, corresponding to the total assets of 19 million 164 thousand and 215 yuan. In addition, 25.73% of the sample industrial enterprises have done advertising in the observation period. The average asset liability rate of all enterprises is 56.65%, the average value of fixed assets is 36.57%, the mean value of intangible assets is 5.10% Table 4 and table 5 show the correlation coefficient between the two main variables and other control variables: "whether the charges are charged" and "the proportion of the discharge fees to the operating income".

Table 3: Descriptive statistics of dependent variables and major independent variables

	Average	standard deviation	Median	minimum value	Maximum value
Sales growth rate	0.0687	0.237	0.103	-1.1358	0.417
Whether or not a discharge fee is charged	0.4336	0.4958	0	0	1
The proportion of discharge fee to business income	0.0014	0.0039	0.0005	0	0.0709
Enterprise age	0.0045	0.9941	0.4348	-3.9	0.7748
Enterprise scale	9.8608	1.4672	9.6639	6.0913	17.8741
Whether it is a state-owned enterprise or not	0.054	0.2261	0	0	1
Asset liability ratio	0.5665	0.2843	0.555	0	1.3825
Proportion of fixed assets	0.3657	0.2145	0.3543	0	0.8597
The proportion of intangible assets	0.051	0.0969	0	0	0.4996
Ratio of income as a percentage of sales	0.0157	0.0881	0.0123	-0.3908	0.2721
advertise	0.2573	0.4373	0	0	1

Table 4: correlation coefficient of "pollution discharge fees" and other control variables

	a1	b	c	d	e	f	g	h
Whether or not a discharge fee is charged (a1)	1							
Enterprise age (b)	-0.1415	1						
Enterprise scale (c)	0.1807	-0.2543	1					
Whether it is a state-owned enterprise or not (d)	0.0454	-0.3589	0.1881	1				
Asset liability ratio (e)	0.0693	-0.1742	0.0825	0.1254	1			
Proportion of fixed assets (f)	0.0611	-0.0015	-0.0079	0.0617	-0.1539	1		
The proportion of intangible assets (g)	0.1227	-0.0715	0.1736	-0.0601	0.0016	-0.0842	1	
Ratio of income as a percentage of sales (h)	0.0223	0.038	0.0093	-0.0711	-0.2585	-0.0421	-0.1407	1
advertise (i)	0.2433	-0.1024	0.3	0.0567	0.0389	-0.0544	0.1497	0.0405

Table 4 analyzes the correlation between "whether the pollution discharge fees is charged" and other variables by using the whole sample of 1333 enterprises. It can be seen from table 4 that the correlation coefficient between "whether collection pollution discharge fees" and other control variables is smaller. The highest is the correlation coefficient of "whether to do advertising" 0.2433. In general, the correlation between variables is low, and it can basically exclude the multiple collinearity between variables. Table 5 analyses the correlation between the "share of the cost of the discharge of discharge" and the other variables, using the observation data of the 578 enterprises that have been levied. The proportion of the cost of pollutant discharge to the operating income. From table 5, it can be seen that "the proportion of discharge fees to operating income" is less than 0.01, except that the proportion of the proportion of the fixed assets is 0.1055, and the correlation coefficient between the other variables is less than 0.01. Overall, the correlation coefficient is the largest correlation between "enterprise age" and "whether state-owned enterprise" or not 0.4304 It can also exclude multiple collinearity between explanatory variables and control variables.

Table 5: correlation coefficient between the proportion of pollution discharge fees and operating income and other control variables

	a2	b	c	d	e	f	g	h
The proportion of discharge fee to business income（a2）	1							
Enterprise age（b）	0.0494	1						
Enterprise scale（c）	-0.0786	-0.278	1					
Whether it is a state-owned enterprise or not（d）	0.0259	-0.4304	0.2573	1				
Asset liability ratio（e）	0.0023	-0.162	0.0755	0.0533	1			
Proportion of fixed assets（f）	0.1055	0.0521	0.047	0.11	-0.1853	1		
The proportion of intangible assets（g)	0.0617	-0.0652	0.1294	-0.0964	0.005	-0.1072	1	
Ratio of income as a percentage of sales(h）	-0.0462	0.1123	0.0691	-0.0706	-0.3058	-0.045	-0.0996	1
advertise（i）	-0.0604	-0.1357	0.2918	0.0518	0.0262	-0.0813	0.0779	0.0387

4. RESULT ANALYSIS

4.1. "Whether or not the discharge fee of an enterprise is levied" as a regression result of explanatory variables

Table 6 shows the results of the regression of the growth rate of industrial enterprises by using a virtual variable "whether to be levied on pollution charges" as an explanatory variable, using a full sample of 1333 enterprises. Because the results obtained from the linear regression model are not significant, we chose to construct a logarithmic linear model. The observation value of 2004 is chosen as the independent variable. The dependent variable is the logarithm of the annual average sales growth rate of an industrial enterprise for 2005-2009 years, excluding abnormal variables, data of 975 enterprises participated in regression analysis. Using clustering robust standard deviation based on two digit industry code, regression using the least square method.Table 6, from column (1) to column (4), is the result of respectively adopt the regression of "Whether or not the discharge fee of an enterprise is levied" separately, and gradually add the remaining control variables, urban dummy variables and industry dummy variables are added respectively. Generally speaking, although not all the regression coefficients of control variables are significant, we focus on the explanatory variables we studied. The results of these four regressions were all significant at 1% level, and the regression coefficients ranged from -0.1440 to -0.2010. Based on the significance of regression coefficient, although the logarithmic linear model slope represents growth rate, we can directly relate the correlation to the explanatory variables. Regression significance based on virtual variables, the coefficients obtained from the four regressions are all negative values, indicating that the average sales growth rate of the enterprises that are charged with pollution discharge fees is lower than that of the enterprises that have not been charged with pollution discharge fees. Due to the "pollution discharge fees" has caused a certain degree of pollution in the production process, we can think that this enterprise adopts the economic mode of "pollution helps growth".

Table 6: Regression results for future sales growth rate of "pollution discharge fees"

	(1)	(2)	(3)	(4)
Whether or not a discharge fee is charged	-0.2010***	-0.1440***	-0.1740***	-0.1520***
	(-0.0461)	(-0.0421)	(-0.0447)	(-0.0423)
Enterprise age		0.0619	0.0686	0.0657
		(-0.0428)	(-0.0488)	(-0.0474)
Enterprise scale		-0.0112	-0.0379	-0.0172
		(-0.0391)	(-0.0375)	(-0.0407)
Whether it is a state-owned enterprise or not		-0.181	-0.0734	-0.117
		(-0.2040)	(-0.1730)	(-0.1790)
Asset liability ratio		-0.19	-0.2720*	-0.165
		(-0.1250)	(-0.1480)	(-0.1260)
Proportion of fixed assets		-0.0759	0.101	0.0184
		(-0.1470)	(-0.1620)	(-0.1590)
The proportion of intangible assets		-0.7010**	-0.5700*	-0.583*
		(-0.3170)	(-0.3080)	(-0.3270)
Ratio of income as a percentage of sales		-0.688	-0.419	-0.517
		(-0.4170)	(-0.4550)	(-0.4230)
advertise		0.0857	0.0778	0.0713
		(-0.0638)	(-0.0723)	(-0.0650)
region dummy variable	Not added	add	Not added	add
industry dummy variable	Not added	Not added	add	add
Intercept item	-1.9540***	-1.7070***	-1.4020***	-1.0230**
	(-0.0399)	(-0.4200)	(-0.4590)	(-0.4260)
Sample observation	975	975	975	975
Adjust the goodness of fit	0.013	0.113	0.083	0.153

Note: the number of brackets is the robust standard deviation of the corresponding regression coefficient · ***, **, * refers to the significance at the level of 1%, 5%, and 10% respectively;

Therefore, the results can be interpreted as theoretically, the growth rate of "pollution helps growth" enterprises is lower than that of "sustainable development" enterprises.

From the above results, it can also be seen that most industrial enterprises choose to refuse technical transformation and equipment renewal, and to pollute the environment at the cost of lower cost to fill their own losses caused by pollution discharge fees. Although this does have a certain degree of economic growth, in theory, environmentally friendly enterprises that choose cleaner production technologies and reduce pollution can also gain economic growth. Moreover, the growth rate of enterprises under the "sustainable development" mode is faster than that of the "pollution changing growth" mode. Therefore, industrial development and environmental protection can coexist, and economic development is not necessarily at the expense of pollution.

Table 7 (1) shows the results obtained from the regression of the 467 enterprises in the "high polluting industries" in the same way, as for the logarithm of the sales growth rate, 342 enterprises were involved in the regression analysis. In the sample of "high pollution industry", the result of "whether to levy pollution charges" was significant at the level of 5%.The regression coefficient of "whether the pollution discharge fees is charged" is -0.2300, and the absolute value of this regression coefficient is greater than the absolute value of regression coefficient in Table 6, it shows that the growth rate of the explanatory variables is higher in the "high pollution" industry, and the environmental pollution level of the industrial enterprises has a greater impact on the sales growth rate. The results show that in the "high pollution" industry "no pollution fee" of enterprises to be levied pollution fees to obtain greater economic growth, compared to the whole industry, "high pollution" industry in this effect is more significant.

Table 7 (2) shows the cross term for the use of full sample regression but the introduction of the cross term, "whether it belongs to the high pollution industry" and its "whether to be levied on pollution charges". In this return, the cross term coefficient indicates that enterprises in "high pollution industry" have more sales growth than the enterprises that have not been levied on pollution discharge fees, the explanatory variable coefficient is significant and the coefficient is negative, which means that the "sustainable development" mode can achieve more sales growth.

Table 7: Effect of "pollution discharge fees" on sales growth rate in industries with different pollution levels

	(1) sub sample of high pollution industry		(2) full sample	
Whether or not a discharge fee is charged	-0.2300**	(-0.0957)	-0.1020**	(-0.0384)
Whether it belongs to the high pollution industry			-0.2520***	(-0.0720)
Whether or not a discharge fee is charged（0） *Whether it belongs to the high pollution industry（1）			0.141	(-0.0928)
Enterprise age	0.0661	(-0.0822)	0.0658	(-0.0474)
Enterprise scale	-0.0406	(-0.0852)	-0.0172	(-0.0407)
Whether it is a state-owned enterprise or not	-0.0356	(-0.3300)	-0.119	(-0.1810)
Asset liability ratio	-0.198	(-0.2590)	-0.16	(-0.1250)
Proportion of fixed assets	-0.0305	(-0.2110)	0.019	(-0.1600)
The proportion of intangible assets	-0.198	(-0.4980)	-0.5830*	(-0.3200)
Ratio of income as a percentage of sales	-0.665	(-0.7290)	-0.513	(-0.4180)
advertise	0.1180*	(-0.0580)	0.0779	(-0.0665)
region dummy variable	add		add	
industry dummy variable	add		add	
Intercept item	-2.3670**	(-1.0590)	‘-1.5970***	-0.44
Sample observation	342		975	
Adjust the goodness of fit	0.201		0.154	

Note: the number of brackets is the robust standard deviation of the corresponding regression coefficient · ***, **, * refers to the significance at the level of 1%, 5%, and 10% respectively;

4.2. "the proportion of pollution discharge fees to operating income".as a regression result of explanatory variables

The regression of the second models is that the explanatory variable is "the proportion of pollution discharge fees to business income", and the sample is 578 enterprises that are charged with pollution discharge fees.Similarly, a logarithmic linear regression model is established for logarithm of sales growth rate, and a total of 421 enterprises' data are involved in regression. The independent variable is the observed value in 2004, because the "Discharge fee accounts for the proportion of operating income" and some control variables are also measured by "the proportion of operating income", this paper uses industrial added value instead of operating income to calculate the proportion of pollutant discharge fees. Using clustering robust standard deviation based on two digit industry code, regression using the least square method. Table 8, from column (1) to column (4), is the result of respectively adopt the regression of "proportion of collected pollution discharge fees" separately, and gradually add the remaining control variables, urban dummy variables and industry dummy variables are added respectively. The sample of column (5) is 257 high polluting enterprises in the enterprises that are charged with pollution discharge fees, after the logarithm, the final 186 enterprises were involved in the regression analysis. The result is not significant, which shows that "the proportion of pollution discharge fees to operating income" has little impact on the "sales growth rate".Although the trend indicates that the two are positively related, pollution may bring economic growth, but because the regression coefficient and equation are not significant, it is impossible to determine whether the percentage of pollution discharge fees will affect sales growth rate.

Table 8: Effect of "share of pollution discharge fees on operating income" on future sales growth rate

	(1)	(2)	(3)	(4)	(5)
The proportion of discharge fee to business income	27.35	9.716	44.61	33	44.16
	-44.19	-41.6	-45.48	-44.43	-48.77
Enterprise age		0.0791	0.0788	0.0761	0.0599
		(-0.0606)	(-0.0712)	(-0.0662)	(-0.1120)
Enterprise scale		-0.0378	-0.0637	-0.0601	-0.0923
		(-0.0514)	(-0.0529)	(-0.0603)	(-0.1100)
Whether it is a state-owned enterprise or not		0.141	0.0503	0.142	0.0067
		(-0.2460)	(-0.2250)	(-0.252)	(-0.5100)

Asset liability ratio		-0.3710*	-0.4640*	-0.346	-0.366
		(-0.2090)	(-0.2720)	(-0.214)	(-0.3780)
Proportion of fixed assets		0.0817	0.271	0.22	-0.167
		(-0.1940)	(-0.2510)	(-0.215)	(-0.2670)
The proportion of intangible assets		-1.4000***	-1.3950**	-1.450**	-1.485
		(-0.4860)	(-0.5790)	(-0.564)	(-0.8430)
Ratio of income as a percentage of sales		-0.299	-0.129	-0.0957	-0.578
		(-0.6930)	(-0.8290)	(-0.766)	(-1.0850)
advertise		0.155	0.134	0.1	0.115
		(-0.0934)	(-0.1240)	(-0.118)	(-0.1610)
region dummy variable	Not added	add	Not added	add	add
industry dummy variable	Not added	Not added	add	add	add
Intercept item	-2.1860***	-1.5980**	0.00276	-0.383	0.329
	(-0.0585)	(-0.5830)	(-0.7460)	(-0.467)	(-1.44)
Sample observation	421	421	421	421	186
Adjust the goodness of fit	0.003	0.158	0.144	0.227	0.324

Note: the number of brackets is the robust standard deviation of the corresponding regression coefficient · ***, **, * refers to the significance at the level of 1%, 5%, and 10% respectively;

The gradual improvement of policies and regulations has made the cost of pollutants more and more expensive. Although the enterprises still exist with low cost and high pollution, this kind of enterprises may change their own interests at low cost for the time being, but with the improvement of the policy and the change of public choice, environmental protection, sustainable and low pollution are the choice of more and more people. The additional losses caused by pollution will exceed the profit brought by low cost, which will lead to a reduction in sales. Compared with the conclusion that the model of "pollution exchange growth" can bring sales growth, the possible reason for this regression result is the improvement of the cost of pollutant discharge. In 2007, the Interim Regulations on the collection and use of pollution discharge fees in Hubei Province promulgated by the Hubei province gave more detailed limits on the collection of pollution discharge fees, especially in respect of air pollution and sewage treatment, we should further divide the accounting for the amount of pollutant discharge in different behaviours and the standard of pollution discharge fees payable. This leads to an increase in the cost of sewage, and the low cost benefits of old equipment can not offset the losses caused by pollution discharge fees. In addition, in the notice on the adjustment of the standards for the adjustment of pollutant discharge fees in Hubei province in 2014, it was pointed out that the charge for pollutants in waste gas and sewage was adjusted to two times that of the original. The environmental protection tax law of the People's Republic of China, which was passed in 2016, has been changed from January 1, 2018 to environmental tax since January 1, 2018. Therefore, in order to promote the construction of ecological civilization, take sustainable development, reduce environmental pollution, the cost of pollution will become higher and higher. The traditional economic growth model of "pollution for growth" is not suitable for the long-term development of enterprises.

A comprehensive consideration the regression results is given to the two regressions obtained from "whether the pollution discharge fees is charged" and "the proportion of pollution discharge fees to business income" as independent variables. It can be seen that there are environmental protection enterprises and polluting enterprises in Hubei's industrial enterprises. On the whole, environment-friendly enterprises can get higher economic growth than polluting enterprises theoretically, companies that choose technological innovation and clean survival will have better prospects. Although there are still companies choosing low - cost and high pollution to meet their economic growth, this model does not assert whether pollution is bound to grow.

5. CONCLUSION

This paper uses the microscopic data of Hubei industrial enterprises to analyze the impact of environmental pollution on its sales growth rate, and explores the sales growth mode of industrial enterprises.It is found that there are environment-friendly enterprises in industrial enterprises, and pollute enterprises exist at the same time. Environmental enterprises can obtain higher economic growth than polluting enterprises. It will have better prospects for the enterprises to choose technological innovation and clean survival.The development of industrial enterprises and environmental protection can coexist. Economic development does not necessarily depend on pollution.Although there are still businesses that choose low cost and high pollution to meet their economic growth, it is not safe to say that pollution can be exchanged for growth.

Therefore, it is the best way for industrial enterprises to choose the "sustainable growth" mode in theory. But in reality, there is still a "pollution - to - growth" growth model, which requires enterprises to reduce the pollution of the environment by accelerating technological innovation. The government should also improve the management system and increase the supervision.If the standard of the discharge fee is low, the polluting enterprises will not have the power to update the equipment to change the production, the low cost of the equipment will bring the high profit, and the discharge fee is not enough to promote the transformation of the enterprise. It is necessary for the government to raise the standards for the collection of pollution discharge fees, improve the environmental access threshold for enterprises, and enhance the depth of the concept of "sustainable development" of industrial enterprises. It is necessary for the government to raise the standards for the collection of pollution discharge fees, improve the environmental access threshold for enterprises, and strengthen the concept of "sustainable development" of industrial enterprises.

6. REFERENCES

Tang W, Fu Y, Wang Z. Technological innovation, technology introduction and transformation of economic growth pattern [J]. Economic research,2014,(7):31-43

Zhang K, Yuan H, Chen Y. Environmental imbalance and scientific and technological progress: review and prospect of research on the relationship between industrial economic development and environmental relations [J]. Industrial economy BBS, 2016,(3):250-252

Bao Q, Shao M and Hou W. Did exports improve employee income [J]. Economic research, 2011, (9) : 41-54.

Zhao W. Research on the role of technology introduction in promoting economic growth -- based on panel data of large and medium-sized industrial enterprises in 1996-2009 [J]. Financial economy, 2012, (8) : 59.

Feng Z. Environmental technology spillover pathway of foreign direct investment -- an empirical study based on the data of China's industrial enterprise survey in 2004 [J]. Journal of Beijing economic management cadre institute, 2015, (3) : 16-17.

Zhang Y, Qin F, Wu Y. "sustainable development" or "pollution for growth" -- an analysis based on the sales growth model of Chinese industrial enterprises [J]. China's industrial economy, 2015, (2) : 89-100.

Pan C. Research on the impact of forward-looking environmental strategy on sustainable competitive advantage of enterprises [D]. Doctoral thesis of jilin university,2017(5).

Wang H. On China's enterprise sales model and sustainable development strategy [J]. China business, 2012, (14) : 35.

Cao L. A brief discussion on how chemical enterprises can do a good job in energy conservation and emission reduction [J]. Science and technology, 2015, (19) : 253.

Chen M. Analysis on the cost of sustainable development of enterprises under the change of economic development mode [J]. Enterprise economy, 2011, (8) : 26-28.

Byrne M.M. Is Growth a Dirty Word? Pollution, Abatement and Endogenous Growth[J].Journal of Development Economics,1997,54(2):261-284.

Chen T, Kokko A, Tingvall P.G. FDI and Spillovers in China:Non-linearity and Absorptive Capacity[J].Journal of Chinese Economic and Business Studies,2011,9(1):1-22.

Kotabe M, Jiang C.X., Murray J.Y. Managerial Ties,Knowledge Acquisition,Realized Absorptive Capacity and New Product Market Performance of Emerging Multinational Companies:A Case of China[J].Journal of World Business,2010,(46):166-176

265: Study on the influence of educational level to the ecological efficiency of urban agglomeration in the middle reaches of Yangtze River and regional differences

Yanhua ZHANG[1,2,3] , Nijun WANG [1] , Zhongyi WANG[1]

[1] the College of Economic and Management, Hubei University of Technology, Nanli Road No.28, Hongshan District, Wuhan City, Hubei Province, China, 2039076986@qq.com
[2] the Research Center of Circular Economy Development in Hubei, Nanli Road No.28, Hongshan District, Wuhan City, Hubei Province, China
[3] the Collaborative Innovation Center of Regional Industrial Ecology Development, Hubei University of Technology, Nanli Road No.28, Hongshan District,Wuhan City, Hubei Province, China

In the past ten years, China's economy has grown steadily. Due to historical development factors, management systems, and technical conditions, the economic development model still suffers from high energy consumption, high emissions, and high pollution. China's resources and environmental pressures continue to increase. In the context of sustainable development, how to coordinate the relations among economic development, resource consumption and environmental protection, reduce resource consumption and pollution emissions, and increase economic output are an important issue for China's current development. We measure the eco-efficiency of cities in three provinces in the middle reaches of the Yangtze River, expand and deform the random model of environmental impact, and discuss the temporal and spatial effects. Then we study the ecological efficiency and population, wealth, and human factors in the middle reaches of the Yangtze River. The relationship between. The research results show that the eco-efficiency of urban agglomerations in the middle reaches of the Yangtze River increases year by year, and the eco-efficiency of some cities in the middle reaches of the Yangtze River varies greatly, and there are significant spatial correlations and dependencies; the level of education based on the number of colleges and universities is positively correlated with ecological efficiency. The improvement of the level will increase people's awareness of environmental protection and conservation, thereby reducing pollution emissions and resource consumption, and the ecological efficiency will be further improved. By exploring the impact of population, economic and human factors on ecological efficiency, we hope to provide reference policy suggestions for urban planning, economic development and environmental protection in China.

Keywords: urban agglomeration in the middle reaches of Yangtze River; ecological efficiency; spatial measurement; educational level; IPAT model

1. INTRODUCTION

In recent years, domestic and foreign scholars have conducted in-depth research on the factors that affect ecological efficiency. There are many studies on the impact of economic factors on ecological efficiency and the influence of population factors on ecological efficiency. Xu Zhongmin's research (2005) shows that the environment is mainly affected by the number of people, the environment is affected by the same proportion of the population, and the increase in wealth also has an impact on the environment; Liu Xie (2008) analyzed the population, economic and social factors of Jiangxi Province for the environment. The impact is that the population has the greatest impact on the environment in Jiangxi Province; Fan et al. (2006) analyzed the impact of population, affluence and technological factors on total CO2 emissions in different countries, and stated that the main driver of CO2 emissions is the level of affluence. He Qiang (2008) and others used the IPAT model to study the impact of factors such as population, technology, economy, and economic structure on the ecological environment, and proved the impact of economic development on environmental quality; Luo Hong et al. (2010) use different economies. - The growth rate studies the impact of economic development on environmental pressures. A few scholars in China have analyzed the impact of factors such as economic development level, regional development level, scientific and technological level, human capital, environmental policy, and industrial structure on regional eco-efficiency on the basis of evaluation of regional eco-efficiency. Fu Lina (2013) found that the ecological efficiency was improved with the adjustment of industrial structure and the increase of research intensity, and technological progress had a positive impact on ecological efficiency; Li Haidong (2012) concluded that regional science and technology, pollution control, environmental policy, industrial structure, and regional ecology There is a significant positive effect on efficiency; Deng Bo's research (2011) results show that per capita schooling can improve ecological efficiency.

As for the spatial effect of regional eco-efficiency, Pan Xingxia (2014) shows that there is a significant positive autocorrelation spatial correlation model for regional eco-efficiency in China, and it has been increasing year by year; Li Jiajia (2016) analyzed the differences in the impact of city size on eco-efficiency in different regions. It shows that the scale of the city has a positive influence on the ecological efficiency, and the significance is affected by the region; Guan Wei's research (2015) finds that the inter-provincial energy eco-efficiency is spatially interactive and dependent, and the spatial effect is significant. The degree of spatial overflow of regional energy eco-efficiency is stronger than that of the impact of the impact of energy eco-efficiency in adjacent areas on the region; Chen Zhenling (2016) builds spatial Dubin model of the relationship between eco-efficiency and urbanization and finds urbanization and ecology The efficiency shows a negative correlation; Xu Shuting (2016) found that China's energy eco-efficiency exhibited significant global spatial agglomeration characteristics at the inter-provincial scale.

Domestic and foreign scholars have deeper research on the ecological efficiency of the population and economic development. When using the environmental impact stochastic model, it is preferred to use the population number P, the wealth degree A, and the technical level T. According to Zhong Xingju's induction (2016) and summary of the IPAT expansion model, scholars at home and abroad are aware of the complexity of T, and gradually deepen their research on T, rather than just using T as a technical level. At the same time, scholars at home and abroad have discovered the spatial effects of regional eco-efficiency. They have used the space panel lag model and the space panel error model to conduct research, and selected Moran’s I and Ceary’ C indices for testing.

2. ANALYSIS OF THE CORRELATION BETWEEN ECOLOGICAL EFFICIENCY AND SPATIAL STRUCTURE OF URBAN AGGLOMERATION IN THE MIDDLE REACHES OF YANGTZE RIVER

2.1. Measurement methods and index selection

Schategger and Sturn first proposed the concept of eco-efficiency in 1990. They have different understandings of eco-efficiency scholars. Among them, the widely recognized is the definition of the National Sustainable Development Business Council: “Provide products that can meet the needs of human life and development. Services not only have price advantages but also consume the earth’s affordable resources, have little impact on the environment, and harmonize the environmental and social developments as ecological efficiency. We understand ecological efficiency as economic output under certain environmental losses and resource consumption.

The concept of sustainable development promoted the concept of eco-efficiency and explored ways to measure eco-efficiency. Eco-efficiency is the ratio of economic output to environmental input resource consumption. Domestic and foreign scholars have developed many methods for measuring eco-efficiency. There are widely used factor analysis methods, analytic hierarchy process, ecological footprint method, DEA method, etc. The advantage of DEA method over other methods is that weights do not use assumptions and data are automatically obtained. To gain weight, the issue of eco-efficiency measurement indicators has been solved. The super-efficiency DEA model allows the efficiency value to be greater than 1, and the efficiency in the super-efficiency DEA model can be ranked and compared.

Based on the above reasons, we chose the super-efficiency DEA model to calculate the ecological efficiency of each city in the middle reaches of the Yangtze River and rank it. Using the super-efficiency DEA model, with

reference to the availability of previous literature and data, we selected industrial sulfur dioxide emissions, industrial wastewater emissions, Industrial smoke and dust emissions are the input indicators of environmental pollution. The total social power consumption, water consumption, and built-up area are used as input indicators for resource consumption, and economic development is used as output. The industrial output value is used as an indicator of output variables. The input-oriented super-efficiency DEA model with constant scale returns was used for measurement. Our data comes from the "China City Yearbook" and the "China Environment Yearbook."

2.2. Analysis of measurement results

Using MYDEA 1.0 software, we calculated the eco-efficiency of 36 prefecture-level cities in Hubei, Hunan, and Jiangxi from 2006 to 2015 and plotted the distribution of inter-city eco-efficiency using the ARCGIS 10.2 software for horizontal comparison among cities. , Draw an eco-efficiency histogram for comparison between years. The analysis of ecological efficiency changes of 36 cities over a decade was conducted using stata to plot the ecological efficiency over time of 36 cities over time. According to the calculation results of ecological efficiency of 36 cities in three provinces, from the time dimension, the three provinces 36 The eco-efficiency of each city has improved during the ten years, and different cities have improved differently. In 2006, the ecological efficiency of Hubei Province was better than that of Jiangxi Province than that of Hunan Province. Jiangxi Province is the province with the fastest increase in eco-efficiency, and the eco-efficiency of prefecture-level cities has Great difference. In the ten years, the ecological efficiency of the three provinces has undergone tremendous changes.

2.3. Spatiotemporal correlation analysis

The natural conditions, industrial structure, education level and economic development level of 36 cities in the three provinces are all different. There are significant differences in the eco-efficiency of different cities. There may be spatial correlation among cities, due to economic spillovers, industrial shifts and cooperation. Even with the spread of pollution and the sharing of resources, there may be spillover effects on ecological efficiency, and the eco-efficiency of neighboring cities may influence each other. The spatial correlation and degree of correlation are verified below, and spatial correlation is tested using Geary's C index and Moran's index.

We used MATLAB software to examine the spatial correlation of the ecological efficiency of 36 cities. The results show that the Moran index of the eco-efficiency of urban agglomerations in the middle reaches of the Yangtze River between 2006 and 2015 is positive, and the Geary's C index is between 0 and 1. Both of them passed the test at a significant level of 5%, indicating that there is a correlation between the distributions of ecological efficiency sub-spaces in the middle reaches of the Yangtze River. According to the calculated ecological efficiency, the ArcGIS 10.2 software was used to plot the comparison of the eco-efficiency map and eco-efficiency for 2006 to 2015.

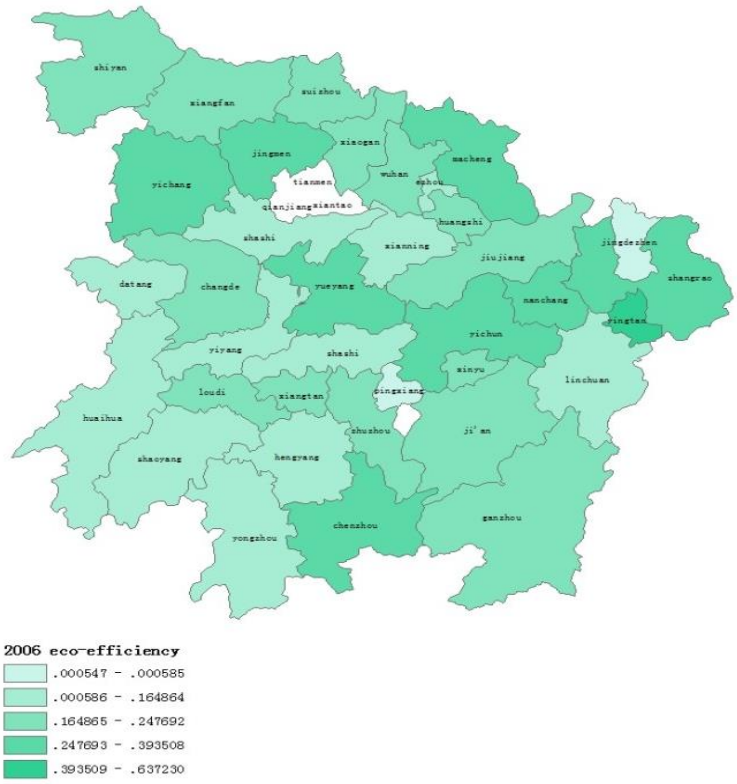

Figure 1: Urban Eco-efficiency in the Middle Reaches of the Yangtze River in 2006

In the past 10 years, the eco-efficiency of all cities has increased. Among them, Zhangjiajie, Changsha, Suizhou, Xianning, and Huanggang have the greatest growth. It can be seen that regardless of the basis of eco-efficiency in 2006, all urban eco-efficiency has increased. With different growth rates, the ranking of eco-efficiency changes, among which the higher ecological efficiency is in Changsha City (1.514491) Huanggang City (1.266725) Suizhou City (1.114256) the lower ecological efficiency is Xiangfan City (0.230235) Jingdezhen City (0.344903) Xinyu City (0.37304) among them, the eco-efficiency of Yingtan City reached a peak in 2010 and then gradually declined. The upward trend of Jingdezhen City and the base difference of eco-efficiency became the only two places in both 2006 and 2015. The eco-efficiency of a few cities has fluctuate slightly over the past 10 years, and it has shown an overall upward trend.

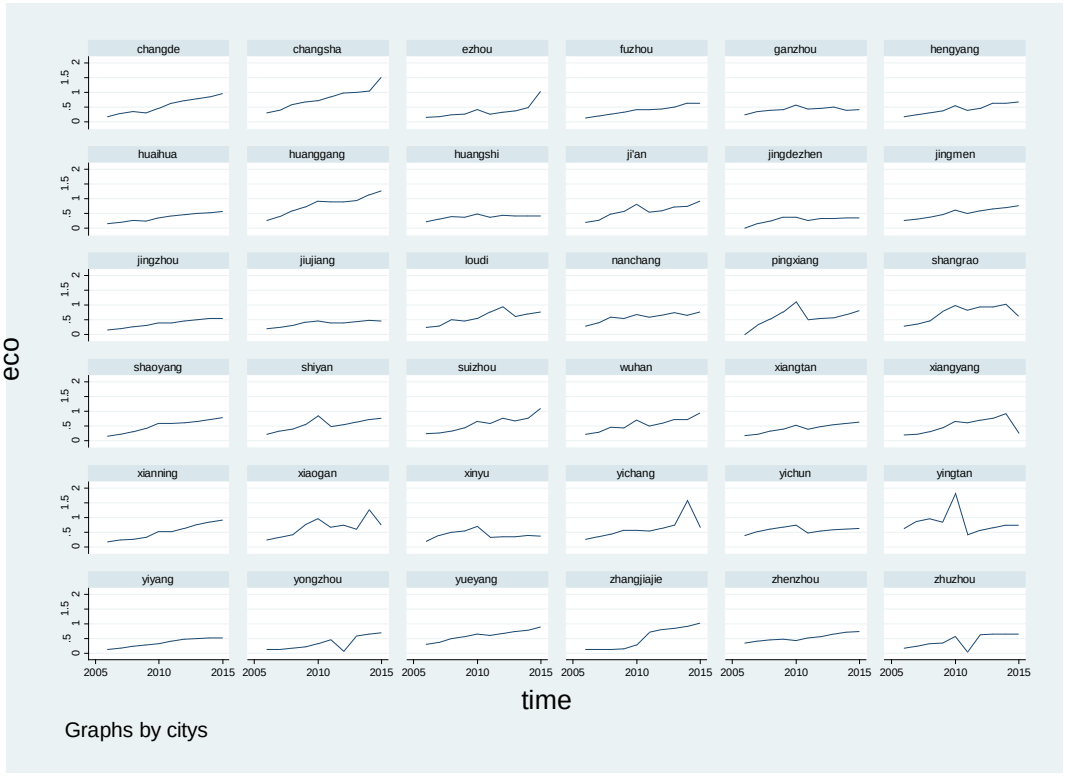

Figure 2: Trend of Ecological Efficiency in the 10 Years of Urban Agglomeration in the Middle Reaches of Yangtze River

Eco-efficiency is only one of the top three cities in Jingdezhen City between 2006 and 2015. This is closely related to the economic development model of Jingdezhen City. Jingdezhen is famous for its ceramics. The ceramic industry with high pollution and high energy consumption is the pillar of the city. Sex industry. With the announcement of Hubei's featured township list, Luotian County and Hunchun County of Huanggang City were respectively given the fame of Sanbao Town and Wengai Town, and Suizhou Guangshui City was rated as a fleshy town. The urban development model is based on agricultural cultivation, with a low level of industrialization, little pollution to the environment and less resource consumption. Changsha, as the capital city of Hunan Province, enjoys more policies and economic support, and has gathered and transformed many industries. Changsha's pillar industries have gradually shifted from traditional construction machinery, automobiles and auto parts to new materials, new energy, and biomedical products. With the transformation of higher-end and low-consumption industries, with the famous Yuelu Mountain, Orange Island and other attractions, the annual revenue generated by the tourism industry can not be underestimated. When accepting the preferential policies as a provincial capital, the environmental constraints will be stricter than other prefecture-level cities, and there will be more thresholds for the introduction of industries, among which the heavily polluting industries will be rejected. Both the policy preferences and constraints have promoted the changes in the eco-efficiency of Changsha City in ten years. The economic development model determines the effect of the population. With cities with scarce human capital, economic development brings people more opportunities and challenges, causing a large number of talents to inflow. In cities where the promotion of industrial upgrading has higher ecological efficiency, slower economic development, single industrial structure, and large population, the influx of foreign residents will cause environmental damage, and the consumption of resources will not increase the economic output and the ecological efficiency will decrease

3. MODEL SETTING AND INDEX SELECTION

3.1. An empirical model of educational efficiency affecting eco-efficiency

The famous IPAT model for studying the impact of human activities on the environment was proposed by the American economists Holdren and Ehrlich in the 1970s. In the IPAT model, the main factors affecting the ecological environment are: technological level, population, wealth, IPAT, I can refer to environmental damage, environmental carrying capacity, resource consumption, etc. The advantage of this model is that it can qualitatively study the influence of factors such as population and economy on the environment, and thus it is widely used. Later scholars have extended and extended this model. Some of the more famous ones are: a, b, c, d are the parameters to be estimated, e is the random error, and a group of scholars improve the model according to different research backgrounds for quantitative study. And establish environmental standards and establish an eco-efficiency ranking system.

This article takes the logarithm of the innovative IPAT mode

$$\ln I_i = \ln a + b \ln P_i + c \ln A_i + d \ln T_i + \ln e_i$$

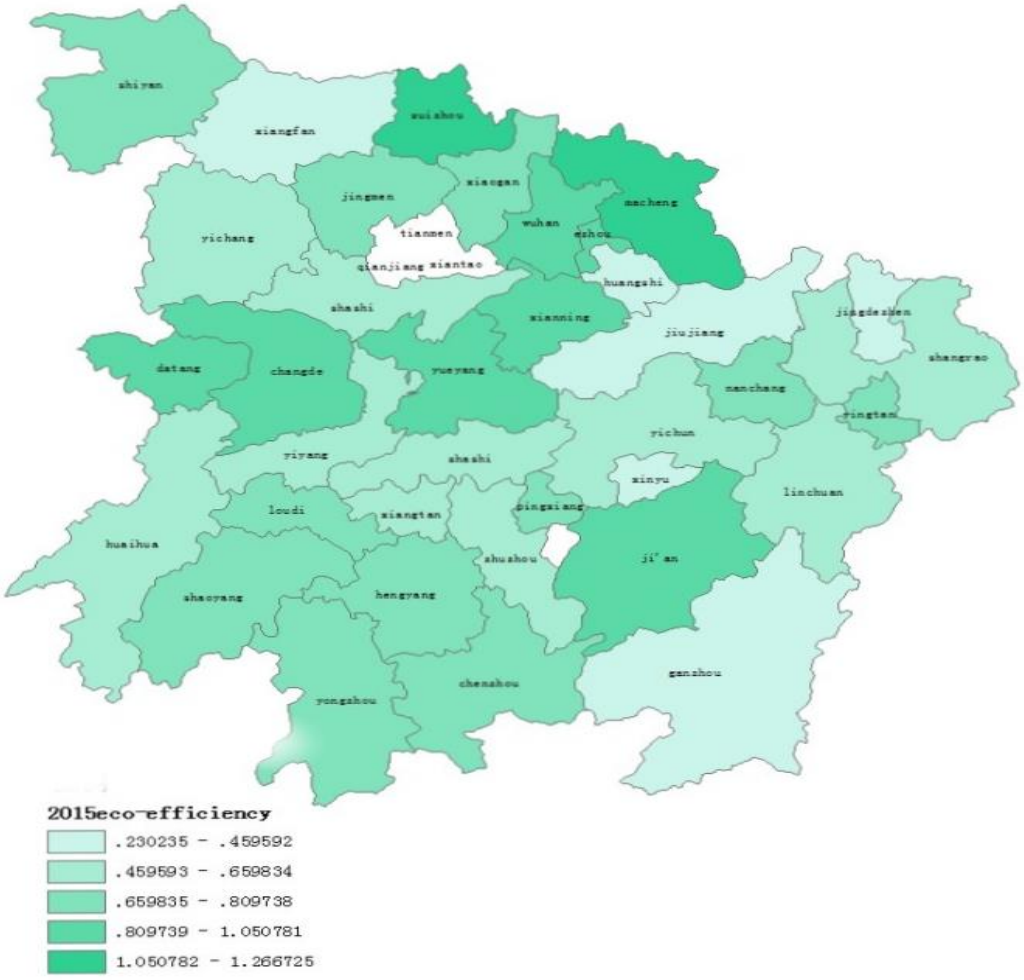

Figure 3: Urban Eco-efficiency in the Middle Reaches of the Yangtze River in 2015

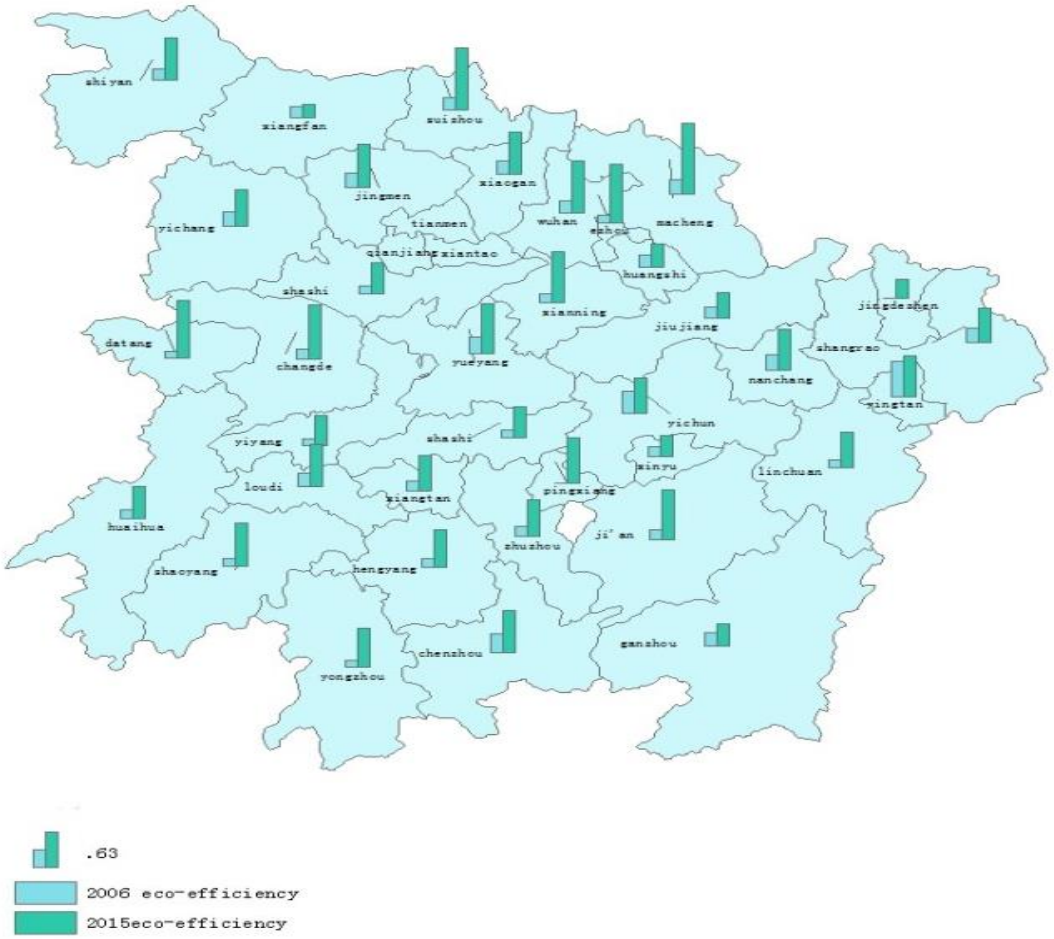

Figure 4: Eco-efficiency comparison chart for 2006-2015

Using the model of deformation expansion, we use ecological efficiency to represent lnI, use the city's population at the end of the year as the operability to represent a city's annual population P, use the regional total output value to represent A, and the regional number of universities to represent the level of education, T, to obtain the following model:

$$ecDEA = \beta_1 + \beta_2 \ln pop + \beta_3 \ln gdp + \beta_4 school + \varepsilon_{it} \quad (1)$$

In the formula, it is a different city, represents the year, represents the individual effect, represents the time effect, is the parameter to be estimated, is a random disturbance item, and represents the (i=1, 2...36) cities and the first (t=1,2.....10) years; ecDEA represents eco-efficiency, pop represents urban population, gdp is urban output value, and school represents education level.

The spatial autocorrelation test results show that there is a spatial correlation between the eco-efficiency of the urban agglomeration in the middle reaches of the Yangtze River, and it is found that the urban eco-efficiency is related to the eco-efficiency of the previous year. Based on this, a spatial econometric model is constructed for empirical analysis.

Urban eco-efficiency has a certain relationship with the urban development model, economic level, and education level. These factors cannot be changed overnight. Based on this, there is reason to speculate that there is a lagging effect on urban eco-efficiency. The following two models are established: the spatial lag model and the spatial error model.

Spatial Lag Model

$$ecDEA_{it} = \beta_i + \beta_t + PWecDEA_{it} + \beta_1 \ln gdp_{it} + \beta_2 \ln pop_{it} + \beta_3 school_{it} + \varepsilon_{it}$$

Spatial error model

$$\begin{cases} ecDEA_{it} = \beta_i + \beta_t + \beta_1 \ln gdp_{it} + \beta_2 \ln pop_{it} + \beta_3 school_{it} + \varepsilon_{it} \\ \varepsilon_{it} = cW_{it} + \mu_{it}, \mu \sim N(0, \sigma_{it}^2) \end{cases}$$

In the formula, p is the spatial auto-regression coefficient, W is the spatial weight matrix, and ε is the random interference term. The construction of the weight matrix W is based on whether the cities are adjacent to each other, adjacent to 1 or 0 otherwise.

Table 1: Estimated factors affecting eco-efficiency

variable	Model One	Model Two	Model There
lngdp	0.2983	0.3292	0.3331
lnpop	-0.1357	-0.192	-0.3802
school	0.0053	0.001	0.0009
C	-3.8043		
Spatial Lag Factors		0.1254	
Spatial error factor			0.1493
Number of samples	360	360	360

3.2. Data sources and indicator selection

Based on the geographical uniqueness and data availability of urban agglomerations in the middle reaches of the Yangtze River, we selected data from 36 prefecture-level cities in Jiangxi, Hunan, and Hubei provinces in the middle reaches of the Yangtze River for the decade from 2006 to 2015. The eco-efficiency of the explanatory variables in the three models was calculated from the super-efficiency DEA model. The data of the explanatory variables were from the Urban Statistical Yearbook and the Environmental Statistics Yearbook. The wealth of control variables is represented by the total urban output value, and the year-end population statistics of the city are used to represent the annual population of the city. The educational level of independent variables is represented by the number of urban universities. There are few studies on the impact of human factors on eco-efficiency. The fundamental reason is the unquantifiable nature of human factors. For the quantification of education level, some scholars use the proportion of the number of students in school, the level of education per capita, and then the assignment, the number of schools Such indicators quantify the level of urban education. Based on operability, we chose the number of urban universities to represent the level of urban education.

4. EMPIRICAL ANALYSIS

4.1. Analysis of the impact of educational level on eco-efficiency

From the model results, it can be seen that in the middle reaches of the Yangtze River, the degree of affluence and education have a positive effect on ecological efficiency. The coefficients of the logarithm of the three models of GDP and the number of schools are significantly positive, and the degree of affluence to ecology. The efficiency promotion effect is obvious. The coefficient of population in the three models is negative, indicating that the urban population in the middle reaches of the Yangtze River has an increase in the ecological efficiency. This may be related to the industrial structure and population quality. The increase in population has accelerated the consumption of local resources and produced greater Environmental pressure, but at the same time, did not bring about corresponding economic growth, resulting in a reduction in ecological efficiency.

The hysteresis factor in the spatial lag model is not significantly zero, and the eco-efficiency has a lagging effect. The environmental foundation and economic foundation will affect the urban ecological efficiency. The spatial error factor in the spatial error model is also notably zero, and there is a spatial correlation in ecological efficiency. The inter-city urban eco-efficiency influences each other, which may lead to the spread of new technologies, the transfer of advantageous industries, and the possibility that they may be troubled by neighbors. Both models show that the ecological efficiency of a city is related to its development base and neighboring cities.

In urban agglomerations in the middle reaches of the Yangtze River, the coefficient of urban education is positive, indicating that the impact of education on urban eco-efficiency is positive. Eco-efficiency increases with the improvement of education. Among the factors affecting urban eco-efficiency, there is a positive relationship between affluence and eco-efficiency, and the population is negatively correlated.

4.2. Province-based differences analysis

Although 36 cities are located in the middle reaches of the Yangtze River, due to differences in geographical location, whether they are provincial capitals, differences in resource endowments, economic development

opportunities, policies and other development conditions, the impact of education on ecological efficiency may be different. Different provinces divided 36 cities into three regions: Hunan, Hubei, and Jiangxi.The FGLS method was used to estimate the model and the following results were obtained.

Table 2: Results of Eco-efficiency Assessment of Educational Levels in Different Provinces and Cities

variable	Hubei	Hunan	Jiangxi
lngdp	0.3331	0.3565	0.3684
lnpop	-0.3802	-0.1384	-0.3551
school	0.0083	0.0077	0.0096
C	-3.009	-3.1446	-4.0011
Number of samples	120	130	110

It can be seen that each factor has different influences on the eco-efficiency of different provincial cities, but the influence direction is the same, the degree of affluence, the contribution of education level to ecological efficiency are positive, and the population is negative. The same amount of output growth has the greatest effect on promoting urban eco-efficiency in Jiangxi Province, which may be related to the economic development basis of Jiangxi Province. Compared with Hunan and Hubei, Jiangxi's economy is relatively weak, its starting point is low, and its ecological efficiency growth is relatively high. It is easy for Hubei Province to have the greatest impact on the ecological efficiency due to the increase of population growth. Hubei Province has the greatest population growth inhibition on ecological efficiency, and the level of education has played an important role in promoting the ecological efficiency of Jiangxi Province.

5. CONCLUSIONS AND INSPIRATION

From the perspective of geographical location, economic development, education level, and urban population, we analyzed the influencing factors of eco-efficiency in the middle reaches of the Yangtze River. Using spatial econometrics to empirically analyze the impact of education and spatial effects on urban eco-efficiency and gain some inspiration.

(1) The eco-efficiency of the urban agglomerations in the middle reaches of the Yangtze River has increased significantly from 2006 to 2015. There are regional differences in ecological efficiency, and the spillover effect of ecological efficiency is obvious. The externality of eco-efficiency makes it difficult for municipal governments to achieve their own ecological efficiency. Only considering partial policies will lead to the tragedy of the commons, pollution emissions will destroy the overall eco-efficiency, and pollution transfer or eviction will be an ineffective means of ignoring neighbors. Only cooperation between cities can be carried out to achieve a win-win situation with eco-efficiency optimisation. Among them, Changsha, Huanggang, and Suizhou have high ecological efficiency, and they can use these cities as the center. The surrounding cities can learn from their development models, cooperate with them, learn green development experiences, form high eco-efficiency zones, and radiate to other surrounding cities. , improve the overall ecological efficiency.

(2) The impact of education on urban eco-efficiency is positive. People's awareness of environmental protection and ways of saving will improve with the improvement of education level. The establishment of public interest classrooms to raise public awareness of environmental protection and introduce green lifestyles will increase the ecological efficiency of their cities.

(3) There is a negative correlation between population and ecological efficiency. Control the population of the city, speed up the construction of surrounding cities through the radiation effects of more developed cities, and conduct demographic drainage, so as to achieve the best balance between urban development and ecological efficiency.

6. REFERENCES

Xu Z-M, Cheng GD. 2005, Impacts of population and affluence on environment in China. Journal of Glaciology and Geocryology, 27(5):767-773(in Chinese)

Liu X, Xiong X, Jia JS. 2008, Effects of social and economic factors on environmental stress in midland of China:A case study in Jiangxi Province. Population Research, 32(3) :75-78(in Chinese)

Fan Y, Liu LC, Wu G, et al. 2006, Analyzing impact factors of CO2 emissions using the STIRPAT model. Environmental Impact Assessment Review, 26:377-395

He Q, Lyu G-M. 2008, Analysis of ecological environmental impact based on IPAT Model: A case study of Beijing. Journal of Central University of Finance and Economics, 12(6) :83-88(in Chinese)

Luo H, Shu J, Lyu L, et al. 2010, Research on environmental pressure-response of Suzhou City based on IPAT model. Research of Environmental Sciences, 23(1) : 116-119 (in Chinese)

Fu L, Chen X, Leng Z. 2013, Study on the Eco-efficiency of Urban Agglomeration Based on Super-efficiency DEA Model: A Case Study of "3+5" Urban Agglomeration in Changsha, Zhuzhou and Xiangtan [J]. China's Population, Resources and Environment, 23(04):169-175.

Li H, Wang S. 2012 , An empirical analysis of the eco-efficiency assessment and influencing factors in the "two-type" social construction - Taking provincial panel data from 2006 to 2009 as an example [J]. Journal of Electronic Science and Technology University (Social Sciences), 14(6):72-77.

Dang B, Zhang X, Guo J. 2011, Research on regional eco-efficiency based on three-phase DEA model[J]. China Soft Science, 92-99.

Pan X. 2014. Research on Regional Ecological Efficiency Evaluation, Influence Factors and Convergence in China [D]. Nanchang University.

Li J, Luo N. 2016, The Impact of Urban Scale on Ecological Efficiency and Analysis of Regional Disparities[J]. China Population, Resources and Environment, 26(02): 129-136

Guan W, Xu S, 2015, The spatial pattern and spatial effect of China's energy eco-efficiency[J]. Acta Geographica Sinica, 70(06): 980-992.

Chen Z. 2016, Eco-efficiency, urbanization and spatial overflow: A study based on the space panel Durbin model [J]. Management Review, 28(11):66-74

Xu S. 2016. Research on the spatio-temporal evolution and influencing factors of energy eco-efficiency in China [D]. Liaoning Normal University,

Zhong X, Long S. 2016, A further understanding of the IPAT model of environmental impact[J]. China Population, Resources and Environment, 26(03): 61-68

266: A fuzzy set based synthetical approach of faulty line selection for single-phase ground fault

Tingkang PENG[1]，Ziqiang XI[2]，Liang SHUAI[3]

[1]Solar Energy Building, Hubei University of Technology, Wuhan, Hubei Province, 430068, China, 1457766941@qq.com
[2]Solar Energy Building, Hubei University of Technology, Wuhan, Hubei Province, 430068, China, 695936405@qq.com
[3]Solar Energy Building, Hubei University of Technology, Wuhan, Hubei Province, 430068, China, 972710028@qq.com

The single-phase earth fault of the distribution network is an important problem that needs to be solved in the grid system fault. The correct selection of the distribution network is the key to solving this problem. Since there are many types of single-phase ground faults, and the corresponding solution for each case will be different, the traditional line selection method is difficult to effectively solve the fault.After comprehensive consideration, this paper designed a fault line selection method,which integrates a large number of single methods and makes comprehensive judgments on a variety of sampled signals, resulting in a more effective and reliable line selection result than before.In this paper, the fuzzy theory is analyzed in detail.We established the measure membership functions and corresponding weight system functions of zero-sequence active power method, zero-sequence current fifth harmonic ratio method and zero-current ratio method.Based on the information fusion theory, a fault line method is designed.Using MATLAB to build two three-phase simulation systems, respectively ungrounded systems and arc suppression coil grounding systems.Then artificially introduce single-phase ground faults at different locations in each system, sample and analyze the three-phase voltage, zero-sequence voltage, three-phase current, and zero-sequence current of each system line under each fault.Finally, use the designed comprehensive line selection method to obtain the simulation result，proving that the method can be used fordistribution net-work neutral point grounding and neutral point via arc suppression coil grounded system. In the end,it is proved by MATLAB simulation that this method is suitable for the selection of line neutral point ungrounded and neutral point arc-suppression coil grounding system as well.The conclusion is that this integrated line selection method can provide more comprehensive and accurate discrimination criteria for line selection than the traditional single line selection method.

Keyword ：Single-phase Fuzzy control MATLAB simulation

1. INTRODUCTION

In China, arc-extinguishing coil grounded or ungrounded system are normally used in the distribution network.The single-phase grounding of the power distribution network is the most prone to failure. When a single-phase ground fault occurs in the distribution network, a small ground current will be generated. Because of the fact that the three-phase line voltage does not change, the user will not be affected in a short time.However, if it is not dealt with as soon as possible, the single-phase ground fault may cause the grid system capacitive current to the ground to be expanded, and then cause a wide range of power failures, causing huge economic losses and casualties.Therefore, we should handle single-phase ground faults promptly and quickly. Correctly selecting the line is the precondition for quickly solving this problem. Therefore, it is of practical significance to study the problem of fault line selection in distribution networks.

Currently, the methods of the single-phase ground fault line selection can be divided into three categories based on the type of signal sampled: selection method based on the steady-state,selection method based on transient amount,and signal injection.Here we mainly discuss zero-sequence current amplitude method, zero-sequence current relative phase method, fifth harmonic component method, and negative sequence current method based on the steady state quantity method.Based on the fuzzy function, we use the membership functions toanalyze the zero-sequence current method, the zero-sequence current ratio method, and the fifth harmonic component method.We focus on a comprehensive selection method,which is based on the fuzzy line theory of integrated line selection method. The features of multiple faults are intelligently combined using multiple line selection methods. Finally, the feasibility of the method is proved by MATLAB simulation.

2. THE ESTABLISHMENT OF THE FUZZY MODEL

2.1. Fuzzy function theory and its application

Fuzzy Function Modeling is a problem that must be solved firstly for actual practical fuzzy methods.The rationality of membership function selection will directly affect the accuracy of fuzzy set quantification.The same fuzzy problem may have many different solutions using the membership functions.Due to the diversity of practical problems, the choice of membership functions does not have a uniform standard.Although the choice of membership functions is subjective, as long as the fuzzy relationships between fuzzy sets are used and analyzed, the membership functions can be scientifically reflected.Membership functions need to be continuously improved in practice. By constantly modifying the membership functions, more scientific and accurate data can be obtained on the results.The commonly used methods of membership numbers are binary contrast ranking method, fuzzy statistics method and so on.Determining the appropriate domain can reduce the operation of fuzzy sets,In determining the universe of the set, the first thing to do is to determine the range of variable sets that can fully map fuzzy sets based on the actual fuzzy problem; the second thing to do is to represent all fuzzy characteristics using the smallest set of discourses.

In determining the domain of fuzzy sets, the focus is to analysis the elements with membership degrees of 1, 0, and 0.5:

(1) Sets with a degree of membership of 1: A set of membership degrees of 1 is the "nucleus" of the fuzzy set, which constitutes the "main value interval" and directly determines the membership function.
(2) A set with a degree of membership of 0: When the degree of membership of an element is 0, the fuzzy set does not contain this element.
(3) Set of domain elements with a degree of membership of 0.5: The most difficult part to determine is the element with a degree of membership of 0.5 in a fuzzy set. If the fuzzy set is the least certain whether a certain element belongs to the set, the element can be assigned an affiliation as the degree of 0.5.There are two methods for determining the most fuzzy point in practical applications:firstly, according to characteristics of the fuzzy set, the most indeterminable element is determined as the most fuzzy point based on experience; and secondly, the element whose membership degree is 1 or 0 and the degree of membership cannot be determined is determined as the most fuzzy point.

Recently, due to the different environment of the single-phase ground fault of the distribution network system, judging the line selection by using a fault criterion cannot ensure the correctness of the line selection.On the basis of information fusion, this chapter designed a method for selecting single-phase ground faults in power distribution networks. The results were obtained by comprehensively judging the multi-criterions of the sampled signals.Next, the membership functions of the zero-sequence current ratio method, zero-sequence active power method, and zero-sequence current fifth harmonic phase ratio method are going to be respectively introduced.

Zero-sequence current ratio method

The zero-sequence current ratio method determines the fault line by comparing the amplitude of the current. The bus zero sequence current is defined as:

Equation 1:

$$I_{00} = -\sum_{i=1}^{n} I_{0i}$$

Equation1 indicates that the line-to-ground capacitance currents of the system, such as bus zero-sequence current values, are in opposite directions.And the zero-sequence current would be equation 2:

Equation 2:

$$|I_0|_{sum} = \sum_{i=0}^{n} |I_{0i}|$$

When a line fails to ground, $I_{00} \approx 0$ .When the bus fails, $I_{00} \approx -\frac{1}{2}|I_0|_{sum}$ .The line fault measure function is inversely proportional to the line zero-sequence current I_{0i} . Therefore, the fault measure function can be expressed as Equation 3 :

Equation 3:

$$\mu_r(i) = \begin{cases} 1 & I_{0i} < -0.5|I_0|_{sum} \\ \dfrac{0.5|I_0|_{sum} - I_{0i}}{|I_0|_{sum}} & -0.5|I_0|_{sum} < I_{0i} < 0.5|I_0|_{sum} \\ 0 & I_{0i} > 0.5|I_0|_{sum} \end{cases}$$

The curve of the membership function of the zero-sequence current fundamental wave ratio method is shown in Figure 1. The zero-sequence current fundamental wave amplitude method not only considers the amplitude, but also considers the phase at the same time.

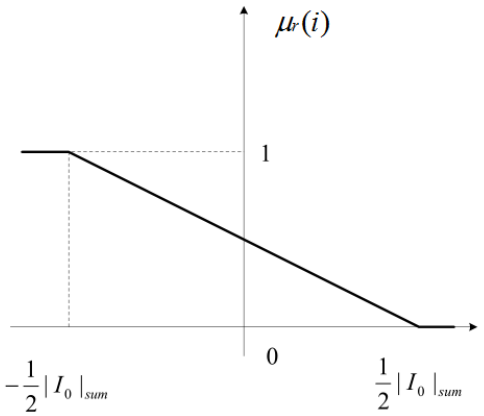

Figure 1: Membership function curve

The fault line zero-sequence current of the distribution network is several times the zero-sequence current of other normal operating conditions.However, if the line is short or grounded with high impedance, the difference between the zero-sequence current of the faulty line and the normal line is small.Therefore, the weight coefficient function can be determined according to the difference of the zero-sequence current, such as Equation 4. The curve is shown in Figure 2.

Equation 4:

$$A_r = \begin{cases} 1 & |I_0|_{\max} \geq 0.5|I_0|_{sum} \\ \dfrac{|I_0|_{\max}}{0.5|I_0|_{sum}} & 0 \leq |I_0|_{\max} < 0.5|I_0|_{sum} \end{cases}$$

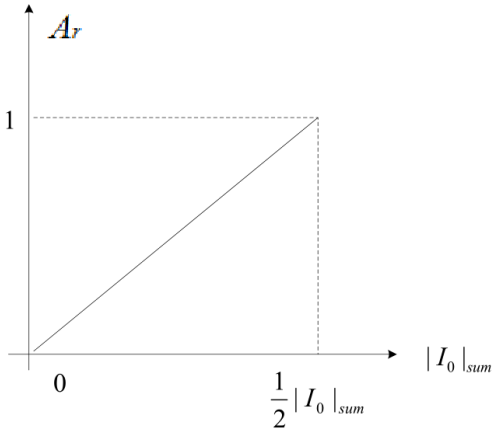

Figure 2: Zero-sequence current weight coefficient function

Zero-sequence active power method

Due to the influence of the impedance of the arc suppression coil, the zero-sequence current of the faulty line is more than several times that of normal operating conditions, and the zero-sequence active power has high sensitivity.The essence of this method is to use the amplitude characteristics of the zero-sequence current after the single-phase earth fault of the distribution network. The inductor current compensated by the arc suppression coil reduces the fault current and easily misjudges the flow of the zero-sequence current.Therefor,we can reduce the accuracy of fault line selection by zero-sequence active power method.

The method for calculating the zero-sequence active power is Equation 5:

Equation 5:

$$P_{0i} = 3U_0 I_{0i} \cos\phi_i = \frac{1}{3T}\int_t^{t+T} 3u_0(t) * 3i_{0i}(t)dt$$

The method for calculating the zero sequence active power of the bus is Equation 6:

Equation 6:

$$P_{00} = \left|P_{0i}\right|_{sum} - \left|P_{0i}\right|_{\max}$$

Among them, $\left|P_{0i}\right|_{\max}$ and $\left|P_{0i}\right|_{sum}$ respectively represent the maximum and total sum of zero-sequence active power of all outgoing lines.

It can be deduced from the equations above that when a ground fault occurs in the distribution network, the probability of the faulty line is directly proportional to its zero-sequence active power value. The membership function of the fault measure is shown in Equation 7 which Indicates that the membership function is proportional to the zero sequence active power.

Equation 7:

$$\mu_a(i) = \frac{\left|P_{0i}\right|}{\left|P_{0i}\right|_{\max}}$$

The zero-sequence active power is greatly influenced by the waveform. The larger the single-phase grounding resistance, the zero-sequence voltage and current waveform distortion will be selected. At this time, the characteristics of the zero-sequence current are less obvious, and then the fault is only caused by the zero-sequence current amplitude. The lower the accuracy of the judgment, the weighted system function of the zero-sequence active power method is determined based on the waveform distortion rate v of the zero-sequence current.

Here is the design of weight system function.When the distortion rate v is greater than 5%, the coefficient is 0; When the distortion rate v is less than 5%, the coefficient is 1; when the waveform distortion rate is greater than 5% and less than 50%, it is a decreasing function. The weight coefficient function is shown in Equation 8 and Figure 3.

Equation 8:

$$A_a=\begin{cases}1 & \nu \le 0.05 \\ -\dfrac{20}{9}\nu+\dfrac{10}{9} & 0.05<\nu<0.5 \\ 0 & \nu>0.5\end{cases}$$

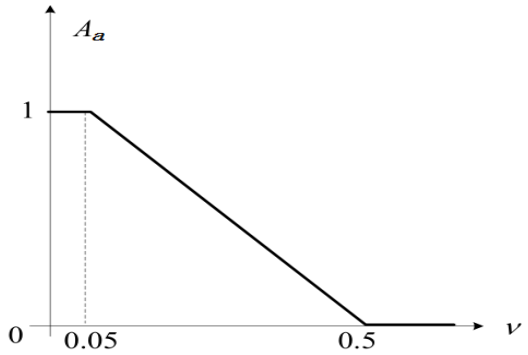

Figure 3. Zero sequence function weight function

Zero-sequence current fifth harmonic ratio phase method

Zero-sequence current fifth harmonic phase ratio method can avoid the interference of arc suppression coil.The fifth harmonic phase ϕ_{5i} is converted in order to use the fifth harmonic phase quantity more effectively,guaranteeing the zero-order voltage fifth harmonic phase BB is a monotonic function in [0,180],like it's shown in Equation 9.

Equation 9:

$$\phi_{5ci}=\begin{cases}\left|\phi_{5i}-90°\right| & \phi_{5i}>0° \\ 180°-\left|\phi_{5i}+90°\right| & \phi_{5i}<0°\end{cases}$$

$\phi_{5ci}=0°$ and $\phi_{5ci}=90°$ (capacitive) are the cases for normal line conditions.And $\phi_{5ci}=180°$ and $\phi_{5ci}=-90°$ (inductive) are the cases for a faulty line.The fault measure membership function is shown as Equation 10.

Equation 10:

$$\mu 5ci(i)=\begin{cases}1-\dfrac{\max\phi_{5ci}}{180°} & i=0 \\ \dfrac{\phi_{5ci}}{180°} & i=1\ldots n\end{cases}$$

And the graph of the subharmonic membership function of the zero-sequence current is shown in Figure 4.

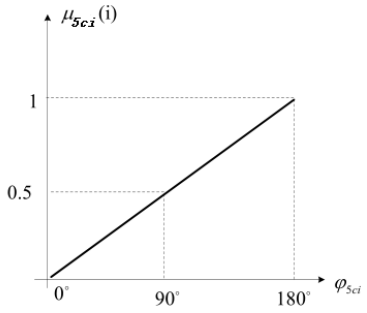

Figure 4: Zero-order current fifth harmonic membership function

After analysis, it can be seen that when a neutral phase ungrounded system experiences a single-phase ground fault, the zero-sequence current harmonic phase of the faulty line is the opposite of the non-faulty line.When the phase is in the third or fourth quadrant, the weight coefficient function value is 1.However, when the zero-order

current fifth harmonic signal is weak, the phase of the non-faulty line will misjudge the fault line selection and reduce the reliability of the weighted system function.When the non-faulty line phase falls more in the third or fourth quadrant, the credibility of the weight coefficient would be lower, and the weight coefficient is shown as Equation 11 where Ln is the number of lines($Ln = n+1$); C_{n5} is the number of phases in the third or fourth quadrant.

Equation 11:

$$A_{5ci} = \begin{cases} 1 & Ln = 1 \\ \dfrac{Ln - Cn_5}{Ln - 1} & Ln < 1 \end{cases}$$

2.2. Fuzzy general selection criteria

According to the principle of information fusion, the fuzzy fault comprehensive selection procedure based on information fusion technology is shown in Figure 5.

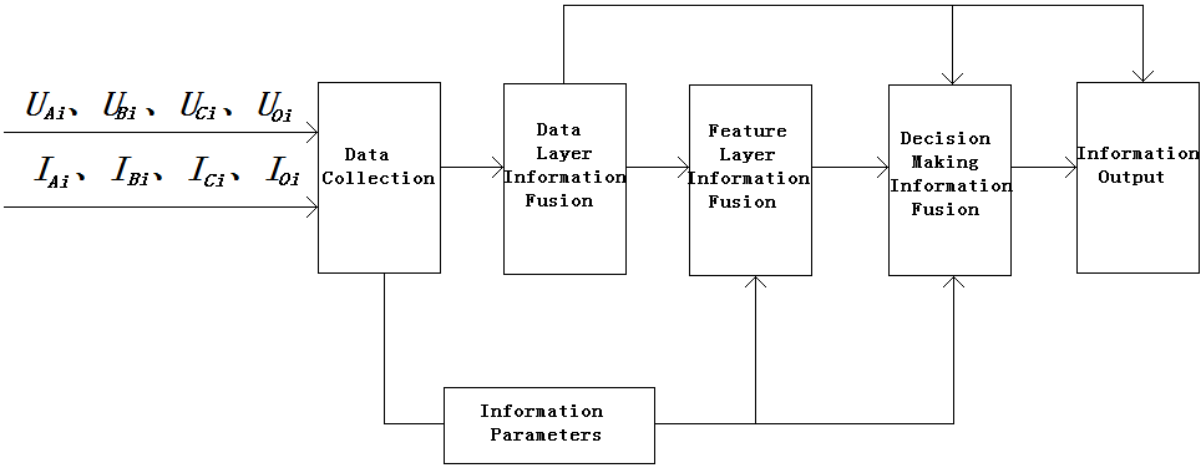

Figure 5: Integrated line selection criteria

The single-phase ground fault voltage and current of the distribution network are transmitted to the line selection device through the transformer, and the fuzzy integrated line selection criteria of the bus and each line can be shown as Equation 12,according to the fuzzy theory of fault comprehensive line selection method,using mathematical tools such as wavelet function to extract fault features such as zero-sequence voltage and current,and calculated by fault measure membership function and weight coefficient function.

Equation 12:

$$P_f = \frac{A_r\mu_r(i) + A_a\mu_a(i) + A_{5ci}\mu_{5ci}(i)}{\sum_{i=0}^{n} A_r\mu_r(i) + A_a\mu_a(i) + A_{5ci}\mu_{5ci}(i)}$$

According to the calculation results, the fault line is selected according to the value of P_f ,and that selected line would be the maximum value is the fault line.

3. MATLAB MODELING AND SIMULATION

3.1. Matlab simulation model

According to the comprehensive line selection method proposed in Chapter 2, this chapter will carry out the relevant simulation of the method.We use a 110kV substation as a model. Switch Breaker2 can realize different neutral grounding methods.Figure 6 shows the simulation model of this system using Matlab/Simulink.

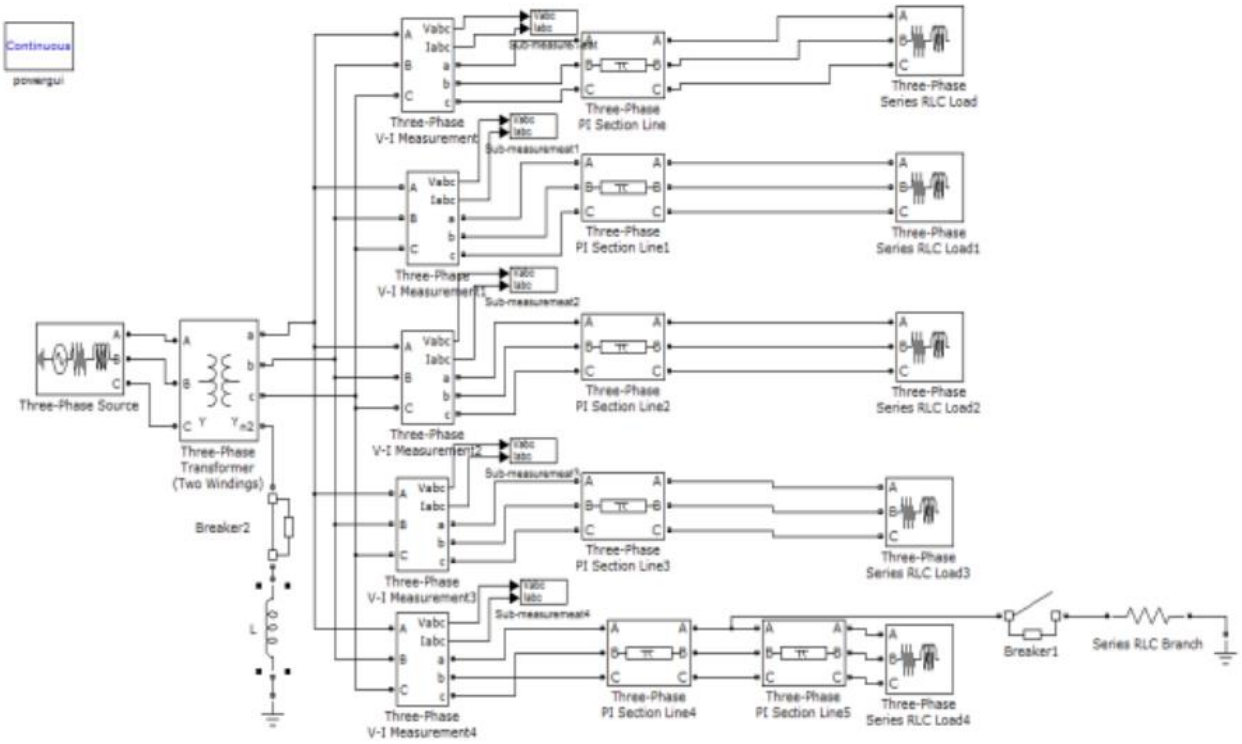

Figure 6: System Simulation Diagram

The positive sequence parameters of the line are: $R_1 = 0.17\Omega / km$, $L_1 = 7.6mH / km$, $C_1 = 0.061\mu F / km$;

The zero sequence parameters of the line are: $R_0 = 0.23\Omega / km$, $L_0 = 34.4mH / km$, $C_0 = 0.038\mu F / km$;

The Power capacity is 300MVA;The Transformers with a voltage rating of 110kV /10kV.And the line lengths are:

$l_1 = 5km, l_2 = 8km, l_3 = 10km, l_4 = 15km, l_5 = 16km$.

3.2. Simulation results

In the Matlab simulation model established in this paper, the time domain simulation of the normal working conditions of the distribution network is performed.

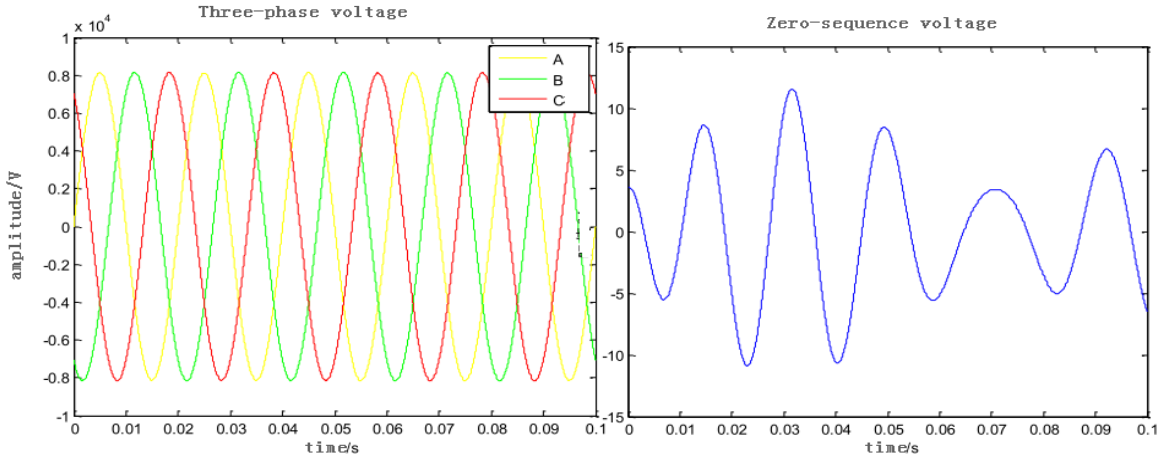

F igure 7: Voltage and zero-sequence voltage of line l5 as Ungrounded system

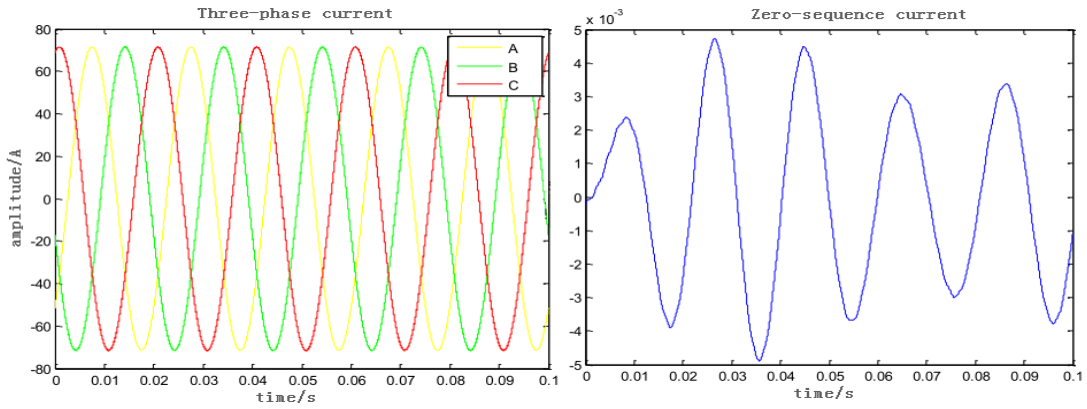

Figure 8: Current and zero-sequence current of line l5 as as Ungrounded system

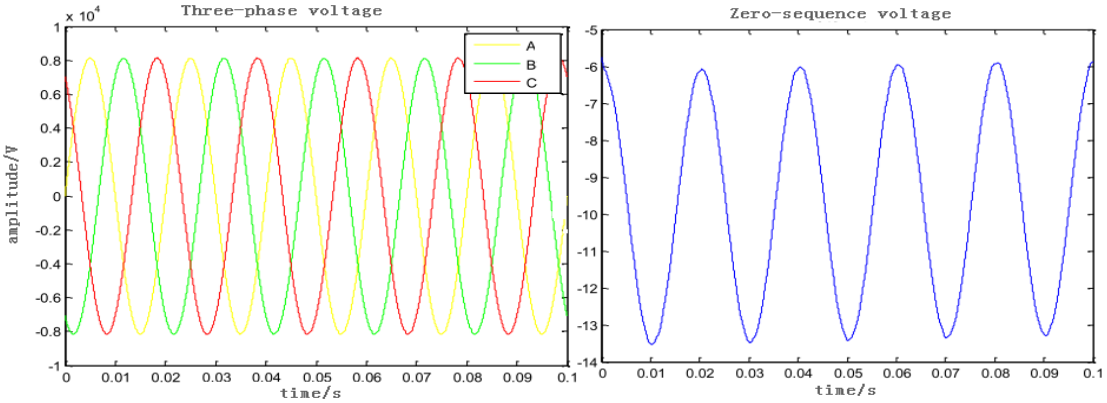

Figure 9: Voltage and zero-sequence voltage of line l5 as arc suppression coil grounding system system

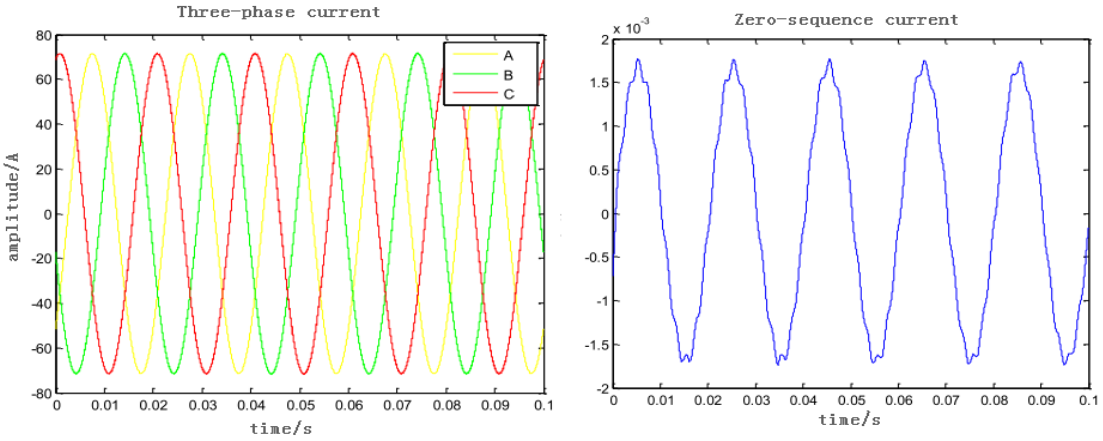

Figure 10: Current and zero-sequence current of line l5 as arc suppression coil grounding system system

From the simulation, it can be seen that when the neutral point is not grounded and the distribution network grounded by the arc suppression coil is in normal operation, due to the asymmetry of the load, the grid will also generate transient voltages.And the zero-sequence voltage of the system is very small, less than 1% of the phase voltage of the grid, and there is basically no zero-sequence current, so it will not affect the stable operation of the power grid.

3.3. Fault integrated line selection in Matlab simulation

Ungrounded distribution network system

Switch Breaker2 into open, assuming a phase-one ground fault in phase A has occurred at 12 km of line l_5.The fault occurs at 0.03s and the ground resistance is 1Ω.The fuzzy integrated line selection simulation results of the ground fault are shown in Table 1.

Table 1: Measure of Ungrounded system fault

Line selection method	Measure of fault					
	Bus	L1	L2	L3	L4	L5
Zero-sequence current ratio method	0.0035	0.5614	0.6175	0.4973	0.5436	0.9871
Zero-sequence active power method	0.1157	0.0936	0.2023	0.2786	0.3945	0.9867
Zero-sequence current fifth harmonic ratio phase method	0.3312	0.3676	0.2136	0.2546	0.4161	0.5979
Fuzzy comprehensive line selection	0.2644	0.4232	0.5067	0.3938	0.4576	0.8967

Arc suppression coil grounding system

Switch Breaker2 into close, assuming a phase-one ground fault in phase A has occurred at 13 km of line l_5.The fault occurs at 0.03s and the ground resistance is 1Ω,and the over compensation is 10%.The fuzzy comprehensive line selection simulation of the system under the single-phase earth fault is shown in Table 2.Table 2 shows that the zero-sequence current ratio method is not accurate in single-phase ground fault line selection in the arc-suppression coil grounding system, but fuzzy comprehensive line selection can accurately determine fault line selection.

Table 2: Measure of Arc suppression coil grounding system fault

Line selection method	Measure of fault					
	Bus	L1	L2	L3	L4	L5
Zero-sequence current ratio method	0.0038	0.4978	0.5064	0.5234	0.5318	0.5478
Zero-sequence active power method	0.0913	0.0826	0.1223	0.1334	0.2168	0.8039
Zero-sequence current fifth harmonic ratio phase method	0.2935	0.2578	0.3356	0.4167	0.4535	0.7168
Fuzzy comprehensive line selection	0.1036	0.1435	0.3089	0.3496	0.3967	0.7034

4. CONCLUSION

The correct selection of distribution network is the premise to solve the single-phase earth fault of the distribution network, and is the basis for the stable operation of the power grid as well.Domestic and foreign scholars and experts introduced Walsh function, fuzzy theory, information integration, neural network, wavelet analysis and other mathematical analysis tools in the study of single-phase ground fault signal characteristics to extract the single-phase ground fault transient signal characteristics more reliably and accurately.However, how to further use single-phase ground fault transient signals for line selection research requires extensive research by scholars and experts.

As it is the fact that there is some uncertainty in current line selection using a single criterion, this paper designed a single-phase ground fault line selection scheme based on fuzzy theory.Based on the theory of fuzzy control, the zero-sequence current ratio method, the zero-sequence active power method, and the zero-order current fifth-order harmonic phase ratio method are used to establish the three single-phase ground fault measure membership functions and the corresponding weight system functions.So here we design the single-phase ground fault integrated line selection method . Through MATLAB simulation, this method was proved to be applicable to the line selection judgment of distribution network neutral point ungrounded and neutral point arc-suppression coil grounding system.Compared with the traditional single line selection method, this method can avoid the possible misjudgment of a single line selection verdict,thus can provide more accurate and rapid selection criteria.This method is more reasonable and can make correct line selection under the influence of various factors. Therefore, this method has higher discrimination accuracy and stability.The comprehensive line selection method based on

membership function can be used as the basis for distinguishing single-phase ground faults.Although this method can solve the problem of fault line selection for ungrounded and arc-suppressed coil grounding systems in distribution networks, this method requires further research so we can find a more reasonable and more complete membership function method to solve the problem of correct line selection in single-phase ground faults in distribution networks.This method still requires actual testing to be able to play its role in practice.

5. REFERENCES

Deaton R J, 1984. Limitations of ground-fault protection schemes on industrial electrical distribution systems..IEEE-IAS-1984 Annual Meeting

Janne A, Olavi M, Kimmo K ,2003 .Intermittent Earth Faults-need to Improve the Existing Feede Earth Fault Protect on Schemes.Barcelona:17th International Conference on Electricity Distribution CIRED

Assef Y, Bastard P, Meunier M, 1996. Artificial Neural Networks for Single Phase Fault Detection inResonant Grounded Power Distribution Systems.LosAngeles:Proc.IEEEPES Transmission and Distribution Conference,566-572.

Ruz F, Fuentes JA, 2001. Fuzzy Decision Making Applied to High Impedance Fault Detection in Compensated Neutral Grounded MV Distribution Systems.Developments in Power System Protection,Conference Publication No.479 IEE 2001,307-310

Yajie L, Keyan L, Xiaoli M，2016. A single-line-to-ground fault diagnosis method in small-current--grounding system based on fuzzy-integral decision fusion technique.2016 China International Conference on Electricity Distribution

Huang Z, Xing C, Fan X, 2011. The Stable State Analysis on the Single-phase Earth Fault of Small Current Grounding System Based on Mathematical Model.2011 International Coriference on Electronics and Optoelectronics

Cao J, Lu J, 2017. Research on fault location method in small current grounding system based on active protection. 2017 4th International Conference on Information Science and Control Engineering:1158-1162

Yundong S, Shun Y, Chunfang Z, 2007. Neural Network Faulty Line Detection Method in Small Current Grounding Systems Based on Rough Set Theory.Proceedings of the 2007 IEEE:3735-3739

Wang Y, Long F, Zuo Z, 2011. Support Vector Machine for Classification and its Application to the Small Current Grounding Fault line Detection in Peterson-Coil-Grounding System.2011 Fourth International Conference on Intelligent Computation Technology and Automation:727-730

Fang C, Rolando B, Dushan B, 2018. A Bidirectional High-Efficiency Transformerless Converter with Common-Mode Decoupling for the Interconnection of AC and DC Grids.IEEE Transactions on Power Electronics:1-1

Zheng S, Liancheng W, Han Z, 2016 A fault line selection method for small current grounding system based on big data.2016 IEEE PES Asia-Pacific Power and Energy Engineering Conference (APPEEC): 2470 – 2474

Xiangxiang W, Dechang Y, 2015. An adaptive fault line selection method based on wavelet packet comprehensive singular value for small current grounding system.2015 5th International Conference on Electric Utility Deregulation and Restructuring and Power Technologies (DRPT): 1110 – 1114

Guping Z, Qiang L, Haihan L, 2015. Improved mathematical morphology transformation and application to single ground fault feature extraction in small current system.2015 5th International Conference on Electric Utility Deregulation and Restructuring and Power Technologies (DRPT): 2431 – 2435

Yuling L, Hui L, 2012. The transient signal analysis of the single phase grounding fault of small current ground power system.2012 International Conference on Wavelet Active Media Technology and Information Processing (ICWAMTIP): 334 - 337

268: An empirical analysis of household energy consumption in Hubei Province under the transition of income class

Yanhua ZHANG[1,2,3], Yunchao XIA[1], Xian YU[1], Mengyuan HU[1]

[1] the College of Economic and Management, Hubei University of Technology, Nanli Road No.28, Hongshan District, Wuhan City, Hubei Province, China, 2039076986@qq.com
[2] the Research Center of Circular Economy Development in Hubei, Nanli Road No.28, Hongshan District, Wuhan City, Hubei Province, China
[3] the Collaborative Innovation Center of Regional Industrial Ecology Development, Hubei University of Technology, Nanli Road No.28, Hongshan District,Wuhan City, Hubei Province, China

The paper used the way of micro-data collection. In the form of a one-to-one survey conducted by the investigator, I visited 16 cities under the jurisdiction of Hubei province, collected 788 valid questionnaires and got the latest data of 2017.Obtained the detailed data on the income level of the residents and the use of various kinds of household energy. The data indicated that the mainly household energy consume in Hubei province are electricity, liquefied petroleum gas, gasoline and firewood. According to the structure and data characteristics of the questionnaire, classified the families according to the annual household income into five types as under 30000 yuan, 30000 to 50000 yuan, 50000 to 100000 yuan, 100000 to 200000 yuan, and more than 200000. Use the Excel and Stata to measure their energy consumption preferences at different income levels. Through analysis, it is found that the energy consumption of households in Hubei Province shows a clear energy mix. The dominant energy portfolio is different for each income level. With the increase of income, the general trend of "complexity to simplicity" has emerged for the choice of energy mix .Resulting in the rapid rise of the energy combination represented by "gasoline + electricity" in the consumption structure. Changes in energy mix also have volatility characteristics. In the energy consumption structure of Hubei Province, the amount of gasoline is the most, equivalent to approximately 7,252,0972 tons of standard coal. Electricity consumption ranks second, which is equivalent to approximately 3,075,721 tons of standard coal. With the help of the expression of the data and the charts. To show the situation about the household energy consumption and the household energy consumption preferences in Hubei Province in 2017.According to the actual situation of energy consumption of the residents to provide reference for the development policy of Hubei province.

Keywords:Micro data; Household Energy Consumption; Energy Consumption ; Energy Mix; Energy consumption Preference

1. INTRODUCTION

The issue of energy consumption has always been the focus of research by Chinese and foreign scholars. From agricultural civilization to industrial civilization to ecological civilization, the replacement of civilization is not based on simple ideological or lifestyle changes. The change in energy demand has led to a radical change in the way of thinking and life of human civilization. At the same time, it will inevitably leave behind the shadow of the previous generation of civilization. At the stage of farming civilization, fuelwood and straw are the motive power for the advancement of mankind. They have mastered the techniques of drilling firewood and using charcoal to retain the fire, allowing human beings to rescue themselves from the threat of survival. In the industrial civilization stage, with the invention and improvement of steam engines and the continuous upgrading of internal combustion engines, coal and petroleum have become the guidelines for humans to embark on the fast lane of development and have mastered the methods of high-efficiency and stable control of energy, allowing rapid connection between humans. The limitations of time and space have freed humanity from connection barriers. At the ecological civilization stage, with the awakening of more people's environmental awareness, the production and life of an era consumes the carbon accumulated in several eras, resulting in visible changes in the climate, so that the efficient development of the cycle of energy to extend the energy cycle development model came into being. More new energy representing ecological interests is being explored. More new energy sources are waiting to be discovered. Because the energy issue is related to the fate of an era, the rise and fall of a society, so a series of topics derived from energy consumption have received attention.

2. LITERATURE REVIEW

Provincial family life energy consumption is one of the sub-topics of energy consumption issues. China is affected by the difference in resource endowment, resulting in more than 62% of domestic energy consumption structure is coal, which has caused China's CO2 emissions have been high in recent years. To cope with climate change caused by CO2 emissions, China has officially launched a nationwide carbon trading market in December 2017, and has included emission-intensive industrial companies in mandatory emission reductions. In the constant technological innovation, most industrial enterprises will reduce energy intensity and reduce energy consumption, but household energy consumption emissions will hardly consider the externalities of the environment, which will hinder the realization of the country's emission reduction targets, and at the same time, due to the dispersion of households' living, Cannot effectively implement monitoring and management, data is not easy to obtain, resulting in the difficulties of quantitative analysis (Wei Chu et al., 2017). In addition, due to the data involved in many private issues also caused great difficulties in the collection of data.

The problem of household energy consumption is more to start with coal consumption because some scholars have found that the range of coal-fired time and severe haze occurrences in northern rural households coincide highly (Zheng Xinye et al., 2015), and found coal by establishing multiple linear regression models. The consumption will be affected by resource endowments, climate differences and income levels (Wei Chu et al., 2017). Because China has a vast territory, climate change and resource endowments vary greatly from place to place. In order to visualize digital data and draw a map of energy use (Huo Molin et al., 2017), we can visually compare spatial differences. The data from the earlier studies came from the statistical yearbooks of the National Bureau of Statistics or provinces and cities. However, compared with the use of time-series data, micro-data can more accurately reflect the actual situation in an area. As a result, micro-data were favored by more and more scholars. The "Chinese Residents' Energy Consumption Survey" is a questionnaire designed based on the actual situation of residents (Zheng Xinye et al., 2016). Although microscopic data is difficult to obtain, due to recent exposure to actual consumption targets, Therefore, it is indeed the best choice to reflect the actual situation in the survey area, and it is relatively more accurate and adaptable than the current method of remote sensing satellite estimation (Huo Molin et al., 2017). On the basis of good data, a sample method for estimating the population was used to aggregate the national data (Zhiguo Rui et al., 2015). At the present stage, most of the analysis of data is the multiple linear regression model, which analyzes the significance between variables. In the field of consumer behaviour, many scholars have used the linear expenditure system model to analyze the relationship between total consumption and income of different energy types (Song Mingming et al., 2017). In order to improve the connotation of the model, they also proposed an extended linear expenditure system model (Zhang Xin et al., 2011) compare the differences in preferences of energy choices for different income levels. In the study of energy consumption structure, the use of the "energy ladder" model is also a very common analysis method (Zhang Haipeng et al., 2010). Although the predecessors have already proposed a good data collection method and improved the data processing model, they are all studying the situation in a large area. The data based on the survey alone is not enough for model analysis, and there are errors if the data is in small areas. Based on the classification of data for expansion, it will be more representative. Prior to this, some scholars have already studied issues related to energy consumption of households, such as policy orientation, energy supply, and so on. This article analyzes energy consumption under different income levels based on survey data.

This article is based on the micro survey data of Hubei Province, mainly through the survey of 16 cities to obtain various energy consumption data under different income conditions, and estimate the average situation of the province according to the proportion of the sample to achieve the purpose of reducing statistical errors. . The purpose of the study is to clearly understand the actual situation of household energy consumption in Hubei Province through various types of energy data and income status, compare the energy selection preferences under different income levels, and observe the actual situation of the energy portfolio and the magnitude of its replacement.

In order to achieve this goal, the first is to sort out the energy consumption data of each city in Hubei province, to estimate the average level within the province through samples, to use the energy ladder model, and to grade according to the level of income, observe the various income levels through the multi-valued Logit model. Under the selection preference, get the relevant conclusions. The main contribution of this paper is a detailed analysis of the use of various energy sources in different household income levels in Hubei Province. With changes in income levels, preferences for various energy and energy combinations, and household energy consumption structure in Hubei Province There is a comprehensive understanding to provide valuable opinions and data for improving energy consumption structure or inducing consumer preferences.

The structure of this paper is as follows. The first part introduces the sources of data and the selection of research methods. The second part uses the results of analysis to compare the preferences of family life energy at different income levels. Finally, draw relevant conclusions and recommendations.

3. DATA SOURCES AND RESEARCH METHODS

3.1. Data sources

Based on the “Household Energy Consumption Survey in Hubei Province,” this article collected specific data on energy consumption for household life. This data was initiated by the Energy Economics Department of Hubei University of Technology. From the winter of 2016, the energy consumption of households in Hubei Province was included. Household survey activities were conducted by the investigators in person at the interviewees' homes to carry out one-on-one interview questionnaire surveys. The design of the questionnaire mainly included the basic information of the respondent's family, household income and expenditure, household energy use, and household electrical appliances. Usage and traffic conditions and the main factors affecting travel. From the actual situation of the residents' living, we should understand the use of various energy sources and the specific usage in the residents' life.

The data used in this paper is mainly the summary of the data of household income and expenditure and household energy in the questionnaire. The questionnaire distributed a total of 3043 data, a total of 1749 questionnaires were recovered, and 788 was obtained in the subsequent collation. Effective data, which covers 16 cities within the province: Huangshi, Huanggang, Enshi, Ezhou, Jingzhou, Jingmen, Qianjiang, Shiyan, Suizhou, Tianmen and Wuhan , Xiantao City, Liyang City, Xianning City, Yichang City, Xiaogan City. In the section of household income and expenditure, the annual income level is selected, which is <30000, 3-50000, 5-100000, 10-200000, and >200,000, and five income levels, and according to the principle of statistics Take the average of 15,000, 40,000, 75,000, 150,000, and 250,000, respectively. In this paper, the data of firewood, liquefied petroleum gas, electricity consumption, and gasoline are used according to the actual conditions, and the conversion is carried out according to the standard coal coefficient.

Table 1: shows the discount coefficient

	Firewood	Liquefied gas	electricity	gasoline
standard coal coefficient	0.56kgce/kg	1.7143kgce/kg	0.1229kgce/(kw.h)	1.4714kgce/kg

3.2. Research methods

This article mainly analyzes the energy mix used by households under different income levels according to the “Energy Ladder” model, and the trend and volatility of alternative energy mixes during the transition of income levels, and compares households with different income levels according to the multi-valued Logit model. Life energy has a preference for firewood, liquefied petroleum gas, electric energy, and gasoline.

First of all, the total amount of samples of four kinds of living energy is collected, and then the total consumption of these four types of energy in the province is estimated from the samples. The total consumption of the four major sources of living energy in Hubei Province was calculated and adjusted according to the proportion of the sample and the level of income. Assume that the sample household uses a variety of energy per household as Mi (where i=1, 2, 3, and 4, respectively, representing fuelwood, liquefied petroleum gas, electricity consumption, and gasoline, the same below), that is, total coal consumption divided by The number of households participating in the survey; At the same time, M1i represents the total consumption of various energy sources divided by the number of households using the energy in households surveyed. Then, the consumption of various energy sources (C_i) for residents' family life can be calculated by the following formula:

$$C_i=M1_i \times R \times P_i \quad (1)；P_I=p \times r_i \quad (2)$$

Among them, M1i represents the average household consumption of various energy sources, the unit is Kgce/household; R is the proportion of households using this energy (%), ri is the proportion (%) of each income level in the sample, P is the family in the area The total number of households, the variable data from the sixth national census.

With the increase in household annual income level, the average household heating coal in rural households is “inverted U-shaped”, which means that within a certain range, when income increases, people’s demand for coal will increase, and when the family economic life After a greater level of improvement, people will choose higher-quality, less polluting energy sources to replace coal-fired fuels and achieve better quality of life. (Zhang Haipeng et al., 2010) shows that neglecting the impact of income will cause greater bias in consumer preferences.

In different income levels, fuelwood, liquefied petroleum gas, electric energy, and gasoline are the main living energy sources. However, the survey data show that, apart from electricity, household energy can be supplied separately. In households, household energy is basically energy. The combination of forms of energy supply, so the use of "energy ladder model" for different income levels of energy portfolio statistics, which to observe the income transition energy combinations to replace the speed and extent of help.

In the analysis of the individual's actual energy consumption behaviour, the Logit model is widely used. In the micro-decision-making process, what factors influence the consumer’s purchase decision of a specific brand or commodity and how it affects it? This is undoubtedly the microfoundation of many economic activities. This is the advantage of the Logit model in distinguishing it from other analytical tools (Chen et al., 2006). In the process of micro-decision making, the choices faced by individuals are often multi-valued, so this paper mainly introduces the multi-valued Logit model into the research on the purchasing preferences of the four kinds of energy needed for living under different income levels in the household life. In the article, the income level Xi has 5 levels, ie all individuals are in the 5 mutually exclusive levels. Using randomization, individuals j use different energy sources at different income levels to produce different random effects:

$$U_{ji}=y_j\beta_i+\varepsilon_{ji} \quad （i=1、2、3、4、5；j=1、2、….）（3）$$

Among them, under the same income level, individual preferences for various energy sources are not affected by income levels. The variables in the Logit model are interpreted as dichotomous variables, and the "most likely" estimate of the "coefficient" is found using the method of generation of the maximum likelihood estimate. By the same token, as the “economic person”, utility maximization is often the pursuit of consumers, so the individual’s preference for that type of energy can be expressed as:

$$P(X_i=\mathrm{i}/\mathrm{y}_j)=\frac{\exp(y_j\beta i)}{\sum_{k=1}^{i}\exp y_j\beta_k} \quad （4）$$

Obviously, the probability of a self-employed household distributed at each level is 1, it`s

$$\sum_{i=1}^{i}P(X_i=\mathrm{i}/\mathrm{y}_j)=1$$

Equation (4) is a natural extension of the binary logit model to the multi-valued logit model. In this case, it is not possible to identify all of them, so usually the largest number of observations is used as a reference item and the corresponding coefficient =0. So the probability of an individual's choice of plan is expressed as:

$$P(X_i=\mathrm{i}/\mathrm{y}_j)=\frac{\exp(y_j\beta i)}{1+\sum_{k=2}^{i}\exp y_j\beta_k} \quad （5）$$

4. HOUSEHOLD CONSUMPTION ENERGY CONSUMPTION ANALYSIS OF HUBEI PROVINCE

4.1. Sample characteristics

According to the "Hubei Provincial Household Energy Consumption Survey," a summary report is made. The income level of the questionnaire is shown in Table 2. The survey on energy consumption in this questionnaire mainly investigated the consumption of straw, firewood, LPG, charcoal, briquette, biogas, gasoline and diesel. According to the results of the survey, in 2016, the household life of Hubei residents was mainly used in four kinds of energy sources: fuelwood, liquefied petroleum gas, electric energy, and gasoline. In all statistical questionnaires, other energy sources, such as biogas, straw, diesel, etc., are used by only a few households. Since the data are scarce and not universal, only the most commonly used four types of energy sources are identified in the pooling.

Table 2: The proportion of different income levels

Income level	Number of households (households)	Accounting (%)
X_1(<30000）	110	13.96%
X_2（3-50000）	205	26.02%
X_3（5-100000）	237	30.08%
X_4（10-200000）	172	21.83%
X_5（>200000）	64	8.12%
total	788	100.00%

The basic situation of household life energy use

According to data compiled, households in Hubei Province can use the average amount of household energy according to the average amount of gasoline they can use. The amount of gasoline used is the most, and is calculated using the standard coal coefficient in the "energy balance sheet" of Hubei Province. The average amount of gasoline used by each household is calculated. Equivalent to 365.01Kgce, in the surveyed households, the penetration rate of gasoline use was 38.71%; the average amount used was electrical energy, the equivalent of standard coal was 155.46Kgce, and in the surveyed households, the electricity penetration rate reached 100%, the data is higher than the average electricity rate estimated by the country; after electricity, the penetration rate of liquefied petroleum gas use is 37.18%. Although the penetration rate is almost the same as gasoline, the amount of gasoline used is almost the amount of liquefied petroleum gas used. 5 times, this is also a provincial characteristic of household energy consumption in Hubei Province. Because electricity and gasoline are used in large quantities and account for a large proportion in the consumption structure, the proportion of fuelwood has become lower. Among the surveyed households, the penetration rate of firewood use is 13.07%.

Among the sampled households surveyed, gasoline is the most used energy and is converted to 365.01 kg of standard coal. However, electricity is the most commonly used energy source, with a utilization rate of 100%, which translates to 155.46 kg of standard coal. In addition, the third-ranked energy consumption structure is fuelwood, which translates to 118.82 kg of standard coal. The average use of liquefied petroleum gas is converted to approximately 70.95 kg of standard coal. From the perspective of the sample as a whole, the energy consumption structure of household life in Hubei Province, the energy represented by electricity and petrol occupies a dominant position. At the same time, the non-commodity energy represented by fuelwood also accounts for a certain proportion.

Energy consumption structure under different income levels

In the basic information collection section of the questionnaire, the income level of the residents was specifically investigated. As shown in Table 2, the income level was divided into five levels. In the income level of 30,000, fuelwood consumption accounted for 42%, ranking first in the consumption structure, followed by gasoline consumption, which was less than 1/3 of the entire consumption structure, followed by electricity consumption, and the least used. The liquefied petroleum gas. In the 3-5 million income level, the rapid growth of electricity consumption, with 32% of the total energy consumption structure is the first, the proportion of 28% of gasoline consumption is basically stable, but the amount of fuel wood is rapidly falling and gasoline consumption Flat, the smallest proportion is still the amount of liquefied petroleum gas. In the 5-10 million income level, electricity consumption rapidly rises, accounting for 47%, becoming the first in the consumption structure, the proportion of fuelwood is further compressed, only 14% share, while the proportion of electricity is slightly It has declined, accounting for 26% of the total. Although LPG is still at the bottom, its share in energy consumption structure remains basically unchanged. At the income level of 100,000 to 200,000, the proportion of gasoline continues to expand, taking up 68% of the consumption structure.

At the same time, the share of firewood, liquefied petroleum gas, and electricity consumption is gradually being compressed, which is 7% respectively. 7% and 18%. In the income level of >200,000, the use of gasoline is still growing, accounting for 80% of the total, and the proportion of fuelwood is the smallest, only 3%. The proportion of electricity consumption and liquefied petroleum gas is also decreasing, accounting for 12% and 5% of the total energy consumption structure.

Table 3: Energy consumption structure（Kgec）

Energy type Household consumption Income level	Firewood usage	Liquefied gas consumption	Electrical usage	gaosline
<30000	262.23	78.78	97.52	183.26
3-50000	144.81	63.87	163.86	146.08
5-100000	88.63	82.94	168.69	306.07
10-200000	69.89	67.46	178.59	662.74
>200000	32.38	45.13	117.00	798.47

As can be seen from Table 3, the four types of energy under the five income levels use a discount amount. At the x1 level, the most used firewood consumption is 262.23 kg of standard coal; in the x2 level, the electricity consumption almost doubles to 163.86 kg. The consumption of standard coal accounted for the first place in the consumption structure; in the x3, x4, and x5 levels, the amount of gasoline used was the largest, and converted to kilograms of standard coal were 306.07, 662.74, and 798.47, respectively. In addition, it can be seen that the amount of firewood used is almost a multiple of the reduction in each income level, the use of liquefied petroleum gas is a decline in volatility, and the transition of electricity consumption with income levels is presented. Out of the "U-shaped inverted", gasoline is showing "U-shaped." As shown in Figure 6. For the electricity consumption, the value of each level is not much different, but when the income is very low and high, there is a case where the electricity consumption is reduced; the amount of gasoline is presented in a hierarchical difference, in the X3, X4 these two In grades, the degree of change is the most dramatic.

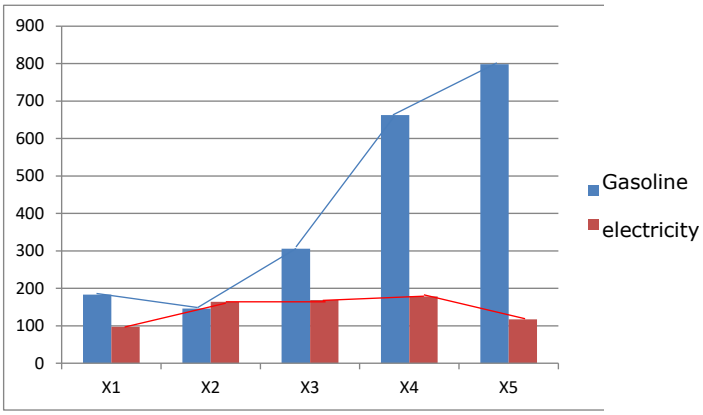

Figure 1: Gasoline and electricity usage of different income levels

Energy consumption mix at different income levels

Referring to the energy ladder model, according to its basic theory, it can be known that while households increase their income, they will gradually increase the use of advanced energy and discard the corresponding low-level energy (Zhang Haipeng et al., 2010). The change in energy consumption structure is not a Jumping process, but in the form of energy combinations to replace each other in the transition phase. Therefore, in the transitional period, the impact of income on energy consumption structure cannot be ignored. According to the survey results, household energy consumption in Hubei Province at different income levels also shows a combination of energy sources, as shown in the table below.

Among the 30,000 income levels, only electricity is used on its own, because Hubei has a higher electricity rate, accounting for 31.82%. In addition, energy sources are all used in the form of two or more energy combinations. Among them, households using two kinds of energy combinations accounted for 39.99%, and those using three types of energy combinations and four kinds of energy combinations accounted for 24.54% and 3.64%, respectively. Among the various household energy consumption mixes, the top four portfolios are “power”, “power+liquefied gas”, “electricity+liquefied gas+gasoline”, and “power+fuelwood” accounting for 31.82% and 25.45%, respectively. 11.82%, 8.18%.

In the income class of 50,000 to 50,000, the same electricity is used alone, accounting for 38.05%. In addition, 40.98% of households use 2 energy combinations, and 16.09% and 4.88% of households use 3 energy combinations and 4 energy combinations, respectively. Among the various household energy consumption mixes, the top 4 combinations are 38.05% and 20.49% respectively for “electricity”, “power+liquefied gas”, “electricity+gasoline”, and “electricity+liquefied gas+gasoline”. 14.15%, 10.73%.

In the 5-10 million income level, electricity can be used alone, accounting for 36.71% of this level. In addition, 40.93% of households use two types of energy combinations, and 18.14% and 4.22% of households use three types of energy combinations and four types of energy combinations, respectively. Among the various household energy consumption mixes, the top four combinations are “power”, “power+gasoline”, “electricity+liquefied gas”, and “power+liquefied gas+gasoline” accounting for 36.71% and 20.25%, respectively. 18.57%, 13.92%.

In the 10-20 million income category, only the electricity can also be separated from the energy mix, accounting for 30.81% of the X4. In addition, 50.47% of households use 2 energy combinations, and 12.78% and 2.33% use 3 energy combinations and 4 energy combinations, respectively. Among the various household energy consumption mixes, the top four combinations are “power+gasoline”, “electricity”, “electricity+liquefied gas”, and “electricity+liquefied gas+gasoline” accounting for 33.14% and 30.81% respectively. 17.44%, 9.88%.

In the income category of >200,000, the same power can only be separated from the energy mix, accounting for 28.13% of the fifth income level. In addition, households using two types of energy sources accounted for 67.19%, and households using three types of energy combinations and four types of energy combinations accounted for 4.69% and 0 respectively. Among the various household energy consumption mixes, the top four groups were 48.44% and 28.13% respectively of “Power + Gasoline”, “Power”, “Power + Liquefied Gas”, and “Power + LPG + Gasoline”. 17.19%, 3.13%.

From the above analysis, a comparison of the proportions of energy combinations between different income levels. It can be seen that in the process of increasing income levels, from the point of view of energy mix, the consumption choices show changes from “complexity to simplicity,” and the proportions of the three energy combinations and the four energy combinations are continuously declining. With the combination of the 3 and 4 types of energy appearing on the third level, the income is at the middle level of the current stage of social development, which not only has the need for advanced energy, but also retains the use of the original low-level energy. Of all energy sources, only electrical energy can be used alone. The proportion of the five income levels in descending order is X2, X3, X1, X4, and X5. As the income level increases, the amount of firewood in the energy mix gradually decreases, but fuelwood has always existed in various income levels and has not been eliminated. At the same time, the “electricity+gasoline” energy portfolio gradually accounts for energy consumption. leading position. In addition, the non-commodity energy represented by fuelwood is gradually being marginalized in different income levels, gradually turning to advanced commodity energy represented by gasoline and electricity, but various energy combinations will follow in the transition of income levels. The degree of transition when income increases is not the same.

In the five income levels, the number of households that use the most is always “electricity+gasoline”, “electricity”, “electricity+liquefied gas”, “electricity+liquefied gas+gasoline”, and the four types of energy combinations are There are also fluctuations in the process of level transitions, but there are differences in the magnitude of fluctuations. The “Electricity + Gasoline” portfolio has been rising steadily with income levels, and the rate of increase has also been expanding. This increase is steeper as income increases; the “Power + LPG” portfolio has been declining, and The trend of decline gradually became gradual; “electricity+liquefied gas+gasoline” conformed to the general trend of “from complexity to simplicity”, and was gradually replaced by a simpler energy combination; “electricity” fluctuates little, each time The degree of decline is almost the same, but this choice of using a single energy source has a decreasing trend. In general, the increase in income also has an impact on the increase in the energy mix. The combination of the two advanced energy sources will gradually affect the use of other energy mixes, which is also a trend of rising income. Single advanced energy cannot quickly assume the pursuit of higher quality of life for households. The combination of low-level energy is not only inefficient but also does not meet the needs of higher quality of life.

Table 4: Households with different income levels and different energy consumption combinations

	<30000		[3,5)0000		[5,10)0000		[10,20)0000		≥200000	
Energy consumption type	households	proportion%	households	proportion%	households	proportion%	households	proportion%	households	proportion%
electricity	35	31.8	78	38.1	87	36.7	53	30.8	18	28.1
Electricity + fuelwood	9	8.2	13	6.3	5	2.1	6	3.5	1	1.6
Electricity + liquefied gas	28	25.5	42	20.5	44	18.6	30	17.4	11	17.2
Electricity + Gasoline	7	6.4	29	14.2	48	20.3	57	33.1	31	48.4
Electricity + fuelwood + liquefied gas	6	5.5	8	3.9	6	2.5	3	1.7	0	0.0
Electricity + fuelwood + gasoline	8	7.3	3	1.5	4	1.7	2	1.2	1	1.6
Electricity + liquefied gas + Gasoline	13	11.8	22	10.7	33	13.9	17	9.9	2	3.1
Electricity + fuelwood + gasoline + liquefied gas	4	3.6	10	4.9	10	4.2	4	2.3	0	0.0
total	110	100.0	205	100.0	237	100.0	172	100.0	64	100.0

4.2. Overall estimate

According to the average value of the sample families obtained by standardizing the fuelwood, liquefied petroleum gas, electricity consumption, and gasoline consumption at the five income levels, then the formula (1) and formula (2) are used in Tables 2 and 3 The data was adjusted to add the average of all types of energy in the sample to the provincial level, and to determine the average amount of energy used by households living in Hubei Province. The adjusted results are shown in Table 9.

Observing and accounting data at the provincial level, in the consumption energy consumption structure of households in Hubei Province, the amount of gasoline used is equivalent to approximately 7,252,208.72 tons of standard coal, which is the first in the consumption structure. Electricity consumption ranks second, which is equivalent to approximately 3087521.48 tons of standard coal. Followed by the amount of firewood and the amount of liquefied petroleum gas, respectively, 2,578,782.44 tons of standard coal and 140,908.14 tons of standard coal. The overall situation of family household energy consumption in Hubei Province is dominated by advanced commodity energy represented by gasoline and electric energy, while low-level non-commodity energy represented by firewood is still used by households of different income levels.

Table 5: Energy use under different income levels across the province（tce）

average income	Firewood usage	Liquefied gas consumption	Electrical usage	gaosline	total
<30000	727016	218410	270353	508077	1723856
3-50000	748179	329995	846636	754783	2679594
5-100000	529404	495429	1007640	1828253	3860726
10-200000	302958	292444	774176	2873020	4242598
>200000	52222	72803	188717	1287957	1601699
total	2359780	1409082	3087521	7252090	14108474

4.3. Multi-valued Logit model

According to the survey results in Table 2, income is divided into five levels and the income level is introduced into the model as a dummy variable. The people surveyed are all distributed among these five income levels, and individuals at each level select the utility-maximizing energy consumption pattern according to their respective income levels. Use stata software to process data, run equation (4), and process results are shown in Table 5.

Because X3 has the largest number of observations, X3 is used as a reference scheme. Under the 5% level of significance, in the class of income less than 30,000, the household energy consumption of households is more inclined to increase the use of fuelwood and reduce the use of electricity; under the income level of 3-5 million, the households still remain. The use of firewood was chosen, but the decrease in the X1 level was reduced, and it tends to reduce the amount of LPG, which tends to slow down the use of gasoline and electricity; in the 100,000-200,000 income category, The increase in income makes households more inclined to the consumption of electricity and gasoline. Among them, the preference for electricity is stronger; in the income class of more than 200,000, gasoline has become the most favored energy source. The energy appetite preferences estimated by MLE may be affected by the energy mix, but the overall trend is consistent with the descriptive analysis in the previous article. With the increase of income level, household energy use tends to replace high-level commodity energy with low-level non-commodity energy. However, non-commodity energy still exists in the household energy consumption structure of various income levels, indicating that the overall energy consumption in Hubei Province is still in the transitional stage from non-commodity energy to commodity energy.

Table 6: Logit regression results

	(1)	(2)	(3)	(4)	(5)
	<30000	[3,5)0000	[5,10)0000	[10,20)0000	≥200000
Fuelwood	0.0005**	0.0002*	Reference method	-0.0001	-0.0008
Liquefied gas	-0.0005	-0.0009		-0.0005	-0.0025*
electricity	-0.0060***	-0.0002		0.0004*	-0.0038***
gasoline	-0.0004	-0.0008***		0.0003***	0.0003**
constant	0.0446	0.0796		-0.4713***	-0.7097***

Note：*p<0.1，**p<0.05，***p<0.01，Significant level

5. CONCLUSION AND SUGGESTION

5.1. Conclusion

Based on the above analysis, the following conclusions can be drawn:

First, the energy used by households in Hubei Province at this stage is mainly gasoline, electricity, liquefied petroleum gas, and fuelwood. Based on the sample data, the situation in the province is estimated and it is found that the electricity rate of electricity reaches 100%, followed by the prevalence of gasoline use. The higher is 38.71%, followed by liquefied petroleum gas and fuelwood respectively, and the penetration rates are 37.18% and 13.07%, respectively. It is worth noting that although the popularity of firewood is not high and only a few households are using it, the total amount is almost the same as other energy sources, and it is clearly regional in the survey of raw data.

Second, the data can be categorized and summarized, and can be divided into five levels according to the income level. The demand for different energy sources is different in different income levels. In the income level of <30,000, the fuel wood consumption accounts for Compared with 42%, it ranks first in the consumption structure. In the 3-5 million income level, the rapid growth of electricity consumption, with 32% of the total energy consumption structure is the first. In the 5-10 million income level, electricity consumption has rapidly increased, accounting for 47% of the total, becoming the first in the consumption structure. At the income level of 100,000 to 200,000, the proportion of gasoline continues to expand, taking up 68% of the consumption structure. At the same time, the share of firewood, liquefied petroleum gas, and electricity consumption is gradually being compressed, which is 7% respectively. 7% and 18%. At a level of >200,000, the use of gasoline is still growing, accounting for 80% of the total.

Thirdly, according to the basic idea of the “Energy Ladder” model in different income levels, it can be seen that apart from the energy consumption of residents, energy can be used alone, and other energy sources are in the form of energy combinations with different shares. With the transition of income levels, the energy mix presents a trend of “complexity to simplicity,” and the energy mix gradually becomes the form of “gasoline+electric energy”, and the energy mix is in the process of simplification. The speed and degree of replacement are not the same.

Fourth, according to the “economic man” theory, individual consumers always satisfy the utility maximization in the consumption process, so the multi-valued Logit model is used to judge the energy selection preference under different income levels, and at the low income level, it is more prone to The use of fuelwood, which represents non-commodity energy sources, tends to be more of a commodity like gasoline at higher income levels. However, the transition from non-commodities to commodities has not ended, as can be seen from the use of firewood. This transitional phase will continue and may continue until no low income level exists.

5.2. Suggestion

First, the introduction of many provincial policies is based on official statistics. However, because official data can only count the approximate amount of energy from large nodes, it is not targeted. Therefore, data collection can establish long-term detection methods, which are led by the government and entrust provincial universities to collect data of the target scope. Multiplicity of the common indicators in different regions is used to determine the actual situation in the province. Although data collection is slow, it can be updated over a long period of time, and it is more accurate to use mathematical statistics that are closest to the individual consumers.

Second, the energy consumption of households is in the form of an obvious energy mix. By stabilizing the price of certain energy in the region, other energy prices within the energy portfolio can be adjusted. Through analysis, we can see that the growth of income will obviously drive the growth of demand for electricity and gasoline. Therefore, Hubei Province must do a good job in the planning of power stations, power supply networks, ladder power, etc., and do a good job in oil reserve and petrochemical development layout planning.

Third, at present, Hubei Province is also vigorously advancing the popularity of new energy in households' family life. However, according to actual surveys, the popularity of biogas is not high in Hubei Province. The calculation data is too small to be considered in this paper. The main reason is that The shortage of installation costs and raw materials can not meet the development needs, so in line with the concept of promoting green and low-carbon development, combined with the development model of circular economy, the promotion of green communities and the establishment of a common biogas generating equipment. In the survey, many of the biomass fuels were wasted, so the formation of intensive use in the community can serve two purposes.

Fourth, based on the stage of energy use transformation in Hubei Province, as the income level rises, residents will gradually reduce the use of firewood. Therefore, new energy technologies can be used to carbonize or crush the gradually reduced fuelwood energy. Mix with the same reduced use of liquefied gas to form a new type of composite energy and improve energy quality.

6. REFERENCES

Wei C, Wang D, Wu W, Xie L. Research on the coal consumption of rural residents in China and its influencing factors[J]. China Population, Resources and Environment, 2017, 27(09): 178-185.

Zhai X, Wang W. Research on the Influencing Factors of Rural Residents' Carbon Emissions in China[J]. Ecological Economy, 2017, 33(01): 73-76.

Zhi G, Yang J, Zhang T, Guan J, Du J, Xue Z, Meng F. Investigation on the burning of coal in rural areas in northern China, estimation of emissions and policy implications[J]. Environmental Sciences Research, 2015,28(08): 1179-1185.

Wu Y, Shen L, Song X, Hu Y. Study on the correlation between energy consumption and residential living standards of urban residential buildings: Taking Chongqing as an example[J]. Building Economy, 2015, 36(07): 116 -120.[5]

Zhao W, Xu Q, Li L, Jiang L, Zhang D, Chen T. Estimation of coal burning and pollutant emissions in the urban-rural junction in the Beijing plain area[J]. Environmental Science Research, 2015,28(06): 869-876.

Chen Z, Gao W, Xie P. The relationship between green lifestyle, green product attitude, and purchase intention: An empirical study based on the market segmentation of two types of green products[J]. Economic Management, 2014, 36(11):166 -177.

Qian Y. The Beijing-Tianjin-Hebei Region needs to focus on the management of rural scattered coal burning[N]. China Environment News, 2013-06-07(002).

Luo K. Research on Green Value Structure Based on Multi-group Structure Equation Model[J].China Polulation.Resources and Environment,2012,22(07):78-84.

Zhang X, Niu S, Zhao C, Hu L. Research on Household Energy Consumption and Carbon Emission in the Process of Urbanization in China[J]. China Soft Science, 2011(09):65-75.

Zhang H, Gou J, Yin H. Empirical analysis of rural household energy consumption demand in rural areas: a model based on double expansion linear expenditure system [J]. China Rural Economy, 2010(07):64-74.

Zhang L. Analysis on the influencing factors of green purchasing behaviour from the perspective of multi-group structural equation model: data from eastern, central and western regions [J]. China Rural Economy, 2010(02):44-56.

Gong Z. The burning of bulk coal in Hebei rural areas becomes an important source of pollution [N]. Economic Information Daily, 2015 - 09 - 28.

Huo M, Zhao J, Xu C, et al. China's scattered coal consumption map and influencing factors [J]. China Power, 2017, 50(1) : 1- 8.

Shi Q, Peng X, Zhang R. Field Survey on Energy Consumption in Rural China: A Case Study of 2 253 Farmers in Shanxi, Zhejiang, and Zhejiang Provinces [J]. Managing the world, 2014(5) :80- 92.

Zheng X, Wei C, Yan Y, et al. China Household Energy Consumption Research Report (2016) [R]. Beijing: Science Press, 2017.

Chen Y, Wang X, Zhu M. Application of Logit Model in Quantitative Marketing Research: Consumer's Empirical Analysis of Consumer Electronics Brand Selection [J]. Business Studies, 2006 (24): 195-199.

Oladokun M G, Odesola I A. Household energy consumption and carbon emissions for sustainable cities – A critical review of modelling approaches[J]. International Journal of Sustainable Built Environment, 2015, 4(2).

Burfurd I, Gangadharan L, Nemes V. Stars and standards: Energy efficiency in rental markets[J]. Journal of Environmental Economics and Management, 2012, 64(2).

269: Study on the transmittance of glass

Weidong BAO[1,2], Qinghua LV*[1,2], Hui LV[1,2], Jiachen CUI[1,2], Yuehong SU[1], Saffa RIFFAT[1,3]

[1]*Hubei Collaborative Innovation Center for High-efficient Utilization of Solar Energy, Hubei University of Technology*
[2]*School of Science, Hubei University of Technology, Hubei, Wuhan, 430068*
[3]*University of Nottingham,UK*
**Corresponding author*

As an important part of battery package, glass is directly used in solar power generation module, which has the ability to transfer and control light. The transmittance of glass is an important factor affecting the conversion efficiency of solar cells. However, it is affected by many factors, such as metal content in glass, calender pattern and preparation method of glass surface film, etc. In this paper, we use COMSOL software to carry out simulation experiments. This paper focuses on how to use the simplest coating method to reduce the reflectivity of glass, to increase the conversion rate of light energy of glass and to improve the overall performance of the system, to reduce the cost of industrial design and to meet the requirements of green industry.

Keywords: glass; transmittance; reflectivity; COMSOL simulation; improvement

1. INTRODUCTION

Energy shortage has become a major problem hindering the development of the world economy, the development of new energy has been widely agreed. As a kind of non-pollution and renewable energy, solar energy has been paid more and more attention to. Glass can not only keep heat, heat insulation, sound insulation, but also provide clean and environmental energy on the basis of conventional lighting and aesthetics. The application of glass can make buildings and roofs generate electricity without pollutant emission. At the same time, the components such as door and window curtain wall have thermal insulation, save energy and achieve the effect of energy saving and environmental protection. Glass is used in buildings to achieve the goal that building materials will be significantly reduced, energy consumption, operating costs and carbon dioxide emissions will be significantly reduced.

The transmittance of solar glass is an important factor that affects the module photoelectric conversion efficiency, and it is also one of the most concerned indicators of glass manufacturers and component manufacturers. The transmittance of solar glass plays an important role in the utilization of solar energy, so how to improve the transmittance of glass has become an important research topic in industry.

2. METHOD FOR IMPROVING LIGHT TRANSMITTANCE OF GLASS

At present, there are three main ways to improve the transmittance of glass: reducing absorption, increasing trapping structure and reducing reflection. To reduce the content of transition metal in glass, to apply calendering pattern to the glass by calender roll and to prepare anti-reflection film on glass are the important ways and means to reduce absorption, increase the structure of trapping light and reduce reflection.

2.1. Improving the transmittance of glass by reducing absorption

The transition metals such as iron, vanadium, cobalt, nickel, copper, chromium, manganese, titanium, cerium, praseodymium, neodymium, aluminum and so on in the glass have the effect of absorbing and scattering light, so that the glass has the ability of colouring. The colouring ability of glass is closely related to the content of these transition metals (Caixin 2012). Reducing the content of transition metal in the glass is an important measure to enhance the transmission efficiency of glass.

2.2. Improving the transmittance of glass by increasing trapping structure

In order to increase the absorption efficiency of the active layer of thin film devices, the trapping structure is formed on the surface of glass. The front surface of glass is treated with hazy surface, and the special pattern is pressed out on the opposite side, thus increasing the transmittance and energy transmittance of glass under long-term sunlight, and then increasing the light energy conversion rate of solar cell module (Tie et al. 2017).

2.3. Improving the transmittance of glass by reducing reflection

Through the glass coating, the glass surface is treated with immaterialness, forming high efficiency anti-reflection film to reduce the reflection to improve the transmittance. As a kind of deep processing method of glass, the coating technology of glass is to reduce the reflection of light by coating an anti-reflection film on the surface of glass and utilizing the phase interference between the anti-reflection film and the glass. A method of increasing the transmission of light. Because the coating technology is relatively simple and the realization method is various, there are many research results and applications in this field. The common methods of preparing anti-reflective films on ultra-white glass surface in reality are mainly true. Blank coating, Chemical Vapor deposition and Sol-Gel method (Huayi 20018).

The third method is to improve the transmittance of glass by glass coating.If we do not consider the energy loss of absorbed light, we only consider reflection and transmission. If the reflection and transmission complement each other, the smaller the reflectivity, the higher the transmittance. Anti-reflection film is based on the principle of reflection light interference cancellation on the surface of the film, which can be divided into single layer anti-reflection film, double layer anti-reflection film and Multilateralism anti-reflection film. As a kind of deep processing method of glass, the coating technology of glass is to reduce the reflection of light by coating an anti-reflection film on the surface of glass and utilizing the phase interference between the anti-reflection film and the glass. A method of increasing the transmission of light.

3. THE PROPERTIES OF THE FILM LAYER MATERIAL

In optical elements, the light energy is lost due to the reflection on the surface of the element. In order to reduce the reflection loss on the surface of the element, transparent dielectric film is often deposited on the surface of the optical element, which is called anti-reflective film.

With the continuous development and research of the anti-reflective film, the coating technology of the optical anti-reflective film is developing continuously. The thickness of the optical anti-reflective film should be controlled at the magnitude of the wavelength of the visible wavelength of 1/4, and the requirement of the uniformity of the film is very harsh. The commonly used films do not make the light intensity of the transmission light maximum, that is to say, the reflection light is not the weakest. And for an anti-reflective film, it is completely anti-reflective to monochromatic light of a certain wavelength. Therefore, the Anti-reflective effect can be improved by multilateralism coating technology, and the line width of transmitted light, that is, frequency width, can also be increased. Mono layer films can only resist the reflection of electromagnetic waves of a certain wavelength. In order to achieve anti-reflection in a larger range and more wavelengths, multilateralism films are used to achieve the purpose of anti-reflection.

The anti-reflective film analysis of the mono layer is as follows：

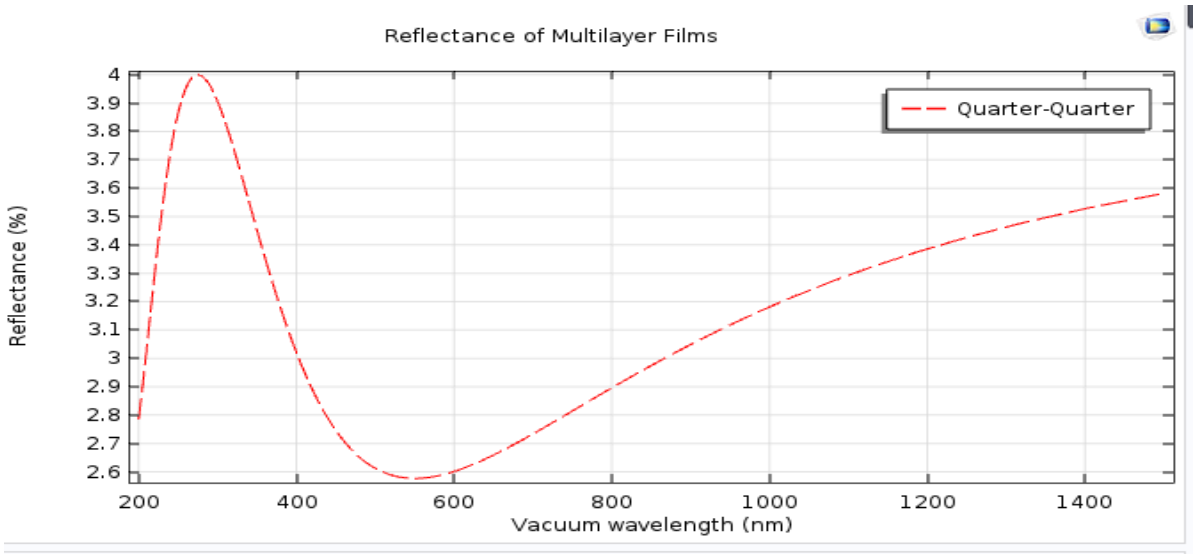

Figure 1

4. THE PRINCIPLE OF IMPROVING THE TRANSMITTANCE OF GLASS COATING

Due to the reflection of the interface, the transmitted light energy is very weak and the transmittance of glass is reduced. Therefore, in order to solve this problem, it is necessary to deposit anti-reflective film on the surface of optical devices. The anti-reflective glass can not only greatly reduce the energy of light reflected in the glass, but also improve the transmittance of glass.

For incident light with a fixed wavelength（λ_0）, when the thickness of the film is satisfied,

$$n_2 d = N\frac{\lambda_0}{2} \qquad N = 0,1,2\cdots(1)$$

the reflectivity is the highest(R_M), and when the thickness of the film is satisfied,

$$n_2 d = (2N+1)\frac{\lambda_0}{4} \qquad N = 0,1,2\cdots(2)$$

the reflectivity is the lowest. When the thickness of the film is

$$2N\frac{\lambda_0}{4}(N\frac{\lambda_0}{2}) \sim (2N+1)\frac{\lambda_0}{4} \qquad N = 0,1,2\cdots(3)$$

The reflectivity varies from $R_{\mathrm{m}} \sim R_M$ when it changes. When the thickness of the film is $\frac{\lambda_0}{4}$ or odd, the reflectivity is the lowest and the intensity of reflected light is very low.When satisfied

$$n_2 = \sqrt{n_1^2 n_s / n_a} \qquad (4)$$

Where:

- n_2d is the optical thickness of the film,
- n_1 and n_2 are the refraction coefficient of the thin film,
- n_s is the refraction coefficient of the glass,
- n_a is the refraction coefficient of the air.

The reflectivity of the film is 0.There is no reflected light and the incident light is completely transmitted. The advantages of a single - layer film are relatively simple ; however , the film layer must be designed in accordance with the formula(2), so that it is difficult to achieve this , and it is difficult to achieve this , and it is also necessary to use a double - layer or multi - layer film to further adequately address these difficulties.

5. SIMULATION ANALYSIS OF PHOTOVOLATAIC GLASS COATING

In industrial application, a single film may not be able to meet the needs of the times in terms of energy saving effect. Therefore, we seek to find the most reasonable results by coating different layers of anti-reflective films on vacuum glass. A simple anti-reflective film is selected to minimize the reflectivity at specific vacuum wavelengths. More complex coatings can reduce the reflectivity of relatively large wavelengths by using multilateralism films with different material properties. The simplest multilateralism coating consists of two different layers of material on the surface of the glass substrate. Each layer has a one-fourth wavelength thickness in the medium; therefore, this design is called a quarter of a wavelength. Membrane theoretically, a quarter of a wavelength film can reduce the reflectivity to zero at a specified wavelength; but normally, there is no material with refractive index. Another advantage of its reflection coefficient of zero. 1 / 4 wavelength layer is that it prevents light from reflecting at a frequency.

In this paper, the substrate is made of glass (n_s=1. 5) and the first film is made of titanium dioxide TiO_2(n_1=1.44). The formula (4) can be used to determine the optimum refractive index of the second layer, and the n_2 reflectivity can be obtained.

By calculation, the optimum （n_2） value is about 1.76. The refraction coefficient of alumina, a common anti-reflective membrane material, is about 1.76. It is more appropriate to use this material. The simulation results are as follows:

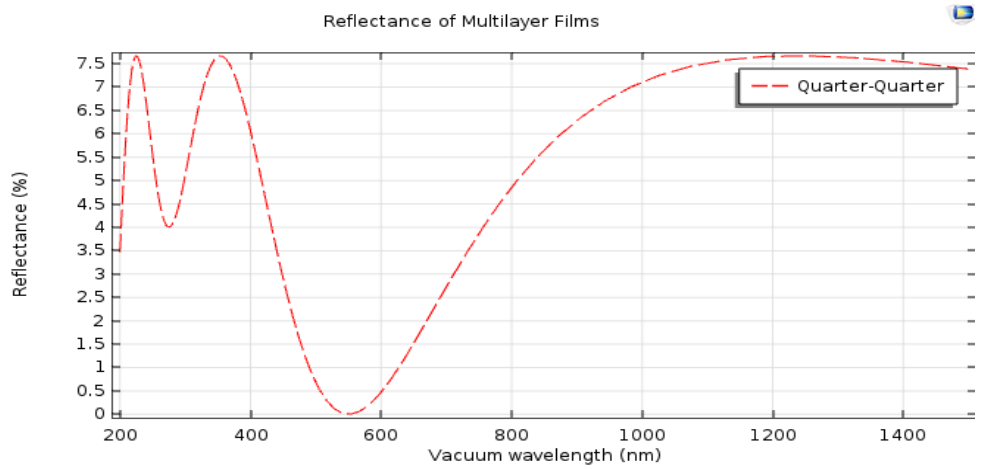

Figure 2

The reflectivity of the film as a quarter-quarter of the vacuum wavelength is shown in figure 1. We know that the reflectivity of ordinary glass is 8 %~ 10%. From figure 1, we can see that the reflectivity has been reduced, but one obvious disadvantage of the two layers of anti-reflection film is that the reflectivity in the visible light band is significantly reduced in the narrow band of one wavelength. For infrared and ultraviolet bands, the refractive index changes little and the value is small.

The reflectance can be reduced over a wider range of wavelengths by using a dielectric film with three or more layers. An example of a three-layer coating is the quarter-half-quarter coating, in which a thin layer of thickness quarter-half-quarter is placed between the two quarter-wavelength layers.

Next, simulate a quarter of a layer and add another Low-e film between two quarter-quarter layers. The material in this interlace is a ZrO and the refraction coefficient is 2.2. Set the thickness to the specified half wavelength thickness. The simulation results are as follows:

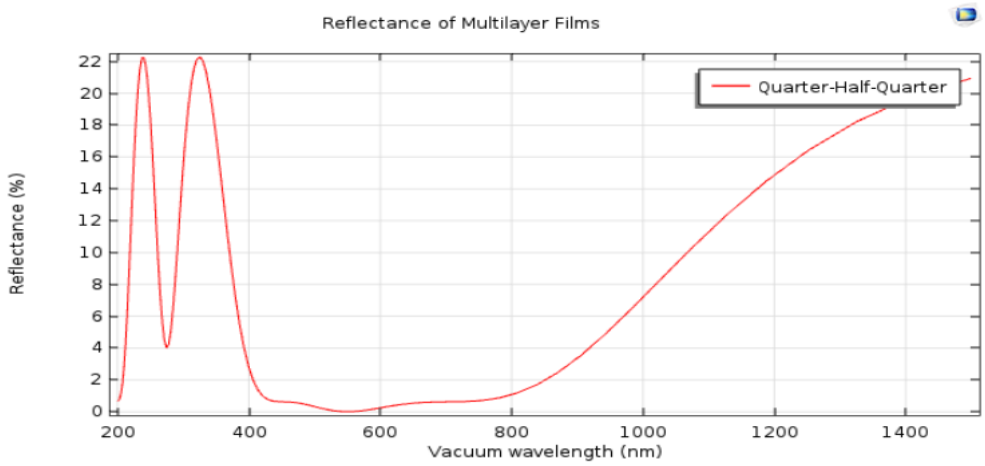

Figure 3

Figure 2 and Figure 3 compare the reflectance of the quarter-quarter and quarter-half-quarter films.Because the refractive indices of real materials are used, the reflectance of the quarter-quarter coating does not decrease to zero. The quarter-half-quarter film exhibits slightly greater reflectance at the center of the band, but the reflectance is reduced over a much wider frequency range.However, for infrared and ultraviolet bands, the reflectivity fluctuates obviously and varies greatly. In practical application, vacuum glass coated with film has better energy saving effect in visible wave band. And it blocks a lot of infrared and ultraviolet radiation. It helps prevent indoor objects from fading.

6. CONCLUSIONS AND FINAL REMARKS

The simulation results show that the reflection coefficient can be reduced by a wider range of wavelengths with three or more anti-reflective layers. There are many ways to improve the transmittance of glass. Compared with other methods to improve the transmittance of glass, the application of anti-reflective film in glass has achieved remarkable results. In the visible light band, the transmittance of anti-reflective film is much higher than that of industry standard. With the development of industry, the requirement of glass is higher and higher. Although it has been widely studied and applied, However, the study of anti-reflective, convenience and economy in the process of application is not enough, and in order to accelerate the application of anti-reflective membrane to solar selective absorption, we need to explore the design of anti-reflective film in the future.

7. ACKNOWLEDGEMENT

This work was supported by International Science & Technology Cooperation Program of China (No. 2016YFE0124300)

8. REFERENCES

Han C.On the Development Potential of Photovoltaic Glass [J].2012(1):55-57.Doors and Windows.

Geng T, Hu J, Yu C, Sheng J, Qin L.Review on Improving the Transmittance of Photovoltaic Glass[J].Silicate Bulletin,2017,36(05):1594-1598.

Huang H.Mechanism Analysis of Antireflective Coating on Glass Surface[J].Foreign Building Materials Science and Technology,2008,29(06):34-38.

Qi L. Preparation and Properties of Microcrystalline Silicon Films by PECVD[D]. Shanghai Normal University,2012.

270: Performance of a three-stage travelling-wave thermoacoustic engine utilizing low-grade heat

Jie ZHANG[1,2], Daming SUN[1,2], Kai LUO[1,2], Honghao PAN[1,2]

[1] *Institute of Refrigeration and Cryogenics, Zhejiang University, Hangzhou 310027, PR China, jiezhang_91@zju.edu.cn*
[2] *Key Laboratory of Refrigeration and Cryogenic Technology of Zhejiang Province, Hangzhou 310027, PR China, jiezhang_91@zju.edu.cn*

Thermoacoustic technology is capable of converting thermal energy into usable energy with the advantages of simple structure, high reliability, and low costs due to the absence of mechanical moving parts. And multi-stage travelling-wave thermoacoustic devices have high potential in recovering low-grade heat source into usable energy which can contribute to ease the energy shortage. In this work, a three-stage travelling-wave thermoacoustic engine has been proposed and studied numerically and experimentally. In the experiment, at the mean pressure of 3.0 MPa and the temperature difference between the hot and cold end of the regenerator of about 285 K, the working frequency is about 20 Hz, the onset temperature difference is 55 K, the pressure amplitude is 278.0 kPa, and the pressure ratio can achieve 1.19, when the working gas is nitrogen; meanwhile, the working frequency is about 55 Hz, the onset temperature difference is 71 K, the pressure amplitude is 194.3 kPa, and the pressure ration can achieve 1.13, when the working gas is helium. Furthermore, an electric generator driven by the three-stage traveling-wave thermoacoustic engine with helium as the working gas was modelled by DeltaEC. And the conversion from low-grade heat to electric energy is verified. A maximum electric power of 1427.2 W and a highest thermal-to-electric efficiency of 10.7% are obtained numerically when the mean pressure is 3.0 MPa and the heating temperature is 623 K.

Keywords: thermoacousitc; travelling-wave; low-grade heat; generator

1. INTRODUCTION

Thermoacoustic engines are capable of converting thermal energy into acoustic power with comparable efficiencies as that of conventional heat engines (Backhaus 1999). Thermoacoustic engines, especially traveling-wave thermoacoustic engines (TWTAE) have great advantages of simple structure, high reliability, and low costs due to the absence of mechanical moving parts. Moreover, low-grade heat, such as solar energy, geothermal energy and industrial waste heat, can be utilized by thermoacoustic engines. By connecting linear alternators to the thermoacoustic engine, the produced acoustic power can be converted into electricity, which is a common use of thermoacoustic engines. For example, Wu et al (2012), constructed a solar-powered traveling-wave thermoacoustic engine which can obtain electric power of 200 W.

The concept of TWTAE is firstly brought by Ceperley (1979), which describes the reversible thermodynamic cycle similar to Stirling cycle with a high thermal efficiency. In particular, the multi-stage TWTAE has become a hot research topic for its lower onset temperature difference and higher energy density. In 2008, de Blok (2012) proposed a four-stage thermoacoustic engine whose onset temperature difference can be as low as 30 K. Since 2008, Luo et al. has developed a double-acting thermoacoustic engine and conducted a series of studies. In 2014, Wu et al. (2014) developed a double-acting thermoacoustic electric generator where the linear alternators were adopted to reduce the length of the resonator, and obtained an electric power of 1.57 kW with a thermal-to-electric efficiency of 16.8% when the hot temperature was 650 °C. Bi et al. (2017) proposed a three-stage looped thermoacoustic electric generator achieved the maximum electric power of 4.69 kW and the highest thermal-to-electric efficiency of 18.4%. Jin et al. (2016) discussed the mechanism of phase adjustment in the looped thermoacoustic engine and analyzed two effective means of phase adjustors, with which the looped three-stage and four-stage thermoacoustic engine could start to oscillate with the hot temperature as low as 29 °C(Jin 2017). Moreover, they focused on the thermoacoustic engine driven by low-grade heat and proposed a thermoacoustic electric generator driven by low-grade heat, in which a highest thermal-to-electric efficiency of 1.51% was achieved at the hot temperature of 120 °C with He-Ar mixture as the working fluid [8]. Besides, Zhang et al. (2015) studied the onset characteristics of a four-stage traveling-wave thermoacoustic engine based on the linear network model and then they considered the impacts of the mean pressure, working substance, hydraulic radius of regenerator, and stage number.

As above, multi-stage TWTAE has been improved significantly in recent years. However, onset characteristics, operating characteristics, and mechanism of acoustic power dissipations of the engine need deeper study. The research focused on the multi-stage TWTAE utilizing low-grade heat is still lacking. In this paper, a three-stage TWTAE has been proposed and onset temperature difference and operating characteristics have been studied numerically and experimentally. Furthermore, an electric generator driven by the three-stage traveling-wave thermoacoustic engine with helium as the working gas was modified by DeltaEC (Ward 2008). And the conversion from low-grade heat to electric energy is verified.

2. EXPERIMENT SETUP

Figure 1 shows the schematic diagram of the three-stage traveling-wave thermoacoustic engine and the photographs of the engine. Every stage of the engine consists of a hot end exchanger(HHX), a stacked-screen regenerator(REG), a main ambient heat exchanger(AHX), a secondary ambient heat exchanger(SAHX), a thermal buffer tube(TBT) and a few tube components, for example, a resonator tube (RT). The REG is the key component where thermoacoustic energy conversion happens, and is filled with stainless steel screens with a mesh number of 125. The HHX is a fin-type heat exchanger with a fin thickness of 0.4 mm and a gap of 0.8 mm. The AHX and SAHX are both of shell-tube type with working gas oscillating inside the stainless steel tubes and the chilling water flowing through the shell sides. The inner diameter of the tubes of AHX is 1.6 mm and the inner diameter of the tubes of SAHX is 2 mm. Three pressure sensors were installed on the RT to measure the output pressure (P1 to P5) of thermoacoustic cores (TACs), locating at 0.1 meter away from the cone-shaped tube connecting to the AHX and SAHX. Huba pressure sensor (511.940603742) was installed at P1, and high-precision dynamic pressure sensors from PCB Piezotronics (102B15) were installed at P2 to P5. K-type thermocouples are used to measure the temperatures of HHXs, import and export cooling water of AHXs. The pressure signals are collected by DAQ card from National Instrument (PC-6123) and the temperature signals are collected by the Keithley digital multimeter 2700. All the signals are collected simultaneously by the self-coded program based on LabVIEW platform.

In the experiments, the temperatures of the AHXs are kept at 25 °C. And the main geometry parameters are given in Table. 1.

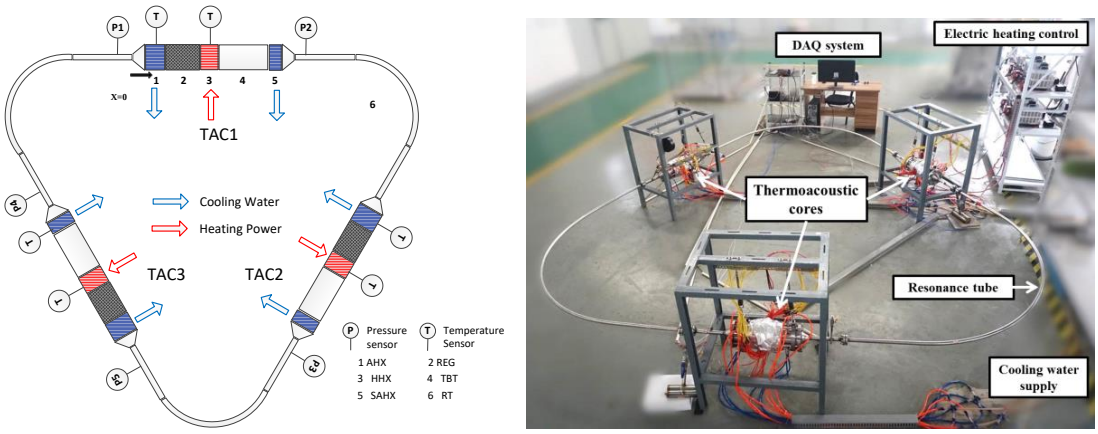

Figure 1: Three-stage traveling-wave thermoacoustic engine (a) schematic (b) photograph

Table 1: Geometry parameters of three-stage TWTAE

Components		d/mm	L/mm	Other dimensions*
Cone1		-	95	-
TAC	AHX	76	60	Shell-tube, porosity 22%, *hydraulic radius*=0.8 mm
	REG	76	60	Stainless mesh, porosity 80%, *hydraulic diameter* =50 μm
	HHX	76	80	Finned, porosity 36%
	TBT	76	125	
	SAHX	76	40	Shell-tube, porosity 14%, *hydraulic radius* =1 mm
Cone2		-	65	-
RT		20	3500	-

3. RESULTS AND DISCUSSTION

3.1. Onset characteristics

Figure 2 shows the onset and damping temperature differences of the hot and cold ends of the regenerators at different mean pressures when helium and nitrogen are the working gases, respectively. The onset and damping temperature differences of helium and nitrogen are lower with the increase of mean pressure. The damping temperature differences are lower than the onset temperature differences. Moreover, the temperature difference of helium is higher than that of nitrogen. For example, when the working gas is helium, the onset temperature difference is 130.1 K and damping temperature difference is 116.1 K at the mean pressure of 2.0 MPa, and the onset temperature difference is 71.0 K and damping temperature difference is 66.6 K at the mean pressure of 4.0 MPa; when the working gas is nitrogen, the onset temperature difference is 84.4 K and damping temperature difference is 60.0 K at the mean pressure of 2.0 MPa, and the onset temperature difference is 43.8 K and damping temperature difference is 35.4 K at the mean pressure of 4.0 MPa. Besides, according to our previous study on the effect of pressure disturbance on the onset temperature and process (Qiu 2006), the onset temperature can be much lower than the ordinary one if an appropriate pressure disturbance is introduced. It seems that the damping temperature difference is the lowest temperature at which the thermoacoustic engine can start to work and maintain the pressure oscillation.

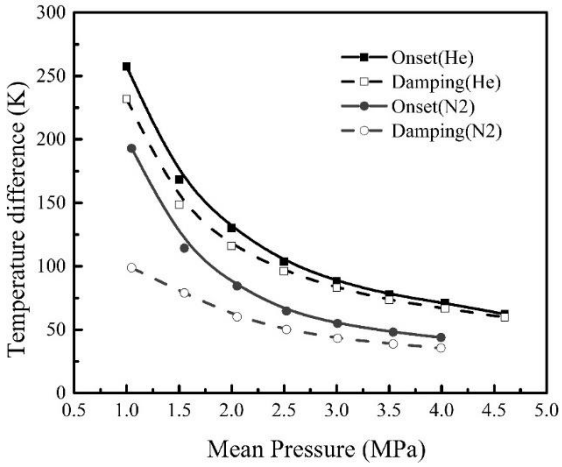

Figure 2: Onset and Damping temperature differences vs. mean pressure

3.2. Operating characteristics

Figure 3 displays the trend of the mean pressure varying with the temperature difference. As shown, the mean pressure is higher with the increase of the temperature difference. Since the molecular mass of nitrogen is larger than that of helium, the growth speed varying with the temperature difference is faster when the working gas is nitrogen, especially the mean pressure is higher than 1.0 MPa. As shown, from 143.0 K to 286.0 K, the mean pressure is 230 kPa higher when the working gas is helium, while the mean pressure is 270 kPa higher when the working gas is nitrogen.

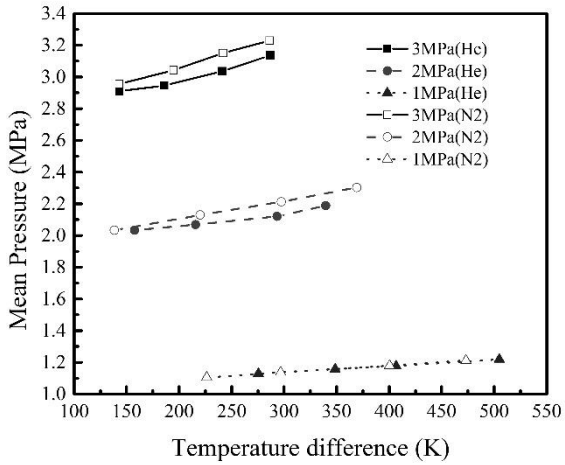

Figure 3: Mean pressure vs. temperature difference

The experimental frequencies and numerical frequencies calculated by DeltaEC of the three-stage TWTAE are given in Figure 4. In Figure 4 (a), the numerical frequencies are larger than the experimental frequencies. For instance, the experimental frequency is 54.1 Hz and the numerical frequency is 55.9 Hz when the charge pressure is 2.0 MPa and the temperature difference is 186.0 K. The relative deviations are from 1.6% to 3.4% when the charge pressure is 2.0 MPa. In Figure 4 (b), the trend of the frequencies when the working gas is nitrogen is similar to that in Figure 4 (a). And the relative deviations are from 2.1% to 4.5% at the charge pressure of 2.0 MPa when the working gas is nitrogen. The power density is higher when the working gas is helium for the frequency is larger.

It is worth noting that the frequencies are higher with the increase of the temperature difference on the whole. However, sometimes the working frequency gets lower firstly after the onset process in the experiment. For example, the frequency is 54.3 Hz at the temperature difference of 143.1K and 54.1 Hz at the temperature difference of 185.9 K when the mean pressure is 2.9 MPa. The probable reason is the singularity of the relationship between the pressure loss and mass flow in the heating tube proposed by Liu (2001). Between the first and second critical points, the pressure loss decreases with the increase of the mass flow. He regarded the phenomenon as a reason resulting to the instability and oscillations of a thermoacoustic engine. After the onset process, the singularity

disappears and the pressure loss increases with the increase of the mass flow. Thus the impedance gets larger under certain condition and the working frequency is lower.

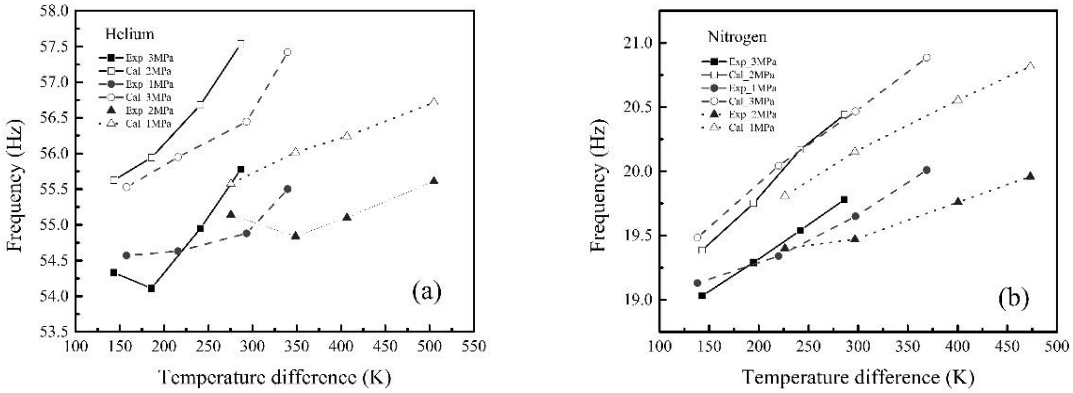

Figure 4: The experimental and numerical frequencies vs. temperature difference (a) helium; (b) nitrogen

The experimental and numerical pressure amplitudes of P1 and P2 are given in Figure 5. In Figure 5 (a), when the working gas is helium, the pressure amplitude is larger while the charge pressure is higher and the temperature difference is larger for both P1 and P2. And the pressure amplitude at P1 is larger than that at P2 in the experiment and calculation. Although the trend of the pressure amplitudes in the experiment and calculation are similar, the deviations between the experiment and calculation can not be ignored and become larger when the temperature difference is larger. When the charge pressure is 2.0 MPa and the temperature difference is 293.3 K, the experimental pressure amplitudes at P1 and P2 are 126.9 kPa, 100.2 kPa, respectively. And the numerical pressure amplitudes at P1 and P2 are 242.5 kPa and 190.5 kPa. The reasons of the large deviations are that the heating power in the calculation is larger than that in the experiment, and non-linear losses exist in the experiment which is ignored in DeltaEC. In Figure 5 (b), when the working gas is nitrogen, the trends of experimental and numerical pressure amplitudes at P1 and P2 are similar to those shown in Figure 5 (a). When the charge pressure is 2.0 MPa and the temperature difference is 297.3 K, the experimental pressure amplitudes at P1 and P2 are 196.3 kPa, 153.8 kPa, respectively. And the numerical pressure amplitudes at P1 and P2 are 270.7 kPa and 228.1 kPa. The deviations between experiment and calculation is smaller when the working gas is nitrogen. Besides, the pressure amplitude is larger when the working gas is nitrogen since the molecular mass of nitrogen is larger than that of helium.

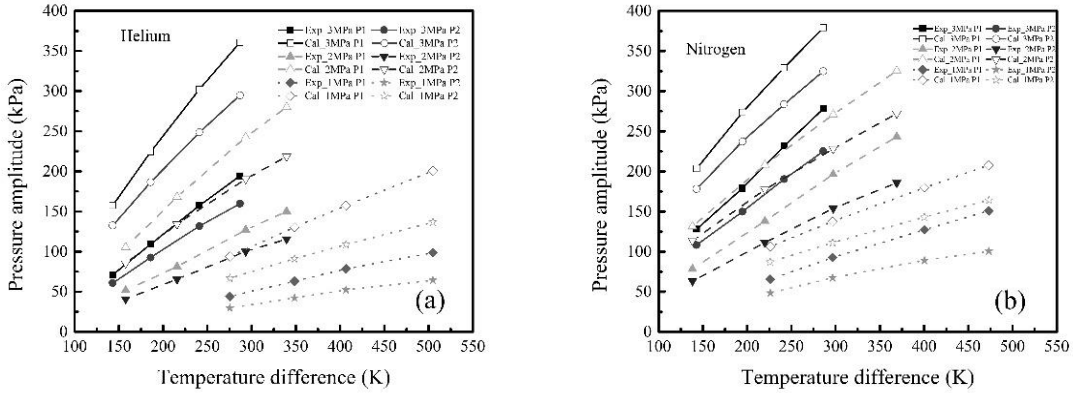

Figure 5: The experimental and numerical pressure amplitudes vs. temperature difference at P1 and P2 (a) helium; (b) nitrogen

The experimental and numerical pressure ratios of P1 and P2 are displayed in Figure 6. Actually, the trend of the pressure ratios change with the temperature difference in Figure 6 is basically consistent with the trend of the pressure amplitude change with the temperature difference in Figure 5 with both helium and nitrogen as the working gas. When the mean pressure is about 3.1 MPa and the temperature difference is about 286 K, the experimental pressure ratios with helium as the working gas at P1 and P2 is 1.13 and 1.11, and the numerical pressure ratios at P1 and P2 is 1.26 and 1.21. Meanwhile, the experimental pressure ratios with nitrogen as the working gas at P1 and P2 is 1.19 and 1.15, and the numerical pressure ratios at P1 and P2 is 1.27 and 1.22. Moreover, the highest pressure ratios obtained in the experiment at P1 and P2 is 1.18 and 1.11 when the working gas is helium under the mean pressure of 1.2 MPa and the temperature difference of 504.9 K. And the highest pressure ratios with nitrogen

as the working gas in the experiment at P1 and P2 is 1.28 and 1.18 under the mean pressure of 1.2 MPa and the temperature difference of 504.9 K. So it is obviously that the pressure ratios will be larger if the mean pressure and the temperature difference are larger. We can see that the three-stage TWTAE has potential under low and medium working temperature. So it is very promising in utilizing waste heat, solar thermal energy, and geothermal energy.

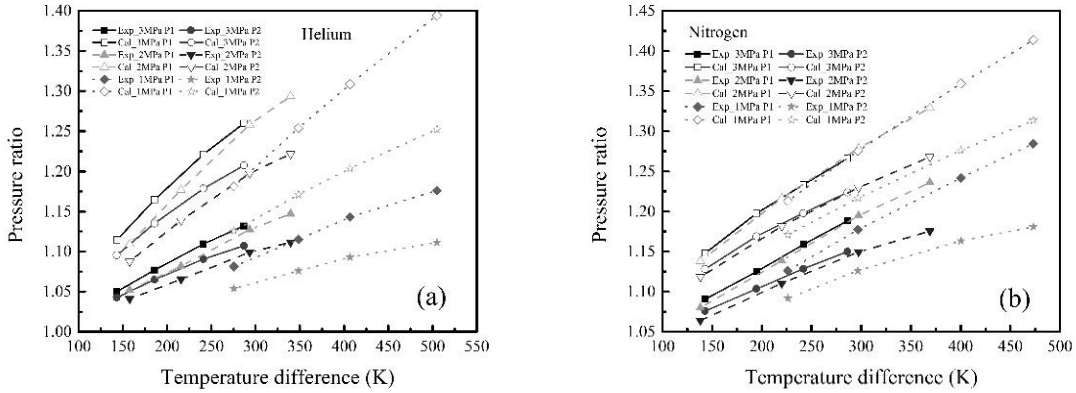

Figure 6: The experimental and numerical pressure ratios vs. temperature difference at P1 and P2 (a) helium; (b) nitrogen

The experimental acoustic power in HHX of TAC 3 (Based on P4 and P5) are shown in Figure 7. As shown, the higher the charge pressure, the more acoustic power. In general, the acoustic power is larger when the working gas is helium. From Figure 3, when the charge pressure is 2 and 3 MPa, the mean pressure is slightly lower when the working gas is helium under the same temperature differences. However, the acoustic power is still larger when the working gas is helium. For instance, when the charge pressure is 3 MPa and the temperature difference is about 286 K, the acoustic power in HHX of TAC 3 is 718.0 W when the working gas is helium, whilst the acoustic power is 558.7 W when the working gas is nitrogen. When the charge pressure is 1 MPa, the onset temperature is higher so that the three-stage TWTAE need to overcome more losses to start to work. And the acoustic power in HHX is firstly lower and then higher when the working gas is helium than that when the working gas is nitrogen.

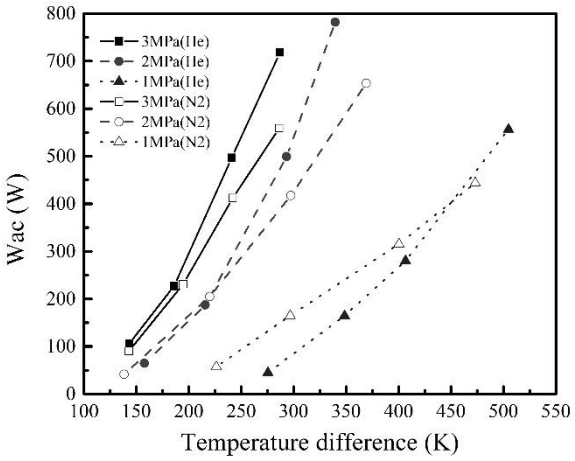

Figure 7: The experimental acoustic power in HHX vs. temperature difference

The experimental heating power for the three-stage TWTAE are displayed in Figure 8. As shown, the higher the charge pressure, the greater the heat capacity of the gas, so more power is required to heat to the same temperature difference. When the working gas is nitrogen, the total heating power is about 6.9 kW under the mean pressure of 3.2 MPa and the temperature difference of 286.2 K. When the mean pressure is 2.3 MPa, the temperature difference is about 369.1 K under the same heating power. When heated to the same temperature, nitrogen requires more heat as the working gas than helium as the working gas. When the mean pressure is 1.2 MPa and the heating power is about 5.4 kW, the temperature difference is 473.2 K when the working gas is nitrogen and 504.9 K when the working gas is helium, respectively.

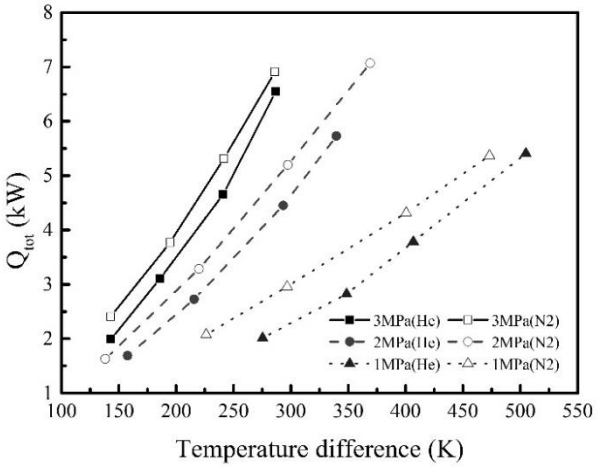

Figure 8: The experimental heating power vs. temperature difference

3.3. Electrical power

The three-stage TWTAE has promising potential in utilizing low-grade heat which is proved experimentally and numerically. An electric generator driven by the three-stage traveling-wave thermoacoustic engine with helium as the working gas was then modified by DeltaEC. The thermoacoustic generator is composed of the three-stage TWTAE and six linear alternators, which are located at the outlet of SAHXs and divided into three pairs. In the model, the mean pressure is 3.0 MPa, the heating temperatures of HHXs are set at 623 K, the cooling temperatures of AHXs and SAHXs are set at 303 K, and the electric capacitance is set at 15.5 μF which is optimised before.

Figure 8 shows the calculated electric power generation and thermal-to-electric efficiency of the three-stage thermoacousitc generator with respect to the load resistance. As shown, the electric power firstly increases, and then decreases. The optimal load resistance is in the range of 90 Ω to 140 Ω, and the maximum electric power is 1427.2 W. The variation trend of the thermal-to-electric efficiency with the load resistance is also shown in Figure 8. The thermal-to-electric efficiency also increases at first, and then decreases. The optimal resistance is in the range of 100 Ω to 120 Ω, and the maximum thermal-to-electric efficiency is 10.7%. It is found that the optimal load resistances needed for the efficiency are different from that for the electric power. This is because the optimal acoustic impedance for thermal-to-acoustic efficiency is different from that for output power. In all, adjusting the load resistance essentially changes the acoustic impedances of the linear alternators, which then determines the output capability of the engine, and further affects the performance of the thermoacoustic generator.

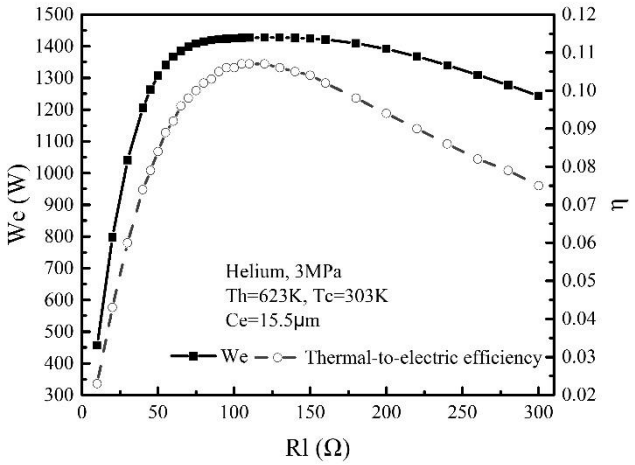

Figure 9: Electric power and thermal-to-electric efficiency varying with the load resistance

4. CONCLUSION

Multi-stage TWTAE has high potential in recovering low-grade heat source into usable energy with the advantages of simple structure, high reliability, and low costs. Thus, a three-stage TWTAE was proposed and studied in this paper.

The performance of the three-stage TWTAE shows the potential in utilizing low-grade heat. In the experiment, at the mean pressure of 3.0 MPa and the temperature difference between the hot and cold end of the regenerator of about 285 K, the working frequency is about 20 Hz, the onset temperature difference is 55 K, the pressure amplitude is 278.0 kPa, and the pressure ratio can achieve 1.19, when the working gas is nitrogen; meanwhile, the working frequency is about 55 Hz, the onset temperature difference is 71 K, the pressure amplitude is 194.3 kPa, and the pressure ration can achieve 1.13, when the working gas is helium.

Furthermore, the numerical results of the thermoacousitc generator verify its ability to convert low-grade heat into electricity. A maximum electric power of 1427.2 W and a highest thermal-to-electric efficiency of 10.7% are obtained numerically when the mean pressure is 3.0 MPa and the heating temperature is 623 K.

5. ACKNOWLEDGEMENT

This work is financially supported by National Natural Science Foundation of China (No. 51676168).

6. REFERENCES

Backhaus S., Swift G.W., 1999. A thermoacoustic Stirling heat engine. Nature, 399, 335-338.

Wu Z, Dai W, Man M, et al., 2012. A solar-powered traveling-wave thermoacoustic electricity generator. Solar Energy, 86(9), 2376-2382.

Ceperley P.H., 1979. A pistonless Stirling engine- The traveling wave heat engine. Journal of the Acoustical Society of America, 66(5), 1508-1513.

de Blok K, 2012. Novel 4-Stage Traveling Wave Thermoacoustic Power Generator[C]// In ASME 2010 3rd Joint US-European Fluids Engineering Summer Meeting collocated with 8th International Conference on Nanochannels, Microchannels, and Minichannels, American Society of Mechanical Engineers, 73—79.

Wu Z, Yu G, Zhang L, et al., 2014. Development of a 3kW double-acting thermoacoustic Stirling electric generator. Applied Energy, 136, 866-72.

Bi T, Wu Z, Zhang L, et al., 2017. Development of a 5kW traveling-wave thermoacoustic electric generator. Applied Energy,185, 1355-1361.

Jin T, Yang R, Wang Y, et al., 2016. Phase adjustment analysis and performance of a looped thermoacoustic prime mover with compliance/resistance tube. Applied Energy, 183, 290-298.

Jin T, Yang R, Wang Y, et al., 2017. Low temperature difference thermoacoustic prime mover with asymmetric multi-stage loop configuration. Scientific Report, 7(1), 7665.

Zhang X, Chang J, 2015. Onset and steady-operation features of low temperature differential multi-stage travelling wave thermoacoustic engines for low grade energy utilization. Energy Conversion and Management, 105, 810-816.

Ward B, Clark J, Swift G.W., 2008. Design environment for low-amplitude thermoacoustic energy conversion. Version 6.2. Users Guide.

Qiu L, Sun D, Tan Y, et al., 2006. Effect of pressure disturbance on onset processes in thermoacoustic engine. Energy Conversion and Management, 47, 1383-1390.

Liu J, Yan J, Lin W, et al., 2001. New explanation on the Mechanism of the Rijke tube. Journal of Xi'an Jiaotong University, 35(3), 221-224.

271: Construction and quantitative analysis of the policy base of energy conservation and emissions reduction in Hubei Province

Wang YI[1], Peng JIANXIN[2]

[1] Wang Yi, School of Economics and Management in Hubei University of Technology, 747739206@qq.com
[2] Peng jianxin, School of Economics and Management in Hubei University of Technology, 756823027@qq.com

With the global climate change intensified and environmental constraints highlighted, China attach great significance to energy conservation and emissions reduction, which has become one of China's basic national policies. Quantitating the analysis of the effectiveness of energy conservation and emissions reduction policies and differing the synergy in those measures are vital to understand the interest game behind the policies as well as the formulation principle of them.

In this paper, we have collected energy conservation and emissions reduction policies between 2012 and 2016 from the public information platform of Hubei provincial government. Through intensive reading, screening and sorting, we have constructed a preliminary energy conservation and emissions reduction policies base. And from three dimensions: policy dynamics, policy measures and policy targets, we have designed a quantitative evaluation model of policy effectiveness and policy synergy of energy conservation and emissions reduction, then empirically analysed the synergistic evolution law of energy conservation and emissions reduction policies in Hubei province. Results have shown that from 2012 to 2016, the number of energy conservation and emissions reduction policies in Hubei province showed an upward trend, but the overall and average policy effectiveness was on the decline; the synergy between policy measures and policy targets has been gradually reduced to a stable range since 2012. Those mean that Hubei province puts a high value on energy conservation and emissions reduction, but there are conflicts between different policies and measures, which make it difficult to achieve the desired policy goals. Meanwhile, we have found that the effectiveness of energy conservation and emissions reduction policies in Hubei Province has a strong correlation with the national government's five-year plan for energy conservation and emissions reduction, which is lack of strategy and systematicness; the emphasis among diversified policies is shifted from single synergy to multiple measures. Finally, we put forward some suggestions on the policy formulation of energy conservation and emissions reduction in Hubei province.

Keywords: Energy conservation and emissions reduction; Policy effectiveness; Policy synergy; Policy evaluation

1. INTRODUCTION

"Energy conservation" means to take all measures that are technically feasible, economically reasonable, environmentally acceptable and socially acceptable to improve the utilization efficiency of energy and resources. "Emission reduction" emphasizes the protection of the ecological environment as well as the reduction of pollutant and greenhouse gas emissions at all links of energy development, production and use. Energy conservation and emissions reduction is controlled through a variety of measures in various fields, in the process of which pollution and greenhouse gas emissions are reduced, so as to achieve economic and social sustainable development. Nowadays, energy conservation and emissions reduction has become the common goal of all countries in the world. In many countries, governments or organizations have taken a series of measures in technology, engineering and economy to vigorously promote energy conservation and emissions reduction. China has now become the world's largest energy consumer, due to the increasingly serious environmental pollution and energy supply shortage, our government needs to solve enormous problems in balancing economic growth and sustainable development. Thereby, it is China's top priorities to actively respond to climate change and further promote pollutant reduction at this stage. In order to achieve sustainable economic development goals, the government must adhere to energy conservation and emissions reduction.

Since the 11th five-year plan period, China has strengthened policy restrictions and gradually formed a long-term policy framework for energy conservation and emissions reduction in 2030. In the process of the gradual improvement and evolution of the policy system, marketing tools have been promoted to the core position. During the “12th Five-Year Plan” period, China initiated carbon trading pilots in seven provinces and cities, among which Hubei transactions were the most active with the market share ranking first in the country. This will be the practice of China's largest market-based emissions reduction policy tool. Although the opening of the carbon emission market has initially achieved certain results, there are still obvious defects in the standardization of the system that policies formulated by the government are subject to externalities such as energy conservation and emissions reduction, public welfare or lack of motivation. In terms of restrictions, energy saving and emission reduction cannot be solved by market mechanisms alone, it requires the government to formulate enormous policies. However, energy conservation and emissions reduction are multidisciplinary and complex. Any single or excessive use of a policy may have adverse effects on the sustainable development of economy and the efficiency of energy conservation and emissions reduction. Therefore, the coordinated use of a variety of macro-control tools can better achieve the set goals. This requires our government, when vigorously promoting energy conservation and emissions reduction, must consider the implementation in the influence of economic growth and social development; must coordinate to promote energy conservation and emissions reduction and other growth targets, making it produce a good synergistic effect at the policy level. Therefore, this paper discusses the coordination status and synergy effectiveness of existing energy conservation and emissions reduction policies in Hubei Province, so as to provide some suggestions for the government to formulate guidance policies.

2. LITERATURE REVIEW

At present, there is a lack of research on energy conservation and emissions reduction. For policy synergy issues, Meijers and Stead et al. (2004) believe that policy synergy refers to the government's management of cross-border issues in the policy development process. These issues go beyond the boundaries of existing policy areas and the scope of responsibilities of individual departments, which needs synergy among multiple entities. However, Camarero and Tamarit consider that policy synergy, an effective way to resolve policy conflicts, is the result of conflicts or competitions between policy targets. Kim (2011) pointed out that the government should adopt policy synergy and other measures to maintain the stability of the policy in environmental changes. Peng and Zhong et al (2008) found that the impact of innovation policy synergy on economic and technical performance has significant directional differences.

China's research on energy conservation and emissions reduction policies focuses on the analysis of its deficiencies and implementation dilemmas; there are few concerns about the synergies of China's energy conservation and emissions reduction policies. Starting from the policy itself, the initial attempt to quantify policies began in 1978. Libecap (1978) categorized various regulations concerning mineral property rights in 15 pre-designed categories, and according to regulations, when the right is defined more detailed and accurate, a score of 1 is assigned. This quantitative processing results are used to statistically analyse policies’ impact. Cools and Brijs, et al. (2012) quantified the policy measures of Flanders traffic policies such as traffic stability, energy taxation and parking fees from the four evaluation criteria: "Hard", "Soft", "Push" and "Pul". Liu et al. (2007) used statistical analysis methods to study the historical evolution path of China's innovation policy from 1980 to 2005. Yan et al. (2006) promulgated our foreign investment industrial policies and their investment catalogues issued by China in 1987, 1995, 1997 and 2002 as the target, weighting various industrial policy categories, measuring foreign industrial policy indices, and studying the effectiveness of foreign investment industrial policies. Peng et al. (2008) took the technological innovation policy as an example, adopted a quantified approach, measured the policy from different dimensions, and used the quantified results to explore the evolution path of policy synergy and its impact on economic performance. Their method sets a good example in the following research. Zhang et al. (2014) collected energy conservation and emissions reduction policies of China from 1978 to 2013. They developed quantitative standards for energy conservation and emissions reduction policies from the three dimensions: policy dynamics, policy measures, and policy targets, then quantified the collected policies, constructed a model to analyse synergy

evolution of those policies by quantitative data. This paper collects energy conservation and emissions reduction policies of Hubei province from 2012 to 2016. Through the above-mentioned policy quantitative research methods, Hubei Province's related policies are analysed in terms of effectiveness of policies, synergies between measures, and target synergy. In addition, based on the analysis of the conclusions and the status of energy conservation and emissions reduction policies in Hubei Province, we can put forward reasonable advice to help the Hubei Provincial Government make subsequently related policies.

3. RESEARCH DESIGN

3.1. Design evaluation system

In order to measure the synergy of policies from the policy content itself, this paper quantifies the energy conservation and emissions reduction policy in Hubei province from three dimensions: policy dynamics, policy measures and policy targets.

Policy dynamics is an indicator reflecting the size of policies' legal effectiveness. In general, the higher the level of institutions promulgated by policies and laws, the greater policies' legal effectiveness and the higher scores of policy dynamics. Policy measures refer to the methods and means adopted by governments when formulating and implementing policies in order to achieve the set goals. Policy targets are considered as the purpose of a policy. These three dimensions of quantification make up for the deficiencies of single indicators in reflecting policy content, thus better mirroring the content validity of policies.

3.2. Build a quantitative model of indicators

Policy dynamics is an indicator that measures the size of policy legal effectiveness; policy measures are indicators that describe the methods used by the policies; policy target is to depict the objectives of the policy. Generally speaking, the greater policy dynamics, the more specific measures used and the clearer goals achieved, the higher overall effectiveness. Therefore, this paper will adopt the quantitative model of Zhang guoxin et al. Equation 1 is used to calculate the overall effectiveness of each year's energy conservation and emissions reduction policies; equation 2 is used to calculate the average effectiveness of each quarter's policies. The exact expression for both is as follows.

Equation 1: Overall effectiveness of each year's policies

$$YTPE_i = \sum_{j=1}^{N_i} pe_j \times pm_j \times pg_j$$

Where:

$YTPE_i$: represents the overall policy effectiveness in year i

N: indicates the number of policies in year i

pe_j: represents the policy dynamics score of article j policy

pm_j: represents the total score of policy measures of article j policy

pg_j: represents the total score of policy targets of article j policy

i: from 2012 to 2016

Equation 2: the average effectiveness of each quarter's policies

$$YPE_i = \frac{\sum_{j=1}^{N_i} pe_j \times pm_j \times pg_j}{N}$$

Where:

YPE_i: represents the average policy effectiveness in year i

The synergy of policy measures or policy targets describes a situation where a policy uses multiple measures or achieves multiple goals. Generally speaking, the greater policy dynamics, the more specific measures or the clearer goals achieved, the synergy of policy measures or policy targets will be better. Therefore, this paper mainly refers to Peng jisheng's measurement model of technological policy synergy. Equation 3 is used to calculate the synergy of each year's policy measures; equation 4 is used to calculate the synergy of each year's energy conservation and emissions reduction policies targets. The exact expression for both is as follows.

Equation 3: the synergy of each year's policy measures

$$PMJ_i = \sum_{j=1}^{N} pe_j \times pm_{jk} \times pm_{jl} \left(k \neq l\right)$$

Where:

PMJ_i: represents the synergy of policy measures in the quarter i

pm_{jk}; pm_{jl}: represent scores of the kth and lth policy measures in the article j policy

k; l: indicate that 2 measures are selected from 6 measures including personnel measures, administrative measures, fiscal and taxation measures, financial measures, guiding measures and other economic measures to consider measures synergy.

Equation 4: the synergy of each year's policies targets

$$PGJ_i = \sum_{j=1}^{N} pe_j \times pg_{js} \times pg_{jt} \left(s \neq t\right)$$

Where:

PGJ_i: represents the policy synergy in year i

pg_{js}; pg_{jt}: represents scores of the sth and tth policy targets in the article j policy

s; t: indicate that 2 targets are selected from 7 targets including pollution prevention, improvement of energy conservation and emissions reduction, establishment of energy conservation and emissions reduction concepts, promotion of industrial upgrading, improvement of energy utilization efficiency, optimisation of energy consumption structure, and promotion of technological transformation in energy conservation and emissions reduction to consider targets synergy

3.3. Energy conservation and emissions reduction policies base

This paper combines the quantified standards developed by Zhang guoxin et al. in the process of studying the co-evolution of energy conservation and emissions reduction policies with the quantitative technological innovation policies standards developed by Peng Jisheng et al. Subsequently, based on the actual situation of the energy conservation and emissions reduction policy in Hubei province, the quantitative standards for energy conservation and emissions reduction policies in Hubei province are obtained from these three dimensions: policy dynamics, policy measures and policy targets.

At first, this paper collects a total of 563 policies on energy conservation and emissions reduction issued by the People's Government of Hubei Province and the General Office of the People's Government of Hubei Province from the Hubei Government Information Disclosure Platform. Among them, there are 97 policies related to energy conservation and emissions reduction from early 2012 to the end of 2016. Later, we conduct a preliminary screening of policies that are highly relevant to energy conservation and emissions reduction. Then, classify and quantify these policies from 3 dimensions: policy dynamics, policy measures and policy targets. Thus, a policy base for energy conservation and emissions reduction in Hubei province has been formed. According to the level and policy type of the promulgation agency for energy conservation and emissions reduction policies in Hubei province, the values of 1, 2, 3, and 4 points are assigned to each policy to reflect the magnitude of policy dynamics. The specific quantitative standards are shown in Table 1.

Table 1: Quantitative standards for energy conservation and emissions reduction policies

Policy Dynamics Score	Score Criteria
Score 4	Measures, regulations, provisions, decisions and interim measures promulgated by the Provincial People's Government (order of the provincial government)
Score 3	Opinions and notifications issued by the Provincial People's Government
Score 2	Implementation opinions and notifications issued by the General Office of the Provincial People's Government
Score 1	Notices and implementation opinions promulgated by the General Office of the Provincial People's Government

According to the research on the classification of policy measures by Kim, Murphy, Meijer and Peng jisheng, et al. as well as the summary of Zhang guoxing, et al., this paper divides the main measures of energy conservation and emissions reduction policies into personnel measures, administrative measures, fiscal and taxation measures, financial measures, guidance measures and other economic measures. In the process of quantification, the value of 5,4,3,2,1 points will be assigned to each policy measure according to the detailed degree of measures and the implementation effectiveness. The quantitative criteria are partly shown in table 2.

Table 2: Quantitative standards for energy conservation and emissions reduction policies measures

Measures	Score	Quantitative standards for policy measures
personnel measures	5	established a special agency to promote energy conservation and emissions reduction; clarified this agency's responsibilities
		trained personnel, improved the level of benefits, and formulated relevant systems
		formulated performance appraisal measures for energy conservation and emissions reduction; improved the incentive and punishment mechanism
	3	clearly proposed to improve energy conservation and emissions reduction related institutions
		commend outstanding personnel and punish those who violate the rules
		evaluate energy conservation and emissions reduction achievements; link the assessment results with the performance of personnel
		no enforcement measures have been formulated or the recognition and punishment methods are unclear
	2	only mention or relate to the above terms
	1	no personnel measures were mentioned
guidance measures	5	vigorously guide individuals or enterprises in energy conservation and emission reduction, and formulate specific implementation measures or plans for publicity
		formulate methods for implementing demonstration projects or pilot projects
		developed a catalogue of product technology promotion
		developed a detailed guidance system
	3	explicitly put forward the need to vigorously implement the promotion of energy conservation and emissions reduction; strengthen the implementation of logo management for energy conservation and environmental protection products
		explicitly stated the need to formulate a list of product consumption recommendations
		explicitly proposed to formulate guidance measures related to energy conservation and emissions reduction
		no relevant implementation measures or related directories have been established
	2	only mention or relate to the above terms
	1	no guidance measures were mentioned

The main policy targets of energy conservation and emissions reduction policies are divided into: pollution prevention, improvement of energy conservation and emissions reduction, establishment of energy concepts, promotion of industrial upgrading, improvement of energy utilization efficiency, optimisation of energy consumption structure, promotion of technological transformation in energy conservation and emissions reduction. According to the degree of government's attitude toward the policy's targets or the degree to which the policy achieves its target, it is assigned 5, 4, 3, 2, and 1 points respectively. The quantification standards are partly shown in Table 3.

Table 3: Quantitative standards for energy conservation and emissions reduction policies targets

Measures	Score	Quantitative standards for policy measures
establishment of energy conservation and emissions reduction concepts	5	requested to increase the promotion of energy conservation and emissions reduction in the province to raise the related awareness
		legally require recognition of relevant groups
		request to make detailed plans to raise public awareness
	3	formulated an implementation plan to increase energy conservation and emissions reduction
		formulated specific measures for public participation in supervision or evaluation
		formulated the implementation method of demonstration or energy conservation logo management
	2	requirements system only involves the above items, but no relevant measures and measures have been introduced
	1	no mention of any idea or scheme for energy conservation and emissions reduction
improvement of energy utilization efficiency	5	mandatory elimination of high energy-consuming backward equipment and renovation
		formulated a clear energy-saving enforcement target and heat-measurement retrofit goals to support energy conservation in all aspects
		formulated a definitive constraint on energy consumption reduction
		implement energy regulation from legislative, price and cost aspects; strengthen the management of power consumption
	3	formulated a plan for implementing the elimination of backward production capacity and upgrading
		established fiscal, taxation, and financial support options or price-based cost incentives to support energy conservation
		formulated an energy-saving product promotion program
		established guidelines for energy consumption limits
	2	only the above clauses are involved, but relevant measures have not been introduced
	1	no measures or policies to improve energy efficiency

4. QUANTITATIVE ANALYSIS OF ENERGY CONSERVATION AND EMISSIONS REDUCTION POLICIES IN HUBEI PROVINCE

4.1. The evolution of the number and effectiveness of policies

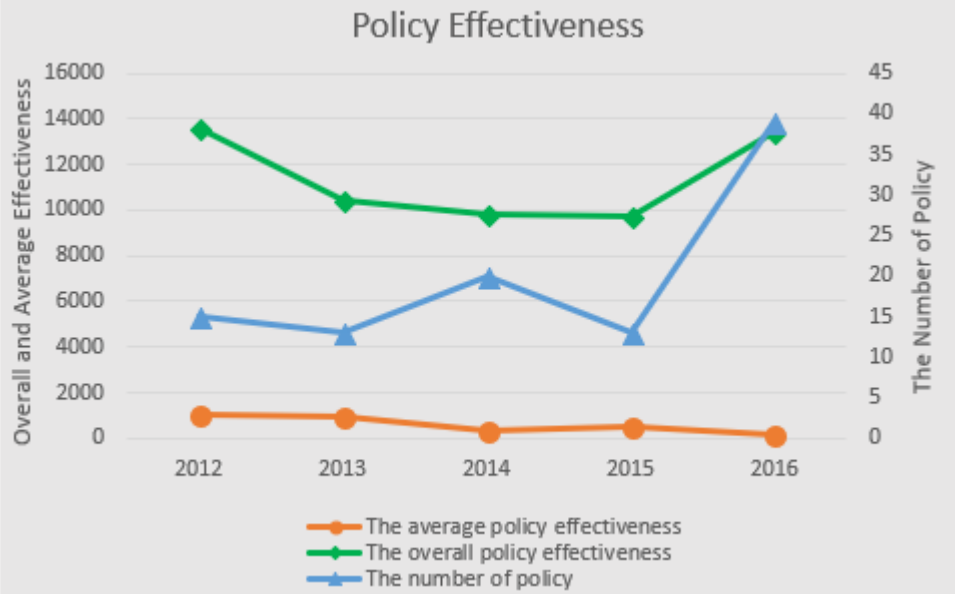

Figure 1: The evolution analysis of policy quantity, overall policy effectiveness and average policy effectiveness

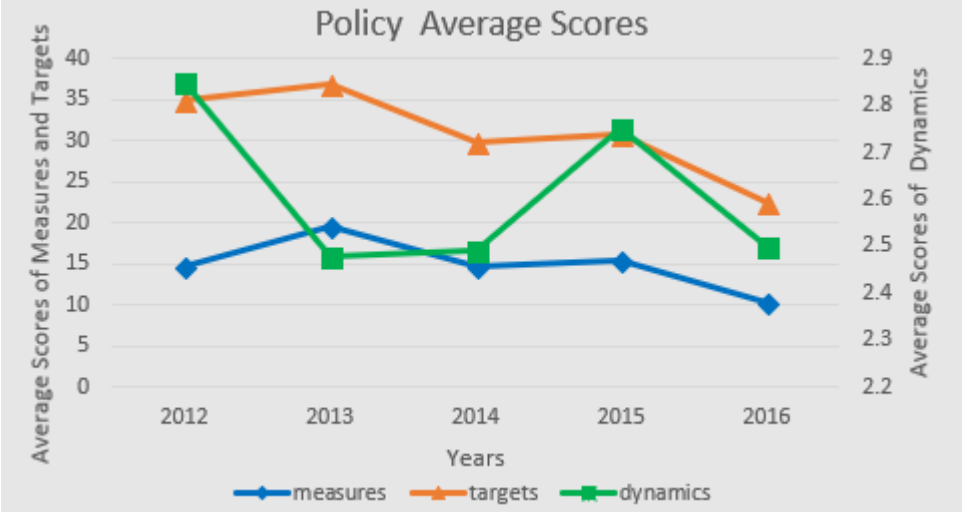

Figure 2: The evolution analysis on the average score of policy dynamics, policy measures and policy targets

This paper analyses the energy conservation and emissions reduction policies issued by Hubei province from the early 2012 to the late 2016, then draws two charts here. Figure 1 shows the evolution process of the number, average and overall effectiveness of energy conservation and emissions reduction policies during this period. It can be seen that in the last five years, Hubei province, the number of energy conservation and emissions reduction policies in general are on the rise, although from 2014 to 2015, the number of policies declined slightly, then began to rise from 2016. In order to realize the binding index of energy consumption and main pollutant emission in the national "Twelve-Five" planning, a lot of energy conservation and emissions reduction policies are often introduced in the first and last year of planning. At the same time, before 2000, most policies on energy conservation and emissions reduction are issued in the form of laws or orders with high policy dynamics, which is an indicator of the legal effect of policies. In recent years, these policies promulgated are mainly supportive, which are relatively low in dynamics and effectiveness. Therefore, the number of policies increases year by year, while their average effectiveness decreases.

From Figure 2, it can be roughly analysed that the average policy effectiveness is gradually reduced. The policy on energy conservation and emissions reduction in Hubei province is less powerful, and the scores of policy measures and policy targets are lower, which result in the decrease of the overall policy effectiveness. The number of policies is the highest in 2016, because it is the beginning year of the 13th five-year plan. This year promulgated more

supporting policies, in order to complete the "Twelve-Five" planning energy conservation and emissions reduction of the binding goal, to promote the economic development, upgrading and efficiency. The overall policy effectiveness is the highest in 2012 (a number of notices were issued for the completion of the "Twelve-Five" plan), then gradually decline until 2015 (energy conservation and emissions reduction policies become more specific which are less forceful, thus the overall effectiveness of these policies decreased accordingly), and subsequently maintained a large increase.

The change of the overall effectiveness of energy conservation and emissions reduction policy in Hubei province is mainly determined by the amount of policy changes, and there is a certain positive correlation, that is, the increase of the overall effectiveness depends on the increasing number of policies instead of its legal effect. This has also led to a continuous decline in policy measure scores, target scores and average dynamic scores between 2012 and 2016. The excessive reduction on policy's legal effect is not only detrimental to the formulation and implementation of systematic and strategic policies on energy conservation and emissions reduction, but also makes its plans more complicated and ineffective. Therefore, the government should strengthen the systematic and strategic construction of our provincial energy conservation and emissions reduction policy to make it moderate.

4.2. Analysis on the synergy evolution of policies measures

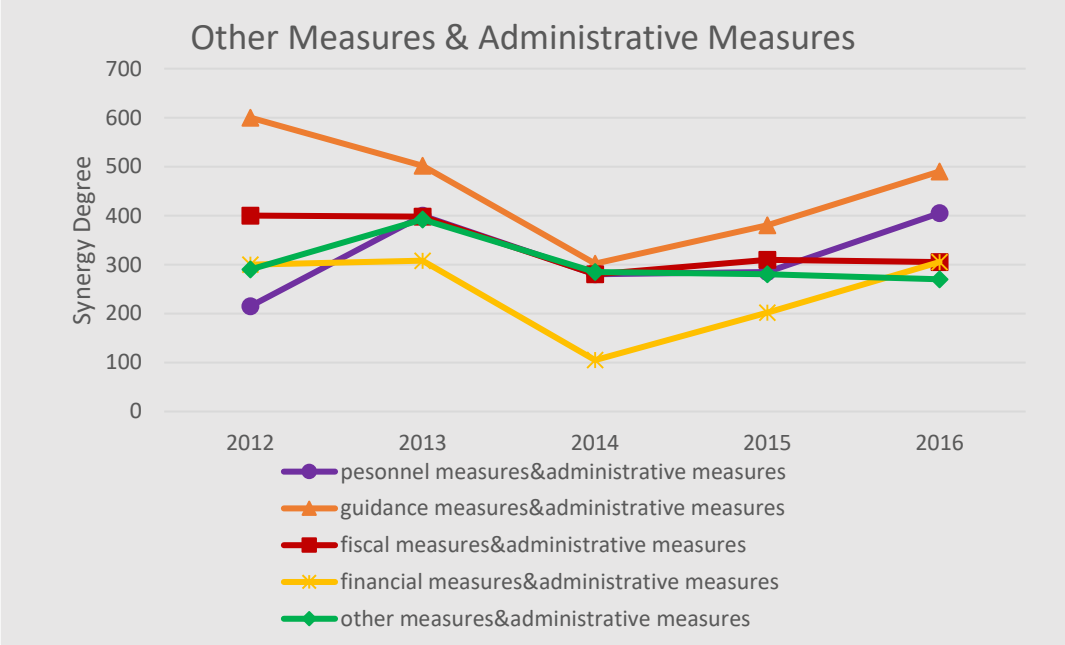

Figure 3: The evolution analysis in the synergy between administrative measures and other measures

The summary table shows that: in the Hubei provincial energy conservation and emissions reduction policy, administrative measures and guidance measures are of the most usage, financial and other economic measures are of the least usage, so this paper choose the most used measures to study the synergy in policies.

As can be seen from Figure 3, there is a strong synergy in different measures. The changes in the synergy of policy measures over the past five years have the following characteristics: first, the policy has been transformed into a synergistic action of multiple measures. In 2012, the policy measures synergy was relatively dispersed, and then became concentrated, because multiple policy measures have been given equal weight ever since. Second, the synergy between financial measures and administrative measures has been paid more and more attention. In Hubei province, where the economic growth is regarded as the main development theme, taking too much administrative measures to interfere with the energy consumption of enterprises to reduce emissions, may hinder its economic development and people's prosperity. However, guidance measures and fiscal measures are limited in scope and intensity, so we should grasp the financial measures which have not received more attention. Similarly, other economic measures should further assist the government in planning and increase the scope and depth of policies.

Figure 4 shows that financial measures, and other economic measures, fiscal and tax measures and personnel measures also present a certain synergy relationship with guidance measures, among which guidance measures and other measures are closer and closer in synergy. The synergy between financial measures and guidance measures indicates that government departments begin to reduce administrative measures while taking advantage of economic leverage and market mechanisms to achieve energy conservation; the synergy between personnel measures and guidance measures reflects that our government attaches importance to the guidance system and personnel training.

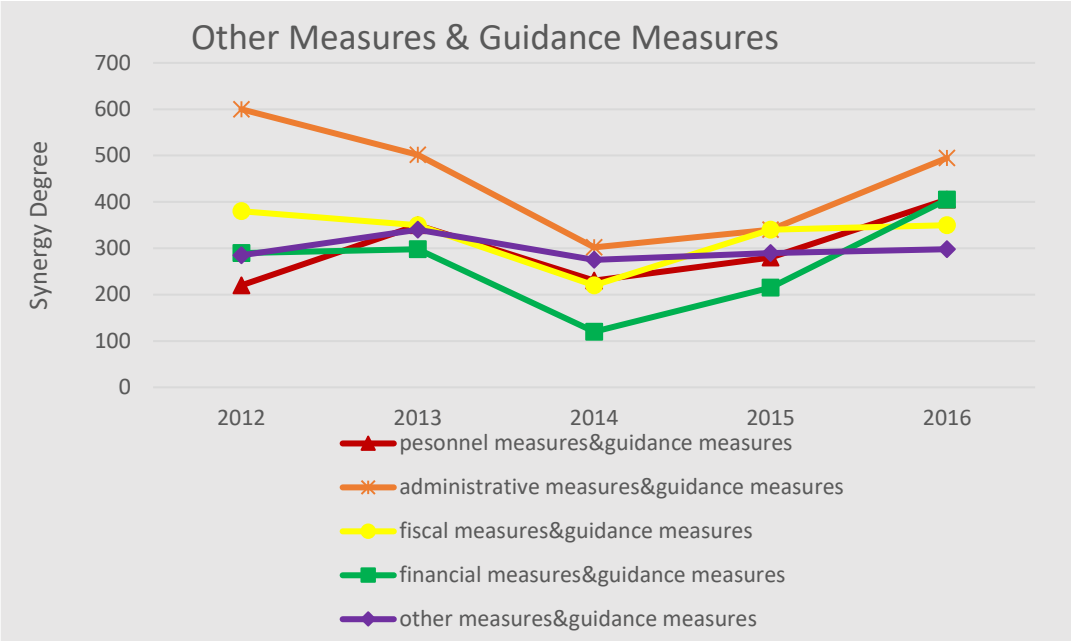

Figure 4: The evolution analysis in the synergy between guidance measures and other measures

4.3. Analysis on the synergy evolution of policies targets

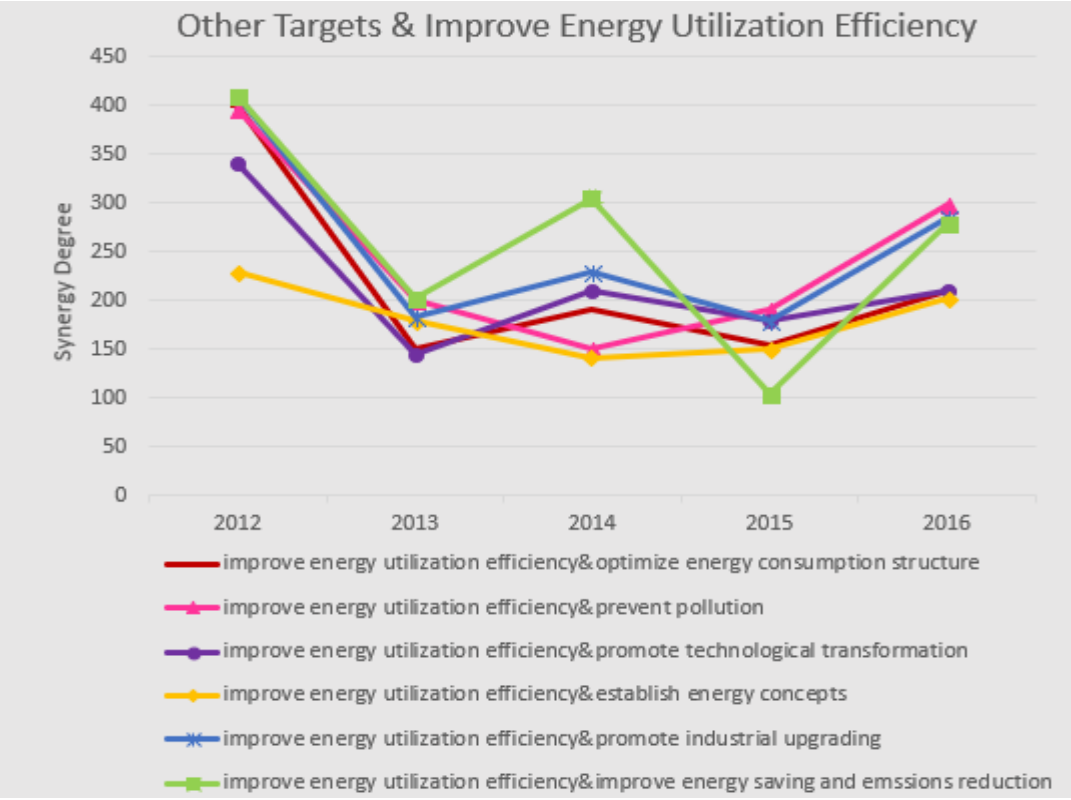

Figure 5: The evolution analysis in the synergy between improvement of energy utilization efficiency and other targets

Since reducing energy consumption and pollutant emissions are the main aims of energy conservation and emissions reduction policy, figure 5 focuses on the synergy between other policy targets and the improvement of energy utilization efficiency. Most of these targets have a high degree of synergy with the improvement of energy utilization efficiency. It is concluded that: the implementation path on energy conservation and emissions reduction in Hubei province should focus on changing the mode of economic growth, the main way of which is to improve the efficiency of energy use, whose basis are optimising energy structure, promoting industrial upgrading, promoting energy conservation and emissions reduction as well.

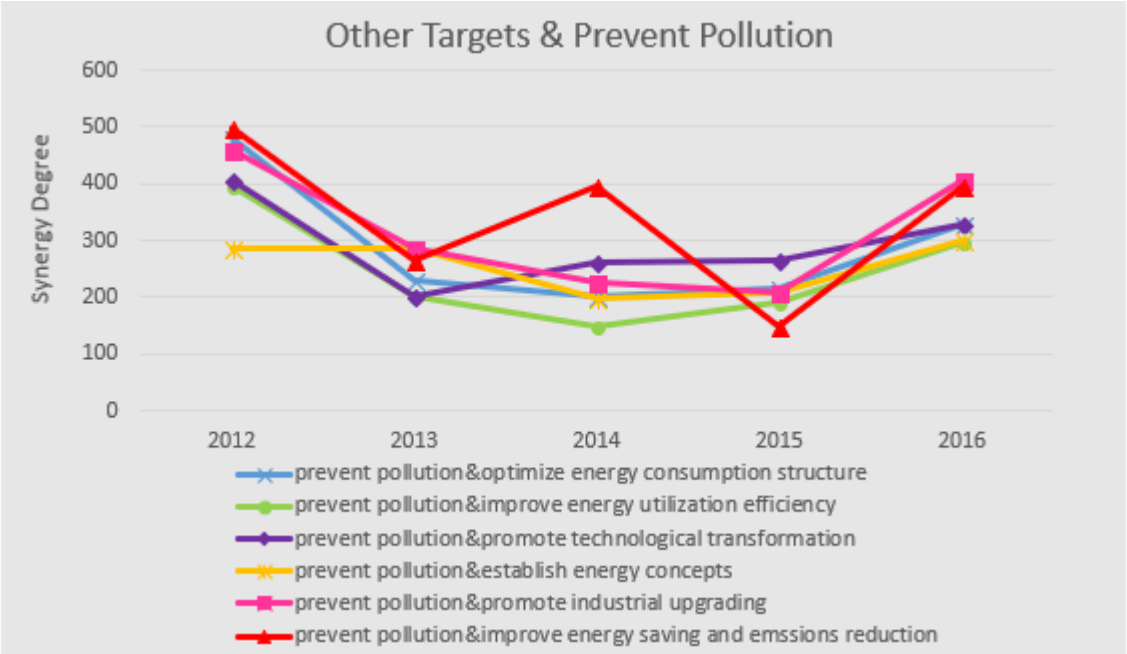

Figure 6: The evolution analysis in the synergy between pollution prevention and other targets

Figure 6 illustrates that there is a good synergy between pollution control and other policy targets. The synergy between pollution prevention and energy conservation and emissions reduction remains high, indicating that the effect of energy conservation and emissions reduction is equal to pollution prevention. In fact, people are the main source of energy consumption and pollutant emission. If the government wants to implement effective policies, it must raise people's awareness on energy conservation and emissions reduction. However, our government pay little attention to this aspect and do not give full play to the initiative of the masses. As Hubei province given priority to coal-dominated energy consumption structure, pollution phenomenon serious, the follow-up policies should lay stress on optimising energy consumption structure and the synergy in policy targets.

5. CONCLUSION AND SUGGESTION

In this paper, we have collected and screened the energy conservation and emissions reduction policies of Hubei province from 2012 to 2016, then scored the policies based on quantitative standards in terms of policy dynamics, policy measures and policy targets. According to the quantitative data, we analysed the synergy evolution of energy conservation and emissions reduction policies in Hubei province. The main conclusions are as follows:

First, the government of Hubei province is paying more and more attention to energy conservation and emissions reduction. The overall effectiveness of these policies in Hubei province has increased as a whole between 2012 and 2016, but their average effectiveness has been reduced, reflecting that there are some defects in the policy formulation. In addition, the increase in the overall policy effectiveness is due to the increase in the number of policies, which lacks strategy and systemicity. The lack of these characteristics mirrors that the formulation of energy conservation and emissions reduction policies in Hubei province focuses on short-term goals rather than long-term planning, which fails to implement the concept of sustainable development.

Second, on the policy targets of synergy, optimisation of energy consumption structure, establishment of energy conservation and emissions reduction concepts, pollution prevention, promotion of industrial upgrading, improvement of energy conservation and emissions reduction, promotion of technological transformation in energy conservation and emissions reduction together with improvement of energy utilization efficiency, have all demonstrated high and better synergy. This indicates that Hubei province has a clear goal in energy conservation and emissions reduction, good energy-saving industry layout and diversified energy conservation industry development (the lead of the carbon emissions trading pilot is a good proof of these targets synergy.)

Third, from the overall point of view, the score that economic leverage guides social actors to actively participate in energy conservation and emissions reduction is not high, indicating that Hubei province's capital investment in energy conservation and emissions reduction is not enough. Besides, in the scoring of energy conservation and emissions reduction policies, personnel measures scores are lower. This shows that Hubei province does not attach importance to the achievement of energy conservation and emissions reduction targets as an important content in the assessment of leading cadres, which helps to play their value-oriented role. In the policy review, it is found that there is a lack of energy conservation and environmental protection supervision, law enforcement as well as the establishment of monitoring platforms for key pollution sources.

Fourth, in the policy scoring, the industrial structure adjustment project, new technology promotion project, and circular economy demonstration project are mentioned in most of the policies, showing that Hubei provincial government has reduced pollutant emission fundamentally, solved the source of energy consumption and emission problems, and achieved the set goals better.

Based on the analysis results in this paper and the current status of energy conservation and emissions reduction policies in Hubei province, the following suggestions are proposed: first, strengthen the cooperative operation mechanism between the main body of policy departments in Hubei province, so as to formulate policy targets of strategic, integrality and pluralism; second, strengthen the intensity of policy formulation in Hubei province and take effective measures to enrich the contents of the energy conservation and emissions reduction management system so as to highlight the attribution, authoritativeness and unity of the Hubei provincial ordinance, so that these policies are obvious and cannot be underestimated; third, strengthen the coordination and combination of different policy measures. The characteristics of energy conservation and emissions reduction activities determine that their policies go beyond the boundary of existing policy areas and the scope of responsibilities of individual departments. No single, excessive emphasis on any one policy can achieve optimal results. Therefore, the Hubei provincial government should enhance the comprehensive utilization of various policy measures in the subsequent policy formulation.

6. REFERENCES

Meijers E, Stead D. 2004. Policy Integration: What does it Mean and How Can it be Achieved? Berlin: Berlin Conference on the Human Dimensions of Global Environmental Change: Greening of Policies Interlinkages and Policy Integration.

Yin H, Pan Z, 2006. Research on the Measurement and Effectiveness of China's Foreign Direct Investment Industry Policy. Managing the World, (7),34.

Kim Y H, 2011. International Policy Coordination Mechanism with Respect to the Moral Hazards of Financial Intermediaries. Economic Modelling, 28(4),1914.

Peng J, Zhong W, Sun W, 2008. Policy Measurement, Policy Synergy Evolution and Economic Performance: an Empirical Study Based on Innovation Policy. Managing the World, (9),25.

Yuan J, Kang J, et al. 2011. Energy Conservation and Emissions Reduction in China—Progress and Prospective. Renewable and Sustainable Energy Reviews, 15(9),4334.

Zhang G, Gao X, et al. 2014. Measurement, Synergy and Evolution of Energy Saving and Emission Reduction Policies in China. China's Population Resources and Environment, 24(12),6274.

Libecap G D, 1978. Economic Variables and the Development of the Law:The Case of Western Mineral Rights. The Journal of Economic History, 38(2),338.

Brijs K, Tormans H, et al. 2012. Optimising the Implementationof Policy Measures Through Social Acceptance Segmentation. Transport Policy, 22,80.

Liu F, Sun Y, 2007. The Process, Trend and Suggestion of the Evolution of China's Science and Technology Policy to Innovation Policy. Soft Science in China, (5),34.

273: New design method for energy slab using artificial neural network (ANN)

Seokjae LEE[1], DongKu KIM[2], Khanh PHAM[3], Sangwoo PARK[4], Hangseok CHOI[5]

[1] School of Civil, Environmental and Architectural Engineering, Korea University, Seoul 02841, Korea, liontjrwo@korea.ac.kr
[2] School of Civil, Environmental and Architectural Engineering, Korea University, Seoul 02841, Korea, dkkim9013@korea.ac.kr
[3] School of Civil, Environmental and Architectural Engineering, Korea University, Seoul 02841, Korea, Khanhpnl199@korea.ac.kr
[4] Department of Civil Engineering and Environmental Sciences, Korea Military Academy, Seoul 01805, Korea, ptstwt@korea.ac.kr
[5] School of Civil, Environmental and Architectural Engineering, Korea University, Seoul 02841, Korea, hchoi2@korea.ac.kr

The energy slab is a ground-coupled heat exchanger consisting of the horizontal ground heat exchanger (HGHE). The HGHE allows circulation of a working fluid through heat exchange pipes, which are buried underground with a horizontal layout, inducing heat transfer between the fluid and the surrounding ground. The energy slab is installed as one component of the floor slab layers to utilize the underground structure as a hybrid heat exchanger. However, a comprehensive design tool for predicting the thermal performance of energy slabs has not been established. In this paper, a new design method for energy slabs using an artificial neural network (ANN) is proposed and compared with the engineering chart for design. Before establishing the design method, it is necessary to accurately identify key influential parameters that may affect the thermal performance of energy slabs. Therefore, the effect of key influential parameters (i.e., the thermal conductivity of ground formations and concrete slab, the flow rate of working fluid, etc.) on the thermal performance of energy slabs was investigated by numerical analysis for ideal conditions. Then, a set of engineering charts constructed through the numerical analysis was implemented by the ANN. From this approach, the thermal performance of energy slabs for a typical condition can be readily predicted without time-consuming numerical simulations. Additionally, this new method can provide the designers with a more practical design tool comparing to the engineering chart. Note that the Bayesian Regularization algorithm with 8 hidden neurons is the optimum learning algorithm, which can maximize the accuracy of prediction.

Keywords: Energy slab, Horizontal ground heat exchanger (HGHE), Artificial neural network (ANN), Numerical analysis

1. INTRODUCTION

The Ground Source Heat Pump (GSHP) system utilizes the geothermal energy in the heating and cooling of buildings by constructing Ground Heat Exchangers (GHEXs) in underground. The GHEXs allow circulating a working fluid through heat exchange pipes to induce heat exchange between the working fluid, the wall of heat exchange pipe and the surrounding medium. While a closed-loop vertical GHEX is mostly used in practice, it demands a high initial investment cost because of the additional drilling of the borehole and the need for the construction area (Boënnec, 2008). Especially, the drilling cost occupies more than 50% of the total construction cost. In this respect, novel types of GHEX have been developed to reduce the construction cost, which can be installed in underground structure elements, e.g., energy textile (Lee et al., 2012), energy pile (Brandl, 2006; De Moel et al., 2004; Morino and Oka, 1994), etc. Among them, the energy slab can be a tactical way to use the underground space for GHEXs effectively. The energy slab is installed as one component of the floor slab layers to utilize the building structure as a hybrid energy structure (Choi, 2012; Choi and Sohn, 2012). Constructing an energy slab is also an effective approach to reducing the construction cost without additional drilling, because it is buried underground with a horizontal layout, and can be constructed not only in new buildings but also in existing structures. Despite these advantages, the design methods or algorithms for predicting the thermal performance of energy slabs have not been established yet.

Two methods have been used to predict the thermal performance of various types of GHEXs. First, Park et al. (2018) used the engineering charts to predict the thermal performance of cast-in-place energy piles. In this method, the thermal performance of energy piles after three months of operation can be predicted. Furthermore, the designer can predict the thermal performance of energy piles for long-term operation (over three months) with consideration of the temperature difference between the ground formation and inlet fluid. Second, a machine learnings such as Artificial Neuron Network (ANN) or Adaptive Neuro-Fuzzy Interference System (ANFIS) were used. Esen and Mustafa (2010), Sun et al. (2015) developed the ANN and ANFIS models to predict the COPs of GHEXs. Moreover, Makasis et al. (2018) conducted a machine learning approach to energy pile design, by inputting annual thermal loads.

In this paper, a new design method for predicting the thermal performance of energy slabs was proposed. First, a Computational Fluid Dynamic (CFD) model was developed for ideal conditions. Then, a family of engineering charts was constructed along with a series of CFD simulations considering key influential parameters that affect the thermal performance of energy slabs (i.e., thermal conductivity of the concrete slab, ground formation and thermal insulation material, the flow rate of working fluid, the initial temperature of surrounding mediums and the interval of heat exchange pipes). Finally, the prediction model for the thermal performance of energy slabs was developed by adopting an ANN model based on CFD simulation data, and the applicability of the developed ANN and engineering charts were evaluated.

2. DEVELOPMENT OF CFD MODEL AND NUMERICAL DATABASE CONSTRUCTION

2.1. Development of CFD model

A CFD model was developed using a commercial 3D FE analysis program, COMSOL Multiphysics. In this numerical model, the heat transfer in the medium by convection and conduction can be accurately simulated (Park et al., 2016, Park et al., 2018). The overview of entire geometry and mesh configuration of the model are shown in Figure. 1. The number of meshes is set to about 80,000 to improve the accuracy of the model, and the 3-D tetrahedral element is used for consisting the geometry. The size of floor and wall concrete slabs working as an energy slab is 5 m X 5 m. The internal space of the concrete slab was modeled with air, and the external surface was surrounded by the underground formation. The thermal properties of each component input into the CFD model are shown in Table 1.

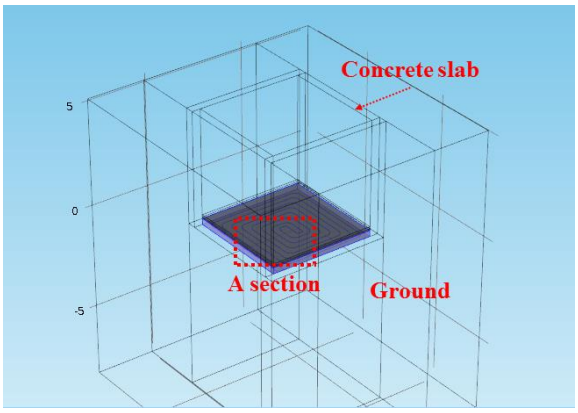

(a) Entire geometry of CFD model

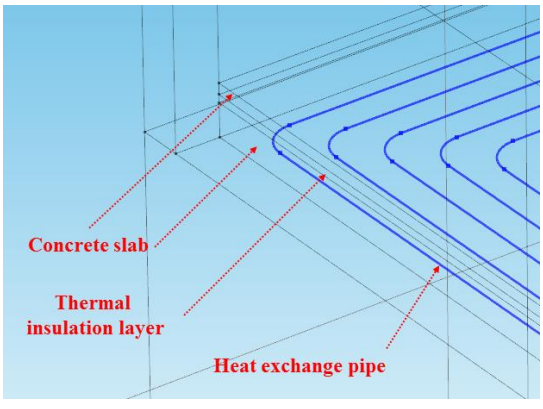

(b) A section

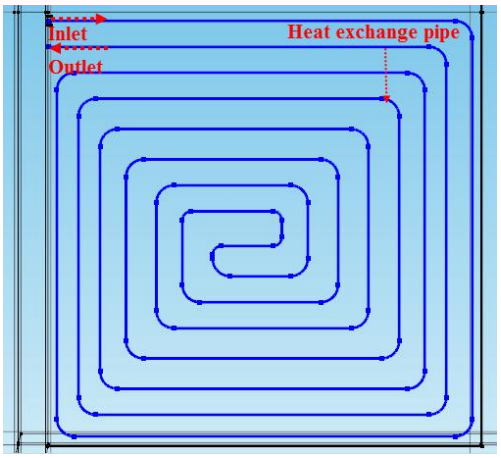

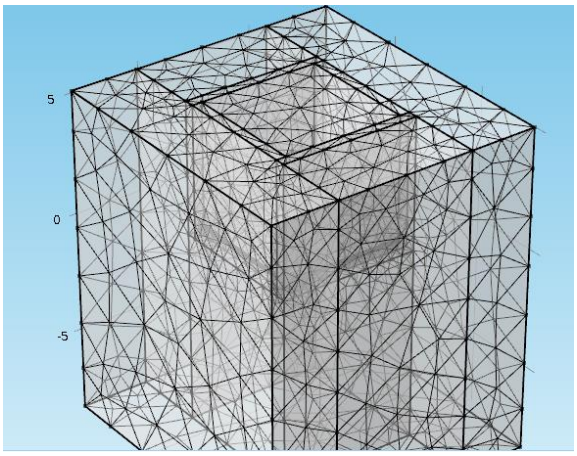

(c) Heat exchange pipe configuration *(d) Mesh configuration*

Figure 1: Overview of developed CFD model

Table 1: Thermal properties of CFD model

Type	Ground formation	Concrete slab	Heat exchange pipe (High-density polyethylene)	Working fluid
Density (kg/m^3)	1,820	3,640	950	998.2
Specific heat capacity (J/kgK)	1,480	840	2,302	4,182
Thermal conductivity (W/mK)	1.3	2.05	0.4	0.6
Viscosity (kg/ms)	-	-	-	0.001

Table 2 shows the applied operation condition of the CFD model. The initial temperatures of ground formation and concrete slabs are assumed to be constant temperature because the structure is installed in an underground formation. The intermittent operation of 8 hours operation - 16 hours pause was considered to simulate a typical commercial building. The inlet fluid temperature was kept at 30℃ during operation to simulate the cooling condition. The internal temperature of the concrete slab is assumed to be 24℃. In order to prevent the degradation of the thermal performance of the energy slab due to the interactions between the energy slab and air inside the underground structure, the thermal insulation layer (i.e., Phenol Foam board, k = 0.018 W/mK) is installed in the floor concrete slab of the CFD model.

Table 2: Operation condition of CFD model

Type	Condition
Operation type	Activating 8 hours–Deactivating 16 hours (intermittent operation)
Flow rate	11.35 liter/min
Inlet temperature	30 ℃ (cooling operation)
Initial temperature of surrounding medium	15 ℃
Internal temperature of concrete slab (underground space)	24 ℃
Thermal conductivity of thermal insulation layer	0.018 W/mK (PF board)

2.2. Construction of database on thermal performance

In this section, the key influential parameters that affect the thermal performance of energy slabs were selected. First, the thermal conductivity of concrete slab and ground formation was considered. As the thermal conductivity of surrounding medium increases, the thermal performance of GHEXs increase (Lee et al., 2010, Park et al., 2011, Kim et al., 2017, Park et al., 2016, Chen et al., 2018). Second, the flow rate of a working fluid is regarded as a significant influential parameter on the thermal performance according to the previous studies (Park, 2016, Misra et al., 2013, Carotenuto et al., 2017). Third, the initial temperature of surrounding medium was considered. The temperature difference between the surrounding medium and inlet fluid shows a linear relation with the thermal performance (Park et al., 2018). As the temperature difference increases, the thermal performance of GHEXs increases. Thus, various temperatures were applied to surrounding medium in the course of simulation while the temperature of Inlet fluid was maintained at 30 ℃. As mentioned in section 2.1, the thermal insulation layer was

installed in the energy slabs to relieve thermal interaction between the energy slab and air inside the underground structure. If the thermal conductivity of thermal insulation material is not low enough to prevent the thermal interaction, the thermal performance of energy slabs would be weakened. Therefore, the thermal conductivity of thermal insulation layer also has to be considered as a key influential parameter. Finally, an interval between each heat exchange pipe also affects the thermal performance due to the existence of thermal interference. As the total pipe length installed in an energy slab increases, the heat exchange amount can also increase while the efficiency and long-term performance significantly decrease. As a result, the total simulation cases were chosen as shown in Table 3. Figures 2 - 7 show engineering charts of energy slabs for design with consideration of the key influential parameters, and comparative evaluations were summarized in Table 4.

*Table 3: Total simulation cases (**Bold**: base condition)*

Type	Applied value				
Thermal conductivity of concrete slab (W/mK)	1.75	1.90	**2.05**	2.30	2.45
Thermal conductivity of ground formation (W/mK)	1.1	1.2	**1.3**	1.4	1.5
Flow rate of working fluid (liter/min)	7.57	9.46	**11.36**	13.25	
Initial temperature of surrounding medium (℃)	13	14	**15**	16	
Thermal conductivity of thermal insulation material (W/mK)	**0.018**	0.05	0.1	0.3	0.5	2.05
Interval of heat exchange pipe (length) (cm)	**30 (76.66 m)**	40 (59.11 m)	50 (49.32 m)	60 (41.47 m)	

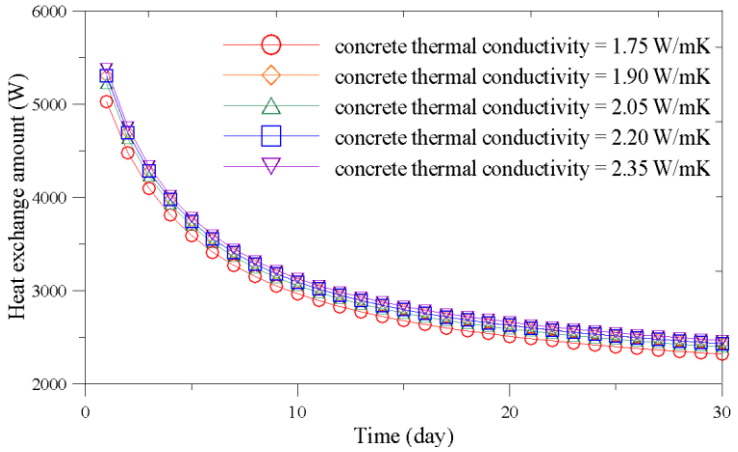

Figure 2: Heat exchange amount according to thermal conductivity of concrete slab

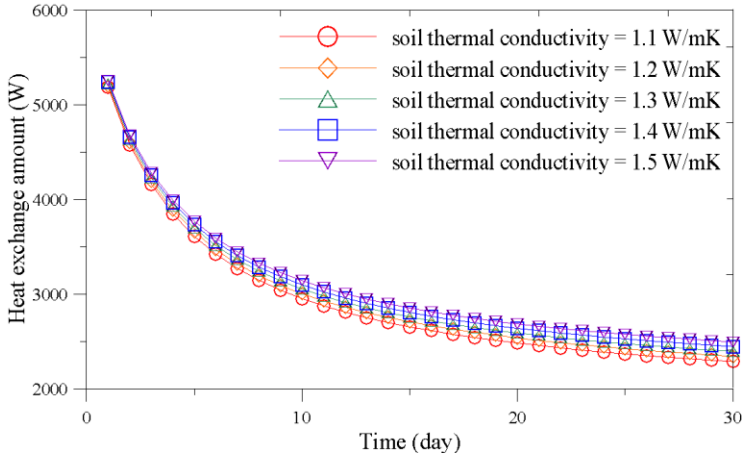

Figure 3: Heat exchange amount according to thermal conductivity of ground formation

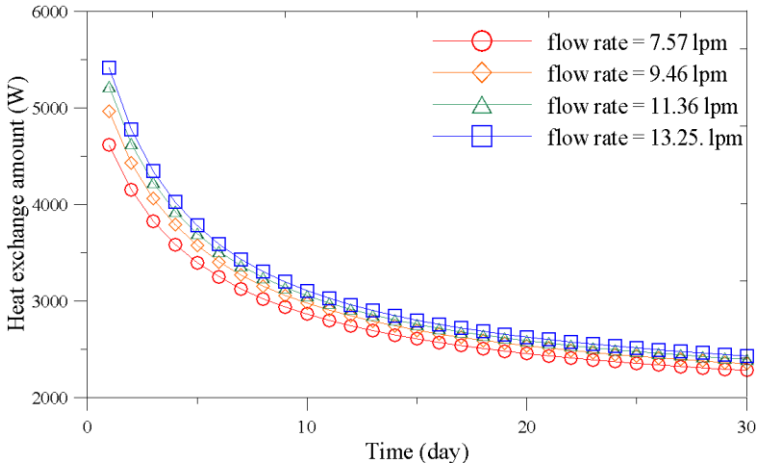

Figure 4: Heat exchange amount according to flow rate of working fluid

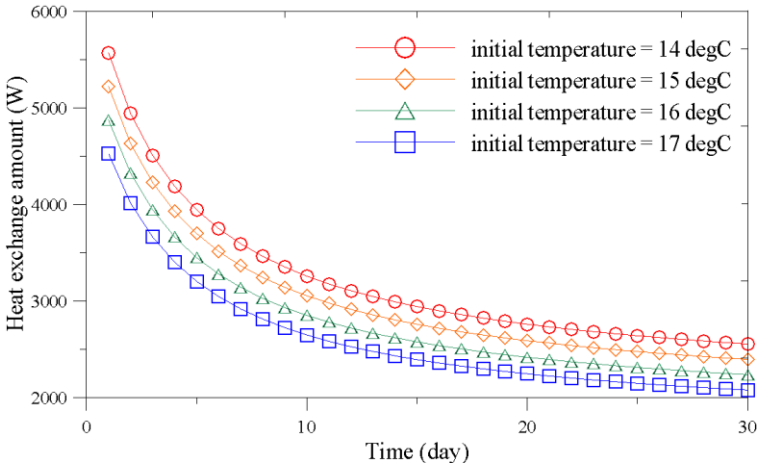

Figure 5: Heat exchange amount according to initial temperature of surrounding medium

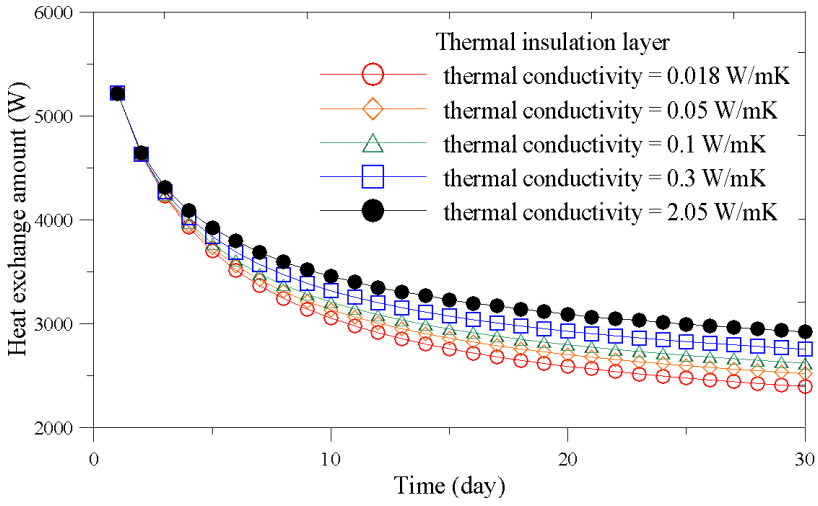

Figure 6: Heat exchange amount according to thermal conductivity of thermal insulation layer

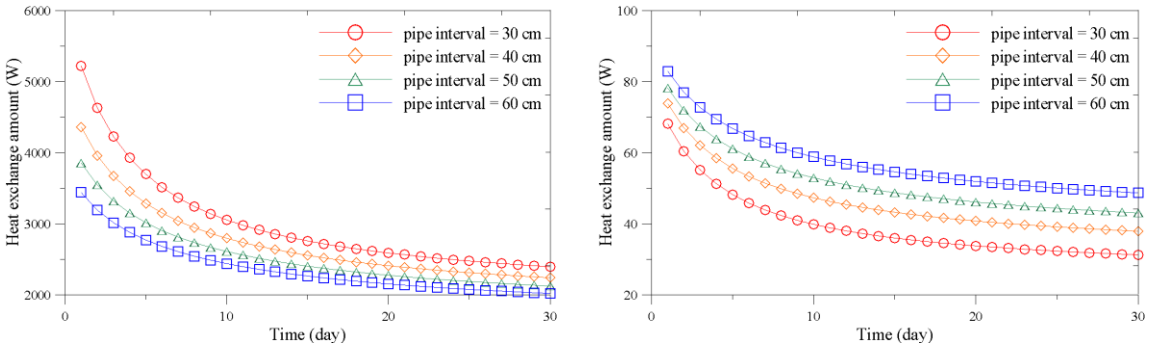

(a) Heat exchange amount of energy slabs *(b) Heat exchange amount per unit pipe length*

Figure 7: Heat exchange amount according to interval of heat exchange pipe

Table 4: Thermal performance of energy slab according to various key influential parameters

Key influential parameter	Conclusion
Thermal conductivity of concrete slab	No significant effect on thermal performance of energy slab
Thermal conductivity of ground formation	As the thermal conductivity of ground formation increases, the thermal performance of energy slab increases.
Flow rate of working fluid	As the flow rate of a working fluid increases, the thermal performance of energy slab increases (non-linear relationship).
Initial temperature of surrounding medium	As the initial temperature of surrounding medium increases, the thermal performance of energy slab decreases
Thermal conductivity of thermal insulation material	As the thermal conductivity of thermal insulation material decreases, the thermal performance of energy slab decreases.
Interval of heat exchange pipe (length)	As the heat exchange pipe interval decreases, the thermal performance of energy slab increase (non-linear relationship).

3. DESIGN METHOD FOR ENERGY SLAB

3.1. Engineering charts for energy slab design

In the previous section, the engineering charts were developed with consideration of various key influential parameters. Total 28 cases of CFD simulations were conducted for the energy slabs. These charts can be used to preliminarily predict the thermal performance of energy slabs without performing time-consuming CFD simulations. For example, If the initial temperature of surrounding medium is 14.5 ℃, the designer can predict the thermal performance of energy slabs after one month as 2500 W (see Figure 8).

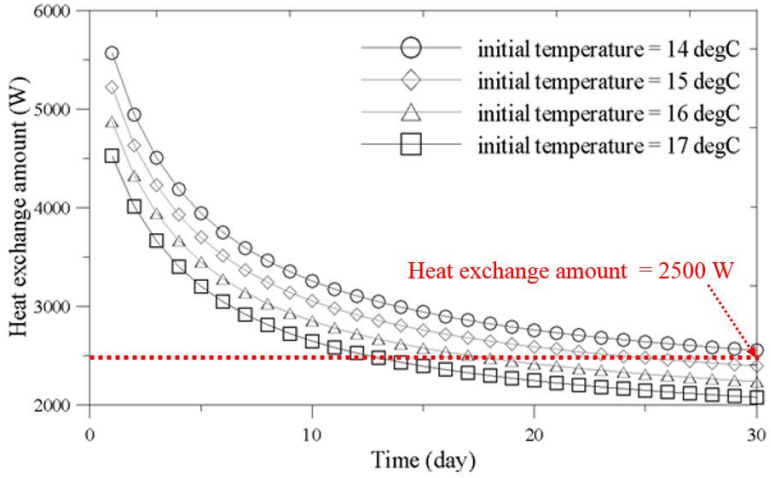

Figure 8: Predicting heat exchange amount of energy slab from engineering charts (example)

In the previous study (Park et al., 2018), engineering charts were constructed with three key influential parameters (i.e., thermal conductivity of ground formation, flow rate of a working fluid, temperature difference between the inlet fluid and surrounding medium), which are considered as the most significant factors in the thermal performance of energy piles. A total of 81 charts was constructed to allow the designer to effectively predict the thermal performance of energy piles. On the other hand, energy slabs are associated with more influential parameters on the thermal performance because of a diversity of pipe configurations and existence of the thermal insulation layer. This demends a great many cases of engineering charts for designing energy slabs, which makes the designers challenging to predict the thermal performance of energy slabs by the conventional method. Consequently, a new effective approach is proposed in this paper to predict the thermal performance of energy slabs.

3.2. Development of design method using ANN

The Artificial Neuron Network (ANN) is an information processing model, which consists of several neurons. In this model, in the course of data training, the neurons learn the relationship between output and input data. Figure 9 shows a schematic of ANN. In the training section, various learning algorithms are adopted, such as Levenberg-Marquardt (LM), Bayesian Regularization (BR), Scaled Conjugate Gradient (SCG), etc. Each learning algorithm possesses unique properties, and the optimal learning algorithm differs according to the characteristics of training data. Additionally, the ANN has a hidden layer, which can extract and store the information of data set. If the number of neurons in the hidden layer is too small to get sufficient information, the accuracy of the ANN model may be signficantly reduced. On the contrary, too many neurons in the hidden layer may lead to getting irregular information and additional learning time. Consequently, it is necessary to define the acceptable learning algorithm and the optimum number of neurons in the hidden layer. In this paper, the LM and BR algorithm were compared to each other according to the number of neurons in the hidden layer. A total of 89 datasets (63 for the training section, 13 for the validation section and 13 for the testing section) was used in the ANN model. Figure 10 shows the ANN model for predicting the outlet temperature that should be used to calculate the heat exchange amount of energy slabs (Equation 1).

Equation 1: Calculating heat exchange amount of energy slabs using outlet temperature $Q = C\,\dot{m}\,\Delta T = C\,\dot{m}\,(T_{in} - T_{out})$

Where:

Q = Heat exchange amount of energy slab (W)

$\dot{m}$ = Flow rate of working fluid (liter/min)

C = specific heat of circulating fluid (J/kgK)

ΔT= temperature difference (℃)

T_{in} = Inlet temperature (℃)

T_{out} = Outlet temperature (℃)

As a result, the BR algorithm with 8 neurons in the hidden layer has the lowest Mean Square Error (MSE) of 0.00142 corresponding to R of 0.997673 (referred to Table 5).

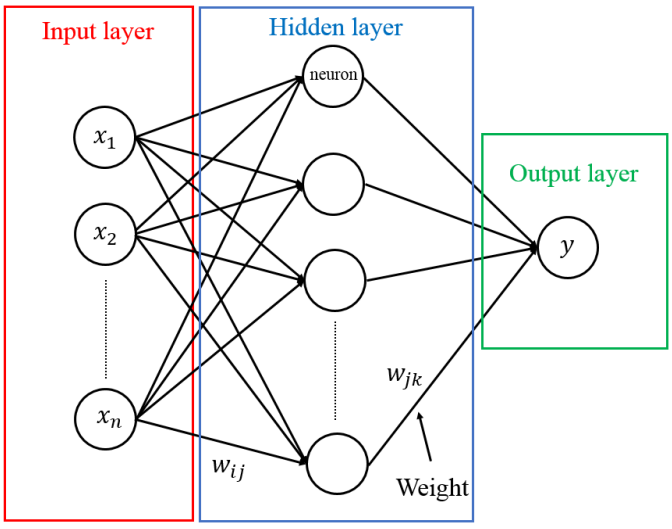

Figure 9: Schematics of ANN structure

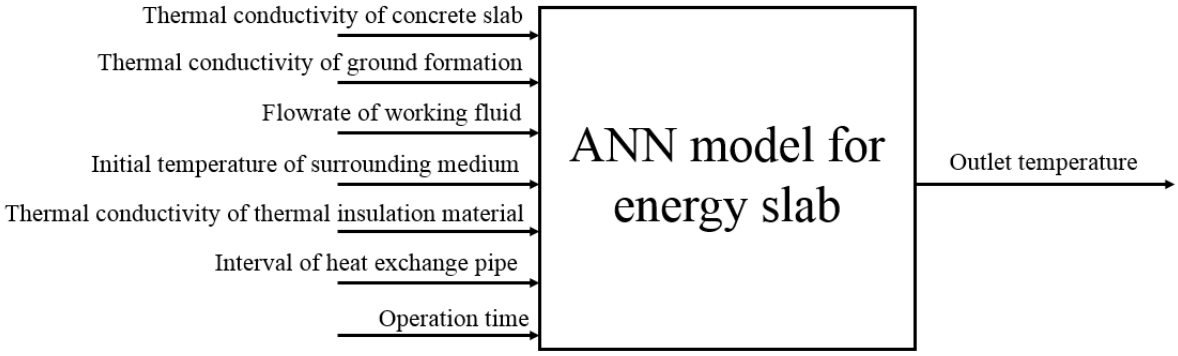

Figure 10: ANN model used for designing energy slabs

Table 5: MSE and R according to the number of neurons in hidden layer

Levenberg-Marquardt algorithm			*Bayesian Regularization*		
The number of neurons	MSE	R	The number of neurons	MSE	R
1	0.02906	0.97720	1	0.025694	0.969834
2	0.02211	0.97591	2	0.031009	0.985444
3	0.01382	0.98799	3	0.003295	0.99734
4	0.01096	0.98480	4	0.007478	0.993684
5	0.01588	0.98700	5	0.004626	0.994469
6	0.01072	0.99004	6	0.006116	0.99418
7	**0.00741**	**0.99097**	7	0.011153	0.981538
8	0.01004	0.98793	**8**	**0.00142**	**0.997673**
9	0.01755	0.98792	9	0.003609	0.997268
10	0.01442	0.98625	10	0.001512	0.998285

To verify the proposed ANN model, the outlet temperature of energy slabs was evaluated with the randomly selected input data between the maximum and minimum input value. Then, the result was compared with the result of CFD numerical analysis that was simulated by applying the same input data in the model. As shown in Table 6, the trained ANN has a good agreement with the numerical simulation in the CFD model. Consequently, the ANN model allows the designers to effectively estimate the thermal performance of energy slabs without time-consuming numerical simulation.

Table 6: Verification of proposed ANN model

Case	Thermal conductivity of concrete slab (W/mK)	Thermal conductivity of ground formation (W/mK)	Flow rate of working fluid (liter/min)	Initial temperature of surrounding medium (℃)	Thermal conductivity of thermal insulation material (W/mK)	Interval of heat exchange pipe (cm)	MSE
1	2.00	1.35	10	15.5	0.018	30	0.53
2	1.80	1.23	8	15.2	0.018	30	0.61

4. CONCLUSION

In this study, a comprehensive design method for energy slabs was discussed. A CFD numerical model was developed to construct a family of engineering charts. Then, a ANN model was trained using the database obtained from a series of CFD simulation. Finally, the ANN model was verified with the developed CFD model. Some important findings are summarized as follows:

1) The thermal conductivity of ground formation, concrete slab and thermal insulation layer, the flowrate of working fluid, the Initial temperature of surrounding medium and the Interval of heat exchange pipe were selected as the key influential parameters on the thermal performance of energy slabs. Among the parameters, the thermal conductivity of concrete slab has the least effect on the thermal performance of energy slabs.
2) In case of the energy slab, the numerous crucial parameters influence the thermal performance of energy slabs compared to the energy piles discussed in the preceding studies. Application of engineering charts

should be limited in designing energy slabs because it is impractical to develop a set of engineering charts to cover the entire variation of the influential parameters.

3) The ANN model was trained using the data selected from the engineering charts. The BR algorithm with 8 hidden layer neuron was found to be an optimum set of the ANN model. Then, the predicted values from the ANN model and the CFD model with randomly selected inputs were compared for verification of the developed ANN model. Consequently, the developed ANN model shows a good agreement with the CFD numerical analysis. This result indicates that the designers can predict the thermal performance of energy slabs accurately with the aid of the developed ANN model without time-consuming and recursive numerical simulations.

5. ACKNOWLEDGEMENT

This research was supported by National Research Foundation of Korea Government (NRF-2014R1A2A2A01007883) and by Korea institute of Energy Technology Evaluation and Planning (KETEP), Ministry of Knowledge Economy (No. 20153030111110).

6. REFERENCES

Brandl, H, 2006. Energy foundations and other thermo-active ground structures**.**56(2), 81-122

Boënnec, O, 2008.Shallow ground energy systems. *Proceedings of the Institution of Civil Engineers-Energy***,** 161(2), 57-61

Carotenuto et al., 2017. Energy piles for ground source heat pump applications: Comparison of heat transfer performance for different design and operating parameters. Applied Thermal Engineering, 124, 1492-1504.

Chen et al., 2018. Efficiency analysis of utilizing phase change materials as grout for a vertical U-tube heat exchanger coupled ground source heat pump system. Applied Thermal Engineering, 130, 698-709.

Choi, 2012. Heating and cooling performance of a ground coupled heat pump system with energy-slab, Korean Journal of Air-Conditioning and Refrigeration Engineering, 24, 196-203

Choi and Sohn, 2012. Performance analysis of energy-slab ground-coupled heat exchanger, Korean Journal of Air-Conditioning and Refrigeration Engineering, 24, 487-496.

De Moel et al., 2010. Technological advances and applications of geothermal energy pile foundations and their feasibility in Australia.*Renewable and Sustainable Energy Reviews*, 14(9), 2683-2696

Esen and Mustafa, 2010. ANN and ANFIS models for performance evaluation of a vertical ground source heat pump system, Expert Systems with Applications, 37(12), 8134-8147.

Kim et al., 2017. Experimental and numerical investigation of thermal properties of cement-based grouts used for vertical ground heat exchanger, Renewable Energy, 112, 260-267.

Lee et al., 2010. Characteristics of thermally-enhanced bentonite grouts for geothermal heat exchanger in South Korea, Science in China Series E: Technological Sciences, 53(1), 123-128.

Lee et al., 2012. Evaluation of thermal performance of energy textile installed in Tunnel, *Renewable Energy*, 42, 11-22.

Makasis et al., 2018. A machine learning approach to energy pile design, Computers and Geotechnics, 97, 189-203.

Misra et al., 2013. CFD analysis based parametric study of derating factor for Earth Air Tunnel Heat Exchanger, Applied Energy, 103, 266-277.

Morino and Oka, 1994. Study on heat exchanged in soil by circulating water in a steel pile, Energy and Buildings, 21, 65-78

Park et al., 2011. Applicability of cement-based grout for ground heat exchanger considering heating-cooling cycles. Science China Technological Sciences, 54(7), 1661-1667.

Park et al., 2016. Effect of borehole material on analytical solutions of the heat transfer model of ground heat exchangers considering groundwater flow. Energies, 9(5), 318.

Park et al., 2018. Engineering chart for thermal performance of cast-in-place energy pile considering thermal resistance, Applied Thermal Engineering, 130, 899-921.

Sun et al., 2015. Case study of performance evaluation of ground source heat pump system based on ANN and ANFIS models, Applied Thermal Engineering, 87, 586-594.

274: Prediction of thermal performance of evacuated tube solar water heater based on deep belief network

Shanting DING[1,2], Qixiao HU[1], Menglan GONG[1], Shurong WEN[3]

[1] School of Mechanical Engineering, Hubei University of Technology, Wuhan, China, Dingst@hbut.edu.cn
[2] Hubei Key Laboratory of Modern Manufacturing Quantity Engineering, Wuhan, China
[3] National Solar Heater water Supervision Inspection Centre of Product Quality, Wuhan, China

As the largest country of solar water heater producer and installation, China has leading position in solar heat utilization in the world. The thermal performance of solar water heater is obtained by heat collection tests and heat loss tests. Because of low solar energy density, random meteorological conditions, and intermittent season nature, the strict test conditions is required in performance assessment. Limited by these conditions, the solar water heaters inspection efficiency is low.

To improve the efficiency, a prediction model based on deep belief neural network (DBN) is presented. Based on the evacuated tube heat transfer theory, the key parameters were determined. According to different daily tests, include the local solar irradiance(G), ambient air temperature(t_a) and cold water temperature(t_b), the measured data(ΔT) obtained under standard or non-standard test conditions. Two-thirds of the data were put in the trained neural network. The rest were put in the tested neural network. The predicted result is close to measured data. It concluded that the DBN can accurately predict the thermal performance of solar water heater by hourly measured data which obtained under standard test conditions or fall short of the standard conditions. Compared to the genetic algorithm and back propagation (GA-BP) model, DBN model is superior in performance predication.

Keywords: deep belief; neural network; prediction model; evacuated tube solar water heater

1. INTRODUCTION

Utilization of clean and renewable energy, the solar water heaters has entered in millions Chinese families. In the 13th Five-Year plan for solar energy development of China, the solar collectors will increase to 800 million m^2.To guarantee high-quality solar water heater product serve people, evaluation of solar heat energy efficiency is necessary for market access.

Obtained from thermal performance testing, the daily useful solar heat energy q17 is the key parameter in solar energy efficiency evaluation. The higher the q17 value, the better the performance of heater collector. GB18706 defines test methods for thermal performance of domestic solar water heating systems. Usually, the thermal performance testing is carried out in the outdoor. According to specific requirements of national standards, testing need procedure 8 hours a day for four days, and the hemispherical solar irradiance at the collector plane shall be higher than 17MJ/m^2. Test condition also include ambient temperature range at 8~39℃ , surrounding air speed lower than 4m/s, cold water temperature set as 20℃,and so on. Affected by the changes of season climate and different geographical of regions, solar energy distribution is unbalanced. The diurnal irradiation changes with time. For the same heater, it would gain different daily solar heat energy value q with different outdoor test condition. Conversion through empirical formulas, the daily useful solar heat energy q17 indicates the performance of solar energy conversion efficiency in standard test conditions. But some test reports show that the results are inconsistent which calculated with different solar irradiance in sunny day or cloudy day.

Many studies show that the evaluation of solar heat energy efficiency is affected by solar irradiance, ambient temperature and surrounding air flow in outdoor thermal performance testing. Wei Feng et al. proved the solar irradiance variation is main factor which result q17 inconsistent (2006). Huang Zhulian et al. studied the influence of environment temperature on useful daily heat gain test of solar water heater. The 10℃ difference of ambient temperature result the useful daily heat value change in ±0.10MJ/m^2, and 20℃ difference result change in ±0.15MJ/m^2 (2011). Yin Zhiqiang et al. proved lower ambient temperature would reduced the energy efficiency grade though lots of tests (2012). Tian Yulan et al. studied on daily solar radiation effect of the thermal performance testing in Nanjin. 86 days of solar radiation monitoring showed that 28% of all days can meet the testing standard. 27 days of solar water heating performance testing according to different daily solar radiations were conducted. The temperature rise in water tank showed positive linear relationship with the daily solar radiation except the daily radiation is high (2015).

In order to improve the efficiency of testing, computer simulation was carried out. The model may be used with hourly values of local solar irradiance, ambient temperature and cold water temperature data to predict annual system performance. However, it is a proprietary product and cannot be modified by the user. Some scholars use neural network technology to predict the performance. Mei Rong built the temperature changing models of solar collector with BP neural networks. Within tests condition it may predict the temperature changing accurately (2012). Li Manfeng et al. built GA-BP neural network model for simulation calculation. The simulation result shows that the GA-BP is more accurately than the mathematical model and BP model (2012). At present, most simulation model is built to predict the change of collector temperature.

As an important theory of machine learning, deep learning has successfully applied to the fields of speech recognition, image recognition and text processing. It can be also used as a discriminate model to predict energy efficiency grade. The prediction would be intelligent and high accuracy. In this paper, the temperature rise changing model based on deep belief neural network is built. It would predict the daily useful solar heat energy q17 by hourly solar irradiance, ambient temperature in a variety of environmental conditions.

2. THE ESTABLISHMENT OF NEURAL NETWORK MODEL

2.1. Physical model of solar water heater

The structure of the solar water heater is shown in Figure 1. The evacuated tube heater collector absorb solar irradiance and convert solar energy into heat energy. The water flow in evacuated tube, and circulated into storage tank with heat siphon phenomenon. After enough natural circulating, water temperature reached stable and consistent.

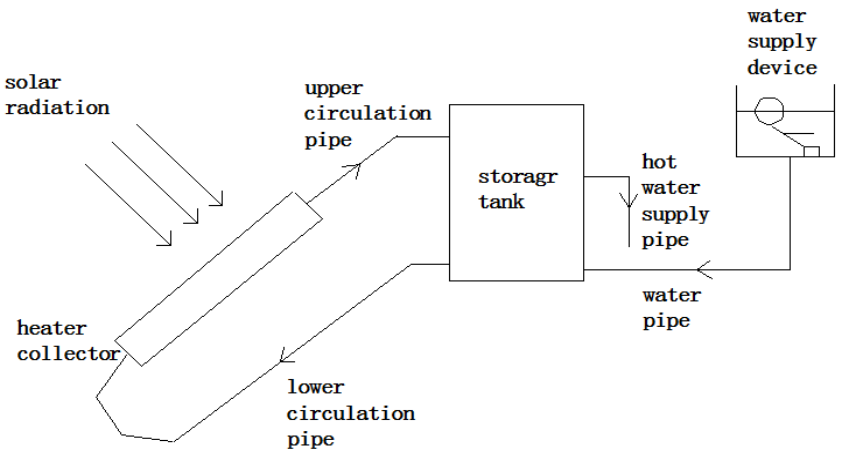

Figure1: Solar water heater structure

According to the energy conservation law, the solar water heater energy is decided on two fronts: the energy of solar irradiance conservation with evacuated tube collector and the loss energy of system by the surrounding environment. Determination of changes in water temperature using average measurements from three sensors in storage tank. In the process of heat collection, the relationship between the change in temperature rise and solar energy conversion and system heat loss is shown as:

Equation 1: the change in temperature rise

$$(mC_p)_s \frac{d\Delta T}{d\tau} = F' A_c G(\tau\alpha)_e - [F' U_L A_c + (UA)_s][\Delta T - (t_a - t_b)]$$

Where:

$(mC_p)_s$= heat capacity of water in storage tank (J/℃)
ΔT= temperature difference between the hot and the cold fluid (K)
$(\tau\alpha)_e$=effective transmittance-absorbance of evacuated tube collector
U_L= heat loss from the collector
$(UA)_s$= heat loss from water in storage tank

GB18706 gave the empirical formulas to calculate the daily useful heat q17 as an indicator for evaluating the thermal performance of water heaters. The relation between q17 and ΔT_{17} is shown as:

Equation 2: the relation between q17 and ΔT_{17}

$$q_{17} = \frac{mc_{pw}\Delta T_{17}}{10^6 A_c}$$

2.2. The temperature rise prediction model based on deep belief network

According to the solar irradiance varies with time, and the indeterminacy of environment condition, it is difficult to detect the useful temperature rise ΔT_{17} accurately. Using the real-time temperature rise detection data and past records, a neural network model is established to predict the useful temperature rise ΔT_{17} . That is :

Equation 3: ΔT_{17}predict in ANN

$$\Delta T_{17} = f(H, v_a, t_a - t_b)|_{H=17, v_a=0, t_a=20}$$

Deep belief network (DBN) is a deep learning generation model with multiple hidden layers, which is constructed by the Restricted Boltzmann Machines (RBM) stack and Back Propagation (BP) network. The learning process can be divided into two stages: one is to train the RBM stack forward by layer and layer, and the other is to use BP algorithm to optimise the inverse parameters. The DBN learning sketch map is shown in Figure 2.

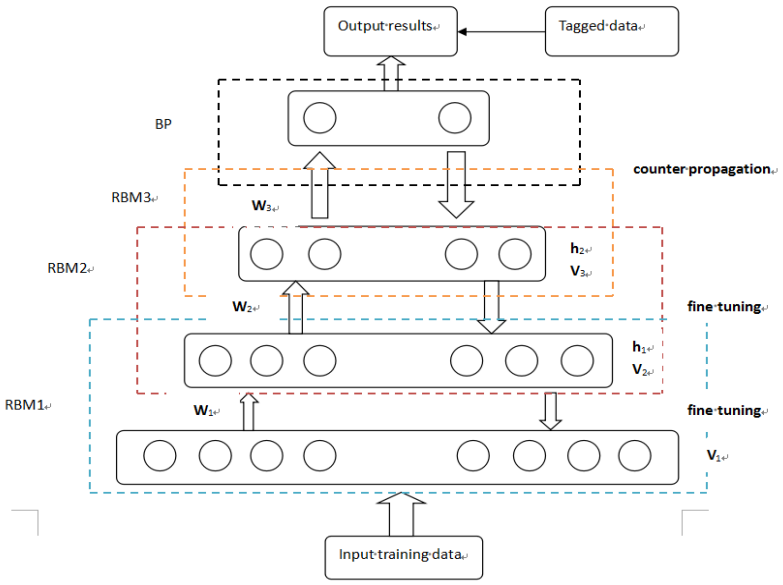

Figure 2: DBN diagrammatic sketch

RBM is a probabilistic undirected graph model, which consists of visual layer V and hidden layer H. W_{ij} is the weight between the *j* visual layer V_j and the *i* hidden layer H_i. Coefficient a_j and b_i are deviations from the visible layer V_j and the hidden layer H_i respectively. The parameters are estimated by the contrast dispersion (CD) algorithm of maximum likelihood estimation. During the training phase, the greedy algorithm is used to train the RBM stack. The output of the upper layer (W_{ij}, a_j, b_i) is the input of the next layer, and the top output is the input of the neural network in the tuning phase. The tuning phase is supervised learning，the learning parameters of each layer fine-tune from top to bottom with the gradient descent algorithm. With the learning parameters of each layer and the learning label, the BP neural network optimise the parameters of trained RBM .The number of network layers in the BP is equal to the RBM stack. The overall depth of DBN depends on the number of RBM stack layers. It is very important to determine the appropriate stack of RBM network layers.

In order to automatically select the depth of the network, the reconstruction error is trained in each RBM layer. For a single RBM, after one iteration, the reconstruction error will be generated between the input visible layer V and the reconstructed visible layer V', which is as follows:

Equation 4: the reconstruction error

$$err = \frac{\sum_{j=1}^{\beta}\sum_{i=1}^{\alpha}(p_{ij} - x_{ij})}{\alpha\beta}$$

Where:

α = single- layer RBM input node number
β = the number of input characteristics
p_{ij}=reconstruction value after single RBM training
x_{ij}= single RBM tag value

If the reconfiguration error difference is greater than the setting ε, the number of layer should be added one, the current stack RBM structure is added up. Otherwise the number should stop add. That is:

Equation 5: the number of layer

$$\begin{cases} L = N_{RBM}, & 0 \le err(k-1) - err(k) \le \varepsilon \\ L = N_{RBM} + 1, & err(k-1) - err(k) > \varepsilon \end{cases}$$

Where:

L = the depth of stacked RBM in DBN
N_{RBM} is the layer of the current stacked RBM
err (k) ,err (k-1)= the reconfiguration error of the current layer and the previous layer
ε = preset value

The setting ε is the key to the accuracy of model. Too large ε would miss the optimal number of network layers, and lead to the large fluctuation of DBN output. By contrast, it would lead to too many layers of DBN and great accumulative error. According to the prediction solar heater model and the performance testing condition, the range of ε is [0.05,0.1]. In this paper it is given as ε=0.07.

3. DATA PROCESSING AND MODEL ANALYSIS

3.1. Data processing

The data from outdoor thermal performance tests for an evacuated tube solar heater by accredited laboratory, the national solar water heater product quality supervision and Inspection Center (Wuhan). The test device meet the requirement of GB18706. In order to obtain the real-time temperature change, temperature sensors were installed in the storage tank. Consider the temperature stratification in the water tank, three sensors were distributed in the upper, middle and lower level. The average of three sensor represent the water temperature. It recorded the temperature data every five minutes. The tests carried out in accordance with the procedure with the same water heater for 8 hours a day for five days. According to the influence of different weather, solar irradiance G is record by times, shown in Figure 3. The 96 samples in standard condition testing were selected as training samples, 24 groups were used as test samples. Before constructing the neural network model, the sample data need to normalization and anti normalization.

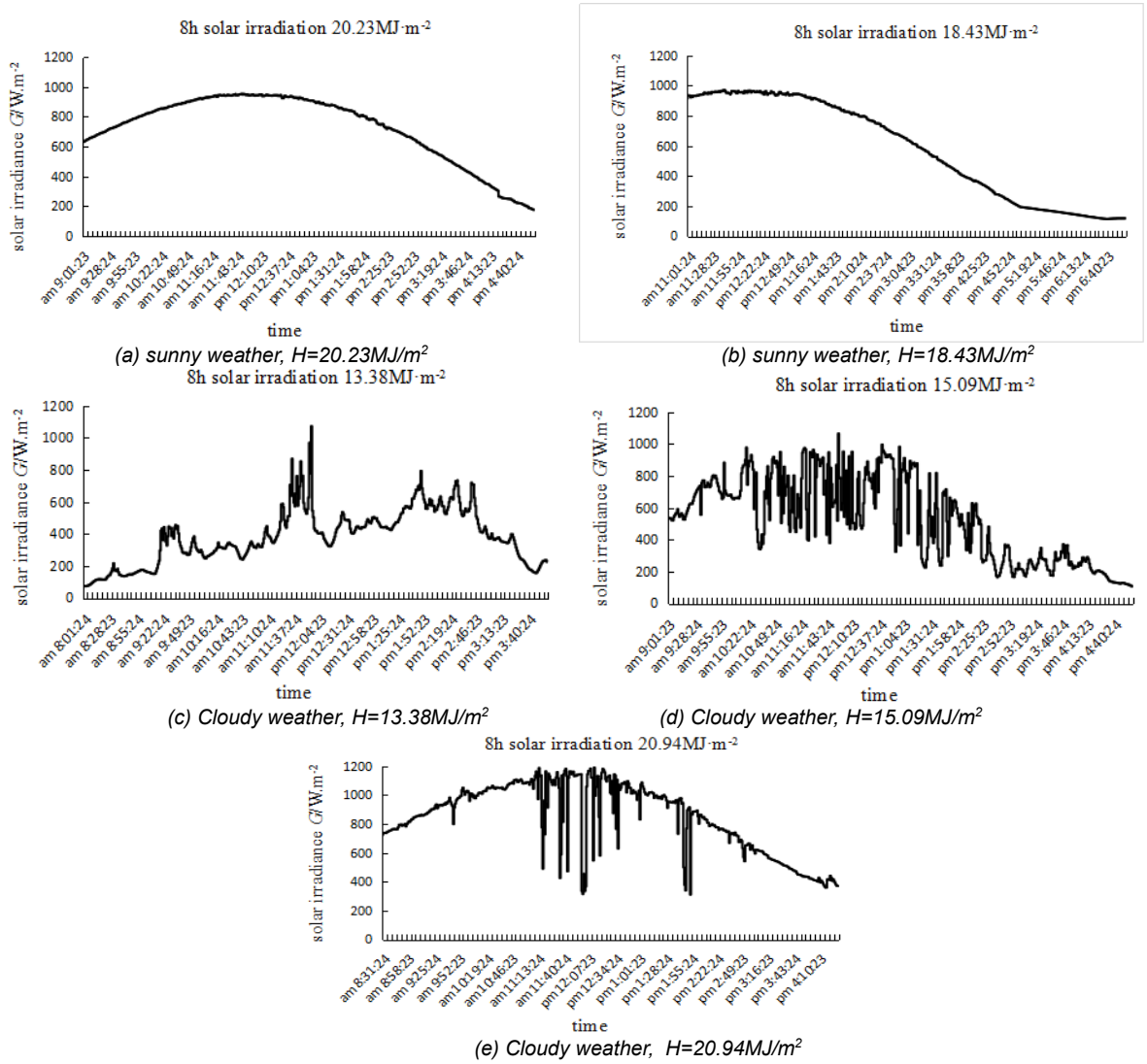

(a) sunny weather, H=20.23MJ/m²

(b) sunny weather, H=18.43MJ/m²

(c) Cloudy weather, H=13.38MJ/m²

(d) Cloudy weather, H=15.09MJ/m²

(e) Cloudy weather, H=20.94MJ/m²

Figure 3: Solar irradiance G changed with time in the time of heat collection test

3.2. The temperature rise model of DBN

According to the DBN program, it established a temperature model to predict useful temperature rise ΔT_{17}. Training in 96 group data, it is 3 stacked RBM generated by the network. Then a greedy algorithm was conducted to obtain

hidden variables. The 3-5-4-1 structure was better prediction stability in 4 layers network depth of DBN. Table 1 presents the comparison of different network depth.

Table 1: Comparison of DBN training errors with different network depth

network depth	network structure	Reconstruction error	prediction error	error variance
3	3-5-1	0.26	0.44	0.08
4	3-5-4-1	0.21	0.34	0.04
5	3-5-4-3-1	0.08	0.38	0.05

Compare with the GA-BP which is an shallow neural network with advantages in wide range of applications, short running time, good global solution and other characteristics. The evaluation of GA-BP network prediction result show that the best number of hidden nodes is 5. After training GA-BP and DBN networks separately, two temperature rise prediction models with 24 groups of test samples were evaluated. Table 2 gives the prediction temperature rise of test data and the predictions of two networks.

Table 2: Test data and prediction of temperature rise by GA/BP and DBN networks

24 group test Data			The prediction of temperature rise (℃)	
Daily Solar radiation(MJ/m^2)	Average surrounding air speed (m/s)	label temperature rise(℃)	DBN	GA-BP
0.70	0.59	1.23	1.24	1.90
1.51	0.54	3.20	3.30	3.08
1.72	0.55	5.30	5.63	5.93
2.63	0.58	7.46	7.54	7.06
3.63	0.57	9.64	9.26	9.24
4.69	0.58	11.89	11.29	11.19
5.78	0.58	14.15	14.29	13.97
6.92	0.57	16.42	16.05	15.98
8.11	0.56	18.72	18.12	18.83
9.25	0.56	20.83	20.21	21.35
10.38	0.57	22.94	23.02	22.82
11.51	0.57	24.89	24.40	24.40
12.59	0.57	26.98	26.55	27.92
13.76	0.57	29.05	28.93	28.50
14.90	0.56	31.12	31.30	30.95
16.02	0.56	33.25	33.95	33.90
17.05	0.57	35.00	34.98	34.83
17.96	0.59	36.87	37.02	36.07
18.86	0.58	38.57	38.02	38.67
19.68	0.58	40.25	40.51	40.13
20.41	0.57	40.76	41.20	40.01
20.64	0.57	41.32	41.98	40.26
20.76	0.56	42.00	42.08	42.90
20.94	0.56	44.26	43.96	44.29

Comparison between the expected output and the network forecast outputs in Figure 4. Figure 4(a) shows both DBN and GA-BP temperature rise prediction models are better. As evaluation index of output performance, smaller average and variance of absolute error showed the accuracy of prediction. DBN prediction absolute error average is 0.34, less than GA-BP(0.46). and DBN error variance down to 0.05, less than GA-BP(0.09) . Figure 4(b) gives a comparison of the absolute error.

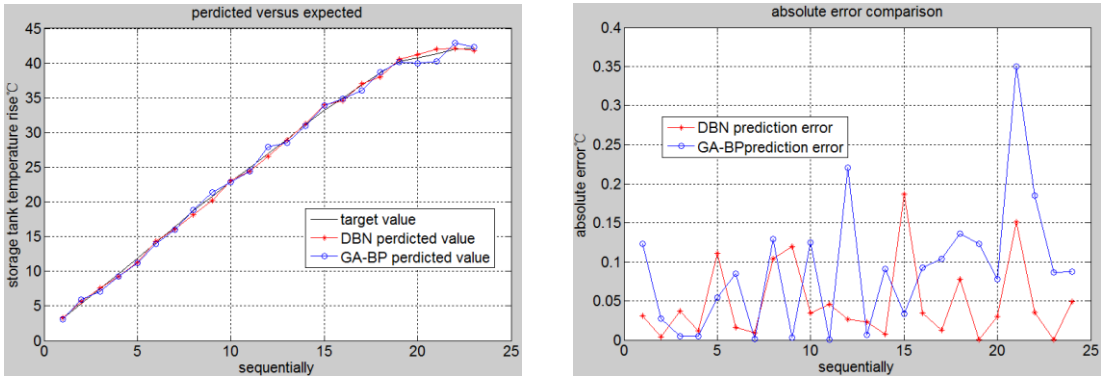

(a) predictions vs expected (b) absolute error

Figure 4: Comparison between the GA-BP and DBN network

3.3. Model verification

The daily solar irradiance G changed time with time. The heat collection test data from different solar irradiance amounts were trained by DBN respectively. The trained model was used to forecast the daily useful temperature rise ΔT_{17}. The daily useful heat q17 is calculated by equation 2. Compare with the calculation of 8h heat collector test value by original conversion equation given by the national standard, as shown in Table 3.

Table 3: Daily useful temperature values and daily useful heat under different day solar irradiance

Daily solar irradiance (MJ/m^2)	Average surrounding air speed (m/s)	calculation of test data		Prediction of DBN	
		Daily temperature rise ΔT_{17} (℃)	Daily useful heat q_{17} (MJ/m^2)	Daily temperature rise ΔT_{17} (℃)	Daily useful heat q_{17} (MJ/m^2)
13.38	0.14	26.17	7.77	35.06	8.20
15.09	0.79	30.42	8.01	35.11	8.21
18.43	0.84	38.6	8.33	34.94	8.17
20.23	0.93	42.43	8.34	34.97	8.18
20.94	0.56	44.26	8.40	35.08	8.20

The daily solar radiation H in test is from 13.38 MJ/m^2 to 20.94 MJ/m^2 in five days. Two days is cloudy which is lower than 16 MJ/m^2 defined by the standard. One day is meet the requirement of 16 MJ/m^2 but the test time less than 8 hours. With the maximum difference of 0.17℃, that the prediction of daily useful temperature rise ΔT_{17} were consistent. The estimated value of daily useful heat energy q17 obtained by two method is shown in Figure 5.

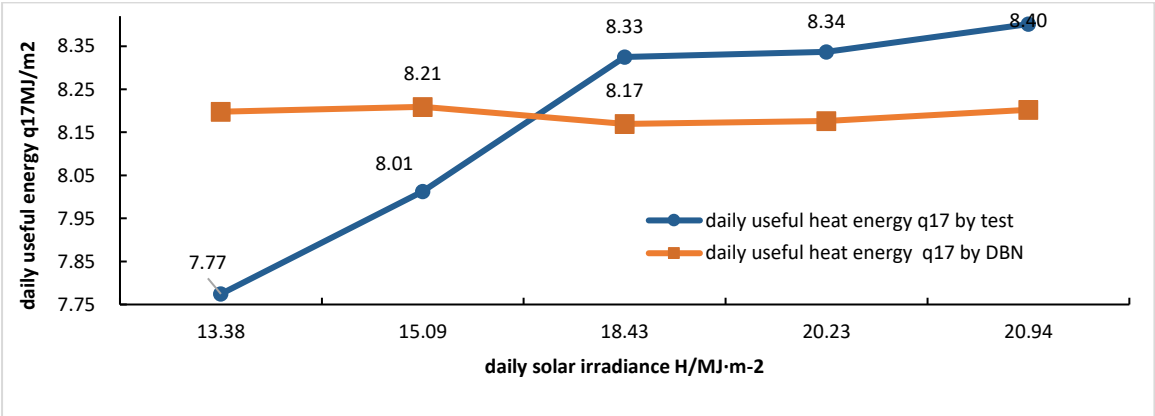

Figure 5: The two method estimates the daily useful energy

Figure 5 shows that whether the value of solar irradiance H is higher or less than 16 MJ/m^2, the q17 prediction by DBN is consistent in q17=8.20, which fluctuation amplitude is not more than 0.04 MJ/m^2. Compared with the results by original equation, the q17 value varies from 7.77 MJ/m^2 to 8.40 MJ/m^2. This shows that the application of the DBN temperature rise prediction method has broken the limitation of environmental conditions.

4. CONCLUSION

Based on the evacuated tube heat transfer theory, a temperature rise prediction model based on deep belief neural network (DBN) is presented. The DBN prediction model is 3-5-4-1 structure and 4 network depth. The solar solar irradiance G , the difference of the average ambient air temperature and the initial water temperature of the water heater (t_a-t_b), the average air rate v_a were the input, the temperature rise ΔT as the label value. After training with test data, the model established. Compared with the GA-BP neural network prediction model, it shows that the DBN network prediction model has higher prediction accuracy and stability. It concluded that the DBN can accurately predict the thermal performance of solar water heater by server hours test data which obtained under standard test conditions or fall short of the standard conditions. The prediction of the temperature rise is also conducive to the development of complementary technology in solar energy and other auxiliary energy.

5. NOMENCLATURE

List of symbols

m	thermally active mass of the collector(kg)	**q**	the daily solar heat energy during period of test (J)
C_{pw}	the specific heat of water (J·/(kg·℃))	**q17**	the daily useful solar heat energy when hemispherical irradiation equal to 17MJ/m^2
A_c	cross sectional area of the tube(m^2)	T_1, T_2	the initial and final average temperatures of the system during measurement period(℃)
G	hemispherical solar irradiance （W/m^2）	ΔT	Temperature difference between the hot and the cold water during measurement period (℃)
H	hemispherical irradiation on the collector plane	ΔT_{17}	Temperature difference between the hot and the cold water when hemispherical irradiation on the collector plane equal to 17MJ/m^2 (℃)
t_a	average ambient temperature during measurement period(℃)	t_{in}, t_{out}	the in-flow and out-flow temperature through the opening of the tube(℃)
t_b	average water temperature in collector at the test begin (℃)	F'	collector efficiency factor

6. REFERENCES

Goodfellow I, Bengio Y, Courville A, 2016. Deep Learning. Massachusetts Institute of Technology.

He Z, 2009. Solar thermal utilization. Beijing: University of Science and Technology of China press, 130-133.

Huang Z, Zhang X, et al, 2011. The influence of ambient temperature on the daily useful heat test of solar water heaters. Architecture Science, S2:136-138.

Lecun Y, Bengio Y, Hinton G, 2015. Deep learning. Nature, 521(7553):43.

Li M, Li S, Fan B, 2012. Simulation study of solar collector based on Genetic Neural Network. Chinese Journal of Electrical Engineering, 32(5):126-130.

Li Z, Gao W, Liu T, et al, 2013.Prediction model of hourly cycle performance of vacuum tube solar water heaters. Renewable energy, 31(12):11-16.

Ma Y, Zhou L, Ma G, 2011. The experimental study on the test conditions for daily useful heat gain. Solar energy, 14: 46-48+51.

Tian Y, Zhu J, Li C, 2014.The research on influence of solar day radiation on thermal performance of solar water heating system. China test, 41(5):107-111.

Wei F, Zhang X, Xing L, 2006.The influence of environmental conditions on the thermal performance of all glass vacuum solar water heating system. Power and energy, 27(2):63-65.

Yin Z, Ma G, et al., 2012. The influence of environment and measurement uncertainty on solar energy water heater energy efficiency grade migration. Solar energy, 18-22.

Zhang Y, Dong H, Zhou E, 2008. Prediction and correction model of thermal performance of heat pipe vacuum tube collector based on BP neural network. Solar energy Journal, 29(6):690-693.

275: Study on the distribution characteristics of stray current in Subway

Xingxing ZHANG[1], Bo FU[2], Manman MAO[3]

[1] Hubei University of Technology, Wuhan, Hubei, 892896549@qq.com
[2] Hubei University of Technology, Wuhan, Hubei, 515412113@qq.com
[3] Hubei University of Technology, Wuhan, Hubei, 904595094@qq.com

As one of the most important transportation for residents, metro has been actively popularized and applied in most major cities in China. Metro often uses DC traction power supply system. The running rail also serves return current. Part of return current in the rail leaks into the soil， which called stray current. With the continuous improvement of metro lines, the disadvantages of stray current have become serious. Based on CDEGS software, this paper builds a metro stray current simulation model, and considers the influence of stray current collection devices such as drain net conductors (DNC)., and the effects of different line conditions and fault types on the distribution of stray current are studied by adjusting the structural parameters. Then, the simulation for multi-locomotive in the power supply interval are established to research the variation of stray current when the running state of each locomotive changes. Simulation results show that the rail longitudinal resistance and insulation layer resistivity have a great impact on the distribution of stray current. The influence of partial insulation layer failure is limited, and only the density of rail leakage current increases locally. When the traction current is constant, the locomotive in the middle of the power supply interval will cause more serious stray current problems. When adjacent locomotives are in an accelerated state in the same interval, the rail potential will increase significantly. The simulation results not only provide a theoretical basis for metro operation and maintenance, but also can guide constructors to take preventive measures in advance in the corresponding location. These measures are very vital for restraining the harmful effects of stray current.

Keywords: metro; stray current; rail longitudinal resistance; insulation layer resistivity

1. INTRODUCTION

As one of the most important means of transportation for residents, the subway has been widely applied in major cities of China. The rapid development of the subway provides a new way for the increasingly serious problem of air pollution control. However, the large-scale and high density operation of the subway brings serious stray current problems (Jian Hua 2016). The stray current is not only harmful to the subway system itself, but also causes huge electrochemical corrosion to the metal equipment along the line and the metal pipeline outside the tunnel. In addition, with the gradual improvement of metro lines, the problem of DC bias caused by stray current to the main transformer of urban power grid is becoming increasingly prominent.

In the present paper, the distribution characteristics of the stray current are analyzed by analytical method. By establishing a multi-layer ground network model, the multiple conductors in the same layer are equivalent to a conductor, and the distribution of stray current in all layers of conductors is analyzed. The analytic method is based on the Kirchhoff's law of current and the law of voltage to establish the structural equation of the stray current network, and the result is derived through the complex formula. This method is to make the conductor with a stereoscopic distribution in the space equivalent to the plane distribution structure in the space the selection of the transition resistance between the layers of each layer usually has errors, and the analytical method is not conducive to analyzing the influence of stray current on each conductor in the ground network system. Based on the CDEGS simulation software, this paper builds a three-dimensional structure simulation model based on the space position of the conductors in the actual tunnel, analyzes the line conditions such as the resistance of the rail, the resistivity of the insulation system ,and the influence caused by operational states of the locomotive position and propulsion current Compared with the analytical method, the results obtained by the above simulation models are more accurate, and the simulation results have important guiding significance for subway maintenance work (Li 2015; Kai 2015).

2. FORMATION MECHANISM AND MODEL ESTABLISHMENT OF STRAY CURRENT.

The subway adopts 750 V or 1500 V DC traction power supply system, and the locomotive withstands the traction current from the contact network, and the rail will do the line track and the reflux rail, and the reflux current will eventually flow to the negative poles of each traction. Due to the internal resistance of the rail, the reflux current forms the voltage difference on the rail, and because the rail and the earth cannot be completely insulated, so some reflux current in the rail will leak into the soil and form a stray current (Zhao 2016). In order to reduce the harm of the stray current to the buried metal around the tunnel, the stray current collection network is usually laid in the cement base under the rail. Most of the stray current will flow back to the negative electrode through the drain net, leaving only a few stray currents flowing into the buried metal, thus greatly reducing the adverse effects of the stray current (see Figure 1) (Pires 2016).

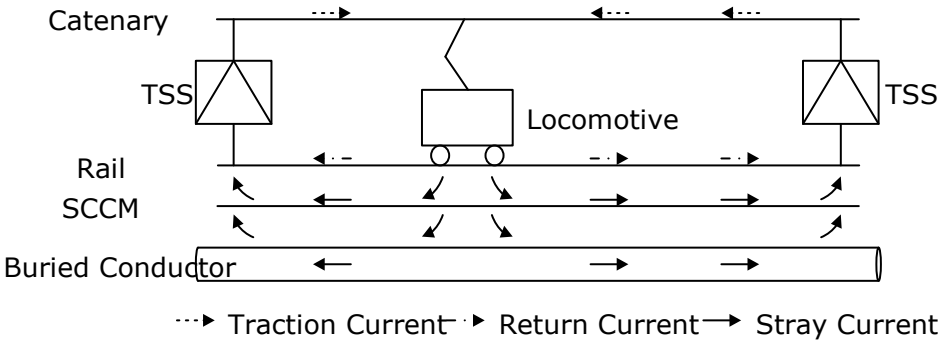

Figure 1: Scheme of a DC traction power system

In this paper, the research model of stray current is established by using the MALZ module of CDEGS software. The spatial structure of the two water soil layer model is used to simulate the concrete structure and soil structure of the tunnel wall, and the analytical method can only simulate the earth structure, and the resistivity of concrete can not be considered. In the model, the locomotive is equivalent to the current source, which stipulates that the current is positive to the right and that the current flows out of the conductor in the positive direction. The rail will be equivalent to a cylindrical conductor, and in order to limit the adverse effects caused by the stray current, the rail and the cement base will be added to the insulation system to increase the transition resistance between the rail and the earth. In China, the resistivity of the insulation system of the new subway line should not be less than 15 ohm km, and the resistivity should not be less than 3 ohm km for the operation line. As the object of this study is the stray current, the insulation fastener and insulation pad model is not set up in this paper, only the influence of the whole insulation system on the distribution of stray current is considered. Cotton (2005) suggests that the insulation system can be equivalent to the insulating layer wrapped around the rail conductor, when the resistivity of the insulation system is 15 Omega. Km, the he resistivity of the insulating layer is 450000 ohms km and the thickness is 10 mm. There are 6 longitudinal steel bars below the rail, and each 50 m uses a transverse conductor

to connect the conductors to form SCCM. The stray current grid model perspective is shown in figure Figure 2 (a), showing the spatial position of each conductor as shown in figure Figure 2 (b). The values of each parameter are shown as shown by Table 1 (Charalambous. 2014; Liu 2017).

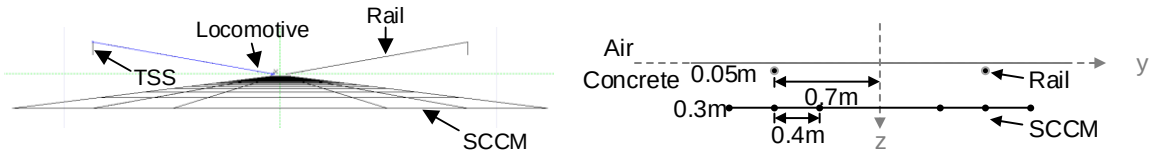

(a) Perspective diagram of the stray current ground network model *(b) Layout map of ground network conductor*

Figure 2: The layout diagram of the stray current ground network model

Table 1: Base Input Data and Assumptions

Parameter	Characteristic	Value
Rail	Resistance	40 m Ω/km
	Radius	0.035 m
	Amount	2 lines
SCCM	Resistance	660 m Ω/km
	Radius	0.008 m
	Amount	6 lines
Insulation mat	Resistivity	450000 Ω.km
	Thickness	10 mm
Spatial structure	Air	1×e^18 Ω.km
	Concrete	2000 Ω.km
	Soil	200 Ω.km

In view of the protection of stray current, a number of design codes have been explained in detail (GB 50157-2013, 2014). In order to protect the safety of passengers and staff, the rail potential should be less than 120 V. When the rail potential is too high, the rail limit device should be put into use immediately. The action threshold is related to the instantaneous value of the rail potential (CJJ 49-92, 1993). In order to prevent the excessive corrosion of the buried metal surrounding the stray current, the mean value of the polarization voltage forward deviation of the discharge network conductor should be less than 0.5 V, and the test time should be less than 30 minutes. When the stray current is serious, the discharge cabinet should be put into use immediately. At this time, the position of SCCM is connected to the negative pole of the traction place, and the action threshold is related to the continuous value of the polarization voltage.

When the stray current is studied by CDEGS, each conductor will be divided into N segments. The length of the conductor section is the calculation step of the software. The more the conductor section is, the more accurate the calculated results are. Reasonable control of the number of segments can effectively improve the computation efficiency and reduce the simulation time. CDEGS can directly read the parameters of each conductor section, including the potential of the conductor section, the longitudinal current and the leakage current. By combining the potential of each conductor section on the same conductor, the potential distribution curve along the conductor can be obtained. The stray current in the ground is the accumulation of leakage current in each segment of the rail, assuming that the location of the conductor segment on the rail is L1, L2, LN, the leakage current of each conductor segment is Ilc (1), Ilc (2), respectively. Ilc (N), the size of the stray current in the Li position is as follows:

$$_{i}I_{sc}(L_i) = \int_1^i I_{lc}(i)di; \quad 1 < i < N \tag{1}$$

According to the above formula, the stray current in different locations along the line can be obtained, and the stray current distribution curve along the line can be obtained.

3. DISTRIBUTION CHARACTERISTICS OF STRAY CURRENT

There are many factors that affect the distribution of stray current, which are mainly divided into two categories, one is the line condition, the other is the locomotive working condition. Two. The line conditions include the change of the internal resistance of the rail and the resistivity of the insulating layer. The locomotive working conditions include the change of the locomotive position, the size of the traction current and so on. In this chapter, by observing

the distribution of rail potential and stray current, the influence of different factors on the above curve distribution is analyzed.

3.1. Influence of line condition on the distribution of stray current

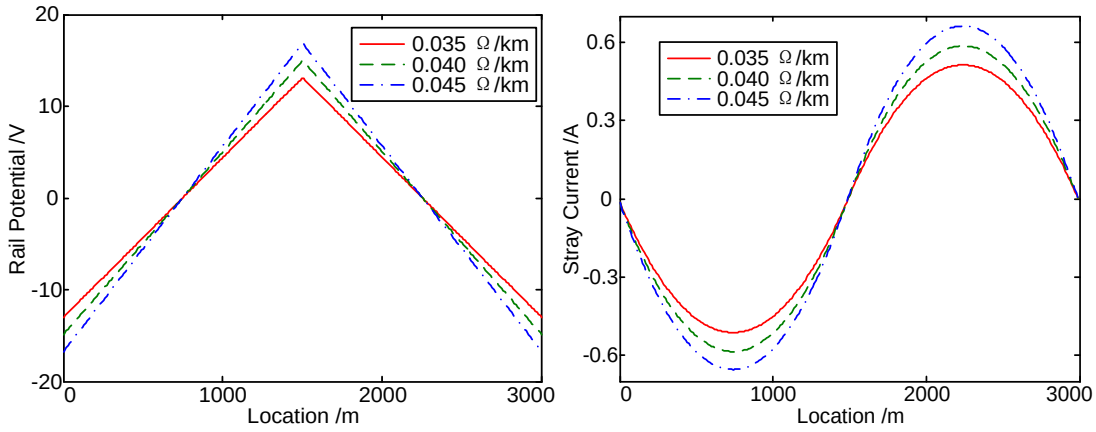

(a) Rail potential *(b) Stray current*

Figure 3: Influence of rail internal resistance on the distribution of various parameters

Table 2: The maximum value of the parameters under the internal resistance of different rail

Rail Resistance (ohms/km)	Rail Potential Maximum (V)	Stray Current Maximum (A)
0.035	13.04	0.51
0.040	14.90	0.59
0.045	16.76	0.66

From the simulation data of Figure 3 and Table 1, it is found that the rail resistance change has a great influence on the rail potential and the distribution of stray current. When the rail resistance rises, the rail potential rises obviously and the total stray current increases. By raising the rail manufacturing process and reducing the internal resistance of rail, the rail potential can be effectively suppressed and the total amount of stray current in the ground can also be reduced.

Rail insulation system has good insulation in the initial stage of subway operation. However, with the long time operation of the subway, a lot of dust will be attached to the insulation fastener and insulation pad. In some cities, the water accumulation in the tunnel may exist in the tunnel because of the poor drainage system of the tunnel, and the resistance of the insulation system is obviously reduced. The above situation will cause the stray current to increase. When the resistivity of the insulating layer is 90000, 270000, 450000 and 630000, the corresponding transition resistance of rail to earth is 3, 9, 15 and 21 respectively, and the distribution of the rail potential and stray current, as shown by Figure 4, is shown by the maximum value of each curve as shown by Table 3.

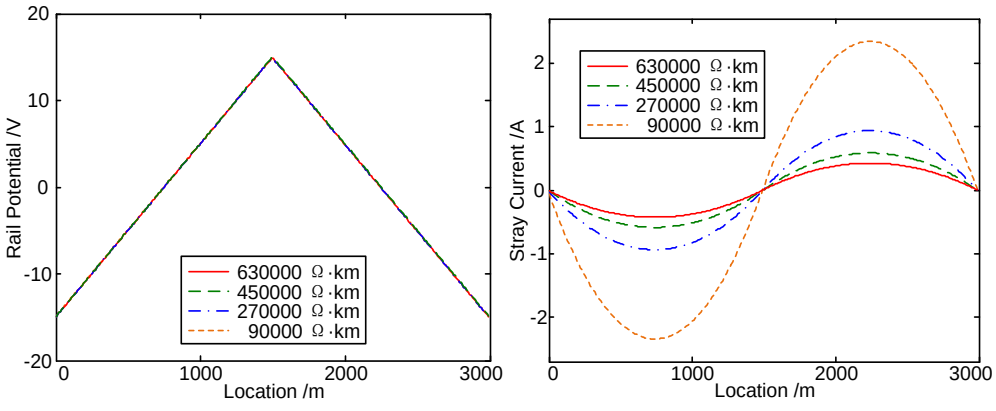

(a) Rail potential *(b) Stray current*

Figure 4: The influence of the resistivity of the insulation system on the distribution of the parameters

Table 3: Maximum parameters of different insulation layers

Insulating Layer Resistivity (ohms • km)	Rail Potential Maximum (V)	Stray Current Maximum (A)
90000	14.89	0.43
270000	14.90	0.59
450000	14.90	0.94
630000	14.90	2.34

According to the above simulation data, when the resistivity of insulation layer rises, the rail potential distribution is not changed obviously, but the stray current changes greatly. With the increase of insulation resistivity, the stray current in the ground decreases significantly, and the rate of stray current decreases rapidly. According to the simulation results, it can be found that when the transition resistance of rail to ground is reduced, the rail potential will not have a greater impact on the rail potential, but it will seriously affect the leakage current of the rail. Therefore, the effect of improving the resistivity of the insulation system to prevent the stray current is obvious. However, it is limited to suppress the stray current by increasing the resistivity of the insulating component only. It is not in line with the construction economy to over increase its resistivity. In the operation and maintenance, the tunnel drying and the reliability of the insulation components can effectively suppress the stray current.

If the maintenance work of the staff is not good, it may lead to a sharp drop in the resistivity of the insulation system in some positions, and even the direct grounding of the rail. In order to simulate the above fault, the insulation breakage of a section of 1m long is set at 800 m, 1100m and 1400m, that is, the rail is directly exposed to the concrete layer, and the resistivity of the outer insulating layer is 0. The simulation results, such as FIGURE 5, are shown.

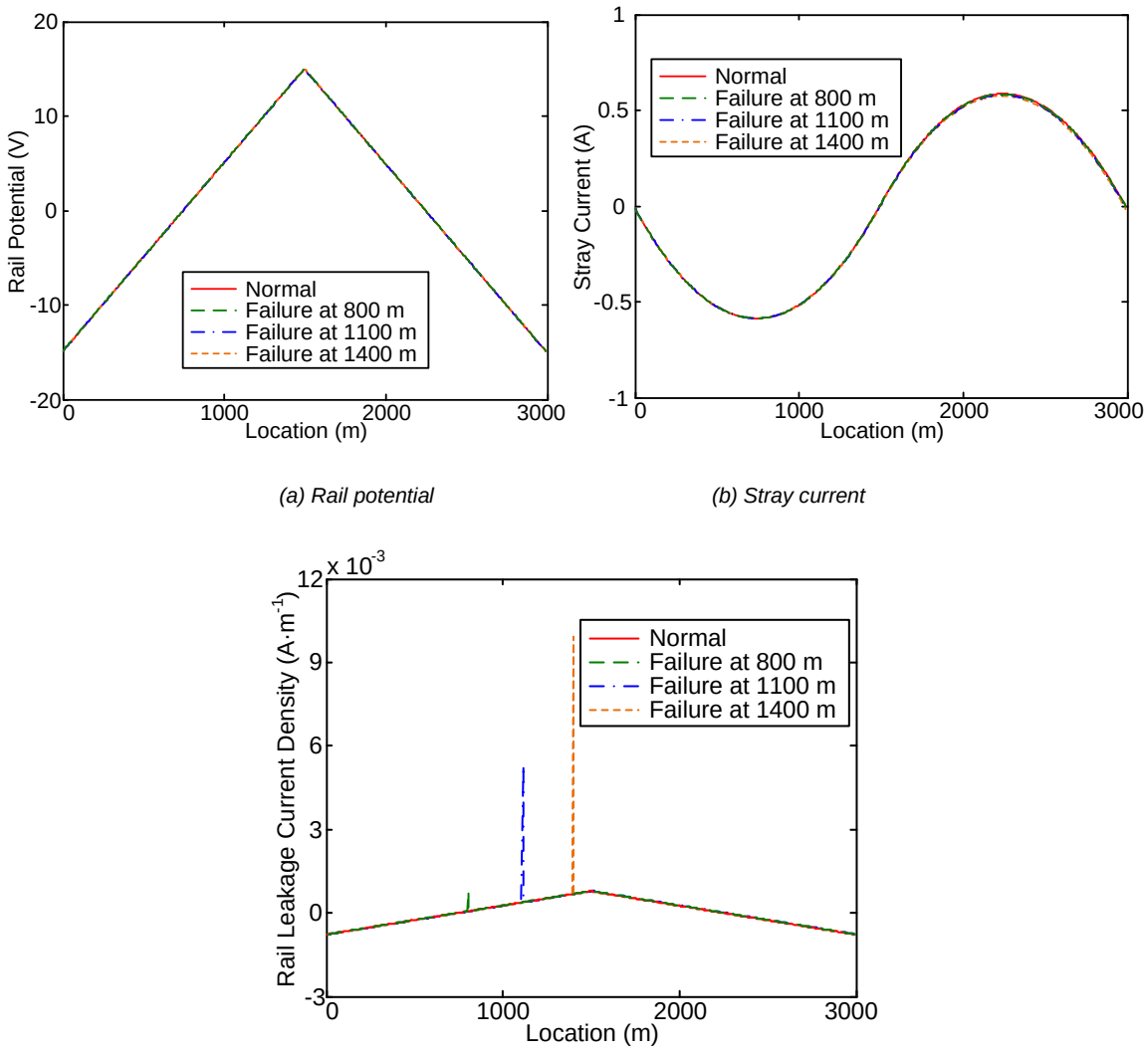

(a) Rail potential

(b) Stray current

(c) Rail leakage current density

Figure 5: Influence of partial breakage of insulating layer on the distribution of various parameters

According to the above simulation results, it is found that when the insulating layer is partially damaged, the rail potential and the ground stray current have no obvious change, which only causes the leakage current density of the damaged position to produce the sudden change of the leakage current density. In addition, by comparing the leakage current density of different damaged locations, it is known that the higher the rail potential, the greater the leakage current density. Because the locomotive is located at 1500m, the leakage current density at the damaged point at

1400m is the largest. Although the leakage current distribution curve of rail leakage will change at the corresponding breakage point, the leakage current at the breakage point has little effect on the rail and the total stray current due to the limited length of damaged interval. Therefore, in the actual project, the partial damage of the insulating layer will not cause significant influence in the short term, but it is necessary to prevent further expansion of the damage range and avoid a large amount of leakage current.

3.2. Influence of locomotive working condition on the distribution of stray current

The running state of locomotive is divided into acceleration, idling and braking, and the pulling force is related to the traction current. The traction current is positive and negative when the locomotive is in acceleration or braking state. When locomotive is in idling condition, the traction current is small and negligible. In order to analyze the influence of the traction current on the rail potential and the stray current, this paper assumes that the locomotive traction current is 2000A, 1000A, -1000A and -2000A respectively. When the locomotive traction current is positive, the locomotive pulls the current into the rail and draws out the current from the rail. When the locomotive traction current is negative, the direction is opposite. The location of the locomotive is still at 1500m, and the simulation results are shown in Figure 6.

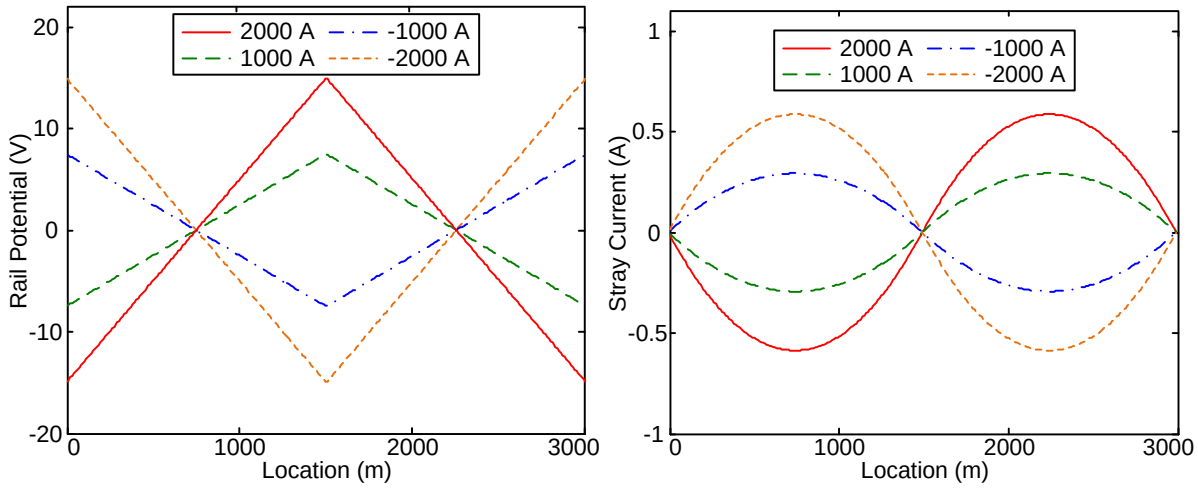

(a) Rail potential *(b) Stray current*

Figure 6: The influence of the change of traction current on the distribution of each parameter

According to Figure 6, it is known that when the traction current is positive, the rail potential is positive, the rail potential at both ends of the line is negative, and the rail potential decreases monotonically from the locomotive position to the two ends. The results are opposite when the traction current is negative. The greater the traction current of locomotive is, the higher the rail potential will be. For the stray current, when the locomotive is in the acceleration state, the stray current flows from the middle point of the line to both sides respectively. The size of the stray current increases first and then decreases, the greater the amplitude of the traction current, the more stray current in the ground. Because the above model is an independent system, the stray current in the ground flows back to the traction station at both ends of the line. According to the stray current distribution curve, the maximum stray current at 750m and 2250m is the most serious influence on the metal equipment around the tunnel.

When the locomotive moves between two stations, the position of the locomotive is always changing. In order to study the influence of locomotive position on the distribution of stray current, it is assumed that the locomotive traction current is 2000A constant, and the locomotive is simulated at 500m, 1000m and 1500m respectively. The distribution of rail potential and stray current is shown as Figure 7. The maximum value of the distribution curve of the stray current is shown as Table 4.

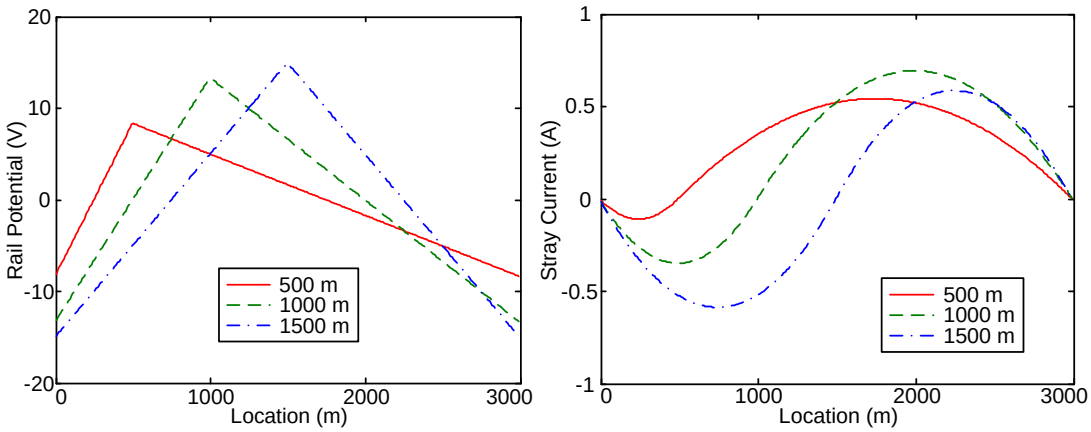

(a) Rail potential *(b) Stray current*

Figure 7: Influence of locomotive position on the distribution of various parameters

Table 4: The maximum stray current of a locomotive at different positions

Locomotive Location (ohms • km)	Left Side Maximum (A)	Right Side Maximum (A)	Total Amount (A)
500	0.11	0.54	0.65
1000	0.35	0.69	1.04
1500	0.59	0.59	1.18

According to Figure 6, when the traction current is the same, the position of the locomotive has great influence on the distribution of rail potential and stray current. The closer the locomotive midpoint is, the greater the rail potential will be. The traction current is different from the rail. When the locomotive is located at 1000m, the maximum value of the stray current appears on one side, but when the locomotive is in the middle point of the locomotive, the peak of the stray current on both sides of the locomotive is the largest, and the overall influence of the stray current on the two sides of the line is more serious than that of the other positions.

Usually, two traction stations and stations form a power supply section, and one or more ordinary stations will be built in one power supply area. When the departure interval is short, there will be a number of locomotives running in the same power supply zone, and the traction current will provide the traction current for these locomotives at the same time. There will be mutual influence between the locomotives. When the locomotive leaves the station, it enters the state of acceleration, the traction current is positive and the amplitude is larger. When the locomotive is about to enter the station, the locomotive will enter the braking state, and the traction current is negative and the amplitude is larger.

In order to study the influence of different locomotive operating conditions on the distribution of rail potential and stray current, this paper sets up two current source excitation at 750m and 2250m, respectively representing 1# locomotives and 2# locomotives, setting accelerated locomotive traction current is 2000A, braking state locomotive traction current is -2000A, analog "Acceleration & Acceleration". And "Acceleration & Deceleration" two conditions, the distribution of rail potential and stray current is shown in Figure 8.

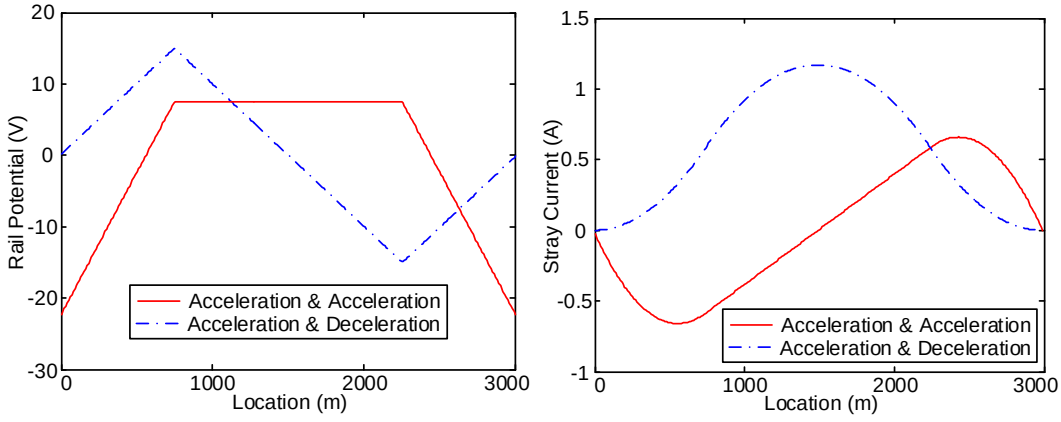

(a) Rail potential *(b) Stray current*

Figure 8: Influence of multi locomotive operation on the distribution of various parameters

According to Figure 7, the running state of multiple locomotives also has obvious influence on the distribution of rail potential and stray current. When the locomotive is in the state of Acceleration & Acceleration, the rail potential is about symmetrical distribution, the rail potential between the locomotives is higher, the maximum value is 7.50V, and appears in the position of the 1# locomotive and the 2# locomotive. Stray current is centrally symmetric, with a maximum value of 0.66A. When the locomotive is in the state of Acceleration & Deceleration, the distribution trend of the rail potential and stray current is opposite to the previous working condition. The maximum rail potential is 14.92V, which appears in the position of the 1# locomotive, the maximum stray current is 1.17A, appearing at the middle point of the power supply interval, and the rail potential is almost equal to the running state of the single locomotive. The maximum rail potential and the stray current are obviously greater than the maximum value of the single vehicle running state.

Therefore, if the locomotive is in the acceleration state in the same interval, it will lead to the centralization of the rail potential distribution. At this time, the stray current in the middle of the line increases and the stray current on both sides decreases, which indicates that the stray current in the middle of the line flows from the rail to the soil and SCCM, and the stray current both sides of the line reflows back to the rail. According to Faraday's law, when the current flows out of the conductor, the conductor is in the anodic corrosion state, and the current will cause electrochemical corrosion to the conductor. Therefore, in the Acceleration & Acceleration state, stray current will corrode the stray current on both sides of the rail and the line. If the locomotive gets the opposite of traction current, the rail leads to the concentration of stray current distribution, and its peak value is obviously larger than that of another. The SCCM corrosion of the stray current on the right side of the rail and the line on the left side of the line is more serious.

Therefore, in order to reduce the negative influence of the rail potential and stray current, control the departure time of the locomotives on the main line, and avoid the two locomotives at the same time in acceleration and braking, which can effectively promote the protection of the stray current.

4. CONCLUSION

Based on CDEGS, a subway distribution network model of stray current is established, and rail and SCCM are built according to actual conditions. In order to study the distribution of stray current, this paper studies the influence of line condition and locomotive operating state on the distribution of rail potential and stray current. The study shows that the increase of longitudinal resistance of rail will obviously raise the rail potential and the total stray current, and the decrease of the resistivity of the insulating layer has little effect on the rail potential, but it is stray and stray. The current will increase; the partial damage of the rail insulation layer has limited influence on the parameters, and the short time will not cause serious failure, but it needs to be maintained in time to prevent further expansion of the damage range. The size of the locomotive traction current will directly affect the parameter amplitude. When the traction current is fixed, when the locomotive runs to the middle point of the interval, the rail potential is the highest and the stray current on both sides of the locomotive is high. When two locomotives are running at the same time in the same power supply range, if the locomotive is in the acceleration state and the braking state respectively, the obtained rails are obtained. The potential and stray current are more serious, which can reduce the negative effects of the stray current by adjusting the departure interval and avoiding the long time in the above working conditions. The simulation results and research conclusions provide a theoretical basis for the protection of stray current, which can guide the staff to do preventive measures in the corresponding position and improve the protection efficiency effectively.

5. REFERENCES

Jian Hua ,L, 2016 , Research on Metro Stray Current Dynamic Probability Distribution and Corrosion Protection[C]. Southwest Jiaotong University.

Li, C, Jian Guo, Z, Ya Dong, F. 2015, Influence of the Track-to-earth Resistance of Subway on Stray Current Distribution[J], High Voltage Engineering, 41(11):3604-3610.

Kai Y. 2015, The Simulation of Metro Stray Current Based on Cdegs[C], Southwest Jiaotong University.

Zhao L P, Li J H, Liu M J. 2016, Simulation and analysis of metro stray current based on multi-locomotives condition[C]. 35th Chinese Control Conference (CCC), Chengdu, 2016:9252-9258.

Pires C L. 2016, What the IEC Tells Us About Stray Currents: Guidance for a Practical Approach[J]. IEEE Electrification Magazine, 4(3):23-29.

Cotton I, Charalambous C, Aylott P, et al. 2005, Stray current control in DC mass transit systems[J]. IEEE Transactions on Vehicular Technology, 54(2):722-730.

Charalambous C A, Aylott P 2014,Dynamic Stray Current Evaluations on Cut-and-Cover Sections of DC Metro Systems[J]. IEEE Transactions on Vehicular Technology, 63(8):3530-3538.

Liu M J, Lin S, Zhao L P, et al. 2017Study on dynamic characteristics of metro stray current based on CDEGS[C]. The 3rd International Conference on Electrical and Information Technologies for Rail Transportation (EITRT 2017), Changsha,:571-578.

GB 50157-2013 Subway design code [S]. Bei Jing: China Construction Industry Press, 2014.

CJJ 49-92. Technical regulations for corrosion protection of stray current in Subway [S], 1993.

277: Experimental and numerical evaluation on influential factors for thermal performance of coaxial-type ground heat exchanger

Kwanggeun OH[1], Seokjae LEE[2], Minkyu KANG[3], Sangwoo PARK[4], Hangseok CHOI[5]

[1] School of Civil, Environmental and Architectural Engineering, Korea University, Seoul 02841, Korea, zhe123@korea.ac.kr
[2] School of Civil, Environmental and Architectural Engineering, Korea University, Seoul 02841, Korea, liontjrwo@korea.ac.kr
[3] School of Civil, Environmental and Architectural Engineering, Korea University, Seoul 02841, Korea, dldnjfwp@korea.ac.kr
[4] Department of Civil Engineering and Environmental Sciences, Korea Military Academy, Seoul 01805, Korea, ptstwt@korea.ac.kr
[5] School of Civil, Environmental and Architectural Engineering, Korea University, Seoul 02841, Korea, hchoi2@korea.ac.kr

Thermal behaviour of Ground Heat Exchanger (GHEX) is affected by environmental factors, operating conditions, and the configuration of heat exchange pipes. Moreover, heat transfer in GHEXs is governed by the convection phenomenon among the circulating fluid, the wall of heat exchange pipe, the borehole grout and the ground formation. The convection is variable with flow conditions within the heat exchange pipe (i.e., laminar or turbulent flow), which is a significant variable in the thermal performance of GHEXs. Especially, in case of coaxial-type GHEXs, the occurrence of turbulent flow with sufficient heat exchange area is considerably critical due to the geometric characteristics of the concentric tube-in-tube configuration. In this paper, the coaxial-type GHEX was constructed in a test bed, and the in-situ thermal performance test (TPT) was carried out to estimate the thermal performance of the coaxial-type GHEX. In addition, a Computational Fluid Dynamic (CFD) model was developed by calibrating with the field test results. In order to simulate turbulent flow inside the pipe, the K-epsilon model was applied. Then, parametric studies were conducted with consideration of various configurations (i.e., depth, inner and outer diameters, and flow rate) to figure out the optimal configuration for coaxial-type GHEXs. As the flow rate and depth increased, the heat exchange amount of coaxial-type GHEX increased. In particular, as the hydraulic diameter increased, the heat exchange amount increased, which means that a reduction in the fluid velocity through the annular space is more dominant in determining the heat exchange amount.

Keywords: Turbulent flow, Coaxial-type Ground Heat Exchanger, In-situ thermal performance test (In-situ TPT), Computational Fluid Dynamic (CFD) model. Parametric study

1. INTRODUCTION

The coaxial-type GHEX has been considered as an alternative to improve the thermal performance of GHEX, which possesses a concentric tube-in-tube configuration. It can provide relatively higher thermal performance than the conventional U-type GHEXs along with securing sufficient heat exchange area and turbulent flow condition inside the pipe in accordance with its configuration (Boënnec, 2008; Carslaw et al., 1959; Mogensen, 1983; Wood et al., 2012).

There have been several studies to evaluate the thermal performance and the heat exchange mechanism of coaxial-type GHEX. The thermal performance of coaxial-type GHEX have been mainly evaluated by numerical analysis depending on pipe material, insulation condition, pipe cross-section, and thermal conductivity of ground (Holmberg et al., 2016; Sliwa& Rosen, 2017; Zanchini et al., 2010a; Zanchini et al., 2010b). In addition, a study on the heat exchange mechanism considering operation condition such as changing flow direction and the flow rate was performed by Holmberg et al. (2016), Eiamsa-ard et al. (2008) and Park et al. (2017). In the results, the flow condition inside the pipe was evaulated as the most significant parameter on the heat exchange efficiency of coaxial-type GHEX.

In this study, experimental and numerical studies for the coaxial-type GHEX were carried out to evaluate the thermal performance of coaxial-type GHEX. First of all, in-situ thermal performance test (TPT) was carried out by constructing a 50-m-deep coaxial-type GHEX in a test bed. Then, a Computational Fluid Dynamic (CFD) model was developed based on the field test data. Finally, parametric studies were conducted to evaluate on influential factors for thermal performance and estimate the optimal configuration of coaxial-type GHEXs.

2. CONSTRUCTION OF COAXIAL-TYPE GROUND HEAT EXCHANGER

The test bed is located in Dangjin-city, Korea. The construction site is composed of low hilly terrain and consisted of the metamorphic and biotite granitic rocks. The 50-m-deep coaxial-type GHEX was constructed in the test bed. The High-density polyethylene (HDPE) and bentonite grouting were used as pipe material and grouting material, respectively. In addition, the diameter of pipe was 75 mm for outer pipe and 40 mm for inner pipe. Figure 1 shows the cross-section of constructed coaxial-type GHEX.

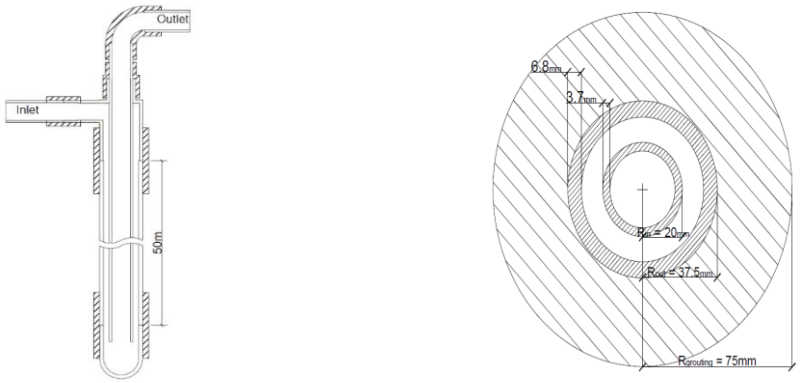

(a) Longitudinal schematic of coaxial-type GHEX (b) Cross section of coaxial-type GHEX

Figure 1: Schematics of coaxial-type GHEX

3. IN-SITU THERMAL PERFORMANCE TESTS

3.1. Overview of in-situ thermal performance test

The in-situ thermal performance test (TPT) was conducted to evaluate the thermal performance of coaxial-type GHEX. The in-situ TPT is a field test method to estimate the heat exchange amount of GHEX by measuring the temperature difference between inlet fluid and outlet fluid after inducing heat exchange under real operation condition. The heat exchange amount of coaxial-type GHEX can be calculated by Equation 1.

Equation 1: Heat exchange amount

$$Q = C \times \dot{m} \times \Delta T$$

Where:

Q = Heat exchange amount (W)

C = Specific heat of circulating fluid (J/kgK)

$\dot{m}$ = Mass flux of circulating fluid (l/min)

ΔT = Temperature difference between the inlet fluid and outlet fluid (℃)

In order to simulate the cooling operation of commercial buildings, artificial intermittent load (i.e., 8 h operating – 16 h pause) was applyed to the GHEX. The flow rate of circulating fluid was determined to be 11 l/min to secure the turbulent flow condition, and the test duration was 7 days. The schematic of experimental setup and testing equipment are shown in Figure 2.

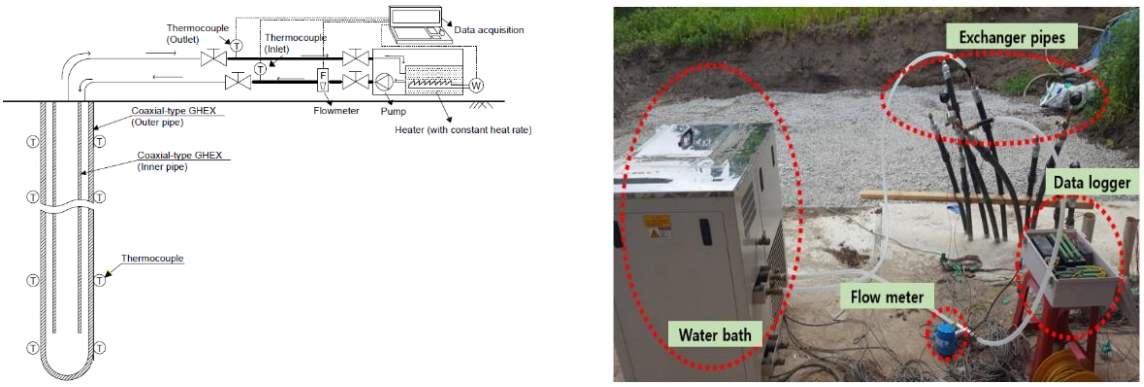

Figure 2: Experimental setup of in-situ TPT

3.2. Result of in-situ thermal performance test

Figure 3 represents the temperature change between inlet and outlet fluid, and the heat exchange amount calculated by using Equation 1. The inlet fluid temperature was maintained at 30℃ to simulate to cooling operation, and outlet fluid temperature estimated after heat exchange was measured. The average heat exchange amount and the average temperature difference between inlet and outlet were calculated to be 2,578 W and 3.26℃, respectively.

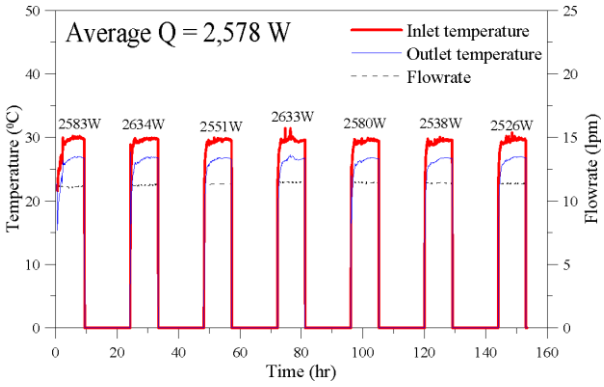

Figure 3: Result of in-situ TPT

However, the heat exchange amount of coaxial-type GHEX will differ with various conditions such as flow rate of working fluid, operation condition, and thermal conductivity of heat transfer medium. Especially, the thermal performance of coaxial-type GHEX was largely influenced by flow condition inside the coaxial tube. In this study, a numerical model was developed to understand the effect of various design parameter on the thermal performance of coaxial-type GHEX. In addition, the sensitivity of each design parameter was evaluated to find the optimum configuration of coaxial-type GHEX.

4. CFD NUMERICAL ANALYSIS

4.1. Overview of numerical modeling

Thermal behaviour of GHEX is affected by various conditions such as environmental factors, operating conditions, and the shape of heat exchange pipe (Park et al, 2017). Generally, heat transfer in GHEX is caused by the convection between fluid flow and pipe wall, and conduction from the pipe wall to the concrete and ground formation.

The heat conduction is caused by the temperature difference between the adjacent medium and the contact area. Therefore, the thermal behaviour is affected by the thermal conductivity of surrounding medium, the temperature difference between the fluid and surrounding material, and contact area of heat exchange pipe. On the other hand, the convection is mainly influenced by the flow condition (i.e., laminar or turbulent flow condition) of the fluid inside the heat exchange pipe. Especially, the thermal behaviour of coaxial-type GHEX is more sensitively affected by the turbulent flow and sufficient heat exchange area due to the geometric characteristic of the concentric tube-in-tube configuration (Boënnec, 2008; Carslaw and Jaeger, 1959; Mogensen, 1983; Wood et al., 2012).

In this chapter, the numerical model was developed to evaluate the thermal behaviour of coaxial-type GHEX depending on various boundary and operation conditions. A Computational Fluid Dynamic (CFD) analysis was adopted to simultaneously consider the convective heat transfer of a working fluid and the heat conduction of surrounding medium. The numerical model was developed based on the field test conditions, and the accuracy of CFD model was verified by comparing with field test results.

The $k-\varepsilon$model is the most popular two-equation model for simulating turbulence flow. It is derived from the transport equation and turbulent dissipation rate. By defining the kinematic eddy-viscosity as the two-equation model, the $k-\varepsilon$ model can reflect the history effects such as convection and diffusion of turbulent energy and can determine the scale of turbulence. The Standard $k-\varepsilon$ model is summarized as follows (Wilcox, 1993; Pope, 2001).

Equation 2: Kinematic Eddy-Viscosity

$$\nu_t = C_\mu \frac{k^2}{\varepsilon}$$

Equation 3: Turbulence Kinetic Energy

$$\frac{\partial k}{\partial t} + \overline{u_j}\frac{\partial k}{\partial x_j} = \tau_{ij}\frac{\partial \overline{u_i}}{\partial x_j} - \varepsilon + \frac{\partial}{\partial x_j}\left[(\nu + \frac{\nu_t}{\sigma_k})\frac{\partial k}{\partial x_j}\right]$$

Equation 4: Dissipation Rate

$$\frac{\partial \varepsilon}{\partial t} + \overline{u_j}\frac{\partial \varepsilon}{\partial x_j} = C_{\varepsilon 1}\frac{\varepsilon}{k}\tau_{ij}\frac{\partial \overline{u_i}}{\partial x_j} - C_{\varepsilon 2}\frac{\varepsilon^2}{k} + \frac{\partial}{\partial x_j}\left[(\nu + \frac{\nu_t}{\sigma_\varepsilon})\frac{\partial \varepsilon}{\partial x_j}\right]$$

Equation 5: Closure Coefficients

$$C_\mu = 0.09 \quad \sigma_k = 1.0 \quad \sigma_\varepsilon = 1.3 \quad C_{\varepsilon 1} = 1.44 \quad C_{\varepsilon 2} = 1.92$$

Where:

ν_t = Kinematic eddy-viscosity

k = Turbulence kinetic energy (m^2/s^2)

$\overline{u}$ = Mean-flow velocity (m/s)

ε = Dissipation rate

Since the Standard $k-\varepsilon$ model is a Partial Differencial Equation (PDE), initial conditions and boundary conditions for the turbulent kinetic energy and turbulent dissipation rate are required. In addition, there is no need to specify the flow-dependent specifications such as mixing length (l_m) in advance of the flow to be analyzed. The fundamental governing equation of non-isothermal flow applied in a numerical model is given by Equation 6 (Panton, 1996).

Equation 6: Governing equation of non-isothermal flow

$$\rho C_p\left(\frac{\partial T}{\partial t} + (\mathrm{u}\cdot\nabla)T\right) = -(\nabla\cdot\mathrm{q}) + \tau\colon\mathrm{S} - \frac{T}{\rho}\frac{\partial \rho}{\partial T}\Big|_p\left(\frac{\partial p}{\partial t} + (\mathrm{u}\cdot\nabla)p\right) + Q$$

Where:

C_p = Specific heat capacity at constant pressure (J/(kg·K))

T = Absolute temperature (K)

q = Heat flux by conduction (W/m^2)

τ = Viscous stress tensor (Pa)

Q = Heat source or sink (W/m^3)

Meanwhile, the energy equation for the one-dimensional incompressible fluid flow inside the pipe is represented in Equation 7 (Lurie, 2008).

Equation 7: Energy equation for the one-dimensional incompressible fluid flow inside the pipe

$$\rho A C_p \frac{\partial T}{\partial t} + \rho A C_p \boldsymbol{u} \cdot \nabla T = \nabla \cdot Ak\nabla T + f_D \frac{\rho A}{2d_h} |\boldsymbol{u}|^3 + Q + Q_{wall}$$

Where:

k = Thermal conductivity (W/mK)

A = Cross section of pipe (m^2)

Q = General heat source (W/m)

Q_{wall} = Heat transfer between the wall of heat exchange pipe and the surrounding grouting material (W/m)

The Q_{wall} can be written by Equation 8 based on the Newton's Law of Cooling where convective heat transfer is proportional to the temperature difference.

Equation 8: Definition of Q_{wall} based on the Newton's Law

$$Q_{wall} = hZ(T_{ext} - T)$$

Where:

Z = Perimeter of the pipe (m)

A = Cross section of pipe (m^2)

h = Heat transfer coefficient ($W/m^2 \cdot K$)

T_{ext} = External temperature outside the pipe (K)

To simulate complex phenomena such as turbulent flow in a coaxial pipe and the heat exchange between a heat exchange pipe, grouting material, and ground, Finite Element (FE) analysis program, COMSOL Multiphysics, was used. CFD module and heat transfer module were applied to simultaneously simulate the turbulent flow in the coaxial pipe and the heat transfer due to it. As a result, thermo-hydro coupled numerical model was developed which can analyze the turbulent flow of non-isothermal fluid in a pipe and heat transfer phenomena.

In order to reduce the computational capacity of the numerical model, the geometry of the cylindrical annular space in which the heat exchange takes place was simplified using two-dimensional axisymmetric geometry. The geometric shape and the mesh configuration of the developed numerical model are shown in Figure 4.

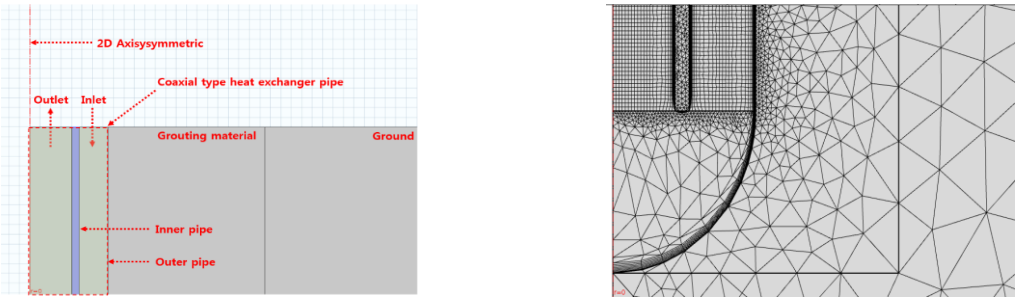

(a) Geometry of numerical model (b) Mesh configuration of connection part

Figure 4: Geometry and mesh configuration of coaxial-type GHEX

The air temperature data measured during the field tests was applied to the top boundary of numerical model, and ground temperature data measured in the test bed was used as initial temperature condition of ground and grouting sections. The fluid inlet temperature and flow rate conditions applied to the inlet boundary of the numerical model were the same as the inlet temperature and flow rate of the field test. The model verification was conducted by comparing the outlet temperature of numerical model with field test results. The material properties of the material applied to the numerical model are represented in Table 1, and the pipe configuration and the type of grouting material were the same as the construction condition of coaxial-type GHEX.

Table 1: Material properties of materials applied in numerical model

Type	Density (kg/m^3)	Specific Heat (J/kgK)	Thermal Conductivity (W/mK)	Viscosity (kg/ms)
Fluid	998.2	4,182	0.6	0.001
Ground	1,820	1,480	2.36	-
Grouting (bentonite)	641	732	0.86	-
Heat exchange pipe (HDPE)	958	1,201	0.4	-

4.2. Verification of developed numerical model

In order to verify the adequacy of the developed numerical model, the outlet temperature of numerical model was compared with field test results by applying the inlet temperature and flow rate of field test to the inlet boundary of numerical model. The result of in-situ TPT performed in the test bed was used as the reference for verifying the accuracy of the numerical model, and the results of comparison is represented in Figure 5.

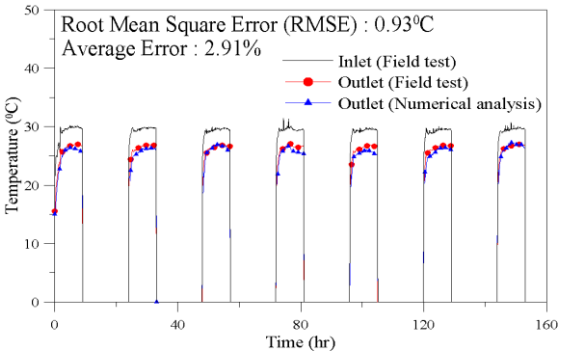

Figure 5: Comparison of in-situ TPT results and numerical analysis results

The average error was calculated to be 2.91%, and the RMSE was calculated to be 0.93℃. According to these results, it is evaluated that the developed numerical model can simulate the field test with high accuracy. It means that the developed numerical model is suitable for simulating the thermal behaviour of coaxial-type GHEX, and it can be used for estimating the thermal performance of coaxial-type GHEX before the construction. Therefore, the parametric studies were performed with various configurations (i.e., depth, inner and outer diameters, and flow rate) using developed numerical model to estimate the main parameters that affect the thermal performance of the coaxial-type GHEX.

5. PARAMETRIC STUDY OF THERMO-HYDRAULIC BEHAVOIR OF COAXIAL-TYPE GHEX

5.1. Overview of parametric study

Since the thermal performance of coaxial-type GHEX is affected by the flow conditions of circulating fluid and the heat exchange properties of the surrounding medium, it is important to understand the sensitivity of each design parameter. Therefore, in this chapter, a series of parametric studies was conducted by developed numerical model to figure out the effect of various design parameter. Since there are many cases of the relationship between the thermal conductivity of heat transfer medium and heat exchange amount (Choi et al., 2008; Park, 2016), parametric studies were focused on the effect of turbulent flow condition on the heat transfer. Therefore, the considered parameters were the flow rate of working fluid, length of heat exchange pipe, and hydraulic diameter of the pipe. The considered ranges of each parameter were summarized as follows:

(1) The parametric studies were performed on the flow rate to figure out the effect of flow rate of working fluid on the thermal performance of coaxial-type GHEX. The reference value for flow rate of working fluid was 11 L/m, and the range of flow rate was determined to be from 5 L/m to 40 L/m.

(2) Generally, the thermal performance of GHEXs increased as the length of heat exchange pipe becomes longer (Holemberg et al., 2016; Park, 2016). Then, in order to evaluate the effect of length of heat exchange pipe on thermal performance of coaxial-type GHEX, 25 m, 100 m, 150 m, and 200 m length pipes were considered in the parametric study.

(3) Hydraulic diameter determined the flow condition in the pipe. In case of the coaxial tube, the hydraulic diameter of the coaxial tube is influenced by the diameter of inner and outer pipes constituting the coaxial tube. Therefore, the range from 15 mm to 60 mm was considered for the hydraulic diameter to compare the effect of turbulent flow on thermal performance of coaxial-type GHEX.

The range of parameters applied in parametric studies was organized in Table 2, and the reference conditions were represented in shaded.

Table 2: Range of parameters applied in parametric studies

Type	Parameters									
Flow rate of working fluid (L/m)	5		11		20		30		40	
Length of pipe (m)	25		50		100		150		200	
Hydraulic diameter (mm)	15	20	25	30	35	40	45	50	55	60

5.2. Effect of flow rate of working fluid

The parametric study for the flow rate of working fluid was conducted for the values of 5 L/m, 20 L/m, 30 L/m, and 40 L/m. According to each flow rate of working fluid, a series of in-situ TPT was simulated for seven days, and the other values except the flow rate were the same as the reference conditions. The heat exchange amount depending on different flow rate are shown in Figure 6, and Table 3 represents the results of parametric study for flow rate.

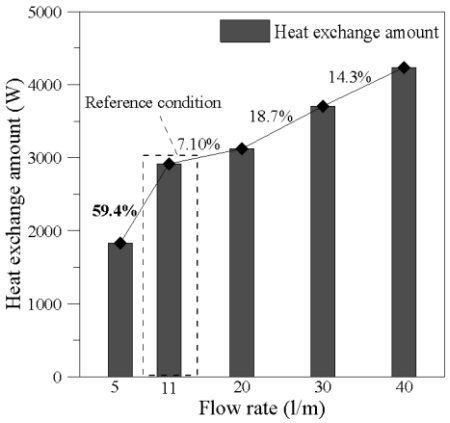

Figure 6: Comparison of heat exchange amount depending on flow rate

Table 3: Results of parametric study for flow rate

Type	Heat exchange amount depending on flow rate				
Flow rate (L/m)	5	11	20	30	40
Heat exchange amount (W)	1,829	2,916	3,123	3,706	4,236

The thermal performance of coaxial-type GHEX increased as the flow rate increased because the increase of the Reynolds number more generates the heat transfer by turbulence. When the flow rate increased from 5 L/m to 11 L/m, the increment of heat exchange amount was the largest at 59.4%. This result indicates that the increment of heat exchange amount is maximized near the limit flow rate of working fluid where the flow condition inside the pipe has started to change from laminar flow to turbulent flow (i.e., 6.66 L/m at this construction conditions). As a result, while a large flow rate of working fluid is required to achieve the high thermal performance in coaxial-type GHEX, the appropriate flow rate should be determined considering the thermal performance to be achieved, boundary flow rate of working fluid capable of generating turbulence, and operating cost.

5.3. Effect of pipe length

Generally, as the length of heat exchange pipe becomes longer, the thermal performance of GHEX also increases (Holemberg et al., 2016; Park, 2016). Similar to the general tendency on pipe length, the heat exchange amount of coaxial-type GHEX increased as the pipe length increased because of the increasing contact area (Figure7 and Table 4).

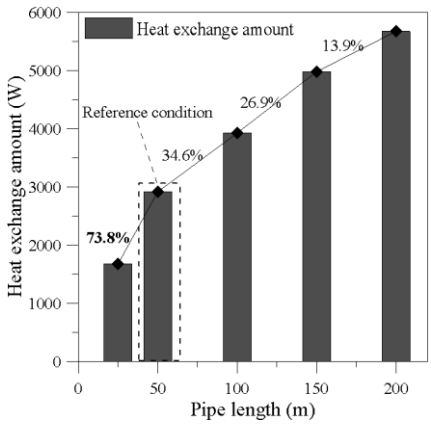

Figure 7: Comparison of heat exchange amount depending on pipe length

Table 4: Results of parametric study for pipe length

Type	Heat exchange amount depending on pipe length				
Pipe length (m)	25	50	100	150	200
Heat exchange amount (W)	1,678	2,916	3,925	4,979	5,671

However, the heat exchange amount was not proportional to the increment of pipe length, and the increasing rate of heat exchange amount decreased as the pipe length increase. Therefore, in actual construction, it is important to determine the drilling depth considering the thermal performance to be achieved and construction cost.

5.4. Effect of hydraulic diameter

As shown in Equation 9, the flow condition through the concentric annular tube is influenced by the hydraulic diameter determined by difference between inner and outer diameter. Therefore, in order to evaluate the effect of flow condition on thermal performance, a variation of hydraulic diameter by changing inner and outer pipe diameter was considered in the parametric study.

Equation 9: Hydraulic diameter of coaxial tube

$$D_h = \frac{4A_c}{P} = \frac{4\pi({D_o}^2 - {D_i}^2)/4}{\pi(D_o + D_i)} = D_o - D_i$$

Where:

D_h = Hydraulic diameter

A_c = Cross-sectional area perpendicular to the flow direction (mm^2)

P = Wetted perimeter (mm)

D_i = Inner pipe diameter (mm)

D_o = Outer pipe diameter (mm)

In order to increase hydraulic diameter, the diameter of inner pipe was fixed at 35 mm and the outer pipe diameter was increased to 100 mm at intervals of 5 mm. As a result, the hydraulic diameter increased from 35 mm for reference condition to 60 mm, and the heat exchange amounts depending on the case of increasing hydraulic diameter were shown in Figure 8. Moreover, in order to evaluate the heat transfer effect of turbulence, the turbulent kinetic energy of the annular space at 25 m depth was calculated at the same time.

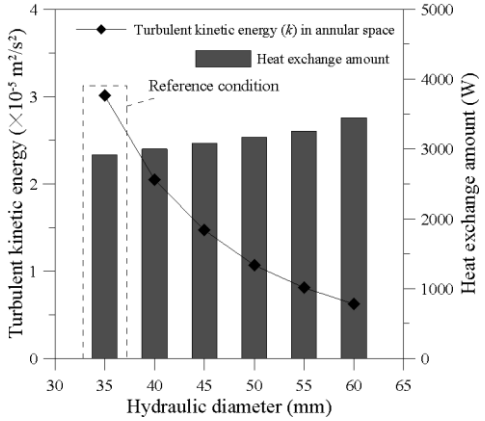

Figure 8: Relation between heat exchange amount and turbulent kinetic energy (Increasing hydraulic diameter)

As the hydraulic diameter increased, the heat exchange amount of coaxial-type GHEX increased. The increment of heat exchange amount was the largest at 5.87% when the hydraulic diameter increased from 55 mm to 60 mm. When the hydraulic diameter was 60 mm, the Reynolds number was less than 4,000, and the flow at this case represented the most significant heat exchange amount even though it is a transition region where turbulence and laminar flow exist at the same time. Conceptually, as the hydraulic diameter increases, the velocity of the internal fluid decreased in the same flow rate of working fluid due to the cross-sectional area of annular space increased. The turbulent kinetic energy was minimum value in the case of the hydraulic diameter at 60 mm, however, the heat exchange amount is maximum value in this case because as the velocity of the internal fluid decreased, sufficient heat exchange time between the working fluid and the heat transfer medium was secured. Therefore, this result suggested that in the case of coaxial-type GHEX, securing sufficient heat exchange time is a more influential factor

than the heat transfer efficiency by the turbulent flow. The results of the parametric study for increasing hydraulic diameter were summarized in Table 5.

Table 5: Results of parametric study for increasing hydraulic diameter

Type	Heat exchange amount depending on hydraulic diameter					
Hydraulic diameter (mm)	35	40	45	50	55	60
Heat exchange amount (W)	2,916	3,000	3,083	3,170	3,256	3,447
Turbulent kinetic energy in annular space ($\times 10^{-5}$m^2/s^2)	3.01	2.05	1.47	1.07	0.811	0.624

On the other hand, The diameter of outer pipe was fixed at 75 mm and the inner pipe diameter was increased to 60 mm at intervals of 5 mm. As a result, the hydraulic diameter decreased from 35 mm for reference condition to 15 mm, and the heat exchange amounts depending on the case of decreasing hydraulic diameter were represented in Figure 6. As the hydraulic diameter decreased, the heat exchange amount decreased. On the contrary to the case of increasing hydraulic diameter, however, the variation of heat exchange amount according to the hydraulic diameter was expressed extremely small. Similar to the case of increasing hydraulic diameter, as the hydraulic diameter decreased, the turbulent kinetic energy increase and it soared dramatically when the hydraulic diameter was 15 mm as shown in Figure 9. The results of parametric study for decreasing hydraulic diameter were summarized in Table 6.

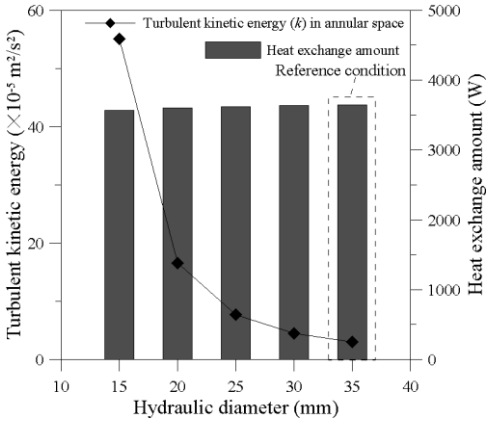

Figure 9: Relation between heat exchange amount and turbulent kinetic energy (Decreasing hydraulic diameter)

Table 6: Results of parametric study for decreasing hydraulic diameter

Type	Heat exchange amount depending on hydraulic diameter				
Hydraulic diameter (mm)	15	20	25	30	35
Heat exchange amount (W)	2,853	2,884	2,895	2,910	2,916
Turbulent kinetic energy in annular space ($\times 10^{-5}$m^2/s^2)	55.1	16.6	7.69	4.5	3.01

To summarize both results, the thermal performance of coaxial-type GHEX decreased as the hydraulic diameter decreased. This is because the decreasing of hydraulic diameter reduced the cross-sectional area of the annular space, leading to an increase in the fluid velocity. Therefore, sufficient heat exchange was not performed due to the lack of residence time for circulating fluid. Also, when the hydraulic diameter was smaller than 35 mm, there was almost no change in the heat exchange amount. In the other words, if the hydraulic diameter was smaller than 35 mm, the improvement of the thermal performance of coaxial-type GHEX due to the increase of the residence time induced by decrease of the fluid velocity was insufficient. In conclusion, the reduction of the fluid velocity through the annular space was more dominant in determining the thermal performance of coaxial-type GHEX than the effect of the turbulent kinetic energy. Therefore, the heat exchange amount of coaxial-type GHEX increased by applying a concentric tube which possesses hydraulic diameter of 35 mm or more. Furthermore, methods for increasing residence time and turbulence effect of the circulating fluid by installing a pin in the annular space should be considered (Eiamsa-ard et al., 2008; Park et al., 2017).

6. CONCLUSION

In order to evaluate thermal behaviours of the coaxial-type GHEX numerically, the CFD model was developed based on the results of field tests. The accuracy of CFD model was verified by comparing the outlet fluid temperature with field tests result when applying the same boundary conditions of field tests. A series of parametric studies was conducted with consideration of various configurations (i.e., length, pipe diameter, and flow rate) to evaluate the effect of various design parameter on the thermal performance of coaxial-type GHEX. From the numerical analyses, some important findings are summarized as follows:

(1) The change of flow rate influenced the thermal performance of coaxial-type GHEX. The increase of turbulent heat transfer effect due to the increase of flow rate increased the thermal performance. In particular, change of thermal performance in the vicinity of the boundary flow rate where the turbulence is generated was the largest, and the flow condition inside the pipe changed from laminar flow to turbulent flow in that case.
(2) The thermal performance of coaxial-type GHEX was improved by increasing the pipe length. The increase of the contact area with the ground improved the thermal performance. However, the increment of thermal performance was not proportional to the variation of pipe length. Therefore, it is important to determine the proper pipe length considering the thermal performance to be achieved and construction cost.
(3) As the hydraulic diameter increased, the thermal performance of coaxial-type GHEX increased. This is because sufficient heat exchange time was secured by decreasing the fluid velocity in annular space. In addition, the effect of improving the thermal performance by reducing the fluid velocity was effective when the hydraulic diameter was 35 mm or more. Therefore, it should be considered that determining the appropriate pipe diameter and installing a pin inside the annular space to generate vortex to maximize retention effect of circulating fluid.

7. REFERENCES

Boennec O. (2008), “Shallow ground energy systems”, Proceedings of the Institution of Civil Engineers, Energy, Vol. 161, No. 2, pp. 57-61.

Carslaw, S. H., Jaeger, J. C. (1959), “Conduction of heat in solids, 2nd ed.”, Oxford Science Publication.

Eiamsa-ard, Smith, et al. (2008), "Turbulent flow heat transfer and pressure loss in a double pipe heat exchanger with louvered strip inserts.", International Communications in Heat and Mass Transfer, Vol. 35, No. 2, pp. 120-129.

Holmberg, H., Acuña, J., Næss, E., & Sønju, O. K. (2016), “Thermal evaluation of coaxial deep borehole heat exchangers”, Renewable Energy, Vol. 97, pp. 65-76.

Lurie, M. V. (2008), “Modeling of oil product and gas pipeline transportation”, WILEY-VCH Verlag GmbH &Co., KGaA, Weinheim

Mogensen, P. (1983) “Fluid to duct wall heat transfer in duct system heat storages”, Document-Swedish Council for Building Research, Vol.16, pp. 652-657.

Panton, R. L. (1996), “Incompressible Flow”, 2nd ed., John Wiley & Sons, Inc.

Park, C. D., Lee, D. H., Park, B. S., Choi, J. (2017) “A Numerical Study on Heat Transfer and Flow Characteristics of a Finned Downhole Coaxial Heat Exchanger”, Transactions of the Korean Society of Mechanical Engineers, B, Vol. 41, No. 2, pp. 79-86.

Park, S., Lee, D., Lee, S., Chauchois, A., & Choi, H. (2017) “Experimental and numerical analysis on thermal performance of large-diameter cast-in-place energy pile constructed in soft ground”, Energy, Vol. 118, pp 297-311.

Park, S., Lee, S., Lee, H., Pham, K., Choi, H. (2016) “Effect of borehole material on analytical solutions of the heat transfer model of ground heat exchangers considering groundwater flow”, Energies, Vol. 9, No. 5, pp 318.

Pope, S. B. (2001). “Turbulent flows”, Cambridge University press.

Sliwa, T. and Rosen, M. A. (2017) “Efficiency analysis of borehole heat exchangers as grout varies via thermal response test simulations”, Geothermics, Vol. 69, pp. 132-138.

Wilcox, D. C. (1993). “Turbulence modeling for CFD (Vol. 2)”, DCW industries.

Wood, C. J., Liu, H., Riffat, S. B. (2012) “Comparative performance of ‘U-tube’ and ‘coaxial’loop designs for use with a ground source heat pump”, Applied Thermal Engineering, Vol. 37, pp. 190-195.

Zanchini, E., Lazzari, S., Priarone, A. (2010a) “Improving the thermal performance of coaxial borehole heat exchangers”, Energy, Vol. 35, No. 2, pp. 657-666.

Zanchini, E., Lazzari, S., Priarone, A. (2010b) “Effects of flow direction and thermal short-circuiting on the performance of small coaxial ground heat exchangers”, Renewable Energy, Vol. 35, No. 6, pp. 1255-1265.

278: Automatic surface detection method of disc solar concent rator based on non-diffractive Moire fringes

Zilong FANG[1], Qinghua LV[2], Xue GONG[3], Qi ZHANG[4], Bowen SU[5], Weidong BAO[6]

[1] Hubei Colllaborative Innovation Center for Hight-efficirnt Utilization of Solar Energy,Hubei University of Te--chnol ogy,903349917@qq.com
[2] Hubei Colllaborative Innovation Center for Hight-efficirnt Utilization of Solar Energy,Hubei University of Te--chnol ogy,382511335 @qq.com
[3]School of Science,Hubei University of Technology,1104617349@qq.com
[4]School of Science,Hubei University of Technology,1256289017@qq.com
[5]School of Science,Hubei University of Technology,915622540@qq.com
[6] Hubei Colllaborative Innovation Center for Hight-efficirnt Utilization of Solar Energy,Hubei University of Te--chnol ogy,baoweidong666@qq.com

According to the demand of disc solar power generation for surface shape detection of concentrator, an automatic surface detection method of disc solar concentrator based on non-diffractive moire fringe is proposed.The measuring principle of this method is described in detail in this paper.The ZEMAX software is used to simulate the optical system, and the non-diffractive moire fringes before and after the surface deformation are simulated.After binarization and fitting, 3D deformation of the concentrator can be obtained, and the shape surface of the condenser can be judged to meet the requirements of production and application.

Keywords: Moire fringr; Solar concentrator; Surface shape detection

1. INTRODUCTION

In recent decades, many feasible methods have been put forward to measure the shape surface of solar condenser, and some methods have been applied in practice. According to their physical principles, these methods can be divided into three categories: the first is based on laser scanning technology. The second and third methods are based on image processing technology. In the photography method and the fringe reflection method, CCD camera is used to capture and record the image information. The VSHOT measurement method based on laser scanning technology is suitable for the measurement of disc and slot condenser with high accuracy, but the collection method is time-consuming and not suitable for measuring long focal length condenser. The photography method can be used to measure any type of solar condenser, but this method requires a large number of mark points on the measured surface, which is time-consuming and of low precision. The deflection method is suitable for high precision measurement of large area mirror surface. At present, laser scanning is the main method to measure the surface shape of disc solar concentrator. The accuracy of this method is very high and can reach 0.1 mrad**.** However, this method requires that the distance between the laser and the mirror is about twice as long as that of the mirror and when the focal length is long, the distance from the laser to the mirror will be very long. Therefore, the scanning accuracy of the laser is required to be very high, which is difficult to achieve (Xiao 2015).

To sum up, based on the fringe reflection method, a non-diffractive moire fringe method is proposed to detect the surface shape of solar surface reflector.

2. MEASURING PRINCIPLE

2.1. Non-diffractive light

After the collimation and beam expansion, the incidence of the light emitted by the laser will be parallel to the axis cone mirror. According to the characteristic that the axial cone mirror can produce non-diffractive light, a zero-order Bessel shape concentric circular ring (no diffractive light) is formed behind the axial cone mirror Wang 2011). Figure 1 shows the principle of producing non-diffractive light after the parallel incidence of the light.

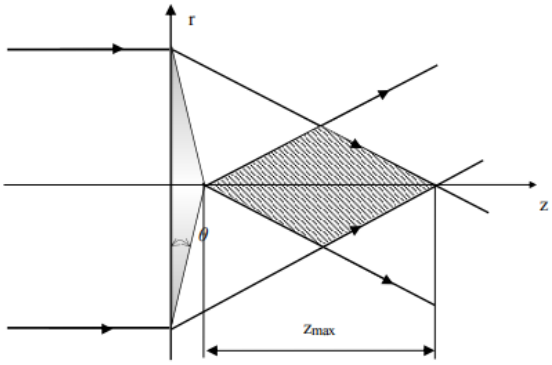

Figure 1: Principle diagram of non-diffractive light generated by axial cone mirror

The cone angle of the axial cone mirror is θ , and its transmission function can be as follows:

$$t(r) = \begin{cases} exp[-i\,k(n-1)r\theta], (r < \frac{D}{2}) \\ 0, (r \geq \frac{D}{2}) \end{cases} \quad (1)$$

Where:

r = incident radius

n= refractive index of the axis cone

D= diameter of the axial cone

k= wave number

λ= wavelength

According to Fresnel diffraction formula, the distribution of light field at z behind the axial cone mirror is as follows (Zhao 1998):

$$E_z = \frac{\pi r_p}{j\sqrt{\lambda z}} J_0\left(k\frac{r_p}{z}r_1\right)\exp\left(jkz + j\frac{k}{2z}{r_1}^2 + j\frac{k}{2z}{r_p}^2 + j\frac{\pi}{4}\right) \tag{2}$$

Ligh distribution:

$$I_z = E_z^* \cdot E_z = \frac{\pi^2 {r_p}^2}{\lambda z} {J_0}^2[k(n-1)\theta r_1] \tag{3}$$

Maximum diffraction distance:

$$Z_{max} = \frac{D}{(n-1)\theta} \tag{4}$$

Where:

r_1 = polar radius of the observation plane

r_p = Stable phase point

It can be seen from the above equations that the transverse intensity distribution of the non-diffractive light which is produced in the maximum non-diffractive distance Z_{max} is the square term of the zero-order Bessel function J_0 of the first kind,after the monochromatic plane wave passes through the axial cone mirror. The specific distribution depends on the refractive index of the axial cone mirror n, the cone angle of the axial cone mirror θ, and the wavelength of the incident light λ (Zhongsheng 2016).

2.2. Non-diffractive moire fringe

If we introduce a beam of non-diffractive light to make the two beams satisfy the coherent conditions and interfere, the interference intensity can be calculated as follows (Zhai 2008):

$$I_M = \left\{\frac{\pi^2 z_1}{\lambda} J_0[k(n-1)\theta r_1] + \frac{\pi^2 z_2}{\lambda} J_0[k(n-1)\theta r_2]\right\}^2 \tag{5}$$

Where:

$r_2 =$ polar radius of the polar coordinate system with the center of the second beam as the origin

Z_1、Z_2= optical path of two beams of light respectively.

The interference intensity is the superposition of the zero-order Bessel function with different positions of the two centers. The central position of two Bessel functions is determined by r_1 and r_2.

The outer loop of the Bessel function is regarded as a periodic function. Two non-diffractive beams with different central positions are superposed, and the interference fringes are distributed in light and dark phases, which is exactly the moire fringes of non-diffractive light. The non-diffractive beam simulated from the formula is shown in the diagram.

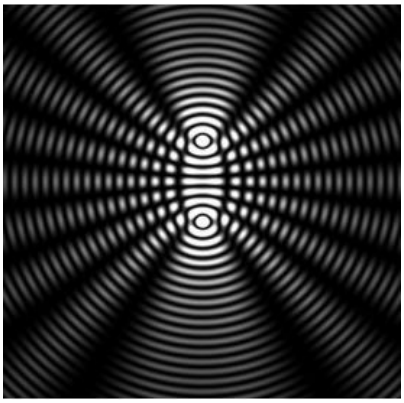

Figure 2: Two beams of non-diffractive light interference superposition

2.3. Measurement scheme

As shown in figure 3, the device structure of the automatic surface detection system for solar concentrator is measured by linear motion and rotation motion. The probe consists of a laser, a collimating beam expander, an axial cone mirror and a splitter prism 1. The laser emitted from the He-Ne laser is illuminated to the axial cone mirror by the collimation system, and then a non-diffractive beam with invariable shape of the central spot is formed. The beam is divided into two beams by the splitter prism, in which the transmitted non-diffractive light is the object beam. The object beam is directly illuminated to a point on the condenser, and the reflected beam changes the angle at which the light is emitted through a precise angle modulator. A non-diffractive moire fringe is formed after the beam of light which is emitted from the angle regulator and the combiner and the reference beam reflected from the splitter prism converge. The magnitude of normal error can be determined according to the shape and number of moire stripes. The non-diffractive moire fringes have the characteristics of amplification, which can further improve the measurement accuracy.

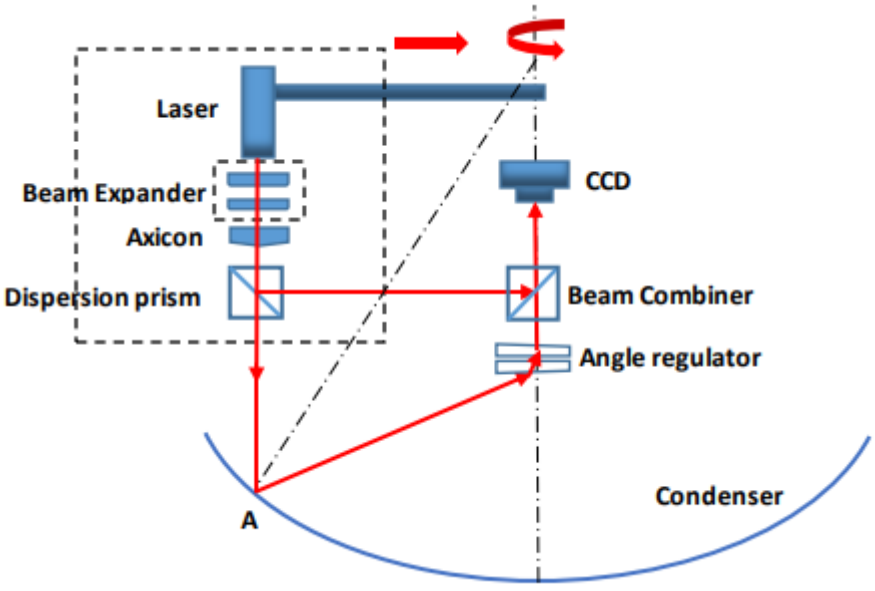

Figure 3: Structure diagram of automatic measuring system for surface of solar concentrator

In the ideal case, the amplitude of the object beam is A_1 and the phase of the object beam on the image plane is φ_1. The amplitude and phase of the reference light are respectively A_2 and φ_2:

$$A_1 = a_1 exp(j\varphi_1) \tag{6}$$

$$A_2 = a_2 exp(j\varphi_2) \tag{7}$$

The complex amplitude of the synthesized light wave is:

$$A_3 = A_1 + A_2 = a_1 exp(j\varphi_1) + a_2 exp(j\varphi_2) \tag{8}$$

The synthetic light intensity is:

$$I_1 = (A_1 + A_2)(A_1 + A_2)^* = A_3 A_3^* = a_1^2 + a_2^2 + 2a_1 a_2 \cos(\varphi_1 - \varphi_2) \quad (9)$$

When the surface of the condenser is deformed, the complex amplitude of the reference light does not change. The phase of the complex amplitude of the object will change with the deformation of the condenser $\Delta\varphi$:

$$A_1 = a_1 exp[j(\varphi_1 + \Delta\varphi)] \quad (10)$$

The light intensity after deformation is:

$$I_2 = a_1^2 + a_2^2 + 2a_1 a_2 \cos(\varphi_1 - \varphi_2 + \Delta\varphi) \quad (11)$$

By subtracting the intensity of light before and after deformation, the following are:

$$I = |I_2 - I_1| = 4a_1 a_2 \sin(\varphi_1 - \varphi_2 + \Delta\varphi/2) \sin(\Delta\varphi/2) \quad (12)$$

The light intensity difference I is a function of the phase change $\Delta\varphi$, and $\Delta\varphi$ changes with the deformation of the condenser. When $\Delta\varphi$ is $2n\pi$ or 0, the subtraction is zero, the intensity of light is invariant and the dark stripes appear. When $\Delta\varphi$ is $2(n+1)\pi$, there are still stripes and bright stripes after subtraction. The subtracted images distribute stripes related with $\Delta\varphi$, which contain the deformation information of the condenser. The error of the condenser can be obtained by the software analysis.

3. FTWARE SIMULATION

3.1. Simulation of testing system

Using ZEMAX optical simulation software, the corresponding optical path platform is built, and the following results are obtained by simulation.

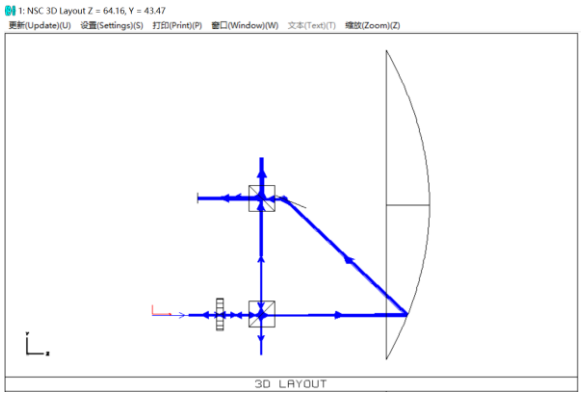

Figure 4: Ideal optical path simulation diagram

The results on the detector are observed with 10 million rays of light. The moire stripes produced by two non-diffractive beams with a certain optical path difference can be seen on the detector (figure 5).

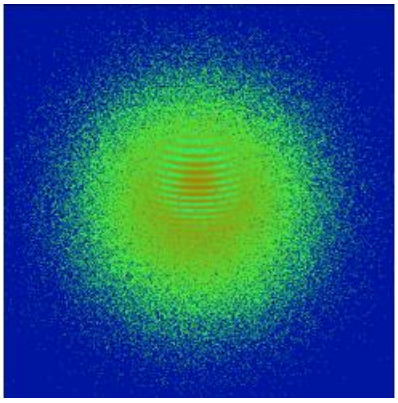

Figure 5: Moire fringes under ideal conditions

3.2. Simulation of Surface error

According to the above ideal light path, as shown in Figure 6, the concentrator is replaced with a plane mirror to simulate the fact that there is a shape plane error at a certain point of the solar concentrator.

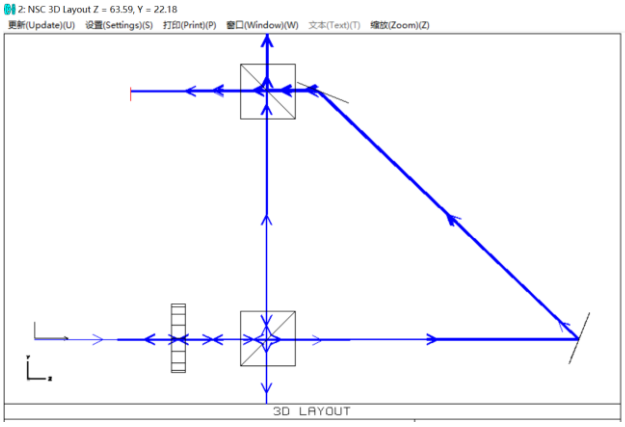

Figure 6: Simulation diagram of actual optical path

The interference fringes are shown in Figure 7

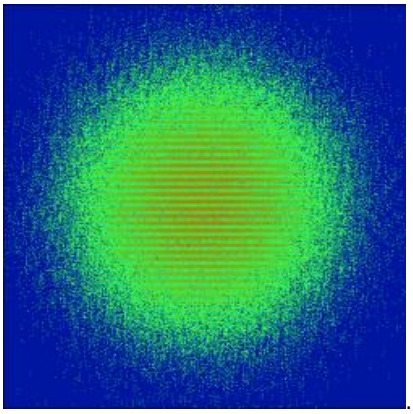

Figure 7: Moire fringes in practice

According to the ideal case obtained from figure 5 and figure 7 and the non-diffractive moire fringe of the actual case, the deformation of the solar concentrator at this point can be judged by subtracting the two images which is shown in Figure 8. After binarization and fitting, the 3D image of the surface of the concentrator can be obtained which is shown in Figure 9. According to the image, it can be determined whether the shape surface of the condenser meets the requirements of production and application.

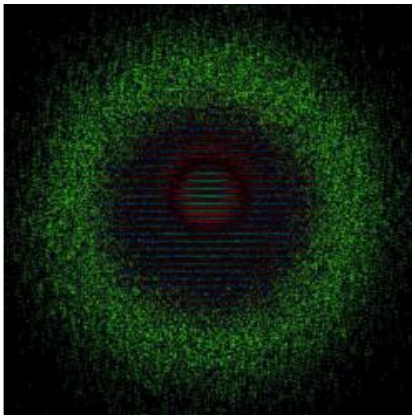

Figure 8: Subtracted image

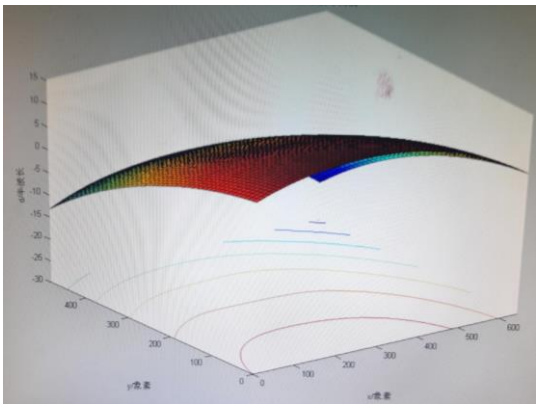

Figure 9: 3D image

4. CONCLUSION

The elliptical light spots reflecting the parabola of the same radius are obtained by CCD camera. The image processing system splices each circle of images and restores the paraboloidal model. The shape error can be obtained by analyzing the moire fringes of the non-diffractive light. By using this method, we can accurately find the exact position of the shape difference and reduce the loss of light caused by the reflector surface error in the process of concentrating light.

5. ACKNOWLEDGEMENT

This work was supported by the National Natural Science Foundation of China (Nos. 51405143, 51575164), open Foundation of Hubei Collaborative Innovation Center for High-efficient Utilization of Solar Energy (No. HBSKFZD2014007)

6. REFERENCES

Xiao J, Study of surface shape measurement of the solar concentrator mirrors in solar thermal power applications[D].University of Chinese Academy of Sciences, 2015.

Wang Z, Wang Q, Meng H, Wang X. Surface roughness measurement based on non-diffracting beam triangulation and gray evaluation[J].Journal of Applied Optics,2011,32(5):909-912.

Zhao B, Li Z. Diffraction property of an axicon in oblique illumination[J].Applied Optics, 1998,37(13):2563-2568.

Zhongsheng Z, Qinghua L, Xuanze W,et al. Measurement of four-degree-of-freedom error motions based on non-diffracting beam[J].Optics Communications,2016,366:168-173

Zhai Z, Zhao B. Experiments and Theoretical Analyses of Non-Diffracting Beams Interference[J]. ACTA OPTICA SINICA,2008,27(8):1503-1507

279: Does technology innovation through "environmental mountains" really exist?

Taking the Central Five Provinces as examples

Yanhua ZHANG [1,2,3], Wenbin LI [1], Weixiang LIU [1]

[1] the College of Economic and Management, Hubei University of Technology, Nanli Road No.28, Hongshan District, Wuhan City, Hubei Province, China, 2039076986@qq.com
[2] the Research Center of Circular Economy Development in Hubei, Nanli Road No.28, Hongshan District, Wuhan City, Hubei Province, China
[3] the Collaborative Innovation Center of Regional Industrial Ecology Development, Hubei University of Technology, Nanli Road No.28, Hongshan District,Wuhan City, Hubei Province, China

As the country's grand strategy, the rise of central China requires a certain industrial structure. To a large extent, the development of industry is the only way to achieve the rise of central China. However, the long-term dual economic structure of industrial development often means more large-scale energy. Demand and deeper environmental pollution deviate from what is explicitly stated in the 13th Five-Year Plan such as the "No Yangtze River Development" and "Ecological Civilization Construction". At present, the drastic increase in water pollution and air pollution that accompany the rapid development of the central industry seems to be able to prove in fact that industrial development is indeed an important factor in causing environmental pollution. We cannot help but ask that industrial development has aggravated environmental degradation in the central region. What? Is it possible for industrial development to co-exist with environmental protection?

Based on the research, we use the environmental externalities to characterize the complex industrial development impacts of the central industry from 2004 to 2016, and empirically examine the impact of regional technological innovation and industrial development on regional environmental pollution. The results of the study show that: Due to the existence of spatial spillover effects, the coupling effect between industrial development and technological innovation has a nonlinear relationship with environmental pollution, showing an inverted "U" type correlation. The current central region (except Jiangxi) has crossed the inflection point at the right end of the model. At an important threshold for industrial transformation, industrial development or reduction in environmental pollution.

Keywords: industry development; technological innovation; correlation effect, environmental pollution

1. INTRODUCTION

Experience has shown that industry promotes economic development, but it is one of the major sources of environmental pollution in today's society; however, according to the empirical analysis of relevant scholars, the synergies brought about by industrial development and scientific and technological innovation may bring about environmental effects. Positive externalities affect this conflict, perhaps conflicting, and perhaps have a deeper correlation.

Some studies show that the externalities brought about by the development of industries certainly exist, but in the different stages of industrial agglomeration, the externalities they exhibit are not the same. This shows that there are more complex mechanisms for industrial agglomeration and environmental pollution. The connection, we know that industry tends to cluster in the process of development, through analogy, then in the process of agglomeration of industrial industry, is there a connection that we do not know? How does the industrial development mechanism for industrial pollution actually work?

In order to promote the coordinated development of industrial development and regional environmental protection, the hypothesis in this paper is that there is a certain non-linear relationship between industrial development and environmental pollution. In the different stages of industrial development, externalities will obviously differ. This paper verifies that there may be a turning point in Chinese externalities and calculates the period when this turning point occurred. This inflection point is quite uncertain and may change accordingly with changes in some factors. This article explores its factors on the premise of this assumption and puts forward corresponding hypotheses:

Hypothesis 1: With the development of the industry, the degree of industrial agglomeration will rise to varying degrees, and at the same time the indicators of scientific and technological innovation will greatly reduce the peak value of the environmental Kuznets curve.

Under the principle of large-scale environmental protection policies, governments at all levels have established a series of industrial parks and conducted a certain amount of pollution control. By 2017, 51 industrial parks nationwide had officially entered the pilot phase of low-carbon industrial parks. The relevant person in charge of the National Development and Reform Commission stated that pilot demonstrations of low-carbon cities, parks, and enterprises should be further deepened. After more than three years of trials, the industrial structure of the participating pilot parks is constantly being optimised and adjusted, while the economy maintains rapid development. Its total energy consumption and carbon emission values and intensity values have declined to varying degrees, and some have reached the advanced level of the domestic industry. Take Yangluo Development Zone as an example: In the past, "garbage dumps" turned into "treasure bowls", and the green recycling of resources is a major industrial feature of Yangluo Development Zone to create low-carbon industrial parks. Greenmem Corporation, located in Wuhan Yangluo Economic Development Zone, is a world-renowned environmental protection enterprise. In the past, electronic waste and used batteries were discarded at will in the city, but now it has established a waste battery system covering 58,000 square kilometers and a population of 38 million. , is a classic example of "urban mines." According to the Kuznets curve, the development of the industry will bring about technological innovation effects, which will gradually reduce the intensity of environmental pollution per unit of GDP, until it reaches a critical value will in turn improve the environment, then the level of scientific and technological innovation will certainly be able to influence the level of The level at which this critical value occurs.

This means that under the continuous development of the industry, the degree of pollution in the environment will be reduced, and as the technology progresses, the peak value of the EKC curve will be further reduced.

Hypothesis 2: The social reform process can greatly reduce the peak of EKC

The social reform force has always been one of the leading forces of environmental protection, and a strong policy can significantly reduce the peak of EKC. When studying the data, we found that SO2, which is our pollution standard, emerged in 2015-2016. The faults, such as SO2 emissions in all five central provinces in 2015 were about 3,428,800 tons, but in 2016, the SO2 emissions in the five central provinces had a sharp drop of nearly half to 16.755 million tons. This is an unbelievable idea. In view of the availability of data, we have temporarily failed to obtain specific changes in the number of employees in related industries in 2016, but it is foreseeable that policy measures have played a crucial role in this period, during this time period, The "Air Pollution Prevention Law" newly revised on January 1st was formally implemented. This is also the first single method revised after the new "Environmental Protection Law" passed. Therefore, this article speculates that the social reform process can greatly reduce the peak of EKC under the stimulation of policy measures.

2. BACKGROUND

Since the end of the last century, different scholars have started to study the issue of environmental pollution from the perspective of foreign direct investment and economic development. Panayotou (1993) has for the first time made the relationship between environmental quality and social benefits an environmental Kuznets curve (EKC): economic. Initial development will lead to increased environmental pollution, but when the economic development breaks through a "turning point", environmental pollution will be alleviated. Crossman and Krueger (1991, 1995) analyzed the nonlinear relationship between pollutants and income in the Kuznets Curve. Jaliland Mahmud (2009) demonstrated the existence of the "inverted U-shape" of the environmental Kutznets through different models and methods. The impact of foreign investment on the one hand has effectively promoted the development of the local industrial economy and on the other hand brought about certain environmental problems. At present, there are mainly two kinds of assumptions: "Pollution Shelters", pointing out that due to environmental taxes and other reasons, The negative environmental externalities and "pollution paradise effect" caused by the development of the industry have pointed out that the development of the industry has weakened the original negative externality problem and the positive externality of the environment has emerged.

Many scholars have studied the environmental externalities formed by the industry and have taken some research progress. However, the research conclusions are quite different. At present, there are three mainstream views:

1. Industrial agglomeration brings negative environmental externalities. Zhang Ke and Wang Dongfang (2014) used the spatial simultaneous equations model to empirically analyze the mechanism between China's economic agglomeration and environmental pollution, and found that economic agglomeration exacerbated environmental pollution and brought negative environmental externalities.

2. Industrial agglomeration to improve environmental pollution. By constructing a spatial economic growth model, Dao-ZhiZengetal. (2009) found that manufacturing agglomeration helps to reduce the “pollution shelter” effect. Li Xiaole (2014) used a threshold model to verify the non-linear relationship between industrial agglomeration and environmental pollution and took the market level as a threshold variable for analysis. He believes that at a low level of marketization, industrial gatherings lead to environmental pollution, but as the level of marketization reaches a certain threshold, industrial agglomeration will improve the environment. Lu Ming and Feng Hao (2014) constructed a population-scale gap model between prefecture-level cities in various provinces from 1993 to 2006 to reflect the level of spatial agglomeration within the provincial-level administrative regions, arguing that spatial agglomeration of economic activities is conducive to reducing the unit GDP industry. Pollution emission intensity. Yang Renfa (2015) used the panel data of 227 cities in China to adopt the threshold regression method and foreign direct investment as the threshold variable. The empirical results show that there is an “inverted U-shaped” nonlinear relationship between industrial agglomeration and environmental pollution.

3. The relationship between industrial agglomeration and environmental pollution cannot be determined. Li Weina et al. (2010) used panel data from 30 manufacturing industry segments in China to analyze that the relationship between China's manufacturing agglomeration and air pollution is “N”. At present, China’s atmospheric pollution increases with the increase in manufacturing concentration. Stage, but the intensity of pollution gradually declines. Yan Fengzhu et al. (2011) investigated the Chinese manufacturing industry using a panel-corrected error model and concluded that industrial agglomeration will effectively reduce pollution emissions in the short term, but there is no causal relationship in the long term. Tan Jiayin and Zhang Yaohui (2015) used panel data of Guangdong Province to find that VEC models have a negative externality effect on industrial improvement in the short term, but there is no inevitable causal relationship between long-term industrial agglomeration and environmental pollution.

3. METHOD

3.1. Model design

In order to examine the relationship between industrial development, technological innovation and environmental pollution, explore industrial development, and test the coupling between industrial development and technological innovation, this paper builds the following model (1) on the basis of linearity, and On the basis of 1), the model of the square model of industrial development was inserted (2), and the interactive items of technological innovation and industrial development were inserted on the basis of model (2). The following three models were obtained:

$$polu_{i,t-1} = \beta_0 + \beta_1 eco_{i,t-1} + \beta_2 v_{i,t-1} + \beta_3 GI_{i,t-1} + \beta_4 tech_{i,t-1} + \beta E_{i,t-1} + \varepsilon_{\mathrm{it}} \quad (1)$$

$$polu_{i,t-1} = \beta_0 + \beta_{11} eco_{i,t-1} + \beta_{12} v_{i,t-1} + \beta_{13} v_{i,t-1}^{\ 2} + \beta_{14} GI_{i,t-1} + \beta_{15} tech_{i,t-1} + \beta_{16} E_{i,t-1} + \varepsilon \quad (2)$$

$$polu_{i,t-1} = \beta_0 + \beta_{21} eco_{i,t-1} + \beta_{22} v_{i,t-1} + \beta_{23} GI_{i,t-1} + \beta_{24} tech_{i,t-1} + \beta_{25} E_{i,t-1} + \beta_{26} v_{i,t-1} \bullet tech_{i,t-1} + \varepsilon \quad (3)$$

Where:

Polui,t-1= level of environmental pollution

i= province

t = time

eco= economic development

v= level of industrial development

GI = government's intensity of environmental input

E= energy intensity

tech =a indicator of technological innovation

ε = error term

Referring to the models of Zeng and Zhao (2009) and Yuan et al. (2015), this paper sets the model as a fixed-effect panel data model, in order to reduce the errors caused by the endogeneity of the model. All lags behind. Where i is the province and t is the time. Polu represents the level of environmental pollution; eco represents the level of regional economic development; v represents the level of industrial development; GI represents the government's intensity of environmental input; E represents energy intensity; tech is an indicator of technological innovation; ε is an error term.

3.2. Data processing and indicator description

Based on the availability of data, the data from the central five provinces from 2004 to 2016 can be directly calculated. The raw data comes from the statistical bulletins of various provinces and cities, the website of the International Bureau of Statistics, and the statistical yearbooks of provinces and cities. Statistical Yearbook, and China Economic Census Yearbook, descriptive statistics for each variable are as follows:

Table 1: Descriptive statistics

Variable		Mean	Std. Dev.	Min	Max	Observations	
polu	overall	745449.6	335502.2	276888.2	1624000	N =	65
	between		321481.6	509764.8	1297697	n =	5
	within		169084.2	-138624.3	1071753	T =	13
eco	overall	16366.04	9330.784	3456.7	40471.79	N =	65
	between		5074.342	10170.08	23710.9	n =	5
	within		8132.805	1208.938	33126.94	T =	13
E	overall	8558761	304927	4320599	1.528445	N =	65
	between		0.0942015	0.7386849	0.9664164	n =	5
	within		0.2928658	0.4224315	1.45984	T =	13
v	overall	7835.94	4631.171	1566	19276	N =	65
	between		2300.441	5231.769	11457.23	n =	5
	within		4141.01	-1642.291	15654.71	T =	13
tech	overall	34383.85	33965	2685	172552	N =	65
	between		14639.07	14583.77	54411.46	n =	5
	within		31296.97	-17084.62	152524.4	T =	13
GI	overall	175934.5	122172.5	39478	651538	N =	65
	between		77150.69	82596.62	292118.5	n =	5
	within		100448.6	8935.923	535353.9	T =	13

The panel data collected data of the five provinces (Anhui, Jiangxi, Henan, Hubei, and Hunan) in the central region, among which:

(1) Environmental pollution level (polu): The evaluation of industrial pollution indicators is too complicated, but a significant indicator of industrial pollution is the air pollution index of SO2. Here, SO2 is used to evaluate the environmental pollution of industrial systems.

(2) Technology innovation (tech): The use of patent applications to measure the level of scientific and technological innovation. Because the amount of patent application acceptance directly reflects the level of technological innovation that the company is free from outside intervention, and there is a time lag between patent applications and authorizations, this paper uses patent acceptance indicators rather than patent authorization indicators.

(3) Other control variables: 1. The regional economic development level is measured by GDP per capita in each region; 2. Energy intensity (E): Because the energy intensity avoids the description deviation of local energy use due to the use of only single energy data, so This article uses energy to measure the level of energy use in an area; 3. The government's input to the environment (GI): The government's investment in the environment must be a direct factor influencing the level of environmental pollution. This article selects the amount of investment in the treatment of industrial pollution in each region to measure; 4. Industry Development Level (V): Use the output value of the secondary industry in each region to measure it.

4. MEASURMENT RESULTS AND ANALYSIS

4.1. Verification of hypothesis one

Based on the econometric model constructed above, the Hausman test was performed on the fixed effect model and the random effect model, and the corresponding panel regression method was selected based on the test results. From Table 2, we can see that each model is basically in a significant state, and the research results are basically consistent with expectations.

Table 2: Results of Panel Regression Data for Five Provinces in Central China from 2004 to 2016

	(1)	(2)	(3)
	m1	m2	m3
VARIABLES	polu	polu	polu
eco	20.55**	28.35***	19.26**
	(9.308)	(8.834)	(7.968)
E	900,725***	1.033e+06***	1.000e+06***
	(143,502)	(137,080)	(124,541)
V	25.73	97.34***	60.17***
	(17.97)	(26.42)	(17.00)
tech	-4.751***	-5.482***	6.910**
	(1.292)	(1.204)	(2.690)
GI	0.192	0.493	0.654**
	(0.351)	(0.334)	(0.316)
V2		-0.00449***	
		(0.00129)	
V*tech			-0.00114***
			(0.000239)
Constant	-433,687**	-893,054***	-820,191***
	(175,985)	(208,817)	(171,086)
Observations	65	65	65
R-squared	0.608	0.675	0.718

Standard errors in parentheses *** p<0.01, ** p<0.05, * p<0.1

Table 3: Hausman test

	(b)	(B)	(b-B)	sqrt(diag(V b-V B
Coefficients	FE	RE	Difference	S.E.
eco	-14.8698	26.62091	-41.4907	10.98045
eco	-74650.7	948993.2	-1023644	295173
v	2.803674	42.02845	-39.2248	9.186871
tech	2.846675	2.027788	0.818887	2.169102
GI	0.133776	0.643965	-0.51019	0.116911
vt	-0.0002	-0.00073	0.000533	0.000227
cons	1007505	-721302	1728807	485966.4

Prob>chi2 = 0.0003 p-value=0.0003 Should use fixed-effect model

Model (1) The linear relationship between innovation and pollution has resulted in significant results. It shows that the role of industrial development in the environment is destructive and has strong pollution characteristics. The coefficient of industrial development is 25.73, and the average industrial development is increased by 100 million yuan. Yuan, the emission of sulfur dioxide increased by 25.73 tons. Scientific and technological innovation has had

a significant positive effect on the environment with an influence coefficient of -4.7751, which can effectively control the deterioration of the environment. This to a certain extent supports the important position of technological progress in the process of pollution control and control.

The model (2) introduces the square of industrial development and examines the nonlinear relationship between industrial development and environmental pollution. At the 10% level of significance, the square of the industrial development has a negative sign on the impact coefficient of environmental pollution, indicating that the industrial development and environmental pollution are in an inverted “U” type relationship. With other factors unchanged, before the output value reached 1.083964 billion yuan, industrial development was positively related to environmental pollution, and industrial development exacerbated environmental pollution. Only when the production value crossed the threshold of 1,083.64 billion, can industry development be possible to the environment. Pollution has played a significant inhibitory role and has become an effective mechanism to promote pollution reduction. According to the original data, Hubei's secondary industry output value reached 1.4375 trillion yuan in 2016, Hunan's secondary industry output value reached 1.371 trillion yuan in 2016, and Henan's secondary industry output value reached 1.92276 trillion yuan in 2016, Anhui Province in 2016. The output value of the secondary industry has reached 1.159 trillion yuan, and the output value of the secondary industry in Jiangxi Province has reached 883 billion yuan in 2016. Except for Jiangxi Province, the central region has generally been on the right of the inverted U-shaped curve, and the level of development has reached the level of reducing pollution. Emission threshold.

In Model (3), we inserted the interaction terms of industrial development and technological innovation, and measured the coupling of industrial development and scientific and technological innovation. The study showed that interaction terms and environmental pollution have a significant negative relationship, which to a certain extent It proves that technological innovation plays a major role in the process of industrial development.

When the level of industrial development is low, the government and industrial enterprises will not pay attention to the environmental pollution caused, because at this time, the competitiveness is insufficient, and it is necessary to damage a certain degree of environmental externalities to support the initial period of difficult development. In the middle period of development, even if companies are inclined to environmental protection, they will not be able to effectively reduce the environmental pollution caused by capital, infrastructure, and technology. Until the industry accumulates to a certain degree, it may be due to knowledge spillovers. As a result, the utilization rate of raw materials is further increased. At the same time, in order to meet the increasing environmental regulatory requirements, companies will invest a certain amount of funds in environmental pollution control, which may lead to a reduction in corporate R&D investment. At this time, pollution control does not exceed its Pollution levels, pollution costs are still high, and the positive externalities of the environment caused by industrial development offset the negative externalities of the environment. With the development of industrial processes, the infrastructure has been continuously improved and the industrial technology is continuously updated. The consumption of industries is becoming less and less. , The system of industries has continued to diversify and finally arrived In terms of threshold, this threshold is mainly broken by the momentum of technological innovation, and continuously reducing its pollution effect, even reducing its original pollution, realizing the more developed industries and the better environment, which is verified to some extent. Our hypothesis 1. The continuous advancement of technology has effectively reduced the peak value of the environmental Kuznets curve.

4.2. Examination of hypothesis 2

Another problem worth pondering in the last model is that the coefficient of GI is not what we expected to be a negative value. On the contrary, this value has always been positive. According to the logic of pure data, the government's environmental protection investment plan has aggravated the environment. Pollution is obviously impossible. The explanation we give for this issue is probably because the government's environmental investment plan is often changed with the severity of the pollution, and secondly because there is a certain degree of stickiness. The effect, the real and other environmental protection planning, and the effective reduction of environmental pollution, the role of environmental planning is shared among other variables or errors.

At the same time, considering the major role that policy factors may play in the analysis, we have analyzed the data of pollution emissions over the years and plotted the relevant line charts, as shown in Figure 1:

Figure 1: Pollution emission trend map of five provinces

1=Hubei 2=Hunan 3=Henan 4= Jiangxi 5= Anhui

According to the table showing that the change of polu is still in a smooth stage before 2015, and according to the data, there was a landslide-like decline during the period 2015-2016, which shows that there may be a time node during this period because we did not enter The factors have led to this major downturn. This factor is currently viewed as a major reason that apart from the fact that large technological innovations have led to a rapid decline in industrial pollution, there is only one reason that some large polluting enterprises have disappeared. There is no particularly unusual volatility in the second output value between 2015 and 2016. The answer is immediately apparent. This is most likely due to policy reasons that led to a large drop in the intensity of this environmental release, but for insurance reasons, we do a comparative analysis to verify our ideas.

Table 4: Results of Panel Regression Data for Five Provinces in Central China from 2004 to 2015

	(1) m1	(2) m2	(3) m3
VARIABLES	polu	polu	polu
eco	28.53***	33.49***	26.62***
	(8.341)	(8.279)	(7.974)
E	884,338***	974,374***	948,993***
	(123,261)	(124,337)	(119,996)
v	16.69	64.08**	42.03**
	(15.58)	(25.03)	(17.81)
tech	-5.153***	-5.546***	2.028
	(1.404)	(1.358)	(3.098)
GI	0.579*	0.648*	0.644*
	(0.341)	(0.329)	(0.326)
v2		-0.00294**	
		(0.00125)	
vt			-0.000729**
			(0.000284)
Constant	-505,549***	-794,426***	-721,302***
	(151,932)	(190,378)	(167,234)
Individual fixed effect test	Fixed	Fixed	Fixed
Observations	60	60	60
R-squared	0.700	0.729	0.733

According to the results of the Hausmann test, both here and in the above table are fixed functions, and the significance is also quite obvious. Other values are not significantly different from the above table. The level of

technology is significant, the coefficient is -5.153, which is greater than In the previous model, by calculating the inflection point, we found that the turning point before 2015 was at 1.0898 trillion yuan, which was much higher than the figure of 1,083.964 billion yuan added in 2016, and the new revision that appeared as a background on January 1, 2016 The "Air Pollution Prevention and Control Law" was formally implemented. This is also the first single method modified after the "Environmental Protection Law" was passed. It can be regarded as the main reason for this node, which to a certain extent supports our hypothesis.

5. CONCLUSIONS AND SUGGESTIONS

Research conclusions using the panel data of the five provinces in the central part of China, the empirical analysis was made on the impact of industrial development, technological innovation capabilities, and the associated effects of industrial development and technological innovation on the intensity of environmental pollution emissions and the total amount of pollution emissions. At the same time, the development of the industry was examined. The key role of technological innovation in the mechanisms that affect environmental pollution (intensity and total volume), the conclusions of this paper are mainly in three aspects: First: Industry development and environmental pollution are inverted "U"

When the level of development is low, industrial development aggravates environmental pollution due to the limitation of objective conditions; and as the level of development continues to increase and the scale of development continues to expand, the level of agglomeration crosses a specific “threshold value,” and industrial agglomeration Positive environmental externalities offset negative externalities and become an effective mechanism for improving environmental quality. Second, the associated effects of industrial development and technological innovation have a significant inhibitory effect on environmental pollution, which explains the role of industrial development in environmental pollution. Technological innovation has played a key role and has affected the position of the "inflection point" in the relationship between the two; Thirdly, it calculated the turning point of the development of the industries in the central region and found that the central five provinces (Anhui, Jiangxi, Henan, Hubei, Hunan) Outside of Jiangxi, all crossing the inflection point, the positive externalities of industrial development are constantly highlighted. Based on the current development status of the industrial industry, it is possible to clarify the development tone of the central region in the coming period of time:

1) Adhering to the national strategy of rejuvenating the country through science and education. Related environmental protection projects and related industries are inseparable from advances in science and technology, and the support of universities. Schools and enterprises are more closely linked, and from the theory to the practice, one-stop environmental protection is carried out. Industrial planning can make some of the original heavily polluting industrial projects significantly improved, so that the original clean production process can be better promoted as an example, so that different companies can communicate with each other to form a cluster, and ultimately better protect the environment in the middle.

2) Adhere to the prevention and control of environmental pollution, because a "Air Pollution Prevention and Control Law", at least in the air pollution industry has emerged a node, it can be seen that the effectiveness of the policy for the environment, can have a law to follow, a large number We control the number of high-pollution companies and raise the corporate threshold. Based on the economic development in 2015-2016, we can be confident that not only will this not reduce economic activity, but it may also be due to the elimination of old companies that cannot keep up with the rhythm and provide new businesses with more There is ample room for development. As a result, the government can appropriately improve the company's environmental supervision, which is beneficial to enhance market vitality.

3) If the industrial park is reviewed, if it is not intentionally deregulating, industrial agglomeration can, to a certain extent, improve the efficiency of resource use and reduce environmental pollution. However, this requires a more rigorous design. How to make companies with strong symbiosis complement and benefit each other reducing the environmental impact of the pollutant discharge is a big problem. At present, some industrial parks have falsely placed a shelf on an industrial park. However, there is no way to achieve significant benefits. These industrial parks should be reduced by preferential policies and support in order to facilitate the development of industry with development potential and a clean development mechanism.

6. REFERENCES

Panayatou, T. , Empirical tests and policy analysis ofenvironmental degradation at different stages of economic devel－opment[R]. Geneva：Working Paper, 1993.

Grossman GM, Krueger AB. EnvironmentalImpacts of the North American Free Trade Agreement [R]. Cambridge: Working Paper, 1991.

Grossman GM, Krueger AB. EnvironmentalImpacts of the North American Free Trade Agreement [R]. Cambridge: Working Paper, 1991.

Jalil A, Mahmud S F, Environment Kuznets Curve for CO_2 Emissions：a Cointegration Analysis for China [J]. EnergyPolicy, 2009, 37（12）：5167-5172.

Zhang K, Wang D-F. The Interaction and Spatial Spillover between Agglomeration an Pollution[J]. Chin Ind Econ, 2014（6）：70-82.

Zeng D Z, Zhao L. Pollution Havens and Industrial Agglomeration ［J］. Journal of Environmental Economics and Management, 2009, 58（2）：141-153.

Li Y. An Empirical Analysis Based on Marketization · Industrial Agglomeration and Environmental Pollution[J]. Statistical and Study, 2014（8）：39-45.

Li W-N, Yang Y-F et al. Manufacturing agglomeration, air pollution and energy saving and emission reduction[J]. Eco nomics and Management, 2010（9）：36-44.

Investigation on the relationship between industrial agglomeration development and environmental pollution -- Evidence from China's manufacturing industry[J]. Studies in Science of Science， 2011（1）：79-83.

Tang, L. Investigation on the relationship between industrial agglomeration development and environmental pollution -- Evidence from China's manufacturing industry[J]. Economics and Management, 2015（6）：82-89.

Yuan Y-J. Internal relations between industrial agglomeration, technological innovation and environmental pollution[J]. Studies in Science of Science， 2015, 33（9）：1340-1347.

Zeng D-Z, Zhao L. Pollution havens and industrial agglomeration[J]. Journal of Environmental Economics and Management . 2009 (2)

283: Research on bicycle rear hub power generation system

Zheng ZHANG[1], Lei DONG[2], Zhefu DU[3], Jiang WANG [4]

[1] Hubei University of Technology, Wuhan, Hubei, 271998085@qq.com
[2]Hubei University of Technology, Wuhan, Hubei 1139018553@qq.com
[3] Hubei University of Technology Wuhan, Hubei, duzhefu@vip.qq.com
[4]Hubei University of Technology, Wuhan, Hubei 1940847553@qq.com

In order to realize the self-supply of the on-board controller of a shared bicycle, a rear hub rotation power generation system is designed and tested and analyzed on a shared bicycle. The experimental system consists of a power generation system, a charging system, and a rectifying-filtering-regulating system. Each of the three subsystems is analyzed and optimised separately, and finally the power generated by the power generation system meets the target of the loss of the on-board controller of the bicycle. Research shows that when the vehicle speed is 10km/h, the charging time is about 32 hours, and when the vehicle speed is 15km/h, the charging time is about 22 hours.

Keywords: Shared bike; Rear hub power; Recycled charging battery; generate power

1. INTRODUCTION

With the improvement of living standards, the way we travel is also constantly improving. For travels with slightly longer distances, we have basically adopted public transport, private cars or subways, but for travels that are not very far away, Bicycle travel is more convenient. As a result, shared bicycle (Faghih-Imani 2016) companies are now prevailing in the market, and many models such as OFO, MOBIKE, and HELLOBIKE have been developed. This type of bicycle has remote control, and it is inevitable to use batteries. If a one-time battery is used, it will inevitably lead to problems such as the need to replace the battery due to lack of power. In order to better solve this kind of problem, this paper has done a rear-wheel hub. Bring generators to power generation tests.

2. SYSTEM COMPOSITION

The design is divided into three parts according to its functional principle: power generation system, charging system and power supply system. The connection of the three parts to the bicycle is shown in Figure 1. Figure 1 shows the main body of the bicycle. The power generation system, charging system and power supply system are all concentrated in the rear hub of the bicycle. The internal hub of the integrated power generation system, charging system and power supply system is shown in Figure 2.

Figure 1: Overall structure

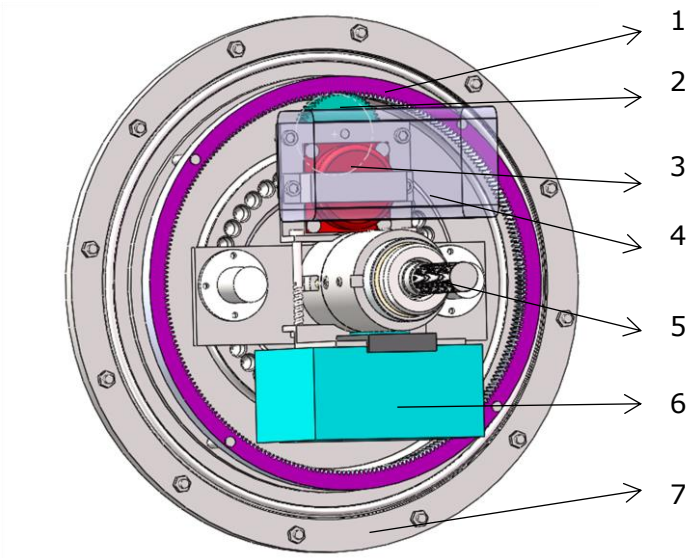

Figure 2: Hub inner view

1 - Internal gears; 2 - External gears; 3 - Micro three-phase alternators; 4 - Recyclable rechargeable lithium batteries; 5 - Center shafts; 6 - Vehicle mounted units; 7 - Sealing caps

2.1. Power system

The system includes a bicycle, a generator and corresponding fixtures, the main role of which is to charge the built-in recyclable rechargeable battery. As shown in figure 2, in the overall structure, only the 1-internal gear and the 7-wheel hub are relatively fixed to the rear wheel of the bicycle and rotate as the bicycle travels; while the other 2, 3, 4, and 5 are fixed with the bicycle frame. When riding, the chemical energy in the human body works by stepping on the bicycle to rotate the rear wheel of the bicycle. The rear wheel is fixed with the 7-hub and the 1-internal gear, so the rear wheel is synchronized with the 7-hub and the 1-internal gear. The 1-internal gear meshes with the 2-outer gear, so the 1-internal gear rotates the 2-external gear. In addition, the 2-outer gear meshes with the pinion on the 3-generator, so the 2-outer gear can drive the generator to work. In this way, the working principle of generating power by cutting the magnetic field generated by the generator through two gear shifts of the rear wheel is realized, and the generated electric energy is stored in the 4-rechargeable battery.

The entire rear hub was designed by solidworks2014 and made of aluminum alloy. There are two gear changes between the 1-internal gear and the generator shaft. Through structural analysis, it can be seen that the two-stage gear transmission relationship satisfies the following formula:

Equation 1: Transmission ratio calculation formula.

$$\mathrm{i} = \frac{r_1}{r_2} * \frac{r_2}{r_3} = \frac{r_1}{r_3}$$

Where:

i = Transmission ratio of rear or internal gear and generator

r_1 = the radius of external gear (mm)

r_2 = the radius of internal gear (mm)

r_3 = the radius of generator gear (mm)

The actual size of r_1 is 127.5mm. The actual size of r_2 is 27.5mm.The actual size of r_3 is 8.5mm.Therefore, The i of the transmission ratio is 15.

The generator speed and the rear wheel speed of the bicycle satisfy the following relationship:

Equation 2: Generator speed.

$$\mathrm{n}_3 = i * n_1$$

Where:

$\mathrm{n}_3 = \mathrm{Generator\ speed}\ (\mathrm{r/min})$

$\mathrm{n}_1 = \mathrm{Rear\ wheel\ speed}$ of the bicycle $(\mathrm{r/min})$

From the equation (2), it can be seen that one revolution of the rear wheel of the bicycle can drive 15 rotations of the generator shaft.

2.2. Charging system

The system includes a charge control circuit and a rechargeable battery (Chauque 2017) that can be recharged. The purpose of the system is to ensure that the battery is safely charged and synchronized to control the state of the battery including the rectification circuit (Kadir 2015), wave filtering (Johnson 2014), regulated voltage circuit (Jung 2018). As lithium batteries are rechargeable batteries, and in order to prolong battery life, the unavoidable factors that mainly damage batteries are dealt with, that is, rectifying, regulating, and filtering circuits are added. Therefore, this part of the circuit is divided into rectification, filtering, voltage regulator circuit and charging circuit.

Rectification circuit, wave filtering and voltage stabilization

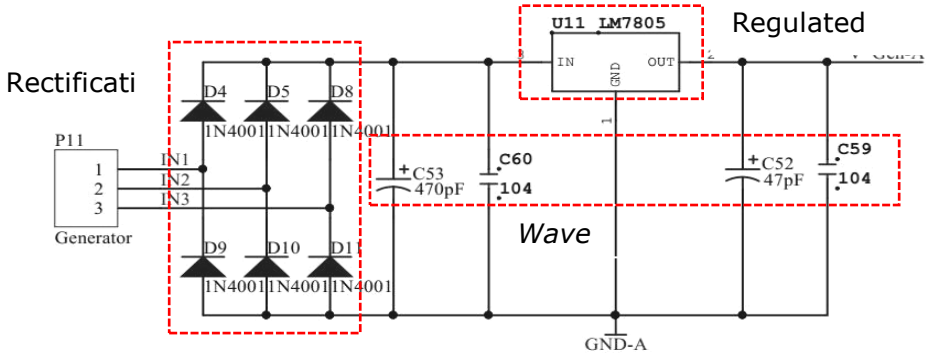

Figure 3: Generator generates current rectification, filtering, voltage stabilization circuit

As shown in Figure 3, this part of the circuit can be subdivided into three parts: rectification, filtering, and regulation. The rectifying circuit can convert the alternating current generated by the three-phase alternator into direct current. Here, the bridge rectifying circuit (Jin 2013) is composed of D4, D5, D6 and D9, D10, and D11 diodes. Because the bridge rectifier circuit can double the AC frequency, it is more conducive to the subsequent filtering. By adding a filter capacitor, AC components can be filtered out, so that the output AC tends to rectify. Finally, after passing through the LM7805 regulator chip, the output voltage can be stabilized at 5V and output to the charging circuit through the V-Gen-A port.

Charging circuit

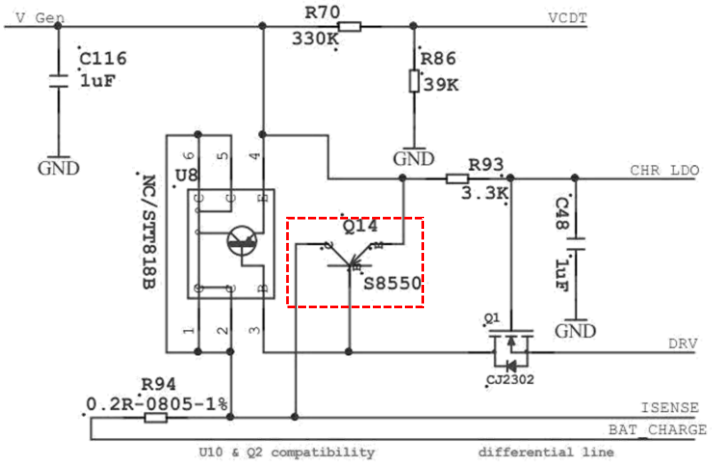

Figure 4: Charge and discharge management circuit

Lithium battery charge and discharge management circuit shown in Figure 4, which V-Gen and V-Gen-A port in Figure 3 connected. In order to facilitate the detection during the experiment, the VCDT is added to the charging voltage detection terminal, and the ISENSE is the charging current detection terminal. BAT_CHARGE is connected to the positive pole of the lithium battery to charge the lithium battery. In order to better protect the lithium battery and prevent the lithium battery from overcharging, a battery charging control circuit is designed. As shown in the box of FIGURE 4, the charging function can be turned on or off through the transistor Q14. When the charging is started, the base current of the transistor Q14 can be adjusted to control the current flowing through the CE terminal of the triode to realize the setting of the charging current.

3. EXPERIMENTAL TESTING AND ANALYSIS

3.1. Experimental program

Because it is difficult to stabilize the speed when riding a bicycle, it is not conducive to testing and analyzing power generation data. Therefore, an equivalent alternative method was chosen for experiments: In order to ensure the stability of the rear wheel speed of the bicycle, we put up the rear wheel of the bicycle and use the pulley to drive

the rear wheel to rotate. In this way, we can control the speed of the rear wheel of the bicycle by controlling the rotation speed of the pulley. Through the conversion of speed and speed, control the bicycle with a controlled speed pulley to test. If we want to test the bicycle's power generation data at a speed of 5km/h, that is, the vehicle speed is 5km/h. Since the diameter of the bicycle rear wheel is 0.61m, then the speed of the bicycle is r=5000/(60*pi*0.61). = 43.5r/min, we adjust the speed of the pulley so that the rear wheel speed is 43.5r/min. By the formula (1) that the transmission ratio is 15, then the generator speed is 653r/min. And so on, you can get the following table 1

Table 1: Bicycle speed and motor speed pairing table

Bicycle speed （km/h）	5	6.738	7.5	10	12	15	20
Bicycle rear wheel speed（km/h）	43.5	58.7	65.3	87.1	104.5	130.6	173.3
generator speed (r/min)	653	880	980	1306	1568	1959	2600

3.2. Rectifier and regulator circuit output test

By adjusting the rotation speed of the pulley, the rotation speed of the generator satisfies the rotation speed requirement of Table 1. In this case, we tested it, as shown in Table 2.

Table 2: Debug data

Bicycle speed（km/h） /generator speed (r/min)	Rectifier output		Regulated voltage output /LM7805	
	V(v)	I(mA)	V_{LM7805}(v)	I_{LM7805}(mA)
5km/h (653r/min)	4.850	123	3.517	77
6.738km/h (880r/min)	6.623	167	4.923	115
7.5km/h (980r/min)	7.694	192	4.973	148
10km/h (1306r/min)	10.480	252	4.979	205
12km/h (1568r/min)	11.930	270	4.976	230
15km/h (1959r/min)	15.817	333	4.989	270
20km/h (2600r/min)	18.405	400	4.965	300

According to the CJ78L05 (Arunkumar 2016) chip manual, when the regulator chip works normally, the input voltage range is 5---20V. It is known from Table 2 that when the vehicle speed is 5km/h, the rectified output voltage is 4.850V. At this time, the output voltage of the rectifying circuit cannot make the voltage regulator chip work normally; when the vehicle speed reaches 6.738km/h, the rectified output voltage is 6.623. When V, the regulator chip can work, can charge the lithium battery, at this time the charging current is relatively small, the charging speed is very slow; when the speed reaches 12km/h, the controller in the USB mode (non-lithium battery-powered) can Normal work; When the speed reaches 20km/h, the rectified output voltage is 18.405V, which is close to the high voltage of the regulator chip input, at this time the input and output current is relatively large, the charging speed is significantly improved; when the speed exceeds 20km/h The chip is turned off and the lithium battery cannot be charged.

3.3. Charging time test

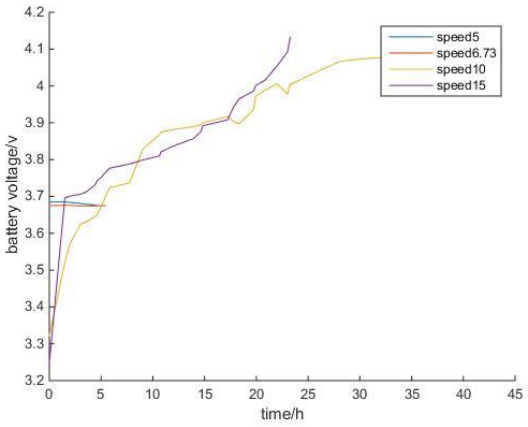

Figure 5: Charging time test at different speeds

As shown in Figure 5, the speed5 curve represents the lithium battery voltage variation at a bicycle speed of 5km/h. Similarly, the speed 6.73 curve represents the lithium battery voltage variation when the bicycle speed is 6.73km/h, and so on.

According to the characteristics of the lithium battery (Wang 2017) when the power is full, the voltage is about 4.1v, and when the voltage is less than 3.7v, the power is less than 20%. It can be seen from the curve situation in the figure that the battery voltage has almost no change at the vehicle speeds of 5km/h and 6.73km/h; at the speeds of 10km/h and 15km/h, the lithium battery voltage appears. Obvious change, when the speed is 10km/h, it takes about 30h to fill the battery, when the speed is 15km/h, it takes about 20h.

4. CONCLUSION

The design scheme achieves the purpose of the bicycle rear wheel dynamic power generation. When the bicycle speed is lower than 6.73km/h, the lithium battery cannot be powered normally. When the bicycle speed is 10km/h, the charging time is about 32 hours, and when the vehicle speed is 15km/h, the charging time is about 22 hours. When the speed exceeds 20km/h, the regulator chip will be disconnected and it will not work properly. The average person's normal riding speed is 12-20km/h, so the charging method is generally feasible.

In this system, there is indeed an improved part of the reference, for example, we can choose not to use the LM7805 regulator chip to exceed the limits of 6.73km/min and 20km/h cap; or we can improve the circuit when it is not normal for lithium batteries In the case of charging, the amount of electricity generated by the generator can be directly used for use. In addition, considering the portability of the device, lightweight composite material should be selected for the hub or frame material (Du 2007), and the utility model can be improved by folding the frame or easily disassembling the body component.

5. REFERENCES

Faghih-Imani A, Eluru N, 2016. Determining the role of bicycle sharing system infrastructure installation decision on usage: Vase study of Montreal BIXI system. *Transportation Research Part A*,94,685-698

Chauque S, Oliva FY, 2017. Lithium titanate as anode material for lithium ion batteries: Synthesis, posttreatment and its electrochemical response. *Journal of Electroanalytical Vhemistry,*799,142-155

Kadir EA, Hu AP, 2015. A bridgeless rectification circuit for Wi-Fi energy harvesting system. *Energy Conversion Congress & Exposition, 421-426*

Johnson KS, Shea TE, 2014. Mutual Inductance in Wave Filters with an Introduction on Filter Design. *Bell System Technical Journal*,4(1),55-111

Jung T-H, Gwon G-H, 2018. Voltage Regulation Method for Voltage Drop Compensation and Unbalance Reduction in Bipolar Low-Voltage DC Distribution System. *IEEE Transactions on Power Delivery*,33, 141-149

Jin C, Liu L, 2013. Simulation analysis of three-phase bridge rectifier circuit of aviation device. *International Conference on Communications,*2,407-409

Arunkumar CM, Mukesh Kumar PC, 2016.An experimental and simulation analysis off voltage regulator using the multisim.International. *Journal of Advanced Research*.,4,631-634

Wang L, Wang Z, 2017. Characteristic Analysis of Lithium Titanate Battery. *Energy Procedia*,105,4444-4449

Du X, Li W, 2007, Application of fiber reinforced composites for sports instruments[j]. *Fiber Composites*, 24(1):14-17.

287: An air quality prediction method based on LSA-SVR

Chunzhi WANG[1], Shang PAN[2], Heng SHI[3], Zhiwei YE[4], Linyu YAN[5]

[1] School of Computer Science, Hubei University of Technology, 28 Nan Li Road, Hongshan District, Wuhan, Hubei Province, China, chunzhiwang@vip.com
[2] School of Computer Science, Hubei University of Technology, 28 Nan Li Road, Hongshan District, Wuhan, Hubei Province, China, shinepans@live.com
[3] School of Computer Science, Hubei University of Technology, 28 Nan Li Road, Hongshan District, Wuhan, Hubei Province, China, chamarry@hotmail.com
[4] School of Computer Science, Hubei University of Technology, 28 Nan Li Road, Hongshan District, Wuhan, Hubei Province, China, weizhiye121@163.com
[5] School of Computer Science, Hubei University of Technology, 28 Nan Li Road, Hongshan District, Wuhan, Hubei Province, China, yanlingyu@hbut.edu.cn

1. INTRODUCTION

With the development of industry, urban air pollution has become increasingly serious. In the face of increasing air pollution, forecasts of air quality are particularly important. Air quality data is highly complex nonlinear time series, and traditional linear methods are difficult to obtain good prediction results. Support vector machine regression is based on statistical machine learning methods. It overcomes the problems of traditional methods and has good robustness and generalization ability. For SVM prediction problems, the choice of model parameters (penalty factor C, kernel function type, and kernel function parameters) has a crucial influence on the accuracy of the prediction results. How to select the model parameters to obtain the optimal prediction results is a hot issue in the current research field of support vector machines. At present, commonly used SVM parameter optimisation methods include genetic algorithm (GA), standard particle swarm algorithm (PSO), and ant colony algorithm (ACO). For SVR difficult to determine the optimal parameters, this paper proposes the LSA-SVR model, and then use the model to simulate the Wuhan Meteorological Station air quality index. Through simulation experiments on Wuhan historical weather data and error analysis and comparison with the traditional SVR and PSO-SVR models, it was found that the LSA-SVR method has a better predict effect.

Keywords: Air Quality Index, Forecasting, Support Vector Regression, Lighting Search Algorithm

In recent years, with the economic development and industrial production, atmospheric haze has become more serious. When people go out, they need constant breathing air to maintain their vital signs. Poor air quality will

cause discomfort in the human respiratory system, will cause respiratory-related diseases, and will also weaken the body's immune system. For this reason, accurately predicting the air quality index based on historical data of urban air quality is great significance.

The earliest prediction of air pollutant concentration was a multiple regression model (Yunhai, Zhang and Caitao et al., 2009).With the development of artificial neural networks, many scholars have studied the use of neural networks to predict the concentration of air pollutants. Russo A, Raischel F and Lind P G (2013) proposed an optimal neural networks with stochastic variables to predict air quality. Ling Yao, Ning Liu and Sheng Jiang (2012) proposed an artificial neural network to estimate multi-source PM2.5. Hui Xie, Fei Ma and Qingyuan Bai (2009) proposed an artificial neural networks to predict indoor air quality. Haiming Zheng and Xiaoxiao Shang (2013) proposed a RBF neural network model to predict the PM2.5 of atmosphere. The presented results are superior to multiple regression models. However, neural networks generally suffer from overfitting due to insufficient training data (Jianchuan Li, Guochuan Qin and Xisen Wen, 2002).

Support Vector Machine (SVM) (Christopher, J, C, Burges 1998) is an efficient learning machine that has good generalization ability in solving small sample and nonlinear problems and has been widely used in classification, time prediction, function estimation and other fields. However, in the prediction of multi-dimensional sample data, there are deficiencies in its efficiency and accuracy.

Wei Liu (2013) used the support vector machine to apply the time quality sequence of urban air quality. In 2016, Hu's PSO-SVM model was applied to air quality prediction (Shiqian Hu, Qianwen Jiang and Bin Lin et al., 2016). Hussain Shareef, Ahmad and Asrul et al., (2015) proposed a new heuristic optimisation algorithm, the Lightning Search Algorithm (LSA), which originated from thunder and lightning Natural phenomenon, through the probability distribution and tortuous characteristics of the discharge body, space discharge body and discharge body of the three kinds of discharges to create a random distribution function to solve the problem to be optimised. LSA has the excellent features of less adjustment parameters, high convergence accuracy and high ability of global search which have been applied in function optimisation, TSP (Traveling Sales-man Problem) optimisation and so on.

2. A LSA-SVR METHOD FOR AIR QUALITY FORECASTING

2.1. Support vector regression

Support Vector Regression (SVR) has good ability to solve linear and non-linear regression problems. Kuanyu Chen (2006) put forward a forecasting method of Taiwan stock exchange market weighted index which used evolutionary SVR. Kim K J (2003) found a method to forecast financial which can predict financial in time series by using SVR. Wei Wang, Yue Liu and Guozheng Li (2005) proposed a method to find out the connection between seismic activity and global seismic activity and sunspots by the model of SVR. Nanye L, Daniel G and Guiherme J et al., (2011) proposed a method to predict the precipitation. Based on the relative spatial delay coordinate reconstruction theory of chaotic dynamical systems and the non-linear fitting performance of support vector machines, He established a prediction model of precipitation based on support vector machines.

The basic idea of Support Vector Regression (SVR) to deal with non-linear regression prediction problems is to map the input sample data into the high-dimensional feature space by using the non-linear mapping $\varphi(\cdot)$ to transform the nonlinear problem into a linear problem.

Equation 1: Linear regression equation.

$$f(x) = \omega\varphi(x) + b$$

Where:

ω = Weight vector of high-dimensional feature space H

$\varphi(\cdot)$ = A mapping that maps the input vector x_i from the input space to the high-dimensional feature space H

b = Bias term of the linear regression equation

According to the principle of structural risk minimization, the $f(x)$ function should minimize the following risk function:

Equation 2: Risk function.

$$R(\omega) = \frac{1}{2}\|\omega\|^2 + C\sum_{i=1}^{n} l(f(x_i) - y_i)$$

Where:

C = The penalty factor

$l(f(x_i)-y_i)$ = A mapping that maps the input vector x_i from the input space to the high-dimensional feature space H

The penalty factor controls the degree of punishment for sample data that exceeds inaccuracy error. According to the characteristics of the air quality index regression prediction, the loss function of this paper selects the linear insensitive loss function. Its expression is:

Equation 3: The loss function

$$l(f(x_i)-y_i)=\max(0,|f(x_i)-y_i|-\varepsilon)$$

Where:

ε = The insensitivity coefficient

The insensitivity coefficient controls the accuracy of the prediction model. Due to the need to deal with data whose function $f(x)$ cannot be regressed with ε accuracy, the relaxation factors ξ and ξ^* are introduced, so the air quality regression prediction problem of the terminal building is converted into the solution to the following minimization problem under the constraint conditions:

Equation 4: The constraint function

$$R(\omega,\xi_i,\xi_i^*)=\frac{1}{2}\|\omega\|^2+C\sum_{i=1}^{n}(\xi_i+\xi_i^*),s.t.\begin{cases}y_i-\omega\varphi(x_i)-b\le\varepsilon+\xi_i\\ \omega\varphi(x_i)+b-y_i\le\varepsilon+\xi_i^*\\ \xi_i,\xi_i^*\ge 0\\ i=1,2,\cdots n\end{cases}$$

Applying the Lagrange multiplier method and the duality principle to equation 4 and introducing a kernel function :

Equation 5: Kernel function

$$K(x_i,x_j)=\varphi(x_i)\varphi(x_j)$$

It satisfies the Mercer condition, the dual problem of equation (4) is:

Equation 6: Duality of equation 4

$$\max\begin{cases}-\frac{1}{2}\sum_{i,j=1}^{n}(\alpha_i-\alpha_i^*)(\alpha_j-\alpha_j^*)K(x_i,x_j)+\\ \sum_{i=1}^{n}(\alpha_i-\alpha_i^*)y_i-\sum_{i=1}^{n}(\alpha_i+\alpha_i^*)\varepsilon\end{cases},s.t.\begin{cases}\sum_{i=1}^{n}(\alpha_i-\alpha_i^*)=0\\ \alpha_i,\alpha_i^*\in[0,C]\end{cases}$$

Where:

α_i,α_i^* = The Lagrange multipliers, they can be calculated by equation 5, when α_i or α_i^* not equal to 0, the independent variable in the sample is called support vector.

The regression function can be expressed as:

Equation 7: The regression function

$$f(x)=\sum_{i=1}^{n}(\alpha_i-\alpha_i^*)K(x_i,x_j)+b$$

Because Gaussian kernel function has the ability to deal well with the complex nonlinear relationship between input and output of samples, and has the advantages of high computational efficiency, fewer parameters and less calculation of parameters (Nanye L, Daniel G and Guiherme J, et al., 2011), Gaussian kernel function:

Equation 8: Gaussian kernel function

$$K(x_i,x)=e^{-\gamma\|x_i-x\|^2}$$

It is selected as the SVR input kernel function. Finally, the decision function as:

Equation 9: The decision function

$$f(x)=\sum_{i=1}^{n}(\alpha_i-\alpha_i^*)e^{-\gamma\|x_i-x\|^2}+b$$

2.2. Lightning search algorithm

The probability characteristics and tortuous characteristics of lightning discharge originate from lightning. In the common manifestation of lightning, the negative ground flash in the downward direction is one of the most studied natural phenomena in lightning research. The LSA proposed by Hussain Shareef is based on the descending negative streak-stage lead propagation mechanism, which is mainly achieved by mathematical modeling of three types of discharge bodies: transitional discharge bodies, space dischargers that are trying to become leaders, and leaded discharge body originating from the group of transitional discharge bodies and representing the best position. LSA solves the problem to be solved by creating a random distribution function based on the discharge probability characteristics and tortuous characteristics of the three types of discharge volume. LSA defines lightning fast particles based on a cascaded lead propagation mechanism as a discharge body. Assuming that each discharge body contains a step leader and a channel, the number of transition discharges represents the initial population size, and each discharge body represents a spatially random candidate solution to a set of problems to be optimised. In this study, the spatially optimal solution the optimise problem is the top position of the pilot discharge body where the maximum energy is currently located.

Under normal conditions, an electric discharge body passing through the atmosphere will lose its kinetic energy when colliding with molecules and atoms in the air. The speed of the electric discharge body can be expressed as:

Equation 10: The discharge body speed

$$v_p=[1-(\frac{1}{\sqrt{1-(\frac{v_0}{c})^2}}-\frac{sF}{mc^2})^{-2}]^{-\frac{1}{2}}$$

Where:

v_p = Discharge body current speed

v_0 = Discharge body initial speed

c = The speed of light

F = Constant ionization rate

m = Discharge body quality

s = The length of the passed path

The equation 8 shows that the speed is a function of the energy at the top of the step leader and the mass of the discharge body. When the mass is small or the travel path is long, the discharge body has almost no potential to be ionized or detected a large space. It can be only ionized or developed nearby space. Therefore, the LSA's exploration and development capabilities can be controlled by the relative energy of the cascade leader.

Another important feature of the discharge body is bifurcation, bifurcation is achieved by creating a symmetrical channel:

Equation 11: Creating a symmetrical channel

$$\overline{p}_i=a+b-p_i$$

Where:

$\overline{p}_i, p_i$ = The two opposite discharge bodies in the one-dimensional problem

a, b = The range boundaries

Through the spatial iterative movement of the three types of discharge bodies, the ultimate energy of the guided discharge body is finally found to be the optimal solution.

Following Figure 1 is a flowchart of the LSA algorithm:

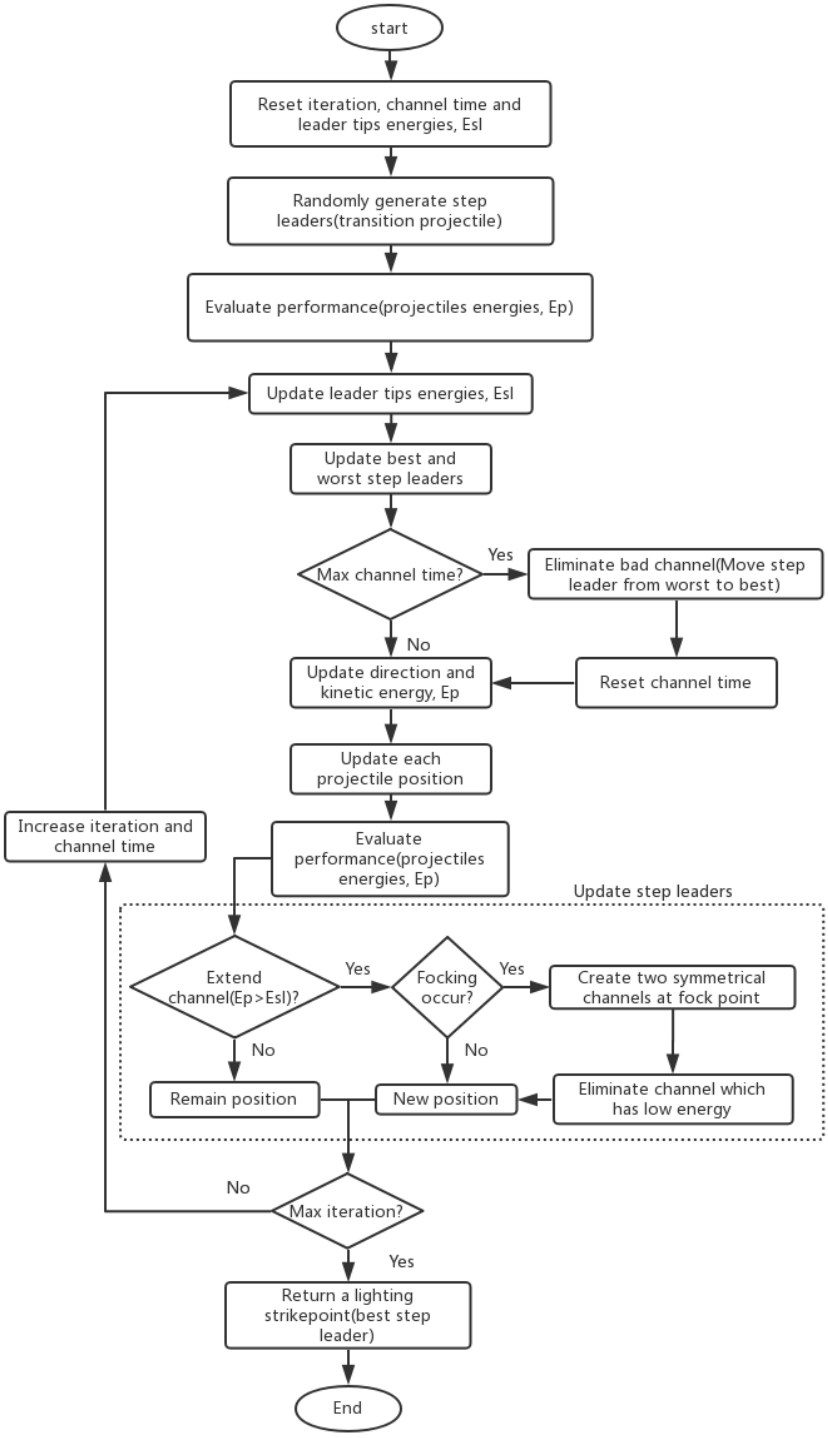

Figure 1: The flowchart of the LSA

2.3. LSA-SVR model parameter optimisation

Vapink V N (1995) proposes a supervised machine learning method that supports vector machine regression (SVR). This method has good effectiveness and can solve the problem of SVM in predicting problems.

This paper uses the newly proposed SVR model, combined with lightning search intelligent optimisation algorithm (LSA) to optimise the model parameters in the SVR model, and finally it get a good air quality prediction effect. These make the air quality predictable. It has considerable benefits for the protection of the environment and people's health.

The optimisation of the parameters of the SVR model mainly lies in obtaining a better solution of the penalty parameter C , kernel function parameter γ .[16]

This paper uses LSA algorithm to optimise SVR parameters. The following flowchart Figure 2 is the flowchart of LSA to optimise SVR parameters

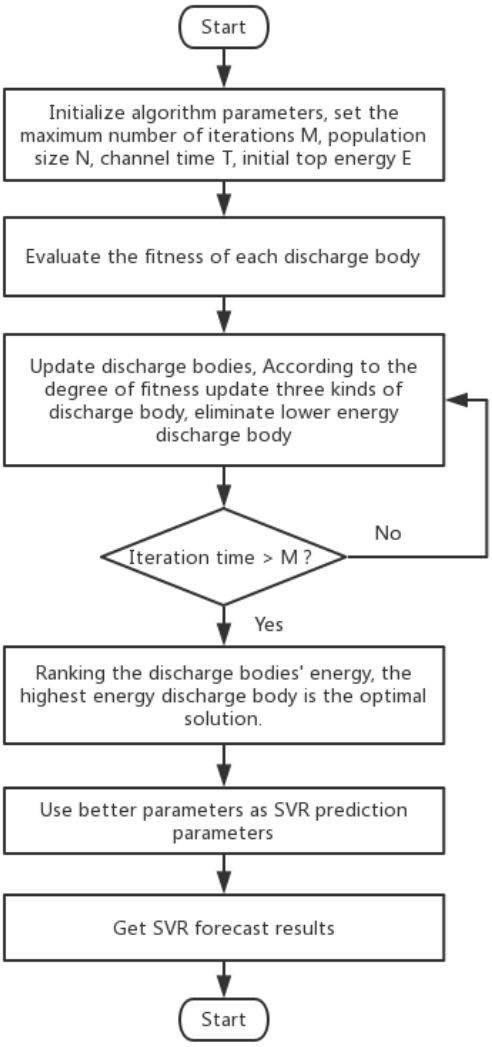

Figure 2: The flowchart of the LSA-SVR

3. SIMULATION EXPERIMENT AND RESULT ANALYSIS

3.1. Simulation experiment

This paper uses historical air quality data from the Chinese Ministry of Environmental Protection and selects 150 days of air quality data from January 2018 to May 2018 in Wuhan as a simulation.

In order to reduce the modeling error and improve the computational efficiency, the data needs to be normalized. In this paper, the data is normalized to [0, 1] using the minimum-maximum normalization method.

Equation 12: Data normalization formula

$$x_i^* = \frac{x_i - x_{\min}}{x_{\max} - x_{\min}}, i = 1, 2, \cdots, n$$

Where:

x_i, x_i^* = Normalized data before and after

$x_{\max}$ = The maximum value in the data

$x_{\min}$ = The minimum value in the data

n = The number of input data

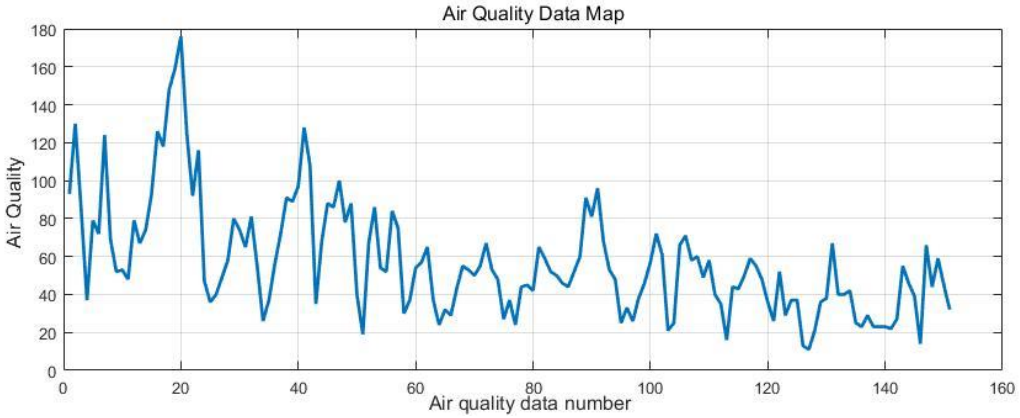

Figure 3: Original air quality data plot

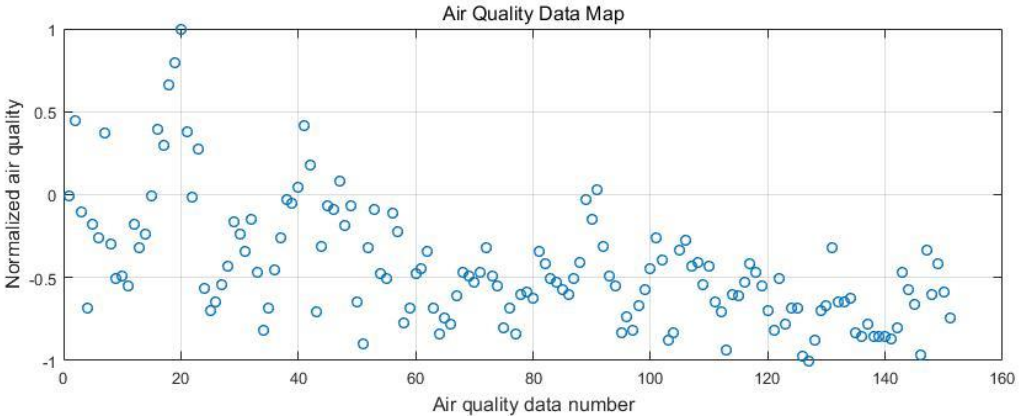

Figure 4: Normalized air quality data plot

Figure 3 shows the air quality data. The data contains real historical air quality data for Wuhan in the past 160 days. The air quality index varies from 11 to 176. As we can see in the figure, on the 20th day, air quality pollution is the most serious, after normalized, the data is showed in figure 4. Through serialization, model error will be reduced and the model training speed will be faster.

In the experiment, the number of iterations was 100, the number of discharge bodies was 50. In order to get better analyse and predict the changes in the air environment in Wuhan in the recent past, 120 days from January to April 2018 were selected as training data. This paper divides the training data and prediction data into 4:1 to increase the accuracy of the training model, and finally select the most recent 30-day data for short-term prediction. Finally, a fitting evaluation is performed to evaluate the accuracy of the model of LSA-SVR.

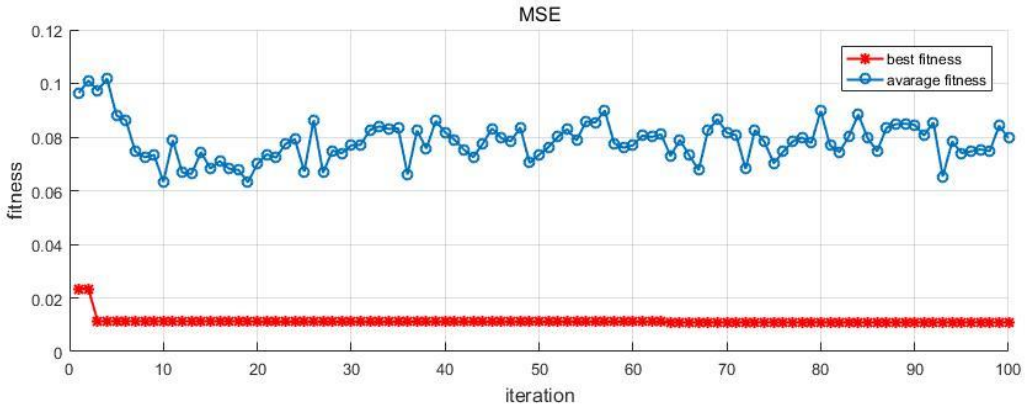

Figure 5: The LSA fitness curve

The figure 5 shows the fitness of LSA's 100 times iteration. Finally, the best disciplinary factor in SVR C = 14.0775, the best Gaussian kernel function parameters γ =0.14.

3.2. Fit evaluation

Fitting the actual data and prediction data, the results show that the LSA-SVR prediction model has a high degree of fit and an accurate prediction capability. This can be seen in Figure 6.

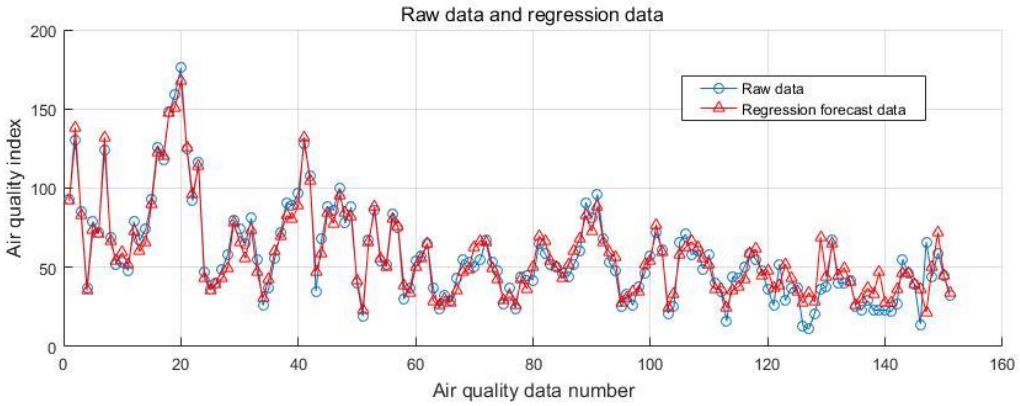

Figure 6: Comparison of raw data and regression forecast data

Then the paper compares the LSA-SVR model with the SVR model and PSO-SVR model and introduces the Mean Square Error and Mean Absolute Error to evaluate the model. The Mean Square Error function is as follows:

Equation 13: Mean Square Error Function

$$MSE = \frac{1}{n}\sum_{i=1}^{n}(y_i - y_t^*)^2$$

Where:

y_i = Actual value of the i-th data

y_t^* = SVR model predictions corresponding to the i-th data

The Mean Absolute Error function is as follows:

Equation 14: Mean Absolute Error Function

$$MAE = \frac{1}{n}\sum_{i=1}^{n}\left|(y_t^* - y_i)\right|$$

Where:

y_i = Actual value of the i-th data

y_t^* = SVR model predictions corresponding to the i-th data

Finally obtained the following error data table

Table 1: Forecast error table

MODEL	MES	MAE
SVR	0.0529	0.1527
PSO-SVR	0.0201	0.1234
LSA-SVR	0.0104	0.1146

After calculating the error, the results in Table 1 show that the LSA-SVR model has better accuracy than the traditional SVR model and PSO-SVR model.

4. CONCLUSION

In nowadays increasingly serious air pollution, it is very important to predict the air quality index in order to give people a healthier guide. The traditional SVR model has simple understanding, few parameters adjustment, and the model is easy to operate, but its prediction accuracy depends to a large extent on the choice of artificial parameters. The PSO-SVR model has the function of automatically optimising parameters, and its accuracy exceeds the original SVR model, but its prediction accuracy is still lacking. The LSA-SVR method proposed in this paper provides a new method for Wuhan air quality prediction. It has higher prediction accuracy and better stability. It providing a reference for better air quality prediction in the future. However, during the course of the experiment, it was found that there were poorly-predicted and inaccurate data points for individual predictions, which required follow-up studies to continue efforts to improve.

5. ACKNOWLEDGEMENTS

This work is funded by the National Natural Science Foundation of China under Grant No. 201701030033, 20170101006, 201701049026, funded by Beijing Shenzhou Taiyue Education Technology, Cisco and Wuhan Soft Cool Network Technology.

6. REFERENCES

Burges, C. J. (1998). A tutorial on support vector machines for pattern recognition. *Data mining and knowledge discovery*, 2(2), 121-167.

Chen, K. Y. (2006). Evolutionary support vector regression modeling for Taiwan stock exchange market weighted index forecasting. *Journal of American Academy of Business*, 8(1), 241-247.

Haiming, Z., & Xiaoxiao, S. (2013, June). Study on prediction of atmospheric PM2. 5 based on RBF neural network. In *Digital Manufacturing and Automation (ICDMA), 2013 Fourth International Conference on* (pp. 1287-1289). IEEE.

Kim, K. J. (2003). Financial time series forecasting using support vector machines. *Neurocomputing*, 55(1-2), 307-319.

Long, N., Gianola, D., Rosa, G. J., & Weigel, K. A. (2011). Application of support vector regression to genome-assisted prediction of quantitative traits. *Theoretical and applied genetics*, 123(7), 1065-1074.

Mustaffa, Z., & Sulaiman, M. H. (2006). Price predictive analysis mechanism utilizing grey wolf optimiser-least, squares support vector machines. *ARPN Journal of Engineering and Applied Sciences*, 2015(11), 17461-17491.

Russo, A., Raischel, F., & Lind, P. G. (2013). Air quality prediction using optimal neural networks with stochastic variables. *Atmospheric Environment,* 79, 822-830.

Shareef, H., Ibrahim, A. A., & Mutlag, A. H. (2015). Lightning search algorithm. *Applied Soft Computing*, 36, 315-333.

Shi-qian Hu, Qian-wen Jiang, Bin Lin, Wei-dong Yi (2016). Monitoring and early warning of air quality based on improved support vector machine. *Journal of Jiangsu University*, 4, 491-496.

Vapnik, V. (2013). *The nature of statistical learning theory*. Springer science & business media.

Wang, W., Liu, Y., & Li, G. (2005). The support vector machine method for time sequence forecasting of strong earthquakes in China's mainland. *Earthquake*, 25(4), 28-34.

Wei Liu. (2013). A research on Support vector machine based model of city's air quality time series prediction. *Electronic Test*, 20, 44-46.

Xie, H., Ma, F., & Bai, Q. (2009, August). Prediction of indoor air quality using artificial neural networks. In *Natural Computation, 2009. ICNC'09. Fifth International Conference on* (Vol. 2, pp. 414-418). IEEE.

Xisen, L. J. Q. G. W., & Niaoqing, H. (2002). Over-Fitting in Neural Network Learning Algorithms and Its Solving Strategies [J]. *Journal of Vibration, Measurement & Diagnosis*, 4, 260‑264.

Yao, L., Lu, N., & Jiang, S. (2012, May). Artificial neural network (ANN) for multi-source PM2. 5 Estimation using surface, MODIS, and meteorological data. In *Biomedical Engineering and Biotechnology (iCBEB), 2012 International Conference on* (pp. 1228-1231). IEEE.

Zhang, Y. H., Cai-tao, S. U. N., & Hong-bin, Y. A. N. G. (2009). PM10 Concentration Forecast Model Based on Stepwise Regression Analysis. *Environmental Science & Technology*, 5, 100-102.

288: Round panel experiment research on flexural toughness of hybrid fiber shotcreting

Feng ZHU[1], Dong-Tao XIA[2], Yan-Fang ZHANG[3]

[1]School of Civil Engineering and Environment Hubei University of Technology,Wuhan , 625213373@qq.com
[2] School of Civil Engineering and Environment Hubei University of Technology,Wuhan , 2390654741@qq.com
[3] School of Civil Engineering and Environment Hubei University of Technology,Wuhan , 843274644@qq.com

In order to investigate the flexural toughness of hybrid fiber shotcreting, The round hybrid fiber shotcreting panel with a diameter of 800mm was placed on the pedestal, which is arranged along the circumference with three cylinders that are 120 degrees to each other, and the center point of the panel was loading with concentrated force until the deflection of center point was at least 45 mm, then the load-deflection curve and energy absorption value were obtained, the effects to the concrete slab on flexural toughness and deflection performance for hybrid fiber shotcreting were investigated, which brought by the different amount of steel fiber volume fraction,steel fiber type and the addition of the polypropylene fibers. The results show that the flexural strength and flexural toughness of shotcreting panel raising with the increased of steel fiber volume fraction. The flexural toughness and crack control ability of ultra-short microfilament steel fibers shotcreting are better than multiple anchor steel fiber shotcreting. When it comes with the hybrid fibershotcreting with 1.2% of ultra-short microfilament steel fibers and 0.11% of the polypropylene fibers, the experimental results show the best flexural toughness and the highest compressive strength.

Keywords: hybrid fiber, shotcreting, flexural toughness, round panel test, energy absorption value

1. INTRODUCTION

Compared with the ordinary shotcreting, the advantages of fiber shotcreting are high bearing capacity, good deformability and flexural toughness. Therefore, it is widely used in the maintenance and reinforcement of underground transportation, tunnel-liner, rock face slope, shell structure, bridge and so on. At present, most of the shotcreting in engineering uses a single fiber, such as steel fiber shotcreting. Because of the concrete is a multi - component, multi – level, non - homogeneous material, the reinforcement and toughening effect of single fiber is more limited. If some other fibers with low modulus of elasticity are added to the steel fiber concrete with high modulus of elasticity, the two kinds of fiber hybrid can be reinforced and toughened step by step in different structural levels and loading stages, and the super position effect can be obtained by stimulating and supplementing each other, which can obviously improve the toughness, crack resistance and other properties of the single fiber shotcreting.

The flexural toughness test of hybrid fiber shotcretingin this paper is based on the round panel test in The Standard Test Method for Fibrous Concrete (CECS13: 2009) which shows the bending destructional forms of hybrid fiber shotcreting. The effects of steel fiber volume fraction steel fiber type and the addition of the polypropylene fibers on mechanical properties for hybrid fiber shotcretingare investigated,and the toughening and anti-cracking mechanism of mixed fiber shotcrete is discussed to give the optimum mix ratio of flexural toughness,which is based on the energy absorption value.

2. TEST SCHEME

Test specimens selected cw01-02 /13 ultra-short microfilament steel fibers and cw03-05 / 30 multiple anchor steel fibers, and durafiber adopted in polypropylene fiber. The characteristic parameters of fibers are shown in Table 1. P. O. 42.5 ordinary Portland cement is used in the matrix concrete with strength grade of C45; gravel particle size of 5 to 10mm is used in the coarse aggregate; fineness modulus of 2.8 in the coarse river sand is selected in fine aggregate; blast furnace slag powder (density: 2. 91g/m3, specific surface area: 459m2 /kg) is selected; FDN2 superplasticizer is used, with water reducedup to 20%; alkali-free liquid accelerator which weighs 8% of the weight of cement is mixed; the amount of silicon powder is 10% of the weight of cement. The basic mixture ratio of the concrete is shown in Table 2. In order to study the influence of steel fiber and polypropylene fiber on the concrete, 6 kinds of mixed fiber forms were selected to make 6 groups of shotcrete specimens, each group of 3 specimens, then the results were averaged. The volume of fiber in each group was shown in Table 3.

Table 1: The characteristic parameters of fibers

Type of fibers	Length /mm	Diameter /mm	Tensile strength /MPa	Number
Ultra-short micro-filament steel fibers	13	0.2	2000	85000
Multi-anchor steel fibers	30	0.5	1000	19800
Polypropylene fibers	12	0.03	276	3.3×107

Table 2: The base mix ratio of concrete/（kg/m3）

Material	Water	Cement	Sand	Gravel	Water reducer	Quick-setting agent	Silicon powder	Blast furnace slag powder
Content	195	481	903	738	4.81	3.848	48.1	48.1

Table 3: The volume content of fiber in each group of specimens and the test results of the average compressive strength of 28-day cubes in each group

Specimen group	The volume content of ultra-short micro-filament steel fibers/%	The volume content of multi-anchor steel fibers/%	The volume content of polypropylene fibers/%	The average of compressive strength fcu/MPa
S1	0	0	0	49.8
S2	0	0.8	0.11	51.2
S3	1.2	0	0	58.1
S4	0.8	0	0.11	55.3
S5	1.2	0	0.11	58.9
S6	0	1.2	0.11	53.4

2.1. Wet shotcreting process and test method

Wet shotcreting process

The test method of shotcreting is wet spray method. Firstly, stir the sand, stone, cement, steel fiber into the 300L dual-forced mixer without water for 3 minutes. Then add the polypropylene fiber into the mixer. After 3 minutes, add

water and silicon powder into the mixer.13 minutes later, concrete will be directly poured into the nozzle through the wet jet machine silo and evenly mixed with quick-setting agent.Then the concrete will be sprayed to the sprayed concrete surface with air compressor by means of the injection molding fiber concrete specimen production method (CECS 13: 2009), with the sprayed surface and the horizontal surface at an angle of 135 °. The spray gun spray vertically to the template from bottom to up, at a distance of about about 1m.

The cube compression and flexural toughness test

The cube compression test piece measures 100mm × 100mm × 100mm, and the cutting plate is made by spray large plate, 3 plates in each group.The specimen size of flexural toughness test is diameter 800mm, thickness 75mm, 3 plates in each group. The mechanical tests are carried out after curing for 28 days under standard curing conditions. The compressive strength of cubes is tested according to Standard Test Method for Mechanical Properties of Common Concrete (GB / T 50081-2002) (Standard Test Method Standard for mechanical properties of GB /T 50081 2002), and the compressive strength value were corrected by the conversion factor of 0.9.

For the determination of flexural toughness of shotcreting, beam bending test method has been used in most of the domestic, which is quite different from the actual shotcreting loading mechanism and can not reflect the fiber three-dimensional direction of the toughening effect, thus making the test results having greater dispersion, so it should not be directly used to test the flexural toughness of shotcreting. However, the round panel test in Standard Test Method for Fibers and Concrete" (CECS 13: 2009) is based on the method of energy injection and uses a three-point support system as a static system. The three cracks are symmetrical to the center of the round panel, and the test results have good consistency. Compared with the traditional test methods, the energy dissipation capacity of the sprayed concrete surface layer under the deformation of the base layer can be truly reflected (Liu 2012; Wang 2005), So the flexural toughness is tested by the round panel method.

Loading equipment selected 300kN computer-controlled electro-hydraulic servo pressure testing machine, a distance of 50mm displacement sensor is installed atthe center of the bottom of the round panel, and the round panel test device shown in Figure 1. In order to eliminate the distortion error between the machine cylinder and the deformation, before the component loading reached 0. 5kN, cylinder displacement is used to controlwith the loading rate of 1mm / min. After reaching 0. 5kN,it uses disc displacement to control, and the loading rate is 3mm / min. The load value and the displacement value at the center of the round panel are measured synchronously by the load cell and the displacement sensor respectively, and the load-displacement curve was recorded and displayed. When the deflection of the center of the round panel reached 45mm, the test was stopped and the energy absorbed by the round panel is calculated according to the load-deflection curve.

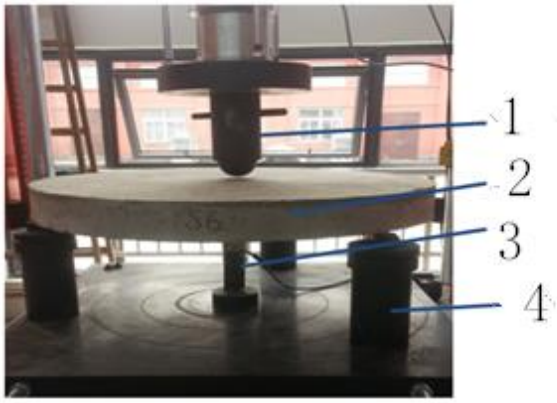

Figure 1: Round panel test device：(1) Load header；(2) Specimen；(3) Motion detector；(4)Pedestal end.

3. EFFECT OF FIBERON COMPRESSIVE STRENGTHOF SHOTCRETING

The average compressive strength of 28-day cubes in each group of samples is shown in Table 3. As is shown in Table 3, the compressive strength of the shotcreting with single steel fiber or hybrid fiber is improved in comparison with the plain shotcreting. The compressive strength of shotcreting with ultra-short micro-filament steel fibers is 6% to 8% higher than that of the shotcreting mixed with multi-anchor steel fibers. However, the addition of polypropylene fiber has almost no effect on the compressive strength of shotcreting.

4. THE FLEXURAL TOUGHNESSOFSHOTCRETING PANEL

4.1. The failure form of shotcreting panel

Plain shotcreting panel

With the loading increasing, plain shotcreting panel S1 quickly breaks into 3 relatively homogeneous rigid block with a bang bang, with a very smooth plate fracture surface, which shows the brittle characteristics of plain shotcreting. The failure form is shown in Figure 2.

Figure 2: The failure form of plain shotcreting panel S1

Hybrid fiber shotcreting panel

In flexural toughness teston hybrid fiber concrete plate S4, when the center deflection of the panel reaches 0. 72mm, the three cracks extend almost simultaneously from the center of the panel to the side of panel, each crack just in the adjacent two ball joints. As the deformation of the center of the panel increases, the cracks gradually extend from the bottom of the panel to the side of the panel. Due to the bridging effect of the fibers crossing the cracks, the cracks develop very slowly. When the center deflection of the plate reaches 28 mm, the panel surface also appeared cracks, where we can observe the steel fiber has been pulled out and the polypropylene fiber has been pulled off at the crack. The panel is not completely broken until the end of the test, which showed its good ductility. It can be seen from the results that the role of fiber bridging cracks can limit the development of cracks in concrete, relieve the stress concentration at the tip of cracks, and delay the time of forming micro cracks through micro cracks (Lu 2010).The failure form is shown in Figure 3.

Figure 3: The failure form of hybrid fiber shotcreting panel S4

The crack growth speed of the hybrid fiber shotcreting panel S2 is faster than the hybrid fiber shotcreting panel S4.When the deflection at the center of the panel reaches 18mm, the crack on the bottom of the panel extends to the front surface of the panel. The flexural cracking process and the failure morphology are basically similar to the hybrid fiber shotcreting panel S4, and the failure morphology is shown in Figure 4. At the end of the test, the crack widths of hybrid fiber shotcreting panel S4 and hybrid fiber shotcreting panel S2 are measured. Three different positions were measured along the radial direction of each main crack. Taking the average of the crack widths for comparison, it can be found that hybrid fiber shotcreting panel S4 is smaller than that of hybrid fiber shotcreting panel S2 by nearly 10%, and the crack control ability of hybrid fiber shotcreting panel S4 is better than that of hybrid fiber shotcreting panel S2.

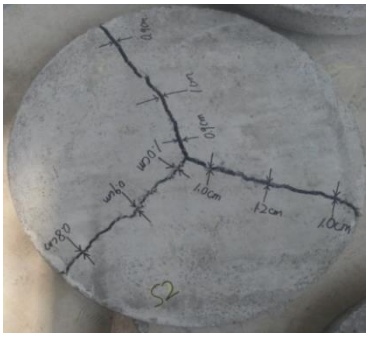

Figure 4: The failure form of hybrid fiber shotcreting panel S2

4.2. The effect of fiber volumecontent on flexural toughness of shotcreting

The load-deflection curves of shotcreting panels S1, S2 and S4 to S6 are shown in Figure 5. When the central deflection of plain shotcreting panel S1 reaches 0.762mm, the ultimate loading is reached. At this moment, the tensile stress of the concrete in the panel tensile zone has reached its ultimate tensile stress, and the concrete is withdrawn from work. Since there is no fiber reinforcement and toughening effect, the micro-cracks rapidly expanded and penetrated, resulting in instability failure. When the deflection value reached 9. 2mm, the flexural strength of plain shotcreting panel dropped to 0.

However, the hybrid fiber shotcreting panel from loading to the destruction process can be divided into three stages, and the hybrid fiber shotcreing panel S5 is analyzed as an example.

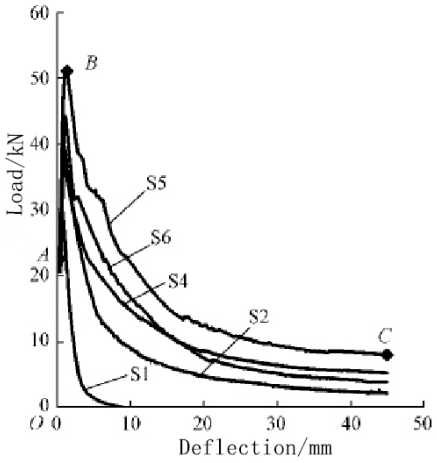

Figure 5: Comparison of load-deflection curve of shotcreting panels S1, S2, S4 and S6

(1) In linear elastic stage: When the central deflection of hybrid fiber shotcreting panel is small, as is shown in Figure 5 in section OA, it is in a linear elastic stage, and micro cracks in concrete do not increase with the increase of loads, but remain in a relatively stable state. Fiber and concrete as a whole are forced together, and the deformation of the two coordinated. At this stage, the flexural properties of the hybrid fiber shotcreting panel is no obvious difference, and the fibers have no obvious influence on the flexural toughness of the hybrid fiber shotcreting panel.

(2) In elastic-plastic stage: the load of hybrid fiber shotcreting panel continues to increase. When the tensile strain of concrete tensile zone reaches the ultimate tensile strain of concrete initial crack, cracks begin to appear at the bottom of the panel. However, the shotcreting panel with fibers exhibits obvious strain hardening characteristics after the initial breaking strength is reached and before the bending ultimate load. At this time, the hybrid fiber shotcreting panel enters the elasto-plastic stage, as is shown in Figure 5 in section AB. The load is transmitted to the fiber through the bond between the fiber and the concrete. The steel fiber can share the load without exceeding the bond with the concrete. The polypropylene fiber can relieve the stress concentration phenomenon of the micro-crack, so as to enhance the toughening effect.

(3) In the unloading stage: as is shown in Figure 5 in section BC, the bond strength between fiber and concrete gradually reaches the limit after the hybrid fiber shotcreting panel reaches the ultimate load, the relative slip happens between the two parts. Some steel fibers has been pulled-out, and the polypropylene fiber has been pulled off, which lead to the hybrid fiber shotcreting panel bending load capacity graduallydecreasing. As the fiber absorbs a

large amount of energy during the pull-out and pull-off process, the decline rate of flexural capacity of the hybrid fiber shotcreting panel tends to be gentle, which obviously improves the flexural toughness of shotcreting panel.

It can be seen from Figure 5 that the slow degree of the load deflection curve of the shotcreting panel with different fiber content are obviously different. The flexural peak loads of hybrid fiber shotcreting panels increased by 28% and 19% respectively when the content of the two kinds of steel fibers of ultra-short micro-filament steel and multi-anchor steel fibers increased from 0.8% to 1.2%. The initial crack deflection increased by nearly 15% and 10%, and the drop section of the load deflection curve of the shotcreting with high steel fiber content is less than the falling section of the shotcreting with low content. The reason is that the increase of the steel fiber content reduces the spacing between the fibers. The more steel fibers there are across the crack, the higher the stress transmission capacity is, the more the restraint of the steel fiber has on the concrete, and the slower the cracks grow. Therefore, with the increase of the steel fiber content, the flexural capacity and flexural toughness of the hybrid fiber shotcreting panels are improved.

4.3. The effect of steel fiber types on the flexural toughness of shotcreting

The flexural toughness of the two steel fiber shotcreting panels are also different under the same fiber content. It can be seen from Figure 5 that when the content of fiber are both 0.8%, the ultimate bending load of hybrid fiber shotcreting panel S4 is almost 10% higher than that of hybrid fiber shotcreting panel S2, and the load-deflection curve drop section is more smooth and full. When the fiber content is 1.2%, the flexural ultimate load of hybrid fiber shotcreting panel S5 is almost 16% higher than that of hybrid fiber shotcreting panel S6. Comparing the crack widths of hybrid fiber shotcreting panel S4 and hybrid fiber shotcreting panel S2, we can see that the plastic deformation capacity of ultra-short microfilament steel fiber shotcreting panel is obviously better than that of multi-anchor fiber steel shotcreting panel.

Although the aspect ratios of the two kinds of steel fibers are similar, the characteristic parameters of the two kinds of steel fibers are obviously different: (1) The tensile strength of the ultra-short micro-filament steel fiber is twice that of the multi-anchor fiber (Table 1). The result showsit obviously raises the pull-out force of steel fiber, and that high tensile strength steel fiber can play a good role in micro-reinforcement; (2) while the diameter of ultra-short microfilament steel fibers is only 0.4 times of the diameter of multi-anchor steel fibers, the number of ultra-short microfilament steel fibers per unit volume is almost 3 times that of multi-anchor steel fibers. Besides, the steel fiber spacing is greatly reduced, the amount of the steel fibers across the cracks increases, it contact with concrete more fully, and the ability to transmit the load is also greatly enhanced, so that the steel fiber reinforced cracking effect is more obvious ; (3) With the fiber's length of only 13mm,the ultra-short microfilament steel fiber belongs to the ultra-short steel fiber, whose Wall Effect is comparatively weak. Compared with the multi-anchor steel fiber, it is more evenly dispersed in the test piece, and the number of intersecting fibers is more, which can effectively prevent the occurrence and development of primary cracks parallel to the interface (Li 2012). Therefore, the hybrid fiber shotcreting with ultra-short micro-filament steel fibers shows better flexural toughness and plastic deformation ability.

4.4. The effect of polypropylene fiber on the flexural toughness of shotcreting

The load deflection contrast curve of the fiber shotcreting panel S3 incorporating a single ultrafine micro-filament steel fiber and the fiber shotcreting panel S5 incorporating a hybrid fiber are shown in Figure 6.

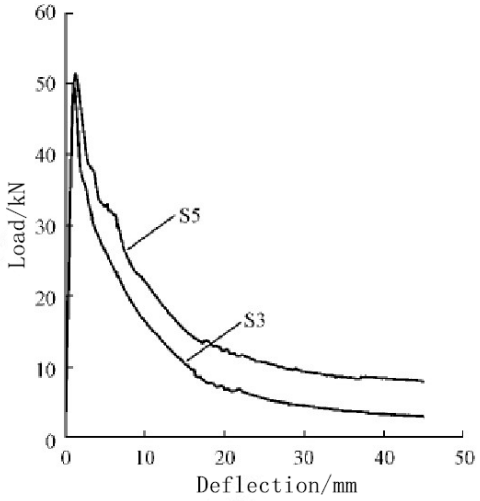

Figure 6: Comparison of load-deflection curve of shotcreting panels S3 and S5

It can be seen from Figure 6 that compared with a single-steel fiber shotcreting panel S3, the flexural peak load of hybrid fiber shotcreting panel S5 is increased by 4% and initial crack deflection of hybrid fiber shotcreting panel S5 is increased by 8%.The peak load-deflection curve of hybrid fiber shotcreting panel S5 decreased more slowly, which shows a good bending deformation performance. Since the diameter of polypropylene fiber is only 3/20 of the ultra-short micro-filament steel fiber, the spacing between the fibers is greatly reduced, the number of polypropylene fibers across the crack increases greatly, and the ability to transmit stress is greatly improved.Since polypropylene fiber has a larger elongation, it does a lot of work in the process of deformation and elongation, passivation of the stress concentration of the primary crack tip, so that the media has evener uniform stress field (Li 2012). Polypropylene fiber can continue to bridge the cracks in concrete after some steel fibers are debonded, which restrains the development of microcracks, thus reducing the brittleness of concrete and improving the crack resistance of concrete. Steel fibers with high modulus of elasticity and polypropylene fibers with low modulus of elasticity form a composite material, which can significantly improve the mechanical properties of shotcreting through the hybrid effect of their bridging action and energy dissipation mechanism in different loading stages and levels (Li 2005). Therefore, the toughening effect of hybrid fibers on shotcreting is not comparable to that of single steel fibers.

4.5. Energy absorption value of hybrid fiber shotcreting

Table 4 shows the average value of the energy absorption correction and the ultimate bending moment when the center deflections of the shotcreting panels reach 5, 10, 20, 40 and 45mm respectively. It can be seen from Table 4 that, the plain shotcreting panel S1 has no fiber bridging cracks and rapidly collapses after cracking, and the average value of the energy absorption correction is low. However, the fiber shotcreting panels S2 ~ S6 with different fibers are different from the plain shotcreting panel S1.Compared with the shotcreting panel S1, the average value of energy absorption correction is improved to some extent. When the fiber shotcreting panel S2 ~ S6 deflected 45mm in the center of the panel, the average value of energy absorption correction was increased by 188%, 279%, 237%, 350% and 257% respectively.

Table 4: The average value of the energy absorption correction and ultimate bending loads of shotcreting panel

Specimen group	The average value of the energy absorption correction					Ultimate bending loads
	Deflection 5mm	Deflection 10mm	Deflection 20mm	Deflection 40mm	Deflection 45mm	
S1	117	135	——	——	——	30.94
S2	127	192	272	370	389	37.08
S3	170	279	394	495	512	49.10
S4	135	215	319	434	456	39.76
S5	190	303	442	580	607	50.99
S6	148	251	369	464	482	44.10

Compared with hybrid fiber shotcreting panel S6 and hybrid fiber shotcreting panel S2, the fiber content of multi-anchor steel fiber increased by 0.4%. When the center deflection of the panel reached 45mm, the average value of energy absorption correction was increased by nearly 24%. It can be seen that the energy absorption capacity of hybrid fiber shotcreting panel increases with the increase of steel fiber content.

Then, compare the energy absorption capacity of hybrid fiber shotcreting panels S5 and S6.Because of the higher tensile strength of the ultra-short microfilament steel fibers, the toughening effect is better and the restraining effect on concrete cracks is stronger, but the hooks at both ends of the multi-anchor steel fibers are straightened in the test, resulting in toughening ability to decline. Therefore, when the deflection of the center of the panel reaches 10, 20, 45mm, compared with the single steel fiber shotcreting panel S6, the average energy absorption correction of hybrid fiber shotcreting panel S5 were increased by 9.7%, 25%, 25.9% respectively.

Compared with the single steel fiber shotcreting panel S3, due to the addition of polypropylene fiber in the mixed fiber shotcreting panel S5, the spacing between the fibers is greatly reduced, and the stress concentration at the crack tip can be passivated. When the steel fiber is gradually slipping and debonding with the shotcreting, the polypropylene fiber can still transfer the tensile stress, which absorbs a large amount of energy due to its deformation and elongation during the plastic deformation of the confined concrete (Ding). Therefore, the energy absorption capacity of hybrid fiber shotcreting was significantly better than that of single steel fiber shotcreting. At the end of the test, the average energy absorption correction of hybrid fiber shotcreting panel S5 is higher than that of the single steel fiber shotcreting panel S3 by 18.6%.

After comparing the load-deflection curve, the average value of the energy absorption correction and the cracking deformability of the shotcreting panel from S2 to S6,it can be seen that the optimal mix ratio of the flexural toughness of hybrid fiber shotcreting is: the volume content of ultra-short micro-filament steel fiber is 1.2%, the volume content of polypropylene fiber is 0. 11%.

5. CONCLUSIONS

(1) The addition of different volume of steel fiber and polypropylene fiber in shotcreting can improve the mechanical properties of shotcreting in different degrees. Compared with plain shotcreting, the compressive strength of hybrid fiber shotcreting is increased by 3% ~ 18%, and maximum bending load is increased 19.8% ~ 64.8%. At the same time, the hybrid fibers can obviously change the brittleness of the shotcreting and improve the ductility of the components.

(2) With the same fiber content, different types of steel fiber have a greater influence on the flexural toughness of fiber shotcreting. The mechanical properties of shotcreting with ultra-short microfilament steel fibers are better than those with multi-anchor steel fibers. When the steel fiber content are 0.8% and 1.2% respectively, the ultimate flexural strength of fiber shotcreting were increased by 44% and 52% , and the width of the cracks is reduced by nearly 10%, which shows a better ability of crack control and plastic deformation.

(3) The energy absorption value of fiber shotcreting is better than that of single steel fiber shotcreting. When the deflection of the center of the panel reaches 45mm, the average energy absorption correction of fiber shotcreting is increased by 18.6%.

(4) The hybrid fiber shotcreting with 1. 2% of ultrashort microfilament steel fibers and 0. 11% of the polypropylene fibers show the best flexural toughness and highest compressive strength.

6. REFERENCES

Huang C-K. Fiber reinforced concrete structures [M]. Beijing: Mechanical Industry Press, 2004.

Morgan DR, Heer E R, Evolution of fiber reinforced shotcrete［J］. Shotcrete Magazine2000，2(2): 811.

Wu Yao, Ke- Ru Wu. The condition of the experiment of concrete tensile stress-strain curve. [J]. Journal of Tongji University: Natural Science Edition, 1996, 24 (2): 142-145.

Xia D-T, Liu X-K, Xia G-Z. J hybrid fiber reinforced high performance concrete flexural toughness study. Journal of Huazhong University of Science and Technology: Natural Science Edition, 2013, 41 (6): 108-112.

CECS 13: 2009 fiber concrete test method standard [S]. Beijing: China Planning Press, 2010.

Standard Test Method Standard for mechanical properties of GB /T 50081 - 2002 common concrete [S]. Beijing: China Construction Industry Press, 2003.

Liu G-P, Wang J-Y. Based on the energy representation method, the test method of the toughness of jet fiber reinforced concrete is summarized. [C] / / The 14th National Conference on fiber concrete conference. Zhengzhou: North China Water Conservancy and Hydropower Press, 2012:123-127.

Wang S-H, Yuan Y. Review of the method of shotcrete test [J]. Journal of Kunming University of Science and Technology: physical edition, 2005, 30 (4): 55-58.

Lu Z-A, Zou Y, Ren Z-G, et al. Experimental research on flexural toughness of fiber high strength concrete [J]. Concrete, 2010, 32 (3): 5-7, 12.

Li Y. Resistance to cracking and toughening and durability of hybrid fiber concrete [M]. Beijing: Science Press, 2012

Li S-J, Wu K. Steel-PP fiber mixed cement-based materials mechanical behaviour [J]. Concrete and Cement Products, 2005, 32(4): 35-37.

Ding Y，Zhang Y，Thomas A. The investigation on strength and flexural toughness of fibre cocktail reinforced self-compacting high performance concrete［J］Construction and Building Ma

292: Research on carbon emission cost accounting and disclosure in the industry manufacturing

Yingchun SONG[1], Wenyi YANG[2], Yaoxin ZHOU[3]

[1] School of Economics and Management, Hubei University of Technology, 7862659@qq.com
[2] School of Economics and Management, Hubei University of Technology, 530524575@qq.com
[3] School of Economics and Management, Hubei University of Technology, 1065234613@qq.com

Manufacturing enterprises are one of the most important sources of carbon emissions. Carbon emission cost accounting is a crucial process of carbon emission cost accounting in the manufacturing Industry. There are differences in the form of carbon emission measurement of different manufacturing enterprises. This paper, based on Schumpeter Innovation Theory, combined with the production process of cement enterprises, reengineering the existing financial accounting process, propose that first carries out carbon verification to obtain carbon emissions, then calculates carbon cost measurement by carbon market price, and finally discloses carbon cost information. The paper also uses a case which belongs to cement manufacturing enterprises to illustrate. Reengineering the existing financial accounting process can solve the difficulties of carbon cost accounting under traditional accounting and provide carbon emission cost information for the internal managers of enterprises.

Keywords: Accounting Process Reengineering, Material flow cost accounting, Carbon emission cost, Carbon emission cost disclosure

1. INTRODUCTION

As corporate social awareness grows, manufacturers should consider the carbon emissions cost to predict the cost of manufacturing and reduce the impact on the environment when they make decisions. However, the current accounting theory system in China cannot accurately account for carbon emissions-related issues such as energy-saving emission reduction and emission control, nor can it fully disclose relevant information. While the material flow cost method originated from German enterprises in the mid-1990s, emphasizing the importance of material loss in accounting. Its basic idea comes from the principle of material balance. It calculates the positive product cost and negative product cost in terms of both quantity and value. Through the analysis of the internal material flow and cost of the company, the waste generated in the production process, the loss of raw materials and the environmental loss are identified. The main link of cost generation provides useful information for improving process and cost control. It is considered the best way to calculate the cost of enterprises from the transparency of input to output process and the visualization of the value conversion process of materials to products This paper will be based on Schumpeter Innovation Theory, combined with the production process of cement enterprises, reengineering the existing financial accounting process. Firstly, the carbon emission verification is carried out to calculate the cost of carbon emission at different stages. Then it carries out accounting and disclosure and uses cement manufacturing companies as examples to explain to provide reference for carbon cost accounting and disclosure of manufacturing enterprises in China.

2. RESEARCH STATUS AND RESEARCH SIGNIFICANCE OF RELATED ISSUES AT HOME AND ABROAD

2.1. Research status at home and abroad

From the definition of carbon emission costs, confirmation and measurement of carbon emission costs and disclosure of carbon emission cost information:

Definition of carbon emission cost

There are four main views on carbon emission costs: the first is that the carbon emission cost is the establishment of carbon emissions costs and resulting compensation including production, manufacturing, logistics, use, and disposal (Janek, 2007). (Ratnatunga & Balachandm,2010); the second is that the carbon emission cost is the sum of all expenses incurred by a company to prevent, plan and control carbon emissions, and the sum of all losses caused by exceeding the established carbon emissions (Yang et al., 2011); the third type of carbon emission cost is the outflow of various economic benefits that can be measured in available currency for the purpose of preventing, controlling, and controlling carbon emissions and achieving expected environmental effects and environmental benefits (Lin & Zhang, 2012); the fourth is based on carbon flow to research the consumption of substances in the company's technological processes (Xiao et al., 2013).

Carbon emission cost accounting model

The cost model in the cost model of Martinez-Sanchez et al. (2015) is divided into budget cost, transfer cost and external cost. Cost model contains three life cycle costs namely the transfer of life cycle cost (Financial Costs Assessment), environmental life cycle cost (Life Cycle Assessment) and social life cycle cost (Socio-economic Assessment). Among them, life cycle cost and environmental life cycle cost include budget cost and transfer cost, and social life cycle cost includes budget and external cost. The carbon emission cost model consists of prevention costs and identification costs and nuclear loss costs (Yang et al., 2011). The cost of carbon flow is divided into the effective utilization value of carbon flow, the value of waste loss and the value of the external environmental damage of the waste (Xiao et al., 2013).

Accounting treatment of carbon emission cost

Tsai et al. (2012) used the activity-based costing method to estimate the environmental cost of exhaust emissions and final finished products of Taiwan's paper industry. Provide information for existing environmental accounting systems to help managers integrate environmental cost information into scientific decisions. D'Onza et al. (2016) used the full cost method to calculate various types of costs when accounting for fixed waste. Martinez-Sanchez et al. (2015) used life cycle accounting to provide economic assessments of fixed waste. Wan et al. (2015) used material flow cost accounting to study the hidden costs of waste in the process flow. Lee (2012) proposes to find out the carbon flow of enterprises and measure their carbon performance from the methods of ecological control.

Using the total life cycle assessment method to measure carbon dioxide emissions, design a three-layer accounting method for emissions accounting: carbon emission from enterprises; indirect emissions from the purchase of electricity or thermal energy and other indirect emissions from extraction, production and purchase materials, and waste management (WRI/WBCSD,2007).

Disclosure of carbon emission cost information

Cowan & Craig (2011) used the theory of legality, voluntary disclosure of emissions provided by Australian companies, and found that even if corporate information disclosure is based on the National Pollutant Inventory provided by Australia, there are likely to be the problem of incomplete disclosure range between businesses. Liu & Zhang (2013) argue that the disclosure of carbon emission costs can draw lessons from the pattern of environmental cost disclosure: in the form of environmental cost information, it is divided into three categories: currency information, non-monetary information, and descriptive information.

2.2. Domestic and foreign research reviews

There is insufficient research on the carbon emission from the micro perspective of enterprises. Overall, domestic and foreign scholars mainly study the impact of carbon emission on the climate environment and the national economy from a macro perspective. More use of life cycle assessment, life cycle theory, activity-based costing, cost of material flow, or the integration of these theories are analyzed, few studies carbon costs from an enterprise micro-perspective. Therefore, this topic will focus on the classification and accounting of carbon emission costs of manufacturing enterprises.

There is also insufficient research on the disclosure of carbon emission costs. Carbon emission cost information is an important reference for enterprise managers to make green production plan, behaviour control and decision making. However, there is currently a lack of research on the disclosure of carbon emission costs in the academic community. By studying the disclosure of carbon emission cost information and promoting the green production of enterprises, it is particularly urgent for enterprises to achieve the goals of transformation development, environmental protection awareness and sustainable development.

2.3. Research significance

Expand the cost accounting theory research. At present, China's traditional cost accounting does not consider the impact of carbon emission costs on enterprises, and the research on the accounting of carbon emission costs can improve the current issue of the lack of cost accounting. This paper is based on Schumpeter innovation theory to improve the existing financial accounting process, and put forward carbon emission verification, carbon cost measurement, carbon cost accounting and disclosure of carbon cost information to fully reveal which expand and enrich the carbon emission cost accounting theory.

Promote the green development of the industry. In our country there are a large number of high input, high consumption, and high emission industries. A low-carbon economy needs to create a circular economy among these enterprises, transform traditional technologies and processes, and re-define and account for costs. Therefore, an urgent need for carbon emissions recognition, measurement and disclosure of information, provide a reference for the development of uniform standards, so as to promote the development of green industry.

3. PROCESS REENGINEERING OF CARBON EMISSION COST ACCOUNTING FOR CEMENT MANUFACTURING ENTERPRISES BASED ON SCHUMPETER INNOVATION THEORY

3.1. Schumpeter innovation theory

Schumpeter believes that innovation and development are closely linked. Schumpeter's innovation includes five aspects: product innovation, process innovation, market innovation, input innovation and organizational innovation. Combined with the characteristics of carbon emission in cement manufacturing enterprises, this paper mainly discusses the process innovation, i.e., reconstructing the existing accounting process. The traditional accounting process is to confirm, measure, record and report after the occurrence of economic business. However, for manufacturing enterprises, the amount of direct and indirect carbon emissions in the production process cannot be obtained, resulting in carbon costs that cannot be measured in traditional accounting. Therefore, based on Schumpeter Innovation Theory, this paper puts forward the accounting process reengineering of carbon emission cost accounting. First, carbon emission verification is carried out, i.e., the enterprises' carbon emissions are calculated, and then calculate the cost of carbon emissions by means of material flow cost method according to the price of carbon market, and finally disclose the cost information of carbon emissions.

3.2. Process reengineering of carbon emission cost accounting for cement manufacturing Enterprises

Carbon emission verification

There are four main types of cement manufacturing processes: wet, dry, preheater and pre-calcined kiln. For the wet process, feedstock slurry enters the kiln, drying, calcining and sintering all occur in the kiln. The drying process

is consistent with the wet process, but dry feedstock enters the kiln. The typical cement manufacturing process is decomposed into three basic stages: raw material preparation — cement kiln production — cement production. Among them, the raw materials are prepared for quarrying, crushing, and grinding of the raw materials. Most of the raw materials are made of limestone. Once the raw materials are grinded, they are homogenized in the silo until the next stage. Once the raw materials in the cement kiln produce clinker, the clinker ball is rolled and mixed with other materials to form cement.

According to the characteristics of the production process of the cement manufacturing enterprise, its carbon emissions are mainly concentrated in the emission of fuel combustion in the production process of the enterprise, the discharge of the industrial production process and the corresponding emission of electricity and heat used in the production process. The emission of fuel combustion mainly includes the combustion of fossil fuels such as physical coal, fuel and other fossil fuels, alternative fuels and the combustion of non-biomass carbon contained in the waste of coordinated disposal. The industrial production process mainly includes emissions from raw acid and salt decomposition and emissions from non-fuel carbon calcinations in raw materials. The net purchase of electricity and heat is carbon dioxide emissions from steam and hot water production by enterprises (2013, The National Development and Reform Commission). Therefore, the carbon emission cost of cement manufacturing enterprises is divided into direct carbon emission cost and indirect carbon emission cost:

The carbon emission cost is based on monetary measurement. The carbon emissions of the cement manufacturing industry can be obtained through the previous steps. And the cost value of carbon emissions can be calculated according to the carbon emissions trading price. At present, China has 7 provinces and cities of Beijing, Tianjin, Shanghai, Chongqing, Hubei, Guangdong and Shenzhen to carry out carbon emissions trading pilot. Each carbon market has carbon trading and market prices, so cement enterprises can trade according to their carbon trading market.

Measurement of carbon emission cost

The direct carbon emission cost refers to the carbon emissions generated by fuel and the carbon emissions produced in the production process of cement manufacturing enterprises.

Equation 1: Carbon emissions cost from fuel combustion

$$CEC_{fc} = \sum_{i=1}^{n} (Q_i \times A_i \times C_i \times O_i) \times 44/12 \times p_0 + \sum_{i=1}^{n} (Q_j \times H_j \times EF_j \times \alpha_j) \times p_0$$

Where:

- CEC_{fc}= carbon emissions Cost from fuel combustion (yuan);
- Qi= net consumption of the i-th fossil fuel during the accounting and reporting period. Solid or liquid fuel (t); Gas fuel (10 Km^3);
- Ai = average low calorific value of the i-th fossil fuel in the accounting and reporting period. Solid or liquid fuel (GJ/t); Gas fuel (GJ/10 Km^3).
- Ci = unit calorific carbon content of the i-th fossil fuel (tC/GJ).
- Oi = carbon oxidation rate of the i-th fossil fuel (%).
- p_0=carbon market price (￥/t).
- i=types of fossil fuels consumed during the accounting and reporting period
- Qj = amount of j-th alternative fuel or waste(t).
- Hj= weighted average low caloric value of the j-th alternative fuel or waste (GJ/t).
- EFj= CO2 emission factor of the j-th alternative fuel or waste (tCO2/GJ).
- α_j = non-biomass carbon content in the j-th alternative fuel or waste (%).
- J=Types of alternative fuels or waste.

Equation 2: Carbon emission cost from the calcining of raw materials

$$CEC_{rm} = (\sum M_1 + M_{bpd} + M_{ckd}) \times [(m_2 - m_3) \times 44/56 + (m_4 - m_5) \times 44/40] \times p_0 + M_6 \times \beta \times 44/12 \times p_0$$

Where:

- CEC_{rmr}= carbon emission cost from the calcining of raw materials (yuan);
- M_1=quality of cement clinker produced (t);
- M_{bpd}=quality of blast dust in furnace bypass (t);
- M_{ckd} =dust quality of kiln head (t);
- m_2=proportion of calcium oxide in clinker (%);
- m_3=proportion of calcium oxide from clinker that is not derived from carbonate decomposition (%);
- m_4=proportion of Magnesium Oxide in the clinker (%);

- m_5=proportion of Magnesium Oxide from clinker that is not derived from carbonate decomposition (%);
- 44/56= Molecular weight conversion between CO2 and CaO.
- 44/12= Molecular weight conversion between CO2 and MgO.

M_2=quality of raw material (t);
- m_5=fuel carbon in raw materials (%);
- p_0=carbon market price (yuan/t).

-- m_2= ratio of cao in clinker (%).
-- m_3= the proportion of cao that is not derived from carbonate decomposition in clinker (%).
-- m_4= ratio of mgo in clinker (%).
-- m_5 = the proportion of mgo that is not derived from carbonate decomposition in clinker (%).
-- 44/56= molecular weight conversion between co2 and cao.
-- 44/12= molecular weight conversion between co2 and mgo.

Equation 3: Electricity emission cost in production process

$$EEC_{PP} = P_1 \times EF_3 \times p_0$$

Where:
- EEC_{PP}= Electricity emission cost in production process (yuan);
- P_1=net purchase of electricity consumed in the production process (MWh);
- EF_3= power CO_2 emission factor (t/MWh);
- p_0=carbon market price (yuan/t).

The cost of indirect carbon emission refers to the carbon emissions produced by the external energy (electricity, heat, steam) consumed by the cement manufacturer in the whole production process of the product.

Equation 4: Electricity emission cost in auxiliary production and management processes

$$EEC_{auxi} = P_2 \times EF_3 \times p_0$$

Where:
- EEC_{auxi}= electricity emission cost in auxiliary production and management processes(yuan);
- P_2=the amount of electricity consumed in the process of auxiliary production and management (MWh);
- EF_3=power CO_2 emission factor (t/MWh);
- p_0=carbon market price (yuan/t).

Record of carbon emission cost

In the whole process of the production of the cement manufacturing enterprise, the material flow cost method is adopted and each quantity center is regarded as the unit of cost accounting. Based on the quantity center, the cost is collected first and then allocated according to a certain distribution method. The cost of the next quantity center consists of semi-finished products transferred from the last volume center, newly invested raw materials, energy and equipment depreciation. Based on the quantity center, the material flow cost method is subdivided into material cost, energy cost, other indirect cost and internal loss cost before the related cost is collected.

No carbon emission cost account is found in the current Level I account of manufacturing enterprises' chart of accounts. In the process of production, due to the cost related to production, it can be calculated directly by "direct carbon emission cost" and "indirect carbon emission cost" of Level 2 account subject according to needs, and can also be calculated by "production costs — direct carbon emission costs" and "production costs — Indirect carbon emission costs". In order to highlight the research content, this paper uses the first method to calculate.

(1) The accounting records of direct carbon emission cost are as follows:

Cost of direct carbon emissions	- Cost of carbon emissions from fuel combustion	×××	
	- Cost of carbon emission from raw material calcination	×××	
	- Emission costs of electricity used in production process	×××	
	- Raw materials and other related subjects		×××

(2) The accounting records of indirect carbon emission cost are as follows:

Cost of indirect carbon emission	—Electrical discharge costs for auxiliary production and management	×××	
	Cash in bank and other related subjects		×××

(3) The accounting records of carrying forward closing carbon emission costs are as follows:

Cost of manufacturer	—Cost of carbon emission	×××	

Cost of direct carbon emissions — Cost of carbon emissions from fuel combustion ×××
Cost of carbon emission from raw material calcination ×××
— Emission costs of electricity used in production process ×××
Cost of indirect carbon emission — Electrical discharge costs for auxiliary production and management ×××

Disclosure of carbon emission cost

The disclosure of carbon emission cost information is divided into both internal and external. There is no fixed format for the internal disclosure of carbon cost information, so enterprises can disclose the quantity and amount of carbon emission costs according to the internal management needs of the enterprises. Since the cost of carbon emissions has been included in the cost of products through accounting, and the information cannot be detected in the existing accounting statements, so it is possible to choose external disclosure or to selectively disclose the carbon emissions cost information of enterprise through the corporate social responsibility report.

4. CASE ANALYSIS OF CARBON EMISSION COST ACCOUNTING AND DISCLOSURE FOR MANUFACTURING ENTERPRISES

The following is a case of cement manufacturing enterprises to illustrate the cost accounting and disclosure of carbon emissions. This case data comes from the production data of a cement enterprise in 2015, which is provided by Li (2017). The cement enterprise not only produces cement clinker, but also produces cement.

In 2015, the total output of cement clinker and the total output of cement were 652061 tons and 846320 tons respectively. In the process of cement production, the ore raw material is consumed, of which the CaO content of the clinker is 66.59%, the content of MgO in the clinker is 0.43%, the CaO content of the non-carbonate form in the clinker is 1.02%, and the MgO content of the non-carbonate form in the clinker is 0.13%. The total amount of dust in the kiln exhaust barrel is 16.37 tons, the amount of clinker calcined bituminous coal is 96847 tons, the amount of diesel oil is 18 tons, the power consumption of raw material preparation is 1770613/kWh, the power consumption of calcining of clinker is 15688848/kWh, the power consumption of auxiliary production and management is 2558992/kWh, the power consumption of cement production is 28687889/kWh, the power generation capacity of cement kiln waste heat is 17171401/kWh and so on. The trading price of carbon emissions is 23.57 yuan /t (taken from the average price of the carbon market in 2015 from the Hubei carbon market).

4.1. Calculation of carbon emission cost in cement manufacturing enterprises

The specific classification of carbon emission costs in cement manufacturing enterprises mainly refers to the standard of “Accounting Method and Report Guide of Greenhouse Gas Emission in China Cement Production Enterprise (Trial Implementation)". Carbon emissions include fuel combustion emission, industrial production process emission and net purchase of electricity and heat corresponding emissions. The specific carbon emission cost data are shown in Table 1:

Table 1: Carbon emission cost calculation table for cement manufacturing enterprises in 2015

Carbon Emission Cost	Emission Source	Carbon Emissions (t)	Carbon Cost (yuan/t)
Direct Carbon Emission Cost	Emissions from Fossil Fuel Combustion	191017.26	4502276.82
	Calcined Emission of By-pass Dust	338097.46	7968957.13
	Calcined Discharge of Kiln Ash		
	Emission Corresponding to Carbonate Decomposition		
	Emission of Non-fuel Carbon Combustion in Raw Material	3678.68	86706.49
Cost of indirect carbon emission	Emissions Corresponding to Power Consumption	24989.12	588993.56
Total	Whole Process of Cement Production	557782.52	13146934.00

Note: the carbon emission data in the table are derived from the carbon emission cost calculated according to the method from " Accounting Method and Report Guide of Greenhouse Gas Emission in China Cement Production Enterprise (Trial Implementation)" in the article of Li et al. (2017).

Calculation of Direct Carbon Emissions Cost and Its Accounting Treatment

According to Table 1 above, the calculation results of direct carbon emission cost are as follows:

(1) Cost of carbon emissions from fuel combustion(CEC_{fc})
=（96847×20.96×0.02618×98%+18×42.652×0.0202×99%）×44/12×23.57=4502276.82(yuan)
That is, cost of carbon emissions from fuel combustion=4502276.82(yuan)

(2) Cost of carbon emission from the calcining of raw materials(CECrm)
= (652061+0+16.37) ×[(66.59%-1.02%)×44/56+(0.43%-0.13%)×44/40] ×23.57+1003276×0.1%×44/12×23.57
That is, cost of carbon emission from the calcining of raw materials=7968957.13+86706.49=8055663.62(yuan)

(3) Electricity emission cost in production process(EECpp)
= (17770613+15688848+28687889-17171401) ×0.5257/1000×23.57=557285.70(yuan)
That is, Electricity emission cost in production process =557285.70 (yuan)

Therefore, accounting entries can be compiled according to the direct carbon emission cost. There is no carbon emission cost subject in Level I accounting subjects of the manufacturing enterprise, but the enterprise can set up Level 2 accounting subject of "direct carbon emission cost" according to the needs of the enterprise, as follows:

Cost of direct carbon emissions —	Cost of carbon emissions from fuel combustion	4502276.82
	— Cost of carbon emission from raw material calcination	8055663.62
	— Emission costs of electricity used in production process	557285.70
	-- Raw materials and other related subjects	13115226.14

Calculation of Indirect Carbon Emissions Cost and Its Accounting Treatment

Electricity emission cost in auxiliary production and management processes (EECauxi)
=2558992×0.5257/1000×23.57=31707.83(yuan)
That is, Electricity emission cost in auxiliary production and management processes =31707.83 (yuan)

Therefore, the accounting records of indirect carbon emission cost are as follows:

Cost of indirect carbon emission —Electrical discharge costs for auxiliary production and management		31707.83
Cash in bank and other related subjects		31707.83

Closing Carbon Emission Cost Carry-forward

At the end of the term, carbon emission costs need to be carried forward. Its accounting records are as follows:

Cost of manufacturer —	Cost of carbon emission	13146933.97
Cost of direct carbon emissions —	Cost of carbon emissions from fuel combustion	4502276.82
	— Cost of carbon emission from raw material calcination	8055663.62
	— Emission costs of electricity used in production process	557285.70
Cost of indirect carbon emission —	Electrical discharge costs for auxiliary production and management	31707.83

4.2. Disclosure of carbon emission costs in cement manufacturing enterprises

Cement enterprises can disclose carbon emission costs in the process of cement production to the corporate management by means of internal carbon emission cost reports. At the same time, the direct carbon emission costs of 13115226.14 yuan and the indirect carbon cost of 31707.83 yuan are disclosed separately in the notes to the accounting statements, and the carbon emission cost information is selectively disclosed through the corporate social responsibility report. For the problems found in the material flow cost accounting method, we can send the countermeasures and suggestions as internal management improvement suggestions to the management department after analysis, and control the damage caused by excessive carbon emissions to the environment.

5. CONCLUSION

This paper, based on Schumpeter Innovation Theory, combined with the production process of cement enterprises, reengineering the existing financial accounting process, first carries out carbon emission verification to obtain carbon emissions, then calculates carbon cost measurement by carbon market price, and finally discloses carbon cost information, and uses cement manufacturing enterprises as a case to illustrate. The innovation of this paper is based on Schumpeter Innovation Theory, and proposes the reengineering of financial accounting process, which can solve the difficulties of carbon cost accounting under traditional accounting and provide carbon emission cost information for the internal managers of enterprises. The limitation of this paper is the data obtained from Li et al. (2017) due to the availability of indicators such as cement carbon emissions. In addition, this paper only pays attention to the calculation of carbon emission costs in the process of production. Because the scope of the investigation is limited, it may miss other aspects of carbon emission cost calculation. Look forward to improving in future research.

6. ACKNOWLEDGEMENTS

This study was supported by the Hubei Circular Economy Development Research Centre Open Fund Project (No. HXFKYJ52).

7. REFERENCES

Lee, K.H., 2012. Carbon accounting for supply chain management in the automobile industry. *Journal of Cleaner Production*, *36*, pp.83-93.

Tsai, W.H., Shen, Y.S., Lee, P.L., Chen, H.C., Kuo, L. and Huang, C.C., 2012. Integrating information about the cost of carbon through activity-based costing. *Journal of Cleaner Production*, *36*, pp.102-111.

D'Onza, G., Greco, G. and Allegrini, M., 2016. Full cost accounting in the analysis of separated waste collection efficiency: A methodological proposal. *Journal of environmental management*, *167*, pp.59-65.

Martinez-Sanchez, V., Kromann, M.A. and Astrup, T.F., 2015. Life cycle costing of waste management systems: Overview, calculation principles and case studies. *Waste management*, *36*, pp.343-355.

Wan, Y.K., Ng, R.T., Ng, D.K. and Tan, R.R., 2015. Material flow cost accounting (MFCA)–based approach for prioritisation of waste recovery. *Journal of Cleaner Production*, *107*, pp.602-614.

Cowan, S. and Deegan, C., 2011. Corporate disclosure reactions to Australia's first national emission reporting scheme. *Accounting & Finance*, *51*(2), pp.409-436.

Luo J, Xiao X., 2011.Material flow cost accounting theory and its application. *East China Economic Management*, (7), pp.113-117.

Lin J, Zhang B., 2012.Research on the Confirmation and Measurement of Corporate Carbon Emission Costs. *Contemporary economic,* (1), pp. 43-45.

Deng M, Luo W., 2010.The environment management accounting research progress -- material flow cost accounting guide content and enlightenment. *East China Economic Management*, (2), pp.90-94.

Deng M, Luo W, Huang L., 2009.Foreign material flow cost accounting research and practice and enlightenment. *Journal of Hunan University of Science and Technology (social science edition)*, (2), pp.78-83.

Li J, Yin J, Wu Q, Wei J, Wang R.,2017. Comparison and Case Analysis of Carbon Emission Calculation in Cement Industry. *China Cement*, (08), pp.83-86.

294: Application of an economical multi-axis automatic solar tracking device for efficiency improvement in solar power systems using Arduino board

Dominic RAMERE[1], Timothy LASEINDE[2]

[1] Tshwane University of Technology, Pretoria, South Africa, rameremd@eskom.co.za
[2] University of Johannesburg, Doornfontein Campus, Johannesburg, South Africa, otlaseinde@uj.ac.za

Solar irradiation is a green and sustainable renewable energy source which is largely harnessed through photovoltaic and thermal cell surfaces. It is one of the fastest growing clean power technologies with high global growth figures, due to its simplicity, affordability, and availability, relative to other renewable energy alternatives. In South Africa, rural urban drift has been on the increase which has contributed to increase in the demand for electric power supply thereby causing undue strain to national power grids. Ironically, the expansion of power generating stations lags behind increasing energy demand. Solar power systems is one of the fastest growing interventions augmenting fossil power and its application is now expanding beyond domestic utilization to commercial and industrial dependence. Due to continuous change in the position of the sun together with other salient factors, only a fraction of the suns energy potential is harnessed. The paper is focused on sharing an optimisation option that has effectively addressed a major gap experienced in conventional solar power system installation as applicable to Light Emitting Diodes (LED) traffic light systems. The continuous movement of the sun limits maximum sun light irradiation absorption and solar trackers are practical solutions to this drawback. The high cost of solar trackers has however been the major limitation to their adoption. The Introduction of microcontroller based solar tracking systems using Arduino board was found to be cost effective, and it improved the efficiency of the solar cells significantly. In the study, the maximum Power Point (MPP) tracking algorithm was designed and developed using multiple-axis servo-motor feedback tracking system, which increased the efficiency of the solar panel array by 23.95%.

Keywords: solar tracking; solar power; Arduino board; optimisation; solar irradiation

1. INTRODUCTION

Electricity generation through solar power is widely used for industrial, commercial and domestic purposes. Gomathy et al. (2012:1110) states, “Government, industry and independent analysis have shown that cost-effective energy efficiency improvements could reduce electricity use by 27% to 75% of total national use within 10-20 years without impacting quality of life or manufacturing output”. Solar energy systems are cost effective energy efficient systems, and they have the advantage of zero harmful gas emissions. They are free of daily running cost compared to fossil powered energy systems (Cha and Lee. 2008), because the suns energy is simply absorbed by photovoltaic and thermal solar systems. The only waste linked to solar energy systems is the e-waste during the disposal phase after the life cycle of its components. However, e-waste is not peculiar to solar systems alone and this cannot be avoided in the current dispensation because almost every system existing today is dependent on electronics. This research deals with power systems supplying power to Light Emitting Diodes (LED) in a typical traffic light system. The topic is useful because load shedding and continuous load balancing of the main grid power supply system is negatively impacting power supply to traffic light systems within the region where this research was carried out. Power failure in this traffic systems lead to long vehicular queues which end up in commotion whenever power supply is not restored quickly.

The use of renewable energy sources as alternative to fossil fuel is continually increasing due to the consciousness for greener environment fuelled by environmental sustainability drives. Government incentives promoting cleaner energy, and rising global prices of fossil fuels is continually increasing the prominence of greener power supply thereby contributing to solar energy demand. Solar energy is free but the process of absorbing the energy requires optimisation due to losses experienced in solar Photovoltaic (PV) and thermal absorbers. Excessive heat on the solar panels and poor orientation of the panels per time have been identified as the two most contributory factor to poor efficiency of solar absorbers. The Maximum Power Point (MPP) varies with solar insolation and seasons, and absorbing maximum solar irradiation is imperative for an efficient system (Mummadi et al, 2002) (Gomathy et al., 2012:1110). Numerous studies have been conducted to develop methods of enhancing efficiency of photovoltaic cells. Generally, increasing the number of cells within an array is the quickest method often considered when energy demand increases. However, the use of solar tracking algorithm enables more energy to be generated by the solar panel without increasing the number of cells in an array (Won et al., 2006:1048). This is so because solar trackers can be designed to maintain perpendicular profile to the sun’s rays whenever there is day light (Eldin et al., 2016:228) (Shah and Shah, 2012:91). In 2012, Eke and Sentruk (2012) of Turkey found that, solar tracker improved power generated by solar cells by 30%. Huang and Sun (2007:677) proved that single-axis solar tracking system increased power output of solar panel by 56%. According to Ghosh and Haldar (2014), the use of solar tracking system can increase the output of solar systems by estimated percentages as high as 60 %. At particular solar insolation levels, there is a unique operating point of the photovoltaic generator wherein the power output will be maximum. It is important to match photovoltaic power output of solar generators with the load, such that the equilibrium operating point coincides with the MPP of the PV source (Mummadi et al., 2002). To overcome this problem, multiple-axis solar tracking system need to be deployed to obtain maximum power obtainable by the solar cells. In 2013, Bawa and Patil (2013:179) used buck dc to dc converter to improve Maximum Power Point Tracking. According to Eldin et al. (2016:230) works on geographical studies, the sun move from East to West. However the design of solar tracking system is required to move on a multiple-axis that can achieve continuous change of direction throughout the day time as the position of the sun changes not only East to West but with angular variations in orientation such as East-West. Senpinar and Cebeci (2012:684) concluded that, two-axis solar tracking systems are the most effective due to the advantage of maintaining constant position to sun without being affected by cloud or other environmental conditions. The tracker must be able to fulfil East to West, and North to South direction changes.

The study involved the development of a low cost microcontroller multi-axis solar tracking system using Arduino board. From literature review carried out in the early stages of the research, the two options available for low cost effective tracking devices were Arduino and Rasberry pi. Arduino board is quite similar to Rasberrry pi due to their cost effectiveness. An Arduino is a microcontroller motherboard which is simply a small computer that can run one program at a time, whereas the raspberry pi runs multiple programs and are more complicated to use than Arduino. The poor adoption of solar tracking devices have been largely linked to the placement location and the high cost of purchasing solar tracking units. As such, a major objective of the study was to improve solar PV array efficiency at low cost. The focus of this paper is to discuss the approach that was adopted for improving efficiency of solar panel array as tested on Light Emitting Diode (LED) traffic light system.

1.1. Photovoltaic cell efficiency with changing solar irradiation

During the daytime, there is big variation in the power delivered by solar cells most especially in the first six hours and the last five hours of the day (Bristow and Campbell, 1984). The sun constantly moves from East to West on daily basis, of which 180 degrees is day and the other 180 degrees is night (Zhan et al., 2013:276). As stated by Laurentiu (2006), the fixed orientation solar panel can only see about 75 degrees of the sun motion, of which only 25% of the solar energy is harnessed, and 75% of the energy is lost.

According to the graph of local solar time shown in figure 1, there is gradual increase in solar insolation from 06:00hrs to 12:00 hours and decline from 12:00 hours to approximately 19:00 hours.

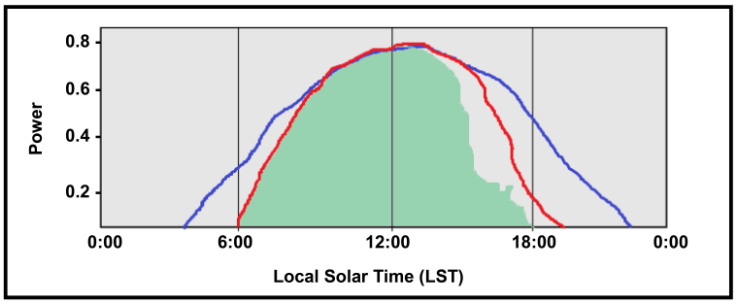

Figure 1: Local solar time

2. SOLAR TRACKING DEVICES

Solar tracking devices enable PV cells to absorb maximum radiant energy from the sun. Through the absorption of maximum sun light, Maximum Power Point (MPP) of solar cells will be achieved and more power will be generated. There are numerous solar power tracking models which are in use for improving the efficiency of solar array. Multiple axis solar tracking system use both East-West and North-South axes for positioning the solar panel (Yusof and Zamri, 2014). This type of solar tracker is accurate in maintaining the perpendicular profile to the sun all the time, even under seasonal changes where there is slight change in the sun's position at sunrise and sunset (Mousazadeh et al., 2009:1800). However, it was stated by Senpinar and Cebeci (2012:685) that two-axis solar tracker arrays have the advantage of maintaining their position without being affected by environmental conditions.

Generally, multiple-axis solar tracking systems have the disadvantage of high construction cost and high energy consumption due to energy required to run the rotating motors. The positioning control of horizontal and vertical directions are done by using two dc motors (Yousen. 1999). Furthermore, the cost of maintaining the motors and control system is much higher in multiple- axis tracking systems than the single axis tracking position systems. From a life cycle perspective, lowering the cost of the system architecture will overcome this disadvantages.

The disadvantage of single axis solar tracking system is that it can tilt only in a single plane and wrong positioning may inconvenience the solar panel. The use of multi-directional tracking systems overcomes this limitation. The movement of solar system need to accommodate all positions relative to the motion of the sun (East-West and North-South). However Iulia Stamatescu et al. (2014:501) described the motion of two-axis solar panels as Azimuth angle (horizontal direction) and Zenith angle (angle of inclination). The study findings showed that the use of low power servo motors carefully designed to move the tracking device hub substantially reduced the power required by the tracking system. Arduino board which belongs to a family of low cost control system was also found to be extremely energy efficient.

2.1. Development of the solar tracking system

Solar trackers are designed using a combination of hardware components and Software control systems. The setup comprises of sensors, comparators, microcontroller circuit, motor drive circuit, and electric motors. Basically, stepper motors or servo motors are usually utilized. These are assembled and programmed to move the platform on which the Photovoltaic cells are mounted. The Arduino board model discussed in this study eliminates some of these components. Figure 2 shows the schematic diagram of how the tracking system operates.

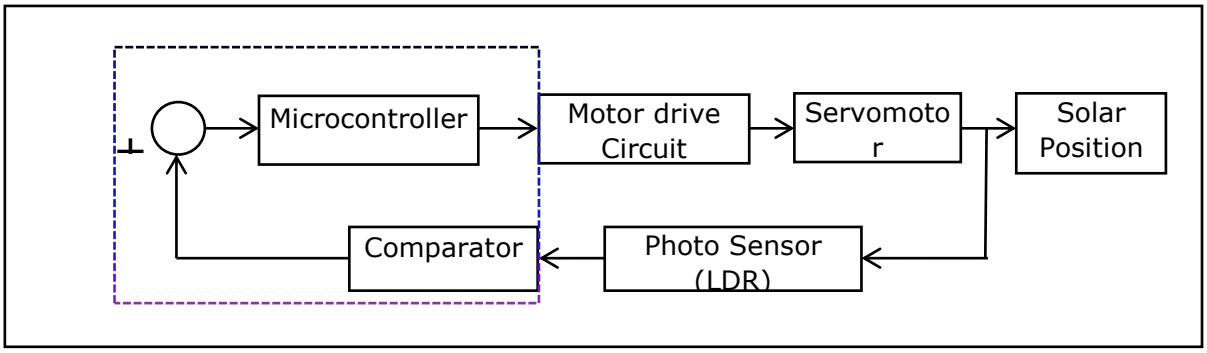

Figure 2: Solar positioning control system

The system was modelled using a power supply device, an Arduino board, a servo motor, and Light Dependent Resistor's (LDR's) which serve as light sensors for detecting the light from the sun. The system is automatically driven relative to the sun to achieve the maximum power point. The solar cells therefore maintain the perpendicular position (90 degrees) to the sun in the sky as the tracking unit twist towards the perpendicular position.

The Photovoltaic position control (Light Dependent Resistor) is the mechanism controlled by electric circuit to position the solar panel perpendicular to the sun in the sky. The tracking system improves the efficiency of solar panel by increasing the duration of radiant energy absorption. Tracking the sun at the highest accuracy degree ensure that concentrated radiant energy is precisely absorbed by the solar panel. The microcontroller is the decision maker that collaborates with motor drive circuit, light sensors, motors for positioning the solar panel support structure direct to sun light.

The light dependent resistors (LDR) detect the light from the sun and are connected to the comparator circuit. The LDRs are attached on the panel, each on opposite direction to the other. The multiple-axis solar tracking system use four (4) LDRs of which each pair is situated at opposite direction to each other. When the solar panel has been positioned perpendicularly, the voltages of all four (4) LDRs will be equal. Unequal voltage generated by the sensors lead the microcontroller to execute the directional change to a new position in line with the suns movement. Figure 3 shows how the sensors are attached on the multiple-axis solar tracking system.

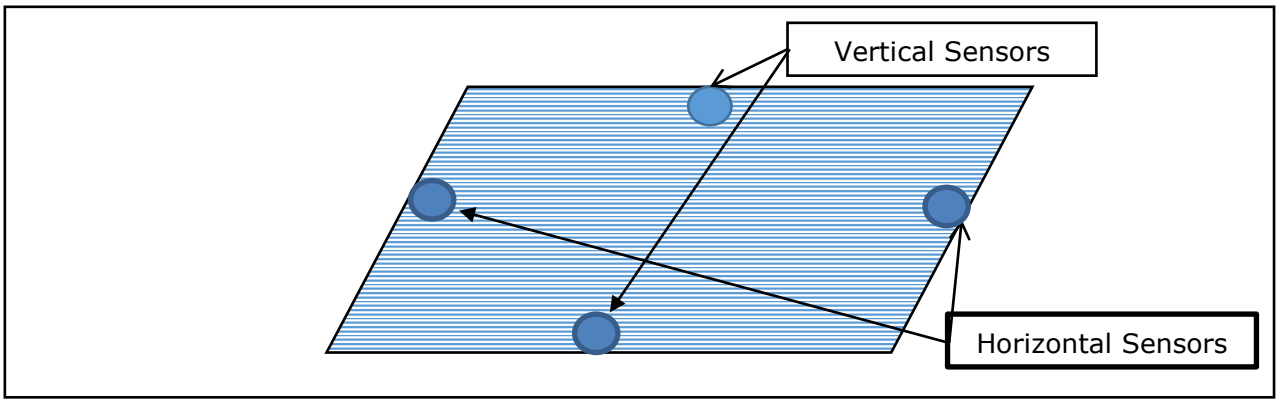

Figure 3: LDR positioning

The comparator circuit compare the difference of the voltage generated by Dependent Resistor (LDR) situated opposite direction of the other attached on the solar panel. The comparator use the voltage divide rule to compare the voltage generated by each LDR. The voltage divide of comparator is mathematically calculated as:

$$V_{min} = 5V\left(\frac{Selected\ R}{Selected\ R + Dark\ R}\right)$$

The resistance value of the LDR is inversely proportional to the light. Increase in the voltage of any LDR triggers the comparator to inform the microcontroller where more sun light is available. Figure 4 shows the relationship between the light and resistance of the LDR.

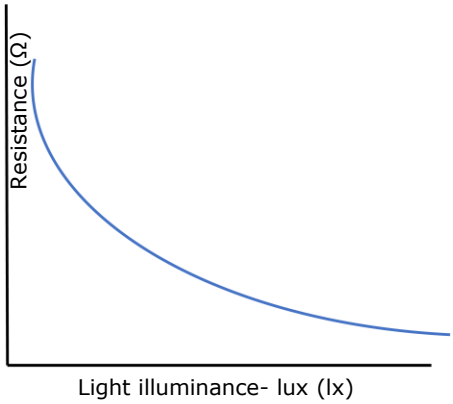

Figure 4: Relationship between light and resistance

The Light Dependant Resistors are connected to the analog input of the Arduino circuit on the pin 23 to 26. The Arduino microcontroller (ATMega328P) has its internal comparator that is used to compare the difference of the voltages generated by the LDRs. The comparator can be the Non-inverting and inverting as shown in figure 5 and figure 6 below.

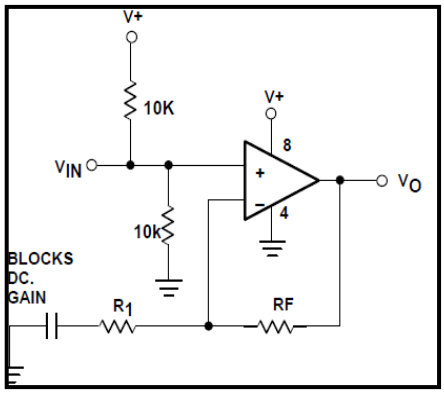

Figure 5: The non-inverting comparator

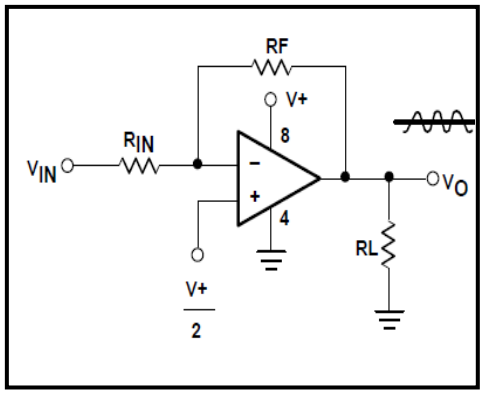

Figure 6: Inverting Comparator

The inverting comparator has input voltage connected to the inverting pin of the comparator and the reference voltage is connected to the non-inverting pin of the comparator. The non-inverting comparator configuration have the input voltage connected to the non-inerting pin of the comparator with the reference voltage connected to the inverting pin of the comparator.

Microcontroller (ATMEGAR328) microchip stores and runs the program memory for the operation of solar tracking system. The microcontroller has the analogue inputs that connects the LDRs to the circuit, and the outputs that give the motor drive circuit the direction of rotations. The microcontroller has 14 digital input/ output of which six (6) was used as Pulse Width Modulator (PWM) and are analog inputs. It operates at the frequency of 16MHz. One of the main advantages of Arduino microcontroller circuit is that their circuit design has connections on both inputs/outputs connections which enables the program installation to perform the required duty. This microcontroller circuit is cheaper and minimizes time and electronic circuits construction cost. The two (2) LDRs are connected to any six (6) analog inputs pins used as comparators and the motor drive circuit is connected to the output pins of the microcontroller. Figure 7 below shows the complete microcontroller Arduino board used for carrying out experiment

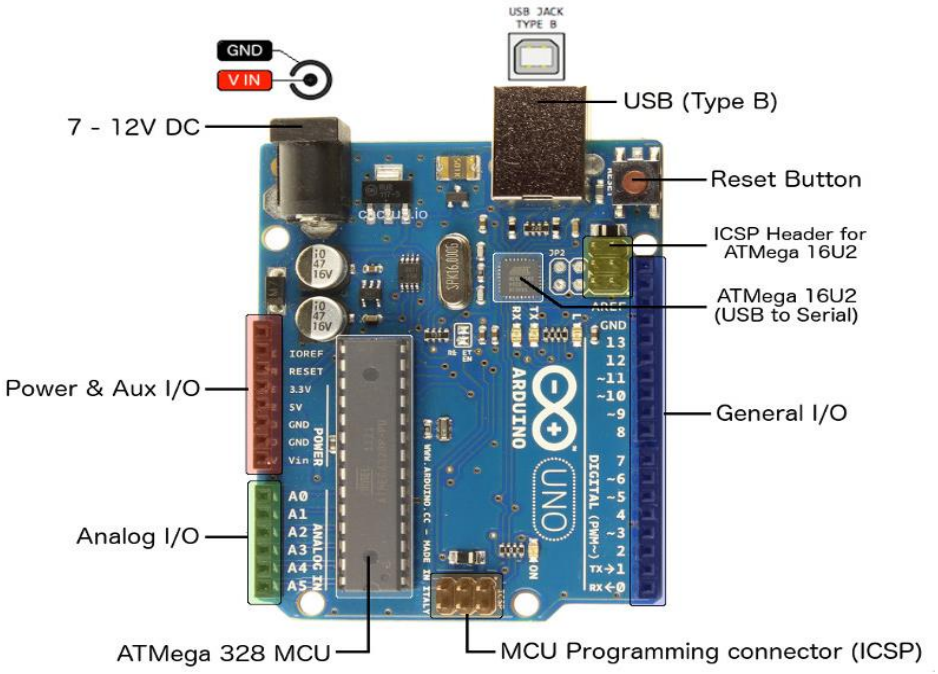

Figure 7: Labelled image of the Arduino Uno Rev 3 Board (Cactus, 2016)

Arduino also has the advantage of carrying out basic multi-function without the use of many circuit diagrams and without upgrading to Rasberry pi. The portable microcontroller has the ability to drive any size of structure with its intelligent program.

2.2. Motor drive circuit and servo-motor (Optional Circuit)

Motor drive circuit will only be applicable for driving the big motor that need more power to rotate. The motor drive circuit of L293D receives the signal for the microcontroller on which direction the motor rotates. The L293D is a multiple high current half-H driver that has bidirectional rotations. It operates at the voltage range between 4.5 to 36V dc. This circuit is designed to drive high voltage/current loads.

The servo-motor form part of mechanical structure for positioning the solar panel to the desired direction executed by the Arduino microcontroller circuit. The motors sizes are chosen based on the torque and load to be driven to achieve the objective of improving the efficiency.

Tests

Traffic light

In the experiment carried out, a 4 watts 300/400 mm red polycarbonate traffic Light Emmiting Diode was used to measure the efficiency of solar panel. The lights operate at the rated voltage of 12 Direct Current (DC).

It is highly important to measure the efficiency of tracked solar panel with reference to the stationary panel. The results was validated by comparison of power generated by stationary and tracked solar panel. Table 1 shows data gathered from a stationary panel and table 2 represents data gathered from tracked solar panel.

Table 1: Data measured from fixed solar panel

Data Collected from Fixed positioned solar panel						
Time	**Input (Photovoltaic panel)**			**Output (LEDs connected to the Battery)**		
	Voltage (V)	**Current (A)**	**Power (W)**	**Voltage (V)**	**Current (A)**	**Power (W)**
05:00	0	0	0	0	0	0
06:00	21.5	0.122	2.621	5.4	0.003	0.0162
07:00	21.4	0.19	4.066	10.1	0.23	2.323
08:00	18.6	0.27	5.022	11.4	0.33	3.762
09:00	17.6	0.36	6.336	12.4	0.36	4.464
10:00	17.7	0.44	7.788	13	0.38	4.94
11:00	17.8	0.48	8.544	13.2	0.39	5.148
12:00	17.9	0.48	8.592	13.5	0.39	5.265
13:00	17.4	0.47	8.187	13.4	0.39	5.226
14:00	17.4	0.41	7.134	13.3	0.38	5.054
15:00	17.7	0.37	6.549	12.9	0.34	4.386
16:00	16.9	0.25	4.225	12.2	0.34	4.148
17:00	16.9	0.12	2.028	11.6	0.34	3.944
18:00	13.9	0.024	0.3336	6.7	0.002	0.0134
19:00	3.6	0.011	0.0396	3.4	0	0

Table 2: Data for tracked solar panel. Test results obtained from Laboratory tests of tracked panels

Data Collected from Tracked solar panel						
Time	**Input (Photovoltaic panel)**			**Output (LEDs connected to the Battery)**		
	Voltage (V)	**Current (A)**	**Power (W)**	**Voltage (V)**	**Current (A)**	**Power (W)**
05:00	0	0	0	0	0	0
06:00	20.2	0.22	4.444	11.2	0.289	3.2368
07:00	18.2	0.33	6.006	12.2	0.36	4.392
08:00	17.9	0.42	7.518	12.9	0.37	4.773
09:00	17.9	0.46	8.234	13.3	0.37	4.921
10:00	17.1	0.51	8.721	13.8	0.39	5.382
11:00	17.9	0.5	8.95	13.9	0.4	5.56
12:00	17.3	0.52	8.996	13.7	0.39	5.343
13:00	18.7	0.46	8.602	13.7	0.39	5.343
14:00	17.6	0.47	8.272	13.6	0.39	5.304
15:00	18.7	0.39	7.293	13.1	0.34	4.454
16:00	17.8	0.37	6.586	13.7	0.4	5.48
17:00	17.2	0.36	6.192	13.1	0.38	4.978
18:00	18.4	0.22	4.048	12.5	0.37	4.625
19:00	17.4	0.006	0.1044	10.1	0.09	0.909

2.3. Measuring of solar efficiency

Efficiency is measured by the comparison of power generated by tracked and stationary solar panels. Mathematically efficiency is the percentage of the ratios of output power into the input power. In this case, power generated by the tracking system was considered as the reference to measure the efficiency. The graph in figure 8 was used to compare the power generated by each solar system.

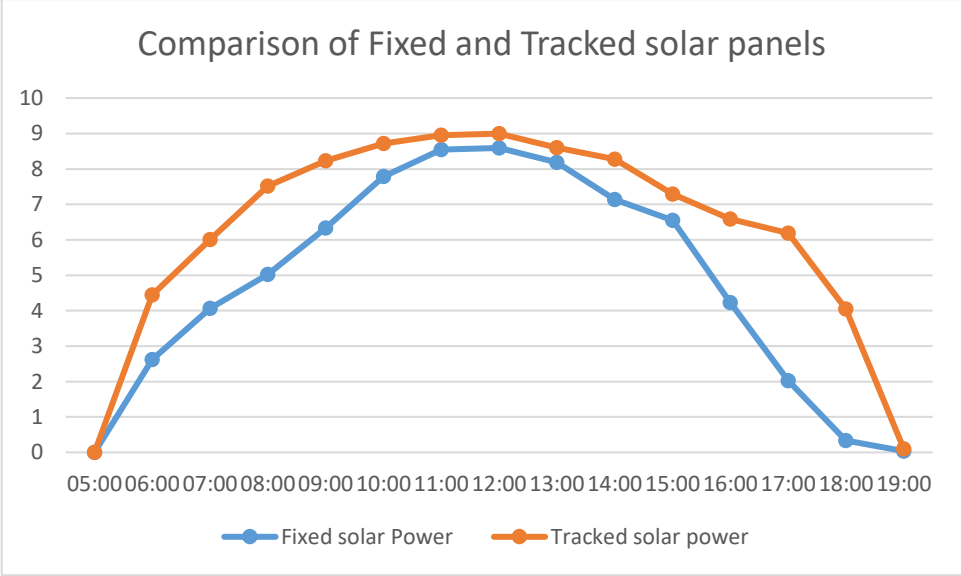

Figure 8: Comparison of energy generated by tracked and stationary solar panels

The tracked solar system has improved the efficiency of solar panel. It is mathematical expressed as:

$$Efficiency = \frac{\left(P_{tracked} - P_{stationary}\right)}{P_{tracked}} \times 100\%$$

$$= \frac{(6.2644 - 4.7643)}{6.2644} \times 100\%$$

$$Efficiency = 23.95\%$$

3. CONCLUSION

The study findings showed that the use of low power servo motors carefully designed to move the tracking device hub substantially reduced the power required by the tracking system. Arduino board which belongs to a family of low cost control system was also found to be extremely energy efficient. Multiple axis solar tracking algorithm improved the power generated by the solar panel with an efficiency improvement of 23.95 %. The study concluded that it is highly important to track the sun at a high degree of accuracy to improve solar irradiation absorption. The developed algorithm has the advantage of space savings compared to adding more solar panels to improve energy generated cum efficiency. The use of Arduino board reduced the system construction cost without depending on complicated, costly and space consuming proprietary infrastructures.

4. REFERENCES

Bawa, D. and Patil, C.Y., 2013. *Fussy control based solar tracking using Arduino Uno*. International Journal of engineering and Innovative Technology. Department of Instrumentation and control, college of Engineering, Pune, pp (179-187). Volume2, Issue 12

Bharti, B.K., 2016. *Dual Axis Solar Tracking System*. *Imperial Journal of Interdisciplinary Research*, *2*(4).

Bristow.K, and Campbell.G,. 1984. *On the relationship between incoming solar radiation and daily maximum and minimum temperature*. Agricultural and forest meteorology.

Cactus, 2016. Entry level Arduino Uno Rev 3 image, www.cactus.io/ Accessed 01 Dec 2017.

Cha,H. and Lee,S., 2008, 0ctober. *Design and implementation of photovoltaic power conditioning system using a current based maximum power point tracking*. In Industry applications society annual meeting, 2008. IAS'08.IEEE (pp.1-5).IEEE

Eldin, S.A., Lin, W.M., Tsai, M.H. and Wang, G.S., 2013, July. *Design and Implementation of the Dual-axis Solar Tracking System*. In *Computer Software and Applications Conference (COMPSAC), 2013 IEEE 37th Annual* (pp. 276-277). IEEE.

Ghosh.S, and Halgar.N,. 2014. *Solar tracking system using AT89C51 Microcontroller and LDR*. International journal of Emerging technology and Advanced engineering.

Gomathy, S., Saravanan,S. and Thangavel, S.,2012, Octomer. *Design and Implementation of Maximum Power Point Tracking (MPPT) algorithm for a standalone PV system*. Elixir international Journal. PP (11110-11114). www.elixirpublishers.com.

Huang, Y.J., Kuo, T.C., Chen, C.Y., Chang, C.H., Wu, P.C. and Wu, T.H., 2009. *The design and implementation of a solar tracking generating power system*. *Eng Lett*, *17*(4), pp.1-5.

Kwon, J.M., Nam, K.H. and Kwon, B.H., 2006. *Photovoltaic power conditioning system with line connection*. IEEE Transactions on Industrial Electronics, 53(4), pp.1048-1054

Laurentiu A., G. Maolea, and F. Ravigan. 2006. *Positioning system for solar panel placed in isolated areas*, Annals of the University of Craiova, Electrical Engineering series No.30

Mousazadeh, H., Keyhani, A., Javadi, A., Mobli, H., Abrinia, K. and Sharifi, A., 2009. *A review of principle and sun-tracking methods for maximizing solar systems output*. *Renewable and sustainable energy reviews*, *13*(8), pp.1800-1818.

Mummadi.V.,Tomonobu.S, and Katsumi.U,. 2002. *Voltage-Base maximum power point tracking control of PV system*. University of the Ryukyus.Japan

Sefa, I., Demirtas, M. and Çolak, I., 2009. *Application of one-axis sun tracking system*. *Energy conversion and Management*, *50*(11), pp.2709-2718.

Shah.S, and Shah.H. 2012. *Dual axis solar tracking system*. Dwarkadas J.Sanghvi College of Engineering.

Stamatescu, I., Fagarasan .I. and Stamatescu, S. 2014. *Design and implementation of a solar-Tracking Algorithm*. 24th DAAM International Symposium on Interlligent Manufacturing and Automation , 2013 Science Direct .pp(500-507).Elsevier

Wang, J.M. and Lu, C.L., 2013. *Design and implementation of a sun tracker with a dual-axis single motor for an optical sensor-based photovoltaic system*. *Sensors*, *13*(3), pp.3157-3168.

Wang, J.M. and Lu, C.L., 2013. *Design and implementation of a sun tracker with a dual-axis single motor for an optical sensor-based photovoltaic system*. *Sensors*, *13*(3), pp.3157-3168.

Yousef, H.A., 1999. *Design and implementation of a fuzzy logic computer-controlled sun tracking system*. In *Industrial Electronics, 1999. ISIE'99. Proceedings of the IEEE International Symposium on* (Vol. 3, pp. 1030-1034). IEEE.

Yousef,H., 1999. *Design ang Implementation of a fuzzy login computer-controlled sun tracking system.* Proceedings of the IEEE International Symposium on Industrial Electronics, Volume3, pp (1030-1034)

Yusof S.H and Zamri, M. 2004.*Modeling and simulation of maximum power point tracker for photovoltaic system*. Power energy conference pp 88-93

Yusof, Y., Sayuti, S.H., Latif, M.A. and Wanik, M.C., 2004, November. *Modeling and simulation of maximum power point tracker for photovoltaic system*. In *Power and Energy Conference, 2004. PECon 2004. Proceedings. National* (pp. 88-93). IEEE.

Zhan, T.S., Lin, W.M., Tsai, M.H. and Wang, G.S., 2013, July. *Design and Implementation of the Dual-axis Solar Tracking System*. In *Computer Software and Applications Conference (COMPSAC), 2013 IEEE 37th Annual* (pp. 276-277). IEEE.

.

295: Zoning of rural medium voltage distribution networks for improving restoration time using distribution automation systems

Dominic RAMERE[1], Timothy LASEINDE[2]

[1] *Tshwane University of Technology, Pretoria Campus, South Africa, rameremd@eskom.co.za*
[2] *University of Johannesburg, Doornfontein Campus Buxton Street, South Africa, otlaseinde@uj.ac.za*

Electricity distribution reliability is a measure of power availability, which is a function of the frequency of interruptions, and the duration of such interruptions. Studies have shown that Medium Voltage (MV) overhead lines are the most significant contributory factors to power outages which lead to poor performance of electrical distribution networks. The research investigated the basis for the poor performance of MV overhead lines in a 22 Kilovolt (KV) radial feeder, in order to develop the most reliable and cost effective optimisation approach for switching device placement which has the potential of improving the performance of MV overhead line distribution networks. A major requirement in power distribution is to supply customers with reliable electricity without interruptions. The research explored and identified causes of electricity supply interruptions, high values of Mega Voltage Ampere (MVA) losses, and the effect of downtimes in terms of number of customers impacted by outages. The findings informed the design of a robust switching device placement algorithm, capable of optimising the performance of a 22KV overhead line, by reducing the number of customers impacted by interruptions, and minimizing MVA losses accordingly. Optimal switching device placement strategy improved restoration time of electricity by isolating only faulty section of network, and minimizing high costs currently associated with scheduled maintenance on the MV lines. On the occurrence of momentary supply interruption, the reclosers automatically restore electric power by their auto-reclose feature. System Average Interruption Duration Index (SAIDI), System Average Interruption Frequency Index (SAIFI), Customer Base Impact Index (CBII), and Mega Voltage Ampere Base Impact Index (MVABII) were used to measure the performance outcomes of the line using customer and MVA data obtained from the feeder. Secondary data comprising information on monthly SAIDI, SAIFI, customers connected per transformer, and MVA data were obtained from the engineering plant department. A switching device placement technique was developed and validated using comparative analysis of the old and new data impact obtained after a pilot implementation phase. The developed technique improved the network performance by reducing the number of customers affected, and MVA losses impacted due to electricity supply interruptions by 30.74 and 25.30 % respectively.

Keywords: Medium voltage; recloser; power distribution optimisation; SAIDI; SAIFI

1. INTRODUCTION

The reliability of electricity supply to customers depends largely on the performance of power generation systems, transmission systems, and distribution system (Carter-Brown et al, 2008). In electrical power distribution systems, frequency of interruptions, outage durations and customer supply losses are the main factors often considered to judge the reliability and performance of distribution networks. According to Sohn et al (2006:941) more customers affected may cause heavy damage by increasing interest in the value-based reliability optimisation. The study was carried out at a robust power distribution network herein referred to as 'feeder A', situated in location A of area B within province C. The study was divided into phases with the ultimate aim of developing a model for improving the reliability of the power distribution network. Key Performance Indicators (KPIs) of Medium Voltage (MV) Overhead line distribution networks were evaluated which is highly important in a bid to identify where and how to improve reliability of electric power supply to customers as required by the utility company. In the power distribution industry, the main problem associated with power systems is lack of stability due to intermittent power failures. Poor reliability is linked to incessant emergence of unforeseen defects (third party influenced, natural causes and hardware failures) which are often complex, and require extensive time to diagnose and repair. Another major challenge is linked to the landscape/geographical expanse MV overhead line distribution networks cover (Hannan, 2011:235). According to Abdi et al (2014), about 70 percent of power failures are estimated as transient faults, and about 30 percent are permanent faults on MV networks. Based on the findings of the study carried out on different feeders within the "feeder A" network, the most contributory factors to poor performance of the MV overhead lines were found to be unplanned interruptions associated with hardware failure, environmental causes, natural occurrences, and third party actions. Unplanned maintenance and major interruptions are the most contributors to the Reticulation Supply Loss Index (RSLI). As highlighted by Hashim et al., (2006: 586), transient faults are commonly caused by defects due to MV line interferences as a result of clashing power lines caused by stormy whether effects. Conversely, permanent faults were mainly associated with broken lines (hardware) and third party activities such as theft and vandalism (Thomas, 2014).

In power system design, the user end expectations need to be factored into the design and these considerations must inform the approach adopted. Customer satisfaction is largely influenced by the level of reliability which is commonly understood by end users as a state where there is continuous uninterrupted power supply round the clock. As power systems designs are becoming advance by the day, the possibility of applying technology for effective network monitoring is now a reality. In this regard, it is important to deploy solutions with some level of intelligence built into them. One of such approaches is the use of switching device placement optimisation technique to improve the performance of MV overhead line distribution network in order to achieve the objective of reducing the possible number of interruptions, outage durations, number of customers affected and MVA loss.

Power systems equipment are highly capital intensive and equipment replacement requires extensive budgeting and planning. For this reason, power system designers try to achieve as much as is possible for system reliability within project budget for the envisaged lifecycle of systems. Due to the problem associated with equipment's life span, eliminating power disruptions is a herculean task. Elimination as against minimization of failures has been a hard to reach goal. In this study, switching devices placement optimisation technique was adapted as a basis for proposing the new technique developed specifically for dividing Medium Voltage (MV) distribution network in "location A" into zones. Protective devices such as fuses, reclosers and isolating switches plays important role in reducing annual failure rate and outage duration and total customer interruption cost (Sohn et al., 2006:941). A total shut down of the power system in location A was not possible during the study, because the cost associated with just a few minutes of downtime is extremely enormous. This posed some limitation to the research at the start, however; during the pilot test phase, various sections of the zones were shut down for the purpose of achieving the planned objectives.

Various methods currently exist for accomplishing performance measurement of different sections of power systems. For MV lines, System Average Interruption Duration Index (SAIDI), System Average Interruption Frequency Index (SAIFI) by (Chatterton. 2004), Mega Voltage Amperes Base Impact index (MVABII) and Customer Base impact index (CBII) are generally considered (Eskom. 2012). The study adopted existing methods and these were applied in developing the optimal switching placement technique discussed in this paper.

2. BACKGROUND

The 22KV overhead line radial feeder in location A is one of the twenty (20) worst performing feeders in its zone within a province in South African power utility. According to Carter-Brown et al (2008), reduced performance is associated with decrease of tariff and less revenue generated. As with most electrical Infrastructure, this overhead line distribution network experiences both planned and unplanned outages (Moradi et al. 2008). Planned outages occur when the equipment is isolated for reasons such as scheduled maintenance and customer request. Unplanned outages occur when power supply from the line is interrupted due to defects, leading to an automatic power trip off by protective devices. Data on restoration and daily sequential reports, Overcurrent (O/C), Sensitive Earth Fault (SEF), and Earth Fault (E/F) protection triggers recloser within the 22KV feeder system available at location A was utilized for the developed model.

Overhead line performance evaluation is important to the utility where the study was conducted because it guides them in identifying where to make improvement on the distribution network. Improving the performance of the distribution networks is important to ensure reliable electricity supply is available to end users (Carter-Brown et al, 2008). The reliability and availability of electricity in distribution network is measured based on number of interruptions or outages and restoration time of supply (Eskom. 2012). It is important to balance between the investment cost and network performance by including reliability criteria of distribution networks (Abiri-Jahromi et al, 2012). To improve reliability, the numbers of unplanned outages must be reduced, and the duration of such outages must be shorter. Frequent power interruptions lead to loss of production in the manufacturing sector. In industries and commercial enterprises, poor supply affects productivity and service delivery, which in turn reduces the revenue generated. Long down time of electricity supply lead to losses of perishable items by domestic users. At the commencement of the research, the 22 kV overhead line at location A had large number of defects which required large amount of human and financial resources for its maintenance.

System Average Interruption Frequency Index (SAIFI) is the Key Performance Indicator (KPI) for measuring the frequency of outages while System Average Interruption Duration index (SAIDI) is the KPI to measure the average yearly outage time (Carter-Brown et al, 2008). The Reticulation Supply Loss Index (RSLI) is used to measure the customer hour losses on MV distribution network (NRS 048-6). According to the SAIDI and SAIFI report, the 22KV feeder in location A is the most significant contributor to the poor performance in area B of Province C. The weekly restoration report shows that it takes technicians unacceptably long durations to restore supply. Conversely, the maximum allowable downtime by power utility standards is three and half hours. The excessive downtime is a function of the long hours spent on fault finding and actual repairs of such faults. The control officer compiles a detailed daily sequential report that shows the frequency, duration and customer hour losses of power outages and restoration on the electric power network based on SAIFI and SAIDI standards. In order to achieve a better distribution system reliability indices fault management must reduce the number of faults, interruption, customers affected, outage duration (Sumper et al .2005).

The study focused on improving the network management through increasing the level of optimal switching devices on Medium Voltage (MV) power network to improve the operating efficiency of medium voltage overhead line distribution networks that in turn will improve the restoration time and reduce number of customers affected by the interruptions and MVA losses. The optimal numbere and placement of sectionalizing switches in MV radial distribution network correspond to technical, regulatory and economic aspect (Esteban et al, 2010:283). According to Abiri-Jahromi et al (2012), automation was used by distribution utilities as a successful investment strategy to enhance reliability and operation efficiency. Distribution network automation system can trim down outage events and increase system reliability (Dehghani, and Dashit, 2011: 508). With the use of switching devices placement technique, there is a hypothesis to support possible improvement in the restoration time and reduction in customer hour losses on feeder A. The approach adopted generated output results that may be applied to optimise the network performance by reducing interruptions, improving restoration time and reducing customer hour losses on the Medium Voltage (MV) overhead lines. The location for pilot phase optimal switching device placement technique implementation was based largely on daily network events, showing critical indicators for improvement.

2.1. Optimisation method

In this research, zone concept optimal switching device placement was utilized to improve the performance of an over-headline distribution network by minimizing the number of customers and Mega Voltage Amperes (MVA) losses by electricity supply interruption. A 22KV overhead line was divided into zones (sections) equipped with intelligent protective devices to achieve the research objective. According to Abiri-Jahromi et al., (2012: 362), there is a critical need for balance between investment cost and network performance by including specific reliability criteria for equipment idleness, loading level and customer per network. It is important to equip the line with the right automation system to minimize interruption that will lead to improvement on the performance. Preliminary studies of past works on Medium Voltage (MV) overhead lines optimisation were reviewed, in order to come up with approaches for switching devices placement to enhance the performance of feeder A 22 KV network. Furthermore, zone concept optimal switching device placement techniques was studied and adopted as a measure for developing a suitable model for optimising the performance of MV overhead line distribution network of the r 22KV power feeder by dividing the network into zones. According to Thomas (2014), determining the optimal number and placement of switching devices within sections of MV overhead line radial distribution network is in correspondence with technical, regulatory and economic aspects. Planning criteria on distribution network is based on analysis of feeder characteristics, existing network performance and experienced based rules (Carter-Brown et al, 2008). The main aim of the study was to deploy optimal switching devices placement technique that will enhance the performance of medium voltage overhead line distribution network by reducing number of customers and MVA losses caused by electricity supply interruption which in return improves the reliability of electricity supply to customers. To assess the reliability of distribution systems, it is important to understand the impact of each supply interruption, outage duration and frequency of occurrence on reliability assessment. The paper discussion is centred on the deployment of zone concept optimal switching devices placement, which are reclosers position on deferent zones of A 22KV overhead line distribution network. Abiri-Jahromi et al., (2012: 363) found that, automated switching devices can reduce the duration and number of customers affected by interruption during transient fault by its fast restoration feature.

2.2. Distribution network automation

In this research, each zone of A 22 KV distribution network is equipped with its recloser to minimize the interrupted area. According to Khan (2015), the placement of protection devices in radial distribution feeder improves network reliability and minimizes the values of reliability indices. Protective devices and switches play important role in reliability of electrical distribution network by minimizing impact of interruption on customers affected and MVA losses (Sohn et al., 2006:941). Billington and Jonnavithula (1996) applied sectionalising switches in primary distribution systems for different applications for reliability improvement, isolation, configuration management and to reconfigure networks. Switching devices selection and cost associated with installations are important in determining the number of distribution automation systems (Billington and Jonnavithula, 1996). In the past, utilities used past experiences, customer data and similar consideration to optimise performance (Billington and Jonnavithula, 1996). However, El-Wafa et al (2002) considered outages, maintenance and investment cost in section of sectionalizing devices placement and number required to optimise the performance.

Auto-reclosers situated closer and behind the faulty part of systems operates to isolate typical faults. Selection switching device is important on automated distribution network, where sectionalising switches are remotely controlled (Billington and Jonnavithula, 1996). Pole Mounted Breakers (PMB) also known as reclosers, sense and interrupt 'fault current' and automatically restore electricity supply after momentary outages. According to the power system philosophy, PMB's isolate faulty distribution network ahead of their position. This equipment automatically isolates faulty part distribution networks ahead of them and report back the change of status and fault information to the control centre (Billington and Jonnavithula, 1996). The breaker are remotely controlled and monitored by the control officer using a control system architecture called Supervisory Control and Data Acquisition (SCADA) for monitoring the continuity of supply to customers and these advanced automation systems are equipped with fault location detection systems (Schneider electricity, 2013).

3. METHODOLOGY

3.1. Zone concept

In the utility company where the study was conducted, power system zone concept was used to divide electricity power networks into zones, separated by intelligent components which include remote controlled reclosers, automatic Sectionalizes, fault path indicators and other methods to handle fault in an optimal technique (Eskom. 2016). The principle of zone concept is to minimize the area affected during power interruptions. Each zone should be equipped with communication for transfer of status indications, measurements, and control commands as required by the secondary distribution application.

3.2. Process of switching device placement selection

It is necessary to position the circuit breakers on the right locations within the distribution network in order for the breakers to optimally serve their required functions. The exposure of unplanned interruptions, and the impact of reliability Key Performance Indicators (KPIs), need to be determined first. In the process of determining the locations for placing circuit breakers, the network length beyond each protective device and the percentage of customers affected by the interruptions were first measured. When the breaker trips, the percentage of the feeder impacted KPI is usually determined based on the zone affected (Leci et al. 2007). It is important to calculate the possibilities of improvement before allocation of each circuit breaker. If no improvement is established, the circuit breakers need to be repositioned to spots where they will serve the desired objectives. Figure 1 shows the decision making process of switching device allocation, while the process of optimisation is shown in figure 2.

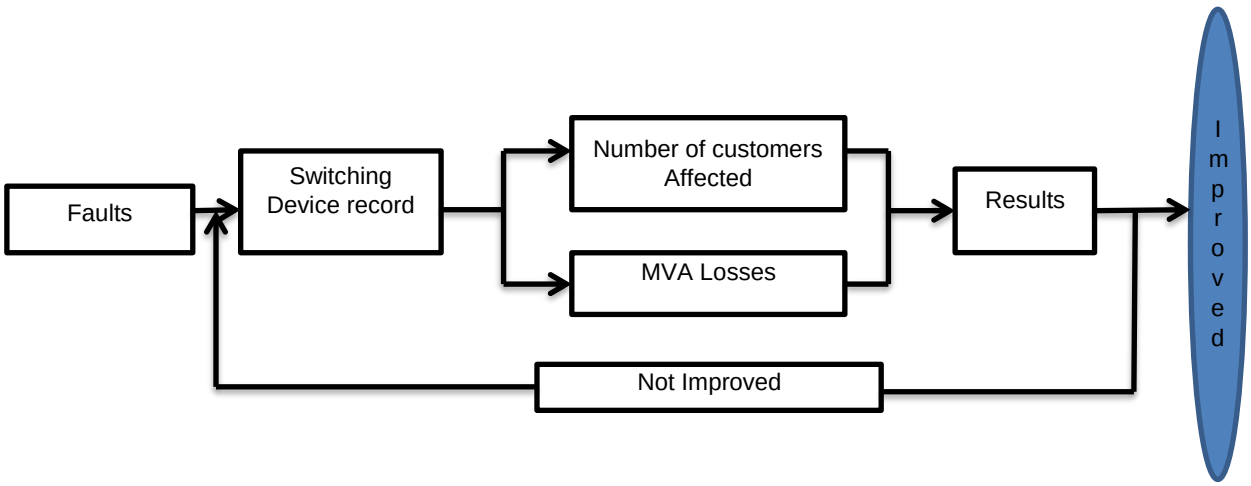

Figure1: Process of switching device allocation decision

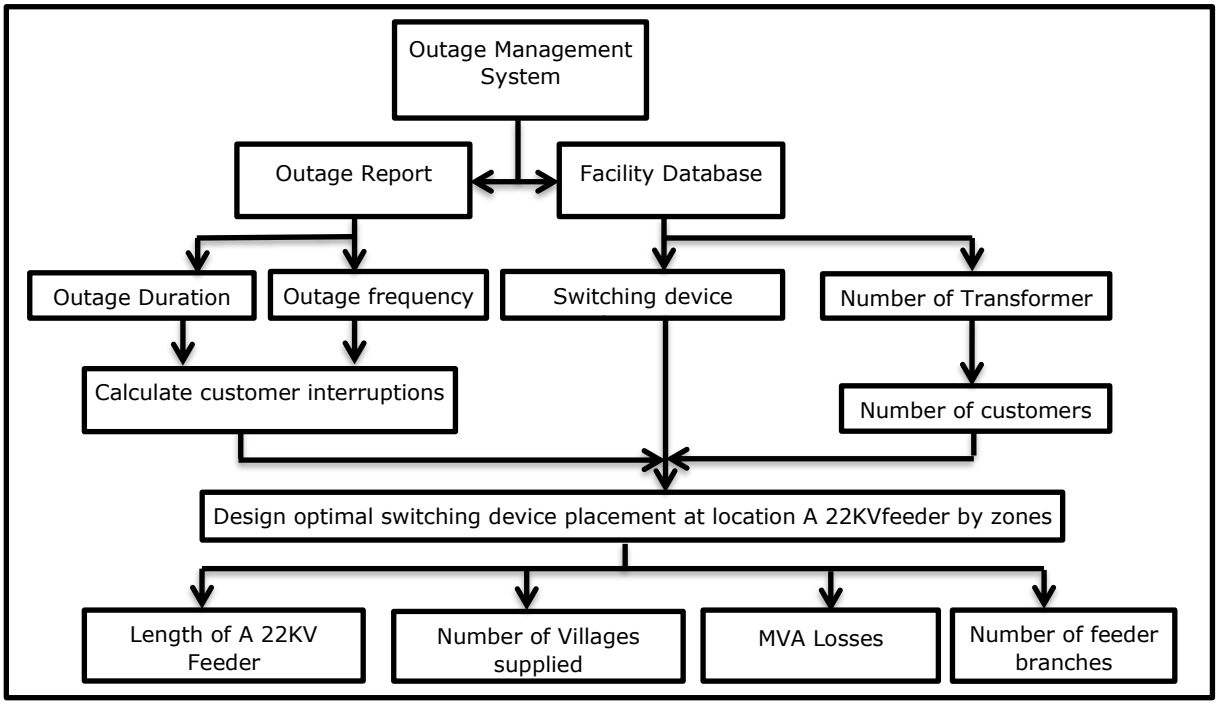

Figure 2: Optimal switching device placement selection process

The process of optimisation started by identifying the gaps in the performance of the feeder A 22KV Medium Voltage (MV) line. Outage management system (OMS) was consulted to check the contributors to the poor performance of the MV overhead line distribution network. The OMS provided the outage report and facility database that contained detailed information about interruptions frequency, duration, switching devices interruptions and customers connected per transformer. In the process of designing the optimal switching device placement model, the number of areas, customers, length of distribution network, power losses (MVA loss) and number of feeder branches were considered.

After the optimisation process, comparison of results was carried out based on data obtained from both the historical data and that of pilot phase of implementation. The comparison of both historical and pilot phase implementation data was validated through improvement on the reliability indices which includes System Average Interruption Duration Index (SAIDI), System Average Interruption Frequency Index (SAIFI), customer base impact index (CBII) and MVA base impact index (MVABII) for location A 22KV feeder.

Feeder A 22KV overhead line zone concept

Due to the length and complexity of the 22KV feeder distribution network especially in the rural villages, determination of the location where faults originates from is a huge challenge. It is highly important to divide this network into zones and subzones, in order to determine the faulty section (area where the faults come from). Dividing the distribution network into zones and subzones helps in minimizing the number of customers affected by interruptions, improves fault finding time, and reduces restoration time thereby reducing electricity supply losses which is in line with the proposition of Khan (2014). In this study, the sequence on figure 2 was followed to achieve effective zone divisions, but subzones were not considered in this stage of the research because it was a pilot implementation phase. In the optimisation process, the overhead line length, number of branches, number of customers, and MVA losses were considered. The switching placement process commenced from the network phase as illustrated on figure 3.

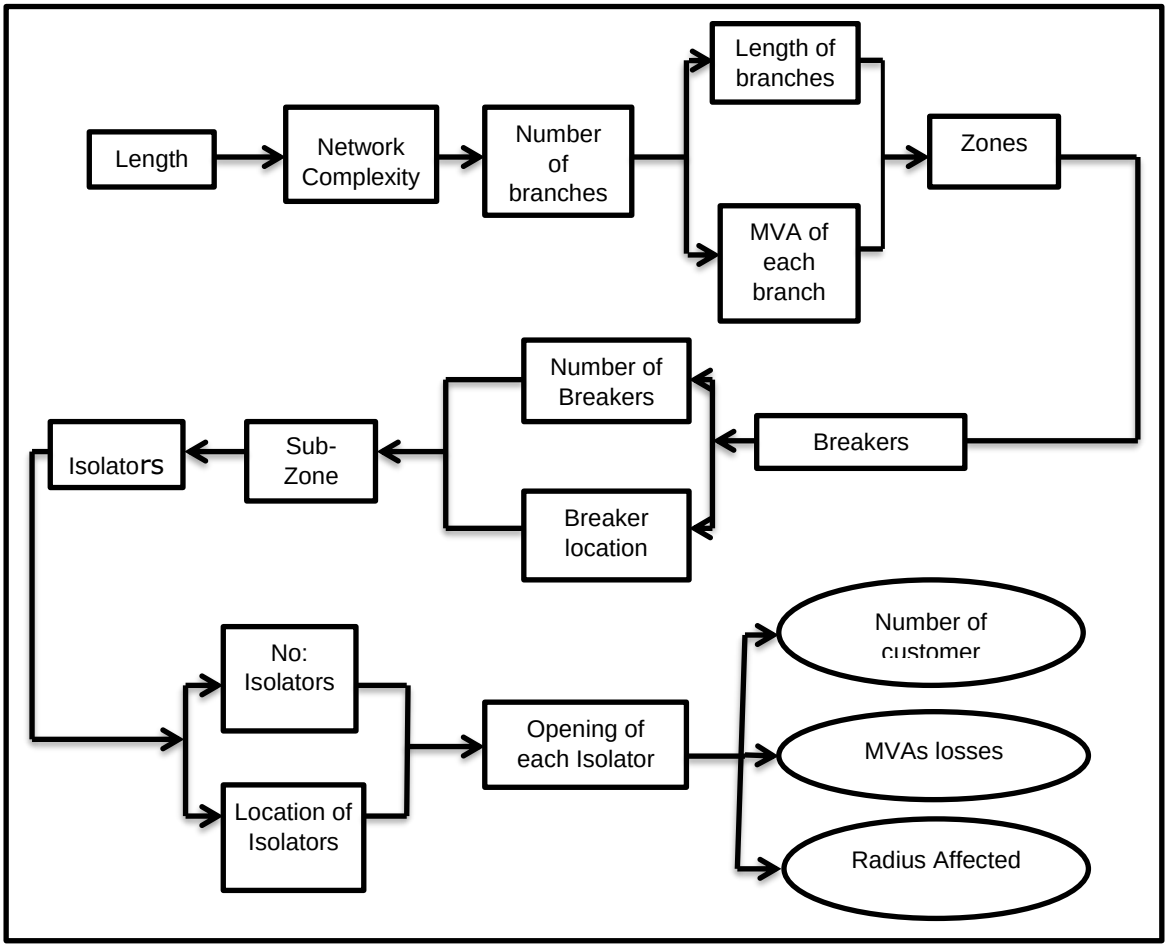

Figure 3: Zone process

Dividing Feeder A 22KV MV overhead lines distribution network into zones, the customer base impact index (CBII) and MVA base impact index (MVABII) need to be considered. The CBII is the ratio of the customer base impacted by the interruption from the total customer base. The MVABII is ratio of MVA base impacted over the total MVA base and can be converted into percentages. They are mathematically expressed as:

Customer Base Impact Index = CBII

$$CBII = \frac{Customer\ base\ impacted}{Total\ MVA\ base} \quad \ldots\ldots\ldots\ldots\ldots\ldots\ldots\ldots\ldots\ldots\ldots\ldots\ldots\ldots\ldots\ldots\ldots\ldots \quad (1)$$

MVA Base Impacted Index (MVABII)

$$MVABII = \frac{MVA\ base\ Impacted}{Total\ MVA\ base} \quad \ldots\ldots\ldots\ldots\ldots\ldots\ldots\ldots\ldots\ldots\ldots\ldots\ldots\ldots\ldots\ldots\ldots\ldots \quad (2)$$

4. RESULT AND DISCUSSION

4.1. Recloser positioning for optimisation

It is important to equip the 22KV feeder with adequate protective devices (reclosers) to prevent the occurrence of unnecessary outage duration, minimize number of customers impacted by interruption and minimize Mega Voltage Amperes (MVA) losses caused by supply interruption. The recloser installed at each zone, validates the direction of fault to technicians and it also minimizes the area impacted by power outages. The Researcher found that, this method minimized the fault finding time by validating possible direction of faults. Recloser positioning technique

designed in figure 4 was used to achieve the research objectives. Figure 4 shows the application of switching device allocation in the 22 KV feeder applicable to this research.

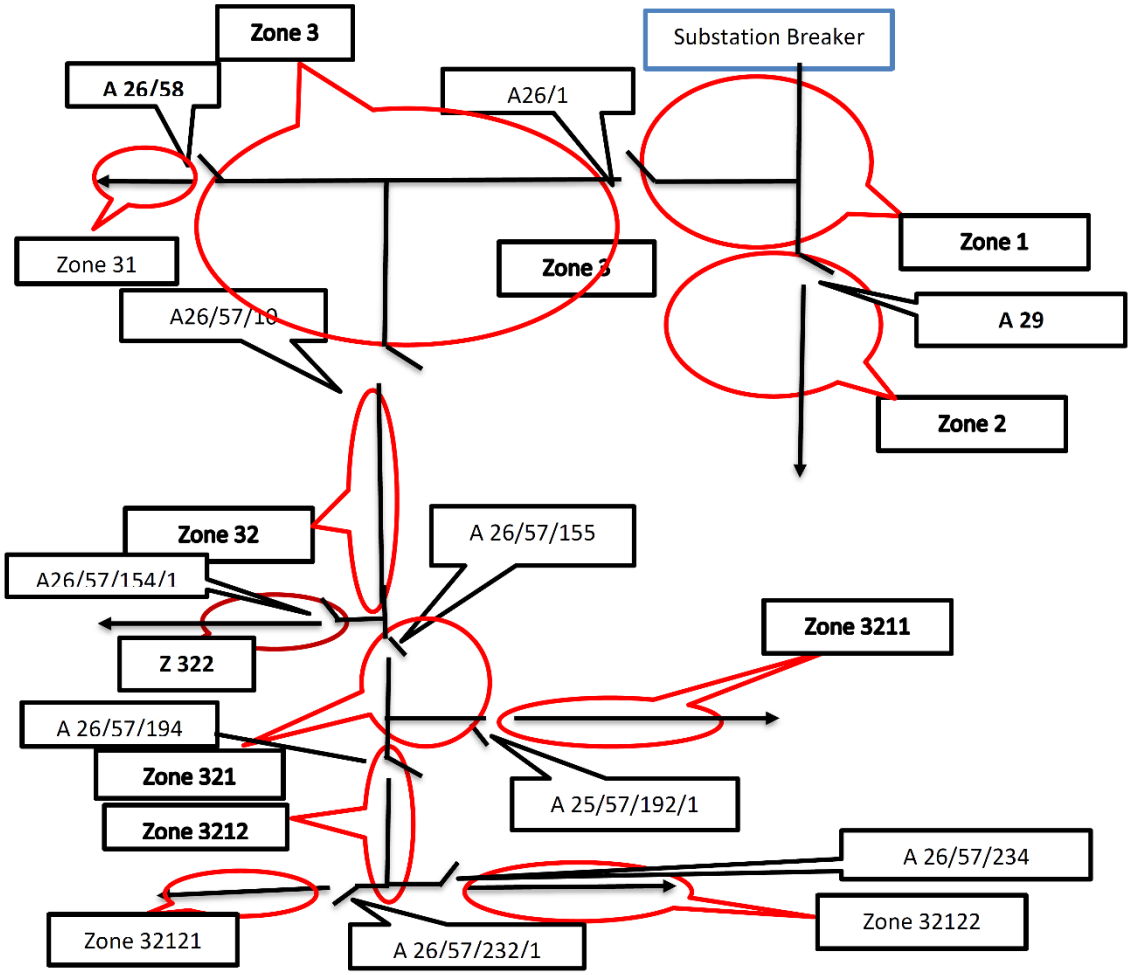

Figure 4: Zone division method

4.2. Recommended length of network beyond the circuit breaker

The recommended distribution network length refers to both backbone (Main line) and / or T-offs (branches and sub-branches of the line). In the process of circuit breaker positioning, the following factors were considered:

- Time taken from the breaker to the closest sectionalising links on fault finding process.
- Fault finding time (Sectionalising time).
- The distance from the recloser to the sectionalising links.
- Number of T-offs (Line branches).

Other factors considered include:

- Dispatching time.
- Time taken to travel from utility offices to site.

The length of the distribution network has significant effect on the fault finding and restoration times. Long and complex line designs with multiple branches requires more time and resources to find the fault location. Faults are dispatched by the Resource management Centre (RMC) to technician. The fault validation process in this research started from the dispatching phase as illustrated in Figure 5. The fault finding process approach adopted is as shown in Figure 5.

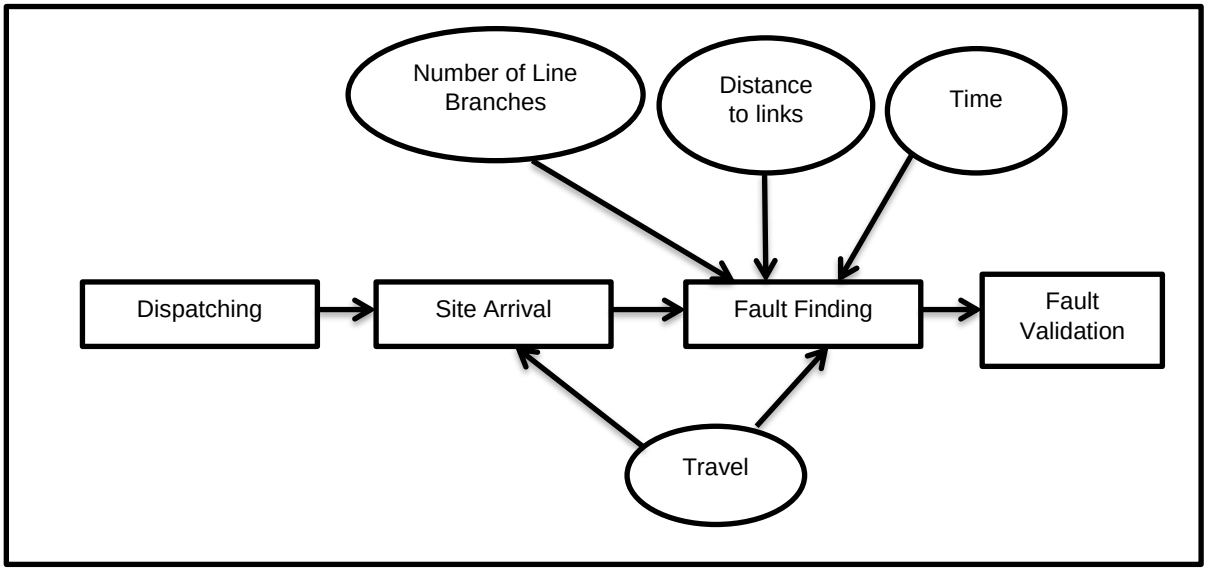

Figure 5: Fault finding process

Recommended MVA of the network beyond the breaker

The recommended MVA of the network refers to the load size. When selecting the location of breakers using the MVA, the following need to be considered:

- Number of transformers and their sizes.
- Number of customers connected to the source.

On the MVA hour loss, the study focused on the number of transformers affected by the opening of each circuit breaker. In this regard, it was important to reduce number of transformers affected by the supply interruption and the outage duration to improve MVA Base impact index (MVABII). The tripping of circuit breakers before optimisation affected large number of customers of different villages and farms. The numbers of customers, outage duration are relatively proportional to power losses. The reduction in the number of customers affected, outage duration and MVA loss lead to improvement in the performance which in turn validate the correct positioning of switching device placement. The diagram in figure 6 shows how to determine MVA hour losses.

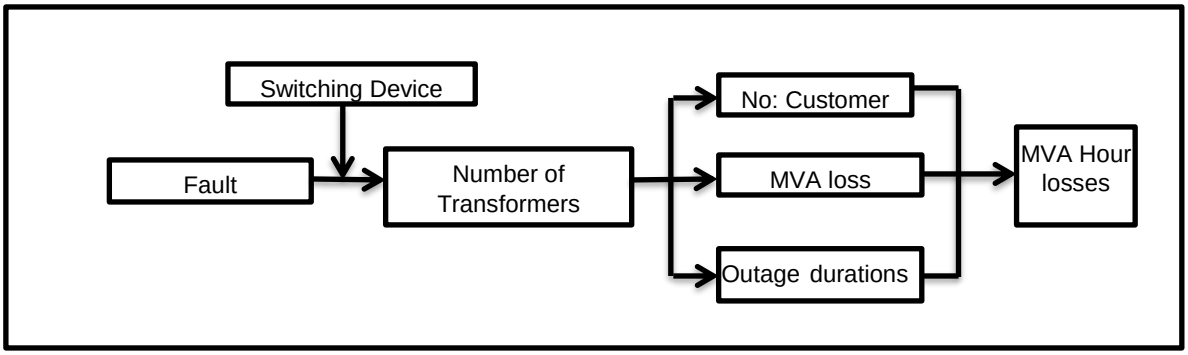

Figure 6: MVA hour losses

The improvement of optimisation is mathematically determined by calculating the change on the percentage of MVA losses and number of customers affected before and after optimisation. Feeder A 22KV feeder was divided into fourteen (14) zones represented by alphabets (A,B,C,…) in column 1 of table 1. The Zones were divided based on the number of customers, line branches, network length and MVA's of transformers connected. The positioning of intelligent protective devices (remote controlled reclosers) on feeder A 22 KV distribution network determined where the zone starts and ends. The occurrence of fault on each section of the line triggers the reclose behind that fault to trip and isolate only that faulty section of the line. The occurrence of fault on that zone, impact certain number of customers and its MVA losses specified in table 1.

The results obtained by comparative analysis of data on zones, before and after optimisation of location A "22KV feeder", is presented using histograms, based on data obtained by measuring the level of improvement of Mega Voltage Ampere (MVA) and by evaluating the total number of customers affected by power supply interruptions. Table 1 shows MVA and the number of customers affected by interruption before and after optimisation within various zones.

Table 1: Data representing improvement based on comparison of the status before and after a pilot implementation phase.

Table 1: An example of a clear table

Zone representation	Zone	No. of customers impacted by interruptions before optimisation	No. of customers impacted by interruptions after optimisation	MVA losses before optimisation	MVA losses after optimisation
A	1	2867	2867	10.245	10.245
B	2	2867	35	10.245	2.857
C	3	2867	2867	10.245	10.245
D	31	2830	2830	7.238	7.238
E	311	2830	2830	7.238	7.238
F	312	2830	2830	7.238	7.238
G	3121	2808	2808	5.438	5.438
H	3122	2787	2787	4.697	4.697
I	31221	2787	2787	4.697	4.697
J	312211	1365	1365	2.316	2.316
K	31222	2787	880	4.697	1.435
L	312221	2787	601	4.697	0.982
M	312222	2787	279	4.697	0.453
N	3123	2787	542	4.697	0.946

The average number of customers affected by the fault at each zone was used to measure the improvement that the method contributed to switching device placement solutions. Referring to table 1, the average number of customers affected per zone were obtained through mathematical computation, using standard empirical steps. MVA losses 1 represent before state while MVA losses 2 represent the losses recorded after the optimisation process. Also, "number of customers impacted 1" represent the total number of customers within each zone affected by interruptions before the optimisation while "number of customers impacted 2" are those affected after the pilot phase of the optimisation process.

The Average MVA loss before and after optimisation was mathematically calculated as shown in figure 7:

$MVA_{avg} = \frac{Total\ MVA\ of\ each\ zone}{Number\ of\ Zones}$.....(3) Where MVA_{avg} = Average Mega Voltage Ampere

Before

$MVA_{avg} = \frac{88.385}{14}$ $MVA_{avg}\ before = \mathbf{6.313\ MVA}$

After

$MVA_{avg} = \frac{Total\ MVA\ of\ each\ zone}{Number\ of\ Zones}$ $MVA_{avg}\ after = \frac{66.025}{14}$

$MVA_{avg} = \mathbf{4.716\ MVA}$

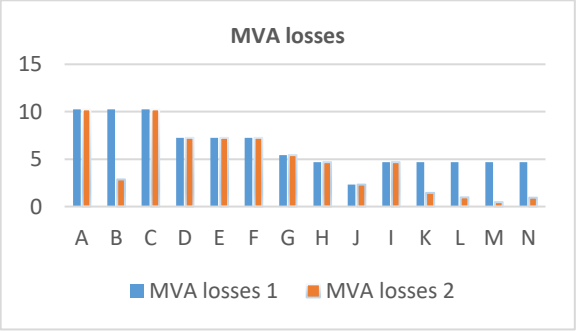

Figure 7: Comparison of MVA losses before and after optimisation

% reduction in MVA losses = $\frac{MVA\ losses\ (6.313 - 4.716)}{MVA\ losses\ (6.313)} x100 = \mathbf{25.30}\%$

The average number of customers affected per zone was mathematically determined as shown in figure 8:

$Customers_{avg} = \frac{Total\ number\ of\ customers\ of\ each\ Zone}{Number\ of\ Zones}$ .. (4) Where $Customers_{avg}$ = Average no. of customers

Before

$Customers_{avg} = \frac{37986}{14}$ $Customers_{avg} = \mathbf{2713\ customers}$

After

$Customers_{avg} = \frac{Total\ number\ of\ customers\ of\ each\ Zone}{Number\ of\ Zones}$

$Customers_{avg} = \frac{26308}{14}$ $Customers_{avg} = \mathbf{1879\ customers}$

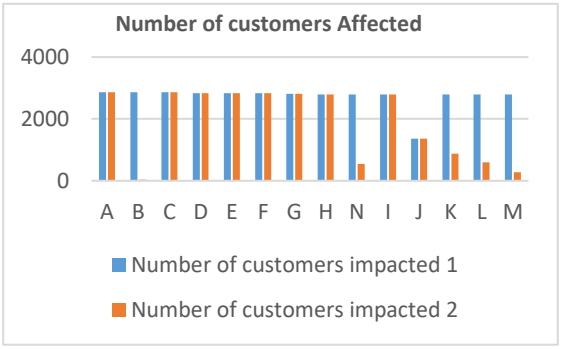

Figure 8: Comparison of number of customers affected before and after optimisation

% reduction in no. of customers affected by interruptions = $\frac{No.of\ customers\ affected\ (before-after)}{No.of\ customers\ affected\ before} x100 = 30.74\%$

5. CONCLUSION AND RECOMMENDATION

Switching device placement optimisation approach significantly improved the performance of location A 22 KV feeder by reducing the MVA losses and the number of customers impacted by electricity supply interruptions. The value of MVA losses and number of customers affected by electricity supply interruption decreased by 30.74% and 25.30% respectively. Due too high cost of Medium Voltage (MV) isolation equipment, optimisation of MV networks is rarely considered within the lifecycle of equipment's but he application of autoreclosers as means of improving the entire system output have proven successful not only in terms of reduction in MVA losses but by providing improved services to end customers. As a recommendation for future research, complete cost models may be explored whereby the losses associated with financial revenue before and after a new model is implemented may be compared putting into consideration the equipment lifespan. The developed model in this research can undergo further improvement and may form part of what will be considered when designing new MV power distribution networks under stringent budget and financial constraints.

6. REFERENCES

Abdi. S, Afshar.K., Bigdeli.N., and Abdi.M,. 2014. *Optimal recloser and autosectionalizer allocation in distribution networks using IPSO-Monte carlo approach*. International Journal of Electrical Power and Energy System.

Abiri-Jahromi.A., Mahmud. F.F.,Masood.P., and Mohsen.M. 2012. *Optimised sectionalizing switch placement strategy in distribution systems*. IEEE Transactions on power Delivery

Billington.R, and Jonnavithula.S,. 1996. *Optimal switching device placement in radial distribution system*.IEEE Trans. Power Del. Vol. 11, no. 3, pp. 1646-1651

Carter-Brown, C., Cameron.M.J., and Du preez. 2008. *Determining the relationship between Eskom distribution network performance and capital investment*. www.Mersa.org.za

Chatterton, B., 2004, October. *Network Reliability Measurement, Reporting, Benchmarking and Alignment with International Practices*. In *AMEU 20th Technical Meeting, Richards Bay*.

Dehghani, N. and Dashti, R., 2011. *Optimisation of recloser placement to improve reliability by genetic algorithm*. *Energy and Power Engineering*, *3*(04), p.508.

Eskom, 2016. *Fault path indicator for overhead line network of up to 132KV standard-part 1*. Eskom Internal publications.

Esteban, A. and Alberto, A., 2010. *Optimal selection and allocation of sectionalizers in distribution systems using fuzzy dynamic programming. Energy and Power Engineering*, *2*(04), p.283.

Hannan, S., Iskandar, N. and Embang, D., 2011, June. *Overhead line reliability indices improvement using self-feeder automation*. In *CIRED Conf. Frankfurt* (pp. 1-4).

Hashim.A.H.,Mohamad.A.M., and Abidin.I.Z. 2006. Determination of auto-recloser location using cost analysis in the sabah electricity distribution network. Power and enegy conference. IEEE International, 587-590.

Improving MV network Efficiency with feeder Automation www.schneider-electricity.com retrieved 21/02/2013

Khan,Z,H. 2015.*Improving the reliability performance of medium voltage network*. Master of Science in electrical engineering. University of Cape Town.

Leci,G.,Starck,J.& Saha,M. 2007. *Advanced automation with zone dividers deployment in distribution network*. ABB

Moradi,A,.Fotuhi-Firuzabad, M.& Rashidi-Nejad, M. 2008. *Optimal switch placement in distribution systems using trinary particle swarm optimisation algorithm*.Vol 23.Issue 1

NRS 048-6 (Edition 3, 2005*): Electricity supply-South African Quality of service*, Part1, Minimum standard

Sohn, J.M., Nam, S.R. and Park, J.K., 2006. *Value-based radial distribution system reliability optimisation*. *IEEE Transactions on Power Systems*, *21*(2), pp.941-947.

Sumper, A., Sudria, A. and Ferrer, F., 2005. *International reliability analysis in distribution networks*. *CITCEA Report for ENDESA RED. Spain*, pp.32-36.

Thomas. R.S.M,. 2014. *Optimising the number and position of reclosers on the medium voltage distribution line to minimize damage to equipment*. University of Pretoria

296: The well-to-wheel analysis of hydrogen enriched compressed natural gas for heavy-duty vehicles

An LCA approach for HCNG fuel cycle

Pralhad GUPTA[1], Fanhua MA[2], Weilin ZHUGE[3], Sijie LUO[4]

[1] Department of Automotive Engineering, Tsinghua University, Beijing, China, pgupta.tsinghua@yahoo.com
[2] Department of Automotive Engineering, Tsinghua University, Beijing, China, mafh@tsinghua.edu.cn
[3] Department of Automotive Engineering, Tsinghua University, Beijing, China, zhugewl@tsinghua.edu.cn
[4] Department of Automotive Engineering, Tsinghua University, Beijing, China, rossdger@mail.tsinghua.edu.cn

Increasing urban air pollution, greenhouse gases, and declining fossil energy sources are the three major problems of transportation sector which drive the use of alternative vehicular fuels to prevent energy shortage, reduce oil dependency, and decrease tailpipe emissions including air pollutants and greenhouse gas emissions. This research work is contextual life cycle analysis of $HCNG^{®}$ in which 20% gaseous hydrogen blended compressed natural gas has been investigated in terms of net energy ratio, GHG value, and cost-effectiveness. A mix of various hydrogen pathways has been considered here based on data adapted from literature reviews and surveys of relevant previous work. The functional unit considered in this study is "per MJ of energy output" from the engine fueled with 0%HCNG and 20%HCNG. The pump-to-wheel has been extracted from Ma, Wang, Ding, and Jiang (2009) which is the paper published from our research team. The well-to-pump data for various hydrogen pathways with a variety of feedstocks has been gathered from literature surveys. Additionally, an engineering economic approach has been used to evaluate cost-effectiveness ratio of CNG and 20%HCNG pathways derived from fuel economy improvement. It has been shown that at pump-to-wheel stage, 7% reduction in fuel consumption can be achieved together with 11% reduction in GHGs, 7% reduction in energy consumption at operation and 7% reduction in total costs (RMB/MJ) for 20%HCNG compared with CNG. In this work, rank has been assigned for every 20%HCNG pathway based on well-to-wheel energy ratio and GHG emissions (1 means 'best and 10 means 'worst') which shows that renewable based hydrogen pathways such as solar, wind and biomass showed dual benefits of lower energy consumption and lower GHG emissions whereas grid electricity-to-hydrogen displayed the worst case in both scenarios. It is also very important to visualize energy consumption by a hydrogen pathway in two perspectives: qualitative and quantitative. Usually, biomass based HCNG pathways may have higher net energy ratio, but the sources are cleaner, and renewable in nature. Net energy ratio is also affected by energy efficiency. The energy efficiency of fossil based pathways such as natural gas, coal, etc. is higher than biomass gasification pathway.

Keywords: Well-to-wheel, HCNG, life cycle analysis, heavy-duty vehicles, fuel cycle

1. INTRODUCTION

1.1. Research motivation

The concept of using hydrogen enhanced compressed natural gas fuel for HDVs has been well understood by many researchers and scientists. Although $HCNG^{®}$ is comparatively more advantageous than conventional CNG in terms of performance and cleaner emissions, the large scale application has not been achieved till now. One of the major barriers to large scale marketization of HCNG is immaturity of 'hydrogen economy' which encompasses hydrogen production, storage, T&D, and HCNG fuelling infrastructure. Therefore, to get the deep insight to HCNG technology, life cycle analysis is an effective choice. The well-to-wheel study of HCNG established on a typical life cycle approach provides an extension to the demonstration projects and test bench experiments of $Hythane^{®}$.

1.2. Previous works

Lyu, Ou, and Zhang (2015) stated that automotive energy is one of the core areas of environmental and climatic issues and is still challenging in overall spectrum which includes technology, economics and sustainability at present. Ou et al. (2010) claimed that compared to conventional diesel buses, AFVs offer dual benefits of energy saving and GHG reduction. Hydrogen is a zero-emitter fuel with a very fast laminar burning speed and extended limit of flammability which ensures possibilities to enrich CNG with hydrogen (Mehra, Duan, Juknelevičius, Ma, & Li, 2017). The transient performance and emission analysis of 20%HCNG by the author (2009) demonstrated that 20% hydrogen enrichment decreases NO_x, CO, NMHC, CH_4 and BSFC by 51%, 36%, 59%, 47%, and 7%, respectively whereas the maximum power remains the same. Genovese, Contrisciani, Ortenzi, & Cazzola, 2011 showed that 5% HCNG enhanced the energy consumption by 4%, 25% HCNG produced the largest reduction of CO_2 by 25% compared with baseline CNG (HDB) operation. The levels of HC emission were constant and could not meet the EEV limits. NO_x reduced by 47% with 5% HCNG ((Genovese et al., 2011)). A chassis dynamometer test bench experiment performed on a passenger car with L4-SI (PFI) engine equipped with a TWC as per NEDC cycle procedure showed that CO and CO_2 was reduced by 19% and 3% respectively whereas HC was almost unchanged. The amount of NO_x increased by 70%. No significant changes occurred in fuel consumption on both basis; mass and energy. Significant benefits from HCNG can only be achieved with an appropriate hydrogen ratio and spark timing (Unich, Morrone, Mariani, & Prati, 2009). Hydrogen fraction, spark timing, and excess air ratio and are the important operating parameters of HCNG. Development of sufficient control system for the HCNG engine is necessary to maintain a balance between maximum performance and minimum exhausts. Development of an infrastructure supporting HCNG use is another big challenge (Ma et al., 2010). (KILGUS, 2005)has claimed that no significant changes in the performance trends of modified HCNG 15% and HCNG 30% occurred compared with baseline CNG vehicle. However, the corresponding fleet of hydrogen vehicles would have the best environmental performance. (Nelsson, Hulteberg, Saint-Just, & Kaiadi, 2010) revealed that if the objective is only CO_2 reduction, HCNG may not be an effective choice as it contributes to only 10% reduction in CO_2 emissions which is easy to achieve just by switching CNG to biogas in various parts of the world. Lastly, this study also proved that HCNG is best suited for the primary goal of air pollution reduction rather than CO_2 reduction (Nelsson et al., 2010).

Huang and Zhang (2006) disclosed that NG-based hydrogen pathway showed the highest WTW energy efficiency and the electricity-to-hydrogen based pathways showed the poorest characteristics. The well-to-wheel energy efficiency of naphtha-to-hydrogen and coal-to-hydrogen lies between WTW energy efficiency of natural gas SMR and electricity-to-hydrogen pathways. According to Ewan and Allen (2005), solar PV seems to have tremendous prospects as a large scale electricity producer which can provide a platform for hydrogen economy but costs of PV technology is a major concern. He also added that biomass is a low carbon intensive technology, direct water splitting solar photo catalysis pathway can be more effective if continuous researches can increase its conversion efficiency to a larger extent. Bartels, Pate, and Olson (2010) claimed that with the pace of technological advancement of alternative technologies, fossil fuels are becoming costlier than alternative sources which clearly is expected to dominate the energy mix in future (Bartels et al., 2010). Turner (2004) proposed that building a larger number of hydrogen production stations with lower capacity is more cost-effective than building a small number of large scale central production sites. Higher volume or mass production supports costs savings. The author also suggested not to spend a tremendous amount of money for CO_2 sequestration rather he emphasized to limit the use of coal in both gasification and electricity generation and leave them unused which is very challenging because of its availability and economic competitiveness (Turner, 2004).

Life cycle cost analysis is defined as the methodical estimation of costs of a system or a product for its full life duration Márquez, Márquez, Fernández, Campos, and Díaz (2012). DeCicco and Ross (1996) proposed an engineering-economic analysis for a fleet of cars with a set of technological improvements focused on fuel economy optimisation. In his work, he also mentioned about estimation of fuel saving payback and cost of conserved energy average. The author also explained the significance of fuel economy improvement in vehicle stock turnover in the form of gasoline consumption reduction.

2. METHODOLOGY

To describe the method of this research work, a basic understanding of components of life cycle analysis is important. This work is based on an integrated two-stage well-to-wheel (WTW) analysis of 20%HCNG fuel for its heavy-duty applications (e.g. passenger city buses). According to ISO 14040, there are basically four components of LCA: definition of goal & scope, LCI or life cycle inventory, LCIA or life cycle impact analysis, and improvement analysis. For any typical LCA, the first and most important thing is the selection of a 'system boundary'. This system boundary is basically a framework of study which provides a detail layout of investigation including 'level of details', 'affordability', 'constraints', and 'scope' of the work.

2.1. System boundary

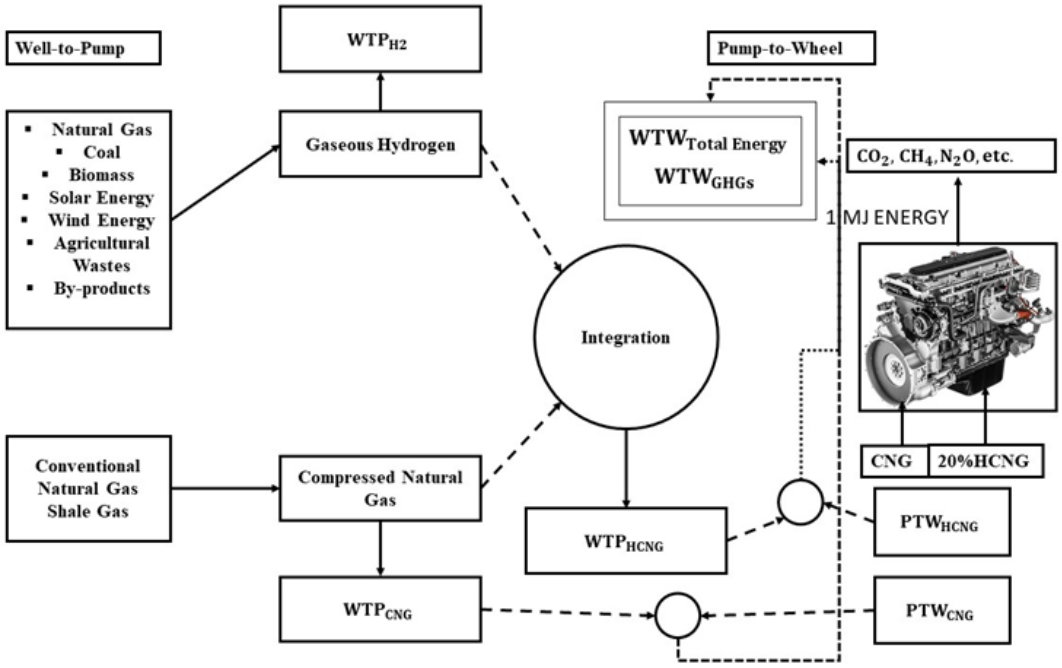

Figure 1: System Boundary

Figure 1 shows the system boundary or study framework for our research. This approach combines the experimental test results of the engine with the data obtained from literature reviews for the upstream well-to-pump. The idea is to calculate the amount of energy required and GHG emitted to produce 1 MJ of energy from the engine including the entire fuel cycle (WTW). Similarly, emission data is available from the test performance data published in (Ma et al., 2009). However, as the data of CO_2 emission was missing, 'carbon balance method' was used to calculate specific CO_2 emission by using mathematical computations supported by given brake specific fuel consumption and emissions data (CH_4, CO, NMHC). Later, all the greenhouse gases were combined to form gCO_{2e}/MJ. The fuel-use system in this framework is an operating engine under a transient test ETC cycle aimed at meeting Euro IV emission requirements with 20% HCNG and suitable operating conditions of equivalence ratio, spark timing, etc. Two parameters have been investigated 'net energy ratio (MJ/MJ)' and 'GHG emission (gCO_{2e}/MJ)'. Both of these findings were made on two scenarios of natural gas i.e. conventional natural gas (CNG) and shale gas (SG). For each of these scenario, baseline i.e. CNG and later SG were compared with 20%HCNG pathways (EU4 ETC) taking in account of various hydrogen pathways. Results differentiate the WTW total energy and WTW GHG emissions between 0% HCNG (CNG) and 20%HCNG including the impacts of each hydrogen and natural gas pair pathways.

This flow diagram shows the step-by-step procedure for this research methodology.

i. The upstream well-to-pump data was chosen from literature reviews which includes various hydrogen pathway mixes.
ii. The well-to-pump inventory data were integrated by a statistical weighted average principle on LHV basis to find the integrated WTP energy use and GHG for 20%HCNG pathways.
iii. Available experimental pump-to-wheel (PTW) data was transformed by appropriate mathematical ways to implement integration of WTP and PTW required by the integration method of GREET which was also used by other previous works (JRC, HASS, LARIVÉ, & JRC, 2014).

iv. CO_2 was calculated for all these operations by using carbon balance method. CO_2, and CH_4 was combined to calculate total GHGs based on their global warming potential values for 100-years' time horizon as suggested by 'Intergovernmental Panel on Climate Change'. The GWP of CO_2, CH_4 and N_2O is assumed as 1, 25 and 298 $gCO_{2,equivalent}$ according to the IPCC report. Then, the well-to-pump inventory was combined with pump-to-wheel inventory for analysis.
v. Cost-effectiveness analysis has been performed using a typical engineering economics approach which has not been shown in Figure 1： for the simplicity.

2.2. Functional unit

The functional unit is an effective way to evaluate comparison between two different fuel options and also an important component in an LCA study. The functional unit has been defined 'per MJ of energy' from the engine.

Functional Unit	WTP	PTW	WTW
Total Energy	$\frac{MJ_{Input}}{MJ_{finished\ fuel}}$	$\frac{MJ_{Input(from\ finished\ fuel)}}{MJ_{1\ MJ\ output\ from\ engine}}$	$\frac{MJ}{MJ_{engine}}$
GHGs	$\frac{gCO_{2e}}{MJ_{finished\ fuel}}$	$\frac{gCO_{2e}}{MJ_{1\ MJ\ output\ from\ engine}}$	$\frac{gCO_{2e}}{MJ_{engine}}$

Note: In other well-to-wheel analyses, it is quite common to find the WTW results in terms of per km basis and per passenger-km for passenger heavy-duty buses (number of passengers*VKT). For example, $\frac{MJ}{km}$ for energy consumption and $\frac{gCO_{2,equivalent}}{km}$ for GHG emissions.

2.3. Data

Pump-to-Wheel Data

Table 1: Unmodified Experimental Data of PTW stage (20%HCNG-ETC Euro IV)

Fuel	CO_2 (g/kWh)	NO_x (g/kWh)	CO (g/kWh)	NMHC (g/kWh)	CH_4 (g/kWh)	BSFC (g/kWh)	Peak Power (kW)
CNG	686.647	4.76	2.45	0.52	4	254	154
20% HCNG	644.389	2.31	1.54	0.21	2.1	236	154

Table 2: Adjusted Pump-to-Wheel Data (Dimensionality Modifications)

Fuel	$PTW_{Total\ Energy}(\frac{MJ}{MJ})$	$PTW_{GHGs}(\frac{gCO_{2e}}{MJ})$
CNG	3.528	217.037
20%HCNG (EU4)	3.278	192.224

Well-to-Pump Data

Table 3: Well-to-Pump Data of Compressed Natural Gas

Code	Study	Energy Source	Process	WTP_{Energy} $(\frac{MJ}{MJ_f})$	WTP_{GHGs} $(\frac{gCO_{2e}}{MJ})$	Code
Con.NG	(Ou, Zhang, Zhang, & Zhang, 2013)	(Coal + Raw NG+ Petroleum)	Conventional Raw NG to NG	1.15	137.81	$NG_{Conv.}$ **[CNG]**
SG-CNG	(Concawe, 2006)	Shale Gas EU	Shale Gas to CNG	0.10	8	$CNG_{Shale\ Gas.}$ **[SG]**

Table 4: Well-to-Pump Data of Gaseous Hydrogen

Code	Study	Energy Source	Process	WTP_{Energy} $(\frac{MJ}{MJ_f})$	WTP_{GHGs} $(\frac{gCO_{2e}}{MJ_f})$	Pathway
NG SMR	(Spath & Mann, 2000)	NG	SMR	1.527	101.049	$GH_2\_NG\_SMR$
Coal Gasification (w/o CCS)	(Djomo & Blumberga)	Coal/No CCS	Gasification	0.710	238.000	$GH_2\_CO\_Gas\_w_o\_C_{Seq.}$
Coal Gasification (w/ CCS)	(Djomo & Blumberga, 2011)	Coal/ CCS	Gasification	0.560	53.917	$GH_2\_CO\_Gas\_w\_C_{Seq.}$
WTH	(Cetinkaya, Dincer, & Naterer, 2012)	Wind Power	Electrolysis	0.082	8.083	$GH_2\_Elect_{WindPower}$
STH	(Cetinkaya et al., 2012)	Solar Power	Electrolysis	0.279	20.101	$GH_2\_Elect_{SolarPower}$
Bio-fermentation	(Djomo & Blumberga, 2011)	Wheat Straw (WS)	Bio-fermentation	1.080	46.667	$GH_2\_BioWS\_Ferm.$
Bio-Gasification	(Djomo & Blumberga, 2011)	Waste Wood	On-site gasification	0.82	11.167	$GH_2\_BioWW\_Ferm.$
Biomethane	(Wulf & Kaltschmitt, 2013)	Biomethane	SMR	0.45	52	$GH_2\_BioCH4\_SMR$
Bio-Electrolysis	(Wulf & Kaltschmitt, 2013)	Straw (herbaceous biomass)	Electrolysis	0.5	90	$GH_2\_Elect_{Bio\_straw}$
Distr. Grid Elect.		Distributed Grid Electricity	Electrolysis	3.79	361.88	$GH_2\_Elect_{Grid}$

Figure 4 shows the well-to-pump total energy consumption and GHG emission for various pathways or hydrogen chosen for this study. Additionally, pathway's code has been assigned for the simplicity and a brief description of the pathway details has been provided.

Governing Equations

Pump-to-Wheel Total Energy

Equation 1: Pump-to-Wheel total energy (MJ/MJ) calculation

$$PTW_{Total\ Energy}\left(\frac{MJ}{MJ}\right) = \left(\frac{BSFC\left(\frac{g}{kWh}\right)}{3.6}\right) * \frac{LHV_f\left(\frac{MJ}{kg}\right)}{1000}$$

Where:

- $\mathrm{LHV_f} =$ lower heating value of fuel
- $\mathrm{BSFC}\left(\frac{\mathrm{g}}{\mathrm{kWh}}\right) =$ brake specific fuel consumption
- $\mathrm{PTW_{Total\ Energy}}\left(\frac{\mathrm{MJ}}{\mathrm{MJ}}\right) =$ total energy required to produce 1 MJ of energy from the engine (downstream)

Pump-to-Wheel GHGs

Carbon Balance Approach:

Equation 2: Carbon balance method for CO2 calculation

$$\frac{M_{C,CH_4}}{M_{CH_4}} * BSFC_{fuel} = \frac{M_{C,CO_2}}{M_{CO_2}} * [CO_2] + \frac{M_{C,CO}}{M_{CO}} * [CO] + \frac{M_{C,NMHC}}{M_{NMHC}} * [NMHC] + \frac{M_{C,CH_4}}{M_{CH_4}} * [CH_4]$$

Where:

- M_i = Molar mass of i − component in exhaust tailpipe
- $M_{C,i}$ = molecular mass of carbon in i − component
- i = $CH_4, CO, CO_2, NMHC$
- [i] = exhaust flow rate (g) per kWh
- $[N_2O] = 0 \frac{g}{kWh}$ (assumption; there was no such tailpipe emissions measured.)

Equation 3: Pump-to-Wheel GWP (gCO2e/MJ) $$PTW_{GHGs} = (CO_2 * 1 + CH_4 * 25 + N_2O * 298)(\frac{g}{3.6\ MJ_f})$$

Where:

- $(CO_2/CH_4/N_2O)$ = measured in $\frac{g}{kWh}$ (1kWh = 3.6 MJ)

Integration of Well-to-Pump Total Energy & GHGs of Hydrogen and CNG to form 20%HCNG

For 20%HCNG operation, the integration of WTP inventory of gaseous hydrogen and compressed natural gas was achieved by using following expression of 'weighted average' on LHV basis.

Equation 4: 2 Integration method for WTP HCNG LCI $$k_{20\%HCNG} = \frac{0.2*k_{H2}*LHV_{H2}+0.8*k_{CNG}*k_{CNG}}{0.2*LHV_{H2}+0.8*LHV_{CNG}}$$

- k = $WTP_{Total\ Energy}$, $WTP_{GHGs,}$ LHV

The GHG was calculated by the following expression for WTP stage combining all greenhouse gases inventory together to form $gCO_{2,equivalent}$ emission.

Equation 5: WTP GHG ($\frac{gCO_{2e}}{MJ_f}$) calculation $$WTP_{GHGs} = (CO_2 * 1 + CH_4 * 25 + N_2O * 298)\left(\frac{gCO_{2e}}{3.6\ MJ_f}\right)$$

WTW Net Energy Ratio & Total GHG Emissions

Equation 6: Net Energy Ratio (MJ/MJ) $$WTW_{Total\ Energy}\left(\frac{MJ}{MJ}\right) = PTW_{Total\ Energy}\left(\frac{MJ_f}{MJ}\right) * \left(1 + WTP_{Energy}\right)\left(\frac{MJ}{MJ_f}\right)$$

Equation 7: WTW GHG $$WTW_{GHGs}\left(\frac{gCO_{2eq}}{MJ}\right) = PTW_{GHGs}\left(\frac{gCO_{2eq}}{MJ}\right) + PTW_{Total\ Energy}\left(\frac{MJ_f}{MJ}\right) * WTP_{GHGs}\left(\frac{gCO_{2eq}}{MJ_f}\right)$$

Where:

- $PTW_{Total\ Energy}\left(\frac{MJ_f}{MJ}\right)$ = amount of energy needed from fuel to produce 1 MJ energy from engine
- $WTP_{Energy}\ (\frac{MJ}{MJ_f})$ = amount of energy needed to produce fuel that contains 1 MJ of energy in it
- $PTW_{GHGs}\ \left(\frac{gCO_{2eq}}{MJ}\right)$ = GHG emitted per MJ of engine output
- $WTP_{GHGs}\ \left(\frac{gCO_{2eq}}{MJ_f}\right)$ = GHG emitted per MJ of energy in the final fuel produced

Adapted from: JRC et al. (2014)

In section 2.2, these parameters have been explained under the heading of 'functional unit'.

3. RESULTS

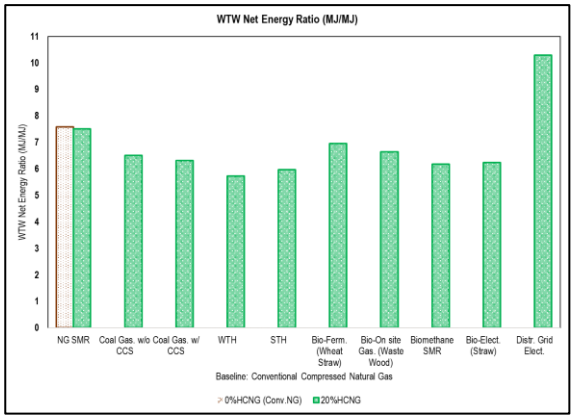

Figure 2: (a) WTW Net Energy Ratio (MJ/MJ)

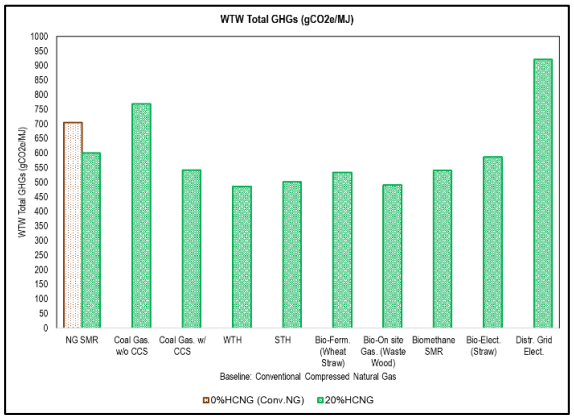

(b) WTW Total GHGs (gCO2e/MJ) [Conventional NG]

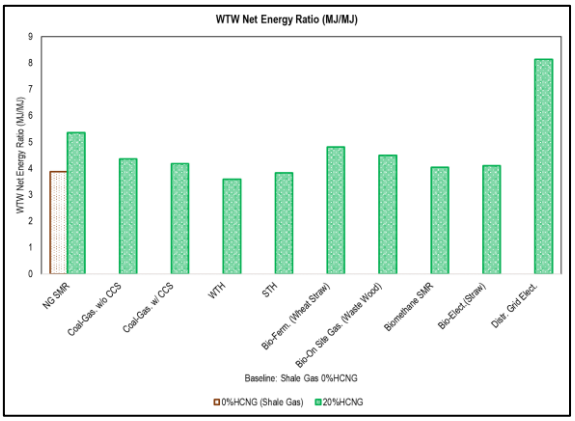

Figure 3: (a) WTW Net Energy Ratio (MJ/MJ)

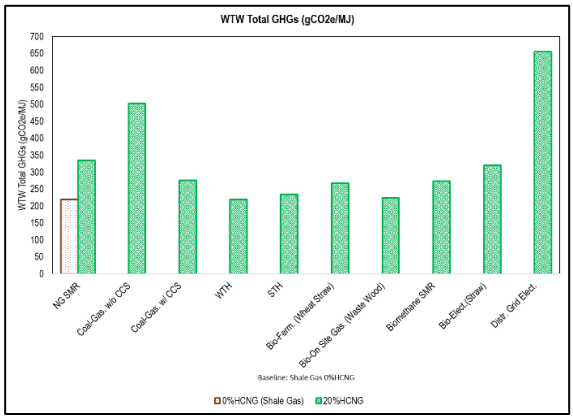

(b) WTW Total GHGs (gCO2e/MJ) [Shale Gas]

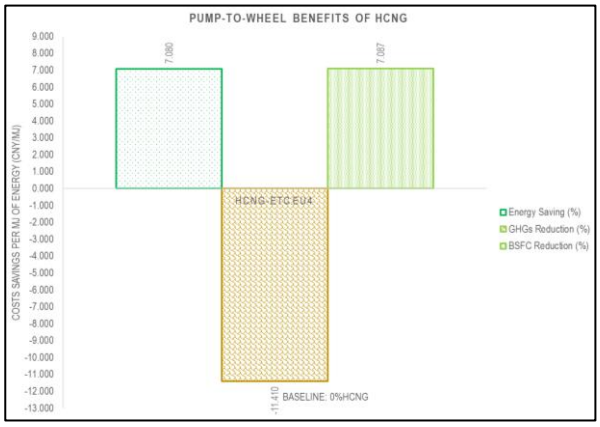

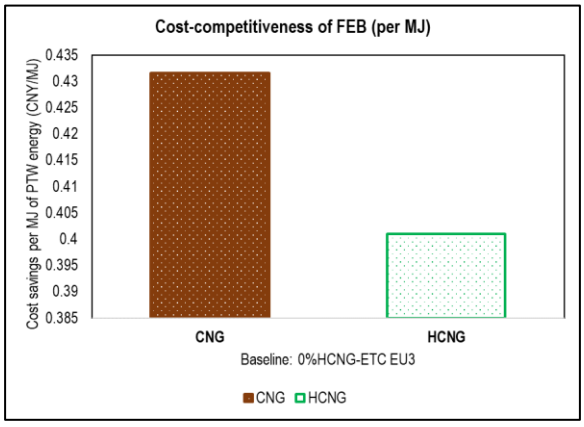

Figure 4: Miscellaneous Benefits of HCNG over CNG

Figure 2 shows the comparison of well-to-wheel net energy ratio and GHG emissions of 20%HCNG pathways with a baseline CNG (conventional natural gas scenario). Figure 3 shows the similar comparison but only difference is that baseline is CNG from shale gas. The net energy ratio and GHGs of 20%HCNG pathways have been assigned rank here where 1 means the best and 10 means the worst scenario for both these NER and GHG. The purpose of ranking is to highlight the effects of hydrogen pathway on 20%HCNG pathways which has been shown in figure 5. In this case, 80% CNG in 20%HCNG comes from conventional natural gas. Figure 4 highlights the pump-to-wheel advantages of 20%HCNG over CNG in terms of energy saving (MJ/MJ), fuel saving (g/kWh), GHGs reduction (gCO2e/MJ), and costs saving (CNY/MJ).

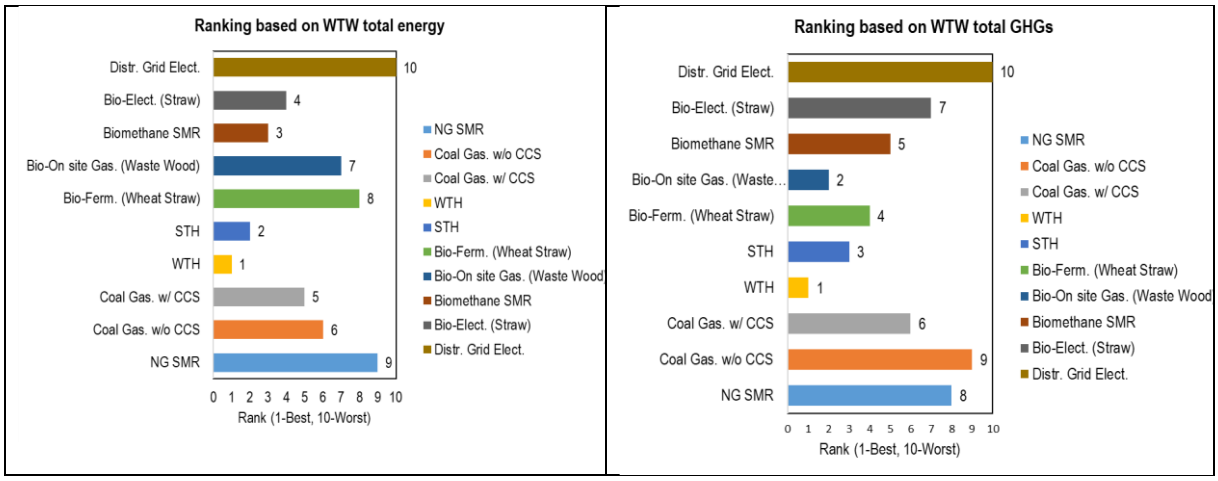

Figure 5: Ranking of Net Energy Ratio & GHG emissions for 20%HCNG Pathways (Conventional NG)

If we compare figure 2 and figure 5, renewable hydrogen pathways such as solar, wind and biomass displayed 'best' scenarios in both energy use and GHG emission perspectives. Grid-electricity based hydrogen is found to be the worst case as majority of the electricity in China as well as in USA is generated from coal and other fossil sources. Furthermore, On-site gasification of waste wood showed 2nd rank in lower GHG emissions but 7th rank in net energy ratio scenario. It means that although the energy consumption is higher in this case, the feedstocks used i.e. waste wood is a cleaner waste-product. Quantitatively, it might be higher, but qualitatively it is clean and sustainable. However, for the near-term future, hydrogen from natural gas steam reforming and coal gasification equipped with CCS facility can be a good choice to cut down emission of conventional NG and coal based pathways. They are preferable as the feedstocks are cheaper, and the technology is quite efficient comparing to other renewable hydrogen options. However, CO_2 sequestration is costlier which is another barrier. Moreover, booming of renewable electricity especially from solar and wind energy with reasonable cost is expected to flourish hydrogen use not just in transportation, but also for residential and industrial applications.

4. DISCUSSION

Figure 2 shows that comparing to conventional natural gas application, 20%HCNG proves dual benefits of lower energy consumption and lower GHG emissions especially in the case of renewable 20%HCNG pathways including solar, wind and biomass energy. At present, natural gas steam reforming is the most mature and widely used technology of hydrogen production. If we compare 0%HCNG with 20%HCNG (NG SMR), energy consumption is slightly increased but there is subsequent reduction in GHG emissions. As 20%HCNG contains 80%CNG, the feedstock of CNG has a significant impact on an entire fuel cycle. Therefore, shale gas can be a futuristic choice of CNG pathway which significantly cuts down GHG emissions and energy use to make 20%HCNG pathways even more efficient and cleaner. This difference has been demonstrated in figure 3. Figure 4 shows that using 20%HCNG, reduces brake specific fuel consumption by 7%, energy consumption by 7%, CO emission by 6.15%, GHGs by 11% as well as total costs of fuel usage (RMB/MJ, derived from fuel economy) by 7%. The cost of CNG and HCNG has been assumed as 4 CNY/kg based on literatures. Figure 5 shows that wind-to-hydrogen pathway of 20%HCNG demonstrated the best case in both NER and GHG scenarios and grid electricity-hydrogen demonstrated the worst. Bio-based pathways although seem to have higher energy consumption, they contribute to lower emissions as the feedstocks are qualitatively cleaner and by-products or wastes. With the integration of CCS (carbon-capture and storage), coal-to-hydrogen pathway can reduce both energy consumption and GHG emissions. Interestingly, coal-hydrogen with CCS seems a better choice than NG SMR in terms of both energy consumption and GHG emissions. However, there are other drawbacks of using CCS and one of them is incremental cost of the technology.

5. CONCLUSION & FUTURE OUTLOOK

There is a great necessity of life cycle analysis of HCNG® in order to achieve marketization and promote large scale commercial use. It is evident that 20%hydrogen enhancement optimises the performance and emission of a conventional CNG vehicle. But, it is very important to consider the downsides of adding 20% hydrogen and get an insight to 'hydrogen economy'. The pathways of hydrogen have a tremendous impact on environment as well as economics. So, it is recommended to perform life cycle analysis and life cycle cost analysis to obtain a detailed and comprehensive cluster of remarks. However, in this research, using data from literature, a simplified but an effective approach has been chosen to perform well-to-wheel analysis of HCNG HDV. The general conclusion can be made as renewable hydrogen pathways can be the best choice of HCNG pathways. It is evident that if in future, these renewable hydrogen pathways get cheaper, technically advanced and energy efficient, 20%HCNG vehicles can get a booming market in a near-term future especially for heavy duty applications such as passenger buses. One of the greatest challenges associated with HCNG vehicular technology is lack of sufficient infrastructure e.g. refuelling stations, high costs of hydrogen generation, and choice of highly carbon-intensive fossil based hydrogen pathways

because of comparatively better maturity and energy efficiency. Additionally, in future, shale gas can be one of the best replacements of conventional compressed natural gas even compared with 20%HCNG pathways

6. REFERENCES

Bartels, J. R., Pate, M. B., & Olson, N. K. (2010). An economic survey of hydrogen production from conventional and alternative energy sources. *International Journal of Hydrogen Energy, 35*(16), 8371-8384.

Cetinkaya, E., Dincer, I., & Naterer, G. (2012). Life cycle assessment of various hydrogen production methods. *International Journal of Hydrogen Energy, 37*(3), 2071-2080.

Concawe, E. (2006). Well-to-wheels analysis of future automotive fuels and powertrains in the European context. *Well-to-TANK Report*.

DeCicco, J., & Ross, M. (1996). Recent advances in automotive technology and the cost-effectiveness of fuel economy improvement. *Transportation Research Part D: Transport and Environment, 1*(2), 79-96.

Djomo, S. N., & Blumberga, D. (2011). Comparative life cycle assessment of three biohydrogen pathways. *Bioresource technology, 102*(3), 2684-2694.

Ewan, B., & Allen, R. (2005). A figure of merit assessment of the routes to hydrogen. *International Journal of Hydrogen Energy, 30*(8), 809-819.

Genovese, A., Contrisciani, N., Ortenzi, F., & Cazzola, V. (2011). On road experimental tests of hydrogen/natural gas blends on transit buses. *International Journal of Hydrogen Energy, 36*(2), 1775-1783.

Huang, Z., & Zhang, X. (2006). Well-to-wheels analysis of hydrogen based fuel-cell vehicle pathways in Shanghai. *Energy, 31*(4), 471-489.

JRC, R. E., HASS, H., LARIVÉ, J.-F., & JRC, L. L. (2014). WELL-TO-WHEELS Report Version 4. a JEC WELL-TO-WHEELS ANALYSIS.

Kilgus, D. (2005). Life Cycle Assessment of a Demonstration Project.

Lyu, C., Ou, X., & Zhang, X. (2015). China automotive energy consumption and greenhouse gas emissions outlook to 2050. *Mitigation and Adaptation Strategies for Global Change, 20*(5), 627-650.

Ma, F., Naeve, N., Wang, M., Jiang, L., Chen, R., & Zhao, S. (2010). Hydrogen-enriched compressed natural gas as a fuel for engines *Natural Gas*: InTech.

Ma, F., Wang, Y., Ding, S., & Jiang, L. (2009). Twenty percent hydrogen-enriched natural gas transient performance research. *International Journal of Hydrogen Energy, 34*(15), 6523-6531.

Márquez, A. C., Márquez, C. P., Fernández, J. G., Campos, M. L., & Díaz, V. G. (2012). Asset Management: Dordrecht: Springer Netherlands.

Mehra, R. K., Duan, H., Juknelevičius, R., Ma, F., & Li, J. (2017). Progress in hydrogen enriched compressed natural gas (HCNG) internal combustion engines-A comprehensive review. *Renewable and Sustainable Energy Reviews, 80*, 1458-1498.

Nelsson, C., Hulteberg, C., Saint-Just, J., & Kaiadi, M. (2010). *HCNG–A Dead End or a Bridge to the Future?* Paper presented at the 18th World Hydrogen Energy Conference. Essen.

Ou, X., Zhang, X., & Chang, S. (2010). Alternative fuel buses currently in use in China: life-cycle fossil energy use, GHG emissions and policy recommendations. *Energy Policy, 38*(1), 406-418.

Ou, X., Zhang, X., Zhang, X., & Zhang, Q. (2013). Life cycle GHG of NG-based fuel and electric vehicle in China. *Energies, 6*(5), 2644-2662.

Spath, P. L., & Mann, M. K. (2000). *Life cycle assessment of hydrogen production via natural gas steam reforming*.

Turner, J. A. (2004). Sustainable hydrogen production. *Science, 305*(5686), 972-974.

Unich, A., Morrone, B., Mariani, A., & Prati, M. (2009). *The impact of natural gas-hydrogen blends on internal combustion engines performance and emissions* (0148-7191).

Wulf, C., & Kaltschmitt, M. (2013). Life cycle assessment of biohydrogen production as a transportation fuel in Germany. *Bioresource technology, 150*, 466-475.

300: Sustainable applications of parks landscaping as an approach to the development of built environment

Abdullah HAREDY[1]

[1] Department of Architectural Engineering, Schools of Engineering, Albaha University, Albaha, Saudi Arabia, aaharedy@bu.edu.sa

Implementing sustainable principals and applications when landscaping parks are vital to the development of built environment. This paper presents guidelines to be considered for the current and future sustainable parks in moderate climate regions in order to put ecotourism, cost effective operation and maintenance, clean environment, promotion of renewable energy, and resource preservation into the effect. In so doing, several parks, located in a moderate climate zones, have been studied from the aspects of location, topography, operation, and landscaping characteristics. Prince Meshari Park located at Al Baha City, Saudi Arabia was considered as a case study to apply all guidelines proposed in this investigation.

Keywords: Sustainable Parks, Cost-effective parks, Environmental balance, landscaping, resource preservation, Ecotourism

1. INTRODUCTION

The importance of built environment and its resource has been recently an issue especially in countries that their climate is moderate I some regions, and are welling to locate parks with limited conditions and resources. As such, and for example, The Kingdom of Saudi Arabia has been locating national parks to motivate tourism with respect to sustainable operation and maintenance, renewable energy applications, and resources preservation under the supervision of City councils. Al Baha city was the most important spot for these developments since it acquires a wide class of green spaces. Therefore, serious consideration has been dedicated to the development of these forests and to come up with guidelines and regulations to be implemented for landscaping and sustainable long-term operation.

This study focuses on reviewing the planning and design considerations of national parks that can be applied in the landscaping stage and the coordination of those areas in order to achieve the desired and optimum solutions that satisfy sustainable development. The paper will conclude a vision and standards for parks landscaping towards sustainable built environment development utilising the case study of Prince Meshari Park, Al Baha City, Saudi Arabia.

The coordination of sustainable parks depends on their design to attract tourists. Thus, the design must bring the parks to the bioclimatic level where cost effective maintenance, visual pleasing atmosphere, can be achieved. Having said that, several aspect should be considered: conservation of limited resources; operational cost; waste reduction; prevention of air, water and soil pollution; organic fertilizing; the life cycle of the grass, organic pest control measures, the selection of suitable plants and trees that can adopt climate and location; the efficiency of irrigation through the use of renewable energy technologies.

2. SUSTAINBLE PARKS COORDINATION AND ECOTOURISM MOTIVATION

Ecotourism is tourism of enjoyment committed to the natural environment and its components, which are carried out without violation of ecosystem nor provoking negative impacts on the components of biodiversity. The environmental tourist focuses on the enjoyment of observing ecosystems and their animals and plants living components in their habitat. He can also be pleased of the historical, cultural and heritage features that characterize the site. Similar to the other kinds of tourism, the ecotourism is tending to be more cultural and less harmful to the environment since, it is identified as green, responsible and sustainable.

Ecotourism is linked significantly to landscaping of parks in the process of ecological balance, and derives its vitality from the coordination of park sites. Thus, it has a mutual interests that maintain the environment from pollution, however, it is improved for the environment, in general, and can preserves normal and wild life. (Arab Organization for Education, 1984). It should be emphasized that the awareness of the important role of parks, both for tourism and for being a strategic reserve for natural resources and genetics banks, requires governmental initiatives to support them with the necessary scientific researches and equipment to achieve their resources preservations. Ecotourism can contribute for economic built environment if they are carefully organized (Al-Sawaf, 1992).

There are many attractive points in the parks, including the show of customs and traditions of local communities, the production of publications, souvenirs, television and radio programs about forests and their types of trees. The integration of ecotourism into the Sustainable Parks Management Plan will contribute to generate sustainable national income, rise the awareness of the importance of preserving biodiversity and natural resources.

3. PARK DESIGN LAYOUTS

There are several layouts for the design of parks, such as the geometric shapes, which are characterized by geometric lines in various forms (linear, oval lines, or any geometric shape proportional to the parameters of the location topography) where symmetry can be achieved. There is also a layout of binary and multiplication symmetry where the design of side flower basins on the main axis of the park is located. Furthermore, a layout is the circular and radiation symmetry can be identified, where the parts of the garden are repeated so that they are all outside the circular loop. Moreover, there is a natural layout that takes into account the simulation of nature and the non-use of geometric shapes while using elements of local materials. There is also a dual layout that combines natural and geometric forms simultaneously, as well as free layout, which frees geometric lines from their forms (1), (Motloch, 2001).

Figure 1: park landscaping systems

4. SUSTAINABLE PLANNING PRINCIPLES OF PARKS

Parks planning is generally attributed to the climatic, inhabitants, and economic, of a city where each individual can be accounted for a specific percentage of its green area (Abdel Hamid Abdel Wahid 1988). However, when planning a park, a set of principals should be observed as follows:

1. The areas allocated for parks must be commensurate with the density of the population that will serve, so that a park should be provided for 2500-5000 people and the required area of the park should be between 2-10 m^2 per inhabitant (Al Moussawi, 2010).
2. The location of a park should be appropriate for use and preferably outside the expansion of the city's future buildings to remain away from the city's congestion and in a safe place away from highways.
3. Considering the topography of a park location by planning the park according to the contour lines.
4. Identifying the streets surrounding a park as well as the streets leading to its entries, taking into account the allocation of parking spaces.
5. Isolating the public park from the surrounding streets with high fences or thick fences of trees and windbreaks, if they are established inside or near the city. However, it cannot be isolated in case of parks are located between natural landscape areas (Bartholomew, 1975).
6. Providing all recreation elements such as Topiaries, bog gardens, paths and drives, lakes with boats, conservatories and lawns in order to achieve the recreational content of the inhabitants, which includes the diversity of perspectives, through the cultivation of different types of trees (Northam, 1984).

Figure 2: parks landscaping principals

5. SUSTAINABLE DESIGN PRINCIPLES OF PARKS

Sustainable park design depends on several factors that should be considered in the design stage such as unity, proportionality, repetition, colours and their degree of compatibility, lighting and shade where the different plants are distributed and selected in terms of density, Figure 2, in an artistic rhythm. Furthermore, parks sustainable design should into account climatic and geological conditions such as solar radiations, soil type, wind direction, topography, selection of suitable plants (Hansen, 2010).

5.1. Selection of plants

Plants are the main component when coordinating a sustainable park unless it includes imported plants. Plants should be carefully chosen according to their growth and properties. The selected plants should perform the required role that is appropriate to its environment, be placed suitably to achieve the purpose of use, whether be placed individually within green areas or as groups for edging the park or for sensory pathways (al-Ghitani, 1982).

5.2. Elements of sustainable park design and landscaping

- **Plant elements**: Several aspects should be considered when selecting a plant for parks: stages of growth; location suitability; eventual mass size; purpose of planting (aesthetic appearance, blocking unfavourable views, dividing spaces, providing shades, or minimising air pollution and wind speed). For each factor, there is a specific type of plant such as climbers, grasses and green spaces, which are green or long-standing grass that cover extended spaces.
- **Structural elements:** The structural elements of parks can be divided into the following: **the required**: parking lots, information centers and ticket office, restrooms, cafeterias and restaurants, souvenir stores. **The possible**: Children's playground, boating, internal transport, place for concerts, exhibitions or fairs. **The disputable**: new monuments, new buildings (pavillions, gazeebos, tea houses, etc.), modern art objects and installations, sports court.

6. WATER SUPPLY AND TREATMENT IN PARKS

The conservation of water is the cornerstone of sustainable park design and landscaping which includes rainwater harvesting and use in irrigation, flushing, pure groundwater, such as wells and eyes. However, if there is an abundance of rainwater, the rain catchment is the right choice for the water supply, provided that a necessary treatment is used before feeding if it is used for drinking and irrigation. It is also possible to utilise the rainwater through the traditional methods, which includes building the stairs and terraces on the slopes of agricultural mountains as in Figure 3 (Lyle, 1993).

Figure 3: Terraces or agricultural debris on the slopes of the mountains are irrigated with rainwater

In addition, water treatment types depend on their source and quality. Groundwater used in drinking is treated with simple processes using sodium hypochlorite and chlorine dioxide. Surface water can also be low turbidity water. `In this case, it is necessary to filter with sand filters and then disinfect them with bleaching. Water treatment with multi-stage filters, which use filtering elements with narrow pores such as ceramics and paper. If the surface water is high turbidity, the treatment must be complete, including the addition of industrial chemical formations such as alum and urine. The drainage and distribution of water such as the system used in Raghadan Park, AL Baha city, Saudi Arabia in buried or descending systems had less impact on the site but are subject to vandalism. Furthermore, local water systems and traditional irrigation systems should be utilized which is based on the construction of agricultural terraces in valleys and slopes of mountains (Al-Ghamdi, 1995).

7. PARKS WASTE MANAGEMENT

This strategy requires the prevention of waste in the parks to rise the awareness of visitors and users and train workers of how to prevent the generation of waste. These systems include either biological analysis of the process of mixing or digestion of anaerobic organic waste biodegradable and reuse of the product in the fertilization of plant

soil or for the use of methane, which is used as an energy source, and should be used techniques that reuse the waste, such as the use of dry toilets and working without water (Beck and Franklin, 2009).

8. ENERGY USE CONTROL

Renewable energy applications can paly a main role in sustainable parks and can have less impact on the built environment than the traditional alternatives. However, before considering energy applications, attention must be paid to the park planning strategies that contribute to reducing energy consumption such as minimising vehicle movements within the parks, precise allocation of buildings and services to the extend that meet victors demands, involving strategies of thermal energy and night lighting. Solar energy systems can also be used for water pumping irrigation (Lindberg and Hawkins, 1998).

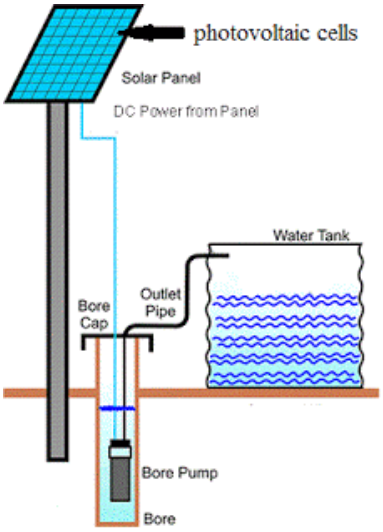

Figure 4: The given diagram depicts the function of a solar power water pump

9. PARKS CASE STUIDIES

KLCC Park Kuala Lumpur, Malaysia: The park in Kuala Lumpur, Malaysia, was designed to illustrate the continuity of the green tropical heritage through the integration of natural human creativity. The park was coordinated through a beautiful and harmonious vision in the bustling and active city centre, Figure 5, in an area of 20 hectares, which is designed by the late Brazilian landscape architect Roberto Burle Marx. The architect used assemblages of trees, shrubs, cement structures, natural stones, traditional Malaysian wood and water multi-static that blending elements of shapes and textures surfaces with the topography of the ground to produce a state-of-the-art design that is attractive (Design Magazine, 2005).

Figure 5: The master plan of KLCC Park Kuala Lumpur

The lake was aesthetically designed to be the focus of the park and to include a musical fountain. There is also a playground for children with an area of 2 hectares. In general, the park design has presented three basic elements: geometrical formations of the water bodies and channels where a bridge connects the sides of the lake. Moreover, the park includes an aesthetic dolphin statue made from the chrome-clad steel. The park was planted with different tree of variety of colours and natural consistency in most of the pillars, sides, edges and terraces Figure 6.

Figure 6: Planted levels of the park

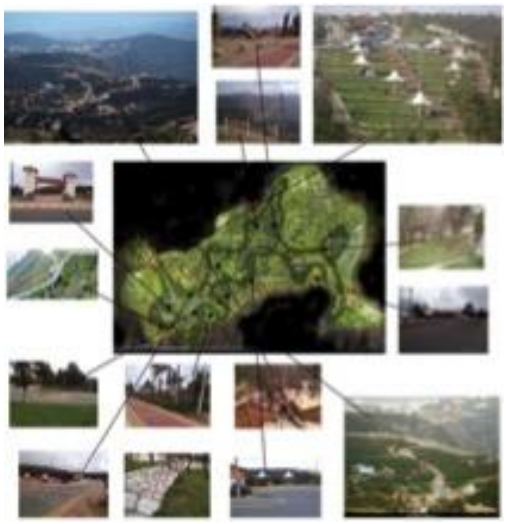

Figure 7: A top view of Raghdan Park

Raghdan Park, AL Baha, Saudi Arabia: Raghdan National Park is located 4 km north-west of Al-Baha city in the south-western part of the Kingdom of Saudi Arabia. It is located on the main road between Al-Baha and Taif, another city to the norht. The park is one of the most beautiful forests in Al-Baha. It is located at an altitude of 1,700 meters above sea level. It overlooks the King Fahd obstacle road, which connects the AL Baha with AL Makhwah, a near city. Its climate is moderated during the summer and rainy in the winter. It is characterized by a wide variety of vegetation and abundant agricultural such as Acacia, Pine and and Juniper (Council of Ministers, 1426). The park has been developed in successive periods and provided with children's play areas, family zones, lightings, internal vehicle movements, sports fields, walkways of 800 meters and utility services. Stone fountains interspersed with flower basins that are fed from established 40 reservoirs of water.

10. PRINCE MESHARI PARK

Current situation: Prince Meshari Park is located in the southwest part of the Kingdom of Saudi Arabia. Prince Mashari Park “Al-Zaraieb Forest” is located between Al-Baha and AL Mandaq, a near city. The climate of the forest is moderate during the summer and rainy in the winter. The forest is characterized by a wide variety of vegetation and abundant agricultural such as Acacia, Pine and Juniper. The park has been developed in successive periods and provided with children's play areas, family zones, lightings, internal vehicle movements, and sports fields. Figure 12 and 13.

Figure 8: The current situation of Prince Mesahri Park

Figure 9: A top view of Prince Mesahri Park

However, the park requires a preparation of an environmental management plan. The plan needs to assess the current situation in detail, and come up with recommendations that will guide the future development of the forest. Thus, the plan needs the following steps to be fulfilled:

- Vegetation survey of the forest. It has been observed that plant safety has been significantly affected by the lack of rainfall in recent years, affecting their growth and intensity in the forest. The project will need to determine whether this is due to water scarcity, development and/or increased use of the forest.
- Identifying the wildlife in the forest, and analysis of historical records - if any - to determine the causes of shrinking or extinction.
- Evaluating the existing facilities (roads, utilities, gazebos, street lighting, etc.).
- Evaluating the location and uses of the seasonal summer shopping festival, which was created by the municipality of the area, and other related matters such as seasonal pollution.

In so doing, several sites were chosen from the park and have been evaluated according to a set of systems and the integrated planning and design principles, which constitute a strategy for the development and sustainable coordination of parks.

Proposed Sustainable Design for the Park: The proposed design should be able to allocate spots for different types activities such as festivals, sports and aquatic playgrounds. It should also include walkways for horses, bicycles, playgrounds for children as well as seating zones. Thus, it was proposed to divide the park into a variety of different environments, namely natural environments, the central garden environment, slope environments, and modern environments that have been exploited for recreational structures. The landscaping considerations of these environments can be summarized as follows:

- Creating irregular shapes of open spaces with various functions and privacy to facilitate their management within the park and to allow partial operation of the park to minimise operational cost.
- The centre part of the park has to be considered as a central pedestrian movement so that it allows easy access to all parts of the park where an open festival space is located surrounded by food trucks and pavilion structures.
- The east part of the park will include outdoor waterfalls where water can run to water ponds that are surrounded by seating zones which represent the local and historical design of the city while maintaining the existing elements such as rock formations and plant.
- On the north side, a garden has been located consisting of a ring pedestrian walkway that is surrounded by an outdoor stage for local arts and traditional tools exhibition.
- The park levels have been used utilised for seating zones while maintaining the existing plants.
- To connect the different zones of the park, a number of main axes have been designed, such as the focal points of the parks and green spaces, the main entrance connecting the park's traditional heritage gate with the park centre, as well as the axis connecting the monument in the middle of the park and the eastern part.
- The north-western part was specified for a zoo area, which coordinated according to the location topography where each animal can enjoy suitable movements.

A network of secondary movement paths has been located between the park different levels.

A number of architectural features have been created to satisfy visitor’s needs such as landmarks and public facilities (car park, kiosk, barbeque facilities, disabled amenities, and toilets. Most important of all, a green hotel was proposed to be located within the park and designed according to the concepts of green codes and equipped with sustainable energy technologies. It was proposed as a governmental initiative to raise the awareness for sustainable development.

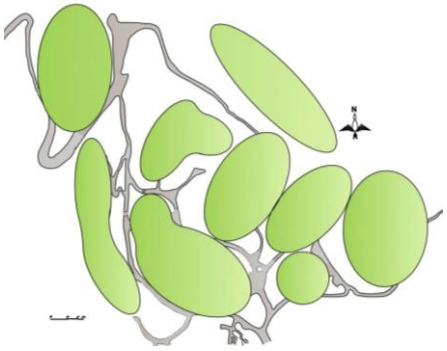

Figure 10: Park landscaping concept dividing it Into different green spaces on different levels

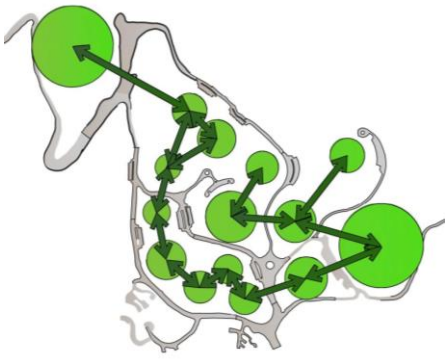

Figure 11: Movement pattern of the park

Figure 12: Utilising the park levels for seating

Figure 13: The master plan of the proposed park

Figure 14: Eastern perspective view of the proposed park

Figure 15: Western perspective view of the proposed park

11. CONCLUSION

The concept of sustainable parks that the Kingdom of Saudi Arabia dedicated great efforts for developing their design, planning and landscaping must be adhered to a variety of practices that responsive to environmental issues with respect to operation management and renewable energy applications. Prince Meshari design proposal is a promising model of what can be a sustainable park. Therefore, a set of principles must be taking into account when sustainable park is considered:

- Taking into account the location conditions (climate, topography, water availability and soil quality).
- Satisfying the sustainable park design principals such as unity, interdependence and repetition in forms of geometrical, natural or both which achieves a functional fit in the distribution of elements and activities within a park.
- Careful attention must be paid to the selection of plants that are suitable for the local environment where plants can be adapted to resist any local harmful insects. Thus, a great saving of money can be achieved for soil fertilization and modification, pest control and irrigation.
- Proposing structural elements such as pavilions, benches and walkways to suit environmental factors
- Taking measures of pest control.
- Using of sustainable harvested wood, composite wood products for landscaping and other agricultural projects as well as the use of flexible wood.
- Products recycling such as glass and rubber from tires and other materials for making products used in paving stones and park furniture.
- Soil control practices including fertilization, maintenance and enhancement of sound soils that support diversity in the terrestrial environment.

Furthermore, as per ISO standards for SME's, industrial, commercial, residential facilities. Energy auditing is a very significant factor that can play a main role for achieving energy efficiency, and reduction of power consumption, which is included in the 2030 Kingdome national vision. With the new primary energy tariffs are imposed, sustainable parks should optimise their energy usage without affecting their operation and processes, therefore maintaining their overheads and profits while increasing their energy efficiency and competitiveness. From this prospective, the demand for energy auditing would become an actual need and popular trend. Thus, technologies such as solar powered trash bin/compactors, rain water harvesting for parks and open spaces, and solar PV systems for energy generation must be applied.

12. REFERENCES

Bartholomew, H, 1975. The Land Use Survey. In, Mayr, H.M and Kohn, CF., Readings in Urban Geography, eds. Chicago Univ., press, Chicago. P.42

Northam, R.M, 1984. Urban Geography, John Wiley and Sons, New York. 1979. P333-Piereall, G. Residential Landscapes, Reston Publishing Co. Inc Reston, Virginia, p23.

Christopher J L, 2006. A Study of Landscape Architecture Design Methods, Master of Landscape Architecture, Alexandria, Virginia, USA.

Motloch J L, 2001. Introduction to Landscape Design 2nd edition, John Wiley &Sons, Inc, Canada.

Hansen G, 2010. Basic Principles of Landscape Design, Florida, cooperative extinction service, University of Florida.

Beck T and Franklin C, 2009. Principles of Ecological Landscape Design, Island Press, Suite 300, 1718 Connecticut Ave., NW, Washington, Dc.

Ceballos-Lascurain H, 1996. Tourism, Eco-tourism, and Protected Areas. Gland, Switzerland: IUCN Publications.

Givoni, B. 1976. Climate & Arohite Ctvke, Building research stoaticeen Iechnion, Israel Institute at technology, second Edirion, London.

Lyle, J.T, 1993. Regenerative Design for Sustainable Development. New York: John Wiley and Sons.

Lindberg, K. Hawkins., D.E, 1998. Eco tourism: Aguidi for planers and Managers. Volume 1, 2 North Berningron, Vermont.

Arab Organization for Education, 1984. Culture and Science, National Parks and Reserves in the Arab World, Tunisia.

Al-Ghitani, M Y, 1982. Flowers and Ornamental Plants and Landscaping, Egyptian Universities House, Alexandria,

Al-Musawi, M A, 2010. Geographical Standards for Green Areas, Gardens and Design Systems in Arab Cities, Saudi Geographical Society,

Al-Sawaf, M D, 1992. Parks and Parks An Environmental and Urban Needs, Mosul University.

The National Forest Strategy and Action Plan for the Kingdom of Saudi Arabia, Council of Ministers, period from 1426 to 1446H under Resolution No. 306 dated 23/12/1426 H.

Wahid A, Hamid A, 1988. Planning and design of green areas, Dar Ghraib for printing - Cairo.

Supreme Commission for Tourism, Saudi Arabia, Final Report, 18. Tourism Development Strategy in Al - Baha Region, Sustainable Tourism Development Plan, 1/2004.

Al-Ghamdi, M H, 1995. Rainwater Management and Investment Strategy for Enhancing Arab Water Security.

Al-Musawi, M A, 2010. Geographical Standards for Green Areas, Gardens and Design Systems in Arab Cities, Saudi Geographical Society.

Design Magazine, 2005. Cairo, Egypt. No. 13.